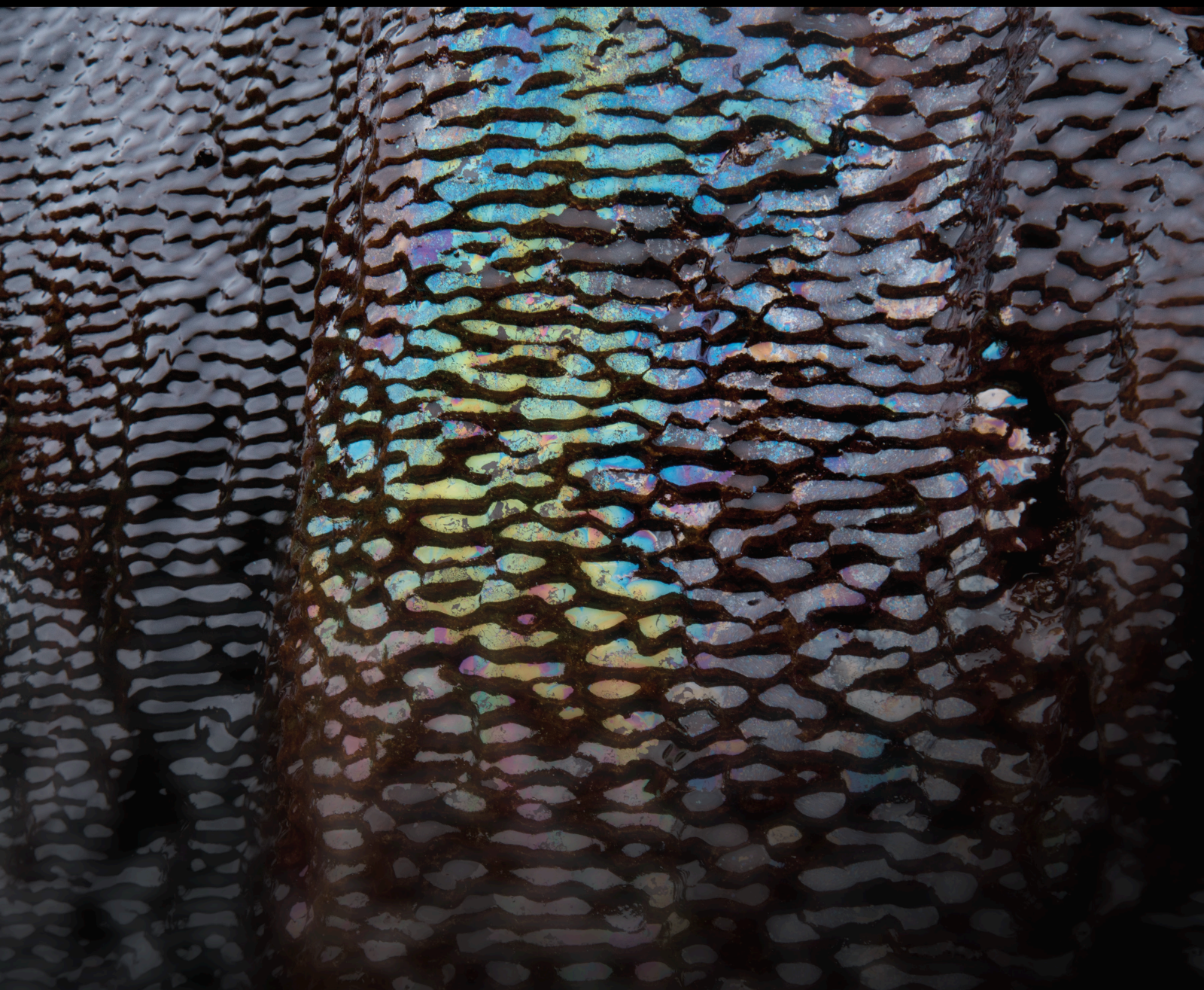


New Applications in Gas Geochemistry

Special Issue Editor in Chief: Francesco Italiano

Guest Editors: Andrzej Solecki, Giovanni Martinelli, Yunpeng Wang, and Guodong Zheng



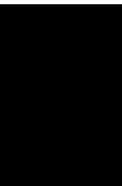


New Applications in Gas Geochemistry

New Applications in Gas Geochemistry

Special Issue Editor in Chief: Francesco Italiano

Guest Editors: Andrzej Solecki, Giovanni
Martinelli, Yunpeng Wang, and Guodong Zheng








Editorial Board

Carmine Apollaro, Italy
Baojun Bai, USA
Maurizio Barbieri, Italy
Julien Bourdet, Australia
Andrea Brogi, Italy
David A. Butterfield, USA
Mauro Cacace, Germany
Isabelle Chambeftort, New Zealand
Shengnan Nancy Chen, Canada
Paola Cianfarra, Italy
Daniele Cinti, Italy
Timothy S. Collett, USA
Nicoló Colombani, Italy
Mercè Corbella, Spain
Henrik Drake, Sweden
Lionel Esteban, Australia
Cinzia Federico, Italy
Paulo Fonseca, Portugal
Francesco Frondini, Italy
Paolo Fulignati, Italy
Paola Gattinoni, Italy
Mauro Giudici, Italy
Fausto Grassa, Italy
Salvatore Inguaggiato, Italy
Francesco Italiano, Italy
Jaewon Jang, Republic of Korea
Luchao Jin, USA
Shinsuke Kawagucci, Japan
Karsten Kroeger, New Zealand
Cornelius Langenbruch, USA
Huazhou Li, Canada
Liangping Li, USA
Marcello Liotta, Italy
Stefano Lo Russo, Italy
Constantinos Loupasakis, Greece
Lin Ma, USA
Judit Mádl-Szonyi, Hungary
Paolo Madonia, Italy
Fabien Magri, Germany
Andrew H. Manning, USA
Micòl Mastrocicco, Italy
Agnes Mazot, New Zealand

Yuan Mei, Australia
Jean-Luc Michelot, France
Ferenc Molnar, Finland
Julie K. Pearce, Australia
Daniele Pedretti, Italy
Marco Petitta, Italy
Christophe Renac, France
Reza Rezaee, Australia
Mohammad Sarmaadivaleh, Australia
Christian Siebert, Germany
Ricardo L. Silva, Canada
Ondra Sracek, Czech Republic
Andri Stefansson, Iceland
Pietro Teatini, Italy
Svetlana G. Tessalina, Australia
Rene Therrien, Canada
Umberta Tinivella, Italy
Tivadar M. Tóth, Hungary
Jinze Xu, Canada
Ye Zhang, USA
Keni Zhang, China
Ling-Li Zhou, Ireland



Contents

New Applications in Gas Geochemistry

Francesco Italiano , Andrzej Solecki , Giovanni Martinelli , Yunpeng Wang , and Guodong Zheng 



Editorial (3 pages), Article ID 4976190, Volume 2020 (2020)

Determination of $\delta^{13}\text{C}$ of Trace Hydrocarbons in Natural Gas Using Syringe Solid Phase Extraction (SSPE) Coupled with Gas Chromatography/Isotope Ratio Mass Spectrometry (GC/IRMS)

Cancan Yan , Zhongping Li , Shutong Li, Zuodong Wang, Lantian Xing, Yan Liu, Weiwei Mou, and Kaiwen Wang

Research Article (10 pages), Article ID 6352378, Volume 2019 (2019)

Nonvolcanic Carbon Dioxide Emission at Continental Rifts: The Bublak Mofette Area, Western Eger Rift, Czech Republic

Horst Kämpf , Alena Sophie Broge , Pouria Marzban , Masoud Allahbakhshi , and Tobias Nickschick 


Research Article (19 pages), Article ID 4852706, Volume 2019 (2019)

Chemical and Noble Gas Isotope Compositions of Formation Gases from a 3 km Deep Scientific Borehole in the Koyna Seismogenic Zone, Western India

Nagaraju Podugu , Satrughna Mishra , Thomas Wiersberg, and Sukanta Roy 




Research Article (16 pages), Article ID 1078942, Volume 2019 (2019)

Gamma Ray and Radon Anomalies in Northern Taiwan as a Possible Preearthquake Indicator around the Plate Boundary

Ching-Chou Fu , Lou-Chuang Lee, Tsanyao Frank Yang, Cheng-Horng Lin, Cheng-Hong Chen, Vivek Walia, Tsung-Kwei Liu, Dimitar Ouzounov, Gioacchino Giuliani, Tzu-Hua Lai, and Peng-Kang Wang


Research Article (14 pages), Article ID 4734513, Volume 2019 (2019)

Isotopic Composition of Abiogenic Gas Produced in Closed-System Fischer-Tropsch Synthesis: Implications for the Origins of the Deep Songliao Basin Gases in China

Zhifu Wei , Yongli Wang , Gen Wang , Xueyun Ma, Wei He, Ting Zhang, Xiaoli Yu, and Yan-Rong Zou



Research Article (13 pages), Article ID 2823803, Volume 2019 (2019)

The Petrogenesis of the Permian Podong Ultramafic Intrusion in the Tarim Craton, Western China: Constraints from C-He-Ne-Ar Isotopes

Mingjie Zhang , Pengyu Feng, Tong Li, Liwu Li, Juerong Fu, Peng Wang, Yuekun Wang, Zhongping Li, and Xiaodong Wang






Research Article (14 pages), Article ID 6402571, Volume 2019 (2019)

Volcanogenic CO₂ Degassing in the Songliao Continental Rift System, NE China


Wenbin Zhao, Zhengfu Guo , Ming Lei, Maoliang Zhang, Lin Ma, Danielle Fortin, and Guodong Zheng 

Research Article (14 pages), Article ID 8053579, Volume 2019 (2019)




Degassing and Cycling of Mercury at Nisyros Volcano (Greece)

A. L. Gagliano , S. Calabrese , K. Daskalopoulou , J. Cabassi, F. Capecchiacci, F. Tassi, S. Bellomo, L. Brusca, M. Bonsignore, S. Milazzo, G. Giudice, L. Li Vigni , F. Parello, and W. D'Alessandro 
Research Article (18 pages), Article ID 4783514, Volume 2019 (2019)



Mofette Vegetation as an Indicator for Geogenic CO₂ Emission: A Case Study on the Banks of the Laacher See Volcano, Vulkaneifel, Germany

Hardy Pfanz , Frank Saßmannshausen, Christiane Wittmann, Benny Pfanz, and Annika Thomalla
Research Article (12 pages), Article ID 9589306, Volume 2019 (2019)

Methane Source and Turnover in the Shallow Sediments to the West of Haima Cold Seeps on the Northwestern Slope of the South China Sea

Junxi Feng , Shengxiong Yang , Hongbin Wang, Jinqiang Liang, Yunxin Fang, and Min Luo 
Research Article (18 pages), Article ID 1010824, Volume 2019 (2019)


Magmatic Signature in Submarine Hydrothermal Fluids Vented Offshore Ventotene and Zannone Islands (Pontine Archipelago, Central Italy)

Francesco Italiano, Davide Romano , Cinzia Caruso, Manfredi Longo , Andrea Corbo, and Gianluca Lazzaro
Research Article (15 pages), Article ID 8759609, Volume 2019 (2019)

The Distribution of Dissolved Methane and Its Air-Sea Flux in the Plume of a Seep Field, Lingtou Promontory, South China Sea

Pengfei Di , Dong Feng , and Duofu Chen 
Research Article (12 pages), Article ID 3240697, Volume 2019 (2019)








Carbon and Hydrogen Isotopic Reversals in Highly Mature Coal-Derived Gases: A Case Study of Paleozoic Gases in the Southern Ordos Basin, China

Dan Liu 
Research Article (23 pages), Article ID 8608596, Volume 2019 (2019)

Evidence of Tectonic Control on the Geochemical Features of the Volatiles Vented along the Nebrodi-Peloritani Mts (Southern Apennine Chain, Italy)


Francesco Italiano, Pietro Bonfanti , and Salvatore Roberto Maugeri 
Research Article (17 pages), Article ID 6250393, Volume 2019 (2019)

Degassing at the Volcanic/Geothermal System of Kos (Greece): Geochemical Characterization of the Released Gases and CO₂ Output Estimation

Kyriaki Daskalopoulou , Antonina Lisa Gagliano , Sergio Calabrese , Lorenza Li Vigni , Manfredi Longo , Konstantinos Kyriakopoulos, Giovannella Pecoraino , and Walter D'Alessandro 
Research Article (16 pages), Article ID 3041037, Volume 2019 (2019)


Contents

Heat and Helium-3 Fluxes from Teide Volcano, Canary Islands, Spain

Mar Alonso , Eleazar Padrón, Hirochika Sumino, Pedro A. Hernández, Gladys V. Melián, María Asensio-Ramos, Fátima Rodríguez, Germán Padilla, Marta García-Merino, Cecilia Amonte, and Nemesio M. Pérez


Research Article (12 pages), Article ID 3983864, Volume 2019 (2019)

Fluid Phase Simulation and Evolution of a Condensate Gas Reservoir in the Tazhong Uplift, Tarim Basin

Rui Deng, Chengsheng Chen, Shuyong Shi, and Yunpeng Wang 



Research Article (15 pages), Article ID 8627698, Volume 2019 (2019)

Towards a Better Knowledge of Natural Methane Releases in the French Alps: A Field Approach

Frédéric Gal , Eric Proust, and Wolfram Kloppmann


Research Article (16 pages), Article ID 6487162, Volume 2019 (2019)

Comparison on Rare Gas Geochemical Characteristics and Gas Originations of Kuche and Southwestern Depressions in Tarim Basin, China

Xiaobo Wang , Caineng Zou, Jian Li, Guoqi Wei, Jianfa Chen, Zengye Xie, Zhisheng Li, Jianying Guo, Shiguo Lin, Songqi Pan, Aisheng Hao , Chunlong Yang, and Xuening Qi

Research Article (15 pages), Article ID 1985216, Volume 2019 (2019)

Occurrence and Origin of H₂S from Volcanic Reservoirs in Niudong Area of the Santanghu Basin, NW China

Xiangxian Ma, Guodong Zheng , Minliang Liang, Dianhe Xie, Giovanni Martinelli , Wasim Sajjad, Wang Xu, Qiaohui Fan, Liwu Li, Li Du, and Yidong Zhao




Research Article (10 pages), Article ID 1279658, Volume 2019 (2019)

²²⁰Rn (Thoron) Geohazard in Room Air of Earthen Dwellings in Vietnam

D#ng Nguy#n-Thuy , H#ng Nguy#n-V#n , Jan P. Schimmelmänn, Nguy#t Th# Anh Nguy#n , Kelsey Doiron , and Arndt Schimmelmänn

Research Article (11 pages), Article ID 7202616, Volume 2019 (2019)

An Areal Assessment of Subseafloor Carbon Cycling in Cold Seeps and Hydrate-Bearing Areas in the Northern South China Sea

Yanping Zhang , Min Luo , Yu Hu, Hongbin Wang, and Duofu Chen 

Research Article (14 pages), Article ID 2573937, Volume 2019 (2019)

Editorial

New Applications in Gas Geochemistry

Francesco Italiano ¹, **Andrzej Solecki** ², **Giovanni Martinelli** ³, **Yunpeng Wang** ⁴,
and Guodong Zheng ⁵

¹INGV, Palermo, Italy

²Institute of Geological Sciences, University of Wrocław, Wrocław, Poland

³ARPA Emilia-Romagna, Bologna, Italy

⁴Guangzhou Institute of Geochemistry, Chinese Academy of Sciences, Guangzhou 510640, China

⁵Key Laboratory of Petroleum Resources, Gansu Province, Northwest Institute of Eco-Environment and Resources, Chinese Academy of Sciences, Lanzhou 730000, China

Correspondence should be addressed to Andrzej Solecki; andrzej.solecki@uwr.edu.pl

Received 21 February 2020; Accepted 21 February 2020; Published 2 July 2020

Copyright © 2020 Francesco Italiano et al. This is an open access article distributed under the Creative Commons Attribution License, which permits unrestricted use, distribution, and reproduction in any medium, provided the original work is properly cited.

Gases present in the Earth crust are important in various branches of human activities. Hydrocarbons are a significant energy resource, helium is applied in many high-tech instruments, and studies of crustal gas dynamics provide insight in the geodynamic processes and help monitor seismic and volcanic hazards. Quantitative analysis of methane and CO₂ migration is important for climate change studies. Some of them are toxic (H₂S, CO₂, CO); radon is responsible for the major part of human radiation dose. The development of analytical techniques in gas geochemistry creates opportunities of applying this science in numerous fields. Noble gases, hydrocarbons, CO₂, N₂, H₂, CO, and Hg vapor are measured by advanced methods in various environments and matrices including fluid inclusions. Following the “Geochemical Applications of Noble Gases”(2009), “Frontiers in Gas Geochemistry” (2013), and “Progress in the Application of Gas Geochemistry to Geothermal, Tectonic and Magmatic Studies” (2017) published as special issues of Chemical Geology and “Gas geochemistry: From conventional to unconventional domains” (2018) published as a special issue of Marine and Petroleum Geology, this volume continues the tradition of publishing papers reflecting the diversity in scope and application of gas geochemistry.

1. Introduction

The aim of this special issue was to collect contributions on the most recent advances in gas geochemistry. The current development of gas geochemical studies is connected not only with introducing advanced techniques combining among other: isotopic studies, gas chromatography, and mass spectrometry applied to hydrocarbons, carbon dioxide, rare gases, H₂S, and Hg vapor, but the application of new geochemical, seismotectonic, and biogeochemical models as well. Gas geochemistry studies results not only in deeper insights in a broad range of geological processes but also in the quantification of the lithosphere, hydrosphere, and atmosphere interactions important both for hydrocarbon and geothermal resources, volcanic and seismic risk, human health, and climate change.

This volume contains a significant number of papers delivered by participants of the 14th International Conference on Gas Geochemistry (ICGG) held in Wrocław-Świeradów, Poland, 24-28 September 2017. The list of contributors has been supplemented by numerous authors who did not participate in the 14th ICGG, whose primary topic was “Gases in the Earth crust, benefits and hazards”. However, all delivered papers stay in line with the primary topic focusing not only on gases as a tool of geochemical, seismotectonic, and petrogenetic studies but also on the environmental risk management.

2. Themes

The 22 papers of this volume can be grouped into 4 general themes. Hydrocarbon gases are the dominant topic and this

volume contains 10 papers aimed at understanding their origin, relationship with geodynamic, and biochemical processes both in oil fields and natural seepages as well.

Zhifu Wei et al. (in this issue) compared the isotopic composition of gas obtained by closed-system Fischer-Tropsch synthesis with a deep Songliao Basin gas which is similar to thermogenic gas and has a trend of a transition to oceanic hydrothermal system abiogenic gas.

Cancan Yan et al. (in this issue) proposed a new technique, syringe solid phase extraction (SSPE), for the enrichment of trace hydrocarbon compounds for isotope analysis (CSIA) with a gas chromatograph (GC) interfaced to an isotope ratio mass spectrometry (IRMS).

Pengfei Di et al. (in this issue) quantified the dissolved methane and its air-sea flux from hydrocarbon seeps from the seafloor to the coastal ocean near the Lingtou Promontory, South China Sea.

Dan Liu (in this issue) studied Paleozoic gases in the southern Ordos Basin, China, with partial or complete isotopic reversals, as examples of isotopic fractionation in over mature coal-derived gases.

Rui Deng et al. (in this issue) studied the impacts of temperature and pressure histories and gas washing on the formation of the condensate gas reservoirs and evolution of the fluid phase and its features in the Tazhong Uplift area in the Tarim Basin of China.

F. Gal et al. (in this issue) investigated hydrocarbon gas seeps located in the French Subalpine Chains in zones of outcropping Jurassic black shales.

Yanping Zhang et al. (in this issue) studied the transfer of carbon from sediments to the water column in the South China Sea by chemosynthetic biotainhabited surface sediments and found that the biogeochemical rates in the northern SCS are generally lower than those in active continental margins and special environments (e.g., the Black Sea), but are comparable with those in passive continental margins.

Xiaobo Wang et al. (in this issue) studied coal-formed gases of the Kuche Depression. Accompanying rare gases in the Kuche Depression were found to be of typical crustal genesis—derived from the radioactive decay of crustal elements.

Junxi Feng et al. (in this issue) studied active cold seeps of Haima that were recently discovered on the northwestern slope of the South China Sea. The analysis of three piston cores from an area characterized by bottom simulating reflectors to the west of Haima suggests that methane seepage probably has persisted at least hundreds to thousands of years with changing methane fluxes.

Xiangxian Ma et al. (in this issue) analyzed mineral and/or chemical compositions and sulfur and carbon isotopes of natural gas, formation water, and rocks of volcanic rock reservoirs in the Niudong area of the Santanghu Oilfields to explain the occurrence and origin of hydrogen sulfide (H_2S). The $\delta^{34}\text{S}$ values of on-well H_2S samples varied in a range of 9.2‰ to 20.5‰, indicating thermochemical sulfate reduction (TSR) and/or thermal decomposition of organic sulfur-bearing compounds (TDS).

Gas geochemistry of volcanic fields was the second dominant topic and this volume contains 7 papers aimed at a broad spectrum of problems starting from understanding

petrogenetic processes via the mechanism of gaseous exhalation to its influence upon plant cover.

Mingjie Zhang et al. (in this issue) measured C, He, Ne, and Ar isotopic compositions of volatiles from magmatic minerals in the Podong ultramafic intrusion. The $\delta^{13}\text{C}$ of CO_2 and CH_4 suggested the magmatic volatile of the mantle mixed with the volatiles of thermogenic and crustal origins. Subduction and devolatilization of altered oceanic crust could be the best mechanism that transported large proportions of air-saturated fluid and crustal components into the mantle source.

A. L. Gagliano et al. (in this issue) performed an extensive survey on Hg concentrations in different matrices (fumarolic fluids, atmosphere, soils, and plants) at the Lakki Plain, Nisyros Island (Greece). The positive correlation with both CO_2 and H_2S in air highlighted the importance of hydrothermal gases as carrier for gaseous elemental mercury. On the other hand, soil Hg concentrations showed no significant correlations with CO_2 and H_2S in the soil gases, whereas it showed a positive correlation with the total S content and an inverse one with the soil pH, evidencing the complexity of the processes involving Hg carried by hydrothermal gases while passing through the soil.

F. Italiano et al. (in this issue) carried out geochemical investigations on submarine hydrothermal fluids vented offshore the Pontine Islands (Tyrrhenian Sea) and revealed the existence of gas vents to the West of Zannone Island and Southwest of Ventotene Island. The geochemical features of the CO_2 -rich gas samples show a clear mantle-derived signature and indicate that cooling Middle Pleistocene magmas are of thermal energy high enough to form an efficient hydrothermal system.

M. A. Amonte et al. (in this issue) performed the first integrated heat flow, CO_2 , and ^3He emission survey across 0.5 km^2 of the summit cone and crater of Teide volcano, Tenerife, Canary Islands, Spain. The calculation of the ^3He /heat ratio for the first time in this volcanic system supports the presence of an important mantle source for the degassing of Teide volcano.

H. Pfanzen et al. (in this issue) studied the relationship between postvolcanic soil degassing and vegetation during spring season in mofette at the banks of the Laacher See, Eifel Mountains. Plant coverage and the number of species decreased significantly in high CO_2 areas. One plant species (marsh sedge, *Carex acutiformis*) proved to be highly mofetophilic and strictly grew on CO_2 degassing sites.

H. Kämpf et al. (in this issue) measured gas flux measurements of cold, mantle-derived CO_2 release at the Bublák mofette field located inside presently seismically active Počátky Plesná fault zone (PPFZ) (Czech republic) and found that en-echelon faults inside of the PPFZ act as fluid channels to depth (CO_2 conduits).

Wenbin Zhao et al. (in this issue) studied bubbling springs and diffuse degassing from soils of the Wudalianchi monogenetic volcanic field in a major continental rift system in NE China. Chemical compositions and C-He isotope analyses revealed that the cold spring gases might originate from the enriched upper mantle, which resulted from the mixing between slab materials (subducted organic sediments and

carbonates) in the mantle transition zone and the ambient depleted mantle. Their results suggest that the CO₂ degassing activities become weaker from early to late in Quaternary.

Gas geochemistry applied to seismic zones studies was the third dominant topic and this volume contains 4 papers aimed at understanding gas exhalation in active seismic zones with their possible application as precursor signals.

Nagaraju Podugu et al. (in this issue) studied helium isotope ratios of 3 km deep research borehole KFD1 in the Koyna reservoir-triggered seismicity region, Western India. Air-corrected helium isotope ratios indicate that helium is a mixture of atmospheric and crustal radiogenic components without mantle contribution.

Ching-Chou Fu et al. (in this issue) described significant increases of soil radon concentrations followed by the increase in gamma rays a few days to a few weeks before earthquakes that occurred in northeastern Taiwan, where the subduction of the Philippine Sea Plate PSP beneath the Eurasian Plate occurs.

F. Italiano et al. (in this issue) studied the southernmost portion of the Apennine chain (Nebrodi-Peloritani Mountains, Sicily, Italy) and revealed a close connection between the tectonic setting and the regional degassing of CO₂-dominated volatiles. Their study yields better insight into the evolution of seismogenesis, considering the fault ruptures as the final stage of a seismic cycle.

K. Daskalopoulou et al. (in this issue) studied natural gas exhalations at the island of Kos. Changes in the degassing areas and significant variations in the geochemical parameters of the released gases were observed both before and after the seismic event; however, no coherent model explaining those changes was obtained.

We also have a fourth domain in environmental and healthy effect of dangerous gases, although there is only one single paper presented: Dương Nguyễn-Thùy et al. (in this issue) described thoron's (220Rn) contribution to radiation exposure and found it significant input in radiation exposure in traditional northern Vietnamese mud house with bare surfaces of dry porous soil dwellings.

3. Concluding Remarks

Since the very beginning, the ICGG has been the forum where we exchange ideas on gas geochemistry. Originally dominated by radon topics, it evolved towards the broad spectrum of gas geochemistry problems. The ICGG 14th chose Świeradów town in Lower Silesia (Poland) due to a historical record of almost 450 years of balneotherapy, with radon as a main curative factor identified in the 20th century. The ICGG 14th commenced in Wrocław—the capital of the Lower Silesia Province with choir concert in the Oratorium Marianum—baroque music hall in the main building of the University of Wrocław. This meeting attracted around 60 delegates performing 36 oral and 20 poster presentations.

During the ending field trip (28–30.09.2017), the participants visited Carpathians Mts. with stop at the Bóbrka oil mine opened in 1854 and still operating as the Ignacy Łukasiewicz Museum of Oil and Gas Industry, geothermal spas of

the Podhale region and the Salt Mine of Wieliczka operating since 13th century.

Proceedings of the meetings are traditionally published as Special Issues in peer-reviewed journals, as in the present case. ICGG continues to attract widespread participation—in the form of oral and poster presentations—from a diverse international audience. We look forward to the 15th ICGG scheduled to be held in Italy in September, 2019.

Conflicts of Interest

We confirm that the Lead Guest Editor and the other Guest Editors have no conflict of interest.

Acknowledgments

This special issue is derived directly from the 14th ICGG held in Wrocław-Świeradów, Poland in September 2017. We would like to thank Giovanni Martinelli for his inspiration to perform 14th ICGG in Poland. We thank all who contributed to the success of the meeting—keynote speakers, oral/poster presenters, and other registrants. We would like to thank the co-organizers: University of Wrocław and Wrocław University of Science and Technology for their organizational and financial support. We also would like to thank Wrocławskie Centrum Akademickie and EXALO Grupa PGNiG for their sponsorship. The editors specially thank academic editors: Andrea Brogi, Andrew H. Manning, Andri Stefansson, and Julien Bourdet for their contribution to this special issue. The papers in this volume were scrutinized by a cadre of reviewers, who cannot be mentioned one by one but they all deserve sincere thanks.

*Francesco Italiano
Andrzej Solecki
Giovanni Martinelli
Yunpeng Wang
Guodong Zheng*

Research Article

Determination of $\delta^{13}\text{C}$ of Trace Hydrocarbons in Natural Gas Using Syringe Solid Phase Extraction (SSPE) Coupled with Gas Chromatography/Isotope Ratio Mass Spectrometry (GC/IRMS)

Cancan Yan^{1,2,3} , Zhongping Li^{1,2,3} , Shutong Li^{1,2,3}, Zuodong Wang^{1,2,3}, Lantian Xing^{1,2,3}, Yan Liu^{1,2,3}, Weiwei Mou^{1,2,3}, and Kaiwen Wang⁴

¹Northwest Institute of Eco-Environment and Resources, Chinese Academy of Sciences, Lanzhou 730000, China

²Key Laboratory of Petroleum Resources, Gansu Province/Key Laboratory of Petroleum Resources Research, Institute of Geology and Geophysics, Chinese Academy of Sciences, Lanzhou 730000, China

³College of Earth Science, University of Chinese Academy of Sciences, Beijing 100049, China

⁴School of Earth Sciences and Gansu Key Laboratory of Mineral Resources in Western China, Lanzhou University, Lanzhou 730000, China

Correspondence should be addressed to Zhongping Li; lizhongping@lzb.ac.cn

Received 15 February 2019; Revised 4 June 2019; Accepted 9 September 2019; Published 21 December 2019

Academic Editor: Giovanni Martinelli

Copyright © 2019 Cancan Yan et al. This is an open access article distributed under the Creative Commons Attribution License, which permits unrestricted use, distribution, and reproduction in any medium, provided the original work is properly cited.

Sample preparation technique, for the analysis of $\delta^{13}\text{C}$ ratios in oil and gas samples, has gradually been recognized as one of the most crucial steps of the whole analytical process. In this study, a new convenient method, syringe solid phase extraction (SSPE), was proposed for measuring $\delta^{13}\text{C}$ in natural gas samples. Based on conditional experiments of temperature and time, SSPE fitted with activated carbon adsorbent was applied with a gas chromatography/isotope ratio mass spectrometry (GC/IRMS) system for trace carbon isotope analysis. The results showed that isotopic fractionation was not clearly observed during the adsorption and desorption process, and the $\delta^{13}\text{C}$ ratios measured by SSPE-GC/IRMS were in good agreement with the known $\delta^{13}\text{C}$ ratios of $\text{CH}_4\sim\text{C}_5\text{H}_{12}$ measured by GC/IRMS with the accuracy all within $\pm 0.48\%$. A natural gas sample was applied to verify the efficiency of this new method, and the obtained results confirmed that SSPE-GC/IRMS is a reliable technique characterized with simplicity, efficiency, and reliability.

1. Introduction

Compound-specific isotope analysis (CSIA) features with a gas chromatograph (GC) interfaced to an isotope ratio mass spectrometry (IRMS) are a reliable sample pretreatment tool for normal level carbon isotope analysis of hydrocarbons in environmental forensics, archaeology, ecology, and gas geochemistry [1–11]. This technique had been widely used in oil and gas geochemistry, for the obtained carbon isotopic ratios can be applied to identify gas genetic origin, characterize gas maturity, and correlate gas with their source rocks. It remains one of fundamental and promising techniques for oil-gas exploration and exploitation of normal level hydrocarbon compounds [10–16].

In general, trace hydrocarbons refer to small molecule volatile hydrocarbons such as $\text{C}_1\sim\text{C}_8$ hydrocarbons in oil and gas geochemistry [17]. Those compounds are widely distributed in natural gas, crude oils, source rocks, sediments, oilfield water, and other types of reservoir fluids. Besides, their $\delta^{13}\text{C}$ ratios contain abundant geochemical information and are considered as an effective proxy associated with oil-gas formation and evolution [18, 19]. However, it is difficult to analyze them directly by CSIA features with GC/IRMS, for those hydrocarbons are always beyond the detection limit of the instrument or very easy to escape during the preparation process [20].

To achieve the analysis of these particular hydrocarbon compounds for various applications, many previous works

have been carried out, and some novel and practical methods such as purge and trap (P&T) and solid phase microextraction (SPME) have been put forward, and these highly efficient techniques made remarkable achievements for pre-concentration of trace volatile or semivolatile organic compounds [21–25]. Though these works greatly improved the detection limit for most trace compounds, these often exhibited selectivity for some hydrocarbon compounds during the extraction process, making the whole analysis quite unfeasible. Therefore, for more intensive measurements of trace light hydrocarbons, the feasibility of these techniques remain to be discussed; the rapid isotopic analysis of trace hydrocarbons is still far from being realized. So, it is quite necessary to develop a new method for the efficient measurement of these compounds for geochemical applications.

In this study, a new technique, syringe solid phase extraction (SSPE), was proposed for the enrichment of trace hydrocarbon compounds with high capacity. In addition, with the consideration of fractionation, the integrated study of time and temperature during the adsorption and desorption process is carried out to determine the optimized experimental condition.

2. Experimental

2.1. Sample Preparation

2.1.1. Standard Sample Preparation. The SSPE preconcentration method was tested by a standard sample; composition of the gas are indicated in Table 1. It consists methane, ethane, propane, isobutane, normal butane, isopentane, and normal pentane, all of them were at trace levels after diluting with helium. The carbon isotopic ratios of different hydrocarbon compounds were also listed in Table 1, and all the $\delta^{13}\text{C}$ were determined by the GC/IRMS system. The determination was assessed by a number of duplicated injections, and the statistical results on these injections of the accuracy were calculated with standard deviations.

2.1.2. Geological Sample Preparation. A natural gas sample from Xiamaling Formation (XML), Sichuan Basin (Table 2), was applied to validate the extract efficiency of the SSPE technique with isobutane, isopentane, pentane, and heptane at the trace level, and all the $\delta^{13}\text{C}$ were determined by the GC/IRMS system.

2.2. Syringe Solid Phase Extraction (SSPE). The improved technique is called syringe solid phase extraction, which consists of three parts: the syringe, the three-way valve, and the extraction part (Figure 1). The syringe was used to hold helium and the natural gas. The three-way valve was used to switch different channels to realize the adsorption and desorption process. And the extraction part, the core part of SSPE technique, was designed to substitute the coated fiber of SPME technique. Adsorbents were filled in the tiny metal tube, and the target compounds can be adsorbed and desorbed by the needle plugging with the aid of the peristaltic pump and the microfurnace.

TABLE 1: Composition and carbon isotopic ratios of the standard sample.

Compound	Formula	$\delta^{13}\text{C}$ (V-PDB, ‰) ($n = 6$)	P_1 (%)	P_2 (%)
Methane	CH_4	-41.84 ± 0.21	50.271	0.084
Ethane	C_2H_6	-29.45 ± 0.17	22.931	0.038
Propane	C_3H_8	-26.70 ± 0.32	7.013	0.012
Isobutane	$i\text{-C}_4\text{H}_{10}$	-26.48 ± 0.31	11.284	0.019
Normal butane	$n\text{-C}_4\text{H}_{10}$	-25.58 ± 0.29	4.418	0.007
Isopentane	$i\text{-C}_5\text{H}_{12}$	-24.78 ± 0.36	3.352	0.006
Normal pentane	$n\text{-C}_5\text{H}_{12}$	-23.12 ± 0.33	0.731	0.001

$\delta^{13}\text{C}$ ratios were all measured by direct injection, and all the ratios were calculated by average values of 6 duplicated injections under the same condition. P_1 : hydrocarbon content of direct injection (each peak area of the hydrocarbon represents their content); P_2 : hydrocarbon content after diluting with helium.

TABLE 2: Composition and peak area of natural gas sample from XML.

Compound	$\delta^{13}\text{C}$ (V-PDB, ‰)	Peak area (mV)
CH_4	-48.20	1.02
C_2H_6	-44.31	1.10
C_3H_8	-41.33	0.99
$i\text{-C}_4\text{H}_{10}$	—	—
$n\text{-C}_4\text{H}_{10}$	-37.28	0.91
$i\text{-C}_5\text{H}_{12}$	—	—
$n\text{-C}_5\text{H}_{12}$	-35.42	0.43
C_6H_{14}	—	—

In this study, SSPE was applied to extract hydrocarbon compounds from natural gas, and all the applications were accomplished by using the metal tube containing adsorbents. In order to select a proper adsorbent, 11 different adsorbents were prepared. Each adsorbent was purified by the microfurnace at 400°C for 5 minutes. The prepared diluted natural gas (diluted with helium) sample was sealed in a glass container (600 mL). Firstly, the SSPE needle should be exposed into the bottle to extract the natural gas sample for 10 minutes at a rate of 3 mL/min. Then, the extracted hydrocarbon compounds should be desorbed for 5 minutes at 300°C . And finally, for the analysis of $\delta^{13}\text{C}$ ratios, the needle needed to be inserted into the GC injection port.

2.3. Optimized Condition Setting

2.3.1. Adsorbents. 3A, 4A, 5A, 13X, Al_2O_3 , silica gel, GDX-101, graphene (TORAY, Japan), 2,6-diphenylfuran porous polymer resin (Tenax), and two types of activated carbon were prepared as the adsorbents of SSPE. Furthermore, in order to validate the extract efficiency, carbon molecular sieve/polydimethylsiloxane/carboxen (CAR/PDMS/carboxen,

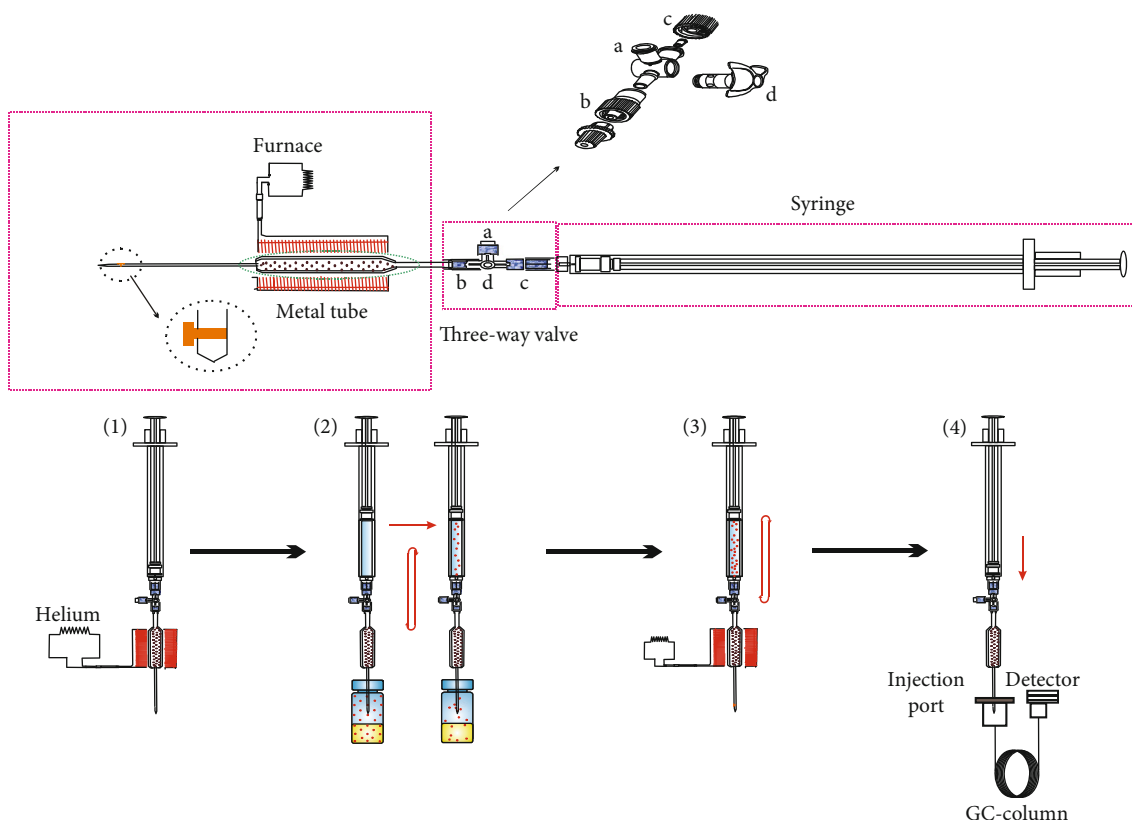


FIGURE 1: Diagram of SSPE structure and its operation procedure. The SSPE process has four steps: (1) heat the metal tube to ensure the adsorbent is completely purified; (2) extract the target hydrocarbon compounds through the natural gas sample; in this step, the sorbent is exposed to the sample and target analytes are separated from the sample matrix and adsorbed on the sorbents; (3) desorb the hydrocarbon compounds with the microfurnace; and (4) inject the hydrocarbons into the GC inlet.

75 μm , Supelco, USA) was selected as the fiber coating of the SPME technique.

2.3.2. Temperature. Six temperature (-20°C , 0°C , 20°C , 40°C , 60°C , and 80°C) were applied to the selection of an optimized adsorption temperature. Similarly, to evaluate the efficiency of desorption temperature, this study compared 10 different desorption temperatures ($50\sim 500^{\circ}\text{C}$, every two adjacent temperatures were at an interval of 50°C).

2.3.3. Time. Ten adsorbent time (1~10 minutes, every two adjacent time were at an interval of 1 minute) were set to evaluate the efficiency characteristics of adsorption time. And the concentration efficiency of 10 desorption time (0.5 minutes, 1 minute, 1.5 minutes, 2 minutes, 3 minutes, 4 minutes, 5 minutes, 6 minutes, 7 minutes, and 8 minutes) was used to measure the desorption time.

2.4. GC-IRMS. A GC-C-IRMS system (Gas Chromatography-Combustion, Agilent 6890, Agilent Technologies, USA; GC Combustion III; Isotope Ratio Mass Spectrometry, Finnigan Delta plus XP, Thermo Fisher, Bremen, Germany) was used to evaluate the SSPE efficiency. Helium ($\geq 99.999\%$) was applied as carrier gas at 4 mL/min. Separation of hydrocarbon compounds was performed on HP-Plot Q (Agilent,

19095P-Q04, 30 m \times 0.53 mm \times 40 μm) column. The temperature of HP-Plot Q column was held at 30°C for 4 minutes, then turned up to 100°C at the rate of $8^{\circ}\text{C}/\text{min}$ and maintained for 4 minutes, and finally increased to 240°C at the rate of $8^{\circ}\text{C}/\text{min}$ and then maintained for 30 minutes. The inlet temperature of the GC was set at 240°C , and all injections were set at split mode at the split ratio of 4:1. The furnace was maintained at 940°C to ensure the individual compound completely oxidized when it flowed through the oxidation ceramic reactor filled with twisted wires (Ni/CuO/Pt). Three standard pure CO_2 gases were used as reference gas for the calculation of $\delta^{13}\text{C}$ of specific compounds. All $\delta^{13}\text{C}$ signatures of analytes are reported relative to the Vienna Pee Dee Belemnite (V-PDB) and expressed as $\delta^{13}\text{C} = \{ [^{13}\text{C}/^{12}\text{C}]_{\text{sample}} / [^{13}\text{C}/^{12}\text{C}]_{\text{standard}} - 1 \} \times 1000$.

3. Results

3.1. Adsorbent Selection. All peak areas of hydrocarbon compounds obtained from the 11 adsorbents are listed in Figure 2(a). For all adsorbents, activated carbon exhibited the best adsorption efficiency, and 4A molecular sieve showed poor adsorptive capacity. Additionally, enrichment coefficient (K) was also considered (Figure 2(b)), which was expressed as the ratio of the concentration (P (%)) of the

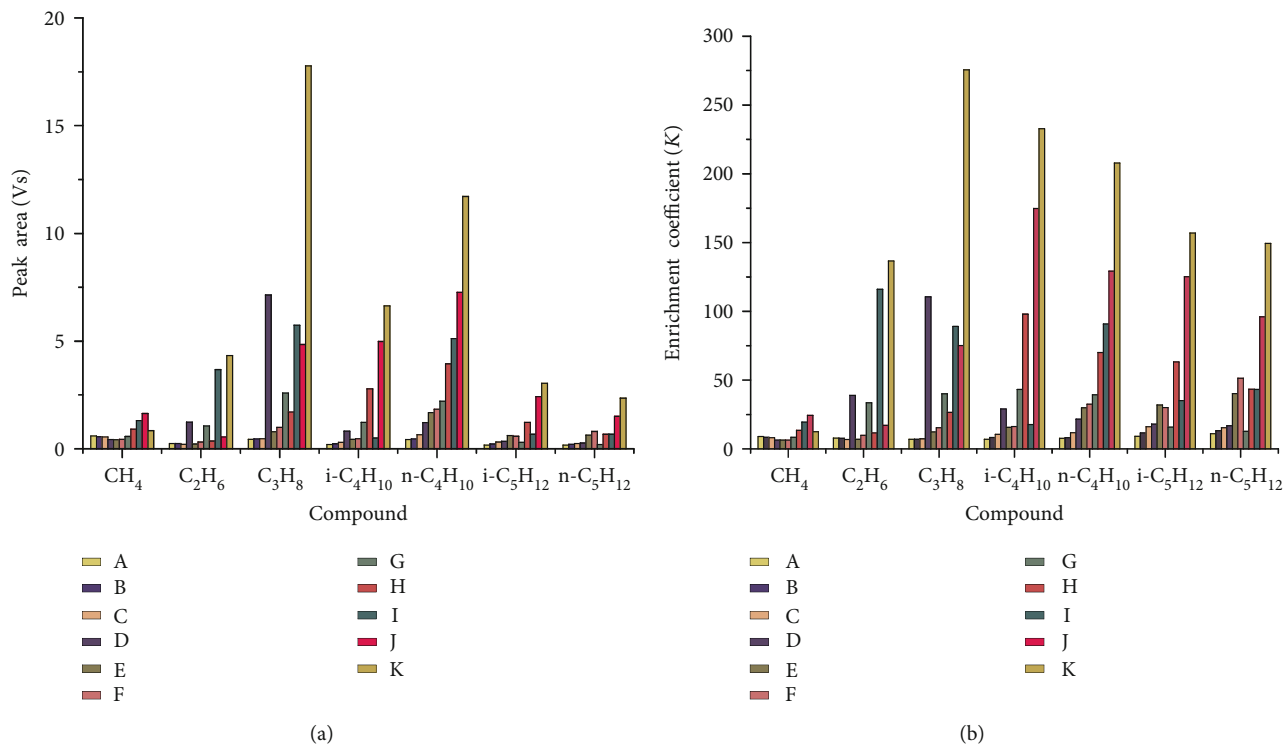


FIGURE 2: Comparison of adsorption efficiency and enrichment coefficient (K) of the 11 adsorbents on CH₄, C₂H₆, C₃H₈, C₄H₁₀, and C₅H₁₂. A: 4A; B: 3A; C: graphene; D: silica gel; E: GDX-101; F: Tenax; G: activated carbon 1; H: ALO; I: 5A; J: 13X; K: activated carbon 2.

same hydrocarbon between the extracted analyte and their corresponding compounds in the gas sample. The result also illustrated that the activated carbon has the best enrichment coefficient. Therefore, it indicated that the activated carbon was suitable for the extraction of hydrocarbons in natural gas, and the following tests were all using activated carbon as adsorbents.

3.2. Temperature Optimization

3.2.1. Adsorption Temperature. Comparing all the adsorption temperature in Figure 3(a), it can be seen that the adsorbent has the best adsorption efficiency at 20°C. The $\delta^{13}\text{C}$ of CH₄, C₂H₆, C₄H₁₀, and C₅H₁₂ varied in a wide range, for the obtained SD-1 were relatively larger than that of the uncertainties of the instrument $\pm 0.5\%$ (CH₄ was 0.97, C₂H₆ was 0.53, i-C₄H₁₀ was 0.70, n-C₄H₁₀ was 0.79, i-C₅H₁₂ was 1.80, and n-C₅H₁₂ was 1.08), whereas C₃H₈ were quite different, with the SD-1 value of 0.40 (Table 3). Additionally, the $\delta^{13}\text{C}$ of CH₄, C₂H₆, i-C₄H₁₀, n-C₄H₁₀, and n-C₅H₁₂ were distributed as follows: CH₄: -43.8~-41.2‰, C₂H₆: -31.4~-30.0‰, i-C₄H₁₀: -26.3~-24.5‰, n-C₄H₁₀: -26.4~-24.7‰, i-C₅H₁₂: -27.3~-22.3‰, and n-C₅H₁₂: -24.0~-21.1‰ (Table 3).

3.2.2. Desorption Temperature. At different desorption temperature, the amount of hydrocarbon compounds released by thermal desorption varies greatly (Figure 3(b)). C₄H₁₀ and C₅H₁₂ could not be thermally desorbed when desorption temperature was below 200°C. Thermal desorption has better adsorption efficiency at the range of 250~350°C. It can be

observed that the standard deviations of the $\delta^{13}\text{C}$ distribution of CH₄~C₅H₁₂ vary in a relatively wide range if CH₄ was 0.44, C₂H₆ was 0.51, C₃H₈ was 0.46, i-C₄H₁₀ was 0.61, n-C₄H₁₀ was 0.44, i-C₅H₁₂ was 0.61, and n-C₅H₁₂ was 0.81, for their $\delta^{13}\text{C}$ ratios were at a relatively large range (Table 3). The $\delta^{13}\text{C}$ ratios of CH₄ were comprised between -42.7 and -41.1‰, C₂H₆ was distributed from -30.4 to -28.4‰, C₃H₈ was clustered between -28.3 and -27.0‰, i-C₄H₁₀ was ranged from -27.4 to -25.7‰, n-C₄H₁₀ was clustered between -27.1 and -26.0‰, i-C₅H₁₂ was located in the range of -25~-23.6‰, and n-C₅H₁₂ ratios were ranged from -25.1 to -22.8‰.

3.3. Time Optimization

3.3.1. Adsorption Time. As shown in Figure 3(c), the best enrichment efficiency of the adsorption time was between 2 and 5 minutes, and the adsorption efficiency of CH₄ remains a relatively stable level with adsorption time changing, but the change of C₂H₆~C₅H₁₂ was more obvious than that of CH₄, especially C₂H₆~C₄H₁₀. Unlike temperature, $\delta^{13}\text{C}$ of CH₄~C₅H₁₂ had a relatively good reproducibility at different adsorption times, which means adsorption time has a relatively little effect on $\delta^{13}\text{C}$ ratios; the standard deviations of CH₄~C₅H₁₂ were all with 0.41‰ (Table 3).

3.3.2. Desorption Time. C₅H₁₂ could not be desorbed before 1.5 minutes, and the adsorption amount of CH₄ and C₅H₁₂ remained in a stable level of the whole desorption process, whereas the changes of the amount of C₂H₆~C₄H₁₀ were

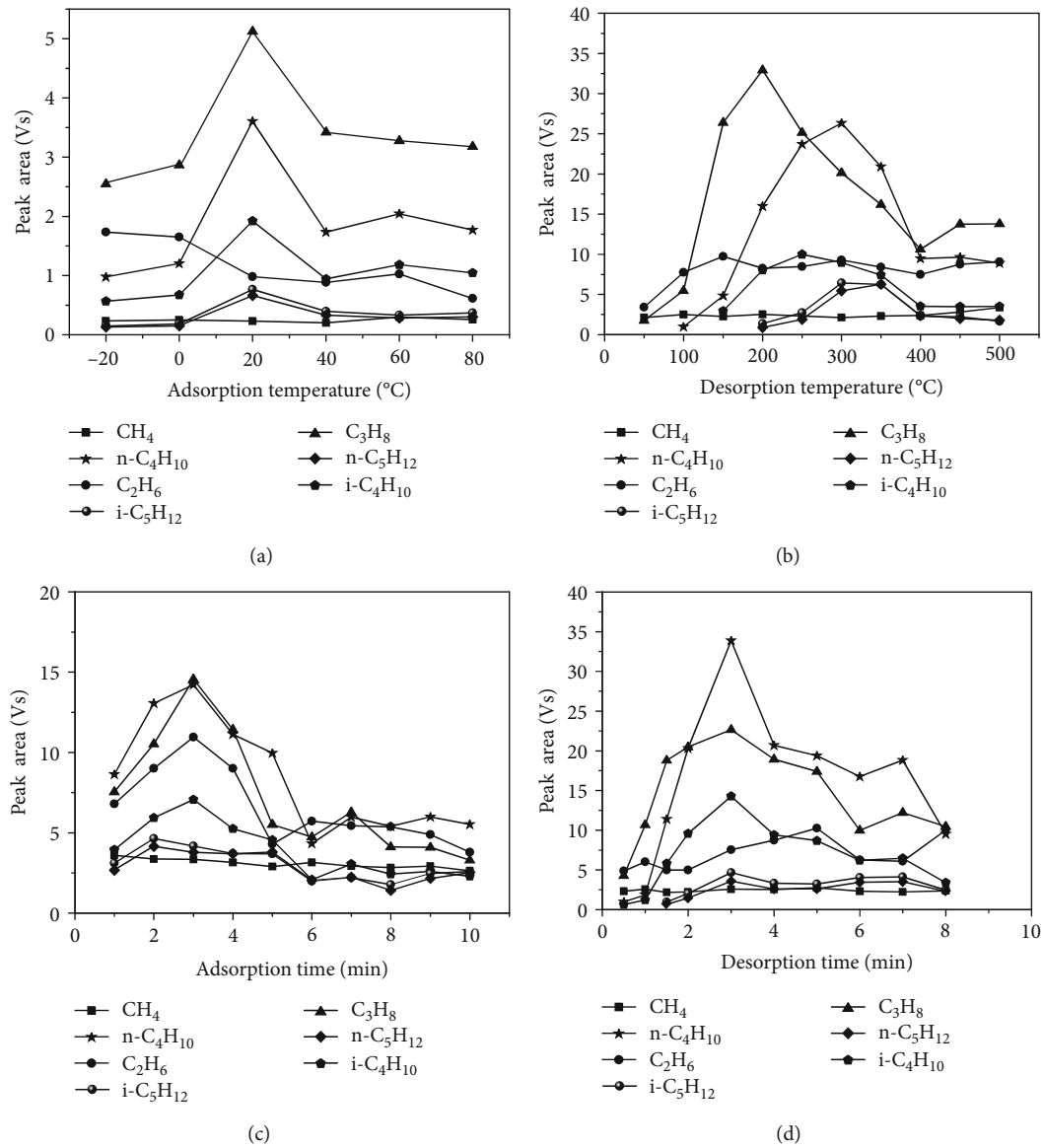


FIGURE 3: Peak areas at different experimental conditions: (a) the adsorption peak areas with adsorption temperatures ranging from 0 to 40°C; (b) the adsorption peak areas at different desorption temperatures from 250 to 350°C; (c) the adsorption peak areas at different adsorption times ranging from 2 to 5 minutes; (d) the adsorption peak areas at different desorption times ranging from 2 to 7 minutes.

TABLE 3: $\delta^{13}\text{C}$ ratios of standard natural gas sample and its SDs at different conditions.

Compound	SD-A	Adsorption temperature (°C)			Desorption temperature (°C)			Adsorption time (s)			Desorption time (s)		
		<i>M</i> (<i>n</i> = 6)	SD-1	SD-2	<i>M</i> (<i>n</i> = 10)	SD-1	SD-2	<i>M</i> (<i>n</i> = 10)	SD-1	SD-2	<i>M</i> (<i>n</i> = 10)	SD-1	SD-2
CH ₄	-41.84	-42.40	0.97	0.40	-41.88	0.44	0.03	-41.55	0.24	0.20	-41.52	0.24	0.23
C ₂ H ₆	-29.45	-30.85	0.53	0.99	-29.78	0.57	0.23	-30.08	0.32	0.44	-29.75	0.80	0.21
C ₃ H ₈	-26.70	-26.96	0.40	0.18	-27.99	0.46	0.91	-27.05	0.42	0.25	-27.62	0.41	0.65
i-C ₄ H ₁₀	-26.48	-25.72	0.70	0.54	-27.03	0.61	0.39	-26.87	0.16	0.28	-21.31	0.33	3.66
n-C ₄ H ₁₀	-25.58	-25.39	0.79	0.13	-25.37	0.44	0.15	-25.60	0.39	0.02	-23.98	0.36	1.13
i-C ₅ H ₁₂	-24.78	-24.97	1.80	0.13	-20.13	0.61	3.29	-25.26	0.41	0.34	-17.25	0.28	5.32
n-C ₅ H ₁₂	-23.12	-22.92	1.08	0.14	-19.71	0.81	2.41	-23.47	0.28	0.25	-16.9	0.44	4.40

SD-A: the average ratios of the standard natural gas sample, V-PDB, ‰; *M*: average ratios at different experimental conditions, V-PDB, ‰; SD-1: standard deviations obtained from average ratios at different experimental conditions; SD-2: standard deviations between STDA and *M*.

TABLE 4: $\delta^{13}\text{C}$ ratios of standard sample at different temperatures ($^{\circ}\text{C}$) and times (min).

Compound	Adsorption temperature (°C)										Desorption temperature (°C)										Adsorption time (min)										Desorption time (min)									
	-20	0	20	40	60	80	50	100	150	200	250	300	350	400	450	500	1	2	3	4	5	6	7	8	9	10	0.5	1	1.5	2	3	4	5	6	7	8				
CH ₄	-44	-42	-42	-41	-42	-43	-41	-41	-41	-41	-42	-41	-42	-41	-42	-43	-42	-41	-41	-41	-42	-42	-41	-42	-42	-42	-41	-45	-42	-42	-42	-42	-42	-41	-42	-41	-42	-41		
C ₂ H ₆	-31	-31	-30.0	-31	-31	-31	-30	-30	-30	-30	-30	-30	-30	-30	-30	-28	-30	-30	-30	-30	-30	-30	-30	-30	-30	-30	-30	-32	-30	-29	-30	-30	-30	-29	-29	-30	-29	-30		
C ₃ H ₈	-27	-27	-27	-28	-27	-27	-28	-27	-28	-28	-28	-27	-28	-28	-28	-27	-28	-27	-27	-27	-27	-26	-26	-27	-27	-27	-27	-28	-29	-27	-28	-28	-28	-28	-28	-28	-28	-28	-28	
i-C ₄ H ₁₀	-25	-26	-26	-26	-25	-26	—	—	-26	-27	-27	-27	-27	-27	-27	-26	-26	-27	-27	-27	-27	-27	-27	-27	-27	-27	-27	-27	-27	-27	-27	-27	-27	-27	-27	-27	-27	-27		
n-C ₄ H ₁₀	-24.7	-25.0	-25.8	-26.4	-24.4	-26.0	—	-26.4	-26.0	-27.0	-26.9	-26.1	-27.0	-26.9	-27.1	-26.3	-25.5	-25.4	-26.2	-25.5	-25.5	-25.0	-25.8	-25.2	-25.4	-25.9	-26.1	-25.1	-25.4	-25.8	-25.1	-25.5	-25.1	-25.3	-25.1	-25.5	-25.1	-25.7		
i-C ₅ H ₁₂	-27	-22	-24	-25	-27	-24	—	—	—	-25	-25	-25	-25	-24	-24	-24	-25	-25	-25	-25	-25	-25	-25	-26	-26	-26	—	—	-25	-25	-25	-26	-26	-26	-25	-25	-25	-25		
n-C ₅ H ₁₂	-22.4	-23.8	-23.5	-22.8	-21.1	-24.0	—	—	—	-24.9	-24.6	-23.1	-24.6	-24.6	-24.3	-22.8	-24.0	-23.9	-23.6	-23.3	-23.2	-23.2	-23.5	-23.5	-23.3	-23.2	—	—	-24.1	-23.5	-24.9	-25.2	-24.8	-25.1	-24.5	-24.5	-24.5			

A Te: adsorption temperature; DTe: desorption temperature; ATi: adsorption time; DTi: desorption time.

larger, and the best adsorption time located in the interval of 2~5 minutes (Figure 3(d)). Comparing the results obtained by adsorption time, it can be seen that except for C_2H_6 (SD-1 was 0.80), the reproducibility of the measurements of 10 desorption times is also satisfied with the uncertainties of the instrument, with the standard deviations all within 0.44‰ (Table 3).

4. Discussion

4.1. Determination of Optimization Conditions. The balance of trace hydrocarbon compounds between adsorbents is critical to optimal condition [26, 27]. Thermal dynamic conditions such as temperature and time are important factors affecting the adsorption efficiency. As temperature increases, both the diffusion ability of the molecules and relative motion between molecules increase; meanwhile, the adsorption rate of adsorbents is faster [20, 26–28]. However, an increase in temperature causes the lower partition coefficient of compounds between the matrix and the adsorbent, thus limiting the amount of the concentrated compound [20, 28]. It is obvious that the SD-1 values of adsorption temperature (0.53~1.80‰, except for C_3H_8) and desorption temperature (CH_4 : 0.44, C_2H_6 : 0.57, C_3H_8 : 0.46, C_4H_{10} : 0.61, C_4H_{10} : 0.44, C_5H_{12} : 0.61, and C_5H_{12} : 0.81) vary greatly, and almost all the standard deviation values are beyond the limit uncertainty of instrument 0.5‰ (Table 3). Thus, this conditional test provided compelling evidence that $\delta^{13}C$ exhibits a considerable influence on isotopic fractionations. Select temperature from Figures 3(a) and 3(b) as follows: 20°C for adsorption temperature and 300°C for desorption temperature, and compare the $\delta^{13}C$ with the average ratios of the standard natural gas sample (Tables 3 and 4), the obtained results are all within 0.47‰ (within 0.50‰). That is, the selected temperatures show little effect on isotopic fractionations, and they can be used as efficiency temperature.

Similarly, equilibrium time is also an important condition that affects the extraction efficiency [28, 29]. Though many researchers may have an empirical understanding of these impacts, there is little explicit clear experiment [20, 30]. The extraction amounts of hydrocarbons remain a relatively stable level after reaching equilibrium, whereas a large change appeared before that state. Different from temperature, except for 0.80‰ of C_2H_6 obtained from desorption time, other SD-1 values of adsorption time and desorption time are all within 0.44‰, which means time may have smaller effects on isotopic fractionations. Additionally, choose the maximum extraction efficiency time to estimate the effect on isotope fractionation, all obtained standard deviations are within 0.5‰ (Figures 3(c) and 3(d)).

The optimized experimental conditions are determined as follows: adsorb the sample at 20°C for 3 minutes and then desorb it at 300°C for 3 minutes. The obtained results of $\delta^{13}C$ values are in good agreement with the $\delta^{13}C$ ratios of direct injection (original standard natural gas, without helium dilution) and SPME (Figure 4). The $\delta^{13}C$ values obtained by these three methods are in good agreement without obvious fractionations (the standard deviations between DI and SSPE are as follows: $\pm 0.15\%$ for CH_4 , $\pm 0.14\%$ for

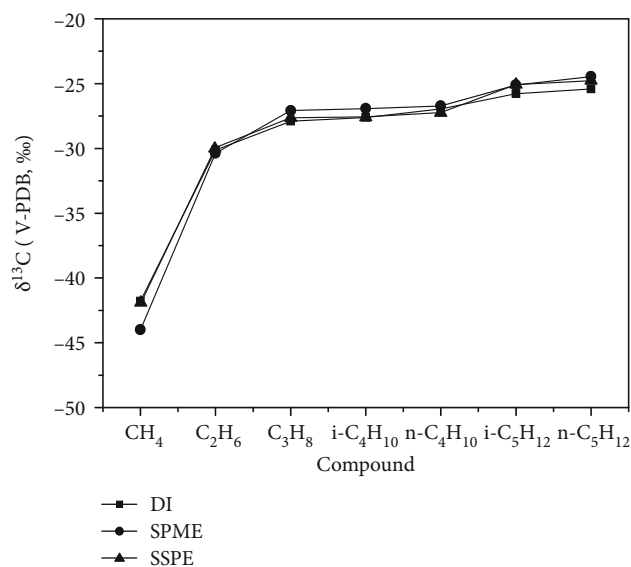


FIGURE 4: Validation of SSPE. DI: direct injection for original standard natural gas sample; SPME: solid phase microextraction for diluted standard natural gas; SSPE: syringe solid phase for diluted standard natural gas.

C_2H_6 , $\pm 0.19\%$ for C_3H_8 , $\pm 0.03\%$ for $i-C_4H_{10}$, $\pm 0.19\%$ for $n-C_4H_{10}$, $\pm 0.49\%$ for $i-C_5H_{12}$, and $\pm 0.45\%$ for $n-C_5H_{12}$). Therefore, this method is a reliable method for trace hydrocarbon preconcentration.

4.2. Geological Sample Verification. After determining the optimization conditions, geological samples are applied to verify the efficiency of SSPE technique, and chromatograms of a natural gas sample obtained by DI, SPME, and SSPE are detected and identified (Figure 5, Table 5). Simultaneously, similar experiments are carried out with SPME technique, and their peak intensities show that the adsorption efficiency of SSPE is higher than SPME (Figures 5(b) and 5(c)). From data given in Table 4, it can be seen that the $\delta^{13}C$ values are all within a reasonable range without carbon isotope fractionation (SD values are all within 0.48), and the intensity of each hydrocarbon obtained by the SSPE method is higher than DI and SPME with the highest intensity of 30000 mV (intensities of DI and SPME are all lower than 2000 mV). Therefore, comparing these values obtained from DI, SPME, and SSPE, it is found that this established SSPE method is reliable for carbon isotope analysis.

4.3. Legacy Issues and Future Prospects. This study facilitates in trace hydrocarbons in natural gas where some barriers and baffles restrict its measurement [25]. For instance, isotopic fractionations appeared obviously with a high temperature (e.g., higher than 350°C), but the mechanism still remains to be solved. So, further insight from this problem needs to be followed up. In addition, considering that the whole sample preconcentration process is completely by manual operation, it is meaningful to expect future improvements for this technique. By optimizing the automation of SSPE technique, better accuracy and precision can be obtained. Additionally,

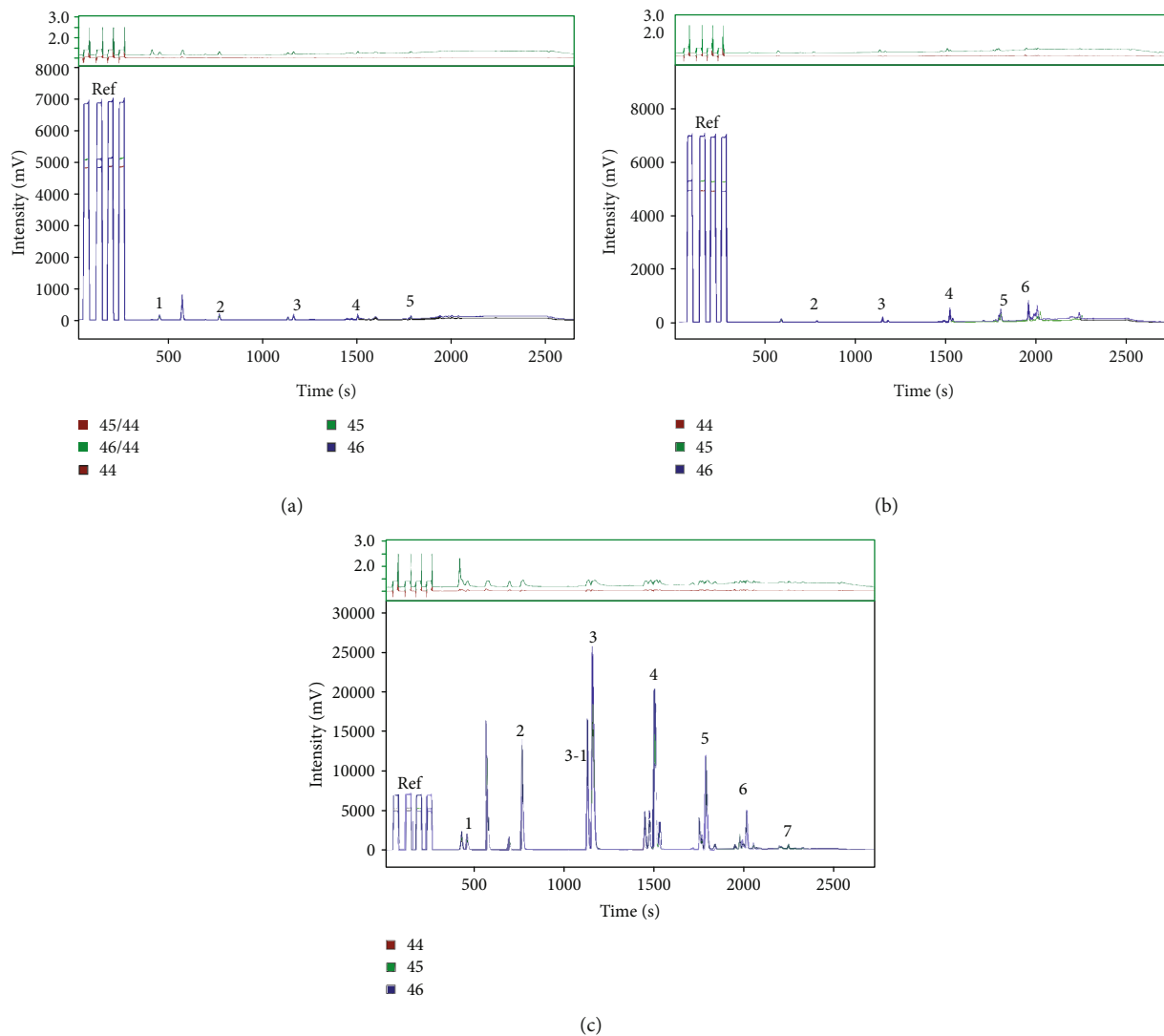


FIGURE 5: Geological sample analysis of DI, SPME, and SSPE: (a) direct injection of 30 μL natural gas sample; (b) SSPE extracted for 30 minutes; (c) SSPE extracted for 3 minutes at 20°C and then desorbed for 3 minutes at 300°C. 1: CH_4 ; 2: C_2H_6 ; 3-1: C_3H_6 ; 3: C_3H_8 ; 4-1: $\text{i-C}_4\text{H}_{10}$; 4-2: C_4H_8 ; 4: $\text{n-C}_4\text{H}_{10}$; 5-1: $\text{i-C}_4\text{H}_{10}$; 5-2: C_5H_{10} ; 5: C_5H_{12} ; 6-1: $\text{i-C}_4\text{H}_{10}$; 6: C_6H_{14} ; 7: C_7H_{16} .

TABLE 5: $\delta^{13}\text{C}$ ratios (‰), S (mV), and SD (‰) obtained from DI, SPME, and SSPE.

Compound	Direct injection		Solid phase microextraction			Syringe solid phase extraction		
	$\delta^{13}\text{C}$	Peak area	$\delta^{13}\text{C}$	Peak area	Standard deviation	$\delta^{13}\text{C}$	Peak area	Standard deviation
CH_4	-48.20	1.02	—	—	—	-47.76	12.50	0.31
C_2H_6	-44.31	1.10	-44.82	0.24	0.36	-44.99	91.70	0.48
C_3H_8	-41.33	0.99	-42.86	0.28	1.08	-41.02	241.44	0.21
$\text{i-C}_4\text{H}_{10}$	—	—	-36.89	0.41	—	-39.42	35.90	—
$\text{n-C}_4\text{H}_{10}$	-37.28	0.91	-40.78	2.40	2.48	-36.84	170.06	0.31
$\text{i-C}_5\text{H}_{12}$	—	—	-38.58	0.58	—	-37.95	9.37	—
$\text{n-C}_5\text{H}_{12}$	-35.42	0.43	-37.76	2.64	1.65	-35.15	29.54	0.19
C_6H_{14}	—	—	-34.58	3.56	—	-36.53	2.82	—

the conditions highlighted in this study can also be applied to simplified studies on source rocks, oilfield water, and other samples for further study.

5. Conclusions

The SSPE-GC/IRMS technique based on SPME-GC/IRMS was conducted on standard and geological samples with different adsorbents, temperatures, and times to determine the optimized experimental condition and achieve the analyzed trace hydrocarbon isotope. For this purpose, the content and $\delta^{13}\text{C}$ were analyzed. The following conclusions can be drawn:

- (1) Activated carbon was selected as the reliable adsorbents, and the optimized condition was determined; adsorb sample at 20°C for 3 minutes and then desorb it at 300°C for 3 minutes. The quality data such as precision and accuracy are acceptable for this technique with the uncertainty of the measurement lower than 0.48 in all cases of the natural gas, which is in accordance with the requirements of the GC-IR/MS
- (2) Apply a sample of Xiamaling formation, Sichuan Basin, for the detection of the SSPE technique; the results showed satisfying extraction efficiency
- (3) The lower detection limits for trace light hydrocarbons required by this technique are achieved and validated, and the requirement of uncertainty was also fulfilled for all hydrocarbons. More hydrocarbons, at the lower content level, than other previous methods proposed in the literature based on the use of SPME-GC-IR/MS have been detected. More hydrocarbons, at the lower content level, than other previous methods proposed in the literature based on the use of SPME-GC-IR/MS have been detected. This technique is quick and simple and increases the selectivity and sensitivity of analysis. And furthermore, the proposed technique is versatile, for it can be applied to detect other samples besides natural gas samples

Data Availability

The data used to support the findings of this study are available from the corresponding author and first author upon request.

Conflicts of Interest

The authors declare that they have no conflicts of interest.

Acknowledgments

Thanks to Prof. Mingjie Zhang and Dr. Ting Zhang for their advices. And this research was financially supported by the National Science Foundation of China (No. 41272145, 41572136, and 41973066) and the “West Light Foundation of Chinese Academy of Sciences.”

References

- [1] M. Hoenig and A.-M. de Kersabiec, “Sample preparation steps for analysis by atomic spectroscopy methods: present status,” *Spectrochimica Acta Part B: Atomic Spectroscopy*, vol. 51, no. 11, pp. 1297–1307, 1996.
- [2] L. H. Keith, W. Crummett, J. Deegan, R. A. Libby, J. K. Taylor, and G. Wentler, “Principles of environmental analysis,” *Analytical Chemistry*, vol. 55, no. 14, pp. 2210–2218, 1983.
- [3] R. M. Smith, “Before the injection—modern methods of sample preparation for separation techniques,” *Journal of Chromatography A*, vol. 1000, no. 1–2, pp. 3–27, 2003.
- [4] B. K. Matuszewski, M. L. Constanzer, and C. M. Chavez-Eng, “Strategies for the assessment of matrix effect in quantitative bioanalytical methods based on HPLC–MS/MS,” *Analytical Chemistry*, vol. 75, no. 13, pp. 3019–3030, 2003.
- [5] A. V. Bridgwater, D. Meier, and D. Radlein, “An overview of fast pyrolysis of biomass,” *Organic Geochemistry*, vol. 30, no. 12, pp. 1479–1493, 1999.
- [6] T. C. Schmidt, L. Zwank, M. Elsner, M. Berg, R. U. Meckenstock, and S. B. Haderlein, “Compound-specific stable isotope analysis of organic contaminants in natural environments: a critical review of the state of the art, prospects, and future challenges,” *Analytical and Bioanalytical Chemistry*, vol. 378, no. 2, pp. 283–300, 2004.
- [7] E. Lichtfouse, “Compound-specific isotope analysis. Application to archaeology, biomedical sciences, biosynthesis, environment, extraterrestrial chemistry, food science, forensic science, humic substances, microbiology, organic geochemistry, soil science and sport,” *Rapid Communications in Mass Spectrometry*, vol. 14, no. 15, pp. 1337–1344, 2000.
- [8] A. Cincinelli, F. Pieri, Y. Zhang, M. Seed, and K. C. Jones, “Compound specific isotope analysis (CSIA) for chlorine and bromine: a review of techniques and applications to elucidate environmental sources and processes,” *Environmental Pollution*, vol. 169, pp. 112–127, 2012.
- [9] B. N. Popp, B. S. Graham, R. J. Olson et al., “Insight into the trophic ecology of yellowfin tuna, *Thunnus albacares*, from compound-specific nitrogen isotope analysis of proteinaceous amino acids,” *Terrestrial Ecology*, vol. 1, pp. 173–190, 2007.
- [10] M. Schoell, “The hydrogen and carbon isotopic composition of methane from natural gases of various origins,” *Geochimica et Cosmochimica Acta*, vol. 44, pp. 649–661, 1979.
- [11] M. J. Whiticar, “Stable isotope geochemistry of coals, humic kerogens and related natural gases,” *International Journal of Coal Geology*, vol. 32, no. 1–4, pp. 191–215, 1996.
- [12] M. Schoell, “Multiple origins of methane in the Earth,” *Chemical Geology*, vol. 71, pp. 1–10, 1999.
- [13] W. J. Stahl, “Carbon and nitrogen isotopes in hydrocarbon research and exploration,” *Chemical Geology*, vol. 20, pp. 121–149, 1977.
- [14] C. J. Clayton, “Effect of maturity on carbon isotope ratios of oils and condensates,” *Organic Geochemistry*, vol. 17, no. 6, pp. 887–899, 1991.
- [15] E. Maslen, K. Grice, P. L. Métayer, D. Dawson, and D. Edwards, “Stable carbon isotopic compositions of individual aromatic hydrocarbons as source and age indicators in oils from western Australian basins,” *Organic Geochemistry*, vol. 42, no. 4, pp. 387–398, 2011.
- [16] J. A. Curiale, “Petroleum geochemistry,” *Encyclopedia of Petroleum Geoscience*, Springer, Cham, 2017.

- [17] R. G. Schaefer and D. Leythaeuser, "Analysis of trace amounts of hydrocarbons (C_2 – C_8) from rock and crude oil samples and its application in petroleum geochemistry," *Physics and Chemistry of the Earth*, vol. 12, pp. 149–156, 1980.
- [18] Y. Huiban, S. Noirez, A. Prinzhofer, J. P. Girard, and J. Chappellaz, "Chemical and isotopic analysis of hydrocarbon gas at trace levels: Methodology and results," *Chemical Geology*, vol. 265, no. 3–4, pp. 363–368, 2009.
- [19] S. M. Abeel, A. K. Vickers, and D. Decker, "Trends in purge and trap," *Journal of Chromatographic Science*, vol. 32, no. 8, pp. 328–338, 1994.
- [20] H. Lord and J. Pawliszyn, "Evolution of solid-phase microextraction technology," *Journal of Chromatography A*, vol. 885, no. 1–2, pp. 153–193, 2000.
- [21] L. Zwank, M. Berg, T. C. Schmidt, and S. B. Haderlein, "Compound-specific carbon isotope analysis of volatile organic compounds in the low-microgram per liter range," *Analytical Chemistry*, vol. 75, no. 20, pp. 5575–5583, 2003.
- [22] G. Contarini and M. Povolò, "Volatile fraction of milk: comparison between purge and trap and solid phase microextraction techniques," *Journal of Agricultural and Food Chemistry*, vol. 50, no. 25, pp. 7350–7355, 2002.
- [23] C. L. Arthur and J. Pawliszyn, "Solid phase microextraction with thermal desorption using fused silica optical fibers," *Analytical Chemistry*, vol. 62, no. 19, pp. 2145–2148, 1990.
- [24] M. Llompart, K. Li, and M. Fingas, "Headspace solid-phase microextraction for the determination of volatile and semi-volatile pollutants in water and air," *Journal of Chromatography A*, vol. 824, no. 1, pp. 53–61, 1998.
- [25] Z. Li, X. Wang, L. Li et al., "Development of new method of $\delta^{13}C$ measurement for trace hydrocarbons in natural gas using solid phase micro-extraction coupled to gas chromatography isotope ratio mass spectrometry," *Journal of Chromatography A*, vol. 1372, pp. 228–235, 2014.
- [26] J. C. Maxwell, "On the dynamical theory of gases," *Philosophical Transactions of the Royal Society of London*, vol. 157, pp. 49–88, 1867.
- [27] F. I. Khan and A. K. Ghoshal, "Removal of volatile organic compounds from polluted air," *Journal of Loss Prevention in the Process Industries*, vol. 13, no. 6, pp. 527–545, 2000.
- [28] A. M. Aljeboree, A. N. Alshirifi, and A. F. Alkaim, "Kinetics and equilibrium study for the adsorption of textile dyes on coconut shell activated carbon," *Arabian Journal of Chemistry*, vol. 10, pp. S3381–S3393, 2017.
- [29] J. Palau, A. Soler, P. Teixidor, and R. Aravena, "Compound-specific carbon isotope analysis of volatile organic compounds in water using solid-phase microextraction," *Journal of Chromatography A*, vol. 1163, no. 1–2, pp. 260–268, 2007.
- [30] W. J. Boecklen, C. T. Yarnes, B. A. Cook, and A. C. James, "On the use of stable isotopes in trophic ecology," *Annual Review of Ecology, Evolution, and Systematics*, vol. 42, no. 1, pp. 411–440, 2011.

Research Article

Nonvolcanic Carbon Dioxide Emission at Continental Rifts: The Bublák Mofette Area, Western Eger Rift, Czech Republic

Horst Kämpf¹, **Alena Sophie Broge**², **Pouria Marzban**³, **Masoud Allahbakhshi**³,
and **Tobias Nickschick**⁴

¹GFZ German Research Centre for Geosciences, Section Organic Geochemistry, Telegrafenberg, 14473 Potsdam, Germany

²Geoscience Centre, Georg-August Universität Göttingen, 37077 Göttingen, Goldschmidtstrasse 3, Germany

³GFZ German Research Centre for Geosciences, Section Physics of Earthquakes and Volcanoes, Telegrafenberg,
14473 Potsdam, Germany

⁴Institute of Geophysics and Geology, Talstrasse 35, 04103 Leipzig, Germany

Correspondence should be addressed to Horst Kämpf; kaempfh@gfz-potsdam.de

Received 14 March 2019; Accepted 2 May 2019; Published 30 October 2019

Guest Editor: Andrzej Solecki

Copyright © 2019 Horst Kämpf et al. This is an open access article distributed under the Creative Commons Attribution License, which permits unrestricted use, distribution, and reproduction in any medium, provided the original work is properly cited.

This study presents the results of gas flux measurements of cold, mantle-derived CO₂ release at the Bublák mofette field (BMF), located inside of the N-S directed Počátky Plesná fault zone (PPFZ). The PPFZ is presently seismically active, located in the eastern part of the Cheb Basin, western Eger Rift, Central Europe. The goal of the work was to identify the linkage between tectonics and gas flux. The investigated area has a size of 0,43 km² in which 1.115 locations have been measured. Besides classical soil CO₂ gas flux measurements using the closed chamber method (West Systems), drone-based orthophotos were used in combination with knowledge of plant zonation to find zones of high degassing in the agriculturally unused part of the BMF. The highest observed soil CO₂ gas flux is 177.926,17 g m⁻² d⁻¹, and the lowest is 0,28 g m⁻² d⁻¹. Three statistical methods were used for the calculation of the gas flux: arithmetic mean, kriging, and trans-Gaussian kriging. The average CO₂ soil degassing of the BMF is 30 t d⁻¹ for an area of 0,43 km². Since the CO₂ soil degassing of the Hartoušov mofette field (HMF) amounts to 23 t d⁻¹ for an area of 0,35 km², the average dry degassing values of the BMF and HMF are in the same magnitude of order. The amount of CO₂ flux from wet mofettes is 3 t d⁻¹ for the BMF and 0,6 t d⁻¹ for the HMF. It was found that the degassing in the BMF and HMF is not in accordance with the pull-apart basin interpretation, based on the direction of degassing as well as topography and sediment fill of the suggested basins. En-echelon faults inside of the PPFZ act as fluid channels to depth (CO₂ conduits). These structures inside the PPFZ show beginning faulting and act as tectonic control of CO₂ degassing.

1. Introduction

The quantification of mass flow between deep reservoirs and the surface is important for understanding deep carbon fluxes, changes of rock and soil atmosphere, influence on biosphere, and connections to atmosphere. Here, we use high-resolution measurement of carbon dioxide flux at the surface to characterize nonvolcanic magmatic volatile systems in the Cheb Basin (CB), western Eger (Ohře) Rift (ER), Czech Republic.

The Cenozoic CB lies in the western part of the Bohemian Massif, Central Europe, and is a structural domain of

the ER, a 300 km long, ENE-WSW striking element of the European Cenozoic Rift System (ECRIS) [1, 2]. The basin-geometry influenced by the intersection of three regional fault zones, the N-S striking Regensburg-Leipzig-Rostock zone (RLRZ), the NW-SE to NNW-SSE striking Cheb-Domazlice Graben, and the ENE-WSW faults of the Eger (Ohře) Graben, Figure 1. The Cheb-Domazlice Graben is controlled at the eastern flank by the Mariánské Lázně fault zone (MLFZ) and the Tachov fault zone (TFZ) at the western flank (Figure 1).

The MLFZ, dipping to SW, is approximately 100 km long morphologically depicted by a 200 m high escarpment at the

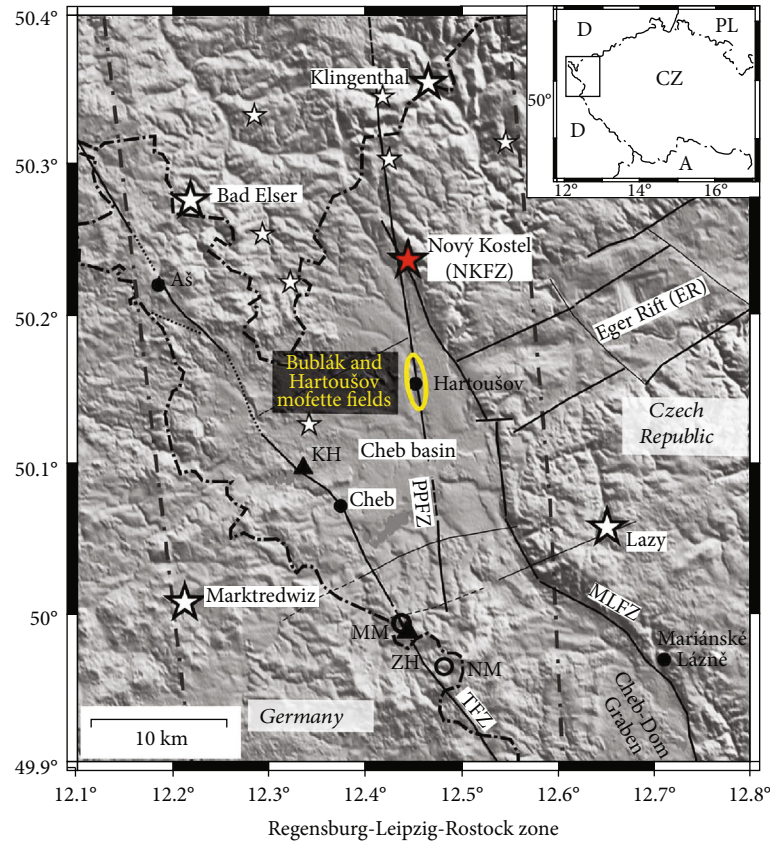


FIGURE 1: Fault zones in the Cheb Basin with Pleistocene scoria cones Železná hůrka (ZH) and Komorní hůrka (KH) (black triangles); black circles mark Mýtina maar (MM) and Neualbenreuth maar (NM); PPFZ Počátky Plesná fault zone, MLFZ Mariánské Lázně fault zone, TFZ Tachov fault zone; white stars point to further locations of swarm earthquake epicentral areas; the red star marks the NKFZ Nový Kostel focal zone [13, 28, 35].

eastern border of the CB [3]. The western flank of the basin is topographically indistinct, influenced by erosional activity [4] and bordered by the similarly NW-SE striking Tachov fault zone. In the north of the basin are the Ore Mountains (Erzgebirge) and in the south the Kaiserwald/Slavkovský les (Kaiserwald). Cenozoic fluvial and lacustrine sediments with a thickness of up to 300 m along the MLFZ fill the basin [4].

West Bohemia and the Vogtland on the German side of the border are known for their “earthquake swarms” (German: “Schwarmbeben”), a term first mentioned by Credner [5] that describes earthquakes of low magnitude but high frequency. Earthquake swarms occur mainly in areas of enhanced crustal fluid activity with Quaternary volcanism [6]. These earthquake swarms, combined with evidence for currently ongoing hidden magmatic processes in the subcontinental lithospheric mantle and mantle-derived CO_2 degassing at the surface in mineral springs and mofettes, make Cheb Basin to a unique area in Europe [7, 8] and one of the best studied nonvolcanic intracontinental rift areas worldwide [9–11].

The youngest volcanic activity in the Cheb Basin is related to the scoria cones Komorní hůrka and Železná hůrka from 0.7 to 0.3 Ma and the two maar diatreme volcanoes of Mýtina and Neualbenreuth that were discovered in 2007 [12] and 2015 [13] (Figure 1).

Within the last 40 years, three swarms that exceeded magnitudes of 4 (1985/86, 2014, and 2018) were observed, with about 90% of the total seismic moment being released in the Nový Kostel focal zone (NKFZ) [14]. The NKFZ is located close to the intersection of the Počátky Plesná fault zone (PPFZ) and the MLFZ (Figure 1). The significance of the PPFZ as a seismically active fault zone was detected by Bankwitz et al. [15]. Through stress analysis of an earthquake swarm in 2008, Vavryčuk [16] found that the PPFZ is a sinistral fault with a direction of $\approx 169^\circ$. The triggering mechanisms for the earthquake swarms in West Bohemia are assumed to be fluids that rise up through the fault zones [6, 7, 17]. On the base of large-scale electrical resistivity tomography and gravity/GPS, data along an E-W striking profile crossing the PPFZ and MLFZ Nickschick et al. [18] mapped the crustal section of the eastern CB up to the depths of more than 1000 m. They proposed a conceptual model in which certain lithological layers (Cenozoic Vildstejn, Cypris, and Main Seam formation) act as caps for the ascending fluids. They hypothesize that any ascending fluid forced along impregnable and impermeable layers, and can only ascent along fractures at the PPFZ and MLFZ.

Aside from the Cheb Basin, CO_2 -dominated degassing occurs at two more degassing centers: Mariánské Lázně and Karlovy Vary [19–22]. These three resemble each other in

that all gases are CO₂-rich (>99 vol% CO₂) with high CO₂ flow and the same level of $\delta^{13}\text{C}$ values, but different levels of ³He/⁴He ratios [8, 19]. On the surface, this causes various degassing phenomena such as more than 100 mineral springs in Fratiškovy Lázně, Mariánské Lázně, and Karlovy Vary; Bad Brambach, Bad Elster, and Sybillenbad and surroundings; and mofettes in Soos, Hartoušov, and Bublák and north of Mariánské Lázně [17, 23]. The Cheb Basin is particularly interesting because of its high R_a values between 3.6 and 5.9 R_a (R_a = measured air-corrected He isotope ratios were divided by the ³He/⁴He of air [³He/⁴He_{air} = 1.384×10^{-6}]) points to almost undisturbed degassing from the lithospheric mantle [8, 17, 19–21]. In the Cheb Basin, the mineral springs escape along the WSW-ENE striking faults of the Eger Graben [23]. The mofettes themselves in Hartoušov and Bublák and north of Mariánské Lázně strike N-S and NW-SE [17, 23].

2. Research Area

The Bublák mofette field (BMF) is located in the Cheb Basin between Hartoušov and Milhostov (Figure 1). It is roughly 1000 m in length and 500 m wide. The Plesná river runs through the area and forms a valley, where wet and dry mofettes—cold emission spots of CO₂—are present. The thickness of Neogene sediments in the HMF (mudstones, sandstones, and lignite coals, deposited in a lacustrine environment) amounts to ~90 m [24]. The crystalline basement up to the final depth of the pilot hole HJB-1 consists of altered or/and weathered Palaeozoic mica schists.

Wet mofettes are pools of groundwater in which CO₂ rises to the surface, hereby leading to the bubbling sound the area was named after (see [17], supplementary data). Sub-surface transport of carbon dioxide is often accompanied by gas bubble collapses that act as noise sources and produce seismic signals. Flores Estrella et al. [25] locate noise sources with seismological investigations. Results suggest the presence of fluid channels to a depth of at least 30 m. The gases consist mainly of CO₂ (>99%), with traces of N₂, O₂, Ar, CH₄, He, and H₂ [26, 27]. Helium ratios were used as an indicator for the origin of the gas. As ³He related to the mantle, a high R_a (³He/⁴He) value points to a mantle origin. The high ³He/⁴He ratios at Bublák of ~5.9 R_a strongly indicate a subcontinental (lithospheric) mantle origin ($6.32 \pm 0.39 R_a$), which is supported by $\delta^{13}\text{C}_{\text{CO}_2}$ from -1.9 up to -4.2‰, higher than MORB (mid-ocean ridge basalt, [7, 19]). During an observation period between March and May 2006, an increase in the ³He/⁴He ratio from 5.9 up to 6.3 R_a at Bublák was observed [26] and interpreted as a hidden intrusion of magmatic material from a deeper source of the lithospheric mantle.

Dry mofettes, on which this work will focus, are visible at the surface in a change of the vegetation that occurs together with high degassing rates in the proximity of small vents (<0.2 m diameter) [28]. This is expressed in crippled vegetation that is less high and brown-colored because of chlorosis, meaning the insufficient production of chlorophyll. Different plant species in

the surrounding areas are also found in the dry mofette areas [29, 30]. Sometimes, the dry mofettes have vegetation-free depressions where soil CO₂ concentration and CO₂ flux are too high for plants to grow [29]. Because the ground in these areas is saturated with CO₂ [28], the organic material does not decompose as fast as in the surrounding areas and accumulates, which leads to an elevated ground level. No molehills exist in the CO₂ mofette areas and corpses of bugs and larger animals found around spots of high degassing [31]. For bugs, these act as natural pitfall traps [30].

Plants in CO₂ mofette fields are grouped into three categories: *mofettophobic* plants “that strictly avoid geogenic soil CO₂ at concentrations above 2–3 %”, whereas those that grow directly above strong CO₂ emanations are *mofettophilic*. Plants, that occur in degassing as well as in control areas are named *mofettovague*” [31, 32]. Sassmanshausen 2010 carried out measurements in the Bublák area in which he related the different plants to CO₂ concentration in different depths in the ground. As seen in [17], the mofettophilic plants consist of low, green, and brown grasses and mofettovague plants in this area are tall, brown grasses.

As the ascent of gases mostly depends on the existence of paths of higher permeability, it is possible to map out these fault zones by means of the gas flow distribution on the surface [23]. In [28], the gas flux was mapped in the Hartoušov mofette field (HMF) about a kilometer south of Bublák. They interpreted the degassing patterns they found as a pull-apart basin-like structure and suggested that the BMF is located in a different pull-apart basin, because of the difference in He-isotope trend and sediment fill ([28], Figure 10, inset).

A pull-apart basin consists of two parallel master strike-slip fault segments the so-called principal displacement zones and the oblique-extensional basin sidewall faults with an angle between them that is usually 30–35°. The proportion of length to width is usually 3:1, and they are shown as depressional structures [33]. According to Yuce et al. [34], who analyzed degassing in the Amik Basin (SE-Turkey), leakage occurs mainly at the basin sidewall faults.

The goal of this work is to check the pull-apart hypothesis proposed by [28] by mapping the CO₂ gas flux in the BMF and to compare it with the results from the HMF. During the course of the measurement, strategy was adjusted to the BMF and further developed.

3. Field Locations and Methods

3.1. Measurement Strategy and Field Locations. The measurements in this work were carried out during two periods in 2017 (August–September) and 2018 (August–October). The region (Bublák and Milhostov areas) is located about one kilometer north of the Hartoušov area, where Kämpf et al. [17] and Nickschick et al. [28] carried out their studies.

As shown in Nickschick et al. [28], an evenly spaced net of measurements is not reliable for dry mofette degassing areas like the Bublák and Milhostov areas because the

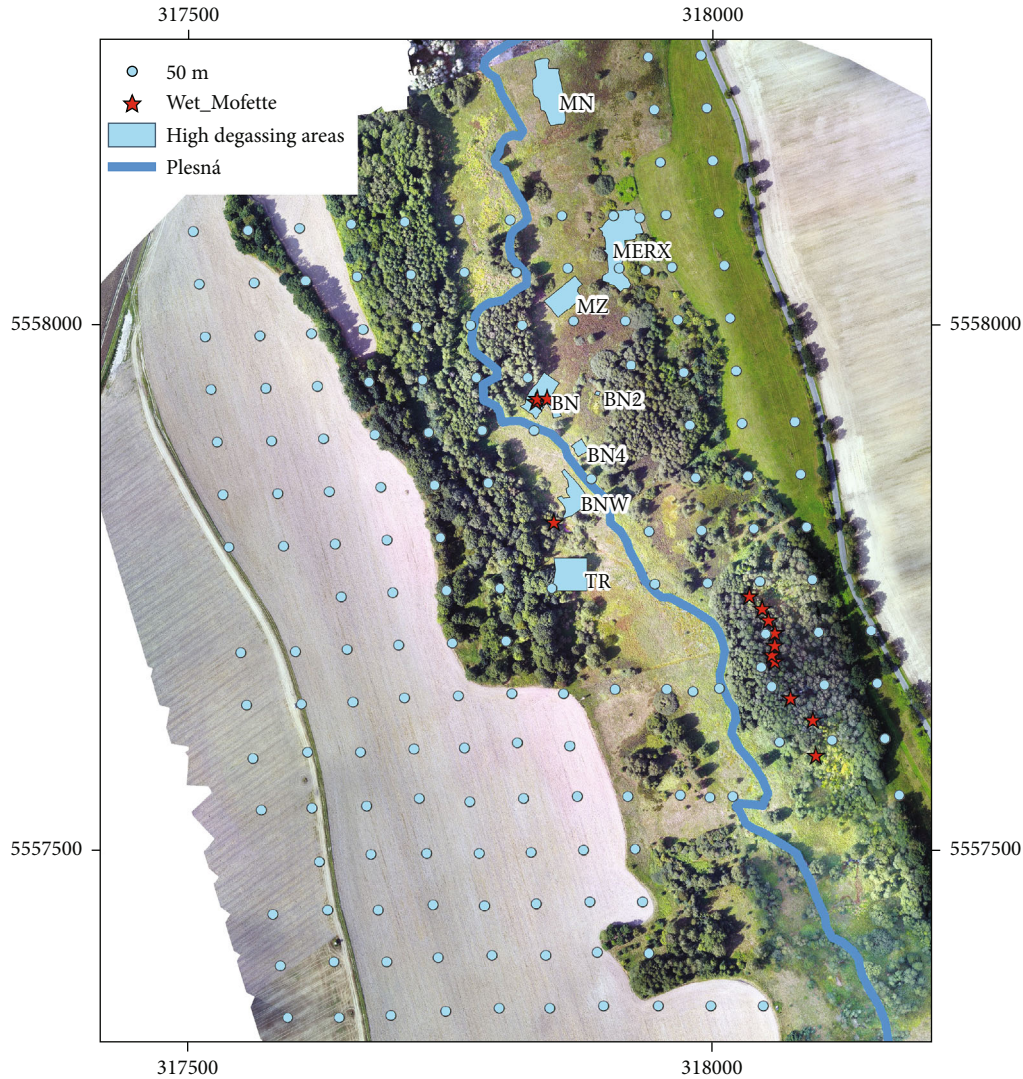


FIGURE 2: Overview of the Bublák and Milhostov areas. MERX: Milhostov East; MZ: Milhostov Central; MN: Milhostov North; BN: Bublák North; BN2: Bublák North 2; BN4: Bublák North 4; BNW: Bublák North-West; TR: trees.

amount of CO_2 discharged by single vents can be over- or underestimated if the sampling position is shifted only by a few decimeters [28]. They advise to use a measurement grid that decreases the distance between the points towards the high degassing zones, followed by proper data analysis. They used $20\text{ m} \times 20\text{ m}$ as the biggest distance for a grid. In a smaller area of the same region, Kämpf et al. [17] used a measurement grid with $10\text{ m} \times 10\text{ m}$ as the highest distance, also decreasing towards the high degassing zones.

Following the methodology of Kämpf et al. [17] and Nickschick et al. [28] on the one side and being restricted by the time at disposal on the other side, it was decided to start with a measurement grid of $50\text{ m} \times 50\text{ m}$ in 2017. This large point spacing for the big grid was chosen to detect high degassing areas and to quantify the background degassing while leaving enough time for accurate measurements. The areas where a high-density grid was placed were shown as brown color in the drone images. This was only possible because, as opposed to Hartoušov, the river valley of the

Bublák area is left in its natural state and not agriculturally used.

While the whole Bublák area is about 415.761 m^2 wide, the resulting eight smaller high degassing areas (Figure 2) are about 6.301 m^2 wide, amounting to 1,5% of the whole area (Table 1). This made it possible to focus on the high degassing zones with accurate measurements.

In 2018 (August-October), the high degassing areas were measured with a smaller spacing that was $2,5\text{ m} \times 2,5\text{ m}$ in the degassing center and $5\text{ m} \times 5\text{ m}$ or $10\text{ m} \times 10\text{ m}$ in the periphery. Some points were impossible to be measured as their locations were too wet or overgrown. Overall, 1.122 points were put, of which 1.115 were measured, each point once.

3.2. Gas Flux Measurements and Meteorological Conditions.

To quantify the rate of discharge at the surface, a portable diffuse flux meter made by West Systems (Italy, closed-chamber method) was used. The device includes both a LI-COR LI-820 CO_2 detector (Table 2) and a WS-HC CH_4 detector,

TABLE 1: Measurement parameters of the areas.

Year	Area name	Abbreviation	Measured area (m ²)	Ratio of measured area to total area (%)	Number of measured points
50 m grid					
2017	50 m	50 m	432.358	100%	179
Detected areas with high degassing					
	Milhostov East	MERX	1.685	0,39%	349
	Milhostov Central	MZ	703	0,16%	132
	Milhostov North	MN	1.337	0,31%	159
	Bublák North	BN	816	0,19%	127
2018	Bublák North 2	BN2	18	0,00%	8
	Bublák North 4	BN4	145	0,03%	23
	Bublák North-West	BNW	612	0,14%	71
	Trees	TR	985	0,23%	67
	Total		6.301	1,46%	936
2017 + 2018			432.358		1.115

TABLE 2: Technical data LICOR LI-820 (LI-COR, uncertainty and upper limit from [28] and the manufacturer's manual).

LI-COR LI-820					
Measurement range	0-20000 ppm				
Accuracy	3 % of measurement		Calibration drift:	Zero drift	<0,15 ppm/°C
Measurement principle	Nondispersive infrared			Span drift	<0,03%/°C
Uncertainty	4% (increases with flux as the chamber is saturated faster)		Upper limit	Up to 600 mol m ⁻² d ⁻¹ accurately measurable	

although the CH₄ detector was not used because the methane concentration of the Bublák mofette amounts to 2,5 ppm only [27] and is overshadowed by the sheer amount of emitted carbon dioxide.

Some of the fluxes were too high to be measured with high accuracy as the chamber filled in just a few seconds and some values were much larger than the accuracy limit of 600 mol m⁻² d⁻¹ and 26.406 g m⁻² d⁻¹, respectively. Nickschick et al. [28] already encountered this problem. To get a better accuracy for the data, they took multiple measurements in this case, as the chamber fills too fast and can only be estimated by repeated measurements.

Calibration of the sensor is only seldom needed and done by an expert. As such, no calibrations must be done during measurement of in the field. To calculate the gas flux, air temperature and barometric pressure also must be measured in the field. Using these, an accumulation chamber factor K is calculated which is multiplied with the value measured in the field in ppm s⁻¹ to obtain the gas flux in mol m⁻² d⁻¹. The calculation for K is done with the following formula (West [36]):

$$K = \frac{86400 * P}{10^6 * R * T_k} * \frac{V}{A}, \quad (1)$$

where K is the accumulation chamber factor, P is the barometric pressure in mbar, R is the gas constant 0,08314510 bar L K⁻¹ mol⁻¹, T_k is the air temperature in Kelvin, V is the volume of the accumulation chamber in

TABLE 3: Specifications of the accumulation chambers (West [36]).

	Chamber A	Chamber B
V	$2,756 * 10^{-3} \text{ m}^3$	$V = 6,878 * 10^{-3} \text{ m}^3$
A	$3,14 * 10^{-2} \text{ m}^2$	$A = 7,116 * 10^{-2} \text{ m}^2$

cubic meters, and A is the area of the accumulation chamber in square meters.

The device uses accumulation chambers with different volumes (Table 3) from which the accumulating gas is pumped to the LICOR-Detector. In the accumulation chambers, the gas is mixed by a fan, so that the CO₂, which is denser than air, does not form a separate layer. During the measurements, the accumulation chambers A (small) and B (big) were used. While chamber A is better for measuring small fluxes due to its increased sensitivity, chamber B is more accurate at gas fluxes above 1.000 g m⁻² d⁻¹ (West [36]).

While performing a measurement, the chosen chamber must be placed as airtight as possible on the ground to prevent an influx of air, especially during windy days [37]. Then, the measurement is started via the software "Fluxmeter" on a handheld computer that is connected to the flux meter by Bluetooth. During measurement, the software shows a curve with time on the x -axis and ppm of CO₂ or CH₄ in the gas in the accumulation chamber on the y -axis. The user now must find the best fit to the

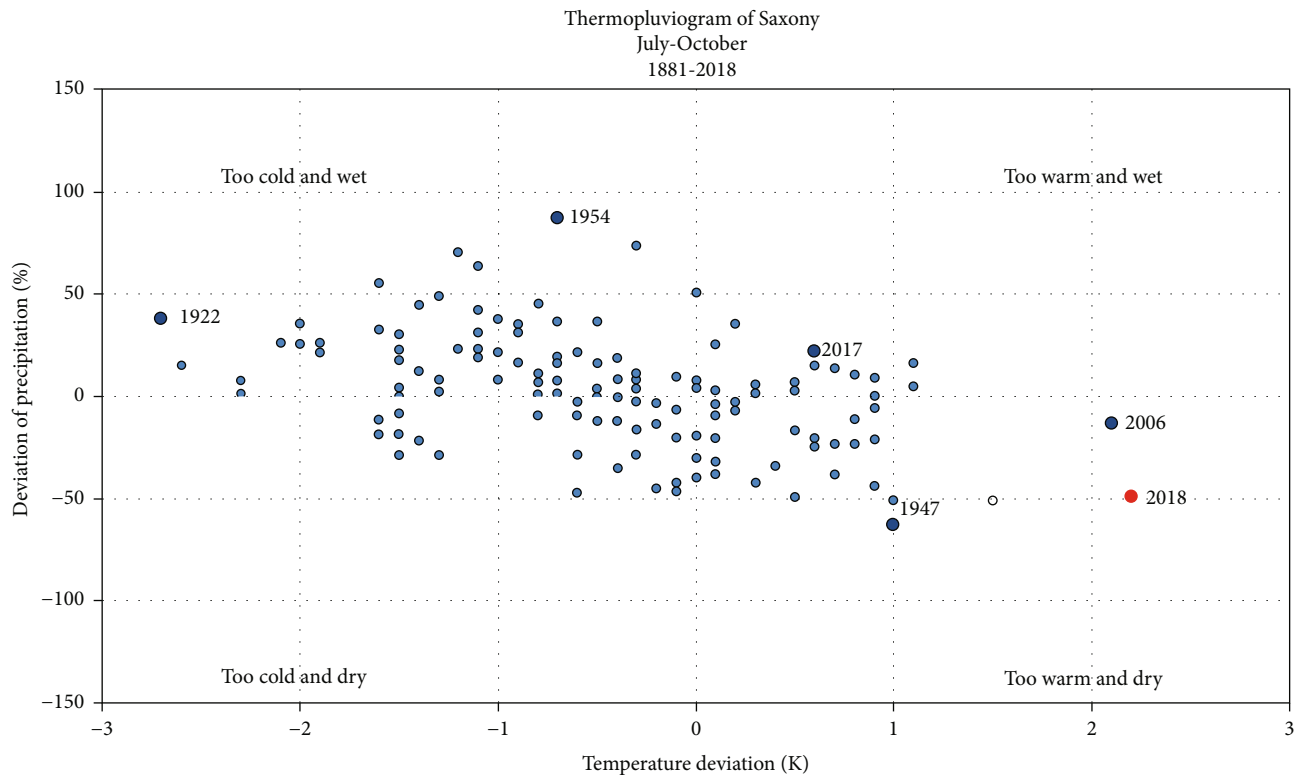


FIGURE 3: Deviation from long-standing average: summer of 2018 as an exceptional summer. Thermopluviogram of the Free State of Saxony, Germany (July-October, 1881-2018); DWD (German Weather Service, personal comm. 17.12.2018).

curve presented on the handheld computer. This method is called the closed chamber method and has been used since 1998, when Chiodini et al. [37] tested it in a volcanic area and found it to be a reliable and quick method.

For measurement, the ground must be dry, as water would show the same signature as CO_2 in the infrared LICOR sensor and falsify the measurements or damage the sensor through condensation [37]. To minimize the risk of this, a desiccant was placed between the accumulation chamber and the sensor. Additionally, measurements in dry periods are generally preferred as rain and soil humidity may influence soil-gas concentrations [38]. This is especially the case in an area such as this one where beneath the soil is a layer of clays [39]. To prevent biogenic influence by plants and to guarantee an airtight environment within the chamber as much as possible, a hole of 30 cm depth was dug before measurements.

As seen in Figure 3, the summer of 2018 in Central Europe including Saxony and working area in the western Eger Rift was exceptional in being the warmest summer and one of the driest summers since 1881. This led to areas that were swampy in the year before being dry and measurable (e.g., surrounding MZ). It was also possible to measure directly after digging the holes because the ground was dry even in 30 cm depth. While 2017 still was relatively warm, it was sometimes necessary to let the ground dry for a day or two after digging the hole. This is also reflected in the thermopluviogram below (Figure 3), where the summer of 2018 is the warmest and one of the driest summers on record,

while the summer of 2017 was still warm, but not nearly as warm as 2018 and a little wetter than average.

3.3. GPS Measurements

3.3.1. Handheld GPS. The points for the 50 m grid were calculated before measuring. To find the correct coordinates in the field, a handheld Garmin GPSMAP 60CSx was used, as the device showed the coordinates in real time. The handheld GPS was used because even though the error of this device and most handheld GPS is in the range of several meters, in the densely vegetated Plesná area, it is still more accurate and quicker than measuring the distance by hand.

3.3.2. Differential GPS. For the areas of high degassing, a point-to-point distance of 2,5 m was used because of the high differences in gas flux and tectonic control of degassing over small distances. As the error of the handheld GPS would have been close to—or sometimes even higher than—the distance between the points themselves, a differential GPS (D-GPS) with a higher accuracy than the handheld GPS was used.

The available D-GPS was a 1200+ by Leica, which uses a reference station that remains stationary during the measurements and a rover antenna which is carried to the data points and collects data for several minutes. As there was a constantly high number of satellites receivable, a single point only took two minutes to measure. Because the D-GPS was only available for two weeks during the second measurement period, measuring all the points would have taken too long.

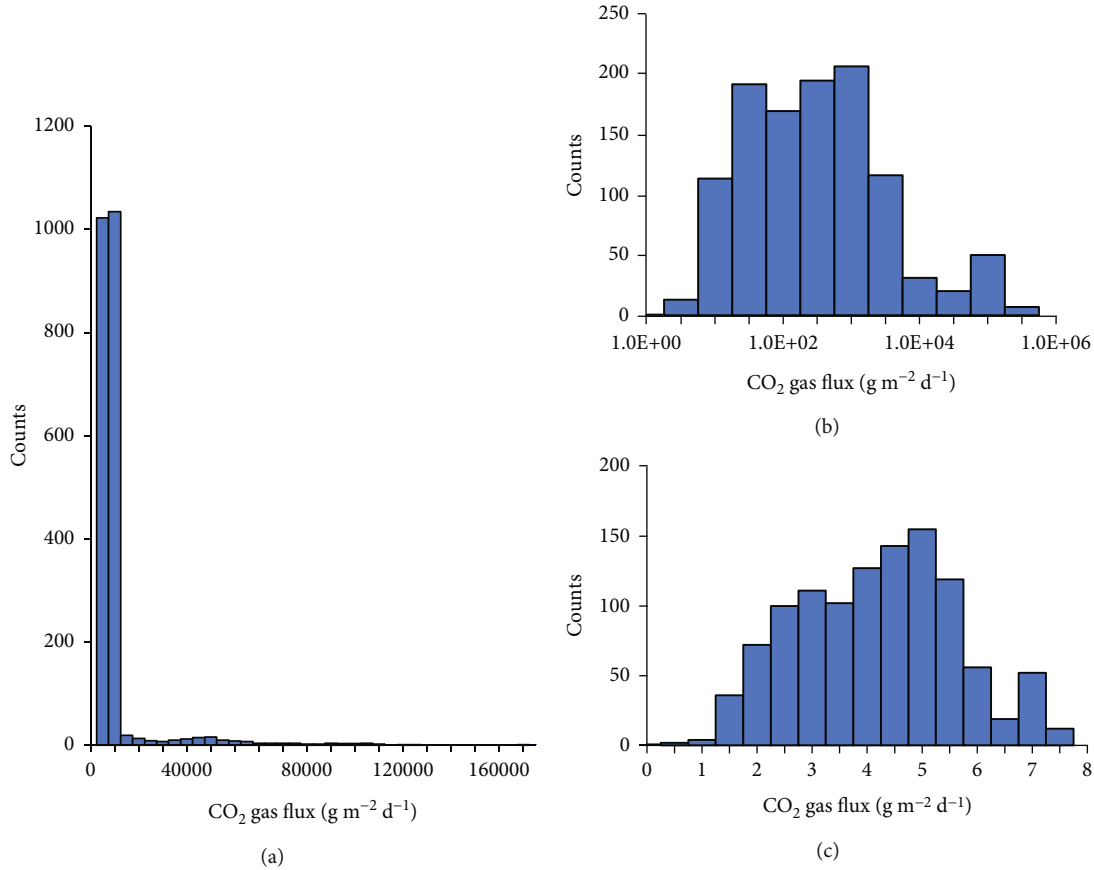


FIGURE 4: Gas flux in g m⁻² d⁻¹: (a) the dataset; (b) displaying the data on a logarithmic scale; and (c) the box-cox transformed dataset with -0,093 as lambda.

Therefore, it was decided to take a high-resolution drone image after digging the holes for the measurements, georeference it, and then insert the points in ArcGIS (Figure 2).

3.4. Drones. During the measurements, multiple drone images were taken. At the beginning of the measuring period in August 2017, an image was taken, providing an overview of the area. In October 2018, a high-resolution drone image was taken to reduce the time needed for the GPS measurements.

To obtain the images, DJI Phantom 4 was used. This drone provides the possibility to take 4K images and has a flight time of 30 minutes. The drone can either be controlled by the user or follow a preset path and automatically take a picture every second. The resulting pictures were stitched together, creating an orthophoto, using the software Agisoft.

The drones have built-in GPS for orientation and geotagging of the images. To get more accurate images, Ground Control Points (GCPs) can be set, whose coordinates were obtained by using the D-GPS and then used for georeferencing. This method was used for the drone image taken in October 2018, which shows the northern part of the area where most dry mofettes are located.

The drone image from 2017 offers less detail but covers the whole area (Figure 2). It is also less accurate because it

did not use GCPs for georeferencing. However, it was useful for identifying degassing structures by their brown color because it was taken in August as opposed to the 2018 image that was taken in October when many of the plants around the mofettes already started changing color.

3.5. Geostatistical Data Analysis

3.5.1. Interpolation of Missing Values. To be able to quantify the gas flux for the whole area as accurately as possible, the values need to be interpolated for the unmeasured areas. This was performed using the Software ArcGIS, which provides various geostatistical methods. After the prediction was done, the calculated values were divided into 1 m² sized cells to obtain the calculated values for each square meter for further calculations.

As the results of this study should be comparable to the results from Nickschick et al. [28], the same methods for data analysis were applied. The used methods were arithmetic mean, ordinary kriging, and trans-Gaussian kriging. An exception to this is the radial basis function, which was not used, as its direct interpolation of the measurement points leads to a severe overestimation of degassing as in Nickschick et al. [28]; the data of this work did not follow a normal/Gaussian distribution (Figure 4(a)), and the standard deviation was very high.

3.5.2. Arithmetic Mean. Gilbert [40] and Lewicki et al. [41] said that the arithmetic mean can be used to estimate the amount of ejected CO₂ if it is normally distributed.

As discussed in [28], the arithmetic mean is not suitable for interpretation due to its high mean and standard deviation that are derived from the skewedness. It is nevertheless the simplest method to calculate an average and overall degassing and might be sensible to use in case no computer with ArcGIS is available and if the person is aware of the errors done by this method.

3.5.3. Ordinary Kriging. Kriging estimates values for locations without measured points. It takes the spatial distribution of the measurement points into consideration but overestimates minima and underestimates maxima [28], (Figure 4(b)). Therefore, the standard deviation will be lower than by using the arithmetic mean, but it will still overrate the actual amount of degassing. The formula for kriging is as follows:

$$\hat{Z}(s_0) = \sum_{i=1}^N \lambda_i Z(s_i), \quad (2)$$

where $Z(s_i)$ is the measured value at the i -th position, λ_i is the unknown weighting for the measured value at the i -th position, s_0 is the predicted position, and N is the number of measured values [42].

3.5.4. Trans-Gaussian Kriging. For non-Gaussian distributions of the measured values, all standard geostatistical methods will provide an incorrect estimation. Normally, a simple transformation such as a data transformation into a logarithmic scale suffices, but here, the data is heavily skewed even after doing so. For trans-Gaussian kriging, the dataset is transformed by using a power transformation such as the box-cox transformation to make the data as normally distributed as possible (Figure 4(c)) and then interpolated by kriging. Afterwards, the data is transformed back by ArcGIS and can be used for further calculations. The formula for the Box-cox transformation for values of λ that are not equal to zero is as follows:

$$X^\lambda = \frac{X^\lambda - 1}{\lambda}, \quad (3)$$

where X is the measured value and λ is the power parameter [43].

The value for λ that would best transform the dataset is -0,093. As ArcGIS only allows values for lambda larger or equal to -0,1, this value was used instead. Please note that also other ways of data transformation exist (such as the normal score transformation in ArcGIS).

4. Results

4.1. Overview of Soil CO₂ Survey. The entire investigated area has a size of 432.358 m² (0,43 km²) in which 1.115 points have been measured (Figure 5). The highest observed gas flux is 177.926,17 g m⁻² d⁻¹ close to the center of the MZ area. The

lowest measured value is 0,28 g m⁻² d⁻¹ and is in the western edge of the 50 m grid. Overall, higher gas fluxes are observed in the floodplain of the Plesná.

The overall degassing varies by several orders of magnitude by using different methods for calculation and visualizes how improper data analysis leads to severely incorrect estimations. 1.638 t d⁻¹ calculated by using the arithmetic mean as an overall value for the degassing is likely to be a huge overestimation due to the influence of the high skewedness. The true overall degassing per day for the area is likely to be between 30 t d⁻¹ and 154 t d⁻¹, calculated by trans-Gaussian kriging and kriging, respectively (Table 4).

As the CO₂ is emitted from small vents, high degassing values occur in their proximity [44] which leads to few measured values contributing to most of the measured CO₂. In this case, 90% of the total CO₂ are discharged by the top 66 highest values which make out 5,9% of all data and 99% by the top 155 (13,9%) values. This again illustrates the high skewedness of the data and the influence of the small degassing channels on the overall degassing.

To estimate the amount of degassing from an external source—in this case from the mantle—the gas fluxes can be divided into three different categories (as seen in [45]). Population A represents the biogenic background degassing with 25 g m⁻² d⁻¹, a value that has been suggested by Kämpf et al. [17] based on carbon isotope measurements of soil gas. This value is close to the 27 g m⁻² d⁻¹ that were calculated as an average for the 50 m raster and thus a sensible estimation for the background degassing by plants and soil in this area. Population B represents a zone of mixture between biogenic and endogenic degassing with an upper limit of 100 g m⁻² d⁻¹. Every value above this belongs to population C and indicates endogenous degassing (Table 5).

It can be stated that 56% of all measured data belong to population C, endogenous. For the surveyed areas, MERX has the highest percentage (77%) for this population. For every area except for 50 m, population C has an average degassing two orders of magnitude higher than populations A and B (Table 5). For population C, area BN24 has the highest average with 10.678 g m⁻² d⁻¹, making up 62% of the total measured values in this area. The lowest average of population C has 50 m with 336 g m⁻² d⁻¹ (3% of all measured values).

4.2. Surveyed Areas. Figures 6 and 7 show the measurement points for the surveyed areas color-coded by their CO₂ soil gas flux. White dots represent population A, and yellow represents population B. Population C has been split into values above 500 g m⁻² d⁻¹ which are shown in red and values between 100 and 500 g m⁻² d⁻¹ in green to make the central areas of the mofettes visible.

4.2.1. 50 m. Only 3% of the values in the 50 m area belong to population C as opposed to the average 56% (Table 5). The highest measured flux is 488,18 g m⁻² d⁻¹ in the forest on the eastern side of the Plesná and the smallest 0,28 g m⁻² d⁻¹ near the southwestern corner of the grid, which is also the smallest measured value overall.

Figure 5 shows that most degassing, higher than background degassing, is in the Plesná valley and not in the

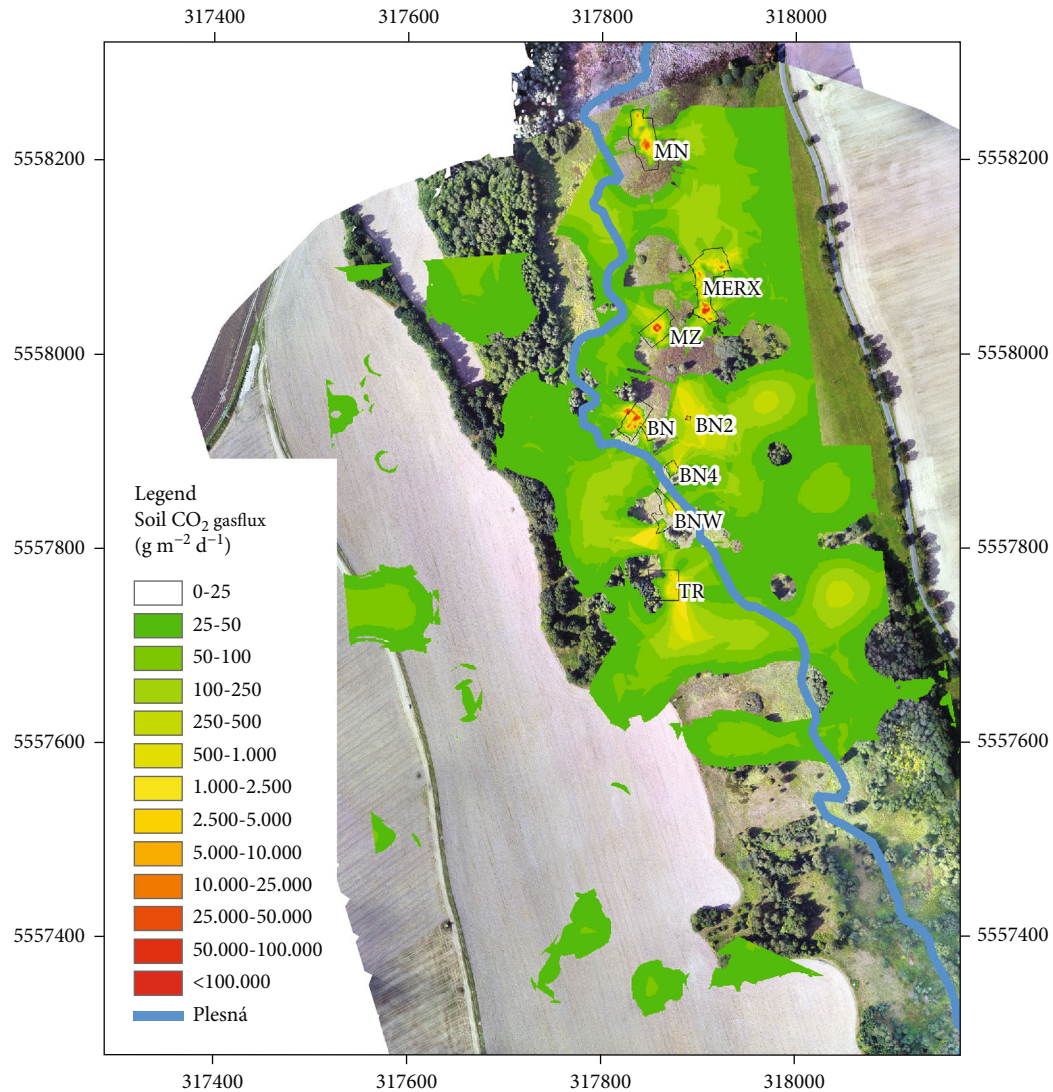


FIGURE 5: Quantified CO₂ soil gas flux for 1 m² after interpolation of 1.115 measuring points in the Bublák mofette field using trans-Gaussian kriging.

TABLE 4: Averages and totals for the whole area through different methods.

Method	Average (g m ⁻² d ⁻¹)	Overall (t d ⁻¹)
Arithmetic mean	3.996	1.638
Kriging	370	154
Trans-Gaussian kriging	73	30

agriculturally used fields in the east of the area. An exception to this is the meadow to the west of the valley where there is constantly slightly higher degassing than the background value. The forest where most of the wet mofettes are located has predominantly low degassing values, except for its north, where the highest degassing value of the 50 m raster was recorded.

4.2.2. Milhostov East (MERX). The Milhostov East area (Figure 6(a)) is the largest area with the most measure-

ment points (Table 6). Most of the area is elongated in a N-S direction and would be oval shaped if not for the degassing close to the field. It consists of multiple anomalies that are distinguishable from each other in Figure 5, but less in Figure 6(a), as most of the area has endogenous degassing. The areas with brown vegetation show an overlap with areas of endogenous degassing. For example, degassing decreases towards the solitary bush in the upper middle of the degassing area.

MERX is the area with the second-highest maximum degassing (125.773,33 g m⁻² d⁻¹). The lowest degassing value is 8,43 g m⁻² d⁻¹. 77% of the measured values belong to population C.

4.2.3. Milhostov Central (MZ). The Milhostov Central area (Figure 6(b)) consists of a singular, round anomaly that is very well visible in the 2017 drone image and Figure 6. The zone of endogenous degassing is bigger than the zone of brown vegetation, but otherwise very similar in shape and location.

TABLE 5: Estimated parameters and partitioned populations of the measured data in the surveyed areas.

Name	Population	Proportion (%)	Average gas flux ($\text{g m}^{-2} \text{ d}^{-1}$)	90% confidence ($\text{g m}^{-2} \text{ d}^{-1}$)		Overall (t d^{-1})
				+	-	
50 m	A (background)	72	11,3	12,1	10,4	0,001
	B (background)	25	38,3	41,1	35,5	0,002
	C (endogenous)	3	336,1	435,2	237,1	0,002
	Total	100	27,3	34,6	20	0,005
MERX	A (background)	5	17,8	19,7	15,9	0,0003
	B (background)	18	63,5	68,7	58,4	0,004
	C (endogenous)	77	6.779,6	8.830,4	4.728,8	1,83
	Total	100	4.911,0	6.413,9	3.408,1	1,83
MZ	A (background)	20	16,8	18,6	15,1	0,0004
	B (background)	26	46,8	51,5	42,1	0,002
	C (endogenous)	55	8.791,3	13.759,8	3.822,7	0,8
	Total	100	6.092,3	9.592,3	2.592,4	0,8
MN	A (background)	15	9,8	11,7	7,8	0,0002
	B (background)	19	52,1	57,9	46,2	0,002
	C (endogenous)	66	4.643,2	6.299,5	2.986,8	0,56
	Total	100	3.549,3	4.923,5	2.175,0	0,56
BN24	A (background)	25	10,1	11,4	8,8	0,0004
	B (background)	13	53,7	62,7	44,7	0,001
	C (endogenous)	62	10.677,5	13.630,8	7.724,3	1,05
	Total	100	6.632,1	8.584,8	4.679,4	1,05
BNW	A (background)	46	6,5	7,7	5,4	0,0002
	B (background)	19	57,3	66,4	48,2	0,001
	C (endogenous)	36	3.082,0	6.021,0	143,1	0,08
	Total	100	1.114,4	2.202,9	25,8	0,08
TR	A (background)	15	12,4	15,3	9,4	0,0001
	B (background)	12	57,2	69,9	44,6	0,0005
	C (endogenous)	73	2.222,7	3.962,3	483,1	0,11
	Total	100	1.634,3	2.921,4	347,1	0,11
Total	A (background)	25	11,4	12,1	10,8	0,003
	B (background)	19	52,8	55,3	50,3	0,01
	C (endogenous)	56	7.098,0	8.401,7	5.794,3	4,43
	Total	100	3.996,0	4.747,7	3.244,2	4,44

In its center, there are multiple vegetation-free depressions. In one of them, the highest degassing value in all the areas ($177.926,17 \text{ g m}^{-2} \text{ d}^{-1}$) was found. The lowest degassing value is $6,85 \text{ g m}^{-2} \text{ d}^{-1}$. 55% of the measured values belong to population C.

4.2.4. Milhostov North (MN). The Milhostov North area (Figure 6(c)) is the northernmost of the measured areas. Like MERX, it is elongated in a roughly N-S direction. It has a large degassing anomaly in the south and a smaller one in the north. The areas with brown vegetation overlap very well with the areas of endogenous degassing.

66% of the measured values belong to population C. The highest degassing value is $79.591,73 \text{ g m}^{-2} \text{ d}^{-1}$, one of the moderate values for maximum degassing. The lowest value in this area is $2,29 \text{ g m}^{-2} \text{ d}^{-1}$ (Table 6).

4.2.5. Bublák North (BN24). As both BN2 and BN4 are small degassing structures, they have been combined with BN for analytic purposes to form BN24 (Figure 7(a)). BN, the largest of these areas, has wet mofettes that have been measured before in addition to the dry degassing area that surrounds these. One of these wet mofettes has been artificially made by drilling. It might be either a large, circular anomaly or multiple clustered small anomalies as there are some points of midhigh degassing among points of very high degassing. To the south of the area, there is an offshoot of high degassing that is obvious in the drone image due to its brown color.

The Bublák North 2 area is the smallest measured degassing area, with an extent of only 18 m^2 . It is located about 40 m to the east of BN in an area that is otherwise covered with water due to a spring close to the road. This degassing area is elevated and therefore dry and measurable. Nine

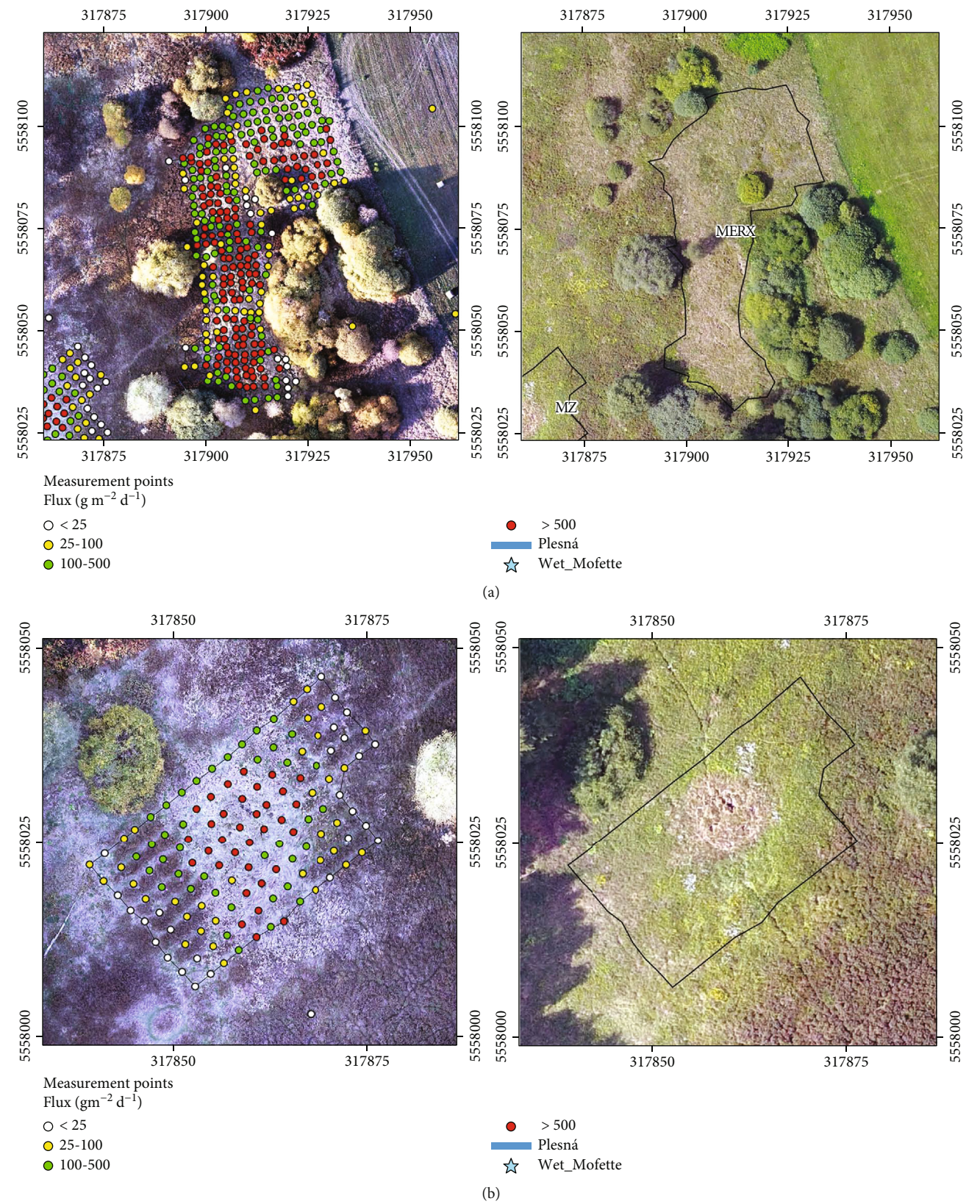


FIGURE 6: Continued.

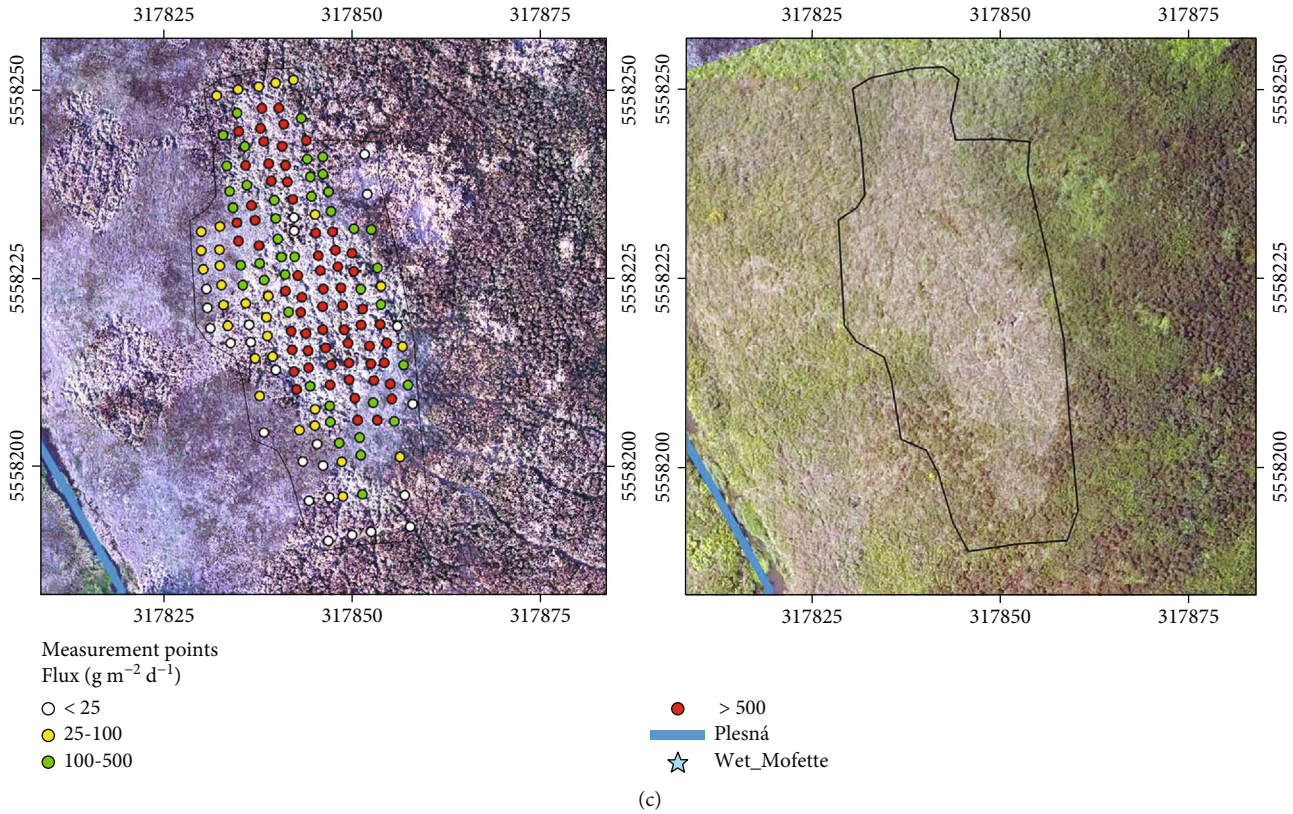


FIGURE 6: Soil CO₂ gas flux for (a) MERX, (b) MZ, and (c) MN. Left: October 2018 drone image with partitioned populations. Right: August 2017 drone image.

points were placed in a cross shape with a spacing of 1 m in the elevated, circular area of which one could not be measured as water started collecting in the hole.

Bublák North 4 by itself is the least prominent anomaly, the maximum of degassing being an order of magnitude lower than the next largest anomaly (Table 6). Nevertheless, it is still visible in the drone images (Figure 7(a)) as an area of brown-colored vegetation exists that is a bit north of the spots with the highest degassing.

62% of the analyzed data for all 3 areas of Bublák North belong to population C. The highest measured value is $60.255,82 \text{ g m}^{-2} \text{ d}^{-1}$ and the lowest $2,89 \text{ g m}^{-2} \text{ d}^{-1}$. In the drone image, due to its size and coloring, BN is easily spotted. BN2 also has an obvious coloring, and BN4 is less visible.

4.2.6. Bublák North-West (BNW). The BNW dry degassing area (Figure 7(b)) was named after the wet mofette Bublák North-West, which is located in the east of that area [17]. Degassing is the highest towards the Plesná and the wet mofette and low in between. The change of color in the vegetation is less obvious in this area compared to other ones, even when looking at the 2017 drone image that is usually better at showing these structures. Figure 7(b) reveals BNW as two separate anomalies of endogenous degassing with a small zone of background degassing in between.

Maximum degassing in this area is $46.386,81 \text{ g m}^{-2} \text{ d}^{-1}$ in the anomaly close to the Plesná, with a minimum of $1,35 \text{ g m}^{-2} \text{ d}^{-1}$, thus being the area with the lowest maximum.

36% of the measured values belong to population C, the smallest share in any of the high degassing areas.

4.2.7. Trees (TR). The trees' area (Figure 7(c)) sits close to a forested area. Due to the shadow in the drone image, the different coloring of the vegetation is hard to see but exists. The 2017 drone image shows areas of brown grass further south of the measured area, which was not possible to see in the field in 2018. The amount of endogenous degassing generally increases with distance to the forested zones. Any further observations on the shape of the degassing zones are hard to make, as not enough points have been placed and measured towards the east.

The highest degassing occurs in the northeast of the area where there are several vegetation-free spots ($49.889,41 \text{ g m}^{-2} \text{ d}^{-1}$) and is lowest in the forested area with $4,06 \text{ g m}^{-2} \text{ d}^{-1}$. 73% of the measured points belong to population C.

5. Discussion

5.1. Measurement Strategy and Field Locations under Consideration of Mofette Vegetation. The zonation of vegetation in mofette areas can be used as a very important indication to subdivide the areas. According to Figure 8, the mofettophobic zone is located where CO₂ gas flux amounts to $< 25 \text{ g m}^{-2} \text{ d}^{-1}$; the mofettovague zone is defined by CO₂ gas fluxes between 25 and $500 \text{ g m}^{-2} \text{ d}^{-1}$. Mofettophilic plants grow at CO₂ gas fluxes $> 500 \text{ g m}^{-2} \text{ d}^{-1}$.

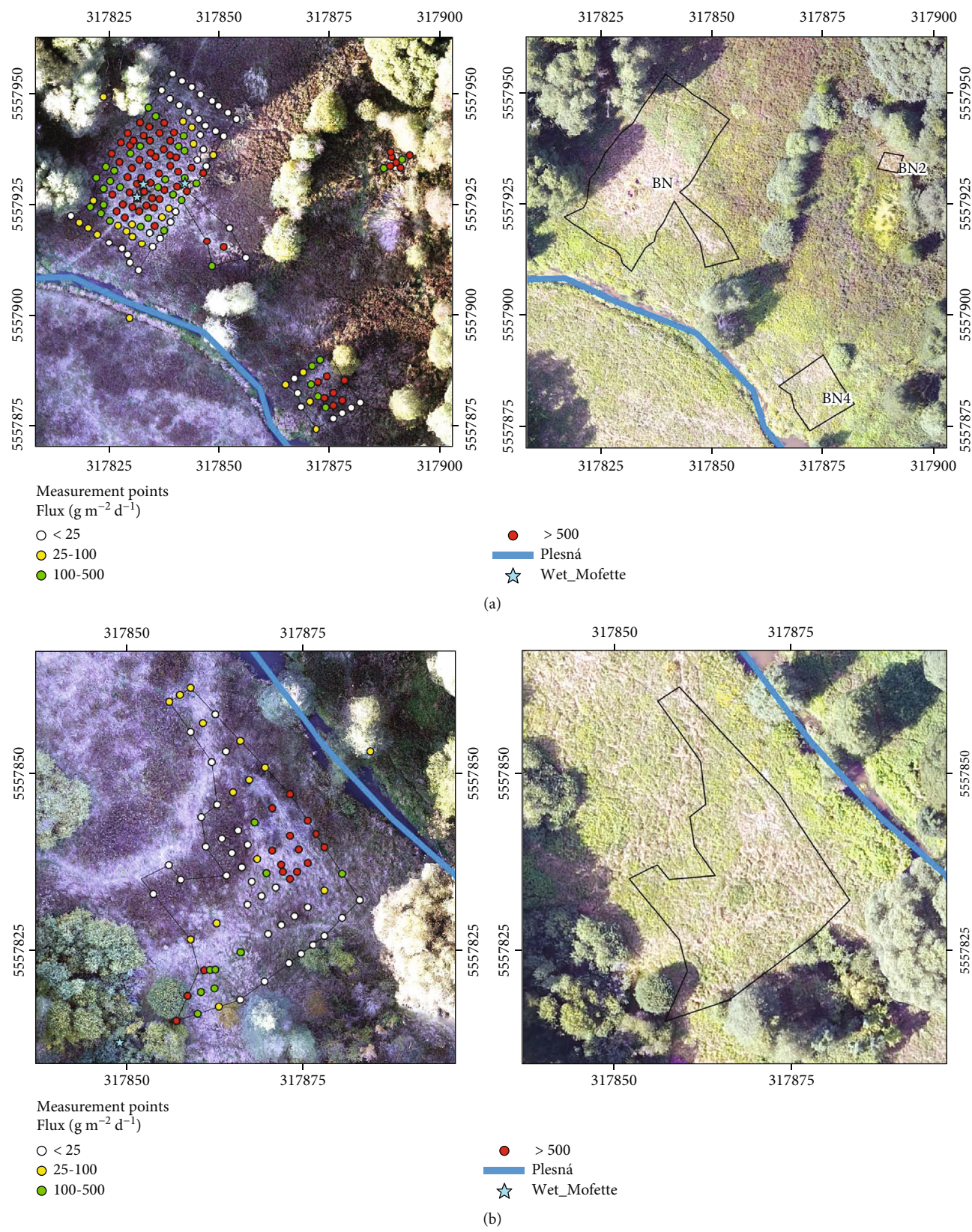


FIGURE 7: Continued.

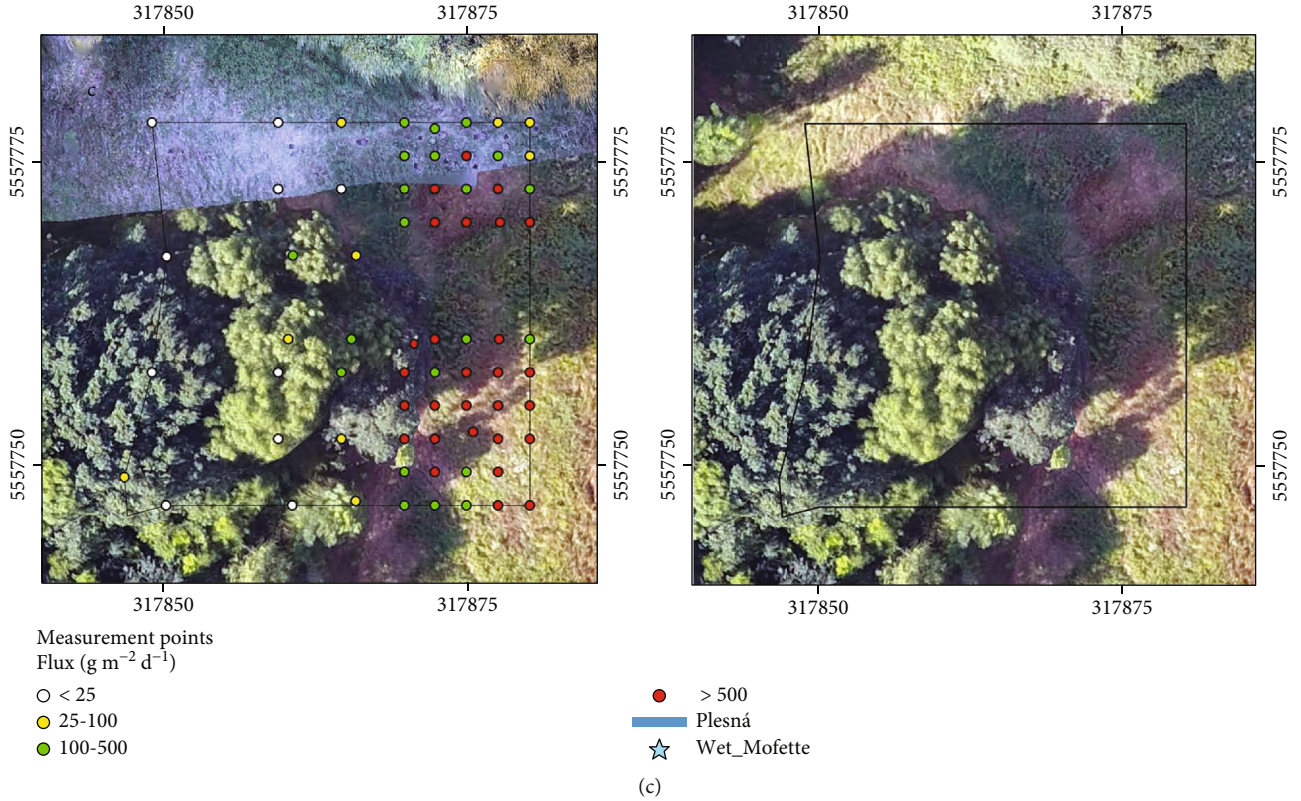


FIGURE 7: Soil CO_2 gas flux for (a) BN24, (b) BNW, and (c) TR. Left: October 2018 drone image with partitioned populations. Right: August 2017 drone image.

TABLE 6: Main parameters of the surveyed areas.

Area	Extension m^2	Average flux $\text{g m}^{-2} \text{d}^{-1}$	Median $\text{g m}^{-2} \text{d}^{-1}$	Min. flux $\text{g m}^{-2} \text{d}^{-1}$	Max. flux $\text{g m}^{-2} \text{d}^{-1}$	Number of points
50 m	432.358	27	14	0,28	488,18	179
MERX	1.685	5.257	326	8,43	125.773,33	349
MZ	703	6.092	128	6,85	177.926,17	132
MN	1.337	3.549	261	2,29	79.591,73	159
BN24	979	6.632	209	2,89	60.255,82	158
BNW	612	1.083	34	1,35	46.386,81	71
TR	985	1.634	334	4,06	49.889,41	67

Sassmannshausen [30] mapped BN24 and MERX botanically and specified mofettophobic, mofettovague, and mofettophilic plant communities and demonstrated a correlation between them and the CO_2 soil gas concentration in different depths. This work proves, as first in the area, the relationship between vegetation and CO_2 gas flux. This is not surprising, as gas concentration and gas flux are mostly related [17, 28] but make mapping of CO_2 gas flux easier because the point spacing can be adjusted according to plant zonality to the presumed gas flux. Areas with mofettophilic vegetation should, for high accuracy, be measured with a point spacing of 2,5 m. In mofettovague areas, this can be stretched to a distance of 5 m. Mofettophobic areas around a mofette can have a spacing of 10 m. Placing at least one row of points around a mofette in the mofettophobic zone would ensure better kriging results.

This relationship is not as clear for BNW, the area with the lowest average degassing and percentage of values in population C except for the 50 m grid. Neither the 2017 nor the 2018 drone image provides clear information about the location of high degassing. Mapping of gas flux solely based on the vegetation will be difficult in such a case and will certainly lead to oversight of some dry mofettes. Other problems for this approach are agriculturally used areas, as there is no chance for the characteristic vegetation to grow. Botanic zonation could be used for defining a measurement strategy for CO_2 gas flux measurements in the highest degassing areas of the agriculturally not used Plesná valley.

5.1.1. GPS Measurements and Drones. The drone images were a great help during the measurements, especially for

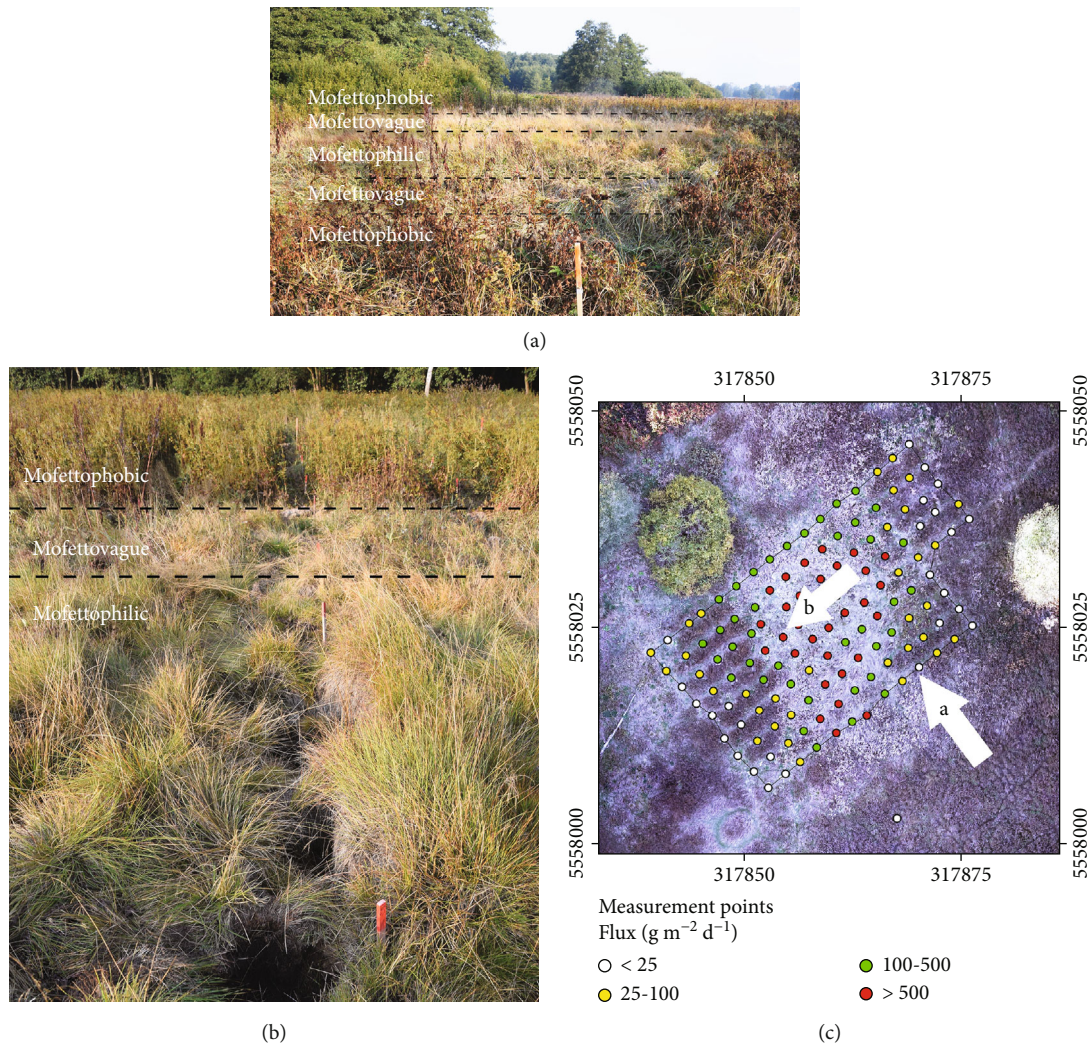


FIGURE 8: Mofette vegetation. (a) View of the MZ from the southern edge to the NW. (b) View of the MZ from the center to the SW. (c) Soil CO₂ gas flux and location and direction of (a) and (b).

locating the high degassing areas. They allow for a better overview than in the field and are good for verifying the high degassing areas. It is sensible to take the images in spring or early summer as the contrast between the types of vegetation is high (Figures 6 and 7).

The combination of GPS measurements and drone images has been proven to be efficient, accurate, and useful. Measuring every single point would have taken at least 37 hours of pure measurement time. Putting the points with ArcGIS still took around 12 hours but freed up valuable time in the field. This method however requires thorough work in the field as one needs to be sure where each point is. Points covered by foliage need to have their coordinates taken with the GPS. Ideally, points should be left untouched between digging the hole and taking drone pictures so that they do not get buried.

5.1.2. Measurement Grid and Data Analysis. Having a point spacing of 50 m × 50 m for the overview grid had advantages, but also disadvantages. A grid of this size

made it possible to measure the high degassing areas very accurately, which was necessary for the study. However, problems that were encountered during data analysis would not have been as bad, if a 20 m × 20 m grid would have been used. Finding the correct parameters for trans-Gaussian kriging proved to be difficult due to the poor point distribution (few high distances, many small distances).

This leads to the trans-Gaussian kriging predicting high degassing values for areas that probably do not actually have these as there is no change in vegetation. This problem occurs especially in areas where high degassing values (population C) are on the outer edge of the grid. This is especially striking around BN2 area (Figure 5), where all the measured points have degassing values above 100 g m⁻² d⁻¹ which leads to a calculated area of high degassing that is much larger than what would be assumed from observations in the field. On the other hand, this partially outweighs the oversight of potential moderate degassing spots that are not visible on the orthophoto or by vegetation changes.

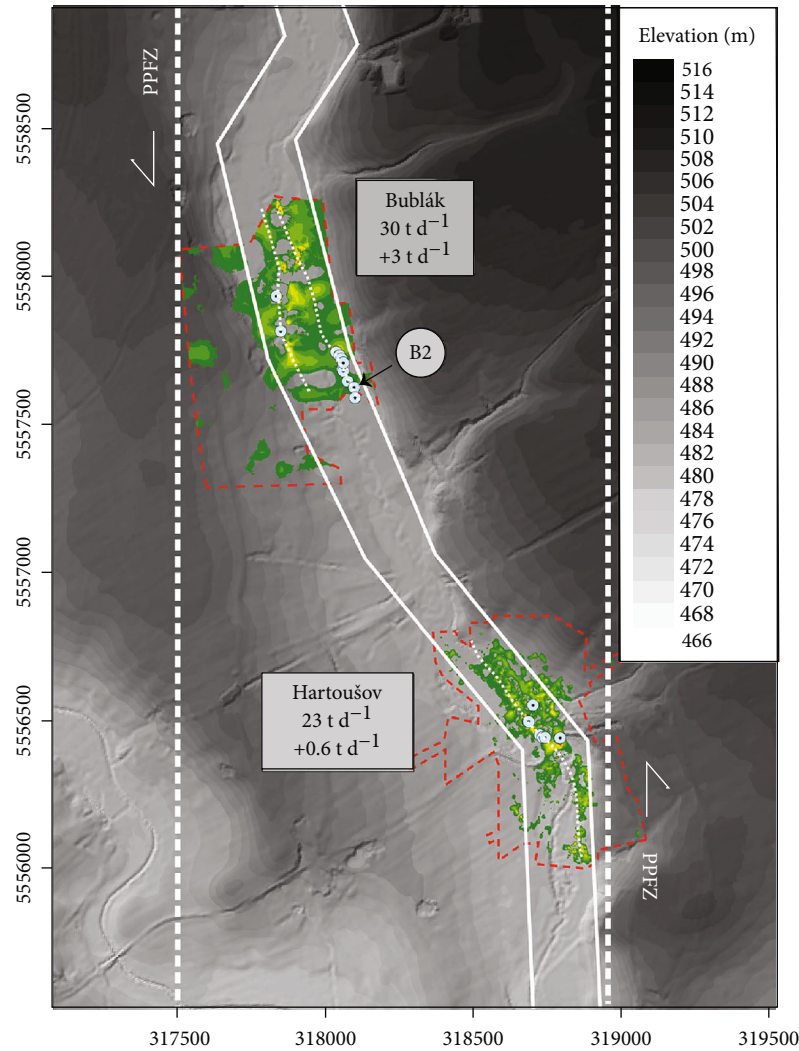


FIGURE 9: Structural setting of the Hartoušov and Bublák mofette fields with the locations of DDS and wet mofettes (blue dots).

For further measurements, the overview raster should be kept to a point distance of $20\text{ m} \times 20\text{ m}$ and areas of high-density measurements should be around 10 m larger than the mofettevague zone to avoid problems with data analysis. Alternatively, a small spacing could be kept for the entire BMF zone, which however would not be economical due to the harsh and sturdy vegetation.

5.2. CO_2 Degassing at the Počátky Plesná Fault Zone: Comparison of Bublák and Hartoušov Mofette Fields. In Figure 9, the results from the gas flux measurements of Nickschick et al. [28] which include the results from Kämpf et al. [17] and this study are shown. Overall, 4,647 measurements were carried out in an area of $780,000\text{ m}^2$ between 2009 and 2018 (April–October). The overall degassing for the HMF is likely somewhere between 23 t d^{-1} and 97 t d^{-1} and for the BMF between 30 t d^{-1} and 154 t d^{-1} with a respective average of $65,2\text{ g m}^{-2}\text{ d}^{-1}$ and $73\text{ g m}^{-2}\text{ d}^{-1}$ for trans-Gaussian kriging. We favor the values of 30 t d^{-1} and 23 t d^{-1} , as they are the results of the geostatistically most solid estimation. There are N-S, NNW-SSE, and

NW-SE striking degassing elements present in both. Therefore, the two mofette fields are comparable in their CO_2 gas flux and tectonics.

From the original interpretation of the fault appearance, some modifications had to be transferred to the location of the PPFZ. Its western part should be moved to the east, to where the N-S striking degassing is located. No changes are necessary for the eastern part.

The distribution of the degassing areas leads to the following two possible interpretations keeping in mind the pull-apart aspect:

- (1) There exist two pull-apart basin-like degassing structures as hypothesized in Nickschick et al. [28]. In this case, the wet mofettes in the BMF form the southern basin sidewall fault as the areas with the highest degassing occur north of them. The dry mofettes would form one of the principal displacement zones. This would mean that, to confirm this theory, surveying for dry degassing areas north of the measured area would be needed.

- (2) Contrary to information from Nickschick et al. [28], only one pull-apart basin-like degassing structure exists. The HMF and BMF would be part of the northern or southern basin sidewall of a pull-apart basin.

The second theory seems to fit the observations better, as the length to width ratio of such a basin could be around 3:1 with an acute angle of around 30°, as most of the earth's pull-apart structures do. In Nickschick et al. [28] and the first theory, this is not kept in mind as the suggested pull-apart basins are not long enough. However, both theories have the problem that, except for the river valley, there is no explicitly depressive topography and the sediment thickness is less in the center of the suggested pull-apart basin than in the margin ([28], Figure 9). This is contrary to what would be expected [34]. Yuce et al. [34] also located the zones of the highest degassing rates at the basin sidewalls. The Bublák dry degassing areas do not follow this direction, but rather the direction of what would be a principal displacement zone, which is also the case for some of the data from Nickschick et al. [28].

A more plausible theory might be that there exists a pattern of en-echelon faults that show the earliest stages of faulting [46] with the active fault segments oriented in N-S (Figure 9). This is in accordance with tectonic interpretation of the PPFZ shear zone fault segments [15, 47], seismological results according to Vavryčuk [16], and reflection seismic evidence of tectonic activity of the PPFZ by Halpaap et al. [48]. Bankwitz et al. [15] pointed out that the surface of the PPFZ corresponds to an about 1 km wide sinistral shear zone consisting of short NNE and NNW striking segments in km scale. The zigzag course of the Plesna river is related to these segments, interpreted as sinistral P- (=NNE) and sinistral Riedel shears (=NNW) inside of the PPFZ. Peterek et al. [47] detected displacement (significant uplift of the eastern flanks of the PPFZ) of age-different river terraces of the Ohře (Eger) river valley at the area where the valley is crossing the PPFZ as evidence of the tectonic activity of the PPFZ from Mid Pleistocene up to Holocene. Inside the PPFZ, Halpaap et al. [48] detected the complete absence of faulting in the sediment strata; meanwhile, the crystalline basement is strongly faulted. We interpreted the degassing structures at the BMF and HMF according to our own results and literature data as pattern of en-echelon faults that show reactivation of preexisting faults at the earliest stages of faulting (Figure 9).

6. Conclusions and Outlook

This study presents the results of CO₂ gas flux measurements of a cold mantle-derived CO₂ release in the western Eger Rift, geodynamically most active area of the European Cenozoic Rift System [8].

The CO₂ gas flux measurements yielded various results:

- (i) The experiments carried out here continue gas flux measurements of the Hartoušov mofette field [17, 28], located 1 km south of the working area. As a

new technique, drone-based orthophotos were used in combination with knowledge of plant zonation in CO₂ mofette fields. For cases where only rough knowledge of the gas flux is necessary, mapping the vegetation can suffice. This, however, is only reliable for areas with high degassing averages that are not agriculturally used.

- (ii) Mofette vegetation can be used as a guide for a reasonable grid spacing, ranging from 2,5 m in mofettophilic areas to 10 m in mofettophobic areas around a dry mofette. For data analysis, a point spacing of 50 m was proved to be problematic. Better results can be achieved by smaller grids, for example, 20 m point spacing as in Nickschick et al. [28].
- (iii) The average, by trans-Gaussian kriging-calculated degassing for the BMF, is 30 t d⁻¹ for an area of 0,43 km². For the HMF, it is 23 t d⁻¹ for an area of 0,35 km². The average degassing values are in the same magnitude of order and show that the two areas are comparable.
- (iv) The hypothesis of pull-apart basins from Nickschick et al. [28] was tested. During the interpretation of the data and using new results from Kämpf et al. [17] and Nickschick et al. [28], it was found that the degassing in the BMF is not in accordance with this interpretation, based on the direction of degassing as well as topography and sediment fill of the suggested basins. Emanate from our own results and literature data, a new model was proposed in which en-echelon faults show beginning faulting while reactivating preexisting faults. The en-echelon faults inside of the PPFZ act as fluid channels to depth (CO₂ conduits).

Data Availability

All the data of the manuscript are included in the tables.

Conflicts of Interest

The authors declare that the research was conducted in the absence of any commercial or financial relationships that could be construed as a potential conflict of interest.

Acknowledgments

We would like to express our gratitude to the German Research Foundation (DFG) for funding this project (KA902/9, 16). The extensive fieldwork in 2017 and 2018 was funded by the expedition funds “ICDP-Eger” of the Helmholtz-Zentrum Potsdam - Deutsches GeoForschungs-Zentrum GFZ. We thank M. Bogdanowitsch and S. Kraus for their scientific contributions during fieldwork. The authors thank Frank Kreienkamp, German Weather Service for the thermopluviogram of the Free State of Saxony. We are grateful to Karin Bräuer (UFZ-Helmholtz Centre for Environmental Research, Germany) for the critical review of the final version of the manuscript.

References

- [1] C. Prodehl, S. Müller, and V. Haak, "The European Cenozoic rift system," in *Continental Rifts: Evolution, Structure, Tectonics, Developments in Geotectonics*, K. H. Olsen, Ed., vol. 25, pp. 133–212, Elsevier, New York, 1995.
- [2] J. Ulrych, J. Dostal, J. Adamovič et al., "Recurrent Cenozoic volcanic activity in the Bohemian Massif (Czech Republic)," *Lithos*, vol. 123, no. 1–4, pp. 133–144, 2011.
- [3] P. Štěpančíková, T. Fischer, J. Stemberk jr., L. Nováková, F. Hartvich, and P. M. Figueiredo, "Active tectonics in the Cheb Basin: youngest documented Holocene surface faulting in Central Europe?," *Geomorphology*, vol. 327, pp. 472–488, 2019.
- [4] P. Rojík, O. Fejfar, J. Dašková et al., "Krušné hory Piedmont basins - Cheb basin," in *Tertiary Basins and Lignite Deposits of the Czech Republic*, J. Pešek, Ed., pp. 143–161, Czech Geological Survey, Prague, 2014.
- [5] H. Credner, "Das vogtländisch-erzgebirgische Erdbeben vom 23. November 1875," *Zeitschrift für die Gesamten Naturwissenschaften*, vol. 48, pp. 246–269, 1876.
- [6] J. Horálek and T. Fischer, "Role of crustal fluids in triggering the West Bohemia/Vogtland earthquake swarms: just what we know (a review)," *Studia Geophysica et Geodaetica*, vol. 52, no. 4, pp. 455–478, 2008.
- [7] K. Bräuer, H. Kämpf, G. Strauch, and S. M. Weise, "Isotopic evidence ($^3\text{He}/^4\text{He}$, $^{13}\text{C}_{\text{CO}_2}$) of fluid-triggered intraplate seismicity," *Journal of Geophysical Research: Solid Earth*, vol. 108, no. B2, 2003.
- [8] K. Bräuer, H. Kämpf, S. Niedermann, G. Strauch, and J. Tesař, "Natural laboratory NW Bohemia: Comprehensive fluid studies between 1992 and 2005 used to trace geodynamic processes," *Geochemistry, Geophysics, Geosystems*, vol. 9, no. 4, 2008.
- [9] S. Brune, S. E. Williams, and R. D. Müller, "Potential links between continental rifting, CO_2 degassing and climate change through time," *Nature Geoscience*, vol. 10, no. 12, pp. 941–946, 2017.
- [10] J. Horálek and T. Fischer, "Intraplate earthquake swarms in West Bohemia/Vogtland (Central Europe)," *JÖKULL*, vol. 60, pp. 67–87, 2010.
- [11] M. Ibs-von Seht, T. Plenefisch, and K. Klinge, "Earthquake swarms in continental rifts — A comparison of selected cases in America, Africa and Europe," *Tectonophysics*, vol. 452, no. 1–4, pp. 66–77, 2008.
- [12] J. Mrlina, H. Kämpf, C. Kroner et al., "Discovery of the first Quaternary maar in the Bohemian Massif, Central Europe, based on combined geophysical and geological surveys," *Journal of Volcanology and Geothermal Research*, vol. 182, no. 1–2, pp. 97–112, 2009.
- [13] J. Rohrmüller, H. Kämpf, E. Geiß et al., "Reconnaissance study of an inferred Quaternary maar structure in the western part of the Bohemian Massif near Neualbenreuth, NE-Bavaria (Germany)," *International Journal of Earth Sciences*, vol. 107, no. 4, pp. 1381–1405, 2018.
- [14] T. Fischer, J. Horálek, P. Hrubcová, V. Vavryčuk, K. Bräuer, and H. Kämpf, "Intra-continental earthquake swarms in West-Bohemia and Vogtland: a review," *Tectonophysics*, vol. 611, pp. 1–27, 2014.
- [15] P. Bankwitz, G. Schneider, H. Kämpf, and E. Bankwitz, "Structural characteristics of epicentral areas in Central Europe: study case Cheb Basin (Czech Republic)," *Journal of Geodynamics*, vol. 35, no. 1–2, pp. 5–32, 2003.
- [16] V. Vavryčuk, "Principal earthquakes: theory and observations from the 2008 West Bohemia swarm," *Earth and Planetary Science Letters*, vol. 305, no. 3–4, pp. 290–296, 2011.
- [17] H. Kämpf, K. Bräuer, J. Schumann, K. Hahne, and G. Strauch, " CO_2 discharge in an active, non-volcanic continental rift area (Czech Republic): Characterisation ($\delta^{13}\text{C}$, $^3\text{He}/^4\text{He}$) and quantification of diffuse and vent CO_2 emissions," *Chemical Geology*, vol. 339, pp. 71–83, 2013.
- [18] T. Nickschick, C. Flechsig, J. Mrlina, F. Oppermann, F. Löbig, and T. Günther, "Large-scale electrical resistivity tomography in the Cheb Basin (Eger Rift) at an ICDP monitoring drill site to image fluid-related structures," *Solid Earth Discussions*, pp. 1–29, 2019, in review.
- [19] K. Bräuer, H. Kämpf, S. Niedermann, and G. Strauch, "Monitoring of helium and carbon isotopes in the western Eger Rift area (Czech Republic): relationships with the 2014 seismic activity and indications for recent (2000–2016) magmatic unrest," *Chemical Geology*, vol. 482, pp. 131–145, 2018.
- [20] W. H. Geissler, H. Kämpf, R. Kind et al., "Seismic structure and location of a CO_2 source in the upper mantle of the western Eger (Ohře) Rift, central Europe," *Tectonics*, vol. 24, no. 5, 2005.
- [21] H. Kämpf, W. H. Geissler, and K. Bräuer, "Combined Gas-geochemical and Receiver Function Studies of the Vogtland/NW Bohemia Intraplate Mantle Degassing Field, Central Europe," in *Mantle Plumes*, J. R. R. Ritter and U. R. Christensen, Eds., pp. 127–158, Springer, Berlin, Heidelberg, 2007.
- [22] F. H. Weinlich, K. Bräuer, H. Kämpf, G. Strauch, J. Tesař, and S. M. Weise, "An active subcontinental mantle volatile system in the western Eger rift, Central Europe: gas flux, isotopic (He, C, and N) and compositional fingerprints," *Geochimica et Cosmochimica Acta*, vol. 63, no. 21, pp. 3653–3671, 1999.
- [23] F. H. Weinlich, J. Tesař, S. M. Weise, K. Bräuer, and H. Kämpf, "Gas flux distribution in mineral springs and tectonic structure in the western Eger Rift," *Journal of the Czech Geological Society*, vol. 43, pp. 91–110, 1998.
- [24] R. Bussert, H. Kämpf, C. Flechsig et al., "Drilling into an active mofette: pilot-hole study of the impact of CO_2 -rich mantle-derived fluids on the geo-bio interaction in the western Eger Rift (Czech Republic)," *Scientific Drilling*, vol. 23, pp. 13–27, 2017.
- [25] E. H. Flores, J. Umlauf, A. Schmidt, and M. Korn, "Locating mofettes using seismic noise records from small dense arrays and matched field processing analysis in the NW Bohemia/Vogtland Region, Czech Republic," *Near Surface Geophysics*, vol. 14, pp. 327–335, 2016.
- [26] K. Bräuer, H. Kämpf, and G. Strauch, "Earthquake swarms in non-volcanic regions: what fluids have to say," *Geophysical Research Letters*, vol. 36, no. 17, 2009.
- [27] K. Bräuer, H. Kämpf, U. Koch, and G. Strauch, "Monthly monitoring of gas and isotope compositions in the free gas phase at degassing locations close to the Nový Kostel focal zone in the western Eger Rift, Czech Republic," *Chemical Geology*, vol. 290, no. 3–4, pp. 163–176, 2011.
- [28] T. Nickschick, H. Kämpf, C. Flechsig, J. Mrlina, and J. Heinicke, " CO_2 degassing in the Hartoušov mofette area, western Eger Rift, imaged by CO_2 mapping and geoelectrical and gravity surveys," *International Journal of Earth Sciences*, vol. 104, no. 8, pp. 2107–2129, 2015.
- [29] T. Rennert and H. Pfanz, "Hypoxic and acidic – soils on mofette fields," *Geoderma*, vol. 280, pp. 73–81, 2016.

- [30] F. Sassmannshausen, "Vegetationsökologische Charakterisierung terrestrischer Mofettenstandorte am Beispiel des westtschechischen Plesná-Tals," Ph.D. thesis, University of Duisburg - Essen, German, 2010.
- [31] H. Pfanz, *Kalter Atem Schlafender Vulkane*, RVDL-Verlag, Köln, 2008, in German.
- [32] H. Pfanz, G. Yüce, A. H. Gulbay, and A. Gokgoz, "Deadly CO₂ gases in the Plutonium of Hierapolis (Denizli, Turkey)," *Archaeological and Anthropological Sciences*, vol. 11, no. 4, pp. 1359–1371, 2019.
- [33] A. Aydin and A. Nur, "Evolution of pull-apart basins and their scale independence," *Tectonics*, vol. 1, no. 1, pp. 91–105, 1982.
- [34] G. Yuce, C. C. Fu, W. D'Alessandro et al., "Geochemical characteristics of soil radon and carbon dioxide within the Dead Sea Fault and Karasu Fault in the Amik Basin (Hatay), Turkey," *Chemical Geology*, vol. 469, pp. 129–146, 2017.
- [35] C. Flechsig, J. Heinicke, J. Mrlina et al., "Integrated geophysical and geological methods to investigate the inner and outer structures of the Quaternary Mýtina maar (W-Bohemia, Czech Republic)," *International Journal of Earth Sciences*, vol. 104, no. 8, pp. 2087–2105, 2015.
- [36] West Systems, "Portable diffuse flux meter with LI-COR CO₂ detector handbook," *Release*, vol. 8, p. 2, 2012.
- [37] G. Chiodini, R. Cioni, M. Guidi, B. Raco, and L. Marini, "Soil CO₂ flux measurements in volcanic and geothermal areas," *Applied Geochemistry*, vol. 13, no. 5, pp. 543–552, 1998.
- [38] M. E. Hinkle, "Environmental conditions affecting concentrations of He, CO₂, O₂ and N₂ in soil gases," *Applied Geochemistry*, vol. 9, no. 1, pp. 53–63, 1994.
- [39] C. Flechsig, R. Bussert, J. Rechner, C. Schütze, and H. Kämpf, "The Hartušov Mofette field in the Cheb Basin, Western Eger Rift (Czech Republic): a comparative geoelectric, sedimentologic and soil gas study of a magmatic diffuse CO₂-degassing structure," *Zeitschrift für Geologische Wissenschaften*, vol. 36, pp. 177–193, 2008.
- [40] R. O. Gilbert, *Statistical Methods for Environmental Pollution Monitoring*, Wiley, New York, 1987.
- [41] J. L. Lewicki, D. Bergfeld, C. Cardellini et al., "Comparative soil CO₂ flux measurements and geostatistical estimation methods on Masaya volcano, Nicaragua," *Bulletin of Volcanology*, vol. 68, no. 1, pp. 76–90, 2005.
- [42] N. Cressie, "Spatial prediction and ordinary kriging," *Mathematical Geology*, vol. 20, no. 4, pp. 405–421, 1988.
- [43] G. E. P. Box and D. R. Cox, "An analysis of transformations," *Journal of the Royal Statistical Society: Series B (Methodological)*, vol. 26, no. 2, pp. 211–243, 1964.
- [44] T. Rennert, K. Eusterhues, V. de Andrade, and K. U. Totsche, "Iron species in soils on a mofette site studied by Fe K-edge X-ray absorption near-edge spectroscopy," *Chemical Geology*, vol. 332–333, pp. 116–123, 2012.
- [45] G. Chiodini, C. Cardellini, M. C. Lamberti et al., "Carbon dioxide diffuse emission and thermal energy release from hydrothermal systems at Copahue–Caviahue Volcanic Complex (Argentina)," *Journal of Volcanology and Geothermal Research*, vol. 304, pp. 294–303, 2015.
- [46] J. D. Muirhead and S. A. Kattenhorn, "Activation of preexisting transverse structures in an evolving magmatic rift in East Africa," *Journal of Structural Geology*, vol. 106, pp. 1–18, 2018.
- [47] A. Peterek, C.-D. Reuther, and R. Schunk, "Neotectonic evolution of the Cheb Basin (Northwestern Bohemia, Czech Republic) and its implications for the late Pliocene to recent crustal deformation in the western part of the Eger Rift," *Zeitschrift für Geologische Wissenschaften*, vol. 39, pp. 335–365, 2011.
- [48] F. Halpaap, M. Paschke, and F. Bleibinhaus, "Shallow reflection seismic evidence of tectonic activity in the Cheb Basin, NW Bohemia," *Studia Geophysica et Geodaetica*, vol. 62, no. 1, pp. 80–101, 2018.

Research Article

Chemical and Noble Gas Isotope Compositions of Formation Gases from a 3 km Deep Scientific Borehole in the Koyna Seismogenic Zone, Western India

Nagaraju Podugu ¹, Satrughna Mishra ¹, Thomas Wiersberg,² and Sukanta Roy ¹

¹Ministry of Earth Sciences, Borehole Geophysics Research Laboratory, Karad 415 114, India

²GFZ German Research Centre for Geosciences, Telegrafenberg, 14473 Potsdam, Germany

Correspondence should be addressed to Nagaraju Podugu; nagarajupodugu@yahoo.com

Received 14 March 2019; Revised 2 June 2019; Accepted 16 August 2019; Published 17 September 2019

Academic Editor: Francesco Italiano

Copyright © 2019 Nagaraju Podugu et al. This is an open access article distributed under the Creative Commons Attribution License, which permits unrestricted use, distribution, and reproduction in any medium, provided the original work is properly cited.

A 3 km deep research borehole KFD1 was drilled in the Koyna reservoir-triggered seismicity region, Western India, between December 2016 and May 2017. The 1967 M 6.3 Koyna earthquake had generated a NNE-SSW trending surface fissure zone in the Nanel-Donichawadi-Kadoli sector. KFD1 is located ~5 km south of Kadoli along the trend of the Donichawadi fault zone. Online gas monitoring was carried out during drilling of KFD1 from 1315 m to 2831 m depth to sample and study the composition of crustal gases. Formation gases CO_2 , CH_4 , H_2 , and He were only observed during water flushing of ~100 m intervals following coring runs. Laboratory analyses of gas samples collected between 1737 m and 2831 m depth revealed concentrations of up to 1200 ppmv CO_2 , 186 ppmv CH_4 , 139 ppmv H_2 , and 12.8 ppmv He. Zones enriched in gases are mostly below the 2100 m depth with significant He enhancement ranging from 4.6 to 7.6 ppmv above the atmospheric value. The He-rich zones correlate well with the zones of anomalous physical and mechanical properties identified from geophysical logs and are characterized by high fracture density as revealed from borehole images, indicating that the borehole punctured multiple fracture zones. The helium concentrations are consistent with those previously observed over the surface fissures near Kadoli, suggesting a southward extension of the Donichawadi fault zone up to the KFD1 site and confirming that the fault zone is permeable even after 50 years of the 1967 Koyna earthquake. $^3\text{He}/^4\text{He}$ ratios of eleven gas samples fall between 0.426 ± 0.022 and $0.912 \pm 0.059 \text{ Ra}$, with $^4\text{He}/^{20}\text{Ne}$ values between 0.3449 ± 0.0091 and 0.751 ± 0.020 . Air-corrected helium isotope ratios indicate that helium is a mixture of atmospheric and crustal radiogenic components but no mantle contribution within 2σ analytical uncertainties.

1. Introduction

It is known that fluids are responsible for various processes occurring at seismogenic depths of active fault zones [1], but if and how fluid overpressure is linked with these processes, the origin and magnitude of fluid overpressure, and the role of fluid pressures in controlling the strength of fault zones are still under debate [2–4]. Fluid migration and fluid-rock interaction play a role in metamorphic reactions, melting and crystallization processes, mass and heat transport, and the deep biosphere and rheological behaviour of rocks in the Earth's crust.

Deep drilling provides an opportunity to examine pristine fluids from the subsurface. In many cases of deep drilling, drilling mud is circulated to stabilize the borehole, to cool the drill bit, and to drag out the rock chips (cuttings) from the borehole. Formation fluids and gases return to the surface with the drilling mud, where they can be monitored and sampled. Mud gas logging is a common technique in the oil and gas industry to evaluate hydrocarbon reservoir rocks and for safety reasons. In the past few decades, online mud gas monitoring and sampling has been carried out in association with several scientific deep drilling programmes in crystalline rocks to obtain information on crustal gases

[5–7]. Hydrocarbons, He, Rn, CO₂, H₂S, and H₂ are usually enriched in subsurface formation fluids relative to the atmosphere, which therefore make these gases suitable for detection of fluid-bearing horizons including shear zones, open fractures, and other zones with enhanced permeability. Also, a number of studies aimed at detecting geochemical precursors of earthquakes have been carried out as there are strong evidences of preferential degassing at active fault zones [8, 9]. Temporal changes in Rn, He, CO₂, N₂, and CH₄ have been recognized as potential tracers of fault systems [10–17]. However, interpretation in terms of the source of the leaking gas is not straightforward as thermal, radiogenic, and geodynamic processes may be involved in degassing at active faults resulting in a complex pattern of degassing from the crust both in space and time [18].

The continuous fluid analysis during drilling of the KTB (German Continental Deep Drilling Program) boreholes led to determining the composition of gases dissolved in drilling fluid and identifying several fluid flow zones with enhanced gas concentrations above the atmospheric abundances [7, 19]. Subsequently, online monitoring of fluids and gases from circulating drilling mud has been successfully conducted in several scientific drilling projects in crystalline and sedimentary strata with a focus on fault zones, e.g., the San Andreas Fault Observatory at Depth (SAFOD) [7, 20–22], the Wenchuan Fault Zone drilling project [23], and the Nankai Trough Seismogenic Zone Experiment (NanTroSEIZE) [24–26]. Online gas monitoring during drilling through fault zones provides information on the origin and spatial distribution of formation gases at seismogenic depths, gas migration, and the fault zone permeability architecture.

The Koyna region, situated in western India, is a well-known site of reservoir-triggered seismicity (RTS), where triggered earthquakes have been occurring in a restricted area of 30 × 20 km² since the impoundment of the Koyna reservoir in 1962 [27–34]. There were no earthquakes reported in the Koyna region prior to impoundment of the reservoir within 50 km of the Koyna dam, but the seismic activity started in the months following the impoundment and increased gradually during the next few years culminating in the $M \sim 6.3$ Koyna earthquake of December 10, 1967 [29, 35]. The RTS was further enhanced by impoundment of the nearby located Warna reservoir in 1985 [36]. Besides the largest triggered earthquake of $M \sim 6.3$, the region has experienced 22 earthquakes of $M \geq 5$, about 200 earthquakes of $M > 4$, and several thousand smaller earthquakes in the past 55 years. The region continues to be active with recurrent, low magnitude earthquakes. A strong correlation between earthquake occurrences and the annual loading and unloading cycles of the Koyna and Warna reservoirs has been established from observations during the past few decades [29, 34, 37]. However, a model to comprehend the genesis of reservoir-triggered earthquakes has remained elusive likely due to lack of direct observations from the near-field of earthquakes. A major research programme involving scientific deep drilling investigations in the Koyna seismogenic zone was taken up in the year 2012 to improve our understanding of the mechanism of triggered earthquakes in the region through near-field observations. As part of this

research initiative, a 3 km deep pilot borehole KFD1 was drilled between December 2016 and May 2017 at Gothane (17°17'57"N, 73°44'19"E), ~10 km SE of Koyna dam (Figure 1). The ground elevation with respect to the mean sea level is 930 m. The pilot hole drilling provided valuable base information for the proposed main borehole to deploy a deep fault zone observatory at ~5 km depth [38, 39].

The pilot hole site is located in close proximity of the Donichawadi fissure zone, the surface manifestation of the 1967 M 6.3 Koyna earthquake (Figure 1(a)). Although ground fissures and cracks were identified at many localities in the region, a regular pattern and continuity of the fissures was evident over a length of 4 km in the Nanel-Donichawadi-Kadoli sector [40]. A soil-helium survey conducted during 1996–1997 across the fissure zone, 5 km north of the KFD1 drill site, showed helium anomalies up to 7 ppm above atmospheric abundance of 5.24 ppm even 30 years after the 1967 earthquake, signifying the activity of the Donichawadi fissure zone through which formation gases are escaping [41] (Figure 1(b)). Along the same alignment of the Donichawadi fissure zone, small cracks were seen in Randiv village, 12 km south-west of Kadoli [40]. Sathe et al. [42] suggested that this fissure zone extends from Baje to Randiv via Donichawadi and Kadoli, which was later supported by Talwani [31] (Figure 1(a)). However, the continuity of the fissures from Donichawadi to Randiv did not gain support from the detailed examination of hill slopes between these two locations [40]. Therefore, it is not clear whether the Donichawadi fault extends further to the south of Kadoli. On the other hand, the trend of the fissure zone is consistent with the seismic activity in the Koyna region during the past few decades [34]. As the Koyna pilot hole site is located close to the Donichawadi fissure zone, we consider that investigations in KFD1 would shed new light on the presence of the active fault zone in the area and the southward extension of the Donichawadi fissure zone.

In the present study, we have carried out online gas monitoring during KFD1 mud drilling and, for the first time, also during air hammer drilling. Eleven gas samples were collected during water flushing after core runs for off-site noble gas isotope studies. The data from online gas analysis (OLGA) and helium isotope data from off-line gas samples are discussed in the context of abundance and composition of gases present in the pilot borehole KFD1, detection of potential fluid-bearing horizons and shear/fracture zones, and confirmation of possible southward extension of the still active Donichawadi fissure zone.

2. Methods

2.1. KFD1 Drilling Operations. Drilling of the Koyna pilot hole KFD1 was mainly done using the air hammer technique except at a few depths where fluid loss or water ingress zones were encountered and at depths where coring was done, in which mud rotary drilling was performed. KFD1 was drilled in three phases. During phase I (December 20, 2016, to January 8, 2017), the borehole was drilled from the surface to 502 m followed by casing and cementation. During phase II (January 11 to March 12, 2017), the borehole penetrated

the basalt-granite intersection at 1251 m and reached a depth of 1503 m, where geophysical logging from 500 m to 1500 m was conducted in the open hole before the borehole was cased and cemented. Finally, during phase III (March 17 to June 11, 2017), the borehole reached the final depth of 3014 m. Cores were obtained using a 9 m long core barrel at intermittent depths starting from 1679 m to 2912 m during eight coring runs. The borehole passed through the base of the Deccan basalt column at 1251 m and continued 1763 m in the underlying granitic basement. All depths are referenced to the Kelly bushing, which was located at 3.5 m elevation with respect to ground level. The basement rocks, comprised mainly of cratonic (tonalite-trondhjemite-granodiorite) gneisses of peninsular India, occur as interlayering of granite, granite gneiss, and varying proportions of migmatitic gneiss [43].

2.2. Experimental Setup for Online Gas Monitoring at KFD1.

The online mud gas monitoring was set up at the KFD1 drill site to determine and analyse the gases which are extracted from the drilling fluid. Gases were routinely monitored in one-minute intervals during all drilling phases (air hammer drilling, core drilling) and during water flushing from the borehole. However, only gas extraction and analysis during water flushing showed the presence of formation gases (i.e., nonatmospheric). Generally, gas from drilling mud comprises air and other components that are mechanically released either as the drill bit crushes the rock or when the drilling intersects permeable strata. The separation of gas from the drilling mud is done mechanically using a custom-built mud gas separator installed in the so-called “possum belly” at the head of the shale shaker screens. The mud gas is extracted from the returning mud and continuously pumped through a plastic tube to the on-site laboratory, where the gas composition is determined. Mud gas always contains a portion of air as the mud tanks and pumps are open to the atmosphere. The formation gases identified in drilling mud derive either from the pore space of the crushed rock or from fluids entering the borehole through open fractures/fault zones. The technique is operationally simple and comparatively inexpensive as it can be easily deployed on drill rigs and requires no additional rig time. However, the technique only works if drill mud circulation is established. The technical details for online mud gas monitoring are discussed in Erzinger et al. [7]. For air hammer drilling, pressurized air is applied in order to run the air hammer and to lift the cuttings to the surface. As the volume of atmospheric gases pumped down the hole is extremely high compared to the concentration of formation gases in crystalline rock, any formation gas that enters the borehole will be highly diluted. The cuttings are separated from the returning gas in a Mathena™ shale gas separator and a portion of the returning gas is introduced to the nearby OLGA laboratory through a plastic tube (Figure 2). The gas flow is adjusted with a flow meter and a membrane pump to build up vacuum, and a water trap condenses the water. On site, the dry gas is analysed with a quadrupole mass spectrometer (QMS, Pfeiffer OmniStar™ GSD 300 with mass range 0–100 amu) to determine relative gas concentrations. The gas is finally

pumped through glass tubes for sampling gases for off-site isotope studies. With the present experimental setup at the KFD1 drill site, the gases N_2 , O_2 , Ar, CO_2 , CH_4 , He, and H_2 are determined at 1-minute sampling intervals with a detection limit of 1 ppmv (parts per million by volume). Prior to gas monitoring at Koyna, the mass spectrometer has been calibrated for the mass scale (to measure at the peak maximum) and for quantification of gas concentrations. For determination of gas concentrations, the measured ion currents are inputted to a solution matrix and the individual concentrations of the components in the gas to be analysed are determined via calibration factors. The calculated concentrations are automatically normalized to 100 vol.-%. Due to the normalization, the concentration determination is within a certain range independent of the inlet pressure of the gas. Nevertheless, the calibration measurements are performed at the same conditions, including gas inlet pressure, as for the gas monitoring experiment (atmospheric pressure).

The calibration factors used for concentration determination are calculated from the analysis of air and a certified gas mixture, composed of N_2 (64.2 vol.-%), CH_4 (30.3 vol.-%), CO_2 (5.12 vol.-%), ethane (1985 ppmv), propane (500 ppmv), Ar (499 ppmv), He (473 ppmv), and H_2S (454 ppmv). Since all calibration factors are given as relative values, a fixed calibration factor (internal standard) is defined with the value 1. In the present study, ^{40}Ar ($m/e = 40$) is used as the internal standard, where all other calibration factors relate to this value. Apart from determination of the calibration factors, the measurement of calibration gas is also used to determine the standard deviations of the measured values. For that purpose, ion currents are averaged over 11 measurement cycles, and the following relative 2σ standard deviation values are obtained for different gas concentration ranges: 100–0.1 vol.-%: $\pm 1\%$, 1000–100 ppmv: $\pm 2\%$, 100–10 ppmv: $\pm 5\%$, <10 ppmv: $\pm 10\%$.

During online measurements, a record of relative gas concentrations versus time is obtained. The data is later converted into gas concentrations versus depth using lag depth versus time data provided by a commercial mud logging company. The lag depth corresponds to the drill bit depth, corrected for the depth drilled during the time interval that the gas needs to reach the surface. During coring operations, the drilling mud is replaced by water after each coring run in order to prepare for air hammer drilling, as the lifting capacity of air hammer drilling is not sufficient to directly blow out the drilling mud of a mud-filled borehole. In the next step, the water in the borehole is progressively flushed out from top to bottom of the borehole in ~ 100 m intervals (Figure 3). Significant amounts of formation gases were detected when the water column was running through the Mathena™ separator. These observed gas enhancements represent the integrated concentration of gas in the respective ~ 100 m depth interval. Sixteen gas samples were collected from different depths in the granitic basement section during the water flushing after core runs, as listed in Table 1. With known total volume of the Mathena separator (~ 12 m³) and water volume introduced to the separator (2.49–3.51 m³), the absolute concentration of helium in each water column can be estimated. Table 1 shows the absolute helium

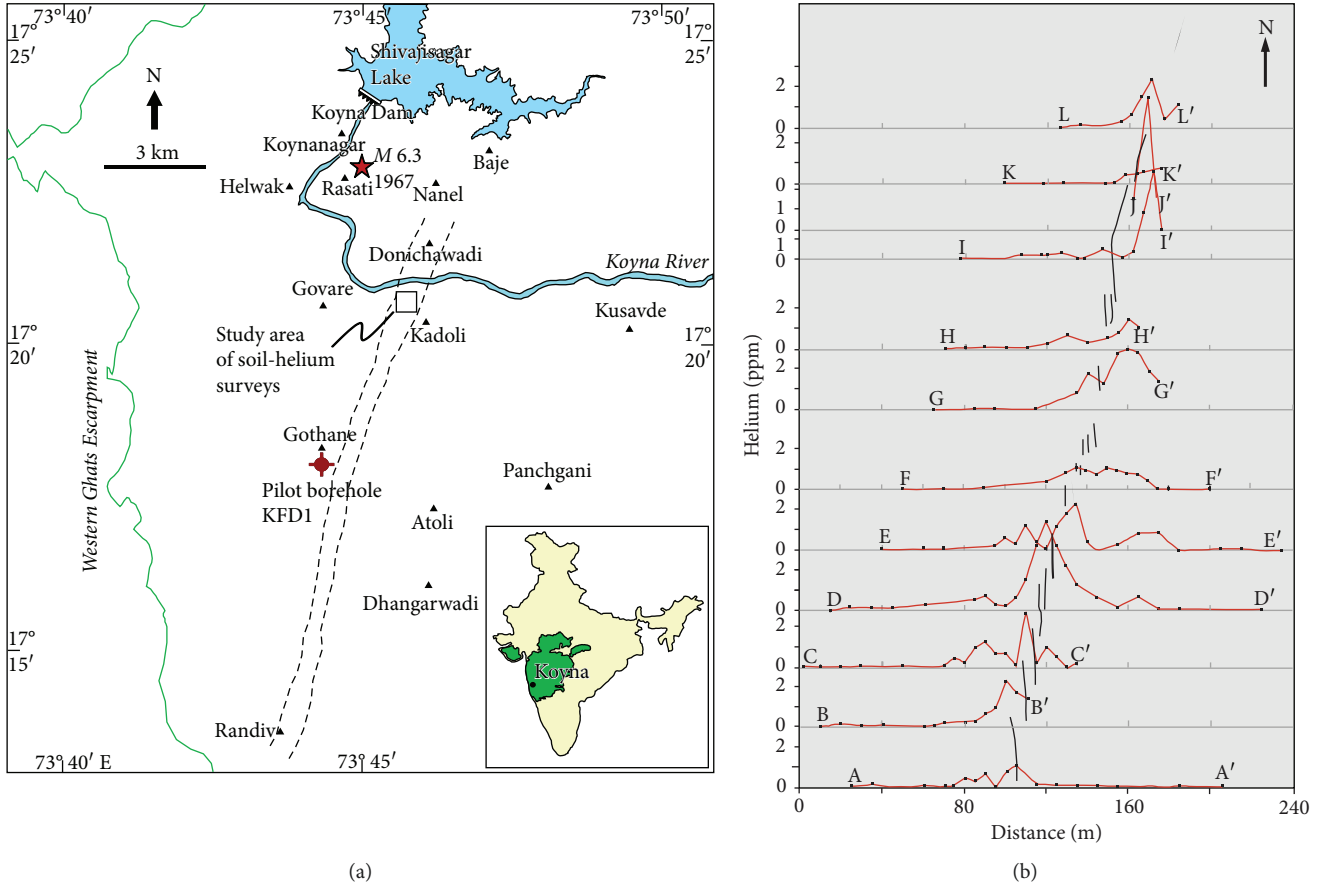


FIGURE 1: (a) Map of the Koyna region showing the locations of the 1967 M 6.3 Koyna earthquake (red star) and the pilot borehole KFD1. The trace of the Donichawadi fissure zone (dashed lines), formed during 1967 earthquake [31, 40], and the study area (square) where the soil-helium surveys were conducted during 1996-1997 are also shown. Inset shows the location of Koyna within the Deccan Traps province (shaded green) on the outline map of India. (b) Map showing the coincidence of the helium anomalies established by soil-helium measurements along 12 traverses (AA', BB', ..., LL') with coseismic en echelon fissures (thick lines) from the 1967 earthquake (Gupta et al. [41]).

concentrations in each water column in millimole, corrected for atmospheric helium input, according to

$$\text{He}_{\text{air-corrected}} = \text{He}_{\text{measured}} - \left[\text{He}_{\text{air}} * \frac{\text{O}_{2(\text{measured})}}{\text{O}_{2(\text{air})}} \right]. \quad (1)$$

Before the water column is introduced into the Mathena separator, the complete separator volume is exchanged several times with air. Hence, any input of residual gas from the degassing of the previous water column seems less likely, which is underlined by the observed significant variation in H_2 concentration between the sample RIH20 (139 ppmv) and the sample RIH21 (50 ppmv). Two core runs were separated by an interval of air hammer drilling, except the 5th and 6th core runs and the 7th and 8th core runs which were done consecutively.

2.3. Borehole Spectral Gamma Ray Logging. Spectral gamma ray logs were taken in association with geophysical well logging in the pilot borehole KFD1. A standard natural gamma ray spectrometry sonde from Schlumberger® was lowered in

the borehole, and data was acquired in the open hole sections 500-1500 m and 1500-3000 m at a logging speed of 240 m/h. Prior to the measurements, the sonde was calibrated with reference sources of ^{40}K , ^{238}U , and ^{232}Th . The spectral gamma ray log measures the natural gamma radiation emanating from a formation split into contributions from each of the major radioisotopic sources K, Th, and U. The characteristic peaks in potassium at 1.46 MeV, the thorium series at 2.62 MeV, and the uranium series at 1.76 MeV are caused by the decay of ^{40}K and short-lived daughter products of the uranium (^{208}Tl) and thorium (^{214}Bi) decay chain. A multichannel analyser is used to determine the amount of radiation coming from the energies associated with each of these major peaks. From the response of the tool and the number of counts in each energy window, the individual concentrations of K, Th, and U in the formation are determined.

2.4. Laboratory Investigations. Sixteen gas samples are analysed with a QMS for the chemical gas composition (^4He , ^{40}Ar , N_2 , O_2 , CH_4 , CO_2 , and H_2), with a gas chromatograph (SRI 8610C) equipped with a flame ionization detector using hydrogen as the carrier gas for hydrocarbons

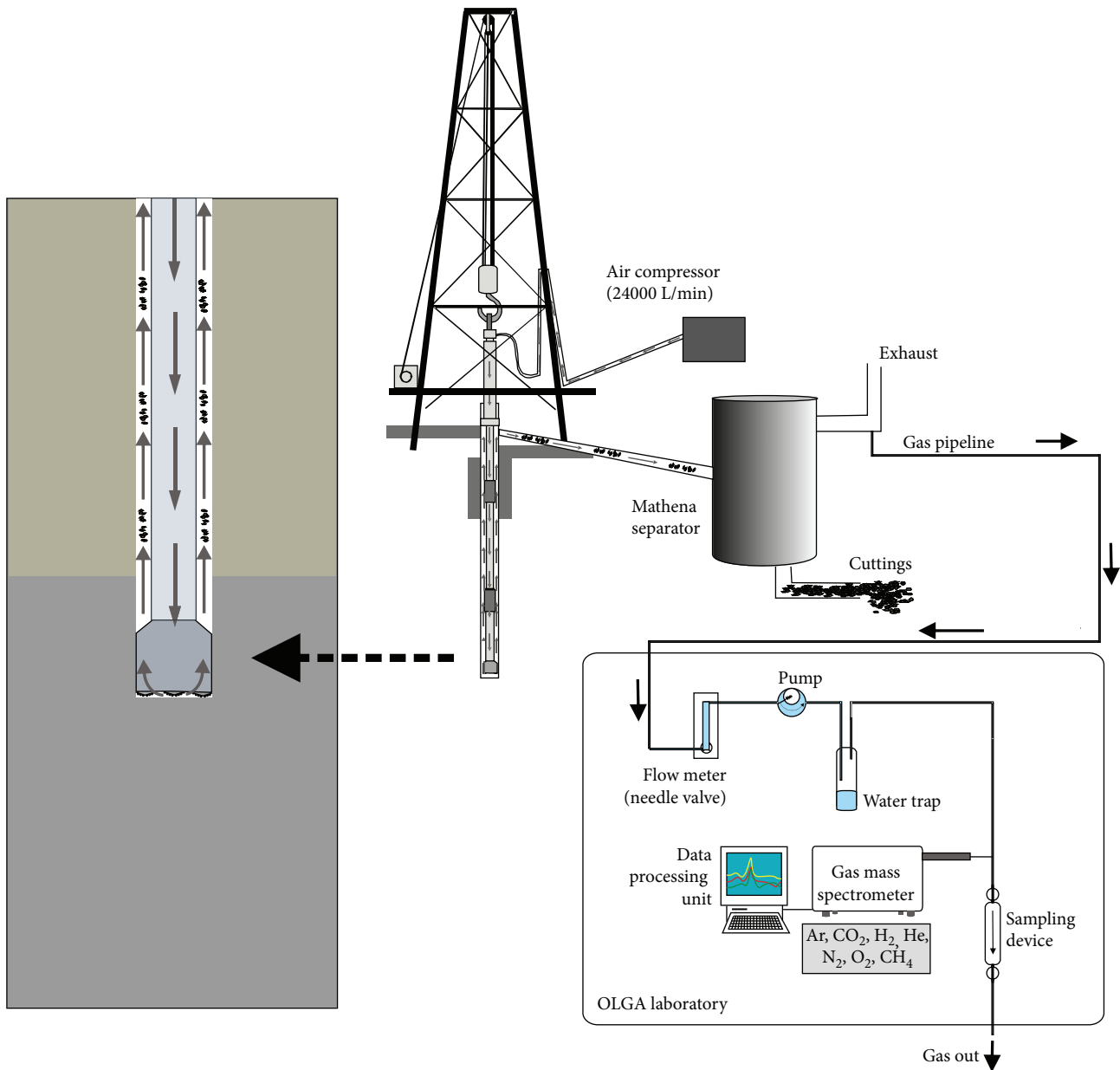


FIGURE 2: Schematic diagram showing the air hammer drilling setup and major components of the OLGA laboratory at the drill site. The Mathena shale gas separator is used to separate gas from borehole cuttings, and the gas is then pumped through a plastic tube to the nearby OLGA laboratory where the gases are determined.

(C1-C4). The gas chromatograph was calibrated with a reference gas (CH₄: 4990 ppmv, C₂H₆: 297.8 ppmv, C₃H₈: 200.3 ppmv, i-C₄H₁₀: 99.4 ppmv, n-C₄H₁₀: 101.7 ppmv, and residual gas: N₂ with traces of CO₂, H₂, and He), followed by eleven measurements of the calibration gas to determine accuracy and precision. Average values of the measurements deviate <2% from the calibration gas concentration for all measured gas species. Relative 2-sigma standard deviations are ≤1% for CH₄, ≤2% for C₂H₆ and C₃H₈, and ≤5% for i/n-C₄H₁₀, indicating that the determinations of all gas species were precise and unbiased.

Eleven samples are analysed for noble gas isotopes with a VG 5400 noble gas mass spectrometer. The following noble gas nuclides have been investigated with the noble gas mass

spectrometer: ³He, ⁴He, ²⁰Ne, ²¹Ne, ²²Ne, ³⁶Ar, ³⁸Ar, ⁴⁰Ar, ⁸⁴Kr, and ¹³²Xe. The procedure for noble gas isotope analyses includes gas purification, mass spectrometric analysis, and data processing and is briefly described in the following (see paper by Niedermann et al. [44] for details). A portion of gas with a predefined volume is introduced in the purification line at constant pressure. Water vapour is condensed in a dry-ice-cooled cold trap. Removal of nitrogen, oxygen, and carbon dioxide is accomplished by passing the sample to two titanium sponge getters, which are cyclically heated. Two Zr-Al getters extract hydrogen, hydrocarbons, and the remaining carbon dioxide. The cleaned gas is then transferred to two cryogenic cold heads. The former allows adsorption of argon, krypton, and xenon at 50 K

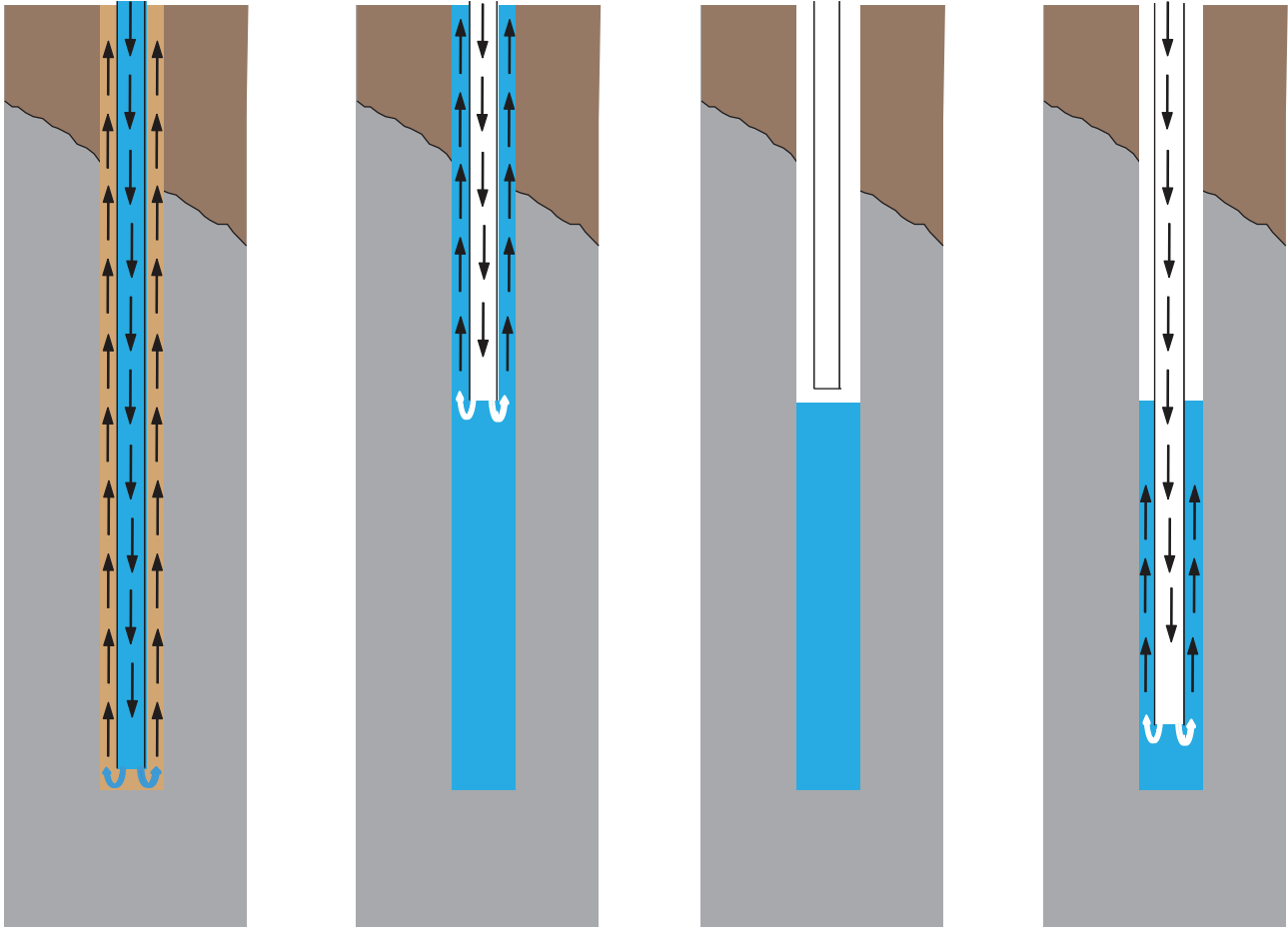


FIGURE 3: Schematic diagram showing (from left to right) replacement of drilling mud by water after each coring run, and the water in the borehole is then progressively flushed out from top to bottom of the pilot borehole KFD1 in ~ 100 m intervals.

temperature, while helium and neon are collected with the second cold head at 11 K. After noble gas adsorption at the cold heads, they are stepwise heated for individual noble gas release and determination. The second cryogenic cold head is heated to 35 K for helium and afterwards to 120 K for neon release. Background concentrations of argon and hydrocarbons are suppressed by a stainless steel frit and an activated charcoal finger that is cooled with liquid nitrogen. Ar, Kr, and Xe are released and measured together by heating the first cold head to 190 K. The measurements in this study are corrected for initial (“blank”) gas concentrations and influences of atmospheric gas following Niedermann et al. [44]. Concentrations of the blanks are typically (in cm^3 STP) as follows: ^4He : $\sim 5 \times 10^{-12}$, ^{20}Ne : $\sim 0.5 \times 10^{-12}$, ^{40}Ar : $\sim 5 \times 10^{-10}$, ^{84}Kr : $\sim 0.05 \times 10^{-12}$, and ^{132}Xe : $\sim 0.02 \times 10^{-12}$ [44, 45]. These concentrations are well below the concentrations in the samples; therefore, a correction was not necessary. Systematic errors by, e.g., incorrect adjustment or inaccurate calibration may bias the accuracy of a noble gas measurement. Such systematic errors shift all measured values in a certain direction. These errors can only be estimated but are likely to be small compared to statistical errors in most cases. Determinable systematic errors in noble gas analytics are, for example, the time-dependent change of

a measured value over the measurement time (up to 40 min) of the measurement cycles (typically 11). Such errors are corrected by extrapolation to the time of gas inlet into the mass spectrometer. All data have been corrected for isobaric interferences and mass discrimination effects. Error limits given in this paper correspond to 2-sigma standard deviations (95.5%) and include statistical uncertainties of the measurement as well as uncertainties of sensitivity and systematic errors of mass discrimination determinations, blanks, and interferences.

3. Data Processing and Results

Except for helium, all noble gas isotopic ratios of our study are indistinguishable from air. Due to clearly distinct helium isotope compositions of different reservoirs and the lower sensitivity for atmospheric contamination, helium isotopes constitute a capable tool to identify the origin of fluids from depth. Helium is not accumulated in the atmosphere, and therefore, the relative atmospheric concentration of helium is low (5.24 ppm). Helium isotope ratios are generally stated as $^3\text{He}/^4\text{He}$ and denoted in atmospheric ratios Ra ($[^3\text{He}/^4\text{He}]_{\text{air}} = 1.39 \times 10^{-6} = 1 \text{ Ra}$). The continental crust is depleted in primordial noble gas nuclides, and its average

TABLE 1: Molecular composition of gas samples collected during water flushing after core run in the pilot hole KFD1 at Gothane, near Koyna, Western India.

Sample	Depth (m)	Flushing after core run #	⁴⁰ Ar (vol.-%) (±1%)	CH ₄ (ppmv) (±5%)	CO ₂ * (ppmv) (±2%)	H ₂ (ppmv) (±5%)	He (ppmv) (±10%)	N ₂ (vol.-%) (±1%)	O ₂ (vol.-%) error = ±1%	C1 (ppmv)	C2 (ppmv)	C3 (ppmv)	i-C ₄ (ppmv)	n-C ₄ (ppmv)	He air-corrected (millimole)
RIH06	2084	5/6	0.983	10	965 (580)	57	6.1	77.8	21.1	14	—	0.4	—	0.3	n.d.
RIH07	2189	5/6	0.982	6	700 (310)	37	5.6	77.6	21.3	5	—	—	—	—	n.d.
RIH08	2295	5/6	0.985	14	32200 (31810)**	63	5.7	77.3	18.4	9	—	—	—	—	n.d.
RIH13	1737	7/8	0.985	48	1005 (620)	45	5.5	77.6	21.3	48	—	—	0.3	—	n.d.
RIH14	1833	7/8	0.996	46	940 (550)	41	6.2	77.7	21.2	60	—	—	—	0.4	0.34
RIH15	1929	7/8	0.999	62	655 (270)	44	7.2	77.6	21.3	65	—	—	0.3	—	0.71
RIH16	2025	7/8	0.991	70	985 (600)	62	7.5	77.8	21.1	69	—	0.3	0.3	—	0.84
RIH17	2121	7/8	0.995	66	930 (540)	34	7.6	77.5	21.4	62	—	—	—	—	0.85
RIH18	2217	7/8	0.992	186	1200 (810)	78	12.8	77.8	21.0	180	—	0.4	—	0.4	2.86
RIH19	2313	7/8	0.989	88	1160 (770)	49	10.1	77.7	21.1	96	—	1.2	—	—	1.83
RIH20	2409	7/8	0.999	140	1180 (790)	139	11.1	77.8	21.1	104	—	—	0.3	—	2.21
RIH21	2514	7/8	0.980	76	1050 (660)	50	10.6	77.8	21.0	66	—	—	—	—	1.95
RIH22	2610	7/8	0.995	52	820 (430)	44	9.9	77.7	21.2	48	—	0.3	0.3	0.6	1.74
RIH23	2687	7/8	0.989	86	970 (580)	46	12.7	77.9	21.0	n.d.	n.d.	n.d.	n.d.	n.d.	3.05
RIH24	2763	7/8	0.999	88	1065 (680)	52	10	77.9	20.9	103	—	—	—	—	1.96
RIH25	2831	7/8	0.992	96	875 (490)	55	9.8	77.9	21.0	78	—	0.5	0.5	0.8	1.93

Gas samples collected during running in and flushing out of water are designated by the prefix RIH. Depths are referenced to the Kelly bushing, which was located at 3.5 m elevation with respect to ground level. *Values in parentheses are air-corrected according to $[\text{CO}_2]_{\text{air-corrected}} = [\text{CO}_2]_{\text{measured}} - ([\text{O}_2]_{\text{measured}} \times [\text{CO}_2]_{\text{air}} / [\text{O}_2]_{\text{air}})$. **Probably an artefact from sample preparation. —: below detection limit (≈ 0.3 ppmv); n.d.: not determined.

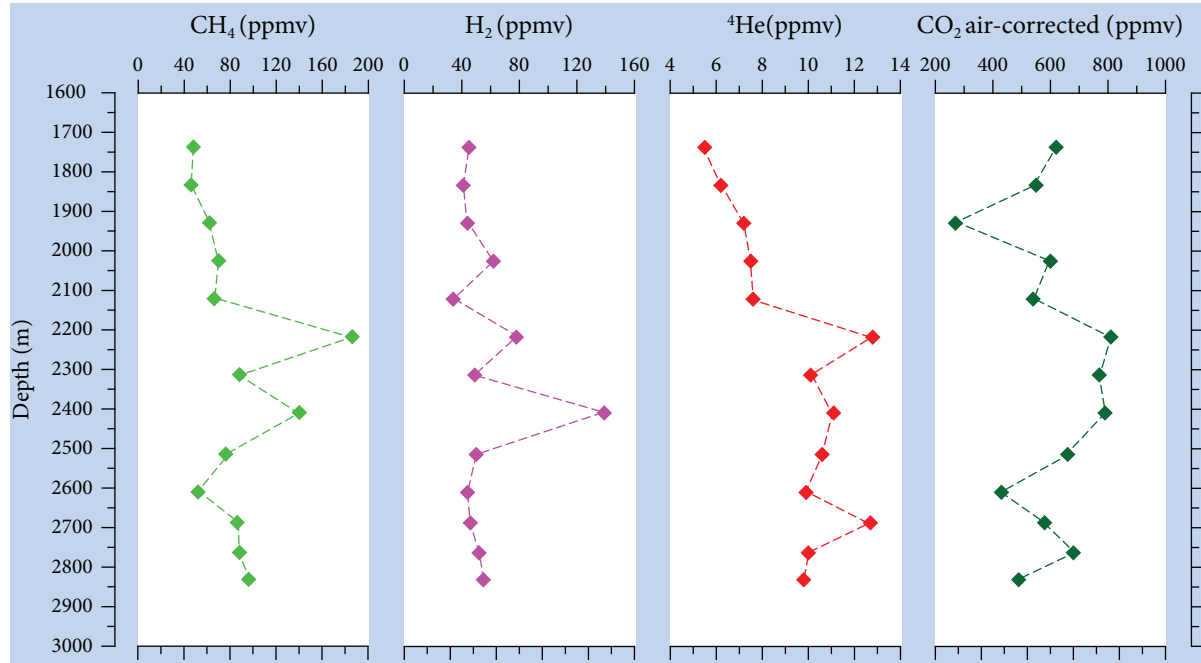


FIGURE 4: Plot showing concentration versus depth profiles of CH₄, H₂, ⁴He, and CO₂ obtained from measurements on gas samples collected during water flushing after core run 7/8.

helium isotope composition (<0.05 Ra) is governed by ³He from the reaction ${}^6\text{Li} (n, \alpha) {}^3\text{H}(\beta^-) {}^3\text{He}$ and ⁴He from the decay of uranium and thorium. Sublithospheric, asthenospheric, and deep mantle reservoirs are characterized by ³He/⁴He ratios of >1 Ra.

Correction of the measured helium isotopic ratios for atmospheric helium is required as gas samples contain a contribution of atmospheric gases. ⁴He/²⁰Ne or ⁴He/³⁶Ar ratios are mostly used to determine the degree of atmospheric contamination. ²⁰Ne and ³⁶Ar are both primordial, i.e., only to a negligible extent affected by ingrowth through radiogenic, nucleogenic, or fissiogenic processes in the continental crust. For our study, the ⁴He/²⁰Ne ratio is used to correct the measured ³He/⁴He ratios in the gas samples according to a method first described by Craig et al. [46], assuming that the continental crust is depleted in primordial noble gas nuclides and ²⁰Ne completely derives from the atmosphere.

Online gas monitoring during drilling has been performed in the Koyna pilot borehole KFD1 starting from the 1315 m to 2831 m depth in the granite-gneiss basement section. In the case of air hammer drilling, the formation gases suffered dilution with the air that was pumped into the borehole, as evident from the gas concentrations that are similar to that of air. Similarly, for the rare cases of mud drilling, no formation gases are detected as the volume of the drilled rock was very low compared to the drilling mud that was pumped downhole. We therefore do not report any gas data from air hammer drilling and mud drilling. The present study is based on data mostly from gas monitoring during water flushing and off-site laboratory studies on gas samples.

The formation gases analysed from online gas monitoring in the 1642–2831 m section during water flushing after the 7th and 8th coring runs are plotted in Figure 4. Sixteen

gas samples from 1737 m to 2831 m are analysed for N₂, O₂, Ar, CO₂, CH₄, H₂, and He. The molecular composition of the gas samples is reported in Table 1. Online gas monitoring together with laboratory analyses of gas samples show that the most abundant formation-derived gases from KFD1 are CO₂, CH₄, H₂, and He. The other gases such as N₂, O₂, and Ar derive from the atmospheric input in the drilling fluid, as indicated by relative proportions of concentrations of these gases indistinguishable from air. All hydrocarbons (C₂H₆, C₃H₈, i-C₄H₁₀, and n-C₄H₁₀) except CH₄ show negligible concentrations. Therefore, the present work emphasises on CO₂, CH₄, H₂, and He data sets. The concentrations of CO₂ reach up to 1200 ppmv (excluding an outlier with 32200 ppmv), CH₄ up to 186 ppmv, H₂ up to 139 ppmv, and He up to 12.8 ppmv. The data also indicates that most gas-rich zones generally occur below the 2100 m depth in the borehole. The measured helium concentrations are observed to be low at ~1800 m, increase substantially at the ~2217 m depth, and maintain the increased level up to the ~2831 m depth. Two prominent peaks, between 2121 m and 2217 m and between 2610 m and 2687 m, are observed.

Eleven gas samples collected from the depth section 1833–2831 m are also analysed for noble gas isotopes. Except for helium, abundances and isotope ratios of all noble gases are atmospheric and not reported here. The measured values of ⁴He/²⁰Ne and ³He/⁴He along with air-corrected ³He/⁴He ratios, the atmospheric contribution to the total helium, and the crustal and mantle-derived helium are listed in Table 2. Air correction of helium isotope ratios has been applied as ⁴He/²⁰Ne ratios for all the samples in the present study are higher than the atmospheric component of 0.319. The data shows that the measured ³He/⁴He ratios are in the range 0.43–0.91 Ra, with ⁴He/²⁰Ne values between 0.34 and

TABLE 2: Noble gas composition of gas samples collected during water flushing after core run 7/8 in the pilot hole KFD1 at Gothane, near Koyana, Western India.

Sample	Depth (m)	^4He (ppmv)	\pm	^{20}Ne (ppmv)	\pm	^{40}Ar (ppmv)	\pm	$^4\text{He}/^{20}\text{Ne}$	\pm	$^3\text{He}/^4\text{He}$ (Ra)	\pm	Crustal contribution (%)	Atmospheric contribution (%)
RIH14	1833	5.96	0.67	17.5	2.0	9900	1100	0.3449	0.0091	0.912	0.059	7.5	92.5
RIH15	1929	6.67	0.75	16.6	1.9	9400	1100	0.406	0.011	0.782	0.032	21.4	78.6
RIH16	2025	7.88	0.88	17.5	2.0	10000	1100	0.455	0.012	0.705	0.036	29.8	70.2
RIH17	2121	7.12	0.80	16.4	1.8	9300	1000	0.440	0.012	0.703	0.050	27.5	72.5
RIH18	2217	12.8	1.4	17.1	1.9	9300	1000	0.751	0.020	0.426	0.022	57.5	42.5
RIH19	2313	10.7	1.2	17.3	1.9	9700	1100	0.624	0.017	0.522	0.027	48.9	51.1
RIH20	2409	12.2	1.4	18.2	2.0	10200	1100	0.682	0.018	0.482	0.034	53.2	46.8
RIH21	2514	11.3	1.3	17.3	1.9	9900	1100	0.659	0.017	0.479	0.020	51.6	48.4
RIH22	2610	10.2	1.1	17.3	1.9	9900	1100	0.593	0.016	0.547	0.028	46.2	53.8
RIH24	2763	9.8	1.1	17.1	1.9	9800	1100	0.574	0.015	0.546	0.018	44.4	55.6
RIH25	2831	10.2	1.1	17.6	2.0	9900	1100	0.588	0.016	0.556	0.030	45.7	54.3

Depths are referenced to the kelly bushing, which was located at 3.5 m elevation with respect to ground level. Gas samples collected during running in and flushing out of water are designated by the prefix RIH. All errors are 2σ .

0.71, which confirms that the samples are a mixture of atmospheric helium and helium from crustal heat production. The low isotope ratios (<1) further confirm that there is no mantle contribution within the analytical uncertainties. The measured $^4\text{He}/^{20}\text{Ne}$ ratios are higher for gas samples below the 2100 m depth (Figure 5(a)). Assuming a value of 0.319 for the $^4\text{He}/^{20}\text{Ne}$ ratio for the atmospheric component, the calculated contribution of air in our samples ranges from 43% to 93% with an average value of 61%. Within 2σ analytical uncertainties, the mantle contribution to the total helium budget is zero for all samples. All samples are a mixture of atmospheric helium and helium from crustal origin (i.e., helium from radioactive decay of uranium and thorium in the continental crust). The same can be seen in the diagram $^3\text{He}/^4\text{He}$ versus $^4\text{He}/^{20}\text{Ne}$ (Figure 5(b)), where all data fall on a hyperbolic mixing curve between air and a crustal helium end-member with $^3\text{He}/^4\text{He} = 0.02$ (i.e., the average crustal production ratio, [47, 48]).

3.1. Comparison between Helium Concentrations from QMS and Noble Gas Isotope Measurements. A comparison has been made between ^4He concentrations obtained from QMS and noble gas isotope measurements for the depth section 1737–2831 m. The mass resolution of the QMS is not sufficient to separate ^3He ($m = 3.016$) from HD ($m = 3.022$); therefore, ^3He can only be determined by noble gas isotope mass spectrometer measurements. Two samples from the 1737 m and 2687 m depth were not analysed for noble gas isotopes, and therefore, ^4He concentration from isotope analysis for those samples are not reported here. As shown in Figure 6, ^4He concentrations from QMS (Table 1) and from noble gas isotope mass spectrometer measurements (Table 2) are in good agreement. Noble gas concentrations determined by noble gas isotope mass spectrometer measurements have been calculated from noble gas nuclide pressure and gas sample inlet pressure. The latter was determined during QMS analysis. We assume that the sample pressure measured by the QMS corresponds to the gas sample inlet pressure when being introduced to the gas line of the

noble gas isotope mass spectrometer measurements. The volume of our sample cylinders for all samples is 250 cc. Given a dead volume of 2 cc for the gas inlet, pressure reduction at the sample inlet in the gas line of the noble gas isotope mass spectrometer is $<1\%$.

In contrast to helium concentrations measured by the noble gas isotope mass spectrometer, the helium concentrations measured by QMS are automatically normalized to 100% as total gas concentration. If the QMS measurement considers all gas species present in the gas phase, then both methods should result in the same helium concentration values (in ppmv). A comparison between the two data sets shows a discrepancy in helium concentration values in the range 0.4–9.9% with an average value of 4.9% and no systematic trend. For four samples, the QMS measurement yields higher helium concentration values, whereas seven samples show the opposite. Given an analytical uncertainty of $\sim 10\%$ for helium concentrations, determined by both methods, the agreement between both data sets is convincing.

4. Discussion

The maximum helium concentrations detected in the 3 km deep pilot borehole KFD1 at Gothane is 12.8 ppmv (by both QMS and noble gas isotope measurements), more than 7 ppmv higher than the atmospheric helium abundance of 5.24 ppmv. Earlier soil-gas helium surveys followed by core drilling carried out between 1995 and 1997 across the Donichawadi fissure zone near Kadoli village provide strong evidence that the fissure zone represents the surface rupture zone of the 1967 earthquake [41]. Helium concentrations exceeding the atmospheric value by 1–7 ppmv coinciding with the surface fissures, which fall off sharply to background value of 0.2 ppmv above atmosphere at a distance of 40–60 m on either side of the fissures, confirm that the fissures constitute the surface expression of a NNE–SSW-oriented seismic fault and that the fault zone had not healed even 30 years after the 1967 earthquake (Figure 1(b)). Elevated helium concentrations detected at depths below 2100 m in the Koyana

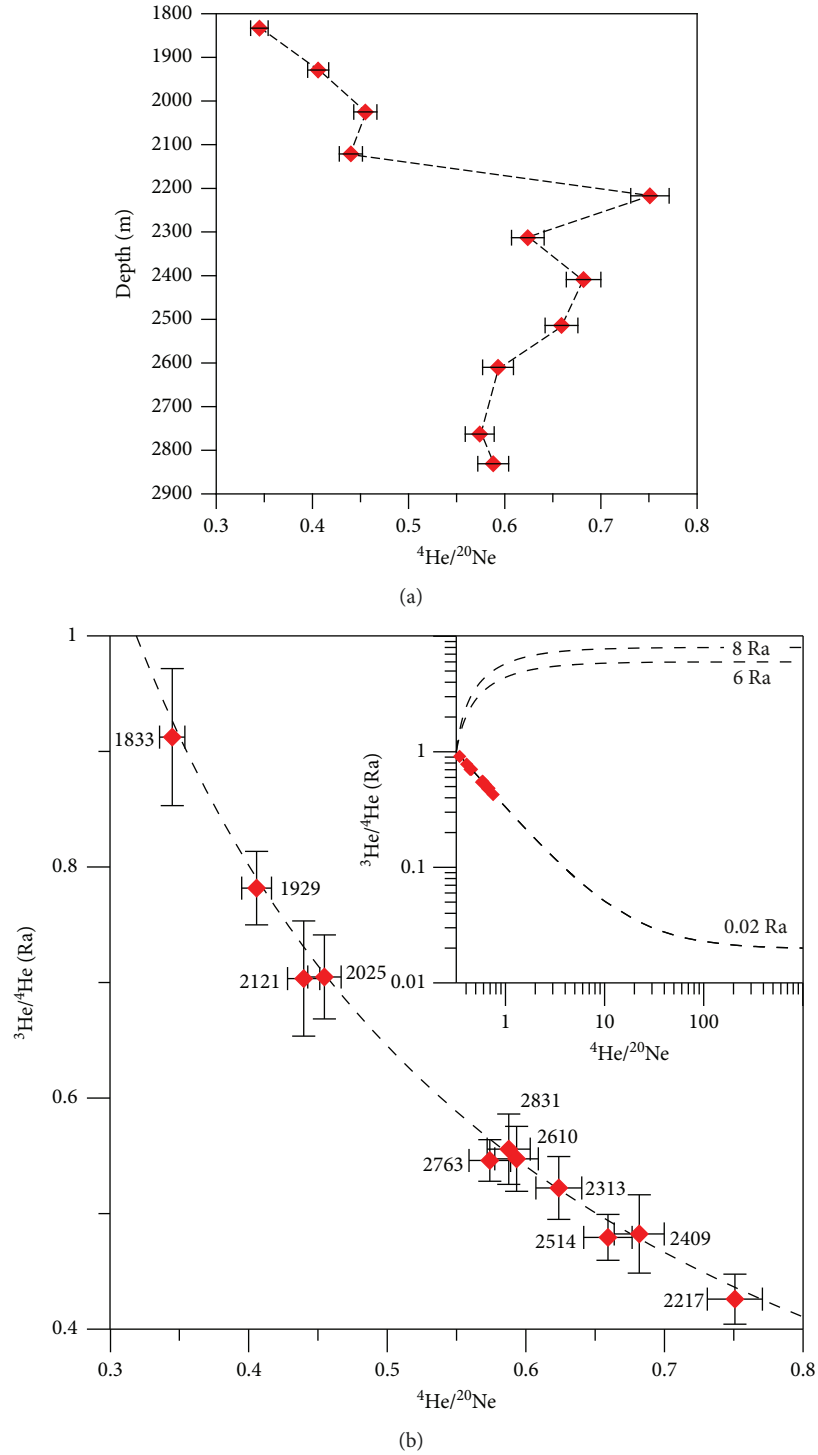


FIGURE 5: Plot showing (a) $^4\text{He}/^{20}\text{Ne}$ versus depth and (b) $^4\text{He}/^{20}\text{Ne}$ versus $^3\text{He}/^4\text{He}$, obtained from isotope measurements on gas samples collected during water flushing after core run 7/8. Error bars indicating uncertainty in the measurement are also shown. Depth of samples in “m” is indicated along with data points in (b). Inset shows mixing hyperbola between air and the continental crust and two different mantle end members (6 Ra for the lithospheric and 8 Ra for the asthenospheric mantle).

pilot borehole KFD1 of the present study are comparable to concentrations observed more than 20 years ago in the Donichawadi fissure zone. Additionally, $^3\text{He}/^4\text{He}$ and $^4\text{He}/^{20}\text{Ne}$ data from the present study reveal that helium gas obtained from the pilot borehole comprises atmospheric helium and

variable contributions of crustal radiogenic helium with no mantle helium.

In general, helium could be a mixture of atmospheric helium ($^3\text{He}/^4\text{He} = 1 \text{ Ra}$; [46, 47]) with different contributions of crustal helium ($^3\text{He}/^4\text{He} < 0.1 \text{ Ra}$) and mantle-

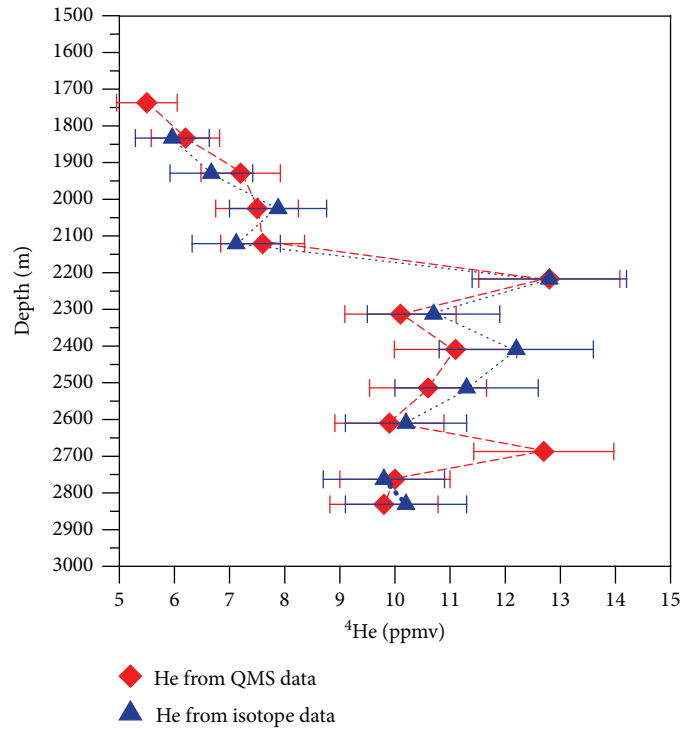


FIGURE 6: ^4He depth profiles from QMS measurements (red) and noble gas isotope analysis (blue) of gas samples collected during water flushing after core run 7/8. Error bars indicating uncertainty in the measurement are also shown. Samples from 1737 m and 2687 m depths were not analysed for noble gas isotopes.

derived helium ($^3\text{He}/^4\text{He} > 1 \text{ Ra}$, e.g., 6 Ra for the lithospheric mantle; [49]). Measured $^3\text{He}/^4\text{He}$ ratios from three soil-gas samples collected above the Donichawadi fissure zone fall between 0.59 and 0.63 Ra [41]. The reported $^3\text{He}/^4\text{He}$ ratios are not air-corrected, leaving open the question of any possible mantle contribution to the total helium budget. With measured helium concentrations of up to 12.24 ppmv (7 ppmv excess helium plus 5.24 ppmv atmospheric helium) and helium isotope compositions of 0.59–0.63 Ra in soil-gas samples, a mantle-derived helium contribution of ~2% would be possible assuming ^{20}Ne concentrations of 16.48 ppmv (atmospheric value). If indeed the Koyna fault gas would contain such a small but significant contribution of a mantle-derived component, questions would arise on the provenance of mantle helium at Koyna (e.g., mantle plume degassing) and its migration mechanisms. Basu et al. [50] determined helium isotope ratios of rock samples from two Deccan alkaline complexes from northern India to be 10–13 Ra. The authors interpret their findings as evidence to support a lower mantle plume origin of Deccan Traps volcanism. Our data, however, clearly point out that no mantle-derived helium is present in any of the samples obtained from the borehole KFD1.

The present study shows that formation gases (CO_2 , CH_4 , H_2 , and He) mostly enter the borehole below 2100 m, with a number of zones of significant He enhancement ranging from 4.6 to 7.6 ppmv above the atmospheric value. The observed gas-rich zones at depths below 2100 m have been compared with data from downhole geophysical logging acquired in the borehole KFD1 [51]. The gas-rich zones cor-

relate well with the zones of anomalous physical and mechanical properties identified from geophysical logs. For comparison, the resistivity and caliper logs are plotted along with the helium concentrations (Figure 7). The logs show a number of localized zones of low resistivity below 2000 m that correspond with the zones of helium enhancement. A number of such zones are also associated with substantial enlargement in borehole diameter. The enlargement in borehole diameter in the form of cavities or washout zones is likely due to the presence of fracture zones in the formation. Electrical (FMI®) and acoustic (UBI®) images acquired in the borehole have shown that these zones contain high fracture density with large number of open fractures, majority of which are oblique to subvertical in orientation. Two typical zones with high fracture density, 2141–2151 m and 2619–2629 m, discovered by electrical and acoustic borehole image logs are shown in Figure 7. These zones are in good agreement with those of gas enrichment observed in our study. On the whole, the present study indicates that the borehole has punctured multiple fracture zones in the subsurface. The association of low resistivity zones with high helium concentrations indicates that the open fractures act as potential pathways for fluid flow in the borehole.

The borehole KFD1 is located ~5 km to the south of Kadoli along the trend of the Donichawadi fault zone (Figure 1(a)). The consistency in concentrations and isotope ratios of soil-gas helium over the fissures near Kadoli and helium from different depths below 2100 m in the borehole KFD1 suggests that the pilot borehole intersects the southward extension of the Donichawadi fault zone

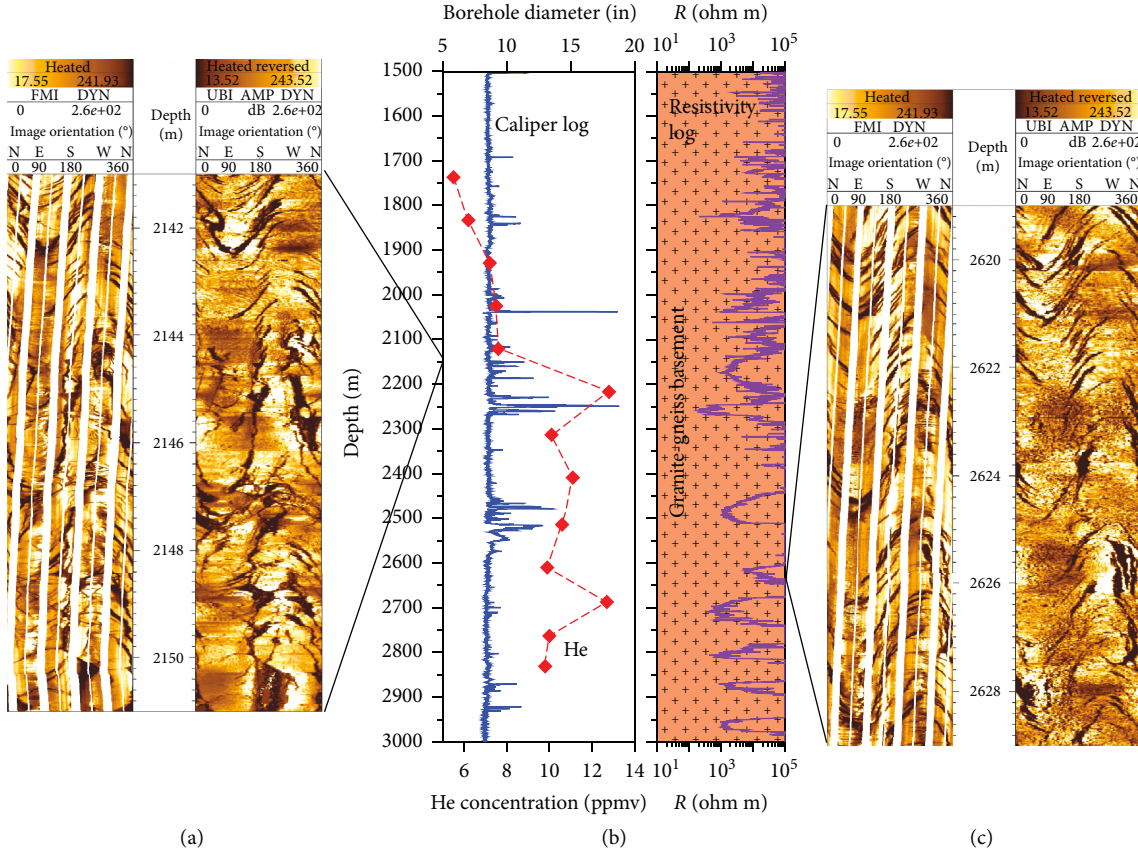


FIGURE 7: Plots showing downhole electrical resistivity (purple line) and caliper (blue line) logs along with helium concentration from QMS measurements (red diamonds) in the granitic basement section 1500-3000 m in the borehole KFD1. High resolution electrical (FMI) and acoustic (UBI) images of two typical depth sections 2141-2151 m (a) and 2619-2629 m (c) showing highly fractured basement rocks corresponding to zones of helium enhancements are also shown.

or its subsidiaries at multiple depths below ~2100 m. Results obtained from both the soil-helium gas study in the Donichawadi fault zone near Kadoli and the present study in the pilot borehole KFD1 demonstrate the possible connection of the Donichawadi fault through fractures zones where the gases migrated from the formation through media such as a borehole. Misra et al. [52] combined field investigations as well as physical and microstructural studies on basement core samples obtained from a 1522 m deep borehole at Rasati near Koyna to demonstrate the extension of the surface fissures into the granite-gneiss basement rocks at different depths beneath the Deccan flood basalt pile. They also suggested the association of these fissures with localized fault zones within the rock unit. Seismological studies including the analysis of seismograms recorded at a local network of 23 surface broadband stations and 6 borehole seismic stations show a distinct NNE-SSW trend of seismicity coinciding with the Donichawadi fault zone, indicating that the fault is still active [53, 54]. This inference gains support from other studies carried out in the Koyna region. Shashidhar et al. [55] carried out detailed studies on the M_w 4.8 earthquake of 14 April 2012, which is among the best monitored and well characterized events in the Koyna region. Using the amplitude inversion and the moment tensor inversion techniques, they show that the depth distribution of the aftershocks

defines a NNE-SSW-trending fault plane dipping about 78° to the WNW, which is consistent with the trend of the Donichawadi fault. Shashidhar et al. [56] studied the earthquakes that occurred during January 2016 and May 2017 in the Koyna region and found that the seismicity is mostly confined to the Donichawadi fault zone during the reservoir drawdown phase (January-May) but occurred in a wider region during the reservoir-refilling phase (June-December). They attributed this pattern to the effect of pore pressure growth and retreat of the pressure front during loading and unloading cycles of the reservoir, respectively. All these studies point out that the seismicity in the Koyna region is mostly concentrated in the vicinity of the Donichawadi fault, which is still controlling the seismotectonics of the Koyna region even 50 years after the occurrence of the 1967 Koyna earthquake.

The present study shows that helium concentration is relatively low above the ~2121 m depth (≤ 7.6 ppmv) followed by a sudden increase of helium at ~2217 m (12.8 ppmv) which is maintained (9.8-12.7 ppmv) up to ~2831 m. To understand the variations with depth, helium data has been compared with Th and U data obtained from the spectral gamma ray log in the borehole KFD1. The decay chains of ^{235}U , ^{238}U , and ^{232}Th are the main sources of radiogenic helium. The proportion of uranium and thorium for the

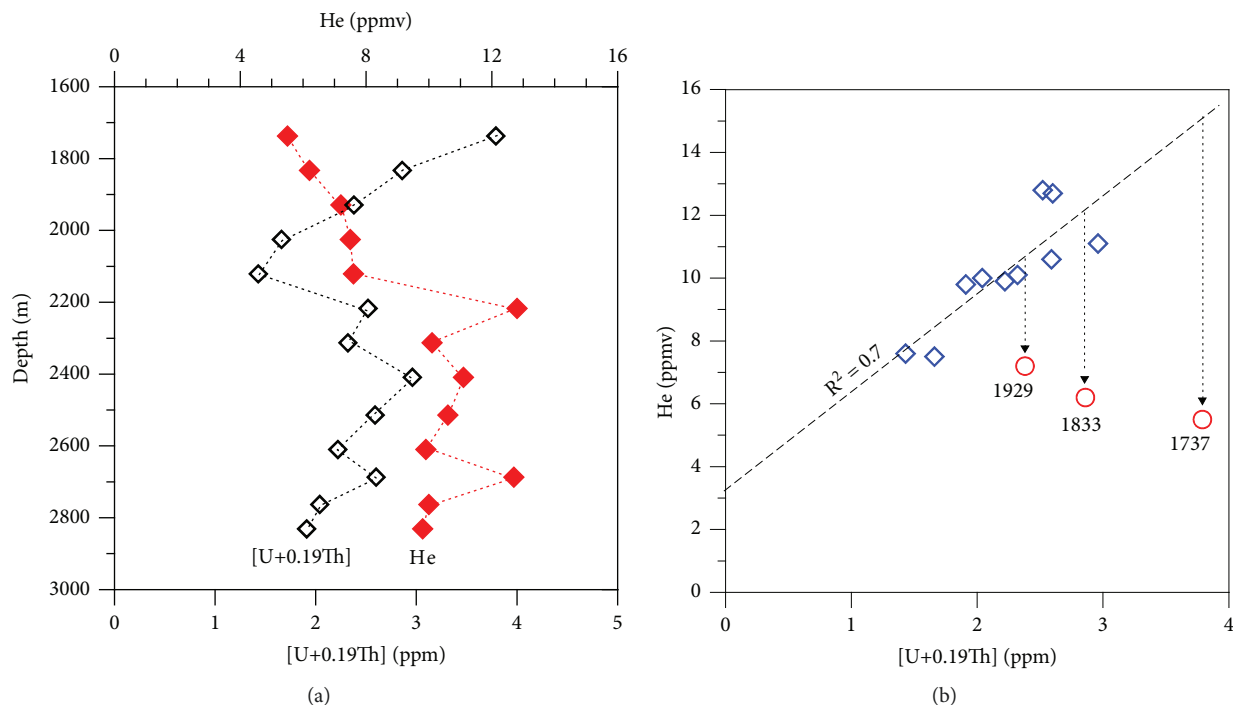


FIGURE 8: (a) Plot showing depth distribution of [U+0.19Th] (black open diamonds) and He (red diamonds). [U+0.19Th] values are averaged over the same ~ 100 m depth intervals as the depth of the water columns from where helium was extracted. (b) Correlation diagram for He versus [U+0.19Th]. Blue open diamonds indicate data from below 2100 m depth, where a positive correlation ($R^2 = 0.70$) is obvious. Red open circles are data from shallower depth which might be affected by helium loss (degassing).

current production of ^4He is [U+0.24Th], sometimes called “effective uranium” (eU). Due to different half-life times of uranium and thorium, this proportion is not constant over geological times and is time-integrated for the last 2.7 Ga (age of the crystalline basement rocks [57]), [U+0.19Th].

Plotting helium concentrations against [U+0.19Th], averaged over the same ~ 100 m depth intervals as for helium, displays a positive correlation for all data points below 2000 m (Figure 8). A linear fit ($R^2 = 0.70$) yields 3.14 ppmv helium per ppm [U+0.19Th]. An interesting observation is that for the shallow samples (< 2000 m), the correlation between [U+0.19Th] and He is not valid. Assuming that the downhole logging data for U and Th are appropriate, the corresponding helium concentration should be between 10 and 14 ppmv, much higher than observed (≤ 7 ppmv, Figure 8). The helium-bearing water column from depths < 2000 m may therefore have undergone significant loss of helium. A possible explanation for helium lost from the water column would be partial helium degassing in the upper two kilometres of the water column in the borehole [48, 58]. Other mechanisms to explain the apparent helium lost in the upper part of the borehole, e.g., diffusion or lower permeability, are less suitable to explain the trend of increasing helium lost with shallower depth.

It should be noted that for all gases investigated in our study (CH_4 , CO_2 , H_2 , and He), significant increase of gas concentrations is observed below the 2100 m depth (Figure 4). Helium (radiogenic) and hydrogen (radiolytic) might be produced by U and Th decay in situ, but this is a little likely for CO_2 and CH_4 . Organic material, which

could serve as a source for in situ production of CO_2 and CH_4 , was not reported in cuttings and cores from KFD1. Moreover, the possibility for generation of organic matter in intact granite-gneiss formation is extremely remote. The only possibility appears to be fracture zones intersecting the borehole in the granitic basement that could serve as potential locales of organic matter or siderophilic bacteria transported along with fluids from the overlying rock mass. As described in the previous section, the granitic basement formation below the 2000 m depth is highly fractured at several depths, which may provide the favourable pathways for fluids to flow in the borehole. Moreover, it is also not clear whether U and Th are located in the rock matrix, as fluids in the fractures could have served as carriers for U and Th. We therefore interpret the helium data as partially deriving from formation pore space around the borehole and partially flowing through open fractures in the borehole. This indicates fluid-controlled migration through permeable strata such as fractures/faults at depths below 2100 m resulting in high helium concentrations relative to depths above 2100 m. Eventually, the presence of permeable fracture/fault zones will have important implications for the pore pressure evolution at depths and the occurrence of reservoir-triggered earthquakes in the Koyna region.

In the present study, online gas monitoring has not shown significant inflow of formation gases during both air hammer and mud drilling. In the case of the former, formation gases in crystalline rock were diluted with the volumes of air pumped down the hole, and in the case of the latter, this was due to the mud weight and the lower

surface to volume ratio of the drill core. However, as gas extraction and analysis during water flushing following each core run showed the presence of anomalous formation gases, the study opens up a new approach to study crustal gases in such scenarios.

Our study, together with the results from the previous soil-gas helium study, demonstrates the presence of helium at seismogenic depths in this region. This suggests that continuous monitoring of deeper gas emanations in the subsurface could be useful to understand temporal gas variations in the fault zones, which in turn could be useful for earthquake precursory studies in this region.

5. Conclusions

Online gas analyses and off-line noble gas isotope studies on eleven gas samples collected during water flushing in the Koyna pilot borehole KFD1 brings out the following conclusions:

- (1) Formation gases (CO_2 , CH_4 , H_2 , and He) mostly enter the borehole at different depths below 2100 m, with significant He enhancement ranging from 4.6 to 7.6 ppmv above the atmospheric value. The He-rich zones correlate well with the zones of anomalous physical and mechanical properties delineated from geophysical logs and are characterized by high fracture density as revealed from borehole images, indicating fluid-controlled migration through permeable strata such as fractures/faults at those depths
- (2) The helium concentrations measured in the borehole below the 2100 m depth are in good agreement with the concentrations observed at the surface more than 20 years ago, which confirms that the Donichawadi fault zone is still permeable, 50 years after the 1967 M 6.3 Koyna earthquake
- (3) Air-corrected helium isotope ratios indicate that helium is composed of atmospheric helium and variable contributions of crustal radiogenic helium with no mantle helium input within 2σ analytical uncertainties
- (4) The presence of helium at seismogenic depths in this region is evident; however, a deeper understanding of fluid migration in time and space and its link to fault processes requires further investigations

Data Availability

The datasets used to support the findings of the study are included within the article.

Conflicts of Interest

The authors declare that they have no conflicts of interest.

Acknowledgments

We thank the Secretary to the Government of India, Ministry of Earth Sciences, for the support and encouragement in carrying out scientific drilling and associated studies in the Koyna region. This work was carried out in collaboration with the International Continental Scientific Drilling Program (ICDP). We are grateful to Harsh Gupta for steering the programme on scientific deep drilling at Koyna and for extended field discussions during the course of the study. Shailesh Nayak provided critical geological inputs during planning and execution. Vyasulu V. Akkiraju, Digant Vyas, Ashish Warhade, and Dinesh Nikalje provided invaluable help during gas monitoring at the drill site, and Deepjyoti Goswami helped with interpretation of image logs. Shivganga Drillers provided valuable logistic support at the drill site. Noble gas isotope analysis was performed at the GFZ Potsdam noble gas laboratory (Section 3.1); we are grateful to Samuel Niedermann and Enzio Schnabel for the tremendous help. The manuscript has benefited from constructive suggestions from two anonymous reviewers. We thank the Director, NCPOR, for facilitating the studies.

References


- [1] S. Hickman, R. Sibson, and R. Bruhn, "Introduction to special section: mechanical involvement of fluids in faulting," *Journal of Geophysical Research: Solid Earth*, vol. 100, no. B7, pp. 12831–12840, 1995.
- [2] J. R. Rice, "Fault stress states, pore pressure distributions, and the weakness of the San Andreas Fault," *International Geophysics*, vol. 51, pp. 475–503, 1992.
- [3] A. Gudmundsson, "Fluid overpressure and stress drop in fault zones," *Geophysical Research Letters*, vol. 26, no. 1, pp. 115–118, 1999.
- [4] J. Imber, R. E. Holdsworth, S. A. F. Smith, S. P. Jefferies, and C. Collettini, "Frictional-viscous flow, seismicity and the geology of weak faults: a review and future directions," *Geological Society, London, Special Publications*, vol. 299, no. 1, pp. 151–173, 2008.
- [5] P. Möller, S. M. Weise, E. Althaus et al., "Paleofluids and recent fluids in the upper continental crust: results from the German Continental Deep Drilling Program (KTB)," *Journal of Geophysical Research: Solid Earth*, vol. 102, no. B8, pp. 18233–18254, 1997.
- [6] W. Bach, D. Naumann, and J. Erzinger, "A helium, argon, and nitrogen record of the upper continental crust (KTB drill holes, Oberpfalz, Germany): implications for crustal degassing," *Chemical Geology*, vol. 160, no. 1–2, pp. 81–101, 1999.
- [7] J. Erzinger, T. Wiersberg, and M. Zimmer, "Real-time mud gas logging and sampling during drilling," *Geofluids*, vol. 6, no. 3, 233 pages, 2006.
- [8] G. V. Rao, G. K. Reddy, R. U. M. Rao, and K. Gopalan, "Extraordinary helium anomaly over surface rupture of September 1993 Killari earthquake, India," *Current Science*, vol. 66, no. 12, pp. 933–935, 1994.
- [9] G. K. Reddy, G. V. Rao, R. U. M. Rao, and K. Gopalan, "Surface rupture of Latur earthquake : the soil-gas helium signature," *Memoir Geological Society of India*, vol. 35, pp. 83–99, 1994.

- [10] C. Y. King, "Radon monitoring for earthquake prediction in China," *Earthquake Prediction Research*, vol. 3, no. 1, pp. 47–68, 1985.
- [11] C. Y. King, "Gas geochemistry applied to earthquake prediction: an overview," *Journal of Geophysical Research: Solid Earth*, vol. 91, no. B12, pp. 12269–12281, 1986.
- [12] D. Thomas, "Geochemical precursors to seismic activity," *Pure and Applied Geophysics*, vol. 126, no. 2-4, pp. 241–266, 1988.
- [13] H. Wakita, Y. Nakamura, and Y. Sano, "Short-term and intermediate-term geochemical precursors," *Pure and Applied Geophysics*, vol. 126, no. 2-4, pp. 267–278, 1988.
- [14] G. M. Reimer, "Prediction of Central California earthquakes from soil-gas helium fluctuations," *Pure and Applied Geophysics*, vol. 122, no. 2-4, pp. 369–375, 1985.
- [15] H. S. Virk, V. Walia, and N. Kumar, "Helium/radon precursory anomalies of Chamoli earthquake, Garhwal Himalaya, India," *Journal of Geodynamics*, vol. 31, no. 2, pp. 201–210, 2001.
- [16] T. F. Yang, C. C. Fu, V. Walia et al., "Seismo-geochemical variations in SW Taiwan: multi-parameter automatic gas monitoring results," *Pure and Applied Geophysics*, vol. 163, no. 4, pp. 693–709, 2006.
- [17] V. Walia, S. Mahajan, A. Kumar et al., "Fault delineation study using soil-gas method in the Dharamsala area, NW Himalayas, India," *Radiation Measurements*, vol. 43, pp. S337–S342, 2008.
- [18] J.-P. Toutain and J. C. Baubron, "Gas geochemistry and seismotectonics: a review," *Tectonophysics*, vol. 304, no. 1-2, pp. 1–27, 1999.
- [19] M. Zimmer and J. Erzinger, "On the geochemistry of gases information and drilling fluids – results from the KTB," *Scientific Drilling*, vol. 5, pp. 101–109, 1995.
- [20] T. Wiersberg and J. Erzinger, "A helium isotope cross-section study through the San Andreas Fault at seismogenic depths," *Geochemistry, Geophysics, Geosystems*, vol. 8, no. 1, 2007.
- [21] T. Wiersberg and J. Erzinger, "Origin and spatial distribution of gas at seismogenic depths of the San Andreas Fault from drill-mud gas analysis," *Applied Geochemistry*, vol. 23, no. 6, pp. 1675–1690, 2008.
- [22] T. Wiersberg and J. Erzinger, "Chemical and isotope compositions of drilling mud gas from the San Andreas Fault Observatory at Depth (SAFOD) boreholes: implications on gas migration and the permeability structure of the San Andreas Fault," *Chemical Geology*, vol. 284, no. 1-2, pp. 148–159, 2011.
- [23] Z. Gong, H. Li, C. Lao, L. Tang, and L. Luo, "Real-time drilling mud gas monitoring records seismic damage zone from the 2008 Mw 7.9 Wenchuan earthquake," *Tectonophysics*, vol. 639, pp. 109–117, 2015.
- [24] S. B. Hammerschmidt, T. Wiersberg, V. B. Heuer, J. Wendt, J. Erzinger, and A. Kopf, "Real-time drilling mud gas monitoring for qualitative evaluation of hydrocarbon gas composition during deep sea drilling in the Nankai Trough Kumano Basin," *Geochemical Transactions*, vol. 15, no. 1, p. 15, 2014.
- [25] T. Wiersberg, A. M. Schleicher, K. Horiguchi, M. L. Doan, N. Eguchi, and J. Erzinger, "Origin and in situ concentrations of hydrocarbons in the Kumano forearc basin from drilling mud gas monitoring during IODP NanTroSEIZE Exp. 319," *Applied Geochemistry*, vol. 61, pp. 206–216, 2015.
- [26] T. Wiersberg, S. B. Hammerschmidt, S. Fuchida, A. Kopf, and J. Erzinger, "Mantle-derived fluids in the Nankai Trough Kumano forearc basin," *Progress in Earth and Planetary Science*, vol. 5, no. 1, 2018.
- [27] H. K. Gupta and B. K. Rastogi, "Developments in Geotechnical Engineering," in *Dams and Earthquakes*, vol. 11, pp. 1–229, Elsevier Scientific Publishing Company, Amsterdam, Netherlands, 1976.
- [28] H. K. Gupta, *Reservoir-Induced Earthquakes*, Elsevier, Amsterdam, Netherlands, 1992.
- [29] H. K. Gupta, "A review of recent studies of triggered earthquakes by artificial water reservoirs with special emphasis on earthquakes in Koyna, India," *Earth-Science Reviews*, vol. 58, no. 3-4, pp. 279–310, 2002.
- [30] H. K. Gupta, "Artificial water reservoir triggered earthquakes," in *Encyclopedia of Solid Earth Geophysics*, H. K. Gupta, Ed., pp. 15–24, Springer, 2011.
- [31] P. Talwani, "Seismotectonics of the Koyna-Warna area, India," *Pure and Applied Geophysics*, vol. 150, no. 3-4, pp. 511–550, 1997.
- [32] H. K. Gupta, C. V. Ramakrishna Rao, B. K. Rastogi, and S. C. Bhatia, "An investigation of earthquakes in Koyna region, Maharashtra for the period October 1973 through December 1976," *Bulletin of the Seismological Society of America*, vol. 70, no. 5, pp. 1838–1847, 1980.
- [33] H. K. Gupta, P. Mandal, and B. K. Rastogi, "How long will triggered earthquakes at Koyna, India continue?," *Current Science*, vol. 82, no. 2, pp. 202–210, 2002.
- [34] H. K. Gupta, K. Arora, N. Purnachandra Rao et al., "Investigations of continued reservoir triggered seismicity at Koyna, India," *Geological Society, London, Special Publications*, vol. 445, no. 1, pp. 151–188, 2017.
- [35] S. K. Guha, P. D. Gosavi, M. M. Varma, S. P. Agarwal, J. G. Padale, and S. C. Marwadi, "Recent seismic disturbances in the Shivajisagar Lake area of the Koyna Hydroelectric Project, Maharashtra, India," Research Report Central Water and Power Research Station, Poona, India, 1968.
- [36] B. K. Rastogi, R. K. Chadha, C. S. P. Sarma et al., "Seismicity at Warna reservoir (near Koyna) through 1995," *Bulletin of the Seismological Society of America*, vol. 87, no. 6, pp. 1484–1494, 1997.
- [37] H. K. Gupta, "Induced seismicity hazard mitigation through water level manipulation at Koyna, India: a suggestion," *Bulletin of Seismological Society of America*, vol. 73, no. 2, pp. 679–682, 1983.
- [38] S. Roy, "Scientific drilling in Koyna region, Maharashtra," *Current Science*, vol. 112, no. 11, p. 2181, 2017.
- [39] N. Podugu, A. Yadav, K. Mallika, D. Goswami, and M. U. Anuradha, "Report on ICDP post-operations international workshop on "scientific deep drilling in Koyna, India"," *Journal of the Geological Society of India*, vol. 91, no. 1, pp. 120–124, 2018.
- [40] GSI, "A geological report on the Koyna earthquake of 11th December, 1967," Report submitted by Officers of the Geological Survey of India, Satara District, Maharashtra State, India, 1968.
- [41] H. K. Gupta, R. U. M. Rao, R. Srinivasan et al., "Anatomy of surface rupture zones of two stable continental region earthquakes, 1967 Koyna and 1993 Latur, India," *Geophysical Research Letters*, vol. 26, no. 13, pp. 1985–1988, 1999.
- [42] R. V. Sathe, A. V. Padke, V. V. Peshwa, and R. K. Sukhatankar, "On the development of fissures and cracks in the region around the Koyna Nagar earthquake affected area," *Journal*

- of University of Poona, Science and Technology Section, vol. 34, pp. 15–19, 1968.
- [43] S. Misra, V. Bartakke, G. Athavale, V. V. Akkiraju, D. Goswami, and S. Roy, “Granite-gneiss basement below Deccan Traps in the Koyna region, western India: Outcome from scientific drilling,” *Journal of the Geological Society of India*, vol. 90, no. 6, pp. 776–782, 2017.
 - [44] S. Niedermann, W. Bach, and J. Erzinger, “Noble gas evidence for a lower mantle component in MORBs from the southern East Pacific Rise: decoupling of helium and neon isotope systematics,” *Geochimica et Cosmochimica Acta*, vol. 61, no. 13, pp. 2697–2715, 1997.
 - [45] T. Wiersberg, S. Süer, N. Güleç, J. Erzinger, and M. Parlaktuna, “Noble gas isotopes and the chemical composition of geothermal gases from the eastern part of the Büyük Menderes Graben (Turkey),” *Journal of Volcanology and Geothermal Research*, vol. 208, no. 3–4, pp. 112–121, 2011.
 - [46] H. Craig, J. E. Lupton, and Y. Horibe, “A mantle helium component in circum-Pacific volcanic gases: Hakone, the Marianas, and Mt. Lassen,” in *Terrestrial Rare Gases*, E. C. Alexander and M. Ozima, Eds., pp. 3–16, Science Societies Press, Tokyo, Japan, 1978.
 - [47] B. A. Mamyrin and L. N. Tolstikhin, *Helium Isotopes in Nature*, Elsevier, New York, NY, USA, 1984.
 - [48] C. J. Ballentine and P. G. Burnard, “Production, release and transport of noble gases in the continental crust,” *Reviews in Mineralogy and Geochemistry*, vol. 47, no. 1, pp. 481–538, 2002.
 - [49] T. J. Dunai and H. Baur, “Helium, neon, and argon systematics of the European subcontinental mantle: Implications for its geochemical evolution,” *Geochimica et Cosmochimica Acta*, vol. 59, no. 13, pp. 2767–2783, 1995.
 - [50] A. R. Basu, P. R. Renne, D. K. DasGupta, F. Teichmann, and R. J. Poreda, “Early and late alkali igneous pulses and a high-³He plume origin for the Deccan flood basalts,” *Science*, vol. 261, no. 5123, pp. 902–906, 1993.
 - [51] D. Goswami, S. Roy, and V. V. Akkiraju, “Delineation of damage zones from 3 km downhole geophysical logs in the Koyna seismogenic zone, western India,” *Journal of Geophysical Research: Solid Earth*, vol. 124, no. 6, pp. 6101–6120, 2019.
 - [52] S. Misra, S. Roy, V. Bartakke, G. Athavale, and H. Gupta, “Fissures and fractures in the Koyna seismogenic zone, Western India,” *Journal of the Geological Society of India*, vol. 90, no. 2, pp. 131–137, 2017.
 - [53] H. K. Gupta, D. Shashidhar, C. R. Mahato et al., “Location of the pilot borehole for investigations of reservoir triggered seismicity at Koyna, India,” *Gondwana Research*, vol. 42, pp. 133–139, 2017.
 - [54] D. Shashidhar, K. Mallika, C. Mahato et al., “A catalogue of earthquakes in the Koyna-Warna region, Western India (2005–2017),” *Journal of the Geological Society of India*, vol. 93, no. 1, pp. 7–24, 2019.
 - [55] D. Shashidhar, N. P. Rao, D. Srinagesh et al., “The 14 April 2012 Koyna earthquake of M_w 4.8: insights into active tectonics of the Koyna region,” *Journal of Seismology*, vol. 17, no. 4, pp. 1345–1353, 2013.
 - [56] D. Shashidhar, K. Mallika, C. R. Mahato, B. S. Maity, and H. V. S. Satyanarayana, “Recent seismicity patterns and micro-earthquake activity on an active intraplate fault system at Koyna-Warna, western India,” *Journal of the Geological Society of India*, vol. 90, no. 6, pp. 798–801, 2017.
 - [57] Y. J. Bhaskar Rao, B. Sreenivas, T. Vijaya Kumar, N. Khadke, A. Kesava Krishna, and E. V. S. S. K. Babu, “Evidence for Neoproterozoic Basement for the Deccan volcanic flows around Koyna-Warna region, Western India: zircon U-Pb age and Hf-isotopic results,” *Journal of the Geological Society of India*, vol. 90, no. 6, pp. 752–760, 2017.
 - [58] T. Torgersen, “Continental degassing flux of ⁴He and its variability,” *Geochemistry, Geophysics, Geosystems*, vol. 11, no. 6, 2010.

Research Article

Gamma Ray and Radon Anomalies in Northern Taiwan as a Possible Preearthquake Indicator around the Plate Boundary

Ching-Chou Fu ¹, **Lou-Chuang Lee**¹, **Tsanyao Frank Yang**^{2†}, **Cheng-Horng Lin**¹,
Cheng-Hong Chen², **Vivek Walia**³, **Tsung-Kwei Liu**², **Dimitar Ouzounov**⁴,
Gioacchino Giuliani⁵, **Tzu-Hua Lai**⁶, and **Peng-Kang Wang**¹

¹*Institute of Earth Sciences, Academia Sinica, Taiwan*

²*Department of Geosciences, National Taiwan University, Taiwan*

³*National Center for Research on Earthquake Engineering, NARL, Taiwan*

⁴*Chapman University, One University Drive, Orange, CA, USA*

⁵*Permanent Foundation G. Giuliani, L'Aquila, Italy*

⁶*Central Geological Survey, MOEA, Taiwan*

[†]*Deceased*

Correspondence should be addressed to Ching-Chou Fu; ccfu@earth.sinica.edu.tw

Received 15 March 2019; Revised 11 June 2019; Accepted 23 June 2019; Published 4 September 2019

Guest Editor: Yunpeng Wang

Copyright © 2019 Ching-Chou Fu et al. This is an open access article distributed under the Creative Commons Attribution License, which permits unrestricted use, distribution, and reproduction in any medium, provided the original work is properly cited.

Taiwan is tectonically situated in an oblique collision zone between the Philippine Sea Plate (PSP) and the Eurasian Plate (EP). Continuous observations of gamma rays at the Yangmingshan (YMSG) station and soil radon at the Tapingti (TPT) station were recorded in the volcanic area and around a major fault zone, respectively, in Taiwan for seismic studies. A number of anomalous high gamma ray counts and radon concentrations at certain times were found. It is noted that significant increases of soil radon concentrations were observed and followed by the increase in gamma rays a few days to a few weeks before earthquakes that occurred in northeastern Taiwan. Earthquakes such as these are usually related to the subduction of the PSP beneath the EP to the north along the subduction zone in northern Taiwan (e.g., $M_L = 6.4$, April 20, 2015). It is suggested that the preseismic activity may be associated with slow geodynamic processes at the subduction interface, leading to the PSP movement triggering radon enhancements at the TPT station. Furthermore, the further movement of the PSP might be blocked by the EP, with the accumulated elastic stress resulting in the increase of gamma rays due to the increase in porosity and fractures below the YMSG station. The continuous monitoring of the multiple parameters can improve the understanding of the relationship between the observed radon and gamma ray variations and the regional crustal stress/strain in north and northeastern Taiwan.

1. Introduction

The island of Taiwan is the result of an oblique collision zone, with a convergence rate of about 8 cm/yr in the direction of 306° [1], between the Philippine Sea Plate (PSP) and the Eurasian Plate (EP) (Figure 1). In the south, the EP underthrusts the PSP to the east along the Manila trench, while to the north, the PSP subducts beneath the EP along the Ryukyu Arc and induces spreading of the Okinawa Trough. The interaction of these two plates generates many earthquakes. The Plio-Pleistocene volcanism of the Tatun Volcano Group

(TVG) is situated both at the northern tip of Taiwan and the western tip of the Ryukyu Arc, which might be associated with the opening of the Okinawa Trough and the postcollisional extension [2–4]. According to previous radiometric dating investigations, two major eruptions of the TVG occurred at 2.5–2.8 Ma and 0.8–0.2 Ma [5–10]. Juang [11] considered the TVG extinct because the last major volcanism occurred from 0.8 to 0.2 BP. Also, Chen and Shen [12] reviewed some records of historical eruptions in northern Taiwan and suggested that volcanism of the TVG has ended.

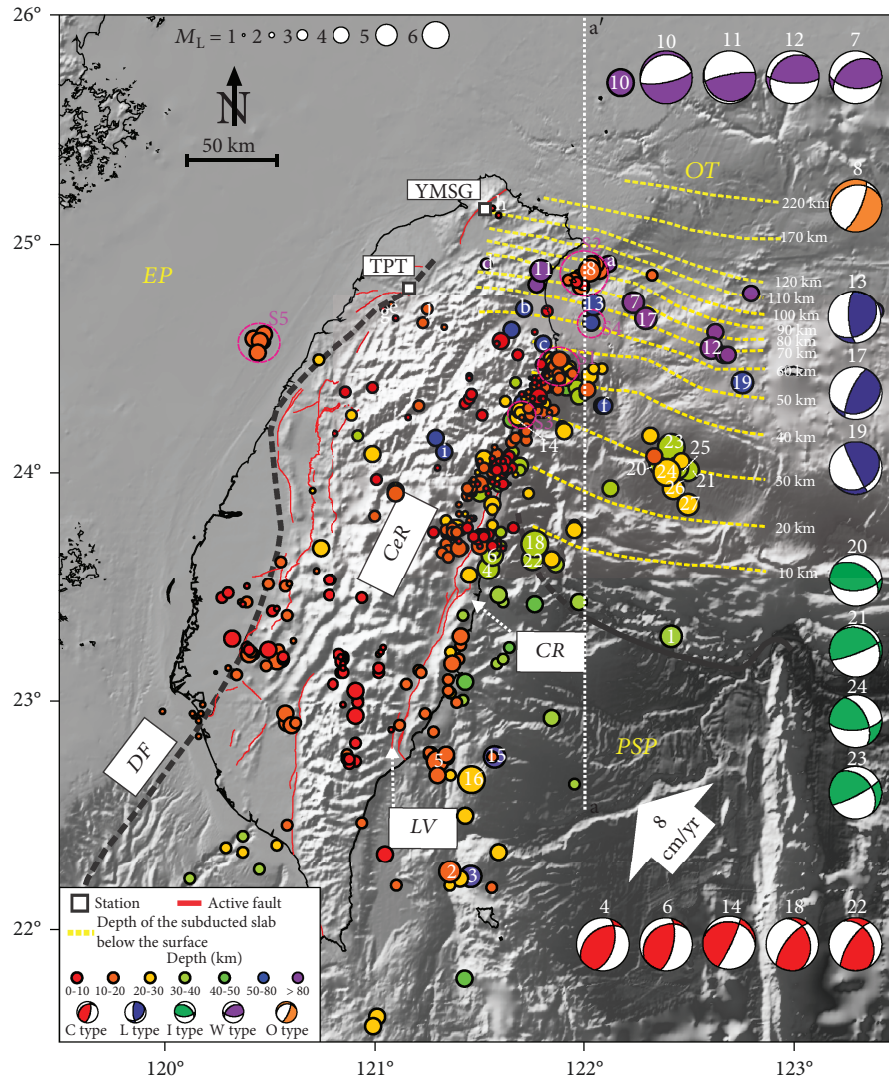


FIGURE 1: The simplified sketch of the regional map and principal tectonic structures around Taiwan shows that the Philippine Sea Plate (PSP) is moving northwest at 8 cm/yr towards the Eurasia Plate (EP). The circle symbols represent the earthquake epicenter with the focal depths corresponding to different colors from July 1, 2014, to June 1, 2015. The open square represents the location of the YMSG gamma ray station and the TPT radon station. The red lines indicate the active fault proposed by the Central Geological Survey of Taiwan [66]. Seismic events with magnitudes larger than five and some specific earthquakes are labeled and listed in Table 2. The yellow dashed lines indicate the isodepth contours between 10 and 220 km. OT = Okinawa Trough; CeR = central range; CR = costal range; LV = Longitudinal Valley; DF = deformation front.

However, Yang et al. [13, 14] and Ohba et al. [15] suggested that a magma chamber might still exist beneath the TVG area based on a high $^3\text{He}/^4\text{He}$ ratio from fumarolic gas and the high $\text{CO}_2/\text{H}_2\text{O}$ ratio of magmatic components. Konstantinou et al. [16] and Wen et al. [17] proposed that magma chambers might exist at depths of 7 to 20 km as indicated by the seismicity characteristics and attenuation structure. Lin [18] proposed the presence of a deep magma reservoir in the lower crust using S-wave shadow and P-wave delay. In recent years, there have been an increasing number of studies in the TVG area focusing on geochemical investigations and monitoring of the gas compositions, soil flux, and hot spring water [19–27] and seismological and geological research, such as seismicity, seismic variations, and ground deformation [16, 28–33], which has provided

more evidences that the TVG could still be active. As the TVG is located close to the Taipei metropolis and two nuclear power plants, long-term monitoring is necessary for providing possible early warnings of volcano-related hazards and major earthquakes.

Radon (^{222}Rn) is the major radioactive gas in this volcanic area. To investigate volcanic activity in the volcanic areas, the monitoring of radon level variations has been considered as a useful tool [20, 27, 34–38]. This research provides another way to record gamma rays related to radon gas emission from underground towards the surface. The anomalous gamma rays may be associated with the radioactive material released during crustal fracturing due to plate motions and geodynamic processes [39]. The objective of this paper is to assess the feasibility of using the gamma ray method to

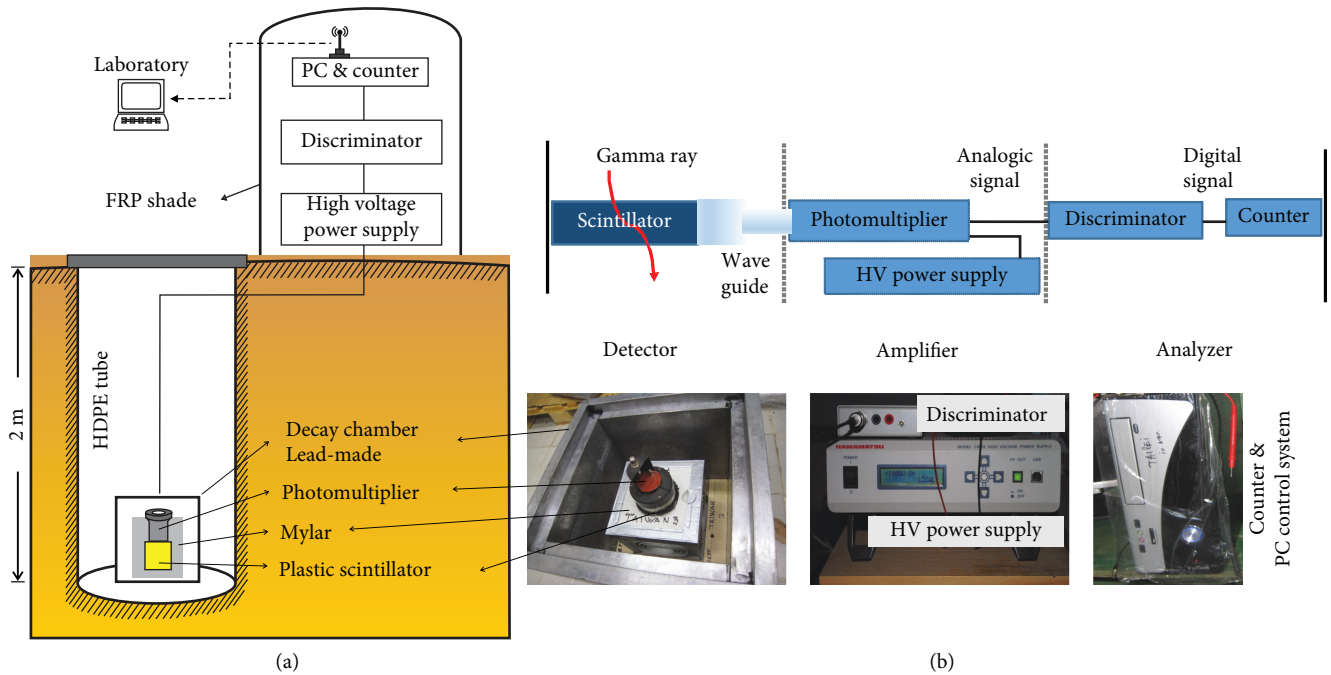


FIGURE 2: (a) Schematic of the gamma ray sensor installation in the YMSG monitoring station. (b) The block diagram and pictures of the gamma sensor assembly.

monitor seismic and volcanic activities in northern Taiwan. The location of the gamma ray station in the Yangmingshan (YMSG) area near the Taiwan Volcano Observatory at Tatun (TVO) was chosen for the first gamma ray observations in a volcanic region of Taiwan. In this study, gamma rays were continually monitored from July 1, 2014, to June 1, 2015. The potential for using a gamma ray anomaly as the possible precursor of earthquake and/or volcanic activity in northern Taiwan was further evaluated on this basis. In order to evaluate the accuracy of possible anomalous gamma ray changes, the radon variations at the Tapingti (TPT) station were chosen for comparison, being located about 70 km southwest of the YMSG gamma ray station.

2. Methodology

Radon is a naturally radioactive noble gas, widely distributed in various places throughout the Earth's crust. Radon is generated in the uranium decay series. The emission of energy from radon can be in the form of alpha or beta particles and gamma rays. Thus, gamma radiation can be used for indirectly determining the radon concentration.

The YMSG monitoring station is equipped with a gamma ray spectrometer with a scintillation counter inside a container made of 7 cm thick lead, inserted in a High-Density Polyethylene (HDPE) tube at a depth of 2 meters (Figure 2). The NE110 gamma ray is a plastic scintillator with a size of 400 mm × 400 mm × 400 mm, connected to photomultipliers with a diameter of 7.6 cm. Any cosmic gamma rays from atmospheric sources can be prevented from reaching the scintillation counter by using the lead box as a decay chamber to provide passive shielding. When radon gas migrates into the lead box, specific gamma rays may be emitted from

^{214}Pb and ^{214}Bi as decay products in the uranium decay series after radon. The energy of the window channel is limited within the range of 250 to 700 keV, which includes the response of gamma rays at 351 keV for ^{214}Pb and 609 keV for ^{214}Bi . The pulse of the chosen energy signal is converted to generate electron currents by the photomultipliers, and then, they are recorded by the discriminator and computer. The description of a similar operation and setting was described in detail by Giuliani et al. [40] and Fu et al. [39]. Meteorological records (e.g., atmospheric pressure, temperature, humidity, and hourly precipitation) are available from a meteorological station of the Central Weather Bureau (CWB) of Taiwan, which is located at a distance of 1 km from the YMSG gamma ray station. Measurements are recorded once every hour and immediately wirelessly transmitted to the server at the Institute of Earth Sciences, Academia Sinica, from the gamma ray and meteorological stations.

The methodology of the operation at the TPT radon station follows that as described in detail by Fu et al. [41]. Seismic data were acquired from the earthquake catalogs of the CWB. In total, there were 482 seismic events with magnitudes (M_L) ranging from 1.4 to 6.7 during the monitoring period in the Taiwan area.

3. Results

The gamma ray results along with meteorological data recorded on an hourly basis at the YMSG station were presented in Figure 3. The gamma counting rate was observed to vary from 589 to 25,020 cph (counts per hour) with an average value of 3,172 cph. During the same period, atmospheric pressure (P_{atm}) varies from 924 to 958 mbar, atmospheric humidity (H_{atm}) from 31 to 100%, and atmospheric

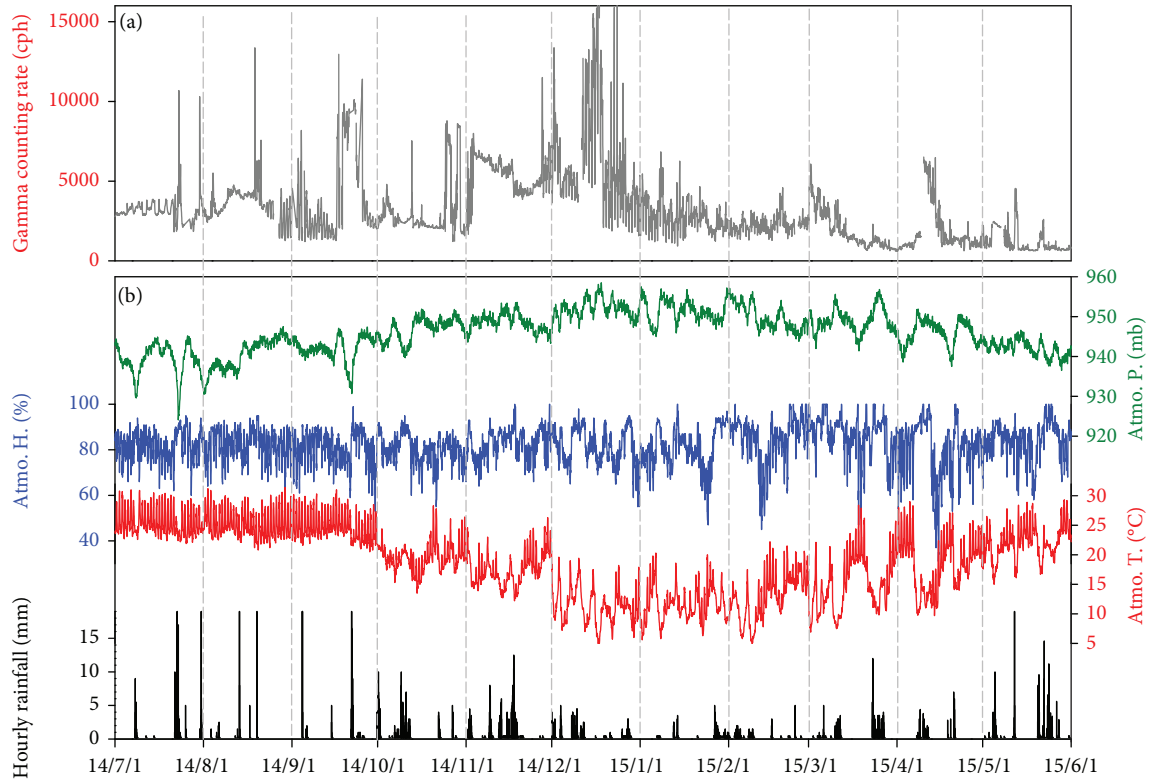


FIGURE 3: Temporal variations of gamma rays at the YMSG station (a) and (b) atmospheric data, including atmospheric pressure (green), humidity (blue), temperature (red), and hourly rainfall (black) (b) from July 1, 2014, to June 1, 2015.

temperature (T_{atm}) from 4.4 to 31.4°C, with the mean value of 946 mbar, 82.3%, and 18.5°C, respectively. Temporal variations of the meteorological factors are not evident. After the initial adjustment for the detector, the gamma counting rate decreases to a low background value of about 1,100 cph for the period from March 15 to June 1, 2015. Substantial increases in the gamma counting rate were observed periodically over the observation period. A wide range of radon gas concentrations in the soil at the TPT station from 7,337 to 31,931 Bq/m³ with an average value of 15,589 Bq/m³ was observed and is shown in Figure 4.

4. Discussion

4.1. The Influence of Meteorological Parameters. Some earlier investigations have revealed that changes in gamma rays may be affected by meteorological factors, such as atmospheric pressure, humidity, temperature, and precipitation [39, 42–46]. Therefore, it is necessary for meteorological effects to be taken into consideration when analyzing gamma ray results. Fu et al. [39] proposed that the air temperature had significant influence on the gamma ray measurements in eastern Taiwan due to a high correlation coefficient between the air temperature and the presence of the gamma ray. However, the influences of meteorological pressure, humidity, and temperature on gamma ray variations were relatively small due to the extremely low correlation coefficients of 0.0178, 0.0022, and 0.0139, respectively, for the study period (Table 1). These low correlation coefficients indicated that

the gamma variations at the YMSG station are not mainly controlled by meteorological parameters.

Fu et al. [39] presumed that the significant decrease in temperature cause reduced sensitivity of electrical sensors. In this study, the marginal effect of atmospheric temperature at the YMSG station, which is situated in a mountainous area (approximately 700 m a.s.l.), may be associated with the relatively small fluctuation of underground temperatures because of the tree shade. To evaluate this possibility, the in situ temperature measurement with a gamma sensor in the monitoring station should be considered in the future.

The temporary, abrupt increase in gamma ray was observed periodically, which may be related to heavy rainfall or precipitation accumulation. This sudden increase in the gamma dose was usually followed by a rapid return to background levels within a few hours after the rain stopped. These observations suggest that short-term (few hours) fluctuations in the rise of gamma rays were partially influenced by a heavy precipitation event, as has been similarly described before [43, 47–49].

For the TPT station, Fu et al. [41] have pointed out that the effects of meteorological parameters on soil radon concentration were insignificant. Therefore, meteorological effects were not taken into consideration during the duration of soil radon concentration anomalies at the TPT station.

4.2. The Relationship between Gamma Ray and Radon Variations and Seismicity. The time series gamma ray data from YMSG was plotted with seismic events, rainfall records, and the radon concentrations of TPT for a period from

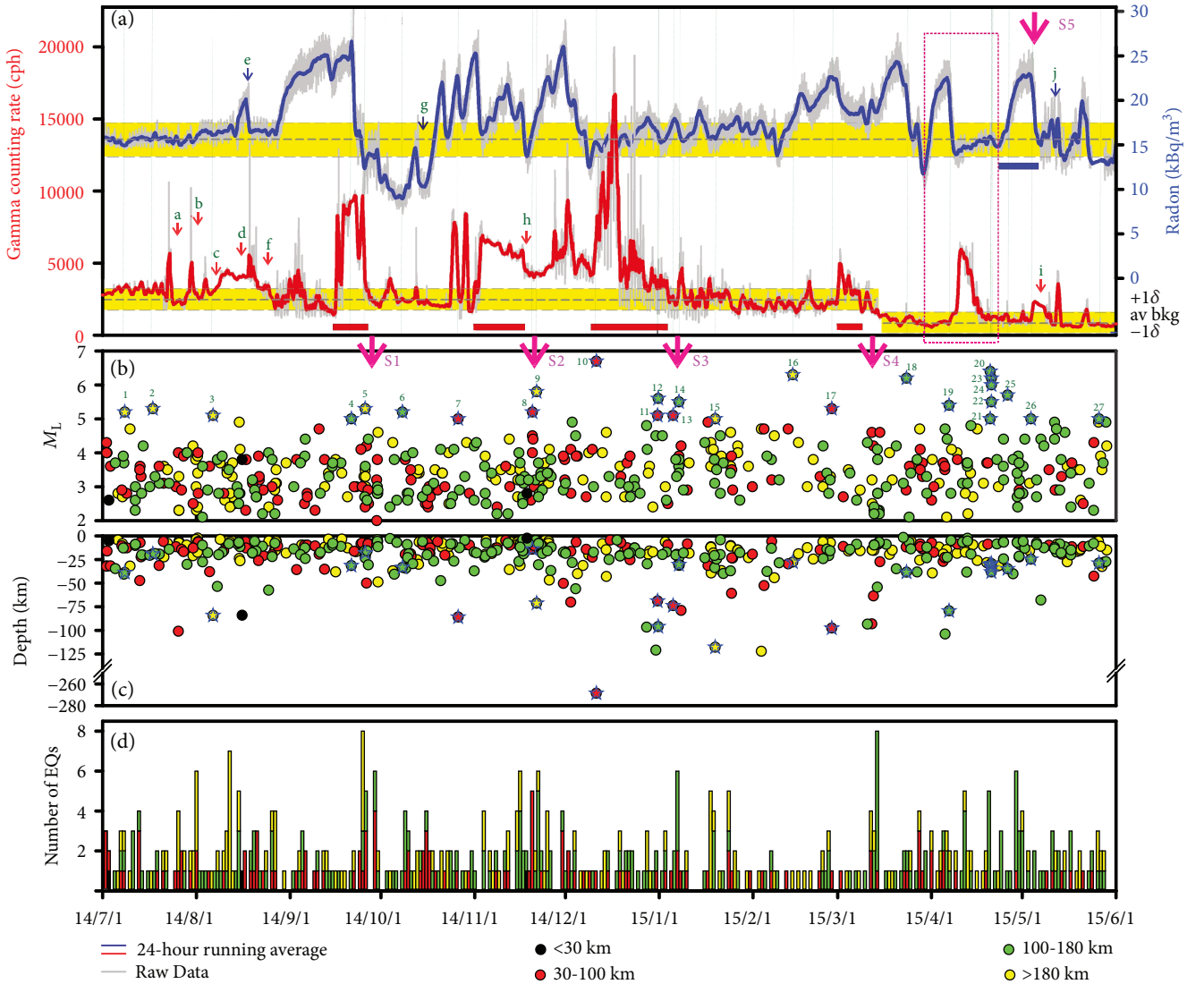


FIGURE 4: The temporal variations of (a) radon and gamma rays from July 1, 2014, to June 1, 2015. Blue and red lines indicate the 24-hour running averages of radon and gamma ray data, respectively; grey lines represent the raw data. Horizontal dashed lines indicate the annual averages of the observed results, and the anomalous threshold value ($\pm 1\sigma$) is included with the yellow bar. The magnitude and depth of earthquakes are plotted in (b) and (c), respectively. The circle symbols in different colors indicate that the epicenter distance of the earthquake to YMSG station was < 30 km (black), 30 to 100 km (red), 100 to 180 km (green), and > 180 km (yellow). Red and blue arrows indicate the specific seismic events. The accumulated number of earthquakes at different distances is also shown as a histogram (d). One specific period of time marked by the dashed rectangle is enlarged in Figure 5.

June 1, 2014, to June 1, 2015, in Figure 4. Many substantial increases in gamma ray and radon concentrations were recorded periodically, and slight diurnal variations were also recorded as shown by the grey line in Figure 4(a). The 24-hour running average of the gamma counting rate and radon concentrations are shown as red and blue lines, respectively, in Figure 4(a) to distinguish their background values. The threshold values were determined using the mean value plus one standard deviation as shown by the grey dashed lines.

The magnitude and depth of the earthquakes were plotted in Figures 4(b) and 4(c), respectively. The seismic event data included the magnitude and depth of the earthquakes, which are sorted by the distances between the YMSG station and the epicenter of the earthquakes for discussing the spatial

distribution of the seismic events. The earthquakes at different distances are plotted in different colors as black, red, green, and yellow circles for distances less than 30 km, 30 to 100 km, 100 to 180 km, and greater than 180 km, respectively. To show the intensity of seismic activity, the accumulated numbers of earthquakes at different distances are also included (Figure 4(d)). The distribution of some specific seismic events is marked in Figure 1, including earthquakes having a magnitude ≥ 5 , an earthquake swarm, and a local earthquake with an epicentral distance less than 30 km to the monitoring station, and the catalog of those earthquakes is listed in Table 2.

The temporal variation of gamma rays and radon shows similar patterns, whereas some high gamma ray

TABLE 1: Correlations between gamma ray variations and meteorological parameters, including atmospheric pressure (P_{atm}), temperature (T_{atm}), and humidity (H_{atm}) during different time periods.

	γ -Rays & P_{atm}	γ -Rays & T_{atm}	γ -Rays & H_{atm}
2014/07	0.2306*	0.0339	0.0064
2014/08	0.1056	0.0585	0.0504
2014/09	0.1105	0.0253	0.0091
2014/10	0.021	0.0095	0.0041
2014/11	0.0316	0.0124	0.0267
2014/12	0.249	0.0171	0.1124
2015/01	0.1932	0.0285	0.3428
2015/02	0.0082	0.0053	0.0405
2015/03	0.0004	0.1215	0.3099
2015/04	0.2202	0.0326	0.3606
2015/05	0.1838	0.02	0.3988

*R-squared values.

and radon concentration peaks in the entire spectrum can also be observed. In addition, it is noted that the increase of soil radon concentrations usually occurred before the change in gamma ray counts. For calculating the anomalies, the anomalous thresholds are found using the average value plus one to three standard deviations [50–52]. In this study, the precursory anomalies were determined as when the running average exceeds one standard deviation, which then can be used to correlate with seismic events (Figure 4 and Table 2).

A comparison of gamma ray data and earthquakes detected by the CWB over the monitoring period indicates that the presence of gamma ray anomalies was quite often accompanied by seismic activity, except for fourteen of twenty-seven marked earthquakes with magnitudes ≥ 5 (1, 2, 3, 4, 5, 9, 14, 15, 16, 18, 19, 22, 25, and 26 in Figure 1 and Table 2). The Events 14 and 22 are considered to be triggered by an earlier earthquake series due to different focal mechanisms and will not be further discussed. Some short-term impulsive gamma ray increases were also recorded with peak values greater than the threshold value before the Events a, b, c, d, f, h, and i. It is noted that the magnitude of those events is smaller than five with a hypocenter depth deeper than 40 km or an epicenter distance of <30 km to the monitoring station. In addition, four significant long-term increases of the gamma ray were also observed from September 15 to 25, 2014, from November 2 to 17, 2014, from December 11, 2014, to January 3, 2015, and from February 28 to March 10, 2015. These anomalies could not be correlated with any significant earthquake, except for the third period. However, the accumulated number of earthquakes displays unusually high seismic activity, such as S1, S2, S3, and S4, which may be related to gamma ray anomaly periods as shown by the red bars in Figure 4(a). These four seismic swarms occurred at a depth of 4 to 50 km from September 26 to 29, 2014, with magnitude 2.0 to 4.4 for S1; at a depth of 4.9 to 71 km from November 20 to 22, 2014, with magnitude 2.7 to 5.2 for S2; at a depth of 23 to 31 km

on January 7, 2015, with magnitude 3.4 to 5.5 for S3; and at a depth of 6 to 93 km from March 12 to 14, 2015, with magnitude 2.2 to 4.6 for S4, respectively. The distance between the epicenters of these four seismic swarms and the YMSG station was approximately 50 to 130 km.

Similarly, the presence of radon anomalies at the TPT station could also be connected with marked seismic events with a magnitude ≥ 5 , except for the Events 1, 2, 3, 5, 9, 11, 12, 13, 14, 15, 16, 19, 22, 25, and 26 in Figure 1 and two local earthquakes (Events e and g). It is noted that the soil radon obviously increased during April 24 to May 3, 2015, and there was a sudden drop in radon concentrations on May 3 followed by an earthquake swarm (S5), which occurred at depths of 11–14 km from May 1 to 15, 2015, with magnitudes 4.2 to 4.9. The distance was approximately 70 km from the epicenter of the earthquake swarm (S5) to the TPT station as shown in Figure 1.

Each gamma ray and radon anomaly is assigned to a definite earthquake and could only be correlated with the precursory anomalous increase a few days to a few weeks before the event occurrence. Each precursory time was illustrated in Figure 5, and the precursory catalog of each seismic event is listed in Table 2.

Figure 5 shows an example for the preearthquake anomalous period of gamma ray and radon results from March 29 to April 22, 2015, before Event 20. Here, ΔT_{Gamma} and ΔT_{Radon} are the time differences between the start time of an anomaly and the earthquake event for the gamma ray and radon anomalies, respectively. In Figure 5, the radon at TPT rose progressively until April 7, 2015, with a peak value of about 23 kBq/m³. A temporal decrease in radon occurred from April 7 to 9, 2015, and the value returned to the background value with a slight variation before Events 20 to 24. Meanwhile, a significant increase in gamma rays at the YMSG was observed from April 7 to 11, 2015, with a peak value of 6,000 cph. Then, a progressive decrease happened from April 11 to 19, 2015, when the gamma counting rates returned to the background value, followed by Events 20 to 24, which occurred at depths of 29–38 km with magnitudes of 5.0 to 6.4 on April 20, 2015. The distance was approximately 150 km from the epicenter of the largest earthquake ($M_L = 6.4$) to the YMSG station. In this case, the significant changes in radon and gamma ray were recorded as precursors about 21 days and 12 days, respectively, before Event 20, which occurred on April 20, 2015.

4.3. Spatial Variation of Related Earthquakes. Most large events could be linked to anomalous changes in gamma rays and radon at both stations (Table 2), and few events were only associated with one of the two anomalies. Anomalies in gamma and/or radon accompanying the relevant earthquake, which can be called the precursory event (PE), and the distribution of those events are shown in Figure 1. For YMSG, two groups of earthquakes may be recognized based on the epicenter distance.

Group A included the PE with an epicenter distance of <30 km and showed anomalous gamma ray changes over a period of a few days (e.g., Event h). The PE with epicenter distances of 30 to 180 km showed anomalies in gamma rays

TABLE 2: Catalog of gamma ray and radon anomalies and related earthquakes occurring in Taiwan from July 1, 2014, to June 1, 2015.

No. ¹	Date	Long. (°E)	Lat. (°N)	Mag. (M_L)	Depth (km)	Distance (km)	$\Delta T_{\text{Radon}}^2$ (day)	$\Delta T_{\text{Gamma}}^2$ (day)	Type
1	2014/7/8 07:06	122.41	23.29	5.2	38.8	224	None	None	—
2	2014/7/17 14:11	121.36	22.25	5.3	19.1	322	None	None	—
3	2014/8/6 11:46	121.46	22.23	5.1	84.2	324	None	None	—
4	2014/9/21 05:14	121.54	23.59	5	31.5	173	21	None	C
5	2014/9/25 18:35	121.3	22.74	5.3	18	269	None	None	—
6	2014/10/8 02:08	121.56	23.65	5.2	33.4	167	15	10	C
7	2014/10/26 12:47	122.23	24.75	5	86.0	81	8	3	W
8	2014/11/20 01:46	122.02	24.89	5.2	13.9	55	17	17	O
9	2014/11/21 11:29	120.13	20.65	5.8	71.3	520	None	None	—
10	2014/12/11 05:03	122.17	25.7	6.7	268.6	86	23	14	W
11	2014/12/31 11:06	121.79	24.89	5.1	68.9	37	None	20	W
12	2014/12/31 15:54	122.6	24.55	5.6	96.1	125	None	20	W
13	2015/1/5 13:53	122.04	24.74	5.1	73.8	67	None	20	L
14	2015/1/7 12:48	121.7	24.26	5.5	30.4	100	None	Unknown	C
15	2015/1/19 11:48	121.57	22.76	5	117.9	265	None	None	—
16	2015/2/14 04:06	121.46	22.66	6.3	27.8	276	None	None	—
17	2015/2/27 00:50	122.29	24.68	5.3	97.6	90	13	11	L
18	2015/3/23 18:13	121.76	23.7	6.2	38.4	162	9	None	C
19	2015/4/6 19:37	122.75	24.4	5.4	79.4	146	None	None	—
20	2015/4/20 09:42	122.37	24.05	6.4	30.6	147	21	12	I
21	2015/4/20 09:49	122.49	24.02	5	30.7	157	21	12	I
22	2015/4/20 19:20	121.75	23.63	5.5	38.3	170	Unknown	Unknown	C
23	2015/4/20 19:45	122.41	24.12	6.2	33.9	143	21	12	I
24	2015/4/20 19:59	122.39	24.01	6	29.4	152	21	12	I
25	2015/4/26 04:01	122.44	24.03	5.7	34.8	153	Unknown	Unknown	—
26	2015/5/3 21:09	122.42	23.94	5	24.8	160	None	None	—
27	2015/5/26 08:56	122.49	23.87	5	28.9	171	7	6	I
a	2014/7/26 00:43	122.11	24.92	4	101	61	None	4	—
b	2014/8/1 12:38	121.6	24.58	4	6.1	64	None	3	—
c	2014/8/5 08:34	121.67	24.4	3.6	38	84	None	3	—
d	2014/8/16 02:51	121.53	24.92	3.8	84	26	None	7	—
e	2014/8/17 06:52	121.04	24.72	2.3	6.2	71	3	None	—
f	2014/8/24 20:39	122.09	24.3	4	57.5	109	None	6	—
g	2014/10/19 17:50	121.1	24.68	2.9	6	70	4	None	—
h	2014/11/18 07:22	121.56	25.16	2.8	2.5	1	None	2	—
i	2015/5/7 04:04	121.33	24.1	4.4	68	119	None	4	—
j	2015/5/9 20:32	121.23	24.66	3.5	10	64	1	None	—

¹The label of relevant earthquakes marked in Figures 1 and 4. ²The time difference between the start time of an anomaly and the earthquake event. “Unknown” indicates that the relationship between an anomaly and the earthquake cannot be identified.

over several days to weeks (e.g., Events 10, 17, and 20) which was identified as Group B. It was noted that no anomaly was found when the distance of the earthquake epicenter was farther than 180 km, such as Events 1, 2, 3, 5, 9, 15, and 16.

A diagram showing the relationship between the depth of the PE and latitude location and the seismic velocity structure along the a-a' line (Figure 1) is presented in Figure 6. The seismic V_p structure was found by using a local earthquake tomography model developed by Wu et al. [53]. The yellow dashed line indicates the possible location of the subduction zone as highlighted by contoured V_p/V_s

values higher than 1.78 [54]. It is noteworthy that a series of the PE located along the subduction zone progressively deepen to the north from ~28 to 268 km deep, except for Event 8. This suggests that an anomaly of gamma rays at the YMSG station may be connected with the geodynamics process within the subduction zone in north and north-eastern Taiwan.

For the TPT, Fu et al. [41] proposed that radon anomalies at the TPT station could be found when a small earthquake has hypocenters shallower than 15 km within 30 km of the monitoring station or when a large earthquake has deeper

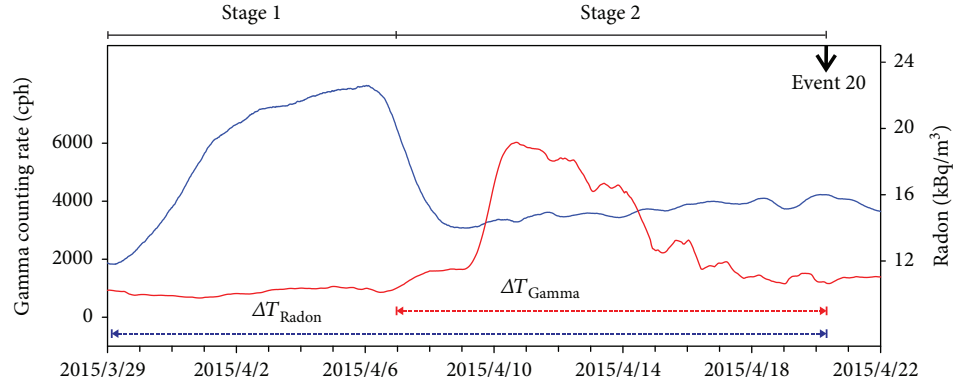


FIGURE 5: Variations of gamma ray and radon data during the period from March 29 to April 22, 2015. The preearthquake anomalous time from the gamma ray and radon results is represented by ΔT_{Gamma} and ΔT_{Radon} , respectively, showing that a radon anomaly occurs earlier than a gamma ray anomaly with respect to an earthquake event.

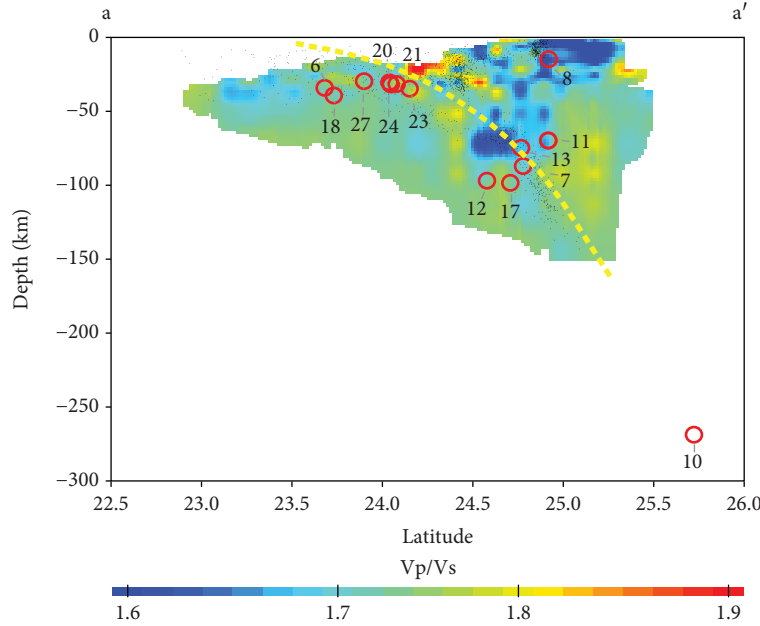


FIGURE 6: The seismic velocity structure transecting northern Taiwan along the a-a' line of Figure 1 is derived based on the local earthquake tomography model by Wu et al. [53]. The dots show the relocated events for $M > 3$ within ± 5 km of the profile. The red open circle means that the projected earthquake with a preanomalous signal is listed in Table 2. Note that the hypocenters get deeper towards the north. The yellow dashed line indicates the subduction boundary between the PSP and the EP.

hypocenters (>20 km) at a greater distance (>45 km). In this paper, the similar anomalies in radon are also confirmed before the near- and far-field earthquakes, such as Events 6, 7, 8, 10, 17, 18, 20, 21, 23, 24, 27, e, g, and j. The preearthquake activities of the far-field events may be transmitted to the region below the TPT site along the major decollement (e.g., [55, 56]) and can facilitate the release of soil gases when squeezed. Hence, radon anomalies could be detected at the TPT station away from the large event [41].

Some fault plane solution diagrams of the studied earthquakes were plotted in Figure 1, and five predominant patterns can be classified. Similarly, Kao et al. [57] proposed five major seismogenic structures in the southernmost Ryukyu Arc-Taiwan region. They were (a) the Collision Seismic

Zone (CSZ, C type), associated with the relative plate convergence between the EP and the PSP along the Longitudinal Valley (e.g., Event 6), (b) the Interface Seismic Zone (ISZ, I type), related to a plate boundary between the EP and the PSP with low-angle thrust faulting to the north with a depth range of 10 to 30 km (e.g., Events 20, 21, 23, 24, and 27), (c) the Wadati-Benioff Seismic Zone (WBSZ, W type), indicating that the earthquakes deeper than ~ 60 km occurred within the Wadati-Benioff zone striking east to west and extending westward beneath NE Taiwan (e.g., Events 7, 10, 11, and 12), (d) the Lateral Compression Seismic Zone (LCSZ, L type), related to a mixture of thrust and oblique strike-slip with P -axes in approximately an east-west direction, roughly parallel to the local strike of the trench-arc system thrust or

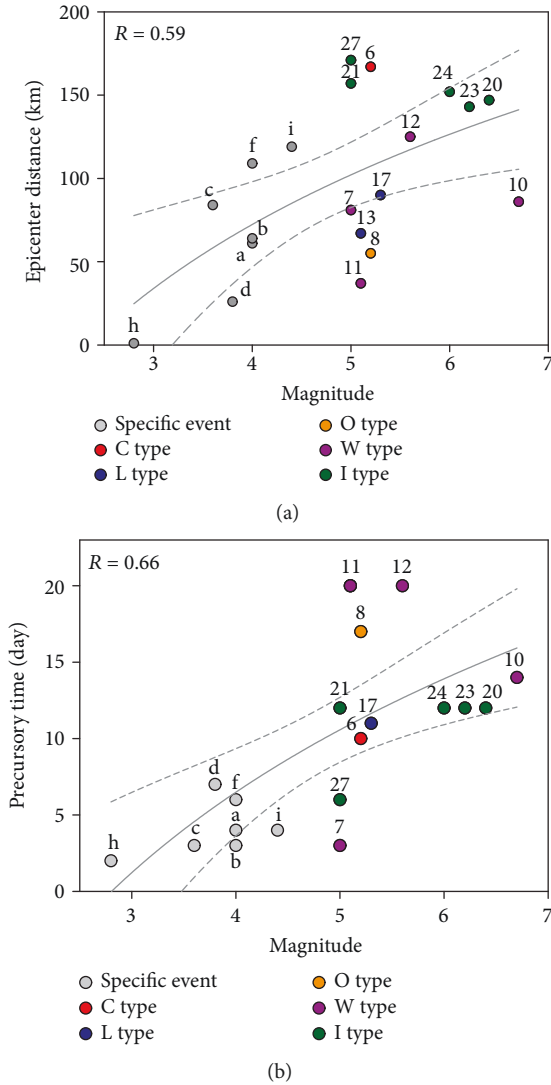


FIGURE 7: Variation diagrams showing the relationship between earthquake magnitude and (a) epicenter distance to the YMSG monitoring site and (b) distribution of the precursory time. Fitted curves are shown as solid lines. Dashed lines indicate the 95% confidence interval of the data set.

oblique-thrust faulting (e.g., Events 13 and 17), and (e) the Okinawa Seismic Zone (OSZ, O type), reflecting the gradual changing state of strain associated with the crustal deformation of the Okinawa opening with a characteristic of shallow earthquakes occurring (e.g., Event 8).

The dependent relationship between the epicenter distance to the YMSG site and the magnitude of the PE was shown in Figure 7(a). A good correlation ($R = 0.66$) was obtained between these variables. The best-fit line may be used to estimate the magnitude of an earthquake with a given epicenter distance. In other words, a larger magnitude of the PE might be distributed in greater epicenter distances of the YMSG station. As mentioned above, when the distance of the earthquake epicenter was farther than 180 km, no anomaly was detected. And the distributions of the PE, including I type, L type, O type, W type, and specific events, get closer towards the YMSG station.

The good correlation between the magnitude of PE and precursory time (ΔT_{Gamma}) was presented in Figure 7(b). The moderate correlation ($R = 0.59$) indicates that it is possible to forecast the magnitude of an impending earthquake. A longer precursory time of gamma ray anomalies appears to be associated with a larger upcoming earthquake, especially the occurrence of I type and W type with high probability. We also found that an anomaly of C type was recorded in only one (Event 6) out of five events, suggesting that C type may be not sensitive for the YMSG station but valuable for the TPT station (Table 2).

The YMSG station is located at the western end of the subduction system in the northern Taiwan area, where the PSP is subducting northward beneath the EP. Furthermore, this region is still seismically active due to continuous convergence and volcanic activity, with changes in high-pressure fluid affected by a deeper pump system [58]. Some microcracks may be also developed during this process, causing the short duration gamma ray anomalies. Similarly, Padrón et al. [59] found that crustal deformation and fracturing during high seismic activity enhance the release of radiogenic helium produced in the crust. Lee et al. [23] reported a short-term negative anomaly of $^3\text{He}/^4\text{He}$ ratios, which indicated that the radiogenic gas release of crustal components affected the degassing system for the short term.

It may be suggested that due to continuous convergence, the preseismic slow slip may occur around the subduction zone before the event. The volumetric expansions of the EP around northern Taiwan then released the additional radiogenic gas from the crustal component. The increase in gamma rays can be attributed to the expansion around the YMSG that produced new fractures for gas and fluid migrations, potentially associated with the slow slip (e.g., Events 6, 7, 8, 10, 17, 20, 21, 23, 24, and 27). A similar explanation of the preseismic slow slip before the Tohoku earthquake was illustrated by Orihara et al. [60].

Hence, based upon the above-mentioned points, the preliminary outline of anomalous data regarding relevant earthquakes can be concluded, which may be associated with the dynamics of the subduction process.

4.4. Relationship between the Tectonic Setting and the Mechanism for Anomalous Signals. The geodynamic setting of the arc-continent collision in Taiwan is well defined by the oblique collision between the PSP and the EP, with the former plate moving about 8 cm/year [1]. To the north of the island lies the Ryukyu subduction zone, which results from the subduction of the PSP beneath the EP. A schematic diagram of the proposed physical mechanism based on the anomalies in radon at TPT and changes in gamma rays at YMSG is shown in Figure 8. Stages 1 to 2 are considered to have occurred successively before the significant earthquake, which occurred along the subduction region. During Stage 1, the prestress caused by the northwestern movement of the PSP may be transmitted by collision with the Kuanyin High along the major decollement to trigger radon enhancements due to the development of microcracks below the TPT station, while no significant changes at the YMSG station occur during this stage. The description of the similar model for

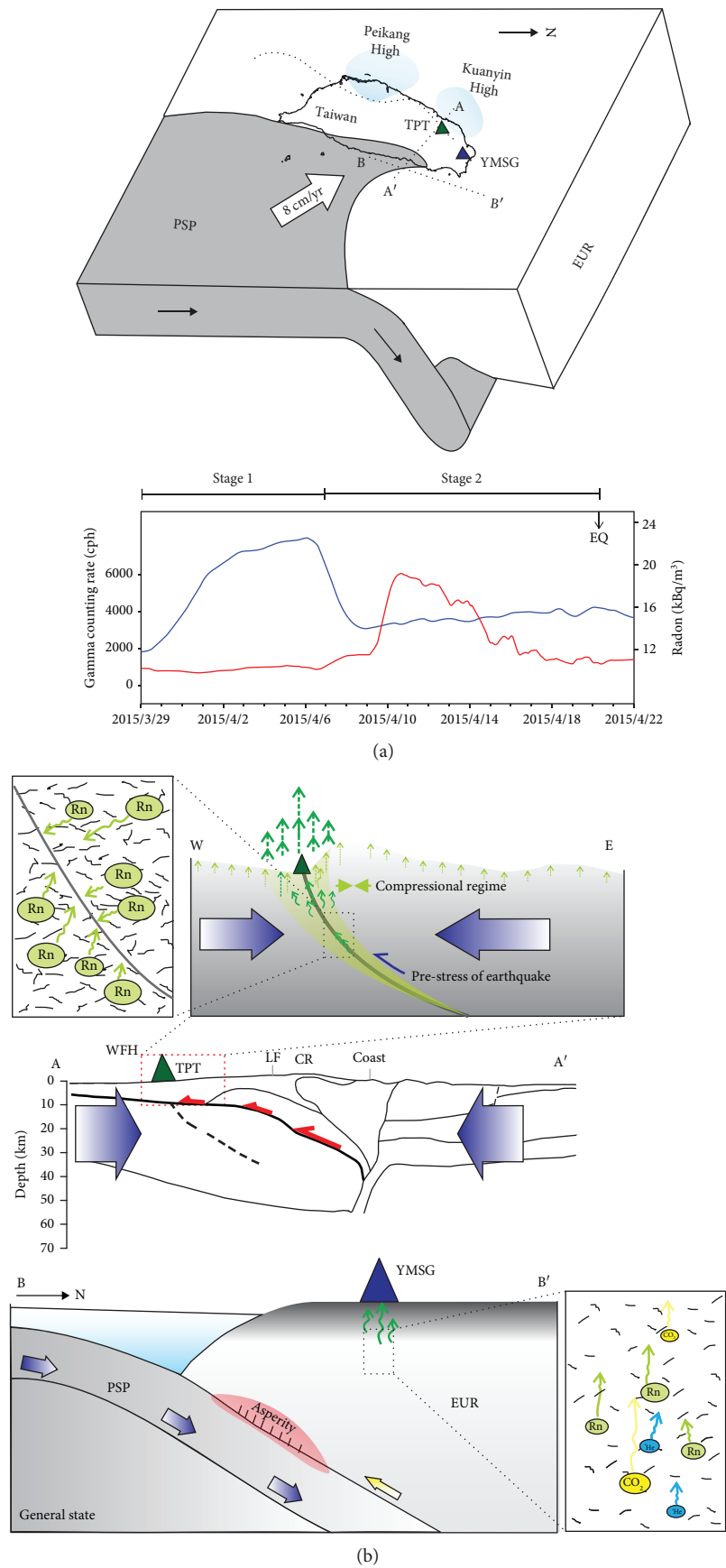


FIGURE 8: Continued.

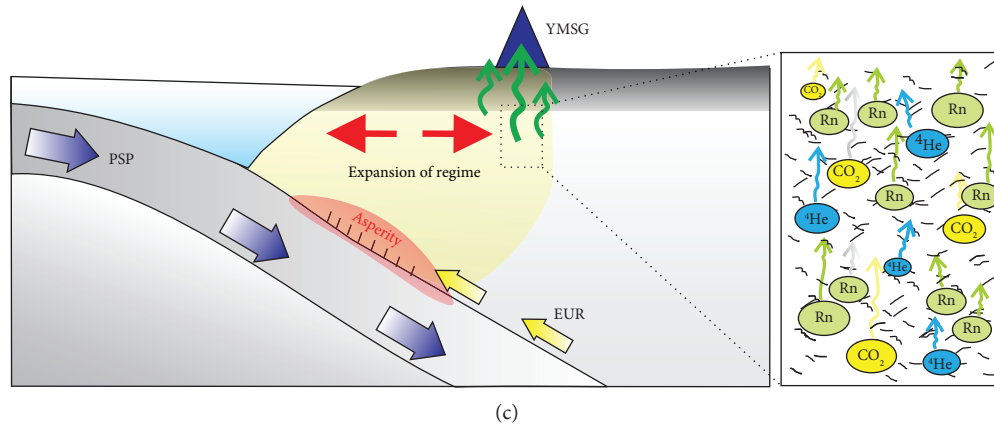


FIGURE 8: (a) A schematic diagram of the proposed physical mechanism based on the gamma ray anomaly of YMSG and radon anomaly at TPT. Stages 1 (b) and 2 (c) are considered to have occurred in order before the significant earthquakes. The schematic diagram showing a crustal-scale cross-section along the geophysical transect (AA' in (a)) modified by Fu et al. [41] is shown in (b).

TPT was described in detail by Fu et al. [41]. At Stage 2, further movement of the PSP may be locked by the EP and accumulated elastic stress results in the increase of radiogenic materials, such as gamma rays and radon gas, due to an increase in the porosity and fractures below the YMSG station.

Based on GPS observations, Rau et al. [61] and Ching et al. [62] concluded that crustal deformations showed the transition of surface strain in the type of tectonic activity from an arc-continent collision to a subduction/back-arc opening in northern Taiwan. Continental collision (around the TPT region) to extension (around the YMSG region) may be associated with the similar geodynamic process of stage 1 to stage 2, respectively, at different time scales.

Therefore, anomalous signals from gamma rays and radon that are attributed to changes in pore pressure by the Coulomb stress changes may be attributed to near/far-field earthquakes or strain-induced changes in permeability within the preparation zone of the earthquake [63–65]. During the build-up of stress by preseismic activity, some of the existing features and the permeability of the fault zone are ruptured. The highly porous and permeable fault zones are then filled with gas and fluid. These closing and opening processes within the fault system are induced by the tectonic stress, which may be responsible for the episodic and/or periodic seismicity in northern and northeastern Taiwan.

5. Conclusions

The major findings of this study are listed below:

- (1) Gamma ray variations are monitored at the YMSG monitoring station, located in the volcanic area of north Taiwan. Results of the temporal gamma ray variations are compared with meteorological records. The marginal effect of atmospheric parameters is observed in gamma ray measurements at the YMSG station
- (2) Under continuous monitoring, many anomalously high radon values at TPT and gamma rays at YMSG

were observed a few days to a few weeks before the seismic events

- (3) Two groups of earthquakes can be identified at the YMSG station based on relevant earthquakes: earthquakes with shallower hypocenters and that are concentrated within 30 km of the monitoring station with a smaller magnitude and the earthquakes with deeper hypocenters and that are distributed at greater distances (~30 to 180 km) from the monitoring site
- (4) The precursory changes in soil radon at the TPT station and gamma rays at the YMSG station may represent the preparation stage of an earthquake. When the observed precursory signals from these two stations with time delay occur, the possible impending large earthquake around the plate boundary in northeastern Taiwan can then be expected, which is located approximately between latitudes 23.9°N and 26.7°N and longitudes 121.3°E and 122.6°E
- (5) Both radon and gamma ray measurements provide a useful tool and act as a good indicator for exploring earthquake precursors, especially in north and northeastern Taiwan

Data Availability

The data used to support the findings of this study are available from the corresponding author upon request.

Disclosure

A preliminary study has been presented as a conference abstract in the 2005 AGU-Fall Meeting.

Conflicts of Interest

The authors declare that they have no conflicts of interest.

Acknowledgments

We dedicate this paper to the late Prof. Tsanyao Frank Yang (TFY), who passed away on the 12th of March 2015. He had worked as a geochemist at the Department of Geosciences, National Taiwan University (NTU), Taiwan, for more than 20 years. His passion for research included setting new standards for relevant measurements, which enables us to present our work here. We thank Messrs. Shin-Jung Lin and Kou-Wei Wu for helping in the operation and maintenance of the monitoring station. The research is supported by grants MOST 107-2116-M-002-019 through the Ministry of Science and Technology (MOST) and MOTC-CWB-106-E-01 from the Central Weather Bureau (CWB), Taiwan. The TEC contribution number for this article is 00151. We would like to thank Uni-edit (<http://www.uni-edit.net>) for editing and proofreading this manuscript. We are also thankful to the editor Yunpeng Wang and the anonymous referee for their valuable comments and suggestions, which helped us to improve the manuscript.

References

- [1] S. B. Yu, H. Y. Chen, and L. C. Kuo, "Velocity field of GPS stations in the Taiwan area," *Tectonophysics*, vol. 274, no. 1-3, pp. 41-59, 1997.
- [2] L. S. Teng, "Extensional collapse of the northern Taiwan mountain belt," *Geology*, vol. 24, no. 10, pp. 949-952, 1996.
- [3] K. L. Wang, S. L. Chung, C. H. Chen, R. Shinjo, T. F. Yang, and C. H. Chen, "Post-collisional magmatism around northern Taiwan and its relation with opening of the Okinawa Trough," *Tectonophysics*, vol. 308, no. 3, pp. 363-376, 1999.
- [4] K. L. Wang, S. L. Chung, S. Y. O'Reilly, S. S. Sun, R. Shinjo, and C. H. Chen, "Geochemical constraints for the genesis of post-collisional magmatism and the geodynamic evolution of the northern Taiwan region," *Journal of Petrology*, vol. 45, no. 5, pp. 975-1011, 2004.
- [5] W. S. Juang and J. C. Chen, "Geochronology and geochemistry of volcanic rocks in northern Taiwan," *Bulletin of Central Geological Survey*, vol. 5, pp. 31-66, 1989.
- [6] S. R. Song, S. Tsao, and H. J. Lo, "Characteristics of the Tatun volcanic eruptions, North Taiwan: implications for a cauldron formation and volcanic evolution," *Journal of the Geological Society of China*, vol. 43, pp. 361-378, 2000.
- [7] S. R. Song, T. F. Yang, Y. H. Yeh, S. Tsao, and H. J. Lo, "The Tatun volcano group is active or extinct?," *Journal of the Geological Society of China*, vol. 43, pp. 521-534, 2000.
- [8] L. S. Teng, "Quaternary tectonics of Taiwan," *Special Publication of the Central Geological Survey*, vol. 18, pp. 1-24, 2007.
- [9] S. J. Tsao, "Potassium-argon age determination of volcanic rocks from the Tatun Volcano Group," *Bulletin of Central Geological Survey*, vol. 9, pp. 137-154, 1994.
- [10] W. H. Wang and C. H. Chen, "The volcanology and fission track age dating of pyroclastic deposits in Tatun Volcano Group," *Acta Geologica Taiwanica*, vol. 28, pp. 1-30, 1990.
- [11] W. S. Juang, "Diversity and origin of quaternary basaltic magma series in northern Taiwan," *Bulletin of the National Museum of Natural Science*, vol. 4, pp. 125-165, 1993.
- [12] C. H. Chen and J. J. S. Shen, "A refined historical record of volcanic eruptions around Taiwan: tectonic implications in the arc-continent collision area," *Terrestrial, Atmospheric and Oceanic Sciences*, vol. 16, no. 2, pp. 331-343, 2005.
- [13] T. F. Yang, " $^3\text{He}/^4\text{He}$ ratios of fumaroles and bubbling gases of hot springs in Tatun Volcano Group, North Taiwan," *Journal of National Park*, vol. 10, no. 1, pp. 73-94, 2000.
- [14] T. F. Yang, Y. Sano, and S. R. Song, " $^3\text{He}/^4\text{He}$ ratios of fumaroles and bubbling gases of hot springs in Tatun Volcano Group, North Taiwan," *Nuovo Cimento della Societa Italiana di Fisica C*, vol. 22, pp. 281-286, 1999.
- [15] T. Ohba, T. Sawa, N. Taira et al., "Magmatic fluids of Tatun volcanic group, Taiwan," *Applied Geochemistry*, vol. 25, no. 4, pp. 513-523, 2010.
- [16] K. I. Konstantinou, C. H. Lin, and W. T. Liang, "Seismicity characteristics of a potentially active Quaternary volcano: the Tatun Volcano Group, northern Taiwan," *Journal of Volcanology and Geothermal Research*, vol. 160, no. 3-4, pp. 300-318, 2007.
- [17] S. Wen, Y. Z. Chang, C. H. Chen, Y. G. Chen, and T. L. Teng, "The seismic velocity and attenuation structure beneath the Tatun volcanic area, Taiwan," *Journal of Asian Earth Sciences*, vol. 54-55, pp. 182-191, 2012.
- [18] C. H. Lin, "Evidence for a magma reservoir beneath the Taipei metropolis of Taiwan from both S-wave shadows and P-wave delays," *Scientific Reports*, vol. 6, no. 1, article 39500, 2016.
- [19] A. Kumar, V. Walia, Y. C. Sung, S. J. Lin, C. C. Fu, and K. L. Wen, "Soil gas survey in and around Shanchiao fault of northern Taiwan for establishing continuous monitoring station," *Acta Geophysica*, vol. 66, no. 5, pp. 1213-1221, 2018.
- [20] A. Kumar, V. Walia, Y. C. Sung et al., "Integrated radon monitoring in Tatun Volcanic Areas of Northern Taiwan," *Terrestrial, Atmospheric and Oceanic Sciences*, vol. 29, no. 3, pp. 261-273, 2018.
- [21] T. F. Lan, T. F. Yang, H. F. Lee et al., "Compositions and flux of soil gas in Liu-Huang-Ku hydrothermal area, northern Taiwan," *Journal of Volcanology and Geothermal Research*, vol. 165, no. 1-2, pp. 32-45, 2007.
- [22] H. F. Lee, T. F. Yang, T. F. Lan, S. R. Song, and S. Tsao, "Fumarolic gas composition of the Tatun Volcano Group, northern Taiwan," *Terrestrial, Atmospheric and Oceanic Sciences*, vol. 16, no. 4, pp. 843-864, 2005.
- [23] H. F. Lee, T. F. Yang, T. F. Lan, C. H. Chen, S. R. Song, and S. Tsao, "Temporal variations of gas compositions of fumaroles in the Tatun Volcano Group, northern Taiwan," *Journal of Volcanology and Geothermal Research*, vol. 178, no. 4, pp. 624-635, 2008.
- [24] C. M. Liu, S. R. Song, Y. L. Chen, and S. Tsao, "Characteristics and origins of hot springs in the Tatun Volcano Group in northern Taiwan," *Terrestrial, Atmospheric and Oceanic Sciences*, vol. 22, no. 5, pp. 475-489, 2011.
- [25] H. Wen, T. F. Yang, T. F. Lan et al., "Soil CO_2 flux in hydrothermal areas of the Tatun Volcano Group, Northern Taiwan," *Journal of Volcanology and Geothermal Research*, vol. 321, pp. 114-124, 2016.
- [26] M. L. I. Witt, T. P. Fischer, D. M. Pyle, T. F. Yang, and G. F. Zellmer, "Fumarole compositions and mercury emissions from the Tatun volcanic field, Taiwan: results from multicomponent gas analyser, portable mercury spectrometer and direct sampling techniques," *Journal of Volcanology and Geothermal Research*, vol. 178, no. 4, pp. 636-643, 2008.

- [27] T. F. Yang, H. Y. Wen, C. C. Fu et al., "Soil radon flux and concentrations in hydrothermal area of the Tatun volcano group, Northern Taiwan," *Geochemical Journal*, vol. 45, no. 6, pp. 483–490, 2011.
- [28] K. I. Konstantinou, C. H. Lin, W. T. Liang, and Y. C. Chan, "Seismogenic stress field beneath the Tatun Volcano Group, northern Taiwan," *Journal of Volcanology and Geothermal Research*, vol. 187, no. 3–4, pp. 261–271, 2009.
- [29] C. H. Lin, K. I. Konstantinou, W. T. Liang et al., "Preliminary analysis of volcanoseismic signals recorded at the Tatun Volcano Group, northern Taiwan," *Geophysical Research Letters*, vol. 32, no. 10, article L10313, 2005.
- [30] C. H. Lin, K. I. Konstantinou, H. C. Pu et al., "Preliminary results from seismic monitoring at the Tatun volcanic area of northern Taiwan," *Terrestrial, Atmospheric and Oceanic Sciences*, vol. 16, no. 3, pp. 563–577, 2005.
- [31] M. Murase, C. H. Lin, F. Kimata, H. Mori, and H. C. Pu, "Volcano-hydrothermal activity detected by precise levelling surveys at the Tatun volcano group in Northern Taiwan during 2006–2013," *Journal of Volcanology and Geothermal Research*, vol. 286, pp. 30–40, 2014.
- [32] H. C. Pu, C. H. Lin, Y. C. Huang et al., "The volcanic earthquake swarm of October 20, 2009 in the Tatun area of northern Taiwan," *Terrestrial, Atmospheric and Oceanic Sciences*, vol. 25, no. 5, pp. 625–635, 2014.
- [33] J. B. H. Shyu, K. Sieh, Y. G. Chen, and C. S. Liu, "Neotectonic architecture of Taiwan and its implications for future large earthquakes," *Journal of Geophysical Research*, vol. 110, no. B8, article B08402, 2005.
- [34] S. Giammanco, K. W. W. Sims, and M. Neri, "Measurements of ^{220}Rn and ^{222}Rn and CO_2 emissions in soil and fumarole gases on Mt. Etna volcano (Italy): implications for gas transport and shallow ground fracture," *Geochemistry, Geophysics, Geosystems*, vol. 8, no. 10, article Q10001, 2007.
- [35] M. Neri, B. Behncke, M. Burton et al., "Continuous soil radon monitoring during the July 2006 Etna eruption," *Geophysical Research Letters*, vol. 33, no. 24, article L24316, 2006.
- [36] M. Neri, E. Ferrera, S. Giammanco et al., "Soil radon measurements as a potential tracer of tectonic and volcanic activity," *Scientific Reports*, vol. 6, no. 1, article 24581, 2016.
- [37] N. M. Pérez, J. M. L. Salazar, P. A. Hernández, T. Soriano, K. Lopez, and K. Notsu, "Diffuse CO_2 and ^{222}Rn degassing from San Salvador volcano, El Salvador, Central America," in *Natural Hazards in El Salvador*, W. I. Rose, J. J. Bommer, D. L. López, M. J. Carr, and J. J. Major, Eds., vol. 375, pp. 227–236, Bulletin of Geological Society of America, 2004.
- [38] J. M. L. Salazar, N. M. Pérez, P. A. Hernández et al., "Precursory diffuse carbon dioxide degassing signature related to a 5.1 magnitude earthquake in El Salvador, Central America," *Earth and Planetary Science Letters*, vol. 205, no. 1–2, pp. 81–89, 2002.
- [39] C. C. Fu, P. K. Wang, L. C. Lee et al., "Temporal variation of gamma rays as a possible precursor of earthquake in the Longitudinal Valley of eastern Taiwan," *Journal of Asian Earth Sciences*, vol. 114, no. 2, pp. 362–372, 2015.
- [40] G. Giuliani, A. Attanasio, and G. Fioravanti, "Gamma detectors for continuous monitoring of radon," *International Environmental Application and Science*, vol. 8, no. 4, pp. 541–550, 2013.
- [41] C. C. Fu, T. F. Yang, C. H. Chen et al., "Spatial and temporal anomalies of soil gas in northern Taiwan and its tectonic and seismic implications," *Journal of Asian Earth Sciences*, vol. 149, pp. 64–77, 2017.
- [42] T. Ichiji and T. Hattori, "Continuous measurement of environmental gamma-ray radiation in Tokyo using Ge semiconductor detector," *Proceedings of the IRPA 11 Conference*, 2000P-4a-288.
- [43] A. Melintescu, S. Chambers, J. Crawford, A. Williams, B. Zorila, and D. Galeriu, "Radon-222 related influence on ambient gamma dose," *Journal of Environmental Radioactivity*, vol. 189, pp. 67–78, 2018.
- [44] M. Takeyasu, T. Iida, T. Tsujimoto, K. Yamasaki, and Y. Ogawa, "Concentrations and their ratio of ^{222}Rn decay products in rainwater measured by gamma-ray spectrometry using a low-background Ge detector," *Journal of Environmental Radioactivity*, vol. 88, no. 1, pp. 74–89, 2006.
- [45] T. Tsvetkova, I. Nevinsky, and V. Nevinsky, "Results of spectral monitoring of environmental gamma background in a fault zone of the Western Caucasus for seismological application," *Radiation Measurements*, vol. 69, pp. 35–49, 2014.
- [46] H. Yamanisi and H. Miyake, "Separation of natural background by using correlation of time-series data on radiation monitoring," *Journal of Nuclear Science and Technology*, vol. 40, no. 1, pp. 44–48, 2003.
- [47] J. L. Burnett, I. W. Croudace, and P. E. Warwick, "Short-lived variations in the background gamma-radiation dose," *Journal of Radiological Protection*, vol. 30, no. 3, pp. 525–533, 2010.
- [48] R. Livesay, C. S. Blessinger, T. Guzzardo, and P. Hausladen, "Rain-induced increase in background radiation detected by Radiation Portal Monitors," *Journal of Environmental Radioactivity*, vol. 137, pp. 137–141, 2014.
- [49] J. F. Mercier, B. L. Tracy, R. d'Armours et al., "Increased environmental gamma-ray dose rate during precipitation: a strong correlation with contributing air mass," *Journal of Environmental Radioactivity*, vol. 100, no. 7, pp. 527–533, 2009.
- [50] C. C. Fu, T. F. Yang, V. Walia et al., "Variations of soil-gas composition around the active Chihshang Fault in a plate suture zone, eastern Taiwan," *Radiation Measurements*, vol. 44, no. 9–10, pp. 940–944, 2009.
- [51] Y. H. Oh and G. Kim, "A radon-thoron isotope pair as a reliable earthquake precursor," *Scientific Reports*, vol. 5, no. 1, article 13084, 2015.
- [52] R. C. Ramola, Y. Prasad, G. Prasad, S. Kumar, and V. M. Choubey, "Soil-gas radon as seismotectonic indicator in Garhwal Himalaya," *Applied Radiation and Isotopes*, vol. 66, no. 10, pp. 1523–1530, 2008.
- [53] Y. M. Wu, C. H. Chang, L. Zhao et al., "Seismic tomography of Taiwan: improved constraints from a dense network of strong motion stations," *Journal of Geophysical Research*, vol. 112, no. B8, article B08312, 2007.
- [54] J. Y. Lin, S. K. Hsu, and J. C. Sibuet, "Melting features along the western Ryukyu slab edge (northeast Taiwan): tomographic evidence," *Journal of Geophysical Research*, vol. 109, no. B12, article B12402, 2004.
- [55] J. Malavielle, "Impact of erosion, sedimentation, and structural heritage on the structure and kinematics of orogenic wedges: analog models and case studies," *GSA Today*, vol. 20, pp. 4–10, 2010.
- [56] J. Suppe, "Mechanics of mountain building and metamorphism in Taiwan," *Memoir of the Geological Society of China*, vol. 4, pp. 67–89, 1981.

- [57] H. Kao, S. J. Shen, and K. F. Ma, "Transition from oblique subduction to collision: earthquakes in the southernmost Ryukyu arc-Taiwan region," *Journal of Geophysical Research*, vol. 103, no. B4, pp. 7211–7229, 1998.
- [58] C. H. Lin and H. C. Pu, "Very-long-period seismic signals at the Tatun Volcano Group, northern Taiwan," *Journal of Volcanology and Geothermal Research*, vol. 328, pp. 230–236, 2016.
- [59] E. Padrón, N. M. Pérez, P. A. Hernández et al., "Diffusive helium emissions as a precursory sign of volcanic unrest," *Geology*, vol. 41, no. 5, pp. 539–542, 2013.
- [60] Y. Orihara, M. Kamogawa, and T. Nagao, "Preseismic changes of the level and temperature of confined groundwater related to the 2011 Tohoku Earthquake," *Scientific Reports*, vol. 4, no. 1, article 6907, 2014.
- [61] R. J. Rau, K. E. Ching, J. C. Hu, and J. C. Lee, "Crustal deformation and block kinematics in transition from collision to subduction: global positioning system measurements in northern Taiwan, 1995-2005," *Journal of Geophysical Research*, vol. 113, no. B9, article B09404, 2008.
- [62] K. E. Ching, M. L. Hsieh, K. M. Johnson, K. H. Chen, R. J. Rau, and M. Yang, "Modern vertical deformation rates and mountain building in Taiwan from precise leveling and continuous GPS observations, 2000-2008," *Journal of Geophysical Research*, vol. 116, no. B8, article B08406, 2011.
- [63] I. P. Dobrovolsky, S. I. Zubkov, and V. I. Miachkin, "Estimation of the size of earthquake preparation zone," *Pure and Applied Geophysics*, vol. 117, no. 5, pp. 1025–1044, 1979.
- [64] R. L. Fleischer, "Dislocation model for radon response to distant earthquakes," *Geophysical Research Letters*, vol. 8, no. 5, pp. 477–480, 1981.
- [65] P. Upton, P. O. Koons, and D. Eberhart-Phillips, "Extension and partitioning in an oblique subduction zone, New Zealand: constraints from three-dimensional numerical modeling," *Tectonics*, vol. 22, no. 6, article 1068, 2003.
- [66] C. W. Lin, W. C. Chang, S. T. Lu, T. S. Shih, and W. C. Huang, "An introduction to the active faults of Taiwan, 2nd edition, explanatory text of the active fault map of Taiwan," in *Special Publication of the Central Geological Survey*, vol. 13, pp. 1–122, 2000.

Research Article

Isotopic Composition of Abiogenic Gas Produced in Closed-System Fischer-Tropsch Synthesis: Implications for the Origins of the Deep Songliao Basin Gases in China

Zhifu Wei¹, Yongli Wang², Gen Wang¹, Xueyun Ma^{1,3}, Wei He^{1,3}, Ting Zhang^{1,3}, Xiaoli Yu^{1,3} and Yan-Rong Zou⁴

¹Key Laboratory of Petroleum Resources Research, Gansu Province, Northwest Institute of Eco-Environment and Resources, Chinese Academy of Sciences, Lanzhou 730000, China

²Key Laboratory of Cenozoic Geology and Environment, Institute of Geology and Geophysics, Chinese Academy of Sciences; CAS Center for Excellence in Life and Paleoenvironment, Beijing 100029, China

³University of Chinese Academy of Sciences, Beijing 100049, China

⁴The State Key Laboratory of Organic Geochemistry, Guangzhou Institute of Geochemistry, Chinese Academy of Sciences, Guangzhou 510640, China

Correspondence should be addressed to Yongli Wang; ylwang@mail.iggcas.ac.cn and Gen Wang; gwang@lzb.ac.cn

Received 10 January 2019; Revised 13 February 2019; Accepted 3 March 2019; Published 28 August 2019

Academic Editor: Francesco Italiano

Copyright © 2019 Zhifu Wei et al. This is an open access article distributed under the Creative Commons Attribution License, which permits unrestricted use, distribution, and reproduction in any medium, provided the original work is properly cited.

In this study, closed-system Fischer-Tropsch synthesis was conducted at 380°C and 30 MPa for 72 h with magnetite as a catalyst. The isotopic composition of the closed-system Fischer-Tropsch synthesis gas and the composition of known abiogenic gas were systematically studied, and the deep Songliao Basin gas was also investigated. The results show that closed-system Fischer-Tropsch synthesis of gaseous hydrocarbon isotopes exhibits a partial reverse order, which includes the reverse order of methane and ethane such as $\delta^{13}\text{C-C}_1 > \delta^{13}\text{C-C}_2 < \delta^{13}\text{C-C}_3$ and $\delta^2\text{H-C}_1 > \delta^2\text{H-C}_2 < \delta^2\text{H-C}_3$. Furthermore, experimental data on the control of NaBH_4 content indicates that the carbon isotopes demonstrate a reverse order on condition that the H_2/CO_2 (mole ratio) is equal to or greater than 4.0; meanwhile, the hydrogen isotopes show a normal order. The deep Songliao Basin hydrocarbon gas component is similar to thermogenic gas and has a trend of a transition to oceanic hydrothermal system abiogenic gas. In addition, the deep Songliao Basin gas isotopic pattern is different from both Lost City and Kidd Creek where the deep Basin gas carbon isotopic pattern has a reverse order, and the hydrogen isotopic pattern has a normal order. Therefore, the deep Basin gas might be a mixture of the oil-type gas and the coal-formed gas, which could be the cause of the isotopic reverse.

1. Introduction

Generally, hydrocarbons are mainly derived from microbial decomposition of organic matter [1–3] and organic matter thermal degradation [2, 4]. However, abiogenic hydrocarbons are produced by chemical reactions that do not directly involve organic matter and are present in trace amounts in high-temperature volcanic/geothermal fluids and magma systems [5–7]. The researchers found that a large proportion of abiogenic hydrocarbons (up to 90 vol.%) associated with low-temperature gas-water rock interactions were present in Precambrian crystalline shield, submarine peridotite

hydrothermal system, continental ophiolite, and serpentinized ultramafic rocks in peridotite blocks [8–12]. Abiogenic gas associated with continental serpentinized ultramafic rock systems have been found in many countries from North America, Europe, and Asia to Oceania [8, 13–18]. Typical characteristics of the gas include a high concentration of methane (CH_4 , usually greater than 80 vol. %), variable amounts of hydrogen (H_2) and C_{2+} alkanes (ethane, propane, and butane), and typical combinations of stable C and H isotopes of CH_4 , which overlap only partially with biological (thermal) gases [9, 19]. In fact, abiogenic gas is related to a process known as Fischer-Tropsch synthesis (FTS) [20–22].

Fischer-Tropsch synthesis (FTS) was first developed by German chemists Franz Fischer and Hans Tropsch in 1926, and it is a chemical process that converts carbon monoxide from coal into liquid hydrocarbon-based fuels and lubricants [23]. Usually, it can be defined as a heterogeneous catalytic reduction of carbon dioxide using molecular hydrogen, which is widely considered to be a process that may lead to the presence of organic compounds in meteorites, submarine hydrothermal systems, and igneous rocks [24–29]. Organic compounds produced by Fischer-Tropsch synthesis (FTS) are used to explain the existence of hydrocarbons in igneous rocks and hydrothermal fluids, and they are involved in a variety of geological processes, including the production of methane and hydrocarbons deep in the crust, which provides nutrients for microorganisms in underground and hydrothermal environments ([30]; Szamtmari, 1989; [22, 27, 31–33]).

It has previously been observed that some abiogenic CO₂ and biogenic hydrocarbon gas reservoirs have been found successively in the Xujiaweizi fault depression of the Songliao Basin [34, 35]. Most of these gases are produced by Ro > 2.0% source rocks and have carbon isotopic reversals ($\delta^{13}\text{C} - \text{C}_1 > \delta^{13}\text{C} - \text{C}_2$; $\delta^{13}\text{C} - \text{C}_2 > \delta^{13}\text{C} - \text{C}_3$) [36]. Their genetic origin has been debated for a long time (e.g., Guo et al. 1997; [37–41]), mainly because of their common carbon isotopic reversals. Previous studies have found that the deep natural gas in the Songliao Basin is dominated by hydrocarbon gas. The carbon isotope composition of methane is relatively heavy (>30.0‰), and the carbon isotopic reversal trend is general, so it is believed that there are abiogenic alkane gases in the Xujiaweizi fault depression, which is considered to be related to mantle degassing ([42]; Guo et al. 1997; [43, 44]). Others have argued that the mixing of different types of natural gas formed by organic matter in the same formation is the main reason for those results [45]. In this study, the experimental data and the isotopic composition of abiogenic gas were systematically studied with closed-system Fischer-Tropsch synthesis and pyrolysis at 380°C and 30 MPa, and the deep Songliao Basin gas was also investigated to provide more information for exploring the sources of the deep Songliao Basin gas.

2. Geological Setting

Songliao Basin is a complex faulted basin in which the Lower Cretaceous is dominated by faulted sedimentation and contains a natural gas reservoir, and the Upper Cretaceous is dominated by depression sedimentation and contains a petroleum reservoir [46]. The Xujiaweizi fault depression is located in the north part of the Songliao Basin (Figure 1(a)). From younger to older, the deep strata of the Xujiaweizi fault depression comprise the Dengloulou Formation, Yingcheng Formation, Shahezi Formation, and Huoshiling Formation (Figure 1(b)) [36]. Among these, the deposition periods of the Huoshiling and Yingcheng formations were the main developing times for volcanic rocks in fault depression, the deposition period of Shahezi Formation was the main developing period for hydrocarbon source rocks in the fault depressions, and the Dengloulou Formation

was the regional cap rock of the natural gas in the deep fault depression [41].

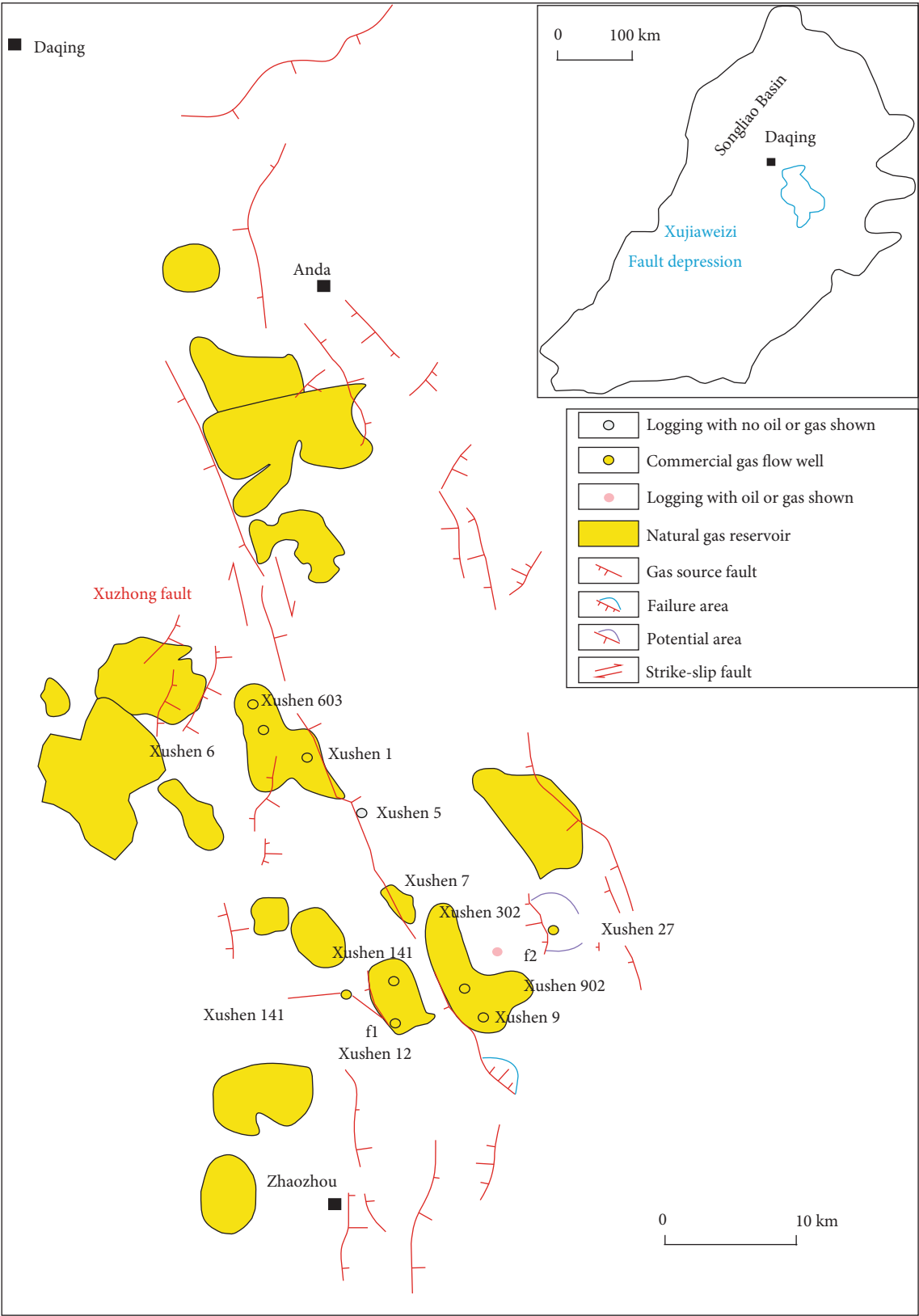
The Xujiaweizi fault depression mainly develops two sets of source rocks of the Lower Cretaceous Shahezi Formation (K₁sh) and Yingcheng Formation (K₁yc). The source rocks of Shahezi Formation are widely distributed, mainly in the central, western, and northern parts of the fault depression, with a thickness of more than 200 m, whereas source rocks in the Yingcheng Formation are mainly distributed in the Xuzhong area and the southern part of the fault depression with a maximum thickness of 160 m. The TOC average values of Shahezi Formation and Yingcheng Formation are 2.43% and 1.41%, respectively [47]. The organic matter types are mainly type III, and the vitrinite reflectance Ro average values are 2.36% and 2.24%, respectively [47]. Both sets of source rocks are in stages of high to overmature evolution. The main deep gas reservoir types include the Dengloulou structural gas reservoir, Yingcheng Formation volcanic lithologic gas reservoir and basement lithologic gas reservoir. The Xujiaweizi fault depression is the most abundant hydrocarbon gas reservoir in volcanic rocks around the world [48] with proven gas reserves exceeding 250 billion cubic meters that have been discovered since the milestone well XS1 was drilled in 2002. Gas fields, such as Wangjiatun, Songfangtun, Changde, Nongan, and Qingshen, have been discovered in the Xujiaweizi fault depression and its surroundings.

3. Fischer-Tropsch Synthesis

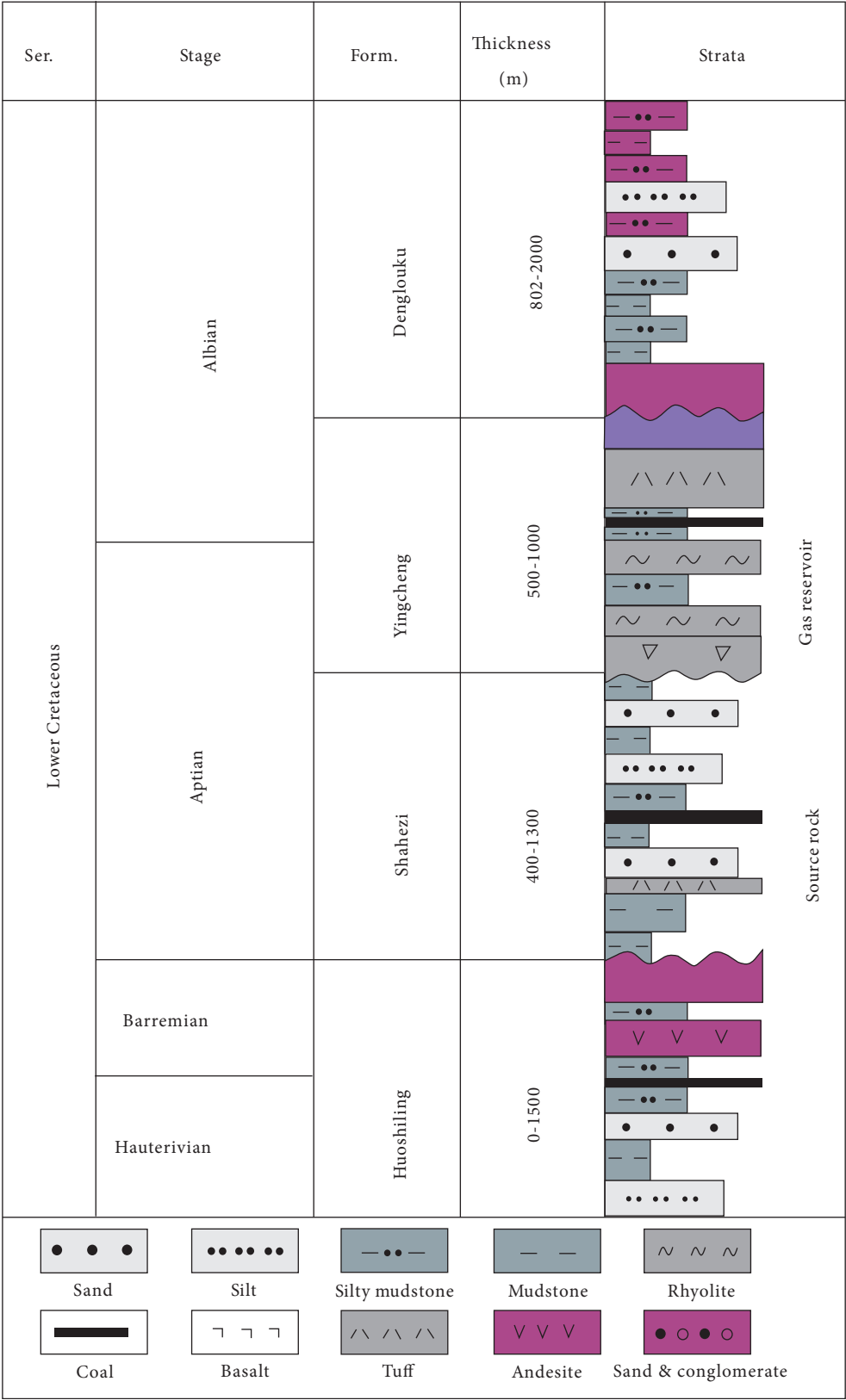
Abiogenic synthesis of hydrocarbons has been discussed since 1940 [49]. Many methods have been described, and although the researchers have not yet reached a conclusion, it is generally believed that hydrocarbons could be produced by reduction of CO₂ via an aqueous Fischer-Tropsch synthesis (FTS) reaction. The Fischer-Tropsch reaction is a common industrial process invented by German scientists Franz Fischer and Hans Tropsch in the 1920s. The mass balance equation is as follows:



Although the first study of FTS began in the early 20th century, the mechanism of hydrocarbon formation from CO and H₂ is still controversial because the whole process is a very complex binding chain that is simultaneously and continuously reacting on the surface of changing metal-oxide-carbide [50–52]. The composition of FTS products differs essentially from the equilibrium composition [53–55]. FTS is a process controlled by kinetics, and the distribution of products depends on the properties of catalysts and synthesis conditions. The main initial step is to adsorb H₂ and CO on the metal surface. The activity and selectivity of catalysts depend mainly on the properties of CO adsorption-desorption-dissociation. Compared to H₂, CO can be adsorbed on metal and oxide surfaces [56]. The simple rules of FTS indicate that more olefins and carbon dioxide are formed on iron catalysts, whereas more alkanes and water are produced on nickel and cobalt catalysts [53]. In hydrothermal systems, carbon dioxide is the most likely reactant,



(a)
FIGURE 1: Continued.



(b)

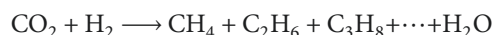
FIGURE 1: Location of the Xujiaweizi Fault Depression (modified from [41]) and the stratigraphic column for the deep strata of Xujiaweizi fault depression (modified from [36]).

and many laboratory experiments [57–63] have shown that saturated hydrocarbons and other organic compounds can be generated by FTS reactions with carbon dioxide as an indirect carbon source. In addition, it has been suggested that in this case, the first stage of the FTS reaction is to form CO by reducing CO₂ by H₂:



4. Experiments and Methods

4.1. Experimental Conditions and Materials. The Xujiaweizi fault depression is a gas-bearing fault depression with the highest exploration degree in the Songliao Basin. The buried depth of the gas reservoir is generally 3000–4000 m with an average of approximately 3500 m [64]. The paleogeothermal gradient in the Xujiaweizi fault depression is higher than the present average value of 4°C/100 m with a maximum of 5°C/100 m at the end of the Cretaceous (~65 Ma) [65, 66]. The maximum temperatures experienced by reservoirs and source rocks thus occurred before the end of the Cretaceous, except in some areas where they may have been influenced by volcanic activity [66, 67]. In this study, the chosen laboratory conditions (380°C and 30 MPa) of the Fischer-Tropsch synthesis experiments might be representative of the thermodynamic conditions of the Songliao reservoir. In addition, two types of material were selected to carry on the Fischer-Tropsch reaction, including the sodium materials, which are NaHCO₃ and NaBH₄. NaHCO₃ is prepared by CO₂ that is taken from the Fangshen-9 Well in the Songliao Basin, China. It has been established that the CO₂ in the Fangshen-9 Well has an abiogenic origin. Therefore, the purpose of choosing CO₂ in the Fangshen-9 Well to simulate the formation process of deep gas in the Songliao Basin was to make the simulation as realistic as possible, allowing for the exploration of the origins of the gas. The CO₂ and NaOH solution is fully reacted and crystallized to obtain NaHCO₃. After these two kinds of materials are mixed, the NaHCO₃ heating decomposition produces water that reacts with NaBH₄ to produce the hydrogen. At a certain temperature and pressure, the hydrogen and carbon dioxide undergo Fischer-Tropsch synthesis. Magnetite is a ubiquitous component of ultramafic-hosted hydrothermal systems (Alt & Shanks, 2003), which is why it was selected for this series of experiments. Magnetite was used as the catalyst in the experiment, and the chemical reaction equation was as follows:



4.2. Experimental Procedure. The pyrolysis experiment was conducted in a closed system following the procedures described in detail by Tao [68]. All pyrolysis experiments were performed in gold cell reactors (50 mm × 4 mm). Approximately 5 mg of NaBH₄, 5 mg of magnetite, and 40 mg of NaHCO₃ prepared by CO₂ were taken from the Fangshen-9 Well in the Songliao Basin, China, and were

loaded into one gold tube, which was then welded on one end. The gold tube was flushed with argon for approximately 15 minutes to ensure complete removal of air and then sealed in an argon atmosphere using arc welding. After that, the sealed gold was placed in a stainless-steel pressure cooker, and then approximately 10 ml of water was placed in a container connected to a pressurized water line. The pressure device consisted of an air compressor and a booster pump that drives high pressure water into an autoclave. The sample in the autoclave was heated to a target temperature in a single oven. During pyrolysis, the pressure in the autoclave was adjusted by adding water from the pump or removing water from the autoclave through a leak valve. The experiment was carried out at a temperature of 380°C and a pressure of 30 MPa for up to 72 h.

4.3. Product Analysis. The pyrolysis products of Fischer-Tropsch synthesis include hydrocarbon gases and nonhydrocarbon gases. In the analysis of hydrocarbon composition, the gold cell was placed in a vacuum system and pierced with a needle, and the gas products were released and collected by a Toppler pump for quantitative analysis. Then, the composition of the gas products was analyzed using Agilent 6890N-Wasson gas chromatography with a PoraPLOT Q capillary column (50 m × 0.53 mm id). The oven temperature was maintained at 70°C for 6 min, then increased from 70°C to 130°C at 15°C/min, from 130°C to 180°C at 25°C/min, and then maintained at 180°C for 4 min. Nitrogen was used as a carrier gas, and experiments were carried out at 180°C using FID and TCD detectors. C₁–C₅ hydrocarbons, H₂S, H₂, and CO₂ (detection limits of CO₂ and H₂: 40 ppmv; H₂S: 150 ppmv; HC: 10 ppmv; precision 2%; 10% at the detection limit) were quantitatively analyzed by using the external standard method.

Gas carbon isotope analysis was performed by gas chromatography-isotope ratio mass spectrometry (GV IsoPrime™ GC-IRMS) with a capillary column (30 m × 0.32 mm). The temperature program was as follows: using helium as a carrier gas, the oven temperature was kept at 60°C for 3 min, rose to 180°C with a 25°C/min heating program, then held at 180°C for 10 min. Gas samples were analyzed in duplicates, and the stable carbon isotopic values are reported in the δ-notation in per mil (‰) relative to VPDB. Precision for individual components in the molecular δ¹³C analysis is ±0.3‰.

GC-IRMS (Finnigan Delta Plus XL) with a capillary column (HP-PLOT, 30 m × 0.32 mm) was used to analyze the hydrogen isotope of hydrocarbon gases (C₁–C₃). The temperature program is as follows: the temperature was held at 50°C for 7 min, and then the temperature rose to 180°C at a rate of 30°C/min. The stable hydrogen isotopic ratio (δ²H) values are reported in the δ-notation in per mil (‰) relative to VSMOW and the reproducibility and precision of isotope values are expected to be ±3‰.

5. Results and Discussion

5.1. Gas Isotope Composition. The Fischer-Tropsch synthesis experiments were carried out under closed-system gold tube-

high pressure vessels at 380°C and 30 MPa. The gas yields and gas isotopic compositions are shown in Table 1. The results show that the carbon isotopes (PDB, ‰) and hydrogen isotopes (SMOW, ‰) of gaseous hydrocarbons exhibited normal order or partial reverse order, which is the reverse order of methane and ethane, such as $\delta^{13}\text{C} - \text{C}_1 > \delta^{13}\text{C} - \text{C}_2 < \delta^{13}\text{C} - \text{C}_3$ and $\delta^2\text{H} - \text{C}_1 > \delta^2\text{H} - \text{C}_2 < \delta^2\text{H} - \text{C}_3$ (Figure 2). Hu et al. [69] also observed that the carbon isotopes have a reverse order or partial reverse order, whereas the Fischer-Tropsch synthesis experiments were carried out under a closed system with an iron-based catalyst for CO and H_2 at 270–300°C, 0.7–2.0 MPa. Other scholars have reported that hydrogen isotopes show $\delta^2\text{H} - \text{C}_1 > \delta^2\text{H} - \text{C}_2 < \delta^2\text{H} - \text{C}_3$ in a hydrothermal system; however, the carbon isotopes of gaseous hydrocarbons are heavier with an increase in carbon number, and carbon isotopes have a normal order [21, 70]. Fu et al. [71] indicated that carbon isotopes do not have a reverse order in a closed system with an iron-based catalyst for CO and H_2 at 400°C, 50 MPa. In addition, Fischer-Tropsch synthesis experiments were carried out in an open system with an iron-based catalyst for CO and H_2 at 260–300°C, 3 MPa, by Taran et al. [72]; the results showed that the carbon isotopes of gaseous hydrocarbons were reversed only for a low conversion rate of CO, and they considered that other processes (such as a simple mixing of two or more end members) or other P-T conditions of the carbon reduction could be responsible for the “inverse” isotopic trend found in meteorites and some natural gases. To this end, FTS experiments were carried out while controlling the NaBH_4 content (Table 1). According to Zhang & Duan [73], the ethane was probably oxidized when the mantle-derived gas was migrated to the crust. Mantle fluids rose to the boundary of lithosphere-asthenosphere, and the composition of the fluids changed from the mixture of $\text{H}_2\text{O}-\text{CH}_4-\text{H}_2-\text{C}_2\text{H}_6$ to the mixture of $\text{H}_2\text{O}-\text{CO}_2-\text{CO}$. The mantle fluids H_2/CO_2 (mole ratio) are generally less than 1.2 under the conditions of high temperature and high pressure. The FTS experimental gaseous hydrocarbons with the control of NaBH_4 carbon content and hydrogen isotope patterns are shown in Figure 3. When the H_2/CO_2 (mole ratio) is less than 1.2, the gas carbon isotopes are a normal order and show a linear increase in carbon numbers; when the H_2/CO_2 (mole ratio) is more than 1.2, the carbon isotopes of methane are heavier than ethane, and the carbon isotopes of C_{2+} are heavier and show a linear increase in carbon numbers. When the H_2/CO_2 (mole ratio) is equal to or greater than 4.0, the carbon isotopes have a reverse order. Compared to carbon isotopes, the hydrogen isotopes show $\delta^2\text{H} - \text{C}_1 < \delta^2\text{H} - \text{C}_2 > \delta^2\text{H} - \text{C}_3$ when H_2/CO_2 (mole ratio) is less than 4.0, and the hydrogen isotopes of propane are close to ethane with an increase in H_2/CO_2 (mole ratio). When H_2/CO_2 (mole ratio) is equal to or greater than 4.0, the hydrogen isotopes of propane are heavier than ethane, and the hydrogen isotopes show a normal order.

5.2. The Characteristics of Abiogenic Gas. Sherwood Lollar et al. [74] used stable isotope signatures to suggest that CH_4 and higher hydrocarbon gases (ethane, propane, and butane)

at Kidd Creek mine on the Canadian Shield are produced abiogenically by water-rock interactions, such as surface-catalyzed polymerization [24, 53], metamorphism of graphite-carbonate bearing rocks [75–77], and other gas-water-rock alteration reactions, such as serpentinization [20, 78–83].

According to Sherwood-Lollar et al. [11], the isotopic pattern of abiogenic gas of Precambrian Shield sites in Canada is shown in Figure 4(a). It was indicated that $\delta^{13}\text{C}$ of methane is the heaviest, which is distributed in $-32\text{‰} \sim -36\text{‰}$ (PDB); however, $\delta^{13}\text{C}$ of ethane is in $-36\text{‰} \sim -39\text{‰}$ which is the lightest in hydrocarbon gas, and C_1-C_2 shows a depletion trend while C_2-C_5 shows a consistent trend of isotopic enrichment in ^{13}C with increasing molecular weight. The pattern of hydrogen isotopic variation had consistent ^2H enrichment with increasing molecular weight, which is a positive sequence (Figure 4(b)). Proskurowski et al. (2008) pointed out that the carbon isotope compositions of C_1 to C_4 hydrocarbons from Lost City fluids are increasingly negative ($\delta^{13}\text{C}$ ranges from -9‰ to -16‰ , PDB) with increasing chain length (Figure 4(a)). The hydrogen isotopic composition of Lost City C_1 to C_3 hydrocarbons shows a similar, although less defined, trend in which molecules with longer chain lengths have similar or slightly lower $\delta^2\text{H}$ values (-120‰ to -170‰ , SMOW) relative to shorter-chain alkanes (Figure 4(b)). As shown in Figure 4, the carbon and hydrogen of the closed-system FTS gaseous hydrocarbon are distributed between the Kidd Creek and Lost City.

5.3. The Deep Gas in the Songliao Basin and Abiogenic Gas

5.3.1. Gas Component. The composition of the deep Songliao Basin hydrocarbon gas [41, 84], Fischer-Tropsch experimental gas (Table 1), and the abiogenic gas of Kidd Creek [11] is shown in Figure 5. As shown in Figure 5, the deep Songliao Basin hydrocarbon gas is similar to thermogenic gas but has a different variation with abiogenic gas and has a trend of a transition to oceanic hydrothermal system abiogenic gas (Proskurowski et al. 2008). Therefore, the deep Basin gas might be a mixture of the oil-type gas and the coal-formed gas, which could be the cause of the isotopic reverse; the closed-system FTS gas is similar to the hydrothermal system and has a trend of transition to the Kidd Creek (Figure 5).

5.3.2. Isotopic Characteristics. Previous studies have found that natural gases in the deep strata of the Songliao Basin are dominated by alkane gases, the carbon isotope composition of methane is heavier ($>-30.0\text{‰}$) and the carbon isotopic reversal trend is general [41]. The carbon isotopes of the deep Songliao Basin hydrocarbon gas become more depleted in ^{13}C with increasing molecular mass ($\delta^{13}\text{C} - \text{C}_1 > \delta^{13}\text{C} - \text{C}_2 > \delta^{13}\text{C} - \text{C}_3 > \delta^{13}\text{C} - \text{C}_4$), which is a reverse order [41]. Wang et al. [84] suggested that natural gases from the Songliao Basin show two different distribution patterns of $\delta^{13}\text{C}$ values due to differences in precursors and mechanisms of hydrocarbon formation as well as the kinetic isotope fractionation of alkane carbon isotopes. Alkanes formed by the degradation of sedimentary organic matter show lighter $\delta^{13}\text{C}-\text{C}_1$ values ($-30.2\text{‰} \sim -58.3\text{‰}$) with

TABLE 1: The gas yields and isotopic composition of the Fischer-Tropsch synthesis.

Sample	T (°C)	P (MPa)	t (hr)	NaHCO ₃ (mg)	NaBH ₄ (mg)	Yields (ml/g NaHCO ₃)					δ ¹³ C (PDB, ‰)			δ ² H (SMOW, ‰)			
						C ₁	C ₂	C ₃	CO ₂	C ₄ +C ₅	CO ₂	C ₁	C ₂	C ₃	C ₁	C ₂	C ₃
NaHCO ₃ +NaBH ₄ +Fe ₃ O ₄	380	30	6	37.07	3.89	1.38	0.18	0.09	0.05	0.04	-36.19	-19.09	-35.12	-33.81	-267.24	-456.62	-180.43
	380	30	18	32.88	5.78	14.10	0.53	0.18	0.08	0.10	-21.37	-20.37	-20.12	-17.63	-269.03	-326.79	-195.21
	380	30	36	36.22	5.52	15.86	0.59	0.22	0.07	0.12	-24.35	-25.93	-22.15	-18.17	-313.52	-305.48	-193.18
	380	30	54	34.33	4.88	18.04	0.69	0.24	0.04	0.16	-23.41	-18.99	-22.78	-18.31	-319.61	-322.91	-205.27
	380	30	72	36.92	5.04	15.86	0.86	0.20	0.03	0.09	-29.57	-13.47	-30.74	-24.73	-306.47	-276.12	-223.56
	380	30	72	39.98	0	n.d.	n.d.	n.d.	26.23	n.d.	-4.94	n.d.	n.d.	n.d.	n.d.	n.d.	n.d.
	380	30	72	39.37	1.26	0.89	0.06	0.03	15.70	0.01	-22.14	-23.72	-33.76	-28.20	-420.10	nd	nd
	380	30	72	40.56	3.84	9.10	0.45	0.17	1.75	0.09	-23.59	-17.00	-13.76	-13.77	-381.59	-296.53	-355.85
	380	30	72	39.61	5.17	12.03	0.76	0.26	0.04	0.17	-23.86	-24.48	-30.61	-25.30	-329.69	-280.31	-293.20
	380	30	72	41.75	6.86	19.01	0.81	0.23	0.05	0.05	-24.10	-17.14	-23.46	-21.42	-320.66	-222.56	-252.33
	380	30	72	40.79	8.48	33.01	4.58	2.26	0.04	1.18	-22.73	-23.79	-21.90	-23.72	-333.06	-240.58	-232.78

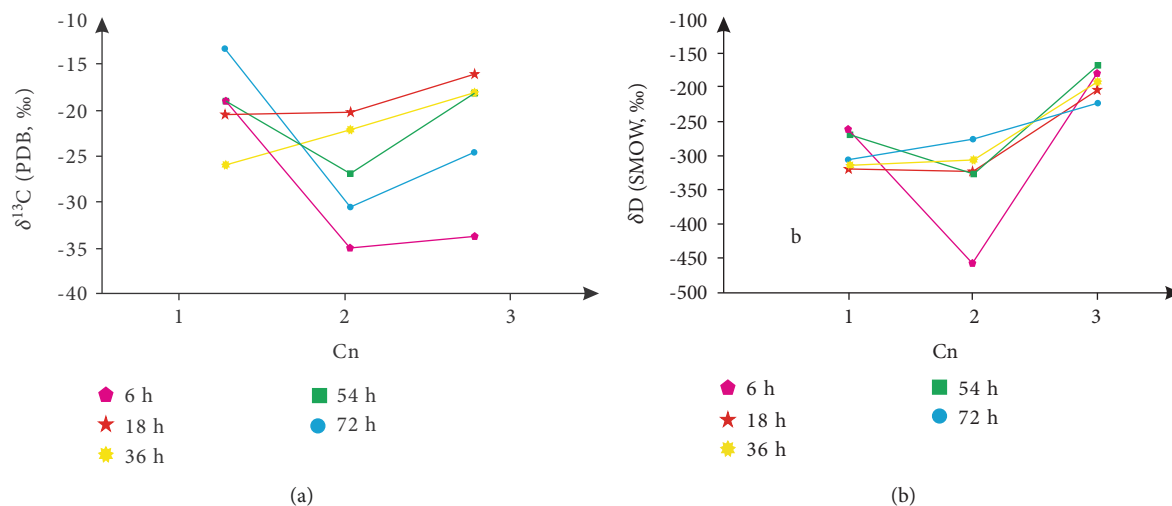


FIGURE 2: The isotopic pattern of the Fischer-Tropsch synthesis gas at different pyrolysis times. (a) The carbon isotopic pattern and (b) the hydrogen isotopic pattern.

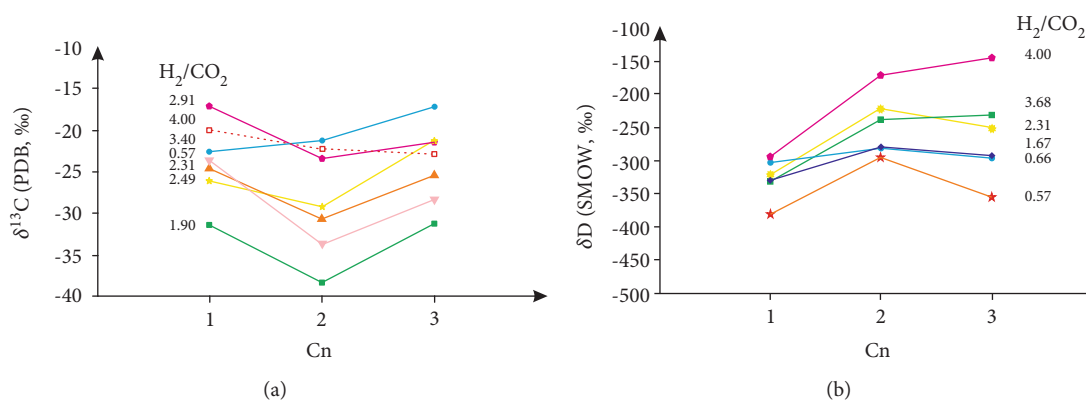


FIGURE 3: The isotopic pattern of closed-system FTS with the control of NaBH_4 content. (a) The carbon isotopic pattern and (b) the hydrogen isotopic pattern.

a normal distribution of $\delta^{13}\text{C}$ values for methane homologues. Abiogenic natural gases show heavier $\delta^{13}\text{C}-\text{C}_1$ values ($-30.5\text{‰} \sim -16.7\text{‰}$) with a reverse distribution of $\delta^{13}\text{C}$ values similar to alkanes from the Murchison meteorite and polymerization, whereas the $\delta^2\text{H}$ values are featured by a normal distribution. Figure 6 shows the carbon-hydrogen isotope variation with carbon numbers (data from Proskurowski et al. 2008; [11, 84]). As shown in Figure 6, the deep Songliao Basin gas isotopic pattern is different for both Lost City and Kidd Creek in which the deep Basin gas carbon isotopic pattern has a reverse order, and the pattern of hydrogen has a normal order. The abiogenic gas of Kidd Creek only shows $\delta^{13}\text{C}-\text{C}_1 > \delta^{13}\text{C}-\text{C}_2$, yet the carbon isotopes of C_{2+} have a normal order, and the carbon and hydrogen isotopes of the Lost City are the reverse order.

5.3.3. Isotope Fractionation. According to previously reported data ([21, 69, 71, 72]; Proskurowski et al. 2008; [84, 85]), the CO/CO_2 and methane carbon isotope

fractionation diagram was added up for different natural environments and experimental conditions (Figure 7). Overall, the CO_2 and methane carbon fractionation is between 15‰ and 25‰ in the natural environments, and under experimental conditions, the CO/CO_2 and methane carbon isotope fractionation changed greatly between 8‰ and 40‰ , which is related to the conversion rate [69, 72]. The conversion of CO/CO_2 and carbon isotope fractionation has a negative correlation. It should be noted that the methane carbon isotope variation is limited to the deep Songliao Basin gas which seems to have nothing to do with the CO_2 carbon isotope (Figure 7). The results suggest that the conversion of mantle CO_2 to synthesize methane is low, and there is a supplement of organic CO_2 , which implied that there is a complicated relationship between the two.

During the formation of abiogenic gas, hydrogen isotope fractionation also occurred (Figure 8). As shown in Figure 8, the carbon isotope and hydrogen isotope fractionation all occurred in abiogenic synthesis to methane, and the

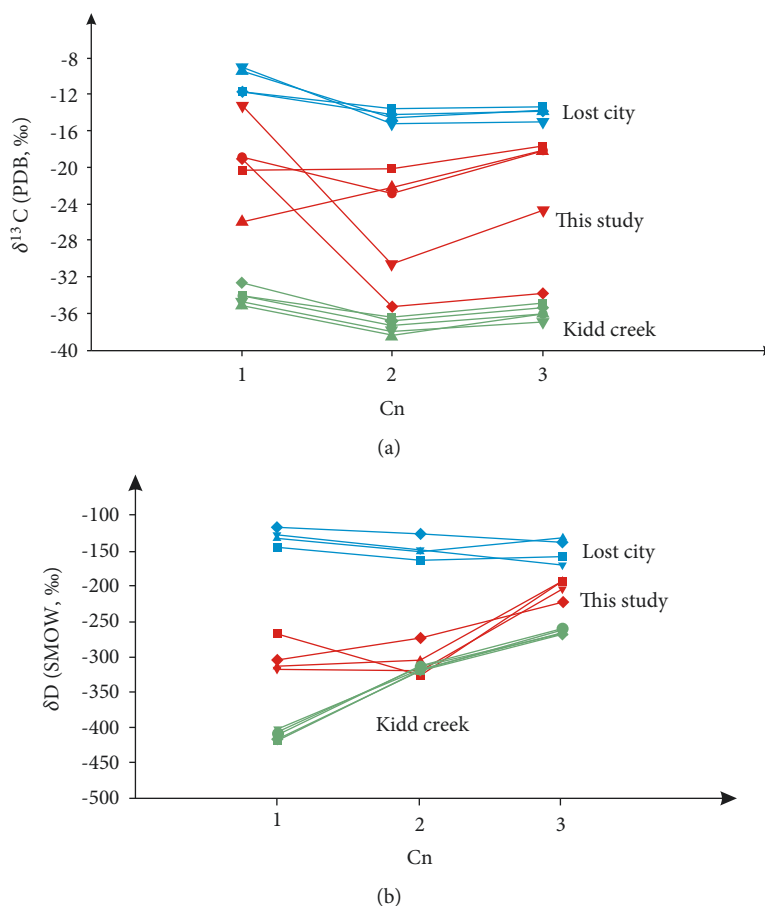


FIGURE 4: The isotopic pattern of abiogenic gas. (a) The carbon isotopic pattern and (b) the hydrogen isotopic pattern; for comparison, the $\delta^{13}\text{C}$ and $\delta^2\text{H}$ values for abiogenic gases occurring at Lost City (Proskurowski et al. 2008) and Kidd Creek [74] are also shown.

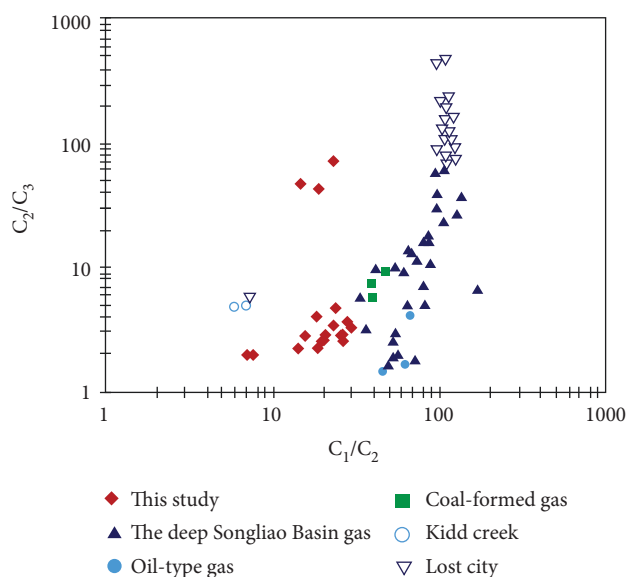


FIGURE 5: Chemical components of the deep Songliao Basin gas and abiogenic gas (the deep Songliao Basin hydrocarbon gas: [84]; the oil-type gas and the coal-formed gas: [68]; Kidd Creek: [11]; Lost city: Proskurowski et al. 2008).

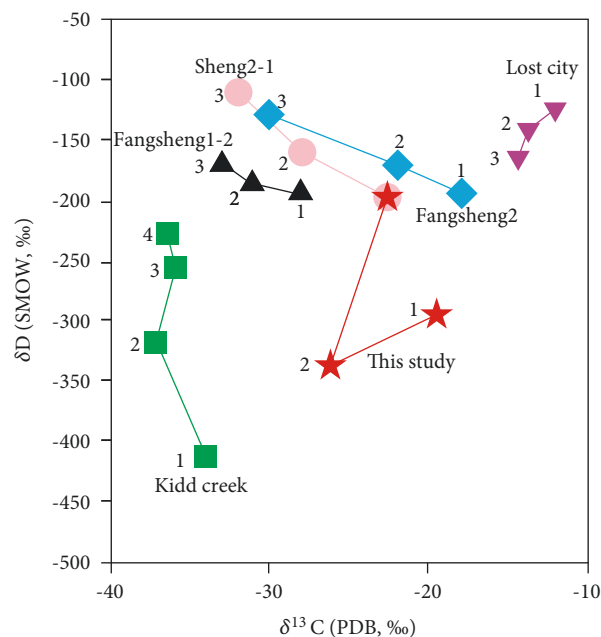


FIGURE 6: Natural gas carbon-hydrogen isotope variation with carbon number (the deep Songliao Basin hydrocarbon gas: [84]; Kidd Creek: [11]; Lost city: Proskurowski et al. 2008).

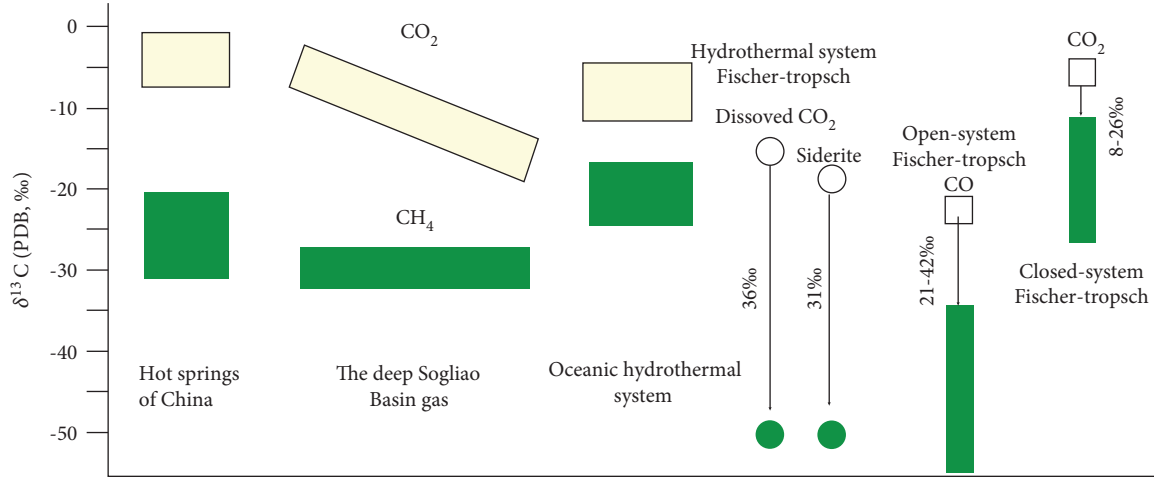


FIGURE 7: Carbon isotope fractionation under different conditions (data from [21, 69, 71, 72]; Proskurowski et al. 2008; [84, 85]).

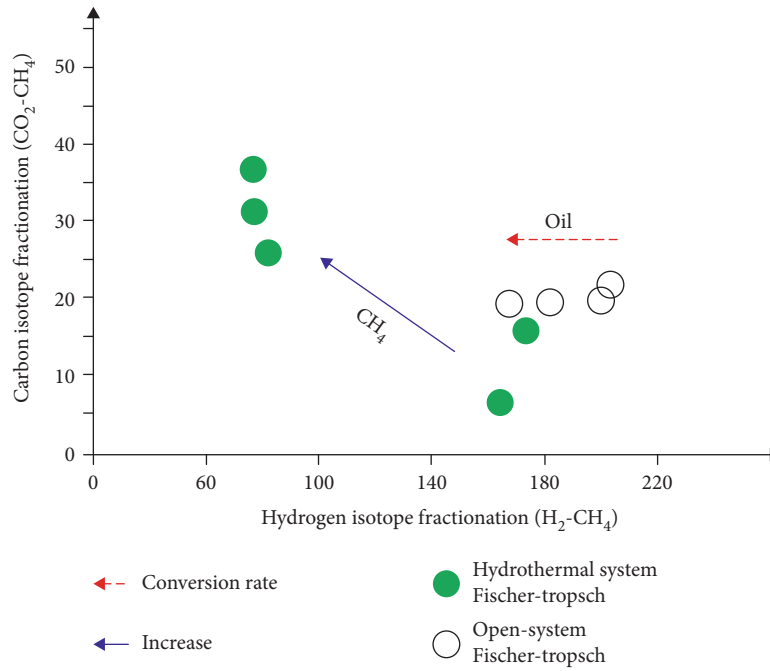


FIGURE 8: Carbon-hydrogen isotope fractionation under different experimental conditions (data from [21, 72]).

carbon isotope fractionation increased with the conversion as the hydrogen isotope fractionation decreased with the conversion. It is estimated that the methane carbon isotope fractionation was in the 20‰ and 25‰, and the early hydrogen isotope fractionation was 170‰ while the late fractionation was 80‰. The carbon isotope and hydrogen isotope fractionation of the condensate oil was 20‰ and 180‰. Closed-system Fischer-Tropsch synthesis experimental data (Table 1) shows that a carbon isotope of methane has increased with a decrease in C_1/C_2 , which means that the carbon isotope fractionation is reduced and is probably related to high conversion and polymerization [11, 84].

6. Conclusion

Closed-system Fischer-Tropsch synthesis and pyrolysis were carried out at 380°C and 30 MPa; the experimental data and the isotopic composition of abiogenic gas were systematically studied, and the deep Songliao Basin gas was also investigated in this study, producing following preliminary conclusions:

(1) The results show that carbon isotopes and hydrogen isotopes of Fischer-Tropsch synthesis gaseous hydrocarbons exhibit normal order or partial reverse order, which is the reverse order of methane and ethane such that $\delta^{13}C - C_1 > \delta^{13}C - C_2 < \delta^{13}C - C_3$ and $\delta^2H - C_1 > \delta^2H - C_2 < \delta^2H - C_3$.

(2) It is suggested that carbon isotopes of gaseous hydrocarbons showed a reversal or a reverse order only at low conversion rates of CO_2 ; when the H_2/CO_2 (mole ratio) is equal to or greater than 4.0, the carbon isotopes show a reverse order, while the hydrogen isotopes show a normal order.

(3) The gas component and isotopic pattern suggests that the deep Songliao Basin gas might be a mixture of oil-type gas and coal-formed gas, which could be the cause of the isotopic reverse.

Data Availability

The experimental data used to support the findings of this study are included within the article.

Conflicts of Interest

The authors declare that they have no conflicts of interest.

Acknowledgments

This work was financially supported by the Chinese Academy of Sciences Key Project (Grant Nos. XDB10010202 and XDB10030404), the National Natural Science Foundation of China (Grant Nos. 41572350 and 41503049), the National Key R&D Program of China (Grant No. 2017YFA0604803), the Western Light Project and the Key Laboratory Project of Gansu (Grant No. 1309RTSA041).

References

- [1] D. D. Rice and G. E. Claypool, "Generation accumulation and resource potential of biogenic gas," *AAPG Bulletin*, vol. 65, pp. 5–25, 1981.
- [2] M. Schoell, "Multiple origins of methane in the earth," *Chemical Geology*, vol. 71, pp. 1–10, 1988.
- [3] M. J. Whiticar, E. Faber, and M. Schoell, "Biogenic methane formation in marine and freshwater environments: CO_2 reduction vs. acetate fermentation-isotope evidence," *Geochimica et Cosmochimica Acta*, vol. 50, no. 5, pp. 693–709, 1986.
- [4] M. Schoell, "The hydrogen and carbon isotopic composition of methane from natural gases of various origins," *Geochimica et Cosmochimica Acta*, vol. 44, pp. 649–661, 1980.
- [5] B. Capaccioni, Y. Taran, F. Tassi, O. Vaselli, G. Mangani, and J. L. Macias, "Source conditions and degradation processes of light hydrocarbons in volcanic gases: an example from El Chichón volcano (Chiapas State, Mexico)," *Chemical Geology*, vol. 206, no. 1–2, pp. 81–96, 2004.
- [6] J. Fiebig, A. B. Woodland, J. Spangenberg, and W. Oschmann, "Natural evidence for rapid abiogenic hydrothermal generation of CH_4 ," *Geochimica et Cosmochimica Acta*, vol. 71, no. 12, pp. 3028–3039, 2007.
- [7] Y. Wang, S. Zhang, and G. Yuce, "Gas geochemistry: from conventional to unconventional domains," *Marine and Petroleum Geology*, vol. 89, pp. 1–3, 2018.
- [8] G. Etiope, M. Schoell, and H. Hosgormez, "Abiotic methane flux from the Chi-maera seep and Tekirova ophiolites (Turkey): understanding gas exhalation from low temperature serpentinization and implications for Mars," *Earth and Planetary Science Letters*, vol. 310, no. 1–2, pp. 96–104, 2011.
- [9] G. Etiope and B. Sherwood Lollar, "Abiotic methane on earth," *Reviews of Geophysics*, vol. 51, no. 2, pp. 276–299, 2013.
- [10] M. A. Sephton and R. M. Hazen, "On the origins of deep hydrocarbons," *Reviews in Mineralogy and Geochemistry*, vol. 75, no. 1, pp. 449–465, 2013.
- [11] B. S. Lollar, G. Lacrampe-Couloume, K. Voglesonger, T. C. Onstott, L. M. Pratt, and G. F. Slater, "Isotopic signatures of CH_4 and higher hydrocarbon gases from Precambrian Shield sites: a model for abiogenic polymerization of hydrocarbons," *Geochimica et Cosmochimica Acta*, vol. 72, no. 19, pp. 4778–4795, 2008.
- [12] G. Yuce, F. Italiano, W. D'Alessandro et al., "Origin and interactions of fluids circulating over the Amik Basin (Hatay, Turkey) and relationships with the hydrologic, geologic and tectonic settings," *Chemical Geology*, vol. 388, pp. 23–39, 2014.
- [13] T. Boschetti, G. Etiope, and L. Toscani, "Abiotic methane in the hyperalkaline springs of Genova, Italy," *Procedia Earth and Planetary Science*, vol. 7, pp. 248–251, 2013.
- [14] C. Boulart, V. Chavagnac, C. Monnin, A. Delacourt, G. Ceuleneer, and G. Hoareau, "Difference in gas venting from ultramafic-hosted warm springs: the example of Oman and Voltri ophiolites," *Ophiolite*, vol. 38, pp. 143–156, 2013.
- [15] W. D'Alessandro, G. Yüce, F. Italiano et al., "Large compositional differences in the gases released from the Kizildag ophiolitic body (Turkey): evidences of prevalingly abiogenic origin," *Marine and Petroleum Geology*, vol. 89, pp. 174–184, 2018.
- [16] G. Etiope, "Abiotic methane in continental serpentinization sites: an overview," *Procedia Earth and Planetary Science*, vol. 17, pp. 9–12, 2017.
- [17] Y. Sano, A. Urabe, H. Wakita, and H. Wushiki, "Origin of hydrogen-nitrogen gas seeps, Oman," *Applied Geochemistry*, vol. 8, no. 1, pp. 1–8, 1993.
- [18] C. Vacquand, E. Deville, V. Beaumont et al., "Reduced gas seepages in ophiolitic complexes: evidences for multiple origins of the $\text{H}_2\text{-CH}_4\text{-N}_2$ gas mixtures," *Geochimica et Cosmochimica Acta*, vol. 223, pp. 437–461, 2018.
- [19] G. Etiope, N. Samardžić, F. Grassa, H. Hrvatović, N. Miošić, and F. Skopljak, "Methane and hydrogen in hyperalkaline groundwaters of the serpentinized Dinaride ophiolite belt, Bosnia and Herzegovina," *Applied Geochemistry*, vol. 84, pp. 286–296, 2017.
- [20] J. Horita and M. E. Berndt, "Abiogenic methane formation and isotopic fractionation under hydrothermal conditions," *Science*, vol. 285, no. 5430, pp. 1055–1057, 1999.
- [21] T. M. McCollom and J. S. Seewald, "Carbon isotope composition of organic compounds produced by abiotic synthesis under hydrothermal conditions," *Earth and Planetary Science Letters*, vol. 243, no. 1–2, pp. 74–84, 2006.
- [22] B. Sherwood Lollar, S. K. Frape, S. M. Weise, P. Fritz, S. A. Macko, and J. A. Welhan, "Abiogenic methanogenesis in crystalline rocks," *Geochimica et Cosmochimica Acta*, vol. 57, no. 23–24, pp. 5087–5097, 1993.
- [23] F. Fischer and H. Tropsch, "Hydrocarbon synthesis at atmospheric pressures from gasification products of coal," *Brantoff Chemistry*, vol. 7, pp. 97–104, 1926.
- [24] D. I. Foustoukos and Seyfried WE Jr, "Hydrocarbons in hydrothermal vent fluids: the role of chromium-bearing catalysts," *Science*, vol. 304, no. 5673, pp. 1002–1005, 2004.

- [25] J. Horita, "Some perspectives on isotope biosignatures for early life," *Chemical Geology*, vol. 218, no. 1-2, pp. 171-186, 2005.
- [26] M. S. Lancet and E. Anders, "Carbon isotope fractionation in the Fischer-Tropsch synthesis and in meteorites," *Science*, vol. 170, no. 3961, pp. 980-982, 1970.
- [27] S. Salvi and A. E. Williams-Jones, "Fischer-Tropsch synthesis of hydrocarbons during sub-solidus alteration of the Strange Lake peralkaline granite, Quebec/Labrador, Canada," *Geochimica et Cosmochimica Acta*, vol. 61, no. 1, pp. 83-99, 1997.
- [28] E. L. Shock, "Geochemical constraints on the origin of organic compounds in hydrothermal systems," *Origins of Life and Evolution of the Biosphere*, vol. 20, no. 3-4, pp. 331-367, 1990.
- [29] G. Yuen, N. Blair, D. J. Des Marais, and S. Chang, "Carbon isotope composition of low molecular weight hydrocarbons and monocarboxylic acids from Murchison meteorite," *Nature*, vol. 307, no. 5948, pp. 252-254, 1984.
- [30] T. J. Gold, "Terrestrial sources of carbon and earthquake outgassing," *Journal of Petroleum Geology*, vol. 1, no. 3, pp. 3-19, 1979.
- [31] N. G. Holm and J. L. Charlou, "Initial indications of abiotic formation of hydrocarbons in the rainbow ultramafic hydrothermal system, Mid-Atlantic Ridge," *Earth and Planetary Science Letters*, vol. 191, no. 1-2, pp. 1-8, 2001.
- [32] D. S. Kelley, J. A. Karson, G. L. Früh-Green et al., "A serpentinite-hosted ecosystem: the Lost City hydrothermal field," *Science*, vol. 307, no. 5714, pp. 1428-1434, 2005.
- [33] J. Potter, A. H. Rankin, and P. J. Treloar, "Abiogenic Fischer-Tropsch synthesis of hydrocarbons in alkaline igneous rocks; fluid inclusion, textural and isotopic evidence from the Lovozero complex, N.W. Russia," *Lithos*, vol. 75, no. 3-4, pp. 311-330, 2004.
- [34] J. X. Dai, Y. Song, C. S. Dai, A. F. Chen, M. L. Sun, Y. S. Liao et al., *Conditions Governing the Formation of Abiogenic Gas and Gas Pools in the Eastern China*, Science Press, Beijing, China, 2000.
- [35] J. X. Dai, "Potential areas for coal-formed gas exploration in China," *Petroleum Exploration and Development*, vol. 34, no. 6, pp. 641-645, 2007.
- [36] H. S. Zeng, J. K. Li, and Q. L. Huo, "A review of alkane gas geochemistry in the Xujiaweizi fault-depression, Songliao Basin," *Marine and Petroleum Geology*, vol. 43, pp. 284-296, 2013.
- [37] J. Dai, Y. Ni, J. Li et al., *Geochemical Characteristics of the Abiogenic Alkane Gases in the Songliao Basin, China*, AAPG Hedberg Conference Natural Gas Geochemistry, Beijing, China, 2011.
- [38] H. Huang, J. Yang, Y. Yang, and X. du, "Geochemistry of natural gases in deep strata of the Songliao Basin, NE China," *International Journal of Coal Geology*, vol. 58, no. 4, pp. 231-244, 2004.
- [39] J. Li, W. Fang, H. Zeng, W. Liu, Y. Zou, and J. Liu, "Possible origins for inverse stable carbon isotopes of gaseous alkanes from the Xujiaweizi fault depression," *Acta Petrolei Sinica*, vol. 32, pp. 54-61, 2011.
- [40] J. Mi, S. Zhang, G. Hu, and K. He, "Geochemistry of coal-measure source rocks and natural gases in deep formations in Songliao Basin, NE China," *International Journal of Coal Geology*, vol. 84, no. 3-4, pp. 276-285, 2010.
- [41] N. Yunyan, D. Jinxing, Z. Qinghua, L. Xia, H. Anping, and Y. Chun, "Geochemical characteristics of abiogenic gas and its percentage in Xujiaweizi Fault Depression, Songliao Basin, NE China," *Petroleum Exploration and Development*, vol. 36, no. 1, pp. 35-45, 2009.
- [42] J. X. Dai, "Identification of various genetic natural gases," *China Offshore Oil and Gas*, vol. 6, no. 1, pp. 11-19, 1992.
- [43] Z. Q. Guo and X. B. Wang, "Discussions on abiogenic gases in the Songliao Basin," *Science in China (Series B)*, vol. 24, no. 3, pp. 303-309, 1994.
- [44] Y. F. Yang, Q. Zhang, H. P. Huang et al., "Abiogenic natural gases and their accumulation model in Xujiaweizi area, Songliao Basin, Northeast China," *Earth Science Frontiers*, vol. 7, no. 4, pp. 523-533, 2000.
- [45] H. P. Huang, "Isotopic reversal in natural gas: an example of deep-strata gases from Xujiaweizi depression, Songliao Basin," *Earth Science-Journal of China University of Geosciences*, vol. 25, no. 6, pp. 617-623, 2000.
- [46] C. W. Huang, "The 10 great advances of petroleum science and technology of CNPC in 2010," *Petroleum Exploration and Development*, vol. 38, no. 2, p. 144, 2011.
- [47] Y. Shang and S. M. Shi, "Geochemical characteristics and genesis of the deep natural gas in Xijiaeweizi fault depression," *Petroleum Geology and Oilfield Development in Daqing*, vol. 34, no. 2, pp. 19-25, 2015.
- [48] Z. Q. Feng, "Volcanic rocks as prolific gas reservoir: a case study from the Qingshen gas field in the Songliao Basin, NE China," *Marine and Petroleum Geology*, vol. 25, no. 4-5, pp. 416-432, 2008.
- [49] G. P. Glasby, "Abiogenic origin of hydrocarbons: an historical overview," *Resource Geology*, vol. 56, no. 1, pp. 83-96, 2006.
- [50] A. Raje and B. H. Davis, "Fischer-Tropsch synthesis: mechanism studies using isotopes," in *Catalysis, Volume 12*, J. J. Spring, Ed., pp. 52-131, The Royal Society of Chemistry, 1996.
- [51] A. Steynberg and M. Dry, *Fischer-Tropsch Technology*, Elsevier, 2004.
- [52] G. P. Van der Laan, A. A. Beenacker, and C. M. Beenacker, "Kinetics and selectivity of the Fischer-Tropsch synthesis: a literature review," *Catalysis Reviews: Science and Engineering*, vol. 41, no. 3-4, pp. 255-318, 1999.
- [53] R. B. Anderson, *The Fischer-Tropsch Synthesis*, Academic Press, Orlando, 1984.
- [54] L. S. Glebov and G. A. Kliger, "Molecular-weight distribution of the Fischer-Tropsch synthesis products," *Russian Chemical Reviews*, vol. 63, pp. 192-202, 1994.
- [55] B. Shi and B. H. Davis, "Fischer-Tropsch synthesis: accounting for chain-length related phenomena," *Applied Catalysis A: General*, vol. 277, no. 1-2, pp. 61-69, 2004.
- [56] A. L. Lapidus and A. Y. Krylova, "On the mechanism of forming of liquid hydrocarbons on co-catalyst," *Russian chemical journal*, vol. 1, pp. 44-55, 2000.
- [57] T. M. McCollom and B. R. T. Simoneit, "Abiotic formation of hydrocarbons and oxygenated compounds during thermal decomposition of iron oxalate," *Origins of Life and Evolution of the Biosphere*, vol. 29, no. 2, pp. 167-186, 1999.
- [58] T. M. McCollom, "Experimental investigation of abiotic synthesis of organic compounds under hydrothermal conditions," *Book of Abstracts 2000; 219th ACS National Meeting*, 2000, San Francisco, CA, USA, March 26-30, 2000, 2000GEOC-028.
- [59] A. I. Rushdi and B. R. T. Simoneit, "Abiotic condensation synthesis of glyceride lipids and wax esters under simulated hydrothermal conditions," *Origins of Life and Evolution of Biospheres*, vol. 36, no. 2, pp. 93-108, 2006.

- [60] A. I. Rushdi and B. R. T. Simoneit, "Abiotic synthesis of organic compounds from carbon disulfide under hydrothermal conditions," *Astrobiology*, vol. 5, no. 6, pp. 749–769, 2005.
- [61] A. I. Rushdi and B. R. T. Simoneit, "Condensation reactions and formation of amides, esters, and nitriles under hydrothermal conditions," *Astrobiology*, vol. 4, no. 2, pp. 211–224, 2004.
- [62] A. I. Rushdi and B. R. T. Simoneit, "Lipid formation by aqueous Fischer-Tropsch-type synthesis over a temperature range of 100 to 400 degrees C," *Origins of Life and Evolution of the Biosphere*, vol. 31, no. 1/2, pp. 103–118, 2001.
- [63] J. S. Seewald, M. Y. Zolotov, and T. McCollom, "Experimental investigation of single carbon compounds under hydrothermal conditions," *Geochimica et Cosmochimica Acta*, vol. 70, no. 2, pp. 446–460, 2006.
- [64] M. Wang, Y. F. Sun, W. G. Wang, Y. Wang, and L. Shi, "Gas generation characteristics and resource potential of the deep source rock in Xujiaweizi fault depression, northern Songliao Basin," *Natural Gas Geoscience*, vol. 25, no. 7, pp. 1011–1018, 2014.
- [65] J. Li, W. Liu, and L. Song, "A study of hydrocarbon generation conditions of deep source rocks in Xujiaweizi fault depression of the Songliao Basin," *Natural Gas Industry*, vol. 26, pp. 21–24, 2006.
- [66] Q. Zhou, Z. Feng, and G. Men, "Present geotemperature and its suggestion to natural gas generation in Xujiaweizi fault-depression of the northern Songliao Basin," *Science in China Series D: Earth Sciences*, vol. 51, no. S1, pp. 207–220, 2008.
- [67] J. Xiao, H. Chen, S. Yang et al., "Gas charging of deep volcanic reservoirs in the northern Songliao Basin: evidence from fluid inclusions," *Acta Petroli Sinica*, vol. 32, pp. 968–975, 2011.
- [68] W. Tao, *Experiments on Natural Gas Generation, Oil Cracking and FTS under High Pressure: Experiments, Kinetics and a Case Study*, Guangzhou Institute of Geochemistry, Chinese Academy of Sciences, Guangzhou, China, 2008.
- [69] G. X. Hu, Z. Y. OuYang, X. B. Wang, and Q. B. Wen, "The Fischer-Tropsch reaction of carbon isotope fractionation under the conditions of the original solar nebula," *Science in China (Series D)*, vol. 27, no. 5, pp. 395–400, 1997.
- [70] F. W. Ji, H. Y. Zhou, and Q. H. Yang, "Abiogenic synthesis of butane and pentane from CO₂ and H₂ under hydrothermal conditions," *Geochemica*, vol. 36, no. 2, pp. 171–175, 2007.
- [71] Q. Fu, B. Sherwood Lollar, J. Horita, G. Lacrampe-Couloume, and W. E. Seyfried Jr, "Abiotic formation of hydrocarbons under hydrothermal conditions: constraints from chemical and isotope data," *Geochimica et Cosmochimica Acta*, vol. 71, no. 8, pp. 1982–1998, 2007.
- [72] Y. A. Taran, G. A. Kliger, and V. S. Sevastianov, "Carbon isotope effects in the open-system Fischer-Tropsch synthesis," *Geochimica et Cosmochimica Acta*, vol. 71, no. 18, pp. 4474–4487, 2007.
- [73] C. Zhang and Z. H. Duan, "A model for C-O-H fluid in the Earth's mantle," *Geochimica et Cosmochimica Acta*, vol. 73, no. 7, pp. 2089–2102, 2009.
- [74] B. Sherwood Lollar, T. D. Westgate, J. A. Ward, G. F. Slater, and G. Lacrampe-Couloume, "Abiogenic formation of alkanes in the Earth's crust as a minor source for global hydrocarbon reservoirs," *Nature*, vol. 416, no. 6880, pp. 522–524, 2002.
- [75] A. A. Giardini and C. A. Salotti, "Kinetics and relations in the calcite-hydrogen reaction and relations in the dolomite-hydrogen and siderite-hydrogen systems," *American Mineralogist*, vol. 54, pp. 1151–1172, 1969.
- [76] J. R. Holloway, "Graphite-CH₄-H₂O-CO₂ equilibria at low-grade metamorphic conditions," *Geology*, vol. 12, no. 8, pp. 455–458, 1984.
- [77] J. F. Kenney, V. A. Kutcherov, N. A. Bendeliani, and V. A. Alekseev, "The evolution of multicomponent systems at high pressures: VI. The thermodynamic stability of the hydrogen-carbon system: The genesis of hydrocarbons and the origin of petroleum," *Proceedings of the National Academy of Sciences*, vol. 99, no. 17, pp. 10976–10981, 2002.
- [78] M. E. Berndt, D. E. Allen, and W. E. J. Seyfried, "Reduction of CO₂ during serpentinization of olivine at 300 °C and 500 bar," *Geology*, vol. 24, no. 4, pp. 351–354, 1996.
- [79] J. L. Charlou, J. P. Donval, Y. Fouquet, P. Jean-Baptiste, and N. Holm, "Geochemistry of high H₂ and CH₄ vent fluids issuing from ultramafic rocks at the rainbow hydrothermal field (36°14'N, MAR)," *Chemical Geology*, vol. 191, no. 4, pp. 345–359, 2002.
- [80] J. L. Charlou and J. P. Donval, "Hydrothermal methane venting between 12°N and 26°N along the Mid-Atlantic Ridge," *Journal of Geophysical Research*, vol. 98, no. B6, pp. 9625–9642, 1993.
- [81] D. S. Kelley, J. A. Karson, D. K. Blackman et al., "An off-axis hydrothermal vent field near the Mid-Atlantic Ridge at 30°N," *Nature*, vol. 412, no. 6843, pp. 145–149, 2001.
- [82] T. M. McCollom and J. S. Seewald, "A reassessment of the potential for reduction of dissolved CO₂ to hydrocarbons during serpentinization of olivine," *Geochimica et Cosmochimica Acta*, vol. 65, no. 21, pp. 3769–3778, 2001.
- [83] D. A. Vanko and D. S. Stakes, "Fluids in oceanic layer 3: evidence from veined rocks, hole 735B, Southwest Indian Ridge," *Proceedings of the Ocean Drilling Program, Scientific Results*, vol. 118, pp. 181–215, 1991.
- [84] X. Wang, Z. Guo, J. Tuo et al., "Abiogenic hydrocarbons in commercial gases from the Songliao Basin," *Science in China (Series D)*, vol. 52, no. 2, pp. 213–226, 2009.
- [85] J. X. Dai, C. N. Zou, S. C. Zhang et al., "Identification the origin of inorganic and organic alkane," *China. Sci. China, Ser. D*, vol. 38, no. 11, pp. 1329–1341, 2008.

Research Article

The Petrogenesis of the Permian Podong Ultramafic Intrusion in the Tarim Craton, Western China: Constraints from C-He-Ne-Ar Isotopes

Mingjie Zhang¹, Pengyu Feng¹, Tong Li¹, Liwu Li², Juerong Fu¹, Peng Wang³,
Yuekun Wang¹, Zhongping Li², and Xiaodong Wang¹

¹Key Lab of Mineral Resources in Western China (Gansu), School of Earth Sciences, Lanzhou University, Lanzhou 730000, China

²Key Lab of Petroleum Resource, Gansu Province, Northwest Institute of Eco-Environment and Resources, CAS, Lanzhou 730000, China

³Sixth Geological Unit, Xinjiang Bureau of Geology and Mineral Exploration, Hami 839000, China

Correspondence should be addressed to Mingjie Zhang; mjzhang@lzu.edu.cn

Received 31 March 2019; Revised 26 June 2019; Accepted 10 July 2019; Published 22 August 2019

Academic Editor: Giovanni Martinelli

Copyright © 2019 Mingjie Zhang et al. This is an open access article distributed under the Creative Commons Attribution License, which permits unrestricted use, distribution, and reproduction in any medium, provided the original work is properly cited.

The Podong Permian ultramafic intrusion is only one ultramafic intrusion with massif Ni-Cu sulfide mineralization in the Pobei layered mafic-ultramafic complex, western China. It is obviously different in sulfide mineralization from the nearby coeval Poyi ultramafic intrusion with the largest disseminated Ni-Cu sulfide mineralization and mantle plume contribution (Zhang et al., 2017). The type and addition mechanism of the confirmed crustal contaminations and possible mantle plume involved in the intrusion formation require evidences from carbon and noble gas isotopic compositions. In the present study, we have measured C, He, Ne, and Ar isotopic compositions of volatiles from magmatic minerals in the Podong ultramafic intrusion. The results show that olivine, pyroxene, and plagioclase minerals in the Podong intrusion have variable $\delta^{13}\text{C}$ of CO_2 (-24.5‰ to -3.2‰). The CH_4 , C_2H_6 , C_3H_8 , and C_4H_{10} hydrocarbon gases show normal or partial reversal distribution patterns of carbon isotope with carbon number and light $\delta^{13}\text{C}_1$ value of CH_4 , indicating the hydrocarbon gases of biogenic origin. The $\delta^{13}\text{C}$ of CO_2 and CH_4 suggested the magmatic volatile of the mantle mixed with the volatiles of thermogenic and crustal origins. Carbon and noble gas isotopes indicated that the Podong intrusion could have a different petrogenesis from the Poyi ultramafic intrusion. Two types of contaminated crustal materials can be identified as crustal fluids from subducted altered oceanic crust (AOC) in the lithospheric mantle source and a part of the siliceous crust. The carbon isotopes for different minerals show that magma spent some time crystallizing in a magma chamber during which assimilation of crustal material occurred. Subduction-devolatilization of altered oceanic crust could be the best mechanism that transported large proportion of ASF (air-saturated fluid) and crustal components into the mantle source. The mantle plume existing beneath the Poyi intrusion could provide less contribution of real materials of silicate and fluid components.

1. Introduction

The Pobei Permian mafic-ultramafic complex is the largest layered complex in China and is composed mainly of more than 20 ultramafic intrusions hosting Ni-Cu sulfide mineralization, which intruded in an early-stage large gabbro intrusion [1–6]. These ultramafic intrusions were assumed to be formed by asthenosphere mantle upwelling induced by a mantle plume [1, 6–11] or lithosphere delamination-

induced basaltic magmatism in a convergent postcollision tectonic geodynamic setting [2, 12–14]. There is about 10 Ma difference of formation age between early-stage gabbro intrusion and lately ultramafic intrusions [3]; therefore, each ultramafic intrusion could be considered as an individual intrusive event.

The Podong ultramafic intrusion in the Pobei complex is only one ultramafic intrusion with massif Ni-Cu sulfide mineralization [3, 4]. The Podong intrusion is composed

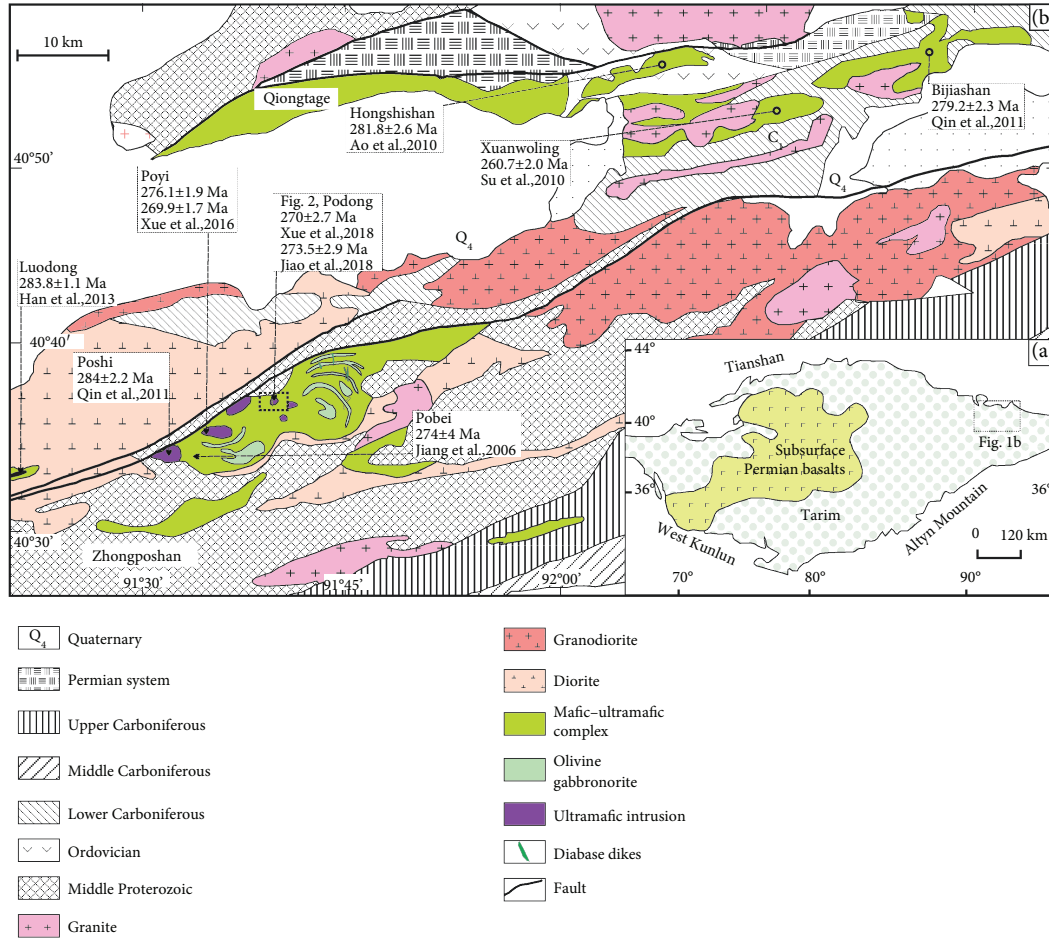


FIGURE 1: Tectonic (a) and geological sketch maps (b) of mafic-ultramafic complexes in the Beishan area, western China (after [7, 10]).

mainly of ilmenite, websterite, troctolite, gabbro, olivine gabbro-norite, and norite, whereas the nearby coeval Poyi (No. 1) ultramafic intrusion contains dunite, wehrlite, troctolite, olivine clinopyroxenite, and olivine gabbro [3, 4]. The Podong Ni-Cu mineralization occurs in gabbro-norite (\pm olivine) with high Ni grade, whereas the Poyi intrusion in the west end of the Pobei complex hosts disseminated sulfide deposit in troctolite and peridotite ultramafic rocks with low Ni grade [4]. The zircon U-Pb age of gabbro-norite in the Podong intrusion is 270 ± 2.7 Ma [3] or 273.5 ± 2.9 Ma [4].

The Podong ultramafic intrusion shows pronounced negative anomalies of Nb, Ta, Ti, Zr, and Hf high field strength elements. The external fluids and siliceous crustal assimilations may have triggered sulfide saturation in the mineralization of the Podong magma [3, 4]. The $\epsilon_{\text{Nd}}(t)$ (-0.61 – $+1.92$) and variable $(^{87}\text{Sr}/^{86}\text{Sr})_i$ (0.7055 – 0.7090) indicated that the Podong parental magma experienced 0–13 wt% contamination of the upper crust [3]. However, the 0–13 wt% upper crust suggested by Sr-Nd isotopes which cannot fully account for the negative Nb-Ta anomalies [3, 4]. Meanwhile, the sulfur isotopic compositions (0.82–2.02‰) cannot completely rule out the addition of external sulfur or fluids in the Podong intrusion [3].

On the other hand, the carbon and noble gas isotopic compositions revealed the information of mantle plume in

the Poyi ultramafic intrusion [10], but indicated the different petrogenesis of No. 4 and 10 ultramafic intrusions at the west end of the Pobei complex, which showed a mixture of different portion of lithospheric mantle, crust, and air [11]. Hence, the type of contaminated crustal materials and the contribution of the mantle plume in the formation of the Podong intrusion require constraints from C and He-Ne-Ar isotopic compositions. An integrated study of C and He-Ne-Ar isotopes of magmatic minerals in the Podong ultramafic intrusion has been carried out to constrain the origins of volatiles, to reveal the type and mechanism of the contaminated crustal material, and to provide insight into the petrogenesis of the Podong ultramafic intrusion.

2. Geological Background

The Podong ultramafic intrusion is located at the center of the Pobei mafic-ultramafic complex in the northeastern margin of the Tarim Craton, western China. The Pobei complex is associated temporally and spatially with the Cantoushan, Bijiashan, Hongshishan, Xuanwoling, and Zhongposhan mafic-ultramafic complexes in the Beishan Paleozoic rift (Figure 1). These coeval Paleozoic magmatisms were intruded extensively into the Proterozoic and Carboniferous strata and hosted the Ni-Cu-Fe mineralization [2, 5, 6, 15, 16].

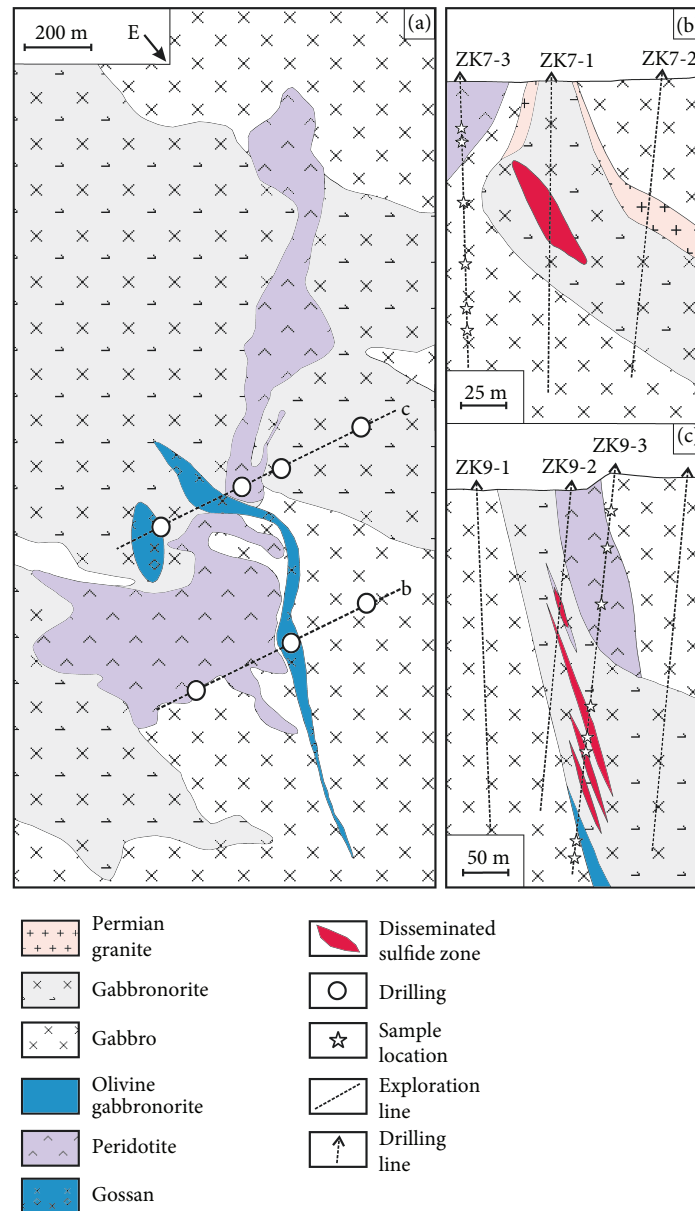


FIGURE 2: Geological sketch map (a) and vertical cross sections at exploration line 7 (b) and line 9 (c) of the Podong ultramafic intrusion, China (after [4]).

The Pobei mafic-ultramafic complex is ~36 km in length and ~8 km in width on the surface (Figure 1). The downward extension of the intrusion exceeds 2400 m [10]. It is predominantly composed of an early-stage huge gabbroic intrusion intruded by more than 20 small sulfide-mineralized ultramafic-troctolitic intrusions, including Poyi (No. 1), Posan (No. 3), Posi (No. 4), and Poshi (No. 10) ultramafic intrusions [2, 5, 13]. The contacts between the ultramafic-troctolite intrusions and the gabbroic intrusion show clear intrusive relations. Country rocks are Proterozoic schists, gneiss, and gneissic granite (Figure 1).

The ultramafic intrusions are commonly composed of dunite, peridotite, pyroxenite, troctolite, and gabbro with significant cumulate rhythmic layers of magmatic minerals [2, 5, 6, 13, 15, 17]. The contacts among the ultramafic

rocks are gradational. The formation ages of the ultramafic intrusions and the early-stage gabbro intrusion are significantly different (Figure 1). The zircon U-Pb isotope ages are 269.9 ± 1.7 Ma for the Poyi ultramafic intrusion [2], 275.8 ± 2.7 Ma for the Posan intrusion [9], and 284.0 ± 2.2 Ma for the Poshi intrusion [1]. The gabbro intrusion has a zircon U-Pb isotope age of 276.1 ± 1.9 Ma [2].

The Podong intrusion surface exposure is ~1400 m in length and 80–400 m in width, with a downward extension > 600 m (Figure 2) [3]. Immediate country rocks are Late Paleozoic gabbros (Figure 2). Many dolerite dykes are present in the south and east of the Podong intrusion and have a zircon U-Pb age of $\sim 280.5 \pm 2.0$ Ma [2]. Drilling confirmed that Podong Ni-Cu sulfide mineralization formed an economic sulfide deposit as steeply dipping net-texture

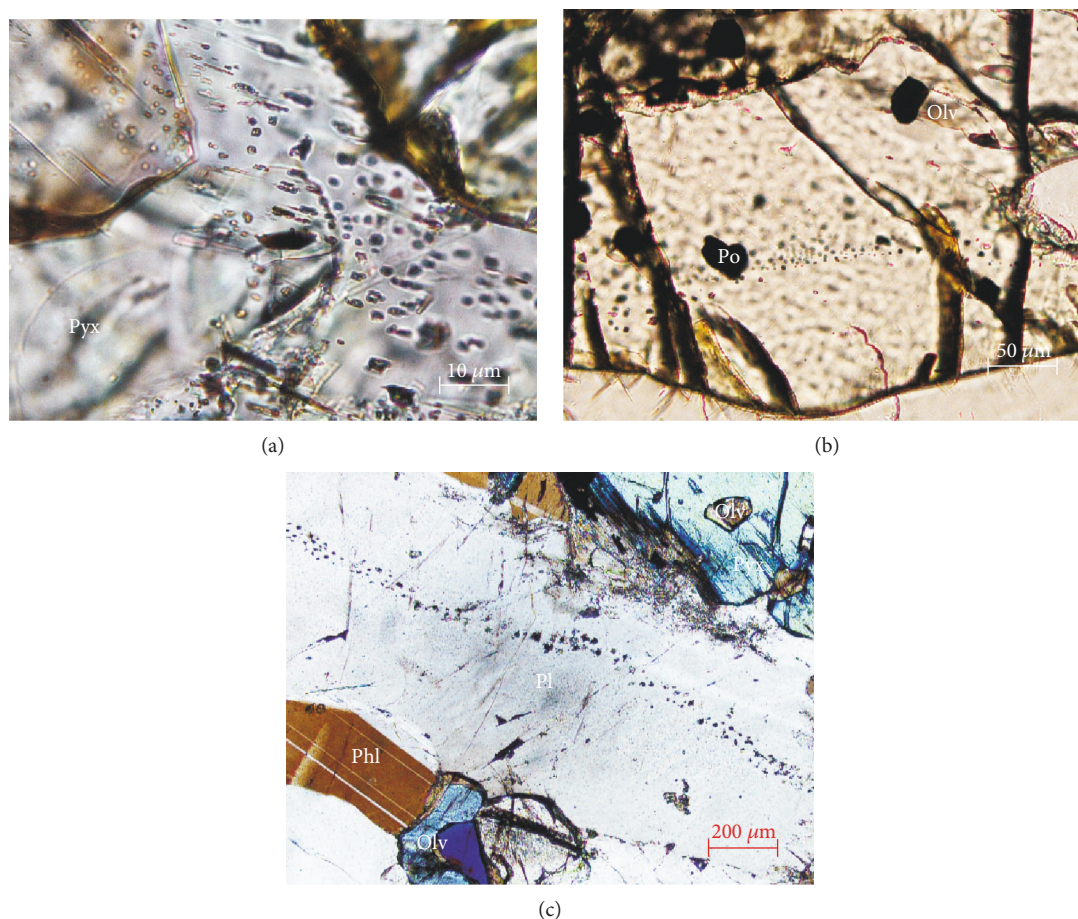


FIGURE 3: Microphotos of different types of fluid inclusions in the Podong ultramafic intrusion, China. (a) Primary fluid inclusions in pyroxene of sample PD73-1, plane polarized light (-); (b) primary fluid inclusions in olivine of sample PD73-2, plane polarized light (-); (c) secondary fluid inclusions in plagioclase of sample PD73-5, perpendicular polarized light (+). Olv = olivine; Pyx = pyroxene; Pl = plagioclase; Phl = phlogopite; Po = pyrrhotite.

sulfide lenses at lines 7 to 9; Ni-Cu sulfide mineralization is mostly associated with gabbro at the center of the intrusion. The sulfide minerals commonly interstitial in the silicate matrix are dominated by pyrrhotite with minor pentlandite and chalcopyrite [3, 4, 18].

3. Sampling and Analytical Methods

3.1. Samples. Twenty-three peridotite, pyroxenite, troctolite, olivine gabbro, and gabbro samples used in this study were sampled from three drill cores (ZK7-3, ZK9-3, and ZK11-3) at exploration lines 7, 9, and 11, respectively, in the Podong ultramafic intrusion. The locations of exploration lines with drilled holes are shown in Figure 2, and the representative exploration profiles and sample locations are shown in Figures 2(b) and 2(c). All the rock samples were cut into polished thin sections. The microscopic petrology is observed using both reflected- and transmitted-light microscopy.

The mineral compositions, texture, and other petrographical characteristics of the Podong ultramafic intrusion are reported in reference [3] and are similar to the Poyi intrusion [10]. Olivine, pyroxene, and plagioclase magmatic

minerals have different types of fluid inclusions and trapped the volatiles in different stages of magmatism (Figure 3). Partial alteration of olivine by serpentine plus secondary magnetite and clinopyroxene by tremolite are observed in the Podong ultramafic intrusion. Plagioclase is generally pristine, with a negligible alteration in the samples.

3.2. Sample Preparation. All the rock samples were observed using petrography microscopy, and the least altered samples were selected for mineral separation. The rock samples were cut into small pieces. The selected rock pieces without weathered surface, visible secondary veins were crushed and sieved 0.2–0.3 mm in diameter portions. The mineral separates were first of all selected by magnetic separation and followed by hand-picking using a binocular microscope.

The samples for carbon isotopic analysis were immersed in 0.3 M HCl for 24 h and then ultrasonically cleansed with analytical grade CH_2Cl_2 , which can remove possible secondary organic components, after which they were rinsed with distilled water until the pH value of the rinsing water reached about 7. The samples for noble gas isotopic analysis were washed with 5% HNO_3 in an ultrasonic bath to remove possible secondary radiogenic components [19].

The cleaned mineral separates were baked at 110°C prior to analysis [10, 20–22].

3.3. Analytical Methods

3.3.1. Carbon Isotope Analysis. Carbon isotopes of CO₂ and CH₄, C₂H₆, C₃H₈, and C₄H₁₀ hydrocarbon gases were analyzed by a GC-C-MS system using a stepwise heating extraction procedure. Carbon isotopes are expressed as $\delta^{13}\text{C} (\text{‰}) = ([^{13}\text{C}/^{12}\text{C}]_{\text{sample}}/[^{13}\text{C}/^{12}\text{C}]_{\text{PDB}} - 1) \times 10^3$ (where PDB (Pee Dee Belemnite) is the reference standard). A well-established online stepwise heating method was used for the extraction of volatiles from the magmatic mineral separates [21, 23, 24].

The gas extraction apparatus is composed of a U-shaped quartz tube, a cold trap, and an adsorption trap of molecular sieve; it is directly connected to a gas chromatography-combustion-mass spectrometry (GC-C-MS) system. The sample of ab. 1 g was loaded into the quartz tube and was degassed in helium carrier gas to remove potentially surface-adsorbed gases at 200°C for 4 h. The molecular sieve was activated at 400°C. The CO₂ and hydrocarbon gases were released for 1 h heating at each interval at 3 temperature intervals of 200–400°C, 400–700°C, and 700–1200°C based on volatile releasing patterns in the Pobei complex [10], and were adsorbed and collected using the molecular sieve tube with liquid nitrogen cooling. Then, the CO₂ and hydrocarbon gases were released and introduced into an Agilent 6890 GC-Delta Plus XP-MS system by helium carrier gas for carbon isotope analysis in the Key Lab of Petroleum Resources, CAS, Lanzhou, China. The extraction and analysis methods of volatiles were described in detail by [10, 21, 25]. The reported $\delta^{13}\text{C}$ (relative to V-PDB) values have a relative error less than 1.01‰.

3.3.2. He, Ne, and Ar Isotope Analysis. The noble gas isotopes from olivine and pyroxene separates were measured using an online vacuum heating Noblesse mass spectrometer system in the Key Lab of Petroleum Resources, CAS, Lanzhou, China. The sample of about 500 mg was wrapped using aluminum foil and was loaded into the Mo crucible of the sample chamber. The aluminum foil and Mo crucible were preheated for >24 h at 600°C and 1700°C, respectively. The noble gas extraction line and the sample were heated at 150°C for >24 h prior to analysis to remove atmospheric or possibly solar-implanted noble gases adsorbed in the samples.

The volatiles in the sample were extracted by one-step heating at 1200°C. The active gases were removed firstly by using a spongy titanium furnace at 800°C. H₂ was removed by Zr-Al getters at room temperature. The purified noble gases were adsorbed in a cryogenic trap at a temperature of 8 K for 20 min. Then, He, Ne, and Ar gases were released for isotope analysis at the cryogenic trap temperature of 15 K, 50 K, and 100 K, respectively. The volume of He, Ne, and Ar was determined for calibration of their concentration. The air of Lanzhou city collected from the top of Gaolan Mountain in Lanzhou city, China was used as an internal standard, which was measured before each sample. No

significant fluctuations were observed during sample analysis. Finally, the measured data were calculated after measuring the voltage ratio of relevant ions from both the standard sample and the sample obtained. The extraction and analysis methods of volatiles are described in detail by [10, 22, 26].

The effect of helium pressure on mass shift was examined and corrected. The mass interferences at $m/z = 22$ of (²⁰Ne)⁺ and (²²Ne)⁺ from (⁴⁰Ar)²⁺ and (¹²C¹⁶O₂)²⁺ were corrected using CO₂²⁺/CO₂⁺ = 0.004. The details of Ne and data correction procedures were described in detail in [22, 26, 27].

4. Results

4.1. The Carbon Isotopic Compositions. The carbon isotopic compositions of CO₂ and CH₄, C₂H₆, C₃H₈, and C₄H₁₀ hydrocarbon gases from the olivine (Olv), pyroxene (Pyx), and plagioclase (Pl) separates in the Podong ultramafic intrusion are listed in Table 1.

The Podong magmatic minerals have variable $\delta^{13}\text{C}$ values of CO₂ (−24.5‰ to −3.2‰). The $\delta^{13}\text{C}_{\text{CO}_2}$ range is similar to the Poyi ultramafic intrusion (−33.6–−2.2‰) in the Pobei complex, China [10], the coeval Zhubu ultramafic intrusion (−22.8–−7.1‰) in the Emeishan large igneous province (LIP) [28], and the coeval Noril'sk ultramafic intrusion (−25.3–−19.0‰) in Siberia LIP [20] which were related to mantle plume. $\delta^{13}\text{C}_{\text{CO}_2}$ values increase from olivine (−24.5–−4.5‰, av. −14.3‰), pyroxene (−22.9–−3.2‰, av. −11.05‰), to plagioclase (−17.2–−6.7‰, av. −11.7‰).

The carbon isotopes of hydrocarbon gases in the Podong intrusion vary in a large range. $\delta^{13}\text{C}_{\text{CH}_4}$ ranges from −42.6 to −18.4‰, $\delta^{13}\text{C}_{\text{C}_2\text{H}_6} = -34.0$ –−18.7‰, $\delta^{13}\text{C}_{\text{C}_3\text{H}_8} = -38.4$ –−7.0‰, and $\delta^{13}\text{C}_{\text{C}_4\text{H}_{10}} = -30.9$ –−22.5‰. The hydrocarbon gases in most of the samples show normal distribution patterns of carbon isotopes with carbon number (Figure 4(a)), and some samples show (partial) reversal distribution patterns (Figure 4(b)), implying different origins of hydrocarbon gases.

4.2. The He, Ne, and Ar Isotopic Compositions. The He, Ne, and Ar abundances and isotopic compositions of the mineral separates in the Podong ultramafic intrusion are listed in Table 2. ³He/⁴He ratios are reported as the R/Ra ratios (i.e., measured ³He/⁴He normalized to the atmospheric ratio, Ra = 1.39 × 10^{−6}). The analytical uncertainties for ³He/⁴He, ²⁰Ne/²²Ne, ²¹Ne/²²Ne, and ⁴⁰Ar/³⁶Ar ratios are listed as 1σ in Table 2.

The ⁴He abundances of olivine and pyroxene minerals in peridotite, pyroxenite, and gabbro in the Podong ultramafic intrusion range from 3.94 × 10^{−6} cm³ · STP/g to 51.81 × 10^{−6} cm³ · STP/g, av. 31.61 × 10^{−6} cm³ · STP/g. The average value of ⁴He abundances in pyroxene (30.73 × 10^{−6} cm³ · STP/g) is lower than that in olivine (av. 37.38 × 10^{−6} cm³ · STP/g). Podong samples show higher ⁴He abundance than the Jinchuan mafic-ultramafic intrusion (0.01–2.56 × 10^{−6} cm³ · STP/g) [22] and the Poyi ultramafic intrusion (0.03–1.09 × 10^{−6} cm³ · STP/g) [10],

TABLE 1: The carbon isotopic compositions (‰, V-PDB) of the mineral separates in the Podong mafic-ultramafic intrusion, China.

Sample no.	Rock	Mineral	T (°C)	$\delta^{13}\text{C}_{\text{CO}_2}$	$\delta^{13}\text{C}_{\text{CH}_4}$	$\delta^{13}\text{C}_{\text{C}_2\text{H}_6}$	$\delta^{13}\text{C}_{\text{C}_3\text{H}_8}$	$\delta^{13}\text{C}_{\text{C}_4\text{H}_{10}}$
PD73-2	Gabbro	Olv	200-400	-24.5	-26.4			
			400-700	-15.7	-31.8	-24.8	-23.2	-29.8
			700-1200	-11.3	-35.5	-23.7	-24.0	-30.9
PD73-3	Gabbro	Pyx	200-400	-10.5				
			400-700	-15.2	-34.7			
			700-1200	-6.3	-38.9			
PD73-4	Gabbro	Pyx	200-400	-18		-21.1	-20.5	
			400-700	-10.6	-20.3			
			700-1200	-5.4	-27.9	-27.9	-38.4	
PD73-5	Gabbro	Pl	200-400	-17.2	-29.8			
			400-700	-11.2	-29.0			
			700-1200	-6.7	-18.9	-26.8	-7.0	
PD73-7	Gabbro	Pyx	200-400	-20.4	-42.6			
			400-700	-10.4	-40.9			
			700-1200	-9.2	-32.4	-24.6	-27.8	-22.5
PD93-3	Gabbro	Pyx	200-400	-8.5	-31.5			
			400-700	-4.3	-22.6			
			700-1200	-6.8	-22.3	-18.7		
PD93-4	Gabbro	Olv	200-400	-22.7	-18.4			
			400-700	-7.1	-28.0	-21.4		
			700-1200	-4.5	-27.1	-23.5		
PD93-5	Gabbro	Pyx	200-400	-22.9				
			400-700	-20.3	-30.1	-29.7		
			700-1200	-16.0	-30.3	-20.8	-29.8	
PD93-7	Gabbro	Pyx	200-400	-14.8				
			400-700	-9.8	-35.8	-34	-28.7	
			700-1200	-10.7	-31.2	-22.5	-25.7	
PD93-8	Gabbro	Pyx	200-400	-17.9	-40.0			
			400-700	-6.1	-36.4	-26.7	-27.9	-24.5
			700-1200	-6.0	-31.5	-24.6		
PD93-9	Gabbro	Pyx	200-400	-8.4	-26.0	-19.6	-26.3	
			400-700	-3.6	-28.3	-23.6	-30.0	
			700-1200	-3.2	-27.2			

Olv: olivine; Pyx: pyroxene; Pl: plagioclase.

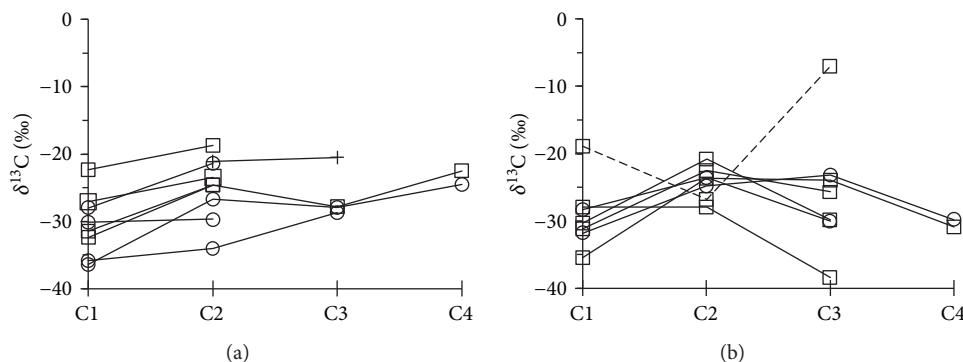
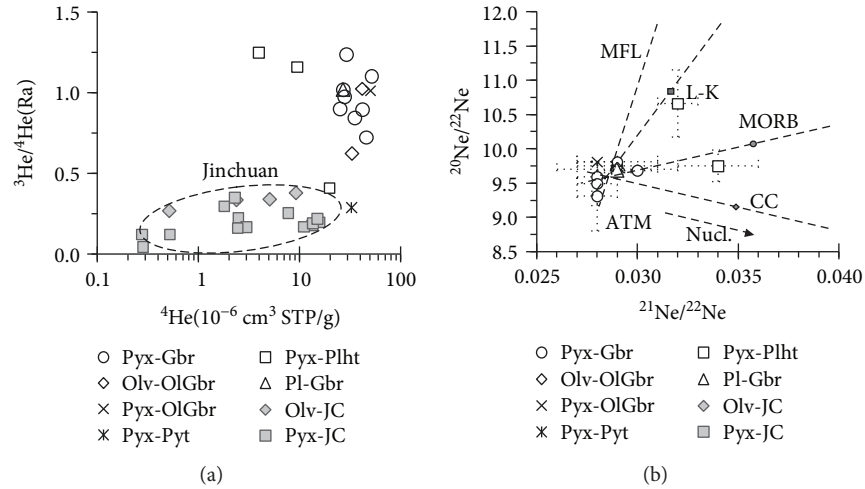


FIGURE 4: The normal (a) and partial reversal (b) carbon isotopic distribution patterns of CH_4 , C_2H_6 , C_3H_8 , and C_4H_{10} with carbon number in the Podong ultramafic intrusion, China.

TABLE 2: He, Ne, and Ar abundances and isotopic compositions of the magmatic mineral separates in the Podong mafic-ultramafic intrusion, western China.

No.	Rock	Mineral	Contents (10^{-6} cm ³ -STP/g)			³ He/ ⁴ He		²⁰ Ne/ ²² Ne		²¹ Ne/ ²² Ne		⁴⁰ Ar/ ³⁶ Ar	
			⁴ He	²⁰ Ne	⁴⁰ Ar	(Ra)	1 σ	R	1 σ	R	1 σ	R	1 σ
PD73-1	Pl lherzolite	Pyx	9.49	0.54	41.96	1.16	0.09	9.75	0.23	0.034	0.013	293.05	1.60
PD73-2	Olv gabbro	Olv	33.04	9.55	359.12	0.62	0.03	9.65	0.01	0.029	0.001	297.86	0.50
PD73-4	Gabbro	Pl	27.04	11.50	11.48	1.02	0.04	9.68	0.01	0.029	0.001	126.48	0.52
PD73-5	Gabbro	Pyx	25.06	18.95	682.78	0.90	0.05	9.59	0.21	0.028	0.001	297.19	0.43
PD73-6	Gabbro	Pyx	45.76	3.43	4.15	0.72	0.02	9.75	0.01	0.029	0.002	177.03	7.30
PD73-7	Gabbro	Pyx	29.05	4.60	96.68	1.24	0.03	9.49	0.32	0.028	0.001	295.19	0.78
PD93-1	Pl lherzolite	Pyx	19.75	0.19	22.34	0.41	0.04			0.031	0.001	395.2	1.10
PD93-2	Pl lherzolite	Pyx	3.94	0.17	15.25	1.25	0.15	10.66	0.49	0.032	0.001	398.11	1.50
PD93-3	Gabbro	Pyx	51.81	33.60	68.55	1.10	0.03	9.81	0.01	0.029	0.002	291.92	1.50
PD93-4	Olv gabbro	Olv	41.72	21.26	744.56	1.03	0.04	9.70	0.01	0.029	0.003	294.92	0.40
PD93-7	Olv gabbro	Pyx	50.24	14.40	490.15	1.01	0.04	9.81	0.01	0.028	0.001	301.11	0.52
PD93-6	Gabbro	Pyx	35.07	11.92	451.08	0.84	0.04	9.68	0.01	0.030	0.001	296.23	0.51
PD93-8	Gabbro	Pyx	41.69	1.17	154.42	0.90	0.03			0.023	0.004	296.15	0.73
PD93-9	Gabbro	Pyx	27.83	4.83	185.88	0.98	0.03	9.31	0.51	0.028	0.001	304.69	0.71
PD113-1	Pyroxenite	Pyx	32.70	0.23	18.24	0.29	0.02			0.031	0.001	285.29	9.69

FIGURE 5: Plots of ³He/⁴He versus ⁴He contents (a) and ²⁰Ne/²²Ne versus ²¹Ne/²²Ne (b) in the Podong ultramafic intrusion, China. Olv: olivine; Pyx: pyroxene; Gbr: gabbro; OlGbr: olive gabbro; Pyt: pyroxenite; Plht: plagioclase lherzolite; ATM: atmosphere [29, 39]; MFL: the mass fractionation line [29, 39]; CC: continental crust [29]; Nucl.: nucleogenic; L-K: Loihi- Kilauea line [26]; MORB: mid-ocean ridge basalts [58].

China (Figure 5(a)). The Jinchuan mafic-ultramafic intrusion in western China hosts the third largest Ni-Cu sulfide deposit in the world and is of a much older formation age (8.31 Ma) [28] than the Podong intrusion. It should have more radiogenic ⁴He* ingrowths produced by U and Th decay after crystallization.

The ³He/⁴He ratios of olivine and pyroxene minerals in the Podong ultramafic intrusion range from 0.29 to 1.25 Ra, av. 0.90 Ra. Olivine in the Podong intrusion shows lower ³He/⁴He ratios (0.60-1.03 Ra, av. 0.82 Ra) than pyroxene (0.29-1.25 Ra, av. 0.92 Ra). The ³He/⁴He ratios of Podong samples are higher than the value of continental crust [29, 30], lower than the

values of the subcontinental lithospheric mantle (SCLM, 6.1 Ra) [31–33], arc-related volcanic fluids (5.37 ± 1.87 Ra) [34], typical MORB (8 ± 1 Ra) [35], and OIB (~8-50 Ra) [30, 36, 37]. Podong samples show lower ³He/⁴He ratios than the nearby coeval Poyi intrusion (1.13-6.15 Ra) [10] and coeval mafic-ultramafic intrusions in the Emeishan LIP (0.078-4.34 Ra, av. 0.78 Ra) [38] but have higher ³He/⁴He ratios than the Jinchuan mafic-ultramafic intrusion, China [22] (Figure 5(a)) with more radiogenic ⁴He* ingrowths.

The ²⁰Ne abundances of the Podong intrusion range from 0.17 to 33.60×10^{-6} cm³ · STP/g with a mean of 9.09×10^{-6} cm³ · STP/g. The ²⁰Ne/²²Ne ratios in the

Podong intrusion vary from 9.31 to 10.66, and the $^{21}\text{Ne}/^{22}\text{Ne}$ ratios range from 0.027 to 0.035 (Figure 5(b)). The $^{20}\text{Ne}/^{22}\text{Ne}$ ratios are lower than the mantle (12.5), higher than the atmospheric value (9.8) [29, 39, 40]. The $^{21}\text{Ne}/^{22}\text{Ne}$ ratios are within the ranges of the atmosphere (0.029) and the solar value (0.033) and are lower than the crust (0.47) and the upper mantle (0.074) [39–43]. $^{20}\text{Ne}/^{22}\text{Ne}$ and $^{21}\text{Ne}/^{22}\text{Ne}$ are plotted around Air and show a trend to the L-K line (Figure 5(b)).

The ^{40}Ar abundances of the Podong intrusion range from 4.15 to $744.56 \times 10^{-6} \text{ cm}^3 \cdot \text{STP/g}$, which is much higher than the Jinchuan intrusion (0.04 – $21.70 \times 10^{-6} \text{ cm}^3 \cdot \text{STP/g}$) [22] and the Poyi intrusion (0.14 – $0.50 \times 10^{-6} \text{ cm}^3 \cdot \text{STP/g}$) [10]. The $^{40}\text{Ar}/^{36}\text{Ar}$ ratios in the Podong intrusion vary from 285.29 to 398.11, which are close to the atmosphere (295.5) and lower than the crust (1650–170000) and the mantle (295.5–8000) [36, 42, 44–46].

5. Discussion

5.1. The Origins of Magmatic Volatiles. The volatiles had occurred in the Poyi and Podong intrusions (Figure 3) and had played a key role in the processes of triggering sulfide saturation and mineralization [3, 4, 10, 11]. The CO_2 and CH_4 volatiles and noble gases released from the Podong samples could be derived from three potential sources: (1) primary volatiles in the Podong magmatism, including mantle-derived volatiles from partial melting of mantle source and contaminated crustal volatiles from subducted plate or country rocks, (2) *in situ* radiogenic noble gas ingrowths produced by U, Th, and K decay after mineral crystallization, and (3) secondary volatiles added by subsequent alteration or regional metamorphism and contaminated air and cosmogenic noble gases. The third source of volatiles absorbed on sample surface is likely negligible in the Podong samples due to fresh core samples with less alteration or metamorphism, as well as sample pretreatment before analysis [22, 41, 47]. Therefore, volatiles released from the Podong samples could be derived from magmatism and radiogenic noble gas ingrowths and can trace the origins of the volatiles.

The volatiles of different origins exhibit markedly different C, He, Ne, and Ar isotopic compositions, which can be used to reveal their sources [10, 21, 22, 28, 37, 48]. The $^3\text{He}/^4\text{He}$ and $^{40}\text{Ar}/^{36}\text{Ar}$ ratios in the Podong intrusion are mainly plotted around the atmosphere (ATM) with a trend toward continental crust and old oceanic crust end-members [22, 29, 39, 49] (crust, Figure 6). The $^{20}\text{Ne}/^{22}\text{Ne}$ and $^{21}\text{Ne}/^{22}\text{Ne}$ ratios of most Podong samples were also plotted around the ATM and show a trend to the L-K line and MORB (i.e., upper mantle, DMM) (Figure 5(b)) [27, 29, 50].

Low $^3\text{He}/^4\text{He}$ ratios of Podong samples could be interpreted as *in situ* radiogenic ^4He ingrowths, crust and air-saturated fluid additions (Figures 5(a) and 6), because mantle-derived He signatures are often diluted by the addition of *in situ* radiogenic ^4He [43] and/or crustal He [29, 30]. The radiogenic ingrowths produced by U, Th, and K decay after crystallization can be deduced by calculation

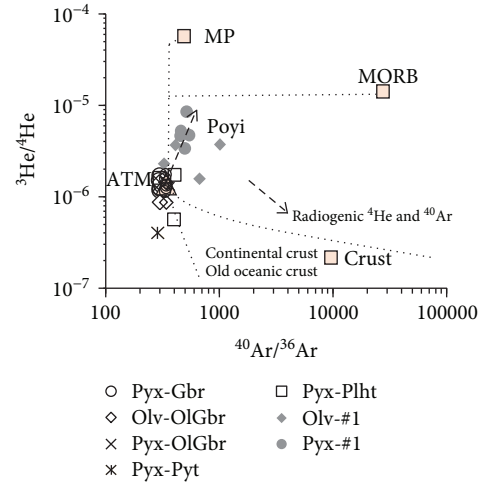


FIGURE 6: Plot of $^{40}\text{Ar}/^{36}\text{Ar}$ versus $^3\text{He}/^4\text{He}$ ratios in the Podong intrusion, China (after [49]). ATM: atmosphere [29, 39]; Crust: continental crust; MORB: depleted mantle for MORB; MP: mantle plume [34, 35]. Data sources: the Poyi ultramafic intrusion, China (#1) [10].

or be identified by the relationship between isotopic ratios and contents of He and Ar.

The amounts of radiogenic $^4\text{He}^*$ contents in the Podong intrusion can be calculated using Graham et al.'s (1987) equation:

$$^4\text{He}^* = 2.80 \times 10^{-8} (4.35 + \text{Th}/\text{U}) [\text{U}] \cdot t (\text{cm}^3 \cdot \text{STP/g}), \quad (1)$$

where t is the formation time in Myr, $[\text{U}]$ is the uranium concentration in ppm, and Th/U is the atomic ratio of Th and U. Using average contents of whole rock Th (0.15, 0.24, and 0.11 ppm) and U (0.04, 0.08, and 0.06 ppm) for lherzolite, pyroxenite, and gabbro, respectively [3, 4], and the crystallization age of the gabbro (270 Ma) in the Podong intrusion [4], the estimated radiogenic $^4\text{He}^*$ contents are 2.45, 4.45, and $2.80 \times 10^{-6} \text{ cm}^3 \cdot \text{STP/g}$ for lherzolite, pyroxenite and gabbro, respectively.

The whole rock K contents (0.07, 0.08, and 0.14 wt%) for lherzolite, pyroxenite and gabbro [3, 4] were used to estimate the radiogenic $^{40}\text{Ar}^*$ contents as 0.11, 0.13 and $0.22 \times 10^{-6} \text{ cm}^3 \cdot \text{STP/g}$ in lherzolite, Pyroxenite and Gabbro, respectively.

The estimated radiogenic $^4\text{He}^*$ and $^{40}\text{Ar}^*$ contents in the Podong ultramafic intrusion range from 2.45 to $4.45 \times 10^{-6} \text{ cm}^3 \cdot \text{STP/g}$ and from 0.11 to $0.23 \times 10^{-6} \text{ cm}^3 \cdot \text{STP/g}$, respectively, and are much lower than the measured values (Table 2). There is no obvious correlation between $^3\text{He}/^4\text{He}$ and ^4He contents, which can rule out significant radiogenic $^4\text{He}^*$ ingrowths in the Podong samples (Figure 5(a)). The obvious correlation between $^{40}\text{Ar}/^{36}\text{Ar}$ ratios and ^{40}Ar contents indicated a certain amount of radiogenic $^{40}\text{Ar}^*$ ingrowths (Figures 7(a) and 7(b)). $^3\text{He}/^4\text{He}$ and $^{40}\text{Ar}/^{36}\text{Ar}$ ratios after deducting radiogenic $^4\text{He}^*$ and $^{40}\text{Ar}^*$ contents show similar ranges to measured values and indicate a large proportion of air and crust origins (Figure 6).

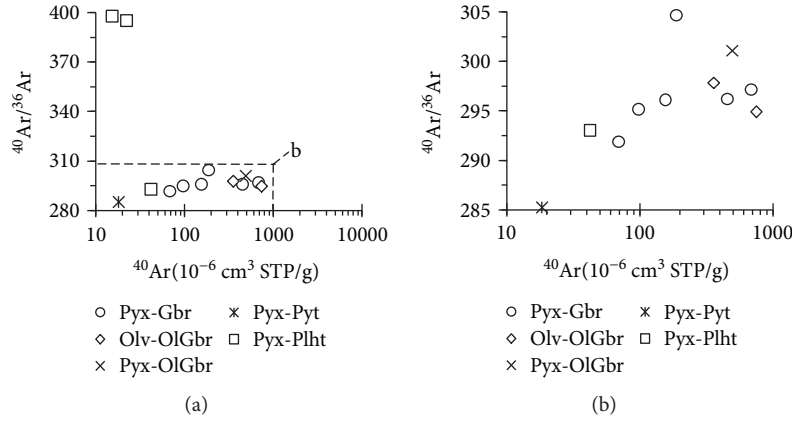


FIGURE 7: Plots of $^{40}\text{Ar}/^{36}\text{Ar}$ versus ^{40}Ar contents (a) and partial enlarged (b) in the Podong intrusion, China.

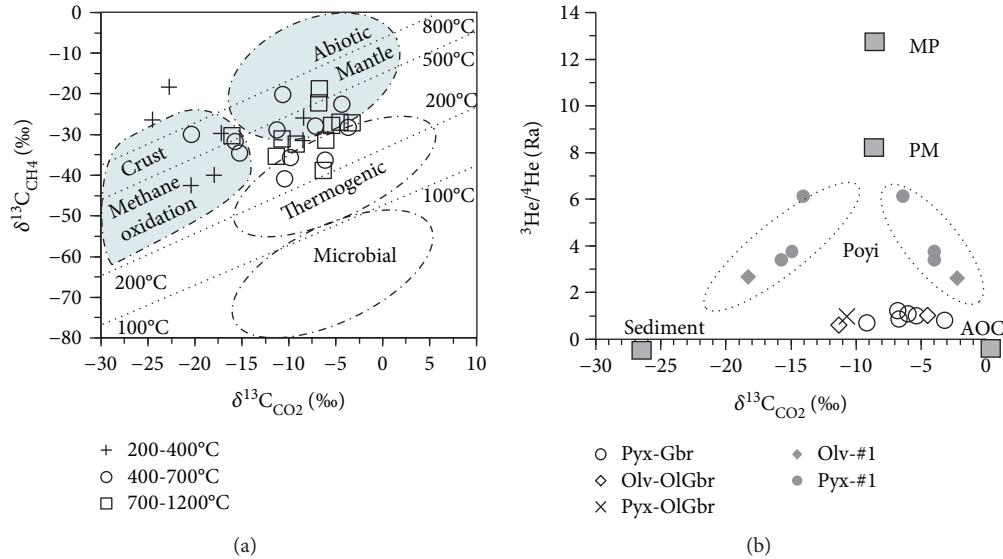


FIGURE 8: The plots of $\delta^{13}\text{C}_{\text{CO}_2}$ (‰, v-PDB) vs. $\delta^{13}\text{C}_{\text{CH}_4}$ (‰, v-PDB) (a, [52]) and the $^3\text{He}/^4\text{He}$ ratios (b, [10]) in the Podong ultramafic intrusion, China. Thermogenic: thermogenic origins [52]; Sediment: sedimentary organic matter [63]; AOC: altered oceanic crust [64]; MP: mantle plume [34]; PM: primitive mantle [34, 40].

The CO_2 and hydrocarbon gases from different origins show distinct carbon isotopic compositions and distribution patterns, which can be used to constrain various terrestrial reservoirs [10, 21, 22, 37, 48, 51]. The CO_2 and CH_4 released at 200-400°C were mainly released from secondary fluid inclusions and cracked primary fluid inclusions (Figure 3(b)), since the atmospheric component adsorbed in the samples is generally degassed at low temperature during step heating [49]. $\delta^{13}\text{C}_{\text{CO}_2}$ and $\delta^{13}\text{C}_{\text{CH}_4}$ values at 200-400°C are plotted into the range associated with methane oxidation and crustal origins (Figure 8(a)) and proved the origin of secondary processes, i.e., alteration.

The CO_2 and hydrocarbon gases released at 400-700°C and 700-1200°C temperature intervals from the Podong samples were mainly released from the fluid inclusions trapped during the magmatic process (Figure 3(a)). $\delta^{13}\text{C}_{\text{CO}_2}$

and $\delta^{13}\text{C}_{\text{CH}_4}$ are plotted into the ranges of the mantle, thermogenic, and crust-methane oxidation origins (Figure 8(a)) [10, 49, 52], indicating that the Podong volatiles originated from the mantle (i.e., abiogenic origin) [53, 54] and were mixed with thermogenic and crustal components. The mantle origin of volatiles is supported by (partial) reversal carbon isotopic distribution pattern of the hydrocarbon gases (Figure 4(b)), i.e., abiogenic hydrocarbon gases. It is also supported by sulfur isotopes of sulfide separates (0.82-2.02‰) [3], similar to typical mantle values ($0 \pm 2\%$). The thermogenic origin refers to the gases formed by thermal decomposition of biogenic organic matter under high geological temperature and pressure conditions and implies a sedimentary source [48]. The crust and thermogenic origins are supported by a normal carbon isotopic distribution pattern (Figure 4(a)).

The C, He, and Ar isotopes depict a mixture of different end-members for the Podong mafic-ultramafic rocks. The proportions of each end-member can be estimated by mass balance calculations of He and Ar isotopic mixing models. The air-saturated fluid (ASF) has low $^3\text{He}/^4\text{He}$ (1 Ra) and $^{40}\text{Ar}/^{36}\text{Ar}$ (298.6) [29, 55]; recycled oceanic crust has low $^3\text{He}/^4\text{He}$ (0.005 Ra) [30] and $^{40}\text{Ar}/^{36}\text{Ar}$ (350) [56]. The upper mantle (UM) or subcontinental lithospheric mantle (SCLM) has high $^3\text{He}/^4\text{He}$ (6.1 Ra) [31–33] and $^{40}\text{Ar}/^{36}\text{Ar}$ (2000) ratios [31]. The SCLM and crust are considered as the only two end-members of the He isotopic mixing model to calculate the proportions of SCLM and crust components due to very low He concentration and the shortest atmospheric residence time (1 to 10 million years) in the atmosphere [22]. Calculation shows 5–26%, av. 18% for SCLM, av. 10% for altered oceanic crust, and av. 72% for ASF, i.e., ATM, when radiogenic $^4\text{He}^*$ has been corrected from silicate mineral separates. The most ATM component could be volatiles from ASF.

5.2. The Additions of Air and Crustal Volatiles. The carbon and noble gas isotopic compositions indicated that a large proportion of air and crustal components had been mixed in the Podong mantle-derived magma (Figures 4(b) and 5(a)). The low $^3\text{He}/^4\text{He}$ ratios and calculated contents of radiogenic $^4\text{He}^*$ imply a large proportion of crustal origin in the Podong intrusion, which was supported by pronounced negative Nb-Ta anomalies and whole-rock Sr-Nd isotopes [4]. Large proportions of air are suggested by low $^{40}\text{Ar}/^{36}\text{Ar}$ and $^{21}\text{Ne}/^{22}\text{Ne}$ ratios in the Podong samples.

The type of assimilated crustal materials in the Podong intrusion was inferred as siliceous materials of the upper crust, pre-Permian sedimentary rocks in region [3], or crustal fluid [4]. The crust siliceous materials contaminated in the Podong magma can not only result in low $^3\text{He}/^4\text{He}$ ratios but also cause the rising of both $^{40}\text{Ar}/^{36}\text{Ar}$ and $^{21}\text{Ne}/^{22}\text{Ne}$ ratios. Meanwhile, a large proportion of siliceous materials (at least 0–13 wt% [3]) should cause a significant increase in the SiO_2 content of the magma system, i.e., more felsic rocks. All of those are not observed in the Podong intrusion (Figure 6). Therefore, large proportions of contaminated crust materials could be fluids, but siliceous materials, as shown above in the calculations of He and Ar isotopic mixing models.

The siliceous and fluids are two types of crustal materials that could exist in the Podong magma. Xue et al. argued that 0–13 wt% crustal contamination suggested by Sr-Nd isotopes in the Podong parental magma cannot fully account for the observed negative Nb-Ta anomalies in the rocks [3], which implied more crustal materials related to negative Nb-Ta anomalies. The fluids associated with the subducted plate could be the best candidate without siliceous materials.

The $\delta^{13}\text{C}_{\text{CO}_2}$ vs. $\delta^{13}\text{C}_{\text{CH}_4}$ plotted the Podong samples into ranges of thermogenic, crust-methane oxidation, and mantle (Figure 8(a)). The normal $\delta^{13}\text{C}$ distribution pattern from CH_4 to C_4H_{10} observed in most Podong samples suggests that hydrocarbon gases should be biogenic organic matters,

i.e., contaminated crustal components in Podong magma could derive from sedimentary organic matters (Figure 4(a)), including sedimentary organic matters from country rocks of magma chamber or/and subducted plate in the magma source. The $\delta^{13}\text{C}_{\text{CO}_2}$ values increase from olivine, pyroxene, to plagioclase and constrain that crustal materials with heavy $\delta^{13}\text{C}$ were added into magma during crystallization in the magma chamber. Therefore, assimilation of crustal material should occur during crystallizing in the magma chamber.

A large proportion of atmosphere component in the Podong intrusion is suggested by Ne and Ar isotopes (Figures 5(b) and 7(b)). $^{20}\text{Ne}/^{22}\text{Ne}$ and $^{21}\text{Ne}/^{22}\text{Ne}$ ratios in the Podong intrusion are mainly plotted around ATM (Figure 5(b)); $^{40}\text{Ar}/^{36}\text{Ar}$ vs. $^3\text{He}/^4\text{He}$ diagram also indicated a large proportion of air in the Podong magma (Figures 5(a), 7(a), and 7(b)). The $^{40}\text{Ar}/^{36}\text{Ar}$ and $^{21}\text{Ne}/^{22}\text{Ne}$ ratios in the Podong intrusion are very low and could be related to the incorporation of atmospheric components [57] or recycled oceanic crust in the source materials [58], although the radiogenic $^{40}\text{Ar}^*$ ingrowths were suggested by calculation and the relationship of $^{40}\text{Ar}/^{36}\text{Ar}$ versus ^{40}Ar content (Figure 7(a)). The $\delta^{13}\text{C}_{\text{CO}_2}$ and $^3\text{He}/^4\text{He}$ ratios of the Podong ultramafic intrusion plotted a trend of the altered oceanic crust (AOC, Figure 8(b)), so a large proportion of atmosphere component could be related to the ASF devolatilization of recycled oceanic crust in the magma source.

5.3. The Petrogenesis and Dynamic Settings of Intrusion. Carbon and noble gas isotopes indicate that the Podong intrusion could have a different petrogenesis from the Poyi ultramafic intrusion (Figures 6 and 8(b)). C-He-Ar and Sr-Nd isotopes indicate that the Podong and Poyi ultramafic intrusions did not share the same mantle source [3]. It is supported by the significant difference of Sr-Nd isotope compositions between the Podong and Poyi coeval mafic-ultramafic intrusions [3]. The Podong intrusion shows lower calculated $\epsilon\text{Nd}(t)$ values and higher initial $(^{87}\text{Sr}/^{86}\text{Sr})_i$ ratios than the coeval Poyi mafic-ultramafic intrusion (see Figure 10a in reference [3]). The Podong ultramafic intrusion could have a magma source of lithospheric mantle, which was metasomatized by slab-derived fluids and/or subducted sediment-derived melt during the previous subduction processes [3]. The Podong magma should be formed by the partial melting of metasomatized lithospheric mantle material with higher $(^{87}\text{Sr}/^{86}\text{Sr})_i$ and lower $\epsilon\text{Nd}(t)$ than Poyi intrusion and was contaminated by the crustal components in the magma chamber.

The $\delta^{13}\text{C}_{\text{CO}_2}$, $^3\text{He}/^4\text{He}$, and $^{40}\text{Ar}/^{36}\text{Ar}$ ratios of the Podong ultramafic intrusion are plotted around the air (ATM) with a trend to the altered oceanic crust (AOC, Figures 6 and 8(b)) and are different from the Poyi ultramafic intrusion. The Poyi intrusion showed a trend to mantle plume with high $^3\text{He}/^4\text{He}$ and $^{40}\text{Ar}/^{36}\text{Ar}$ ratios [10] (Figure 8(b)). Mantle plume has a $^3\text{He}/^4\text{He}$ value of ~ 12.7 Ra [36] and $^{40}\text{Ar}/^{36}\text{Ar}$ of 1200 [50]. The high $^3\text{He}/^4\text{He}$ ratios of 8–50 Ra observed in many mantle

plumes are from an ancient reservoir created within the first 100 Myr of solar system histories [36, 59, 60]. The noble gas isotopes had not completely homogenized in the mantle due to low recycling efficiency in the mantle compared to the lithophile elements [59]. The primordial noble gases that supply mantle plumes are not distributed throughout the whole lower mantle or are localized in a region of the deep mantle [59]. The mantle plume existing beneath the Poyi intrusion could provide less contribution of real materials (e.g., of silicate and fluid components) in the Podong magma because the associated Podong mafic dykes show similar Sr-Nd isotope ranges to the coeval Poyi mafic-ultramafic intrusion [3], i.e., Podong magmatism could be a little older (270 ± 2.7 Ma [3] or 273.5 ± 2.9 Ma [4]) than the Poyi magma (269.9 ± 1.7 Ma [2]) associated mantle plume.

The ATM and crustal components added in the Podong magma could be derived from either subducted sedimentary organic matter in the mantle source or contaminations from country rocks in magma chambers or rising conduit. The subduction of the oceanic crust can effectively transport air and crust components into the mantle [7, 40, 50] because the recycled oceanic crust has low He contents, extremely low $^3\text{He}/^4\text{He}$ (<0.1 Ra) [61], and relatively low $^{40}\text{Ar}/^{36}\text{Ar}$ (350) [46]; meanwhile, subducted oceanic crust has variable $\delta^{13}\text{C}_{\text{CO}_2}$ values ranging from -26‰ for type I organic-rich sediments of altered ocean crust (AOC) to 0‰ for marine carbonate [10, 62, 63].

The correlations between $^3\text{He}/^4\text{He}$ ratio vs. both $^{40}\text{Ar}/^{36}\text{Ar}$ and $\delta^{13}\text{C}_{\text{CO}_2}$ indicated the contribution from altered oceanic crust (AOC, Figures 6 and 8) in the Podong intrusion [64, 65]. $\delta^{13}\text{C}_2 > \delta^{13}\text{C}_3$ in most samples demonstrate type I organic materials from oceanic sedimentary [48]. The $\delta^{13}\text{C}_{\text{CO}_2}$ and $\delta^{13}\text{C}_{\text{CH}_4}$ variations in the Podong volatiles are suggestive of methane oxidative activity (Figure 8(a)), which provides further evidence of a contribution from altered oceanic crust [10]. All the evidences make the subducted altered ocean crust (AOC) as probable end-member to explain the C-He-Ne-Ar isotopic compositions of the Podong samples (Figure 8(b)). This is consistent with a subduction-modified mantle source suggested by LILE rich and Nb and Ta depletion [4, 13] because subduction-related magma is commonly characterized by pronounced negative Nb-Ta anomalies.

The noble gases are stored in sedimentary organic matter with air-saturated fluid (ASF) and are highly soluble in hydrous minerals such as amphibole and phlogopite [44]. The fluid-related components from the altered oceanic crust with low K, U, and Th contents could be the favorite candidate for added air and crustal components, which were supported by contributions from water or other volatile phases in the Podong intrusion [3, 4]. The water and other fluids in the parental magma were indicated by common occurrence of hornblende and phlogopite in the intrusion (Figure 3(c)) [3]. Enhanced recycling of subducted altered oceanic components to the mantle source region can account for the relatively low ratios of He, Ne, and Ar isotopes.

6. Conclusions

The C and He-Ne-Ar isotopic data of the Podong ultramafic intrusion provide the evidence for air and crustal origins as well as petrogenesis.

- (1) Most of the Podong magmatic minerals show normal carbon isotopic distribution patterns of CH_4 , C_2H_6 , C_3H_8 , and C_4H_{10} that indicated hydrocarbon gases of sedimentary origin. The variable $\delta^{13}\text{C}_{\text{CO}_2}$ and light $\delta^{13}\text{C}_{\text{CH}_4}$ suggested that the mantle-derived magmatic volatiles were mixed with thermogenic and crustal components
- (2) Low $^3\text{He}/^4\text{He}$, $^{21}\text{Ne}/^{22}\text{Ne}$, and $^{40}\text{Ar}/^{36}\text{Ar}$ ratios indicated a large proportion of air and crustal components mixed in the Podong intrusion. Two types of contaminated crustal materials can be identified as crustal fluids from the altered oceanic crust and siliceous crust materials. The crustal materials of country rock were assimilated during magma crystallizing in the chamber
- (3) Carbon and noble gas isotopes indicated that the Podong intrusion could have a different petrogenesis from the nearby coeval Poyi ultramafic intrusion. Subducted oceanic plate added air and crustal fluids released from altered oceanic crust with a large proportion of ASF into the magma SCLM source. The mantle plume beneath the Poyi intrusion could contribute less real material of silicate and fluid components

Data Availability

The manuscript is a self-contained data article; the entire data used to support the findings of this study are included within the article. If any additional information is required, this is available from the corresponding author upon request to mjzhang@lzu.edu.cn.

Additional Points

Highlight. The Podong ultramafic intrusion hosts the only massif Ni-Cu sulfide mineralization in the Pobei layered mafic-ultramafic complex, China, and had different petrogenesis with fewer mantle plume contributions from the nearby coeval the Poyi intrusion related mantle plume (Zhang et al., Chem. Geol., 2017).

Conflicts of Interest

The authors declare that there are no conflicts of interest regarding the publication of this paper.

Acknowledgments

This study was financially supported by NSF of China (41872075, 41572136, 41502143, 41473062, and 41372095),

STEP program (Grant no. 2019QZKK0704), Gansu Key Lab of Petrol. Res. (SZDKFJJ20170603), and DPHEC (20120211110023). We thank Gang Deng, Jiangwei Zhang, Zhaowei Zhang, Qingyan Tang, Jianping Li, Zhe Song, Chunhui Cao and Li Du for their assistance in fieldwork, sampling, and experimental works.

References

- [1] K. Qin, B. Su, P. A. Sakyi et al., "SIMS zircon U-Pb geochronology and Sr-Nd isotopes of Ni-Cu-Bearing Mafic-Ultramafic Intrusions in Eastern Tianshan and Beishan in correlation with flood basalts in Tarim Basin (NW China): Constraints on a ca. 280 Ma mantle plume," *American Journal of Science*, vol. 311, no. 3, pp. 237–260, 2011.
- [2] S. C. Xue, C. Li, K. Z. Qin, and D. M. Tang, "A non-plume model for the Permian protracted (266–286 Ma) basaltic magmatism in the Beishan–Tianshan region, Xinjiang, Western China," *Lithos*, vol. 256–257, pp. 243–249, 2016.
- [3] S. Xue, K. Qin, C. Li, Z. Yao, E. M. Ripley, and X. Wang, "Geochronological, mineralogical and geochemical studies of sulfide mineralization in the Podong mafic-ultramafic intrusion in northern Xinjiang, western China," *Ore Geology Reviews*, vol. 101, pp. 688–699, 2018.
- [4] J. Jiao, X. Leng, S. Duan, M. Xia, H. Rui, and L. Tan, "Petrogenesis and metallogenic characteristics of the Early Permian Podong Cu-Ni sulfide deposit, northeastern margin of the Tarim plate," *Acta Petrologica Sinica*, vol. 34, no. 8, pp. 2211–2222, 2018.
- [5] S. H. Yang, M. F. Zhou, P. C. Lightfoot et al., "Re–Os isotope and platinum-group element geochemistry of the Pobei Ni–Cu sulfide-bearing mafic-ultramafic complex in the northeastern part of the Tarim Craton," *Mineralium Deposita*, vol. 49, no. 3, pp. 381–397, 2014.
- [6] B. Su, K. Qin, P. A. Sakyi et al., "Geochronologic-petrochemical studies of the Hongshishan mafic-ultramafic intrusion, Beishan area, Xinjiang (NW China): petrogenesis and tectonic implications," *International Geology Review*, vol. 54, no. 3, pp. 270–289, 2012.
- [7] Q. Tang, M. Zhang, W. Li, M. Yu, Z. Zhang, and Y. Wang, "Geodynamic setting and metallogenic potential of Permian large-sized mafic-ultramafic intrusions in Beishan area, Xinjiang, China," *Geology in China*, vol. 42, no. 3, pp. 468–481, 2015.
- [8] Y. Liu, X. Lu, C. Wu et al., "The migration of Tarim plume magma toward the northeast in Early Permian and its significance for the exploration of PGE–Cu–Ni magmatic sulfide deposits in Xinjiang, NW China: As suggested by Sr–Nd–Hf isotopes, sedimentology and geophysical data," *Ore Geology Reviews*, vol. 72, pp. 538–545, 2016.
- [9] J. Ma, X. Lu, Y. Liu et al., "The impact of early sulfur saturation and calc-crustal contamination on ore-forming process in the Posan mafic-ultramafic complex: derived from the shallow depleted mantle, Beishan region, NW China," *Journal of Asian Earth Sciences*, vol. 118, pp. 81–94, 2016.
- [10] M. Zhang, Q. Tang, C. Cao et al., "The origin of Permian Pobei ultramafic complex in the northeastern Tarim craton, western China: evidences from chemical and C–He–Ne–Ar isotopic compositions of volatiles," *Chemical Geology*, vol. 469, pp. 85–96, 2017.
- [11] P. Feng, M. Zhang, L. Li et al., "The noble gas isotopic constrains on the petrogenesis of mafic-ultramafic intrusions in the western end of the Pobei complex, Xinjiang, northwestern China," *Acta Petrologica Sinica*, vol. 34, no. 11, pp. 3445–3454, 2018.
- [12] X. Y. Song, L. M. Chen, Y. F. Deng, and W. Xie, "Syncollisional tholeiitic magmatism induced by asthenosphere upwelling owing to slab detachment at the southern margin of the Central Asian Orogenic Belt," *Journal of the Geological Society*, vol. 170, no. 6, pp. 941–950, 2013.
- [13] M. Z. Xia, C. Y. Jiang, C. Li, and Z. D. Xia, "Characteristics of a newly discovered Ni–Cu sulfide deposit hosted in the Poyi ultramafic intrusion, Tarim Craton, NW China," *Economic Geology*, vol. 108, no. 8, pp. 1865–1878, 2013.
- [14] S. Xue, K. Qin, C. Li et al., "Geochronological, petrological and geochemical constraints on Ni–Cu sulfide mineralization in the Poyi ultramafic-troctolitic intrusion in the northeast rim of the Tarim Craton, western China," *Economic Geology*, vol. 111, no. 6, pp. 1465–1484, 2016.
- [15] B. Su, K. Qin, H. Sun, and H. Wang, "Geochronological, petrological, mineralogical and geochemical studies of the Xuanwoling mafic-ultramafic intrusion in Beishan area, Xinjiang," *Acta Petrologica Sinica*, vol. 26, no. 11, pp. 3283–3294, 2010.
- [16] B. X. Su, K. Z. Qin, M. Santosh, H. Sun, and D. M. Tang, "The Early Permian mafic-ultramafic complexes in the Beishan Terrane, NW China: Alaskan-type intrusives or rift cumulates?," *Journal of Asian Earth Sciences*, vol. 66, pp. 175–187, 2013.
- [17] S. J. Ao, W. J. Xiao, C. M. Han, Q. G. Mao, and J. E. Zhang, "Geochronology and geochemistry of early Permian mafic-ultramafic complexes in the Beishan area, Xinjiang, NW China: implications for late paleozoic tectonic evolution of the southern Altaids," *Gondwana Research*, vol. 18, no. 2–3, pp. 466–478, 2010.
- [18] H. Wang, P. Wang, J. Li, J. Feng, G. Deng, and X. Lv, "A tentative discussion on features of mafic-ultramafic rocks and exploration methods in Pobei area of Ruqiang, Xinjiang," *Geology in China*, vol. 42, no. 3, pp. 777–784, 2015.
- [19] M. Moreira and P. Madureira, "Cosmogenic helium and neon in 11 Myr old ultramafic xenoliths: Consequences for mantle signatures in old samples," *Geochemistry, Geophysics, Geosystems*, vol. 6, no. 8, article Q08006, 2005.
- [20] Q. Tang, M. Zhang, C. Li, M. Yu, and L. Li, "The chemical compositions and abundances of volatiles in the Siberian large igneous province: constraints on magmatic CO₂ and SO₂ emissions into the atmosphere," *Chemical Geology*, vol. 339, pp. 84–91, 2013.
- [21] M. Zhang, P. Hu, Y. Niu, and S. Su, "Chemical and stable isotopic constraints on the nature and origin of volatiles in the sub-continental lithospheric mantle beneath eastern China," *Lithos*, vol. 96, no. 1–2, pp. 55–66, 2007.
- [22] M. Zhang, Q. Tang, P. Hu, X. Ye, and Y. Cong, "Noble gas isotopic constraints on the origin and evolution of the Jinchuan Ni–Cu–(PGE) sulfide ore-bearing ultramafic intrusion, Western China," *Chemical Geology*, vol. 339, pp. 301–312, 2013.
- [23] M. F. Miller and C. T. Pillinger, "An appraisal of stepped heating release of fluid inclusion CO₂ for isotopic analysis: A preliminary to $\delta^{13}\text{C}$ characterisation of carbonaceous vesicles at the nanomole level," *Geochimica et Cosmochimica Acta*, vol. 61, no. 1, pp. 193–205, 1997.
- [24] P. H. Barry, D. R. Hilton, E. Füri, S. A. Halldórsson, and K. Grönvold, "Carbon isotope and abundance systematics of

- Icelandic geothermal gases, fluids and subglacial basalts with implications for mantle plume-related CO₂ fluxes,” *Geochimica et Cosmochimica Acta*, vol. 134, pp. 74–99, 2014.
- [25] Z. Li, X. Wang, L. Li et al., “Development of new method of $\delta^{13}\text{C}$ measurement for trace hydrocarbons in natural gas using solid phase micro-extraction coupled to gas chromatography isotope ratio mass spectrometry,” *Journal of Chromatography A*, vol. 1372, pp. 228–235, 2014.
- [26] C. Cao, M. Zhang, Q. Tang et al., “Noble gas isotopic variations and geological implication of Longmaxi shale gas in Sichuan Basin, China,” *Marine and Petroleum Geology*, vol. 89, pp. 38–46, 2018.
- [27] T. Zhang, M. Zhang, B. Bai, X. Wang, and L. Li, “Origin and accumulation of carbon dioxide in the Huanghua depression, Bohai Bay basin, China,” *AAPG Bulletin*, vol. 92, no. 3, pp. 341–358, 2008.
- [28] M. Zhang, S. L. Kamo, C. Li, P. Hu, and E. M. Ripley, “Precise U–Pb zircon–baddeleyite age of the Jinchuan sulfide ore-bearing ultramafic intrusion, western China,” *Mineralium Deposita*, vol. 45, no. 1, pp. 3–9, 2010.
- [29] C. J. Allègre, T. Staudacher, and P. Sarda, “Rare gas systematics: formation of the atmosphere, evolution and structure of the Earth’s mantle,” *Earth and Planetary Science Letters*, vol. 81, no. 2–3, pp. 127–150, 1987.
- [30] C. J. Ballentine and P. G. Burnard, “Production, release and transport of noble gases in the continental crust,” *Reviews in Mineralogy and Geochemistry*, vol. 47, no. 1, pp. 481–538, 2002.
- [31] T. J. Dunai and H. Baur, “Helium, neon, and argon systematics of the European subcontinental mantle: Implications for its geochemical evolution,” *Geochimica et Cosmochimica Acta*, vol. 59, no. 13, pp. 2767–2783, 1995.
- [32] C. Gautheron and M. Moreira, “Helium signature of the subcontinental lithospheric mantle,” *Earth and Planetary Science Letters*, vol. 199, no. 1–2, pp. 39–47, 2002.
- [33] C. Gautheron, M. Moreira, and C. Allègre, “He, Ne and Ar composition of the European lithospheric mantle,” *Chemical Geology*, vol. 217, no. 1–2, pp. 97–112, 2005.
- [34] D. R. Hilton, T. P. Fischer, and B. Marty, “Noble gases and volatile recycling at subduction zones,” *Reviews in Mineralogy and Geochemistry*, vol. 47, no. 1, pp. 319–370, 2002.
- [35] K. A. Farley, J. H. Natland, and H. Craig, “Binary mixing of enriched and undegassed (primitive?) mantle components (He, Sr, Nd, Pb) in Samoan lavas,” *Earth and Planetary Science Letters*, vol. 111, no. 1, pp. 183–199, 1992.
- [36] A. R. Basu, R. J. Poreda, P. R. Renne et al., “High-³He plume origin and temporal-spatial evolution of the Siberian flood basalts,” *Science*, vol. 269, no. 5225, pp. 822–825, 1995.
- [37] D. R. Hilton and D. Porcelli, “3.7 - Noble gases as mantle tracers,” in *Treatise on Geochemistry (Second Edition)*, vol. 3, pp. 293–325, 2014.
- [38] T. Hou, Z. Zhang, X. Ye, J. Encarnacion, and M. K. Reichow, “Noble gas isotopic systematics of Fe–Ti–V oxide ore-related mafic–ultramafic layered intrusions in the Panxi area, China: the role of recycled oceanic crust in their petrogenesis,” *Geochimica et Cosmochimica Acta*, vol. 75, no. 22, pp. 6727–6741, 2011.
- [39] P. Sarda, T. Staudacher, and C. Allegre, “Neon isotopes in submarine basalts,” *Earth and Planetary Science Letters*, vol. 91, no. 1–2, pp. 73–88, 1988.
- [40] P. Sarda, M. Moreira, T. Staudacher, J. G. Schilling, and C. J. Allegre, “Rare gas systematics on the southernmost Mid-Atlantic Ridge: constraints on the lower mantle and the Dupal source,” *Journal of Geophysical Research*, vol. 105, no. B3, pp. 5973–5996, 2000.
- [41] J. P. Benkert, H. Baur, P. Signer, and R. Wieler, “He, Ne, and Ar from the solar wind and solar energetic particles in lunar ilmenites and pyroxenes,” *Journal of Geophysical Research*, vol. 98, no. E7, pp. 13147–13162, 1993.
- [42] R. K. O’Nions and I. N. Tolstikhin, “Behaviour and residence times of lithophile and rare gas tracers in the upper mantle,” *Earth and Planetary Science Letters*, vol. 124, no. 1–4, pp. 131–138, 1994.
- [43] M. Ozima and F. A. Podosek, *Noble Gas Geochemistry*, Cambridge University Press, Cambridge, UK, 2nd edition, 2002.
- [44] M. A. Kendrick, M. Honda, D. Gillen, T. Baker, and D. Phillips, “New constraints on regional brecciation in the Wernecke Mountains, Canada, from He, Ne, Ar, Kr, Xe, Cl, Br and I in fluid inclusions,” *Chemical Geology*, vol. 255, no. 1–2, pp. 33–46, 2008.
- [45] M. Moreira, J. Kunz, and C. Allegre, “Rare gas systematics in popping rock: isotopic and elemental compositions in the upper mantle,” *Science*, vol. 279, no. 5354, pp. 1178–1181, 1998.
- [46] T. Staudacher, P. Sarda, S. H. Richardson, C. J. Allègre, I. Sagna, and L. V. Dmitriev, “Noble gases in basalt glasses from a Mid-Atlantic Ridge topographic high at 14°N: geodynamic consequences,” *Earth and Planetary Science Letters*, vol. 96, no. 1–2, pp. 119–133, 1989.
- [47] D. Lal, “In situ-produced cosmogenic isotopes in terrestrial rocks,” *Annual Review of Earth and Planetary Sciences*, vol. 16, no. 1, pp. 355–388, 1988.
- [48] M. Zhang, Q. Tang, C. Cao et al., “Molecular and carbon isotopic variation in 3.5 years shale gas production from Longmaxi Formation in Sichuan Basin, China,” *Marine and Petroleum Geology*, vol. 89, pp. 27–37, 2018.
- [49] M. Moreira and P. Sarda, “Noble gas constraints on degassing processes,” *Earth and Planetary Science Letters*, vol. 176, no. 3–4, pp. 375–386, 2000.
- [50] D. W. Graham, “Noble gas isotope geochemistry of mid-ocean ridge and ocean island basalts: characterization of mantle source reservoirs,” *Reviews in Mineralogy and Geochemistry*, vol. 47, no. 1, pp. 247–317, 2002.
- [51] Q. Tang, M. Zhang, Y. Wang et al., “The origin of the Zhubu mafic-ultramafic intrusion of the Emeishan large igneous province, SW China: Insights from volatile compositions and C–Hf–Sr–Nd isotopes,” *Chemical Geology*, vol. 469, pp. 47–59, 2017.
- [52] Y. Ueno, K. Yamada, N. Yoshida, S. Maruyama, and Y. Isozaki, “Evidence from fluid inclusions for microbial methanogenesis in the early Archaean era,” *Nature*, vol. 440, no. 7083, pp. 516–519, 2006.
- [53] B. Sherwood Lollar, S. K. Frape, S. M. Weise, P. Fritz, S. A. Macko, and J. A. Welhan, “Abiogenic methanogenesis in crystalline rocks,” *Geochimica et Cosmochimica Acta*, vol. 57, no. 23–24, pp. 5087–5097, 1993.
- [54] B. Sherwood Lollar, G. Lacrampe-Couloume, K. Voglesonger, T. C. Onstott, L. M. Pratt, and G. F. Slater, “Isotopic signatures of CH₄ and higher hydrocarbon gases from Precambrian Shield sites: A model for abiogenic polymerization of

- hydrocarbons," *Geochimica et Cosmochimica Acta*, vol. 72, no. 19, pp. 4778–4795, 2008.
- [55] J. Y. Lee, K. Marti, J. P. Severinghaus et al., "A redetermination of the isotopic abundances of atmospheric Ar," *Geochimica et Cosmochimica Acta*, vol. 70, no. 17, pp. 4507–4512, 2006.
- [56] T. Staudacher and C. J. Allegre, "Recycling of oceanic crust and sediments: the noble gas subduction barrier," *Earth and Planetary Science Letters*, vol. 89, no. 2, pp. 173–183, 1988.
- [57] J. Yamamoto, I. Kaneoka, S. Nakai, H. Kagi, V. S. Prikhod'ko, and S. Arai, "Evidence for subduction-related components in the subcontinental mantle from low $^3\text{He}/^4\text{He}$ and $^{40}\text{Ar}/^{36}\text{Ar}$ ratio in mantle xenoliths from Far Eastern Russia," *Chemical Geology*, vol. 207, no. 3–4, pp. 237–259, 2004.
- [58] G. Czuppon, T. Matsumoto, M. R. Handler, and J. I. Matsuda, "Noble gases in spinel peridotite xenoliths from Mt Quincan, North Queensland, Australia: undisturbed MORB-type noble gases in the subcontinental lithospheric mantle," *Chemical Geology*, vol. 266, no. 1–2, pp. 19–28, 2009.
- [59] S. Mukhopadhyay, "Early differentiation and volatile accretion recorded in deep-mantle neon and xenon," *Nature*, vol. 486, no. 7401, pp. 101–104, 2012.
- [60] N. A. Starkey, F. M. Stuart, R. M. Ellam, J. G. Fitton, S. Basu, and L. M. Larsen, "Helium isotopes in early Iceland plume picrites: Constraints on the composition of high $^3\text{He}/^4\text{He}$ mantle," *Earth and Planetary Science Letters*, vol. 277, no. 1–2, pp. 91–100, 2009.
- [61] D. Chavrit, R. Burgess, H. Sumino et al., "The contribution of hydrothermally altered ocean crust to the mantle halogen and noble gas cycles," *Geochimica et Cosmochimica Acta*, vol. 183, pp. 106–124, 2016.
- [62] Z. Cheng, Z. Zhang, T. Hou et al., "Decoupling of Mg–C and Sr–Nd–O isotopes traces the role of recycled carbon in magnesio碳酸atites from the Tarim Large Igneous Province," *Geochimica et Cosmochimica Acta*, vol. 202, pp. 159–178, 2017.
- [63] M. Schidlowski, "A 3,800-million-year isotopic record of life from carbon in sedimentary rocks," *Nature*, vol. 333, no. 6171, pp. 313–318, 1988.
- [64] C. G. Macpherson, D. R. Hilton, J. M. D. Day, D. Lowry, and K. Gronvold, "High- $^3\text{He}/^4\text{He}$, depleted mantle and low- $\delta^{18}\text{O}$, recycled oceanic lithosphere in the source of central Iceland magmatism," *Earth and Planetary Science Letters*, vol. 233, no. 3–4, pp. 411–427, 2005.
- [65] S. Shilobreeva, I. Martinez, V. Busigny, P. Agrinier, and C. Laverne, "Insights into C and H storage in the altered oceanic crust: Results from ODP/IODP Hole 1256D," *Geochimica et Cosmochimica Acta*, vol. 75, no. 9, pp. 2237–2255, 2011.

Research Article

Volcanogenic CO₂ Degassing in the Songliao Continental Rift System, NE China

Wenbin Zhao,^{1,2,3} Zhengfu Guo^{1,2,3} , Ming Lei,^{1,2,3} Maoliang Zhang,^{1,2,3} Lin Ma,^{1,2,3} Danielle Fortin,⁴ and Guodong Zheng^{5,6} 

¹Key Laboratory of Cenozoic Geology and Environment, Institute of Geology and Geophysics, Chinese Academy of Sciences, Beijing 100029, China

²CAS Center for Excellence in Life and Paleoenvironment, Beijing 100044, China

³College of Earth and Planetary Sciences, University of Chinese Academy of Sciences, Beijing 100049, China

⁴Department of Earth and Environmental Sciences, University of Ottawa, Ottawa, Ontario, Canada K1N 6N5

⁵Northwest Institute of Eco-Environment and Resources, Chinese Academy of Sciences, Lanzhou 730000, China

⁶Key Laboratory of Petroleum Resources, Gansu Province, Lanzhou 730000, China

Correspondence should be addressed to Zhengfu Guo; zfguo@mail.iggcas.ac.cn

Received 26 January 2019; Revised 14 May 2019; Accepted 17 June 2019; Published 19 August 2019

Academic Editor: Giovanni Martinelli

Copyright © 2019 Wenbin Zhao et al. This is an open access article distributed under the Creative Commons Attribution License, which permits unrestricted use, distribution, and reproduction in any medium, provided the original work is properly cited.

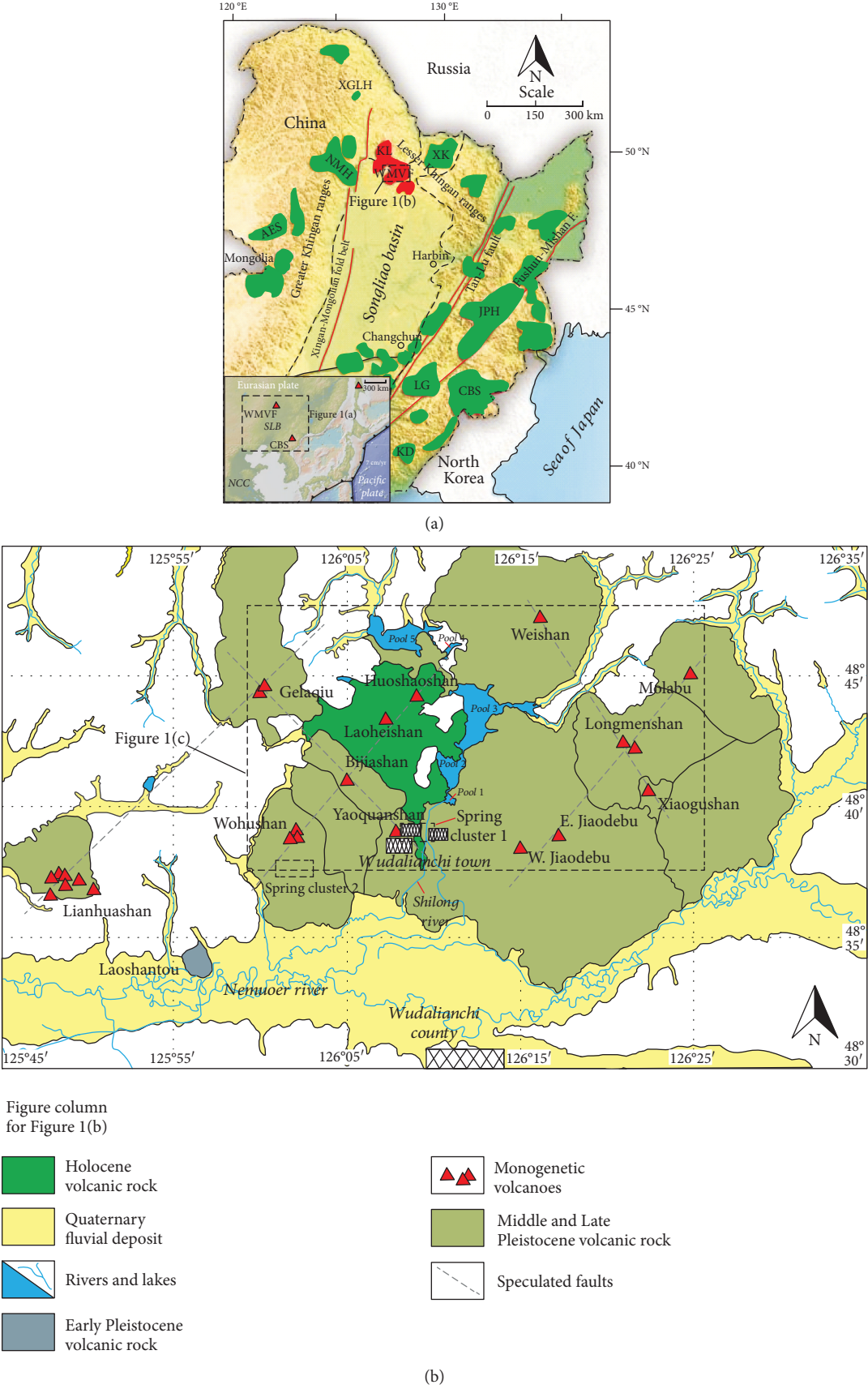
The Wudalianchi monogenetic volcanic field (WMVF) is located in the Songliao basin within a major continental rift system in NE China. Bubbling springs and diffuse degassing from soils are typical features of the WMVF. Chemical compositions and C-He isotope analyses revealed that the cold spring gases might originate from the enriched upper mantle (EM), which resulted from the mixing between slab materials (subducted organic sediments and carbonates) in the mantle transition zone (MTZ) and the ambient depleted mantle. These EM-derived volatiles experienced variable degrees of crustal input, including both continental organic metasediments and crustal carbonates during their ascending path to the surface. The estimated results of the degassing CO₂ fluxes, combined with previous geophysical evidence, suggest that the CO₂ degassing activities become weaker from early to late in Quaternary.

1. Introduction

Continental rift systems, together with the related intraplate volcanism, have been regarded as a possible trigger of deep-derived CO₂ degassing into the atmosphere and long-term climate change [1–6]. Positive spatial correlation between CO₂ discharges and the extensional tectonic regimes confirms that the continental rift systems are critical pathways for deep carbon degassing from the Earth's interior to the exosphere [6]. Research on continental rift lengths and paleoatmospheric CO₂ concentrations over the last 200 million years also indicates that continental fragmentation may control the atmospheric CO₂ levels via massive CO₂ degassing in rift systems [4]. Intraplate volcanism along continental rift systems is primarily derived from the metasomatized mantle [7]. Under these conditions, the reduction of the peri-

dotite solidus due to the presence of volatiles allows for partial melting of the upper mantle at depth and thus for the release of large amounts of CO₂ into the atmosphere via extensive volcanism [4, 5, 8, 9].

The Songliao basin in NE China has experienced long-term extension-induced continental rifting since the Late Mesozoic as indicated by many intraplate volcanoes (Figure 1(a)) [10]. Based on both petrogenesis and geophysical evidences, these Cenozoic volcanic activities have been considered to be linked to the stagnant Pacific slab materials in the mantle transition zone (MTZ) [11–15]. However, the origin and evolution of magma degassing in the continental rift system involving the deep subduction of oceanic slab are poorly understood [16, 17]. Located at the northern margin of the Songliao continental rift system in East Asia (Figure 1(a)), the Wudalianchi monogenetic volcanic field





(c)

FIGURE 1: (a) Geological and tectonic map showing the locations of major faults and Cenozoic basaltic volcanic fields in NE China (modified from Liu et al. [10]). The inset shows the location of Eastern China. Abbreviations of Cenozoic volcanic fields in NE China are as follows: WMVF: Wudalianchi monogenetic volcanic field; XK: Xunke; KL: Keluo; NMH: Nuominhe; XGLH: Xiaogulihe; AES: Aershan; JPH: Jingpohu; LG: Longgang; CBS: Changbaishan; KD: Kuandian; SLB: Songliao basin; NCC: North China craton. (b) Geological map of WMVF (modified from Zhao et al. [23]). (c) Geomorphologic map showing the location of monogenetic volcanoes and cold springs in WMVF. Red dots represent the location of the soil CO_2 flux survey, and the stars represent the sample locations.

(WMVF) is characterized by extensive CO_2 degassing, i.e., cold bubbling springs, diffused CO_2 emissions from soils, and volcanogenic fault systems (Figure 1(b)). CO_2 is supposed to be of mainly magmatic origin, but the mechanisms of deep CO_2 formation are still debated. Some authors [18–21] indicated a binary mixing between the depleted mantle- and upper crust-derived volatiles. Other authors [22] hypothesized partial melting of a subcontinental lithospheric mantle (SCLM) metasomatized by ancient fluids.

In this paper, we report the first soil CO_2 flux measurements in the WMVF. Additionally, new data on the chemical and C-He isotopic composition of gases associated with four cold springs located in the area are presented and used to gain insights into the mechanisms responsible for CO_2 formation at depth.

2. Geological Setting

The Wudalianchi monogenetic volcanic field (WMVF) is an active K-rich volcanic region located in a continental rift system in NE China (Figure 1(a)). Its latest eruption dates back to 1721 AD (e.g., Laoheishan and Huoshaoshan volcanoes, Figures 1(b) and 1(c)) [23, 24]. The WMVF basement consists of Archean granites, Mesozoic andesite, and granite intrusions [25]. Limestones and marine carbonate sediments have been present in outcrops in the ambient Songliao basin since the Mesozoic age [26, 27]. During the Cenozoic period, dispersed calc-alkaline, tholeiitic, and alkali basaltic rocks were formed in Northeastern China [10], which constitute

the eastern part of the Asian tectono-magmatic province that extends from Lake Baikal, Siberia, to Eastern China [28].

Cenozoic volcanic activity has formed 800 km^2 of lava flows, which includes the middle Pleistocene to Holocene volcanic activity in WMVF (Figure 1(b)) [23, 24]. These fissure-central-type eruptions are controlled by NE- to NNW-striking fractures or deep faults [23, 29], which are linked to the continental rift systems in East Asia [30, 31]. Deep buried faults provided potential rising channels for the magma [23], which finally led to the unique volcanic landscapes seen nowadays in WMVF [24], such as linear rows of scoria cones (Figures 1(b) and 1(c)), dominant tectonic weakness direction enlarged by erosion (e.g., Huoshaoshan volcanic cone, Figure 2(e)), and overlapping scoria cones (e.g., Wohushan volcanic cone, Figure 1(c)). All of these features were used in the past to locate feeding fissures beneath the monogenetic volcanoes in continental rift systems [32].

Seismic tomography studies have shown the presence of a magma reservoir under the Weishan volcano in WMVF (Figures 1(b) and 1(c)), which is considered as evidence for partial melting in a shallow magma chamber at 7–13 km depth [33]. Surface manifestation of such activity is mainly expressed as cold-mineral bubbling springs with high p_{CO_2} and low water temperature (generally between 4 and 7°C), prevalently distributed on the flanks or at the margin of the active volcanic cones (Figure 1(c)) [18, 21], and located roughly at the same elevation (about 300 to 320 m.a.s.l., Figure 1(c)). The Hualin spring (HLQ) is located at the eastern slope of the Huoshaoshan volcanic cone (Figures 1(c))



FIGURE 2: Photos showing the Fanhua spring (a), Hualin spring in August 2017 (b) and April 2019 (c), basaltic lava flow under the thin pumiceous deposits beside the Laoheishan volcanic cone (d), and dominant tectonic weakness direction enlarged by erosion in the Huoshaoshan volcanic cone (e).

and 2(b)) and shows the highest water temperature (24°C) in the WMVF. The North, South, and Fanhua cold springs are located east of the Yaoquanshan volcano and west of the Shilong river (Figure 1(c)) and are characterized by water temperatures lower than 10°C .

3. Sampling and Analytical Methods

3.1. Soil CO_2 Flux Measurements. Soil CO_2 fluxes were measured *in situ* using soil diffuse gas flux meters based on the accumulation chamber method (Figure 2(d)), which was firstly reported by Chiodini et al. [34]. The edge of the

inverted cylindrical chamber was sealed with damp soil to diminish air contamination of the soil gases in the chamber [35]. The measurement sites were located near the main volcano-structural features of the region and preferentially placed on uncovered ground to minimize the influence of the vegetation on the measured fluxes (Figure 1(c)). The temperature was measured *in situ* at a depth of 10 cm, and the location was recorded (measured with a Garmin GPSMAP 60SCx) at each measurement point (see details in Supplementary Material). 92 measurement points were made during stable suitable weather and similar atmospheric conditions in August and September 2017. In order to compare

the CO₂ emission rate of the new erupted region with that of the whole WMVF, additional 38 points were considered on the southeastern slope of the Laoheishan volcanic cone (Figures 1(c) and 2(d)), whose last activity occurred about 300 years ago.

3.2. Spring Gas Sampling and Composition Analysis. Gas samples from four cold bubbling springs (Figures 1(c) and 2) were collected by means of the drainage method using lead-bearing glass bottles [16]. The temperature of the spring water was measured *in situ* using a portable thermometer. Chemical and isotopic compositions of the gas samples were measured in the Key Laboratory of Petroleum Resources Research, Institute of Geology and Geophysics, Chinese Academy of Sciences (IGGCAS), Lanzhou, China. The chemical composition of the gas samples was determined using a MAT 271 mass spectrometer. The $\delta^{13}\text{C}_{\text{CO}_2}$ was analyzed with a Delta Plus XP mass spectrometer. All samples were analyzed for the helium isotope composition ($^3\text{He}/^4\text{He}$) using a Noblesse noble gas mass spectrometer. Detailed analytical procedures are described in Luo et al. [36] and Zhang et al. [37].

4. Results

4.1. Degassing Flux of Soil CO₂. We obtained a broad range of soil CO₂ fluxes (1.1 to $161.5 \text{ g m}^{-2} \text{ d}^{-1}$) and soil temperatures (18.1°C to 33.3°C ; Supplementary Table S1), which demonstrate high variability of soil CO₂ emissions in WMVF. In the log probability plot (Figure 3(a)), our analytical data could be basically divided into the following three groups by two inflection points on the skewed curve [38]: less than $5 \text{ g m}^{-2} \text{ d}^{-1}$ (Group A), 5 – $60 \text{ g m}^{-2} \text{ d}^{-1}$ (Group B), and more than $60 \text{ g m}^{-2} \text{ d}^{-1}$ (Group C), characterized by average soil CO₂ flux values of $3.5 \text{ g m}^{-2} \text{ d}^{-1}$, $17.6 \text{ g m}^{-2} \text{ d}^{-1}$, and $92.1 \text{ g m}^{-2} \text{ d}^{-1}$, respectively (Figure 3(a)). These groups may represent different sources of soil CO₂ based on Chiodini et al. [39]: (i) biological source with low soil CO₂ flux (e.g., soil respiration or pedochemical process, Group A) and (ii) geological source with high soil CO₂ flux (e.g., magmatic or hydrothermal related carbon degassing, Group C). In particular, Group B with intermediate soil CO₂ fluxes may represent the mixture of biological and geological sources (Figure 3(a)). The average soil CO₂ flux of the whole WMVF was calculated using the weighted mean method, which is $18.7 \text{ g m}^{-2} \text{ d}^{-1}$. Using the same statistical method, an average soil CO₂ flux of $11.8 \text{ g m}^{-2} \text{ d}^{-1}$ was obtained for the SE slope of the Laoheishan volcanic cone (Figure 3(b)).

Caracausi et al. [40] proposed that size-normalized CO₂ fluxes inversely correlate with the ages from the last eruptions, which means that active outgassing of volatiles from magmatic bodies would occur for a long time after the last volcanic activity. However, the average soil CO₂ flux in the SE slope of the Laoheishan volcanic cone, which experienced the latest eruption, is lower than that in the whole WMVF (Figure 3). Considering the dispersed cold springs, and the decoupling of soil temperatures and CO₂ fluxes (with a correlation coefficient of 0.0714) in WMVF, we suggest that the

resulting weak degassing is due to the solidification and/or cooling down of the underlying magma body beneath the Laoheishan in about 300 years. Our proposal is in good agreement with crustal electric conductivity studies that a rivet-shaped block with high resistivity, which was considered as the result of solidified magma chamber, is distributed beneath the Laoheishan-Huoshashan volcanic chain (Figure 1) [41].

In this study, 50 sequential Gaussian simulations were performed over a grid of 108001 square cells ($1 \times 1 \text{ m}$) covering an area of 0.11 km^2 in the southeastern slope of the Laoheishan volcano (Figure 4). Total CO₂ output in the selected area of the Laoheishan volcano (ca. 0.11 km^2) is 536.3 t/yr ($\sigma = 43.2 \text{ t/d}$), which is a preliminary survey or first-order estimation of diffusive CO₂ degassing in WMVF.

4.2. Chemical and C-He Isotopic Compositions of Cold Spring Gases. The chemical and C-He isotopic compositions of gases from the WMVF cold springs are listed in Table 1. Our analytical results are in excellent agreement with previous studies (Supplementary Table S3) [18–22], which suggest no distinct changes in chemical and isotopic compositions of the spring gases during the last 20 years.

4.2.1. Chemical Composition. Our results show that most of the gas samples from the Wudalianchi cold springs are characterized by high CO₂ content (higher than 90%) and low O₂ content (lower than 1.29%) and N₂ content (3.2%–8.7%) (Table 1), with the exception of the samples from the Fanhua spring (FHQ17 and FHQ18), which are characterized by low CO₂ content (76.7%–80.2%) and relatively high O₂ (~3.66%) and N₂ content (15.8%–22.6%). N₂/Ar ratios of the WMVF samples in this study range from 27 to 75, suggesting an interaction between helium-rich components, air-saturated water (ASW, N₂/Ar ≈ 40 , temperature dependent), and air (N₂/Ar = 83.6) [44, 45], as shown by the linear trend from the high He/Ar to ASW and air endpoints (Figure 5(a)). CO₂/³He ratios ($(0.1\text{--}29.5) \times 10^9$; Table 1 and Figure 6) were calculated using CO₂/He and $^3\text{He}/^4\text{He}$ ratios, which overlap those of typical arc-related volatiles ($(4.5\text{--}29) \times 10^9$, [46]) and depleted mantle (1.5×10^9 , [46]), indicating CO₂ addition and/or loss during volatile ascending processes (Figure 5(b)).

4.2.2. C-He Isotopic Compositions. The isotopic composition of carbon and helium has been successfully used to quantify the carbonate vs. sediment contribution from subducted slab material recycling [46] and the mantle vs. crustal contribution [44], respectively, in hydrothermal and volcanic gases worldwide.

The $\delta^{13}\text{C}$ -CO₂ values of the spring gas samples from the WMVF fall between -7.3‰ and -2.5‰ (versus VPDB, Table 1), overlapping with the compositional fields reported for arc-related volatiles (-9.1‰ to -1.3‰ , [46]). Some samples show relatively heavier carbon isotope compositions when compared to upper mantle values ($-6.5 \pm 2.5\text{‰}$, [46]), suggesting a possible contribution from inorganic carbon-rich components (carbonate rocks, $0 \pm 2\text{‰}$, [53]).

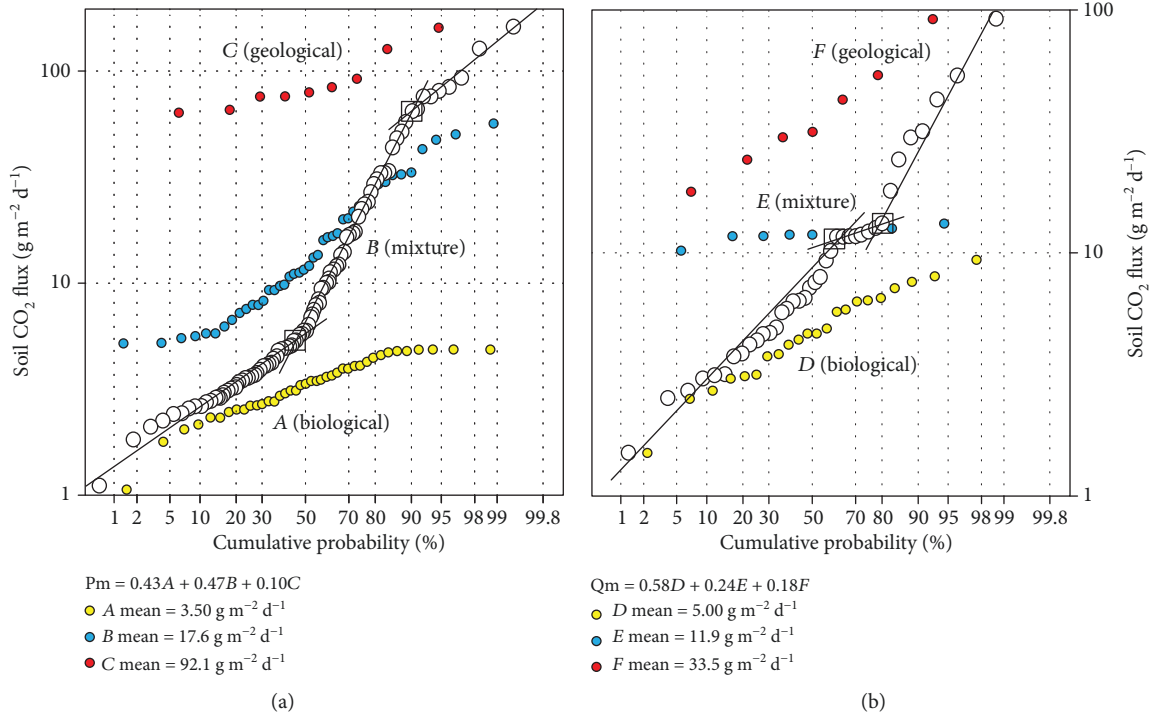


FIGURE 3: Cumulative probability plot of calculated soil CO₂ fluxes in the whole WMVF (a) and SE slope of the Laoheishan volcanic cone (b). Black solid lines represent the partition components of Groups A, B, and C and D, E, and F.

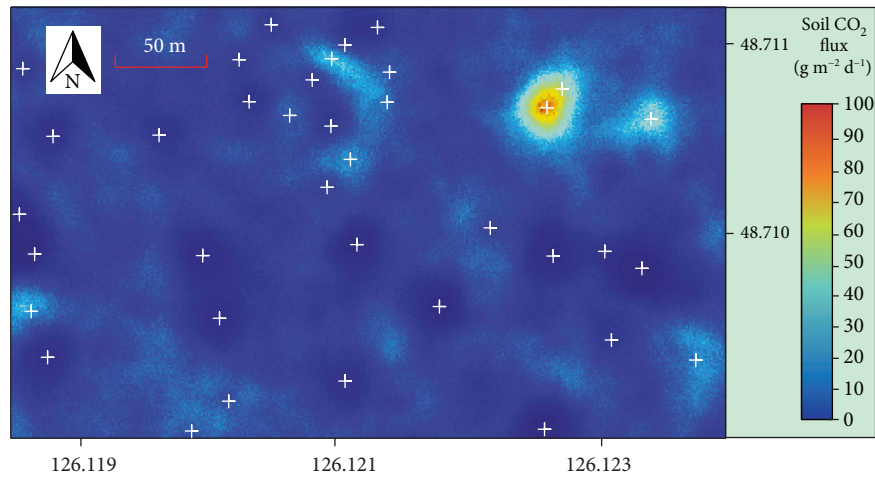


FIGURE 4: CO₂ flux map in the SE slope of the Laoheishan volcanic cone obtained by sequential Gaussian simulations.

Measured $^3\text{He}/^4\text{He}$ ratios (R_M) of the WMVF gas samples range between $2.26R_A$ and $3.18R_A$ (Table 1), suggesting an obvious contribution from the mantle-derived ^3He (Figures 5–7). Such intermediate helium ratios are lower than those of both the depleted MORB-source mantle (DMM, $8 \pm 1R_A$, [52]) and the subcontinental lithospheric mantle (SCLM, $^3\text{He}/^4\text{He} = 6.1 \pm 0.9R_A$, [50]), which point to a mixed origin of volatiles from the upper mantle and an end member with high radiogenic ^4He (e.g., crustal materials, $0.02R_A$, [42]) (Table 2 and Figure 7). As the X values are high (>150) for all the samples of this study (Table 1), there is little difference between measured (R_M/R_A) and air-corrected

(R_C/R_A) helium ratios (Table 1), which indicates little influence from air contamination. Gas samples from the Fanhua spring show higher $^4\text{He}/^{20}\text{Ne}$ (145–359) and He/Ar ratios (0.28–0.43) (Table 1) than those of the air ($^4\text{He}/^{20}\text{Ne} = 0.32$, [42]; $\text{He}/\text{Ar} = 0.0005$, [54]), which indicate that the high N_2 and low CO_2 contents do not result from the air contamination in the Fanhua spring gases.

5. Discussion

5.1. Carbon Provenance of Volatiles in WMVF. Zhang et al. [16] proposed that the upper mantle (DMM) and slab-

TABLE 1: Chemical and C-He isotopic compositions of the spring gases in the WMVF.

Sample no.	T (°C)	N ₂ (%)	O ₂ (%)	Ar (%)	CO ₂ (%)	CH ₄ (%)	He (ppm)	He/Ar	N ₂ /Ar	⁴ He/ ²⁰ Ne	R _M /R _A	X	R _C /R _A	δ ¹³ C (‰)	CO ₂ / ³ He (×10 ⁹)
NYQ17	9.2	8.0	0.35	0.16	91.1	0.07	129	0.08	50	182	2.64	713	2.64	-7.2	1.9
NYQ18	7.7	8.7	0.55	0.18	90.5	0.14	278	0.15	49	153	3.10	597	3.10	-5.6	0.8
BYQ17	7.8	3.4	0.32	0.06	95.8	0.10	379	0.64	58	685	2.26	2675	2.26	-7.3	0.8
BYQ18	6.5	3.2	0.25	0.07	96.5	0.38	18	0.03	46	40	3.16	155	3.17	-6.0	12.1
HLQ17	19.8	4.6	0.88	0.08	94.1	0.02	10	0.01	58	38	2.34	150	2.35	-5.0	29.5
HLQ18	24.0	4.9	1.29	0.09	93.7	0.04	433	0.48	54	72	2.97	281	2.98	-2.6	0.5
FHQ17	12.7	15.8	3.66	0.25	80.2	0.08	718	0.28	62	145	2.81	568	2.81	-4.3	0.3
FHQ18	16.0	22.6	0.21	0.43	76.7	0.89	1845	0.43	53	359	3.18	1401	3.18	-2.5	0.1

(1) R_M/R_A is the observed $^3\text{He}/^4\text{He}$ ratio divided by the $^3\text{He}/^4\text{He}$ ratio in the air (1.39×10^{-6} , [42]). (2) $X = (^4\text{He}/^{20}\text{Ne})_M / (^4\text{He}/^{20}\text{Ne})_{\text{Air}} \times (\beta_{\text{Ne}}/\beta_{\text{He}})$, where β represents the Bunsen coefficients assuming a groundwater recharge temperature of 10°C ($\beta_{\text{Ne}}/\beta_{\text{He}} = 1.25$, [43]), $(^4\text{He}/^{20}\text{Ne})_M$ is the measured ratio of samples, and $(^4\text{He}/^{20}\text{Ne})_{\text{Air}}$ is the ratio of the air (0.32, [42]). (3) R_C/R_A is the air-corrected Helium isotope ratio by applying the following formula [44]: $R_C/R_A = ((R_M/R_A) \times X - 1)/(X - 1)$.

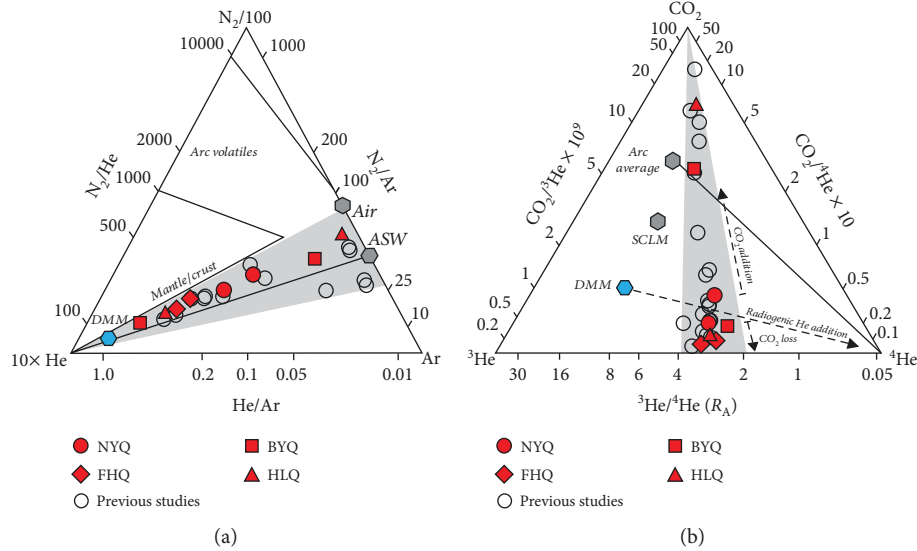


FIGURE 5: Triangle plot of N₂-He-Ar (a) and CO₂-³He-⁴He (b) for the cold spring gases in WMVF (modified from Giggenbach et al. [47]). Filled and open symbols represent, respectively, data in this study and published data in [18–22, 48]. The compiled data in previous studies are available in Supplementary Table S3. Abbreviations: NYQ: South spring; BYQ: North spring; FHQ: Fanhua spring; HLQ: Hualin spring; ASW: air-saturated water; Arc average: arc-related volatiles ($^3\text{He}/^4\text{He} = 5.4 \pm 1.9R_A$, [49]; $\text{CO}_2/^3\text{He} = (4.5\text{--}29) \times 10^9$, [46]); SCLM: subcontinental lithospheric mantle ($^3\text{He}/^4\text{He} = 6.1 \pm 0.9R_A$, [50]; $\text{CO}_2/^3\text{He} = 4 \times 10^9$, [51]); DMM: depleted MORB-source mantle ($^3\text{He}/^4\text{He} = 8 \pm 1R_A$, [52]; $\text{CO}_2/^3\text{He} = 1.5 \times 10^9$, [46]).

derived components related to the deep subduction of the Pacific plate, including the slab carbonate (CAR) and subducted organic sediments (ORS), are involved in the CO₂ inventory of the volatiles in the Changbaishan volcanic fields in NE China, which are similar to those from arc volcanism [46, 58–60]. The CO₂/³He ratio remains constant as the gas phase separates from molten basalt, because of the similar solubilities of CO₂ and He in melts [61]. Figure 6(a) shows the relationship between CO₂/³He ratios and δ¹³C values of cold spring gases in the WMVF, whereas the CO₂/³He ratios of the dataset show marked disparity (Table 1; Figures 5(b) and 6).

Samples with CO₂/³He ratios lower than that of DMM are thought to result from the physical-chemical fractionation of CO₂ to He [46, 61] or variable CO₂/³He ratios of

continental crustal contribution [62]. However, these samples with low CO₂/³He ratios in the WMVF basically have constant $^3\text{He}/^4\text{He}$ (R_A) ratios when compared to those within the three end members (Figures 7 and 6(b)), which eliminate the additional contribution from the crustal origin. Phase separation within the shallow aquifer can potentially fractionate elemental CO₂/³He ratios due to the greater solubility of CO₂ in the aqueous solution relative to that of the helium [43, 63], especially in low-temperature systems. For example, Sano et al. [64] suggested that a positive correlation between observed CO₂/³He ratios and temperatures of fumaroles and springs results from the differences in solubility. We thus suggest that the He-CO₂ fractionation in the cold shallow aquifer would act as the first-order controlling factor on these low CO₂/³He samples, including gas samples from the

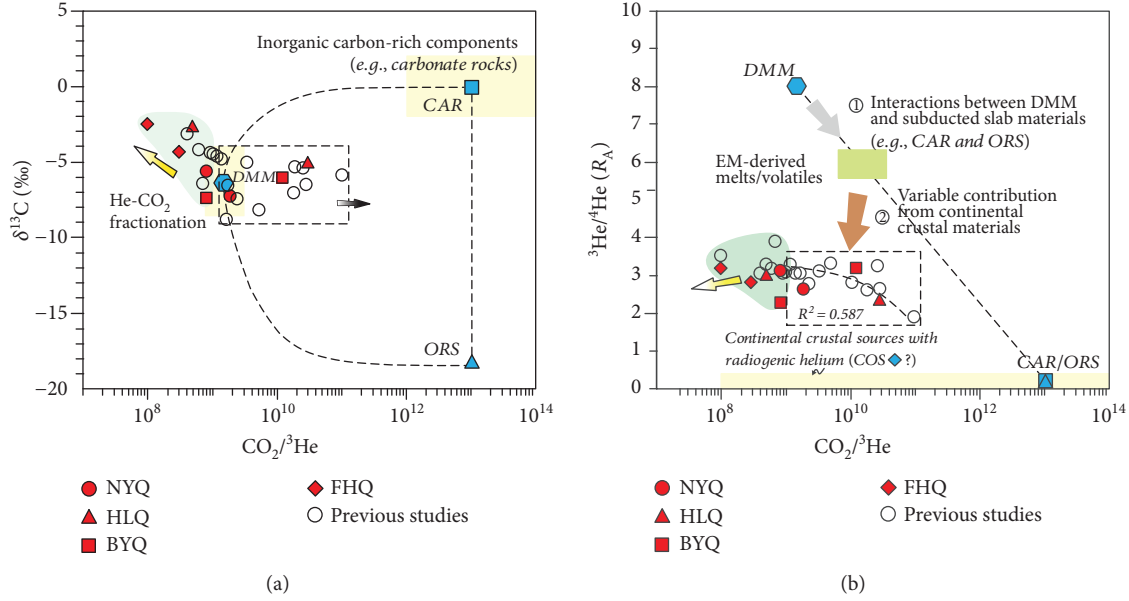


FIGURE 6: (a) $\delta^{13}\text{C}$ (‰) versus $\text{CO}_2/{}^3\text{He}$ ratios for cold spring gases from WMVF. The yellow arrow denotes the effects of He- CO_2 fractionation on the samples outside the mixing envelope. (b) ${}^3\text{He}/{}^4\text{He}$ (R_A) versus $\text{CO}_2/{}^3\text{He}$ ratios for cold spring gases from WMVF. Abbreviations and reference values for end members are as follows: CAR: carbonate rocks ($\delta^{13}\text{C} = 0 \pm 2\%$, [53]); ORS: organic sediments ($\delta^{13}\text{C} = -18.5\%$, [35]). The ${}^3\text{He}/{}^4\text{He}$ (R_A) ratios of CAR and ORS end members are assumed to be $0.02R_A$ [66] and the $\text{CO}_2/{}^3\text{He}$ values ranging from 10^{12} to 10^{14} [62]. The $\text{CO}_2/{}^3\text{He}$ ratios of DMM are ranging from 7.5×10^8 to 3×10^9 , with an average of 1.5×10^9 [46]. The continental crustal source has a wide range of $\text{CO}_2/{}^3\text{He}$ ratios based on [62]. Data source and symbols are as in Figure 5.

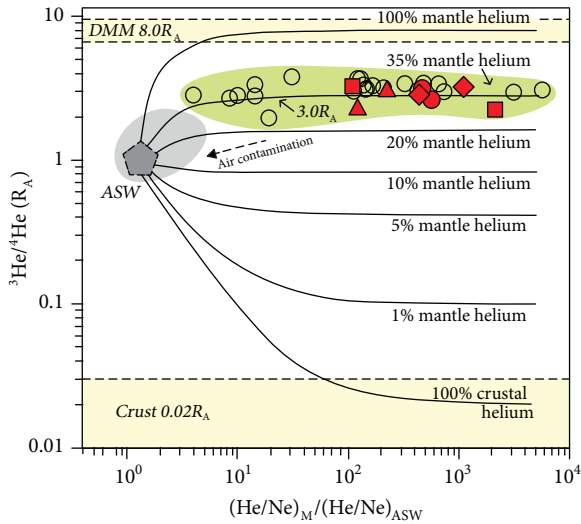


FIGURE 7: ${}^3\text{He}/{}^4\text{He}$ (R_A) versus $(\text{He}/\text{Ne})_M/(\text{He}/\text{Ne})_{\text{ASW}}$ for cold spring gases in WMVF. The calculated binary mixing curves between the air-saturated water (ASW) and crust-mantle mixtures with variable proportions of mantle helium (e.g., 100%, 35%, 20%, 10%, 5%, 1%, and 0%) are shown. Reference values for end members are as follows: ASW: ${}^3\text{He}/{}^4\text{He} = 0.987R_A$ [55], crust: ${}^3\text{He}/{}^4\text{He} = 0.02R_A$ [42] and ${}^4\text{He}/{}^{20}\text{Ne} = 3500$ [56], and DMM: ${}^4\text{He}/{}^{20}\text{Ne} = 5000$ [57]. Data source and symbols are as in Figure 5.

Fanhua spring, which are characterized by relatively high N_2 contents, low CO_2 contents, and low $\text{CO}_2/{}^3\text{He}$ ratios (Table 1; Figures 5 and 6). Considering this process, the orig-

inal $\text{CO}_2/{}^3\text{He}$ ratios of gas samples may be higher than the observed values, as shown by the black arrow in Figure 6(a).

Samples within the mixing trajectories have contributions from DMM, ORS, and CAR end members (Figure 6(a)) [16, 46] and are used to calculate the proportion of their contributions to the total carbon inventory in the WMVF, as shown in Table 2. In this calculation, elemental fractionation and its effect on C-He isotope systematics are not considered. We took the average $\delta^{13}\text{C}$ (-18.5%) of metamorphosed reduced carbon as that of the ORS end member when considering the potential fractionation during the subduction [16, 65]. If the contribution from continental crustal materials is not taken into account, an average proportion of subducted organic sediments (ORS) would be 24% (Table 2). The upper mantle and slab carbonate-derived carbon are the principal contributors to the carbon budget, with an average total contribution of 76% (Table 2), which is analogous to carbon inventories of worldwide arc magma-related volatiles [46, 58–60].

The diagram of ${}^3\text{He}/{}^4\text{He}$ (R_A) versus $\text{CO}_2/{}^3\text{He}$ ratios of volcanic or hydrothermal volatiles has provided important constraints on the origin of carbon [35, 61]. In Figure 6(b), the ${}^3\text{He}/{}^4\text{He}$ values of the studied samples within the mixing curves (Figure 6(a)) are negatively correlated with $\text{CO}_2/{}^3\text{He}$ ratios ($R^2 = 0.587$), further supporting the mixing between DMM or EM end member (both with high- R_A and low- $\text{CO}_2/{}^3\text{He}$ ratios) and subducted slab materials (CAR/ORS end member with low- R_A and high- $\text{CO}_2/{}^3\text{He}$ ratios) [67]. However, these samples are obviously located away from the above mixing line (Figure 5(b)), which shows a binary mixing trend between EM-derived volatiles

TABLE 2: Estimated carbon sources for the spring gas samples in WMVF.

Sample no.	Reference	$\delta^{13}\text{C}$ (‰)	$\text{CO}_2/^3\text{He}$ ($\times 10^9$)	DMM	Carbon inventory		M+C
					ORS	CAR	
HLQ17	This study	-5.0	29.5	0.05	0.25	0.70	0.75
NYQ17	This study	-7.2	1.9	0.79	0.11	0.10	0.89
BYQ18	This study	-6.0	12.1	0.12	0.28	0.60	0.72
HL2	[21]	-5.3	18.8	0.08	0.26	0.66	0.74
FH2	[21]	-8.2	5.1	0.29	0.34	0.37	0.66
BY1	[21]	-6.5	28.5	0.05	0.33	0.61	0.66
NYQ	[18]	-5.1	27.0	0.06	0.26	0.69	0.76
WBQ	[18]	-5.8	97.6	0.02	0.30	0.68	0.70
DZT	[18]	-7.4	2.3	0.65	0.17	0.18	0.83
SG2	[20]	-6.6	1.7	0.88	0.05	0.07	0.95
Average				0.30	0.24	0.46	0.76

and continental crustal materials with variable $\text{CO}_2/^3\text{He}$ ratios (Figure 6(b)) [62].

5.2. Origin and Evolution of the Volatiles in the WMVF

5.2.1. C-He Isotope Systematics and End-Member Parameters. In the C-He isotope systematics based on Van Soest et al. [59], $^3\text{He}/^4\text{He}$ ratios coupled with $\delta^{13}\text{C}_{\text{CO}_2}$ values were applied to quantitatively constrain the evolution of volatiles (Figure 8). Following the deep subduction scenario, upper mantle (DMM), slab carbonate (CAR), and organic sediments (ORS) are involved in the origin of volatiles in the WMVF, which exhibited variable contribution of continental crustal components, including organic metasediments (COS) and crustal carbonate (CAR) during their ascending process (Figures 6(b) and 8). Reference values for associated parameters of end members used in the modelling calculation are listed in Table 3.

Helium concentration of the ORS end member was calculated based on the U-Th decay of the global subducting sediments (GLOSS with high SiO_2 content; see details in the Supplementary Material) with reservoir accumulation age of 2.2 Ga in the MTZ constrained by the lead isotope [13]. The COS end member was assumed to have a helium ratio equal to that of the bulk continental crust ($0.02R_A$, [66]). Considering the potential fractionation effects of the He- CO_2 system, the samples with lower $\text{CO}_2/^3\text{He}$ ratios than DMM (Figure 6) were not considered for further discussion when calculating the C-He isotope systematics (Figure 8). The results of the C-He isotope mixing calculations between different end members are listed in Supplementary Tables S5 and S6.

5.2.2. Nature of the Upper Mantle Enriched by CAR and ORS with respect to Melts beneath the WMVF. Melting of subducted carbonates (CAR) and/or organic sediments (ORS) would release volatiles, i.e., carbon dioxide [70], and generate hydrous-carbonated plumes (HCPs, [71]) and ORS-related silicate melts under the P-T conditions of the MTZ. Based on the C-He isotope systematics, binary mixing between car-

bonate and ambient depleted upper mantle was first considered to produce the carbonated peridotite (CP) (Figure 8). Interaction between CP and ORS-derived silicate melts would produce enriched upper mantle (EM), which is considered as the primary source of WMVF volatiles (Figures 6(b) and 8).

The best-fit mixing trajectory with $K = 1.71$ for mixing between ORS and CP was estimated based on an optimal $\text{CO}_2/^3\text{He}$ ratio of 10^{13} due to the lack of carbon contents in the assumed ORS end member, which lies above all the WMVF samples (Figure 8). K represents the ratio of He/C values between CP and ORS according to Van Soest et al. [59]. The carbon content (12618 ppm) in the ORS end member is obtained by calculation of the optimal K coefficient (1.71). The reasonable upper and lower limits for the CP-ORS mixing are marked by mixing trajectories with K values of 17.1 and 0.171, which yield $\text{CO}_2/^3\text{He}$ ratios of 10^{14} and 10^{12} [62], respectively.

As indicated by the C-He isotope systematics, EM-like $^3\text{He}/^4\text{He}$ and $\delta^{13}\text{C}$ ratios beneath WMVF are marked by $5.8R_A$ and -9.7‰ ($5.5\text{--}6.1R_A$, -10.3 to -9.1‰ ; Figures 8 and 9(b)), respectively. Such C-He isotopes indicate an involvement of 10% (in average; ranging from 8% to 13%) carbonate and 13% (in average; ranging from 11% to 15%) ORS-derived silicate melts in the depleted mantle source, along with the Nd-Mg isotope information from potassic basalts in the WMVF (Supplementary Material). Partial melting of the enriched upper mantle (EM) source would produce basaltic magmas and concomitant initial volatiles in the WMVF (Figures 8 and 9(b)).

5.2.3. Crustal Contribution of the Ascending EM-Derived Volatiles. Previous studies have shown that up to 6 km of sediments piled up and underwent significant heating subsidence associated with the early Cretaceous rifting in the Songliao basin [29, 31]. Buried materials consisted of carbonate sediments (CAR) and shallow organic metasediments (COS) [26, 27]. $\text{CO}_2/^3\text{He}$ ratios and C-He isotope values of the gas samples in the WMVF display obvious mixing evolution trends between the EM source and crustal components

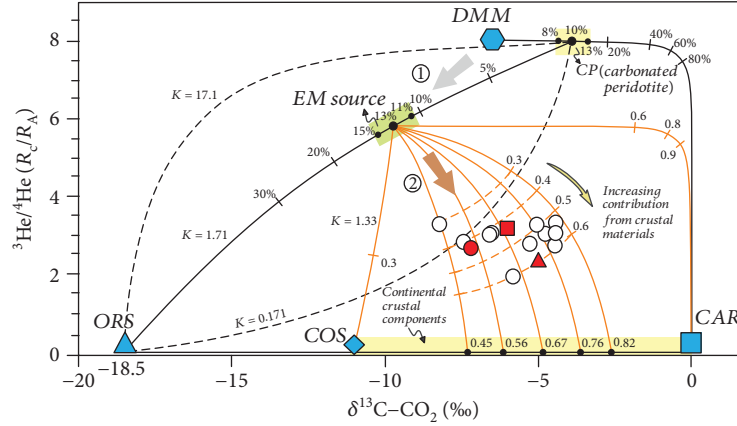


FIGURE 8: C-He isotope systematics showing a two-stage model for cold spring gases in WMVF. Stage 1: interactions between slab-derived melts (CAR and ORS) in MTZ and the depleted upper mantle (DMM); stage 2: the different proportions of crustal contribution (COS and CAR) during the ascending process of EM-derived volatiles. COS represents the continental organic metasediments.

TABLE 3: Reference values for associated parameters of DMM, CAR, ORS, and COS end members used in C-He isotope systematics.

End member	$\delta^{13}\text{C}_{\text{CO}_2}$ (‰)	C contents (ppm)	$^3\text{He}/^4\text{He}$ (R_A)	He contents (ppm)	$\text{CO}_2/{}^3\text{He}$ ($\times 10^9$)
DMM	-6.5 ^a	1920 ^b	8 ^a	0.0288 ^b	1.5 ^a
CAR	0 ^c	11400 ^d	0.05 ^e	0.00023 ^d	1000-100000 ^f
ORS	-18.5 ^g	12618 ^j	0.05 ^e	0.0667 ^j	1000-100000 ^f
COS	-11 ^h	Unknown	0.02 ⁱ	Unknown	0.1-100000 ^f

Data sources: ^a[46], ^b[37], ^c[53], ^d[59], ^e[68], ^f[62], ^g[65], ^h[69], and ⁱ[66]. ^jCalculated based on U-Th decay.

which consists of different proportions of COS and CAR (Figures 6(b) and 8). As indicated by the C-He isotope mixing calculation, the proportion of crustal components (including COS and CAR) ranges from 30% to 60% of the overall carbon budget of the EM source-derived volatiles (Figure 8). In this binary mixing model, continental carbonate sediments (CAR) represent 45% to 82% of the crustal components (Figure 8).

5.3. Genetic Model of Deep CO_2 Emissions in the Songliao Continental Rift System. C-He isotope systematics provide constraint on the source region of volatiles collected at the surface in the WMVF. Following the Pacific oceanic crust deep subduction scenario, we proposed a two-stage model to explain the evolution process of cold spring gases in the WMVF. Firstly, the interactions between the depleted mantle and carbonated silicate melts (CAR and ORS) derived from a stagnant Pacific oceanic slab in the mantle transition zone (MTZ) produce an enriched upper mantle beneath WMVF (Figure 9(b)); secondly, EM-derived initial volatiles underwent different proportions of crustal input, including carbonates (CAR) and organic metasediments (COS) in the continental crust during their arising process (Figures 6(b), 8, and 9(a)). Deep-fed CO_2 is emitted into the atmosphere through spring bubbles and diffusive soil CO_2 emissions in the adjacent areas (Figures 9(a)).

This model provides an integrated constraint on the source region of cold spring gases (e.g., He and C isotopes)

for further understanding the carbon cycling processes in the Songliao continental rift system beneath East Asia, which is supported by petrogenesis of potassic basalts erupted in 1721 AD [11–13] and evidence from seismic tomographic studies [14, 72]. The interactions between the MTZ-derived melts and the ambient upper mantle provide a plausible hypothesis to explain the lithospheric thinning, extensive continental rifting, Cenozoic intraplate basaltic volcanism, and magma-related degassing in East Asia (Figure 9(b)) [14, 16, 71].

6. Conclusions

Our modeling calculated results indicate that the average soil CO_2 flux in the Laoheishan volcano ($11.8 \text{ g m}^{-2} \text{ d}^{-1}$) is lower than that of the whole WMVF ($18.7 \text{ g m}^{-2} \text{ d}^{-1}$), which suggest weak degassing of the solidified underlying magma body beneath the Laoheishan volcano. On the basis of the C-He isotope mixing simulation results, we propose a two-stage model to constrain the provenance and evolution of volatiles in the WMVF. The first stage is concerned with the interactions between the depleted upper mantle (DMM) and the accumulated Pacific oceanic slab materials (CAR and ORS) in the MTZ and finally results in the formation of the enriched mantle source region (EM), which is considered as the primary source of cold spring gases in the WMVF. The second stage is related to the crustal contamination

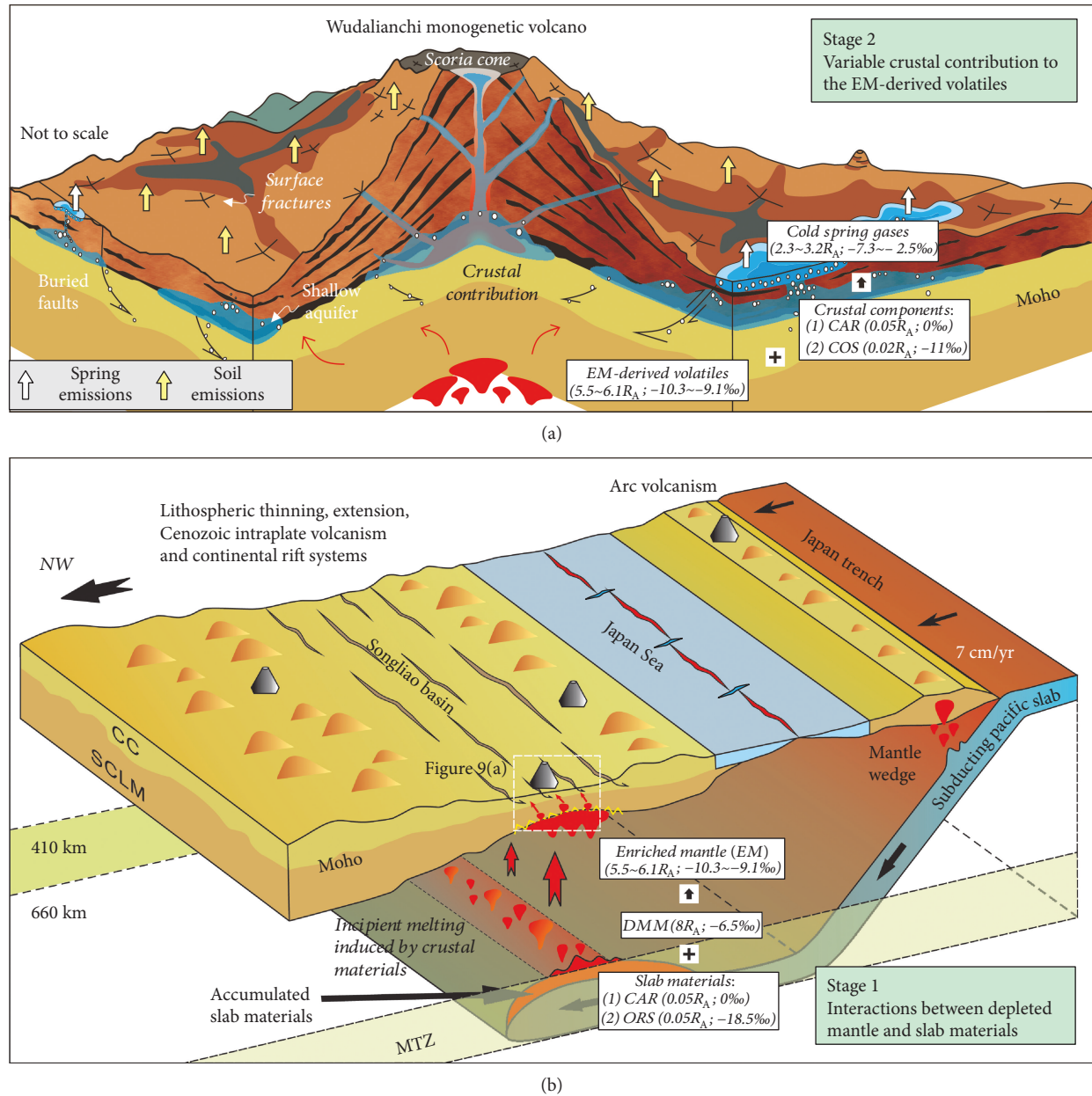


FIGURE 9: Genetic model of the cold spring gases in WMVF. (a) Crustal contribution to the EM-derived volatiles. (b) A schematic map shows the interactions between the depleted mantle and the slab materials in the MTZ. Abbreviations are as follows: MTZ: mantle transition zone; Moho: Mohorovičić discontinuity; SCLM: subcontinental lithospheric mantle; CC: continental crust.

(including continental organic metasediments and carbonates) when the CO_2 -dominated gases rise to the surface.

Data Availability

The chemical and C-He isotope data of spring gases used to support the findings of this study are included within the article and the supplementary material.

Conflicts of Interest

The authors declare that they have no conflicts of interest.

Acknowledgments

This work was funded by the Strategic Priority Research Program of the Chinese Academy of Sciences (Grant No. XDB26000000), the Key Research Project of Frontier Sciences of the Chinese Academy of Sciences (Grant No. QYZDY-SSW-DQC030), and the National Science Foundation of China (Grant Nos. 41572321 and 41702361). We thank Drs. Lihong Zhang and Yutao Sun for interpreting the soil flux data. Drs. Liwu Li, Zhongping Li, Li Du, Lantian Xing, and Hengliang Gao are acknowledged for help in analyzing the samples.

Supplementary Materials

The Supplementary Materials file provides additional tables/figures and data mentioned in the revised manuscript, including (1) measured soil CO₂ fluxes of whole WMVF (Table S1) and SE slope of the Laoheishan volcanic cone (Table S2), (2) chemical and C-He isotopic compositions of spring gases in this and previous studies (Table S3), (3) detailed reference values for associated parameters (Table S4) and results (Table S5 and S6) in C-He isotope systematics, and (4) detailed reference values for associated parameters (Table S7) and results (Table S8 and Figure S1) in the Nd-Mg isotope coupling calculation. (*Supplementary Materials*)

References

- [1] W. Hutchison, T. A. Mather, D. M. Pyle, J. Biggs, and G. Yirgu, "Structural controls on fluid pathways in an active rift system: a case study of the Aluto volcanic complex," *Geosphere*, vol. 11, no. 3, pp. 542–562, 2015.
- [2] H. Lee, J. D. Muirhead, T. P. Fischer et al., "Massive and prolonged deep carbon emissions associated with continental rifting," *Nature Geoscience*, vol. 9, no. 2, pp. 145–149, 2016.
- [3] J. D. Muirhead, S. A. Kattenhorn, H. Lee et al., "Evolution of upper crustal faulting assisted by magmatic volatile release during early-stage continental rift development in the East African Rift," *Geosphere*, vol. 12, no. 6, pp. 1670–1700, 2016.
- [4] S. Brune, S. E. Williams, and R. D. Müller, "Potential links between continental rifting, CO₂ degassing and climate change through time," *Nature Geoscience*, vol. 10, no. 12, pp. 941–946, 2017.
- [5] S. F. Foley and T. P. Fischer, "An essential role for continental rifts and lithosphere in the deep carbon cycle," *Nature Geoscience*, vol. 10, no. 12, pp. 897–902, 2017.
- [6] G. Tamburello, S. Pondrelli, G. Chiodini, and D. Rouwet, "Global-scale control of extensional tectonics on CO₂ earth degassing," *Nature Communications*, vol. 9, no. 1, article 4608, 2018.
- [7] T. O. Rooney, W. R. Nelson, L. Dosso, T. Furman, and B. Hanan, "The role of continental lithosphere metasomes in the production of HIMU-like magmatism on the Northeast African and Arabian plates," *Geology*, vol. 42, no. 5, pp. 419–422, 2014.
- [8] N. H. Sleep, "Stagnant lid convection and carbonate metasomatism of the deep continental lithosphere," *Geochemistry Geophysics Geosystems*, vol. 10, no. 11, article Q11010, 2009.
- [9] W. Hutchison, T. A. Mather, D. M. Pyle et al., "The evolution of magma during continental rifting: new constraints from the isotopic and trace element signatures of silicic magmas from Ethiopian volcanoes," *Earth and Planetary Science Letters*, vol. 489, pp. 203–218, 2018.
- [10] J. Liu, J. Han, and W. S. Fyfe, "Cenozoic episodic volcanism and continental rifting in Northeast China and possible link to Japan Sea development as revealed from K-Ar geochronology," *Tectonophysics*, vol. 339, no. 3–4, pp. 385–401, 2001.
- [11] T. Kuritani, J. I. Kimura, E. Ohtani, H. Miyamoto, and K. Furuyama, "Transition zone origin of potassic basalts from Wudalianchi volcano, Northeast China," *Lithos*, vol. 156–159, pp. 1–12, 2013.
- [12] H. C. Tian, W. Yang, S. G. Li, S. Ke, and Z. Y. Chu, "Origin of low $\delta^{26}\text{Mg}$ basalts with EM-I component: evidence for interaction between enriched lithosphere and carbonated asthenosphere," *Geochimica et Cosmochimica Acta*, vol. 188, pp. 93–105, 2016.
- [13] X. J. Wang, L. H. Chen, A. W. Hofmann et al., "Mantle transition zone-derived EM1 component beneath NE China: geochemical evidence from Cenozoic potassic basalts," *Earth and Planetary Science Letters*, vol. 465, pp. 16–28, 2017.
- [14] G. C. Richard and H. Iwamori, "Stagnant slab, wet plumes and Cenozoic volcanism in East Asia," *Physics of the Earth and Planetary Interiors*, vol. 183, no. 1–2, pp. 280–287, 2010.
- [15] W. Wei, J. O. S. Hammond, D. Zhao, J. Xu, Q. Liu, and Y. Gu, "Seismic evidence for a mantle transition zone origin of the Wudalianchi and Halaha volcanoes in Northeast China," *Geochemistry, Geophysics, Geosystems*, vol. 20, no. 1, pp. 398–416, 2019.
- [16] M. Zhang, Z. Guo, Y. Sano, Z. Cheng, and L. Zhang, "Stagnant subducted Pacific slab-derived CO₂ emissions: insights into magma degassing at Changbaishan volcano, NE China," *Journal of Asian Earth Sciences*, vol. 106, pp. 49–63, 2015.
- [17] M. Zhang, Z. Guo, J. Liu et al., "The intraplate Changbaishan volcanic field (China/North Korea): a review on eruptive history, magma genesis, geodynamic significance, recent dynamics and potential hazards," *Earth-Science Reviews*, vol. 187, pp. 19–52, 2018.
- [18] J. Du, S. Li, Y. Zhao, J. Ren, R. Sun, and H. Duanmu, "Geochemical Characteristics of Gases from the Wudalianchi Volcanic Area, Northeastern China," *Acta Geologica Sinica - English Edition*, vol. 73, no. 2, pp. 225–229, 1999.
- [19] Z. Shangguan, C. Zhao, and L. Gao, "Carbon isotopic compositions of the methane derived from magma at the active volcanic regions in China," *Acta Petrologica Sinica*, vol. 22, pp. 1458–1464, 2006.
- [20] Z. Shangguan and C. Wu, "Geochemical features of magmatic gases in the regions of dormant volcanos in China," *Acta Petrologica Sinica*, vol. 24, pp. 2638–2646, 2008.
- [21] X. Mao, Y. Wang, O. V. Chudaev, and X. Wang, "Geochemical evidence of gas sources of CO₂-rich cold springs from Wudalianchi, Northeast China," *Journal of Earth Science*, vol. 20, no. 6, pp. 959–970, 2009.
- [22] S. Xu, G. Zheng, S. Nakai, H. Wakita, X. Wang, and Z. Guo, "Hydrothermal He and CO₂ at Wudalianchi intra-plate volcano, NE China," *Journal of Asian Earth Sciences*, vol. 62, pp. 526–530, 2013.
- [23] Y. W. Zhao, N. Li, Q. C. Fan, H. Zou, and Y. G. Xu, "Two episodes of volcanism in the Wudalianchi volcanic belt, NE China: evidence for tectonic controls on volcanic activities," *Journal of Volcanology and Geothermal Research*, vol. 285, pp. 170–179, 2014.
- [24] L. Xiao and C. Wang, "Geologic features of Wudalianchi volcanic field, Northeastern China: implications for Martian volcanology," *Planetary and Space Science*, vol. 57, no. 5–6, pp. 685–698, 2009.
- [25] L. Zhang, X. Zhou, J. Ying et al., "Geochemistry and Sr-Nd-Pb-Hf isotopes of Early Cretaceous basalts from the Great Xinggan Range, NE China: implications for their origin and mantle source characteristics," *Chemical Geology*, vol. 256, no. 1–2, pp. 12–23, 2008.

- [26] C. Huang, G. J. Retallack, C. Wang, and Q. Huang, "Paleoatmospheric $p\text{CO}_2$ fluctuations across the Cretaceous–Tertiary boundary recorded from paleosol carbonates in NE China," *Palaeogeography Palaeoclimatology Palaeoecology*, vol. 385, pp. 95–105, 2013.
- [27] Y. Gao, D. E. Ibarra, C. Wang et al., "Midlatitude terrestrial climate of East Asia linked to global climate in the late cretaceous," *Geology*, vol. 43, no. 4, pp. 287–290, 2015.
- [28] T. L. Barry and R. W. Kent, "Cenozoic magmatism in Mongolia and the origin of central and east Asian basalts," in *Mantle Dynamics and Plate Interactions in East Asia Geodynamics*, M. F. J. Flower, S. L. Chung, C. H. Lo, and T. Y. Lee, Eds., pp. 347–364, American Geophysical Union, Washington, D. C., 1998.
- [29] Y. Wang and H. Chen, "Tectonic controls on the Pleistocene–Holocene Wudalianchi volcanic field (Northeastern China)," *Journal of Asian Earth Sciences*, vol. 24, no. 4, pp. 419–431, 2005.
- [30] J. Ren, K. Tamaki, S. Li, and Z. Junxia, "Late Mesozoic and Cenozoic rifting and its dynamic setting in Eastern China and adjacent areas," *Tectonophysics*, vol. 344, no. 3–4, pp. 175–205, 2002.
- [31] R. Zhang, Q. Wu, L. Sun, J. He, and Z. Gao, "Crustal and lithospheric structure of Northeast China from S-wave receiver functions," *Earth and Planetary Science Letters*, vol. 401, pp. 196–205, 2014.
- [32] H. U. Schmincke, *Volcanism*, Springer, Berlin, Heidelberg, 2004.
- [33] Z. Li, S. Ni, B. Zhang et al., "Shallow magma chamber under the Wudalianchi volcanic field unveiled by seismic imaging with dense array," *Geophysical Research Letters*, vol. 43, no. 10, pp. 4954–4961, 2016.
- [34] G. Chiodini, R. Cioni, M. Guidi, B. Raco, and L. Marini, "Soil CO_2 flux measurements in volcanic and geothermal areas," *Applied Geochemistry*, vol. 13, no. 5, pp. 543–552, 1998.
- [35] M. Zhang, Z. Guo, Y. Sano et al., "Magma-derived CO_2 emissions in the Tengchong volcanic field, SE Tibet: implications for deep carbon cycle at intra-continent subduction zone," *Journal of Asian Earth Sciences*, vol. 127, pp. 76–90, 2016.
- [36] M. Luo, H. Huang, P. Zhang, Q. Wu, and D. Chen, "Origins of gas discharging from the Qiangtang Basin in the northern Qinghai–Tibet Plateau, China: evidence from gas compositions, helium, and carbon isotopes," *Journal of Geochemical Exploration*, vol. 146, pp. 119–126, 2014.
- [37] L. Zhang, Z. Guo, Y. Sano et al., "Flux and genesis of CO_2 degassing from volcanic-geothermal fields of Gulu-Yadong rift in the Lhasa terrane, South Tibet: Constraints on characteristics of deep carbon cycle in the India-Asia continent subduction zone," *Journal of Asian Earth Sciences*, vol. 149, pp. 110–123, 2017.
- [38] A. J. Sinclair, "Selection of threshold values in geochemical data using probability graphs," *Journal of Geochemical Exploration*, vol. 3, no. 2, pp. 129–149, 1974.
- [39] G. Chiodini, S. Caliro, C. Cardellini, R. Avino, D. Granieri, and A. Schmidt, "Carbon isotopic composition of soil CO_2 efflux, a powerful method to discriminate different sources feeding soil CO_2 degassing in volcanic-hydrothermal areas," *Earth and Planetary Science Letters*, vol. 274, no. 3–4, pp. 372–379, 2008.
- [40] A. Caracausi, M. Paternoster, and P. M. Nuccio, "Mantle CO_2 degassing at Mt. Vulture volcano (Italy): relationship between CO_2 outgassing of volcanoes and the time of their last eruption," *Earth and Planetary Science Letters*, vol. 411, pp. 268–280, 2015.
- [41] Y. Zhan, G. Zhao, J. Wang, Q. Xiao, J. Tang, and I. I. Rokityansky, "Crustal electric conductivity structure for Wudalianchi volcanic cluster in the Heilongjiang province, China," *Acta Petrologica Sinica*, vol. 22, no. 6, pp. 1495–1502, 2006.
- [42] M. Ozima and F. A. Podosek, *Noble Gas Geochemistry*, Cambridge University Press, London, 1983.
- [43] R. F. Weiss, "Solubility of helium and neon in water and seawater," *Journal of Chemical & Engineering Data*, vol. 16, no. 2, pp. 235–241, 1971.
- [44] D. R. Hilton, "The helium and carbon isotope systematics of a continental geothermal system: results from monitoring studies at Long Valley caldera (California, U.S.A.)," *Chemical Geology*, vol. 127, no. 4, pp. 269–295, 1996.
- [45] T. H. E. Heaton and J. C. Vogel, "Gas concentrations and ages of groundwaters in Beaufort group sediments, South Africa," *Water South Africa*, vol. 5, no. 4, pp. 160–170, 1979.
- [46] Y. Sano and B. Marty, "Origin of carbon in fumarolic gas from island arcs," *Chemical Geology*, vol. 119, no. 1–4, pp. 265–274, 1995.
- [47] W. F. Giggenbach, Y. Sano, and H. Wakita, "Isotopic composition of helium, and CO_2 and CH_4 contents in gases produced along the New Zealand part of a convergent plate boundary," *Geochimica et Cosmochimica Acta*, vol. 57, no. 14, pp. 3427–3455, 1993.
- [48] R. Sun, Z. Pan, Y. Pan, and S. Yang, "Escaping gas He isotope assaying of the outcrop spring and study on the volcanic activity in Wudalianchi area," *Seismological Research of Northeast China*, vol. 24, no. 1, pp. 61–65, 2008.
- [49] D. R. Hilton, T. P. Fischer, and B. Marty, "Noble gases and volatile recycling at subduction zones," *Reviews in Mineralogy and Geochemistry*, vol. 47, no. 1, pp. 319–370, 2002.
- [50] C. Gautheron and M. Moreira, "Helium signature of the subcontinental lithospheric mantle," *Earth and Planetary Science Letters*, vol. 199, no. 1–2, pp. 39–47, 2002.
- [51] D. Hahm, D. R. Hilton, M. Cho, H. Wei, and K. R. Kim, "Geothermal He and CO_2 variations at Changbaishan intra-plate volcano (NE China) and the nature of the sub-continental lithospheric mantle," *Geophysical Research Letters*, vol. 35, no. 22, article L22304, 2008.
- [52] D. R. Hilton and H. Craig, "A helium isotope transect along the Indonesian archipelago," *Nature*, vol. 342, no. 6252, pp. 906–908, 1989.
- [53] J. Hoefs, *Stable Isotope Geochemistry*, Springer, Berlin Heidelberg, 2009.
- [54] J. M. de Moor, T. P. Fischer, Z. D. Sharp et al., "Gas chemistry and nitrogen isotope compositions of cold mantle gases from Rungwe Volcanic Province, southern Tanzania," *Chemical Geology*, vol. 339, pp. 30–42, 2013.
- [55] S. L. Klemperer, B. M. Kennedy, S. R. Sastry, Y. Makovsky, T. Harinarayana, and M. L. Leech, "Mantle fluids in the Karakoram fault: helium isotope evidence," *Earth and Planetary Science Letters*, vol. 366, pp. 59–70, 2013.
- [56] P. H. Barry, D. R. Hilton, T. P. Fischer, J. M. de Moor, F. Mangasini, and C. Ramirez, "Helium and carbon isotope systematics of cold 'mazuku' CO_2 vents and hydrothermal gases and fluids from Rungwe Volcanic Province, southern Tanzania," *Chemical Geology*, vol. 339, pp. 141–156, 2013.
- [57] Y. Sano, T. Tominaga, Y. Nakamura, and H. Wakita, " $^3\text{He}/^4\text{He}$ ratios of methane-rich natural gases in Japan," *Geochemical Journal*, vol. 16, no. 5, pp. 237–245, 1982.

- [58] Y. Sano and S. N. Williams, "Fluxes of mantle and subducted carbon along convergent plate boundaries," *Geophysical Research Letters*, vol. 23, no. 20, pp. 2749–2752, 1996.
- [59] M. C. Van Soest, D. R. Hilton, and R. Kreulen, "Tracing crustal and slab contributions to arc magmatism in the Lesser Antilles island arc using helium and carbon relationships in geothermal fluids," *Geochimica et Cosmochimica Acta*, vol. 62, no. 19–20, pp. 3323–3335, 1998.
- [60] A. M. Shaw, D. R. Hilton, T. P. Fischer, J. A. Walker, and G. E. Alvarado, "Contrasting He–C relationships in Nicaragua and Costa Rica: insights into C cycling through subduction zones," *Earth and Planetary Science Letters*, vol. 214, no. 3–4, pp. 499–513, 2003.
- [61] B. Marty and A. Jambon, " $C/{}^3He$ in volatile fluxes from the solid earth: implications for carbon geodynamics," *Earth and Planetary Science Letters*, vol. 83, no. 1–4, pp. 16–26, 1987.
- [62] R. K. O'Nions and E. R. Oxburgh, "Helium, volatile fluxes and the development of continental crust," *Earth and Planetary Science Letters*, vol. 90, no. 3, pp. 331–347, 1988.
- [63] H. Stephen and T. Stephen, *Solubilities of inorganic and organic compounds, binary systems (1), part 1*, Pergamon press, New York, 1963.
- [64] Y. Sano, J. I. Hirabayashi, T. Oba, and T. Gamo, "Carbon and helium isotopic ratios at Kusatsu-Shirane volcano, Japan," *Applied Geochemistry*, vol. 9, no. 4, pp. 371–377, 1994.
- [65] J. Cook-Kollars, G. E. Bebout, N. C. Collins, S. Angiboust, and P. Agard, "Subduction zone metamorphic pathway for deep carbon cycling: I. Evidence from HP/UHP metasedimentary rocks, Italian Alps," *Chemical Geology*, vol. 386, pp. 31–48, 2014.
- [66] J. E. Lupton, "Terrestrial inert gases isotope tracer studies and clues to primordial components in the mantle," *Annual Review of Earth and Planetary Sciences*, vol. 11, no. 1, pp. 371–414, 1983.
- [67] R. J. Poreda, A. W. A. Jeffrey, I. R. Kaplan, and H. Craig, "Magnetic helium in subduction-zone natural gases," *Chemical Geology*, vol. 71, no. 1–3, pp. 199–210, 1988.
- [68] J. N. Andrews, "The isotopic composition of radiogenic helium and its use to study groundwater movement in confined aquifers," *Chemical Geology*, vol. 49, no. 1–3, pp. 339–351, 1985.
- [69] J. Hoefs and M. Frey, "The isotopic composition of carbonaceous matter in a metamorphic profile from the Swiss Alps," *Geochimica et Cosmochimica Acta*, vol. 40, no. 8, pp. 945–951, 1976.
- [70] R. Dasgupta, M. M. Hirschmann, and A. C. Withers, "Deep global cycling of carbon constrained by the solidus of anhydrous, carbonated eclogite under upper mantle conditions," *Earth and Planetary Science Letters*, vol. 227, no. 1–2, pp. 73–85, 2004.
- [71] I. Safonova, S. Maruyama, and K. Litasov, "Generation of hydrous-carbonated plumes in the mantle transition zone linked to tectonic erosion and subduction," *Tectonophysics*, vol. 662, pp. 454–471, 2015.
- [72] D. Zhao, S. Maruyama, and S. Omori, "Mantle dynamics of Western Pacific and East Asia: insight from seismic tomography and mineral physics," *Gondwana Research*, vol. 11, no. 1–2, pp. 120–131, 2007.

Research Article

Degassing and Cycling of Mercury at Nisyros Volcano (Greece)

A. L. Gagliano ¹, **S. Calabrese** ^{1,2}, **K. Daskalopoulou** ^{2,3}, **J. Cabassi**^{4,5}, **F. Capecchiacci**^{4,5}, **F. Tassi**^{4,5}, **S. Bellomo**¹, **L. Brusca**¹, **M. Bonsignore**⁶, **S. Milazzo**², **G. Giudice**¹, **L. Li Vigni** ¹, **F. Parello**² and **W. D'Alessandro** ¹

¹Istituto Nazionale di Geofisica e Vulcanologia, Sezione di Palermo, Via U. La Malfa 153, 90146 Palermo, Italy

²University of Palermo, Dip. Scienze della Terra e del Mare, Via Archirafi 36, 90123 Palermo, Italy

³National and Kapodistrian University of Athens, Dept. of Geology and Geoenvironment, Panestimioupolis, 15784, Ano Ilissia, Greece

⁴University of Florence, Dip. Scienze della Terra, Via La Pira 4, 50121 Florence, Italy

⁵Consiglio Nazionale delle Ricerche, IGG, Via La Pira 4, 50121 Florence, Italy

⁶Consiglio Nazionale delle Ricerche, IAMC, UOS di Capo Granitola, via del Mare 3, 91021 Campobello di Mazara (TP), Italy

Correspondence should be addressed to S. Calabrese; sergio.calabrese@gmail.com

Received 7 February 2019; Revised 6 May 2019; Accepted 1 July 2019; Published 14 August 2019

Guest Editor: Guodong Zheng

Copyright © 2019 A. L. Gagliano et al. This is an open access article distributed under the Creative Commons Attribution License, which permits unrestricted use, distribution, and reproduction in any medium, provided the original work is properly cited.

Nisyros Island (Greece) is an active volcano hosting a high-enthalpy geothermal system. During June 2013, an extensive survey on Hg concentrations in different matrices (fumarolic fluids, atmosphere, soils, and plants) was carried out at the Lakki Plain, an intracaldera area affected by widespread soil and fumarolic degassing. Concentrations of gaseous elemental mercury (GEM), together with H₂S and CO₂, were simultaneously measured in both the fumarolic emissions and the atmosphere around them. At the same time, 130 samples of top soils and 31 samples of plants (*Cistus creticus* and *salvifolius* and *Erica arborea* and *manipuliflora*) were collected for Hg analysis. Mercury concentrations in fumarolic gases ranged from 10,500 to 46,300 ng/m³, while Hg concentrations in the air ranged from high background values in the Lakki Plain caldera (10–36 ng/m³) up to 7100 ng/m³ in the fumarolic areas. Outside the caldera, the concentrations were relatively low (2–5 ng/m³). The positive correlation with both CO₂ and H₂S in air highlighted the importance of hydrothermal gases as carrier for GEM. On the other hand, soil Hg concentrations (0.023–13.7 µg/g) showed no significant correlations with CO₂ and H₂S in the soil gases, whereas it showed a positive correlation with total S content and an inverse one with the soil pH, evidencing the complexity of the processes involving Hg carried by hydrothermal gases while passing through the soil. Total Hg concentrations in plant leaves (0.010–0.112 µg/g) had no direct correlation with soil Hg, with *Cistus* leaves containing higher values of Hg with respect to *Erica*. Even though GEM concentrations in the air within the caldera are sometimes orders of magnitude above the global background, they should not be considered dangerous to human health. Values exceeding the WHO guideline value of 1000 ng/m³ are very rare (<0.1%) and only found very close to the main fumarolic vents, where the access to tourists is prohibited.

1. Introduction

Volcanoes and geothermal areas are natural sources of environment pollutants potentially dangerous for human health. Paroxysmal eruptions and passive degassing emit huge amounts of gases such as CO₂, H₂S, SO₂, and HF, including gaseous elemental mercury (GEM) [1–4]. Trace metals, being associated with uprising gases, are usually found at consider-

able concentrations in hydrothermal fluids [5]. Even at very low concentrations, they can have a strong impact on the atmosphere and hydrosphere and consequently on the biosphere [6].

Among the volcanic trace volatile elements, mercury (Hg) is one of the most environmentally significant [7] because of its extreme mobility and toxicity [8]. The biogeochemistry of Hg is extremely complex due to the exchanges

between atmospheric, terrestrial, and marine pools [9]. These processes are mainly driven by microbial activity, dark abiotic and photochemical reactions affecting Hg speciation and bioaccumulation [10]. It is emitted in several forms: elemental (metallic) Hg and inorganic and organic Hg compounds. Metallic Hg (Hg^0) is highly volatile due to its high vapour pressure and may experience long-range transport in the air due to its relatively long half-life in the atmosphere (1–2 years [11]). Monovalent and divalent Hg are both soluble in water; divalent Hg (Hg^{II}) is more stable and common in the environment than monovalent (Hg^{I}). This form also may undergo complexation, precipitation with inorganic ligands, and sorption onto the soil matrix. The toxicological properties of Hg for the environment and human health depend on the physical and chemical form in which it occurs. Hg vapours, for example, are very dangerous if inhaled, due to their ability to reach the lungs causing pulmonary oedema, pain, and peeling of the respiratory epithelium of the bronchi [12, 13].

Mercury, as a constituent of volcanic and geothermal fluids [14, 15], is discharged in water and released into the atmosphere as Hg^0 being associated with reducing noncondensable gases [16, 17].

In the last decades, many authors underlined the correlation between Hg and H_2S in discharged hydrothermal fluids (e.g., [18]), as testified by the formation of solid cinnabar (HgS) at the fumarolic vents. Hydrogen sulphide is a toxic pollutant; it is corrosive and poses severe concerns for human health [19, 20].

Nisyros Island is a quiescent volcano releasing hydrothermal gases from several fumarolic emissions and also diffusively through the soil. The hydrothermal fluids of Nisyros are rich in H_2S [21–23], and their diffuse emission creates an extremely acidic environment in soils affected by the hydrothermal degassing [24, 25].

Here, we report the results of an extensive survey on Hg concentrations in different media (fumarolic fluids, atmosphere, soils, and plants) at the Lakki Plain, an area intensively impacted by hydrothermal degassing on Nisyros Island. Even though the geogenic degassing of Nisyros Island has been greatly studied, most of the research conducted was mainly concentrated on the gaseous C compounds and the noble gas composition of the fumaroles. The significance and novelty of this work, with respect to the existing literature, is to add Hg on the puzzle. Furthermore, to the best of our knowledge, this is so far the first study that attempts to define the Hg cycling in an active volcanic/geothermal system by taking into consideration such a great variety of media. Gaseous elemental mercury (GEM) concentrations, together with H_2S and CO_2 in soil gas, were determined in both the fumarolic emissions and ambient air. Similarly, the relationships between fumarolic activity and Hg in the soils were investigated, comparing Hg concentrations to temperature, pH, hydrothermal gas, and the elemental concentrations of C, N, and S measured in the same soils. Leaves of two plant species (*Cistus* and *Erica*) were also collected and their Hg and S contents determined. Finally, a preliminary estimation of the Hg output to the atmosphere from the hydrothermal area of Nisyros was carried out.

2. Study Area

Nisyros Island (Figure 1) is a quiescent volcano located in the easternmost volcanic group of the South Aegean Active Volcanic Arc (SAAVA [26]). The volcanic edifice developed in the last 200 ka through five distinguished stages [27, 28] led to the formation of a caldera of about 4 km in diameter. The most recent activity consisted of hydrothermal explosions forming several phreatic craters, the last of which occurred in 1887 [27]. The Lakki Plain (Figure 1) represents the southeastern remnants of the calderic depression after the emplacement of a series of volcanic domes filling up the northwestern part. Fumarolic fields are currently active in this area, mainly within the hydrothermal craters strongly controlled by fracturing along the main NW- and NE-trending active fault systems [29], and are fed by a >1000 m deep hydrothermal system having a temperature of 300–350°C [30, 31]. The hydrothermal craters form three main groups (Figure 1): the oldest comprises the Kaminakia craters, the second consists of the Stefanos crater, whereas the third corresponds to the youngest area where a postcalderic dome (Lofos) is placed and includes the Phlegeton, Megalos Polybotes, and Mikros Polybotes craters [31, 32]. Water vapour (91–99%) is the main component of the fumarolic fluids, followed by CO_2 and H_2S [22]. The estimated total CO_2 and H_2S outputs are close to 1 kg/s and <0.3 kg/s, respectively [31, 32].

3. Materials and Methods

After the collection of few samples in 2009 and 2010, a multidisciplinary field campaign was carried out on June 2013 at the Lakki Plain, where soil gases, soils, and vegetation were sampled, and Hg, H_2S , and CO_2 concentrations in the air were measured.

A total of 106 soil gas samples was collected at the Lakki Plain mostly in the fumarolic areas of Kaminakia, Stefanos, Mikros Polybotes, and Phlegeton craters and in the areas of Ramos and Lofos (Figure 1). Soil gases were sampled at 50 cm depth using a Teflon tube of 5 mm ID equipped with a tight plastic syringe to avoid air contamination. Soil gas sampling sites were the same as those of the top soils. H_2S and CO_2 analysis was carried out on the overpressurised vials using a Micro GC MSHA CP-4900 having 3 independent modules. Soil temperature was measured at 20 cm depth by using thermal probes and a digital thermometer; these measurements were carried out 10–15 min after the insertion of the thermal probe in the soil in order to achieve thermal equilibrium.

Top soils were collected from the first 3 cm depth at 130 spots at the Lakki Plain. Soil samples were dried, homogenized, and powdered. An aliquot of the homogenized samples was used for the analysis of total Hg, which was performed using a DMA-80 analyser (an atomic absorption spectrophotometer, Milestone, Wesleyan University, Middletown, CT, USA). About 10 mg of dry soil was loaded into specific nickel boats and analysed according to the US-EPA 7473 method [33]. Accuracy was checked by running replicates of the reference materials NCSDC7701

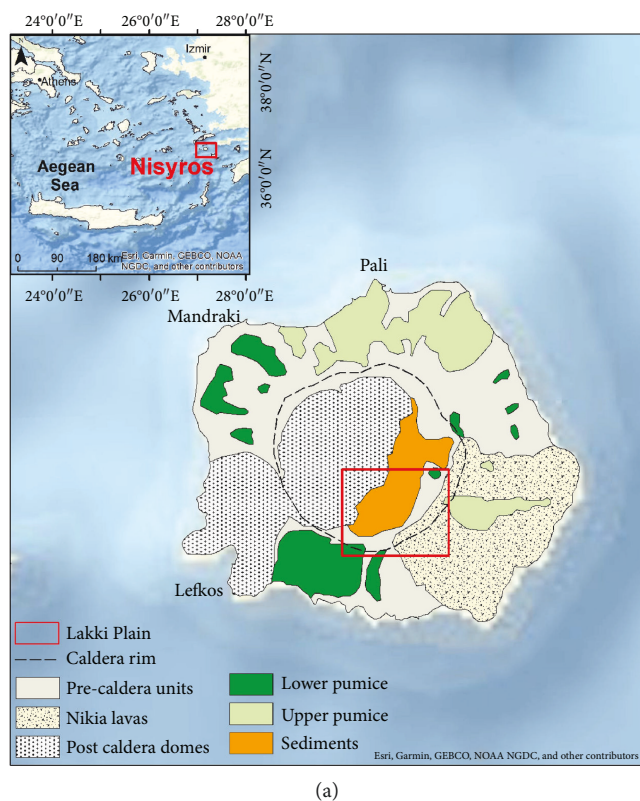


FIGURE 1: Simplified geologic map of the island of Nisyros (a) and sampling areas within the Lakki Plain (b). A = Stefanos crater; B = Kaminakia crater; C = Ramos fumaroles; D = Phlegeton crater; E = Mikros Polybotes; F = Lofos dome.

(0.015 ± 0.006 mg/kg) and MESS3 (0.091 ± 0.009 mg/kg). Bench quality control material was measured at the start of each analytical run (set of 15 samples) for quality assurance and control. The measured values were, on average, within $\pm 8\%$ of the recommended values.

Total C, N, and S were analysed on powdered samples by elemental analysis (Elementar Vario EL Cube, Hanau). The technique is based on “purge and trap” separation (C, N, and S), following high-temperature incineration (induction furnace) in a pure oxygen atmosphere and at a constant temperature exceeding 1150°C for the sample, with WO_3 as catalyst. Helium was used as the carrier gas. Detection limits were 0.04 wt% for C and 0.003 wt% for N and S.

Soil pH values were measured using a specific combination electrode on soil suspensions that were made with deionized water with a soil/solution weight ratio of 1/2.5 [34].

A passive biomonitoring survey was carried out in order to determine the total Hg content in two local spontaneous plants and evaluate the possible contamination by Hg gas emissions. The collected vegetation consisted of 17 leaf samples of the genus *Erica* (*manipuliflora* and *arborea* spp.) and 14 leaf samples of the genus *Cistus* (*creticus* and *salvifolius* spp.). Both the plant species have evergreen leaves and grow widespread as small shrubs (10–50 cm height) in the Lakki Plain where soil degassing is at a lower level. To enhance the interpretation, soil samples were collected along a buffer area of few tens of centimetres close to the sampled plants.

One sample of vegetation and soil was collected outside the caldera as local background blank. The sampling sites and the sampled plants were chosen randomly; for each site, three separate plants in a buffer area of 1.5 m were sampled and merged to obtain the final sample. Vegetation samples were dried in the oven at temperature below 40°C and powdered by agate planetary ball mill to avoid contamination. Analysis of total Hg was made with the use of PerkinElmer Inc. SMS 100 Solid Mercury Analysis. Each sample was heated in an oxygen-rich furnace to release all the decomposition products including Hg. These products were then carried in a stream of O_2 to a catalytic section of the furnace; halogens and/or oxides of N and S were trapped on the catalyst. The remaining vapour was then carried to an amalgamation cell that selectively trapped Hg. After the system was flushed with O_2 to remove any remaining gas or decomposition products, the amalgamation cell was rapidly heated, releasing Hg vapour. Flowing O_2 carried the Hg vapour through an absorbance cell positioned in the light path of a single wavelength atomic absorption spectrophotometer. Absorbance was measured at the 253.7 nm wavelength as a function of the Hg concentration in the sample.

Collection of total gaseous mercury (TGM) was performed with gold-coated bead traps (Au traps), through which atmospheric air was pumped at flow rates between 0.5 and 0.6 L/min [35] over collection periods ranging from 2 to 60 min. At three fumaroles, the gas was collected downstream of a vapour condenser sucking with a

graduated 100 mL syringe and sent to the same Au traps through a three-way valve [36]. The collected Hg was then measured by cold vapour atomic fluorescence spectrometry (CVAFS), based on the conventional thermal-desorption amalgamation technique (relative standard deviation < 15%; EPA Method IO-5; [33, 35, 37]). The results obtained were multiplied by the sampling volume and expressed in ng/m^3 .

The simultaneous real-time measurements of gaseous elemental mercury (GEM), CO_2 , H_2S , and meteorological parameters (air temperature, pressure, and relative humidity) were carried out by coupling portable instruments (similarly to what was proposed by [20]). GEM was measured with a Lumex® RA-915M, which is an atomic absorption spectrometer with a Zeeman effect with high-frequency modulation of light polarization (ZAAS-HFMLP). The separation of the spectral lines (at $\lambda = 254 \text{ nm}$) is operated by a permanent external magnetic field, into which a source of radiation (Hg lamp) is placed [38, 39]. The Zeeman background correction and the multipath analytical cell provide high selectivity and sensitivity [39]. The instrument operates at a flow rate of 10 L/min, whereas its rechargeable battery allows up to 8 h of continuous measurements. The detection limit is 2 ng/m^3 , while the accuracy of the method is 20% from 2 to $50,000 \text{ ng/m}^3$ [38, 39]. The remaining parameters were measured with a Multi-GAS analyser manufactured by INGV-Palermo. Atmospheric gas was drawn into the sampler with an air pump at 1.2 L/min through a $1 \mu\text{m}$ Teflon membrane particle filter and was pumped through a $\text{CO}_2/\text{H}_2\text{O}$ gas detector (Licor LI-840 NDIR closed-path spectrometer) and a series of electrochemical sensors for SO_2 (0–200 ppm; 3ST/F electrochemical sensor by City Technology Ltd.) and H_2S (0–50 ppm; EZ3H electrochemical sensor by City Technology Ltd.) detection. The sensors were housed in a weather-proof box mounted on a backpack frame and were calibrated, before and after fieldwork, with standard calibration gases (200 ppm SO_2 , 50 ppm H_2S , and 3014 ppm CO_2) mixed with ultrapure nitrogen to provide a range of desired concentrations [4, 40].

The spatial coordinates for each concentration value were simultaneously acquired through a GPS signal. All instruments were synchronized and set to high-frequency acquisition (every two seconds: 0.5 Hz). Measurements were carried out along four (Polybotes, Kaminakia, Stefanos, and Lofos) transect walks (about 15 km path, with a mean speed of 1.5 km/h) across the Lakki Plain caldera. The raw data have been processed by a dedicated software (RatioCalc [41]) that allows a derivation of mass ratios of various compounds (e.g., $\text{CO}_2/\text{H}_2\text{S}$, GEM/CO_2 , and $\text{GEM}/\text{H}_2\text{S}$).

Dataset from the gas soil and air surveys were used to define the threshold values of Hg, H_2S , and CO_2 . Data were processed following Sinclair's portioning method extracting the main populations [42]. This method consists in the definition of single populations through the inflection points (main populations) or changes in direction (secondary populations) of the curvature on the probability plot by visual analysis. Finally, data were plotted by using the GIS platform; distribution maps were drawn and ranked according to the identified populations.

4. Results

4.1. Fumarolic Gases and Atmosphere. In 2009, TGM was measured with Au traps in the atmosphere at 9 sampling sites at different distances from the main fumarolic vents. These sampling sites were previously investigated by D'Alessandro et al. [43] measuring H_2S concentrations in the atmosphere with passive samplers. The traps were placed in a range of distance always longer than 10 m and up to about 2 km from the fumarolic vent. Mercury values ranged from 9.4 to 420 ng/m^3 (Table 1). Although not directly comparable due to the different and sometimes not overlapping measuring time intervals (2–60 min for TGM and 4 hours to 5 days for H_2S), the two datasets show a positive correlation (Figure 2), with the highest values close to the fumaroles and the lowest on the caldera rim.

In 2010, further 5 measurements with Au traps were performed. Two measurements were made in the atmosphere at less than 1 m far from the two main fumarolic vents and gave concentrations of 2360 and 4530 ng/m^3 (Table 1). Three fumarolic vents were investigated by performing measurements on the undiluted hydrothermal fluid collected at the outlet of a condenser; results provided values from 10,500 to $46,300 \text{ ng/m}^3$ (Table 1). The composition of the contemporaneously collected gases was published by [44].

In 2013, GEM measured with Lumex® gave atmospheric concentrations from 2 to 7132 ng/m^3 . Values measured with the Multi-GAS ranged from $393 \mu\text{mol/mol}$, which is the background atmospheric value, up to saturation of the sensor ($\sim 4000 \mu\text{mol/mol}$) for CO_2 , from $0.2 \mu\text{mol/mol}$ up to saturation of the sensor ($\sim 60 \mu\text{mol/mol}$) for H_2S , and from 0.39 to $1.34 \mu\text{mol/mol}$ for SO_2 . Saturated values, about 0.1% for CO_2 and 1.6% for H_2S , were not considered for Hg/CO_2 and $\text{Hg}/\text{H}_2\text{S}$ calculations.

4.2. Soils. All parameters measured in the soil samples of the fumarolic areas of the Lakki Plain are shown in Table 2. Total Hg ranged from 0.023 to $13.7 \mu\text{g/g}$ of dry soil. Soil temperatures measured at 20 cm depth varied between 25.5 and 100°C , while concentrations of H_2S and CO_2 at 50 cm depth ranged from <0.001 to 17.8% vol and from 0.28 to 75.3% vol, respectively. Elemental C, N, and S contents in the soil were in the range 0.06–2.63, 0.004–0.23, and 0.014–56.3 weight %, respectively. Soil pH varied from 0.71 to 7.30.

4.3. Plants. Total Hg concentrations in the leaves collected from the Lakki Plain are summarized in Table 3. Data analysis showed the Hg range from 0.014 to $0.066 \mu\text{g/g}$ for *Erica* leaves and from 0.010 to $0.112 \mu\text{g/g}$ for *Cistus* leaves. The Hg concentrations in the soils sampled near the plants vary from 0.045 to $0.619 \mu\text{g/g}$ with a pH ranging from 4.21 to 5.55 (Table 2). The highest pH value is 7.30 and was measured outside the caldera; the value is representative of the local background for the soils collected close to the plants (Table 2).

5. Discussion

5.1. Mercury in the Fumarolic Fluids of Nisyros. Analyses of Hg directly on fumarolic fluids have rarely been performed.

TABLE 1: Total gaseous mercury (TGM) measured with Au traps in the atmosphere and in hydrothermal fluids at Nisyros.

Sample		Date (dd/mm/yyyy)	Time (min)	Flux (dm ³ /min)	Volume (m ³)	TGM (ng/m ³)
Stefanos 1	(4)	31/08/2009	5	0.5	0.0025	266
Stefanos 2	(5)	31/08/2009	5	0.5	0.0025	163
Emporio	(24)	01/09/2009	50	0.5	0.025	17.3
Volcano Cafe	(8)	01/09/2009	30	0.5	0.015	54.1
Polybotes bottom	(2)	02/09/2009	2	0.5	0.0010	222
Polybotes rim	(3)	02/09/2009	5	0.5	0.0025	133
Kaminakia	(9)	03/09/2009	5	0.5	0.0025	420
Phlegeton	(1)	04/09/2009	5	0.5	0.0025	188
Nikia	(19)	06/09/2009	60	0.6	0.036	9.4
Phlegeton		31/08/2010	5	0.5	0.0025	4530
Kaminakia		31/08/2010	5	0.5	0.0025	2360
AM fumarole		31/08/2010	n.a.	n.a.	0.00025	46,300
K6 fumarole		31/08/2010	n.a.	n.a.	0.0002	41,200
PP9S fumarole		31/08/2010	n.a.	n.a.	0.0002	10,500

Sampling sites of 2009 and IDs in brackets are the same as in [43]; fumaroles sampled in 2010 are the same as in [44]. n.a. = not applicable.

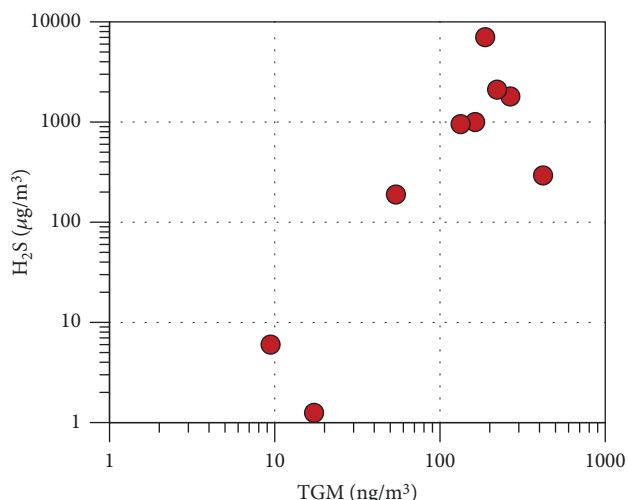


FIGURE 2: Total gaseous mercury in the atmosphere vs. atmospheric H₂S concentrations. H₂S data from [43].

The values reported in literature related to several fumaroles worldwide [3, 35, 45–49] cover a broad range from 1400 to 1,828,000 ng/m³ (Table 4). The values resulting from the three fumaroles sampled at Nisyros fall within this range. Correlating the obtained Hg values with the major composition of the fumarolic gases [44], Hg/H₂S and Hg/CO₂ ratios ranging from 0.36×10^{-7} to 3.3×10^{-7} and from 0.76×10^{-8} to 3.5×10^{-8} , respectively, were observed. The results obtained are coherent with values provided by other fumarolic fields at world scale (Table 4).

The measured Hg/H₂S and Hg/CO₂ ratios should be regarded as lower limit values since water soluble Hg^{II} species plausibly are lost within the fumarolic condensate collected by the sampling device. As evidenced in previous studies, the lost Hg fraction could represent a significant part of the total emitted Hg. Bagnato et al. [49] suggested that up to 70% of the total Hg emitted from the Bocca Grande (BG)

fumarole (Phlegrean Fields, southern Italy) remained in the collected condensate. However, of the 70 fumarolic samples in which Nakagawa [36, 45, 46] measured Hg both in the gas and in the condensed vapour, only in 8 of the samples was the Hg found in the condensed fraction that represented more than 20% of the total. Nevertheless, further studies will be necessary to ascertain the quantity of Hg lost in the condensed steam in the fumaroles of Nisyros.

5.2. Mercury in the Atmosphere of the Lakki Plain Area. Background values of atmospheric GEM in pristine unpolluted areas in the northern hemisphere are below 2 ng/m³, though a decreasing trend in the last decades was recognized [50]. In volcanic/geothermal areas, measured values are often significantly higher than the natural background (tens to hundreds of ng/m³, Table 5). This holds true also for the fumarolic area of the Lakki Plain at Nisyros both for the point measurements with Au traps and for measurements performed along transects with Lumex®.

The data acquired in the air with the Lumex® and Multi-GAS were plotted as described by Sinclair [42] and are shown in Figure 3. The CO₂ probability plot (Figure 3(a)) identifies three main populations (A, B, and C). The A population comprises 64.6% of the data with values ranging from 392 to 431 ppm and refers to the local atmospheric CO₂ background, which is close to the global atmospheric value of unpolluted air in 2013 (395 ppm [51]). Population B (33.3% of the data; CO₂ 431–561 ppm) is the population with CO₂ level slightly higher than average atmospheric air, probably due to diffuse soil degassing. Population C (2.1% of the data) includes the highest values (up to >4000 ppm), indicating a significant fumarolic CO₂ contribution to the atmosphere.

Based on the probability plot (Figure 3(b)), the H₂S dataset can be divided into four populations: A includes very low H₂S concentrations (<0.47 ppm, 5% of the values); B population with values from 0.47 to 2.11 ppm (50% of the data) indicating a slight fumarolic contribution; C

TABLE 2: Analytical composition of soils and soil gases at the Lakki caldera.

Site	E	N	Hg ($\mu\text{g/g}$)	N (%)	C (%)	S (%)	pH	H ₂ S (%)	CH ₄ (%)	CO ₂ (%)	T ($^{\circ}\text{C}$ @ 20 cm)
1*	518465	4049840	0.023	n.d.	n.d.	0.014	7.30	n.d.	n.d.	n.d.	n.m.
Mandraki	512418	4051816	0.039	n.d.	n.d.	n.d.	n.m.	n.d.	n.d.	n.d.	n.m.
2*	515026	4047948	0.18	n.d.	n.d.	1.319	4.60	n.d.	n.d.	n.d.	n.m.
3*	515008	4047754	0.40	n.d.	n.d.	0.728	5.20	n.d.	n.d.	n.d.	n.m.
4*	514836	4047603	0.58	n.d.	n.d.	0.723	4.74	n.d.	n.d.	n.d.	n.m.
5*	514702	4047912	0.40	n.d.	n.d.	0.524	4.70	n.d.	n.d.	n.d.	n.m.
6*	514617	4048285	0.40	n.d.	n.d.	0.392	5.55	n.d.	n.d.	n.d.	n.m.
7*	514608	4048481	0.37	n.d.	n.d.	0.306	4.95	n.d.	n.d.	n.d.	n.m.
8*	514541	4048566	0.49	n.d.	n.d.	0.786	4.86	n.d.	n.d.	n.d.	n.m.
9*	514659	4048676	0.54	n.d.	n.d.	0.451	4.21	n.d.	n.d.	n.d.	n.m.
10*	514830	4048652	0.14	n.d.	n.d.	1.049	4.80	n.d.	n.d.	n.d.	n.m.
11*	514861	4048610	0.21	n.d.	n.d.	1.115	5.02	n.d.	n.d.	n.d.	n.m.
12*	514979	4048382	0.18	n.d.	n.d.	0.575	5.16	n.d.	n.d.	n.d.	n.m.
13*	515081	4048259	0.15	n.d.	n.d.	1.155	4.92	n.d.	n.d.	n.d.	n.m.
14*	515130	4048399	0.25	n.d.	n.d.	0.741	5.31	n.d.	n.d.	n.d.	n.m.
15*	515210	4048719	0.21	n.d.	n.d.	0.764	5.48	n.d.	n.d.	n.d.	n.m.
16*	515402	4048152	0.36	n.d.	n.d.	0.666	4.87	n.d.	n.d.	n.d.	n.m.
17*	515296	4048377	0.64	n.d.	n.d.	0.426	5.04	n.d.	n.d.	n.d.	n.m.
N-St-1	514990	4048141	0.28	n.d.	n.d.	9.215	2.42	n.d.	n.d.	n.d.	n.m.
N-St-3	515020	4048123	0.39	n.d.	n.d.	1.643	2.66	n.d.	n.d.	n.d.	n.m.
N-St-5	515050	4048108	1.57	n.d.	n.d.	7.278	2.70	n.d.	n.d.	n.d.	n.m.
N-St-7	515096	4048083	1.28	n.d.	n.d.	8.566	2.58	n.d.	n.d.	n.d.	n.m.
N-St-9	515156	4048052	0.42	n.d.	n.d.	6.960	2.07	n.d.	n.d.	n.d.	n.m.
N-St-10	515131	4048186	0.29	n.d.	n.d.	3.988	2.31	n.d.	n.d.	n.d.	n.m.
N-St-11	515119	4048163	0.25	n.d.	n.d.	2.415	2.97	n.d.	n.d.	n.d.	n.m.
N-St-13	515092	4048121	1.25	n.d.	n.d.	4.263	3.04	n.d.	n.d.	n.d.	n.m.
N-St-15	515048	4048049	1.77	n.d.	n.d.	6.231	2.71	n.d.	n.d.	n.d.	n.m.
N-St-17	515032	4048046	1.25	n.d.	n.d.	9.823	2.65	n.d.	n.d.	n.d.	n.m.
N-St-19	515015	4047998	0.81	n.d.	n.d.	17.844	1.92	n.d.	n.d.	n.d.	n.m.
N-St-21	514998	4047968	0.31	n.d.	n.d.	7.576	2.63	n.d.	n.d.	n.d.	n.m.
N-St-23	515115	4048009	0.39	n.d.	n.d.	11.536	2.00	n.d.	n.d.	n.d.	n.m.
N-St-24	515160	4048086	0.61	n.d.	n.d.	10.849	2.13	n.d.	n.d.	n.d.	n.m.
N-St-27	515021	4048167	0.20	n.d.	n.d.	6.597	2.12	n.d.	n.d.	n.d.	n.m.
N-St-28	514958	4048098	0.31	n.d.	n.d.	4.751	2.05	n.d.	n.d.	n.d.	n.m.
023 A	514689	4048508	1.59	0.053	0.800	8.447	1.87	10.28	0.092	47.35	n.m.
024 A	514677	4048516	0.72	0.024	0.261	0.869	2.79	17.75	0.15	75.27	n.m.
025 A	514663	4048529	1.78	0.021	0.421	2.569	1.96	14.93	0.13	64.31	n.m.
026 A	514652	4048510	0.15	0.018	0.060	0.779	2.98	7.63	0.083	45.21	n.m.
027 A	514667	4048507	0.23	0.027	0.103	1.632	2.92	10.20	0.11	53.84	n.m.
028 A	514695	4048526	0.21	0.035	0.097	8.916	1.14	6.82	0.067	35.73	n.m.
029 A	514706	4048510	0.71	0.011	0.070	3.492	2.77	n.d.	n.d.	n.d.	n.m.
030 A	514661	4048504	0.34	0.013	0.328	1.245	2.60	17.83	0.15	75.22	n.m.
031 A	514644	4048505	1.48	0.009	0.074	6.968	2.02	7.01	0.073	38.55	n.m.
032 A	514635	4048488	0.33	0.013	0.095	1.986	2.99	5.67	0.071	36.07	n.m.
033 A	514643	4048490	3.44	0.007	0.198	16.260	1.30	10.06	0.10	56.13	n.m.
034 A	514621	4048490	0.41	0.019	0.070	2.536	2.96	n.d.	n.d.	n.d.	n.m.
035 A	515124	4048615	0.81	0.020	0.443	24.468	1.05	n.d.	n.d.	n.d.	n.m.

TABLE 2: Continued.

Site	E	N	Hg ($\mu\text{g/g}$)	N (%)	C (%)	S (%)	pH	H ₂ S (%)	CH ₄ (%)	CO ₂ (%)	T ($^{\circ}\text{C}$ @ 20 cm)
036 A	515148	4048631	0.46	0.065	0.424	1.057	2.58	bdl	0.04	9.26	n.m.
037 A	515157	4048651	1.09	0.009	0.159	0.915	2.73	0.005	0.011	5.80	n.m.
039 A	515475	4048182	0.34	0.022	0.367	0.783	4.15	bdl	0.0002	2.27	n.m.
040 A	515500	4048166	0.68	0.040	0.693	1.045	3.15	bdl	0.0004	8.99	n.m.
041 A	515510	4048159	5.03	0.016	0.418	2.593	1.39	0.66	0.48	26.32	n.m.
042 A	515535	4048127	0.76	0.032	0.388	33.506	1.92	0.19	0.24	13.25	n.m.
043 A	515553	4048105	0.54	0.021	0.228	1.973	3.35	0.012	0.0019	13.50	n.m.
044 A	515554	4048112	0.33	0.079	0.974	2.424	3.73	bdl	0.0005	1.60	n.m.
045 A	515394	4048180	0.62	0.019	0.434	4.352	2.79	0.013	0.14	13.10	n.m.
047 A	515465	4048096	0.19	0.035	0.587	0.254	4.80	bdl	0.0005	7.66	n.m.
048 A	515409	4048079	0.11	0.010	0.255	1.322	2.88	0.016	0.11	8.36	n.m.
049 A	515414	4048050	0.79	0.020	0.961	2.672	1.87	bdl	0.49	30.67	n.m.
050 A	515418	4048013	0.61	0.022	0.935	2.159	1.64	2.15	0.90	43.68	n.m.
051 A	515432	4048003	0.32	0.011	0.151	1.512	3.32	bdl	0.22	27.23	n.m.
053 A	515482	4047984	1.05	0.016	0.259	3.954	3.28	0.022	0.25	25.17	n.m.
054 A	515512	4047995	0.15	0.021	0.220	0.933	3.27	n.d.	n.d.	n.d.	n.m.
186 A	515546	4048080	1.22	0.023	0.243	4.280	3.45	0.10	0.30	25.24	n.m.
189 A	515530	4047998	0.14	0.027	0.173	1.238	3.41	bdl	0.0015	5.25	n.m.
212 A	515204	4048707	0.37	0.093	1.777	1.018	3.77	bdl	0.0003	3.36	n.m.
239 A	514958	4048062	0.20	0.009	0.164	40.328	1.33	0.19	0.023	2.80	n.m.
240 A	514990	4048077	0.31	0.006	0.107	4.842	2.48	n.d.	n.d.	n.d.	n.m.
241 A	515032	4048070	0.81	0.022	0.382	5.690	1.25	17.12	0.68	72.01	n.m.
242 A	515024	4048127	0.23	0.021	0.081	1.653	3.47	0.10	0.028	7.30	n.m.
244 A	515088	4048170	0.39	0.024	0.194	1.497	3.17	0.015	0.052	13.83	n.m.
247 A	515100	4048146	0.34	0.034	0.451	1.752	2.80	0.006	0.0008	9.53	n.m.
248 A	515122	4048111	0.41	0.014	0.178	3.216	2.23	1.67	0.16	20.21	n.m.
249 A	515107	4048092	0.21	0.032	0.782	5.172	2.00	n.d.	n.d.	n.d.	n.m.
251 A	515081	4048103	1.44	0.059	0.637	4.563	2.73	bdl	0.0005	9.50	n.m.
254 A	515013	4048047	0.82	0.046	1.047	3.610	1.59	13.75	0.58	61.71	n.m.
255 A	515039	4048033	0.63	0.051	0.780	56.276	2.22	14.97	0.70	68.74	n.m.
256 A	515020	4047981	0.58	0.013	0.252	2.399	1.55	0.087	0.052	6.46	n.m.
257 A	514986	4047992	0.58	0.024	0.728	2.908	1.68	1.79	0.26	29.13	n.m.
259 A	515143	4048093	0.48	0.009	0.152	10.040	1.77	6.86	0.22	32.79	n.m.
N301	515310	4048583	0.30	0.058	0.868	0.727	4.35	bdl	0.0002	0.40	27.3
N302	515384	4048514	0.33	0.031	0.596	0.695	4.09	bdl	0.0005	0.86	30.5
N303	515479	4048463	0.70	0.230	2.625	1.521	3.75	0.048	0.0004	1.55	30.5
N304	514864	4048679	0.47	0.006	0.073	1.956	1.66	9.97	0.21	62.78	66.2
N305	514856	4048673	0.33	0.007	0.091	3.981	1.45	12.63	0.21	63.93	100.0
N307	514848	4048677	0.47	0.010	0.118	3.730	1.28	16.84	0.26	74.73	53.5
N308	514851	4048680	0.27	0.009	0.088	3.461	1.22	16.47	0.25	74.90	61.1
N309	515695	4048364	0.41	0.031	0.419	8.140	3.39	0.008	0.077	21.24	32.2
N310	515688	4048334	0.50	0.149	1.875	1.215	3.56	0.11	0.0018	20.25	31.1
N311	515663	4048292	0.15	0.200	2.337	1.172	3.61	0.002	0.0015	8.10	30.9
N312	515658	4048288	0.13	0.030	0.427	2.740	3.15	bdl	0.006	26.14	34.9
N313	515227	4048688	0.17	0.046	0.612	0.407	4.20	bdl	0.0005	0.99	36.7
N314	515207	4048667	0.64	0.022	0.300	2.017	2.65	bdl	Bdl	2.07	33.6
N315	515190	4048650	0.26	0.104	2.265	0.772	3.66	bdl	0.0006	6.09	38.9
N316	515173	4048628	0.21	0.058	1.144	0.953	3.52	bdl	0.001	10.21	44.4
N317	515153	4048604	0.22	0.020	0.563	16.470	1.15	0.025	0.06	12.64	54.0

TABLE 2: Continued.

Site	E	N	Hg ($\mu\text{g/g}$)	N (%)	C (%)	S (%)	pH	H ₂ S (%)	CH ₄ (%)	CO ₂ (%)	T ($^{\circ}\text{C}$ @ 20 cm)
N318	515134	4048595	0.32	0.028	0.743	5.035	1.50	0.68	0.10	15.61	51.5
N319	515109	4048583	0.17	0.016	0.171	3.427	1.32	0.004	0.044	10.57	45.9
N320	515095	4048585	0.47	0.029	0.801	3.667	1.49	1.15	0.13	20.46	59.4
N321	515092	4048601	0.70	0.007	0.069	1.620	2.34	0.006	0.03	6.39	43.0
N323	515126	4048638	2.15	0.004	0.109	11.050	1.15	11.38	0.46	59.42	69.8
N324	515139	4048658	0.28	n.d.	n.d.	n.d.	0.78	bdl	0.67	75.00	53.0
N325	515162	4048676	0.23	0.006	0.125	2.415	1.18	0.19	0.09	13.18	48.0
N326	515174	4048697	1.12	0.008	0.245	2.506	1.34	1.61	0.17	21.95	56.4
N327	515621	4048254	0.15	0.016	0.373	3.286	1.48	8.75	1.26	69.20	59.5
N328	515640	4048269	0.29	0.049	0.358	0.900	2.74	bdl	0.16	15.86	28.3
N329	515590	4048259	0.22	0.127	1.928	1.711	3.60	bdl	0.0005	0.38	30.2
N330	515573	4048248	0.44	0.069	0.847	1.570	3.91	bdl	0.0007	3.30	31.8
N331	515526	4048255	0.19	0.099	0.907	1.025	4.67	bdl	0.0005	0.65	30.0
N332	515484	4048245	0.49	0.041	0.717	1.986	3.38	bdl	0.0006	0.50	29.0
N334	515452	4048158	0.19	0.132	2.133	0.675	3.53	0.002	0.0004	3.50	27.8
N335	515486	4048116	0.24	0.085	2.210	0.455	4.15	0.009	0.0005	6.25	33.5
N336	515510	4048081	13.7	0.055	1.812	14.620	0.75	bdl	0.0005	0.28	25.5
N337	515504	4048034	0.056	0.020	0.400	0.352	3.28	bdl	0.0014	8.66	32.0
N338	515473	4048051	0.10	0.034	0.597	0.308	4.10	bdl	0.0005	7.66	33.9
N339	515476	4048008	0.10	0.033	0.751	0.373	4.16	bdl	0.0003	12.43	32.3
N340	515442	4048027	0.31	0.067	1.680	1.502	3.40	bdl	0.0005	14.50	31.9
N341	515444	4048067	0.25	0.039	0.615	1.095	3.07	bdl	0.0005	6.79	31.9
N342	515431	4048111	0.48	0.010	0.124	0.843	4.08	bdl	0.0004	6.16	34.2
N343	515418	4048135	1.15	0.040	0.409	0.825	3.26	0.066	bdl	6.76	31.2
N344	514870	4047612	0.64	0.012	0.194	2.015	2.61	0.038	0.16	26.36	42.8
N345	514849	4047608	0.49	0.065	0.320	0.501	3.41	0.044	0.077	12.06	51.3
N346	514830	4047587	0.12	0.025	0.605	2.853	0.98	0.33	0.48	39.57	56.8
N347	514847	4047594	0.72	0.010	0.138	2.454	3.37	0.004	0.054	17.16	42.9
N348	514857	4047579	0.36	0.008	0.426	1.658	1.34	0.72	0.28	27.30	56.9
N349	514866	4047588	2.75	0.015	0.953	0.475	2.24	bdl	0.009	8.08	43.4
N350	514841	4047574	0.33	0.012	0.675	2.538	0.85	bdl	0.27	20.88	58.1
N351	514849	4047568	0.64	0.010	0.298	4.228	0.72	1.76	0.69	36.59	62.8
N352	514868	4047562	6.93	0.011	0.665	7.972	0.71	7.16	1.91	74.48	51.7
N353	514881	4047577	9.00	0.009	0.241	1.968	0.80	bdl	0.094	6.63	51.8

Sites 1 and Mandraki are background sites outside the Lakki caldera. n.d. = not determined; n.m. = not measured; bdl = below detection limit (<0.002 for H₂S; <0.0002 for CH₄). Easting (E) and northing (N) are expressed as UTM coordinates WGS84, all sites belonging to sector 35S. Data of S concentrations and pH of samples from 1 to 17 and from N-St-1 to N-St-28 are taken from [24]. *Samples collected close to the plants of Table 3.

population (2.11–57 ppm, 43.5% of the data) indicating a significant H₂S input into the atmosphere; D population (1.5% of the data) includes values > 57 ppm of H₂S up to saturation of the sensor in the vicinity of the active fumaroles, suggesting a significant contribution of the hydrothermal fluids released from the subsurface.

Three distinct populations can be recognized (A < 8.5 , B from 8.5 to 44.9, and C up to 7132 ng/m³; 12.2%, 82.8%, and 5.0%, respectively) for GEM concentrations in the air (Figure 3(c)) that were measured with the Lumex® instrumentation.

In Figure 4, an example of H₂S, CO₂, and GEM concentrations measured in the atmosphere through transect walk

within the Lakki Plain is shown. GEM, H₂S, and CO₂ concentration peaks, in correspondence with the fumaroles of Phlegeton, show a good match, confirming the interdependence of these gaseous compounds and their common origin from the fumaroles. The main fumarolic emissions were clearly highlighted by anomalously high Hg concentrations (up to ~ 600 ng/m³) with respect to the surrounding air masses (~ 30 ng/m³). GEM concentrations above background values measured away from the main fumarolic vents were probably due to soil degassing. The Lakki Plain and especially the main hydrothermal craters are sites of strong hydrothermal degassing with CO₂ fluxes up to 6175 g/m²/day [52]. Mercury fluxes from the soil have not

TABLE 3: Hg and S concentrations in plant leaves collected in the Lakki Pain, Nisyros.

ID	Erica		ID	Cistus	
	Total Hg ($\mu\text{g/g}$)	Total S ($\mu\text{g/g}$)		Total Hg ($\mu\text{g/g}$)	Total S ($\mu\text{g/g}$)
1 NY-E	0.026	1180	1 NY-C	0.010	1080
2 NY-E	0.046	6340	2 NY-C	0.037	5950
3 NY-E	0.028	2210	3 NY-C	0.022	2420
4 NY-E	0.014	2310			
5 NY-E	0.025	1410	5 NY-C	0.055	2550
6 NY-E	0.019	1540	6 NY-C	0.019	2290
7 NY-E	0.016	2840	7 NY-C	0.056	5290
8 NY-E	0.066	2560	8 NY-C	0.112	3350
9 NY-E	0.036	3630			
10 NY-E	0.023	4360			
11 NY-E	0.039	4280	11 NY-C	0.025	3570
12 NY-E	0.030	1480	12 NY-C	0.028	2430
13 NY-E	0.036	2960	13 NY-C	0.095	4260
14 NY-E	0.065	2640	14 NY-C	0.027	2340
15 NY-E	0.024	2110	15 NY-C	0.029	2860
16 NY-E	0.023	2540	16 NY-C	0.077	3610
17 NY-E	0.034	1460	17 NY-C	0.112	3140

Soil samples identified with the numbers from 1 to 17 in Table 2 were collected close to the plant samples with the above corresponding numbers.

TABLE 4: Total gaseous mercury (TGM) concentrations in fumarolic gases.

Area	TGM (ng/m^3)	References
Fumaroles Japan (>100 sites)	1400-1,828,000	[36, 45, 46]
Kilauea, Hawaii (U.S.A.)	274-1031	[47]
Colima volcano (Mexico)	470-1442	[47]
White Island, New Zealand (fumarole 3)	22,000-38,000	[48]
Yellowstone caldera, U.S.A. (9 fumaroles)	415-30,000	[3]
Solfatara di Pozzuoli, Italy (fumarole BG)	93,500	[49]
Nisyros, Greece	10,500-46,300	This study

TABLE 5: Atmospheric Hg concentrations, Hg/S and Hg/CO₂ ratios, and total Hg outputs of fumarolic fields at closed-conduit volcanic systems.

Area	Hg atmosphere (ng/m^3)	Hg/S ($\times 10^{-6}$)	Hg/CO ₂ ($\times 10^{-8}$)	Total Hg output (kg/a)	References
Las Pailas, Rincon de la Vieja, Costa Rica	n.r.	8.4	0.14-1.7	0.8-2.4	[4]
Las Hornillas, Miravalles volcano, Costa Rica	n.r.	2.01	0.35-10	4-12	[4]
Poas, Costa Rica	n.r.	0.03	n.r.	1.6-2	[4]
Tatun volcanic field, Taiwan	5.5-292	2.4-5	4-40	5-50	[71]
La Fossa crater, Vulcano, Italy	4.8-339	0.48-1.3	6 \pm 0.3	0.4-7	[72]
Yellowstone caldera, U.S.A.	n.r.	n.r.	0.16-0.26	15-56	[3]
Mt. Lassen fumaroles, Cascades, U.S.A.	n.r.	n.r.	2-22	96-167	[3]
Solfatara di Pozzuoli, Italy	n.r.	n.r.	1.3	7	[49]
Solfatara di Pozzuoli, Italy	n.r.	n.r.	1.34	2	[54]
La Soufriere, Guadeloupe, Lesser Antilles	15-189	3.2	n.r.	0.8	[73]
Nea Kameni, Greece	4.5-121	n.r.	0.1-0.34	0.2-2	[53]
White Island, New Zealand	73-89	0.13-0.25	1.43-2.47	n.r.	[48]β
Nisyros, Greece (fumaroles)	n.a.	0.03-0.16	0.76-3.5	0.7	This study
Nisyros, Greece (atmosphere: Au traps)	9.4-420	n.a.	n.a.	n.a.	This study
Nisyros, Greece (atmosphere: Lumex®)	2-7132	11-68	1.5-8.2	1.9	This study

n.r. = not reported; n.a. = not applicable.

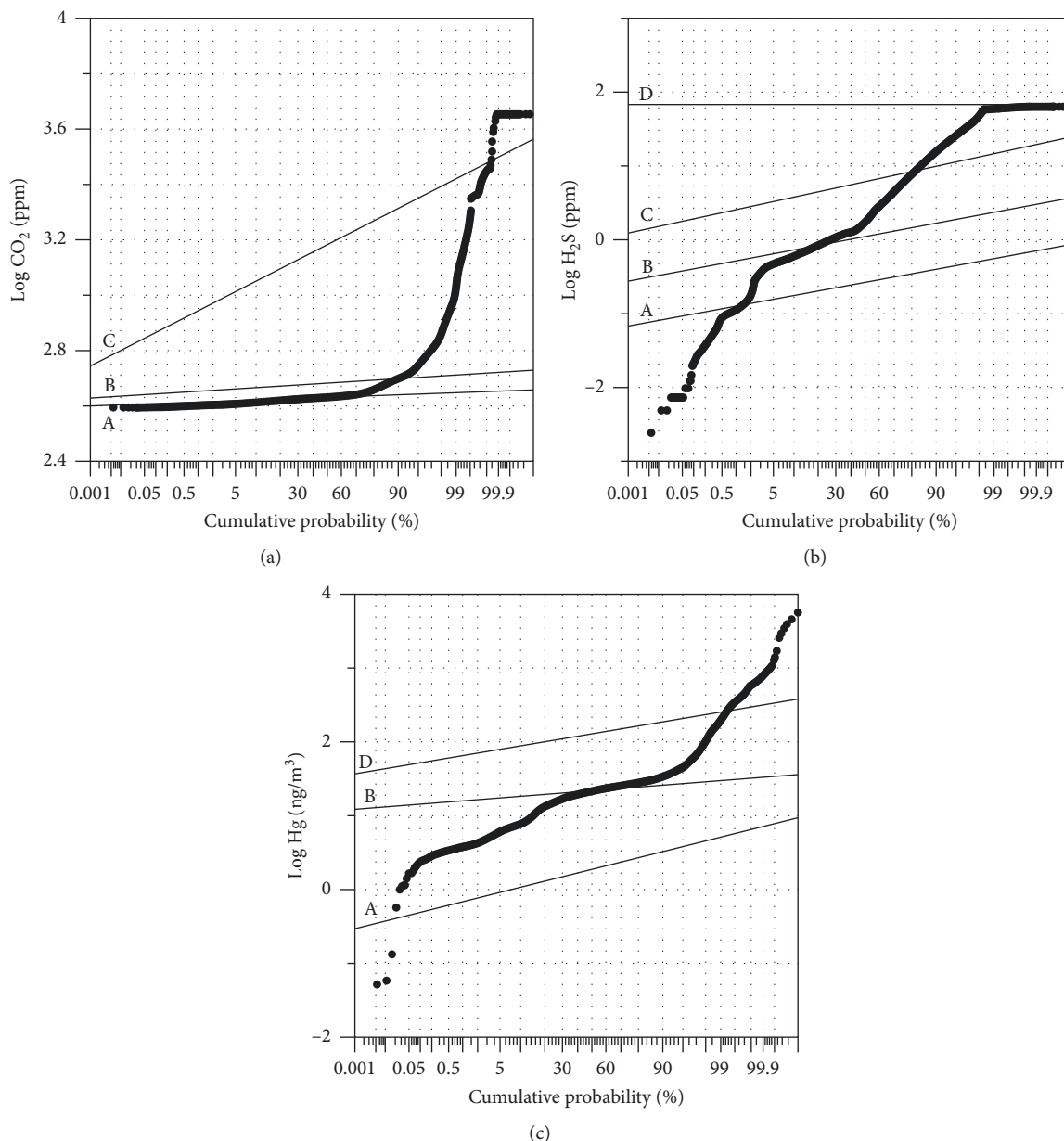


FIGURE 3: Probability plots of CO_2 (a), H_2S (b), and GEM (c) concentrations in the atmosphere of the Lakki Plain.

been measured at Nisyros, but as reported from the literature [3, 49, 53, 54], soils at geothermal and hydrothermal systems also emit gaseous Hg. Nevertheless, the previous authors found Hg fluxes ($1\text{--}2000 \mu\text{g}/\text{m}^2/\text{day}$) that are many orders of magnitude lower than those of CO_2 , with the latter gas often acting as carrier for Hg.

5.3. Mercury in the Soil. The soils of the Lakki Plain are strongly weathered by past and present fumarolic activity. This can be recognized by the widespread presence of secondary alteration minerals, mainly sulfates [24, 25]. The main drivers of the alteration process are fumarolic H_2O and H_2S . The former is the main carrier of thermal energy, which is reflected in soil temperatures reaching up to the

boiling temperature of water. Soil temperatures provide indications regarding the hydrothermal uprising gases, allowing the identification of the actively degassing areas. High temperatures are to be considered related to both high fluxes of hydrothermal fluids and the enrichment of the hydrothermal component in the soil gases. The temperature distribution map at 20 cm depth indicates temperatures above 30°C in all the investigated sites, except for some points along the western flank of the Kaminakia crater (Figure 5(a)). Higher temperatures, from 50 to 100°C , were recorded at the southern part of the Stefanos crater, at Phlegeton and Mikros Polybotes (Figure 5(a)).

Hydrogen sulphide in the fumarolic gases of Nisyros is the third most abundant species after H_2O and CO_2 [22].

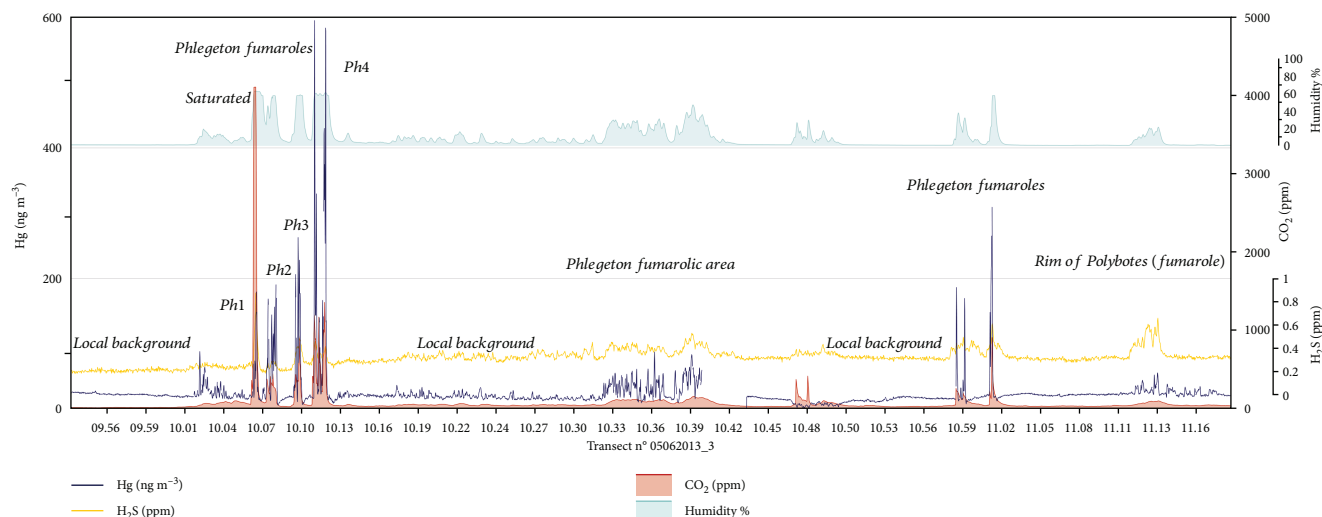


FIGURE 4: Concentrations in the atmosphere of H₂S, CO₂, and GEM measured through a transect walk inside the Lakki Plain and close to the main fumaroles (Ph = Phlegeton).

In the soil gases, on a dry basis, it represents up to nearly 18% vol. Within the soil, H₂S is oxidised by atmospheric O₂ forming sulfuric acid [55, 56], by the net reaction



Such reaction is responsible for the high S contents of the analysed soils (median ~2%, max ~56% (Table 2)) and the very low values of soil pH (from 0.71 to 5.55 (Table 2)). Both parameters show an inverse relationship (Figure 6(a)) indicating that, at the most actively exhaling zones, more sulfuric acid is produced and more sulfur is deposited.

The total amount of Hg trapped in the soil was plotted in a probability plot. As for the Hg concentrations in the air, three populations were detected (Figure 7); a secondary population containing the higher values was detected as indicated by the black arrow in Figure 7. High Hg concentrations were measured in the soil close to the main fumarolic vents (Figure 5(b)). As for sulfur, the inverse relationship between soil Hg and soil pH (Figure 6(b)) supports the transport and the deposition of Hg by fumarolic fluids. Daskalopoulou et al. [24] evidenced that also other volatile elements like As, Bi, Pb, Sb, Se, and Te are enriched in the soils of the Lakki Plain that are mostly affected by hydrothermal gases.

The accumulation of Hg in the soil matrix does not depend solely on the amount of Hg carried by the uprising hydrothermal gases but also on the soil retention capacity. Many studies demonstrated that Hg in soils shows generally a good correlation with soil organic matter (SOM). Ottesen et al. [57] evidenced such positive correlation at the continental scale, based on the analysis of more than 4000 soil samples from 33 countries in Europe. Martin et al. [58] found that the same correlation holds true for the volcanic soils of Mt. Etna. Elemental carbon, which can be considered a proxy for SOM, in the soils of the Lakki Plain does not show any correlation with the measured Hg values. This probably depends on the fact that most of the sampled soils are totally

devoid of vegetation, limiting the presence of SOM to some vegetal debris and microbial communities. The low content of SOM may therefore not contribute much to Hg accumulation in the soils of the Lakki Plain. Sulphide, which could also react with Hg, is also very scarce in the surface soil levels due to the oxidising environment [24].

Soil temperatures are thought to play an important role in Hg retention in soils. This parameter has probably a contrasting effect because higher soil temperatures indicate stronger hydrothermal gases transporting more Hg from the depth, but at the same time, higher soil temperatures presuppose also a faster remobilization of Hg from the soils because of its high volatility [3].

Although hydrothermal gases like CO₂ and H₂S show their maxima close to the main fumarolic areas (Figures 5(d) and 5(e)), no correlation with soil Hg could be evidenced (*p* value 0.77 and 0.83, respectively, and correlation index 0.04 and 0.02, respectively). However, even though both soil and gas samples were collected at the same time and in the same place, they are not totally comparable as CO₂ and H₂S were measured on the gas phase collected at the 50 cm depth while Hg was measured on the solid phase at the soil surface. Nevertheless, a better correlation was expected.

5.4. Mercury in the Plants. Plant leaves present lower concentrations with respect to the soils where they grow, while the local background in both plant leaves and soils shows very low concentrations in total Hg. Results show a range of values regarding the total Hg concentrations that seem to be positively correlated with the intensity of the fumarolic activity. The highest concentrations were measured in sites located close to the hydrothermal drill and the craters of Stefanos, Phlegeton, Mikros Polybotes, and Kaminakia, confirming the impact of the hydrothermal activity on the surrounding environment.

Regarding the availability of soil Hg to plants, it is considered to be low as there is a tendency for Hg to accumulate in

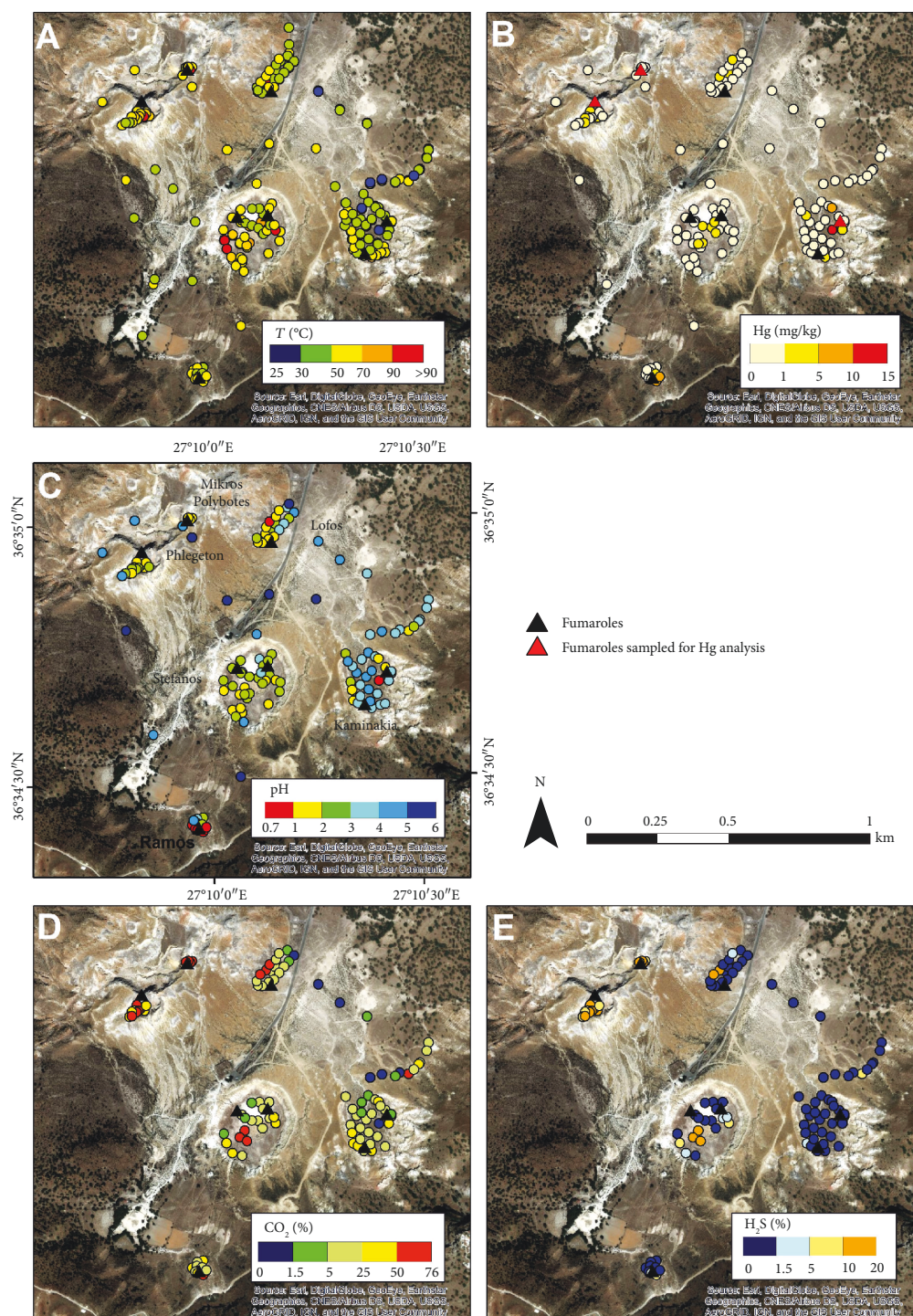


FIGURE 5: Distribution maps of soil temperature (a), Hg soil concentrations (b), soil pH (c), soil CO₂ (d), and H₂S (e) concentrations in the Lakki Plain area.

the roots, indicating that the roots serve as a barrier to Hg uptake [59, 60]. Mercury concentration in aboveground parts of plants appears to depend largely on foliar uptake of Hg⁰ volatilized from the soil [61, 62] and therefore on the age of the plant and the time of day and year [63]. The transfer of Hg (gaseous forms) from the atmosphere

occurs by dry and wet deposition (rain and snow) and enters into the organism by the stomata of the leaves through the transpiration process [59, 61, 64, 65]. The soil-plant correlation diagram (Figures 8(a) and 8(b)) shows that *Cistus* samples were enriched in Hg with respect to *Erica* presenting a moderately good positive correlation.

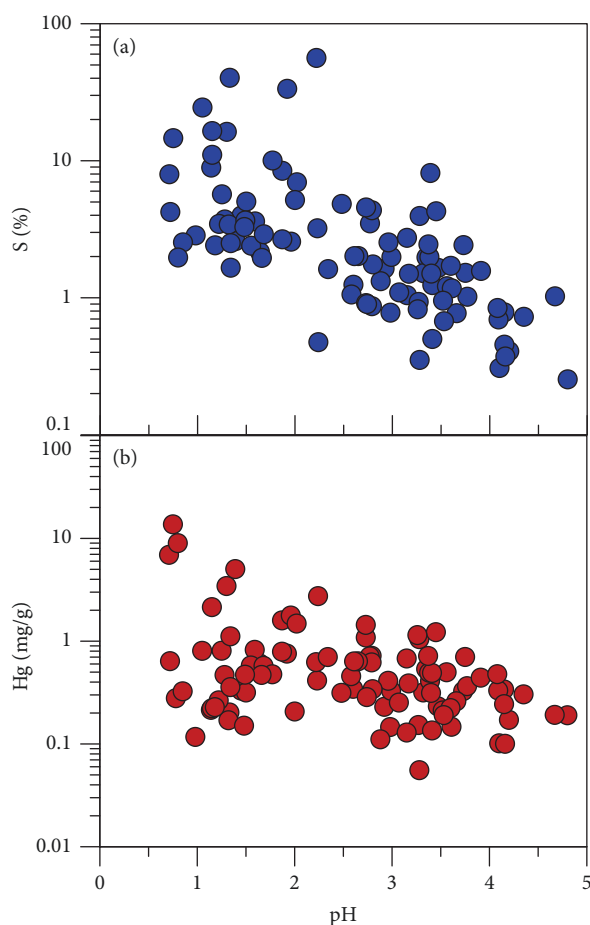


FIGURE 6: Soil total sulfur (a) and total Hg (b) concentrations vs. soil pH binary diagrams.

Taking into consideration that Hg uptake is mostly through the leaves and the samples of both species were collected on the same day, the relatively high concentrations of total Hg in the *Cistus* samples can be justified by the higher specific surface area of its leaflets with respect to *Erica*'s. Additionally, equally important factors that should be taken into consideration are the solar radiation and the humidity. These two factors along with the specific surface area of the leaflets may possibly explain the elevated Hg concentration of the local background sample that was noticed at Erica. It is worth mentioning that the local background samples of both species were collected at a place located close to the sea, at noontime during summer period.

On the other hand, sulfur is an essential macronutrient for plant growth. Its uptake and distribution are tightly controlled by the environmentally induced changes in nutrient demand [66, 67]. Therefore, the high concentrations in S as well as the good correlation between the soil and plant samples in both species can be regarded as mainly caused by its uptake by the roots through the metabolic processes of the plants (Figures 8(c) and 8(d)). Nevertheless, the contribution of the transpiration process via the stomata of the leaves may also be important.

5.5. Environmental and Human Health Issues. Mercury is considered to be among the most toxic metals that could be taken by the human body through different pathways [13], especially concerning methylated species. Furthermore, its deleterious effects can be enhanced through its biomagnification along the trophic chain [11]. One of the primary uptake paths of Hg is through the inhalation of GEM. For the World Health Organization [68], atmospheric concentrations of Hg in the range of 15,000–30,000 ng/m³ may have adverse effects on humans (tremors, renal tubular effects, change in plasma enzymes, and others). However, using an uncertainty factor of 20, the same organization proposed a guideline value for Hg concentration in air of 1000 ng/m³ [68].

At the same time, the US Occupational Safety and Health Administration considered a permissible occupational exposure limit for GEM of 100,000 ng/m³ in the air [69], while the National (US) Institute for Occupational Safety and Health (NIOSH) established a recommended exposure limit for GEM of 50,000 ng/m³ as a time-weighted average (TWA) for up to a 10 h workday and a 40 h workweek [69]. The American Conference of Governmental Industrial Hygienists assigned to GEM a threshold limit value of 25,000 ng/m³ as a TWA for a normal 8 h workday and a 40 h workweek [69]. The minimum risk level (MRL) for chronic inhalation of GEM is 200 ng/m³ [69, 70]. The MRL is an estimate of the daily human exposure to a hazardous substance that is likely to be without appreciable risk of adverse health effects over a specified duration of exposure. The US EPA reference concentration for inhalation is calculated to be 300 ng/m³ (TWA) [69].

Taking into consideration the above limits and thresholds, it may be deduced that, although the atmospheric GEM concentrations within the Nisyros Caldera are sometimes many orders of magnitude above the global background, they do not represent a general hazard for human health. The area is yearly visited by many tens of thousands of tourists, but the zones where they arrive show GEM concentrations rarely exceeding the MRL. Areas exceeding the WHO guideline value of 1000 ng/m³ are very close to the main fumarolic vents where tourists are not allowed to go and where other toxic gases of higher danger are present (i.e., H₂S [19]). Moreover, people who work all day in the area (ticket operators, owner, and employees of the Volcano Café) spend most of their time in areas with atmospheric GEM concentrations well below the occupational limits and generally also below the MRL. Probably, only volcanologists that take gas samples from the main fumaroles may be exposed to atmospheric GEM levels of a few thousands of ng/m³ for some hour, which has still to be considered a low exposition. Even though results propose no particular risk, a more complete survey is highly suggested to have a more accurate picture.

5.6. Total Output from the Hydrothermal System of Nisyros. It has long been established that the contribution of volcanic activity to the total natural emissions of Hg to the atmosphere is substantial [2, 4, 47]. However, due to the limited number of data available, significant uncertainties on the annual emissions of volcanic Hg still remain. Estimates range

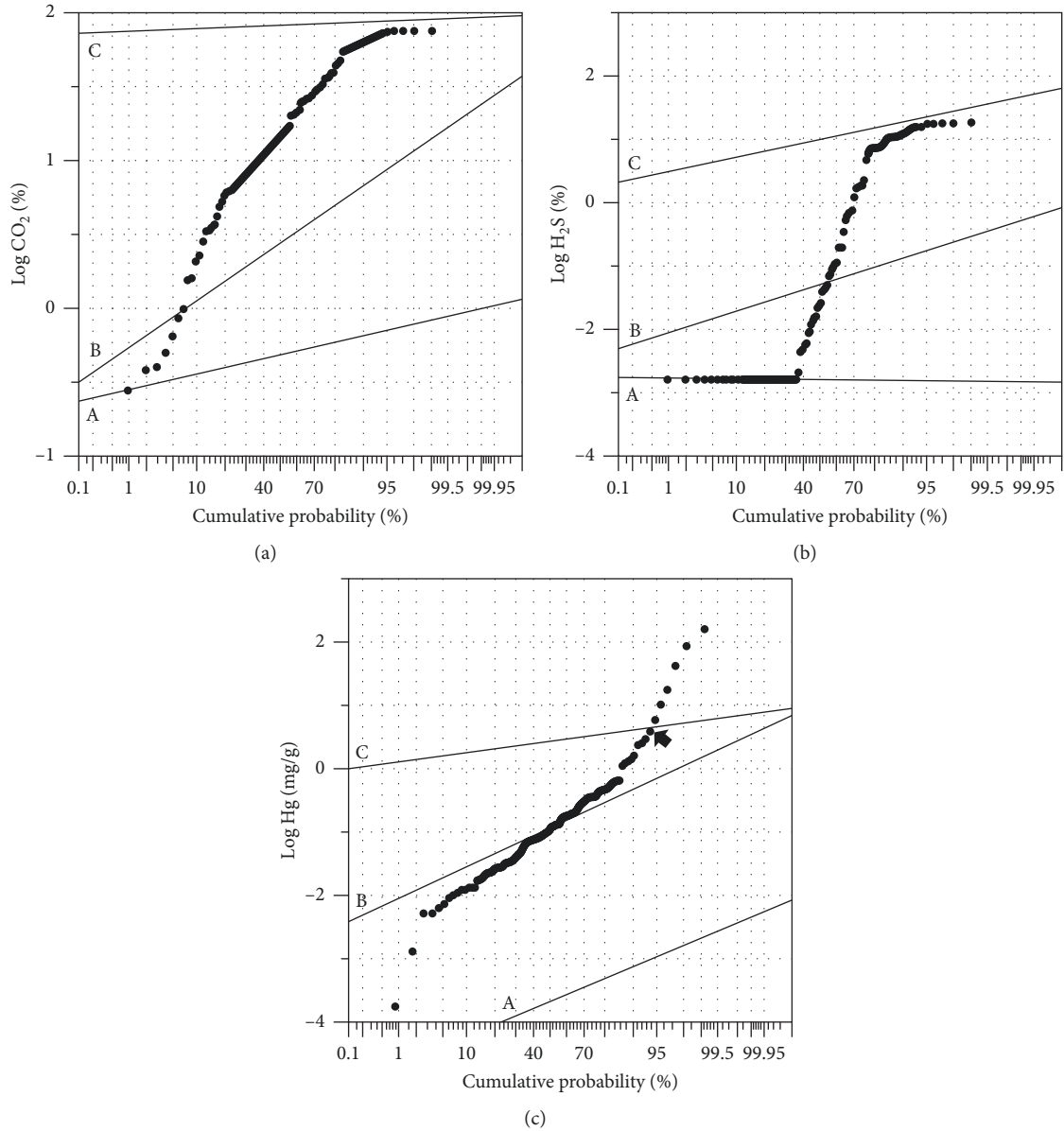


FIGURE 7: Probability plots of total CO₂ (a) and H₂S (b) concentrations in the soil gas and Hg (c) concentrations in the soils of the Lakki Plain.

between 0.6 and 1000 t/a representing a proportion that varies from <1% up to 50% of total natural emissions [2, 4, and references therein]. The strongest contribution (90%) of the total output of volcanic Hg derives from explosive eruptions while the rest derives from passive degassing [2]. Emissions of single open-conduit volcanoes like Etna (Italy), Ambrim (Vanuatu), or Masaya (Nicaragua) are in the order of units to tens of t/a [4], pointing to strong underestimation of global volcanic outputs lower than 50 t/a. The contribution of fumarolic emissions from closed-conduit volcanoes is instead very limited as it is found in the range from 0.2 to 167 kg/a (0.0002-0.167 t/a (Table 5)).

Most of the Hg flux estimations from volcanic systems have been indirectly obtained cross-correlating the measured

SO₂ fluxes with the Hg/SO₂ ratios measured in the volcanic plume [4]. Such method cannot be used for low-temperature fumarolic areas because magmatic SO₂ is strongly scrubbed by the hydrothermal system. To obtain output estimates for such areas, different methods have been proposed. One of which is the measurement of Hg fluxes from the soils with accumulation chambers (dynamic flux chambers or static closed chambers) and the consequent integration of the fluxes over the whole hydrothermal area. Such method was applied only few times [49, 53, 54]. Another method is the cross-correlation of the total CO₂ release of the fumarolic area with the Hg/CO₂ ratio being measured either in the fumarolic fluids or in the air close to the vents [4]. Both methods give the order of magnitude of

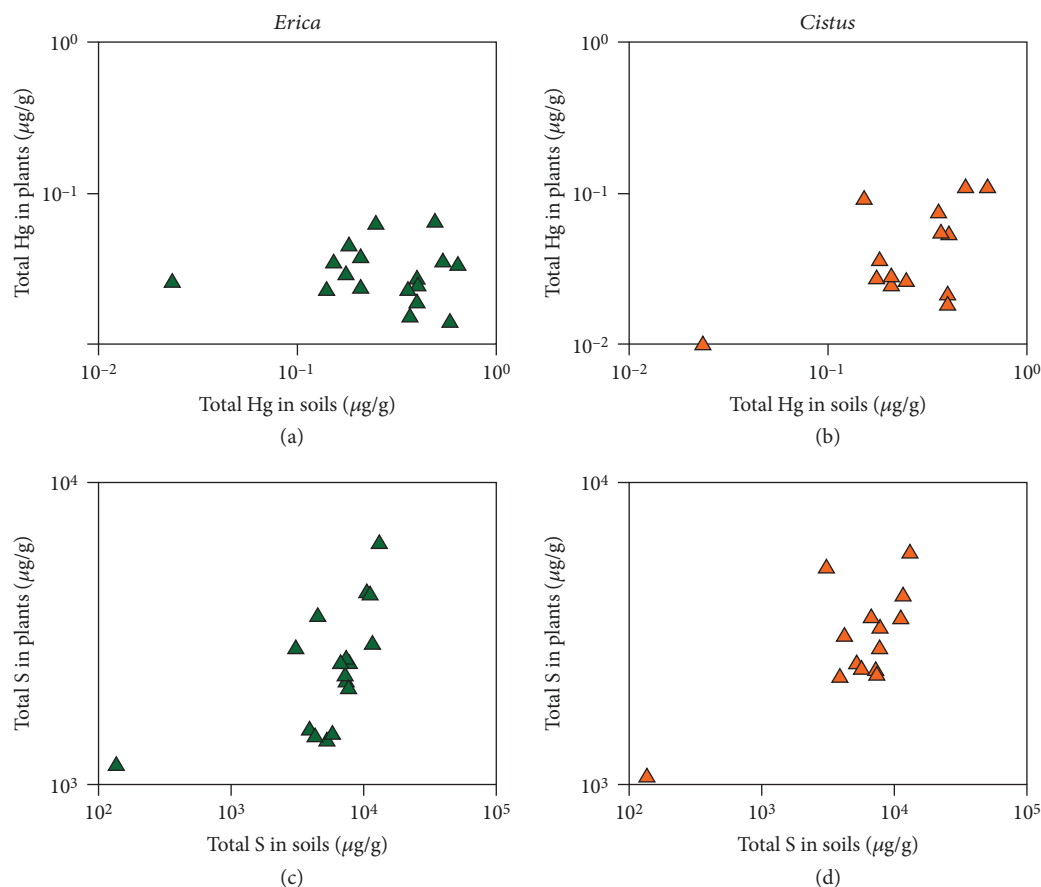


FIGURE 8: Correlation plots that present in the upper part the total Hg concentrations in soils and (a) *Erica* and (b) *Cistus* and in the lower part the total S concentrations in soils and (c) *Erica* and (d) *Cistus* collected in the Lakki Plain.

the Hg output, but they coherently confirm much lower outputs of fumarolic areas with respect to open-conduit volcanoes. Following the second approach, a rough estimation of the Hg output of Nisyros can be obtained considering the total CO_2 output, as determined by Bagnato et al. [53], which is 84 t/d, and the Hg/ CO_2 ratios measured in the fumaroles that range from 0.8×10^{-8} to 3.5×10^{-8} (median value = 2.3×10^{-8}) or in the air ranging from 1.5×10^{-8} to 8.2×10^{-8} (median value = 6.3×10^{-8}), corresponding to the total Hg output of 0.7 and 1.9 kg/a, respectively. Such figures fall in the lower range of the outlet values for fumarolic areas (Table 5).

6. Conclusions

Mercury and its compounds are highly toxic for humans and ecosystems. Volcanic and hydrothermal emissions are major natural sources of Hg in the atmosphere. At Nisyros, a potentially active volcano with intense and widespread degassing activity, real-time measurements of GEM showed concentrations up to 7132 ng/m^3 within the Lakki Plain. The good correlation between Hg and the main fumarolic gases (H_2O , CO_2 , and H_2S) confirms the hydrothermal origin of the former. In the fumarolic gases, Hg was estimated in the range $10,500\text{--}46,300 \text{ ng/m}^3$; these values should be considered the lower limit due to the plausible Hg loss

within the condensing fumarolic vapour. Relatively high Hg concentrations were also identified in the soils; the accumulation of Hg in the soil matrix is dependent on both the amount carried by the upflowing hydrothermal gases and the soil ability to fix a part of it. The lack of vegetation at the crater area maybe responsible of the poor correlation between elemental C and Hg in the soil. No bioavailability through the roots was noticed in the plants collected at the Lakki Plain. The slightly high concentrations of the vegetation samples could have therefore been caused by the transpiration process that takes place in the stomata of the leaves, making *Cistus* a better candidate for biomonitoring investigations with respect to *Erica* due to the greater specific area of its leaves.

The aforementioned synoptic analysis of the results highlights that more than one matrix can be affected by hydrothermal Hg from the degassing activity. Furthermore, it underscores that Hg concentrations are positively correlated with the distance of the sample/measurement from the emission point. Even though the measured Hg concentrations were enhanced and at cases exceed the WHO limits in terms of inhalation, they seem to be of minor risk for human health as the exposure is for a limited time and the access for nonvolcanologists is prohibited. However, an uptake originating from the trophic chain should not be disregarded.

Data Availability

Data will be available on request.

Disclosure

K. Daskalopoulou's present address is GFZ-German Research Centre for Geosciences, Potsdam, Brandenburg, Germany. F. Capecchiacci's present address is Istituto Nazionale di Geofisica e Vulcanologia, Osservatorio Vesuviano, Naples, Italy. G. Giudice's present address is Istituto Nazionale di Geofisica e Vulcanologia, Osservatorio Etneo, Catania, Italy.

Conflicts of Interest

The authors declare that they have no conflicts of interest.

Acknowledgments

We are grateful to Emanuela Bagnato, who made the measurements of the Au traps at the University of Palermo, to Mario Sprovieri who allowed us to make the measurements of Hg in the soils at the laboratories of the Consiglio Nazionale delle Ricerche, IAMC, UOS di Capo Granitola, and to Jens Fiebig, Artemis Kontomichalou, and Konstantinos Kyriakopoulos for their help in the field. We kindly acknowledge the owner of the Volcano Café, Mr. Sideris Kontogiannis, for his logistical support to all volcanologists working in the Nisyros Caldera (and also for many beers spent for free and for the delightful music of his Cretan Lyra at dusk). Finally, we would like to thank the municipality of Nisyros Island for its hospitality and generosity.

References

- [1] M. S. Gustin, "Are mercury emissions from geologic sources significant? A status report," *Science of The Total Environment*, vol. 304, no. 1-3, pp. 153-167, 2003.
- [2] D. M. Pyle and T. A. Mather, "The importance of volcanic emissions for the global atmospheric mercury cycle," *Atmospheric Environment*, vol. 37, no. 36, pp. 5115-5124, 2003.
- [3] M. A. Engle, M. S. Gustin, F. Goff et al., "Atmospheric mercury emissions from substrates and fumaroles associated with three hydrothermal systems in the western United States," *Journal of Geophysical Research*, vol. 111, no. D17, article D17304, 2006.
- [4] E. Bagnato, G. Tamburello, G. Avard et al., "Mercury fluxes from volcanic and geothermal sources: an update," *Geological Society, London, Special Publications*, vol. 410, no. 1, pp. 263-285, 2015.
- [5] S. Metz and J. H. Trefry, "Chemical and mineralogical influences on concentrations of trace metals in hydrothermal fluids," *Geochimica et Cosmochimica Acta*, vol. 64, no. 13, pp. 2267-2279, 2000.
- [6] A. Kabata-Pendias and A. Pendias, *Trace Elements in Soils and Plants*, CRC, third ed edition, 2001.
- [7] R. P. Mason, W. F. Fitzgerald, and F. M. M. Morel, "The biogeochemical cycling of elemental mercury: anthropogenic influences," *Geochimica et Cosmochimica Acta*, vol. 58, no. 15, pp. 3191-3198, 1994.
- [8] C. H. Lamborg, C. M. Tseng, W. F. Fitzgerald, P. H. Balcom, and C. R. Hammerschmidt, "Determination of the mercury complexation characteristics of dissolved organic matter in natural waters with "reducible Hg" titrations," *Environmental Science & Technology*, vol. 37, no. 15, pp. 3316-3322, 2003.
- [9] W. F. Fitzgerald, R. P. Mason, and G. M. Vandal, "Atmospheric cycling and air-water exchange of mercury over mid-continental lacustrine regions," *Water, Air & Soil Pollution*, vol. 56, no. 1, pp. 745-767, 1991.
- [10] F. M. M. Morel, A. M. L. Kraepiel, and M. Amyot, "The chemical cycle and bioaccumulation of mercury," *Annual Review of Ecology and Systematics*, vol. 29, no. 1, pp. 543-566, 1998.
- [11] W. F. Fitzgerald and C. H. Lamborg, "Geochemistry of mercury in the environment," in *Environmental Geochemistry, Treatise on Geochemistry*, H. Holland and K. Turekian, Eds., pp. 1-47, Elsevier, 2007.
- [12] T. W. Clarkson and L. Magos, "The toxicology of mercury and its chemical compounds," *Critical Reviews in Toxicology*, vol. 36, no. 8, pp. 609-662, 2006.
- [13] WHO, *Exposure to Mercury: A Major Public Health Concern*, World Health Organization and United Nations Environment Programme, Geneva, Switzerland, 2007.
- [14] H. L. Barnes and T. M. Seward, "Geothermal systems and mercury deposits," in *Geochemistry of Hydrothermal Ore Deposits*, H. L. Barnes, Ed., pp. 699-736, John Wiley & Sons, New York, 3rd ed. edition, 1997.
- [15] E. Bagnato, A. Aiuppa, F. Parello et al., "Degassing of gaseous (elemental and reactive) and particulate mercury from Mount Etna volcano (Southern Italy)," *Atmospheric Environment*, vol. 41, no. 35, pp. 7377-7388, 2007.
- [16] D. A. Nimick, R. R. Caldwell, D. R. Skaar, and T. M. Selch, "Fate of geothermal mercury from Yellowstone National Park in the Madison and Missouri Rivers, USA," *Science of The Total Environment*, vol. 443, pp. 40-54, 2013.
- [17] D. E. Robertson, E. A. Creclius, J. S. Fruchter, and J. D. Ludwick, "Mercury emissions from geothermal power plants," *Science*, vol. 196, no. 4294, pp. 1094-1097, 1977.
- [18] S. Vitolo and M. Seggiani, "Mercury removal from geothermal exhaust gas by sulfur-impregnated and virgin activated carbons," *Geothermics*, vol. 31, no. 4, pp. 431-442, 2002.
- [19] W. D'Alessandro, L. Brusca, K. Kyriakopoulos, G. Michas, and G. Papadakis, "Hydrogen sulphide as a natural air contaminant in volcanic/geothermal areas: the case of Sousaki, Corinthia (Greece)," *Environmental Geology*, vol. 57, no. 8, pp. 1723-1728, 2009.
- [20] J. Cabassi, F. Tassi, S. Venturi et al., "A new approach for the measurement of gaseous elemental mercury (GEM) and H₂S in air from anthropogenic and natural sources: examples from Mt. Amiata (Siena, Central Italy) and Solfatara Crater (Campi Flegrei, Southern Italy)," *Journal of Geochemical Exploration*, vol. 175, pp. 48-58, 2017.
- [21] L. Marini and J. Fiebig, "Fluid geochemistry of the magmatic-hydrothermal system of Nisyros (Greece)," *Mémoires de Géologie (Lausanne)*, vol. 44, p. 192, 2005.
- [22] J. Fiebig, F. Tassi, W. D'Alessandro, O. Vaselli, and A. B. Woodland, "Carbon-bearing gas geothermometers for volcanic-hydrothermal systems," *Chemical Geology*, vol. 351, pp. 66-75, 2013.
- [23] K. Daskalopoulou, S. Calabrese, F. Grassa et al., "Origin of methane and light hydrocarbons in natural fluid emissions: a

- key study from Greece,” *Chemical Geology*, vol. 479, pp. 286–301, 2018.
- [24] K. Daskalopoulou, S. Calabrese, S. Milazzo et al., “Trace elements mobility in soils from the hydrothermal area of Nisyros (Greece),” *Annals of Geophysics*, vol. 57, Fast Track 2, 2014.
- [25] S. Venturi, F. Tassi, O. Vaselli et al., “Active hydrothermal fluids circulation triggering smallscale collapse events: the case of the 2001–2002 fissure in the Lakki Plain (Nisyros Island, Aegean Sea, Greece),” *Natural Hazards*, vol. 93, no. 2, pp. 601–626, 2018.
- [26] P. Nomikou, D. Papanikolaou, and V. J. Dietrich, “Geodynamics and volcanism in the Kos-Yali-Nisyros volcanic field,” in *Nisyros Volcano - The Kos - Yali - Nisyros Volcanic Field*, Series: Active Volcanoes of the World, V. J. Dietrich and E. Lagios, Eds., pp. 13–55, Springer International Publishing, 2018.
- [27] J. C. Hunziker and L. Marini, *The geology, geochemistry and evolution of Nisyros Volcano (Greece). Implications for the volcanic hazards*, no. 44, 2005 *Memoires de Geologie (Lausanne)*, 2005.
- [28] V. J. Dietrich, “Geology of Nisyros Volcano,” in *Nisyros Volcano - The Kos - Yali - Nisyros Volcanic Field*, Series: Active Volcanoes of the World, V. J. Dietrich and E. Lagios, Eds., pp. 145–201, Springer International Publishing, 2018.
- [29] V. J. Dietrich, G. Chiodini, and F. M. Schwandner, “The hydrothermal system and geothermal activity,” in *Nisyros Volcano - The Kos - Yali - Nisyros Volcanic Field*, Series: Active Volcanoes of the World, V. J. Dietrich and E. Lagios, Eds., pp. 57–102, Springer International Publishing, 2018.
- [30] T. Brombach, S. Caliro, G. Chiodini, J. Fiebig, J. C. Hunziker, and B. Raco, “Geochemical evidence for mixing of magmatic fluids with seawater, Nisyros hydrothermal system, Greece,” *Bulletin of Volcanology*, vol. 65, no. 7, pp. 505–516, 2003.
- [31] S. Caliro, G. Chiodini, D. Galluzzo et al., “Recent activity of Nisyros volcano (Greece) inferred from structural, geochemical and seismological data,” *Bulletin of Volcanology*, vol. 67, no. 4, pp. 358–369, 2005.
- [32] W. D’Alessandro, A. L. Gagliano, K. Kyriakopoulos, and F. Parello, “Hydrothermal methane fluxes from the soil at Lakki plain (Nisyros, Greece),” in *Proceedings of the 13th International Congress of the Geological Society of Greece*, vol. 47no. 3, pp. 1920–1928, Chania, Crete, Greece, September 2013, Bulletin of the Geological Society of Greece.
- [33] US EPA, “Method 7473 (SW-846): mercury in solids and solutions by thermal decomposition, amalgamation, and atomic absorption spectrophotometry,” 1998, February 2019, <https://www.epa.gov/sites/production/files/2015-07/documents/epa-7473.pdf>.
- [34] G. W. Thomas, “Soil pH and soil acidity,” in *Methods of soil analysis - Part 3 Chemical methods*, Book Series, D. L. Sparks, Ed., no. 5pp. 475–490, Soil Sci. Soc. Am, 1996.
- [35] R. Ebinghaus, S. G. Jennings, W. H. Schroeder et al., “International field intercomparison measurements of atmospheric mercury species at Mace head, Ireland,” *Atmospheric Environment*, vol. 33, no. 18, pp. 3063–3073, 1999.
- [36] R. Nakagawa, “Estimation of mercury emissions from geothermal activity in Japan,” *Chemosphere*, vol. 38, no. 8, pp. 1867–1871, 1999.
- [37] US EPA, *Method IO-5: Sampling and Analysis for Atmospheric Mercury. Compendium of Methods for the Determination of Inorganic Compounds in Ambient Air*, Center for Environmental Research Information Office of Research and Development, US Environmental Protection Agency, Cincinnati, OH, 1999.
- [38] S. E. Sholupov and A. A. Ganeyev, “Zeeman atomic absorption spectrometry using high frequency modulated light polarization,” *Spectrochimica Acta Part B: Atomic Spectroscopy*, vol. 50, no. 10, pp. 1227–1236, 1995.
- [39] S. Sholupov, S. Pogarev, V. Ryzhov, N. Mashyanov, and A. Stroganov, “Zeeman atomic absorption spectrometer RA-915+ for direct determination of mercury in air and complex matrix samples,” *Fuel Processing Technology*, vol. 85, no. 6–7, pp. 473–485, 2004.
- [40] A. Aiuppa, C. Federico, G. Giudice, and S. Gurrieri, “Chemical mapping of a fumarolic field: La Fossa Crater, Vulcano Island (Aeolian Islands, Italy),” *Geophysical Research Letters*, vol. 32, no. 13, article L13309, 2005.
- [41] G. Tamburello, “Ratiocalc: software for processing data from multicomponent volcanic gas analyzers,” *Computers & Geosciences*, vol. 82, pp. 63–67, 2015.
- [42] A. J. Sinclair, “Selection of threshold values in geochemical data using probability graphs,” *Journal of Geochemical Exploration*, vol. 3, no. 2, pp. 129–149, 1974.
- [43] W. D’Alessandro, A. Aiuppa, S. Bellomo et al., “Sulphur-gas concentrations in volcanic and geothermal areas in Italy and Greece: characterising potential human exposures and risks,” *Journal of Geochemical Exploration*, vol. 131, pp. 1–13, 2013.
- [44] J. Fiebig, S. Hofmann, F. Tassi, W. D’Alessandro, O. Vaselli, and A. B. Woodland, “Isotopic patterns of hydrothermal hydrocarbons emitted from Mediterranean volcanoes,” *Chemical Geology*, vol. 396, pp. 152–163, 2015.
- [45] R. Nakagawa, “Amounts of mercury discharged to atmosphere from fumaroles and hot spring gases in geothermal areas,” *Nippon Kagaku Kaishi*, vol. 1984, no. 5, pp. 709–715, 1984.
- [46] R. Nakagawa, “Amounts of mercury discharged to atmosphere from fumaroles in geothermal areas of Hokkaido,” *Nippon Kagaku Kaishi*, vol. 1985, no. 4, pp. 703–708, 1985.
- [47] J. C. Varekamp and P. R. Buseck, “Global mercury flux from volcanic and geothermal sources,” *Applied Geochemistry*, vol. 1, no. 1, pp. 65–73, 1986.
- [48] B. W. Christenson and E. K. Mroczek, “Potential reaction pathways of Hg in some New Zealand hydrothermal environments,” in *Volcanic, Geothermal, and Ore-Forming Fluids: Rulers and Witnesses of Processes within the Earth*, S. F. Simmons and I. Graham, Eds., vol. 10, pp. 111–132, Spec. Publ. Soc. Economic Geologists, 2003.
- [49] E. Bagnato, F. Parello, M. Valenza, and S. Caliro, “Mercury content and speciation in the Phlegrean Fields volcanic complex: evidence from hydrothermal system and fumaroles,” *Journal of Volcanology and Geothermal Research*, vol. 187, no. 3–4, pp. 250–260, 2009.
- [50] N. Pirrone, S. Cinnirella, A. Dastoor et al., “Atmospheric pathways, transport and fate,” *Technical Background Report for the Global Mercury Assessment 2013*, AMAP/UNEP. Arctic Monitoring and Assessment Programme, Oslo, Norway/UNEP Chemicals Branch, Geneva, Switzerland, 2013.
- [51] NOAA-ESRL, “National Oceanic & Atmospheric Administration – Earth System Research Laboratory – Global Monitoring Division,” 2019, February 2019, ftp://aftp.cmdl.noaa.gov/products/trends/co2/co2_annmean_gl.txt.
- [52] C. Cardellini, G. Chiodini, and F. Frondini, “Application of stochastic simulation to CO₂ flux from soil: mapping and quantification of gas release,” *Journal of Geophysical Research*, vol. 108, no. B9, article 2425, 2003.

- [53] E. Bagnato, G. Tamburello, A. Aiuppa, M. Sprovieri, G. E. Vougioukalakis, and M. Parks, "Mercury emissions from soils and fumaroles of Nea Kameni volcanic centre, Santorini (Greece)," *Geochemical Journal*, vol. 47, no. 4, pp. 437–450, 2013.
- [54] F. Tassi, J. Cabassi, S. Calabrese et al., "Diffuse soil gas emissions of gaseous elemental mercury (GEM) from hydrothermal-volcanic systems: an innovative approach by using the static closed-chamber method," *Applied Geochemistry*, vol. 66, pp. 234–241, 2016.
- [55] V. W. Lueth, R. O. Rye, and L. Peters, "'Sour gas' hydrothermal jarosite: ancient to modern acid-sulfate mineralization in the southern Rio Grande Rift," *Chemical Geology*, vol. 215, no. 1–4, pp. 339–360, 2005.
- [56] D. R. Zimbelman, R. O. Rye, and G. N. Breit, "Origin of secondary sulfate minerals on active andesitic stratovolcanoes," *Chemical Geology*, vol. 215, no. 1–4, pp. 37–60, 2005.
- [57] R. T. Ottesen, M. Birke, T. E. Finne et al., "Mercury in European agricultural and grazing land soils," *Applied Geochemistry*, vol. 33, pp. 1–12, 2013.
- [58] R. S. Martin, M. L. I. Witt, G. M. Sawyer et al., "Bioindication of volcanic mercury (Hg) deposition around Mt. Etna (Sicily)," *Chemical Geology*, vol. 310–311, pp. 12–22, 2012.
- [59] M. Lodenius, "Use of plants for biomonitoring of airborne mercury in contaminated areas," *Environmental Research*, vol. 125, pp. 113–123, 2013.
- [60] A. Pérez-Sanz, R. Millán, M. J. Sierra et al., "Mercury uptake by *Silene vulgaris* grown on contaminated spiked soils," *Journal of Environmental Management*, vol. 95, no. 2012, pp. S233–S237, 2012.
- [61] L. Fay and M. S. Gustin, "Investigation of mercury accumulation in cattails growing in constructed wetland mesocosms," *Wetlands*, vol. 27, no. 4, pp. 1056–1065, 2007.
- [62] L. Windham-Myers, J. A. Fleck, J. T. Ackerman et al., "Mercury cycling in agricultural and managed wetlands: a synthesis of methylmercury production, hydrologic export, and bioaccumulation from an integrated field study," *Science of the Total Environment*, vol. 484, no. 1, pp. 221–231, 2014.
- [63] M. D. Tabatchnick, G. Nogaro, and C. R. Hammerschmidt, "Potential sources of methylmercury in tree foliage," *Environmental Pollution*, vol. 160, no. 1, pp. 82–87, 2012.
- [64] L. Poissant, H. H. Zhang, J. Canário, and P. Constant, "Critical review of mercury fates and contamination in the Arctic tundra ecosystem," *Science of the Total Environment*, vol. 400, no. 1–3, pp. 173–211, 2008.
- [65] A. Adjorlolo-Gasokpoh, A. A. Golow, and J. Kambo-Dorsa, "Mercury in the surface soil and cassava, *Manihot esculenta* (flesh, leaves and peel) near goldmines at Bogoso and Prestea, Ghana," *Bulletin of Environmental Contamination and Toxicology*, vol. 89, no. 6, pp. 1106–1110, 2012.
- [66] N. Yoshimoto, E. Inoue, K. Saito, T. Yamaya, and H. Takahashi, "Phloem-localizing sulfate transporter, Sultr1;3, mediates re-distribution of sulfur from source to sink organs in *Arabidopsis*," *Plant Physiology*, vol. 131, no. 4, pp. 1511–1517, 2003.
- [67] P. Buchner, C. E. E. Stuijver, S. Westerman et al., "Regulation of sulfate uptake and expression of sulfate transporter genes in *Brassica oleracea* as affected by atmospheric H₂S and pedospheric sulfate nutrition," *Plant Physiology*, vol. 136, no. 2, pp. 3396–3408, 2004.
- [68] WHO, *Air quality guidelines for Europe. WHO Regional Publications European Series 91*, World Health Organization Regional Office for Europe, Copenhagen, 2000.
- [69] US OSHA, "Health and safety (Hg). Occupational Hazards," 2007, March 2018, <https://www.osha.gov/SLTC/mercury/index.html>.
- [70] EPA/ATSDR, "National Mercury Cleanup Policy Workgroup: action levels for elemental mercury spills," 2012, February 2019, http://www.atsdr.cdc.gov/emergency_response/Action_Levels_for_Elemental_Mercury_Spills_2012.pdf.
- [71] M. L. I. Witt, T. P. Fischer, D. M. Pyle, T. F. Yang, and G. F. Zellmer, "Fumarole compositions and mercury emissions from the Tatun Volcanic field, Taiwan: results from multi-component gas analyser, portable mercury spectrometer and direct sampling techniques," *Journal of Volcanology and Geothermal Research*, vol. 178, no. 4, pp. 636–643, 2008.
- [72] A. Aiuppa, E. Bagnato, M. L. I. Witt et al., "Real-time simultaneous detection of volcanic Hg and SO₂ at La Fossa Crater, Vulcano (Aeolian Islands, Sicily)," *Geophysical Research Letters*, vol. 34, no. 21, article L21307, 2007.
- [73] E. Bagnato, P. Allard, F. Parello, A. Aiuppa, S. Calabrese, and G. Hammouya, "Mercury gas emissions from La Soufrière Volcano, Guadeloupe Island (Lesser Antilles)," *Chemical Geology*, vol. 266, no. 3–4, pp. 267–273, 2009.

Research Article

Mofette Vegetation as an Indicator for Geogenic CO₂ Emission: A Case Study on the Banks of the Laacher See Volcano, Vulkaneifel, Germany

Hardy Pfanz , Frank Saßmannshausen, Christiane Wittmann, Benny Pfanz, and Annika Thomalla

Institute of Applied Botany and Volcano Biology, Faculty of Biology, University of Duisburg-Essen, 45117 Essen, Germany

Correspondence should be addressed to Hardy Pfanz; hardy.pfanz@uni-due.de

Received 28 January 2019; Accepted 7 June 2019; Published 8 August 2019

Academic Editor: Giovanni Martinelli

Copyright © 2019 Hardy Pfanz et al. This is an open access article distributed under the Creative Commons Attribution License, which permits unrestricted use, distribution, and reproduction in any medium, provided the original work is properly cited.

A geogenic CO₂ emitting site (mofette U1) at the banks of the Laacher See, Eifel Mountains, was chosen to study the relationship between heavy postvolcanic soil degassing and vegetation during spring season. To test any interrelation between soil CO₂ degassing and vegetation, soil chemism (pH, water content, conductivity, and humus content) and vegetation studies (number of species, plant-soil coverage) were performed. Geogenic soil degassing patterns of carbon dioxide and oxygen were clearly inhomogeneous, resembling soil porosity and distinct permeation channels within the soil. CO₂ concentrations ranged from zero to 100%. Soil CO₂ increased, while soil oxygen decreased with increasing soil depth. There was a reasonable correlation between CO₂ degassing and soil pH as well as soil conductivity. Soil organic matter (SOM) resembled soil water distribution. The number of plant species (from a total of 69 species) as well as plant coverage strongly followed geogenic CO₂ degassing. The total number of growing species was highest in low CO₂ soils (max. 17 species per m²) and lowest at high CO₂-emitting sites (one species per m²). Plant coverage followed the same pattern. Total plant coverage reached values of up to 84% in slightly degassing soils and only 5–6% on heavy CO₂-venting sites. One plant species proved to be highly mofettophilic (marsh sedge, *Carex acutiformis*) and strictly grew on CO₂ degassing sites. Most other species like grove windflower, spring fumewort, fig buttercup, wood bluegrass, addersmeat, and common snowberry showed a mofettophobic behavior and strictly avoided degassing areas. Specific plant species can thus be used to detect and monitor pre- or postvolcanic CO₂ degassing.

1. Introduction

Mofettes are sites with dry CO₂ gas exhalations at ambient temperatures. The gaseous CO₂ originates from magma chambers or from Earth mantle degassing. It moves upward through fissures and cracks within the rocks [1–3]. Along its path, it reacts with wet and dry soil phases, finally exerting its influence on organisms living either within the subterranean soil or directly on the soil surface [4–10]. Depending on the local geological and hydrogeological conditions, the upward migration of CO₂ gas may appear at the surface either as dry CO₂ emanation (mofette) or as CO₂-rich mineral water. Several publications already described the effects of the potentially acidic gas of dry CO₂ emanations on the

soil phase [11–13], on soil insects, nematode worms, and spiders [14–16], on soil microbiota [for review see [5]], and on vegetation. Most authors describe the effects of enhanced geogenic CO₂ on physiological and ecophysiological processes, or anatomical and morphological adaptations of plants [6–8, 17–22]. Only a few references can be found on the special vegetation of these sites—the mofette vegetation [17, 23–26].

The present paper studies a natural, terrestrial mofette site at the Laacher See volcano, where CO₂ from the Laacher See volcano still reaches the surface, influencing ecosystems. The quiet volcano is part of the east Eifel Volcanic field belonging to the West European Rift System. The last eruptive phase of the Laacher See volcano is about 13,000 years

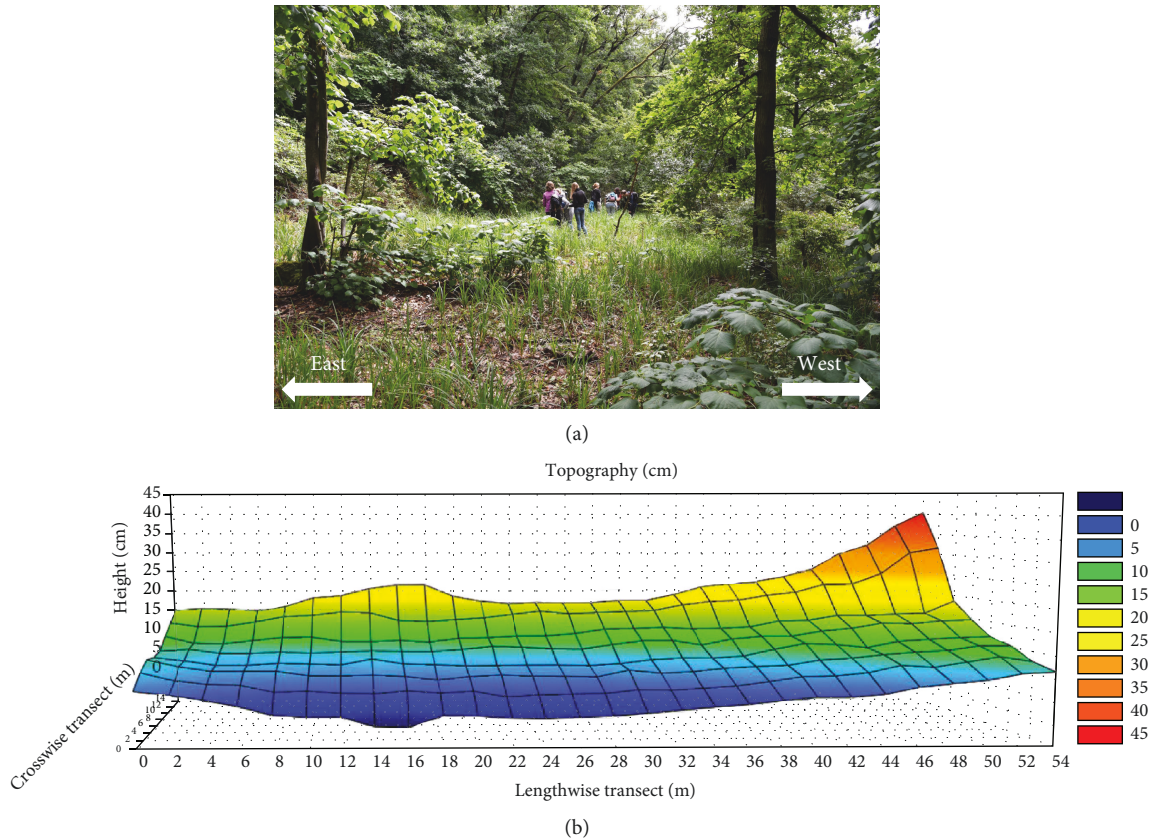


FIGURE 1: Photo from the U1 mofette as seen from north to south in June 2015. The dominating ground vegetation in the mofette is marsh sedge (*Carex acutiformis*). Several linden trees and oaks grow on the edge. The eastern bank of the Laacher See and the walking trail are located on the right side of the picture (a). Topography of the U1 mofette at the lower terrace of the eastern rim of the Laacher See caldera viewed from the Western side. North side is left and south right of the picture (b).

ago [27]. The aim of this work was to find out to which extent geogenic CO_2 concentrations within the soil influence soil chemism and allow or inhibit plant life. It was furthermore of great interest to figure out whether specific plant species can be used as biological indicators to detect and monitor otherwise nondetected volcanic CO_2 emissions.

2. Material and Methods

2.1. Site Description. The study area “U1 mofette” (Figure 1(a)) is located on the first terrace on the eastern inner flanks of the Laacher See Volcano, Eifel Mountains, Germany (see also [28]), just 5 m from the southern wall of the ruins of the so-called Jesuiten-Villa (a two-stored stone house used by the monks to celebrate their free days). It belongs to the cadastral district “Bei der rechten Erde” and extents parallel to the banks of the Laacher See. The terrace is the result of the second drainage phase of the lake performed in 1844 (first drainage in 1164; [29]). As the area is located within a forest, mostly half-light and only rarely full-light conditions prevail, with some heavily shaded parts at the upper left part of the area. Topographically, the U1 area is flat with the highest part in the SE corner (Figure 1(b)). The first 54 m of the 80–90 m long area was

under investigation. In the lake close to the mofette area, CO_2 bubbles indicate visible geogenic gas emission [30].

2.1.1. Sampling and Measurements. The area was chosen to study the relationship between geogenic soil degassing of carbon dioxide and the prevailing vegetation and between soil gas and selected geochemical and soil biological parameters. Seven transects with 2 m spacing and a total length of 54 m were laid out parallel to the lakeshore line. The hiking trail marked the western (lower) end of the study area (Figures 1(a) and 1(b)). All measurements were made at each 2 m intersection of the transect lines, resulting in 224 individual sample spots. Soil gas concentrations (CO_2 and O_2) were measured at all 224 spots at four different soil depths (10, 20, 40, and 60 cm), by coring holes into the soil and inserting gas tight tubing. During the measurements, the holes were closed with a lid to avoid air mixing during the actual measurements. The gas measurements were carried out with a portable landfill gas analyser GA2000 (Geotechnical Instruments, England) equipped with water and dust filters. Problems occurred when the ground was wet or waterlogged, as liquid water would damage the sensitive cells of the analyser. Polyethylene and Teflon tubing (1 cm diameter) was used to enlarge the measuring radius. Readings were recorded after several seconds to one minute.

Gas flux was performed at each grid intersection using a portable diffuse carbon dioxide flux meter system (West Systems Portable diffuse flux meter carbon dioxide high-flux, Pisa, Italy). The device consists of an accumulation chamber (type B), a CO₂ IR detector (Polytron, Dräger), and a PDA palmtop (Brand, Acer n300) for data communication, evaluation, and storage.

The CO₂ flux measurement method is based on the measurement of rising CO₂ concentration versus time in terms of ppm s⁻¹. If the gas concentration inside the chamber is constant, linear regression is used to calculate the gas flux F [moles·m⁻²·day⁻¹] by the following equation:

$$F = K * s \quad (1)$$

where K is the accumulation chamber factor and s is the slope of the flux curve, determined by linear regression.

K is calculated by the following equation:

$$K = \frac{86400 * P}{106 * R * T} * \frac{V}{A} \quad (2)$$

where P is the barometric pressure (hPa), R is the gas constant 0.08314510 (L·bar·K⁻¹·mol⁻¹), T is the air temperature (K), V is the chamber net volume (6.186*10⁻³ m³), and A is the chamber inlet net area (3.140*10⁻² m²). P was measured with the GA2000 and T with a thermocouple thermometer.

2.2. Soil Analysis. After determination of the soil gas, soil cores were taken very close to the points of the gas measurements. A standard soil borer (Pürkhauer; Thomas Müller, Germany) was used, and samples were taken between soil depths of 7 to 13 cm. This depth range was thought to reflect the main rooting horizon of herbaceous plants [31]; this soil depth is also the approximate range of the aerated surface soil [32]. The fresh samples were placed in small airtight plastic cylinders and stored cool until analysis.

Soil water content was determined by drying the soil samples of known fresh weight at 75°C for three days in an oven and reweighing after cooling to room temperature in a desiccator. Dry soil samples were ground, and soil pH was measured with a pH electrode (WTW, Germany) in bi-distilled water (750 mg dry soil in 15 ml water). After pH determination, soil conductivity was determined in the same solution using a conductivity meter (inoLab Multi 9420 IDS, WTW, Germany).

To determine soil organic matter (SOM), 1 g of ground, dry soil was heated (450°C for 18 hours) in an oven (muffle furnace; Heraeus, Germany), cooled to room temperature in a desiccator, and reweighed (for details see [33]).

2.3. Vegetation Analysis. Vegetation cover was estimated according to [34]. Londo's decimal scale has some advantages over the most commonly used scale of [35]. The decimal scale is a pure dominance scale that uses smaller steps of maximal 10%. The more precise information about the plots' vegetation cover leads to better correlations with the abiotic factors. On the other hand, a transformation into

the Braun-Blanquet scale can be arranged without great difficulty [36].

All measurements were carried out at stable weather conditions during a one-week period in February 2013. Vegetation analysis was done in May 2013.

2.4. Statistical Analysis. Statistical analysis was carried out using MS Excel (Microsoft, USA), SigmaPlot 11.0 (Systat Software, USA), and SPSS (SPSS, USA). Multivariable statistical analysis was done using multiattribute analysis based on canonical correspondence analysis (CCA; CANOCO 4.5 program). Probable correlations between plant habitat parameters, plant species composition, and plant distribution can thus be detected [37].

3. Results and Discussion

3.1. Degassing Patterns

3.1.1. Soil Gas Concentrations. Geogenic CO₂ degassing was clearly heterogeneous within the selected area. At 10 cm soil depth, high [CO₂] were found in a line running nearly diagonal from the left upper corner to the area close to the lower right part (Figure 2(a)). At this depth, CO₂ extremes evolved as isolated islands surrounded by lower values.

Soil gas concentrations clearly changed with soil depth. Carbon dioxide increased with increasing soil depth whereas oxygen values decreased at deeper soil horizons (Figures 2(a)–(d) and 3(a)–(d)). Yet the principal “diagonal” degassing pattern was still visible although at a soil depth of 60 cm the whole area showed highly increased CO₂ values. Thus, at deeper soil horizons, a clear broadening of the degassing pattern occurs which narrows when the gas moves upward to the soil surface. Sometimes, the narrowing of CO₂ concentrations at lower soil depths is evident as small channels are formed showing the vertical gas-transducing chimneys. The transect illustration shows the modification of gas permeation pathways with soil depth.

There are two selected transects of the U1 mofette (Figure 4). The upper panel nicely shows two CO₂ gas chimneys (at 12 m and 42 m) emerging at a soil depth of ca. 30 cm further narrowing to a diameter of less than 50 cm finishing at the very soil surface. Gas concentration at the surface thus reaches 80–100% CO₂. Another CO₂ channel (at 36 m) does not reach the actual soil surface but ends at 10 cm soil depth (Figure 4). A less permeable or impermeable soil layer transiently or permanently locks the permeating gas in pockets.

The same is true for oxygen, although in this case a narrowing of oxygen channels with increasing soil depths is visible (Figure 4(b)). Between 8 and 14 m and at point 48 m and 54 m, high O₂ concentrations can be measured even at a soil depth of 40–50 cm. At 54 m, oxygen concentrations are high at even deeper soil levels (Figure 4). At these locations, control plants (mofettophobes) could easily grow.

Also for oxygen, a more or less diagonal concentration pattern from the left upper corner to the right lower corner of the area is seen (Figures 3(a)–3(d)). Yet in contrast to the [CO₂], an inverse pattern is found for [O₂] (Figures 2 and 3). At spots with high [CO₂], low [O₂] is found and vice

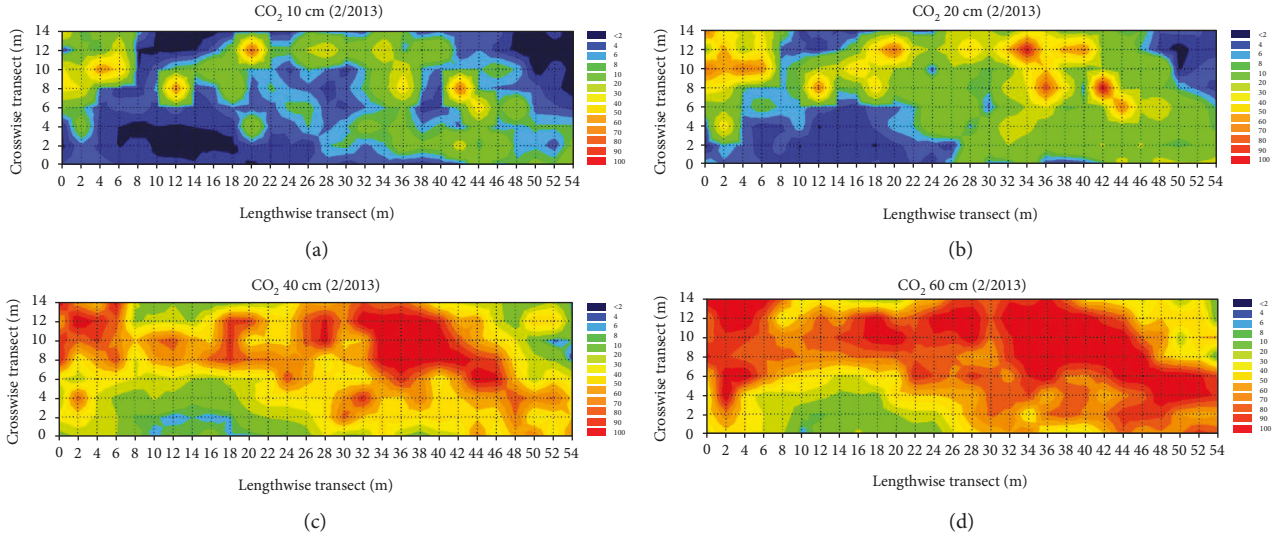


FIGURE 2: (a–d) Soil CO_2 concentrations within the U1 mofette (14×54 m). Measurements were done at each intersection of the 1×2 m grid. CO_2 concentrations at four different soil depths are given: (a) 10 cm, (b) 20 cm, (c) 40 cm, and (d) 60 cm. The colour bar indicates the gas concentration ranges. Orientation of the site as in Figure 1(b). CO_2 concentrations are given in %.

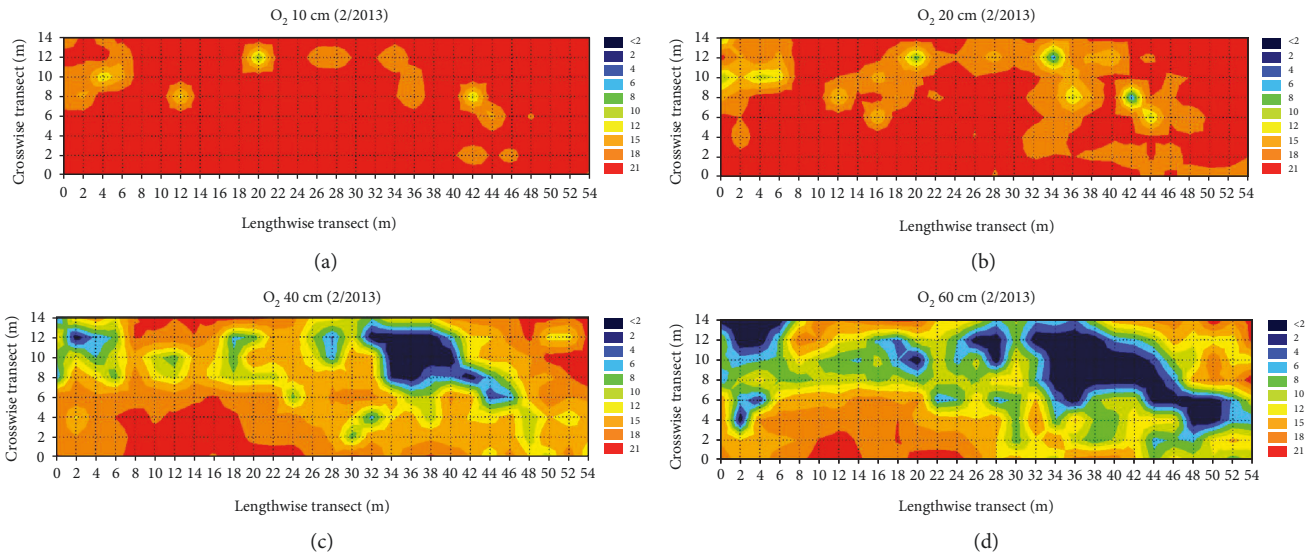


FIGURE 3: (a–d) Soil O_2 concentrations within the U1 mofette. Measurements were performed at each intersection of the 1×2 m grid. O_2 concentrations at four different soil depths are given: (a) 10 cm, (b) 20 cm, (c) 40 cm, and (d) 60 cm. The colour bar indicates the gas concentration ranges. Orientation of the site as in Figure 1(b). CO_2 concentrations are given in %.

versa. If CO_2 migrates towards the surface, mainly by diffusion and advective processes, it leads to a dilution of the in situ soil gas composition. Vodnik et al. [10] have already published the inverse proportionality between carbon dioxide and oxygen concentrations at mofette sites.

Oxygen concentrations $< 2\%$ were only apparent at soil depths below 40 cm. Nevertheless, even at a soil depth of 20 cm, the main rooting zone of many plants, $[\text{O}_2]$ below 15% (slightly hypoxic conditions) can be found in many spots.

3.1.2. CO_2 Fluxes. Additional to the CO_2 concentrations, soil CO_2 fluxes within the U1 mofette were determined directly on the soil surface (Figure 5). Care was taken to avoid the

inclusion of vegetation inside the accumulation chamber. As measurements were performed in February, also, biotic CO_2 evolution by the soil edaphon is expected to be reduced due to the cooler winter temperatures. Postvolcanic soil CO_2 fluxes nicely paralleled soil CO_2 concentrations. Again, CO_2 fluxes were clearly inhomogeneous within the area and a diagonal degassing pattern of enhanced CO_2 flux is seen through the mofette area with the highest CO_2 emission rates in the upper left corner of the area. Rates of $600 \text{ moles } \text{CO}_2 \text{ m}^{-2} \text{ soil surface day}^{-1}$ were seen in two heavily degassing islands (Figure 5). As with the $[\text{CO}_2]$, the upper right corner and the lower left part of the mofette still act as control sites ($2\text{--}8 \text{ moles } \text{CO}_2 \text{ m}^{-2} \text{ soil surface day}^{-1}$).

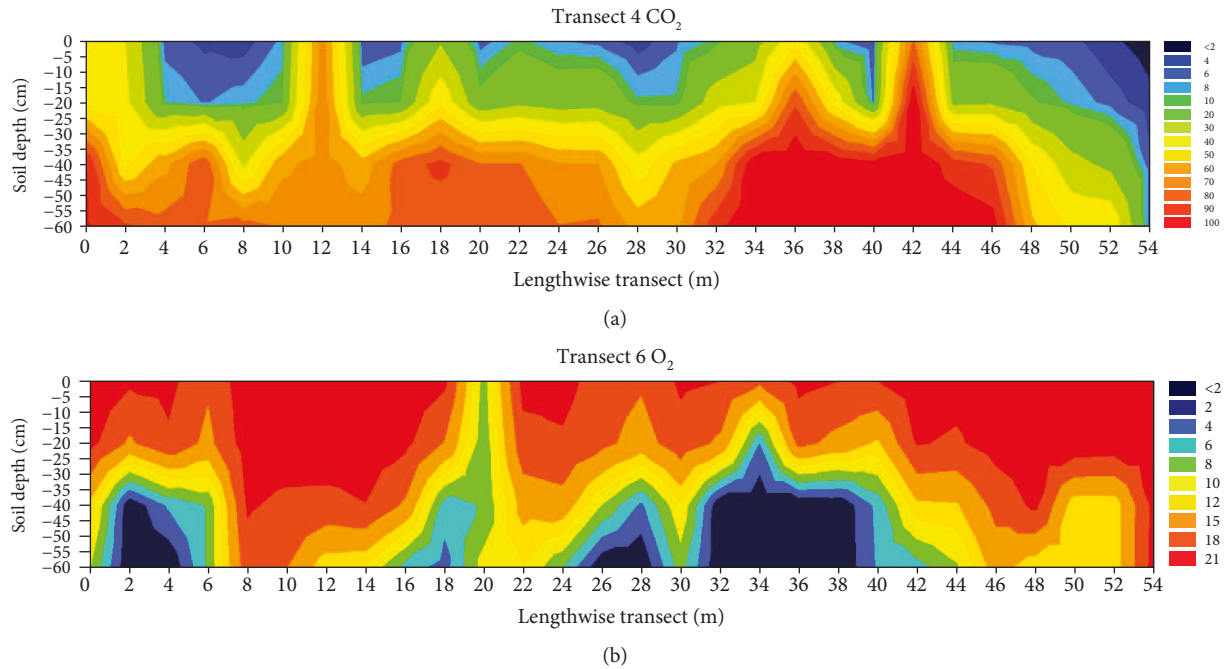


FIGURE 4: Vertical sections of CO₂ (a) and O₂ (b) concentrations showing the prevailing gas channels. Two different transects for the two different gases were chosen. (a) CO₂ concentrations are shown in linear transect 4. Up to five CO₂ channels can be seen from which four are reaching the soil surface. (b) Transect 6 is used to illustrate oxygen channels through the soil. CO₂ concentrations are given in %.

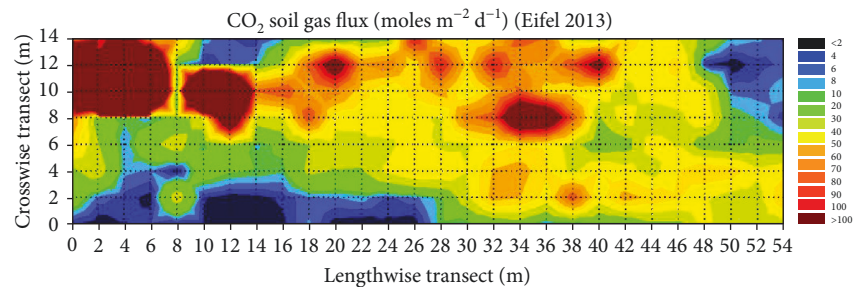


FIGURE 5: CO₂ soil fluxes in moles m⁻² d⁻¹ as measured at each intersection of the 1 × 2 m grid within the U1 mofette. Orientation of the site as in Figure 1(b).

3.1.3. Gas Permeation Barriers. Interestingly, soil penetration data underline the gas permeation pathways established by gas concentration measurements. Soil rigidity data obtained with a penetrometer clearly mark the microsities of low and high gas permeability (Figure 6(b)). Higher soil density or compactness occurs in loamy or otherwise clogged soil parts or in soil with a high skeleton content (stones, stone fragments). These soil characteristics reduce or even do not permit at all the upward migration of the CO₂ gas toward the surface.

Following the data from the soil surface down to a soil depth of 80 cm, it becomes clear that the higher the soil resistance, the lower the actual CO₂ penetration or concentration. Soil hardness is extremely heterogeneous within the area but increases with soil depth. Due to the inhomogeneity of this parameter, a three-dimensional network of vertical and horizontal soil channels is formed allowing gas penetration only in distinct directions. A three-dimensional pattern of easy penetration and prohibited sites is thus formed. The picture

of soil gas concentrations nicely mirrors this diffusional barrier pattern (Figures 2 and 6(b)).

Even the extractable skeleton content in the soil somehow reflects the gas emission pattern (Figure 6(a)). The topsoil has a low content of stones and fragments in high gas emission zones (diagonal line from top left to bottom right), whereas in the upper right corner of the mofette, 50% of dry matter belongs to the soil skeleton. Naturally, the stone fragments are not a perfect hindrance to gas permeation per se. Penetrating gas could easily circumvent isolated stone fragments within the soil. The concentration of stones just reflects the presence of larger blocks and a solid lithosphere in the lower ground.

3.2. Physicochemical Soil Parameters

3.2.1. Soil Water. Figure 6(c) shows values for the soil water content within the mofette area. At the time of our measurements, the water content of the area ranged between 10 and

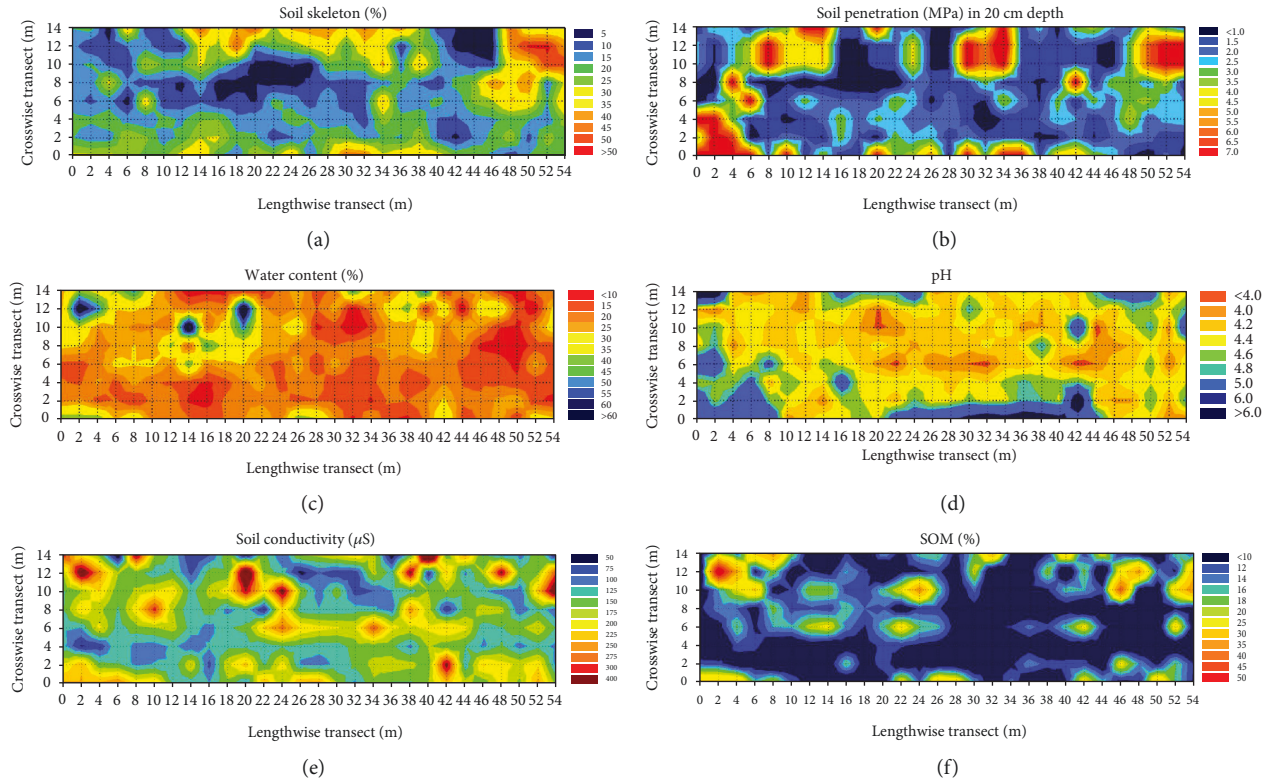


FIGURE 6: (a–f) Soil skeleton content (a) and soil rigidity (b) of the U1 mofette as measured by stone extraction and weight and by soil penetration using a penetrometer. Water content (c), soil pH (d), soil conductivity (e), and soil organic matter (SOM) (f) are also given. Orientation of the site as in Figure 1(b).

30%, with an average between 20 and 30%. Dry sites with a water content less than 10% occurred in larger islands on the upper border and a site in the upper right corner. Also, around the lower margin (14–16 m), a drier island was seen. Only three very small islands in the upper left corner contained more water and reached values of up to 60%. The position of these islands corresponds to the position of the three main vents, characterized by high CO_2 fluxes and high soil CO_2 concentrations at 10 cm depth and thereunder (Figures 2 and 5).

3.2.2. Soil pH. Ascending geogenic carbon dioxide permeates through different soil phases, and due to its high solubility in water, it dissolves in soil water according to temperature, atmospheric pressure, and actual gas concentration and/or flux. Dissolved CO_2 rapidly dissociates in water producing protons thus acidifying the aqueous soil phases as long as buffering capacities are below a certain limit [38–40]. To check whether the CO_2 -permeated mofette soil already shows acidification, soil pH was determined within the U1 mofette at each grid intersection (Figure 6(d)). It can be said *cum grano salis* that there is a reasonable correlation between soil pH and the prevailing CO_2 concentrations. The measured values ranged between pH 3.6 and pH 6.4 with a clear diagonal pattern where slightly more acidic soils prevail. Higher pH values (around 5.5 to 6) occur at microsites with lower CO_2 concentrations/fluxes. Yet two regions clearly differ. At the right end of the area and between 10 and 20 m (lowest transect) in front of the area, pH values are quite

low (pH ca. 4.4–4.0) although $[\text{CO}_2]$ concentrations are not enhanced. [10, 41] already described this pH-lowering effect with accordant results from mofette fields in Slovenia whereas [42] found no effects for three Japanese CO_2 springs [see also [12, 13]]. Our findings are in line with a recent study of [43] which showed that persistent CO_2 leakage affects the soil chemical composition, altering soil from slight alkaline to acidic over a period of 38 treatment days. [44] laid a transect through a gas vent in Italy and found that across the transition zone, between vent core and background, soil pH values dropped quickly from 4.5 to 3.8, which resulted in a clear influence on the chemical composition of the soil. Most oxide concentrations decreased, while parameters such as cation exchange capacity, loss on ignition, and total organic carbon began to increase. These chemical soil conditions will certainly affect nutrient availability or uptake [7], root functioning [45, 46], and the above ground processes of photosynthesis [7, 19].

3.2.3. Soil Organic Matter. Stagnant soil water and hypoxic soil conditions should also affect the formation of soil organic matter [SOM; [11, 47, 48]]. Therefore, the total SOM content was analysed in all soil samples (Figure 6(f)). Positive relationships between SOM and soil water have been published several times [49–51]. The accumulation of dead biomass in wet soils is thought to be the consequence of a disturbed mineralisation. It may be explained by the oxygen requirement of most litter-decomposing animals, fungi, and bacteria. A sufficient oxygen supply cannot be maintained when

the soil pores are filled with water because the diffusion rate of oxygen in water is 10,000 times lower than that in a gaseous medium [52]. In mephitic soils, oxygen is deprived by the pure presence of enhanced CO₂. The SOM pattern of the mofette (Figure 6(f)) largely reflects the distribution of soil water (Figure 6(c)) with the highest SOM contents in the upper left and right corner of the mofette area.

3.3. Vegetation

3.3.1. Number of Plant Species. In the present study, 69 different plant species were counted within the mofette area during a quantitative species survey in May 2013 (Table 1). Most species could be determined to the species level. In four juvenile and pathogenically affected specimens, only the genus could be determined (*Cirsium*, *Chaerophyllum*, *Dryopteris*, and *Epilobium*). The plants found are in good agreement with those found by others in that area [53–55]. As the total number of species as well as the soil coverage of each single species was estimated in each 2 m² square, occurrence and soil coverage of each species could well be correlated with the degassing pattern of CO₂ and O₂ in the soil.

Comparing the pattern of the number of species per area within the U1 mofette with the prevailing CO₂ degassing pattern, it becomes evident that high species numbers (up to 17 per 2 m²) only occur at sites of diminished CO₂ presence (Figures 2 and 7). Two locations with a high number of species become apparent. On the left upper corner, a diagonal pattern (from 7/16 to 2/2) and a spot on the lower middle (3/30 to 3/44) are evident. Both areas are defined by very low [CO₂]. In contrast, the species number is small at sites of higher CO₂ emission (CO₂ diagonal emission). One to four different species are found at CO₂ extremes.

3.3.2. Plant Coverage. The same observation is made when plant coverage is correlated with the CO₂ degassing pattern (Figure 7(b)). The plant coverage of 41 to 84% is found only at sites of low CO₂ emission. A linear transect from the upper left corner to the upper right corner of the area shows high plant coverages at low CO₂ concentrations. A larger island in the middle of the area also shows high plant coverage and low CO₂ concentrations at lower soil levels (Figure 7). At high CO₂ concentrations (and fluxes), plant coverage can be as low as 4–10%. These results are in line with findings of [44] who reported on a naturally occurring gas vent located within a Mediterranean pasture ecosystem (Latera geothermal field, central Italy). They found no vegetation within the 6 m wide center of the vent where CO₂ concentrations > 95% were determined; an approximately 20 m wide halo surrounding the core formed a transition zone, over which a gradual decrease in [CO₂] and a rapid decrease in CO₂ fluxes could be observed. In the transition zone, grasses dominated near the vent core. They were progressively replaced by clover and a greater plant diversity distant from the vent center. However, this study had not provided a full characterization of the botanical taxa.

3.3.3. Mofettophilic and Mofettophobic Plants. Correlating the growth patterns of selected plants and the degassing pattern within the designated mofette area, it turns out that just

TABLE 1: List of species of the U1 mofette found during a quantitative survey in May 2013.

	<i>Alliaria petiolata</i>	<i>Anemone nemorosa</i>
	<i>Carex acutiformis</i>	<i>Carex hirsutella</i>
	<i>Cardamine hirsuta</i>	<i>Cerastium holosteoides</i>
	<i>Chaerophyllum</i> spec.	<i>Cirsium</i> spec.
	<i>Corydalis solida</i>	<i>Dactylis glomerata</i>
	<i>Dentaria bulbifera</i>	<i>Deschampsia cespitosa</i>
	<i>Dianthus carthusianorum</i>	<i>Dryopteris filix-mas</i>
	<i>Dryopteris</i> spec.	<i>Epilobium</i> spec.
	<i>Equisetum</i> spec.	<i>Galeopsis tetrahit</i>
	<i>Galium aparine</i>	<i>Galium odoratum</i>
	<i>Geranium robertianum</i>	<i>Geum urbanum</i>
Herbaceous plants/ferns	<i>Hieracium murorum</i>	<i>Hypericum perforatum</i>
	<i>Lapsana communis</i>	<i>Melica mutica</i>
	<i>Mercurialis perennis</i>	<i>Moehringia trinervia</i>
	<i>Mycelis muralis</i>	<i>Poa annua</i>
	<i>Poa nemoralis</i>	<i>Polygonatum multiflorum</i>
	<i>Potentilla sterilis</i>	<i>Polygonum</i> spec.
	<i>Senecio sylvaticus</i>	<i>Ranunculus ficaria</i>
	<i>Stellaria media</i>	<i>Stellaria holostea</i>
	<i>Teucrium scordium</i>	<i>Taraxacum officinale</i>
	<i>Veronica chamaedrys</i>	<i>Veronica hederifolia</i>
	<i>Veronica officinale</i>	<i>Vinca minor</i>
	<i>Cornus sanguinea</i>	<i>Crataegus monogyna</i>
	<i>Crataegus oxyacantha</i>	<i>Euonymus europaeus</i>
	<i>Lonicera periclymenum</i>	<i>Hedera helix</i>
Shrubs and subshrubs	<i>Ribes petraeum</i>	<i>Rosa</i> spec.
	<i>Rubus fruticosus</i> agg.	<i>Sambucus nigra</i>
	<i>Symphoricarpos albus</i>	<i>Syringa vulgaris</i>
	<i>Acer platanoides</i>	<i>Acer pseudoplatanus</i>
	<i>Carpinus betulus</i>	<i>Fagus sylvatica</i>
Trees	<i>Fraxinus excelsior</i>	<i>Malus domestica</i>
	<i>Prunus avium</i>	<i>Quercus petraea</i>
	<i>Tilia platyphyllos</i>	
	<i>Atrichum undulatum</i>	<i>Plagiomnium affine</i>
Mosses	<i>Polytrichum commune</i>	

one single plant species clearly follows the degassing pattern of CO₂. Marsh sedge (*Carex acutiformis* Ehrh.) grows in great densities directly above strongly degassing areas within

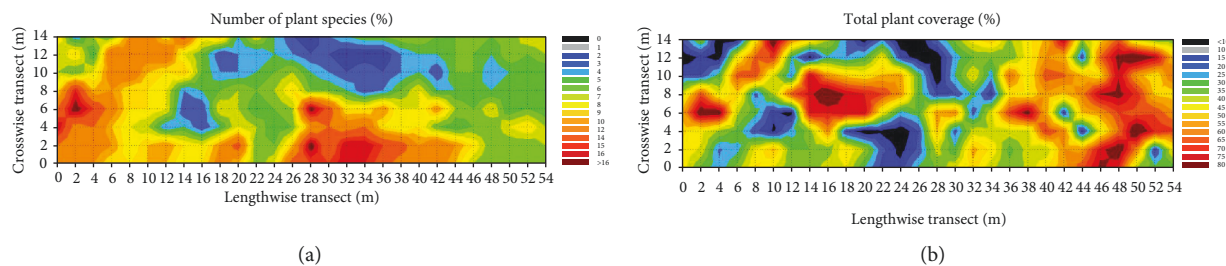


FIGURE 7: Species number per area (a) and total plant coverage (b) within the U1 mofette. The number of different plant species per 2 m² area is given. Plant/soil coverage is given in percent plant surface area per given soil surface. Orientation of the site as in Figure 1(b).

the mofette (Figure 1(a); Figure 8). There is no growth of *Carex* on the top right and lower left corner with less or nearly no CO₂ emission. Being a highlight to half-light loving species, marsh sedge is absent on the top left corner of the area, although CO₂ emission is maximal. The dense canopy formed by beech and limewood trees strongly prevents its growth. Mirroring the CO₂ degassing pattern, *Carex acutiformis* is thought to be the only *eu-mofettophilic* (CO₂-indicating) species in the study area. It is worth mentioning that on other sites also *Carex* species have a high affinity for CO₂ and act as geogas bioindicators. In NW-Czech mofette areas, *Carex nigra* is strictly mofettophilic, whereas in a Yellowstone NP site, *Carex aquatica* plays that part (Pfan, Tercek, King, unpubl).

Quite in contrast to the growth pattern of *Carex acutiformis* are those of grove windflower (*Anemone nemorosa*), spring fumewort (*Corydalis solida*), fig buttercup (*Ranunculus ficaria*), wood bluegrass (*Poa nemoralis*), two-flower melic grass (*Melica mutica*), and addersmeat (*Stellaria holostea*) (Figure 9).

These species clearly avoid growing on degassing sites and occur only on control plots. The growth pattern of some species marks a linear or half-moon-like structure in the upper left corner of the site (running from 7/10-16 to 2/2). This is true for *A. nemorosa*, *P. nemoralis*, *S. holostea*, and *R. ficaria* (Figure 9). To a certain extent, it is also true for *Carpinus betulus*, *Melica mutica*, and *Corydalis solida* (not shown). The upper right part of the area and the lower part in front are also covered.

Two other species like common snowberry (*Symphoricarpos albus*) and Robert geranium (*Geranium robertianum*) cover the lower part of the nongassing area (Figure 10), while common periwinkle (*Vinca minor*), bulbiferous coralwort (*Dentaria bulbifera*), and common honeysuckle (*Lonicera periclymenum*) occupy the nongassing locations at the right rim of the area. Depending on the species, specific mofettophobic plants overgrew either the whole control site or just the light degassing sites. In some cases, mofettophobes grew only at certain low-gas locations. This observation may be explained by the differences in soil permeability, soil water, soil pH, nutrient availability, and shading by tree canopy.

3.3.4. CCA. Canonical correspondence analyses (CCA) were carried out on all environmental and individual species abundance data [37]. In order to exclude random results, plant species were used only if soil coverage of individuals

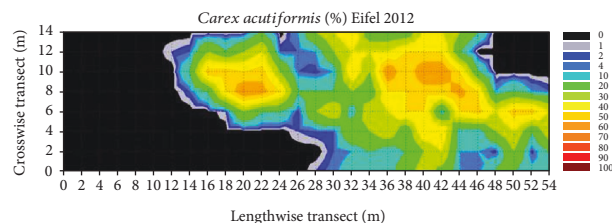


FIGURE 8: Exact growth sites of *Carex acutiformis* within the study site in % coverage. The colour bar decodes the coverage of the plant. Orientation of the site as in Figure 1(b).

was higher than 5% per area. Species response curves were performed on plant species, with at least one representative from each of the species groups distinguished in CCA. The category “mofettophilic and mofettophobic” [according to [17]] was assessed from CCA diagrams and species response curves for those species, which had their optimum (higher densities) in patches with >2-3% CO₂ concentrations.

The canonical correspondence analyses CCA (Figures 11(a)–11(b)) revealed strong correlations between environmental measures and plant species.

The strongest environmental vectors separated the plant species into two to three species groups (Figure 11). Group 1 corresponded to high CO₂ concentration and consisted of one single species, namely, marsh sedge (*Carex acutiformis*; Figure 8). In some analyses, also, *Tilia platyphyllos* was added to that group. In contrast, group 2 was grouped clearly at the lowest CO₂ emission sites and consisted of more species (*Vinca minor*, *Symphoricarpos albus*, *Stellaria holostea*, *Poa nemoralis*, and *Melica mutica*). Group 3 consisted of varying plant species and was grouped around either slightly acidic soil pH values, soil moisture, SOM, or soil density. Depending on analysis, several species stayed near the plot origin of the diagram, revealing neither positive nor negative correlations to any of the respective environmental measures.

CCA thus corroborate the findings of the distribution of species according to the geogenic soil gas emission. Marsh sedge proved to be the only real “*eu-mofettophilic*” plant species within the measured area.

4. Conclusion

Postvolcanic CO₂ gas leakage still occurs around the Laacher See resulting in distinct, dry CO₂ emanations sites (mofettes). Our results indicate that this CO₂ degassing significantly

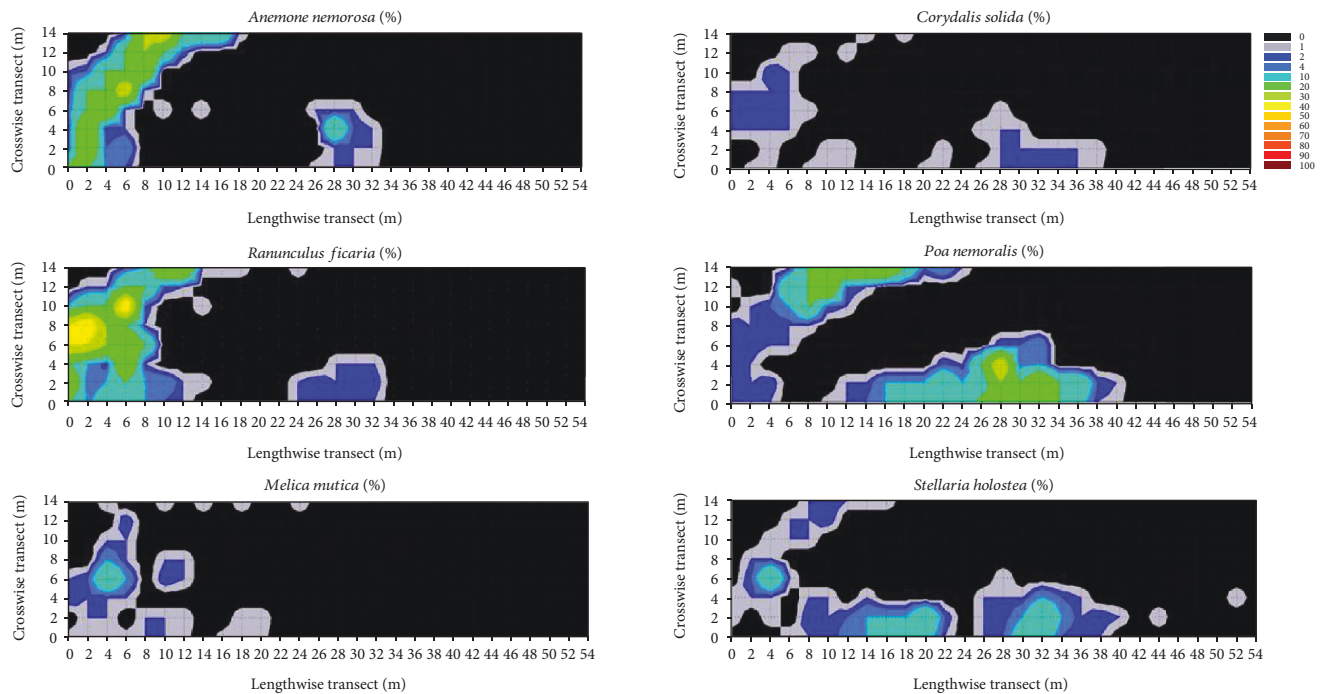


FIGURE 9: Growth sites (in % coverage) of selected mofettophobic plants within the study site. From top left to bottom right: *Anemone nemorosa*, *Corydalis solida*, *Ranunculus ficaria*, *Poa nemoralis*, *Melica mutica*, and *Stellaria holostea*. The colour bar decodes the coverage of the plant. Orientation of the site as in Figure 1(b).

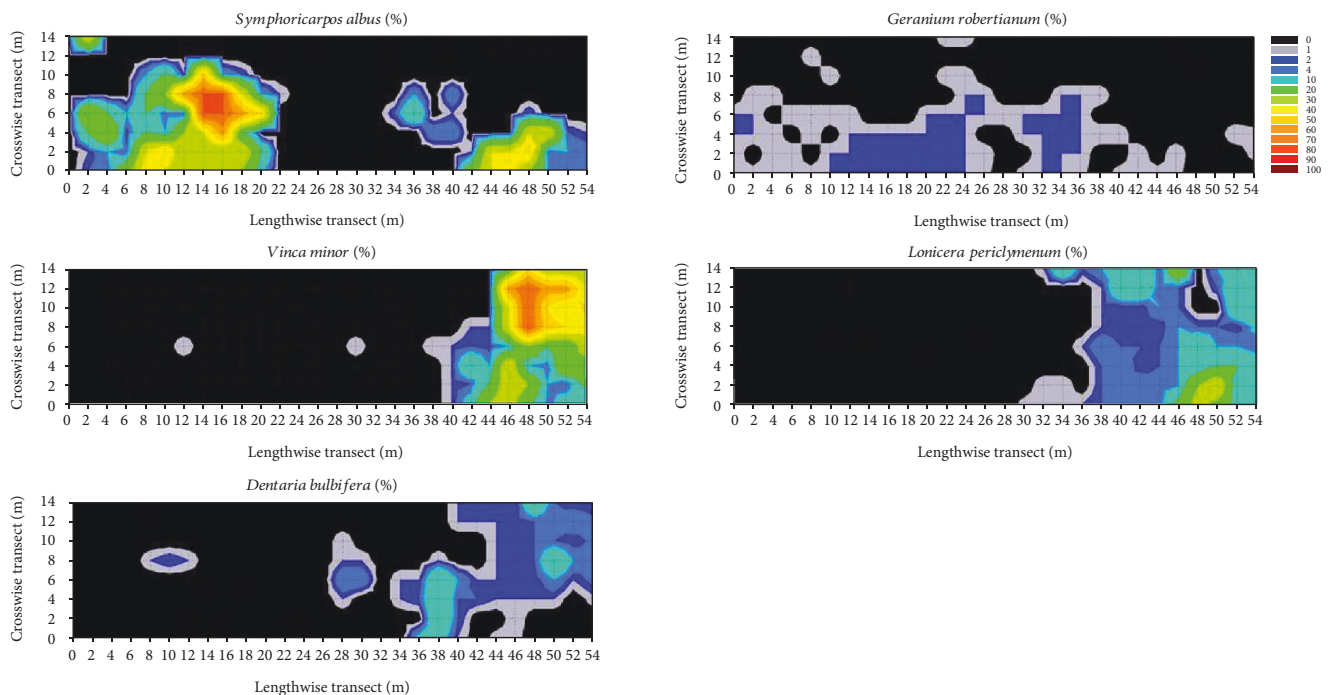


FIGURE 10: Growth sites (in % coverage) of selected mofettophobic to mofettovague plants within the study site. From top left to bottom right: *Symphoricarpos albus*, *Geranium robertianum*, *Vinca minor*, *Lonicera periclymenum*, and *Dentaria bulbifera*. The colour bar decodes the coverage of the plant. Orientation of the site as in Figure 1(b).

affects the terrestrial soil ecosystem. The living organisms within this ecosystem appear to have adapted to the locally high CO_2 concentrations through species substitution or

adaption, with a shift towards hypoxic and acidophilic adaptations. In the case of plants, an azonally growing helophyte, namely, marsh sedge (*C. acutiformis*), is able to grow on

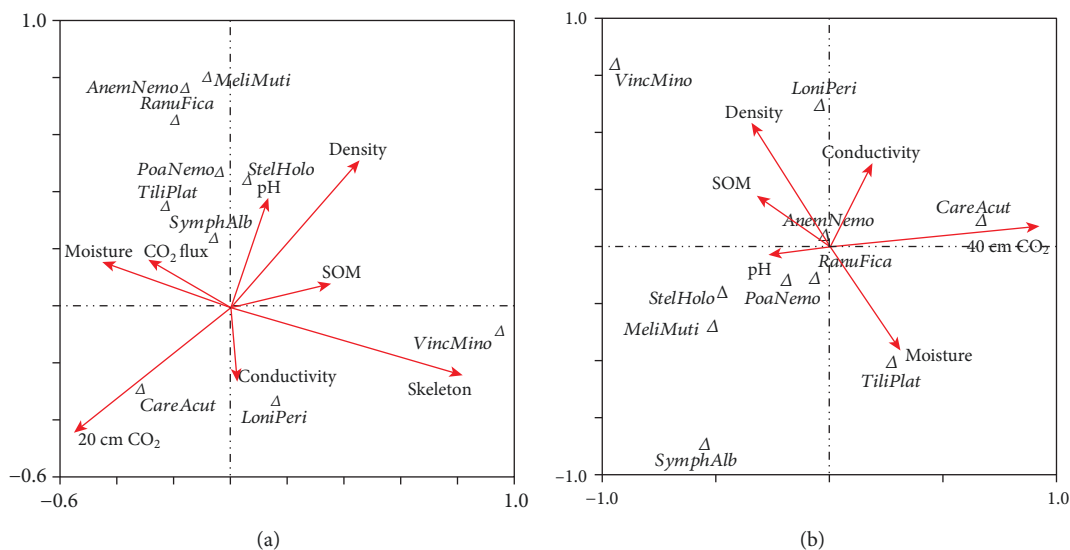


FIGURE 11: (a–b) CCA (CANOCO 4.5) of selected soil parameters, CO₂ concentrations in (a) 20 cm and (b) 40 cm soil depths (arrows), and plant species (triangles) in the U1 mofette. AnemNemo: *Anemone nemorosa*; CareAcut: *Carex acutiformis*; LoniPeri: *Lonicera periclymenum*; MeliMuti: *Melica mutica*; PoaNemo: *Poa nemoralis*; RanuFica: *Ranunculus ficaria*; StelHolo: *Stellaria holostea*; SymphAlb: *Symphoricarpos albus*; TiliPlat: *Tilia platyphyllos*; VincMino: *Vinca minor*. Eigenvalues for (a): 0.529, 0.425, 0.267, and 0.066, and (b): 0.460, 0.341, 0.210, and 0.046 (data sampling in February and May 2013).

highly gas-emitting soils. Its ability to supply oxygen to its roots enables the sedge to establish at hypoxic and concomitantly acidic soils. In this area, *C. acutiformis* is the only really eu-mofettophilic plant species which can be used to biologically indicate geogenic CO₂ emissions. Yet in other mofettic places, there are different *Carex* species showing a high affinity for CO₂; they act as geogas bioindicators. In NW Czech mofette areas, *Carex nigra* is strictly mofettophilic, whereas in a Yellowstone NP site, *Carex aquatica* plays that part (Pfan, Tercek, King, unpubl).

The competent, botanical characterization of mofette sites and the identification of eu-mofettophilic (CO₂ indicating) and mofettophobic (CO₂-avoiding) plant species may help to map gas-emitting tectonic structures with a combination of vegetation data, supported by [CO₂] measurements, and may provide easily detectable plant indicators for geogenic (pre- or postvolcanic) CO₂ emission.

Whether knowledge on CO₂ gas indicator plants will also help to identify gas leaks in artificial CO₂ storage fields (CCS) is still a matter of debate.

Data Availability

We cannot share the data with other colleagues at present on a public scale as we are producing more scientific papers with these data. In this case, we have a time series over several years where these data are included. After publishing the follow-up papers, we may allow public access to the data.

Additional Points

Highlights. Indicative plants can hint geogenic carbon dioxide exhalations—mofettophilic plants. Most plants avoid

growth on high degassing sites—mofettophobic plants. Gas diffusion clearly follows cracks and soil fissures and is not homogeneous within the area. Geogenic soil CO₂ gas flux clearly follows gas concentration patterns.

Conflicts of Interest

The authors declare that there is no conflict of interest regarding the publication of this paper.

Acknowledgments

We want to thank Christa Kosch for her extremely valuable help in the field as well as in the laboratory. The help of Nina Hennigfeld, Annika Pelz, and Christian Baakes is gratefully acknowledged. Sabine Kühr helped in various soil analytics. Cordial thanks are also due to the Deutsche Vulkanologische Gesellschaft (Heinz Lempertz, Wolfgang Riedel, Rainer Hippchen, Wolfgang Kostka, and Walter Müller) as well as forester Karl Hermann Gräf for their help in getting necessary permissions as well as practical and financial support. We are indebted to Mrs. Claudia Uhl and Mr. Stefan Backes, Struktur- und Genehmigungsdirektion Koblenz Nord, Referat Naturschutz, for the permission to study the area and to the Department of Geosciences of the Friedrich Schiller University of Jena (Profs. Heide, Büchel, and Viereck) for many scientific discussions.

References

- [1] G. Chiodini, C. Cardellini, A. Amato et al., “Carbon dioxide Earth degassing and seismogenesis in central and southern Italy,” *Geophysical Research Letters*, vol. 31, no. 7, 2004.

- [2] J. Heinicke, G. Martinelli, and L. Telesca, "Geodynamically induced variations in the emission of CO₂ gas at San Faustino (Central Apennines, Italy)," *Geofluids*, vol. 12, no. 2, 132 pages, 2012.
- [3] A. Minissale, "Origin, transport and discharge of CO₂ in Central Italy," *Earth-Science Reviews*, vol. 66, no. 1-2, pp. 89–141, 2004.
- [4] I. Maček, A. J. Dumbrell, M. Nelson, A. H. Fitter, D. Vodnik, and T. Helgason, "Local adaptation to soil hypoxia determines the structure of an arbuscular mycorrhizal fungal community in roots from natural CO₂ springs," *Applied and Environmental Microbiology*, vol. 77, no. 14, pp. 4770–4777, 2011.
- [5] I. Maček, "A decade of research in mofette areas has given us new insights into adaptation of soil microorganisms to abiotic stress," *Acta Agriculturae Slovenica*, vol. 101, no. 2, pp. 209–217, 2013.
- [6] H. Pfan, D. Vodnik, C. Wittmann, G. Aschan, and A. Raschi, "Plants and Geothermal CO₂ Exhalations — Survival in and Adaptation to a High CO₂ Environment," in *Progress in Botany*, K. Esser, U. Lüttge, W. Beyschlag, and J. Murata, Eds., vol. 65 of Progress in Botany, pp. 499–538, Springer, Berlin, Heidelberg, 2004.
- [7] H. Pfan, D. Vodnik, C. Wittmann et al., "Photosynthetic performance (CO₂-compensation point, carboxylation efficiency, and net photosynthesis) of timothy grass (*Phleum pratense* L.) is affected by elevated carbon dioxide in post-volcanic mofette areas," *Environmental and Experimental Botany*, vol. 61, no. 1, pp. 41–48, 2007.
- [8] A. Raschi, F. Miglietta, R. Tognetti, and P. R. van Gardingen, *Plant Responses to Elevated CO₂ – Evidence from Natural Springs*, Cambridge University Press, Cambridge, 1997.
- [9] M. Vejputsková, A. Thomalla, T. Čihák, B. Lomský, and H. Pfan, "Growth of *Populus tremula* on CO₂-enriched soil at a natural mofette site," *Dendrobiology*, vol. 75, pp. 3–12, 2016.
- [10] D. Vodnik, D. Kastelec, H. Pfan, I. Maček, and B. Turk, "Small-scale spatial variation in soil CO₂ concentration in a natural carbon dioxide spring and some related plant responses," *Geoderma*, vol. 133, no. 3-4, pp. 309–319, 2006.
- [11] T. Rennert, K. Eusterhues, H. Pfan, and K. U. Totsche, "Influence of geogenic CO₂ on mineral and organic soil constituents on a mofette site in the NW Czech Republic," *European Journal of Soil Science*, vol. 62, no. 4, pp. 572–580, 2011.
- [12] T. Rennert and H. Pfan, "Geogenic CO₂ affects stabilization of soil organic matter," *European Journal of Soil Science*, vol. 66, no. 5, pp. 838–846, 2016.
- [13] T. Rennert and H. Pfan, "Hypoxic and acidic – soils on mofette fields," *Geoderma*, vol. 280, pp. 73–81, 2016.
- [14] B. Balkenhol, K. Hohberg, and H. Pfan, "Spiders in mofette fields- survival of the toughest in natural carbon dioxide springs?," *Ecological Indicators*, vol. 69, pp. 749–757, 2016.
- [15] K. Hohberg, H.-J. Schulz, B. Balkenhol et al., "Soil faunal communities from mofette fields: effects of high geogenic carbon dioxide concentration," *Soil Biology and Biochemistry*, vol. 88, pp. 420–429, 2015.
- [16] D. Russell, H.-J. Schulz, K. Hohberg, and H. Pfan, "The collembolan fauna of mofette fields (natural carbon-dioxide springs)," *Soil Organisms*, vol. 83, pp. 489–505, 2011.
- [17] H. Pfan, *Mofetten – kalter Atem schlafender Vulkane*, RVDG Verlag, Köln, 2008.
- [18] B. Turk, H. Pfan, D. Vodnik et al., "The effects of elevated CO₂ in natural CO₂ springs on bog rush (*Juncus effusus* L.) plants. Effects on shoot anatomy," *Phyton*, vol. 42, pp. 13–23, 2002.
- [19] D. Vodnik, H. Pfan, I. Maček, D. Kastelec, S. Lojen, and F. Batič, "Photosynthesis of cockspear (*Echinochloa crus-galli* (L.) Beauv.) at sites of naturally elevated CO₂ concentration," *Photosynthetica*, vol. 40, no. 4, pp. 575–579, 2002.
- [20] D. Vodnik, H. Pfan, C. Wittmann et al., "Photosynthetic acclimation in plants growing near a carbon dioxide spring," *Phyton*, vol. 42, pp. 239–244, 2002.
- [21] D. Vodnik, H. Šircelj, D. Kastelec, I. Maček, H. Pfan, and F. Batič, "The effects of natural CO₂ enrichment on the growth of maize," *Journal of Crop Improvement*, vol. 13, no. 1-2, pp. 193–212, 2005.
- [22] D. Vodnik, U. Videmšek, M. Pintar, I. Maček, and H. Pfan, "The characteristics of soil CO₂ fluxes at a site with natural CO₂ enrichment," *Geoderma*, vol. 150, no. 1-2, pp. 32–37, 2009.
- [23] M. Kaligarič, "Vegetation patterns and responses to elevated CO₂ from natural CO springs at Strmec (Radenci, Slovenia)," *Acta Biologicae Sloveniae*, vol. 44, pp. 31–38, 2001.
- [24] F. Selvi, "Acidophilic grass communities of CO₂-springs in central Italy: composition, structure and ecology," in *Plant responses to elevated CO₂*, A. Raschi, F. Miglietta, R. Tognetti, and P. R. Gardingen, Eds., pp. 114–133, Cambridge University Press, 1997.
- [25] F. Selvi, "Flora of the mineral CO₂-spring Bossoleto (Rapolano Terme, Tuscany) and its relevance to ecological research," *Atti della Società Toscana di Scienze Naturali, Memorie, Serie B*, vol. 105, pp. 23–30, 1998.
- [26] F. Selvi and I. Bettarini, "Geothermal biotopes in central-western Italy from a botanical view point," in *Ecosystem response to CO₂. The MAPLE project results*, A. Raschi, F. P. Vaccari, and F. Miglietta, Eds., pp. 1–12, Luxembourg, 1999.
- [27] H. U. Schmincke, C. Park, and E. Harms, "Evolution and environmental impacts of the eruption of Laacher See Volcano (Germany) 12,900 a BP," *Quaternary International*, vol. 61, no. 1, pp. 61–72, 1999.
- [28] A. Goepel, M. Lonschinski, L. Viereck, G. Büchel, and N. Kukowski, "Volcano-tectonic structures and CO₂-degassing patterns in the Laacher See basin, Germany," *International Journal of Earth Sciences*, vol. 104, no. 5, pp. 1483–1495, 2015.
- [29] K. Grewe, "Der Fulbertsollen am Laacher See. Eine Ingenieurleistung des hohen Mittelalters," *Zeitschrift Archaeologie des Mittelalters*, vol. 7, pp. 107–142, 1979.
- [30] P. A. Philippson, *Der Laacher See. Verhandlungen des Naturhistorischen Vereins der Preussischen Rheinlande und Westfalens*, S. Bonn, 1926.
- [31] H. Ellenberg, H. E. Weber, R. Düll, V. Wirth, W. Werner, and D. Paulißen, *Zeigerwerte von Pflanzen in Mitteleuropa*, Göttingen, 1992.
- [32] J. Richter, *Der Boden als Reaktor. Modelle für Prozesse in Böden*, Stuttgart, 1986.
- [33] R. Bochter, *Boden und bodenuntersuchungen für den unterricht in chemie, biologie und geographie. Praxis-Schriftenreihe*, Abt. Chemie, Bd, Köln, 1995.
- [34] G. Londo, "The decimal scale for releves of permanent quadrats," *Vegetatio*, vol. 33, no. 1, pp. 61–64, 1976.
- [35] J. Braun-Blanquet, *Pflanzensoziologie*, Wien, 1964.

- [36] H. Dierschke, *Pflanzensoziologie*, Stuttgart, 1994.
- [37] J. Leps and P. Smilauer, *Multivariate Analysis of Ecological Data Using CANOCO*, Cambridge University Press, Cambridge, first ed edition, 2012.
- [38] M. Hajnos, *Buffer Capacities of Soils. Encyclopedia of Earth Science Series*, pp. 94-95, 2014.
- [39] H. Pfanz, "Apoplastic and symplastic proton concentrations and their significance for metabolism," in *Ecophysiology of Photosynthesis*, E.-D. Schulze and M. M. Caldwell, Eds., Springer Verlag, Berlin, 1994.
- [40] G. Schaller, "pH changes in the rhizosphere in relation to the pH-buffering of soils," *Plant and Soil*, vol. 97, no. 3, pp. 439-444, 1987.
- [41] U. Videmšek, A. Hagn, M. Suhadolc et al., "Abundance and diversity of CO₂-fixing bacteria in grassland soils close to natural carbon dioxide springs," *Microbial Ecology*, vol. 58, no. 1, pp. 1-9, 2009.
- [42] Y. Onoda, T. Hirose, and K. Hikosaka, "Effect of elevated CO₂ levels on leaf starch, nitrogen and photosynthesis of plants growing at three natural CO₂ springs in Japan," *Ecological Research*, vol. 22, no. 3, pp. 475-484, 2007.
- [43] X. Zhang, X. Ma, Z. Zhao, Y. Wu, and Y. Li, "CO₂ leakage-induced vegetation decline is primarily driven by decreased soil O₂," *Journal of Environmental Management*, vol. 171, pp. 225-230, 2016.
- [44] S. E. Beaubien, G. Ciotoli, P. Coombs et al., "The impact of a naturally occurring CO₂ gas vent on the shallow ecosystem and soil chemistry of a Mediterranean pasture (Latera, Italy)," *International Journal of Greenhouse Gas Control*, vol. 2, no. 3, pp. 373-387, 2008.
- [45] I. Maček, H. Pfanz, V. Francetič, F. Batič, and D. Vodnik, "Root respiration response to high CO₂ concentrations in plants from natural CO₂ springs," *Environmental and Experimental Botany*, vol. 54, no. 1, pp. 90-99, 2005.
- [46] I. Maček, D. Vodnik, H. Pfanz, E. Low-Décarie, and A. J. Dumbrell, "Chapter Six - Locally extreme environments as natural long-term experiments in ecology," *Advances in Ecological Research*, vol. 55, pp. 283-323, 2016.
- [47] M. F. Cotrufo, A. Raschi, M. Lanini, and P. Ineson, "Decomposition and nutrient dynamics of *Quercus pubescens* leaf litter in a naturally enriched CO₂ Mediterranean ecosystem," *Functional Ecology*, vol. 13, no. 3, pp. 343-351, 1999.
- [48] D. J. Ross, K. R. Tate, P. C. D. Newton, R. H. Wilde, and H. Clark, "Carbon and nitrogen pools and mineralization in a grassland gley soil under elevated carbon dioxide at a natural CO₂ spring," *Global Change Biology*, vol. 6, no. 7, pp. 779-790, 2000.
- [49] J. A. Baldock and P. N. Nelson, "Soil organic matter," in *Handbook of soil science*, M. E. Sumner, Ed., pp. B25-B84, Boca Raton, 2000.
- [50] F. Scheffer and P. Schachtschabel, *Lehrbuch der Bodenkunde*, Thieme Verlag, Stuttgart, 12. ed. edition, 1989.
- [51] R. Warncke-Grüttner, *Ökologische untersuchungen zum nährstoff- und wasserhaushalt in niedermooren des westlichen Bodenseegebiets*, Dissertationes Botanicae, Bd, Berlin, 1990.
- [52] W. Larcher, "Ökophysiologie der Pflanzen," in *Leben, Leistung und Stressbewältigung der Pflanzen in ihrer Umwelt*, Stuttgart, 2001.
- [53] H. Andres, "Aus der Pflanzenwelt des Laacher Sees," *Verh. Naturhistor. Ver. Preuß. Rheinl. Westf.*, vol. 83, pp. 65-81, 1926.
- [54] G. Rahm, "Pflanzen vom Laacher See und seiner umgebung," *Aus Natur und Kultur der Eifel*, vol. 6, pp. 1-76, 1923.
- [55] T. Wolf, "Flora von Laach. Zum Gebrauch bei botanischen Exkursionen," in (1983): *Ars liturgica*, A. A. Häußling and J. Leonhard, Eds., Maria Laach, Germany, 1868.

Research Article

Methane Source and Turnover in the Shallow Sediments to the West of Haima Cold Seeps on the Northwestern Slope of the South China Sea

Junxi Feng ^{1,2}, Shengxiong Yang ¹, Hongbin Wang,¹ Jinqiang Liang,¹ Yunxin Fang,¹ and Min Luo ^{3,4}

¹MLR Key Laboratory of Marine Mineral Resources, Guangzhou Marine Geological Survey, Guangzhou 510075, China

²School of Marine Sciences, Sun Yat-sen University, Guangzhou 510006, China

³Shanghai Engineering Research Center of Hadal Science and Technology, College of Marine Sciences, Shanghai Ocean University, Shanghai 201306, China

⁴Laboratory for Marine Geology, Qingdao National Laboratory for Marine Science and Technology, Qingdao 266061, China

Correspondence should be addressed to Shengxiong Yang; yangshengxiong@gmgs.cn and Min Luo; mluo@shou.edu.cn

Received 16 February 2019; Revised 7 May 2019; Accepted 27 May 2019; Published 5 August 2019

Academic Editor: Giovanni Martinelli

Copyright © 2019 Junxi Feng et al. This is an open access article distributed under the Creative Commons Attribution License, which permits unrestricted use, distribution, and reproduction in any medium, provided the original work is properly cited.

The Haima cold seeps are active cold seep areas that were recently discovered on the northwestern slope of the South China Sea (SCS). Three piston cores (CL30, CL44, and CL47) were collected within an area characterized by bottom simulating reflectors to the west of Haima cold seeps. Porewater profiles of the three cores exhibit typical kink-type feature, which is attributed to elevated methane flux (CL30) and bubble irrigation (CL44 and CL47). By simulating the porewater profiles of SO_4^{2-} , CH_4 , PO_4^{3-} , Ca^{2+} , Mg^{2+} , and dissolved inorganic carbon (DIC) in CL44 and CL47 using a steady-state reaction-transport model, we estimated that the dissolved SO_4^{2-} was predominantly consumed by anaerobic oxidation of methane (AOM) at rates of $74.3 \text{ mmol m}^{-2} \text{ yr}^{-1}$ in CL44 and $85.0 \text{ mmol m}^{-2} \text{ yr}^{-1}$ in CL47. The relatively high AOM rates were sustained by free gas dissolution rather than local methanogenesis. Based on the diffusive Ba^{2+} fluxes and the excess barium contents in the sediments slightly above the current SMTZ, we estimated that methane fluxes at core CL44 and CL47 have persisted for ca. 3 kyr and 0.8–1.6 kyr, respectively. The non-steady-state modeling for CL30 predicted that a recent increase in upward dissolved methane flux was initiated ca. 85 yr ago. However, the required time for the formation of the barium front above the SMTZ at this core is much longer (ca. 2.2–4.2 kyr), which suggests that the depth of SMTZ possibly has fluctuated due to episodic changes in methane flux. Furthermore, using the model-derived fractions of different DIC sources and the $\delta^{13}\text{C}_{\text{DIC}}$ mass balance calculation, we estimated that the $\delta^{13}\text{C}$ values of the external methane in cores CL30, CL44, and CL47 are -74.1‰ , -75.4‰ , and -66.7‰ , respectively, indicating the microbial origin of methane. Our results suggest that methane seepage in the broader area surrounding the Haima cold seeps probably has persisted at least hundreds to thousands of years with changing methane fluxes.

1. Introduction

Methane in marine sediments as dissolved gas in porewater or free gas (bubbles) depending on its in situ solubility is a significant component of the global carbon cycle. Methane could also exist in an ice-like solid as gas hydrate if the in situ gas hydrate solubility concentration is oversaturated at suitable pressure-temperature conditions [1]. The base of the gas hydrate reservoir in marine sediments is present as a

characteristic discontinuity known as a bottom-simulating reflector (BSR), which results from the occurrence of free gas beneath the gas hydrate stability zone (GHSZ) [2]. The great majority of methane is consumed by the microbial consortium via anaerobic oxidation of methane within the sulfate-methane transition zone (SMTZ) where methane meets sulfate diffusing downwards from seawater (AOM: $\text{CH}_4 + \text{SO}_4^{2-} \rightarrow \text{HCO}_3^- + \text{HS}^- + \text{H}_2\text{O}$) [3, 4]. Through this, reaction methane is converted to dissolved inorganic carbon

(DIC) which could be partially removed from solution by authigenic carbonate precipitation [5, 6]. Therefore, AOM largely prevents dissolved methane from entering water column and plays a significant role in marine carbon cycling.

Gas bubble rise is a particularly effective mechanism for transporting methane through the sediment and into the bottom water because gas ascension can be faster than bubble dissolution [7] and methane gas cannot directly be consumed by microorganisms [8]. The rising methane gas bubbles emitting from the seafloor can mix bottom seawater down into the sediment column over several meters. The resulting kink-type porewater profiles are supposed to be stable for several years to decades even after active gas bubble ebullition has ceased [7]. Enhancement in upward methane flux could also result in kink-type or concave-up porewater profiles [9–12]. Hence, these types of nonlinear porewater profiles can thus be used to estimate the timing of (sub)recent methane pulse and provide insights into the dynamics of methane seepage and the underlying gas hydrate reservoir [10, 11, 13, 14].

At the steady-state condition, Ba^{2+} diffusing upward into the sulfate-bearing zone above the SMTZ precipitates as barite and forms the authigenic barium fronts ($\text{Ba}^{2+} + \text{SO}_4^{2-} \rightarrow \text{BaSO}_4$) [15]. When buried beneath the sulfate-bearing zone, barite tends to dissolve and release Ba^{2+} into the porewater below the SMTZ due to unsaturation. Through this cycling, authigenic barium fronts would be stably developed just above the SMTZ [15–17]. The content of authigenic barite depends on the upward diffusive Ba^{2+} flux and the duration that the SMTZ has persisted at a given depth interval. The time required for barium front formation above the SMTZ could thus be calculated based on the depth-integrated excess barium contents and the porewater dissolved barium concentration gradients assuming a constant upward Ba^{2+} flux. Therefore, the authigenic barium fronts in sediments can be used to trace present and past SMTZ and associated methane release events as well as the duration of methane seepage that has persisted under a given methane flux [16–20].

Methane seepages are widespread on the northern slope of the South China Sea (SCS) as revealed by authigenic carbonates collected at more than 30 cold seep sites [21–26]. The Haima cold seeps were recently discovered on the northwestern slope of SCS [25]. Several sites with gas bubbling identified by hydroacoustic anomalies, and shallow gas hydrates were found around this area [27–31]. Recent studies have shown a pronounced temporal change in methane seepages and a potential lateral migration of methane-bearing fluid along more permeable sand-bearing layer at Haima cold seeps [25, 32, 33]. Nevertheless, our quantitative understanding of the methane dynamics in this area remains scarce.

In this study, we present porewater geochemical data of three piston cores (CL30, CL44, and CL47) collected to the west of Haima cold seeps, including concentrations of sulfate (SO_4^{2-}), calcium (Ca^{2+}), magnesium (Mg^{2+}), barium (Ba^{2+}), phosphate (PO_4^{3-}), methane (CH_4), and DIC as well as the carbon isotopic compositions of DIC. Using a steady-state reaction-transport model, we quantify the methane turnover rates in CL44 and CL47 which are mainly supplied by rising

free gas. The kink in the porewater profiles of CL30 was reconstructed using a non-steady-state modeling approach assuming a recent increase in methane flux. In addition, authigenic Ba enrichments were used to constrain the durations that the current or past methane seepages have persisted. Furthermore, a simple mass balance model of DIC and $\delta^{13}\text{C}_{\text{DIC}}$ was applied to explore the methane source.

2. Geological Background

The northern SCS is characterized as a Cenozoic, Atlantic-type passive continental margin [34], where the marginal basins generally underwent two stages of evolution, including the rift stage and the postrift thermal subsidence stage [35]. Qiongdongnan Basin is a northeastern trended Cenozoic sedimentary basin which developed on the northwestern part of the SCS [36]. Covered by sedimentary materials of up to 10 km, the depositional environment of the basin initially transformed from lacustrine to marine conditions and later from neritic to bathyal, starting from Eocene till present [37]. During the rifting stage, numerous half-grabens and sags were developed. After that, postrift thermal subsidence occurred and a thick sediment sequence dominated by mudstones was deposited in the basin since Miocene. Collectively, the sedimentation rates and the present-day geothermal gradient are both high in the Qiongdongnan Basin [38]. The thick sediment sequences, high geothermal gradient along with faulting and/or diapirism, have facilitated the generation and migration of the hydrocarbons in the basin [39]. The widely distributed bottom-simulating reflectors and gas chimneys identified in the Qiongdongnan Basin were linked to the accumulation of gas hydrate [40, 41].

The active Haima cold seeps have been discovered in the southern uplift belt of the Qiongdongnan Basin on the lower continental slope of the northwestern SCS during R/V Haiyang-6 cruises in 2015 and 2016. Abundant chemosynthetic communities, methane-derived authigenic carbonates, and massive gas hydrates were found at the Haima cold seeps [25]. The dating of bivalve shells and seep carbonates revealed episodic changes in seepage activity [25]. Other features of methane seeps, such as acoustic plume, acoustic void, chimney structures, and pockmarks, were also reported at the Haima cold seeps and its surrounding area [27–31, 42]. The sampling sites are ca. 20 to 30 kilometers west of the Haima cold seeps, where BSR is well developed (Fang Y., unpublished data). The bathymetric investigation has shown a relatively flat topography, and the water depths range from 1250 to 1300 m in the study area (Figure 1).

3. Materials and Methods

3.1. Sampling and Analytical Methods. Three piston cores (CL30, CL44, and CL47) were collected from the southern Qiongdongnan Basin west to the Haima cold seeps at water depths ranging from 1255 m to 1301 m during the R/V Haiyang-4 cruise conducted by Guangzhou Marine Geological Survey in 2014 (Figure 1 and Table 1). The sediments of the three cores mainly consist of greyish-green silty clay. Notably, the sediments at the bottom of core CL44 yielded

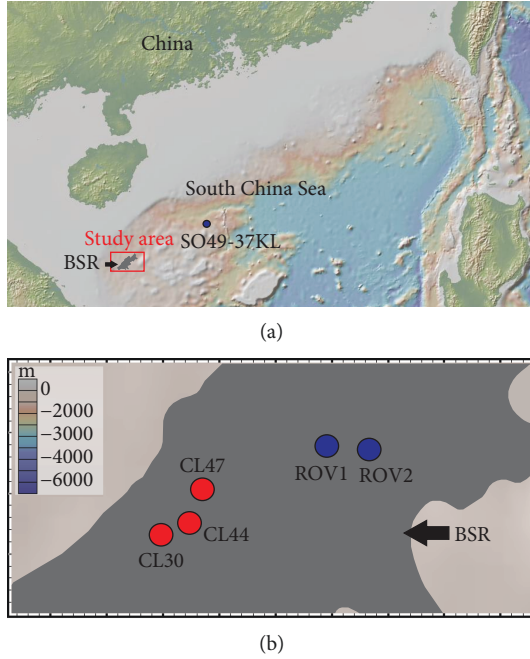


FIGURE 1: (a) Location of the study area. The grey area represents the subsurface area linedated by seismic investigation. The location of the reference core SO49-37KL (blue circle) is also shown. (b) Locations of sampling sites (red dots) and the Haima cold seeps (blue dots).

TABLE 1: Information on the studied cores from the northwestern South China Sea.

Site	Water depth (m)	Seafloor temperature ($^{\circ}\text{C}$)	Core length (cm)
CL30	1255	3.3	630
CL44	1279	3.2	752
CL47	1301	3.1	775

a strong odour of hydrogen sulfide. Porewater samples were then collected onboard using Rhizon samplers with pore sizes of the porous part of approximately 0.2 mm at intervals of 20 cm for CL44 and 60 cm for CL30 and CL47. All the porewater samples were preserved at $\sim 4^{\circ}\text{C}$ until further analyses.

PO_4^{3-} concentrations were measured onboard using the spectrophotometric method according to Grasshoff et al. [43] with a UV-Vis spectrophotometer (Hitachi U5100). The precision for phosphate was $\pm 3.0\%$. 10 ml of sediments was added to 20 ml empty vials onboard to replace the 10 ml headspace needed for the chromatograph injection. The concentrations of hydrocarbon gas were measured onboard using the gas chromatograph method (Agilent 7890N). The precision for methane measurements was $\pm 2.5\%$ [44]. Porosity and density were determined from the weight loss before and after freeze-drying of the wet sediments using a cutting ring with definite mass (15 g) and volume (9.82 cm^3) onboard at core CL44. The porosity and density were calculated assuming a density of the porewater of 1.0 g cm^{-3} .

The offshore analyses of porewater samples for core CL44 and for cores CL30 and CL47 were performed at the Nanjing University and the Third Institute of Oceanography, State Oceanic Administration, respectively. For core CL44, SO_4^{2-} , Ca^{2+} , and Mg^{2+} were measured using the standard method of ion chromatography (Metrohm 790-1, Metrosep A Supp 4-250/Metrosep C 2-150). The relative standard deviation was less than 3%. Ba^{2+} concentrations were measured by inductively coupled plasma mass spectrometry (ICP-MS, Finnigan Element II). Before measurement, samples were prepared by diluting in 2% HNO_3 with 10 ppb of Rh as an internal standard. The analytical precisions were estimated to be $<5\%$ for Ba^{2+} . For cores CL30 and CL47, SO_4^{2-} , Ca^{2+} , and Mg^{2+} concentrations were determined on a Thermo Dionex ICS-1100 ion chromatograph after a 500-fold dilution using ultrapure water [44]. Porewater samples were prepared by diluting in 2% HNO_3 with 10 ppb of Tb as an internal standard before analysis for Ba^{2+} using the ICP-MS (Thermo Fisher iCAPQ). The analytical precisions were estimated to be $<5\%$ for Ba^{2+} .

For core CL44, DIC concentrations and $\delta^{13}\text{C}_{\text{DIC}}$ values were determined using a continuous flow mass spectrometer (Thermo Fisher Delta-Plus). 0.5 ml porewater was treated with pure H_3PO_4 in a glass vial at 25°C . The CO_2 produced was stripped with He and transferred into the mass spectrometer through the measurement of the $\delta^{13}\text{C}$ value [45]. For cores CL30 and CL47, the DIC concentrations and carbon isotopic ratios were determined via a continuous flow mass spectrometer (Thermo Delta V Advantage). A 0.2 ml porewater sample was treated with pure H_3PO_4 in a glass vial at 25°C . The CO_2 produced was stripped with He and transferred into the mass spectrometer through which the $\delta^{13}\text{C}$ values were measured. The analytical precisions were better than 0.2‰ for $\delta^{13}\text{C}$ and better than 2% for DIC concentration [44].

The particulate organic carbon (POC) contents were determined using the potassium dichromate wet oxidation method. The relative standard deviation of the POC content is $<1.5\%$. The aluminium (Al), silicon (Si), and titanium (Ti) concentrations of the sediment samples at cores CL30, CL44, and CL47 were analyzed using PANalytical AXIOSX X-ray fluorescence spectrometry (XRF). The analytical precisions were estimated to be $<2\%$ for Al, Si, and Ti. The contents of Ba, zircon (Zr), and rubidium (Rb) in bulk sediments were determined using a PerkinElmer Optima 4300DV ICP-OES after digestion using HCl, HF, and HClO_4 acid mixture. Rhodium was added as an internal standard for calculating the concentrations of the trace elements. The analytical precisions were estimated to be $<2\%$ for Ba, Zr, and Rb. The carbonate (CaCO_3) contents of the sediment samples were determined by titration with EDTA standard solution. The analytical precisions were estimated to be $<2\%$. For grain size measurements, approximately 0.5 g of the unground sample was treated with 10% (v/v) H_2O_2 for 48 h to oxidize organic matter and then dispersed and homogenized in sodium hexametaphosphate solution using ultrasonic vibration for 30 s before being analyzed by a laser grain size analyzer (Mastersizer 2000). The detection limit ranged from $0.5\text{ }\mu\text{m}$ to $2000\text{ }\mu\text{m}$. Particles $<4\text{ }\mu\text{m}$ in size were classified

TABLE 2: Rate expressions of the reactions considered in the model.

Rate	Kinetic rate law*
Total POC degradation (wt.% C yr ⁻¹)	$R_{\text{POC}} = \left(0.16 \cdot \left(a_0 + \frac{x}{v_s} \right)^{-0.95} \right) \cdot \text{POC}$
POM degradation via sulfate reduction (mmol cm ⁻³ yr ⁻¹ of SO ₄ ²⁻)	$R_{\text{SR}} = 0.5 \cdot R_{\text{POC}} \cdot \frac{K_{\text{SO}_4^{2-}} / \left([\text{SO}_4^{2-}] + K_{\text{SO}_4^{2-}} \right)}{f_{\text{POC}}}$
Methanogenesis (mmol cm ⁻³ yr ⁻¹ of CH ₄)	$R_{\text{MG}} = 0.5 \cdot R_{\text{POC}} \cdot \frac{K_{\text{SO}_4^{2-}} / \left([\text{SO}_4^{2-}] + K_{\text{SO}_4^{2-}} \right)}{f_{\text{POC}}}$
Anaerobic oxidation of methane (mmol cm ⁻³ yr ⁻¹ of CH ₄)	$R_{\text{AOM}} = k_{\text{AOM}} \cdot [\text{SO}_4^{2-}] [\text{CH}_4]$
Authigenic Ca-carbonate precipitation (mmol cm ⁻³ yr ⁻¹ of Ca ²⁺)	$R_{\text{CP-Ca}} = k_{\text{Ca}} \cdot \left(\frac{[\text{Ca}^{2+}] \cdot [\text{CO}_3^{2-}]}{K_{\text{SP}}} - 1 \right)$
Authigenic Mg-carbonate precipitation (mmol cm ⁻³ yr ⁻¹ of Mg ²⁺)	$R_{\text{CP-Mg}} = k_{\text{Mg}} \cdot \left(\frac{[\text{Mg}^{2+}] \cdot [\text{CO}_3^{2-}]}{K_{\text{SP}}} - 1 \right)$
Gas bubble irrigation (mmol cm ⁻³ yr ⁻¹)	$R_{\text{Bui}} = \alpha_1 \cdot \frac{\exp(L_{\text{irr-x}}/\alpha_2)}{1 + \exp(L_{\text{irr-x}}/\alpha_2)} \cdot (C_0 - C_x)$
Gas bubble dissolution (mmol cm ⁻³ yr ⁻¹ of CH ₄)	$R_{\text{diss}} = k_{\text{MB}} \cdot (L_{\text{MB}} - [\text{CH}_4])$

* f_{POC} converts between POC (dry wt.%) and DIC (mmol cm⁻³ of porewater): $f_{\text{POC}} = \text{MWC}/10\Phi/(1 - \Phi)/\rho_s$, where MWC is the molecular weight of carbon (12 g mol⁻¹), ρ_s is the density of dry sediments, and Φ is the porosity.

as clay, 4 to 63 μm as silt, and larger than 63 μm as sand. The analytical precision is better than 3%.

3.2. Diffusive Flux Calculation. To calculate the diffusive Ba²⁺ fluxes below the kink at cores CL30, CL44, and CL47, equations (1) and (2) were used assuming a steady-state condition [46]:

$$J_x = -\varphi D_s \frac{dC}{dx}, \quad (1)$$

$$D_s = \frac{D_0}{1 - \ln(\varphi)^2}, \quad (2)$$

where J_x represents the diffusive flux of Ba²⁺ (mmol m⁻² yr⁻¹), φ is the porosity, D_0 is the diffusion coefficient for seawater (m² s⁻¹), D_s is the diffusion coefficient for sediments (m² s⁻¹), C is the concentration of barium (mmol l⁻¹), and x is the sediment depth (m). The average of sediment porosity of core CL44 (0.69) is applied to cores CL30 and CL47.

3.3. Estimating the Accumulation Time of Diagenetic Barite. The total amount of excess Ba within the interval of the barium peak was calculated using an integral equation:

$$A_x = \int_u^v C_x \cdot \rho \cdot (1 - \varphi), \quad (3)$$

where $\int_u^v C_x$ is the integral value of barium concentration in a peak from a depth interval from u to v , ρ and φ are the average grain density and porosity of the sediments, respectively.

Under the premise of a constant diffusive upward flux of Ba²⁺ into the sulfate-bearing zone, the time needed for barium front formation was calculated using the equation:

$$t_x = \frac{A_x}{J_x}. \quad (4)$$

In this case, t_x is the time for barite enrichment, A_x is the depth-integrated excess barium content within a peak, and J_x is the upward diffusive flux of Ba²⁺. The diffusive flux was calculated using equations (1) and (2). D_s is the tortuosity- and temperature-corrected diffusion coefficient of Ba²⁺ in the sediment, calculated from the diffusion coefficient in free solution (D_0) of 4.64, 4.62, and 4.61 $\times 10^{-6}$ cm² s⁻¹ (3.3, 3.2, and 3.1°C) for CL30, CL44, and CL47, respectively, according to Boudreau [47].

3.4. Reaction-Transport Model. A one-dimensional, steady-state, and reaction-transport model was applied to simulate one solid (POC) and six dissolved species including SO₄²⁻, CH₄, DIC, PO₄³⁻, Ca²⁺, and Mg²⁺. The model is modified from previous simulations of methane-rich sediments [48–51], and a full description of the model is shown in Supplementary Materials. All the reactions considered in the model and the expression of kinetic rate are listed in Table 2.

Solid species are transported through the sediments only by burial with prescribed compaction, which is justified because we are only concerned with the anoxic diagenesis below the bioturbated zone. For sites CL44 and CL47, solutes are considered to be transported by molecular diffusion, porewater burial, and gas bubble irrigation, whereas for site CL30, solutes are regarded to be transported by molecular diffusion and porewater burial. Rising gas bubbles facilitate

the exchange of porewater and bottom water as they move through tube structures in soft sediments [7]. Although this process was not observed directly, there are evidences implying that it is a significant pathway for transporting methane into the upper 10 m of sediment at sites CL44 and CL47 and driving the mixture of porewater and seawater in the upper two meters (see Section 5.1). The induced porewater mixing process was described as a nonlocal transport mechanism whose rate for each species is proportional to the difference between solute concentrations at the sediment surface C_0 (mmol cm⁻³) and at depth below the sediment surface C_x (mmol cm⁻³) (R_{Bui} , Table 2). Bubble irrigation is described by parameters α_1 (yr⁻¹) and α_2 (cm) that define the irrigation intensity and its attenuation below the irrigation depth L_{irr} (cm), respectively [49]. The latter can be determined by visual inspection of the porewater data (see Results) whereas α_1 is a model fitting parameter. For the sake of parsimony, α_2 is assumed to be constant for both sites.

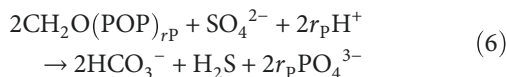
Although dissolution of gas was allowed to occur over the whole sediment column, the rising methane gas was not explicitly modeled. The rate of gas dissolution, R_{diss} (mmol cm⁻³ yr⁻¹), was described using a pseudo-first-order kinetic expression of the departure from the local methane gas solubility concentration, L_{MB} (mmol cm⁻³), where k_{MB} (yr⁻¹) is the kinetic constant for gas bubble dissolution (Table 2). Methane only dissolves if the porewater is undersaturated with respect to L_{MB} :



L_{MB} was calculated for the in situ salinity, temperature, and pressure using the algorithm in [52]. k_{MB} was constrained using the dissolved sulfate and DIC data (see below).

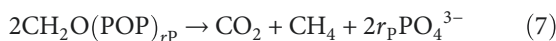
Major biogeochemical reactions considered in the model are particulate organic matter (POM) degradation via sulfate reduction, methanogenesis, AOM, and authigenic carbonate precipitation. Organic matter mineralization via aerobic respiration, denitrification, and metal oxide reduction were ignored since these processes mainly occur in the surface sediments which were mostly lost during coring.

POM is chemically defined as $\text{CH}_2\text{O}(\text{POP})_{r_p}$, where CH_2O and POP denote particulate organic carbon and phosphate, respectively. The total rate of POM mineralization, R_{POC} (wt.% C yr⁻¹), is calculated by the power law model from [53] that considers the initial age of organic matter in surface sediments, a_0 (yr) (Table S2). POM mineralization coupled to sulfate reduction follows the stoichiometry:



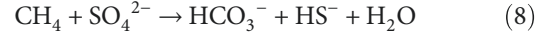
where r_p is the ratios of particulate organic phosphate to carbon. It is assumed to be the typical ratios as 1/106 [48].

When sulfate is almost completely consumed, the remaining POM is degraded via methanogenesis:



The dominant pathways of methanogenesis in marine sediments are organic matter fermentation and CO₂ reduction [54]. Their net reactions at steady state are balanced with equivalent amounts of CO₂ and CH₄ being produced per mole of POM degraded [55]. Therefore, the reaction of methanogenesis is a net reaction.

Methane is considered to be consumed by AOM [3]:



The rate constant for AOM, k_{AOM} (cm³ mmol⁻¹ yr⁻¹), is tuned to the sulfate profiles within the SMTZ.

The loss of Ca²⁺ and Mg²⁺ resulting from the precipitation of authigenic carbonates as Ca-calcite and Mg-calcite ((Ca²⁺, Mg²⁺) + HCO₃⁻ → (Ca, Mg)CO₃ + H⁺) was simulated in the model using the thermodynamic solubility constant as defined in [56] (Table 2). A typical porewater pH value of 7.6 was used to calculate CO₃²⁻ from modeled DIC concentrations [57]. (Ca, Mg)CO₃ was not simulated explicitly in the model.

The length of the simulated model domain was set to 1000 cm. Upper boundary conditions for all species were imposed as fixed concentrations (Dirichlet boundary) using measured values in the uppermost sediment layer where available. For CL44 and CL47, a zero concentration gradient (Neumann-type boundary) was imposed at the lower boundary for all the species. For CL30, a zero concentration gradient was imposed at the lower boundary for all the species except CH₄. CH₄ concentration at the lower boundary was a tunable parameter constrained from the SO₄²⁻ profile. The model was solved using the NDSolve object of MATHEMATICA V. 10.0. The steady-state simulations were run for 10⁷ yrs to achieve the steady state with a mass conservation of >99%. Further details on the model solutions can be found in Supplementary Materials. For the non-steady-state modeling of CL30, a fixed methane concentration in equilibrium with the gas hydrate solubility constrained by local seafloor temperature, pressure, and salinity was defined as the lower boundary of methane [58]. The extrapolation of sulfate concentrations in the upper 3.5 m to zero was taken as the initial condition prior to the increase in methane flux (Supplementary Materials). The basic model construction and kinetic rate expressions as well as the upper and lower boundary conditions for other species were identical to those in the steady-state model.

4. Results

4.1. General Geochemical Trends. The depth profiles of SO₄²⁻ concentration showed kink-type features at all the three cores (Figures 2–4 and Table 3). At site CL30, SO₄²⁻ concentrations decreased gradually above a kink at ~3.5 mbsf and the gradient became steeper below that depth towards the SMTZ at ~4.7 mbsf (Figure 2). In contrast, SO₄²⁻ concentrations at sites CL44 and CL47 displayed near-seawater values in the upper ~2 mbsf above the kinks and then decreased sharply down to the SMTZ located at ~7 and ~6.8 mbsf, respectively (Figures 3 and 4). Ca²⁺ and Mg²⁺ concentrations showed similar trends, with gradual decrease in the upper layers at

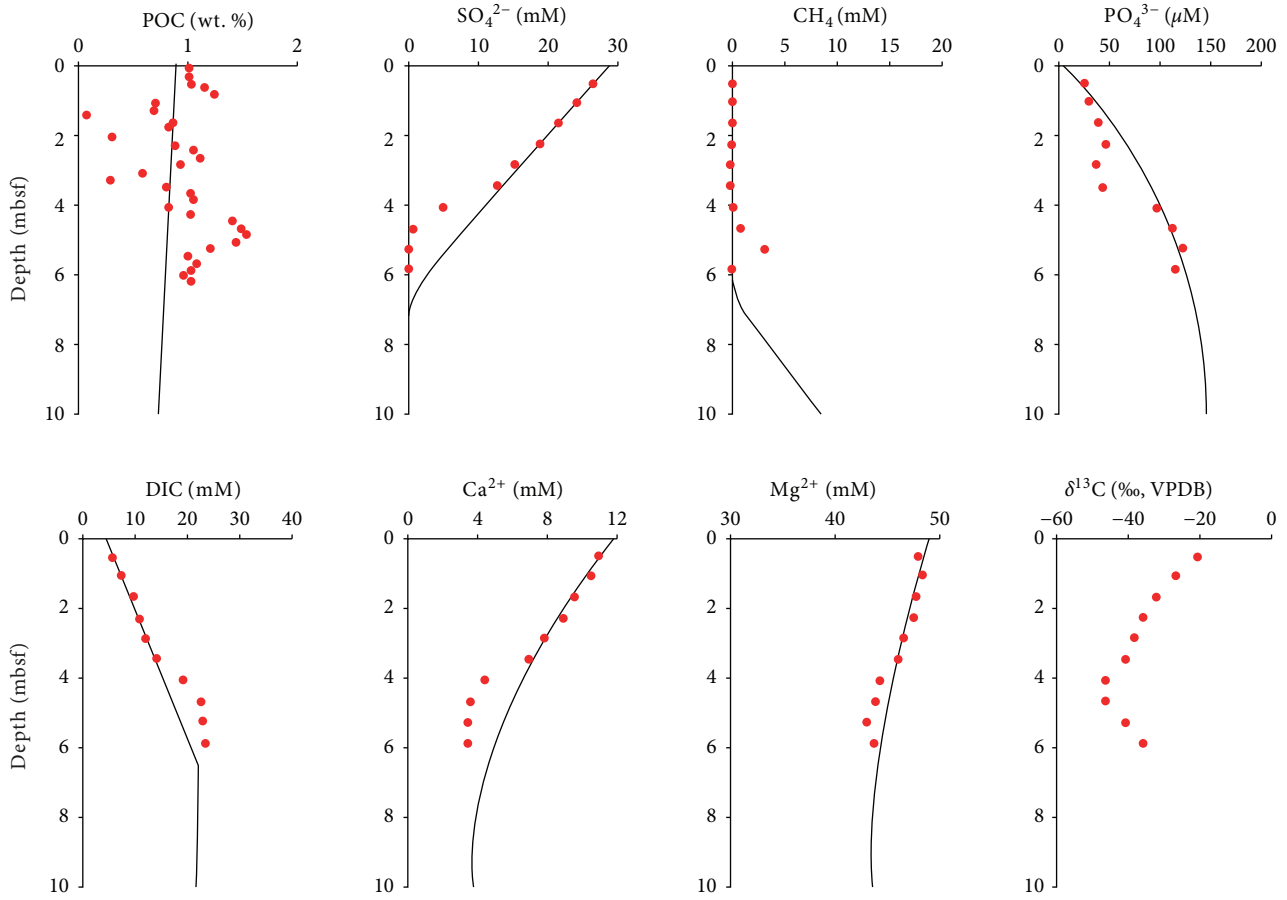


FIGURE 2: Measured (dots) and simulated (curves) depth profiles of core CL30. Down-depth concentration of particulate organic carbon (POC), sulfate (SO_4^{2-}), methane (CH_4), phosphate (PO_4^{3-}), dissolved inorganic carbon (DIC), calcium (Ca^{2+}), magnesium (Mg^{2+}), and $\delta^{13}\text{C}_{\text{DIC}}$ is shown.

core CL30 and close to seawater concentration above the kinks at cores CL44 and CL47. Ca^{2+} and Mg^{2+} concentrations declined sharply below the kinks due to ongoing carbonate precipitation and reached minimum at the SMTZ (Figures 2–4 and Table 3). Concentrations of DIC and PO_4^{3-} showed opposite trends to SO_4^{2-} , being depleted within the upper layer and enriched below it with the maximum at the SMTZ (Figures 2–4 and Table 3). Moreover, CH_4 concentrations at the three cores sharply increased below the SMTZ. The scatter in the CH_4 contents was due to the degassing during core retrieval. The DIC concentrations increased with depth and reached maximum at the SMTZ, with opposite trends of $\delta^{13}\text{C}_{\text{DIC}}$ values (minimum values: -46.4‰ for CL30, -41.0‰ for CL44, and -38.8‰ for CL47) (Figures 2–4 and Table 3).

Vertical profiles of CL30, CL44, and CL47 for pore-water barium concentrations and sediment barium contents together with barium/aluminium (Ba/Al) ratios are shown in Figure 5. Dissolved Ba^{2+} concentrations display maxima of 60.8, 38.6, and 58.5 μM below the SMTZ, respectively, and decreased upward towards the SMTZ (Figure 5). Bulk sediment Ba concentrations range from 306 to 957 mg kg^{-1} (Table S6) with averages of 461 mg kg^{-1} for CL30, 502 mg kg^{-1} for CL44, and 502 mg kg^{-1} for CL47. High Ba concentrations of bulk sediments at each core occur over narrow depth

intervals (0.3–0.8 m) above the present SMTZ (Figure 5). Peak Ba concentrations within these zones reach 957, 741, and 790 mg kg^{-1} and appear at approximately 4.3, 5.9, and 6.3 mbsf at cores CL30, CL44, and CL47, respectively. The refractory amount of solid phase barium at these cores amounts to 530, 550, and 590 mg kg^{-1} , respectively, which is considered to represent the “background” levels of solid phase barium [16]. Ba contents were normalized to Al in order to account for variations in lithology. Depth intervals with Ba content higher than these “background” levels are referred to as “Ba fronts.” At each core examined, the Ba fronts exist within 1.5 m above the depth of current SMTZ (Figure 5). The distance between the peak Ba concentration and the depth of sulfate depletion is approximately 0.4 m at CL30, 1.1 m at CL44, and 0.5 m at CL47.

POC contents at all the sites did not follow a general downward trend with average contents as 0.97% for CL30, 1.05% for CL44, and 1.05% for CL47 (Figures 2–4 and Table S6). The sediments in the study cores are mainly composed of silt and clay. At sites CL30 and CL44, the relative fractions of silt and clay are nearly constant with depth and the fractions of sand remain low values with depth except at ~320 cm in CL30 displaying elevated sand fraction (Figure S2). At site CL47, the sand fractions are low with depth in the interval of 0–200 cm, followed by

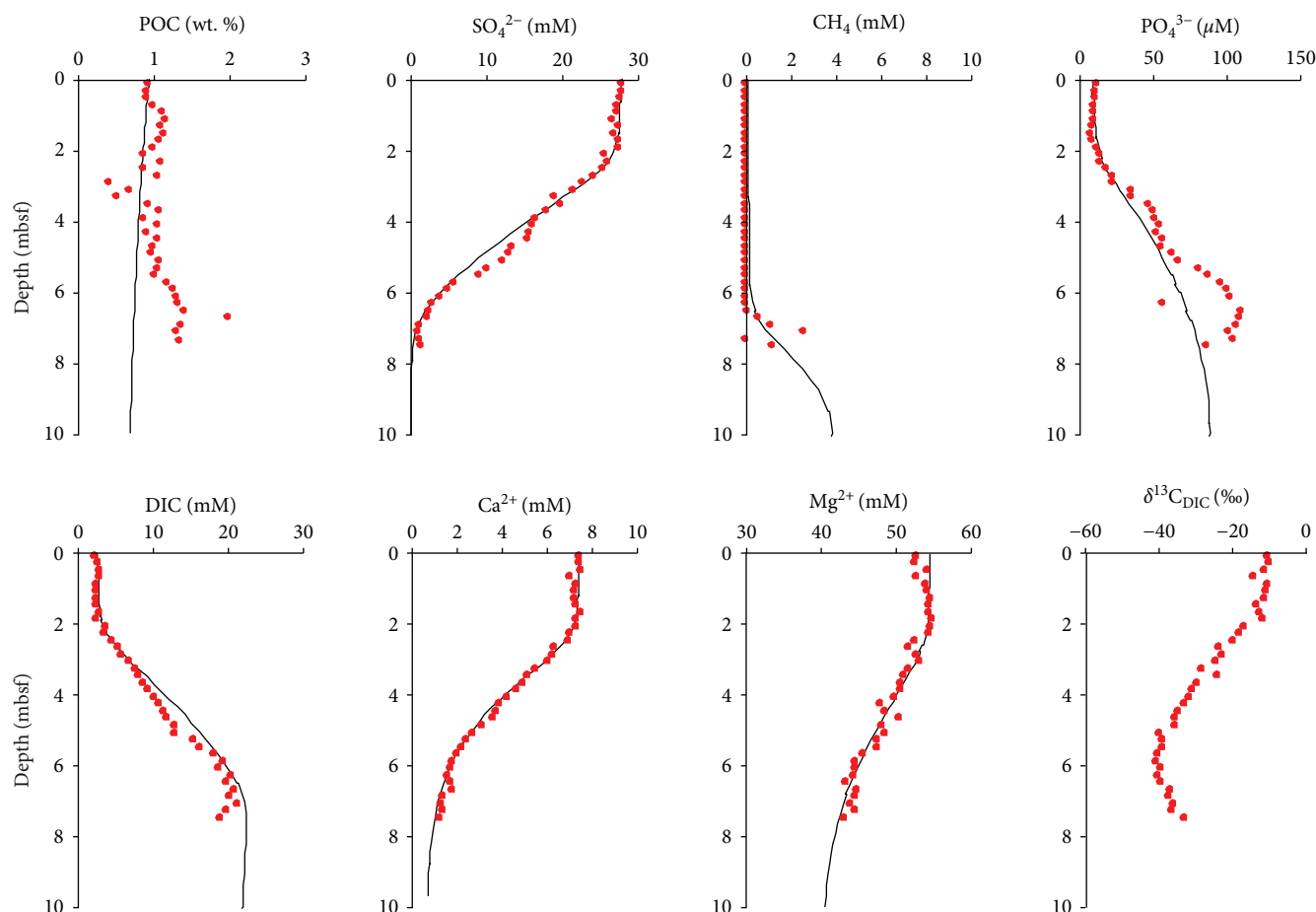


FIGURE 3: Measured (dots) and simulated (curves) depth profiles of core CL44. Down-depth concentration of POC, SO_4^{2-} , CH_4 , PO_4^{3-} , DIC, Ca^{2+} , Mg^{2+} , and $\delta^{13}\text{C}_{\text{DIC}}$ is shown.

an increase in sand fraction with two peaks at the depth of ~ 270 and ~ 430 cm. Below 500 cm, the sand fraction almost decreased to zero (Figure S2).

4.2. Timing of Authigenic Barite Front Accumulation. Dissolved barium fluxes towards the SMTZ were $1.58 \text{ mmol m}^{-2} \text{ yr}^{-1}$ for CL30, $1.54 \text{ mmol m}^{-2} \text{ yr}^{-1}$ for CL44, and $1.61 \text{ mmol m}^{-2} \text{ yr}^{-1}$ for CL47. The calculated time required for the formation of barite front is about 3.2, 3.0, and 1.3 kyr for the three cores, respectively, using an average porosity of 0.69 taken from CL44 (Table S5). Variations of porosity from 0.65 to 0.75 yield the time for barite front formation ranging between 2.2 and 4.2 kyr for CL30 and between 0.8 and 1.6 kyr for CL47. Sensitivity tests of the background Ba content, Ba^{2+} fluxes, and porosity are shown in Figures S5&S6.

4.3. Reaction-Transport Modeling. The modeled profiles and reaction rates are shown in Figures 2–4 and Table 4, respectively. The model parameters used to derive these results are listed in Tables S2–S4. The steady-state modeling reproduced the measured concentrations of SO_4^{2-} , DIC, Ca^{2+} , Mg^{2+} , and PO_4^{3-} at sites CL44, CL47, and CL30 above the kink with obvious discrepancies between modeled and measured concentrations of CH_4 due to aforementioned degassing

during core recovery (Figures 2–4). At site CL30, the model failed to reproduce the concentration gradients of SO_4^{2-} , DIC, Ca^{2+} , Mg^{2+} , and PO_4^{3-} below the kink (~ 3.5 mbsf) which is likely caused by a transient condition that is not considered in the steady-state model.

The sulfate concentration profile with a kink at site CL30 (Figure 2) could be explained by a recent increase in upward methane flux [9]. The linear extrapolation of the sulfate concentrations in the upper 3.5 m to zero sulfate concentration was taken as the initial condition for the non-steady-state model. Under this condition, the sulfate profile was fitted by a fixed CH_4 concentration (67 mM) at the lower boundary in equilibrium with the gas hydrate solubility under the conditions of in situ S , T , and P . A sudden increase in CH_4 concentration reproduces the observed SO_4^{2-} concentration profile after running the model for ~ 85 yr (Figure 6). The increase in methane flux resulted in a prominent increase in the depth-integrated AOM rate from $30.1 \text{ mmol m}^{-2} \text{ yr}^{-1}$ ($t = 0$ yr) to $140 \text{ mmol m}^{-2} \text{ yr}^{-1}$ ($t = 85$ yr).

The initial age of the organic matter was tuned until a good fit was obtained for the PO_4^{3-} . The mean total depth-integrated rates of POC degradation were about 3 times higher at sites CL44 and CL47 (55.2 and $58.1 \text{ mmol m}^{-2} \text{ yr}^{-1}$) than that at site CL30 ($18.8 \text{ mmol m}^{-2} \text{ yr}^{-1}$) (Table 4). The rates of POC degradation through sulfate reduction

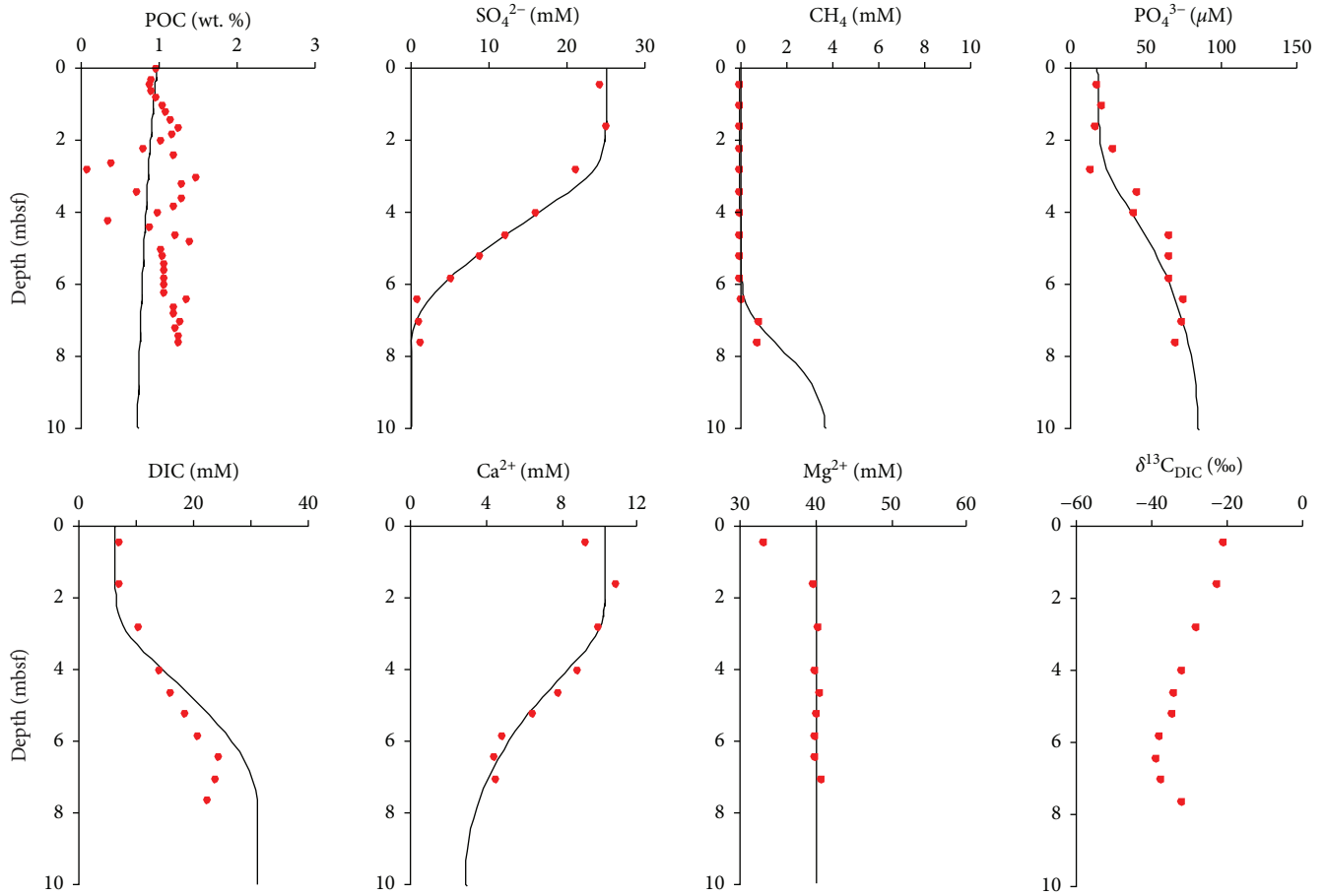


FIGURE 4: Measured (dots) and simulated (curves) depth profiles of core CL47. Down-depth concentration of POC, SO_4^{2-} , CH_4 , PO_4^{3-} , DIC, Ca^{2+} , Mg^{2+} , and $\delta^{13}\text{C}_{\text{DIC}}$ is shown.

(POCSR) were 7.6, 23.9, and 25.1 $\text{mmol m}^{-2} \text{yr}^{-1}$ at cores CL30, CL44, and CL47, respectively. In contrast to the relatively low rates of POCSR, AOM dominated the sulfate consumption with rates of 30.1, 74.3, and 84.7 $\text{mmol m}^{-2} \text{yr}^{-1}$ for CL30, CL44, and CL47, respectively. The AOM rates were mainly sustained by an external methane source, and methanogenesis contributed only a negligible amount of methane (Table 4). The AOM consumes almost all the CH_4 with benthic CH_4 fluxes of 0.49, 2.0, and 2.7 $\text{mmol m}^{-2} \text{yr}^{-1}$ at sites CL30, CL44, and CL47, respectively.

5. Discussion

5.1. Formation Mechanisms of the Nonlinear Porewater Profiles. The sulfate concentration profiles of the porewater in marine sediments depend on the availability of labile organic matter amenable to sulfate reducers, diffusive/advective methane flux, and depositional conditions [9, 59–64]. Combination of these factors would result in linear, kink, concave-up, concave-down, and sigmoidal (S-shape) type sulfate concentration trends in marine sediments [9].

The porewater profiles of the three study cores exhibit kink-type features. The plausible mechanisms for the occurrence of the kink-type profile include (1) irrigation and sea-

water intrusion due to biological, physical, and hydrological processes; (2) changes in the sedimentation rate or porosity due to depositional events; and (3) changes in methane flux and upward advection of fluid [14]. Bioirrigation has been shown to generally occur in a decimeter scale in the surface sediments [65, 66]. In fact, no macroorganisms were observed in the study cores below the upper few centimeters of sediment. The lithology of the upper two-three meters of the sediments in the study cores was dominated by fine-grained hemipelagic sediments mainly consisting of silty clay without any discernible abnormal deposition (Figure S2). Although deep-water turbidity current channel and fan systems are well developed in the study region [67], the homogeneous grain size distributions in cores CL44 and CL47 reveal that the sediment above the kinks of sulfate was not impacted by turbidites, which are typically characterized by upward grading in grain size. The C-M plot also suggests the absence of turbidites in the study cores (Figure S2 [68]). Moreover, by comparing the depth profiles of CaCO_3 content in CL44 and CL47 with that in an adjacent core (SO49-37KL) with established Marine Isotope Stage, we found that the upper ~2 m sediments of CL44 and CL47 represent normal hemipelagic background deposition during the Holocene (Figure S3) [69, 70]. The

TABLE 3: Concentrations and isotope ratios of various dissolved components at cores CL30, CL44, and CL47.

Depth (cmbsf)	CH ₄ (mM)	SO ₄ ²⁻ (mM)	Ca ²⁺ (mM)	Mg ²⁺ (mM)	PO ₄ ³⁻ (μM)	Ba ²⁺ (μM)	DIC (mM)	δ ¹³ C _{DIC} (‰, VPDB)
CL30								
55	0.0016	26.7	10.9	47.9	27.0	23.0	6.0	-20.4
110	0.0012	24.4	10.5	48.3	31.5	19.8	7.6	-26.0
170	0.0010	21.7	9.5	47.6	41.0	17.9	10.1	-31.9
230	0.0051	19.0	8.9	47.5	49.9	17.6	11.1	-35.4
290	0.0012	15.4	7.9	46.5	39.2	9.9	12.4	-38.0
350	0.0000	13.1	7.0	46.1	45.5	20.0	14.3	-40.5
410	0.0056	5.3	4.5	44.3	97.2	16.1	19.2	-45.7
470	0.8752	1.0	3.7	43.8	112	46.5	22.8	-46.4
530	3.2660	0.4	3.5	43.1	122	53.5	23.0	-40.0
590	0.1318	0.2	3.4	43.7	116	60.8	23.7	-35.7
CL44								
10	0.0012	27.9	7.4	52.7	11.9	0.3	2.2	-10.9
30	0.0004	27.9	7.4	52.4	10.1	0.3	2.6	-10.5
50	0.0008	27.6	7.5	54.1	10.4	0.2	3.0	-12.1
70	0.0003	27.2	7.0	52.7	9.3	0.2	3.0	-14.8
90	0.0020	27.3	7.3	53.8	9.6	0.2	2.4	-10.9
110	0.0005	26.7	7.2	54.0	9.1	0.2	2.4	-11.6
130	0.0005	27.4	7.2	54.5	8.3	0.2	2.4	-11.9
150	0.0008	26.9	7.3	54.3	7.1	0.2	2.5	-14.1
170	0.0007	27.5	7.5	54.3	8.1	0.2	3.0	-13.1
190	0.0006	27.5	7.3	54.7	10.9	0.2	2.5	-12.1
210	0.0005	25.6	7.3	54.6	13.2	0.2	3.8	-17.2
230	0.0017	25.9	7.0	54.2	13.7	0.2	3.5	-18.5
250	0.0009	25.3	6.9	52.5	17.7	0.2	4.6	-20.4
270	0.0018	24.1	6.3	51.6	22.3	0.3	5.5	-24.0
290	0.0018	22.6	6.2	52.6	22.6	0.4	5.9	-23.1
310	0.0014	21.5	6.0	53.0	35.1	0.3	6.8	-25.0
330	0.0011	19.0	5.5	51.6	35.6	0.3	7.7	-28.8
350	0.0017	19.7	5.1	51.0	47.3	0.3	8.1	-24.3
370	0.0020	17.9	4.9	50.5	49.8	0.3	8.8	-30.1
390	0.0015	16.4	4.6	50.5	50.8	0.4	9.5	-31.2
410	0.0020	16.0	4.2	49.7	54.9	0.6	10.2	-31.9
430	0.0012	15.6	3.9	47.8	52.1	0.5	11.0	-33.4
450	0.0021	15.4	3.7	48.4	56.5	0.5	11.6	-35.1
470	0.0022	13.2	3.6	50.3	55.4	0.6	12.0	-35.7
490	0.0019	12.8	3.1	48.0	63.6	0.7	13.1	-35.8
510	0.0026	12.0	2.7	48.4	67.1	0.8	13.1	-39.9
530	0.0027	10.0	2.4	47.5	81.9	1.0	15.5	-39.1
550	0.0024	8.9	2.2	47.4	88.0	1.3	16.3	-39.3
570	0.0034	5.6	2.0	45.5	96.7	2.5	18.2	-40.5
590	0.0039	4.7	1.8	44.6	101	4.9	19.5	-41.0
610	0.0028	3.7	1.7	44.5	103	11.0	18.9	-39.7
630	0.0022	2.7	1.6	44.2	57.0	19.3	20.5	-40.5
650	0.0442	2.3	1.7	43.3	111	22.2	19.9	-39.6
670	0.5139	2.1	1.8	44.7	109	31.7	21.1	-37.1
690	1.1022	0.9	1.4	44.5	107	37.9	20.4	-37.4
710	2.5450	0.8	1.3	43.9	102	38.6	21.5	-36.1
730	0.0086	0.9	1.4	44.6	105	37.4	20	-36.8

TABLE 3: Continued.

Depth (cmbsf)	CH ₄ (mM)	SO ₄ ²⁻ (mM)	Ca ²⁺ (mM)	Mg ²⁺ (mM)	PO ₄ ³⁻ (μM)	Ba ²⁺ (μM)	DIC (mM)	δ ¹³ C _{DIC} (‰, VPDB)
750	1.1475	1.1	1.2	43.0	86.8	36.0	19.2	-33.3
CL47								
55	0.0008	24.9	9.2	33.1	18.3	21.3	6.7	-21.1
110	0.0006				21.1			
170	0.0004	26.0	10.9	39.7	16.4	13.6	6.8	-22.9
230	0.0008				28.2			
290	0.0008	21.9	10.0	40.2	13.8	14.8	10.0	-28.5
350	0.0009				44.7			
410	0.0009	16.5	8.8	39.8	43.1	13.9	13.7	-32.1
470	0.0006	12.7	7.8	40.4	66.4	16.9	15.9	-34.0
530	0.0006	9.3	6.5	40.0	65.9	13.7	18.2	-34.7
590	0.0007	5.4	4.9	39.7	66.4	25.9	20.6	-38.2
650	0.0773	1.1	4.5	39.8	76.3	52.0	24.2	-38.8
710	0.7947	1.2	4.6	40.6	74.5	58.5	23.5	-37.4
770	0.7692	1.4			70.2		22.1	-32.1

relatively constant ratios of Ti/Al, Si/Al, and Zr/Rb above the kinks indicate a stable input of detrital fraction (Figure S4). In contrast, the layers at the interval of ~1.4 to ~4.2 mbsf in CL44 and ~1.8 to ~5 mbsf in CL47 exhibiting high Si, Ti, and Zr/Rb contents and coarser grain sizes (Figure S4) suggest elevated input of detrital fraction during sea-level lowstands [71, 72]. In addition, the flat seafloor topography in the study area also precludes the occurrence of abrupt depositional event such as landslide (Figure 1). Therefore, it is unlikely that the irrigation-like feature in CL44 and CL47 was caused by mass-transport deposits [44]. Furthermore, there is no indicator for upward fluid advection at sites CL44 and CL47.

We argue that the cause for the formation of the irrigation-like porewater profiles is probably the bubble irrigation by rising free gas through escaping tubes [7, 12, 51]. Such features were observed at the nearby Haima cold seeps and attributed to bubble irrigation or a recent increase in methane flux [33]. Moreover, BSR and acoustic blanking which are indicative of free gas accumulation were identified in the study area (Fang Y., unpublished data). Hence, gas bubble irrigation is the most likely mechanism to explain the observed profiles at cores CL44 and CL47.

At core CL30, the sediments consist of homogenous silty clay without discernible abnormal deposition and the sulfate concentrations decrease gradually without maintaining seawater-like values above the kink at 3.5 mbsf (Figure 2). We thus hypothesize that the kink in the sulfate profile at core CL30 results from a (sub)recent increase in the upward methane flux, similar to the scenario reported in the Sea of Marmara, the continental margin offshore Pakistan, the slope area south of Svalbard, the Niger Delta, the southern SCS, and so on [10–13, 44]. A simplified numerical model exercise, assuming a diffusional porewater system with POCSR and AOM as the only biogeochemical reactions, was used to demonstrate this scenario (Figure 6). The assumption of diffusive transport of porewater species is warranted because

it has been suggested that porewater solute distributions are dominated by diffusion even if free gas transport and fluid advection exist [14, 73].

The current barite front is located at about 4.2–6.4 mbsf, very close to the current SMTZ (4.7–7 mbsf), indicating that the barite front might form in the recent past to the present day induced by a recent enhancement of methane flux [11]. Actually, the measured SO₄²⁻ concentration profile can be reproduced after a sudden increase in CH₄ concentration lasting for ~85 yr. On the other hand, based on the calculated diffusive Ba²⁺ fluxes and the depth-integrated Ba contents, the time required to form the observed authigenic barite front above the current SMTZ is about 2.2–4.2 kyr for CL30, given the uncertainties of porosity. The difference of estimated duration of constant methane flux between these two approaches may suggest that the barite front was not a result of the recent increase in methane flux inducing the kink-type sulfate profile. Instead, it is more likely that the SMTZ has experienced several fluctuations in depth, considering the episodic pulses of upward methane flux which have occurred in this area as shown by previous studies [25, 32, 33]. However, this decoupled record between sediments and porewaters is commonly observed at cold seeps [74–77] and is considered to reflect the variations of methane fluxes and the resulting SMTZ in the sedimentary column [74]. Observations and numerical modeling suggest that the response of porewater geochemical signatures is more rapid on time-scales of months to centuries than the accumulation of authigenic barite deposits on timescales of decades to hundred thousands of years [11, 12, 14, 16–19, 74]. On the whole, our results suggest that combining porewater data with sedimentary barite front records may provide important clues for better understanding of the evolution of methane seepage.

5.2. Methane-Related Carbon Cycling and Source of Methane.

Based on the simulation results derived from the steady-state modeling, AOM consumed ~80%, 76%, and 77% of sulfate in

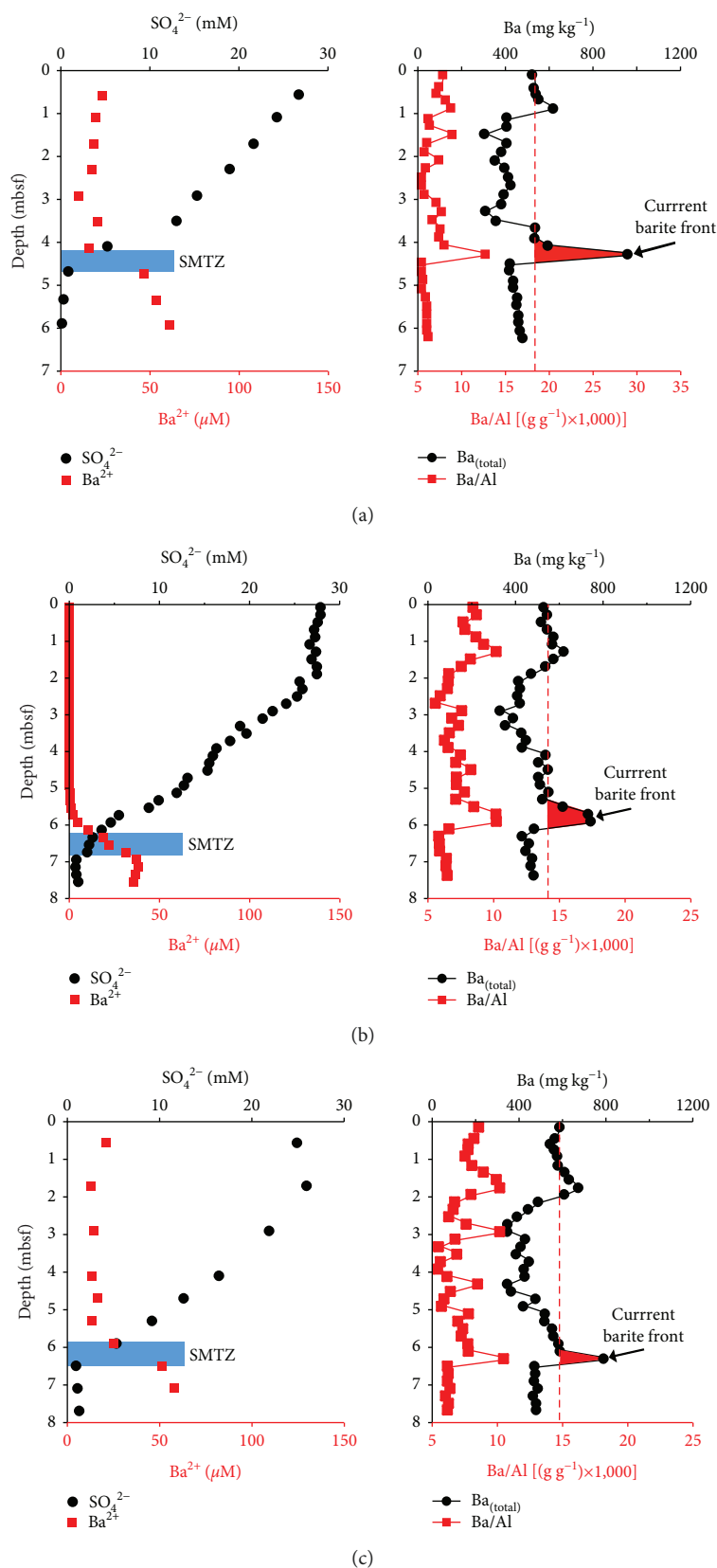


FIGURE 5: Concentration depth profiles of dissolved barium (Ba^{2+}), sulfate (SO_4^{2-}), and solid-phase total barium (Ba_{total}), barium/aluminium ratios (Ba/Al), and diagenetic barium (shown as red peaks) for cores CL30 (a), CL44 (b), and CL47 (c). Blue bands mark the SMTZ. Pink dash lines indicate the background barium contents based on the distribution of barium content. Barium contents above background represent diagenetic barite enrichments (red polygons).

TABLE 4: Depth-integrated simulated turnover rates and benthic methane fluxes based on the steady-state modeling.

	CL30	CL44	CL47	Unit
F_{POC} : total POC mineralization rate	18.8	55.2	58.1	$\text{mmol m}^{-2} \text{yr}^{-1}$ of C
F_{OSR} : sulfate reduction via POC degradation	7.6	23.9	25.1	$\text{mmol m}^{-2} \text{yr}^{-1}$ of SO_4^{2-}
F_{ME} : methane formation via POC degradation	3.6	3.7	4.0	$\text{mmol m}^{-2} \text{yr}^{-1}$ of CH_4
F_{DISS} : gas dissolution	28.4	73.3	84.7	$\text{mmol m}^{-2} \text{yr}^{-1}$ of CH_4
F_{AOM} : anaerobic oxidation of methane	30.1	74.3	85.0	$\text{mmol m}^{-2} \text{yr}^{-1}$ of CH_4
$F_{\text{CP-Ca}}$: authigenic CaCO_3 precipitation	3.0	2.2	5.6	$\text{mmol m}^{-2} \text{yr}^{-1}$ of C
$F_{\text{CP-Mg}}$: authigenic MgCO_3 precipitation	5.4	7.1	0	$\text{mmol m}^{-2} \text{yr}^{-1}$ of C
Sulfate consumed by AOM	79.8	75.7	77.2	%
Benthic flux of CH_4 at SWI	0.5	1.9	2.7	$\text{mmol m}^{-2} \text{yr}^{-1}$ of CH_4
Percentage of CH_4 flux from depth	88.0	95.0	95.3	%
Percentage of CH_4 consumed by AOM	94.1	96.5	95.8	%

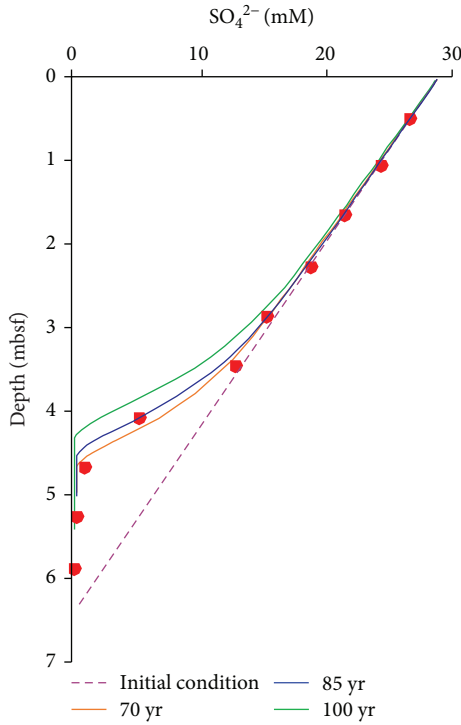


FIGURE 6: Evolution of the sulfate profile over time from simulation of non-steady-state porewater profiles of core CL30.

CL30, CL44, and CL47, respectively. AOM thus acts as an efficient barrier preventing methane from being released into the water column at the studied cores. This is supported by the low $\delta^{13}\text{C}_{\text{DIC}}$ values at the SMTZs mainly derived from methane. AOM increases porewater alkalinity by producing bicarbonate and results in the precipitation of authigenic carbonates as shown by the decrease in Ca^{2+} and Mg^{2+} concentrations with depth (Figures 3–6).

In addition, the $\delta^{13}\text{C}_{\text{DIC}}$ values below the SMTZ become more positive than those at the SMTZ. The reversal in $\delta^{13}\text{C}_{\text{DIC}}$ below the SMTZ is caused by the generation of ^{13}C -enriched DIC via local methanogenesis at the methanogenic zone [63, 78]. The ^{13}C -enriched DIC would migrate into

the SMTZ from the methanogenic zone and “dilute” the ^{12}C pool of DIC in porewater. Thus, in a closed system, DIC generated by local methanogenesis is an important source of DIC in the carbon budget within the SMTZ [78, 79].

Based on the modeling results of methane turnovers, the depth-intergrated AOM rates at cores CL30, CL44, and CL47 are about 8 to 21 times of the in situ methanogenesis rates (Table 4). Therefore, the relative proportions of external methane sources contributed to the total methane pool are 88%, 95%, and 95% at cores CL30, CL44, and CL47, respectively. This indicates that the majority of methane fuelling AOM at the SMTZ was sourced from subsurface sediments. There are two general pathways for producing methane in marine sediments, including microbial methane generated via CO_2 reduction or the fermentation of reduced carbon substrates (e.g., acetate and methanol; [80]) and thermogenic methane formed via thermal cracking of organic matter and/or heavy hydrocarbons [81]. The $\delta^{13}\text{C}$ values of methane are generally distinct between these two types of methane. The $\delta^{13}\text{C}$ values of microbial methane typically range from -50‰ to -110‰ [80], whereas those of thermogenic methane range from -30‰ to -50‰ [81].

Because $\delta^{13}\text{C}$ values of headspace methane in the sediments are absent in the study area, porewater DIC content and $\delta^{13}\text{C}_{\text{DIC}}$ are utilized to constrain the origin of methane. Generally, porewater DIC in marine sediments is mainly derived from (1) the DIC that is diffusing from the overlying seawater into the sediments or the seawater DIC trapped within sediments during burial, (2) the DIC generated by the degradation of sedimentary organic matter, (3) the DIC produced by AOM, and (4) the residual DIC derived from methanogenesis [82, 83]. In order to obtain the carbon isotopic composition of DIC derived from external methane, we applied a simple four-end-member mixing model. The four end-members are (1) seawater-derived DIC trapped within sediments during burial (SW), (2) DIC produced by POC SR, (3) DIC derived from external methane (EM) via AOM, and (4) DIC generated by *in situ* methanogenesis (ME). Note that methane production via local methanogenesis was assumed to be competently recycled by AOM. As a result, the carbon isotopic composition of DIC produced by local methanogenesis was identical to that of organic matter (OM) [82–84]. In

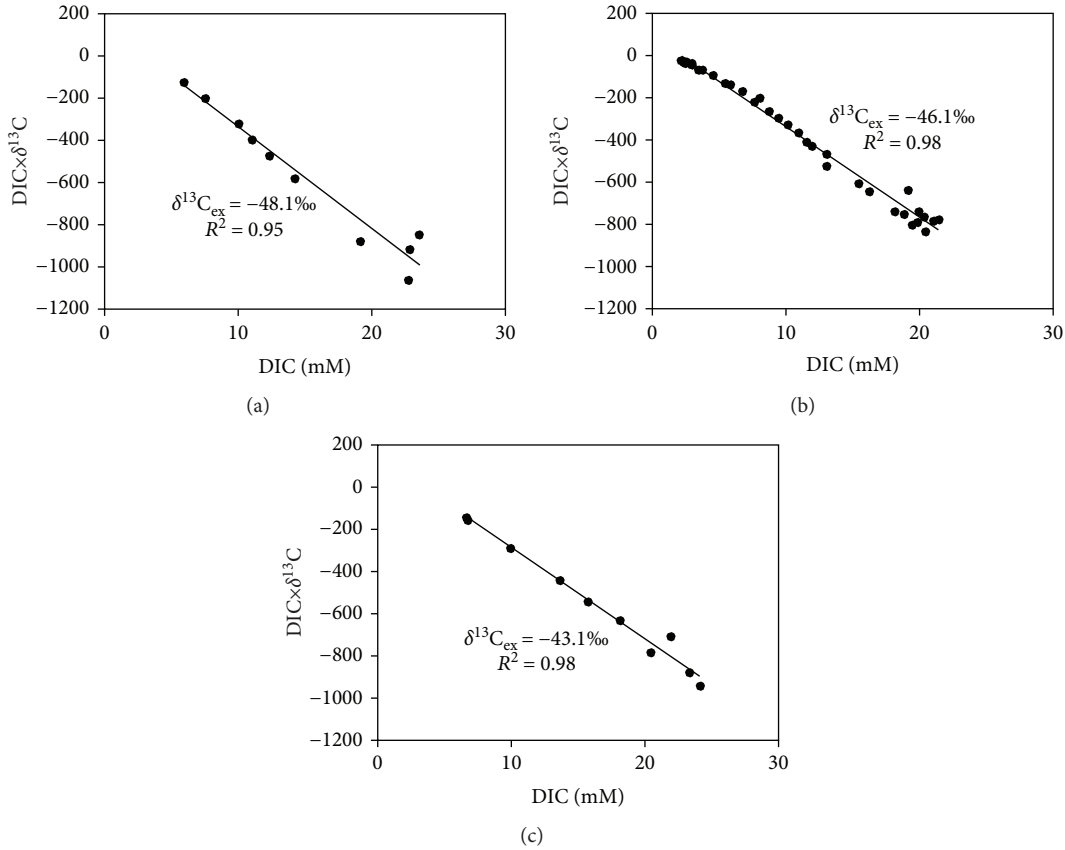


FIGURE 7: Plots of DIC vs. $\text{DIC} \times \delta^{13}\text{C}$. The $\delta^{13}\text{C}_{\text{ex}}$ were calculated using the linear regression of $\text{DIC} \times \delta^{13}\text{C}$ vs. DIC for CL30 (a), CL44 (b), and CL47 (c).

TABLE 5: Fractions of DIC from different sources contributed to the total DIC pool and $\delta^{13}\text{C}$ values from different sources.

Core ID	$\delta^{13}\text{C}_{\text{SMTZ}}$ (‰, VPDB)	$\delta^{13}\text{C}_{\text{ex}}$ (‰, VPDB)	$\delta^{13}\text{C}_{\text{SW}}$ (‰, VPDB)	$\delta^{13}\text{C}_{\text{OM}}$ (‰, VPDB)	X_{SW} (%)	X_{ME} (%)	X_{OSR} (%)	X_{AOM} (%)	$\delta^{13}\text{C}_{\text{methane}}$ (‰, VPDB)
CL30	-46.4	-48.1	0	-20	9.8	6.6	28.0	55.5	-74.1
CL44	-41.0	-46.1	0	-20	9.8	5.3	34.3	50.6	-75.4
CL47	-38.8	-43.1	0	-20	8.7	5.2	32.9	53.1	-66.7

a closed system, $\delta^{13}\text{C}$ balance of the porewater DIC pool at the SMTZ can be expressed by

$$\begin{aligned} \delta^{13}\text{C}_{\text{ex}} = & (X_{\text{SW}}) * (\delta^{13}\text{C}_{\text{SW}}) + (X_{\text{OSR}}) \\ & * (\delta^{13}\text{C}_{\text{OM}}) + (X_{\text{AOM}}) * (\delta^{13}\text{C}_{\text{EM}}) \\ & + (X_{\text{ME}}) * (\delta^{13}\text{C}_{\text{OM}}), \end{aligned} \quad (9)$$

where X is the proportion of DIC contributed to the total DIC pool and the subscripts SW, OSR, AOM, and ME refer to DIC derived from seawater, organic matter, external methane, and local methanogenesis, respectively. The X_{SW} values are estimated as typical seawater DIC concentration (2.1 mM) divided by DIC concentration at the SMTZ, and the $\delta^{13}\text{C}_{\text{SW}}$ is assumed to be 0‰. The $\delta^{13}\text{C}$ value of sedimentary organic matter in sediment of the SCS (-20‰; [85]) is used for the $\delta^{13}\text{C}_{\text{OM}}$. The overall $\delta^{13}\text{C}$ of DIC derived

from methanogenesis is equal to the $\delta^{13}\text{C}_{\text{OM}}$ assuming that methane produced by local methanogenesis was completely converted to DIC by AOM [84]. The contribution fractions of OSR, AOM, and local methanogenesis shown as X_{OSR} , X_{AOM} , and X_{ME} are calculated from the steady-state modeling. The $\delta^{13}\text{C}_{\text{ex}}$ can be acquired from a regression of porewater $\delta^{13}\text{C}_{\text{DIC}} \times \text{DIC}$ vs. DIC (Figure 7). The regression commonly shows linear in seep-impacted sediments, thus providing definitive $\delta^{13}\text{C}_{\text{DIC}}$ supplied to porewater [82, 86, 87]. The $\delta^{13}\text{C}_{\text{ex}}$ values and the contribution fractions estimated from the model are listed in Table 5. The estimated $\delta^{13}\text{C}_{\text{EM}}$ values in the shallow sediments are -74.1‰ (CL30), -75.4‰ (CL44), and -66.7‰ (CL47), suggesting the external methane migrating into the shallow sediments is microbial in origin [83, 88]. The absence of higher hydrocarbons in headspace gas samples also supports the microbial origin of methane in the study area.

Previous studies have suggested that microbial methane was the main hydrocarbon source with minor contributions of oil-derived compounds and pyrolysis gas at the Haima cold seeps [32, 33, 89, 90]. Gas chimney structures, which are well developed around the Haima cold seeps, might serve as conduits for the upward migration of biogenic gas from the underlying free gas reservoir beneath the GHSZ to shallow sediments [29, 42]. This observation suggests that microbial methane at the study sites might be derived from an underlying free gas reservoir trapped beneath the GHSZ.

5.3. Implications of the Time Constraint on Methane Seepage. Based on the diffusive dissolved barium flux and the excess barium content in the sediments, the time for the observed barite enrichments just above the current SMTZ is estimated to be about 3 kyr and 0.8–1.6 kyr for CL44 and CL47, respectively, given the uncertainties of porosity. These results suggest that the SMTZ has been fixed at the current sediment depth for a time period of at least several thousand years at these sites. The irrigation-type sulfate profiles are possibly maintained by continuous mixing of seawater into the sediment over these time periods, like the case in the pockmark sediments of Congo Fan [74]. Furthermore, the depth of SMTZ was speculated to have fluctuated due to variations in methane flux as suggested by the difference in the estimated duration of the barite enrichment and the recent increase methane flux at CL30. Overall, our results show that the methane flux has been fluctuating over the last hundreds to thousands of years in the vicinity of Haima cold seeps.

In fact, methane seepages around the Haima cold seeps are characterized by distinct periodicity of seep activities during the past several thousands of years. Radiocarbon ages of bivalve shells suggest that a major seepage event occurred during the period of 6.1 to 5.1 ka B.P., followed by a subordinate seepage event spanning from 3.9 to 2.9 ka B.P. at the Haima cold seeps [25]. The widespread occurrence of dead bivalves on the seafloor reflects a decline in current seepage intensity [25]. Moreover, modeling of porewater profiles at the Haima cold seeps predicts that gas hydrate formation in the seepage center started at least 150 yr B.P. and the subsequent sealing of gas hydrates favored the lateral migration of methane-rich fluids in the coarser, more permeable interval [33]. Sedimentation dynamics, including sediment instabilities and mass wasting, may trigger the destabilization of the gas hydrate reservoir and the resulting occurrence of methane seepage. The evolution and fate of methane seepage are also considered to be affected by local fluid flow dynamics and associated migration of both free gas and methane-rich fluids along fractures, as well as the redirection of gas supply from the reservoir due to pore space clogging by gas hydrate in shallow sediments [25, 33]. The exact mechanism of the changes in methane flux around the Haima cold seeps area is beyond the scope of this study. Despite this, our quantitative study provides some constraint on the duration of methane seepage and may have implication for understanding the evolution of methane seepage in the petroliferous Qiongdongnan Basin.

6. Conclusions

This study is aimed at understanding the methane source and turnover as well as provide some constraints on the timing of methane seepage to the west of “Haima cold seeps.” The steady-state reaction-transport modeling of SO_4^{2-} , CH_4 , DIC, PO_4^{3-} , Ca^{2+} , and Mg^{2+} in CL44 and CL47 suggests that gas bubble transport may lead to the irrigation-like feature in the upper 2 m and relatively high AOM rates ($74.3 \text{ mmol m}^{-2} \text{ yr}^{-1}$ for CL44 and $85.0 \text{ mmol m}^{-2} \text{ yr}^{-1}$ for CL47). The time required for the enrichment of authigenic barium fronts slightly above the current SMTZ is approximately 3 kyr for CL44 and 0.8–1.6 kyr for CL47, respectively. In contrast, a recent increase in methane flux (prior to ~85 yr) is the likely cause of the kink at 3.5 m of the sulfate profile in CL30 demonstrated by the transient-state modeling. The estimated time required for the formation of the diagenetic barium peak just above the current SMTZ was 2.2–4.2 kyr at this core. The discrepancy in the time estimates constrained by two different approaches suggests that the position of SMTZ possibly has fluctuated due to variation in methane flux at the site. In addition, based on the four DIC end-member mixing calculation, the $\delta^{13}\text{C}$ values of the external methane in cores CL30, CL44, and CL47 are -74.1‰, -75.4‰, and -66.7‰, respectively. This is indicative of the biogenic origin of external methane from an underlying reservoir. Our results suggest that methane seepage exists in a broader area in the vicinity of the “Haima cold seeps” and the methane fluxes may have fluctuated frequently for the last several hundreds to thousands of years.

Data Availability

The data used to support the findings of this study are included within the main text and the supplementary materials.

Conflicts of Interest

The authors declare that they have no conflicts of interest.

Acknowledgments

We thank the crew of the Haiyang-4 exploration ship for collecting the piston cores. We are also grateful to our colleagues from GMGS for their collection and analysis to the porewater and sediment samples. The authors appreciate Dr. T. Yang (Nanjing University) and Dr. X. J. Yin (Third Institute of Oceanography, Ministry of Natural Resources) for the help with the geochemical analyses. This study was supported by the National Key R&D Program of China (Grant: 2018YFC0310006), the China Postdoctoral Science Foundation (Grant: 2017M622654), the open-funds of Key Laboratory of Marine Mineral Resources, Ministry of Land and Resources (KLMMR-2017-A-08), the National Special Project on Gas Hydrate of China (Grant: GZH201100301), and the National Natural Science Foundation of China (Grant: 41730528, 41806074).

Supplementary Materials

In Table S1, reaction terms of all species used in the model are listed. Table S2 presents the summary of model parameters and boundary conditions used in the steady-state model, whereas Table S3 lists the derived and measured parameters used in the steady-state model. Parameters used in the nonsteady-state model are listed in Table S4. In Table S5, porosity and dry grain density of core CL44 are listed. Table S6 lists the solid-phase element contents, Ba/Al, Ti/Al, Si/Al, and Zr/Rb ratios, as well as POC and CaCO₃ contents of cores CL30, CL44, and CL47. Table S7 shows the grain size parameters of the studied cores. In addition, Figure S1 displays the measured (symbols) and modelled (curve) porosity of core CL44. Figure S2 shows the grain size parameters of the sediment cores. Figure S3 displays the downcore variations in carbonate contents and the age models of the studied cores. Figure S4 shows the Ti/Al, Si/Al, Zr/Rb, and carbonate contents of the sediments cores. Figure S5 details the uncertainty evaluation of the formation times of the diagenetic barium enrichments considering variable solid-phase barium background contents and porosities, whereas Figure S6 shows the uncertainty evaluation of the formation times of the diagenetic barium enrichments considering variable Ba²⁺ fluxes and porosities. In summary, Tables S1–S4 are the detailed descriptions of the reaction-transport models. Tables S5–S7 and Figure S1 are the datasets of the geotechnical and geochemical proxies of sediment samples, which contribute to the concentration depth profiles in Figure 5 of this manuscript. Figures S2–S4 show downcore variations in the geotechnical and geochemical proxies of sediment cores. Figures S5 and S6 are the sensitivity analysis of the formation times of the diagenetic barium enrichments. (*Supplementary Materials*)

References

- [1] A. G. Judd and M. Hovland, *Submarine Fluid Flow, the Impact on Geology, Biology, and the Marine Environment*, Cambridge University Press, Cambridge, 2007.
- [2] T. Yuan, G. D. Spence, R. D. Hyndman, T. A. Minshall, and S. C. Singh, “Seismic velocity studies of a gas hydrate bottom-simulating reflector on the northern Cascadia continental margin: amplitude modeling and full waveform inversion,” *Journal of Geophysical Research: Solid Earth*, vol. 104, no. B1, pp. 1179–1191, 1999.
- [3] R. O. Barnes and E. D. Goldberg, “Methane production and consumption in anoxic marine sediments,” *Geology*, vol. 4, no. 5, pp. 297–300, 1976.
- [4] A. Boetius, K. Ravensschlag, C. J. Schubert et al., “A marine microbial consortium apparently mediating anaerobic oxidation of methane,” *Nature*, vol. 407, no. 6804, pp. 623–626, 2000.
- [5] R. Luff, J. Greinert, K. Wallmann, I. Klauke, and E. Suess, “Simulation of long-term feedbacks from authigenic carbonate crust formation at cold vent sites,” *Chemical Geology*, vol. 216, no. 1–2, pp. 157–174, 2005.
- [6] W. Ussler III and C. K. Paull, “Rates of anaerobic oxidation of methane and authigenic carbonate mineralization in methane-rich deep-sea sediments inferred from models and geochemical profiles,” *Earth and Planetary Science Letters*, vol. 266, no. 3–4, pp. 271–287, 2008.
- [7] M. Haeckel, B. P. Boudreau, and K. Wallmann, “Bubble-induced porewater mixing: a 3-D model for deep porewater irrigation,” *Geochimica et Cosmochimica Acta*, vol. 71, no. 21, pp. 5135–5154, 2007.
- [8] S. Sommer, O. Pfannkuche, P. Linke et al., “Efficiency of the benthic filter: biological control of the emission of dissolved methane from sediments containing shallow gas hydrates at Hydrate Ridge,” *Global Biogeochemical Cycles*, vol. 20, no. 2, 2006.
- [9] C. Hensen, M. Zabel, K. Pfeifer et al., “Control of sulfate pore-water profiles by sedimentary events and the significance of anaerobic oxidation of methane for the burial of sulfur in marine sediments,” *Geochimica et Cosmochimica Acta*, vol. 67, no. 14, pp. 2631–2647, 2003.
- [10] P. Halbach, E. Holzbecher, T. Reichel, and R. Moche, “Migration of the sulphate–methane reaction zone in marine sediments of the Sea of Marmara—can this mechanism be tectonically induced?,” *Chemical Geology*, vol. 205, no. 1–2, pp. 73–82, 2004.
- [11] D. Fischer, J. M. Mogollón, M. Strasser et al., “Subduction zone earthquake as potential trigger of submarine hydrocarbon seepage,” *Nature Geoscience*, vol. 6, no. 8, pp. 647–651, 2013.
- [12] W. L. Hong, M. E. Torres, J. L. Carroll et al., “Seepage from an arctic shallow marine gas hydrate reservoir is insensitive to momentary ocean warming,” *Nature Communications*, vol. 8, no. 1, article 15745, 2017.
- [13] A. de Prunelé, L. Ruffine, V. Riboulot et al., “Focused hydrocarbon-migration in shallow sediments of a pockmark cluster in the Niger Delta (Off Nigeria),” *Geochemistry, Geophysics, Geosystems*, vol. 18, no. 1, pp. 93–112, 2017.
- [14] W. L. Hong, S. Sauer, G. Panieri et al., “Removal of methane through hydrological, microbial, and geochemical processes in the shallow sediments of pockmarks along eastern Vestnesa Ridge (Svalbard),” *Limnology and Oceanography*, vol. 61, no. S1, pp. S324–S343, 2016.
- [15] M. E. Torres, G. Bohrmann, and E. Suess, “Authigenic barites and fluxes of barium associated with fluid seeps in the Peru subduction zone,” *Earth and Planetary Science Letters*, vol. 144, no. 3–4, pp. 469–481, 1996.
- [16] G. R. Dickens, “Sulfate profiles and barium fronts in sediment on the Blake Ridge: present and past methane fluxes through a large gas hydrate reservoir,” *Geochimica et Cosmochimica Acta*, vol. 65, no. 4, pp. 529–543, 2001.
- [17] N. Riedinger, S. Kasten, J. Gröger, C. Franke, and K. Pfeifer, “Active and buried authigenic barite fronts in sediments from the Eastern Cape Basin,” *Earth and Planetary Science Letters*, vol. 241, no. 3–4, pp. 876–887, 2006.
- [18] G. T. Snyder, A. Hiruta, R. Matsumoto et al., “Pore water profiles and authigenic mineralization in shallow marine sediments above the methane-charged system on Umitaka Spur, Japan Sea,” *Deep Sea Research Part II Topical Studies in Oceanography*, vol. 54, no. 11–13, pp. 1216–1239, 2007.
- [19] S. Kasten, K. Nöthen, C. Hensen, V. Spieß, M. Blumenberg, and R. R. Schneider, “Gas hydrate decomposition recorded by authigenic barite at pockmark sites of the northern Congo Fan,” *Geo-Marine Letters*, vol. 32, no. 5–6, pp. 515–524, 2012.
- [20] L. F. Fan, S. Lin, C. W. Hsu, Y. T. Tseng, T. F. Yang, and K. M. Huang, “Formation and preservation of authigenic pyrite in



- the methane dominated environment," *Deep-Sea Research Part I*, vol. 138, pp. 60–71, 2018.
- [21] D. F. Chen, Y. Y. Huang, X. L. Yuan, and L. M. Cathles III, "Seep carbonates and preserved methane oxidizing archaea and sulfate reducing bacteria fossils suggest recent gas venting on the seafloor in the northeastern South China Sea," *Marine and Petroleum Geology*, vol. 22, no. 5, pp. 613–621, 2005.
 - [22] X. Han, E. Suess, Y. Huang et al., "Jiulong methane reef: microbial mediation of seep carbonates in the South China Sea," *Marine Geology*, vol. 249, no. 3–4, pp. 243–256, 2008.
 - [23] H. Tong, D. Feng, H. Cheng et al., "Authigenic carbonates from seeps on the northern continental slope of the South China Sea: new insights into fluid sources and geochronology," *Marine and Petroleum Geology*, vol. 43, pp. 260–271, 2013.
 - [24] D. Feng and D. Chen, "Authigenic carbonates from an active cold seep of the northern South China Sea: new insights into fluid sources and past seepage activity," *Deep Sea Research Part II Topical Studies in Oceanography*, vol. 122, pp. 74–83, 2015.
 - [25] Q. Liang, Y. Hu, D. Feng et al., "Authigenic carbonates from newly discovered active cold seeps on the northwestern slope of the South China Sea: constraints on fluid sources, formation environments, and seepage dynamics," *Deep Sea Research Part I Oceanographic Research Papers*, vol. 124, pp. 31–41, 2017.
 - [26] D. Feng, J. W. Qiu, Y. Hu et al., "Cold seep systems in the South China Sea: an overview," *Journal of Asian Earth Sciences*, vol. 168, pp. 3–16, 2018.
 - [27] Y. Bai, H. Song, Y. Guan, J. Chen, and B. Liu, "Structural characteristics and genesis of pockmarks in the northwest of the South China Sea derived from reflective seismic and multi-beam data," *Chinese Journal of Geophysics*, vol. 57, pp. 2208–2222, 2014.
 - [28] B. Liu and S. Liu, "Gas bubble plumes observed at north slope of South China Sea from multi-beam water column data," *Haiyang Xuebao*, vol. 39, pp. 83–89, 2017.
 - [29] L. Yang, B. Liu, M. Xu, S. Liu, Y. Guan, and Y. Gu, "Characteristics of active cold seepages in Qiongdongnan Sea Area of the northern South China Sea," *Chinese Journal of Geophysics*, vol. 61, pp. 2905–2914, 2018.
 - [30] B. Zhao, S. Liu, L. Li, and J. Guo, "Distribution pattern of cold seeps in South China Sea and its geological significance," *Marine Geology Frontiers*, vol. 34, pp. 32–43, 2018.
 - [31] J. Ye, J. Wei, J. Liang et al., "Complex gas hydrate system in a gas chimney, South China Sea," *Marine and Petroleum Geology*, vol. 104, pp. 29–39, 2019.
 - [32] X. Wang, N. Li, D. Feng et al., "Using chemical compositions of sediments to constrain methane seepage dynamics: a case study from Haima cold seeps of the South China Sea," *Journal of Asian Earth Sciences*, vol. 168, pp. 137–144, 2018.
 - [33] Y. Hu, M. Luo, Q. Liang et al., "Pore fluid compositions and inferred fluid flow patterns at the Haima cold seeps of the South China Sea," *Marine and Petroleum Geology*, vol. 103, pp. 29–40, 2019.
 - [34] B. Taylor and D. E. Hayes, "The tectonic evolution of the South China Basin," in *The Tectonic and Geologic Evolution of Southeast Asian Seas and Islands*, D. E. Hayes, Ed., vol. 23 of Geophysical Monograph Series, , pp. 89–104, AGU, 1980.
 - [35] K. Ru and J. D. Pigott, "Episodic rifting and subsidence in the South China Sea," *AAPG Bulletin*, vol. 70, pp. 1136–1155, 1986.
 - [36] T. Lüdmann and H. K. Wong, "Neotectonic regime on the passive continental margin of the northern South China Sea," *Tectonophysics*, vol. 311, no. 1–4, pp. 113–138, 1999.
 - [37] X. Xie, R. D. Müller, S. Li, Z. Gong, and B. Steinberger, "Origin of anomalous subsidence along the northern South China Sea margin and its relationship to dynamic topography," *Marine and Petroleum Geology*, vol. 23, no. 7, pp. 745–765, 2006.
 - [38] X. Shi, H. Jiang, J. Yang, X. Yang, and H. Xu, "Models of the rapid post-rift subsidence in the eastern Qiongdongnan Basin, South China Sea: implications for the development of the deep thermal anomaly," *Basin Research*, vol. 29, no. 3, pp. 340–362, 2017.
 - [39] Q. Sun, J. Cartwright, T. Lüdmann, S. Wu, and G. Yao, "Three-dimensional seismic characterization of a complex sediment drift in the South China Sea: evidence for unsteady flow regime," *Sedimentology*, vol. 64, no. 3, pp. 832–853, 2017.
 - [40] X. Wang, S. Wu, S. Yuan et al., "Geophysical signatures associated with fluid flow and gas hydrate occurrence in a tectonically quiescent sequence, Qiongdongnan Basin, South China Sea," *Geofluids*, vol. 10, no. 3, 368 pages, 2010.
 - [41] G. Hui, S. Li, L. Guo et al., "Source and accumulation of gas hydrate in the northern margin of the South China Sea," *Marine and Petroleum Geology*, vol. 69, pp. 127–145, 2016.
 - [42] J. Wang, S. Wu, X. Kong et al., "Subsurface fluid flow at an active cold seep area in the Qiongdongnan Basin, northern South China Sea," *Journal of Asian Earth Sciences*, vol. 168, pp. 17–26, 2018.
 - [43] K. Grasshoff, K. Kremling, and M. Ehrhardt, *Methods of Seawater Analysis, Third, Completely Revised and Extended Edition*, Wiley-VCH, Weinheim, Germany, 1999.
 - [44] J. Feng, S. Yang, J. Liang et al., "Methane seepage inferred from the porewater geochemistry of shallow sediments in the Beikang Basin of the southern South China Sea," *Journal of Asian Earth Sciences*, vol. 168, pp. 77–86, 2018.
 - [45] T. Yang, S. Y. Jiang, J. H. Yang et al., "Dissolved inorganic carbon (DIC) and its carbon isotopic composition in sediment pore waters from the Shenhu area, northern South China Sea," *Journal of Oceanography*, vol. 64, no. 2, pp. 303–310, 2008.
 - [46] H. D. Schulz, "Quantification of early diagenesis: dissolved constituents in pore water and signals in the solid phase," in *Marine Geochemistry*, H. D. Schulz and M. Zabel, Eds., pp. 73–124, Springer, Berlin, Germany, 2006.
 - [47] B. P. Boudreau, *Diagenetic Models and Their Implementation: Modelling Transport and Reactions in Aquatic Sediments*, Springer-Verlag, Berlin, 1997.
 - [48] K. Wallmann, G. Aloisi, M. Haeckel, A. Obzhairov, G. Pavlova, and P. Tishchenko, "Kinetics of organic matter degradation, microbial methane generation, and gas hydrate formation in anoxic marine sediments," *Geochimica et Cosmochimica Acta*, vol. 70, no. 15, pp. 3905–3927, 2006.
 - [49] P. C. Chuang, A. W. Dale, K. Wallmann et al., "Relating sulfate and methane dynamics to geology: accretionary prism offshore SW Taiwan," *Geochemistry, Geophysics, Geosystems*, vol. 14, no. 7, pp. 2523–2545, 2013.
 - [50] M. Luo, A. W. Dale, K. Wallmann et al., "Estimating the time of pockmark formation in the SW Xisha Uplift (South China Sea) using reaction-transport modeling," *Marine Geology*, vol. 364, pp. 21–31, 2015.
 - [51] M. Luo, A. W. Dale, L. Haffert et al., "A quantitative assessment of methane cycling in Hikurangi Margin sediments

- (New Zealand) using geophysical imaging and biogeochemical modeling,” *Geochemistry, Geophysics, Geosystems*, vol. 17, no. 12, pp. 4817–4835, 2016.
- [52] Z. Duan, N. Møller, J. Greenberg, and J. H. Weare, “The prediction of methane solubility in natural waters to high ionic strength from 0 to 250 °C and from 0 to 1600 bar,” *Geochimica et Cosmochimica Acta*, vol. 56, no. 4, pp. 1451–1460, 1992.
- [53] J. J. Middelburg, “A simple rate model for organic matter decomposition in marine sediments,” *Geochimica et Cosmochimica Acta*, vol. 53, no. 7, pp. 1577–1581, 1989.
- [54] M. J. Whiticar, E. Faber, and M. Schoell, “Biogenic methane formation in marine and freshwater environments: CO₂ reduction vs. acetate fermentation—isotope evidence,” *Geochimica et Cosmochimica Acta*, vol. 50, no. 5, pp. 693–709, 1986.
- [55] E. A. Solomon, A. J. Spivack, M. Kastner, M. E. Torres, and G. Robertson, “Gas hydrate distribution and carbon sequestration through coupled microbial methanogenesis and silicate weathering in the Krishna-Godavari Basin, offshore India,” *Marine and Petroleum Geology*, vol. 58, pp. 233–253, 2014.
- [56] F. J. Millero, “Thermodynamics of the carbon dioxide system in the oceans,” *Geochimica et Cosmochimica Acta*, vol. 59, no. 4, pp. 661–677, 1995.
- [57] R. E. Zeebe and D. A. Wolf-Gladrow, *CO₂ in Seawater: Equilibrium, Kinetics and Isotopes*, Elsevier, U. K., 2001.
- [58] P. Tishchenko, C. Hensen, K. Wallmann, and C. S. Wong, “Calculation of the stability and solubility of methane hydrate in seawater,” *Chemical Geology*, vol. 219, no. 1–4, pp. 37–52, 2005.
- [59] C. Niewohner, C. Hensen, S. Kasten, M. Zabel, and H. D. Schulz, “Deep sulfate reduction completely mediated by anaerobic methane oxidation in sediments of the upwelling area off Namibia,” *Geochimica et Cosmochimica Acta*, vol. 62, no. 3, pp. 455–464, 1998.
- [60] M. Zabel and H. D. Schulz, “Importance of submarine landslides for non-steady state conditions in pore water systems — lower Zaire (Congo) deep-sea fan,” *Marine Geology*, vol. 176, no. 1–4, pp. 87–99, 2001.
- [61] M. Schmidt, C. Hensen, T. Mörz et al., “Methane hydrate accumulation in “Mound 11” mud volcano, Costa Rica forearc,” *Marine Geology*, vol. 216, no. 1–2, pp. 83–100, 2005.
- [62] T. Tréude, J. Niggemann, J. Kallmeyer et al., “Anaerobic oxidation of methane and sulfate reduction along the Chilean continental margin,” *Geochimica et Cosmochimica Acta*, vol. 69, no. 11, pp. 2767–2779, 2005.
- [63] M. Kastner, G. Claypool, and G. Robertson, “Geochemical constraints on the origin of the pore fluids and gas hydrate distribution at Atwater Valley and Keathley canyon, northern Gulf of Mexico,” *Marine and Petroleum Geology*, vol. 25, no. 9, pp. 860–872, 2008.
- [64] W. L. Hong, E. A. Solomon, and M. E. Torres, “A kinetic-model approach to quantify the effect of mass transport deposits on pore water profiles in the Krishna–Godavari Basin, Bay of Bengal,” *Marine and Petroleum Geology*, vol. 58, pp. 223–232, 2014.
- [65] R. C. Aller and J. Y. Aller, “Meiofauna and solute transport in marine muds,” *Limnology and Oceanography*, vol. 37, no. 5, pp. 1018–1033, 1992.
- [66] C. Meile, C. M. Koretsky, and P. V. Cappellen, “Quantifying bioirrigation in aquatic sediments: an inverse modeling approach,” *Limnology and Oceanography*, vol. 46, no. 1, pp. 164–177, 2001.
- [67] S. Yuan, S. Wu, T. Lüdmann et al., “Fine-grained Pleistocene deepwater turbidite channel system on the slope of Qiongdongnan Basin, northern South China Sea,” *Marine and Petroleum Geology*, vol. 26, no. 8, pp. 1441–1451, 2009.
- [68] R. Passega, “Grain size representation by CM patterns as a geologic tool,” *Journal of Sedimentary Petrology*, vol. 34, no. 4, pp. 830–847, 1964.
- [69] J. Schönfeld and H. R. Kudrass, “Hemipelagic sediment accumulation rates in the South China Sea related to late Quaternary sea-level changes,” *Quaternary Research*, vol. 40, no. 3, pp. 368–379, 1993.
- [70] J. Qian, *Paleoceanography for the Late Quaternary in the South China Sea*, China Science Press, Beijing, 1999, (in Chinese).
- [71] Y. Hu, L. Chen, D. Feng, Q. Liang, Z. Xia, and D. Chen, “Geochemical record of methane seepage in authigenic carbonates and surrounding host sediments: a case study from the South China Sea,” *Journal of Asian Earth Sciences*, vol. 138, pp. 51–61, 2017.
- [72] Y. Xu, L. Liu, H. Zhou et al., “Submarine landslide identified in DLW3102 core of the northern continental slope, South China Sea,” *Journal of Ocean University of China*, vol. 17, no. 1, pp. 147–155, 2018.
- [73] J. H. Kim, M. E. Torres, J. Choi, J. J. Bahk, M. H. Park, and W. L. Hong, “Inferences on gas transport based on molecular and isotopic signatures of gases at acoustic chimneys and background sites in the Ulleung Basin,” *Organic Geochemistry*, vol. 43, pp. 26–38, 2012.
- [74] K. Nöthen and S. Kasten, “Reconstructing changes in seep activity by means of pore water and solid phase Sr/Ca and Mg/Ca ratios in pockmark sediments of the northern Congo Fan,” *Marine Geology*, vol. 287, no. 1–4, pp. 1–13, 2011.
- [75] A. Mazumdar, P. Dewangan, H. M. João et al., “Evidence of paleo-cold seep activity from the Bay of Bengal, offshore India,” *Geochemistry, Geophysics, Geosystems*, vol. 10, no. 6, 2009.
- [76] Y. C. Lim, S. Lin, T. F. Yang, Y. G. Chen, and C. S. Liu, “Variations of methane induced pyrite formation in the accretionary wedge sediments offshore southwestern Taiwan,” *Marine and Petroleum Geology*, vol. 28, no. 10, pp. 1829–1837, 2011.
- [77] L. M. Wehrmann, S. P. Templer, B. Brunner, S. M. Bernasconi, L. Maignien, and T. G. Ferdelman, “The imprint of methane seepage on the geochemical record and early diagenetic processes in cold-water coral mounds on Pen Duick Escarpment, Gulf of Cadiz,” *Marine Geology*, vol. 282, no. 1–2, pp. 118–137, 2011.
- [78] S. Chatterjee, G. R. Dickens, G. Bhatnagar et al., “Pore water sulfate, alkalinity, and carbon isotope profiles in shallow sediment above marine gas hydrate systems: a numerical modeling perspective,” *Journal of Geophysical Research*, vol. 116, no. B9, 2011.
- [79] M. Luo, L. Chen, S. Wang, W. Yan, H. Wang, and D. Chen, “Pockmark activity inferred from pore water geochemistry in shallow sediments of the pockmark field in southwestern Xisha Uplift, northwestern South China Sea,” *Marine and Petroleum Geology*, vol. 48, pp. 247–259, 2013.
- [80] M. J. Whiticar, “Carbon and hydrogen isotope systematics of bacterial formation and oxidation of methane,” *Chemical Geology*, vol. 161, no. 1–3, pp. 291–314, 1999.

- [81] W. M. Sackett, "Carbon and hydrogen isotope effects during the thermocatalytic production of hydrocarbons in laboratory simulation experiments," *Geochimica et Cosmochimica Acta*, vol. 42, no. 6, pp. 571–580, 1978.
- [82] W. S. Borowski, N. Cagatay, Y. Ternois, and C. K. Paull, "Data report: carbon isotopic composition of dissolved CO₂, CO₂ gas, and methane, Blake-Bahama Ridge and northeast Bermuda Rise, ODP Leg 172," in *Proceedings of the Ocean Drilling Program, 172 Scientific Results*, L. D. Keigwin, D. Rio, G. D. Acton, and E. Arnold, Eds., pp. 1–16, ODP Publications, 2000.
- [83] Y. Chen, W. Ussler III, H. Haflidason et al., "Sources of methane inferred from pore-water $\delta^{13}\text{C}$ of dissolved inorganic carbon in pockmark G11, offshore Mid-Norway," *Chemical Geology*, vol. 275, no. 3–4, pp. 127–138, 2010.
- [84] Y. Hu, M. Luo, L. Chen et al., "Methane source linked to gas hydrate system at hydrate drilling areas of the South China Sea: porewater geochemistry and numerical model constraints," *Journal of Asian Earth Sciences*, vol. 168, pp. 87–95, 2018.
- [85] F. Chen, J. Chen, H. Jin, and H. Li, "Correlation of $\delta^{13}\text{C}$ origin surface sediments with sinking particulate matter in South China Sea and implication for reconstructing paleo- environment," *Acta Sedimentology Sinica*, vol. 30, pp. 340–345, 2012.
- [86] X. Hu and D. J. Burdige, "Enriched stable carbon isotopes in the pore waters of carbonate sediments dominated by seagrasses: evidence for coupled carbonate dissolution and reprecipitation," *Geochimica et Cosmochimica Acta*, vol. 71, no. 1, pp. 129–144, 2007.
- [87] X. Hu, W. J. Cai, Y. Wang, S. Luo, and X. Guo, "Pore-water geochemistry of two contrasting brine-charged seep sites in the northern Gulf of Mexico continental slope," *Marine Chemistry*, vol. 118, no. 3–4, pp. 99–107, 2010.
- [88] G. E. Claypool and K. A. Kvenvolden, "Methane and other hydrocarbon gases in marine sediment," *Annual Review of Earth and Planetary Sciences*, vol. 11, no. 1, pp. 299–327, 1983.
- [89] Q. Liang, S. Yang, J. Liang, and J. Tao, "The submarine seepage features of Haima cold seeps in the western part of the northern slope of the South China Sea," in *The 3rd Seafloor Observation Symposium*, Qingdao, October 2016.
- [90] H. Guan, D. Birgel, J. Peckmann et al., "Lipid biomarker patterns of authigenic carbonates reveal fluid composition and seepage intensity at Haima cold seeps, South China Sea," *Journal of Asian Earth Sciences*, vol. 168, pp. 163–172, 2018.

Research Article

Magmatic Signature in Submarine Hydrothermal Fluids Vented Offshore Ventotene and Zannone Islands (Pontine Archipelago, Central Italy)

Francesco Italiano,¹ Davide Romano ^{1,2} Cinzia Caruso,¹ Manfredi Longo ¹,
Andrea Corbo,¹ and Gianluca Lazzaro¹

¹Istituto Nazionale di Geofisica e Vulcanologia, Palermo 90146, Italy

²Dipartimento di Scienze Matematiche e Informatiche, Scienze Fisiche e Scienze della Terra (MIFT), Università di Messina, Messina 98166, Italy

Correspondence should be addressed to Davide Romano; dromano@unime.it

Received 15 March 2019; Revised 28 May 2019; Accepted 23 June 2019; Published 22 July 2019

Academic Editor: Andrea Brogi

Copyright © 2019 Francesco Italiano et al. This is an open access article distributed under the Creative Commons Attribution License, which permits unrestricted use, distribution, and reproduction in any medium, provided the original work is properly cited.

Geochemical investigations carried out on submarine hydrothermal fluids vented offshore the Pontine Islands (Tyrrhenian Sea) revealed the existence of gas vents to the W of Zannone Island and SW of Ventotene Island. The geochemical features of the CO₂-rich gas samples show a clear mantle-derived signature with ³He/⁴He of 3.72-3.75 Ra and 1.33 Ra at Zannone and Ventotene, respectively. Gas geochemistry denotes how CO₂-rich gases undergo fractionation processes due to CO₂ dissolution to a variable extent favoring enrichment in the less soluble gas species, i.e., CH₄, N₂, and He. The carbon isotope composition of CO₂, expressed as δ¹³C vs. V-PDB, ranges from -0.71 and -6.16‰ at Zannone to 1.93‰ at Ventotene. Preliminary geothermometric and geobarometric estimations indicate equilibrium temperatures in the range of 150-200°C at Zannone and >200°C at Ventotene besides H₂O pressures in the range of 5 bar and 20 bar at Zannone and Ventotene, respectively. Although the latest volcanic activity at the Pontine Archipelago is dated Middle Pleistocene, the combination of the new geochemical information along with geothermometric estimations indicates that cooling magmas are likely releasing enough thermal energy to form an efficient hydrothermal system.

1. Introduction

The Central Mediterranean Sea and the Italian Peninsula have been affected by intense Neogene and Quaternary Volcanism. In this sector, the geodynamic processes, framed in the Alpine Orogeny, are expressed by the subduction of the Adriatic microplate under the Eurasian plate and by the opening of the Tyrrhenian back-arc basin [1–4]. These different processes had a prominent role in the genesis, evolution, and migration of partial melts [5–12]. The igneous activity of the Tyrrhenian Sea and its eastern margin triggers the development of several geothermal systems. Hydrothermal fields in the Southern Tyrrhenian Sea are present around seamounts [13–15], in the Aeolian Archipelago [16–19], in front of Capo Vaticano [20, 21], along the coast of Ischia Island

[17], and in the Bay of Naples [22, 23]. All these zones are characterized by CO₂-rich emissions and are commonly associated with the occurrence of magmatic bodies underneath the seafloor. It is accepted that seeping processes are driven by active tectonic lineaments able to control the emission rates and likely responsible for past explosive events [24]. Geochemical features of the thermal fluids provide important information on both the current status of cooling magma batches intruding the upper crust and interaction processes taking place between rising fluids and hosting rocks.

The Pontine Archipelago hosts some examples of submarine geothermal systems connected to a quiescent magmatic activity. The Plio-Pleistocene volcanic rocks from the Pontine Island Volcanoes have a hybrid geochemical

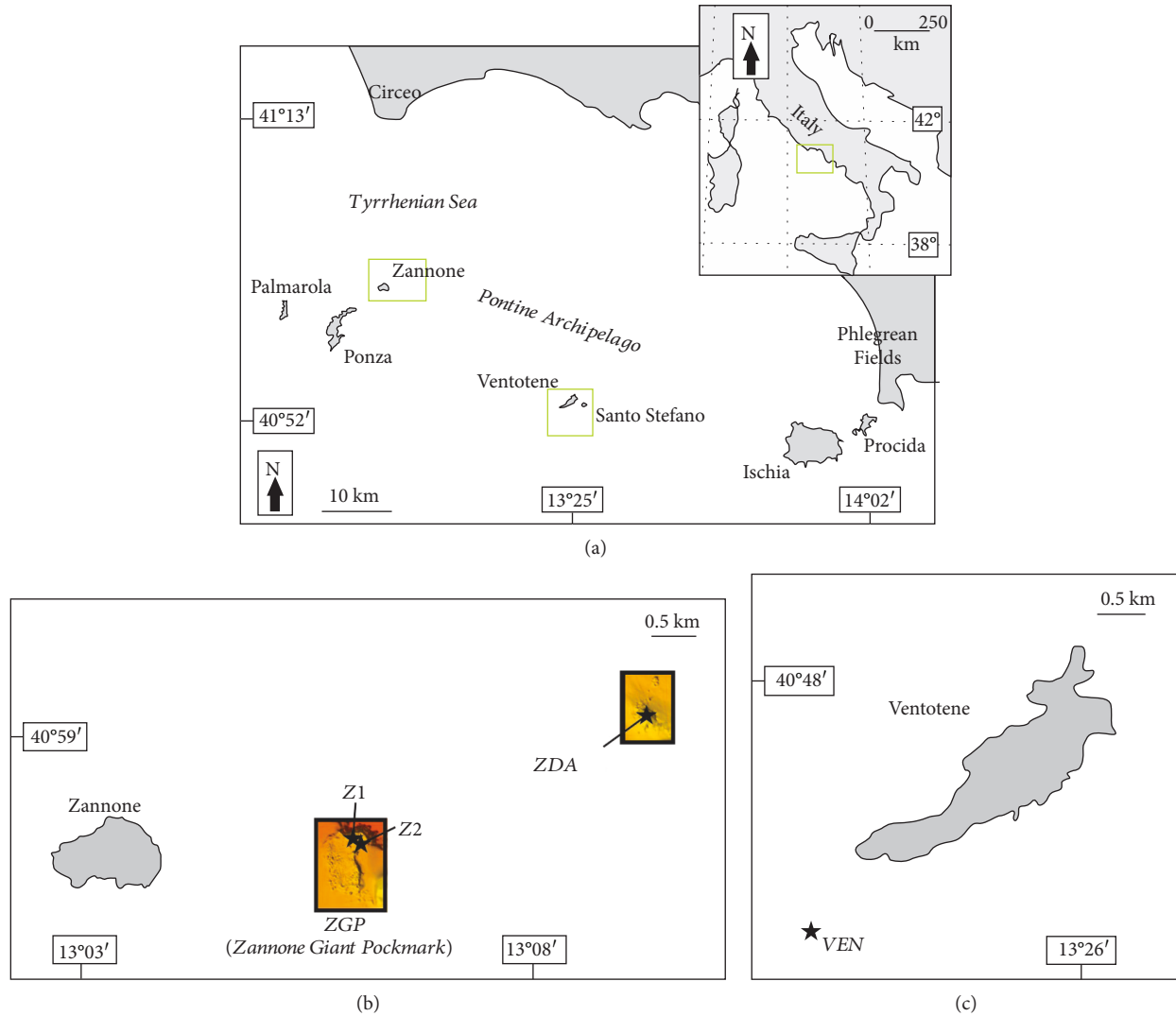


FIGURE 1: (a) Sketch map of the central Tyrrhenian margin with the location of the areas investigated; (b) location map of the Zannone studied sites (after Martorelli et al. [27]). See Ingrassia et al. [26] and Martorelli et al. [27] for further information; (c) location map of the VEN site lying south to the island of Ventotene.

composition showing island arc and OIB signatures ([9] and references therein). Cadoux et al. [25] pointed out that Pontine Volcanism switched from orogenic magmas emplaced in a syn- to late-collisional context to transitional-type magmas emplaced in a late- to post-collisional stage. The current status of the Pontine Island Volcanism is only expressed by a persistent submarine hydrothermal activity. Several wide and depressed hydrothermal areas have recently been discovered offshore the island of Zannone during morphobathymetric investigations [26, 27] and to the SW of the Ventotene coast during deep diving activity. The hydrothermal activity takes place mainly along NE-SW- and NW-SE-oriented tectonic structures, dissecting the Latium and Campanian continental margins in structural highs (e.g., Ponza-Zannone high) and deep sedimentary basins (e.g., Ventotene and Palmarola basins).

Starting from the first constraints provided by the geochemical features of the hydrothermal fluids collected off-

shore the Zannone Island during the “Bolle” cruise in 2014, further investigations were carried out by the oceanographic cruise in 2017 with the aim of obtaining useful insights on the submarine hydrothermal systems of the Pontine Islands.

This paper describes and discusses the geochemical features of the submarine hydrothermal fluids discharged offshore the Zannone and Ventotene islands focusing on the geochemical features of the vented gases. The results show how thermal energy of magmatic origin is still available over the archipelago providing significant perspectives for geothermal energy exploration.

2. Geovolcanological and Hydrothermal Settings

The Pontine Archipelago is located in the Central Tyrrhenian Sea, less than 30 km to the west of the Italian coast, and is composed of five major islands, from NW to SE: Palmarola,

Ponza, Zannone, Ventotene, and Santo Stefano (Figure 1(a)). The volcanic rocks are emplaced over a metamorphic basement overlaid by a Meso-Cenozoic sedimentary succession made up of Late Triassic to Eocene clays, dolostones, limestones, and marls, followed by Miocene flysch deposits [28, 29]. Over the whole archipelago, the prevolcanic substratum only crops out in the northeastern side of Zannone Island [29]. The compressive stress regime has driven the development of a north to northeast verging fold-thrust belt made of a pile of nappes [28]. Starting from the Plio-Pleistocene age, the Alpine belt underwent an extensional deformation [1, 30–32], which has alternatively been interpreted as either a back-arc extension related to an ongoing subduction [33] or as a consequence of a hot asthenosphere flow resulting from the cessation of Adriatic plate subduction [34] or as a divergent plate boundary [35].

The archipelago consists of two different sectors: the northwestern (including Ponza, Palmarola, and Zannone Islands) and the southeastern (including Ventotene and Santo Stefano Islands). The volcanic rocks from the northwestern group display several differences in terms of age and composition in contrast to the rocks forming the southeastern group. Ponza, Palmarola, and Zannone are characterized by the emplacement of calc-alkaline and peralkaline rhyolites showing an age of 4.2 to 1.5 Ma [25]. Only the island of Ponza exhibits a 1.0 Ma old trachytic episode [25, 36–38]. The Pleistocene trachytes are K-alkaline in composition and show a close similarity to the Campanian and Ernici-Roccamonfina products [8, 9, 25, 37]. Paone [39] suggested that calc-alkaline and peralkaline rhyolites were originated from partial melting of a mafic lower crust. On the contrary, Conte et al. [40] indicated that they were derived by fractional crystallization processes of basic orogenic magmas derived from a metasomatised mantle source. The volcanic products include lava flows, domes, and hydromagmatic tuffs.

During the Middle Pleistocene, the volcanic activity shifted eastward to the Ventotene-Santo Stefano area. The development of the two edifices was accompanied by a compositional change. They are indeed mainly represented by basalts and trachybasalts, with minor quantities of shoshonites, latites, and phonolites [9]. They show an age of 0.8–0.13 Ma [41, 42] and are made of lava flows, domes, and pyroclastic materials as fallout, flow, and surge deposits. Pyroclastics are characterized by the presence of sialic, mafic, and ultramafic xenoliths [43].

Submarine hydrothermal systems were recently identified off the islands of Zannone and Ventotene. Off the coast of Zannone, active venting of hydrothermal fluids is located in the northwestern and in the eastern sectors of the insular shelf (Figure 1(b)). Their spatial distribution suggests an active role of the NE-SW-oriented faults affecting the Tyrrhenian offshore of the Latium and Campanian regions. The hydrothermal fields are large depressions up to 10–15 m deep, lying between 110 and 150 m water depth marked by an NNW-SSE elongated shape interpreted as the coalescence of craters connected to explosive events [26]. The depressions developed on sandy wedges considered as low-stand deposits are topped by a thin layer made of mud-sand deposits of the

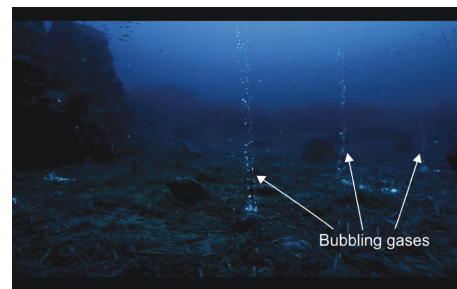


FIGURE 2: Bubbling gases and white patches associated with warm waters vented off Ventotene Island. The hydrothermal fluids occur on a flat area, in water depth varying from 80 to 85 m.

TABLE 1: Location and information of the collected samples. The coordinate reference system is UTM WGS84 zone 33 N.

Site	Locality	Date	Depth (m)	North	East
Z1	Zannone	Feb 2017	134	4537446	340310
Z2	Zannone	Feb 2017	127	4537416	340409
ZDA	Zannone	Feb 2017	147	4539421	345021
VEN	Ventotene	Aug 2018	80	4515668	365025

Holocene age. The hydrothermal fluids are vented all over the depressions and consist of both bubbling gas and thermal water discharges.

An unknown hydrothermal area was discovered off the southwestern coast of Ventotene at a depth of 80 m by diving activity (Figure 1(c)), revealing the presence of bubbling gases. The area was characterized by the presence of warm waters seeping through the seafloor as shown by white patches of bacterial mats made of sulfur precipitates, as well as by several mounds and cones covered by hydrothermal oxides and sulphides (Figure 2). The volcanic rocks outcropping at the seafloor consist of a porphyritic volcanic rock with olivine and pyroxene phenocrysts set in an altered groundmass (Di Bella M., personal communication).

3. Sampling and Analytical Methods

During the 2017 cruise, three vertical casts for water column profiles were carried out using a rosette equipped with a CTD (Conductivity Temperature Depth) and Niskin bottles. Locations and coordinates (UTM-WGS84) of the sites studied are listed in Table 1 and plotted in Figure 1. Fourteen marine water samples were collected from different depths and at the sea bottom (see Tables 1 and 2) for geochemical analyses of the circulating waters and the dissolved gases. Two thermal water samples were collected using a Remote Operated Vehicle (ROV) by a syringe operated by the ROV arm, by inserting a syringe directly into the vent and sucking the water. The temperature at the seafloor was measured using a customized INGV waterproof smart temperature sensor, built to directly operate inside the hydrothermal vents up to a depth of 600 m. The water samples were collected in triplicate and stored as “as is

TABLE 2: Chemical analyses of the water samples. Concentrations in mg/l. Local seawater composition is reported for comparison.

Sample ID	Site	Depth (m)	Type	Sampling method	T (°C)	pH	EC (mS/cm)	Li	Na	K	Mg	Ca	F	Cl	Br	SO ₄	HCO ₃
2	Z1	50	Water column	Niskin	14.5	8.19	45.95	bdl	12189	453	1439	471	bdl	22036	bdl	3118	171
5	Z1	134	Water column	Niskin	14.4	8.04	45.86	bdl	12488	484	1492	503	bdl	21775	bdl	3032	189
9	Z2	127	Water column	Niskin	14.4	8.19	45.84	bdl	12471	486	1487	489	bdl	21874	bdl	2865	189
13	ZDA	120	Water column	Niskin	14.3	8.22	45.78	bdl	12189	476	1454	482	bdl	21904	bdl	2950	171
14	ZDA	147	Water column	Niskin	14.3	8.19	45.78	bdl	12482	481	1479	492	bdl	21977	bdl	2964	171
15	Z2	124	Thermal waters	ROV	60	n.a.	n.a.	bdl	12234	457	1443	465	bdl	22705	bdl	3165	n.a.
16	ZDA	145	Thermal waters	ROV	56	n.a.	n.a.	bdl	12210	450	1438	476	bdl	22302	bdl	3121	n.a.
<i>Seawater</i>						8.15		0.17	10468	348	1331	411	1.3	18952	65	2648	135

n.a. = not analyzed. bdl = below detection limits (detection limits for Li = $2.12E-02$; F = $4.78E-02$; Br = $1.91E-01$).

sample” (i.e., not filtered and not acidified), filtered ($0.45\ \mu\text{m}$ filter), and “filtered and acidified” (HNO_3 Suprapur-grade acid). The samples for dissolved gas analysis were collected directly from the Niskin bottles and stored in 240 ml glass serum-type bottles sealed in the field by silicon/rubber septa using special pliers. All the samples were collected to avoid even the tiniest bubbles to prevent atmospheric contamination and stored on-board upside-down with the necks immersed in water.

The vented gases were collected by Remote Operated Vehicles (ROV) at Zannone and by diving at Ventotene. The gases offshore Zannone areas were collected in 2014 [27] and in 2017 (this work) using a ROV equipped with a gas sampling system made up of four small funnels connected to 240 ml serum-type bottles. The system was fitted to the front of the ROV with the inverted funnels slipped inside the bottle necks (Figure 3). The ROV pilot placed the system over a gas vent, and the funnel allowed the gas bubbles to be driven into the bottle, where the gas accumulated displacing the seawater out of the bottle. At the end of the dive, when the ROV was back to the surface, an operator sealed the bottles with a gas-tight cap when they were still underwater operating on board of a rubber boat. All the samples collected in the serum-type bottles were stored upside-down with the necks submerged in seawater to minimize gas exchanges with the atmosphere through the cap before undergoing laboratory analysis [44]. A deep-sea dive was carried out in August 2018 off the SW Ventotene coast (Figure 1 and Table 1) to collect the bubbling gases directly from the emission points at the seafloor using an inverted funnel connected to two-way glass bottles. The equipment was filled by marine water to avoid any atmospheric contamination; then, the funnel was placed over the venting gas, and the gas sample was collected by water displacement.

One gas sample from Ventotene and two gas samples from Zannone were analyzed.



FIGURE 3: Sampling system for the bubbling gases off Zannone (depth in the range of 120-150 m bsl). The ROV was equipped with a homemade sampling system composed of four small funnels connected to 240 ml serum-type bottles. The system, fitted to the front of the ROV, allows to collect bubbles by placing the funnel on the venting gases (see text for more information).

The chemical and isotope analysis of dissolved and bubbling gases as well as of the collected waters was carried out at the geochemical laboratories of INGV-Palermo. $T^\circ\text{C}$, pH, and electrical conductivity EC in all the marine water samples were determined by on-board measurements. The pH and EC were measured by electronic instruments calibrated in situ using buffer solutions. In the laboratory, the chemical analysis of the major and minor ions was carried out by ion chromatography (Dionex ICS-1100) on both filtered ($0.45\ \mu\text{m}$), acidified (100 ml HNO_3 Suprapur) water samples (Na, K, Mg, and Ca), as well as on untreated samples (F, Cl, Br, and SO_4). The HCO_3 concentration was determined by standard titration procedures with hydrochloric acid.

The chemical composition of the dissolved and bubbling gases was determined by gas chromatography (GC) using an Agilent equipped with a double TCD-FID detector and argon as carrier gas. Typical analytical uncertainties were within $\pm 5\%$. The bubbling gas samples had been admitted to the GC by a syringe, while the dissolved gases were extracted from the 240 ml water samples after equilibration at constant temperature with a host gas (high-purity argon) injected into the sample bottle through the rubber septum (for further details see [45, 46]).

The He-isotope ratio in the bubbling gases was analyzed by the injection of the gas to the purification line directly from the sample bottles. The isotope composition of dissolved He was analyzed by headspace equilibration, following the method proposed by Italiano et al. [46]. After purification in the high vacuum, He and Ne were then cryogenically separated and admitted into mass spectrometers. The $^3\text{He}/^4\text{He}$ ratio was determined by a GVI Helix SFT static vacuum mass spectrometer. The $^4\text{He}/^{20}\text{Ne}$ ratio was evaluated by peak intensities on the same Helix SFT mass spectrometer. Helium isotope composition is expressed as R/R_A , namely, $^3\text{He}/^4\text{He}$ of the sample versus the atmospheric $^3\text{He}/^4\text{He}$ ($R_A = 1.386 \times 10^{-6}$). Some values were corrected for the atmospheric contamination of the sample (R_C/R_A) on the basis of the $^4\text{He}/^{20}\text{Ne}$ ratio [47]. Typical uncertainties in the range of low ^3He samples are within $\pm 5\%$.

The carbon isotope composition of CO_2 ($\delta^{13}\text{C}$) of the bubbling gases was analyzed by a Delta Plus XP IRMS equipped with a Thermo TRACE GC interfaced with Thermo GC/C III. The Thermo TRACE gas chromatograph was equipped with a Poraplot-Q column ($30\text{ m} \times 0.32\text{ mm}$ i.d.), and the oven was held at a constant temperature of 50°C with the flow rate of carrier gas (He 5.6 grade) kept at a constant flux of 0.8 cc/min .

$\delta^{13}\text{C}$ values of the total dissolved carbon ($\delta^{13}\text{C}_{\text{TDC}}$) were measured on 0.2 ml of water sample introduced in bottles where high-purity helium was injected to remove atmospheric CO_2 (Thermo Scientific GasBench II). The device consists of an autosampler tray kept in a thermostatic rack. $150\text{--}200\text{ }\mu\text{l}$ of 100% H_3PO_4 was automatically injected into the vials kept at 70°C for 18 h . Then, the temperature of the thermostatic rack was lowered to 25°C , and the carbon isotope composition of CO_2 produced by acidification was analyzed by a Thermo Scientific Delta V Advantage continuous flow mass spectrometer coupled with Thermo Scientific GasBench II. The results are reported as $\delta^{13}\text{C}\text{‰}$ vs. V-PDB (Vienna-Pee Dee Belemnite) standard; standard deviation of the $^{13}\text{C}/^{12}\text{C}$ ratio was $\pm 0.15\text{‰}$.

4. Results

The analytical results including chemical isotopic ratios of helium, carbon, and $^4\text{He}/^{20}\text{Ne}$ are listed in Tables 2, 3, and 4. Data for local seawater composition are reported as a reference. The hot waters discharged by hydrothermal vents at Zannone show an outlet temperature up to 60°C . The concentration of the major ions (Na^+ , K^+ , Mg^{2+} , Ca^{2+} , Cl^- , SO_4^{2-} , and HCO_3^-) is particularly high with respect to those of local seawater (Table 2), and Cl is the dominant

anion in all samples, with a concentration approximately higher by 10% than seawater.

The composition of the dissolved gases from offshore Zannone is listed in Table 3 and expressed in ccSTP/L (cm^3 at Standard Temperature and Pressure per liter of seawater). The concentrations of dissolved CO_2 , CH_4 , and CO are orders of magnitude higher than those in the ASSW (air-saturated seawater).

Bubbling gases from the submarine gas vents of Zannone and Ventotene show a dominance of CO_2 with concentrations above 90% by vol (Table 3). The typical atmospheric species O_2 and N_2 display low values: O_2 in the range of 0.16% vol at both localities, whereas the N_2 content increases from 1.4% at Ventotene to 3.4% at Zannone. The CH_4 concentration is below 1% .

The $^3\text{He}/^4\text{He}$ isotope ratios in the dissolved gases show values similar to those of atmospheric air ($^3\text{He}/^4\text{He} = 1.386 \times 10^{-6}$). The $^4\text{He}/^{20}\text{Ne}$ ratio (Table 4) shows a slight deviation from 0.283 which is assumed to be representative for $^4\text{He}/^{20}\text{Ne}$ in ASSW [48]. The $^4\text{He}/^{20}\text{Ne}$ ratio of the bubbling gases is above 25 indicating low atmospheric contamination, whereas the R/R_A ($^3\text{He}/^4\text{He}$ of the sample versus the atmospheric $^3\text{He}/^4\text{He}$) ratio increases from 1.33 Ra at Ventotene (sample #19) to $3.72\text{--}3.75\text{ Ra}$ at Zannone (samples #17 and 18).

The $\delta^{13}\text{C}_{\text{CO}_2}$ values for the bubbling gases from Zannone are -0.71 and -6.16‰ (samples #17 and 18), while those of $\delta^{13}\text{C}_{\text{TDC}}$ determined in the dissolved gases ranges between -0.35‰ and -1.51‰ (Table 4). In contrast, the bubbling gases from Ventotene (sample #19) display a positive $\delta^{13}\text{C}_{\text{CO}_2}$ value (1.93‰). In this study, the carbon isotope composition of methane was determined in the bubbling gases from Zannone (samples #17 and 18) only, and the recorded values are -45.5 and -44.2‰ (Table 4).

5. Discussion

5.1. Marine and Thermal Waters. The scenario of the hydrothermal fluids vented at the Pontine Island seafloor is very similar in terms of deposits, gas bubbles, and thermal waters seepage to that of the submarine environment of the Aeolian Islands and other hydrothermal systems of the Mediterranean area. As shown by the analytical results, the geochemical features of the waters and gases collected off Zannone and Ventotene are also very similar to those taken off the Greek Islands (e.g., Milos and Kos [49–51]) and the Aeolian Islands (e.g., Panarea [52]).

As already observed, for the thermal waters vented off Panarea Island [52], the water samples from Zannone are enriched in anions and cations with respect to those of the local seawater (Table 2). The distribution of samples in the Na vs. Cl and Na+K vs. Ca diagrams (Figures 4(a) and 4(b)) suggests the existence of a “concentrated seawater,” likely related to boiling of seawater heated by the ascending hot gases. The release of calcium and potassium from host rocks, and the consequent concentration increase of those cations into the thermal waters with respect to the local seawater, can be explained by exchange reactions enhanced by H^+ from the acidic volcanic fluids. As an example, a reaction

TABLE 3: Chemical composition of the dissolved (D) and bubbling gases (B).

Sample ID	Site	Depth (m)	Type	Sampling method	He	H ₂	O ₂	N ₂	CO	CH ₄	CO ₂
1	Z1	20	D	Niskin	bdl	bdl	3.53	9.24	2.69E-05	3.1E-04	0.46
2	Z1	50	D	Niskin	bdl	bdl	3.36	9.66	2.69E-05	3.8E-04	0.48
3	Z1	80	D	Niskin	bdl	1.53E-04	3.79	9.40	2.15E-05	3.8E-04	0.46
4	Z1	100	D	Niskin	bdl	bdl	3.79	9.82	2.85E-05	4.7E-04	0.64
5	Z1	134	D	Niskin	bdl	1.87E-04	3.56	6.66	2.07E-05	3.7E-04	0.53
6	Z2	50	D	Niskin	bdl	bdl	3.74	9.56	1.71E-05	4.7E-04	0.42
7	Z2	80	D	Niskin	bdl	bdl	3.63	9.37	2.85E-05	4.0E-04	0.45
8	Z2	100	D	Niskin	bdl	bdl	4.38	9.49	bdl	3.0E-04	0.42
9	Z2	127	D	Niskin	bdl	bdl	3.55	9.81	2.69E-05	4.6E-04	0.64
10	ZDA	50	D	Niskin	bdl	1.68E-03	4.16	8.06	bdl	6E-05	0.41
11	ZDA	80	D	Niskin	bdl	6.28E-04	4.43	8.93	bdl	1.22E-04	0.43
12	ZDA	100	D	Niskin	bdl	bdl	2.61	6.50	9.11E-05	2.9E-04	0.41
13	ZDA	120	D	Niskin	bdl	1.73E-04	4.62	9.10	3.98E-05	1.5E-04	0.78
14	ZDA	147	D	Niskin	bdl	bdl	4.83	9.84	2.27E-05	4.9E-04	0.73
	ASSW				4.80E-05		4.80	9.60		1.0E-6	0.24
17	Z2	127	B	ROV	3.12E-03	1.19E-02	0.016	3.410	3.7E-05	0.985	94.62
17 Rec	Z2	127	B	ROV	3.12E-03	1.19E-02	—	3.353	3.7E-05	0.986	94.68
18	Z2	125	B	ROV	5.63E-02	1E-03	15.26	77.57	2.2E-04	9	0.145
18 Rec	Z2	125	B	ROV	1.85E-01	3.28E-03	—	69.31	7.22E-04	29	0.475
19	VEN	80	B	Two-way glass bottle	4.6E-04	bdl	0.18	1.37	1.82E-04	0.163	98.17
11-BT1*	ZGP	129	B	ROV	7.9E-03	7.0E-04			1.9E-04	2.6E-04	50.94
12-BT1*	ZGP	129	B	ROV	8.2E-03	9.0E-04			1.3E-04	2.6E-04	55.08
13-BT4*	ZGP	127	B	ROV	5.8E-03	bdl			1.9E-04	1.9E-04	54.22

Dissolved gas concentrations are given in ccSTP per liter of seawater. Bubbling gas composition is expressed in vol%. Values for ASSW (air-saturated seawaters) are reported as reference. bdl = below detection limits (detection limits for He, H₂, and CO in the dissolved gases = 5E-06 ccSTP; detection limits for He and H₂ in the bubbling gases = 2E-06). Rec = recalculated concentrations; see text for details. * Reactive gases and labels after Martorelli et al. [27].

TABLE 4: Helium and carbon isotopic composition of the dissolved (D) and bubbling gases (B). The ³He/⁴He ratios are normalized to the atmospheric helium isotopic composition and expressed as R/Ra where R is the isotopic ratio of the sample and Ra the atmospheric one.

Sample ID	Site	Depth (m)	Type	Sampling method	R/Ra	He/Ne	R/Ra _c	Error	δ ¹³ C _{CO2}	δ ¹³ C _{CH4}	δ ¹³ C _{TDIC}	CO ₂ / ³ He
5	Z1	134	D	Niskin	0.91	0.283	—	0.0152	—	n.a.	-0.52	
9	Z2	127	D	Niskin	0.91	0.316	—	0.0143	—	n.a.	-1.51	
13	ZDA	120	D	Niskin	0.80	0.344	—	0.0140	—	n.a.	-0.35	
14	ZDA	147	D	Niskin	0.87	0.511	—	0.0178	—	n.a.	-0.53	
17	Z2	127	B	ROV	3.72	92.19	3.73	0.0325	-0.71	-45.50	—	5.86E + 09
18	Z2	125	B	ROV	3.75	51.78	3.76	0.0302	-6.16	-44.28	—	
19	VEN	80	B	Two-way glass bottle	1.33	25.26	1.34	0.0230	1.93	n.a.	—	1.14E + 11
11-BT1*	ZGP	129	B	ROV	3.49	7.71	3.60	0.02420	n.a.	-43.70	—	
12-BT1*	ZGP	129	B	ROV	3.50	7.11	3.62	0.02434	n.a.	n.a.	—	
13-BT4*	ZGP	127	B	ROV	3.41	5.47	3.56	0.02395	n.a.	n.a.	—	

R/Ra_c is the ³He/⁴He ratio corrected for the atmospheric contamination (see text for details). n.a. = not analyzed; * Data and labels after Martorelli et al. [27].

like $1.5\text{KAlSi}_3\text{O}_8 + \text{H}^+ = 0.5\text{KAl}_3\text{Si}_3\text{O}_{10}(\text{OH})_2 + \text{K}^+ + 3\text{SiO}_2$ is a typical hydrothermal alteration moving potassium from K-feldspars to hydrothermal fluids. Similar alteration reac-

tions involving plagioclase and other minerals of the volcanic rocks are responsible for the enrichment in calcium and sodium [52, 53].

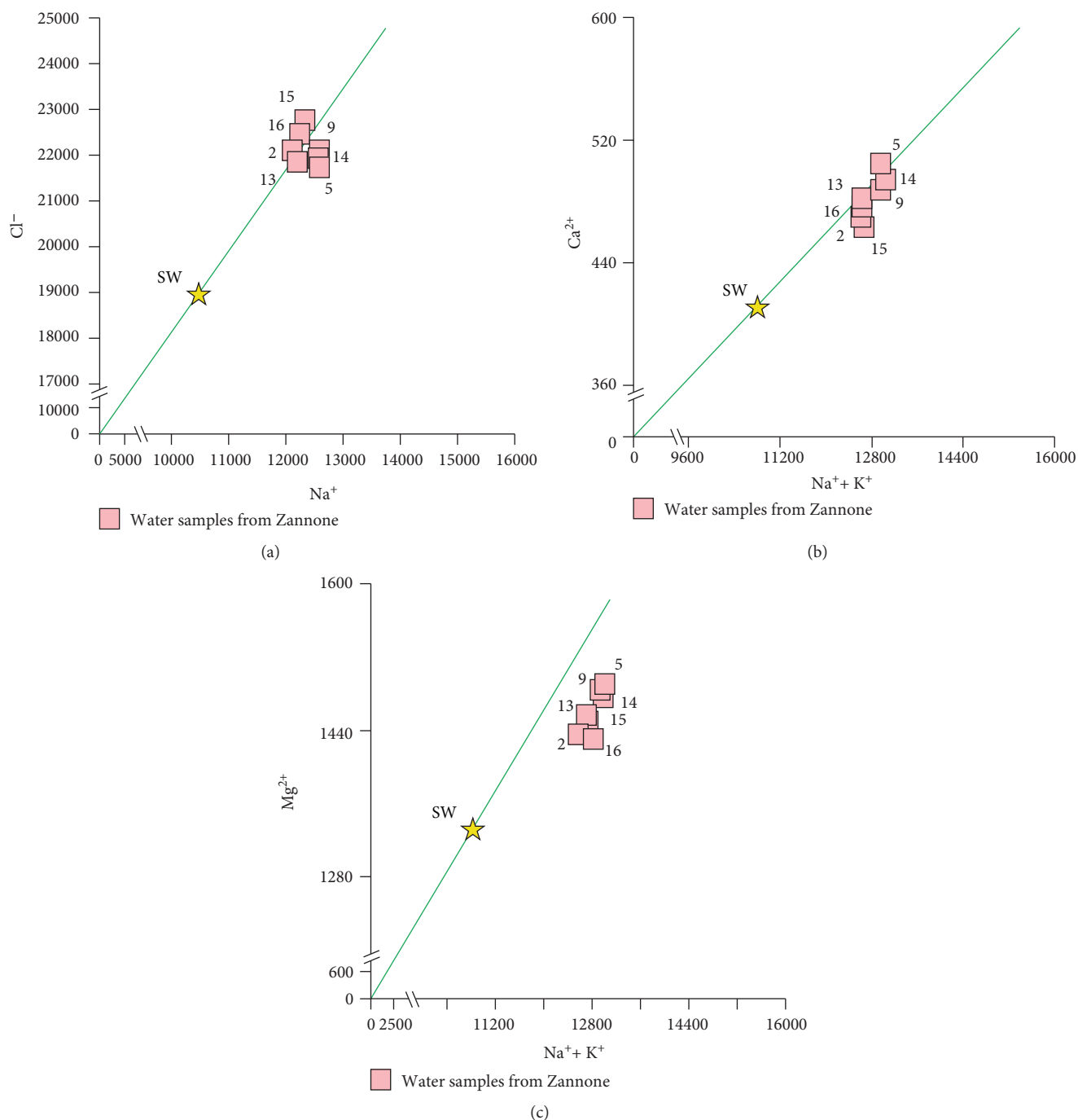


FIGURE 4: Geochemical features of water samples from Zannone. The star indicates the local seawater. (a) Na vs. Cl (mg/l) binary diagram; (b, c) Ca and Mg vs. Na+K concentrations (mg/l).

The chloride concentration is sometimes higher than that of the local seawater due to phase separation [54] or from the dissolution of magmatic hydrogen chloride [55]. According to the Na+K vs. Mg diagram (Figure 4(c)), the water samples are slightly depleted in magnesium in comparison to a “concentrated seawater” having a Na+K content of around 13000 mg/l. Magnesium is commonly removed from solution when seawater is heated or during high-T reactions with rocks [56, 57]. The general

decrease in magnesium concentration is caused by the formation of Mg-rich secondary minerals during water-rock reactions [58].

Italiano and Nuccio [52] interpreted all the above-mentioned features as a mixing of seawater with thermalized marine waters modified by high-temperature interactions with the hosting rocks and proposed the existence of a deep geothermal system fed by magmatic fluids released by a cooling magma body.

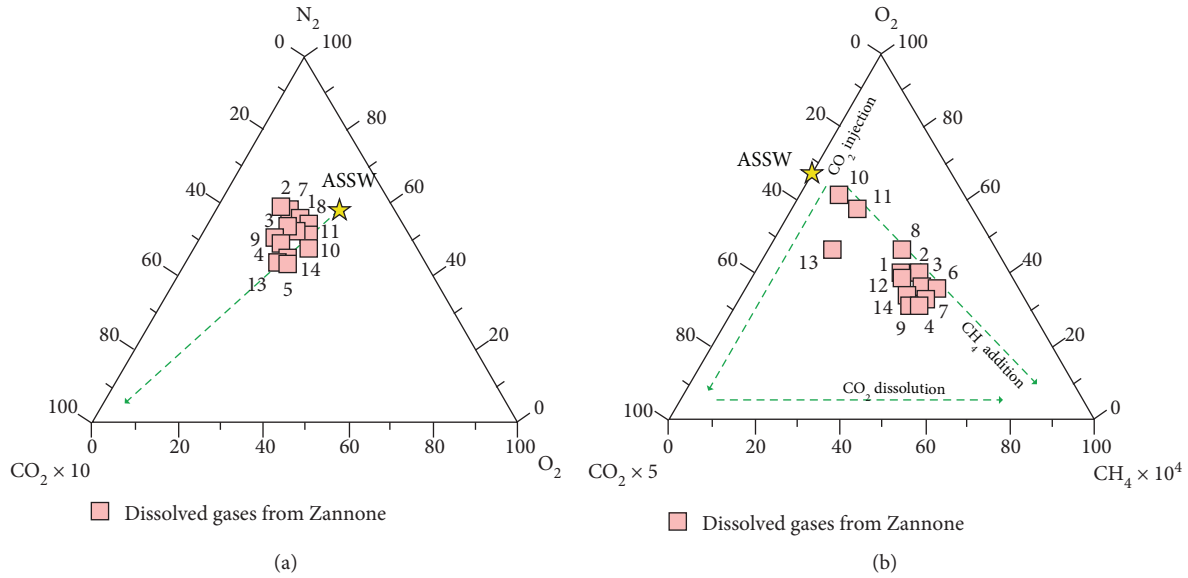


FIGURE 5: Geochemical relationships for dissolved gases. The star indicates the ASSW (air-saturated seawater). (a) The relative concentrations of CO₂, O₂, and N₂. The dashed line indicates a trend of CO₂ injection in an ASSW; (b) relative concentrations CH₄, O₂, and CO₂. Volcanic/hydrothermal-derived components (CO₂-CH₄) are plotted together with a typical dissolved atmospheric component (O₂). The dashed lines represent trends of CO₂ and CH₄ injection and CO₂ dissolution due to GWI.

5.2. Bubbling and Dissolved Gases. The analytical results for all the dissolved gases from Zannone have been plotted in the CO₂-O₂-N₂ ternary diagram (Figure 5(a)). Samples falling along the ASSW-CO₂ mixing line clearly suggest the presence of a CO₂-rich input. The occurrence of gas-water interaction (GWI) is highlighted in the O₂-CO₂-CH₄ ternary diagram (Figure 5(b)) since samples experienced enrichment in the less soluble species (such as CH₄) along with CO₂ dissolution. Our results for dissolved gases are in agreement with those reported by Martorelli et al. ([27]; see Table 3 and Figure 4).

The bubbling gases were collected by ROV at Zannone (125-127 m depth; Table 3) and by divers at Ventotene (80 m depth). The ROV sampling techniques provided samples with variable atmospheric contamination. Sample #19 taken by divers at Ventotene and one sample (#17) collected by ROV in 2017 at Zannone are CO₂-dominated (94.6-98.1 vol%) and thus denote their magmatic origin as expected. Gas-water interaction (GWI) processes may however affect the final composition of gases collected in the marine environment causing (i) the dissolution of highly soluble species, (ii) CO₂ fractionation, and (iii) enrichment in atmospheric components dissolved in seawater (i.e., N₂ and O₂).

Contrastingly, sample #18 in Table 3 displays high amounts of atmospheric-derived components (O₂ and N₂) associated with a very low CO₂ and high CH₄ and helium contents. Besides the high O₂ and N₂ content, that is related to atmospheric contamination of the sample, the high helium and CH₄ concentrations (564 ppm and 9% by volume, respectively) are worth of notice, as a consequence of a large extent of GWI. Considering that the gases released by hydrothermal systems derive from reducing environments and are thus expected to be O₂ free, we recalculated

their composition subtracting the atmospheric contamination. Assuming that sample #17, after the removal of air contamination, represents the pristine gas composition, we restored the gas composition considering the concentration ratios of the less soluble gases (He/CH₄, He/N₂). Table 3 displays for gas samples #17 and 18 both the analytical results and the recalculated gas composition (labeled as "Rec").

The isotopic analysis of helium of sample #17 provides a further indication that only the sampling bottle used for the gas-chromatographic analysis suffered an accidental contamination. As shown in Table 4, both samples #17 and 18 display consistent results with high ⁴He/²⁰Ne ratios denoting negligible air contamination.

5.3. Origin of the Vented Fluids. The helium isotope ratios determined for all the dissolved gases collected within the hydrothermal field off Zannone show atmospheric contamination to variable extents as revealed by the ⁴He/²⁰Ne ratios close to the atmospheric one (0.283; [48]). On the R/Ra (uncorrected) vs. ⁴He/²⁰Ne diagram in Figure 6, they cluster very close to the typical ASSW (air-saturated seawater) end-member. On the other hand, the bubbling gases sampled at Ventotene and Zannone suffer a negligible atmospheric contamination as shown by the high ⁴He/²⁰Ne ratio (>25). The corrected values range from 1.34 at Ventotene (sample #19) to 3.73-3.76 at Zannone (samples #17 and 18), clearly indicating a contribution of mantle-derived He [59]. On the R/Ra (uncorrected) vs. ⁴He/²⁰Ne diagram (Figure 6), the bubbling gases from Ventotene and Zannone plot in the intermediate zone separating the uncontaminated MORB and the crustal ranges, relatively close to the binary mixing line between an atmospheric and a contaminated mantle source. The ³He/⁴He ratio (3.72-3.75 Ra) observed at Zannone (samples #17 and 18) is comparable to those at

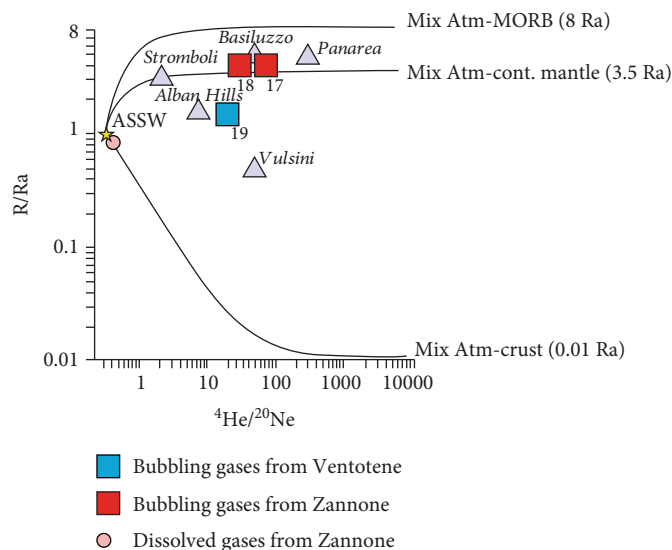


FIGURE 6: Helium isotopic ratios (as R/Ra) and $^4He/^{20}Ne$ relationships. The theoretical black lines represent binary mixing trends for atmospheric helium with helium from crust and mantle sources. The assumed end-members are ASSW (yellow star) with $Ra = 1$ and He/Ne ratio = 0.267; crust with $R/Ra = 0.01$ and $^4He/^{20}Ne = 5000$; MORB-type mantle with $R/Ra = 8$ and $^4He/^{20}Ne = 1000$; contaminated mantle by crustal fluids due to subduction of continental crust having $Ra = 3.5$ and $^4He/^{20}Ne = 1000$. Data for bubbling gases from Panarea and Basiluzzo [16], Stromboli [60], Vulcini [61], and Alban Hills [62] are plotted for comparison.

Stromboli, Panarea, and Basiluzzo (2.8–4.4 Ra ; [16, 60]), while the lower value (1.33 Ra) observed at Ventotene (sample #19) displays a strong affinity with the helium isotope composition of gases from the Roman Comagmatic Province (lower than 2 Ra ; [61, 62]). It is worth of notice that the helium isotopic ratios (Table 4) for samples collected off Zannone in 2014 and 2017 provide consistent results with $^3He/^4He$ in the range of 3.56–3.70 Ra that highlight the magmatic contribution to the vented gases. Outcomes from the R/Ra (uncorrected) vs. $^4He/^{20}Ne$ diagram (Figure 6) suggest that the helium isotope composition in the gases from Zannone and Ventotene can be interpreted as a mixture of a mantle and a crustal component or a fractionated He depleted in 3He because of the long-lasting degassing of the magmatic bodies; however, it denotes the presence of magmatic gases in agreement with the chemical composition.

The carbon isotope composition of methane (in the range from -45.5 to -44.2‰) in the bubbling gases from Zannone (samples #17 and 18) indicates a clear thermogenic derivation ruling out any biogenic contribution. The inorganic origin of the hydrothermal gases is confirmed by the $\delta^{13}C_{CO_2}$, being -0.71‰ (sample #17) and -6.16‰ (sample #18) and by the $\delta^{13}C_{TDC}$ of the CO_2 dissolved in the water samples ranging from -1.51‰ to -0.35‰. As CO_2 is a common gas coming from a variety of sources marked by different $\delta^{13}C$ signatures, the typical isotopic signature of the different sources has to be considered. Typical $\delta^{13}C$ values for some of them are organic CO_2 in the range of -24‰ [63], mantle CO_2 $\delta^{13}C = -6 \pm 2‰$ [64], and CO_2 from marine carbonates $\delta^{13}C = \sim 0 \pm 2‰$ [65]. Moreover, the high reactivity of carbon dioxide and its high solubility in marine waters are responsible fractionation processes able to modify the pristine isotope composition. Therefore, identifying the exact source/sources

involved in the CO_2 production is not always possible using only CO_2 data. According to these limitations, the isotope signature of the CO_2 from Zannone ($\delta^{13}C_{CO_2} = -0.71$ and -6.16‰) could be carefully considered as a mixture of a gaseous contribution derived from a crustal source and a magmatic CO_2 component. The heavier value obtained for the bubbling gases from Ventotene ($\delta^{13}C_{CO_2} = 1.93‰$; sample #19) can be interpreted as a stronger contribution of “crustal” CO_2 or, alternatively, it highlights a less GWI during gas uprising. Considering the $CO_2/^3He$ ratios of samples #17 and 19 (Zannone and Ventotene islands; Table 4) besides the $\delta^{13}C_{CO_2}$ values, a higher contribution of crustal, probably limestone-type products, can be proposed for gases vented at Ventotene in contrast to a larger contribution of magmatic-type volatiles for Zannone island.

According to Martorelli et al. [27], the mantle component identified in the hydrothermal fluids currently vented off-shore Zannone originates in residual magma batches intruded into the crust and never erupted. Direct mantle degassing has been excluded [27] due to permeability limitations induced by the local crustal thickness of about 25 km (see Italiano et al. [66] for further information). Considering that the crustal thickness all along the Tyrrhenian margin of Central Italy is comparable [67], we may also expect that the mantle-derived signature identified at Ventotene is related to the degassing of magma bodies intruded at a relatively shallow crustal level.

With regard to the crustal component, recent studies (i.e., Martelli et al. [68, 69]) pointed out that the Plio-Quaternary volcanic activity from the Roman Comagmatic Province and from the central and eastern sectors of the Aeolian Island reflects an origin in a mantle source contaminated by crustal fluids related to the subduction of the Ionian-Adriatic plate.

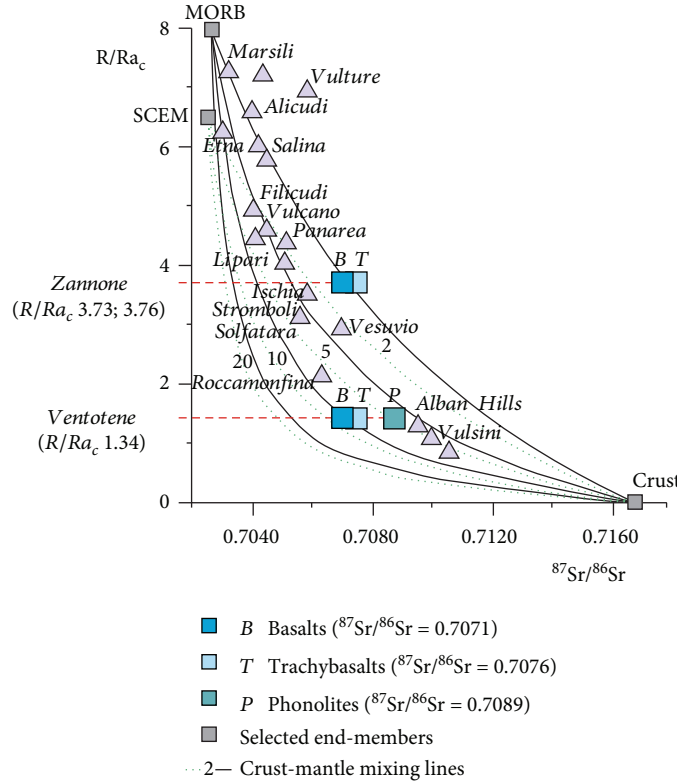


FIGURE 7: $^{87}\text{Sr}/^{86}\text{Sr}$ versus R/R_{a_c} for solid and gas samples from the Tyrrhenian area (modified after Martorelli et al. [27]). The lines are binary mixing between MORB-type mantle and SCEM-type mantle (Subcontinental European Mantle; Dunai and Baur [70]) with a crustal end-member. Numbers (2, 5, 10, and 20) indicate the k value ($k = (\text{He}/\text{Sr})_{\text{crust}}/(\text{He}/\text{Sr})_{\text{mantle}}$) for each curve. Assumed values for mantle and crust end-members: $^3\text{He}/^4\text{He}_{\text{radiogenic}} = 0.01 \text{ Ra}$ [77]; $^3\text{He}/^4\text{He}_{\text{MORB}} = 8 \text{ Ra}$ [78]; $^3\text{He}/^4\text{He}_{\text{SCEM}} = 6.5 \text{ Ra}$ [70]; $^{87}\text{Sr}/^{86}\text{Sr}_{\text{radiogenic}} = 0.720$ [79]; and $^{87}\text{Sr}/^{86}\text{Sr}_{\text{asthenosphere}} = 0.7030$ [80]. $\text{He}_{\text{cont crust}} = 5 \times 10^{-5} \text{ cm}^3 \text{ STP/g}$ [81]; $\text{He}_{\text{HIMU}} = 5 \times 10^{-7} \text{ cm}^3 \text{ STP/g}$ [78]; $\text{Sr}_{\text{cont crust}} = 333 \text{ ppm}$ [82]; and $\text{Sr}_{\text{MORB}} = 16.4 \text{ ppm}$ [83]. Data after D'Antonio et al. [71], Barberi et al. [72], Martelli et al. [68], and Italiano et al. [15].

Moreover, Conte et al. [40] assumed that the genesis of the Pontine magmas has to be referred to as partial melting processes of a mantle source contaminated by crustal components recycled via subduction. Hence, contamination of the mantle reservoir might be the main factor responsible for the crustal component observed in the hydrothermal fluids.

In order to constrain the magmatic source of the geothermal fluids, the R/R_{a_c} - $^{87}\text{Sr}/^{86}\text{Sr}$ diagram (He-Sr relationship) is used (Figure 7). The plot shows binary mixing trends between a crustal end-member and two mantle end-members represented by MORB and SCEM (Subcontinental European Mantle; [70]). He and Sr data from volcanic edifices of the Tyrrhenian area have also been plotted for comparison; most of them refer to values obtained for the same rock sample [15, 68]. The He isotopic ratio observed at Zannone was interpreted [27] as a degassing of cooling mantle-derived magmas having a composition similar to the Pleistocene trachytes (i.e., the Ventotene basalts/trachybasalts). With regard to the hydrothermal fluids emitted SW of Ventotene Island, three different Pleistocene samples belonging to the shoshonitic-type suite outcropping over the island are plotted assuming that those rock types release helium with the same isotopic ratio determined in the bubbling gas ($1.34 R_{a_c}$). The Sr isotopic ratios for those

rocks are basalts $^{87}\text{Sr}/^{86}\text{Sr} = 0.70709$ [71], trachybasalts $^{87}\text{Sr}/^{86}\text{Sr} = 0.70758$ [71], and phonolites $^{87}\text{Sr}/^{86}\text{Sr} = 0.7089$ [72]. The diagram highlights that the helium isotope ratio of $1.34 R_{a_c}$ is consistent with a crust-mantle mixture for all the three Ventotene samples, as they plot within the 5 and 10 binary mixing lines between the values of Roccamonfina and those of the Roman Comagmatic Province (Alban Hills and Vulcini). These results suggest that the Ventotene gases may be deriving from a magmatic source, simply reproducing a crust-mantle mixture. Both basic (basaltic/trachybasaltic) and intermediate magmas (phonolitic) derived from a contaminated mantle source can attain the recorded helium isotopic ratio. Furthermore, they rule out the possibility that the current exhalative activity can be supplied by acidic magmas of anatectic origin.

5.4. Geothermometric and Geobarometric Considerations. Following the assumption that the submarine hydrothermal fluids vented at Zannone and Ventotene may equilibrate inside a geothermal reservoir at some level beneath the seafloor, we propose the existence of a reservoir kept at boiling conditions by the thermal energy released by cooling magma batches intruded at shallow crustal levels. We constrained the chemical-physical conditions (pressure, temperature,

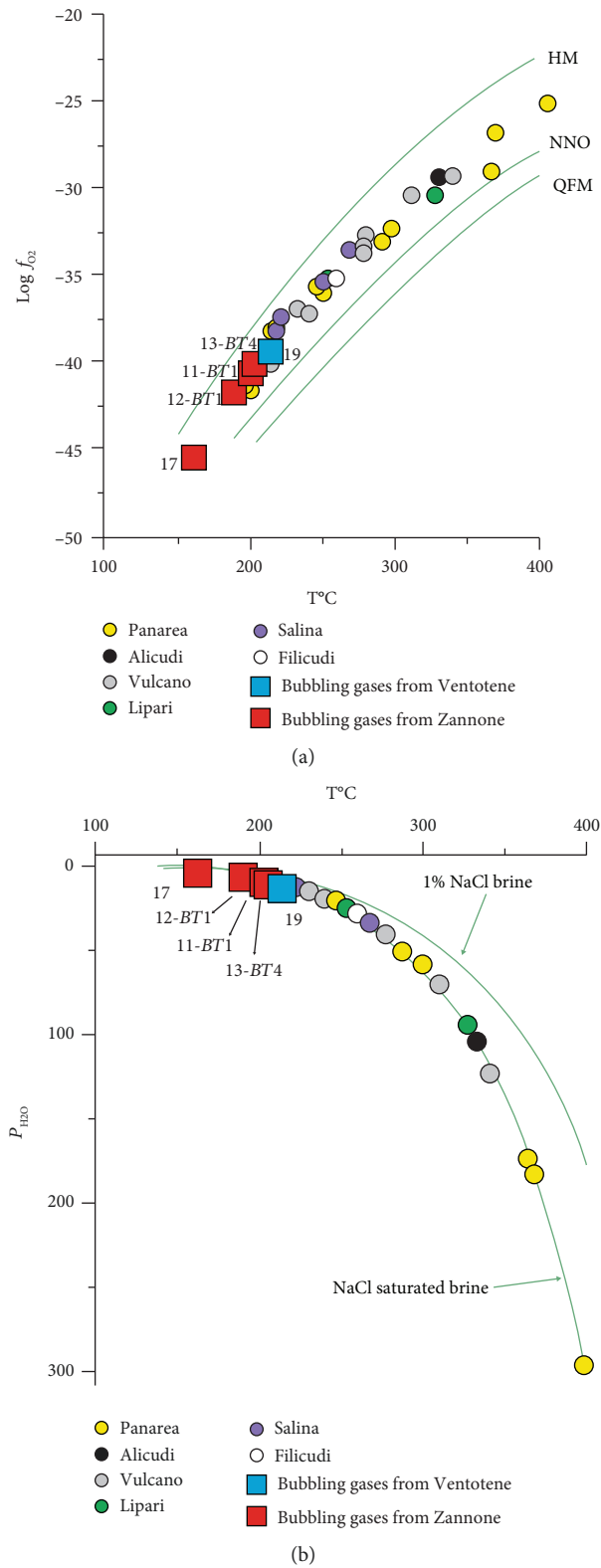


FIGURE 8: Geothermometric and geobarometric estimations for the bubbling gases from Zannone and Ventotene (see text and Section 1 of Supplementary Materials for details). B-Z2 and B-VEN were analyzed in this paper; B1, B2, and B3 after Martorelli et al. [27]: (a) temperature vs. oxygen fugacity (expressed as $\log f_{\text{O}_2}$) diagram; geothermometric estimations for the submarine hydrothermal systems of the Aeolian Islands are reported for comparison. The solid buffers quartz–fayalite–magnetite (QFM), nickel–nickel oxide (N–NO), and hematite–magnetite (HM) are plotted as reference (after Eugster and Wones [84]). (b) Estimated equilibrium pressure of the hydrothermal reservoirs. The pressure is shown on the vertical axis as $P_{\text{H}_2\text{O}}$ (bars). The boiling curves for saturated NaCl and 1%NaCl waters (brines) are shown. $P_{\text{H}_2\text{O}}$ by using the estimated equilibrium temperatures.

and redox) that buffer the chemical composition of the hydrothermal fluids at the reservoir level, using the reactive gases CO , CH_4 , and CO_2 as already used for geothermometric and geobarometric estimations in geothermal systems (e.g., Giggenbach [73], Fiebig et al. [74], and references therein) and also for submarine hydrothermal fluids [52]. Among the reactive gases, hydrogen was not considered due to its reactivity that causes unpredictable H_2 losses during fluid upraising.

Giggenbach [75] and Italiano and Nuccio [52] observed how the temperature estimations based on the system H_2O , CO_2 , CH_4 , and CO assumed to be at boiling conditions are reasonably valid in the range between 100 and 400°C.

In the case of the fluids vented off the Zannone and Ventotene islands, further assumptions and limitations are taken into account as we deal with fluids collected at a depth greater than 120 m bsl. Considering the very high CO_2 solubility in seawater during gas-water interaction (GWI) processes and the observed enrichment of CO and CH_4 (Table 3), we expect that the CO_2/CO and CO_2/CH_4 ratios have been modified during thermal fluid upraise. As observed by Italiano et al. [44], the system adopted is more sensitive to the CO and CH_4 concentrations than that of CO_2 , implying that although GWI induces modifications in the chemical composition, the estimated equilibrium temperatures do not change very much even in the case of, even large, CO_2 content changes. The solubility coefficients of CO and CH_4 are similar and about one order of magnitude lower than that of CO_2 ; thus, they do not alter their abundance ratios (see Section 2 of Supplementary Materials (available here)). Moreover, the slow CO and CH_4 reaction kinetics allows them to keep the deep equilibrium conditions during fluids' upraising. Equations (5) and (6) in Section 1 of Supplementary Materials show how the equilibrium constants are a function of temperature and oxygen fugacity. The water molecule dissociation ($\text{H}_2\text{O} = \text{H}_2 + \frac{1}{2}\text{O}_2$) is a function of temperature, and the f_{O_2} is buffered by the mineral assemblage (quartz, olivine, hematite, magnetite, and nickel) of the host volcanic rocks.

Only the bubbling gases are considered for the geothermometric estimations, and the results plotted on the already adopted temperature f_{O_2} graph (Figure 8(a)) show that even in the case of the Pontine Islands, the samples fall between two theoretical f_{O_2} buffers proving that equilibrium is attained at the geothermal system level. The estimations show equilibrium temperatures of 156°C for Zannone (sample #17) and 213°C for Ventotene (sample #19). These results indicate the existence of a geothermal system beneath each of the two islands. The estimated geotemperatures have been used to constrain the depth of the geothermal reservoir, namely, its $P_{\text{H}_2\text{O}}$ according to the T - $P_{\text{H}_2\text{O}}$ relationship for 2 M and NaCl-saturated waters ($\log f_{\text{H}_2\text{O}} = 5.479 - 2047/T$; [76]). $P_{\text{H}_2\text{O}}$ results to be of 5 and 20 bar at Zannone (sample #17) and Ventotene (sample #19), respectively (Figure 8(b)). Moreover, the geothermometric and geobarometric estimations for the bubbling gases collected at Zannone by Martorelli et al. [27] (samples 11-BT1, 12-BT1, and 13-BT4 in Table 3) indicate consistent results

with equilibrium temperatures in the range of 190–200°C and $P_{\text{H}_2\text{O}}$ of 13–18 bars (Figure 8).

6. Concluding Remarks

The Zannone and Ventotene offshore is widely floored by hydrothermal features. Active seeping occurs along regional tectonic lineaments affecting the Central Tyrrhenian continental margin. Faults and fractures create several releasing zones broadly marked by different fluid-escape morphologies such as cones, mounds, and pockmarks. The vented fluids are composed of bubbling gases and hot thermal waters discharged at temperatures up to 60°C. The occurrence of GWI processes, highlighted by the chemical composition of dissolved and bubbling gases, is responsible for the geochemical features of the collected gas phase. Helium and carbon isotope analyses indicate that geothermal fluids are the result of a mixing of mantle and crustal components: the mantle component comes from residual magma batches intruded at shallow crustal depths, whereas the crustal contribution mainly reflects the metasomatism of the upper mantle by crustal fluids recycled via subduction of the Adriatic plate.

Geothermobarometric estimations as well as the chemical composition of fluids collected in the Pontine Archipelago (marine waters, hot thermal waters, and bubbling gases) mark the occurrence of geothermal systems located at various depths beneath the seafloor. The vented thermal waters display the enrichment of major ions in comparison to the local seawater, reflecting mixing of seawater with marine water modified by high-temperature interaction with the hosting rocks. The calculated equilibrium temperatures fall in the range 150–400°C already estimated for the Aeolian Islands (Figure 8). At Zannone and Ventotene, the helium isotopic signature (1.34–3.76 R_a) clearly indicates a magmatic input probably provided by the same cooling magmatic bodies trapped in the shallow crust that feed the geothermal reservoirs. Our future challenge is to search for brand new hydrothermal features on the seafloor all around the Pontine Islands in order to constrain the total energy budget for the Pontine Archipelago.

Data Availability

The data on gas and water geochemistry used to support the findings of this study are included within the article. In order to strengthen our assumptions, we used some geochemical data from previously reported studies which have been cited.

Conflicts of Interest

The authors declare that there are no conflicts of interest regarding the publication of this paper.

Acknowledgments

This work was financially supported by Ritmare funds. The authors are extremely grateful to Francesco Salerno, Mariano Tantillo, Aldo Sollami, and Ygor Oliveri for their support in the laboratory work. The authors wish to thank Mr. Roberto

Rinaldi for his invaluable discovery and sampling of the gas bubbling of Ventotene.

Supplementary Materials

The supplementary materials detail the method applied in this paper to calculate the equilibrium temperatures (Section 1). Moreover, the solubility coefficients of the main species composing the hydrothermal gas emissions are listed in Section 2. (*Supplementary Materials*)

References

- [1] A. Malinverno and W. B. F. Ryan, "Extension in the Tyrrhenian Sea and shortening in the Apennines as result of arc migration driven by sinking of the lithosphere," *Tectonics*, vol. 5, no. 2, pp. 227–245, 1986.
- [2] L. Jolivet and C. Faccenna, "Mediterranean extension and the Africa-Eurasia collision," *Tectonics*, vol. 19, no. 6, pp. 1095–1106, 2000.
- [3] R. Sartori, "The Tyrrhenian backarc basin and subduction of the Ionian lithosphere," *Episodes*, vol. 26, no. 3, pp. 217–221, 2003.
- [4] C. Faccenna, C. Piromallo, A. Crespo-Blanc, L. Jolivet, and F. Rossetti, "Lateral slab deformation and the origin of the western Mediterranean arcs," *Tectonics*, vol. 23, no. 1, 2004.
- [5] A. Argnani and C. Savelli, "Cenozoic volcanism and tectonics in the southern Tyrrhenian Sea: space-time distribution and geodynamic significance," *Journal of Geodynamics*, vol. 27, no. 4–5, pp. 409–432, 1999.
- [6] A. Peccerillo, "Potassic and ultrapotassic magmatism: compositional characteristics, genesis and geologic significance," *Episodes*, vol. 15, no. 4, pp. 243–251, 1992.
- [7] A. Peccerillo, "Multiple mantle metasomatism in Central-Southern Italy: geochemical effects, timing and geodynamic implications," *Geology*, vol. 27, no. 4, pp. 315–318, 1999.
- [8] A. Peccerillo, Ed., *Plio-Quaternary Volcanism in Italy. Petrology, Geochemistry, Geodynamics*, Springer-Verlag Berlin Heidelberg, 2005.
- [9] A. Peccerillo, Ed., *Cenozoic Volcanism in the Tyrrhenian Sea Region*, Springer International Publishing, 2nd edition, 2017.
- [10] M. Lustrino, "Phanerozoic geodynamic evolution of the circum-Italian realm," *International Geology Review*, vol. 42, no. 8, pp. 724–757, 2000.
- [11] C. Savelli, "Late Oligocene to recent episodes of magmatism in and around the Tyrrhenian Sea: implications for the processes of opening in a young inter-arc basin of intra-orogenic (Mediterranean) type," *Tectonophysics*, vol. 146, no. 1–4, pp. 163–181, 1988.
- [12] C. Savelli, "Two-stage progression of volcanism (8–0 Ma) in the Central Mediterranean (southern Italy)," *Journal of Geodynamics*, vol. 31, no. 4, pp. 393–410, 2001.
- [13] J. Lupton, C. de Ronde, M. Spivieri et al., "Active hydrothermal discharge on the submarine Aeolian Arc," *Journal of Geophysical Research*, vol. 116, no. B2, 2011.
- [14] S. L. Walker, S. Carey, K. L. Bell et al., *Near-bottom water column anomalies associated with active hydrothermal venting at Aeolian arc volcanoes, Tyrrhenian Sea, Italy*, American Geophysical Union, 2012.
- [15] F. Italiano, A. de Santis, P. Favali, M. Rainone, S. Rusi, and P. Signanini, "The Marsili volcanic seamount (southern Tyrrhenian Sea): a potential offshore geothermal resource," *Energies*, vol. 7, no. 7, pp. 4068–4086, 2014.
- [16] F. Italiano, "Hydrothermal fluids vented at shallow depths at the Aeolian islands: relationships with volcanic and geothermal systems," *FOG Freiberg Online Geology*, vol. 22, pp. 55–60, 2009.
- [17] T. L. Maugeri, G. Bianconi, F. Canganella et al., "Shallow hydrothermal vents in the southern Tyrrhenian Sea," *Chemistry and Ecology*, vol. 26, Supplement 1, pp. 285–298, 2010.
- [18] T. Monecke, S. Petersen, M. D. Hannington et al., "Explosion craters associated with shallow submarine gas venting off Panarea island, Italy," *Bulletin of Volcanology*, vol. 74, no. 9, pp. 1937–1944, 2012.
- [19] S. Graziani, S. E. Beaubien, S. Bigi, and S. Lombardi, "Spatial and temporal pCO₂ marine monitoring near Panarea Island (Italy) using multiple low-cost GasPro sensors," *Environmental Science & Technology*, vol. 48, no. 20, pp. 12126–12133, 2014.
- [20] M. Loreto, F. Pepe, R. De Ritis et al., "On the relationships between tectonics and volcanism in the offshore Capo Vaticano, SE Tyrrhenian Sea, during the Plio-Pleistocene," *Rendiconti Online della Società Geologica Italiana*, vol. 31, no. 1, pp. 85–98, 2014.
- [21] M. F. Loreto, F. Italiano, D. Deponte, L. Facchin, and F. Zgur, "Mantle degassing on a near shore volcano, SE Tyrrhenian Sea," *Terra Nova*, vol. 27, no. 3, pp. 195–205, 2015.
- [22] S. Passaro, S. Genovese, M. Sacchi et al., "First hydroacoustic evidence of marine, active fluid vents in the Naples Bay continental shelf (Southern Italy)," *Journal of Volcanology and Geothermal Research*, vol. 285, pp. 29–35, 2014.
- [23] S. Passaro, S. Tamburrino, M. Vallefucio et al., "Seafloor doming driven by degassing processes unveils sprouting volcanism in coastal areas," *Scientific Reports*, vol. 6, no. 1, article 22448, 2016.
- [24] J. Heinicke, F. Italiano, R. Maugeri et al., "Evidence of tectonic control on active arc volcanism: the Panarea-Stromboli tectonic link inferred by submarine hydrothermal vents monitoring (Aeolian arc, Italy)," *Geophysical Research Letters*, vol. 36, no. 4, 2009.
- [25] A. Cadoux, D. L. Pinti, C. Aznar, S. Chiesa, and P. Y. Gillot, "New chronological and geochemical constraints on the genesis and geological evolution of Ponza and Palmarola volcanic islands (Tyrrhenian Sea, Italy)," *Lithos*, vol. 81, no. 1–4, pp. 121–151, 2005.
- [26] M. Ingrassia, E. Martorelli, A. Bosman, L. Macelloni, A. Sposato, and F. L. Chiocci, "The Zannone Giant Pockmark: first evidence of a giant complex seeping structure in shallow-water, central Mediterranean Sea, Italy," *Marine Geology*, vol. 363, pp. 38–51, 2015.
- [27] E. Martorelli, F. Italiano, M. Ingrassia et al., "Evidence of a shallow water submarine hydrothermal field off Zannone Island from morphological and geochemical characterization: implications for Tyrrhenian Sea Quaternary volcanism," *Journal of Geophysical Research: Solid Earth*, vol. 121, no. 12, pp. 8396–8414, 2016.
- [28] R. Bartole, D. Savelli, M. Tramontana, and F. C. Wezel, "Structural and sedimentary features in the Tyrrhenian margin off Campania, southern Italy," *Marine Geology*, vol. 55, no. 3–4, pp. 163–180, 1984.
- [29] D. De Rita, R. Funiciello, D. Pantosti, F. Salvini, A. Sposato, and M. Velonà, "Geological and structural characteristics of

- the Pontine Islands (Italy) and implications with the evolution of the Tyrrhenian margin," *Memorie della Societa Geologica Italiana*, vol. 36, no. 7, pp. 55–65, 1986.
- [30] N. Zitellini, M. Marani, and A. Borsetti, "Post-orogenic tectonic evolution of Palmarola and Ventotene basins (Pontine Archipelago)," *Memorie della Societa Geologica Italiana*, vol. 27, pp. 121–131, 1984.
- [31] M. I. Marani, M. A. Taviani, F. A. Trincardi, A. Argnani, A. M. Borsetti, and N. Zitellini, "Pleistocene progradation and post-glacial events of the NE Tyrrhenian continental shelf between the Tiber river delta and Capo Circeo," *Memorie della Societa Geologica Italiana*, vol. 36, pp. 67–89, 1986.
- [32] M. Marani and N. Zitellini, "Rift structures and wrench tectonics along the continental slope between Civitavecchia and C. Circeo," *Memorie della Societa Geologica Italiana*, vol. 35, no. 2, pp. 453–457, 1986.
- [33] A. Frepoli and A. Amato, "Contemporaneous extension and compression in the Northern Apennines from earthquake fault-plane solutions," *Geophysical Journal International*, vol. 129, no. 2, pp. 368–388, 1997.
- [34] L. Carmignani and R. Kligfield, "Crustal extension in the northern Apennines: the transition from compression to extension in the Alpi Apuane core complex," *Tectonics*, vol. 9, no. 6, pp. 1275–1303, 1990.
- [35] S. Stein and G. F. Sella, "Pleistocene change from convergence to extension in the Apennines as a consequence of Adria microplate motion," in *The Adria Microplate: GPS Geodesy, Tectonics and Hazards*, N. Pinter, G. Gyula, J. Weber, S. Stein, and D. Medak, Eds., vol. 61 of Nato Science Series: IV: Earth and Environmental Sciences, pp. 21–34, Springer, Dordrecht, Netherlands, 2006.
- [36] F. Bellucci, M. Grimaldi, L. Lirer, and A. Rapolla, "Structure and geological evolution of the island of Ponza, Italy: inferences from geological and gravimetric data," *Journal of Volcanology and Geothermal Research*, vol. 79, no. 1–2, pp. 87–96, 1997.
- [37] A. M. Conte and D. Dolfi, "Petrological and geochemical characteristics of Plio-Pleistocene volcanics from Ponza Island (Tyrrhenian Sea, Italy)," *Mineralogy and Petrology*, vol. 74, no. 1, pp. 75–94, 2002.
- [38] E. Martorelli, F. L. Chiocci, A. M. Conte, M. Bellino, and A. Bosman, "Affioramenti vulcanici sottomarini dell'Arcipelago Pontino occidentale: caratteri petrologici e morfoacustici," in *GEOITALIA 2003: 4 Forum Italiano di Scienze Della Terra - Federazione Italiana di Scienze Della Terra*, pp. 16–18, Bellaria, Italia, 2003.
- [39] A. Paone, "Petrogenesis of trachyte and rhyolite magmas on Ponza Island (Italy) and its relationship to the Campanian magmatism," *Journal of Volcanology and Geothermal Research*, vol. 267, pp. 15–29, 2013.
- [40] A. M. Conte, C. Perinelli, G. Bianchini, C. Natali, E. Martorelli, and F. L. Chiocci, "New insights on the petrology of submarine volcanics from the Western Pontine Archipelago (Tyrrhenian Sea, Italy)," *Journal of Volcanology and Geothermal Research*, vol. 327, pp. 223–239, 2016.
- [41] N. Métrich, *Mecanismes d'évolution a l'origine des magmas potassiques d'Italie centrale et meridionale. Exemples du Mt. Somme-Vesuve, des Champs Phlegreens et de l'Ile de Ventotene*, [Ph.D. thesis], University Paris-Sud, Orsay, 1985.
- [42] N. Métrich, R. Santacroce, and C. Savelli, "Ventotene, a potassic quaternary volcano in central Tyrrhenian Sea," *Rendiconti della Società Italiana di Mineralogia e Petrologia*, vol. 43, pp. 1195–1213, 1988.
- [43] B. De Vivo, K. Torok, R. A. Ayuso, A. Lima, and L. Lirer, "Fluid inclusion evidence for magmatic silicate/saline/CO₂ immiscibility and geochemistry of alkaline xenoliths from Ventotene Island, Italy," *Geochimica et Cosmochimica Acta*, vol. 59, no. 14, pp. 2941–2953, 1995.
- [44] F. Italiano, A. Sasmaz, G. Yuce, and O. O. Okan, "Thermal fluids along the East Anatolian Fault Zone (EAFZ): geochemical features and relationships with the tectonic setting," *Chemical Geology*, vol. 339, pp. 103–114, 2013.
- [45] F. Italiano, P. Bonfanti, M. Ditta, R. Petrini, and F. Slejko, "Helium and carbon isotopes in the dissolved gases of Friuli region (NE Italy): geochemical evidence of CO₂ production and degassing over a seismically active area," *Chemical Geology*, vol. 266, no. 1–2, pp. 76–85, 2009.
- [46] F. Italiano, G. Yuce, I. T. Uysal, M. Gasparon, and G. Morelli, "Insights into mantle-type volatiles contribution from dissolved gases in artesian waters of the Great Artesian Basin, Australia," *Chemical Geology*, vol. 378–379, pp. 75–88, 2014.
- [47] Y. Sano and H. Wakita, "Precise measurement of helium isotopes in terrestrial gases," *Bulletin of the Chemical Society of Japan*, vol. 61, no. 4, pp. 1153–1157, 1988.
- [48] J. Holocher, F. Peeters, W. Aeschbach-Hertig et al., "Experimental investigations on the formation of excess air in quasi-saturated porous media," *Geochimica et Cosmochimica Acta*, vol. 66, no. 23, pp. 4103–4117, 2002.
- [49] P. R. Dando, D. Stüben, and S. P. Varnavas, "Hydrothermalism in the Mediterranean Sea," *Progress in Oceanography*, vol. 44, no. 1–3, pp. 333–367, 1999.
- [50] W. D'Alessandro, K. Daskalopoulou, S. Calabrese, M. Longo, K. Kyriakopoulos, and A. L. Gagliano, "Gas geochemistry and preliminary CO₂ output estimation from the island of Kos (Greece)," in , Article ID 17332EGU General Assembly Conference Abstracts, vol. 19, Vienna, Austria, 2017.
- [51] K. Daskalopoulou, A. L. Gagliano, S. Calabrese et al., "Gas geochemistry and CO₂ output estimation at the island of Milos, Greece," *Journal of Volcanology and Geothermal Research*, vol. 365, pp. 13–22, 2018.
- [52] F. Italiano and P. M. Nuccio, "Geochemical investigations of submarine volcanic exhalations to the east of Panarea, Aeolian Islands, Italy," *Journal of Volcanology and Geothermal Research*, vol. 46, no. 1–2, pp. 125–141, 1991.
- [53] F. Italiano and C. Caruso, "Detection of fresh and thermal waters over an island with extinct volcanism: the island of Salina (Aeolian arc, Italy)," *Procedia Earth and Planetary Science*, vol. 4, pp. 39–49, 2011.
- [54] K. L. Von Damm, L. G. Buttermore, S. E. Oosting et al., "Direct observation of the evolution of a seafloor 'black smoker' from vapor to brine," *Earth and Planetary Science Letters*, vol. 149, no. 1–4, pp. 101–111, 1997.
- [55] A. H. Truesdell, J. R. Haizlip, H. Armannsson, and F. D'Amore, "Origin and transport of chloride in superheated geothermal steam," *Geothermics*, vol. 18, no. 1–2, pp. 295–304, 1989.
- [56] R. M. Prol-Ledesma, C. Canet, M. A. Torres-Vera, M. J. Forrest, and M. A. Armienta, "Vent fluid chemistry in Bahía Concepción coastal submarine hydrothermal system, Baja California Sur, Mexico," *Journal of Volcanology and Geothermal Research*, vol. 137, no. 4, pp. 311–328, 2004.

- [57] E. Valsami-Jones, E. Baltatzis, E. H. Bailey et al., "The geochemistry of fluids from an active shallow submarine hydrothermal system: Milos island, Hellenic volcanic arc," *Journal of Volcanology and Geothermal Research*, vol. 148, no. 1-2, pp. 130-151, 2005.
- [58] H. D. Schulz and M. Zabel, Eds., *Marine Geochemistry*, Springer-Verlag Berlin Heidelberg, 2nd edition, 2006.
- [59] C. J. Ballentine, R. Burgess, and B. Marty, "Tracing fluid origin, transport and interaction in the crust," *Reviews in Mineralogy and Geochemistry*, vol. 47, no. 1, pp. 539-614, 2002.
- [60] S. Inguaggiato and A. Rizzo, "Dissolved helium isotope ratios in ground-waters: a new technique based on gas-water re-equilibration and its application to Stromboli volcanic system," *Applied Geochemistry*, vol. 19, no. 5, pp. 665-673, 2004.
- [61] A. Minissale, W. C. Evans, G. Magro, and O. Vaselli, "Multiple source components in gas manifestations from north-central Italy," *Chemical Geology*, vol. 142, no. 3-4, pp. 175-192, 1997.
- [62] M. L. Carapezza and L. Tarchini, "Accidental gas emission from shallow pressurized aquifers at Alban Hills volcano (Rome, Italy): geochemical evidence of magmatic degassing?," *Journal of Volcanology and Geothermal Research*, vol. 165, no. 1-2, pp. 5-16, 2007.
- [63] P. Deines, D. Langmuir, and R. S. Harmon, "Stable carbon isotope ratios and the existence of a gas phase in the evolution of carbonate ground waters," *Geochimica et Cosmochimica Acta*, vol. 38, no. 7, pp. 1147-1164, 1974.
- [64] Y. Sano and B. Marty, "Origin of carbon in fumarolic gas from island arcs," *Chemical Geology*, vol. 119, no. 1-4, pp. 265-274, 1995.
- [65] J. Veizer, D. Ala, K. Azmy et al., " $^{87}\text{Sr}/^{86}\text{Sr}$, $\delta^{13}\text{C}$ and $\delta^{18}\text{O}$ evolution of Phanerozoic seawater," *Chemical Geology*, vol. 161, no. 1-3, pp. 59-88, 1999.
- [66] F. Italiano, M. Martelli, G. Martinelli, and P. M. Nuccio, "Geochemical evidence of melt intrusions along lithospheric faults of the Southern Apennines, Italy: Geodynamic and seismogenic implications," *Journal of Geophysical Research: Solid Earth*, vol. 105, no. B6, pp. 13569-13578, 2000.
- [67] A. Minissale, "Origin, transport and discharge of CO_2 in central Italy," *Earth-Science Reviews*, vol. 66, no. 1-2, pp. 89-141, 2004.
- [68] M. Martelli, P. M. Nuccio, F. M. Stuart, R. Burgess, R. M. Ellam, and F. Italiano, "Helium-strontium isotope constraints on mantle evolution beneath the Roman Comagmatic Province, Italy," *Earth and Planetary Science Letters*, vol. 224, no. 3-4, pp. 295-308, 2004.
- [69] M. Martelli, P. M. Nuccio, F. M. Stuart, V. di Liberto, and R. M. Ellam, "Constraints on mantle source and interactions from He-Sr isotope variation in Italian Plio-Quaternary volcanism," *Geochemistry, Geophysics, Geosystems*, vol. 9, no. 2, 2008.
- [70] T. J. Dunai and H. Baur, "Helium, neon, and argon systematics of the European subcontinental mantle: implications for its geochemical evolution," *Geochimica et Cosmochimica Acta*, vol. 59, no. 13, pp. 2767-2783, 1995.
- [71] M. D'Antonio, L. Civetta, and P. di Girolamo, "Mantle source heterogeneity in the Campanian region (south Italy) as inferred from geochemical and isotopic features of mafic volcanic rocks with shoshonitic affinity," *Mineralogy and Petrology*, vol. 67, no. 3-4, pp. 163-192, 1999.
- [72] F. Barberi, S. Borsi, G. Ferrara, and F. Innocenti, "Contributo alla conoscenza vulcanologica e magmatologica delle Isole dell'Archipelago Pontino," *Memorie della Societa Geologica Italiana*, vol. 6, no. 4, pp. 581-606, 1967.
- [73] W. F. Giggenbach, "Geothermal gas equilibria," *Geochimica et Cosmochimica Acta*, vol. 44, no. 12, pp. 2021-2032, 1980.
- [74] J. Fiebig, G. Chiodini, S. Caliro, A. Rizzo, J. Spangenberg, and J. C. Hunziker, "Chemical and isotopic equilibrium between CO_2 and CH_4 in fumarolic gas discharges: generation of CH_4 in arc magmatic-hydrothermal systems," *Geochimica et Cosmochimica Acta*, vol. 68, no. 10, pp. 2321-2334, 2004.
- [75] W. F. Giggenbach, "Redox processes governing the chemistry of fumarolic gas discharges from White Island, New Zealand," *Applied Geochemistry*, vol. 2, no. 2, pp. 143-161, 1987.
- [76] G. Chiodini, L. Marini, and M. Russo, "Geochemical evidence for the existence of high-temperature hydrothermal brines at Vesuvio volcano, Italy," *Geochimica et Cosmochimica Acta*, vol. 65, no. 13, pp. 2129-2147, 2001.
- [77] R. K. O'Nions and E. R. Oxburgh, "Helium, volatile fluxes and the development of continental crust," *Earth and Planetary Science Letters*, vol. 90, no. 3, pp. 331-347, 1988.
- [78] M. Moreira and M. D. Kurz, "Subducted oceanic lithosphere and the origin of the 'High μ ' basalt helium isotopic signature," *Earth and Planetary Science Letters*, vol. 189, no. 1-2, pp. 49-57, 2001.
- [79] C. J. Hawkesworth and R. Vollmer, "Crustal contamination versus enriched mantle: $^{143}\text{Nd}/^{144}\text{Nd}$ and $^{87}\text{Sr}/^{86}\text{Sr}$ evidence from the Italian volcanics," *Contributions to Mineralogy and Petrology*, vol. 69, no. 2, pp. 151-165, 1979.
- [80] B. Marty, T. Trull, P. Lussiez, I. Basile, and J. C. Tanguy, "He, Ar, O, Sr and Nd isotope constraints on the origin and evolution of Mount Etna magmatism," *Earth and Planetary Science Letters*, vol. 126, no. 1-3, pp. 23-39, 1994.
- [81] C. J. Allègre, T. Staudacher, and P. Sarda, "Rare gas systematics: formation of the atmosphere, evolution and structure of the Earth's mantle," *Earth and Planetary Science Letters*, vol. 81, no. 2-3, pp. 127-150, 1987.
- [82] K. Hans Wedepohl, "The composition of the continental crust," *Geochimica et Cosmochimica Acta*, vol. 59, no. 7, pp. 1217-1232, 1995.
- [83] D. R. Hilton, J. A. Hoogewerff, M. J. Van Bergen, and K. Hammerschmidt, "Mapping magma sources in the east Sunda-Banda arcs, Indonesia: constraints from helium isotopes," *Geochimica et Cosmochimica Acta*, vol. 56, no. 2, pp. 851-859, 1992.
- [84] H. P. Eugster and D. R. Wones, "Stability relations of the ferruginous biotite, annite," *Journal of Petrology*, vol. 3, no. 1, pp. 82-125, 1962.

Research Article

The Distribution of Dissolved Methane and Its Air-Sea Flux in the Plume of a Seep Field, Lingtou Promontory, South China Sea

Pengfei Di ¹, Dong Feng ^{1,2,3} and Duofu Chen ^{2,3}

¹CAS Key Laboratory of Ocean and Marginal Sea Geology, South China Sea Institute of Oceanology, Chinese Academy of Sciences, Guangzhou, Guangdong 510301, China

²Laboratory for Marine Mineral Resources, Qingdao National Laboratory for Marine Science and Technology, Qingdao 266061, China

³Shanghai Engineering Research Center of Hadal Science and Technology, College of Marine Sciences, Shanghai Ocean University, Shanghai 201306, China

Correspondence should be addressed to Pengfei Di; pfd@scsio.ac.cn

Received 24 January 2019; Accepted 18 June 2019; Published 14 July 2019

Academic Editor: Giovanni Martinelli

Copyright © 2019 Pengfei Di et al. This is an open access article distributed under the Creative Commons Attribution License, which permits unrestricted use, distribution, and reproduction in any medium, provided the original work is properly cited.

Methane (CH₄), the most abundant hydrocarbon gas in the atmosphere, plays an important role in global climate change. Quantifying the dissolved methane and its air-sea flux from hydrocarbon seeps is therefore of great importance. Large quantities of natural gas are emitted from the seafloor to the coastal ocean near the Lingtou Promontory, South China Sea. We quantified concentrations of methane in surface and bottom waters at 48 stations in a 56 km² study area. High spatial variability in dissolved methane concentrations was observed in the surface mixed layer (0.5 m water depth) and bottom water (water-sediment interface), with values ranging from 2.90 nmol L⁻¹ to 13570.02 nmol L⁻¹ and from 4.98 nmol L⁻¹ to 31740.02 nmol L⁻¹, respectively. The significant difference between concentrations of dissolved methane in surface and bottom waters suggests that most of the methane emitted from the seafloor is dissolved in the water column. The dissolution of methane in seawater may result in local oxygen depletion that may lead to ecological effects. The δ¹³C values of dissolved methane ranging from −59.76‰ to −48.59‰ indicate a mixture of biogenic and thermogenic gas sources. The average air-sea methane flux of Yinggehai Basin was 672.57 μmol m⁻² d⁻¹, which cannot be ignored in environment assessment. Coastal regions, especially with hydrocarbon seeps in shallow waters of the continental margin, may therefore be an important source of methane to the atmosphere.

1. Introduction

After water vapor and CO₂, methane (CH₄) is the most important greenhouse gas in the atmosphere and plays an important role in global climate change. Methane is produced in oceanic sediments either by methanogens or through the breakdown of organic molecules [1, 2]. Modern-day atmospheric methane concentrations of 1.77 ppmv (parts per million by volume) are more than twice the preindustrial value of 0.71 ppm [3, 4]. Compared with carbon dioxide, methane is a more potent greenhouse gas, having a global warming potential that is 23 times higher on a 100 yr timescale [3, 4]. It is estimated that methane is released into the atmosphere worldwide at a rate of about 503–610 Tg yr⁻¹ [5]. Although

hydrocarbon seeps release about 8–65 Tg yr⁻¹ of methane into the ocean [6], only 4–15 Tg yr⁻¹ of methane is released into the atmosphere, accounting for about 1%–2% of the global atmospheric methane flux [7–12]. These values reveal that methane undergoes a complicated set of processes (involving both anaerobic and aerobic oxidation) in the ocean, with more than 85% of methane being consumed before reaching to the sea surface [13–16]. However, there is still substantial uncertainty surrounding estimates of the size and nature of methane sources and sinks and how their variations can affect atmospheric methane concentrations.

Natural hydrocarbon seeps in marine environments are widely distributed on the seabed of almost all continental margins, which are important sources of methane and other

greenhouse gases to the ocean and the atmosphere [9, 17–19]. Quantifying methane discharge from hydrocarbon seeps and its flux to the atmosphere is a major unsolved issue regarding the marine methane cycle. Hydrocarbon seeps may release methane dissolved in pore waters or, in the case of oversaturation, in the form of gas bubbles into the ocean [9, 17, 18, 20, 21]. When methane is emitted as gas bubbles, a fraction of the methane in the bubbles dissolves in the seawater via gas exchange during the bubbles' transport to the seawater surface, and the methane flux depends on release depth, bubble diameter, and the buoyancy force of the plume [22–24]. Methane can be released directly into the atmosphere from rising gas bubbles mainly in shallow waters (<100 m) while methane bubbles emitted from deep waters tend to become fully dissolved in the water column before reaching to the ocean surface. It has been shown that the flux and vertical transport of this methane are controlled by physical processes such as vertical mixing, turbulent diffusion, and upwelling [24, 25]. Bubble dissolution leads to patches of higher methane concentrations in the water column (from tens of nmol L^{-1} up to several $\mu\text{mol L}^{-1}$), for example, in the Coal Oil Point seep field [19]. However, the dissolved methane flux arising from the dissolution of gas bubbles during transit through the water column or from the discharge of methane-rich pore fluids from the sediment into the water column is particularly difficult to quantify. The quantification of this indirect flux is critical for understanding the marine hydrocarbon contribution to the total atmospheric methane source.

Coastal regions are important sources of methane ($13 \text{ Tg CH}_4 \text{ yr}^{-1}$) to the atmosphere [5, 26, 27]. Hundreds of hydrocarbon seeps are discovered in the coastal regions of Yinggehai Basin [28–30]. However, the distribution of dissolved methane and its air-sea fluxes has not been quantified. Sources and sinks of the seeping methane remain unclear. Here, we determined the distribution of dissolved methane from seawater samples and estimated the methane air-sea flux in the Lingtou Promontory seep area.

2. Study Area

The Yinggehai Basin, located to the southwest of Hainan Island ($16^\circ 50' - 20^\circ 00' \text{N}$, $107^\circ 00' - 111^\circ 50' \text{E}$), is one of the world's largest hydrocarbon seep regions [28, 31–33]. The basin is characterized by abundant hydrocarbon seeps, pockmarks, and mud volcanoes on the seabed [28, 31–33]. More than 120 hydrocarbon seeps have been found on the seabed at water depths of <50 m along the eastern edge of the basin near the western coast of Hainan Island. At these seeps, the gas rises to the sea surface to form a nearshore bubble zone [28]. The total gas flux emitted from these hydrocarbon seeps to the water surface has been estimated as $294\text{--}956 \text{ m}^3 \text{ yr}^{-1}$ based on the displacement of water estimated using an inverted funnel [28], whereas a total methane flux of 4.84×10^4 to $6.84 \times 10^4 \text{ m}^3 \text{ yr}^{-1}$ has been estimated for these seeps based on extrapolation of data obtained over 420 h using a gas flux measuring device on one hydrocarbon seep [29, 30, 34].

The Lingtou Promontory seep field is one of the most active areas in the Yinggehai Basin for natural hydrocarbon

seepage [29, 30]. Over 20 perennial hydrocarbon seeps are emitting gases within an area measuring approximately $580 \text{ m} \times 160 \text{ m}$ located $\sim 300 \text{ m}$ offshore Lingtou Promontory in Hainan Province, at water depths of 3–20 m (Figure 1(a)). It has been observed that gas bubbles (each up to 1–2 cm in diameter) are being emitted continuously from the hydrocarbon seeps on the seafloor (Figures 1(b) and 1(c)) and that these bubbles rise to the sea surface at about 10 cm s^{-1} and release their gases into the atmosphere [29, 30, 35]. Methane is released at rates ranging from 0.807×10^4 to $1.14 \times 10^4 \text{ m}^3 \text{ yr}^{-1}$ from 20 hydrocarbon seeps in the Lingtou Promontory seep area, assuming that the hydrocarbon seeps have a similar gas flux [29, 30]. However, this region has not been surveyed for dissolved methane distributions and air-sea fluxes to date.

3. Methods

On 19–20 August 2015, 96 seawater samples were sampled at 48 stations to quantify the dissolved methane concentration distribution along 4 west-east (W-E) transects from near-shore to the Yinggehai Basin (Figure 1(a) and Table 1). Sampling was carried out with a 5 L Niskin bottle coupled to a conductivity-temperature-depth (CTD) probe (RBR XR420) and a dissolved oxygen sensor (RBR) for the online monitoring of salinity, temperature, pressure, and dissolved oxygen (DO) concentrations in surface waters (0.5 m depth sampling level) and at the sea-sediment interface (bottom-water samples). The CTD sensors were calibrated to a temperature range of $2\text{--}35^\circ \text{C}$ with a resolution of 0.002°C , to a salinity range of $0\text{--}70 \text{ mS cm}^{-1}$ with a resolution of 0.001 mS cm^{-1} , and to a depth range of $0\text{--}6000 \text{ m}$ with a resolution of 0.001 m . The dissolved O_2 sensor could detect within the range $0\text{--}500 \mu\text{M}$ (saturation $0\text{--}120\%$) with a resolution of $<1 \mu\text{M}$ (saturation 0.4%) [36].

All water samples, once collected, were stored in 122 mL crimp-top sample bottles. All sample bottles were flushed with two volumes of water and filled completely to eliminate bubbles. Two to three drops of saturated HgCl_2 were added to the samples after collection, and the bottles were immediately capped with butyl rubber stoppers and crimp-sealed. To prevent the headspace gas from escaping through the rubber stopper, all bottles were stored stopper-side down until analysis. All samples were transported to the laboratory, and a 10 mL N_2 headspace was introduced into each bottle as described by Valentine et al. [37]. Two aliquots of the headspace were each analyzed for methane using a Wason/HP complete gas composition analyzer at the Guangzhou Institute of Geochemistry, Chinese Academy of Science (CAS), Guangzhou, China. Replicate analyses of samples yielded a precision of $\pm 2\%$ for samples with methane content. The methane concentration dissolved in seawater was calculated as described in Johnson et al. [38]:

$$C_L = C_G \left(\frac{\beta RT}{22.356} + \frac{V_G}{V_L} \right), \quad (1)$$

where C_L is the concentration of the gas to be measured in the liquid phase before equilibrium, C_G is the concentration

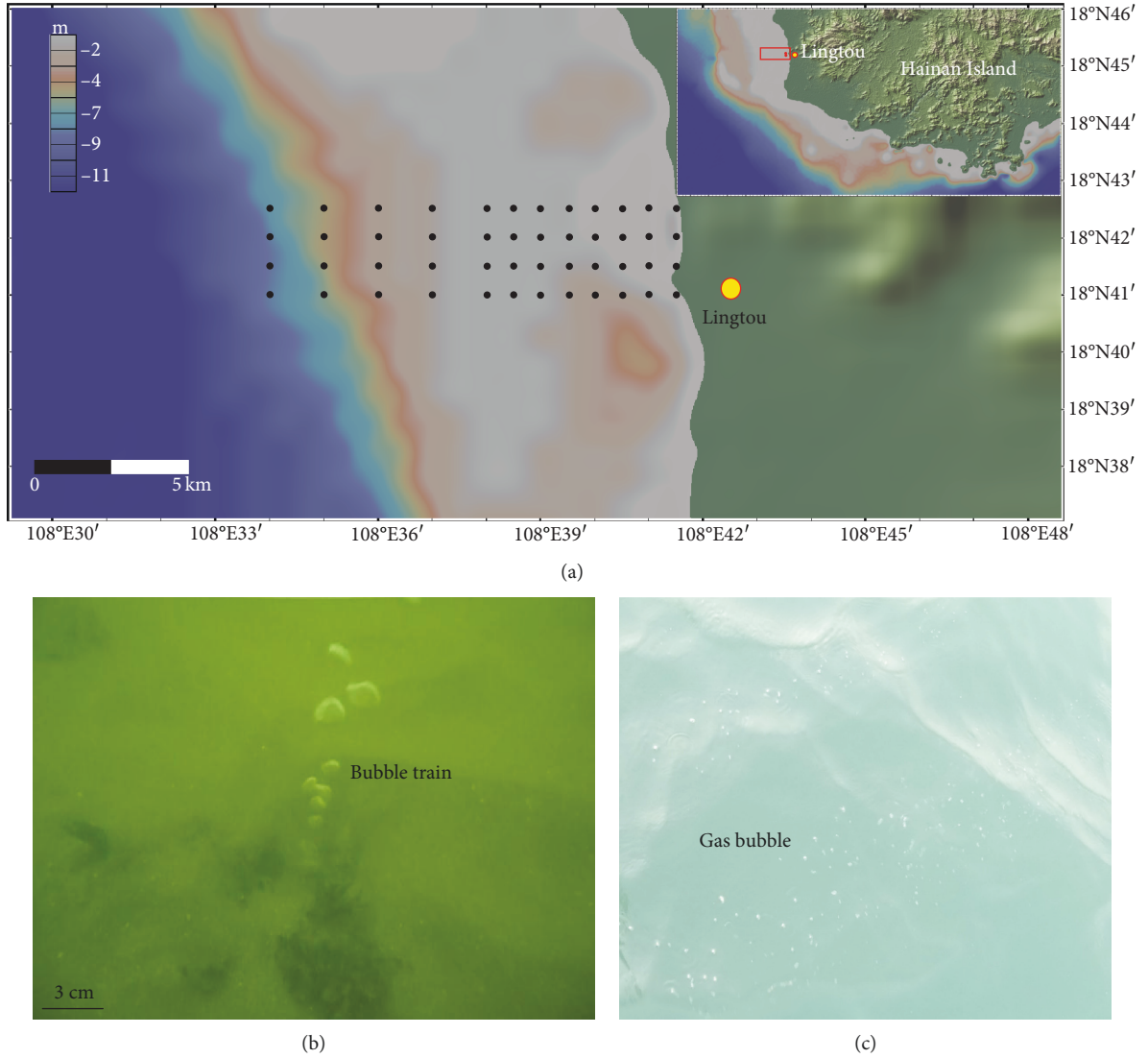


FIGURE 1: (a) Bathymetric map of the hydrocarbon seep area near Lingtou Promontory. The red dots show the distribution of the nearshore hydrocarbon seeps, and the black dots are the seawater sample grid. (b) Photograph of rising irregular gas bubbles from a seep site. (c) Gas bubbles at the sea surface.

of the gas to be measured in the gas phase after equilibrium, β is the Bunsen solubility of the gas to be measured ($\text{L L}^{-1} \text{atm}^{-1}$), R is the gas constant ($\text{L atm. mol}^{-1} \text{K}^{-1}$), and 22.356 is the molecular volume of methane (L mol^{-1}).

Seawater samples with high dissolved methane concentrations were analyzed to determine the stable carbon isotope composition of methane. Stable carbon isotope analyses were conducted using an isotope ratio mass spectrometer at the Guangzhou Institute of Geochemistry, CAS, Guangzhou, China. All isotopic ratios are presented in the δ notation with respect to the Vienna Pee Dee Belemnite (VPDB) standard and have an analytical error of $<1\%$.

The air-sea methane flux (F) was calculated as described in Leifer and MacDonald [39]:

$$F = K_w(C_w - C_a), \quad (2)$$

where K_w is the transfer velocity for methane at in situ temperatures (cm hr^{-1}), C_w is the measured dissolved methane concentration in seawater (nM), and C_a is the air-equilibrated seawater methane concentration (nM), which was calculated for in situ temperatures and salinities using the Bunsen solubility data of Wiesenburg and Guinasso [40]. We have assumed, for these calculations, an atmospheric methane mixing ratio of 1.80 ppmv, which in turn assumes an annual increase of ~ 7 ppbv [3]. The resulting flux is given in units of $\mu\text{mol m}^{-2} \text{d}^{-1}$. The determination of the transfer velocity, K_w , has been thoroughly discussed in Wanninkhof et al. [41]. For our purposes, we used the following relationship, as suggested by Wanninkhof [42], for wind speeds of $<15 \text{ m s}^{-1}$:

$$K_w = 0.24 * U^2 \left(\frac{Sc_{\text{CH}_4}}{660} \right)^{-0.5}, \quad (3)$$

TABLE 1: The CH_4 concentrations of bottom and surface seawater, as well as the O_2 concentration, temperature, water depth, salinity of all the sites, and the $\delta^{13}\text{C}_{\text{CH}_4}$ values in seawater and bubbles from the Lingtou Promontory seep area.

Station	Latitude	Longitude	Water depth (m)	CH_4 concentration (nmol L^{-1})	$\delta^{13}\text{C}$ (‰)	O_2 concentration (mL)	Salinity (‰)	Temperature (°C)
Dot 1	18°41'52"	108°41'13"	0.50	3.18	—	7.81	32.72	29.67
			4.10	10.00	—	8.13	32.62	29.38
Dot 2	18°41'37"	108°40'29"	0.50	11.27	—	7.57	33.14	29.37
			5.31	5472.08	—	7.82	33.21	29.16
Dot 3	18°41'58"	108°39'30"	0.50	7.19	—	7.42	33.41	29.21
			6.48	9.93	—	7.91	33.38	29.13
Dot 4	18°41'58"	108°38'57"	0.50	12.09	—	7.49	33.48	28.92
			7.10	11.06	—	7.94	33.37	29.00
Dot 5	18°42'02"	108°38'28"	0.50	19.74	—	7.31	33.49	29.12
			7.50	23.80	—	7.38	33.33	29.09
Dot 6	18°42'01"	108°37'51"	0.50	36.10	—	7.59	33.43	28.82
			8.07	10.95	—	7.49	33.26	28.61
Dot 7	18°42'02"	108°37'01"	0.50	19.55	—	7.43	33.39	28.84
			7.30	4.98	—	7.63	33.35	28.71
Dot 8	18°41'57"	108°35'58"	0.50	64.70	—	7.48	33.36	28.74
			5.34	28.54	—	7.82	33.24	28.74
Dot 9	18°41'58"	108°35'00"	0.50	9.65	—	7.39	33.39	28.71
			6.30	26.31	—	7.64	33.32	28.68
Dot 10	18°42'01"	108°34'00"	0.50	68.95	—	6.94	33.36	28.86
			7.67	9.13	—	7.23	33.36	28.78
Dot 11	18°42'27"	108°34'02"	0.50	7.62	—	7.01	33.37	28.96
			6.41	79.85	—	7.47	33.36	28.81
Dot 12	18°42'27"	108°35'01"	0.50	1500.49	—	7.29	33.39	28.90
			6.55	17.73	—	7.27	33.27	28.88
Dot 13	18°42'32"	108°36'00"	0.50	975.45	—	6.85	33.47	29.21
			5.22	50.36	—	7.19	33.39	29.05
Dot 14	18°42'43"	108°38'31"	0.50	11.43	—	7.02	33.41	29.42
			5.94	7.35	—	7.23	33.32	29.31
Dot 15	18°42'28"	108°38'35"	0.50	12.45	—	6.93	33.4	29.27
			7.36	45.40	—	7.15	33.38	29.23
Dot 16	18°42'25"	108°39'02"	0.50	10.56	—	7.17	33.38	29.28
			6.11	11.54	—	7.41	33.33	29.21
Dot 17	18°42'24"	108°39'34"	0.50	6.80	—	6.96	33.36	29.32
			7.38	65.62	—	7.13	33.38	29.28
Dot 18	18°42'33"	108°39'59"	0.50	26.09	—	7.04	33.35	29.47
			6.79	22.54	—	7.26	33.31	29.45
Dot 19	18°42'30"	108°40'31"	0.50	4140.60	—	7.12	33.23	29.68
			6.42	17.98	—	7.38	32.98	29.66
Dot 20	18°42'35"	108°41'05"	0.50	16.67	—	7.18	33.17	30.04
			5.48	9.01	—	7.67	33.15	30.02
Dot 21	18°41'59"	108°41'04"	0.50	19.15	—	7.22	33.17	29.98
			4.94	9.42	—	7.85	33.22	29.93
Dot 22	18°41'59"	108°41'29"	0.50	14.95	—	7.58	32.96	30.32
			4.7	390.64	—	8.08	32.93	30.31

TABLE 1: Continued.

Station	Latitude	Longitude	Water depth (m)	CH ₄ concentration (nmol L ⁻¹)	$\delta^{13}\text{C}$ (‰)	O ₂ concentration (mL)	Salinity (‰)	Temperature (°C)
Dot 23	18°40'59"	108°40'59"	0.50	12318.50	-59.17	7.15	33.04	29.55
			3.44	2313.53	—	7.23	33.08	29.49
Dot 24	18°41' 59.5"	108°40'29"	0.50	45.89	—	7.2	33.34	29.29
			4.45	31740.02	-59.54	7.36	33.34	29.28
Dot 25	18°40'59"	108°40'03"	0.50	13577.35	-59.76	7.26	33.34	29.23
			4.45	—	—	7.39	33.33	29.22
Dot 26	18°40'56"	108°39'15"	0.5	33.25	—	7.16	33.37	29.19
			3.72	209.05	—	7.12	33.38	29.16
Dot 27	18°40'59"	108°38'59"	0.5	171.06	—	7.18	33.39	29.22
			5.55	10.04	—	7.2	33.23	29.17
Dot 28	18°40' 59.9"	108°38'29"	0.5	12.23	—	7.12	33.38	29.31
			6.08	435.28	—	7.22	33.34	29.23
Dot 29	18°40' 59.5"	108°37'59"	0.5	8.84	—	7.17	33.38	29.22
			7.01	8.69	—	7.26	33.29	29.12
Dot 30	18°40' 59.3"	108°36'58"	0.5	107.98	—	7.2	33.39	28.68
			7.03	22.35	—	7.19	33.33	28.65
Dot 31	18°40' 59.7"	108°35' 58.2"	0.5	6.17	—	7.15	33.39	28.71
			5.74	23386.77	-48.59	7.2	33.25	28.66
Dot 32	18°41'01"	108°34' 59.4"	0.50	2.90	—	7.09	33.37	29.03
			5.75	9.99	—	7.25	33.27	28.87
Dot 33	18°40' 59.7"	108°33'58"	0.50	22.08	—	7.08	33.34	28.93
			6.96	5.17	—	7.2	33.32	28.75
Dot 34	18°41' 31.6"	108°34'00"	0.50	9.80	—	7.04	33.35	29.05
			10.38	171.94	—	7.29	33.12	28.79
Dot 35	18°41' 29.4"	108°35'01"	0.50	115.34	—	7.14	33.36	29.07
			9.76	107.83	—	7.3	33.32	29.04
Dot 36	18°41' 28.6"	108°36'02"	0.50	7.82	—	7.08	33.39	28.86
			6.52	101.58	—	7.23	33.28	28.85
Dot 37	18°41' 28.9"	108°37'01"	0.50	8.51	—	7.18	33.45	28.94
			5.27	547.26	—	7.22	33.3	28.81
Dot 38	18°41' 29.8"	108°38'01"	0.50	4.01	—	7.07	33.47	29.53
			6.70	573.54	—	7.17	33.35	29.14
Dot 39	18°41' 29.9"	108°38' 38.6"	0.5	7.69	—	7.04	33.43	29.57
			8.21	4.98	—	7.24	33.34	29.15
Dot 40	18°41' 29.8"	108°39'01"	0.5	250.93	—	7.14	33.65	29.49
			8.06	162.68	—	7.29	33.59	29.19
Dot 41	18°41' 29.3"	108°39' 30.7"	0.5	24.02	—	7.01	33.66	29.49
			7.59	9.10	—	7.18	33.64	29.18
Dot 42	18°41'29"	108°40'01"	0.5	7.75	—	7.24	33.35	29.56
			6.99	65.26	—	7.35	33.37	29.41
Dot 43	18°41' 28.4"	108°40' 31.1"	0.5	4.13	—	7.33	33.44	29.75
			6.37	233.55	—	7.42	33.34	29.65
Dot 44	18°41' 58.4"	108°39' 59.7"	0.5	28.80	—	7.1	33.8	29.59
			5.81	21.07	—	7.38	33.72	29.53

TABLE 1: Continued.

Station	Latitude	Longitude	Water depth (m)	CH ₄ concentration (nmol L ⁻¹)	δ ¹³ C (‰)	O ₂ concentration (mL)	Salinity (‰)	Temperature (°C)
Dot 45	18°41′	108°41′	0.5	153.62	—	7.46	33.16	30.09
	31.2″	11.8″	6.15	122.29	—	7.93	33.14	29.98
Dot 46	18°40′	108°41′04″	0.5	551.39	—	7.72	33.15	30.2
	54.6″		5.23	495.30	—	8.12	33.12	30.12
Dot 47	18°40′	108°41′	0.5	7.73	—	7.9	32.86	30.42
	58.7″	29.2″	5.35	169.94	—	8.02	32.76	30.25
Dot 48	18°41′	108°41′	0.5	19.05	—	7.89	32.79	30.49
	32.4″	35.4″	3.45	187.42	—	8.32	32.61	30.41
Dot 49	18°42′0.2″	108°41′	0.5	14.00	—	8.05	32.82	30.49
		28.1″	3.6	11.92	—	8.59	32.7	30.3
YG*	18°41′ 15.7″	108°41′ 37.0″	5.00	—	-35.98	—	—	—
Ys-1*	18°41.136′	108°41.304′	0.50	—	-35.51	—	—	—

*Data are taken from Huang et al. [28] and Di et al. [35].

where U is the average wind speed at 10 m above the water surface at the time of measurement and Sc_{CH_4} was determined from Wanninkhof [42] using

$$Sc_{CH_4} = A + Bt + Ct^2 + Dt^3 + Et^4, \quad (4)$$

where t is the in situ temperature (°C). Values for constants A (2102.2), B (-131.54), C (4.4931), D (-0.08676), and E (0.00070663) were taken from Wanninkhof [42].

Average wind speed data were measured using a revolving vane anemometer (GM8901, range: 0.3–45 m s⁻¹) at 0.5 m above sea level on-board and corrected to a standard height of 10 m by applying the following power law:

$$\frac{V_h}{V_{10}} = \left(\frac{h}{10}\right)^{0.13}, \quad (5)$$

where V_h is the mean wind speed at a height of h , V_{10} is the mean wind speed at 10 m, and h is the effective height of the anemometer above the mean sea level. The air-sea flux was calculated for all the surface water samples. Owing to the potential inaccuracy of wind speed measurements and the parameterizations of the gas transfer velocity, there may be uncertainties surrounding the air-sea flux data.

4. Results and Discussion

4.1. Concentrations of Dissolved Methane. Methane concentrations for the 96 seawater samples collected at the Ling-tou Promontory seep area are all above ~2 nmol L⁻¹ of the atmospheric equilibrium concentration (Table 1) [43]. The methane concentrations of surface seawater samples range from 2.90 nmol L⁻¹ to an anomalously high value of 13577.35 nmol L⁻¹ close to the hydrocarbon seep sites (Figure 2(a)). The average concentration for the surface

seawater samples is 704.40 nmol L⁻¹, which is much higher than the maximal value in surface waters (~1800 nmol L⁻¹) measured in the Santa Barbara Channel (Coal Oil Point), one of the most active known hydrocarbon seep areas in the world [39]. The methane concentrations of the bottom-water samples range from 4.98 nmol L⁻¹ to 31740.02 nmol L⁻¹ with an average value of 1376.75 nmol L^{-0.1}. The dissolved methane concentration data for the bottom-water samples reveal a distinct gas plume situated at the seafloor (Figure 2(b)). The anomalously high concentrations of methane dissolved in bottom waters are higher than the surface methane concentrations but much lower than the maximum methane concentration (2500 μmol L⁻¹) measured by the methane sensor at the hydrocarbon seep sites [29] as well as the calculated saturated methane concentration (1413 μmol L⁻¹) for conditions of 29°C, 0.538 mol kg⁻¹ salinity, and 1.26 bar pressure [44]. Similar results have been reported in other gas seepage areas, such as the North Sea, south of the Dogger Bank, and Tommeliten, the central North Sea [45]. The difference value of the dissolved methane concentrations between surface waters and bottom waters may be attributed to removal by microbial methane oxidation and lateral dispersion by physical transport, favored by strong tidal currents and ocean current [43, 45–47].

Exceptionally high methane concentrations usually point to hydrocarbon seepage. Measurements of methane concentration can be used to detect a gas plume situated near the seafloor, and the transect profiles can reveal discrete maxima that indicate whether the methane released from gas bubbles was emitted from the hydrocarbon seeps or from a horizon where methane from different sources converge. We divided our data into four transects from north to south along the shore. Along the fourth transect, two stations with extremely high methane concentrations were found to be associated with locations of intense hydrocarbon seepage at water depths of 3–20 m (Figure 3). One station with high methane

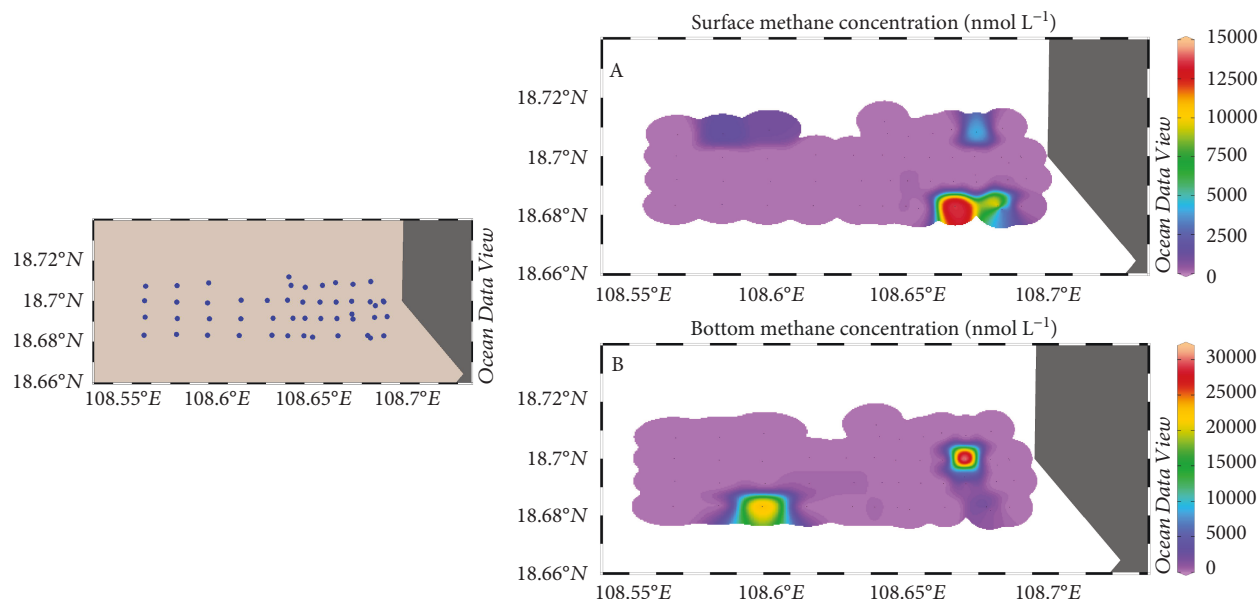


FIGURE 2: The distribution of dissolved methane concentrations in bottom waters and surface waters, respectively. The plot was generated using the Ocean Data View Version 4.5.7 (<https://odv.awi.de>) gridding weighted averages.

concentrations is close to the shore of the Lingtou Promontory at the surface, which indicates that methane was released from a horizon where different sources of methane converge. The other station with high methane concentrations is far offshore and in bottom waters, which indicates that methane was released from gas bubbles emitted from the hydrocarbon seeps. The high methane concentrations in bottom waters along the second and third transects, which eventually decrease offshore (Figure 3), indicate that methane is released from seafloor seeps. Surface methane concentrations were mostly in equilibrium with atmospheric concentrations along the second and third transects. Dissolved methane concentrations along the north transect were lower than in the other three transects, and surface methane concentrations were mostly in equilibrium with the atmosphere except for two locations (Figure 3), indicating that methane was being transported from nearby seafloor emissions by ocean currents. A similar result has been observed at 20 m water depth in the Coal Oil Point seep field near Santa Barbara, California [39].

4.2. Controls on Methane Distribution. Owing to the shallow depths (<20 m) and strong tidal currents, thermal or haline stratification does not occur in the Lingtou Promontory seep area because there are no salinity and temperature gradients between the surface and bottom waters (Figure 4). Due to the strong tidal currents and ocean currents, the dissolved O_2 concentrations remain in approximate equilibrium with atmospheric concentrations, with no gradients between the surface and bottom waters (Figure 4). In addition, the dissolved methane concentrations are not correlated with dissolved O_2 concentration, salinity, and temperature (Figure 4). Although dissolved methane concentrations in bottom waters were statistically higher than that in surface waters, the difference (on average ~48.8%) was much larger

than that in the nearshore shallow coast area of the North Sea (on average ~14%) [43], because gas bubbles are transported a long distance by ocean currents when they have risen to the sea surface. Hence, on account of the shallow depths and well-mixed water column, there is a loss of methane between the bottom and surface waters, unlike in deeper and stratified areas such as Tommeliten and south of the Dogger Bank [43].

The observed bubble emissions are responsible for generating the gas plume in the Lingtou Promontory (Figure 1). The methane maxima above the seafloor observed in the vertical profiles indicate a gaseous methane input from the seabed. Furthermore, the fact that methane maxima were observed above the seafloor suggests gas deposition from bubble dissolution. When gas bubbles rise through the water column, they expand because of the decrease in hydrostatic pressure and at the same time decrease in volume because of dissolution [48]. Owing to the dominating effect of the decrease in bubble size, the net buoyancy force decreases during ascent, and methane is deposited at water depths where hydrostatic equilibrium is reached and bubbles cannot continue moving. However, on account of the shallow water depths, the gas bubbles ($d = 1 - 2$ cm) contain approximately 95% methane on reaching the sea surface [24]. Therefore, there is little loss of methane from gas bubbles as they ascend from the bottom to the surface.

4.3. Air-Sea Methane Flux. Air-sea methane emission fluxes were estimated for water sampled at 0.5 m water depth in the surface mixed layer. The estimated fluxes range between 1.4 and 13058.44 $\mu\text{mol m}^{-2} \text{d}^{-1}$ in the nearshore Lingtou Promontory (Figure 5). The median value is 672.57 $\mu\text{mol m}^{-2} \text{d}^{-1}$, which is approximately four times the reported rate of methane emission in Santa Barbara Channel (Coal Oil Point; 180 $\mu\text{mol m}^{-2} \text{d}^{-1}$), one of the

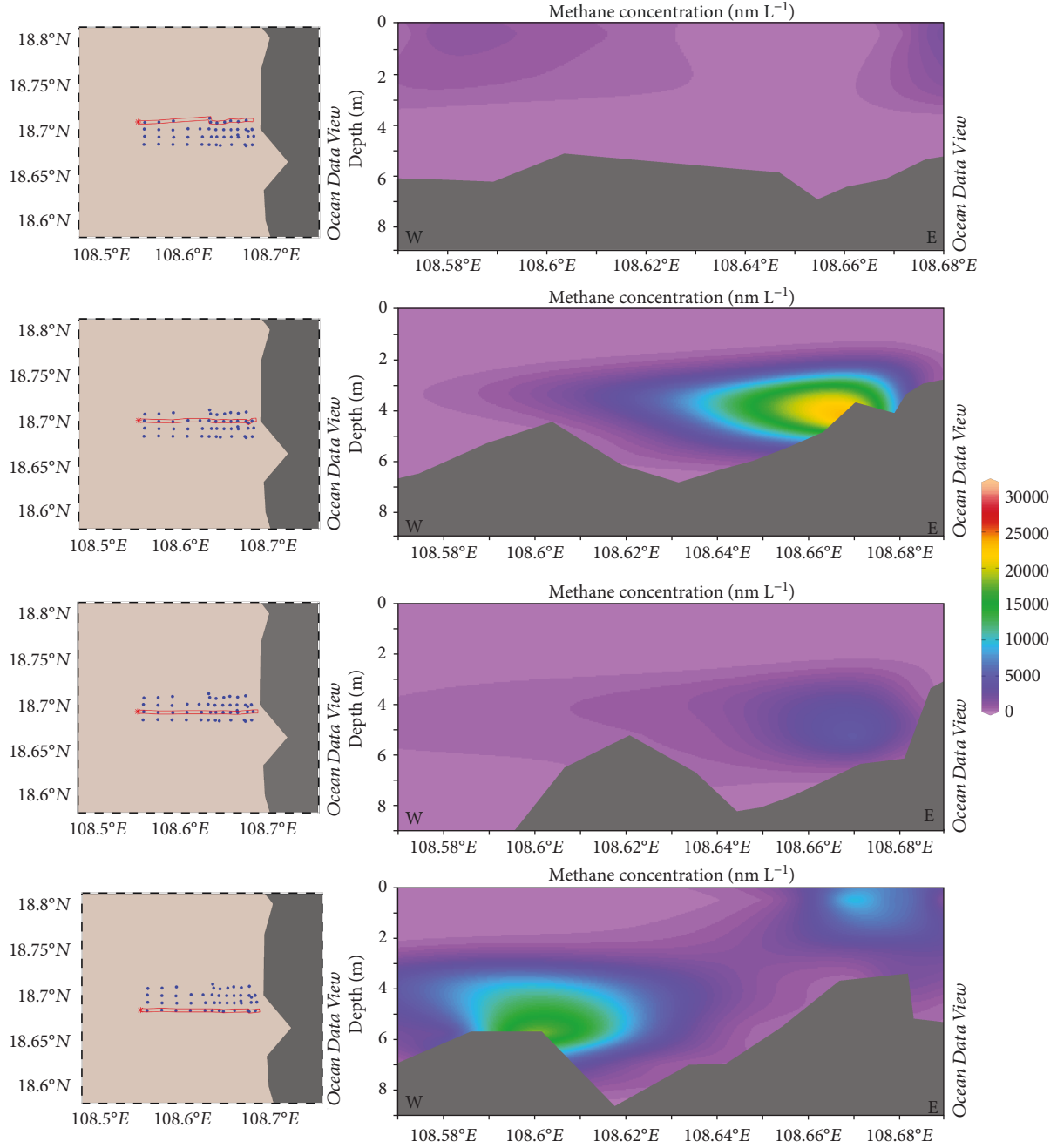


FIGURE 3: East-west transects of dissolved methane concentrations at the Lingtou Promontory seep area. The red stars are the starting point.

most active marine seep areas in the world [39]. The mean value is 18 times higher than the global average flux values for continental shelves (21.6 to $36.29 \mu\text{mol m}^{-2} \text{d}^{-1}$ [26]) and four orders of magnitude higher than values characteristic of the open ocean (0.2 – $0.5 \mu\text{mol m}^{-2} \text{d}^{-1}$) [49]. However, it has been estimated that 0.807×10^4 to $1.14 \times 10^4 \text{ m}^3 \text{yr}^{-1}$ of methane is emitted from hydrocarbon seeps [29, 30]. The total air-sea flux of methane in the nearshore Lingtou Promontory seep area is negligible compared with the flux of the methane bubbles. By analogy with the Lingtou Promontory seep area, other coastal regions of the Yinggehai Basin, such as the Yinggehai riv-

ulet mouth, Yazhou Bay, the Nanshan Promontory, and the Tianya Promontory (shallower than 50 m), may emit more than $672.57 \mu\text{mol m}^{-2} \text{d}^{-1}$ of methane to the atmosphere [28]. Therefore, the coastal regions of the Yinggehai Basin in the hydrocarbon seep areas are significant sources of methane to the atmosphere, and the air-sea methane fluxes were probably underestimated.

4.4. Methane Source. Methane-rich fluids forming gas flares at the seafloor migrate along faults and/or stratigraphic boundaries. Orange et al. [50] and Forrest et al. [51] have shown that the linear arrangement of hydrocarbon seeps on

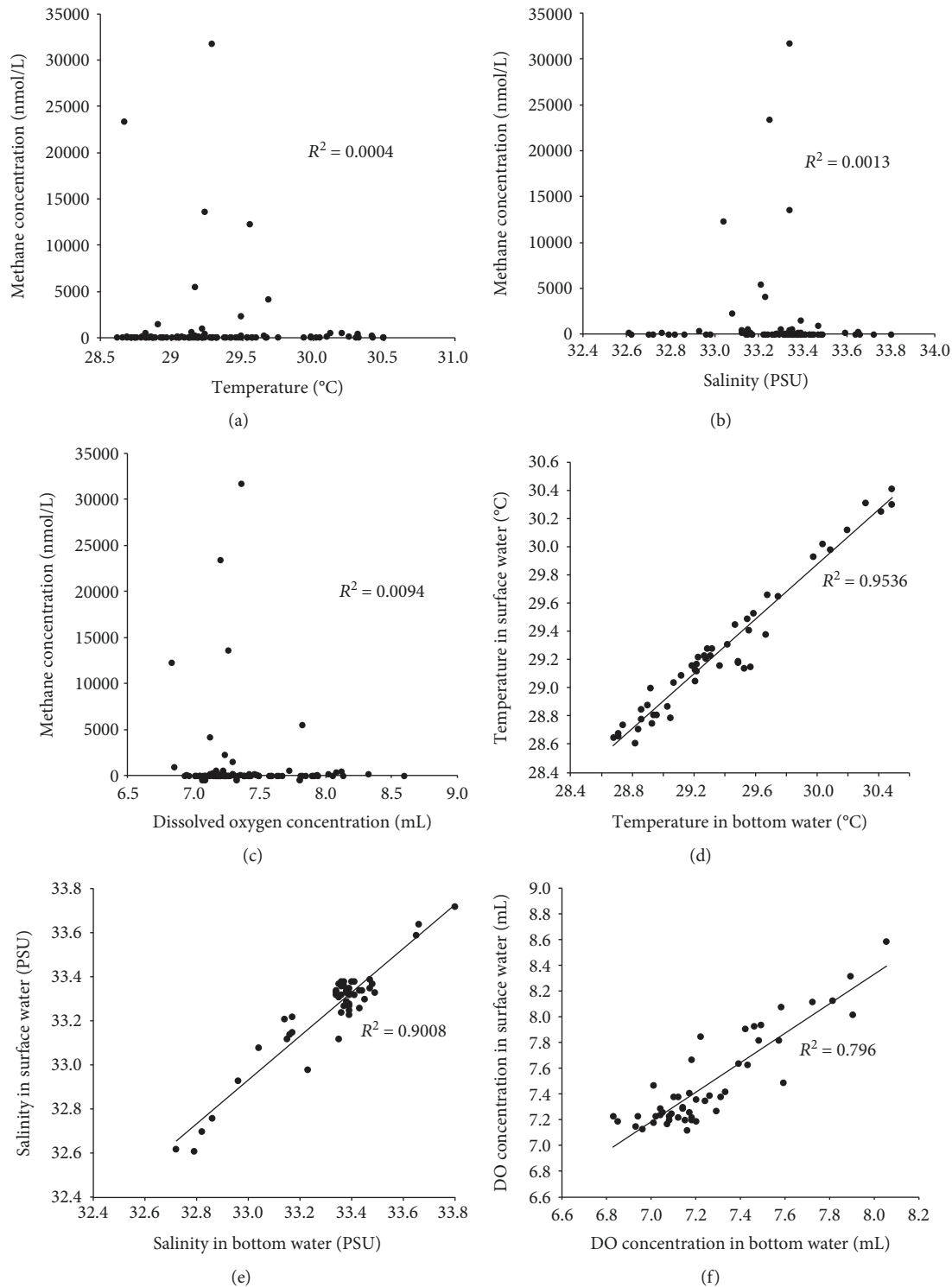


FIGURE 4: Dissolved methane concentrations in relation to dissolved oxygen concentration (a), salinity (b), and temperature (c) and comparison of temperature, salinity, and dissolved O_2 concentration in surface and bottom water (d–f).

the seabed is controlled by a neighboring fault. All gas bubble flares located along the shore of Hanna Island are in the vicinity of the No. 1 Fault [28, 35]. Generally, anomalously high methane concentrations in seawater are associated with hydrocarbon seeps, such as the COP seep area and the western Spitsbergen shelf, which are in turn related to adjacent

faults [39, 52–55]. In the Lingtou Promontory seep area, we further suggest that the sandy sediments facilitate the migration of methane-rich fluid to the seafloor. Hence, we assume fluid migration along structural pathways, particularly the No. 1 Fault. In addition, according to the seismic profile of the central diapir zone in the Yinggehai Basin, methane-

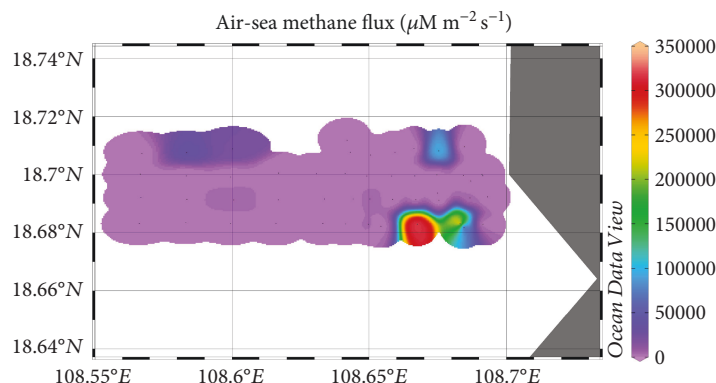


FIGURE 5: The air-sea flux of methane at the Lingtou Promontory seep area. The average wind speed in this area was 5.1 m s^{-1} .

rich fluids may be expelled by mud diapirs and migrate along the dipping strata [56]. A similar phenomenon was also reported for the offshore Prins Karls Forland at ~250 m water depth [57].

To further constrain the sources of methane, we measured the stable carbon isotopic composition of dissolved methane in four water samples with high methane concentrations that had been collected from Lingtou Promontory seep area. The $\delta^{13}\text{C}_{\text{CH}_4}$ values of two of these samples were -59.76‰ and -48.59‰ (Table 1). The fact that $\delta^{13}\text{C}_{\text{CH}_4}$ values in a sea-surface and sea-sediment interface sample are similar suggests that aerobic microbial oxidation is negligible in shallow waters (<10 m).

The $\delta^{13}\text{C}_{\text{CH}_4}$ values of gas bubbles collected from seeps and from the sea surface in the study area are -35.98‰ and -35.51‰ , respectively (Table 1) [28, 35]. These $\delta^{13}\text{C}_{\text{CH}_4}$ values are distinctly higher than those measured in seawater, which reflects the mixing of methane from gas bubbles with biogenic methane generated in sediments. Without background $\delta^{13}\text{C}_{\text{CH}_4}$ values from the bottom and the surface ocean, we could not fully establish the mixing fraction of the methane. Notably, we were able to smell sulfurous odors in sediments collected in the shallow waters of the Lingtou Promontory seep area. It is concluded that the methane originally discharged at the seafloor was oxidized before sampling. However, we do not discount the possibility that the methane could have been removed by migration or preferential microbial oxidation [58, 59].

5. Conclusions

We observed high spatial variability in dissolved methane concentrations in surface and bottom waters in the Lingtou Promontory seep area. Dissolved methane concentrations in surface waters and bottom waters range from 2.90 to $13577.35 \text{ nmol L}^{-1}$ and from 4.98 to $31740.02 \text{ nmol L}^{-1}$, respectively, indicating oversaturation at all stations. The persistent anomalously high methane concentrations in seawater indicate an efficient transfer of dissolved methane from the seafloor to the surface waters. Furthermore, $\delta^{13}\text{C}$ values of the dissolved methane in the studied seawater range from

-59.76‰ to -48.59‰ , indicating a mixed thermogenic and biogenic methane from the sediment. The measured average methane flux ($\sim 672.57 \text{ } \mu\text{mol m}^{-2} \text{ s}^{-1}$) is much higher than values characteristic of continental shelves. It is suggested that the coastal regions of Yinggehai Basin may emit more than $672.57 \text{ } \mu\text{mol m}^{-2} \text{ d}^{-1}$ of methane to the atmosphere. Coastal regions, especially shallow hydrocarbon seep areas, on the continental margin may therefore be an important hot spot of methane emissions to the atmosphere.

Data Availability

The data used to support the findings of this study are available from the corresponding author upon request.

Conflicts of Interest

The authors declare that there are no conflicts of interest regarding the publication of this paper.

Acknowledgments

We thank Dr. Baojia Huang for providing the coordinates of the gas seeps. This study was partially supported by the National Key R&D Program of China (2017YFC0307704) and the National Natural Science Foundation of China (41676046 and 41730528).

References

- [1] D. A. Stolper, M. Lawson, C. L. Davis et al., "Formation temperatures of thermogenic and biogenic methane," *Science*, vol. 344, no. 6191, pp. 1500–1503, 2014.
- [2] A. Wilhelms, S. R. Larter, I. Head, P. Farrimond, R. di-Primio, and C. Zwach, "Biodegradation of oil in uplifted basins prevented by deep-burial sterilization," *Nature*, vol. 411, no. 6841, pp. 1034–1037, 2001.
- [3] IPCC, *Climate Change 2013 – The Physical Science Basis – Contribution of Working Group I to the Fifth Assessment Report of the Intergovernmental Panel on Climate Change*, Cambridge University Press, 2013.
- [4] IPCC, *IPCC fourth assessment report (AR4), in Climate Change 2007: The Physical Science Basis. Contribution of Working Group I to the Fourth Assessment Report of the*

- Intergovernmental Panel on Climate Change*, Cambridge University Press, 2007.
- [5] G. Rehder, R. S. Keir, E. Suess, and T. Pohlmann, "The multiple sources and patterns of methane in North Sea waters," *Aquatic Geochemistry*, vol. 4, no. 3/4, pp. 403–427, 1998.
 - [6] V. Ramaswamy, O. Boucher, J. Haigh et al., "Radiative forcing of climate change," in *Climate Change*, pp. 349–416, Cambridge University Press, Cambridge, UK, 2001.
 - [7] M. Hovland, A. G. Judd, and R. A. Burke Jr., "The global flux of methane from shallow submarine sediments," *Chemosphere*, vol. 26, no. 1–4, pp. 559–578, 1993.
 - [8] G. Etiope, "Natural emissions of methane from geological seepage in Europe," *Atmospheric Environment*, vol. 43, no. 7, pp. 1430–1443, 2009.
 - [9] A. G. Judd, M. Hovland, L. I. Dimitrov, S. Garcia Gil, and V. Jukes, "The geological methane budget at continental margins and its influence on climate change," *Geofluids*, vol. 2, no. 2, 126 pages, 2002.
 - [10] A. G. Judd, "Natural seabed gas seeps as sources of atmospheric methane," *Environmental Geology*, vol. 46, no. 8, pp. 988–996, 2004.
 - [11] D. Wuebbles and K. Hayhoe, "Atmospheric methane: trends and impacts," in *Non-CO₂ Greenhouse Gases: Scientific Understanding, Control and Implementation*, pp. 1–44, Springer, Netherlands, 2000.
 - [12] D. J. Wuebbles and K. Hayhoe, "Atmospheric methane and global change," *Earth-Science Reviews*, vol. 57, no. 3–4, pp. 177–210, 2002.
 - [13] W. S. Reece, "Oceanic methane biogeochemistry," *Chemical Reviews*, vol. 107, no. 2, pp. 486–513, 2007.
 - [14] A. Boetius, K. Ravensschlag, C. J. Schubert et al., "A marine microbial consortium apparently mediating anaerobic oxidation of methane," *Nature*, vol. 407, no. 6804, pp. 623–626, 2000.
 - [15] K. Knittel and A. Boetius, "Anaerobic oxidation of methane: progress with an unknown process," *Annual Review of Microbiology*, vol. 63, no. 1, pp. 311–334, 2009.
 - [16] P. Regnier, A. W. Dale, S. Arndt, D. E. LaRowe, J. Mogollón, and P. van Cappellen, "Quantitative analysis of anaerobic oxidation of methane (AOM) in marine sediments: a modeling perspective," *Earth-Science Reviews*, vol. 106, no. 1–2, pp. 105–130, 2011.
 - [17] K. A. Campbell, "Hydrocarbon seep and hydrothermal vent paleoenvironments and paleontology: past developments and future research directions," *Palaeogeography, Palaeoclimatology, Palaeoecology*, vol. 232, no. 2–4, pp. 362–407, 2006.
 - [18] A. Judd and M. Hovland, *Submarine Fluid Flow, the Impact on Geology, Biology, and the Marine Environment*, Cambridge University Press, 2007.
 - [19] L. Naudts, J. Greinert, J. Poort et al., "Active venting sites on the gas-hydrate-bearing Hikurangi Margin, off New Zealand: diffusive- versus bubble-released methane," *Marine Geology*, vol. 272, no. 1–4, pp. 233–250, 2010.
 - [20] S. Mau, M. B. Heintz, and D. L. Valentine, "Quantification of CH₄ loss and transport in dissolved plumes of the Santa Barbara Channel, California," *Continental Shelf Research*, vol. 32, pp. 110–120, 2012.
 - [21] M. D. Tryon, K. M. Brown, and M. E. Torres, "Fluid and chemical flux in and out of sediments hosting methane hydrate deposits on Hydrate Ridge, OR, II: hydrological processes," *Earth and Planetary Science Letters*, vol. 201, no. 3–4, pp. 541–557, 2002.
 - [22] J. Greinert and D. F. McGinnis, "Single bubble dissolution model—the graphical user interface SiBu-GUI," *Environmental Modelling & Software*, vol. 24, no. 8, pp. 1012–1013, 2009.
 - [23] P. Linke, S. Sommer, L. Rovelli, and D. F. McGinnis, "Physical limitations of dissolved methane fluxes: the role of bottom-boundary layer processes," *Marine Geology*, vol. 272, no. 1–4, pp. 209–222, 2010.
 - [24] D. F. McGinnis, J. Greinert, Y. Artemov, S. E. Beaubien, and A. Wüest, "Fate of rising methane bubbles in stratified waters: how much methane reaches the atmosphere?," *Journal of Geophysical Research*, vol. 111, no. C9, article C09007, 2006.
 - [25] G. Rehder, R. W. Collier, K. Heeschen, P. M. Kosro, J. Barth, and E. Suess, "Enhanced marine CH₄ emissions to the atmosphere off Oregon caused by coastal upwelling," *Global Biogeochemical Cycles*, vol. 16, no. 3, pp. 2–1–2–11, 2002.
 - [26] H. W. Bange, U. H. Bartell, S. Rapsomanikis, and M. O. Andreae, "Methane in the Baltic and North seas and a reassessment of the marine emissions of methane," *Global Biogeochemical Cycles*, vol. 8, no. 4, pp. 465–480, 1994.
 - [27] R. C. Upstill-Goddard, J. Barnes, T. Frost, S. Punshon, and N. J. P. Owens, "Methane in the southern North Sea: low-salinity inputs, estuarine removal, and atmospheric flux," *Global Biogeochemical Cycles*, vol. 14, no. 4, pp. 1205–1217, 2000.
 - [28] B. Huang, X. Xiao, X. Li, and D. Cai, "Spatial distribution and geochemistry of the nearshore gas seepages and their implications to natural gas migration in the Yinggehai Basin, offshore South China Sea," *Marine and Petroleum Geology*, vol. 26, no. 6, pp. 928–935, 2009.
 - [29] P. Di, D. Feng, and D. Chen, "In-situ and on-line measurement of gas flux at a hydrocarbon seep from the northern South China Sea," *Continental Shelf Research*, vol. 81, pp. 80–87, 2014.
 - [30] P. Di, D. Feng, and D. Chen, "Temporal variation in natural gas seep rate and influence factors in the Lingtou promontory seep field of the northern South China Sea," *Terrestrial, Atmospheric and Oceanic Sciences*, vol. 25, no. 5, pp. 665–672, 2014.
 - [31] B. Huang, X. Xiao, and X. Li, "Geochemistry and origins of natural gases in the Yinggehai and Qiongdongnan Basins, offshore South China Sea," *Organic Geochemistry*, vol. 34, no. 7, pp. 1009–1025, 2003.
 - [32] B. Huang, X. Xiao, and W. Zhu, "Geochemistry, origin, and accumulation of CO₂ in natural gases of the Yinggehai Basin, offshore South China Sea," *AAPG Bulletin*, vol. 88, no. 9, pp. 1277–1293, 2004.
 - [33] B. Huang, X. Xiao, Z. Hu, and P. Yi, "Geochemistry and episodic accumulation of natural gases from the Ledong gas field in the Yinggehai Basin, offshore South China Sea," *Organic Geochemistry*, vol. 36, no. 12, pp. 1689–1702, 2005.
 - [34] P. Di, Q. Chen, and D. Chen, "Quantification of methane fluxes from hydrocarbon seeps to the ocean and atmosphere: development of an *in situ* and online gas flux measuring system," *Journal of Ocean University of China*, vol. 16, no. 3, pp. 447–454, 2017.
 - [35] P. Di, D. Feng, and D. Chen, "The distribution and variation in the gas composition of macro-seeps on the near-shore Lingtou Promontory in the South China Sea," *Acta Oceanologica Sinica*, vol. 35, no. 11, pp. 120–125, 2016.

- [36] A. H. Knap, A. E. Michaels, A. Close, H. Ducklow, and A. Dickson, "Protocols for the Joint Global Ocean Flux Study (JGOFS) core measurements," *JGOFS Report Nr. 19*, 1996.
- [37] D. L. Valentine, D. C. Blanton, W. S. Reeburgh, and M. Kastner, "Water column methane oxidation adjacent to an area of active hydrate dissociation, Eel river Basin," *Geochimica et Cosmochimica Acta*, vol. 65, no. 16, pp. 2633–2640, 2001.
- [38] K. M. Johnson, J. E. Hughes, P. L. Donaghay, and J. M. Sieburth, "Bottle –calibration static head space method for the determination of methane dissolved in seawater," *Analytical Chemistry*, vol. 62, no. 21, pp. 2408–2412, 1990.
- [39] I. Leifer and I. MacDonald, "Dynamics of the gas flux from shallow gas hydrate deposits: interaction between oily hydrate bubbles and the oceanic environment," *Earth and Planetary Science Letters*, vol. 210, no. 3–4, pp. 411–424, 2003.
- [40] D. A. Wiesenburg and N. L. Guinasso, "Equilibrium solubilities of methane, carbon monoxide, and hydrogen in water and sea water," *Journal of Chemical & Engineering Data*, vol. 24, no. 4, pp. 356–360, 1979.
- [41] R. Wanninkhof, W. E. Asher, D. T. Ho, C. Sweeney, and W. R. McGillis, "Advances in quantifying air–sea gas exchange and environmental forcing," *Annual Review of Marine Science*, vol. 1, no. 1, pp. 213–244, 2009.
- [42] R. Wanninkhof, "Relationship between wind speed and gas exchange over the ocean revisited," *Limnology and Oceanography: Methods*, vol. 12, no. 6, pp. 351–362, 2014.
- [43] A. V. Borges, W. Champenois, N. Gypens, B. Delille, and J. Harlay, "Massive marine methane emissions from near-shore shallow coastal areas," *Scientific Reports*, vol. 6, no. 1, article 27908, 2016.
- [44] Z. Duan and S. Mao, "A thermodynamic model for calculating methane solubility, density and gas phase composition of methane-bearing aqueous fluids from 273 to 523 K and from 1 to 2000 bar," *Geochimica et Cosmochimica Acta*, vol. 70, no. 13, pp. 3369–3386, 2006.
- [45] S. Mau, M. Römer, M. E. Torres et al., "Widespread methane seepage along the continental margin off Svalbard - from Bjørnøya to Kongsfjorden," *Science Reports*, vol. 7, no. 1, article 42997, 2017.
- [46] S. Mau, T. Gentz, J. H. Körber et al., "Seasonal methane accumulation and release from a gas emission site in the central North Sea," *Biogeosciences*, vol. 12, no. 18, pp. 5261–5276, 2015.
- [47] J. A. Screen and I. Simmonds, "The central role of diminishing sea ice in recent Arctic temperature amplification," *Nature*, vol. 464, no. 7293, pp. 1334–1337, 2010.
- [48] I. Leifer and R. K. Patro, "The bubble mechanism for methane transport from the shallow sea bed to the surface: a review and sensitivity study," *Continental Shelf Research*, vol. 22, no. 16, pp. 2409–2428, 2002.
- [49] T. S. Rhee, A. J. Kettle, and M. O. Andreae, "Methane and nitrous oxide emissions from the ocean: a reassessment using basin-wide observations in the Atlantic," *Journal of Geophysical Research*, vol. 114, no. D12, article D12304, 2009.
- [50] D. L. Orange, H. G. Greene, D. Reed et al., "Widespread fluid expulsion on a translational continental margin: mud volcanoes, fault zones, headless canyons, and organic-rich substrate in Monterey Bay, California," *Geological Society of America Bulletin*, vol. 111, no. 7, pp. 992–1009, 1999.
- [51] M. J. Forrest, J. Ledesma-Vázquez, W. Ussler III, J. T. Kulongoski, D. R. Hilton, and H. G. Greene, "Gas geochemistry of a shallow submarine hydrothermal vent associated with the El Requesón fault zone, Bahía Concepción, Baja California Sur, México," *Chemical Geology*, vol. 224, no. 1–3, pp. 82–95, 2005.
- [52] J. Knies, E. Damm, J. Gutt, U. Mann, and L. Pinturier, "Near-surface hydrocarbon anomalies in shelf sediments off Spitsbergen: evidences for past seepages," *Geochemistry, Geophysics, Geosystems*, vol. 5, no. 6, 2004.
- [53] E. Damm, A. Mackensen, G. Budéus, E. Faber, and C. Hanfland, "Pathways of methane in seawater: plume spreading in an Arctic shelf environment (SW-Spitsbergen)," *Continental Shelf Research*, vol. 25, no. 12–13, pp. 1453–1472, 2005.
- [54] I. Leifer and D. Culling, "Formation of seep bubble plumes in the Coal Oil Point seep field," *Geo-Marine Letters*, vol. 30, no. 3–4, pp. 339–353, 2010.
- [55] S. Mau, M. B. Heintz, F. S. Kinnaman, and D. L. Valentine, "Compositional variability and air–sea flux of ethane and propane in the plume of a large, marine seep field near Coal Oil Point, CA," *Geo-Marine Letters*, vol. 30, no. 3–4, pp. 367–378, 2010.
- [56] P. F. Di, H. G. Huang, B. J. Huang, J. X. He, and D. F. Chen, "Seabed pockmark formation associated with mud diapir development and fluid activities in the Yinggehai Basin of the South China Sea," *Journal of Tropical Oceanography*, vol. 31, pp. 26–36, 2012.
- [57] A. Rajan, J. Mienert, and S. Bünz, "Acoustic evidence for a gas migration and release system in Arctic glaciated continental margins offshore NW-Svalbard," *Marine and Petroleum Geology*, vol. 32, no. 1, pp. 36–49, 2012.
- [58] A. Prinzhofer and É. Pernaton, "Isotopically light methane in natural gas: bacterial imprint or diffusive fractionation," *Chemical Geology*, vol. 142, no. 3–4, pp. 193–200, 1997.
- [59] S. D. Mendes, M. C. Redmond, K. Voiggritter, C. Perez, R. Scarlett, and D. L. Valentine, "Marine microbes rapidly adapt to consume ethane, propane, and butane within the dissolved hydrocarbon plume of a natural seep," *Journal of Geophysical Research: Oceans*, vol. 120, no. 3, pp. 1937–1953, 2015.

Research Article

Carbon and Hydrogen Isotopic Reversals in Highly Mature Coal-Derived Gases: A Case Study of Paleozoic Gases in the Southern Ordos Basin, China

Dan Liu ^{1,2}

¹*Institute of Geology and Geophysics, Chinese Academy of Sciences, Beijing 100029, China*

²*Institute of Earth Science, Chinese Academy of Sciences, Beijing 100029, China*

Correspondence should be addressed to Dan Liu; liudan@mail.iggcas.ac.cn

Received 12 February 2019; Revised 13 May 2019; Accepted 11 June 2019; Published 11 July 2019

Academic Editor: Francesco Italiano

Copyright © 2019 Dan Liu. This is an open access article distributed under the Creative Commons Attribution License, which permits unrestricted use, distribution, and reproduction in any medium, provided the original work is properly cited.

The compositional carbon isotopic series $\delta^{13}\text{C}-\text{CH}_4 < \delta^{13}\text{C}-\text{C}_2\text{H}_6 < \delta^{13}\text{C}-\text{C}_3\text{H}_8 < \delta^{13}\text{C}-\text{C}_4\text{H}_{10}$ is common in thermogenic gases. With the exploration of deeper strata, however, isotopic reversals ($\delta^{13}\text{C}-\text{CH}_4 > \delta^{13}\text{C}-\text{C}_2\text{H}_6 > \delta^{13}\text{C}-\text{C}_3\text{H}_8$) in overmature unconventional shale gases and conventional (coal-derived) gases have been identified. Paleozoic gases in the southern Ordos Basin, China, with partial or complete isotopic reversals, were studied as examples of isotopic fractionation in overmature coal-derived gases. Isotopic compositions of gases of different maturities from the Ordos Basin and shale gases from around the world were compared. Results indicate that carbon isotopic series are related to maturity. Complete isotopic reversal occurs mostly in regions with vitrinite reflectance (R_o) $> 2.4\%$. Where $2.4\% > R_o > 2.0\%$, almost all gases display partial isotopic reversal, with $\delta^{13}\text{C}-\text{CH}_4 > \delta^{13}\text{C}-\text{C}_2\text{H}_6$ or $\delta^{13}\text{C}-\text{C}_2\text{H}_6 > \delta^{13}\text{C}-\text{C}_3\text{H}_8$. Carbon isotopic reversal in coal-derived gases is not caused by abiotic origin, the mixing of gases from different types of source rock, abiotic polymerization, wet gas cracking, and other mechanisms that contribute to reversal in shale gases. Based on the unique structure of coaly source rock and the geology of the Ordos Basin, closed-system aromatization-polycondensation reactions are considered the most likely cause of carbon isotopic reversal. During the reactions, isotopically light gases are generated by recombination of previously formed hydrocarbons and residual kerogen-coal. Hydrogen isotopic reversal in the southern Ordos Basin might also be caused by aromatization-polycondensation reactions.

1. Introduction

The carbon isotopic composition of natural gas can be used to determine its origin, source, and maturity [1, 2]. In thermogenic gas reactions, $^{12}\text{C}-^{12}\text{C}$ bonds usually break before $^{12}\text{C}-^{13}\text{C}$ bonds, resulting in kinetic isotopic fractionation [2] and causing natural gas to follow two evolutionary trends, with carbon isotopes becoming heavier as the component carbon number increases, forming a positive isotopic series with $\delta^{13}\text{C}-\text{CH}_4 < \delta^{13}\text{C}-\text{C}_2\text{H}_6 < \delta^{13}\text{C}-\text{C}_3\text{H}_8 < \delta^{13}\text{C}-\text{C}_4\text{H}_{10}$, and with each component C becoming enriched in ^{13}C as gas maturity increases [1].

As exploration of Paleozoic gas in the Ordos Basin has expanded into the southern part of the basin, more gases have been found to have carbon and hydrogen isotopic reversals. Most previous studies have attributed the partial

carbon isotopic reversal ($\delta^{13}\text{C}-\text{CH}_4 < \delta^{13}\text{C}-\text{C}_2\text{H}_6 > \delta^{13}\text{C}-\text{C}_3\text{H}_8$) of Ordos gases to the mixing of gases generated from different source rocks [3], (Yang et al., 2012), [4–7]. Recent studies have reported complete carbon isotopic reversals ($\delta^{13}\text{C}-\text{CH}_4 > \delta^{13}\text{C}-\text{C}_2\text{H}_6 > \delta^{13}\text{C}-\text{C}_3\text{H}_8$) in Ordos gases [8–12], with all suggesting that such reversals are caused by high temperatures ($> 200^\circ\text{C}$), with isotopic reversal in shale gas having the same mechanism. However, there are problems with this explanation as follows: (1) shale gas is an oil-type gas generated from type I and type II kerogen, whereas Ordos gas is mainly coal derived and generated from type III kerogen, with different gas-generation reactions occurring in these sources; (2) complete carbon isotopic reversal is universal in overmature shale gases [13–15], but not all overmature coal-derived gas has complete carbon isotopic reversals, as in gas from the southern Ordos Basin [16]; and

(3) gases in the southern Ordos Basin display unique characteristics that differ from those of overmature shale gas, such as the evolutionary trend of hydrogen isotopes.

Here, the geochemical characteristics of southern Ordos gas and shale gas are compared, with isotopic fractionation of overmature coal-derived gas being considered separately from shale gas. Geochemical data for gases from other fields in the Ordos Basin with different maturities are considered to elucidate isotopic evolution in the Ordos Basin. The cause of hydrogen isotopic reversal in the southern Ordos Basin is also discussed.

2. Geological Setting

The Ordos Basin is the second largest sedimentary basin in China, with Paleozoic strata occurring over an area of $>250,000 \text{ km}^2$ [16]. This basin is a petroliferous cratonic basin with stable subsidence, depression displacement, visible torsion, and multiple cycles of deposition [8]. Several giant gas fields, each containing >100 billion cubic metres (bcm) of proven gas reserves, have been discovered in the Paleozoic strata of the basin, with most gas being in the upper Paleozoic reservoirs such as the Sulige, Shenmu, Daniudi, and Yan'an gas fields. Upper Paleozoic and lower Paleozoic-Ordovician carbonate rocks provide the reservoir in the Jingbian field (Figure 1). Exploration of the Jingbian field has increased recently, with many wells being drilled in the overmature southern Jingbian area, targeting both lower and upper Paleozoic gas systems [16] and providing an unprecedented opportunity to improve our understanding of the geochemistry of overmature gas systems.

2.1. Source Rocks. The predominant source rock of Paleozoic gases is Carboniferous-Permian (C-P) coal and mudstone. Ordovician marine carbonates contribute only minor amounts of gas owing to their low organic content. Previous studies indicate that gases of the Sulige, Daniudi, Shenmu, Wushenqi, Yulin, Zizhou, and Mizhi fields were all produced from upper Paleozoic coaly source rocks [4, 17–20]. The origin of Jingbian gas, from the lower Paleozoic-Ordovician Majiagou formation, is still unresolved, although the prevailing view is that it was produced mainly from upper Paleozoic coal measures, migrated downward, and mixed with oil-type gas from lower Paleozoic-Ordovician source rocks [11, 21].

2.2. Reservoirs. The two main reservoirs in the Paleozoic strata of the Ordos Basin are the upper C-P paralic and continental clastic reservoir and lower Paleozoic (Ordovician) marine carbonate reservoir. Most natural gas from the Sulige, Daniudi, Shenmu, Wushenqi, Yulin, Zizhou, and Mizhi fields is produced from the upper Paleozoic reservoirs, with tight sandstones of the Permian Shanxi and Xiashihezi formations being the major reservoirs. Gas of the Jingbian field is produced from both the upper and lower Paleozoic reservoirs, with the major lower Paleozoic reservoir being the fifth member (O_1m_5) of the Majiagou formation.

2.3. Caprocks. Caprocks of the lower Paleozoic reservoirs are Carboniferous bauxitic mudstones that are $<10 \text{ m}$ thick, coal measures that are $15\text{--}40 \text{ m}$ thick, and argillaceous

dolomite and marlstone [21]. The regional seal of the upper Paleozoic reservoirs consists of stable, laterally distributed, Shangshihezi and Shiqianfeng formation lacustrine mudstones [16].

2.4. Thermal History and Gas Charge Model. During the Late Triassic-Early Jurassic ($T_3\text{--}J_1$), at the threshold of hydrocarbon generation, the gas first accumulated within C-P source rocks. During the Late Jurassic-Early Cretaceous (J-K₁), $>1000 \text{ m}$ of J-K₁ sediment was deposited, with a maximum depth of $>4000 \text{ m}$ and a maximum palaeogeothermal temperature of $160\text{--}200^\circ\text{C}$. Most C-P gases were generated during this period and migrated to nearby upper Paleozoic C-P reservoirs between source rocks. Driven by buoyancy and abnormal pressure, the gases also migrated directly upward or downward into the lower Paleozoic reservoirs over distances of $<200 \text{ m}$ [16, 21, 22]. From the end of the Early Cretaceous, thick strata were eroded and gas generation terminated, with the temperature reducing to the current $99.6\text{--}113.5^\circ\text{C}$ [23].

3. Sampling and Analysis

3.1. Data Analyses. Geochemical characteristics of 199 gas samples from Paleozoic reservoirs in the Ordos Basin gas fields, including the Jingbian, Yan'an, Sulige, Shenmu, and Daniudi fields (Figure 1), are presented in Table 1. The data pertain to 94 samples from previous studies [9, 16], 41 from newly collected samples in this study, and 64 recorded in the geochemical database of the Exploration and Development Research Institute, Changqing Oil Company (EDRICOC), Xi'an, China. Eight of the 27 samples of Feng et al. [9] were analysed for rare-gas isotopes (Table 1). Data for the gas samples were obtained using similar techniques [11, 16] to ensure consistency. The maturity of the upper Paleozoic source rocks in the Ordos Basin increases from north to south, and the gases come from similar source rocks, so a comparison of isotopic compositions of gases in these fields may provide information on the evolution of coal-derived gases based on geological setting. Lower Paleozoic South Jingbian gases are included in the discussion of the origin of isotopic reversal. Shale gas from the Sichuan Basin and other basins with different maturities is included to provide information on differences between coal-derived and oil-type gases (data for shale gas were obtained from [13–16, 24–31]). Shale gases also display isotopic reversal in high maturity conditions, providing insight into the origin of unusual geochemical characteristics of overmature coal-derived gases.

3.2. Geochemical and C–H Isotopic Analyses. Analyses of gas composition and C and H isotopic ratios were conducted at the Institute of Petroleum Exploration and Development (RIPED), Langfang, China. A Hewlett Packard HP7890A capillary gas chromatograph was used to determine hydrocarbon compositions with a PLOT Al_2O_3 column ($50 \text{ m} \times 0.53 \text{ mm}$).

Carbon isotopic compositions were determined by gas chromatography–combustion–isotope ratio mass spectrometry

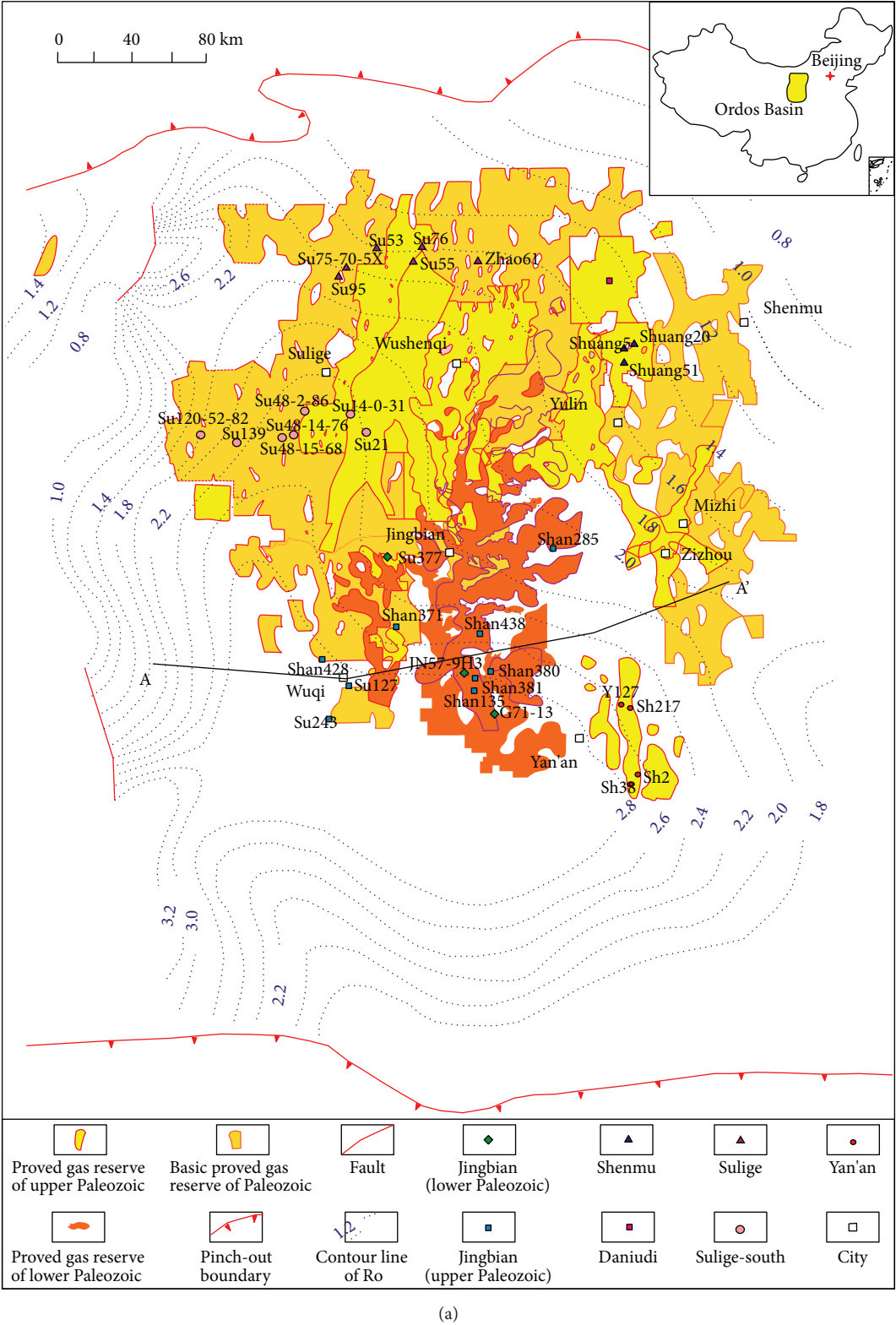
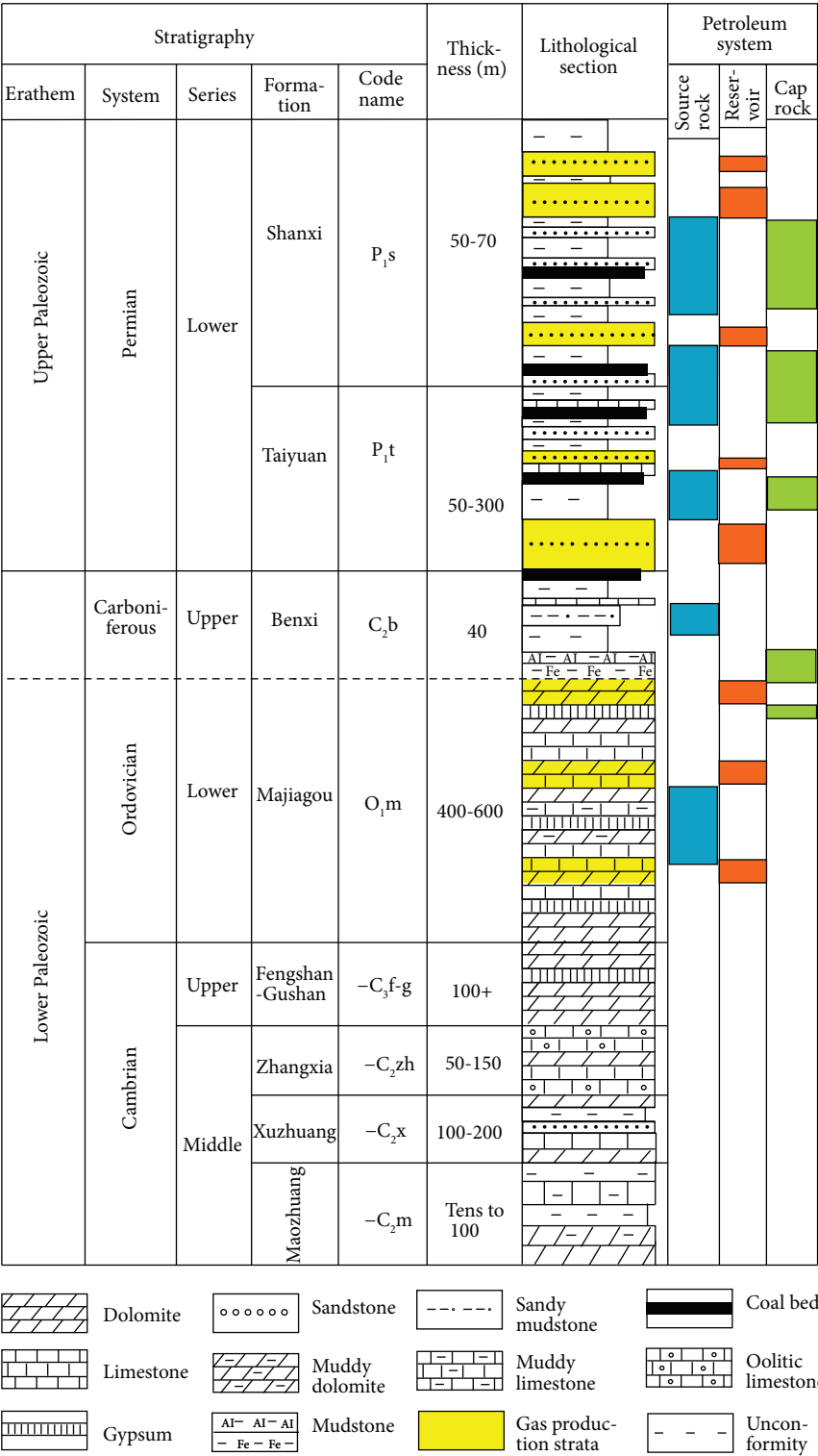


FIGURE 1: Continued.



(b)

FIGURE 1: Continued.

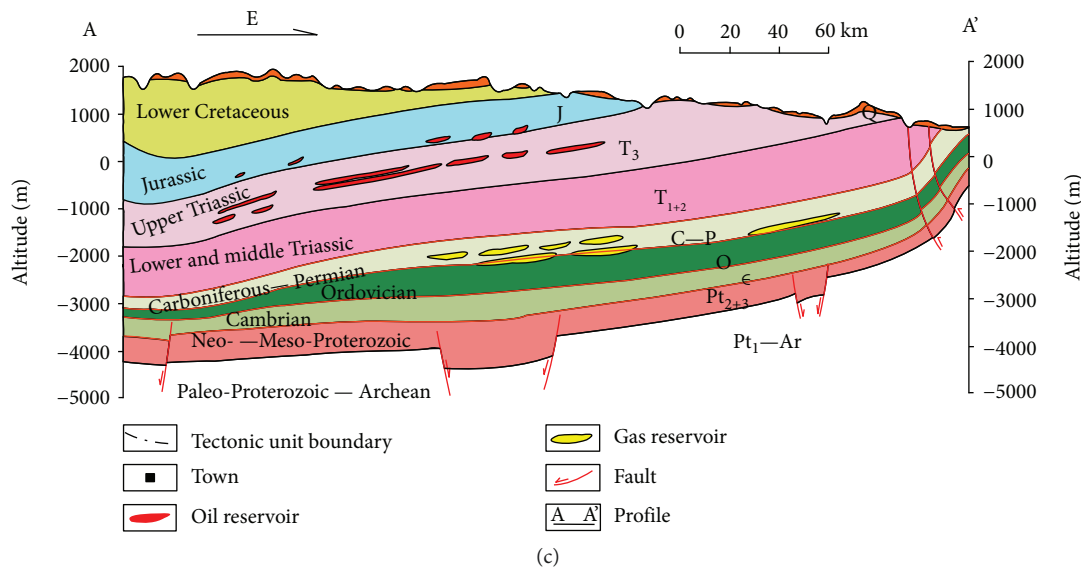


FIGURE 1: (a) Maturity map of the upper Paleozoic strata of the Ordos Basin, with sample locations labelled by well name (after [16]); (b) stratigraphic column of the Paleozoic strata of the Ordos Basin (after [16]); (c) cross section for Ordos Basin (after [16]).

(GC-C-IRMS; Thermo Delta V Advantage). Each sample was analysed three times, yielding an analytical precision of $\pm 0.3\%$. Results are reported relative to Vienna Pee Dee Belemnite (VPDB). Hydrogen isotopes were analysed by GC-thermal conversion-IRMS (GC-TC-IRMS; Finnigan MAT 253), using a HP-PLOTQ GC column (30 m \times 0.32 mm). Analytical precision was $\pm 3\%$. Hydrogen isotopic compositions are reported relative to Vienna Standard Mean Ocean Water (VSMOW). The detailed analytical procedure is described in Feng et al. [9].

3.3. He Isotopic Composition. Seventeen gas samples were analysed at RIPED for He content and $^3\text{He}/^4\text{He}$ ratios using a sampling system attached to an IRMS. The natural gas cylinder was connected to the injection port of the instrument through a pressure relief valve, with the pipeline evacuated to ultrahigh vacuum. Sampling was controlled by an injection valve, and the gas was purified of hydrocarbons, N_2 , O_2 , CO_2 , H_2S , and H_2 , by a zirconium base furnace. He, Ne, Ar, Kr, and Xe were separated cryogenically and analysed by MS. Based on internationally recognized contents of inert gases in air, the relative standard deviations of He content and $^3\text{He}/^4\text{He}$ ratio were $\pm 3.4\%$ and $\pm 4.5\%$, respectively.

4. Results

4.1. Natural Gas Composition. Southern Ordos Basin gases from the Yan'an and South Jingbian gas fields are of high dryness, with dryness coefficients (C_1/C_{1-5}) > 0.962 (Table 1), and their cumulative contents of heavier hydrocarbon components (C_{2-5}) are low (Figure 2). Ethane content is 0.05%–2.68% (mean 0.51%), and propane content is $< 0.60\%$ for Paleozoic gases from both fields. Concentrations of nonhydrocarbon gases, including CO_2 and N_2 , vary widely. CO_2 and N_2 concentrations in the Yan'an gas field are relatively low at 0.56%–31.54% (mean 4.38%) and 0.00%–32.68%

(mean 5.23%), respectively, whereas the nonhydrocarbon content of South Jingbian gas is high, with its methane content being relatively low. The CO_2 content of lower Paleozoic gas from the Jingbian gas field is 0.44%–31.54% (mean 6.61%), whereas the N_2 content of upper Paleozoic gas is 0.26%–33.7% (mean 7.07%). The high CO_2 content of lower Paleozoic South Jingbian gas is probably due to its carbonate reservoir. Upper Paleozoic gases are contained in Carboniferous-Permian reservoirs, whereas lower Paleozoic gases are from Ordovician carbonate reservoirs, and it is likely that the high CO_2 content of the latter arose from the cracking of Ordovician carbonates. High temperatures are necessary for the thermal cracking of carbonate, whereas the existence of acidic water in the Ordovician reservoir [16] makes the generation of CO_2 possible at any temperature.

Gases from the central and northern Ordos Basin (Sulige, Shenmu, and Daniudi fields) have compositions different to those of gases from the southern basin (South Jingbian and Yan'an fields; Figure 2). Gases from the central and northern fields are relatively wet, with dryness coefficients < 0.983 (mean 0.941); their heavy hydrocarbon contents are higher (ethane mean 3.04%); and nonhydrocarbon contents lower (N_2 and CO_2 means 1.86% and 3.07%, respectively). These characteristics are consistent with the R_o distribution of source rocks in the Ordos Basin (Figure 1). Differences in hydrocarbon content indicate that gases from the southern Ordos Basin have been exposed to higher palaeogeothermal stress and were generated in a later evolutionary stage, whereas their nonhydrocarbon content could be explained by some secondary mechanism occurring in a late maturity stage.

4.2. Carbon Isotopic Compositions of Alkanes and CO_2 . Gas $\delta^{13}\text{C}\text{-CH}_4$ values in the upper Paleozoic reservoir of the South Jingbian and Yan'an gas fields range from -21.02%

TABLE 1: Composition and carbon isotopes of Paleozoic gas in Ordos Basin.

Field	Well	Strata	Depth	CH ₄	C ₂ H ₆	C ₃ H ₈	iC ₄ H ₁₀	nC ₄ H ₁₀	iC ₅ H ₁₂	nC ₅ H ₁₂	C ₅ +	CO ₂	N ₂	CH ₄	C ₂ H ₆	C ₃ H ₈	C ₄ H ₁₀	CO ₂	δD (‰), VSMOW	³ He/ ⁴ He	Rare gas ⁴⁰ Ar/ ³⁶ Ar	R ₀ -Dai %	Reference
Yan'an	Sh2	P ₂ h		96.68	0.73	0.09	0.02	0.06				1.41	1.07	-29.2	-30.7	-31.9	-12.9	-168	-190	6.64 ± 0.7	1920.30 ± 25.82	2.34	
	Sh217	P ₂ h		96.30	0.62	0.05						2.27	0.76	-27.6	-34.9		-0.2	-170	-183			3.04	
	Sh6	P ₁ s		96.32	0.76	0.07						1.97	0.86	-28.1	-30.5	-30.4	-9.1	-168	-187			2.80	
	Sh36	P ₁ s		93.90	0.43	0.02						4.93	0.72	-29.2	-35.4		-3.6	-166	-182			2.34	
	Sh38	P ₁ s		95.91	0.42	0.03						3.11	0.53	-28.2	-36.1		-1.1	-167	-185	5.88 ± 0.78	1370.44 ± 18.29	2.75	
	Y127	P ₁ s		93.45	0.43	0.03						5.72	0.37	-29.3	-33.7	-30.7	-0.2	-168	-184	5.21 ± 0.63	1180.46 ± 15.65	2.30	
	Sh210	P ₁ s		93.39	0.43	0.03						5.86	0.30	-29.7	-34.9	-34.5	-0.1	-168	-187			2.15	
	Sh212	P ₁ s		93.24	0.41	0.02						5.63	0.69	-29.7	-35.1	-34.5	-0.7	-167	-184	5.39 ± 0.77	1402.27 ± 18.16	2.15	
	Sh209	P ₁ s		89.90	0.42	0.02						9.08	0.57	-28.9	-34.7		-1.70	-190				2.46	
	Sh217-1	P ₁ s		94.45	0.30	0.02						4.79	0.43	-29.3	-34.0		2.4	-167	-178	7.23 ± 0.9	880.228 ± 13.31	2.30	
	Sh225	P ₁ s		93.87	0.42	0.03						5.01	0.67	-28.8	-34.1		-0.9	-163	-167			2.50	
	Sh231	P ₁ s		93.14	0.40	0.02						5.96	0.47	-29.4	-34.4	-34.0	0.2	-168	-197	5.95 ± 0.71	1116.57 ± 15.41	2.26	
	Sh12	C ₂ b		95.31	0.53	0.04						3.51	0.59	-30.6	-37.2	-35.8	-0.6	-165	-183	7.49 ± 1.41	1008.78 ± 12.97	1.80	
	Sh37	C ₂ b		96.60	0.42	0.03						2.74	0.22	-30.8	-37.1	-37.3	-2.1	-170	-173	7.66 ± 1.04	894.07 ± 11.38	2.09	
	Sh48	C ₂ b		94.89	0.52	0.04						4.29	0.25	-29.9	-36.5		1.7	-163	-186			2.75	
	Sh56	P ₁ s		95.96	0.48	0.03	0.00					3.00	0.47	-28.2	-35.0	-33.7	-1.66					2.46	
Y201	P ₁ s		97.48	0.39	0.04	0.00	0.00				1.37	0.65	-28.9	-34.9	-32.3	-1.66					2.38		
Sh28-1	P ₁ s		97.39	0.41	0.02	0.00	0.00				1.52	0.39	-29.1	-36.8		-1.65	-189				2.80		
Y186	P ₁ s		95.98	0.42	0.02	0.00	0.00				2.97	0.40	-28.1	-36.4	-35.5	-1.65					2.34		
Sh26	P ₁ s		97.15	0.37	0.02	0.00	0.00				2.14	0.24	-29.2	-35.5		-1.63					2.58		
Sh25	P ₁ s		95.84	0.43	0.02	0.00	0.00				3.15	0.48	-28.6	-36.2		-1.66	-193				3.09		
Y175	C ₂ b		96.49	0.62	0.05	0.00	0.00				2.16	0.59	-27.5	-33.4	-33.3	-1.64	-178				2.94		
Sh229	P ₁ s		94.74	0.47	0.03	0.00	0.00				4.16	0.47	-27.8	-34.5	-33.5	-1.67					2.62		
Sh228	P ₁ s		94.68	0.41	0.03	0.00	0.00				4.30	0.46	-28.5	-35.2	-34.7	-1.67	-186				2.71		
Sh214	P ₁ s		94.86	0.43	0.03	0.00	0.00				4.14	0.43	-28.3	-35.4		-1.68					2.89		
Sh207	P ₁ s		95.94	0.28	0.02	0.00	0.00				3.09	0.56	-27.9	-33.7		-1.67					2.75		
Y161	P ₁ s		95.37	0.47	0.03	0.00	0.00				3.53	0.47	-28.2	-34.5		-1.67					0.34		
Standard deviation																							
Tong25	P ₂ h ₄		2647	90.81	2.68	0.60	0.12	0.12	0.06	0.03	0.00	0.78	4.86	-21.0	-21.1	-22.2		4.16	1.98	6.91		8.89	
Shan281	P ₂ h		3522	79.55	0.97	0.16	0.02	0.02	0.01	0.01	0.02	1.30	18.06	-31.3	-35.5	-32.9						1.67	
Shan285	C ₂ b		3150	94.85	1.25	0.14	0.02	0.02	0.00	0.00	0.01	3.37	0.26	-33.6	-33.9	-33.0						1.14	
Shan381	P ₂ h ₈		3237	92.37	1.12	0.15	0.02	0.02	0.02	0.01	0.01	1.06	5.20	-26.4	-27.4	-29.4						3.68	
Su353	P ₁ s ₁		3498	93.12	1.11	0.17	0.02	0.02	0.01	0.00	0.01	1.86	3.69	-24.1	-25.6	-28.7						5.39	
Shan438	C ₂ b		3525	93.02	1.06	0.14	0.02	0.02	0.01	0.00	0.01	4.62	1.11	-30.3	-36.7	-36.3						1.95	
Shan303	P ₂ h ₈		3093	88.47	0.90	0.20	0.02	0.02	0.01	0.00	0.00	2.02	8.36	-27.7	-31.8	-29.3						3.01	
Su222	P ₁ s ₁		3795	93.01	0.95	0.17	0.01	0.02	0.01	0.00	0.01	1.42	4.41	-27.2	-28.6	-30.4						3.24	
Shan380	P ₂ h ₈		3306	90.58	0.94	0.13	0.01	0.01	0.01	0.00	0.01	1.13	7.18	-24.5	-28.3	-29.3						5.05	
Shan437	P ₂ h ₈		3453	80.74	0.76	0.20	0.01	0.01	0.00	0.00	0.00	2.25	16.02	-28.8	-31.8	-30.1						2.49	
Shan135	P ₂ h ₈		3378	95.80	0.99	0.13	0.01	0.03	0.01	0.00	0.00	1.15	1.88	-25.9	-29.0	-30.1						3.98	
Shan292	P ₁ s ₂		3363	86.13	0.77	0.22	0.01	0.01	0.00	0.00	0.00	0.99	11.86	-26.8	-31.2	-29.3						3.47	
Su243	P ₂ h ₈		4038	92.81	0.80	0.14	0.01	0.01	0.00	0.00	0.00	0.56	5.51	-26.2	-28.9	-30.6						3.82	
Shan316	P ₂ h ₈		3217	93.21	0.72	0.19	0.01	0.01	0.00	0.00	0.01	2.74	3.10	-27.9	-32.6	-29.6						2.91	

TABLE 1: Continued.

Field	Well	Strata	Depth	CH ₄	C ₂ H ₆	C ₃ H ₈	iC ₄ H ₁₀	nC ₄ H ₁₀	iC ₅ H ₁₂	nC ₅ H ₁₂	C ₅ +	CO ₂	N ₂	CH ₄	δ ¹³ C (‰), VPDB	δD (‰), VSMOW	³ He/ ⁴ He	Rare gas ⁴⁰ Ar/ ³⁶ Ar	R ₀ -Dai %	Reference		
South Jingbian- lower Paleozoic	Shan428	P ₁ s ₁	3927	90.20	0.67	0.11	0.01	0.01	0.00	0.00	0.02	3.21	5.79	-28.1	-29.2	-29.3			2.82			
	Shan340	P ₂ h ₈	3046	66.02	0.47	0.09	0.01	0.01	0.00	0.00	0.01	0.71	32.68	-26.9	-32.2	-29.7			3.39			
	Shan339	P ₁ s ₂	3527	93.31	0.59	0.10	0.02	0.02	0.01	0.01	0.00	3.34	2.58	-29.1	-34.2			2.39				
	Su127	P ₂ h ₈	3899	94.46	0.63	0.10	0.01	0.01	0.00	0.00	0.02	1.20	3.59	-29.0	-33.7	-34.1			2.42			
	Yi6	P ₂ h ₈	2149	65.72	0.40	0.04	0.00	0.00	0.00	0.00	0.00	0.14	33.70	-32.3	-36.8			1.42				
	Shan341	P ₁ s ₂	3188	93.77	0.44	0.09	0.01	0.02	0.01	0.01	0.00	3.09	2.55	-28.0	-35.7			2.84				
	Shan323	P ₁ s ₁	3751	93.70	0.50	0.07	0.01	0.01	0.00	0.00	0.00	3.66	2.06									
	Shan441	P ₂ h ₈	3266	95.13	0.47	0.05	0.00	0.00	0.00	0.00	0.01	2.66	1.68	-27.0	-31.5	-28.7			3.37			
	Shan429	P ₁ s ₂	3146	93.52	0.46	0.04	0.00	0.00	0.00	0.00	0.00	2.72	3.25	-28.8	-34.2	-35.5			2.51			
	Shan383	P ₂ h ₈	3160	89.97	0.41	0.05	0.00	0.00	0.00	0.00	0.02	4.26	5.31	-27.4	-32.0	-29.6			3.12			
	Shan383	P ₁ s ₁	3214	92.71	0.41	0.05	0.00	0.00	0.00	0.00	0.00	3.15	3.67	-27.5	-32.2	-29.8			3.10			
	Shan441	P ₁ s ₂	3389	92.78	0.33	0.03	0.00	0.00	0.00	0.00	0.00	3.67	3.16	-27.0	-31.5	-28.7			3.37			
	Shan429	P ₁ s ₂	3232	93.42	0.36	0.02	0.00	0.00	0.00	0.00	0.00	3.34	2.86	-29.8	-35.7	-30.5			2.12			
	Yi8	P ₁ s ₂	2164	91.82	0.23	0.02	0.00	0.00	0.00	0.00	0.00	0.42	7.51	-31.3	-31.4	-30.8			1.66			
	Shan371	P ₂ h ₈	3921	93.33	0.22	0.02	0.00	0.00	0.00	0.00	0.00	4.61	1.82	-32.5	-34.3	-30.1			1.37			
	Shan340	C ₂ b	3186	77.56	0.17	0.00	0.00	0.00	0.00	0.00	0.00	1.21	21.05	-28.8	-32.0	-31.2			2.51			
	G69-9C3	P ₂ h ₈		94.95	0.72	0.09	0	0.01	0	0	0	3.31	0.85	-27.6	-29.3	-30	-9.2	-157	-163	-178	3.04	
	G69-9C4	P ₂ h ₈		95.54	0.84	0.09	0.01	0.01	0	0	0	2.64	0.79	-27.2	-28.4	-29.6	-5.3	-158	-165	-167	3.24	
															2.57	3.43	2.53	2.76	0.71	1.41	7.78	This study

South
Jingbian-
lower
Paleozoic

Dai et al.,
[16]

Database of
EDRIGOC

TABLE 1: Continued.

Field	Well	Strata	Depth	CH ₄	C ₂ H ₆	C ₃ H ₈	iC ₄ H ₁₀	nC ₄ H ₁₀	iC ₅ H ₁₂	nC ₅ H ₁₂	C ₅ +	CO ₂	N ₂	CH ₄	C ₂ H ₆	C ₃ H ₈	C ₄ H ₁₀	CO ₂	δD (‰), VSMOW	³ He/ ⁴ He	Rare gas ⁴⁰ Ar/ ³⁶ Ar	R ₀ -Dai %	Reference	
Main component (%)																								
δ ¹³ C (‰), VPDB																								
Shennu	Shan441	O ₁ m ₅	3486	85.03	0.21	0.04	0.02	0.03	0.02	0.01	0.00	14.65	0.00	-32.16	-36.8	-29.7							1.44	
	Shan373	O ₁ m ₅	4003	92.36	0.30	0.03	0.00	0.00	0.00	0.00	0.00	5.93	1.37	-32.70	-33.6	-25.6							1.32	
	Shan322	O ₁ m ₅	3965	85.01	0.25	0.03	0.01	0.01	0.00	0.00	0.00	2.07	12.63	-34.04	-37.9	-33.4							1.06	
	Su222	O ₁ m ₅	4001	92.26	0.27	0.03	0.00	0.00	0.00	0.00	0.00	5.67	1.76	-32.68	-34.2	-30.0							1.32	
	Shan377	O ₁ m ₅	3305	95.86	0.27	0.03	0.00	0.00	0.00	0.00	0.00	2.80	1.05	-32.92	-36.5								1.27	
	Su222	O ₁ m ₅	3942	90.87	0.24	0.03	0.00	0.00	0.00	0.00	0.00	4.82	4.04	-31.80	-33.6	-29.6							1.53	
	Shan323	O ₁ m ₅	3936	93.29	0.25	0.02	0.00	0.00	0.00	0.00	0.00	6.44	0.00	-34.41	-36.3	-31.3							1.00	
	Su127	O ₁ m ₅	4072	84.28	0.19	0.01	0.00	0.00	0.00	0.00	0.00	7.41	8.11	-32.72	-35.7	-30.6							1.32	
	Su379	O ₁ m ₅	3810	89.40	0.05	0.00	0.00	0.00	0.00	0.00	0.00	7.98	2.57	-36.48	-39.4								0.71	
	Yu70	O ₁ m ₅	2762	97.81	1.07	0.40	0.07	0.10	0.01	0.01	0.01	0.44	/	-30.83	-33.6	-28.3							1.79	
	Shan339	O ₁ m ₅	3606	93.51	0.72	0.13	0.02	0.02	0.01	0.01	0.01	3.43	2.12	-31.59	-37.3	-29.4							1.58	
	Shan430	O ₁ m ₅	3959	55.54	0.27	0.05	0.00	0.01	0.00	0.00	0.01	31.54	12.58	-31.21	-32.7	-26.2							1.68	
	Shan323	O ₁ m ₅	3895	91.14	0.40	0.06	0.01	0.01	0.01	0.00	0.00	5.93	2.43	-33.39	-35.9	-30.1							1.18	
	Shan438	O ₁ m ₅	3486	94.92	0.41	0.03	0.00	0.00	0.00	0.00	0.00	3.99	0.63	-31.73	-37.8	-33.3							1.55	
	Shan265	O ₁ m ₅	3450	96.09	0.38	0.06	0.00	0.01	0.00	0.00	0.00	4.26	0.25	-30.98	-37.3	-32.8							1.75	
	Shan430	O ₁ m ₅	3994	79.63	0.29	0.04	0.00	0.00	0.00	0.00	0.00	0.01	6.25	13.78	-32.16	-33.8	-27.4						1.44	
	Shan434	O ₁ m ₅	3558	92.74	0.35	0.03	0.00	0.00	0.00	0.00	0.00	0.01	4.07	2.77	-31.56	-35.8	-30.6						1.59	
	Shan441	O ₁ m ₅	3486	85.03	0.21	0.04	0.02	0.03	0.02	0.01	0.00	14.65	0.00	-32.16	-36.8	-29.7							1.44	
	Shan373	O ₁ m ₅	4003	92.36	0.30	0.03	0.00	0.00	0.00	0.00	0.00	5.93	1.37	-32.70	-33.6	-25.6							1.32	
	Shan322	O ₁ m ₅	3965	85.01	0.25	0.03	0.01	0.01	0.00	0.00	0.00	2.07	12.63	-34.04	-37.9	-33.4							1.06	
	Su222	O ₁ m ₅	4001	92.26	0.27	0.03	0.00	0.00	0.00	0.00	0.00	5.67	1.76	-32.68	-34.2	-30.0							1.32	
	Shan377	O ₁ m ₅	3305	95.86	0.27	0.03	0.00	0.00	0.00	0.00	0.00	2.80	1.05	-32.92	-36.5								1.27	
	Su222	O ₁ m ₅	3942	90.87	0.24	0.03	0.00	0.00	0.00	0.00	0.00	4.82	4.04	-31.80	-33.6	-29.6							1.53	
	Shan323	O ₁ m ₅	3936	93.29	0.25	0.02	0.00	0.00	0.00	0.00	0.00	6.44	0.00	-34.41	-36.3	-31.3							1.00	
	Su127	O ₁ m ₅	4072	84.28	0.19	0.01	0.00	0.00	0.00	0.00	0.00	7.41	8.11	-32.72	-35.7	-30.6							1.32	
	Su379	O ₁ m ₅	3810	89.40	0.05	0.00	0.00	0.00	0.00	0.00	0.00	7.98	2.57	-36.48	-39.4								0.71	
Standard deviation																								
														1.72	2.21	2.19	1.98	4.76	4.85	5.89	29.14		0.48	
Shennu	Shuang0-13	P ₂ h	2990	91.55	4.66	0.95	0.22	0.19	0.10	0.05	0.23	1.62	0.41	-35.9	-23.5	-22.3	-22.2	-198	-157	-152			0.78	
	Shuang0-3	P ₂ s ₁	2878	91.33	4.95	1.03	0.19	0.20	0.09	0.04	0.19	1.56	0.38	-36.5	-24.8	-23.7	-23.0	-196	-161	-159			0.71	
	Shuang10-5	P ₂ h ₈	2888	92.17	3.78	0.75	0.16	0.15	0.07	0.03	0.14	2.22	0.51	-36.1	-23.8	-22.8	-22.0	-195	-157	-156			0.76	
	Shuang10-9	P ₂ h ₈	3105	91.62	4.18	0.85	0.19	0.17	0.08	0.04	0.13	2.28	0.44	-36.5	-23.5	-22.3	-21.7	-199	-157	-154			0.71	
	Shuang11-15C1	P ₂ h ₈	3008	91.34	4.20	0.88	0.18	0.17	0.08	0.04	0.26	2.50	0.33	-36.4	-23.3	-22.3	-21.7	-200	-159	-156			0.72	
	Shuang11-15C3	P ₂ h ₈	3206	91.69	3.81	0.76	0.16	0.15	0.08	0.04	0.25	2.74	0.29	-36	-23.2	-22.2	-21.5	-200	-158	-158			0.77	
	Shuang11-4C5	P ₂ h	2990	89.42	6.92	1.53	0.25	0.27	0.12	0.07	0.22	0.57	0.57	-36.8	-25.4	-24.2	-23.8	-198	-161	-155			0.68	
	Shuang9-12	P ₂ h ₈	2996	92.17	3.09	0.60	0.14	0.11	0.06	0.03	0.16	3.36	0.26	-35.9	-23.2	-21.8	-21.1	-193	-156	-155	4.84 ± 1.19	772.18 ± 10.06	0.78	This study
	Shuang20	P ₁ t	2960	91.37	4.40	0.80	0.14	0.15	0.07	0.04	0.21	2.46	0.34	-36.2	-25.8	-24.2	-23.5	-193	-163	-160			0.75	
	Shuang21-11	P ₂ h ₈	2983	91.61	4.10	0.75	0.14	0.13	0.06	0.03	0.14	2.66	0.36	-35.9	-24.1	-22.9	-21.0	-195	-159	-157			0.78	
	Shuang3	P ₁ s ₂	2990	91.49	4.48	0.88	0.20	0.17	0.09	0.04	0.21	2.17	0.24	-36.7	-23.2	-22	-21.7	-199	-156	-152			0.69	
	Shuang5-19	P ₂ h ₈	3146	92.12	4.00	0.79	0.16	0.15	0.07	0.04	0.16	2.12	0.36	-36.5	-23.9	-22.7	-22.2	-197	-158	-157	4.54 ± 0.81	1096.35 ± 14.2	0.71	
	Shuang6-18	P ₂ h ₈ t	2853	91.77	4.00	0.83	0.17	0.17	0.08	0.04	0.16	2.46	0.29	-36.7	-23.7	-22.4	-21.8	-198	-157	-156			0.69	
	Shuang6-19	P ₂ h ₈	2933	91.65	4.28	0.89	0.18	0.18	0.09	0.04	0.15	2.26	0.25	-37	-23.8	-22.4	-21.9	-201	-161	-159			0.65	
	Shuang7-11	P ₂ h ₆	2872	93.09	4.09	0.86	0.17	0.18	0.09	0.05	0.25	0.53	0.63	-36.7	-24.7	-23.1	-22.5	-197	-161	-155			0.69	
	Shuang7-12	P ₂ h	3083	92.58	3.93	0.74	0.16	0.15	0.08	0.04	0.18	1.78	0.34	-36.1	-23.4	-22.2	-21.9	-199	-157	-155			0.76	

Field	Well	Strata	Depth	CH ₄	C ₂ H ₆	C ₃ H ₈	iC ₄ H ₁₀	nC ₄ H ₁₀	iC ₅ H ₁₂	nC ₅ H ₁₂	Main component (%)	CO ₂	N ₂	CH ₄	C ₂ H ₆	C ₃ H ₈	C ₄ H ₁₀	CO ₂	δD (‰), VSMOW	Rare gas ⁴⁰ Ar/ ³⁶ Ar	R _s -Dai %	Reference			
	Shuang8-12	P ₂ h	2927	94.43	2.63	0.41	0.09	0.10	0.06	0.03	0.10	1.97	0.17	-37.3	-24.7	-26.4	-25.6	-12.3	-185	-189	-178	0.62			
	Shuang8-17C3	P ₂ h	3026	92.08	4.18	0.86	0.19	0.18	0.09	0.05	0.26	1.82	0.26	-36.6	-25.6	-23.4	-22.4	-197	-163	-156	+	0.70			
	Shuang8-8	P ₂ h ₈	2891	91.46	5.53	1.16	0.20	0.24	0.10	0.05	0.18	0.37	0.65	-37.1	-25.1	-24.3	-23.6	-198	-161	-158		0.64			
	Shuang9-11	P ₂ h ₈	2891	91.44	4.42	0.88	0.21	0.18	0.09	0.04	0.24	2.22	0.26	-36	-23.1	-22	-21.7	-199	-156	-152		0.77			
	Shuang9-11H2	P ₁ t	5043	91.97	3.39	0.61	0.14	0.11	0.06	0.03	0.19	3.21	0.26	-35.6	-22.8	-22	-21.0	-198	-155	-157		0.82			
	Shuang9-12	P ₂ h ₈	2899	92.26	3.57	0.68	0.15	0.13	0.07	0.03	0.16	2.63	0.31	-36.5	-23.2	-22.1	-21.1	-198	-157	-156		0.71			
	Shuang9-13H2	P ₁ s ₂	4264	91.34	4.77	1.06	0.25	0.22	0.11	0.05	0.26	1.61	0.30	-36	-23.2	-22.1	-21.9	-198	-156	-154		0.77			
	Shuang8-17c1	P ₁ s+P ₂ h		90.92	4.94	1.16	0.24	0.26	0.13	0.07	0.37	0.52	1.37	-37.5	-22.8	-22.8	-22.3	-1.2	-192	-149	-146	0.60			
				Standard deviation																					
	Su53	P ₁ s, P ₂ h		86.05	8.36	2.17	0.37	0.44	0.00	0	1.13	0.72	0.72	-35.6	-25.3	-23.7	-23.9	-202	-165	-160		0.82			
	Su75	P ₂ h		92.47	3.92	0.66	0.11	0.11	0.00	0	1.30	1.10	1.10	-33.2	-23.8	-23.4	-22.4	-194	-163	-157		1.22			
	Su76	P ₁ s, P ₂ h		86.41	8.37	2.33	0.39	0.51	0.00	0	0.13	1.21	1.21	-35.1	-24.6	-24.4	-24.4	-203	-165	-161		0.89			
	Su53-78-46H	P ₁ s, P ₂ h		89.82	6.21	1.24	0.22	0.24	0.00	0	0.93	0.87	0.87	-33.9	-23.9	-23.0	-23.2	-198	-165	-156		1.09			
	Su75-64-5X	P ₂ h		89.45	6.36	1.26	0.22	0.24	0.00	0	0.13	0.93	0.93	-33.5	-24.0	-23.3	-22.8	-199	-167	-159		1.16			
	Su76-1-4	P ₂ h		90.38	6.03	1.18	0.21	0.22	0.00	0	0.82	0.71	0.71	-32.7	-23.6	-22.9	-23.0	-198	-168	-165		1.32			
	Zhao61	P ₁ s		88.98	6.83	1.53	0.31	0.37	0.00	0	0.55	0.85	0.85	-33.2	-23.5	-23.3	-23.2	-194	-159	-154		1.22			
	M137-13	P ₁ s		94.19	3.77	0.53	0.11	0.09	0.00	0	0.71	0.39	0.39	-33.0	-23.2	-22.4	-21.1	-182	-156	-145		1.26			
	Zhou35-28	P ₁ s ₂		94.81	2.97	0.44	0.06	0.07	0.00	0	1.2	0.37	0.37	-32.5	-25.7	-23.6	-23.3	-181	-164	-157		1.36			
	Yu69	P ₁ s ₂		94.93	2.85	0.4	0.06	0.06	0.00	0	1.27	0.35	0.35	-32.8	-26.3	-24.1	-21.7	-179	-162	-151		1.30	Dai et al., [16]		
	Mi38-13A	P ₁ s ₂		94.53	3.04	0.45	0.08	0.07	0.00	0	1.34	0.37	0.37	-33.1	-25.0	-22.8	-22.0	-181	-155	-141		1.24			
	Zhou21-24	P ₁ s ₂		94.22	3.12	0.48	0.08	0.07	0.00	0	1.58	0.32	0.32	-32.7	-25.1	-23.2	-22.2	-183	-163	-155		1.32			
	Yu45	P ₁ s ₂		94.17	3.12	0.48	0.08	0.08	0.00	0	1.58	0.36	0.36	-33.2	-25.2	-23.1	-22.5	-183	-164	-155		1.22			
	Mi40-13	P ₁ s ₂		94.45	2.99	0.45	0.07	0.07	0.00	0	1.52	0.32	0.32	-32.8	-25.3	-23.3	-22.4	-183	-167	-155		1.30			
	Zhou25-38	P ₁ s ₂		94.67	2.87	0.42	0.06	0.07	0.00	0	1.4	0.38	0.38	-32.6	-25.7	-23.3	-22.9	-185	-165	-154		1.34			
	Su11-18-36	P ₂ h ₈		90.16	5.5	1.15	0.21	0.21	0.00	0	1.47	0.94	0.94	-33.0	-23.3	-22.3	-22.9	-196	-165	-167		1.26			
	Su75-70-5x			90.7	5.19	1.02	0.18	0.18	0.00	0	1.48	0.93	0.93	-32.8	-23.6	-23.1	-22.7	-196	-166	-170		1.30			
	Su55			88.96	7.07	1.47	0.22	0.27	0.00	0	0.68	0.88	0.88	-35.1	-24.6	-24.1	-24.8	-202	-164	-173		0.89			
	Su76-15-18			85.63	8.18	2.56	0.47	0.64	0.00	0	0.41	1.29	1.29	-35.7	-25.3	-24.8	-24.8	-205	-164	-167		0.81			
	Sunan9-61			88.28	5.49	1.16	0.74	0.23	0.00	0	1.47	1.77	1.77	-32.3	-20.4	-17.7	-18.5	-190	-161	-155		1.41			
				Standard deviation																					
	Su21	P ₁ s, P ₂ h		92.39	4.48	0.83	0.13	0.14	0.00	0	0.99	0.68	0.68	-33.4	-23.4	-23.8	-22.7	-194	-167	-163		1.18			
	Su95	P ₂ h		92.24	3.95	0.66	0.11	0.11	0.00	0	1.64	1.00	1.00	-32.5	-23.9	-24.0	-22.7	-193	-167	-160		1.36			
	Su139	P ₁ s, P ₂ h		93.16	3.05	0.51	0.07	0.07	0.00	0	1.31	1.45	1.45	-30.4	-24.2	-26.8	-23.7	-192	-178	-180		1.92			
	Su336	P ₁ s, P ₂ h		90.20	1.40	0.15	0.02	0.01	0.00	0	0.00	8.06	8.06	-28.7	-22.6	-25.1		-189	-169	-168		2.54			
	Su14-0-31	P ₁ s, P ₂ h		93.00	4.05	0.65	0.11	0.10	0.00	0	1.20	0.59	0.59	-32.0	-23.8	-24.7	-22.0	-196	-168	-172		1.48			
	Su48-2-86	P ₁ s		92.85	4.00	0.63	0.11	0.10	0.00	0	1.44	0.57	0.57	-31.7	-23.2	-24.3	-22.3	-190	-172	-170		1.55	Dai et al., [16]		
	Su48-14-76	P ₁ s, P ₂ h		92.73	3.48	0.65	0.13	0.11	0.00	0	1.47	1.14	1.14	-33.5	-22.8	-24.2	-22.2	-192	-172	-171		1.16			
	Su48-15-68	P ₂ h ₈		92.79	3.28	0.61	0.11	0.12	0.00	0	1.70	1.07	1.07	-29.8	-23.4	-25.0	-22.6	-195	-170	-172		2.12			
	Su77-2-5	P ₂ h		89.90	5.53	1.24	0.24	0.27	0.00	0	1.46	0.70	0.70	-30.8	-22.7	-23.3	-22.9	-194	-168	-164		1.80			
	Su77-6-8	P ₂ h ₈		89.90	5.80	1.24	0.22	0.24	0.00	0	0.60	0.79	0.79	-33.6	-23.9	-24.1	-23.5	-201	-165	-165		1.14			
	Su120-52-82	P ₁ s, P ₂ h		91.64	3.69	0.64	0.11	0.10	0.00	0	2.58	0.93	0.93	-31.1	-23.3	-25.6	-23.6	-192	-176	-179		1.71			
	Yu85	P ₁ s ₂		93.83	2.83	0.39	0.06	0.06	0.00	0	1.22	1.48	1.48												

TABLE 1: Continued.

Field	Well	Strata	Depth	CH ₄	C ₂ H ₆	C ₃ H ₈	iC ₄ H ₁₀	nC ₄ H ₁₀	iC ₅ H ₁₂	nC ₅ H ₁₂	C ₆ + C ₇	CO ₂	N ₂	CH ₄	δ ¹³ C (‰), VPDB				δD (‰), VSMOW			³ He/ ⁴ He	Rare gas ⁴⁰ Ar/ ³⁶ Ar	R ₀ -Dai %	Reference
															C ₂ H ₆	C ₃ H ₈	C ₄ H ₁₀	CO ₂	CH ₄	C ₂ H ₆	C ₃ H ₈				
Daniudi	Yu30	P ₁ s ₂		94.1	3.14	0.48	0.07	0.08	0.00	0	0	1.62	0.38	-33.1	-23.0	-23.4	-21.7	-183	-161	-154				1.24	
	Su77-4-6	P ₂ h ₈		90.95	5.1	1.14	0.21	0.24	0.00	0	0	0.21	0.93	-33.5	-23.7	-24.0	-23.3	-198	-161	-166				1.16	
	Su14-8-45	P ₂ h ₈		92.97	3.93	0.74	0.13	0.00	0	0	0	1.1	0.77	-33.2	-24.3	-24.3	-23.0	-188	-170	-165				1.22	
	Su14-18-36	P ₁ s ₁		93.08	3.92	0.73	0.13	0.14	0.00	0	0	1.13	0.66	-33.4	-24.0	-24.3	-22.8	-190	-170	-172				1.18	
	Su14-11-09	P ₂ h ₈		92.52	3.78	0.75	0.16	0.17	0.00	0	0	1.18	1.1	-31.6	-24.0	-24.2	-22.6	-188	-167	-173				1.58	
	Su48-13-79C3			92.82	3.33	0.61	0.12	0.12	0.00	0	0	1.55	1.18	-30.2	-22.9	-23.4	-21.9	-187	-171	-168				1.99	
	Su120-42-84	P ₂ h ₈		91.15	4.19	0.79	0.15	0.14	0.00	0	0	2.25	1.04	-31.9	-23.6	-24.7	-22.7	-190	-165	-173				1.50	
	Sunan3-45			79.77	4.53	0.96	0.23	0.17	0.00	0	0	0.04	13.93	-31.3	-22.1	-22.8	-20.7	-188	-166	-169				1.66	
				Standard deviation																			0.39		
	D66-3	P ₁ h ³		97.49	1.90	0.30	0.06	0.06	0.06	0.06	0.06	0.09	0.00	-35.8	-26.1	-24.8	-24.2	-181						0.80	
	DK19	P ₁ h ³		96.46	1.85	0.27						0.67	0.59	-34.4	-25.7	-24.3	-22.0						1.00		
	D16	P ₁ x ³		94.37	2.52	0.26	0.06	0.09	0.09	0.09	0.09	0.37	1.96	-34.7	-26.7	-26.7	-24.4						0.95		
	DK13	P ₁ x ³		94.49	1.71	0.31						0.28	2.55	-34.7	-25.6	-24.2	-22.4						0.95		
	DK14	P ₁ x ³		93.94	1.79	0.27						0.26	2.98	-35.0	-25.6	-24.2	-22.4						0.91		
	DK30	P ₁ x ¹		85.73	2.83	0.50	0.08	0.10	0.10	0.10	0.10	0.10	1.83	-34.3	-25.9	-25.3	-25.4	-181					1.02		
DP 14	P ₁ x ¹		87.91	8.07	2.32	0.34	0.43	0.43	0.43	0.43	0.42	0.00	-37.4	-25.7	-25.3	-24.6	-201					0.61			
D66-28	P ₁ x ¹		88.87	7.94	1.86	0.28	0.30	0.30	0.30	0.30	0.42	0.00	-37.7	-25.2	-24.2	-23.4	-197					0.58			
D1-1-154	P ₁ x ¹		90.49	6.23	1.59	0.25	0.31	0.31	0.31	0.31	0.64	0.10	-37.1	-25.9	-26.5	-24.5	-197					0.64	Dai et al., [16]		
DK29	P ₁ x ¹		88.67	6.88	2.24	0.49	0.46	0.46	0.46	0.46	0.55	0.15	-34.7	-25.4	-23.8	-22.8	-189					0.95			
D1-4-110	P ₁ s ¹		91.51	4.86	1.13	0.18	0.19	0.19	0.19	0.19	1.89	0.00	-34.1	-24.8	-23.2	-22.3	-186					1.05			
D10	P ₁ s ²		81.15	4.01	0.85	0.27	0.32	0.32	0.32	0.32	1.12	9.71	-36.0	-24.0	-23.5	-23.3						0.77			
D1-4-107	P ₁ s ²		89.30	6.39	2.31	0.44	0.42	0.42	0.42	0.42	0.65	0.00	-33.3	-24.8	-23.0	-22.6	-179					1.20			
D24	P ₁ s ²		87.95	6.92	1.83	0.45	0.63	0.63	0.63	0.63	0.33	1.49	-36.7	-25.4	-25.0	-24.5						0.69			
D12-1	P ₁ s ²		89.91	6.85	1.78	0.30	0.24	0.24	0.24	0.24	0.65	0.00	-35.8	-24.5	-23.5	-22.7	-193					0.80			
D47-47	C ₃ f ²		90.89	5.80	1.48	0.25	0.28	0.28	0.28	0.28	0.73	0.00	-37.5	-26.1	-24.6	-24.2	-204					0.60			
D35	C ₃ f ²		90.31	5.70	1.26	0.19	0.20	0.20	0.20	0.20	1.98	0.00	-37.9	-25.2	-23.4	-21.9	-197					0.56			
D35-22	C ₃ f ²		90.41	5.60	1.22	0.18	0.19	0.19	0.19	0.19	2.11	0.00	-37.7	-25.0	-23.1	-22.6	-195					0.58			
ES1			93.96	3.62	0.87	0.14	0.23	0.23	0.23	0.23	0.20	0.81	-33.5	-25.1	-24.6	-23.6	-11.6	-189	-168	-170	3.2 ± 0.44	1019.38 ± 14.22	1.16		
ES4			93.71	3.57	0.86	0.15	0.22	0.22	0.22	0.22	0.19	1.08	-33.3	-24.5	-23.2	-22.9	-6.8	-186	-166	-172	3.37 ± 0.4	989.672 ± 16.45	1.20		
Jin11			93.69	3.57	0.87	0.14	0.20	0.20	0.20	0.20		1.34	-33.8	-25	-24.5	-23.6	-187	-171	-179	3.41 ± 0.41	799.17 ± 10.43	1.10			
ESP2			93.74	3.64	0.85	0.12	0.17	0.17	0.17	0.17	1.32	0.00	-33.2	-25.3	-24.9	-24.4	-190	-173	-183	3.07 ± 0.47	1175.25 ± 16.44	1.22			
J11P4H			93.87	3.71	0.92	0.13	0.19	0.19	0.19	0.19	0.03	1.04	-33.1	-25.1	-24.6	-23.6	-189	-170	-158				1.24	This study	
Jin26			93.79	3.67	0.90	0.20	0.01	0.01	0.01	0.01	0.09	1.13	-33.7	-25.6	-25.3	-23.8	-22.8	-190	-175	-162	3.44 ± 0.64	853.49 ± 13.63	1.12		
DP84			85.20	8.16	1.92	0.27	0.32	0.32	0.32	0.32	2.96	0.90	-36.7	-23.8	-23.1	-22.7	-7.2	-219	-161	-138			0.69		
DK13			92.72	3.29	0.76	0.11	0.12	0.12	0.12	0.12	2.63	0.32	-35.2	-25.3	-24.6	-23.1	-4.7	-191	-170	-151			0.88		
DK3			95.20	2.87	0.55	0.08	0.08	0.08	0.08	0.08	0.52	0.78	-35.6	-25.1	-22.7	-23.0	-12.4	-193	-166	-145			0.82		
DK6			89.95	5.96	1.54	0.25	0.29	0.29	0.29	0.29	1.28	0.52	-36.8	-24.7	-24.1	-23.5	-9.2	-209	-169	-158			0.68		

The R₀-Dai was calculated by the formula $\delta^{13}\text{C} - \text{CH}_4 = 14.12\text{gRo} - 34.39$ [32].

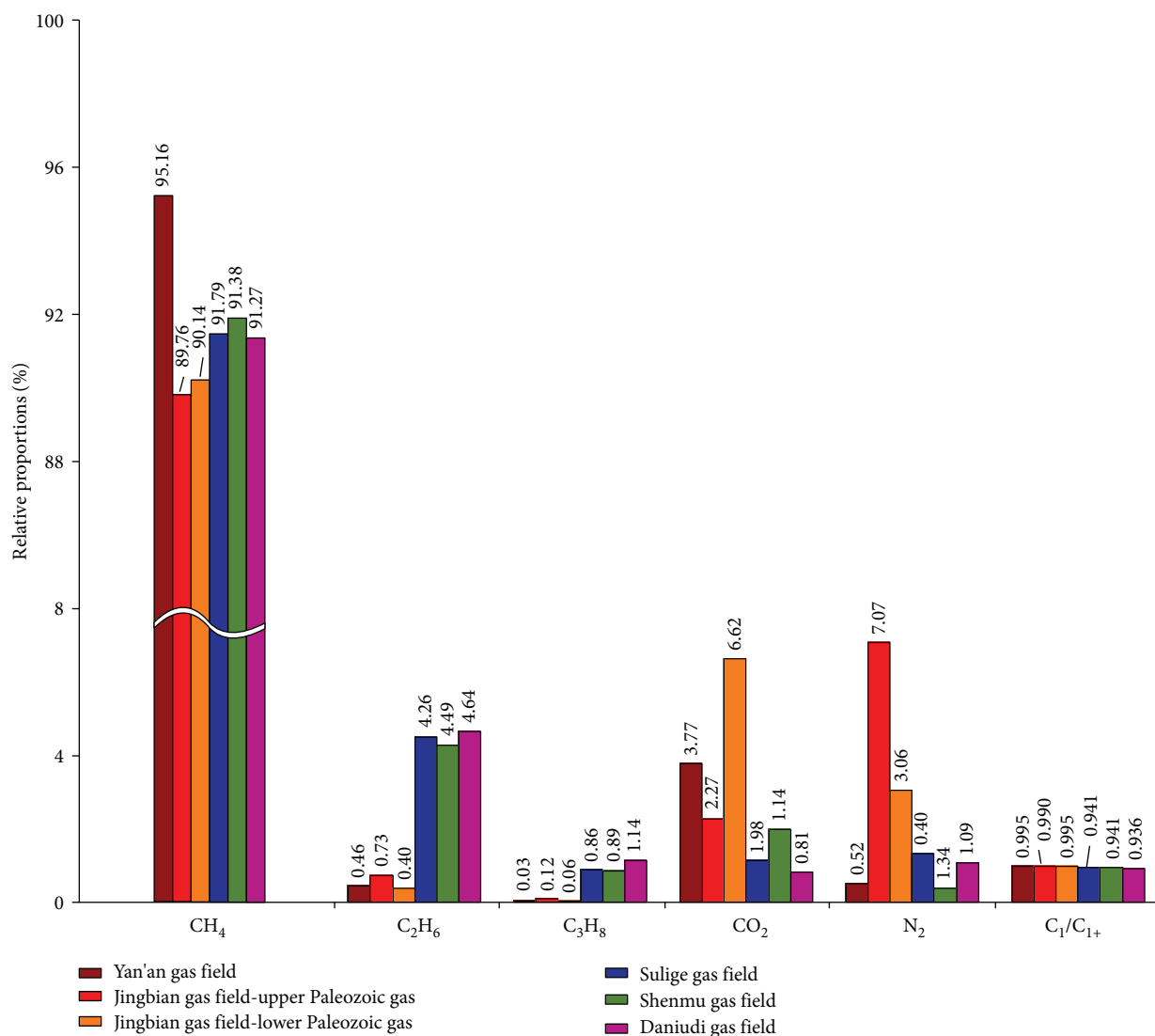


FIGURE 2: Relative proportions and dryness coefficients of gas components of natural gas in gas fields of the Ordos Basin.

to -33.62‰ (SD 2.57‰) and -27.5‰ to -30.8‰ (SD 0.85‰), respectively, with heavier isotopic compositions than those of upper Paleozoic coal-derived gases from other Ordos Basin gas fields such as the Sulige, Shenmu, and Daniudi fields (Table 1; Figure 3). In contrast, most upper Paleozoic gases from the southern Ordos Basin have unusually light $\delta^{13}\text{C}\text{-C}_2\text{H}_6$ values, with those of South Jingbian gas averaging -31.5‰ and Yan'an gas averaging -34.8‰ , which are lighter than typical coal-derived gases ($\geq 29\text{‰}$). Equivalent vitrinite reflectance values of the sources of gases of the upper Paleozoic South Jingbian and Yan'an are in the range $1.14\text{--}5.39\text{‰R}_o$ (SD 1.45‰R_o) and $1.80\text{--}3.09\text{‰R}_o$ (SD 0.34‰R_o), respectively, with the reflectance values of most of these gases being in the range $2.0\text{--}3.5\text{‰R}_o$, based on the relationship proposed by Dai et al. [32] for gases generated from type III kerogen-coal ($\delta^{13}\text{C}\text{-CH}_4 = 14.12; 34.39\text{‰R}_o$), consistent with measured vitrinite reflectance of coal source rocks in the upper Paleozoic strata (Figure 1).

Compared with upper Paleozoic South Jingbian gases, lower Paleozoic gases contain alkanes more depleted in ^{13}C , with $\delta^{13}\text{C}\text{-CH}_4$ values of -27.00‰ to -36.48‰ (mean -32.05‰ , SD 1.72‰) and $\delta^{13}\text{C}\text{-C}_2\text{H}_6$ values of -28.10‰ to -39.42‰ (mean -35.06‰ , SD 2.21‰). The equivalent vitrinite reflectance of lower Paleozoic gas sources, calculated as proposed by Dai et al. [32] for coal-derived gas, is in the range $0.71\text{--}3.35\text{‰R}_o$ (mean 1.50‰R_o , SD 0.48‰R_o). Calculated R_o values for lower Paleozoic source rocks of South Jingbian gas are lower than those of upper Paleozoic source rocks in the same region (Figure 1), indicating two possibilities: that the gas is not coal-derived and the calculation method is therefore inapplicable or that the gases were generated from other coal source rocks of lower maturity than the upper Paleozoic source rocks. Jurassic coaly source rock has lower maturity than C-P coaly source rock, although it produces mainly oil and there is no pathway for any gas generated to migrate to the lower Paleozoic reservoir,

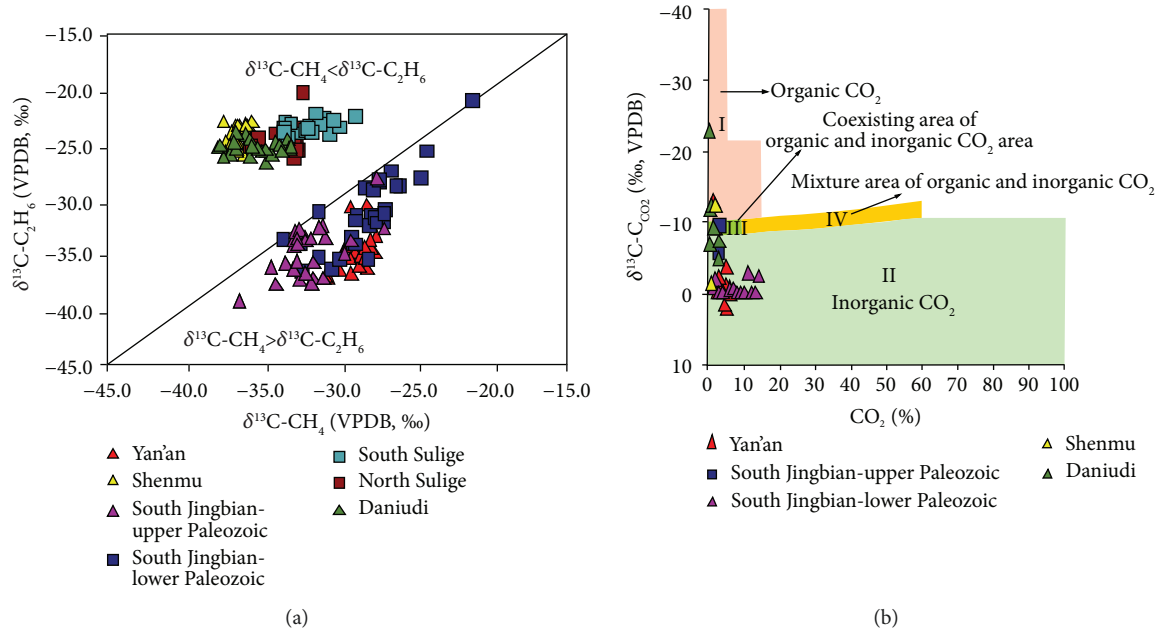


FIGURE 3: (a) Plot of $\delta^{13}\text{C}-\text{C}_2\text{H}_6$ versus $\delta^{13}\text{C}-\text{CH}_4$; (b) relationship between $\delta^{13}\text{C}-\text{CO}_2$ and CO_2 content of gases in different gas fields of the Ordos Basin (modified from [33]). Note: symbols for samples from different areas of the Ordos Basin are used in all subsequent figures.

precluding the second possibility. Type I and type II kerogen occur in lower Paleozoic Ordovician source rocks [11, 34], so oil-type gases generated there could be mixed with lower Paleozoic gases, and the R_o - $\delta^{13}\text{C}-\text{CH}_4$ relationship is not applicable to mixed gases. It appears, therefore, that geochemical differences between lower and upper Paleozoic South Jingbian gases indicate that they are produced from different sources.

Thrasher and Fleet [35] reported that the $\delta^{13}\text{C}$ values for large gas accumulations (over 15 vol.% of CO_2) are in the range -10‰ to 0‰ , suggesting an inorganic origin. In contrast, gas accumulations that have less than 15 vol.% of CO_2 and low $\delta^{13}\text{C}-\text{CO}_2$ values ($<10\text{‰}$) are of organic origin. Dai et al. [33] reviewed the distribution of $\delta^{13}\text{C}-\text{CO}_2$ values in Chinese basins and proposed a model of CO_2 production in which gases of organic origin contain $<15\%$ CO_2 with $\delta^{13}\text{C}-\text{CO}_2$ values below -10‰ , whereas gases of inorganic origin contain $>60\%$ CO_2 with $\delta^{13}\text{C}-\text{CO}_2$ values of -8‰ to -3‰ . The $\delta^{13}\text{C}-\text{CO}_2$ values of 23 Ordos Basin gas samples range from -12.9‰ to 10.9‰ , with 20 having values above -8‰ (Figure 3(b), Table 1), indicating an inorganic origin. Considering that a unit of thick limestone occurs in the Benxi (C_2b) and Taiyuan (P_1t) formations in the Ordos Basin, it is likely that CO_2 was produced by the cracking of inorganic carbonates. The C-P coaly source rock generated organic acid while approaching and reaching maturation [16], with the palaeotemperature reaching 160 – 200°C . These factors created a favourable environment for the generation of CO_2 .

4.3. Hydrogen Isotopic Composition. The hydrogen isotopic composition of methane ($\delta\text{D}-\text{CH}_4$) of natural gas in the southern Ordos Basin is heavy compared with that of the

other gas fields (Figure 4(a)). Yan'an gas $\delta\text{D}-\text{CH}_4$ values range from -163.0‰ to -170.0‰ (mean -166.6‰ , SD 1.98‰). Lower Paleozoic South Jingbian gases have similar hydrogen isotopic compositions, with $\delta\text{D}-\text{CH}_4$ values of -157‰ to -171‰ (mean -165.33‰ , SD 4.85‰). The heavy $\delta\text{D}-\text{CH}_4$ values of Yan'an and South Jingbian gases are consistent with their high maturities. The hydrogen isotopic compositions of ethane ($\delta\text{D}-\text{C}_2\text{H}_6$) of southern Ordos Basin gases are light compared with those of gases from all other Ordos Basin fields (Table 1). The $\delta\text{D}-\text{C}_2\text{H}_6$ values of Yan'an gases range from -167.0‰ to -197.0‰ (mean -184.3‰ , SD 6.91‰), whereas those of South Jingbian gases range from -173.0‰ to -191.0‰ (mean -182.0‰ , SD 5.89‰). Gases of the southern Ordos Basin thus display hydrogen isotopic reversal ($\delta\text{D}-\text{CH}_4 > \delta\text{D}-\text{C}_2\text{H}_6$) (Figure 4(b)).

4.4. Carbon Isotopic Reversal in Gases from the Southern Ordos Basin. Carbon isotopic reversal is a distinctive feature of Paleozoic natural gas of the southern Ordos Basin (Figure 5). The lower Paleozoic South Jingbian gases all display partial reversal ($\delta^{13}\text{C}-\text{CH}_4 > \delta^{13}\text{C}-\text{C}_2\text{H}_6 < \delta^{13}\text{C}-\text{C}_3\text{H}_8$), whereas upper Paleozoic gases display partial ($\delta^{13}\text{C}-\text{CH}_4 > \delta^{13}\text{C}-\text{C}_2\text{H}_6 < \delta^{13}\text{C}-\text{C}_3\text{H}_8$) or complete ($\delta^{13}\text{C}-\text{CH}_4 > \delta^{13}\text{C}-\text{C}_2\text{H}_6 > \delta^{13}\text{C}-\text{C}_3\text{H}_8$) reversals, and Yan'an gases display complete reversals. For all Ordos Basin upper Paleozoic gas fields, there is a strong relationship between maturity (indicated by R_o values) and carbon isotopic series (Figures 1(a) and 5; Table 2).

On the basis of the new data and the results of previous studies, some preliminary conclusions can be drawn as follows. A large portion of the gases with complete carbon isotopic reversal appears in regions with $R_o > 2.4\%$, but not all gases from such regions display complete reversal (some

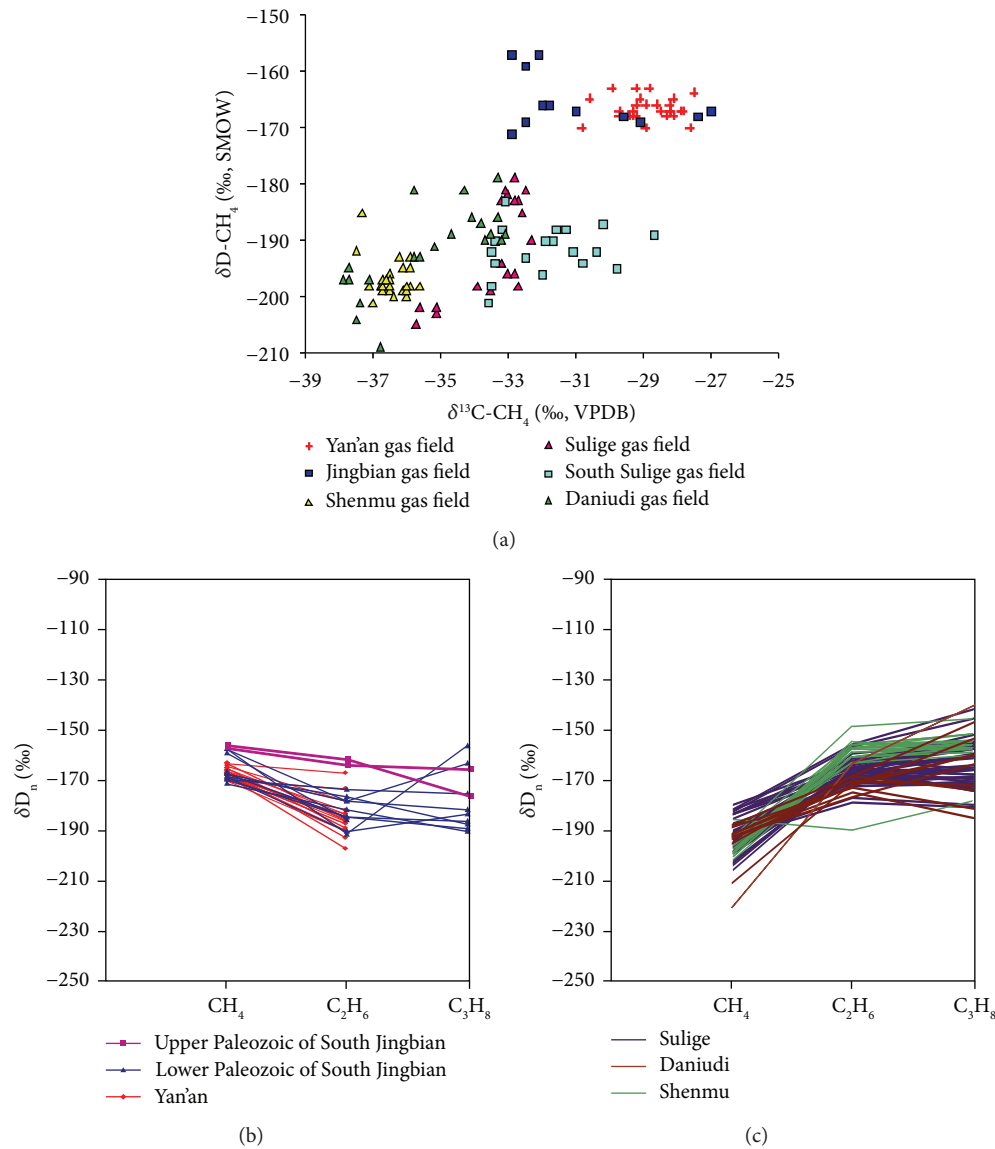


FIGURE 4: (a) Plot of $\delta D-CH_4$ versus $\delta^{13}C-CH_4$; (b) hydrogen isotopic series of alkanes in lower and upper Paleozoic gases of South Jingbian and Yan'an gas fields (all gases show hydrogen isotopic reversal with $\delta D-CH_4 > \delta D-C_2H_6$); (c) hydrogen isotopic series of alkane gases in Sulige, Daniudi, and Shenmu gas fields (with positive hydrogen isotopic series).

have partial reversals); in regions with $2.4\% > R_o > 2.0\%$, almost all gases display partial reversals, some with $\delta^{13}C-CH_4 > \delta^{13}C-C_2H_6$ and others with $\delta^{13}C-C_2H_6 > \delta^{13}C-C_3H_8$; and most gases from regions with $R_o < 2.0\%$ display positive carbon isotopic series. The correlation between carbon isotopic series in Paleozoic Ordos Basin gases and gas maturity indicates that isotopic reversal may be caused by elevated temperatures.

4.5. Carbon Isotopic Evolution in Gases of Different Maturity.

As observed for shale gases of varying maturity, carbon isotopic compositions of methane and ethane indicate different evolutionary trends, with $\delta^{13}C-CH_4$ values increasing with decreasing wetness and $\delta^{13}C-C_2H_6$ values first increasing and then decreasing with decreasing wetness (Figure 6). The evolution of mainly coal-derived natural gases in the

Paleozoic strata of the Ordos Basin can be divided into two zones in terms of $\delta^{13}C-C_2H_6$ versus wetness trends: a prerollover zone with wetness of $>2.0\%$ and a rollover zone with wetness of $<2.0\%$ (Figure 6(a)). Paleozoic gases from the South Jingbian and Yan'an fields are distributed mainly in the rollover zone, where $\delta^{13}C-C_2H_6$ values become more negative with decreasing wetness. Upper Paleozoic gases from the Sulige, Shenmu, and Daniudi fields are distributed in the prerollover zone, where $\delta^{13}C$ values of ethane become heavier with decreasing wetness (Figure 6(a)). $\delta^{13}C-C_2H_6$ rollover occurs with wetness of $<2.0\%$ (this study), whereas for shale gases it occurs with wetness of $<5.0\%$ [15]. A possible cause of this difference is that at the same maturity level, shale gases that originated from types I and II kerogen contain more wet gases than do coal-derived gases that originated from type III kerogen, owing to the different structures

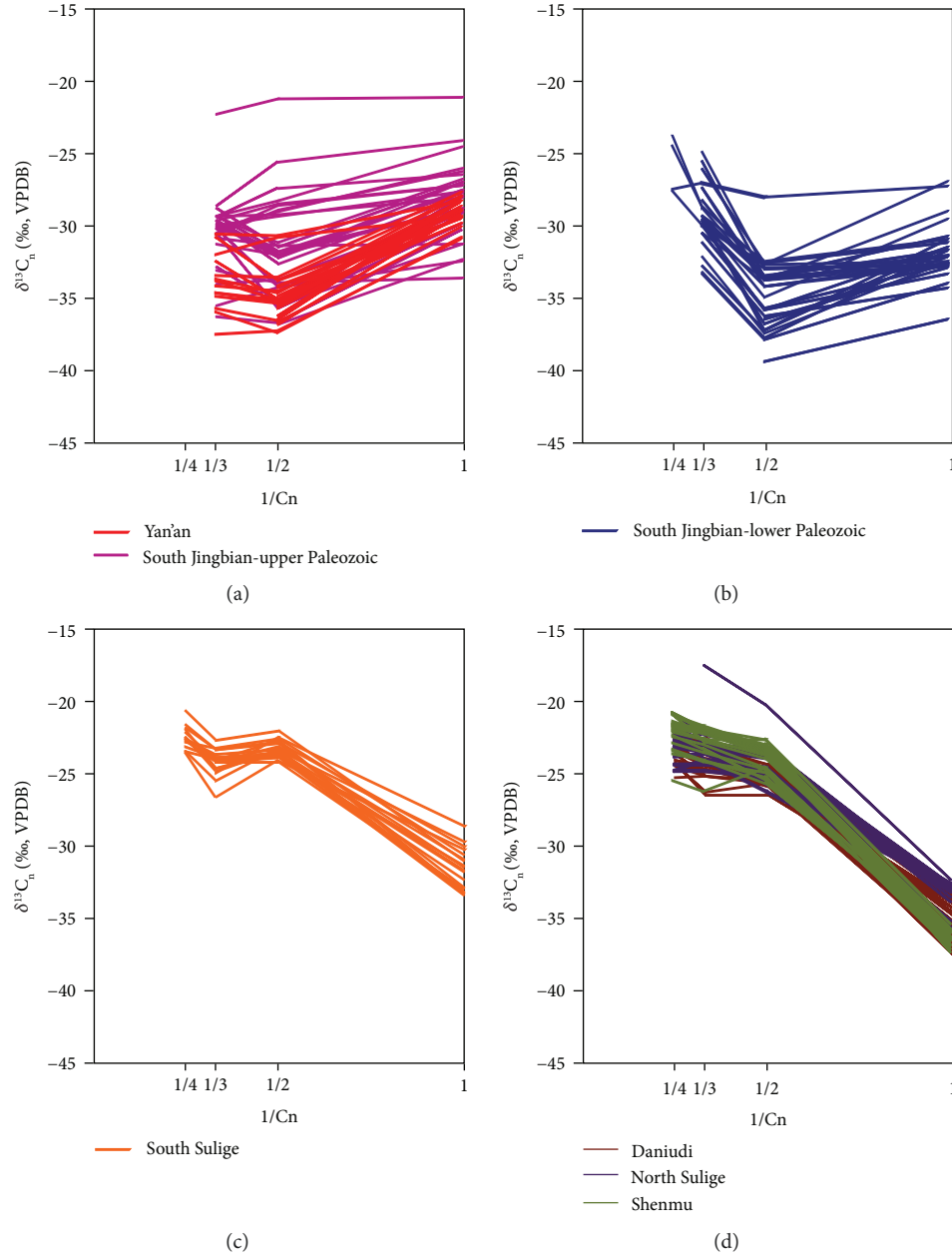


FIGURE 5: Carbon isotopic series of alkane gases in (a) Yan'an and upper Paleozoic South Jingbian gas fields; (b) lower Paleozoic South Jingbian field; (c) southern Sulige field; and (d) Daniudi, northern Sulige, and Shenmu gas fields.

TABLE 2: Relationship between maturity and carbon isotopic series in the Ordos Basin.

Gas field	Source rock maturity	Carbon isotopic series	Detailed carbon isotopic series
Yan'an/South Jingbian	$R_o > 2.4\%$	Complete reversal	$\delta^{13}C-CH_4 > \delta^{13}C-C_2H_6 > \delta^{13}C-C_3H_8$
South Jingbian	$R_o > 2.0\%$	Partial reversal	$\delta^{13}C-CH_4 > \delta^{13}C-C_2H_6 < \delta^{13}C-C_3H_8$
South Sulige	$R_o > 2.0\%$	Partial reversal	$\delta^{13}C-CH_4 < \delta^{13}C-C_2H_6 > \delta^{13}C-C_3H_8$
North Sulige, Shenmu, and Daniudi	$R_o < 2.0\%$	Positive series	$\delta^{13}C-CH_4 < \delta^{13}C-C_2H_6 < \delta^{13}C-C_3H_8$

of parent sources. In the case of shale gas, the retained petroleum could closely contact the kerogen and/or source rock mineralogy, so the cracking rate of the crude oil is much ear-

lier than the conventional gas formation [36]. The $\delta^{13}C-C_2H_6$ content of Ordos gases increases with decreasing wetness (Figure 6(b)).

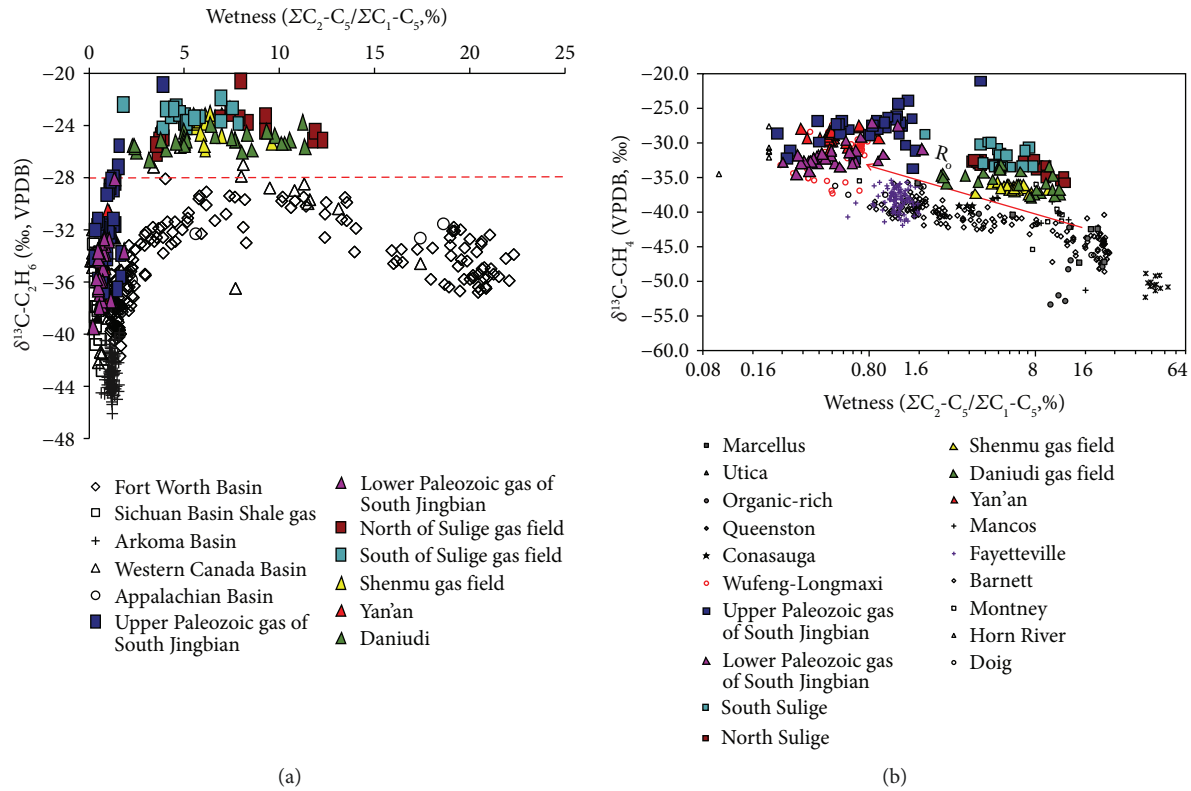


FIGURE 6: (a) $\delta^{13}\text{C}-\text{C}_2\text{H}_6$ versus wetness (modified from [15]); (b) $\delta^{13}\text{C}-\text{CH}_4$ versus wetness (modified from [15]). (Data sources for shale gas in (a) and (b) are as follows: [13, 24–27, 29, 30]; from [14–16, 28, 31]).

5. Discussion

5.1. Source of Natural Gas. Numerous models have been proposed to identify the origin of hydrocarbon gases. One of the most widely used models is the Bernard diagram, which combines $(\text{C}_1/\text{C}_2+\text{C}_3)$ and $\delta^{13}\text{C}-\text{CH}_4$ values. Whiticar [37] modified the diagram after Bernard et al. [38] and Faber and Stahl [39] to identify primary gases and gases altered by secondary effects. Based on previous work, Dai et al. [40] developed a similar model by plotting $(\text{C}_1/\text{C}_2+\text{C}_3)$ versus $\delta^{13}\text{C}-\text{CH}_4$ values for natural gases with different origins from various basins in China, with the model being especially applicable for gas identification in China. A modified Dai plot (Figure 7) of the data in Table 1 reveals that most gases of the Sulige, Shenmu, and Daniudi fields are derived from type III kerogen coaly source rocks, supporting results of previous studies [16]. However, the source of Paleozoic gases in the southern Ordos Basin is more complicated. As shown in Figure 7, data for most upper Paleozoic South Jingbian and Yan'an gases plot in the field of “coal-type gas,” whereas data for lower Paleozoic gases of South Jingbian plot in either the field of “cracking gas from oil and type II kerogen” or the field of “coal-type gas.” This pattern indicates that the upper Paleozoic gas of the southern Ordos Basin is mainly coal-type gas derived from coaly source rocks, whereas the lower Paleozoic gas of the southern Ordos Basin is a mixture of coal-type gas and oil-type gas.

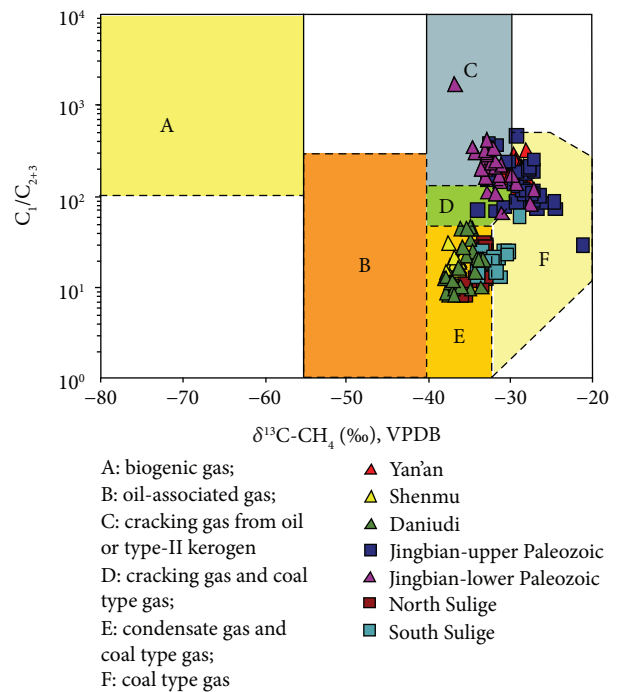


FIGURE 7: Plot of $\text{C}_1/\text{C}_{2+3}$ ratio versus $\delta^{13}\text{C}-\text{CH}_4$ (modified after [38–40]).

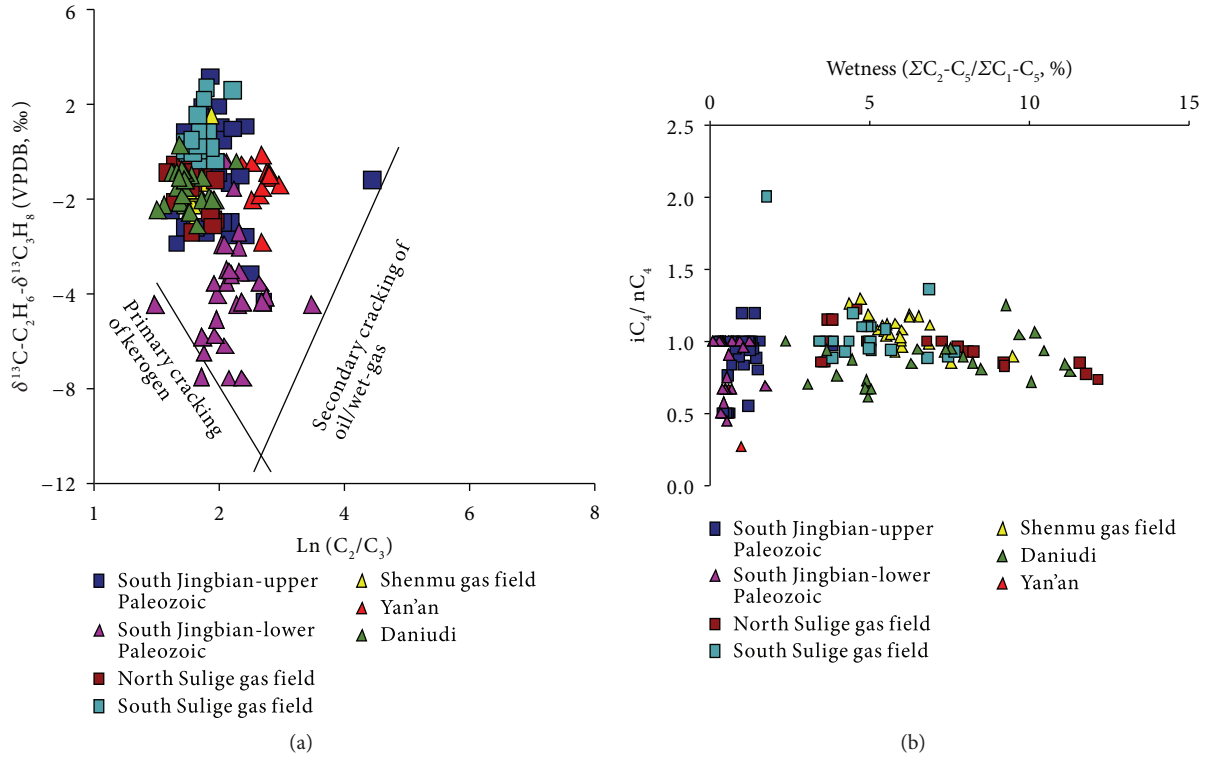


FIGURE 8: (a) Relationship between $\delta^{13}\text{C-C}_2\text{H}_6 - \delta^{13}\text{C-C}_3\text{H}_8$ and gas wetness (the trending line for primary cracking and secondary cracking was modified from [44]); (b) relationship between iC_4/nC_4 and gas wetness (modified from [44]).

5.2. Origin of Carbon Isotopic Reversals

5.2.1. Possible Causes for the Carbon Isotopic Reversals. There are four possible causes of carbon isotopic reversal as follows.

(1) *Inorganic Origin.* Inorganic gases are formed by Fischer-Tropsch synthesis when mantle degassing releases CO_2 or CO , forming hydrocarbons by reduction with reversed carbon isotopic compositions [41]. Such gases are typically characterized by $\delta^{13}\text{C-CH}_4 > \delta^{13}\text{C-C}_2\text{H}_6 > \delta^{13}\text{C-C}_3\text{H}_8 > \delta^{13}\text{C-C}_4\text{H}_{10}$, with $\delta^{13}\text{C-CH}_4 > -25\text{‰}$ [42]. Of the 107 Paleozoic gas samples from the southern Ordos Basin, 15 have complete carbon isotope reversal ($\delta^{13}\text{C-CH}_4 > \delta^{13}\text{C-C}_2\text{H}_6 > \delta^{13}\text{C-C}_3\text{H}_8$), whereas others have partial reversal with $\delta^{13}\text{C-CH}_4 > \delta^{13}\text{C-C}_2\text{H}_6 < \delta^{13}\text{C-C}_3\text{H}_8$, or there are no $\delta^{13}\text{C-C}_3\text{H}_8$ data (Table 1). The $\delta^{13}\text{C-CH}_4$ value is less than -25‰ for all except three samples. As the $^3\text{He}/^4\text{He}$ value of mantle helium is higher than that of crust-sourced helium, the ratio R/R_a , a comparison of the $^3\text{He}/^4\text{He}$ ratio of sample (R) against the atmospheric ratio (R_a), can be used to distinguish whether mantle-derived inorganic gas was injected into the natural gas-producing system [40]. Mantle-sourced helium in all cases has R/R_a ratios of >0.1 [42]. R/R_a values for gases in the southern Ordos are all <0.1 . It is therefore concluded that the helium in the Paleozoic gases of the southern Ordos Basin is not mantle-derived, suggesting an “organic origin” of the associated hydrocarbon gases.

(2) *Mixing.* Some studies have suggested that the isotopic reversal observed in the southern Ordos Basin was caused

by the mixing of coal-derived and oil-type gases from source rock containing type I-II kerogen [3], (Yang et al., 2012), [4, 7]. This cause can easily be excluded. To generate gas mixtures with the light carbon isotopic composition of ethane, the oil-type gas end-member should have $\delta^{13}\text{C-C}_2\text{H}_6$ lighter than the mixed gases. $\delta^{13}\text{C-C}_2\text{H}_6$ values of most samples are less than -32‰ , with the lightest being -39.42‰ (Table 1); however, the lightest $\delta^{13}\text{C-C}_2\text{H}_6$ values of oil-type gases found in Paleozoic reservoirs range from -30.0‰ to -32.0‰ [10, 43]. Even with all of the ethane in the mixture being oil-type gas, it would not account for the carbon isotopic characteristics observed here.

(3) *Wet-Gas Cracking.* This model involves the mixing of primary gas generated directly from kerogen cracking and secondary gas generated from intermediate kerogen products. The wet-gas cracking model produces a positive relationship between $\ln(C_2/C_3)$ and $\delta^{13}\text{C-C}_2\text{H}_6 - \delta^{13}\text{C-C}_3\text{H}_8$ with increasing thermal stress [44] during the secondary cracking process and an initial increase followed by a rapid decrease in iso-butane/n-butane (iC_4/nC_4) ratios with respect to the decrease in wetness (due to the lower stability of iC_4 than nC_4 at high maturity; [15]). The relationship between $\ln(C_2/C_3)$ and $\delta^{13}\text{C-C}_2\text{H}_6 - \delta^{13}\text{C-C}_3\text{H}_8$ in the Ordos data (Figure 8(a)) indicates that secondary cracking of wet gas does not occur in gases of the southern Ordos Basin. If cracking was the main cause of isotopic reversal, the trend of $\ln(C_2/C_3)$ would be expected to first decrease and then increase with increasing $\delta^{13}\text{C-C}_2\text{H}_6 - \delta^{13}\text{C-C}_3\text{H}_8$, as shown for Barnett and Fayetteville shale gases [44]. This trend is

not evident here (Figure 8(a)), indicating that wet-gas cracking cannot be the main cause of carbon isotopic reversal in the southern Ordos Basin. There is no obvious rollover pattern of iC_4/nC_4 versus wetness in Ordos Basin data (Figure 8(b)), suggesting that cracking of wet gas may have occurred.

(4) *Abiotic Polymerization*. Under conditions of ultrahigh temperatures and pressures, similar to those at which inorganic gases are generated, polymerization processes could alter carbon isotope distributions to be similar to those of inorganic gases [45]. If abiotic polymerization occurred, carbon isotopic separation of $1000\ln(\sigma_{C_2-C_1})$ would be expected to decrease as thermal stress increased. As more wet gases were polymerized with increasing thermal stress, wetness would be expected to increase. Taking $1000\ln(\sigma_{C_2-C_1})$ as an indicator of thermal stress, the dryness indicator $C_1/(C_2+C_3)$ should decrease with decreasing $1000\ln(\sigma_{C_2-C_1})$ if the gases were generated by polymerization. Zeng et al. [45] suggested that gases from the Songliao field with isotopic reversals were generated by abiotic polymerization, and the trend for their data is plotted in Figure 9 for comparison. As shown in Figure 9, there is an initial increase and then decrease of $C_1/(C_2+C_3)$ ratios with increasing $1000\ln(\sigma_{C_2-C_1})$ values for the Songliao gases. However, for data from the present study, $C_1/(C_2+C_3)$ ratios of Ordos Basin gases continue to increase with increasing $1000\ln(\sigma_{C_2-C_1})$ (Figure 9). If the gas had been generated by polymerization, $C_1/(C_2+C_3)$ ratios should decrease in the high-maturity stage. Abiotic polymerization thus cannot be the main cause of carbon isotopic reversal in gases of the southern Ordos Basin.

Other models have been proposed to explain carbon isotopic reversal in overmature shale gases, including mass transport [46], water-kerogen redox reactions [47, 48], and other reactions involving transition metals [13, 49]. However, as southern Ordos Basin gases are stored in organic-poor sandstone and carbonates, fractionation through gas movement is unlikely to be the main cause of isotopic reversal. Nor could the other reactions be the cause because the conditions required for these reactions do not occur in the Ordos Basin.

5.2.2. Closed-System Aromatization-Polycondensation Model.

It is clear that geological conditions should be taken into account in explaining carbon isotopic reversal of southern Ordos Basin gases. Dieckmann et al. [50] conducted closed-system pyrolysis experiments with a type III kerogen Taglu Sequence sample, demonstrating that large amounts of gas are generated at extreme levels of thermal stress, with $\delta^{13}C$ values of methane falling to values 10‰ lighter than those of open systems. They suggested that neoformed materials produced during low-maturity stages become active at high maturities ($R_o > 2.5\%$) and recombine with residual kerogen or coal to form gases through aromatization-polycondensation reactions. Furthermore, Erdmann and Horsfield [51] have shown that closed-system pyrolysis of type II/III kerogen of the heater formation results in recombination reactions, which act as sources of gas beyond the

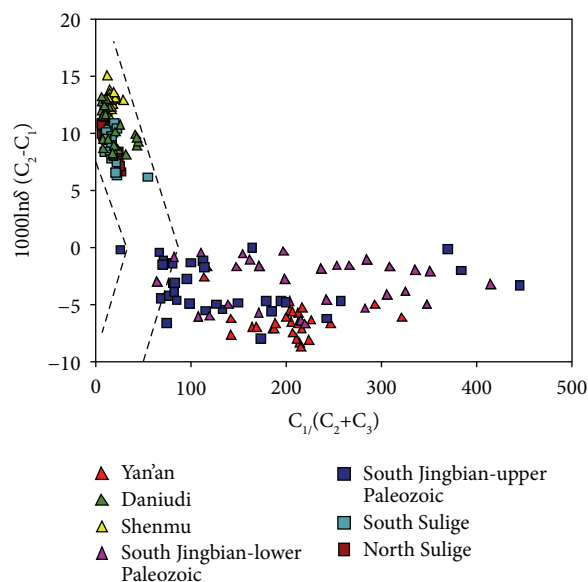


FIGURE 9: Plot of isotopic separation $1000\ln(\sigma_{C_2-C_1})$ versus $C_1/(C_2+C_3)$, where $\sigma_{C_2-C_1} = (1000 + \delta^{13}C-C_2H_6)/(1000 + \delta^{13}C-CH_4)$ (modified after Zeng et al., 2008, the dashed line indicated the expected trend for gas generated by abiotic polymerization).

normal thermal conditions of oil-to-gas cracking, with aromatic compounds, phenols, and short n-alkyl chains being the main products formed from type III kerogen. Aromatization-polycondensation reactions are well known as major processes taking place during coal maturation [52–54]. In the mechanism proposed by Dieckmann et al. [50] and Erdmann and Horsfield [51], some neoformed macromolecules with relatively light carbon isotopic compositions were generated in low-maturity stages and preserved in the closed system. In overmature stages, these neoformed macromolecules react with residual kerogen or coal to form short-chain alkanes depleted in ^{13}C . Such reactions could generate alkanes with light carbon isotopic compositions in the overmature stage.

Mahlstedt and Horsfield [36] showed that the results of Dieckmann et al. [50] and Erdmann and Horsfield [51] were applicable to natural maturation and also discovered that the ability of source rocks to generate late gas (the gas generated through aromatization-polycondensation at high maturity) is related to the initial organic-matter structure, depositional environment, and precursor biota. The heterogeneous aromatic and/or phenolic type II/III and type III coals from fluvial-deltaic-terrestrial environments are most favourable for late gas generation (Yang et al., 2015). The C-P source rock of the Ordos Basin contains Shanxi (P_1s), Taiyuan (P_1t), and Benxi (C_2b) coals and mudstones, with these coaly source rocks having been precipitated in such an environment, with the shore and shallow water delta environment gradually transitioning to a tidal flat or terrestrial swamp. Over long periods, large areas of coal seam sediment were formed. The maceral composition of the source rocks includes vitrinite (Table 3), indicating a terrestrial origin. The sedimentary environment of the upper Paleozoic source

TABLE 3: Geochemical parameters of upper Paleozoic source rocks of Ordos Basin [55, 56].

Item		Organic carbon (%)	Chloroform bitumen A (%)	Total hydrocarbon (ppm)	Maceral composition (%)		
					Vitrinite	Fusinite	Inertinite
		Max/min Average					
Shanxi formation	Coal	89.17/49.28	2.45/0.1	6699.93/519.9	90.2/43.8	54/6.3	12.3/0
		73.6	0.8	2539.8	73.6	24	4.6
	Mudstone	19.29/0.07	0.5/0.0024	524.96/519.85	47/8	87/51.8	20.3/0
		2.25	0.04	163.8	20.5	72	7.4
Taiyuan formation	Coal	83.2/3.83	1.96/0.03	4463/222	98.8/21.2	63.7/1.3	15.1/0
		74.7	0.61	1757.1	64.2	32.1	3.7
	Mudstone	23.38/0.1	2.95/0.003	1904.64/15	82/8.3	89.3/15.3	34.5/0.3
		3.33	0.12	361.6	38	53.3	8.4
	Limestone	6.29/0.11	0.43/0.0026	2194.53/88.92			
		1.41	0.08	493.2			
Benxi formation	Coal	80.26/55.38	0.97/0.41		93.3/72	25.2/6.7	2.8/0
		70.8	0.77		87.2	16	1.4
	Mudstone	11.71/0.05	0.44/0.0024	1466.34/12.51	47.8/12.3	59.8/12.3	39.5/0.3
		2.54	0.065	322.73	24.5	44	18.2

Note: this table has also been used in Liu et al., [57].

rocks indicates that they were favourable precursors for late gas generation.

The geological setting of the southern Ordos Basin provides conditions similar to those essential for such reactions, including type III coaly source rock, high thermal maturity, and a closed system. Most southern Ordos Basin gases were formed from thick coaly source rocks with high maturities and high quality. Large amounts of gas were generated in short time periods and stored in nearby tight sandstone reservoirs with thick caprocks and with gas migration being hindered by the stable basement. Paleozoic gas thus accumulated near its source. Therefore, southern Ordos Basin gas fields have conditions approximating closed systems in which aromatization-polycondensation reactions may occur.

A special example for comparison is the gas of the Kela2 gas field in the Tarim Basin, which was also generated from overmature ($R_o > 2.0\%$) coaly source rocks, but do not display carbon isotopic reversal [16], because the Kela2 gas field is an open system, with neoformed materials having expired before the overmature stage.

If aromatization-polycondensation reactions took place in the southern Ordos Basin gas fields under study here, the gases generated would contain isotopically light methane, ethane, and propane. However, as the amounts of methane > ethane > propane in the residual alkanes generated from kerogen cracking, a small addition of newly formed gas would result in rollover of $\delta^{13}\text{C}-\text{C}_3\text{H}_8$, whereas rollover of $\delta^{13}\text{C}-\text{CH}_4$ would require a larger amount. This would result in two trends: (1) with increasing maturity, rollover of $\delta^{13}\text{C}-\text{C}_3\text{H}_8$ would occur first, followed by $\delta^{13}\text{C}-\text{C}_2\text{H}_6$, and although isotopically light C_1 was added, residual heavy C_1 would dominate the gas mixture with insignificant changes in $\delta^{13}\text{C}-\text{CH}_4$, and rollover of $\delta^{13}\text{C}-\text{CH}_4$ would occur last; (2) as $^{13}\text{C}_3$ became depleted more rapidly than $^{13}\text{C}_1$ and $^{13}\text{C}_2$, reversal of $\delta^{13}\text{C}-\text{C}_2\text{H}_6$ and $\delta^{13}\text{C}-\text{C}_3\text{H}_8$ would occur first, with reversal of $\delta^{13}\text{C}-\text{CH}_4$ and $\delta^{13}\text{C}-\text{C}_2\text{H}_6$ occurring later.

The evolution of carbon isotopic compositions in Ordos Basin gas fields appears to follow these two processes (Figures 6(a), 6(b) and 10(a)). The rollover points of $\delta^{13}\text{C}-\text{CH}_4$, $\delta^{13}\text{C}-\text{C}_2\text{H}_6$, and $\delta^{13}\text{C}-\text{C}_3\text{H}_8$ occur at different wetness and thermal maturities, with wetness of $\delta^{13}\text{C}-\text{CH}_4$, $\delta^{13}\text{C}-\text{C}_2\text{H}_6$, and $\delta^{13}\text{C}-\text{C}_3\text{H}_8$ being 1.2%, 2.0%, and 5.0%, respectively (Figures 6(a), 10(a) and 10(b)). With respect to increasing maturity in the whole basin, the reversal of $\delta^{13}\text{C}-\text{C}_3\text{H}_8 < \delta^{13}\text{C}-\text{C}_2\text{H}_6$ occurs first in the south Sulige field (R_o 2.0%–2.6%), then reversal of $\delta^{13}\text{C}-\text{C}_2\text{H}_6 < \delta^{13}\text{C}-\text{CH}_4$ occurs in the South Jingbian field ($2.0\% < R_o < 3.8\%$), whereas complete reversal occurs only where $R_o > 2.4\%$.

5.3. Hydrogen Isotopic Reversal. A unique characteristic of the southern Ordos Basin gas fields is the hydrogen isotopic reversal ($\delta\text{D}-\text{CH}_4 > \delta\text{D}-\text{C}_2\text{H}_6$). Rollover of $\delta\text{D}-\text{CH}_4$ has been observed in overmature shale gases worldwide [13–15]. Although southern Ordos Basin gases show a rollover of $\delta\text{D}-\text{C}_2\text{H}_6$ (Figure 11(a)), Figure 11(b) indicates that $\delta\text{D}-\text{CH}_4$ values continue to increase as wetness decreases, which differs from the trend observed for overmature shale gases, although both gas types display hydrogen isotopic reversal ($\delta\text{D}-\text{CH}_4 > \delta\text{D}-\text{C}_2\text{H}_6$).

The hydrogen isotopic reversal of methane has been reported in overmature unconventional and conventional gases [13–15]. The temperature of the reservoirs can reach 200–350°C, and at such temperatures, hydrocarbon reactions can be impacted by the presence of water [47] and redox-active transition metals [58]. Most previous studies attributed the phenomenon to isotopic exchange between CH_4 and H_2O at high temperatures, leading to reversal of $\delta\text{D}-\text{CH}_4$ and $\delta\text{D}-\text{C}_2\text{H}_6$ and rollover of $\delta\text{D}-\text{CH}_4$ with increasing maturity. Gases that have undergone isotopic exchange between CH_4 and H_2O can be recognized by increasing CO_2 content with decreasing wetness and decreasing $\delta^{13}\text{C}-\text{CO}_2$ with decreasing wetness [15].

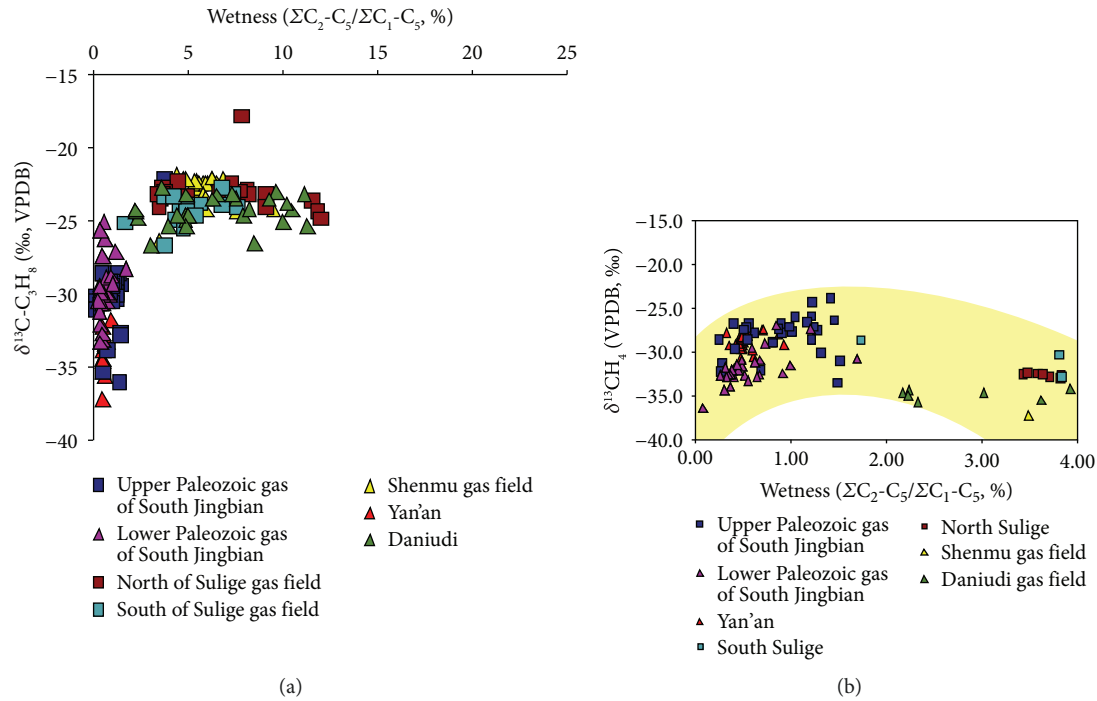


FIGURE 10: (a) $\delta^{13}\text{C}-\text{C}_3\text{H}_8$ versus gas wetness (modified from [15]); (b) detailed plot of $\delta^{13}\text{C}-\text{CH}_4$ versus gas wetness with a wetness range of 0%–4%.

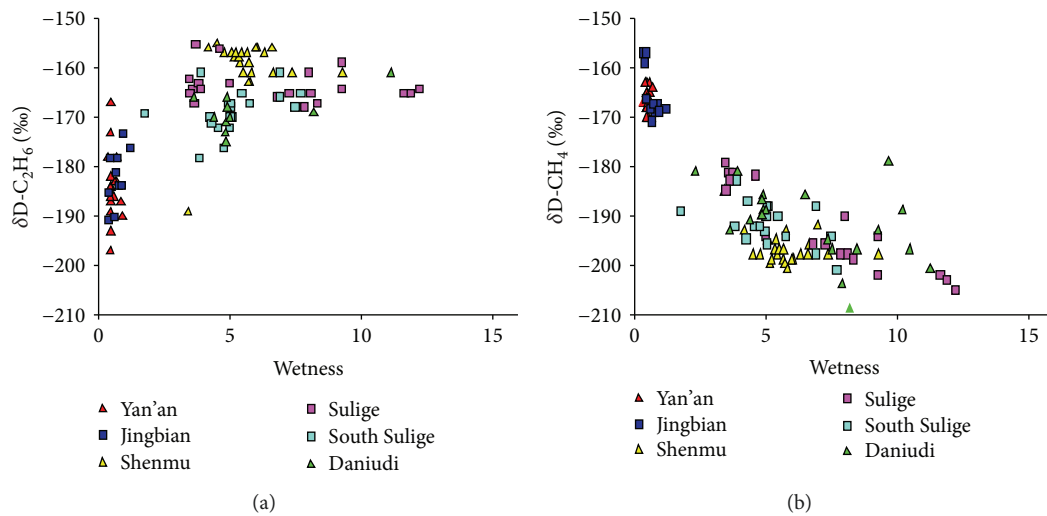


FIGURE 11: (a) $\delta\text{D}-\text{C}_2\text{H}_6$ versus wetness of the gases from different gas fields in the Ordos Basin; (b) $\delta\text{D}-\text{CH}_4$ versus wetness of the gases from different gas fields in the Ordos Basin.

Evolutionary trends of CO_2 content and $\delta^{13}\text{C}-\text{CO}_2$ with decreasing wetness are illustrated in Figure 12. CO_2 contents of southern Ordos Basin gases are higher than those of other gases in the Ordos Basin (Figure 12(a)), but there is no apparent relationship between $\delta^{13}\text{C}-\text{CO}_2$ and wetness (Figure 12(b)). Figure 3(b) indicates that CO_2 is of inorganic origin, and its $\delta^{13}\text{C}-\text{CO}_2$ values are much heavier than those of overmature shale gases. These factors indicate that the high CO_2 contents were not generated from reactions of CH_4 and H_2O , and isotopic exchange between CH_4 and H_2O at high temperatures cannot be the cause of hydrogen

isotopic reversal in the southern Ordos Basin. Moreover, recent work on the clumped isotopic composition of methane indicates that all hydrogen atoms in methane (and ethane and propane) are from organic matter and that a contribution of hydrogen from water is unlikely [59].

The main difference between the hydrogen isotopic compositions of southern Ordos Basin gases and other overmature gases is that rollover of hydrogen isotopes in the former occurs with $\delta\text{D}-\text{C}_2\text{H}_6$ whereas the latter occurs with $\delta\text{D}-\text{CH}_4$. This is attributed to simultaneous rollover of carbon and hydrogen isotopes (i.e., both carbon and

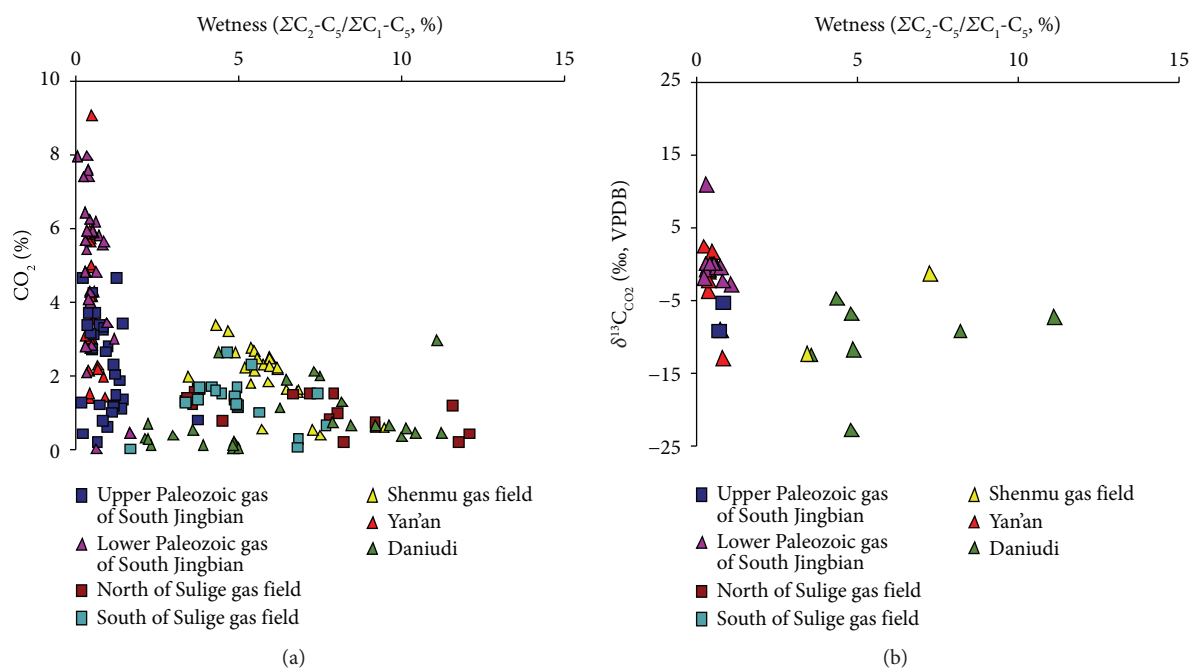


FIGURE 12: (a) CO₂ content versus wetness (modified from [15]); (b) $\delta^{13}C$ -CO₂ versus wetness (modified from [15]).

hydrogen isotopes of methane continue increasing with maturity, whereas those of ethane increase at first and then decrease, indicating that the rollover of carbon and hydrogen isotopes occur through the same process, possibly at the same time).

In the late gas-generation stage, when the first formed moieties recombined with residual kerogen to form methane and ethane, the process should have followed a similar isotopic fractionation rule to that of primary gas generation. That is, the ^{12}C - ^{12}C bonds in all C- 1H molecules have lower activation energy (are easier to break) than those in molecules containing at least one 2H , and the remaining reactants (the residual kerogen) become 2H -enriched, whereas the gas products become 2H -depleted [60]. In the late gas-generation stage, the cracking of earlier-generated C_{6+} moieties would have released alkanes with lighter hydrogen isotopic compositions than those of alkanes originating from late kerogen. These gases with light hydrogen isotopes mixed with the existing gases with much heavier hydrogen isotopes, causing the isotopic rollover of ethane. As the amount of ethane was much smaller than that of methane, a small amount of mixing would have easily caused the hydrogen isotopic composition of the mixed ethane to be lighter, resulting in the rollover. This is consistent with the recent work of Ni et al. [61].

6. Conclusions

- (1) Paleozoic natural gases in the southern Ordos Basin display carbon isotopic reversals, and the gases are not of inorganic origin. Modelled carbon isotope trends of mixed gases containing varying proportions of oil-type and coal-derived gases show that carbon

isotopic reversals are not caused by the mixing of different types of gases. Moreover, because of the different geological setting between conventional coal-derived gas and unconventional shale gas, the mechanisms for carbon isotopic reversal in shale gas could not be applied to explain the reversal in southern Ordos gases. The wetness of southern Ordos gases decreases rather than increases with incremental increases in thermal stress, indicating that abiotic polymerization was not the cause of the carbon isotopic reversal

- (2) Given the evolutionary trend of $\delta^{13}C$ -CH₄, $\delta^{13}C$ -C₂H₆, and $\delta^{13}C$ -C₃H₈ and the geological background of the southern Ordos Basin, carbon isotopic reversal in southern Ordos gases is best explained by a closed-system aromatization-polycondensation model, during which some neoformed macromolecules with relatively light carbon isotopic compositions were generated at a low-maturity stage and preserved in the closed system. During the overmature stage, these neoformed macromolecules reacted with the residual kerogen/coal structure to form short-chain alkanes depleted in ^{13}C through aromatization-polycondensation reactions. The evolutionary trend of δD -CH₄ and δD -C₂H₆ in the Ordos Basin also suggests that the hydrogen isotopic reversal was caused by aromatization-polycondensation reactions

Data Availability

The data used to support the findings of this study are included within the article.

Disclosure

The manuscript has been presented at the 2019 Goldschmidt as a short abstract: <https://goldschmidt.info/2019/abstracts/abstractView?id=2019005642>.

Conflicts of Interest

The author declares no conflicts of interest.

Acknowledgments

The author thanks Professor W. Z. Zhang and Q. F. Kong of the Petroleum Exploration and Development Research Institute, Changqing Oilfield Company, PetroChina, for contributing data and supporting sample collection. The author also appreciates the careful reviews and constructive suggestions of the anonymous reviewers. This study was supported by the National Natural Science Foundation for Young Scientists of China (Grant No. 41702161).

References

- [1] W. J. Stahl and B. D. Carey Jr., "Source-rock identification by isotope analyses of natural gases from fields in the Val Verde and Delaware basins, west Texas," *Chemical Geology*, vol. 16, no. 4, pp. 257–267, 1975.
- [2] Y. Tang, J. K. Perry, P. D. Jenden, and M. Schoell, "Mathematical modeling of stable carbon isotope ratios in natural gases," *Geochimica et Cosmochimica Acta*, vol. 64, no. 15, pp. 2673–2687, 2000.
- [3] A. P. Hu, J. Li, W. Z. Zhang, Z. S. Li, L. Hou, and Q. Y. Liu, "Geochemical characteristics and origin of gases from the Upper, Lower Paleozoic and the Mesozoic reservoirs in the Ordos Basin, China," *Science in China Series D: Earth Sciences*, vol. 51, no. S1, Supplement I, pp. 183–194, 2008.
- [4] J. Dai, D. Gong, Y. Ni, C. Yu, and W. Wu, "Genetic types of alkane gases in giant gas fields with proven reserves over $1000 \times 10^8 \text{ m}^3$ in China," *Energy Exploration & Exploitation*, vol. 32, no. 1, pp. 1–18, 2014.
- [5] D. Gong, J. Li, I. Ablimit et al., "Geochemical characteristics of natural gases related to late Paleozoic coal measures in China," *Marine and Petroleum Geology*, vol. 96, pp. 474–500, 2018.
- [6] C. Yu, S. P. Huang, D. Y. Gong, F. R. Liao, J. Li, and Q. W. Sun, "Partial reversal cause of carbon and hydrogen isotope compositions of natural gas: a case study in Sulige gas field, Ordos Basin," *Acta Petrolei Sinica*, vol. 34, Supplement 1, pp. 92–101, 2013.
- [7] J. Zhao, W. Zhang, J. Li, Q. Cao, and Y. Fan, "Genesis of tight sand gas in the Ordos Basin, China," *Organic Geochemistry*, vol. 74, pp. 76–84, 2014.
- [8] J. X. Dai, Y. Y. Ni, S. P. Huang et al., "Origins of secondary negative carbon isotopic series in natural gas," *Natural Gas Geoscience*, vol. 27, no. 1, pp. 1–7, 2016.
- [9] Z. Feng, D. Liu, S. Huang, D. Gong, and W. Peng, "Geochemical characteristics and genesis of natural gas in the Yan'an gas field, Ordos Basin, China," *Organic Geochemistry*, vol. 102, pp. 67–76, 2016.
- [10] Q. F. Kong, W. Z. Zhang, J. F. Li, and C. L. Zan, "Origin of natural gas in Ordovician in the west of Jingbian Gasfield, Ordos Basin," *Natural Gas Geoscience*, vol. 21, no. 1, pp. 71–80, 2016.
- [11] D. Liu, W. Zhang, Q. Kong, Z. Feng, C. Fang, and W. Peng, "Lower Paleozoic source rocks and natural gas origins in Ordos Basin, NW China," *Petroleum Exploration and Development*, vol. 43, no. 4, pp. 591–601, 2016.
- [12] X. Xia, J. Chen, R. Braun, and Y. Tang, "Isotopic reversals with respect to maturity trends due to mixing of primary and secondary products in source rocks," *Chemical Geology*, vol. 339, pp. 205–212, 2013.
- [13] R. C. Burruss and C. D. Laughrey, "Carbon and hydrogen isotopic reversals in deep basin gas: evidence for limits to the stability of hydrocarbons," *Organic Geochemistry*, vol. 41, no. 12, pp. 1285–1296, 2010.
- [14] B. Tilley and K. Muehlenbachs, "Isotope reversals and universal stages and trends of gas maturation in sealed, self-contained petroleum systems," *Chemical Geology*, vol. 339, pp. 194–204, 2013.
- [15] J. Zumberge, K. Ferworn, and S. Brown, "Isotopic reversal ('rollover') in shale gases produced from the Mississippian Barnett and Fayetteville formations," *Marine and Petroleum Geology*, vol. 31, no. 1, pp. 43–52, 2012.
- [16] J. X. Dai, C. N. Zou, and W. Li, *Large Coal-Derived Gas Fields in China and Their Sources*, Science Press, Beijing, 2014.
- [17] H. Guoyi, L. Jin, S. Xiuqin, H. Zhongxi et al., "The origin of natural gas and the hydrocarbon charging history of the Yulin gas field in the Ordos Basin, China," *International Journal of Coal Geology*, vol. 81, no. 4, pp. 381–391, 2010.
- [18] S. Huang, X. Fang, D. Liu, C. Fang, and T. Huang, "Natural gas genesis and sources in the Zizhou gas field, Ordos Basin, China," *International Journal of Coal Geology*, vol. 152, no. SI, pp. 132–143, 2015.
- [19] S. Huang, C. Yu, D. Gong, W. Wu, and F. Liao, "Stable carbon isotopic characteristics of alkane gases in tight sandstone gas fields and the gas source in China," *Energy Exploration & Exploitation*, vol. 32, no. 1, pp. 75–92, 2014.
- [20] X. Wu, Q. Liu, J. Zhu et al., "Geochemical characteristics of tight gas and gas-source correlation in the Daniudi gas field, the Ordos Basin, China," *Marine and Petroleum Geology*, vol. 79, pp. 412–425, 2017.
- [21] J. Dai, J. Li, X. Luo et al., "Stable carbon isotope compositions and source rock geochemistry of the giant gas accumulations in the Ordos Basin, China," *Organic Geochemistry*, vol. 36, no. 12, pp. 1617–1635, 2005.
- [22] R. Yang, Z. He, G. Qiu, Z. Jin, D. Sun, and X. Jin, "A late Triassic gravity flow depositional system in the southern Ordos Basin," *Petroleum Exploration and Development*, vol. 41, no. 6, pp. 724–733, 2014.
- [23] Z. He and C. Deng, "Discovery and exploration in Jingbian gas field of Ordos Basin," *Marine Origin Petroleum Geology*, vol. 10, no. 2, pp. 37–42, 2005.
- [24] R. J. Hill, D. M. Jarvie, J. Zumberge, M. Henry, and R. M. Pollastro, "Oil and gas geochemistry and petroleum systems of the Fort Worth Basin," *AAPG Bulletin*, vol. 91, no. 4, pp. 445–473, 2007.
- [25] R. C. Johnson and D. D. Rice, "Occurrence and geochemistry of natural gases, Piceance Basin, Northwest Colorado," *AAPG Bulletin*, vol. 77, pp. 980–998, 1990.
- [26] A. M. Martini, L. M. Walter, and J. C. McIntosh, "Identification of microbial and thermogenic gas components from Upper Devonian black shale cores, Illinois and Michigan basins," *AAPG Bulletin*, vol. 92, no. 3, pp. 327–339, 2008.

- [27] S. G. Osborn and J. C. McIntosh, "Chemical and isotopic tracers of the contribution of microbial gas in Devonian organic-rich shales and reservoir sandstones, northern Appalachian Basin," *Applied Geochemistry*, vol. 25, no. 3, pp. 456–471, 2010.
- [28] J. C. Pashin, M. R. McIntyre-Redden, S. D. Mann, D. C. Kopaska-Merkel, M. Varonka, and W. Orem, "Relationships between water and gas chemistry in mature coalbed methane reservoirs of the Black Warrior Basin," *International Journal of Coal Geology*, vol. 126, pp. 92–105, 2014.
- [29] N. D. Rodriguez and R. P. Philp, "Geochemical characterization of gases from the Mississippian Barnett Shale, Fort Worth Basin, Texas," *AAPG Bulletin*, vol. 94, no. 11, pp. 1641–1656, 2010.
- [30] D. Strapoć, M. Mastalerz, A. Schimmelmann, A. Drobniak, and N. R. Hasenmueller, "Geochemical constraints on the origin and volume of gas in the New Albany Shale (Devonian–Mississippian), eastern Illinois Basin," *AAPG Bulletin*, vol. 94, no. 11, pp. 1713–1740, 2010.
- [31] W. Wu, D. Dong, C. Yu, and D. Liu, "Geochemical characteristics of shale gas in Xiasiwan area, Ordos Basin," *Energy Exploration & Exploitation*, vol. 33, no. 1, pp. 25–41, 2015.
- [32] J. X. Dai and H. Qi, "Relationship of $\delta^{13}\text{C}_{\text{R}_0}$ of coal-derived gas in China," *Chinese Science Bulletin*, vol. 34, pp. 690–692, 1989.
- [33] J. X. Dai, Y. Song, C. Dai, and D. Wang, "Geochemistry and accumulation of carbon dioxide gases in China," *AAPG Bulletin*, vol. 80, pp. 1615–1626, 1996.
- [34] Q. Liu, M. Chen, W. Liu, J. Li, P. Han, and Y. Guo, "Origin of natural gas from the Ordovician paleo-weathering crust and gas-filling model in Jingbian gas field, Ordos Basin, China," *Journal of Asian Earth Sciences*, vol. 35, no. 1, pp. 74–88, 2009.
- [35] J. Thrasher and A. J. Fleet, "Predicting the risk of carbon dioxide "pollution" in petroleum reservoirs," in *Organic geochemistry: Developments and applications to energy, climate, environment and human history: Proceedings 17th International Meeting on Organic Geochemistry*, pp. 1086–1088, San Sebastian, Spain, September 1995.
- [36] N. Mahlstedt and B. Horsfield, "Metagenetic methane generation in gas shales I. Screening protocols using immature samples," *Marine and Petroleum Geology*, vol. 31, no. 1, pp. 27–42, 2012.
- [37] M. J. Whiticar, "Stable isotope geochemistry of coals, humic kerogens and related natural gases," *International Journal of Coal Geology*, vol. 32, no. 1–4, pp. 191–215, 1996.
- [38] B. B. Bernard, J. M. Brooks, and W. M. Sackett, "Light hydrocarbons in recent Texas continental shelf and slope sediments," *Journal of Geophysical Research*, vol. 83, no. C8, pp. 4053–4061, 1978.
- [39] E. Faber and W. Stahl, "Geochemical surface exploration for hydrocarbons in North Sea," *AAPG Bulletin*, vol. 68, pp. 363–386, 1984.
- [40] J. X. Dai, X. G. Pei, and H. F. Qi, *China Natural Gas Geology, vol. 1*, Petroleum Industry Press, Beijing, 1992.
- [41] T. M. McCollom and J. S. Seewald, "Carbon isotope composition of organic compounds produced by abiotic synthesis under hydrothermal conditions," *Earth and Planetary Science Letters*, vol. 243, no. 1–2, pp. 74–84, 2006.
- [42] P. D. Jenden, D. R. Hilton, I. R. Kaplan, and H. Craig, "Abiogenic hydrocarbons and mantle helium in oil and gas fields," in *The Future of Energy Gases - USGS Professional Paper 1570*, D. G. Howell, Ed., pp. 31–56, United States Geological Survey, 1993.
- [43] J. K. Mi, X. M. Wang, and G. Y. Zhu, "Origin determination of gas from Jingbian gas field in Ordos basin collective through the geochemistry of gas from inclusions and source rock pyrolysis," *Acta Petrologica Sinica*, vol. 28, no. 3, pp. 859–869, 2012.
- [44] A. A. Prinzhofer and A. Y. Huc, "Genetic and post-genetic molecular and isotopic fractionations in natural gases," *Chemical Geology*, vol. 126, no. 3–4, pp. 281–290, 1995.
- [45] H. Zeng, J. Li, and Q. Huo, "A review of alkane gas geochemistry in the Xujiaweizi fault-depression, Songliao Basin," *Marine and Petroleum Geology*, vol. 43, pp. 284–296, 2013.
- [46] Q. R. Passey, K. M. Bohacs, W. L. Esch, R. Klimentidis, and S. Sinha, "From oil-prone source rock to gas-producing shale reservoir – geologic and petrophysical characterization of unconventional shale-gas reservoir," in *Proceedings of International Oil and Gas Conference and Exhibition in China*, Beijing, China, June 2010.
- [47] M. D. Lewan, "Experiments on the role of water in petroleum formation," *Geochimica et Cosmochimica Acta*, vol. 61, no. 17, pp. 3691–3723, 1997.
- [48] L. C. Price, "A possible deep-basin high-rank gas machine via water organic-matter redox reactions," in *Geologic Studies of Deep Natural Gas Resources*, T. S. Dyman and V. A. Kuuskraa, Eds., pp. H1–H29, USGS, Denver, 2001.
- [49] Y. Tang and X. Y. Xia, "Quantitative assessment of shale gas potential based on its special generation and accumulation processes," in *AAPG Convention and Exhibition of AAPG Search and Discovery Article #90124*, Houston, TX, USA, April 2011.
- [50] V. Dieckmann, R. Ondrak, B. Cramer, and B. Horsfield, "Deep basin gas: new insights from kinetic modelling and isotopic fractionation in deep-formed gas precursors," *Marine and Petroleum Geology*, vol. 23, no. 2, pp. 183–199, 2006.
- [51] M. Erdmann and B. Horsfield, "Enhanced late gas generation potential of petroleum source rocks via recombination reactions: evidence from the Norwegian North Sea," *Geochimica et Cosmochimica Acta*, vol. 70, no. 15, pp. 3943–3956, 2006.
- [52] F. Behar, M. Vandenbroucke, S. C. Teermann, P. G. Hatcher, C. Leblond, and O. Lerat, "Experimental simulation of gas generation from coals and a marine kerogen," *Chemical Geology*, vol. 126, no. 3–4, pp. 247–260, 1995.
- [53] J. R. Levine and W. E. Edmunds, *Structural geology, tectonics, and coalification, Carboniferous Geology of the Anthracite Fields of Eastern Pennsylvania and New England*, Geological Society of America, Coal Division, 1993.
- [54] M. Teichmüller and R. Teichmüller, "The significance of coalification studies to geology: a review," *Bulletin des Centres de Recherches Exploration-Production Elf-Aquitaine*, vol. 5, no. 2, pp. 491–534, 1981.
- [55] Z. X. He, A. Q. Fei, and T. H. Wang, *The Ordos Basin Evolution and Hydrocarbon*, Petroleum Industry Press, Beijing, 2003.
- [56] Z. X. He, J. H. Fu, S. L. Xi, S. T. Fu, and H. P. Bao, "Geological features of Sulige gas field," *Acta Petrologica Sinica*, vol. 24, no. 2, pp. 6–12, 2003.
- [57] D. Liu, C. Yu, S. Huang, C. Fang, Z. Feng, and Q. Kong, "Using light hydrocarbons to identify the depositional environment of source rocks in the Ordos Basin, central China," *Energy Exploration & Exploitation*, vol. 33, no. 6, pp. 869–890, 2015.
- [58] J. S. Seewald, M. Y. Zolotov, and T. McCollom, "Experimental investigation of single carbon compounds under hydrothermal

- conditions,” *Geochimica et Cosmochimica Acta*, vol. 70, no. 2, pp. 446–460, 2006.
- [59] X. Xia and Y. Gao, “Mechanism of linear covariations between isotopic compositions of natural gaseous hydrocarbons,” *Organic Geochemistry*, vol. 113, pp. 115–123, 2017.
- [60] Y. Tang, Y. Huang, G. S. Ellis et al., “A kinetic model for thermally induced hydrogen and carbon isotope fractionation of individual *n*-alkanes in crude oil,” *Geochimica et Cosmochimica Acta*, vol. 69, no. 18, pp. 4505–4520, 2005.
- [61] Y. Ni, J. Gao, J. Chen, F. Liao, J. Liu, and D. Zhang, “Gas generation and its isotope composition during coal pyrolysis: potential mechanism of isotope rollover,” *Fuel*, vol. 231, pp. 387–395, 2018.

Research Article

Evidence of Tectonic Control on the Geochemical Features of the Volatiles Vented along the Nebrodi-Peloritani Mts (Southern Apennine Chain, Italy)

Francesco Italiano,¹ Pietro Bonfanti^{1,2} ,² and Salvatore Roberto Maugeri² 

¹*Istituto Nazionale di Geofisica e Vulcanologia (INGV), Sezione di Palermo, 90146, Italy*

²*Istituto Nazionale di Geofisica e Vulcanologia (INGV), Sezione di Catania Osservatorio Etneo, 95125, Italy*

Correspondence should be addressed to Pietro Bonfanti; pietro.bonfanti@ingv.it

Received 15 February 2019; Revised 30 April 2019; Accepted 30 May 2019; Published 4 July 2019

Academic Editor: Andrew H. Manning

Copyright © 2019 Francesco Italiano et al. This is an open access article distributed under the Creative Commons Attribution License, which permits unrestricted use, distribution, and reproduction in any medium, provided the original work is properly cited.

Investigations carried out over the southernmost portion of the Apennine chain (Nebrodi-Peloritani Mountains, Sicily, Italy) reveal a close connection between the tectonic setting and the regional degassing of CO₂-dominated volatiles. The geochemical features of the collected gases show that the pristine composition has been modified by gas-water interaction (GWI) and degassing processes. The ³He/⁴He isotopic ratio in the range of 0.7–2.8 Ra highlights variable contributions of mantle-derived helium, representing an unusual feature for the crustal regime of the study areas characterized by the widespread presence of ⁴He-producer metamorphic rocks. The degassing of mantle helium is coherent with the tectonics and related to the NW-SE extensional regime of the Calabro-Peloritan Arc (CPA). We propose that the degassing regime as well as the geochemical features of both the dissolved and bubbling gases is closely connected to the strain accumulation rate, inducing almost no temporal changes and insignificant deep-originated fluid contributions to the locked fault volumes. Investigations including discrete and continuous monitoring and degassing-rate estimations are useful tools to gain a better insight into the evolution of seismogenesis, considering the fault rupture as the final stage of a seismic cycle.

1. Introduction

Results of studies on fluid/fault relationships have widely shown the role of fluids both as triggering agents of seismic shocks and as fast carriers of information on processes occurring at deep levels, making them useful tools in gaining a better insight into the evolution of seismogenic processes. The Apennines are well known to be a still-developing chain, with tectonic movements driven by a large number of active faults often recognized as seismogenetic [1, 2]. The Southern portion of the Apennines, the Calabro-Peloritan Arc (CPA), develops over an area that has been struck by some of the most destructive seismic events ever seen in Europe (e.g., Messina 1908 and Calabria 1905, 1783). Indeed, its complicated tectonic setting has been satisfactorily constrained only in recent times and remains under investigation. The CPA is

a major tectonic structure running across northeastern Sicily and Calabria (Figure 1). The Nebrodi and Peloritani mountains stretch E-W along the Northern Ionian and Tyrrhenian coasts for about 100 km.

The presence of thermal springs besides the degassing occurring over some areas (evidenced by bubbling gases in thermal waters and shallow sea waters) is a clue to the close connection of the fluids' circulation pattern with the local tectonic structures. This paper accounts for the results of a fluid collection carried out over the Nebrodi and Peloritani Mts over the period 2004–2006. More samples collected in 2002, 2003, and 2007 were added to the time series of some of the most important sites. The survey aimed at defining the origin as well as the interactions of the fluids circulating over the area in order to evaluate possible relationships with local tectonic structures.

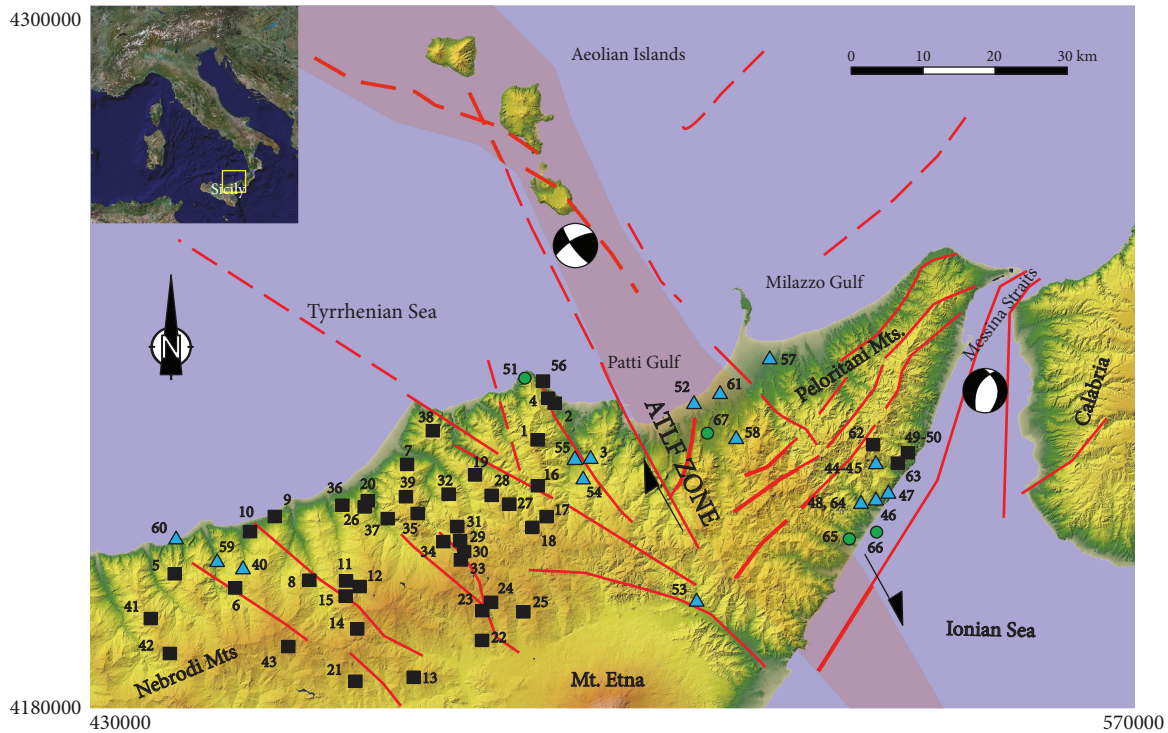


FIGURE 1: Sketch map of the study area (Nebrodi-Peloritani Mountains, Southern Apennines, Sicily, Italy) with the location of the sampling sites and the main tectonic lines (red lines). The beach balls show the focal mechanisms associated with some main shocks. Black square: spring; blue triangle: well; green circle: bubbling gas.

Improving the knowledge of the geochemical features of the fluids and their behaviour in the geodynamic context of the area can provide new information leading to a better understanding of local tectonic settings along with new tools for an insight into the development of the seismogenesis (stress accumulation, deformation, strain release, etc.).

The study area is characterized by the venting of geothermal fluids over both the Tyrrhenian and Ionian coasts, as well as by gas emissions over areas crossed by the Aeolian-Tindari-Letojanni fault (ATLF) system (Figure 1). The gases are mainly dissolved in groundwater and vented as a separate phase only in a few sites.

2. Geologic and Tectonic Setting

The current tectonic framework of the Calabro-Peloritan Arc (CPA) results from the N-S Africa-Eurasia convergence during the Neogene-Quaternary at a rate of 1–2 cm/yr during the last 5–6 My [3–7]. Despite this, a rapid E to SE motion affected the CPA at a rate of 5–6 cm/yr, with an uplift between 0.5 and 1.2 mm/year, in the last 1–0.7 My, mainly accommodated by normal faulting [8–10]. This NE corner of the chain exhibits an uplift with the highest rate in proximity to the Messina Strait (along the Ionian coast) and lower uplift rates along the Tyrrhenian coasts [11].

The motion is related to the roll-back of the subjacent Ionian transitional to oceanic slab and back-arc expansion in the Tyrrhenian Sea [12–14]. During the middle-late

Pleistocene, roll-back and subduction slowed to less than 1 cm/yr [15].

The current structural framework of northern Sicily is the result of the Plio-Pleistocene activation of a complex network of fractures related to a W-E trending right-lateral regional shear zone extending from the Pantelleria Rift to the Aeolian Islands [16–20]. Some of these structures are still active and responsible for the shallow seismicity occurring both in inland Sicily and in the northern offshore in the Tyrrhenian Sea. Focal mechanisms are typically characterized by strike-slip and oblique kinematics consistent with low-dip NW-SE to NNW-SSE trending *P*-axes [21–26], roughly consistent with the global convergence direction between the European and African plates [11, 27–31].

The seismological and geodetic data depict two main crustal domains marked by different stress regimes: a compressive domain in the northern Sicilian offshore and an extensional domain in northeastern Sicily and southern Calabria [24, 32–36]. The transition between the two domains occurs along the Aeolian-Tindari-Letojanni fault (ATLF) system which has been interpreted as a transfer crustal zone between the northern Sicily offshore thrust belt in the Tyrrhenian Sea and the accretionary wedge offshore the eastern Calabria in the Ionian Sea [29, 32, 37] or as a lithospheric tear fault bounding the western edge of the subducting Ionian slab [13, 38–41]. Extension, however, although at an immature tectonic stage, also occurs in a narrow band to the west of the ATLF in northern Sicily as

documented by seismology and structural studies [25, 42]. In the field, the ATLF is formed by NW-SE-oriented en echelon segments characterized by prevailing right-transpressional movements in the Aeolian sector [43, 44] and by transtensional motion in the northern Sicily sector [45]. Seismological, geological, and geodetic data evidence that the ATLF is very active with more than 1500 earthquakes (maximum magnitude = 4.5) occurring in the past 30 years in its northern portion. Fault plane solutions reveal prevailing normal faulting coupled with dextral solutions along the inland part of the ATLF [25]. Figure 1 summarizes the above-mentioned information alongside the distribution of the sampling sites.

Recent geodetic observations coupled to geological constraints have served to better elucidate the interplay of crustal blocks of the Nebrodi-Peloritani area [46]. The ATLF juxtaposes north-south contraction between Sicily and the Tyrrhenian block with northwest-southeast extension in northeastern Sicily and Calabria (Nebrodi-Peloritani chains). As a matter of fact, the Africa-Eurasia convergence in Sicily and southern Calabria is nowadays expressed by two different tectonic and geodynamic domains: a roughly N-S compression over the western region caused by continental collision and a NW-SE extension to the east (Calabro-Peloritan Arc) related to the S-E-directed expansion. The ATLF right-lateral shear zone accommodates the different deformation patterns of these two domains from the Ionian Sea (north of Mt. Etna) to the Aeolian Islands across the Peloritani chain, thus crossing our study area.

3. Methods

3.1. Field Investigations and Sample Collection. A suite of 158 samples taken at 67 different sites has been collected along the Nebrodi-Peloritani chain, the southernmost portion of the Apennines. They include natural springs, fountains, and boreholes as well as bubbling gases from thermal and cold ponds spread over an area > 2500 km².

Table 1 lists the sample locations, the coordinates (in WGS84 notation), and the field data; Table 2, the analytical results for the dissolved gases (43 from the Nebrodi sector and 19 on the Peloritani sector); and Table 3 (8 different sites), the bubbling (free) gases. The samples are listed using ID numbers as well as the site names. The ID number identifies the site; thus, bubbling and dissolved gases taken at the same site display the same ID number but are listed in different tables.

To carry out dissolved gas analyses, water samples were collected and stored in 240 ml Pyrex bottles sealed in the field using silicon/Teflon septa and purpose-built pliers, following the methodology and instrumentation described in Italiano et al. [47–49]. All of the samples were collected taking care to avoid even the tiniest bubbles in order to prevent atmospheric contamination.

To recover a pure gas sample, we collected gas bubbles using an inverted funnel placed on top the bubbles, driving them towards a Pyrex bottle of about 50 ml in volume with two vacuum-type valves at both ends. The sampling bottle was washed by the gas coming from the funnel and the

sample taken by closing the two valves after a volume of at least one order of magnitude larger than that of the sampling bottle had been passed through.

All of the samples (dissolved and free gases) were analyzed for the chemical and isotopic composition of carbon (CO₂) and He.

3.2. Analytical Methods. Field measurements of temperature, pH, redox potential (Eh), and electrical conductivity (EC) were performed by a multiparameter device (Multi 350i, Weilheim) (Table 1).

In the laboratory, the chemical and isotopic composition (He and C) of the bubbling and dissolved gases were determined using the same analytical equipment. The dissolved gases were extracted after equilibrium was reached at constant temperature with a host-gas (high-purity argon) injected in the sample bottle through the rubber septum (for further details, see Italiano et al. [47, 49]). Chemical analyses were carried out by gas chromatography (PerkinElmer Clarus 500 equipped with a double TCD-FID detector) using argon as the carrier gas. Typical uncertainties are within ±5%.

Helium isotope analyses were performed on gas fractions extracted following the same procedure as for the gas chromatography and purified following methods described in the literature [50–52]. The purified helium fraction (either of dissolved or of bubbling gases) was analyzed by a static vacuum mass spectrometer (GVI5400TFT) that allows the simultaneous detection of ³He and ⁴He ion beams, thereby keeping the ³He/⁴He error of measurement to very low values. Typical uncertainties in the range of low-³He samples are within ±1%. During the same analytical procedure, the ⁴He/²⁰Ne ratio was measured by peak intensities on the mass spectrometer.

The isotopic composition of the total dissolved carbon ($\delta^{13}\text{C}_{\text{TDC}}$) was measured in a sample of 2 ml of water introduced into containers injected with high-purity helium to remove atmospheric CO₂. The water samples were acidified with phosphorus pentoxide in an autosampler to ensure complete release of CO₂ from acidified waters. CO₂ was then directly admitted to a continuous flow mass spectrometer (AP2003). The results are reported in ‰ units relative to the V-PDB (Vienna Pee Dee Belemnite) standard; standard deviation of the ¹³C/¹²C ratio was ±0.2‰.

4. Results

4.1. Chemical and Isotopic Composition. Table 2 shows the chemical and isotopic data of the bubbling gases as well as their He and C isotopic compositions and ⁴He/²⁰Ne and CO₂/³He ratios.

CO₂ is by far the main component of the bubbling gases with concentrations always above 90%, but sample Rodi Milici (after [53]) which has a composition dominated by N₂ (96.1%) with CO₂ content is as low as 0.01% with a large amount of O₂. The sample is largely air contaminated and also suffered from gas-water interactions as shown by the high helium and negligible CO₂ content (Table 2). The composition of the dissolved gas phase was calculated from

TABLE 1: List of the sample sites with their location and field data.

Sample #	Site name	Type	Latitude	Longitude	Date	T (°C)	pH	EC ($\mu\text{S cm}^{-1}$)	Eh (mV)
1	Boffe	S	4218339	493362	31/05/2006	17.3	6.6	567	11.7
2	Usignolo	S	4223182	495604	31/05/2006	14	7.4	307	183
3	Belvedere	W	4213960	500401	31/05/2006	n.d.	6.2	373	n.d.
4	Margherita	S	4223774	494811	31/05/2006	17.2	6.8	n.d.	n.d.
5	Lettosanto	S	4203485	446098	26/10/2006	14.5	8.1	430	320
6	Sampieri	S	4201594	453979	26/10/2006	22	7.2	313	141
7	Leone	S	4215364	476353	26/10/2006	15	7.7	439	234
8	S. Mamma	S	4201769	463060	26/10/2006	17.9	7.8	743	251
9	Ramosa	S	4210970	459344	26/10/2006	18.9	6.6	795	-18.7
10	Ficuzza	S	4209011	455969	31/10/2006	20.1	6.6	807	218
11	Moglie	S	4201393	467921	31/10/2006	13.1	8.1	286	256
12	Pilieggi	S	4200639	469645	31/10/2006	13.4	7.2	454	158
13	Cesarò	S	4188208	475206	31/10/2006	15.7	7.4	414	153
14	Torti	S	4194100	469379	31/10/2006	10.1	7.1	117.4	163
15	Muto	S	4199383	467806	31/10/2006	11.2	7.5	224	151
16	Sulipani	S	4210175	493398	16/11/2006	12.7	6.8	251	244
17	Giangalia	S	4206137	494519	16/11/2006	10.1	8.0	333	297
18	Pace	S	4204674	492680	16/11/2006	11.3	8.0	278	195
19	Sfaranda	S	4212196	485181	16/11/2006	14.9	7.1	349	212
20	Agrifoglio	S	4210452	471272	16/11/2006	15.9	7.9	983	195
21	Mezzalora	S	4188364	467379	22/11/2006	9.7	8.4	487	59
22	Margio Salice	S	4192999	484963	22/11/2006	11.9	7.9	511	124
23	Chiusitta	S	4197148	484907	22/11/2006	9	7.5	382	172
24	Tre Arie	S	4198001	486223	22/11/2006	9	8.0	291	58
25	Zarbata	S	4196816	490269	22/11/2006	9.7	7.3	330	196
26	S. Domenica	S	4209724	470900	22/11/2006	13.8	7.5	358	205.8
27	Piano Soprano	S	4207559	489767	22/11/2006	11.7	7.4	397	220
28	Casitti	S	4208940	487512	22/11/2006	11.4	8.0	287	193
29	Jardini	S	4205291	482034	23/11/2006	11.4	7.8	321	193.8
30	Fossaneve	S	4204120	482502	23/11/2006	8.6	7.6	126.5	19
31	Titi bassa	S	4207272	481640	23/11/2006	13.9	7.4	434	198
32	S. Anna	S	4209106	481785	23/11/2006	12	7.5	387	177
33	Balestra	S	4204036	482514	23/11/2006	7.2	7.1	109	132
34	S. Pietro	S	4205385	479831	23/11/2006	13.8	7.8	264	181
35	Filipelli	S	4208702	477706	23/11/2006	10.5	7.8	367	187
36	Iria	S	4209929	468000	29/11/2006	15.6	7.7	848	147
37	Abate	S	4208184	473990	29/11/2006	14.5	7.7	309	106
38	Feudo	S	4218642	480320	29/11/2006	15.4	6.3	300	280
39	Favarotta	S	4210817	476145	29/11/2006	13.7	7.5	388	261
40	Palamara	W	4204231	455414	20/12/2006	17	7.5	648	101
41	Neviera	S	4197698	443048	20/12/2006	10.6	6.9	161.9	35
42	Ramata	S	4193148	445498	20/12/2006	10.4	7.5	378	-28
43	Nocita	S	4193948	459898	20/12/2006	8.0	7.0	57	69
44	Marino SPA 1	W	4206888	537429	08/01/2004	28.1	6.12	6070	-178.5
45	Marino SPA 2	W	4206888	537429	07/04/2004	22.3	6.07	2120	112.9
45	Marino SPA 2	W	4206888	537429	06/05/2004	23.3	6.11	2270	158.0
45	Marino SPA 2	W	4206888	537429	18/10/2004	25	6.13	2630	-228.0
46	Parco Giochi	W	4206515	537444	04/02/2004	16.5	7.1	980	67.5

TABLE 1: Continued.

Sample #	Site name	Type	Latitude	Longitude	Date	T (°C)	pH	EC ($\mu\text{S cm}^{-1}$)	Eh (mV)
47	Berlinghieri	W	4206465	537262	04/02/2004	21.5	7.2	1002	124.5
48	La Magnolia 1	W	4206434	537276	01/06/2005	31.1	5.65	41000	-70.8
49	Granata	S	4206973	537759	23/03/2005	22.5	5.96	35600	-10
50	Granata 1	S	4206973	537759	24/03/2005	22.1	6.14	992	161
51	Calavà	B	4226175	493509	28/08/2002	n.d.	n.d.	n.d.	n.d.
52	Terme Vigliatore	S	4221034	513801	27/02/2006	30.4	6.8	4030	n.d.
53	Chiappe	S	4195686	512328	01/03/2007	16	n.d.	524	-274
54	Pintaudi	W	4211772	500245	26/01/2006	18.2	7.93	5100	-223
55	Biondo	W	4213979	498283	26/01/2006	16.5	6.67	557	n.d.
56	Fetente	S	4226066	494050	27/02/2006	14.9	7.40	6990	210
57	La Malfa	W	4226742	523732	12/01/2007	n.d.	n.d.	n.d.	n.d.
58	Acqua rugiada	S	4216468	519311	25/02/2004	n.d.	n.d.	n.d.	n.d.
59	Pezzino	W	4206270	452884	19/02/2004	17.3	7.20	1032	455
60	Canneto	W	4208324	446323	19/02/2004	15.8	7.43	1028	453
61	Maio	W	4222264	517189	11/04/2007	22.8	7.15	597	n.d.
62	Fontana WP43	S	4214022	536220	18/01/2007	n.d.	n.d.	n.d.	n.d.
63	Scuderi	S	4211597	536559	18/01/2007	n.d.	n.d.	n.d.	n.d.
64	La Magnolia 2	W	4206434	537276	28/04/2005	n.d.	n.d.	n.d.	n.d.
65	Ali	B	4206058	537395	28/08/2002	n.d.	n.d.	n.d.	n.d.
66	Gas in seawater	B	4206473	538547	23/03/2005	n.d.	n.d.	n.d.	n.d.
67	Rodi Milici *	B	4216796	513441	n.a.	n.d.	n.d.	n.d.	n.d.

Geographical coordinates UTM WGS84; EC: electrical conductivity; S: spring; W: well; B: bubbling gas; n.d.: not analyzed; n.a.: not available. *Data after [53]. See Figure 1 for sample locations.

the gas-chromatographic analyses, combining the solubility coefficients (Bunsen coefficient “ β ,” $c_{\text{gas}}/\text{ml}_{\text{water}}$ STP) of each gas species, the volume of gas extracted (cm^3), and the volume of the water sample and the equilibration temperature, as shown in the following equation:

$$G_C = \{ [G_{gc}] * V\gamma_e + ([G_{gc}] * \beta_G * VW) \} VW^{-1} * V\gamma_e * \frac{V\gamma_i^{-1}}{100}, \quad (1)$$

where G_C is the concentration of the selected gas specie, G_{gc} is its concentration measured by gas chromatography (vol%), and $V\gamma_e$ and $V\gamma_i$ represent the extracted and introduced gas volumes, respectively, while VW is the volume of the analyzed water sample (see also [47, 49] for further details). All volumes are carefully measured at the equilibration temperature. Data for dissolved gas compositions are expressed in $\text{cm}^3\text{STP/L}_{\text{H}_2\text{O}}$ and listed in Tables 3(a) and 3(b), as well as the amount of dissolved air (air% in Tables 3(a) and 3(b)). The air content estimation is based on the oxygen content and represents the minimum amount of dissolved air at the sampling site. Oxygen, in fact, can be consumed because of bacterial activity as well as oxidation reactions likely occurring during the water circulation; the percentage of atmospheric components during infiltration might be much higher. As we assume that the deep volatiles are oxygen-free, we recalculated the gas composition removing the atmospheric

components (since atmospheric nitrogen is calculated from the oxygen content, for some sites, it might be underestimated). The gas analyses recalculated in vol%, allowing us a comparison with the analytical results of the bubbling gases, are listed in Tables 4(a) and 4(b) together with the helium and carbon isotopic compositions and the He/Ne ratios.

5. Discussion

5.1. Fluid Geochemistry. The chemical composition of the bubbling gases (Table 2) shows that CO_2 is the most abundant component with the concentration always above 95% by vol. The only exception is represented by the sample #67 (Rodi Milici, Table 2; after [53]), whose CO_2 content is the lowest of the entire dataset. Considering the high He concentration, this sample is a very fractionated gas, which lost almost all the CO_2 likely for intense GWI. It is noteworthy that it was possible to recover a free gas phase only over the Peloritani chain. The main difference in the gas chemistry is related to the amount of CH_4 and N_2 (Table 2) that besides CO_2 are the main components in crustal gases. All the CO_2 -dominated volatiles are here classified as of deep origin, where the term “deep” may indicate an origin from either crustal or mantle/magmatic environments.

The composition of the dissolved gases (Tables 3(a) and 3(b)) shows the presence of air-derived gases (N_2 and O_2) along with the nonatmospheric gases CO_2 and CH_4 . The estimated amount of dissolved air is significantly lower in the samples collected from the Peloritani chain

TABLE 2: Chemical and isotopic composition of the bubbling gases from vents located along the Peloritani chain.

Site ID	Site	Data	He	Ne	O ₂	N ₂	CH ₄	CO ₂	$\delta^{13}\text{C}$	R/Ra	ϵ	He/Ne	CO ₂ / ³ He
48	La Magnolia 1	23/03/2005	<	<	<	3.26	3.4E-02	95.9	-2.15	<	<	<	<
48	La Magnolia 1	28/04/2005	4.7E-03	3.6E-05	0.03	2.0	2.1E-02	95.9	-2.15	0.67	0.0035	132.11	2.17E+10
48	La Magnolia 1	02/03/2006	4.7E-03	4.3E-05	24.0	6.0	2.2E-03	71.3	<	0.67	0.0049	108.66	1.63E+10
49	Granata	28/08/2002	1.5E-04	3.6E-06	<	0.27	4.6E-03	99.7	<	0.70	0.0161	24.23	6.77E+11
49	Granata	11/09/2002	1.8E-04	1.3E-05	<	0.40	1.2E-02	99.5	-1.03	0.70	0.0255	14.20	5.76E+11
49	Granata	23/03/2005	1.8E-04	1.6E-05	<	0.73	5.7E-03	98.3	-1.13	0.68	0.0076	11.36	5.72E+11
49	Granata	28/04/2005	1.6E-04	9.4E-06	<	0.81	7.2E-03	98.1	<	0.68	0.0104	17.48	6.33E+11
49	Granata	02/03/2006	2.4E-04	5.1E-05	0.0	1.1	1.5E-06	97.8	-1.30	0.90	0.0131	4.63	3.32E+11
49	Granata	06/04/2006	1.8E-04	2.6E-05	0.7	4.1	5.4E-03	93.7	<	0.71	0.0108	7.18	5.11E+11
51	Calavà	28/08/2002	2.0E-03	1.8E-05	0.41	1.62	5.4E-01	97.38	<	2.48	0.0243	115.35	1.39E+10
51	Calavà	11/09/2002	2.7E-03	3.2E-05	0.62	2.35	6.9E-01	96.40	<	2.46	0.0233	84.10	1.06E+10
51	Calavà	25/02/2004	2.5E-03	1.4E-05	0.73	2.75	8.1E-01	95.72	<	2.50	0.0206	171.03	1.12E+10
51	Calavà	01/04/2004	1.9E-03	1.3E-05	0.47	2.12	5.6E-01	95.68	<	2.55	0.0206	146.63	1.40E+10
51	Calavà	26/05/2004	1.5E-03	6.9E-06	0.35	1.61	5.1E-01	98.24	<	2.52	0.0239	216.59	1.87E+10
51	Calavà	28/06/2004	1.5E-03	1.9E-05	0.42	1.63	5.6E-01	97.17	<	2.54	0.0301	80.29	1.80E+10
51	Calavà	18/07/2004	2.1E-03	2.5E-05	0.28	1.62	5.2E-01	97.73	<	2.52	0.0321	84.43	1.30E+10
51	Calavà	15/10/2004	<	<	2.68	11.06	4.4E-01	84.46	<	<	<	<	<
51	Calavà	15/05/2005	2.2E-03	1.4E-05	0.48	2.22	6.7E-01	96.52	<	2.47	0.0129	150.42	1.30E+10
51	Calavà	12/08/2005	1.7E-03	1.1E-05	0.2	1.65	5.4E-01	97.38	<	2.49	0.0094	160.56	1.64E+10
52	Terme Vigliatore	06/05/2004	1.0E-05	8.7E-06		0.046	4.8E-03	99.76	<	1.51	0.2850	1.21	4.53E+12
52	Terme Vigliatore*	—	<	<	<	4×10^{-2}	6.0E-05	99.9	<	<	<	<	<
64	La Magnolia 2	28/04/2005	3.1E-03	5.1E-05	<	1.44	1.5E-02	97.0	<	0.67	0.0043	60.26	3.36E+10
65	Ali	28/08/2002	1.5E-04	6.2E-06	<	0.3	4.6E-03	99.7	<	0.70	0.0161	24.23	6.75E+11
65	Ali	11/09/2002	1.8E-04	1.3E-05	1.4	5.7	1.2E-02	93.5	<	0.70	0.0255	14.20	5.40E+11
65	Ali	11/11/2003	1.6E-04	1.7E-05	<	1.0	4.8E-03	99.5	<	0.67	0.0392	9.67	6.63E+11
66	Gas in sea water	23/03/2005	6.6E-03	<	0.3	4.2	6.0E-02	96.4	-1.71				
67	Rodi Milici *	—	8.1×10^{-2}	<	1.36	96.1	1.3E-01	0.01	<	2.14	<	99.52	5.4E+04

Data in vol%; <: below detection limits or not analyzed; ϵ : error of the isotopic determination reported for all of the R/Ra data. *Data after [53].

than in those from the Nebrodi Mts. (Tables 3(a) and 3(b)): it ranges between 8.94 and 84.53% for the latter samples and from 0.01 to 53% for the former (Peloritani chain) with the exception of two samples (#62 and 63, Table 1(b)) showing air content as high as 87 and 88%, respectively. The relationships between atmospheric (O₂) and nonatmospheric gas species in the dissolved gases (Tables 3(a) and 3(b)) are shown in Figure 2.

The arrows show the trends produced by the addition of CO₂ and CH₄ to an atmospheric gas assemblage as well as the effect of gas-water interactions (GWI) on the CO₂ dissolution. The graph clearly shows the presence of fluids from a crustal and/or a mantle source over the whole study area that interact with the groundwater changing their original atmospheric-derived gas assemblage. Gas-water interactions (GWI) allow dissolution of deep gas species as a consequence of the solubility coefficients of each of them, the temperature, and the flux intensity towards the surface.

The recalculated gas analyses show that even in the case of dissolved gases, the deep volatiles are always made by a CO₂-dominated gas assemblage despite a widely different extent of atmospheric contamination, namely, the

air-derived/deep-originated volatile mixing proportion (Tables 3(a) and 3(b)).

It is worth noting that the investigated area is from 30 to more than 60 km away from the volcanic districts of Mt Etna and the Aeolian Islands and there is no evidence of melt intrusions in shallow crustal levels supporting the release of mantle-derived volatiles as already observed in other portions of the Southern Apennines [54].

5.2. Helium and Carbon Isotopes. The helium and carbon systematics may provide the necessary information to constrain the origin of the CO₂-dominated volatiles. It is well accepted that the isotopic ratio of helium is a very sensitive tracer of volatile mixing in volcanic and tectonic systems located near the Earth's surface. During earth evolution and differentiation, the production of radiogenic ⁴He (alpha particles) as a function of U and Th concentrations modified the pristine ³He/⁴He ratio leading to a wide range of isotopic ratios both in the crust (from less than 0.01 to 0.05 Ra, where Ra is the atmospheric ³He/⁴He value of 1.39×10^{-6}) and in the mantle (e.g., $1.2 \pm 0.1 \times 10^{-5}$; ~8 Ra; [55–58]; 6.5 Ra in the Sub Continental European Mantle (SCEM) [59]).

TABLE 3: Chemical composition of the dissolved gas phase.

(a)

Sample #	Site name	Type	Date	He	Ne	O ₂	N ₂	CH ₄	CO ₂	Air%
1	Boffe	S	31/05/2006	2.94E-05	1.02E-04	4.73	11.09	8.45E-05	39.62	24.38
2	Usignolo	S	31/05/2006	1.11E-04	1.64E-04	2.33	11.19	2.40E-04	1.37	44.82
3	Belvedere	W	31/05/2006	5.96E-05	1.90E-04	2.70	14.65	1.48E-04	69.10	8.93
4	Margherita	S	31/05/2006	6.76E-05	2.11E-04	4.71	10.30	7.20E-05	13.07	47.96
5	Lettosanto	S	26/10/2006	2.72E-05	7.05E-05	5.27	11.81	1.01E-04	1.27	82.09
6	Sampieri	S	26/10/2006	3.76E-05	7.43E-05	4.79	11.07	4.35E-05	8.27	56.71
7	Leone	S	26/10/2006	2.05E-05	6.65E-05	5.58	12.78	<	4.69	69.25
8	S. Mamma	S	26/10/2006	1.37E-05	4.60E-05	5.20	11.40	4.35E-05	3.66	73.46
9	Ramosa	S	26/10/2006	2.55E-05	7.88E-05	2.61	11.85	1.23E-03	47.40	12.04
10	Ficuzza	S	31/10/2006	3.04E-05	9.50E-05	2.61	12.21	5.07E-04	37.70	35.57
11	Moglie	S	31/10/2006	3.20E-05	8.94E-05	5.26	11.84	3.62E-04	1.27	81.86
12	Pilegi	S	31/10/2006	4.15E-05	1.25E-04	3.08	12.11	2.03E-03	21.24	24.17
13	Cesarò	S	31/10/2006	1.09E-05	2.82E-05	4.96	11.20	<	4.29	69.33
14	Torti	S	31/10/2006	2.83E-05	8.11E-05	6.82	16.89	2.04E-04	6.90	63.69
15	Muto	S	31/10/2006	2.37E-05	7.80E-05	5.28	11.31	2.39E-04	1.27	84.53
16	Sulipani	S	16/11/2006	2.23E-05	5.61E-05	1.88	11.78	1.53E-05	20.26	15.87
17	Giangalia	S	16/11/2006	2.29E-05	8.80E-05	4.92	10.31	3.71E-04	2.23	80.62
18	Pace	S	16/11/2006	3.53E-05	1.11E-04	4.76	11.39	2.82E-04	3.17	70.47
19	Sfaranda	S	16/11/2006	5.80E-05	1.69E-04	4.98	10.32	1.99E-04	8.22	60.59
20	Agrifoglio	S	16/11/2006	2.53E-05	8.65E-05	4.28	10.97	6.65E-05	8.54	51.48
21	Mezzalora	S	22/11/2006	2.52E-05	4.79E-05	1.96	7.28	9.89E-03	2.14	49.24
22	Margio Salice	S	22/11/2006	1.09E-05	3.25E-05	5.57	11.48	3.71E-04	3.95	75.87
23	Chiusitta	S	22/11/2006	1.32E-05	5.46E-05	3.38	10.67	2.83E-04	9.65	40.80
24	Tre Arie	S	22/11/2006	1.84E-05	6.91E-05	4.38	9.61	5.62E-05	2.87	74.32
25	Zarbata	S	22/11/2006	3.21E-05	6.77E-05	3.26	11.42	5.20E-05	12.39	34.47
26	S. Domenica	S	22/11/2006	2.24E-05	8.16E-05	2.58	10.03	2.55E-05	6.60	38.39
27	Piano Soprano	S	22/11/2006	2.52E-05	7.90E-05	3.08	9.76	<	12.39	34.87
28	Casitti	S	22/11/2006	1.80E-05	5.08E-05	5.23	11.51	<	1.34	82.71
29	Jardini	S	23/11/2006	2.64E-05	6.72E-05	5.43	13.72	3.05E-04	3.12	69.67
30	Fossaneve	S	23/11/2006	2.12E-05	6.31E-05	4.87	11.27	5.64E-03	1.39	79.43
31	Titi bassa	S	23/11/2006	2.04E-05	6.36E-05	3.84	10.68	1.94E-05	6.75	51.62
32	S. Anna	S	23/11/2006	3.53E-05	1.19E-04	5.16	13.06	3.81E-05	4.74	64.28
33	Balestra	S	23/11/2006	1.47E-05	5.33E-05	3.35	11.45	<	9.53	39.39
34	S. Pietro	S	23/11/2006	1.57E-05	5.45E-05	4.39	9.79	4.04E-05	1.97	77.75
35	Filipelli	S	23/11/2006	1.80E-05	5.68E-05	5.04	11.94	2.46E-03	4.34	67.60
36	Iria	S	29/11/2006	2.85E-05	9.63E-05	3.31	12.07	2.03E-04	7.84	40.73
37	Abate	S	29/11/2006	2.84E-05	7.94E-05	5.22	11.22	3.11E-05	2.80	77.65
38	Feudo	S	29/11/2006	2.10E-05	6.81E-05	4.60	10.88	2.33E-05	30.64	28.51
39	Favarotta	S	29/11/2006	3.60E-05	8.44E-05	4.95	11.56	2.33E-05	6.13	62.50
40	Palamara	W	20/12/2006	4.74E-05	1.37E-04	3.70	14.21	1.61E-03	12.22	35.14
41	Neviera	S	20/12/2006	4.21E-05	1.20E-04	2.05	11.83	1.75E-03	13.42	21.47
42	Ramata	S	20/12/2006	3.16E-05	9.53E-05	4.46	11.13	1.07E-03	8.45	53.00
43	Nocita	S	20/12/2006	4.39E-05	1.12E-04	4.90	10.50	5.83E-04	4.20	71.52
ASW				4.06E-05		5	9.80	1.00E-06	0.23	

(b)

Sample #	Site name	Type	Date	He	Ne	O ₂	N ₂	CH ₄	CO ₂	Air%
44	Marino SPA 1	W	08/01/2004	4.84E-04	8.38E-05	0.27	3.05	1.32E-02	509.71	0.15
44	Marino SPA 1	W	07/04/2004	2.57E-04	7.26E-05	0.23	2.61	9.24E-03	615.63	0.21
44	Marino SPA 1	W	06/05/2004	1.03E-04	3.51E-05	0.21	2.83	7.57E-03	499.69	0.12
44	Marino SPA 1	W	18/10/2004	1.61E-04	8.22E-05	0.10	3.54	6.40E-03	502.41	0.06
45	Marino SPA 2	W	08/01/2004	2.26E-04	6.10E-05	0.99	3.10	1.94E-03	664.14	0.43
45	Marino SPA 2	W	07/04/2004	1.47E-04	5.87E-05	0.84	2.62	7.45E-04	616.56	0.06
45	Marino SPA 2	W	06/05/2004	9.49E-05	2.71E-05	0.87	2.74	1.00E-03	606.51	0.43
45	Marino SPA 2	W	18/10/2004	6.94E-05	7.15E-05	0.10	3.54	6.40E-03	502.41	0.39
46	Parco Giochi	W	04/02/2004	2.64E-03	3.02E-04	2.05	17.02	1.22E-04	18.30	15.67
46	Parco Giochi	W	03/03/2004	2.49E-03	1.25E-04	3.48	<	<	13.00	32.58
46	Parco Giochi	W	07/04/2004	1.07E-03	2.36E-04	1.84	43.65	<	32.07	6.80
46	Parco Giochi	W	06/05/2004	1.12E-03	1.99E-04	3.76	16.36	<	9.83	35.90
46	Parco Giochi	W	12/10/2004	1.33E-03	1.30E-04	1.98	16.51	8.41E-04	55.01	7.69
46	Parco Giochi	W	18/10/2004	2.65E-03	1.22E-04	2.56	17.38	3.99E-04	48.95	10.63
46	Parco Giochi	W	28/12/2004	2.89E-04	1.50E-04	3.42	12.71	4.65E-04	18.13	28.55
46	Parco Giochi	W	10/02/2005	1.22E-03	2.51E-04	2.62	13.10	<	17.73	22.36
46	Parco Giochi	W	09/03/2005	6.10E-05	1.20E-04	3.42	14.60	6.49E-03	14.17	30.42
46	Parco Giochi	W	29/04/2005	1.06E-03	2.59E-04	1.72	14.02	2.28E-04	14.30	16.35
46	Parco Giochi	W	01/06/2005	2.12E-03	1.06E-04	2.93	16.14	1.01E-04	16.23	23.75
47	Berlinghieri	W	04/02/2004	1.34E-03	1.38E-04	1.66	10.14	6.98E-04	20.25	14.80
47	Berlinghieri	W	03/03/2004	1.86E-03	1.40E-04	2.11	11.45	1.91E-03	22.12	16.93
47	Berlinghieri	W	07/04/2004	1.36E-03	1.72E-04	2.27	11.12	2.35E-03	22.45	18.10
47	Berlinghieri	W	06/05/2004	1.37E-03	1.69E-04	3.10	15.31	6.38E-05	24.56	20.61
47	Berlinghieri	W	08/07/2004	6.68E-04	2.37E-04	2.86	11.79	<	16.71	26.11
47	Berlinghieri	W	12/10/2004	5.68E-04	1.47E-04	2.27	12.70	6.15E-04	20.44	18.31
47	Berlinghieri	W	18/10/2004	3.11E-04	8.79E-05	2.04	14.06	5.69E-03	20.21	16.05
47	Berlinghieri	W	03/03/2006	1.19E-03	8.36E-05	0.06	5.65	3.65E-04	0.49	2.95
47	Berlinghieri	W	06/04/2006	1.16E-03	8.84E-05	0.88	6.86	9.86E-05	0.51	30.49
48	La Magnolia	W	01/06/2005	<	<	0.13	4.29	8.84E-03	535.13	0.07
48	La Magnolia	W	29/06/2005	3.10E-04	7.83E-05	0.10	0.99	3.37E-03	483.37	0.06
48	La Magnolia	W	04/08/2005	7.27E-05	1.08E-05	0.06	2.26	4.62E-03	488.27	0.04
48	La Magnolia	W	14/09/2005	3.19E-05	3.01E-05	0.03	1.04	2.32E-03	52.67	0.16
48	La Magnolia	W	14/02/2006	6.77E-05	3.61E-05	0.08	3.68	9.07E-03	1065.52	0.12
48	La Magnolia	W	14/06/2006	<	<	0.12	2.31	4.74E-03	71.70	0.44
48	La Magnolia	W	18/07/2006	6.32E-05	3.52E-05	0.04	0.90	3.05E-03	795.63	0.01
49	Granata	S	23/03/2005	2.90E-05	1.01E-04	0.04	4.47	7.05E-04	373.87	0.03
49	Granata	S	13/10/2005	2.03E-05	1.56E-05	0.03	8.56	1.01E-03	359.08	0.02
49	Granata	S	02/03/2006	1.96E-05	3.62E-05	0.20	12.67	7.71E-04	39.24	1.11
49	Granata	S	06/04/2006	6.25E-05	3.73E-05	0.02	6.47	6.10E-04	29.76	0.12
50	Granata 1	S	24/03/2005	7.08E-05	1.14E-04	0.03	3.92	<	310.31	0.02
50	Granata 1	S	28/04/2005	4.12E-05	5.80E-05	0.05	4.15	3.93E-04	348.19	0.04
52	Terme Vigliatore	S	27/02/2006	2.12E-05	3.67E-05	0.08	2.11	4.20E-03	530.14	0.05
52	Terme Vigliatore	S	27/04/2006	1.68E-05	3.92E-05	0.05	1.74	4.85E-03	609.16	0.03
52	Terme Vigliatore	S	26/05/2006	7.27E-05	1.66E-04	0.08	7.79	7.45E-03	763.34	0.02
52	Terme Vigliatore	S	26/06/2006	4.48E-05	4.63E-05	0.05	2.88	4.37E-03	617.45	0.02
53	Chiappe	S	01/03/2007	4.85E-05	1.37E-04	0.03	7.76	3.79	22.21	0.27
53	S. Giorgio	S	11/10/2006	4.30E-03	1.60E-04	0.05	18.30	6.18E-01	432.18	0.03
53	S. Giorgio	S	18/02/2007	<	<	0.02	10.41	8.20E-03	43.02	0.12

TABLE 3: Continued.

Sample #	Site name	Type	Date	He	Ne	O ₂	N ₂	CH ₄	CO ₂	Air%
54	Pintaudi	W	26/01/2006	2.45E-05	4.85E-05	3.54	10.81	7.23E-03	8.26	44.79
54	Pintaudi	W	27/02/2006	3.01E-05	7.49E-05	3.96	10.41	3.25E-03	6.75	53.63
55	Biondo	W	26/01/2006	1.86E-05	4.00E-05	0.09	11.51	1.26E-03	0.44	2.23
55	Biondo	W	27/02/2006	3.53E-05	6.32E-05	0.15	12.42	4.97E-03	1.79	3.07
55	Biondo	W	26/06/2006	3.38E-05	4.02E-05	0.01	10.5	4.81E-04	0.41	0.36
55	Biondo	W	10/10/2006	2.91E-05	4.39E-05	0.03	11.68	1.20E-02	0.55	0.73
56	Fetente	S	27/02/2006	2.91E-05	4.39E-05	4.73	10.34	2.95E-05	10.12	53.71
57	La Malfa	W	12/01/2007	3.88E-05	1.19E-04	2.45	10.32	1.15E-04	37.92	13.84
58	Acqua rugiada	S	25/02/2004	2.17E-04	7.45E-05	0.16	5.96	2.40E-02	482.20	0.10
59	Pezzino	W	19/02/2004	3.64E-05	1.12E-04	4.23	9.25	<	12.31	46.91
60	Canneto	W	19/02/2004	4.97E-05	1.64E-04	2.34	10.78	<	19.23	20.70
61	Maio	W	11/04/2007	<	<	0.26	16.97	1.82E-03	25.02	1.75
62	Fontana WP43	S	18/01/2007	2.58E-05	7.51E-05	5.51	11.38	2.92E-05	1.23	87.01
63	Scuderi	S	18/01/2007	5.43E-05	1.35E-04	5.92	12.11	<	1.18	88.17
ASW				4.06E-05		5	9.80	1.00E-06	0.23	

Data in ccSTP/L_{H₂O}. (a) Samples from the Nebrodi Mts; (b) samples from the Peloritani Mts. The site number is the same as reported on the graphs. S: spring; W: well; <: below detection limits or not analyzed.

The helium isotopic ratio observed in the gases dissolved in the groundwater of the Nebrodi and Peloritani chains, ranging from 0.5 to 1.85 Ra (Tables 4(a) and 4(b)) and increasing to 0.67–2.54 Ra (Table 2) in the bubbling gases of the Peloritani area, indicating significant ³He injections, thus pointing to a mantle origin for those volatiles.

Figure 3 plots the ³He/⁴He ratios (expressed as R/Ra values) versus the ⁴He/²⁰Ne ratio and includes results of both dissolved (Tables 4(a) and 4(b)) and bubbling (Table 2) gases. Assuming all neon to be of atmospheric origin, the ⁴He/²⁰Ne ratio provides an indication of the presence of an atmospheric-derived component in the gas assemblage.

The plot shows that the dissolved gases, although extracted from groundwater equilibrated with the atmosphere, display ⁴He/²⁰Ne ratios remarkably higher than the ASW. In particular, the ratios over the Peloritani Mts are higher than those from the Nebrodi Mts, most likely as a consequence of a larger contribution of CO₂-dominated, He-rich gases. Moreover, the isotopic composition of helium in both dissolved and bubbling gases of the Peloritani samples denotes a broadly higher contribution of mantle-type helium that might seem surprising, considering the geology of this portion of the chain, with its outcrops of high-grade metamorphic rocks (micaschists, gneiss) normally enriched in radioactive, ⁴He-producing elements.

The CO₂-³He-⁴He plot of Figure 4 shows the occurrence of GWI, inducing CO₂ loss, as bicarbonate ions in the pH range of the collected waters (Table 1).

The information is consistent with that from the geochemical features of the dissolved helium and its isotopic composition. The affinity of the heavy ¹³C for the liquid phase is responsible for the observed C fractionation depicting the increasing δ¹³C trend of the dissolved carbon species (total dissolved carbon (TDC)). The process is commonly

observed in CO₂-rich waters (e.g., Eastern Alps [47] and Southern Apennines [60]) with the exception of waters with the presence of gas bubbling (gas oversaturated) where C isotopic fractionation is induced by CO₂ escaping (e.g., East Anatolian Fault Zone (EAFZ) [48]; Figure 5).

To evaluate the extent that mantle volatiles contribute to the dissolved gas phase and to the soils, as well as elemental fractionations between He and CO₂, the correlations between CO₂/³He versus CO₂ (Figure 6(a)) and He (Figure 6(b)) were evaluated.

The CO₂/³He ratios along the Nebrodi-Peloritani chain spans over five orders of magnitude (from 5 × 10⁸ to 5 × 10¹³) covering the range proposed for mantle (2 × 10⁹ for MORBs [61]) and crustal continental fluids (10¹⁴ [62]). The samples from the two sections of the chain, however, span over different ranges: 10¹⁰–10¹² for the Nebrodi area and the whole range for the Peloritani chain.

Since He isotope ratios can only be modified by the admixture of He with a different isotopic signature, i.e., from a different reservoir, the coexistence of low ³He/⁴He ratios (namely, high crustal He component) and low, mantle-like CO₂/³He ratios suggests that the ratio is modified by a mixing of crustal and mantle-derived helium, or alternatively, the crustal component ratios span over a wide range due to chemical CO₂ fractionation.

The data are plotted on Figures 6(a) and 6(b) where the arrows in (a) display two concomitant trends here interpreted as (1) CO₂ addition to the ASW-type waters because of regional degassing and (2) increase in helium concentration because of CO₂ loss during GWI. Almost all the samples from the Nebrodi Mts and a group of samples from the Peloritani show CO₂/³He ratios in the range of 10¹⁰–10¹² broadly lower than the ratios detected for the dissolved gases from the Peloritani area.

TABLE 4: (a, b) Recalculated chemical composition for the Nebrodi (a) and Peloritani Mts. (b) after air removal. Isotopic composition of He and total dissolved carbon are reported as well as the He/Ne and $\text{CO}_2/{}^3\text{He}$ ratios.

(a)													
Sample #	Site name	Type	Date	He	Ne	N_2	CH_4	CO_2	He/Ne	R/Ra	ε	$\text{CO}_2/{}^3\text{He}$	$\delta^{13}\text{C}_{\text{TDC}}$
2	Usignolo	S	31/05/2006	1.4E-03	2.0E-03	45.98	2.9E-03	16.66	0.677	0.86	0.018	1.04E+10	-13.00
6	Sampieri	S	26/10/2006	3.6E-04	7.1E-04	9.01	4.2E-04	79.19	0.51	0.60	0.015	2.65E+11	-15.04
21	Mezzalora	S	22/11/2006	4.4E-04	8.3E-04	31.87	1.7E-01	37.05	0.527	0.83	0.046	7.34E+10	-8.68
25	Zarbata	S	22/11/2006	1.8E-04	3.8E-04	19.77	2.9E-04	69.83	0.474	0.86	0.031	3.24E+11	-12.42
39	Favarotta	S	29/11/2006	4.2E-04	9.9E-04	10.44	2.7E-04	72.17	0.427	0.90	0.031	1.36E+11	-12.82

(b)													
Sample #	Site name	Type	Date	He	Ne	N_2	CH_4	CO_2	He/Ne	R/Ra	Error	$\text{CO}_2/{}^3\text{He}$	$\delta^{13}\text{C}_{\text{CO}_2}$
44	Marino SPA 1	W	08/01/2004	9.4E-05	5.5E-04	0.49	2.6E-03	99.50	5.78	0.67	0.01	1.13E+12	<
44	Marino SPA 1	W	07/04/2004	<	<	0.43	2.1E-03	99.57	3.54	0.69	0.011	2.48E+12	<
44	Marino SPA 1	W	06/05/2004	<	<	0.47	1.7E-03	99.53	2.93	0.71	0.04	4.92E+12	<
44	Marino SPA 1	W	18/10/2004	4.2E-05	1.5E-04	0.35	1.5E-03	99.65	1.95	0.71	0.014	3.16E+12	<
45	Marino SPA 2	W	08/01/2004	2.0E-05	6.0E-05	0.49	1.5E-03	99.51	3.71	0.66	0.017	3.19E+12	<
45	Marino SPA 2	W	07/04/2004	3.2E-05	6.2E-05	0.66	1.3E-03	99.33	2.5	0.74	0.026	4.10E+12	<
45	Marino SPA 2	W	06/05/2004	3.4E-05	1.3E-04	0.19	2.9E-04	99.81	3.5	0.7	0.027	6.58E+12	<
45	Marino SPA 2	W	18/10/2004	<	0.0E+00	0.17	1.4E-04	99.83	0.97	0.78	0.024	6.68E+12	<
46	Parco Giochi	W	04/02/2004	<	0.0E+00	0.14	8.7E-05	99.86	8.73	0.7	0.007	7.09E+09	<
46	Parco Giochi	W	03/03/2004	2.4E-05	5.9E-05	0.17	1.2E-04	99.83	19.97	0.69	0.006	5.43E+09	<
46	Parco Giochi	W	07/04/2004	1.6E-05	5.5E-05	0.18	1.7E-04	99.81	4.54	0.69	0.009	3.13E+10	<
46	Parco Giochi	W	06/05/2004	1.4E-05	1.3E-05	0.66	1.3E-03	99.33	5.64	0.68	0.013	9.26E+09	<
46	Parco Giochi	W	12/10/2004	8.4E-03	7.3E-02	35.33	3.9E-04	58.03	10.27	0.63	0.006	4.69E+10	<
46	Parco Giochi	W	18/10/2004	3.8E-02	7.5E-01	24.68	<	63.10	21.76	0.63	0.007	2.10E+10	<
46	Parco Giochi	W	28/12/2004	1.5E-03	6.7E-03	51.85	<	44.36	1.93	0.65	0.006	6.95E+10	<
46	Parco Giochi	W	10/02/2005	5.8E-03	3.3E-02	31.26	<	51.19	4.87	0.64	0.006	1.64E+10	<
46	Parco Giochi	W	09/03/2005	3.7E+00	9.6E+01	0.00	<	<	0.51	1.19	0.037	1.40E+11	<
46	Parco Giochi	W	29/04/2005	2.0E-03	2.0E-02	17.46	1.2E-03	81.06	4.114	0.63	0.005	1.53E+10	<
46	Parco Giochi	W	01/06/2005	4.3E-03	9.4E-02	18.29	6.5E-04	79.44	19.916	0.63	0.004	8.81E+09	<
47	Berlinghieri	W	04/02/2004	1.2E-03	2.3E-03	18.53	1.9E-03	74.06	9.76	0.67	0.006	1.6E+10	<
47	Berlinghieri	W	03/03/2004	4.7E-03	2.3E-02	24.62	0.0E+00	68.27	13.26	0.67	0.006	1.27E+10	<
47	Berlinghieri	W	07/04/2004	2.7E-04	1.4E-04	25.57	2.9E-02	63.23	7.91	0.67	0.01	1.76E+10	<
47	Berlinghieri	W	06/05/2004	4.2E-03	1.7E-02	36.03	9.1E-04	56.90	8.08	0.68	0.013	1.9E+10	<
47	Berlinghieri	W	08/07/2004	7.9E-03	1.6E-01	30.21	3.7E-04	60.22	2.82	0.67	0.009	2.7E+10	<
47	Berlinghieri	W	12/10/2004	0.0E+00	0.0E+00	51.41	2.8E-04	48.37	3.87	0.69	0.01	3.75E+10	<
47	Berlinghieri	W	18/10/2004	4.9E-03	4.8E-02	22.01	2.6E-03	74.12	3.53	0.64	0.016	7.34E+10	<
47	Berlinghieri	W	03/03/2006	6.3E-03	8.3E-02	21.06	6.4E-03	74.56	14.2	0.67	0.006	4.38E+08	-8.61
47	Berlinghieri	W	06/04/2006	4.6E-03	3.7E-02	19.25	8.0E-03	76.45	13.12	0.62	0.009	5.07E+08	-8.25
48	La Magnolia	W	01/06/2005	4.0E-03	3.2E-02	22.22	1.9E-04	71.98	<	<	<	1.79E+12	<
48	La Magnolia	W	29/06/2005	2.9E-03	8.1E-03	20.61	0.0E+00	72.10	3.961	0.69	0.007	7.13E+12	<
48	La Magnolia	W	04/08/2005	2.0E-03	7.6E-03	23.96	2.1E-03	70.65	6.72	0.67	0.014	1.34E+13	<
48	La Magnolia	W	14/09/2005	1.0E-03	3.6E-03	28.28	1.9E-02	66.30	1.06	0.82	0.021	6.35E+11	<
48	La Magnolia	W	14/02/2006	1.4E-03	0.0E+00	15.40	6.6E-03	81.17	1.87	0.84	0.016	8.79E+12	0.54
48	La Magnolia	W	14/06/2006	3.1E-03	0.0E+00	21.78	3.1E-03	72.25	<	<	<	1.41E+12	<
48	La Magnolia	W	18/07/2006	6.3E-03	0.0E+00	23.63	1.2E-02	68.98	1.8	0.58	0.012	2.52E+13	<
49	Granata	S	23/03/2005	2.0E-02	2.8E-01	88.94	6.0E-03	8.05	0.29	0.72	0.08	1.29E+13	1.82
49	Granata	S	13/10/2005	2.0E-02	2.6E-01	63.16	1.7E-03	8.85	1.31	0.71	0.027	1.79E+13	<

TABLE 4: Continued.

Sample #	Site name	Type	Date	He	Ne	N ₂	CH ₄	CO ₂	He/Ne	R/Ra	Error	CO ₂ / ³ He	δ ¹³ C _{CO2}
49	Granata	S	02/03/2006	<	<	0.67	7.6E-04	99.33	0.54	0.73	0.012	1.97E+12	3.03
49	Granata	S	06/04/2006	<	<	0.54	9.3E-04	99.45	1.68	0.71	0.011	4.84E+11	<
50	Granata 1	S	24/03/2005	5.7E-05	2.3E-04	0.75	1.6E-03	99.25	0.62	0.62	0.008	5.09E+12	<
50	Granata 1	S	28/04/2005	1.5E-05	1.0E-04	0.17	7.0E-04	99.83	0.71	0.91	0.026	6.68E+12	<
52	Terme Vigliatore	S	27/02/2006	6.5E-06	6.9E-06	0.44	9.4E-04	99.56	0.58	0.98	0.116	1.84E+13	<
52	Terme Vigliatore	S	27/04/2006	2.3E-04	5.6E-04	1.83	4.3E-03	98.16	0.43	0.76	0.015	3.44E+13	<
52	Terme Vigliatore	S	26/05/2006	3.5E+01	6.5E+01	0.00	<	<	0.44	0.77	0.008	9.8E+12	<
52	Terme Vigliatore	S	26/06/2006	7.2E-06	2.6E-05	0.33	8.5E-04	99.67	0.97	0.48	0.009	2.08E+13	<
53	Chiappe	S	01/03/2007	<	<	0.79	3.0E-03	99.20	0.353	0.69	<	4.76E+11	-7.09
53	S. Giorgio	S	11/10/2006	8.6E-05	1.5E-04	2.82	6.4E-03	97.16	26.859	1.85	0.026	3.9E+10	-15.94
53	S. Giorgio	S	18/02/2007	4.1E-06	3.0E-06	0.10	3.8E-04	99.90	<	<	<	<	-16.33
54	Pintaudi	W	26/01/2006	<	<	2.50	4.7E-03	97.49	0.506	0.81	0.041	3.00E+11	<
54	Pintaudi	W	27/02/2006	<	<	1.38	4.3E-03	98.60	0.402	0.99	0.056	1.63E+11	<
55	Biondo	W	26/01/2006	<	<	0.21	3.6E-04	99.79	0.466	0.79	0.043	2.16E+10	<
55	Biondo	W	27/02/2006	<	<	0.00	<	<	0.56	0.7	0.036	5.19E+10	<
55	Biondo	W	26/06/2006	7.7E-06	2.2E-06	1.16	1.9E-04	98.84	0.84	0.7	0.026	1.67E+10	<
55	Biondo	W	10/10/2006	5.5E-06	7.2E-06	2.31	2.7E-04	97.68	<	<	<	<	<
56	Fetente	S	27/02/2006	3.8E-05	2.1E-05	23.59	1.5E-03	76.14	0.66	1.3	0.071	1.93E+11	<
57	La Malfa	W	12/01/2007	1.7E-04	2.9E-04	17.77	1.7E-03	82.21	0.326	0.79	<	8.93E+11	-13.82
58	Acqua rugiada	S	25/02/2004	2.3E-05	1.4E-05	1.23	<	98.77	2.91	1.13	0.022	1.41E+12	<
59	Pezzino	W	19/02/2004	1.2E-05	8.3E-06	1.15	1.1E-04	98.85	0.33	1.21	0.232	2.01E+11	<
60	Canneto	W	19/02/2004	1.1E-04	0.0E+00	3.73	3.1E-05	96.26	0.3	1.11	0.155	2.52E+11	<
61	Maio	W	11/04/2007	4.1E+01	5.9E+01	0.00	<	<	0.343	<	<	4.21E+10	-16.77
62	Fontana WP43	S	18/01/2007	4.0E-06	2.3E-06	0.37	7.9E-04	99.63	0.403	0.81	<	1.88E+10	<
63	Scuderi	S	18/01/2007	<	<	0.39	8.4E-04	99.61	0.506	0.84	<	1.93E+11	<

Data in vol%. See text for details. <: below detection limits or not analyzed; ϵ : error of the isotopic determination reported for all of the R/Ra data. Carbon isotopic ratios are expressed as $\delta\text{‰}$ units vs. PDB. $\delta^{13}\text{C}_{\text{TDC}}$ and $\delta^{13}\text{C}_{\text{CO2R}}$: isotopic composition of the total inorganic carbon and recalculated gaseous CO₂, respectively.

It is of note that only samples from the Peloritani Mts show an antirelated CO₂/³He-He relationship as a consequence of GWI processes with CO₂ loss due to dissolution. In addition, the CO₂/³He ratio vs. [CO₂] content (Figure 6(b)) demonstrates a correlation trend indicating that whatever the GWI-induced CO₂ loss, samples from the Nebrodi Mts are characterized by broadly lower CO₂ content. The group of samples from the Peloritani area, marked by low He content with high ³He/⁴He ratios, denotes a different composition of the pristine gas phase.

6. Fluid/Fault Relationships

The active degassing of CO₂-dominated volatiles is considered responsible for the deep-originated dissolved gases we detected in the groundwater collected over the Nebrodi-Peloritani area. Although it was almost unexpected in the geologic context of the Southern Apennines, the evidence that a large amount of CO₂-dominated volatiles feeds the groundwater circulating over the study area indicates the close connection of the fluids' geochemistry with the ATLF tectonic structure.

There is no evidence of melt intrusions in shallow crustal levels capable of releasing ³He-enriched fluids as already detected in other Apennine areas (e.g., [54]); thus, we propose that the presence of mantle fluids is related to lithospheric structures that, enhancing the vertical permeability, allow depressurization at the level of the upper mantle and the degassing of deep-originated fluids. A possible circulation model can be summarized as follows: CO₂-dominated fluids are produced by the partial melting of the upper mantle induced by depressurization due to lithospheric faults; the mantle-originated fluids are driven toward the surface through the 25-30 km thick crustal layers by the ATLF zone; the mantle volatiles permeate shallow crustal levels where crustal-type helium (⁴He) is originated by a wide range of metamorphic rocks; a further mixing occurs as the volatiles move across the groundwater circulating at relatively shallow depths where they suffer GWI (e.g., gas dissolution as a function of Bunsen coefficients and boundary pressure and temperature conditions) and mix with the atmospheric components (mainly represented by O₂ and N₂).

The upraising of large amounts of mantle-originated volatiles (as shown by the ³He content) at Ali Terme (Ionian

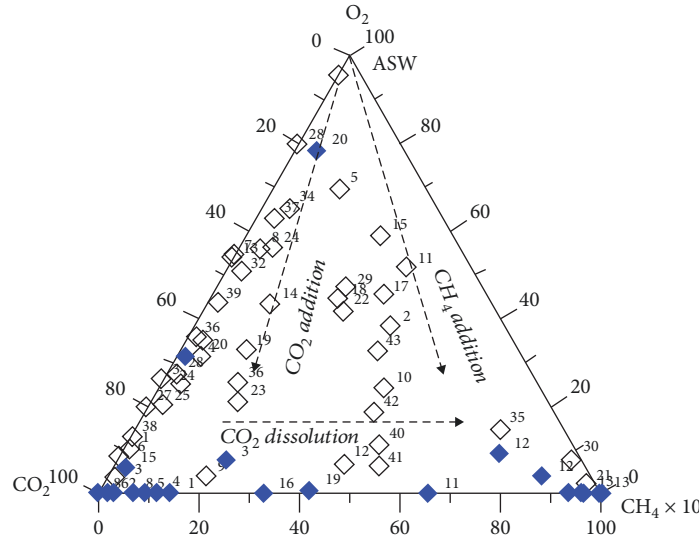


FIGURE 2: CH_4 - O_2 - CO_2 composition of the gases dissolved in the studied waters. The dashed arrows show the trends produced by the addition and dissolution of CO_2 and addition of CH_4 to an atmospheric gas assemblage (see text for details). ASW: air saturated water. Open black marks: samples from Nebrodi Mts; blue filled marks: samples from Peloritani Mts. Labels refer to sample numbers as in Tables 1–4.

Sea) and Capo Calavà (Tyrrhenian Sea) coincides with areas where the ATLF zone crosses the E-W-trending normal faults [63] on the Tyrrhenian Sea and the NE-SW normal structure of the Ionian Sea. The latter area that includes the eastern Peloritani area (Messina Strait and Ionian coasts, Figure 1) is shaped by a complex network of normal and transtensional faults [64] with extensional and right-lateral transtensional tectonics in the southern Messina Strait. This complex tectonic network looks to be able to generate high permeability zones where mantle volatiles can be driven to the surface, in full agreement with the obtained results.

On the other hand, the area is characterized by high strain rate (SR) [65], where the contemporary creeping of the upper and the lower crust may produce that high permeability zone where the mantle fluids move towards the surface without significant temporal changes, in full agreement with our findings. In terms of the escape of fluids, we found the highest CO_2 flow rates at the eastern side of the area (Peloritani chain). By contrast, the Nebrodi area, to the west of the ATLF, seems to accumulate strain at lower rates acting as a locked fault marked by lower CO_2 degassing rates and lower mantle volatile content. The ATLF zone cannot be simply described as a boundary line; however, it is a zone where many different fault segments separate locked fault volumes from areas where dilatancy goes on. Following the model proposed by Riguzzi et al. [65], the elastic energy accumulates in those areas where faults are locked and the strain rate (SR) is lower. High SR areas can be interpreted as regions where both the upper and the lower crust are creeping or alternatively where tectonic loading is more effective. Vice versa, lower strain rates suggest the presence of locked faults in a later stage in the seismic cycle [65]. Doglioni et al. [66] proposed that during an interseismic

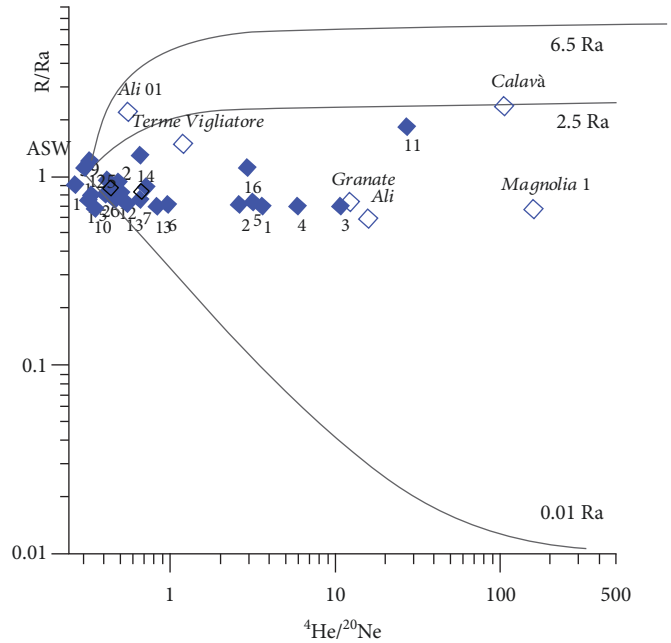


FIGURE 3: Helium isotopes (normalized to the atmosphere) vs. $^4\text{He}/^{20}\text{Ne}$ ratios. The samples represent a mixing between the atmosphere and a radiogenic-type end member. The mixing boundary lines are built with the following end members: atmosphere (as dissolved air) $R/Ra = 1$ vs. $^4\text{He}/^{20}\text{Ne} = 0.285$; mantle (Sub Continental European Mantle (SCEM)) $R/Ra = 6.5$ vs. $^4\text{He}/^{20}\text{Ne} = 1000$ (Dunai and Baur [59]); and continental crust $R/Ra = 0.01$ vs. $^4\text{He}/^{20}\text{Ne} = 1000$. Symbols and labels are as in Figure 2 (dissolved gas samples). Open blue marks refer to bubbling gases from Peloritani Mts.

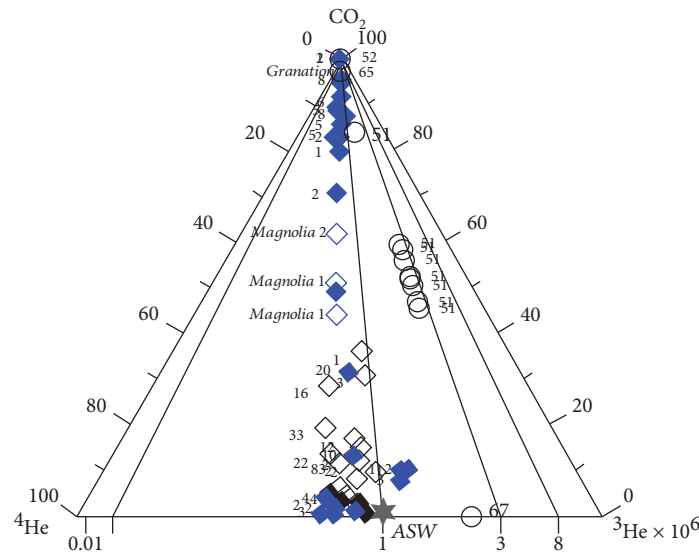


FIGURE 4: ${}^3\text{He}$ - ${}^4\text{He}$ - CO_2 diagram. The graph shows the occurrence of CO_2 dissolution phenomena occurring at variable extents for the sampled sites (grey lines). All the samples plot to the left of the grey line showing that their ${}^3\text{He}$ content is always below the atmospheric. The helium isotopic ratio is mainly a binary mixing between the atmosphere and a ${}^4\text{He}$ -rich end member, and the grey lines also indicate constant ${}^3\text{He}/{}^4\text{He}$ ratios. Symbols and labels are as in Figure 3. Open circles refer to bubbling gases from the Calavà and Ali areas.

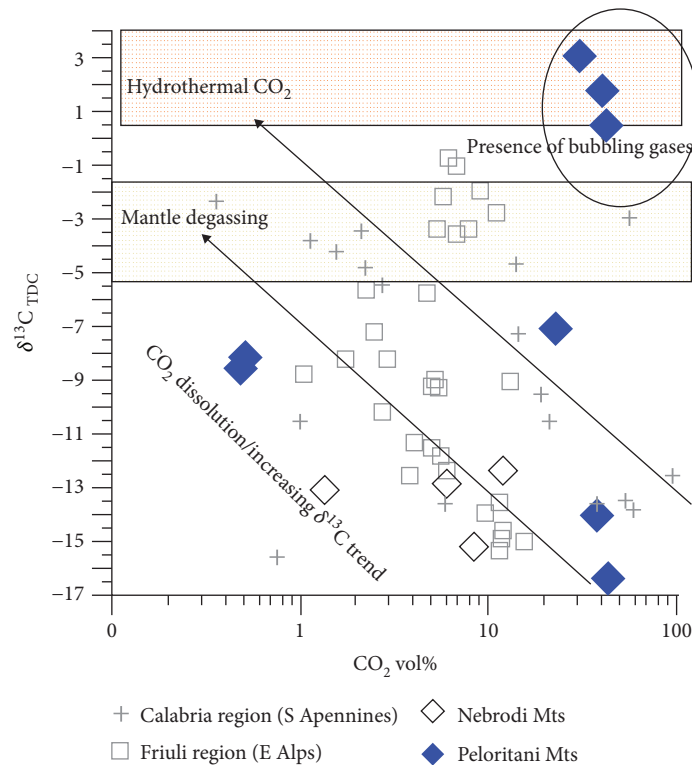


FIGURE 5: CO_2 content vs. $\delta^{13}\text{C}_{\text{TDC}}$. The plot shows carbon isotopic fractionation due to the occurrence of GWI interactions and degassing. The chemical fractionation due to CO_2 dissolution during GWI induces isotopic fractionation of the carbon species. The evidence that the higher the CO_2 content in the dissolved gases, the lower the isotopic composition of the TDC, indicates that the origin of the dissolved carbon is mainly due to the preferential dissolution of the heavy carbon isotope as bicarbonate ion. Samples from the Southern Apennines (grey crosses) after Italiano et al. [60]; samples from the Eastern Alps (grey squared symbols) after Italiano et al. [47]. Other symbols are as in Figure 2.

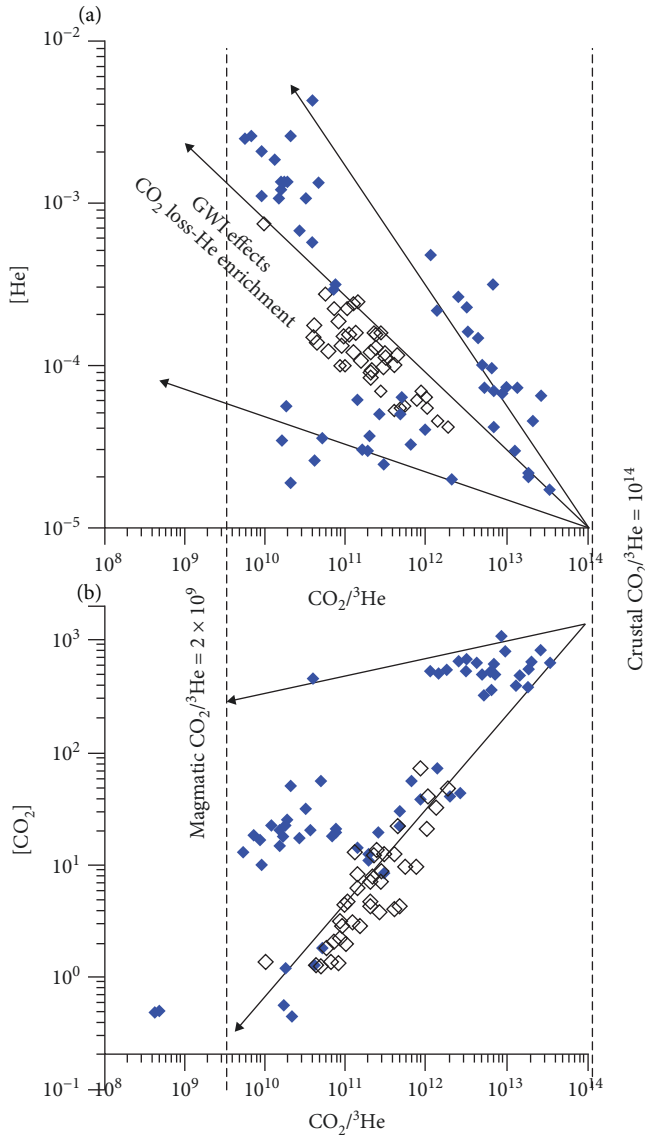


FIGURE 6: CO_2 - ${}^3\text{He}$ relationships. $\text{CO}_2/{}^3\text{He}$ vs. CO_2 content (ml/l STP) (a) and (b) $\text{CO}_2/{}^3\text{He}$ vs. $[\text{He}]$. The sample distribution on (a) shows trends of CO_2 dissolution at variable extents (arrows) with almost constant ${}^3\text{He}$ content. (b) Combines (a) with the information that helium isotopes do not denote simple crust/mantle mixes (see text); however, variable $\text{CO}_2/{}^3\text{He}$ ratios at constant ${}^3\text{He}/{}^4\text{He}$ ratios are possible results of subsequent elemental fractionation. All error bars are within the symbol size. $\text{CO}_2/{}^3\text{He}$ end members are in the range of 2×10^9 (mantle-type volatiles) and 1×10^{14} crustal volatiles (vertical dashed lines). Symbols are as in Figure 2; labels not reported for a readable figure.

period, the brittle-ductile transition zone separates the brittle upper crustal layers, where the faults are almost locked, from the deeper shear zones where the ductile deep crust/shallow mantle layers are constantly creeping. In terms of the geochemical features of the fluids and their temporal behaviour, this model implies that deep, mantle-originated volatiles (marked, for example, by high helium isotopic ratios) are continuously released at the level of the ductile, upper mantle level. They cannot easily move toward the surface over areas

marked by very low SR due to absence of creeping that is the lack of discontinuities where fluids can move across. Contrastingly significant contribution of mantle-type fluids and high degassing rates can be expected over areas undergoing dilatancy, namely, where high SR produce measurable crustal deformation due to creeping activity that allows a fast and, in terms of masses, significant contribution of mantle-derived volatiles.

The CPA is one of the highest seismic risk-prone territories in Italy and includes areas with both high and low strain rate accumulation [65], thus representing a suitable test site to better understand the behaviour of the fluids with respect to the tectonic setting.

7. Conclusions

The investigations carried out on the volatiles vented over the CPA show that a huge amount of CO_2 is daily dissolved in the groundwater. The dissolved gases carry helium with a typical, although variable, mantle signature here interpreted as induced by the lithospheric character of the ATLF.

During the evolution of the seismic cycle, deep lithospheric faults are able to drive mantle-derived fluids to the surface and to change the mixing proportions with the shallow fluids. Following the model proposed by Doglioni et al. [66], we may detect significant contribution of deep fluids over an area accumulating strain at a high rate in full agreement with the geochemical features of the fluids vented over the Peloritani and Nebrodi mountains. Due to high seismicity of the area, further investigations, including discrete and continuous monitoring activity as well as accurate estimations of the degassing rates, may provide a better insight in defining the role of the fluids during the final stage of a seismic cycle. Overall, an integrated approach coupling fluid geochemistry with accurate mapping of the actual SR analysis could represent an effective tool in order to better constrain those areas exposed to high seismic risk.

Data Availability

The data used to support the findings of this study are included within the article.

Conflicts of Interest

The authors declare that there is no conflict of interest regarding the publication of this paper.

Acknowledgments

We acknowledge the thorough and constructive reviews of two anonymous referees, which greatly improved the manuscript. The authors are also indebted to Prof. Alessandro Tripodo and Dott. Giuseppe Sabatino for their help during the field work. Mauro Martelli and Andrea Rizzo are kindly acknowledged for their support during the laboratory work. The research work was supported by the Istituto Nazionale di Geofisica e Vulcanologia (INGV)-DPC grants, S2 and V5 projects, Research Unit-Italiano.

References

- [1] R. Basili, G. Valensise, P. Vannoli et al., "The Database of Individual Seismogenic Sources (DISS), version 3: summarizing 20 years of research on Italy's earthquake geology," *Tectonophysics*, vol. 453, no. 1-4, pp. 20-43, 2008.
- [2] DISS Working Group, *Database of Individual Seismogenic Sources (DISS), version 3.2.1: a compilation of potential sources for earthquakes larger than M 5.5 in Italy and surrounding areas*, Istituto Nazionale di Geofisica e Vulcanologia, 2018, <http://diss.rm.ingv.it/diss/>.
- [3] F. Barberi, F. Innocenti, G. Ferrara, J. Keller, and L. Villari, "Evolution of Eolian arc volcanism (southern Tyrrhenian Sea)," *Earth and Planetary Science Letters*, vol. 21, no. 3, pp. 269-276, 1974.
- [4] A. Malinverno and W. B. F. Ryan, "Extension in the Tyrrhenian Sea and shortening in the Apennines as result of arc migration driven by sinking of the lithosphere," *Tectonics*, vol. 5, no. 2, pp. 227-245, 1986.
- [5] J. F. Dewey, M. L. Helman, S. D. Knott, E. Turco, and D. H. W. Hutton, "Kinematics of the western Mediterranean," *Geological Society, London, Special Publications*, vol. 45, no. 1, pp. 265-283, 1989.
- [6] M. Boccaletti, R. Nicolich, and L. Tortorici, "The Calabrian arc and the Ionian Sea in the dynamic evolution of the Central Mediterranean," *Marine Geology*, vol. 55, no. 3-4, pp. 219-245, 1984.
- [7] E. Patacca, R. Sartori, and R. Scandone, *Tyrrhenian basin and Apenninic arcs. Kinematic relations since late Tortonian times*, vol. 45, Memorie della Società Geologica Italiana, 1990.
- [8] C. Monaco and L. Tortorici, "Active faulting in the Calabrian arc and eastern Sicily," *Journal of Geodynamics*, vol. 29, no. 3-5, pp. 407-424, 2000.
- [9] S. Catalano and G. De Guidi, "Late Quaternary uplift of northeastern Sicily: relation with the active normal faulting deformation," *Journal of Geodynamics*, vol. 36, no. 4, pp. 445-467, 2003.
- [10] S. Catalano, G. De Guidi, G. Romagnoli, S. Torrisi, G. Tortorici, and L. Tortorici, "The migration of plate boundaries in SE Sicily: influence on the large-scale kinematic model of the African promontory in southern Italy," *Tectonophysics*, vol. 449, no. 1-4, pp. 41-62, 2008.
- [11] L. Ferranti, J. S. Oldow, B. D'Argenio et al., "Active deformation in southern Italy, Sicily and southern Sardinia from GPS velocities of the Peri-Tyrrhenian geodetic Array (PTGA)," *Bollettino della Società Geologica Italiana*, vol. 127, pp. 299-316, 2008.
- [12] E. Gueguen, C. Doglioni, and M. Fernandez, "On the post-25 Ma geodynamic evolution of the western Mediterranean," *Tectonophysics*, vol. 298, no. 1-3, pp. 259-269, 1998.
- [13] C. Faccenna, C. Piromallo, A. Crespo-Blanc, L. Jolivet, and F. Rossetti, "Lateral slab deformation and the origin of the western Mediterranean arcs," *Tectonics*, vol. 23, no. 1, 2004.
- [14] G. Rosenbaum, M. Gasparon, F. P. Lucente, A. Peccerillo, and M. S. Miller, "Kinematics of slab tear faults during subduction segmentation and implications for Italian magmatism," *Tectonics*, vol. 27, no. 2, 2008.
- [15] C. Faccenna, T. W. Becker, F. P. Lucente, L. Jolivet, and F. Rossetti, "History of subduction and back-arc extension in the Central Mediterranean," *Geophysical Journal International*, vol. 145, no. 3, pp. 809-820, 2001.
- [16] M. Boccaletti, G. Cello, and L. Tortorici, "Strike-slip deformation as a fundamental process during the Neogene-Quaternary evolution of the Tunisian-Pelagian area," *Annales Tectonicae*, vol. 4, p. 16, 1990.
- [17] F. Ghisetti and L. Vezzani, "Thin-skinned deformation of the Western Sicily thrust belt and relationships with crustal shortening mesostructural data on the M. Kumeta-Alcantara fault zone and related structures," *Bollettino della Società Geologica Italiana*, vol. 103, p. 28, 1984.
- [18] I. Finetti and A. Del Ben, "Geophysical study of the Tyrrhenian opening," *Bollettino di Geofisica Teorica ed Applicata*, vol. 28, p. 81, 1986.
- [19] G. Giunta, D. Luzio, F. Agosta et al., "An integrated approach to investigate the seismotectonics of northern Sicily and southern Tyrrhenian," *Tectonophysics*, vol. 476, no. 1-2, pp. 13-21, 2009.
- [20] G. Giunta, F. Nigro, A. Renda, and A. Giorgianni, *The Sicilian-Maghrebides Tyrrhenian Margin: A Neotectonic Evolutionary Model*, vol. 119, Memorie della Società Geologica Italiana, 2000.
- [21] A. Frepoli and A. Amato, "Fault plane solutions of crustal earthquakes in southern Italy (1988-1995): seismotectonic implications," *Annali di Geofisica*, vol. 43, pp. 437-467, 2000.
- [22] S. Pondrelli, A. Morelli, G. Ekstrom, S. Mazza, E. Boschi, and A. M. Dziewonski, "European-Mediterranean regional centroid-moment tensors: 1997-2000," *Physics of the Earth and Planetary Interiors*, vol. 130, no. 1-2, pp. 71-101, 2002.
- [23] S. Pondrelli, A. Morelli, and G. Ekstrom, "European-Mediterranean regional centroid-moment tensor catalog: solutions for years 2001 and 2002," *Physics of the Earth and Planetary Interiors*, vol. 145, no. 1-4, pp. 127-147, 2004.
- [24] S. Pondrelli, S. Salimbeni, G. Ekstrom, A. Morelli, P. Gasperini, and G. Vannucci, "The Italian CMT dataset from 1977 to the present," *Physics of the Earth and Planetary Interiors*, vol. 159, no. 3-4, pp. 286-303, 2006.
- [25] G. Neri, G. Barberi, G. Oliva, and B. Orecchio, "Spatial variations of seismogenic stress orientations in Sicily, South Italy," *Physics of the Earth and Planetary Interiors*, vol. 148, no. 2-4, pp. 175-191, 2005.
- [26] G. Giunta, F. Nigro, A. Renda, F. Andaloro, A. Giorgianni, and V. Sparacino, "The structural and morphotectonic framework of the NW Sicilian Maghrebides, in a seismotectonic perspective," *Studi Geologici Camerti*, vol. 5, 2002.
- [27] C. Hollenstein, H. G. Kahle, A. Geiger, S. Jenny, S. Goes, and D. Giardini, "New GPS constraints on the Africa-Eurasia plate boundary zone in southern Italy," *Geophysical Research Letters*, vol. 30, no. 18, 2003.
- [28] F. Pepe, G. Bertotti, and S. Cloetingh, "Tectono-stratigraphic modelling of the North Sicily continental margin (southern Tyrrhenian Sea)," *Tectonophysics*, vol. 384, no. 1-4, pp. 257-273, 2004.
- [29] A. Billi, D. Presti, B. Orecchio, C. Faccenna, and G. Neri, "Incipient extension along the active convergent margin of Nubia in Sicily, Italy: Cefalù-Etna seismic zone," *Tectonics*, vol. 29, no. 4, 2010.
- [30] G. Lavecchia, F. Ferrarini, R. de Nardis, F. Visini, and M. S. Barbano, "Active thrusting as a possible seismogenic source in Sicily (southern Italy): some insights from integrated structural-kinematic and seismological data," *Tectonophysics*, vol. 445, no. 3-4, pp. 145-167, 2007.

- [31] M. Mattia, M. Palano, V. Bruno, F. Cannavo, A. Bonaccorso, and S. Gresta, "Tectonic features of the Lipari-Vulcano complex (Aeolian archipelago, Italy) from 10 years (1996-2006) of GPS data," *Terra Nova*, vol. 20, no. 5, pp. 370-377, 2008.
- [32] G. Neri, G. Barberi, G. Oliva, and B. Orecchio, "Tectonic stress and seismogenic faulting in the area of the 1908 Messina earthquake, South Italy," *Geophysical Research Letters*, vol. 31, no. 10, 2004.
- [33] L. Ferranti, C. Monaco, D. Morelli, F. Antonioli, and L. Maschio, "Holocene activity of the Scilla fault, southern Calabria: insights from coastal morphological and structural investigations," *Tectonophysics*, vol. 453, no. 1-4, pp. 74-93, 2008.
- [34] M. Mattia, M. Palano, V. Bruno, and F. Cannavo, "Crustal motion along the Calabro-Peloritano Arc as imaged by twelve years of measurements on a dense GPS network," *Tectonophysics*, vol. 476, no. 3-4, pp. 528-537, 2009.
- [35] E. Serpelloni, R. Bürgmann, M. Anzidei, P. Baldi, B. Mastrolobo Ventura, and E. Boschi, "Strain accumulation across the Messina Straits and kinematics of Sicily and Calabria from GPS data and dislocation modeling," *Earth and Planetary Science Letters*, vol. 298, no. 3-4, pp. 347-360, 2010.
- [36] M. Cuffaro, F. Riguzzi, D. Scrocca, and C. Doglioni, "Coexisting tectonic settings: the example of the southern Tyrrhenian Sea," *International Journal of Earth Sciences*, vol. 100, no. 8, pp. 1915-1924, 2011.
- [37] S. Goes, D. Giardini, S. Jenny, C. Hollenstein, H. G. Kahle, and A. Geiger, "A recent tectonic reorganization in the South-Central Mediterranean," *Earth and Planetary Science Letters*, vol. 226, no. 3-4, pp. 335-345, 2004.
- [38] R. Nicolich, M. Laigle, A. Hirn, L. Cernobori, and J. Gallart, "Crustal structure of the Ionian margin of Sicily: Etna volcano in the frame of regional evolution," *Tectonophysics*, vol. 329, no. 1-4, pp. 121-139, 2000.
- [39] C. Doglioni, M. Ligi, D. Scrocca et al., "The tectonic puzzle of the Messina area (southern Italy): insights from new seismic reflection data," *Scientific Reports*, vol. 2, no. 1, 2012.
- [40] G. Rosenbaum and G. S. Lister, "Neogene and quaternary roll-back evolution of the Tyrrhenian Sea, the Apennines, and the Sicilian Maghrebides," *Tectonics*, vol. 23, no. 1, 2004.
- [41] C. Chiarabba, P. De Gori, and F. Speranza, "The southern Tyrrhenian subduction zone: deep geometry, magmatism and Plio-Pleistocene evolution," *Earth and Planetary Science Letters*, vol. 268, no. 3-4, pp. 408-423, 2008.
- [42] A. Billi, G. Barberi, C. Faccenna, G. Neri, F. Pepe, and A. Sulli, "Tectonics and seismicity of the Tindari Fault System, southern Italy: crustal deformations at the transition between ongoing contractional and extensional domains located above the edge of a subducting slab," *Tectonics*, vol. 25, no. 2, 2006.
- [43] G. Ventura, "Tectonics, structural evolution and caldera formation on Vulcano Island (Aeolian archipelago, southern Tyrrhenian Sea)," *Journal of Volcanology and Geothermal Research*, vol. 60, no. 3-4, pp. 207-224, 1994.
- [44] R. Mazzuoli, L. Tortorici, and G. Ventura, "Oblique rifting in Salina, Lipari and Vulcano Islands (Aeolian Islands, southern Italy)," *Terra Nova*, vol. 7, no. 4, pp. 444-452, 1995.
- [45] F. Ghisetti, "Relazioni tra strutture e fasi trascorrenti e distensive lungo i sistemi Messina-Fiumefreddo, Tindari-Letojanni e Alia-Malvagna (Sicilia nord-orientale): uno studio microtettonico," *Geologica Romana*, vol. 18, p. 35, 1979.
- [46] M. Palano, L. Ferranti, C. Monaco et al., "GPS velocity and strain fields in Sicily and southern Calabria, Italy: updated geodetic constraints on tectonic block interaction in the Central Mediterranean," *Journal of Geophysical Research: Solid Earth*, vol. 117, no. B7, 2012.
- [47] F. Italiano, P. Bonfanti, M. Ditta, R. Petrini, and F. Slejko, "Helium and carbon isotopes in the dissolved gases of Friuli region (NE Italy): geochemical evidence of CO₂ production and degassing over a seismically active area," *Chemical Geology*, vol. 266, no. 1-2, pp. 76-85, 2009.
- [48] F. Italiano, A. Sasmaz, G. Yuce, and O. O. Okan, "Thermal fluids along the East Anatolian Fault Zone (EAFZ): geochemical features and relationships with the tectonic setting," *Chemical Geology*, vol. 339, pp. 103-114, 2013.
- [49] F. Italiano, G. Yuce, I. T. Uysal, M. Gasparon, and G. Morelli, "Insights into mantle-type volatiles contribution from dissolved gases in artesian waters of the Great Artesian Basin, Australia," *Chemical Geology*, vol. 378-379, pp. 75-88, 2014.
- [50] D. R. Hilton, "The helium and carbon isotope systematics of a continental geothermal system: results from monitoring studies at Long Valley caldera (California, U.S.A.)," *Chemical Geology*, vol. 127, no. 4, pp. 269-295, 1996.
- [51] Y. Sano and H. Wakita, "Precise measurement of helium-isotopes in terrestrial gases," *Bulletin of the Chemical Society of Japan*, vol. 61, no. 4, pp. 1153-1157, 1988.
- [52] F. Italiano, G. Martinelli, and P. M. Nuccio, "Anomalies of mantle-derived helium during the 1997-1998 seismic swarm of Umbria-Marche, Italy," *Geophysical Research Letters*, vol. 28, no. 5, pp. 839-842, 2001.
- [53] S. Giammanco, M. Palano, A. Scaltrito, L. Scarfi, and F. Sortino, "Possible role of fluid overpressure in the generation of earthquake swarms in active tectonic areas: the case of the Peloritani Mts. (Sicily, Italy)," *Journal of Volcanology and Geothermal Research*, vol. 178, no. 4, pp. 795-806, 2008.
- [54] F. Italiano, M. Martelli, G. Martinelli, and P. M. Nuccio, "Geochemical evidence of melt intrusions along lithospheric faults of the southern Apennines, Italy: geodynamic and seismogenic implications," *Journal of Geophysical Research: Solid Earth*, vol. 105, no. B6, pp. 13569-13578, 2000.
- [55] D. R. Hilton, K. Hammerschmidt, G. Looock, and H. Friedrichsen, "Helium and argon isotope systematics of the Central Lau Basin and Valu Fa Ridge - evidence of crust mantle interactions in a back-arc basin," *Geochimica et Cosmochimica Acta*, vol. 57, no. 12, pp. 2819-2841, 1993.
- [56] D. R. Hilton, K. Hammerschmidt, S. Teufel, and H. Friedrichsen, "Helium isotope characteristics of Andean geothermal fluids and lavas," *Earth and Planetary Science Letters*, vol. 120, no. 3-4, pp. 265-282, 1993.
- [57] K. A. Farley and E. Neroda, "Noble gases in the Earth's mantle," *Annual Review of Earth and Planetary Sciences*, vol. 26, no. 1, pp. 189-218, 1998.
- [58] M. Ozima and G. Igarashi, "The primordial noble gases in the Earth: a key constraint on Earth evolution models," *Earth and Planetary Science Letters*, vol. 176, no. 2, pp. 219-232, 2000.
- [59] T. J. Dunai and H. Baur, "Helium, neon, and argon systematics of the European subcontinental mantle - implications for its geochemical evolution," *Geochimica et Cosmochimica Acta*, vol. 59, no. 13, pp. 2767-2783, 1995.
- [60] F. Italiano, P. Bonfanti, L. Pizzino, and F. Quattrocchi, "Geochemistry of fluids discharged over the seismic area of

the southern Apennines (Calabria region, southern Italy): implications for fluid-fault relationships,” *Applied Geochemistry*, vol. 25, no. 4, pp. 540–554, 2010.

- [61] B. Marty and A. Jambon, “ C^3He in volatile fluxes from the solid earth: implications for carbon geodynamics,” *Earth and Planetary Science Letters*, vol. 83, no. 1-4, pp. 16–26, 1987.
- [62] R. K. O’Nions and E. R. Oxburgh, “Heat and helium in the earth,” *Nature*, vol. 306, no. 5942, pp. 429–431, 1983.
- [63] G. Barreca, V. Bruno, F. Cultrera, M. Mattia, C. Monaco, and L. Scarfi, “New insights in the geodynamics of the Lipari-Vulcano area (Aeolian archipelago, southern Italy) from geological, geodetic and seismological data,” *Journal of Geodynamics*, vol. 82, pp. 150–167, 2014.
- [64] C. Doglioni, F. Innocenti, and G. Mariotti, “Why Mt Etna?,” *Terra Nova*, vol. 13, no. 1, pp. 25–31, 2001.
- [65] F. Riguzzi, M. Crespi, R. Devoti, C. Doglioni, G. Pietrantonio, and A. R. Pisani, “Geodetic strain rate and earthquake size: new clues for seismic hazard studies,” *Physics of the Earth and Planetary Interiors*, vol. 206-207, pp. 67–75, 2012.
- [66] C. Doglioni, S. Barba, E. Carminati, and F. Riguzzi, “Fault on-off versus coseismic fluids reaction,” *Geoscience Frontiers*, vol. 5, no. 6, pp. 767–780, 2014.

Research Article

Degassing at the Volcanic/Geothermal System of Kos (Greece): Geochemical Characterization of the Released Gases and CO₂ Output Estimation

Kyriaki Daskalopoulou ^{1,2}, Antonina Lisa Gagliano ³, Sergio Calabrese ^{1,3},
Lorenza Li Vigni ³, Manfredi Longo ³, Konstantinos Kyriakopoulos,²
Giovannella Pecoraino ³ and Walter D'Alessandro ³

¹Università degli Studi di Palermo, Dipartimento di Scienze della Terra e del Mare, via Archirafi, 36, 90123 Palermo, Italy

²National and Kapodistrian University of Athens, Department of Geology and Geoenvironment, Panepistimioupolis, Ano Ilisia, 15784 Athens, Greece

³Istituto Nazionale di Geofisica e Vulcanologia, Sezione di Palermo, via Ugo la Malfa 153, 90146 Palermo, Italy

Correspondence should be addressed to Walter D'Alessandro; walter.dalessandro@ingv.it

Received 10 December 2018; Accepted 2 April 2019; Published 26 June 2019

Guest Editor: Andrzej Solecki

Copyright © 2019 Kyriaki Daskalopoulou et al. This is an open access article distributed under the Creative Commons Attribution License, which permits unrestricted use, distribution, and reproduction in any medium, provided the original work is properly cited.

Forty-five gas samples have been collected from natural gas manifestations at the island of Kos—the majority of which are found underwater along the southern coast of the island. On land, two anomalous degassing areas have been recognized. These areas are mainly characterized by the lack of vegetation and after long dry periods by the presence of sulfate salt efflorescence. Carbon dioxide is the prevailing gas species (ranging from 88 to 99%), while minor amounts of N₂ (up to 7.5%) and CH₄ (up to 2.1%) are also present. Significant contents of H₂ (up to 0.2%) and H₂S (up to 0.3%) are found in the on-land manifestations. Only one of the underwater manifestations is generally rich in N₂ (up to 98.9%) with CH₄ concentrations of up to 11.7% and occasionally extremely low CO₂ amounts (down to 0.09%). Isotope composition of He ranges from 0.85 to 6.71 R/R_A, indicating a sometimes-strong mantle contribution; the highest values measured are found in the two highly degassing areas of Paradise beach and Volcania. C-isotope composition of CO₂ ranges from -20.1 to 0.64‰ vs. V-PDB, with the majority of the values being concentrated at around -1‰ and therefore proposing a mixed mantle—limestone origin. Isotope composition of CH₄ ranges from -21.5 to +2.8‰ vs. V-PDB for C and from -143 to +36‰ vs. V-SMOW for H, pointing to a geothermal origin with sometimes-evident secondary oxidation processes. The dataset presented in this work consists of sites that were repeatedly sampled in the last few years, with some of which being also sampled just before and immediately after the magnitude 6.6 earthquake that occurred on the 20th of July 2017 about 15 km ENE of the island of Kos. Changes in the degassing areas along with significant variations in the geochemical parameters of the released gases were observed both before and after the seismic event; however, no coherent model explaining those changes was obtained. CO₂ flux measurements showed values of up to about 10₄ g × m⁻² × d⁻¹ in both the areas of Volcania and Kokkino Nero, 5 × 10⁴ g × m⁻² × d⁻¹ at Paradise beach, and 8 × 10⁵ g × m⁻² × d⁻¹ at Therma spring. CO₂ output estimations gave values of 24.6, 16.8, 12.7, and 20.6 t × d⁻¹, respectively, for the above four areas. The total output of the island is 74.7 t × d⁻¹ and is comparable to those of the other active volcanic/geothermal systems of Greece (Nisyros, Nea Kameni, Milos, Methana, and Sousaki).

1. Introduction

The southern Aegean Sea is one of the most tectonically active regions of western Eurasia, where fast convergence of

the Aegean microplate and the Eastern Mediterranean lithosphere (the front part of the African plate) occurs. The African plate subducts underneath the Aegean-Anatolian microplate at a rate of about 1 cm/a [1, 2], and the microplate

overrides the Eastern Mediterranean [3], resulting also in the generation of a volcanic arc [4]. The South Active Aegean Volcanic Arc (SAAVA) was built on Paleozoic-Mesozoic basement rocks (Alpine basement) that were deformed during the Tertiary by the Hellenide orogeny [5]. During the Lower Pliocene, the rate of convergence between the two continental margins increased and initiated the volcanism and the development of several hydrothermal systems at the SAAVA (e.g., [4, 6–10]).

Kos island is part of the Kos-Nisyros-Gyali volcanic system of the SAAVA, located at the SE edge of the Aegean Sea and formed at around 5 Ma, at the beginning of the Pliocene [1, 3, 11–13]. The geologic units of Kos consist of alluvial deposits with greenschists and flysch in the northern part of the island, lacustrine and terrestrial deposits of the Pliocene age in the central part with tuffs, and ignimbrites of the Quaternary age that cover the southern part of the island [14]. The most prominent volcanic formation on the island is the Kos Plateau Tuff (KPT). It is related to a caldera formed by an explosive eruption that occurred 161 ka ago, which is considered to be the largest explosive Quaternary eruption in the Eastern Mediterranean [15]. The tectonic evolution of the island is controlled by the dominant WNW-ESE and NE-SW faults, which are related to extensional processes and volcanic activity that took place during the Pleistocene and Pliocene [16, 17]. The volcanic island of Kos has been active for at least 3 million years [18] and continued to be active until recent times (e.g., [4, 6–10]). Some geothermal areas of particular interest have been identified in the island. The Volcania area is located 1 km northeast from the rim of Kefalos caldera [19]. It consists of a 1 km diameter basin with 14 small circular areas with evident signs of present and/or past hydrothermal alteration mainly arranged along two intersecting lineaments. These areas (5–20 m across) are devoid of vegetation and are usually covered by whitish altered deposits that contain sulfates and occasionally native sulfur [19]. Furthermore, hydrothermal activity is noticeable along the island with the most important sites being (i) the thermal spring of Therma, which is emerging on the beach close to Cape Fokas [20], (ii) the ferruginous spring of Kokkino Nero rich in CO_2 [21], and (iii) the intensively degassing area of Paradise beach at Kefalos Bay.

Geogenic carbon emissions have a critical impact on the carbon cycle [22, 23] and are regarded as one of the reasons of global climate changes on long time scales. Gas emissions from such sources strongly contribute to the increasing concentrations of greenhouse gases in the atmosphere, with methane and carbon dioxide playing a fundamental role [24, 25]. Moreover, earth degassing defines relations among flux, tectonic structures [26, 27], and volcanic activity [28, 29]. The aim of this study is to estimate the total CO_2 output of Kos island and to investigate the possible relation of these manifestations and anomalous areas with the geodynamically active area of Greece. This work presents new chemical and isotope data about the main gas manifestations of the island both on land and underwater. The collected data are interpreted together with literature data in order to determine the origin of the gases and the postgenetic processes that affect them. Finally, some considerations about possible

variations on gas geochemistry induced by the earthquake ($M_w = 6.6$) on the 20th of July 2017 with an epicenter close to the island are made.

2. Methods

Bubbling gases of Kos island were sampled using an inverted funnel positioned above the emission point of the highest flux, whereas soil gases were collected by inserting a pipe in the soil at >50 cm in depth and driving the gas by a syringe and a 3-way valve. Dry gases were collected in glass flasks equipped with two stopcocks.

In the laboratory, the concentrations of He , H_2 , H_2S , O_2 , N_2 , CO_2 , and CH_4 on the samples were analysed by an Agilent 7890B gas chromatograph combined with a Micro GC analyser by INFICON. A single amount of gas sample is simultaneously split into the loops of the two combined systems. Concentrations of CO_2 and H_2S have been determined by the Micro GC analyser with He as the carrier and equipped with a PoraPLOT U column and TCD detector while all the other gases had been determined by the GC system with Ar as the carrier and equipped with a 4 m Carbo-sieve S II column. A TCD detector was used to measure the concentrations of He , H_2 , O_2 , and N_2 and a FID detector for that of CH_4 . The analytical errors were less than 10% for He and less than 5% for the remaining gases.

The $^{13}\text{C}/^{12}\text{C}$ ratios of CO_2 (expressed as $\delta^{13}\text{C}\text{-CO}_2\text{‰}$ V-PDB) were measured with a Finnigan Delta S mass spectrometer after purification of the gas mixture by standard procedures using cryogenic traps (precision $\pm 1\sigma = 0.1\text{‰}$). Carbon and hydrogen isotopes of CH_4 were measured using a Thermo TRACE GC interfaced to a Delta Plus XP gas source mass spectrometer and equipped with a Thermo GC/C III (for carbon) and with GC/TC peripherals (for hydrogen). The $^{13}\text{C}/^{12}\text{C}$ ratios are reported as $\delta^{13}\text{C}\text{-CH}_4$ values with respect to the V-PDB standard ($\pm 1\sigma = 0.2\text{‰}$) while the $^2\text{H}/^1\text{H}$ ratios are reported as $\delta^2\text{H}\text{-CH}_4$ values with respect to the V-SMOW standard ($\pm 1\sigma = 2.0\text{‰}$).

The abundance and isotope composition of He , and the $^4\text{He}/^{20}\text{Ne}$ ratios, were determined by separately admitting He and Ne into a split flight tube mass spectrometer (Helix SFT). Helium isotope compositions are given as R/R_A , where R is the ($^3\text{He}/^4\text{He}$) ratio of the sample and R_A is the atmospheric ($^3\text{He}/^4\text{He}$) ratio ($R_A = 1.386 \times 10^{-6}$). The analytical errors were generally <1%. The $^4\text{He}/^{20}\text{Ne}$ ratio was used to correct the measured values for the atmospheric contamination, and the corrected values are indicated as R_C/R_A [30]. The analytical results of the collected samples as well as their coordinates are presented in Table 1.

Flux maps were drawn according to the dataset obtained from the three field campaigns that took place in the period from October 2015 to October 2017 (Table 2). Measurements were always made during dry and stable weather conditions. CO_2 flux was measured at Volcania, Kokkino Nero, Paradise beach, and Therma with the accumulation chamber method at more than 600 sites (>500 points per km^2) with portable soil fluxmeters (West Systems, Italy) based on the accumulation chamber method [31]. Flux values were determined at each site from the rate of CO_2 concentration increase in the

TABLE 1: Coordinates and analytical results of the collected gas samples.

No.	Sample	Sector	Coordinates E N	Date dd-mm-yy	He	H ₂	O ₂	N ₂ μmol/mol	CH ₄	CO ₂	H ₂ S	R/R _A	⁴ He/ ²⁰ Ne	δ ¹³ C-CO ₂ ‰ vs. V-PDB	δ ¹³ C-CH ₄ ‰ vs. V-PDB	δ ² H-CH ₄ ‰ vs. V-SMOW
1	Therma	35S	528211	4077679	<3	<2	1700	13100	70	958000	n.d.	n.d.	n.d.	n.d.	n.d.	n.d.
2	Therma	35S	528211	4077679	27	<2	660	44700	290	930000	n.d.	n.d.	n.d.	-3.35	2.8	n.d.
3	Therma	35S	528211	4077679	2.43	<2	1100	8900	50	995000	<5	1.04	2.92	-3.11	n.d.	n.d.
4	Therma	35S	528211	4077679	2.5	<2	530	9300	64	989000	<5	1.44	40.6	-3.46	2.4	36
5	Therma	35S	528211	4077679	7	1.6	1800	19100	110	982000	<5	1.39	23.0	-1.12	n.d.	n.d.
6	Therma	35S	528211	4077679	16	<2	2000	33100	210	949000	<5	1.49	30.5	-3.28	n.d.	n.d.
7	Therma	35S	528211	4077679	9.2	<2	1300	23800	160	958000	n.d.	1.45	55.7	-2.50	n.d.	n.d.
8	Therma Sea	35S	528211	4077679	16	<2	2500	42400	280	955000	<5	1.55	44.1	-3.04	n.d.	n.d.
9	Paradise	35S	500794	4068393	17	<2	3200	10800	11300	953000	n.d.	6.60	25.6	-1.06	n.d.	n.d.
10	Paradise	35S	500794	4068393	12	<2	790	3600	9300	966000	n.d.	6.59	43.9	-0.60	-19.8	n.d.
11	Paradise	35S	500794	4068393	14	2	190	4100	9700	986000	n.d.	6.66	27.8	-0.98	n.d.	n.d.
12	Paradise	35S	500794	4068393	28	<2	14700	34400	20900	900000	n.d.	6.67	34.1	-0.33	n.d.	n.d.
13	Paradise	35S	500794	4068393	12	<2	<100	3400	10000	968000	n.d.	6.70	112	-0.94	n.d.	n.d.
14	Paradise	35S	500794	4068393	23	<2	8400	19600	19200	937000	<5	6.55	49.0	-0.76	-19.5	n.d.
15	Paradise	35S	500794	4068393	14	<2	3100	8600	12100	959000	<5	6.49	223	-0.11	-19.5	-136
16	Paradise	35S	500794	4068393	12	<2	1700	5800	10000	980000	<5	6.27	270	-0.92	-20.1	-122
17	Paradise	35S	500794	4068393	17	<2	1800	8800	12100	972000	<5	n.d.	n.d.	-1.06	-20.0	-126
18	Paradise	35S	500794	4068393	16	<2	2200	7300	11000	977000	<5	n.d.	n.d.	-0.87	-20.6	-133
19	Paradise	35S	500794	4068393	12	<2	800	4100	9700	987000	<5	n.d.	n.d.	-1.82	n.d.	n.d.
20	Paradise	35S	500794	4068393	14	9	13300	46900	10800	915000	<5	6.71	90.7	-1.04	n.d.	n.d.
21	Paradise	35S	500794	4068393	21	2.2	6700	23200	15700	931000	<5	6.53	269	-0.67	-20.1	-124
22	Kokkino Nero	35S	521902	4078954	<3	<2	50	12300	520	966000	n.d.	n.d.	n.d.	-3.13	-21.5	n.d.
23	Kokkino Nero	35S	521902	4078954	5	3.1	3200	13600	3000	978000	<5	2.39	12.78	-1.94	-18.3	n.d.
24	Kokkino Nero	35S	522116	4078886	4.3	30	2700	8300	3100	991000	<5	n.d.	n.d.	n.d.	n.d.	n.d.
25	Kokkino Nero	35S	522116	4078886	5	<2	120	7200	3200	974000	36	n.d.	n.d.	-1.46	-19.5	-143
26	Kokkino Nero	35S	522116	4078886	6	<2	150	10500	3600	994000	<5	n.d.	n.d.	-1.43	-20.0	-104
27	Kokkino Nero	35S	522116	4078886	7	<2	1200	22600	3600	969000	<5	n.d.	n.d.	-1.70	n.d.	n.d.
28	Kokkino Nero	35S	522116	4078886	5	<2	1500	14500	3000	967800	<5	2.48	3.99	-1.48	-21.1	-92
29	Kokkino Nero	35S	521911	4075842	3.3	295	3500	24400	2400	980000	673	n.d.	n.d.	-0.97	-18.2	n.d.
30	Kokkino Nero	35S	521911	4075842	4	2.3	530	4000	2700	972000	2700	n.d.	n.d.	-2.09	n.d.	n.d.
31	Kefalos	35S	497339	4065831	24	15	3700	33000	25700	906000	<5	5.60	92.9	-0.59	-9.9	-71
32	Kefalos	35S	497339	4065831	18	27	3294	25100	23900	946000	<5	6.21	92.8	0.64	-12.2	-54
33	Kefalos	35S	497339	4065831	18	95	5800	35300	24200	902000	<5	6.01	192	-0.68	-12.4	-66
34	Agia Irini	35S	520916	4075676	0.94	<2	2600	6600	40	970000	15	0.85	5.86	-2.52	n.d.	n.d.
35	Agia Irini	35S	520916	4075676	0.34	<2	6219	14600	42	968000	<5	2.19	1.35	-2.24	n.d.	n.d.

TABLE 1: Continued.

No.	Sample	Sector	Coordinates E N	Date dd-mm-yy	He	H ₂	O ₂	N ₂ μmol/mol	CH ₄	CO ₂	H ₂ S	R/R _A	⁴ He/ ²⁰ Ne	δ ¹³ C-CO ₂ ‰ vs. V-PDB	δ ¹³ C-CH ₄ ‰ vs. V-SMOW	δ ² H-CH ₄ ‰ vs. V-SMOW
36	Agia Irini	35S	520916 4075676	16-10-17	0.90	<2	9500	26800	97	956000	<5	1.57	0.61	-2.11	n.d.	n.d.
37	Agia Irini spring	35S	520916 4075676	16-10-17	<3	<2	8900	36000	330	947000	<5	n.d.	n.d.	-3.21	n.d.	n.d.
38	Agia Irini 2	35S	521910 4075843	28-09-15	412	<2	2000	613000	117000	256000	<5	3.67	81.5	-0.82	-16.1	-75
39	Agia Irini 2	35S	521910 4075843	30-09-16	446	<2	2200	989000	6200	900	<5	3.88	48.2	-20.1	-12.4	-14
40	Agia Irini 2	35S	521910 4075843	16-10-17	220	<2	2600	343000	82900	548000	<5	3.62	66.2	-1.52	n.d.	n.d.
41	Volcania	35S	499783 4068858	27-09-15	36	65	810	30500	20600	926000	62	n.d.	n.d.	-0.43	-14.0	-115
42	Volcania	35S	499783 4068858	27-09-15	44	49	340	12400	23500	943000	1200	n.d.	n.d.	-0.55	-19.0	-132
43	Volcania	35S	499783 4068858	27-09-15	44	2.9	310	4000	23100	947000	851	6.71	1066	-0.50	-18.0	-128
44	Volcania	35S	499783 4068858	20-03-14	34	1980	10100	75400	21000	877000	54	n.d.	n.d.	0.25	n.d.	n.d.
45	Volcania	35S	499783 4068858	16-10-17	19	26	13000	74800	14500	882000	<5	5.73	8.94	-0.51	-14.1	-110

n.d.: not determined.

TABLE 2: Statistics on the populations identified in the CO₂ flux dataset.

Site	Pop.	Count	Min Log CO ₂ (g × m ⁻² × d ⁻¹)	Max	Mean	St. dev.
Volcania	A	19	-1.000	0.763	0.362	0.446
	B	405	0.778	3.332	2.147	0.641
	C	16	3.423	4.001	3.619	0.183
Kokkino Nero	A	22	-0.356	1.289	0.818	0.378
	B	95	1.378	3.464	2.572	0.594
	C	13	3.534	4.158	3.786	0.219
Therma	B	13	1.127	4.024	2.755	0.845
	C	17	4.042	5.953	4.793	0.603
Paradise	C	12	2.754	4.726	4.031	0.604

chamber and are expressed in grams per square meter per day ($\text{g} \times \text{m}^{-2} \times \text{d}^{-1}$) after conversion from volumetric to mass concentrations considering atmospheric pressure and temperature values. IR spectrometers with different measurement ranges ($0 - 20 \text{ mmol} \times \text{mol}^{-1}$ for the Licor LI820 and double range of $0 - 10 \text{ mmol} \times \text{mol}^{-1}$ and $0 - 1000 \text{ mmol} \times \text{mol}^{-1}$, respectively, for the Dräger Polytron) were used. This resulted in a measuring range of $10 - 20000 \text{ g} \times \text{m}^{-2} \times \text{d}^{-1}$ for the Licor LI820 spectrometer with accumulation chamber A and a range of up to $900000 \text{ g} \times \text{m}^{-2} \times \text{d}^{-1}$ for the Dräger Polytron spectrometer with accumulation chamber B and high measuring range—the reproducibility being always better than 20%. Chamber A has an area of 0.031 m^2 and a volume of 0.0028 m^3 , while chamber B has the same area and a volume of 0.0062 m^3 . Particular care was taken to follow the recommendations for flux measurements in volcanic/geothermal environments made by Lewicki et al. [32].

The soil temperature was measured only at few places and only in the last campaign by means of a digital thermocouple (error $\pm 0.3^\circ\text{C}$ in the range from -100 to 200°C).

The CO₂ datasets acquired from Volcania, Kokkino Nero, and Therma were used to estimate the total CO₂ flux from these areas.

To define the CO₂ threshold value, CO₂ flux data were processed following the Sinclair's portioning method extracting the main populations (Table 2; [33]). This method consists in the definition of single populations through the inflection points (main populations) or changes in direction (secondary populations) of the curvature on the probability plot by visual analysis.

Following the stochastic simulation approach, CO₂ flux maps were drawn. The data were converted by normal score transformation to follow a Gaussian distribution. The normal score transformed data was used to compute omnidirectional variograms and interpolated with the sequential Gaussian simulation (sGs) method by using the executable "sgsim" of GSLIB [34] and performing 100 equiprobable realizations for each area. The grid resolution was $5 \times 5 \text{ m}$. The final maps were produced averaging the results of the 100 realizations, using the E-type postprocessing method.

Zonal Statistics on the three CO₂ flux maps, performed by using the ArcMap 10.3 (ESRI) Spatial Analyst tool, was used to estimate the total CO₂ output considering only flux values above the background threshold value for each area.

3. Results

In the period from 2009 to 2017, 10 sampling campaigns took place in the island of Kos and 45 gas samples were collected. Twenty-three of them were collected underwater at various depths ($<10 \text{ m}$; Figure 1); five are soil gases whereas the remaining ones are gases bubbling in thermal waters. Literature data were also taken into consideration for comparison [14, 35, 36]. Names, sampling date, coordinates, chemical concentrations, and isotope values are presented on Table 1. Additionally, during the last three campaigns, more than 600 CO₂ flux measurements were performed covering part of the island (both on land and on the sea surface) including 4 intensively degassing areas: 135000 m^2 in Volcania (445 points), 250000 m^2 in Kokkino Nero (133 points), 1100 m^2 in Therma (29 points), and 600 m^2 in Paradise beach (12 points). Results of the flux measurements are presented in Table S1.

3.1. Gas Geochemistry. Gases collected from Kos island show that CO₂ is the prevailing gas species (generally more than $800000 \mu\text{mol} \times \text{mol}^{-1}$ and up to $995000 \mu\text{mol} \times \text{mol}^{-1}$; Figure 2). The majority of these samples display N₂/O₂ ratios higher than those of air and/or air-saturated water (ASW), indicating that the atmospheric component of meteoric water has been modified by redox reactions that took place either in the subsoil or in the aquifers. However, few samples present high concentrations of atmospheric gases (O₂ up to $99000 \mu\text{mol} \times \text{mol}^{-1}$ and N₂ up to $989000 \mu\text{mol} \times \text{mol}^{-1}$), pointing to a strong contamination by an atmospheric component (Figure 2(b)). Helium ranges from 0.34 to $511 \mu\text{mol} \times \text{mol}^{-1}$, while CH₄ ranges from 40 to $118000 \mu\text{mol} \times \text{mol}^{-1}$. Hydrogen and H₂S, typical hydrothermal gases, present significant concentrations (up to 1900 and $2700 \mu\text{mol} \times \text{mol}^{-1}$, respectively) in the soil gases, whereas in the underwater emissions, they are mostly below detection limits.

The isotope composition of He shows values from 0.85 to $6.71 R/R_A$ with the highest values being found in the Paradise beach samples. Regarding the $^4\text{He}/^{20}\text{Ne}$ ratio, values of up to 1066 are observed. Carbon isotope composition of CO₂ in the island is in the range of -20.07 to $+0.64\text{‰}$ vs. V-PDB, although almost all samples fall within a narrower range (-3.5 and 0‰). The isotope composition of CH₄ varies from -21.5 to -2.8‰ vs. V-PDB for C and from -143 to $+36\text{‰}$ vs. V-SMOW for H.

3.2. CO₂ Fluxes and Soil Temperatures. CO₂ flux measurements for the areas under investigation gave values that range from <0.1 to $898000 \text{ g} \times \text{m}^{-2} \times \text{d}^{-1}$. The highest values were measured in Paradise beach and Therma spring (median 9540 and 15100 ; maximum 23100 and $898000 \text{ g} \times \text{m}^{-2} \times \text{d}^{-1}$, respectively) with the use of the floating chamber method. The two soil degassing areas of Volcania and Kokkino Nero

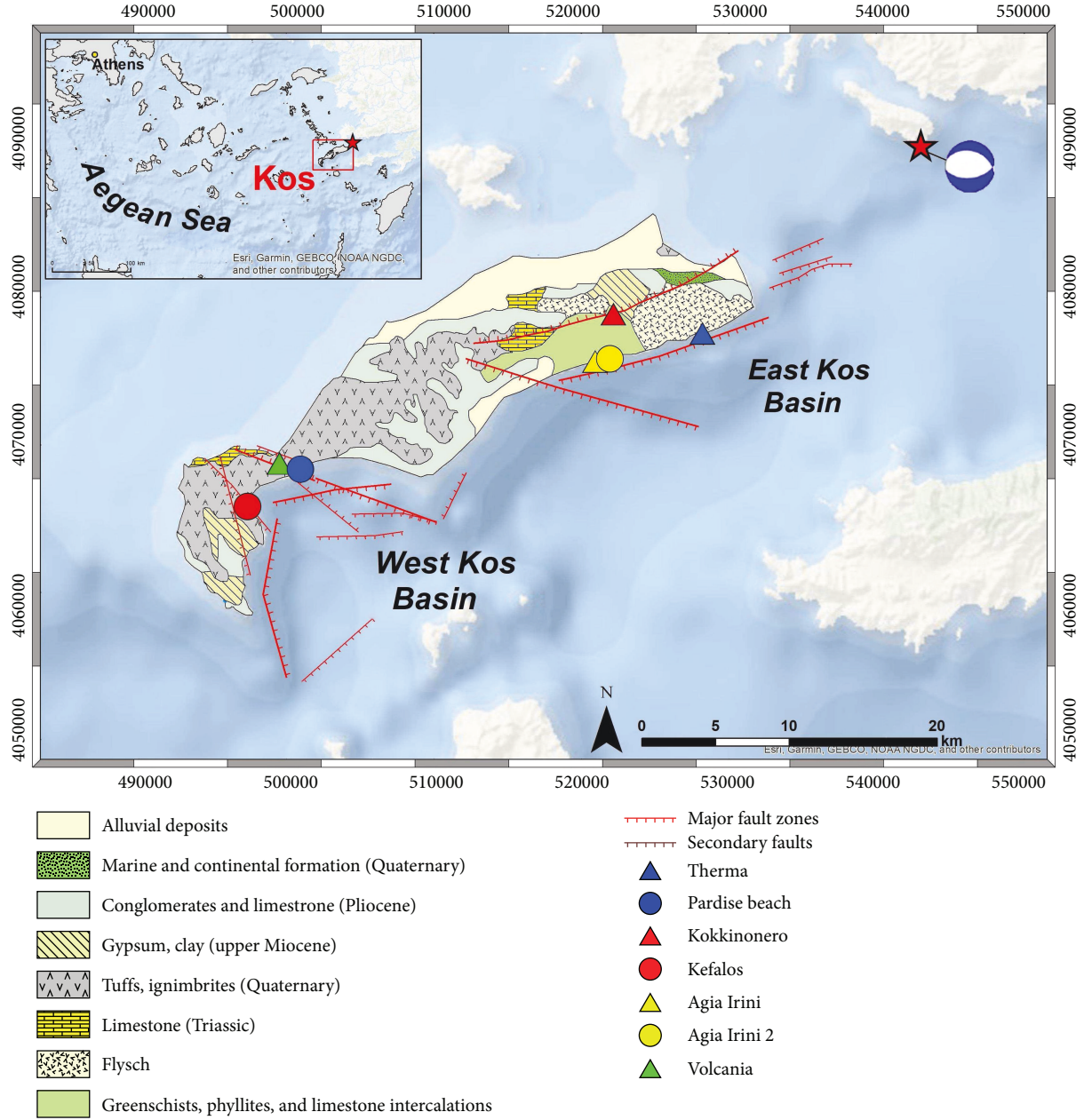


FIGURE 1: Simplified geological map of the island of Kos (modified after [14, 37]) with the geographical position of the gas sampling points. The earthquake epicenter ($M_w = 6.6$) on the 20th of July 2017 is indicated by a red star. Hypocentral depth (11 km) and focal mechanism are taken from [38].

showed the following median values: $169 \text{ g} \times \text{m}^{-2} \times \text{d}^{-1}$ and $345 \text{ g} \times \text{m}^{-2} \times \text{d}^{-1}$, respectively, whereas the maximum values were $10200 \text{ g} \times \text{m}^{-2} \times \text{d}^{-1}$ and $14400 \text{ g} \times \text{m}^{-2} \times \text{d}^{-1}$, respectively. Due to failure of the temperature probe, the temperature was not measured in the first campaign. Only few measurements were made in the second and third campaigns, and they were mainly concentrated in the highest CO_2 flux measuring points. These measurements were taken at 50 cm in depth and gave values that were approaching the annual mean atmospheric temperature (22°C) excluding significant water vapour upflow at both Volcania and Kokkino Nero.

The portioning method of Sinclair [33] was applied to extract data populations from the dataset. Three main populations, i.e., “background (A),” “intermediate (B),” and “hydrothermal (C)” (Table 2), were identified from the CO_2 flux datasets. The “background” population includes values from 0.1 to $5.8 \text{ g} \times \text{m}^{-2} \times \text{d}^{-1}$ at Volcania and values from 0.44 to $19 \text{ g} \times \text{m}^{-2} \times \text{d}^{-1}$ at Kokkino Nero; background population was not identified in the dataset acquired from Therma while at Paradise beach, only the “hydrothermal” population was present. The “intermediate” population includes values from ~ 6 to $2000 \text{ g} \times \text{m}^{-2} \times \text{d}^{-1}$ at Volcania, values from 23 to 2500

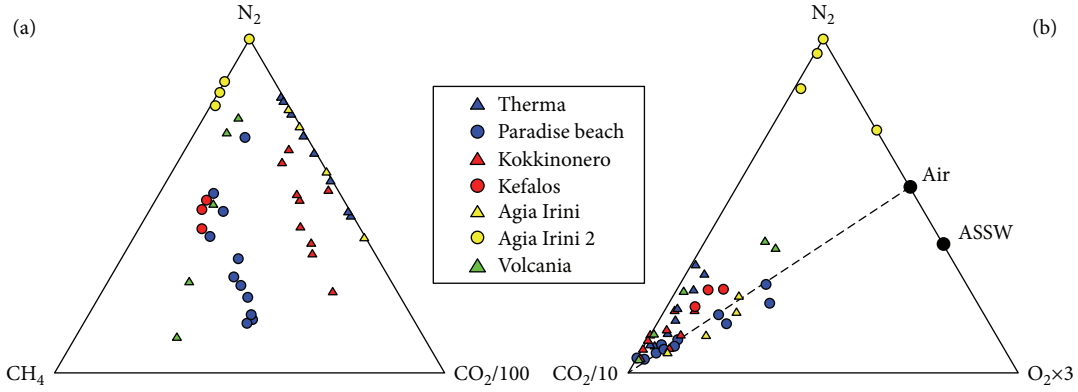


FIGURE 2: (a) $\text{CO}_2\text{-N}_2\text{-CH}_4$ and (b) $\text{CO}_2\text{-N}_2\text{-O}_2$ ternary diagrams. On diagram (b), the typical values of air and ASSW after [39] are also plotted.

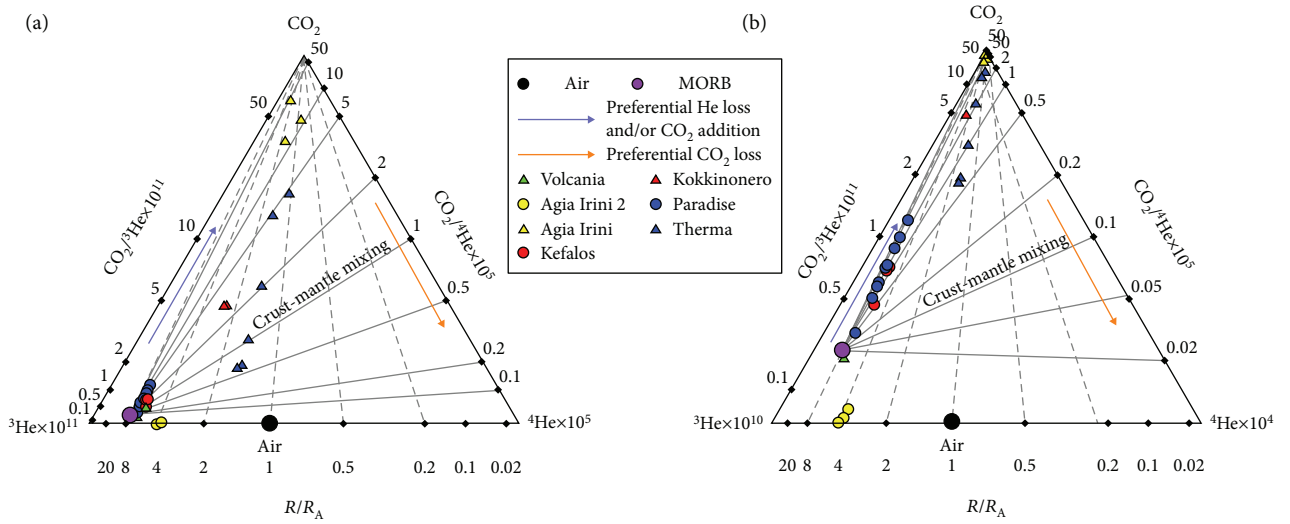


FIGURE 3: (a) $\text{CO}_2\text{-}^3\text{He-}^4\text{He}$ ternary diagram and (b) $\text{CO}_2\text{-}^3\text{He-}^4\text{He}$ ternary diagram with CO_2 multiplied 10 times. Lines represent mixing lines between mantle-derived and crustal volatiles. Dashed lines show the effects of shallow-level phase separation.

$\text{g} \times \text{m}^{-2} \times \text{d}^{-1}$ at Kokkino Nero, and values from 13 to $150 \text{ g} \times \text{m}^{-2} \times \text{d}^{-1}$ at Therma. The “hydrothermal” population includes values from 2500 to $\sim 15000 \text{ g} \times \text{m}^{-2} \times \text{d}^{-1}$ at Volcania and Kokkino Nero and values of up to 53100 and $898000 \text{ g} \times \text{m}^{-2} \times \text{d}^{-1}$ for Paradise beach and Therma, respectively.

Table 2 summarizes the number of points contributing to each population of the dataset and the statistical parameters.

According to the identification of background population from the probability plot, the threshold values used for estimation of the CO_2 flux from the Volcania area were $6 \text{ g} \times \text{m}^{-2} \times \text{d}^{-1}$ and $23 \text{ g} \times \text{m}^{-2} \times \text{d}^{-1}$ for Kokkino Nero, while no background value was used for Paradise beach and Therma.

4. Discussion

4.1. Origin of the Gases and Secondary Processes Affecting Their Composition. Carbon dioxide is the carrier phase for mantle-derived fluids. The combination of C and He isotope ratios is a useful tool to evaluate the origin of fluids. Helium

isotope ratios are used to distinguish between crustal and upper mantle-derived components. In order to identify general controls on the CO_2 characteristics of Kos island, we plotted the data on a $\text{CO}_2\text{-}^3\text{He-}^4\text{He}$ ternary diagram (Figure 3; [40]). The binary mixing trajectories between MORB-type mantle fluids ($R/R_A = 8$, $\text{CO}_2/^3\text{He} = 2 \times 10^9$) and various crustal volatile endmembers ($0.01 R_A$, $\text{CO}_2/^3\text{He} = 10^{10}\text{-}10^{15}$), as well as the general trends expected from addition and/or loss of a particular volatile phase, are also plotted in the diagram. Results propose a mantle origin for He that at points arrives close to the MORB endmember. Samples from Agia Irini and Therma represent products of variable amounts of mixing between mantle-derived and crustal volatiles with a preferential CO_2 addition and/or He loss. On the other hand, Agia Irini 2 is found on the base of the triangle with $\text{CO}_2/^3\text{He}$ ratios lower than those of the MORB, indicating CO_2 removal, possibly caused by the higher solubility of CO_2 with respect to He in aquatic environments (Figure 3(b)).

For the evaluation of the geologic processes' effects, the $\text{CO}_2\text{-He}$ data are plotted on the R/R_A vs. $^4\text{He}/^{20}\text{Ne}$ and

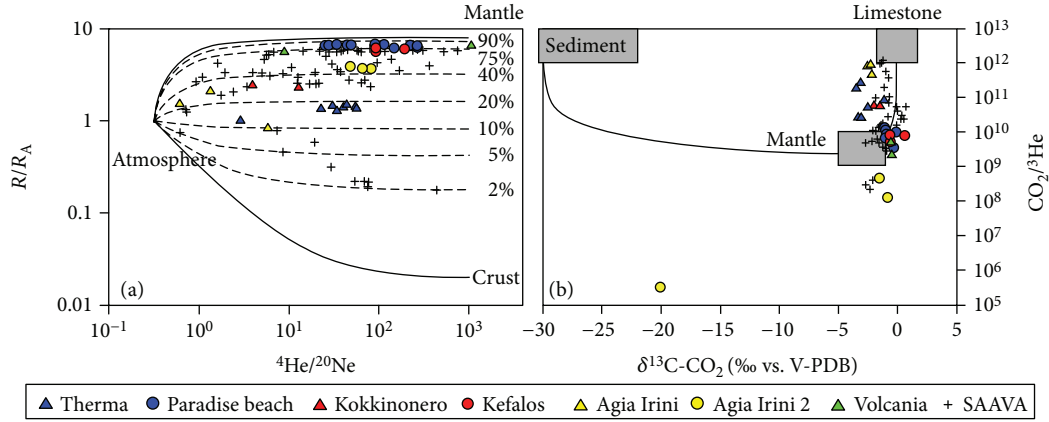


FIGURE 4: (a) Binary plot of R/R_A vs. $^4\text{He}/^{20}\text{Ne}$ of the Hellenic gas emissions. The mixing lines between the atmosphere and mantle and between the atmosphere and crust are also plotted. Dashed lines represent mixing between the atmosphere and endmembers, with different percentages of mantle contribution; (b) binary plot of $\text{CO}_2/{}^3\text{He}$ vs. $\delta^{13}\text{C}-\text{CO}_2$. The compositions for sediments, MORB-like mantle, and limestone endmembers are as follows: $\delta^{13}\text{C}-\text{CO}_2 = -30\text{‰}$, -5‰ , and 0‰ , respectively, and $\text{CO}_2/{}^3\text{He} = 1 \times 10^{13}$, 2×10^9 , and 1×10^{13} , respectively, [41]. SAAVA data from [14, 35, 36, 42–44].

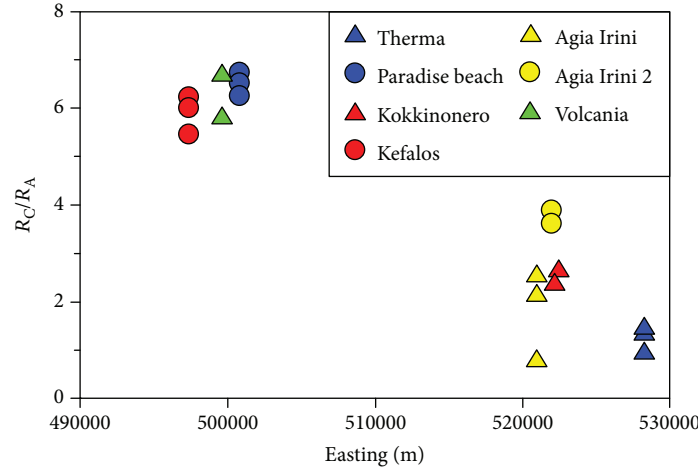


FIGURE 5: Geographical distribution of the R_C/R_A values of the gas samples collected on Kos island.

$\text{CO}_2/{}^3\text{He}$ vs. $\delta^{13}\text{C}-\text{CO}_2$ binary diagrams (Figure 4). In the aforementioned diagrams, the binary mixing curves that display the trends drawn by mixtures of the atmospheric component with different mantle and crustal sources [30], as well as the typical values of sediment, limestone, and mantle-derived CO_2 [41], are also plotted. Literature data of gas manifestations along the SAAVA [14, 35, 36, 42–44] are plotted for comparison.

Only few samples show an important atmospheric contribution for He, as they plot close to the atmospheric end-member (Figure 4(a)). Most of the samples display a mixed crustal-mantle contribution always within the range of the SAAVA samples (up to 85% of mantle contribution). In particular, samples from Therma, Kokkino Nero, and Agia Irini present medium to low mantle contributions for He (up to 35% considering a MORB-type source), whereas data of Paradise beach, Kefalos, and Volcania display a relatively higher range (75–80%) with respect to the aforementioned areas.

The distribution of the R_C/R_A values seems to follow a geographical distribution with the highest values collected

in the western part of the island, while the lower ones are concentrated in the eastern part (Figure 5). Many volcanic systems show an approximately regular radial distribution of the R/R_A values with the highest values being found close to the main volcanic or geothermal vents. Examples can be found at Nevado del Ruiz [45], Mt. Ontake [46], Lesser Antilles islands [47], Cascades [48], and Mt. Elbrus [49]. Such geographical pattern is generally explained with an increase in the contribution of both crustal (radiogenic) and atmospheric He components when the aquifer water reequilibrates with air, going from the main magmatic feeding system towards the peripheral areas [50]. However, in the present case, no active or recent volcanic conduit can be recognized on the island. Nevertheless, it is worth noting that the westernmost sampled gas manifestations are found along the supposed margin of the caldera that formed after the KPT explosive eruption. Along the margin of this structure, many other volcanic systems have been grown since that eruption (i.e., Nisyros, Strongyli, Pacheia, and Pergousa). It may be therefore hypothesized

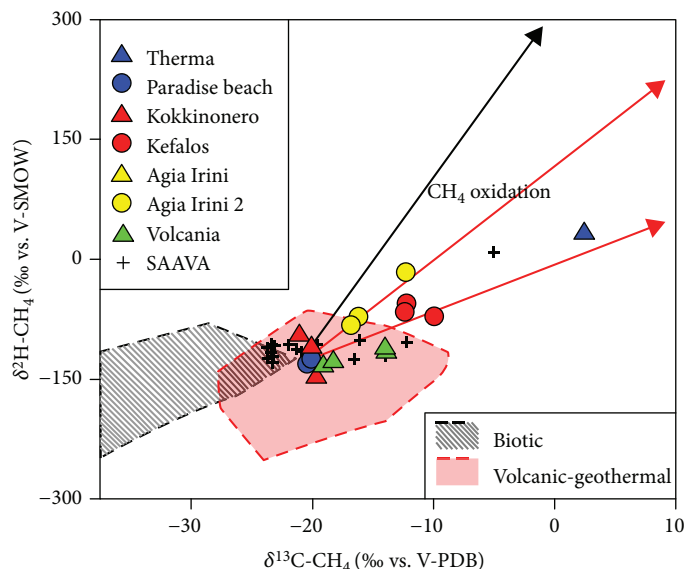


FIGURE 6: Modified Schoell binary diagram [65] of $\delta^2\text{H}-\text{CH}_4$ and $\delta^{13}\text{C}-\text{CH}_4$ ratios for the Hellenic gas discharges. Slopes of biogenic oxidation and abiogenic oxidation of CH_4 are plotted as red- and black-colored lines, respectively. SAAVA data from [43].

that the westernmost gas manifestations of Kos are connected to a deep mantle source by the presence of the ring faults of the caldera. At present, in the area, there is no surface sign of thermal anomalies that could point to the presence of a geothermal system possibly fed by an ascending magma batch. On the contrary, the easternmost sampling sites are found away from the caldera margins, mostly along the main tectonic structures, and are, at least in the case of Therma, related to thermal water circulation. Deep-rooted faults frequently constitute channels of high permeability that facilitate the migration of mantle fluids [51]. The strong difference in He isotope composition between the two groups of sampling sites may be explained also with the different geologic substrate of the two areas. In the western part of the island, young volcanic formations prevail, while in the eastern part, mostly older metamorphic rocks crop out. The latter could be the source of the crustal component that lowers the R/R_A values of the gases collected in the eastern part of Kos.

Moreover, gases collected in Kos along with those of SAAVA are found in the mixing line between mantle and limestone endmembers, while the contribution of the organic sediments is trivial (Figure 4(b)). Samples of Paradise beach, Volcania, and Kefalos are those with the highest mantle component showing $\text{CO}_2/{}^3\text{He}$ ratios similar to those of the MOR gases. Samples collected in Agia Irini 2 present $\text{CO}_2/{}^3\text{He}$ ratios lower than those of the MOR range indicating a relative CO_2 loss (Figures 3 and 4(b); [52–55]).

Hydrothermal hydrocarbon production can be described by two main mechanisms that deal with the biotic and abiotic origins of methane [56]. Considering this, the origin of CH_4 can be investigated using the classification diagram of Schoell [57, 58]. Thermogenic CH_4 has been reported to exhibit $\delta^{13}\text{C}-\text{CH}_4$ values that range from -50 to -30‰ and $\delta^2\text{H}-\text{CH}_4$ values ≤ 150 ‰ (e.g., [57–61]), whereas microbial CH_4 usually has $\delta^{13}\text{C}-\text{CH}_4$ values ≤ 50 ‰ (e.g., [60–62]).

Samples collected in Kos island as well as samples of the SAAVA [43] plot in the field of volcanic geothermal systems and thus, a geothermal origin is suggested for CH_4 (Figure 6). Exceptions are the samples collected at Kefalos, Agia Irini 2, and Therma, which sometimes present extremely (sample no. 2 of Therma) positive isotope values (for both C and H), pointing to CH_4 oxidation processes. Inorganic oxidation of CH_4 [63] in some samples cannot be ruled out. However, it is noticeable that the isotope fractionations of organic oxidation and inorganic oxidation of CH_4 follow different fractionation paths. The former follows $\Delta\text{H}/\Delta\text{C}$ slopes ranging from 5.9 to 13 ([64] and references therein) and the latter a slope of 21 [63]. Daskalopoulou et al. [43] considered $\delta^{13}\text{C} \approx -21$ ‰ and $\delta^2\text{H} \approx -130$ ‰ values that cluster the majority of the samples as the most probable values of the isotope composition of geothermal CH_4 in the Greek geothermal systems before oxidation. Based on that, the $\Delta\text{H}/\Delta\text{C}$ values, comprised between 3.8 and 13.6, are mostly overlapping the typical range of biogenic oxidation processes pointing towards the consumption by methanotrophic microorganisms. It is worth noting that the sites showing signs of methane oxidation are those presenting the lowest gas emission fluxes. The slower uprise of the gases allows a longer interaction with the methanotrophic microorganisms before bubble emission and therefore a higher consumption and a consequent fractionation of methane. This justifies the sometimes-strongly positive values that, considering the abovementioned starting $\delta^{13}\text{C}-\text{CH}_4$ value, indicate a residual fraction of CH_4 of about 0.4 [61].

4.2. Possible Influence of Seismic Activity on Fluid Geochemistry. Fluids play an important role in earthquake generation by reducing the friction between the fault blocks [66–68] and transporting upper mantle energy with geochemical anomalies that occur before, during, and after earthquakes [69]. Therefore, heat flow and tectonics are

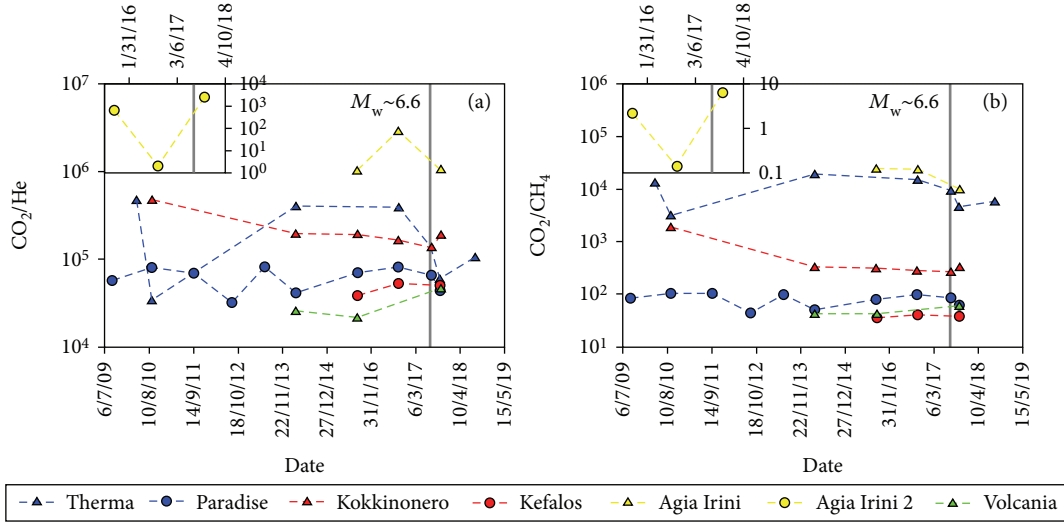


FIGURE 7: Time series plot of (a) CO_2/He ratios and (b) CO_2/CH_4 values between 2009 and 2018 in the island of Kos, with the data of Agia Irini 2 being plotted in the inset. The seismic event on the 20th July 2017 is noted with a gray line.

related to both active faults and geothermal anomalies, and for that reason, many earthquake epicenters occur worldwide in areas with elevated heat flow [66, 67]. Many researchers have studied the relations between seismicity and geochemistry and have noticed changes in the physicochemical parameters, the ground deformation, the gas flow rate, and the isotope composition of the gases (e.g., Kobe, Japan [70]; Kamchatka, Russia [71]; El Salvador, Central America [72]; Nisyros, Greece [73]; and Campi Flegrei, Italy [74]).

An earthquake of $M_w \sim 6.6$ occurred in the Gulf of Gökova between the areas of Bodrum and Kos on the 20th of July 2017. Heavy damages were noticed in both areas with the strongest intensities being recorded in the latter (United States Geological Survey (USGS)). Karasözen et al. [38] attributed this event to a normal fault gently dipping ($\sim 37^\circ$) northwards. This fault reached the sea bottom along a more than 10 km long E-W trending line generating tsunami waves that added further damages in Kara Ada island, Bodrum, and Kos island [75, 76].

Our campaigns included the systematic gas collection in the period from 2009 to 2018, thus including the seismic event. Three of the sampling sites were specifically resampled on the 26th of July 2017, 6 days after the main shock. In almost each area, results indicate a decrease in CO_2 and an increase in both He and CH_4 concentrations postseismically (Figure 7). This can be explained by a possible CO_2 loss and a consequent relative enrichment of He and CH_4 ; the difference in solubility may lead to extreme enrichments in the less soluble gases when a gas mixture rises through nonsaturated waters, especially when the gas/water ratio is very low [77]. This is probably the case of the gas collected 10 months before the seismic event at Agia Irini 2.

Furthermore, the collected gases evidenced variations in the R_C/R_A ratios (Figure 8). In particular, all sites but one (Paradise beach), where He isotopes were measured,

showed increased R_C/R_A ratios at about 10 months before the earthquake. On the contrary, Paradise beach shows at that time a relative minimum, which is subsequently increased to the highest measured value 6 days after the earthquake. Helium isotopes at Therma present a slightly lower value with respect to the previous and subsequent samples. It is worth mentioning that Therma is the site closest to the epicenter and also the second site presented in this work, where He isotopes were measured 6 days after the seismic event. All seven localities along the island present R_C/R_A ratios greater than those typical for crustal production ($R_C/R_A \approx 0.05$; [78]), revealing the presence of mantle-derived He throughout the fault zones (Table 1; Figures 3 and 4(a)). It is worth noting that all the sampling sites can be related to tectonic structures (Figure 1) that represent a preferential pathway for geogenic degassing. The strain induced by both the impending earthquake and the subsequent aftershock sequence may either induce variations in the permeability of these tectonic structures [79] or induce release of gases from magmatic or geothermal systems [36, 73].

The $\delta^{13}\text{C}-\text{CO}_2$ values (Figure 8(a)) show also important variations that may be attributed to different processes like

- degassing of CO_2 from the geothermal waters that results in both the decrease of the CO_2 contents in the geothermal water and the increase of the $\delta^{13}\text{C}$ values of the residual dissolved fraction
- addition/dissolution of CO_2 into groundwater, which leads to partial dissolution ($\text{CO}_{2(\text{aq})}$), hydration (HCO_3^-), and dissociation into HCO_3^- and then CO_3^{2-} . The fractionation factor between HCO_3^- and $\text{CO}_{2(\text{g})}$ (ϵ) is temperature dependent [80–82], and therefore, at temperatures encountered at the sampling localities ($<100^\circ\text{C}$), gaseous CO_2 progresses towards lower $\delta^{13}\text{C}$ values with increased dissolution (i.e., decreasing CO_2)

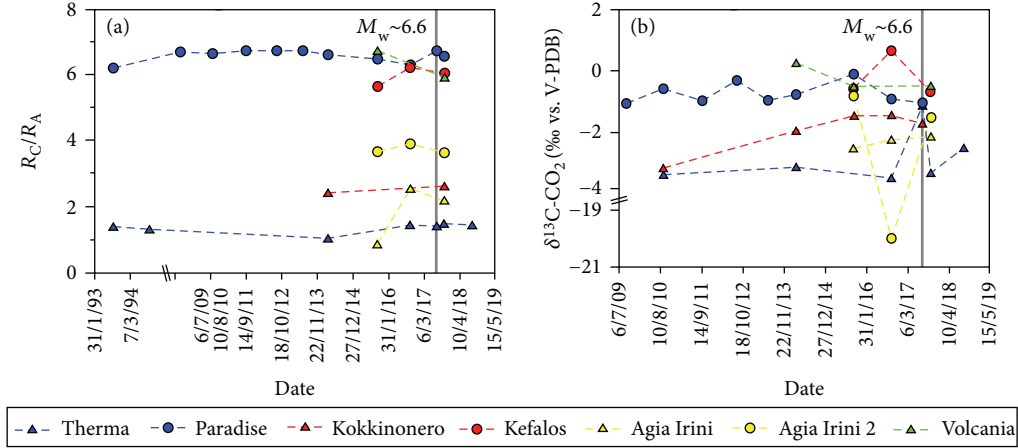


FIGURE 8: Time series plot of (a) R_C/R_A ratios and (b) $\delta^{13}\text{C-CO}_2$ values between 1993 and 2018 in the island of Kos. In order to eliminate the variable of the atmospheric contamination, the R_C/R_A values were used. The seismic event on the 20th July 2017 is noted with a gray line.

(c) dissolution/precipitation of the mineral calcite, where C isotope values become higher in the solid phase relative to the CO_2 in the geothermal water [83] and, consequently, also in this case, $\delta^{13}\text{C}$ values and CO_2 contents decrease in the residual gas phase

(d) mixing of gases with isotopically different CO_2

The variation of $\delta^{13}\text{C-CO}_2$ values in Figure 8(a) is significantly stronger than the variation of R_C/R_A values. A strong decrease in $\delta^{13}\text{C-CO}_2$ values is observed at Agia Irini 2, 10 months before the seismic event and, coherently with the variations in the chemical composition, may be attributed to CO_2 dissolution processes. A reduction in gas upflow rate induced by the impending earthquake can be the cause. Relatively lower $\delta^{13}\text{C-CO}_2$ values can be noticed also in the samples taken at Paradise beach just before and immediately after the earthquake. Conversely, at other sites, the $\delta^{13}\text{C}$ values are increasing either slightly and constantly like in the case of Agia Irini and Kokkino Nero or more spike like as seen at Kefalos (10 months before) and Therma (6 days after). None of these variations could be definitely linked to a particular process. Mixing of heavier carbon may derive from fracturing and dissolution of carbonate minerals of the limestones in the sedimentary series or marbles in the metamorphic sequence.

Along with the variations in the chemical and isotope compositions, changes in the degassing areas were also witnessed. In particular, in the submarine manifestations of Paradise beach, the degassing area became wider and a remarkable increase in the flux was observed. Raised water temperatures (at least at Therma) and gas fluxes were also recorded in the areas closer to the epicenter (Therma, Agia Irini, and Agia Irini 2). However, due to the lack of repeated flux measurements and the sometimes-incoherent temporal variations in chemical composition, R_C/R_A and $\delta^{13}\text{C-CO}_2$, no conclusions regarding the pre- and postseismic changes can be reached in the present work.

4.3. Total CO_2 Output Estimation. The CO_2 total output estimation is performed following a stochastic approach obtaining the most probable CO_2 output value for each of the three investigated areas (Volcania, Kokkino Nero, and Therma). Such data processing is used to produce the CO_2 distribution maps for the three areas (Figure 9).

Analysing the “background” populations extracted from the data, some differences between the datasets are noticed. The background threshold of Volcania is nearly one order of magnitude lower than that obtained from Kokkino Nero. This discrepancy can be referred to the soil assemblage. In fact, the soil at Volcania is more altered and less covered by vegetation even in the low-flux areas with respect to the soil at Kokkino Nero. The strong alteration of the soils in the Volcania area is probably due to past fumarolic activity [19]. The amount of CO_2 produced by the biomass at Volcania is lower than that produced at Kokkino Nero, and, consequently, the CO_2 threshold value is higher at Kokkino Nero.

The Therma dataset was mainly acquired along the shore with most of the data acquired on the water surface. The biomass producing CO_2 in this area was almost absent, and all the CO_2 upflow can be addressed to the hydrothermal component. The intermediate population in the Volcania and Kokkino Nero areas represents the mixing of the background component, the hydrothermal component (higher values), and/or the air mixing/dilution (lower values); the intermediate population obtained from the Therma dataset can be addressed to the hydrothermal component mixed with air. As in this site, the CO_2 flux is highly sustained reaching the extraordinary value of $898000 \text{ g} \times \text{m}^{-2} \times \text{d}^{-1}$ and the CO_2 upflow rate is so high to reduce and in some way prevent the air dilution. Almost all flux measurements included in the hydrothermal population were made with the floating chamber on the water of the artificial pool created for thermal bath purposes. On the contrary, almost all measurements referring to the intermediate population were made on the shores surrounding the pool. The shores are made of highly permeable coarse gravel favouring air circulation. This

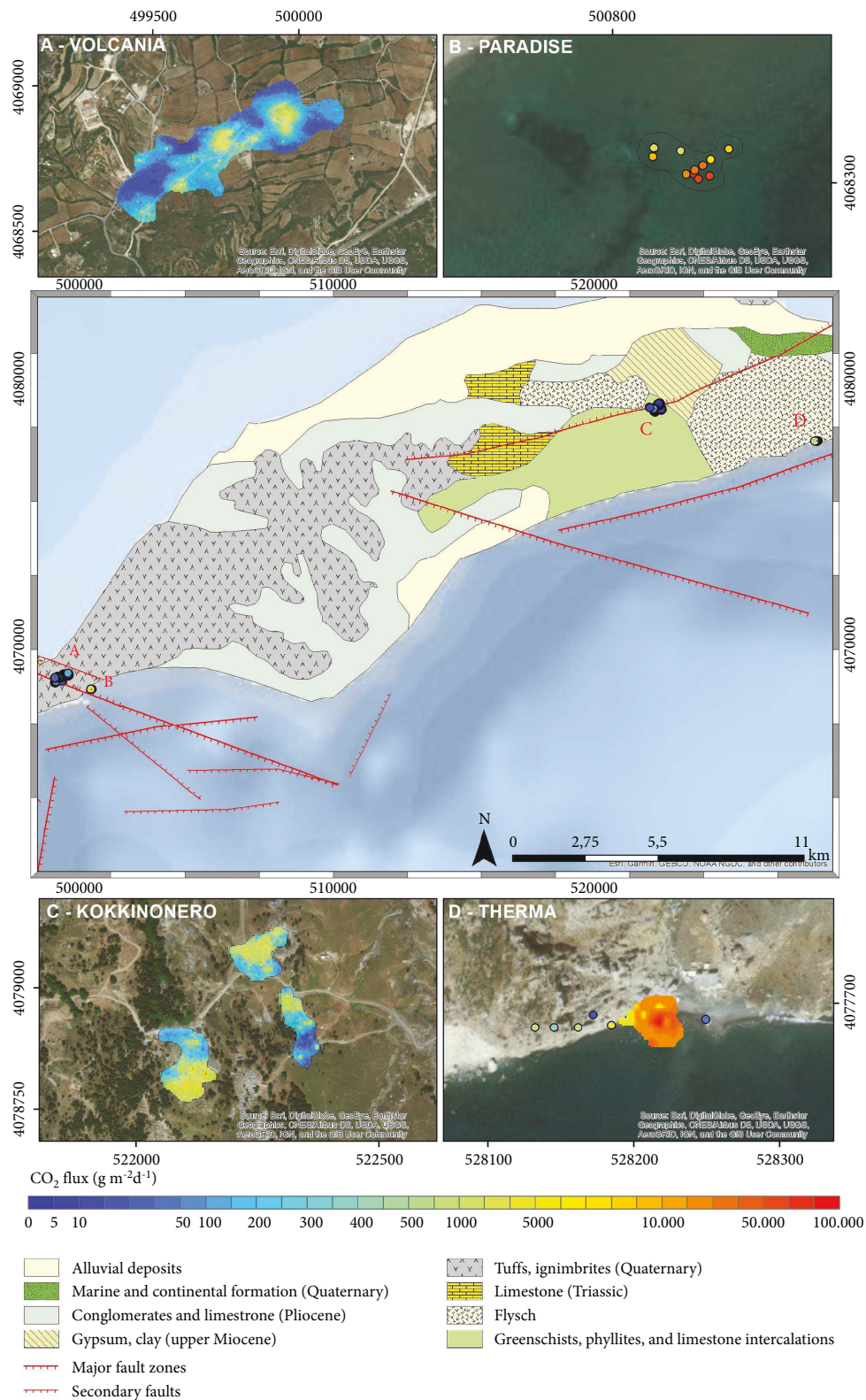


FIGURE 9: Distribution maps of soil CO₂ flux measurements at Kos. (c) The map of the central part of the island showing all measured points. (a, b, d, and e) Areas with more detailed sample density: Volcania (a), Paradise beach (b), Therma (d), and Kokkino Nero (e).

may explain also the low amount of data included in the intermediate population at Therma and its high upper limit ($3225 \text{ g} \times \text{m}^{-2} \times \text{d}^{-1}$).

The sGs produced an E-type map with the mean expected value for each cell. The total CO₂ output was obtained, for each area, summing all cell values above the threshold

TABLE 3: CO₂ output estimations.

Site	Area km ²	CO ₂ flux ^a t × d ⁻¹
Volcania	0.135	24.6
Kokkino Nero	0.250	16.8
Therma	0.0011	20.6
Paradise	0.0006	12.7

^aThe flux is calculated considering only values above the background threshold.

TABLE 4: CO₂ output from the volcanic/geothermal systems along the SAAVA.

Volcanic system	Reference	t × d ⁻¹
Sousaki	[86]	54
Methana	[87]	2.6
Milos	[44]	30.5
Nea Kameni	[31]	15
	[88]	38
Nisyros	[7]	67.8
	[89]	84
Kos	Present work	74.7

multiplied by the surface covered by each cell. The total CO₂ outputs estimated by sGs for Volcania, Kokkino Nero, and Therma are 24.6, 16.8, and 20.6 t × d⁻¹, respectively (Table 3). At Paradise beach, the number of flux measuring points was not enough to produce a map with the sGs method. Therefore, to estimate the CO₂ output of this area, we multiplied the output area by the average of the flux values obtaining a value of 12.7 t × d⁻¹. All the four investigated areas sum up an estimated total CO₂ flux for the island of Kos of about 74.7 t × d⁻¹. Such value falls within the range reported for the other volcanic/geothermal systems along the SAAVA (Table 4) where outputs as low as 2.6 (Methana) and up to 84 t × d⁻¹ (Nisyros) have been obtained. All these values fall at the lower end of the output estimations of volcanic systems worldwide [84, 85] and typical of quiescent volcanic systems.

5. Conclusions

Gas emissions are spread over the volcanic island of Kos and are expressed as hot springs, underwater bubbling, and sulfate salt efflorescence. Results have proposed a mixed mantle-limestone origin for CO₂, which is the prevailing gas species, whereas an up to 85% mantle contribution has been recognized for He. Gas components such as H₂, H₂S, and CH₄ have indicated a geothermal origin within a still not recognized reservoir beneath the island. Gas manifestations as well as anomalous degassing areas can be related to important tectonic structures. The active tectonics of the area often results in seismic activity with the recent earthquake (20th July 2017— $M_w \sim 6.6$) causing a tsunami phenomenon

and heavy damages on the island. Variations in both the chemical and isotope compositions and changes in the degassing areas and the physicochemical parameters of the systems have been observed. These have been possibly caused due to changes in mixing ratios of fluids of different origins and in the flux of uprising gases, although it has not been made possible to interpret all variations univocally.

The four main degassing areas (Volcania, Paradise beach, Kokkino Nero, and Therma) that have been recognized present sometimes very high flux values ($>10^5 \text{ g} \times \text{m}^{-2} \times \text{d}^{-1}$). The total CO₂ output for Kos has been estimated in 74.7 t × d⁻¹. This estimation has been in the range of values typical for the volcanic geothermal systems along the SAAVA and in the lower end of the worldwide volcanic output estimations

Data Availability

The data on gas geochemistry used to support the findings of this study are included within the article. The CO₂ flux data are included within the supplementary information file.

Conflicts of Interest

The authors declare that they have no conflicts of interest.

Acknowledgments

We kindly acknowledge the help of the Marine warrant officer Ilias Simadakis who gave us the permission to collect samples, the owner of “Kardamena Watersports Center” Mr. Nikos Nikolakopoulos who gave us one of his boats, and Mr. Yannis Limperis who accompanied us to the points of interest. CO₂ flux measurements would have not been possible without the friendly help of Salvatore Inguaggiato who gave us the device that he manages. All analyses were made at the laboratories of the INGV of Palermo, and we are grateful to all the following laboratories responsables and technicians: G. Capasso, F. Grassa, M. Martelli, Y. Oliveri, A. Rizzo, F. Salerno, A. Sollami, and M. Tantillo.

Supplementary Materials

MS Office Excel file “Table S1” containing the coordinates and the values of all the CO₂ flux measurements made on the island of Kos. (*Supplementary Materials*)

References

- [1] J. Jackson, “Rates of active deformation in the Eastern Mediterranean,” in *Recent Evolution and Seismicity of the Mediterranean Region*. NATO ASI Series (Series C: Mathematical and Physical Sciences), vol. 402, pp. 53–64, Springer, Dordrecht, 1993.
- [2] M. J. R. Wortel and W. Spakman, “Subduction and slab detachment in the Mediterranean-Carpathian region,” *Science*, vol. 290, no. 5498, pp. 1910–1917, 2000.
- [3] D. McKenzie, “Active tectonics of the Mediterranean region,” *Geophysical Journal International*, vol. 30, no. 2, pp. 109–185, 1972.


- [4] M. Fytikas, F. Innocenti, P. Manetti, A. Peccerillo, R. Mazzuoli, and L. Villari, "Tertiary to Quaternary evolution of volcanism in the Aegean region," *Geological Society London Special Publications*, vol. 17, no. 1, pp. 687–699, 1985.
- [5] G. Pe-Piper and D. J. W. Piper, *The Igneous Rocks of Greece*, Gebrüder Borntraeger, Berlin, 2002.
- [6] G. A. Papadopoulos, M. Sachpazi, G. Panopoulou, and G. Stavrakakis, "The volcanoseismic crisis of 1996–1997 in Nisyros, SE Aegean Sea, Greece," *Terra Nova*, vol. 10, no. 3, pp. 151–154, 1998.
- [7] S. Caliro, G. Chiodini, D. Galluzzo et al., "Recent activity of Nisyros volcano (Greece) inferred from structural, geochemical and seismological data," *Bulletin of Volcanology*, vol. 67, no. 4, pp. 358–369, 2005.
- [8] J. Gottsmann, H. Rymer, and L. K. Wooller, "On the interpretation of gravity variations in the presence of active hydrothermal systems: insights from the Nisyros caldera, Greece," *Geophysical Research Letters*, vol. 32, no. 23, 2005.
- [9] E. Lagios, V. Sakkas, I. Parcharidis, and V. Dietrich, "Ground deformation of Nisyros volcano (Greece) for the period 1995–2002: results from DInSAR and DGPS observations," *Bulletin of Volcanology*, vol. 68, no. 2, pp. 201–214, 2005.
- [10] G. Pe-Piper, D. J. W. Piper, and C. Perissoratis, "Neotectonics and the Kos Plateau Tuff eruption of 161 ka, South Aegean arc," *Journal of Volcanology and Geothermal Research*, vol. 139, no. 3–4, pp. 315–338, 2005.
- [11] X. Le Pichon and J. Angelier, "The Hellenic arc and trench system: a key to the neotectonic evolution of the Eastern Mediterranean area," *Tectonophysics*, vol. 60, no. 1–2, pp. 1–42, 1979.
- [12] D. J. Papanikolaou, "Geotectonic evolution of the Aegean," *Bulletin of Geological Society of Greece*, vol. 18, pp. 33–48, 1993.
- [13] J. Jackson, "Active tectonics of the Aegean region," *Annual Review of Earth and Planetary Sciences*, vol. 22, no. 1, pp. 239–271, 1994.
- [14] G. La Ruffa, C. Panichi, T. Kavouridis, V. Liberopoulou, J. Leontiadis, and A. Caprai, "Isotope and chemical assessment of geothermal potential of Kos island, Greece," *Geothermics*, vol. 28, no. 2, pp. 205–217, 1999.
- [15] D. J. W. Piper, G. Pe-Piper, and D. Lefort, "Precursory activity of the 161 ka Kos Plateau Tuff eruption, Aegean Sea (Greece)," *Bulletin of Volcanology*, vol. 72, no. 6, pp. 657–669, 2010.
- [16] E. Lagios, D. Galanopoulos, B. A. Hobbs, and G. J. K. Dawes, "Two-dimensional magnetotelluric modelling of the Kos island geothermal region (Greece)," *Tectonophysics*, vol. 287, no. 1–4, pp. 157–172, 1998.
- [17] D. J. Papanikolaou and E. Lekkas, *Miocene Tectonism in Kos, Dodecanese Islands*, IESCA Abstract, Izmir, 1990.
- [18] O. Bachmann, "The petrologic evolution and pre-eruptive conditions of the rhyolitic Kos Plateau Tuff (Aegean arc)," *Central European Journal of Geosciences*, vol. 2, no. 3, pp. 270–305, 2010.
- [19] J.-M. Bardintzeff, P. Dalabakis, H. Traineau, and R. Brousse, "Recent explosive volcanic episodes on the island of Kos (Greece): associated hydrothermal parageneses and geothermal area of Volcania," *Terra Research*, vol. 1, no. 1, pp. 75–78, 1988.
- [20] S. Varnavas, D. Panagiotaras, and P. Megalovasilis, "Chemical characteristics of a submarine hydrothermal system offshore Kos island, on the Hellenic volcanic arc," *Rapports et Procès Verbaux de la Commission Internationale Pour L'Exploration Scientifique de la mer Mediterranee*, vol. 35, no. 1, pp. 104–105, 1998.
- [21] V. Hatzivasileiou, *History of Island of Kos Ancient, Medieval and Modern*, Municipality of Kos, Kos Greece, 2013.
- [22] P. Delmelle and J. Stix, "Volcanic gases," in *Encyclopedia of Volcanoes*, pp. 877–896, Academic Press, 1999.
- [23] W. C. Evans, M. L. Sorey, B. M. Kennedy, D. A. Stonestrom, J. D. Rogie, and D. L. Shuster, "High CO₂ emissions through porous media: transport mechanisms and implications for flux measurement and fractionation," *Chemical Geology*, vol. 177, no. 1–2, pp. 15–29, 2001.
- [24] A. Mazzini, H. Svensen, S. Planke et al., "When mud volcanoes sleep: insight from seep geochemistry at the Dashgil mud volcano, Azerbaijan," *Marine and Petroleum Geology*, vol. 26, no. 9, pp. 1704–1715, 2009.
- [25] W.-L. Hong, G. Etiope, T. F. Yang, and P.-Y. Chang, "Methane flux from miniseepage in mud volcanoes of SW Taiwan: comparison with the data from Italy, Romania, and Azerbaijan," *Journal of Asian Earth Sciences*, vol. 65, pp. 3–12, 2013.
- [26] J. L. Lewicki and S. L. Brantley, "CO₂ degassing along the San Andreas Fault, Parkfield, California," *Geophysical Research Letters*, vol. 27, no. 1, pp. 5–8, 2000.
- [27] G. Yüce, C. C. Fu, W. D'Alessandro et al., "Geochemical characteristics of soil radon and carbon dioxide within the Dead Sea Fault and Karasu Fault in the Amik Basin (Hatay), Turkey," *Chemical Geology*, vol. 469, pp. 129–146, 2017.
- [28] D. Granieri, R. Avino, and G. Chiodini, "Carbon dioxide diffuse emission from the soil: ten years of observations at Vesuvio and Campi Flegrei (Pozzuoli), and linkages with volcanic activity," *Bulletin of Volcanology*, vol. 72, no. 1, pp. 103–118, 2010.
- [29] F. Viveiros, C. Cardellini, T. Ferreira, S. Caliro, G. Chiodini, and C. Silva, "Soil CO₂ emissions at Furnas volcano, São Miguel Island, Azores archipelago: volcano monitoring perspectives, geomorphologic studies, and land use planning application," *Journal of Geophysical Research*, vol. 115, no. B12, 2010.
- [30] Y. Sano and H. Wakita, "Geographical distribution of ³He/⁴He ratios in Japan: implications for arc tectonics and incipient magmatism," *Journal of Geophysical Research*, vol. 90, no. B10, pp. 8729–8741, 1985.
- [31] G. Chiodini, R. Cioni, M. Guidi, B. Raco, and L. Marini, "Soil CO₂ flux measurements in volcanic and geothermal areas," *Applied Geochemistry*, vol. 13, no. 5, pp. 543–552, 1998.
- [32] J. L. Lewicki, D. Bergfeld, C. Cardellini et al., "Comparative soil CO₂ flux measurements and geostatistical estimation methods on Masaya volcano, Nicaragua," *Bulletin of Volcanology*, vol. 68, no. 1, pp. 76–90, 2005.
- [33] A. J. Sinclair, "Selection of threshold values in geochemical data using probability graphs," *Journal of Geochemical Exploration*, vol. 3, no. 2, pp. 129–149, 1974.
- [34] C. V. Deutsch and A. G. Journel, *GSLIB: Geostatistical Software Library and User's Guide*, Oxford University Press, New York, NY, USA, 2nd edition, 1998.
- [35] A. Minissale, V. Duchi, N. Kolios, M. Nocenti, and C. Verrucchi, "Chemical patterns of thermal aquifers in the volcanic islands of the Aegean arc, Greece," *Geothermics*, vol. 26, no. 4, pp. 501–518, 1997.
- [36] A. Shimizu, H. Sumino, K. Nagao, K. Notsu, and P. Mitropoulos, "Variation in noble gas isotopic composition

- of gas samples from the Aegean arc, Greece,” *Journal of Volcanology and Geothermal Research*, vol. 140, no. 4, pp. 321–339, 2005.
- [37] P. Nomikou and D. Papanikolaou, “Extension of active fault zones on Nisyros volcano across the Yali-Nisyros Channel based on onshore and offshore data,” *Marine Geophysical Research*, vol. 32, no. 1-2, pp. 181–192, 2011.
- [38] E. Karasözen, E. Nissen, P. Büyükakpınar et al., “The 2017 July 20 Mw 6.6 Bodrum–Kos earthquake illuminates active faulting in the Gulf of Gökova, SW Turkey,” *Geophysical Journal International*, vol. 214, no. 1, pp. 185–199, 2018.
- [39] R. Kipfer, W. Aeschbach-Hertig, F. Peeters, and M. Stute, “Noble gases in lakes and ground waters,” *Reviews in Mineralogy and Geochemistry*, vol. 47, no. 1, pp. 615–700, 2002.
- [40] W. F. Giggenbach, Y. Sano, and H. Wakita, “Isotopic composition of helium and CO₂ and CH₄ contents in gases produced along the New Zealand part of a convergent plate boundary,” *Geochimica et Cosmochimica Acta*, vol. 57, no. 14, pp. 3427–3455, 1993.
- [41] Y. Sano and B. Marty, “Origin of carbon in fumarolic gas from island arcs,” *Chemical Geology*, vol. 119, no. 1-4, pp. 265–274, 1995.
- [42] A. L. Rizzo, A. Caracausi, V. Chavagnac et al., “Kolumbo submarine volcano (Greece): an active window into the Aegean subduction system,” *Scientific Reports*, vol. 6, no. 1, article 28013, 2016.
- [43] K. Daskalopoulou, S. Calabrese, F. Grassa et al., “Origin of methane and light hydrocarbons in natural fluid emissions: a key study from Greece,” *Chemical Geology*, vol. 479, pp. 286–301, 2018.
- [44] K. Daskalopoulou, A. L. Gagliano, S. Calabrese et al., “Gas geochemistry and CO₂ output estimation at the island of Milos, Greece,” *Journal of Volcanology and Geothermal Research*, vol. 365, pp. 13–22, 2018.
- [45] Y. Sano, H. Wakita, and S. N. Williams, “Helium isotope systematics at Nevado del Ruiz volcano, Colombia: implications for the volcanic hydrothermal system,” *Journal of Volcanology and Geothermal Research*, vol. 42, no. 1-2, pp. 41–52, 1990.
- [46] Y. Sano, Y. Nishio, S. Sasaki, T. Gamo, and K. Nagao, “Helium and carbon isotope systematics at Ontake volcano, Japan,” *Journal of Geophysical Research*, vol. 103, no. B10, pp. 23863–23873, 1998.
- [47] P. Jean-Baptiste, P. Allard, E. Fourré, F. Parello, and A. Aiuppa, “Helium isotope systematics of volcanic gases and thermal waters of Guadeloupe island, Lesser Antilles,” *Journal of Volcanology and Geothermal Research*, vol. 283, pp. 66–72, 2014.
- [48] M. O. Saar, M. C. Castro, C. M. Hall, M. Manga, and T. P. Rose, “Quantifying magmatic, crustal, and atmospheric helium contributions to volcanic aquifers using all stable noble gases: implications for magmatism and groundwater flow,” *Geochemistry, Geophysics, Geosystems*, vol. 6, no. 3, 2005.
- [49] B. G. Polyak, V. Y. Lavrushin, and I. L. Kamensky, “Mantle helium traces in the Elbrus–Kazbek sector of the Greater Caucasus and adjacent areas,” *Chemical Geology*, vol. 266, no. 1-2, pp. 57–66, 2009.
- [50] Y. Sano and T. P. Fischer, “The analysis and interpretation of noble gases in modern hydrothermal systems,” in *The Noble Gases as Geochemical Tracers*, pp. 249–317, Springer-Verlag, Berlin Heidelberg, 2013.
- [51] A. Paonita, M. Longo, S. Bellomo, W. D’Alessandro, and L. Brusca, “Dissolved inert gases (He, Ne and N₂) as markers of groundwater flow and degassing areas at Mt Etna volcano (Italy),” *Chemical Geology*, vol. 443, pp. 10–21, 2016.
- [52] C. J. Ballentine, R. Burgess, and B. Marty, “Tracing fluid origin, transport and interaction in the crust,” *Reviews in Mineralogy and Geochemistry*, vol. 47, no. 1, pp. 539–614, 2002.
- [53] C. J. Ballentine, M. Schoell, D. Coleman, and B. A. Cain, “300-Myr-old magmatic CO₂ in natural gas reservoirs of the West Texas Permian basin,” *Nature*, vol. 409, no. 6818, pp. 327–331, 2001.
- [54] B. Sherwood Lollar, C. J. Ballentine, and R. K. Onions, “The fate of mantle-derived carbon in a continental sedimentary basin: integration of C/He relationships and stable isotope signatures,” *Geochimica et Cosmochimica Acta*, vol. 61, no. 11, pp. 2295–2307, 1997.
- [55] B. Sherwood Lollar, R. K. O’Nions, and C. J. Ballentine, “Helium and neon isotope systematics in carbon dioxide-rich and hydrocarbon-rich gas reservoirs,” *Geochimica et Cosmochimica Acta*, vol. 58, no. 23, pp. 5279–5290, 1994.
- [56] Y. Taran and W. Giggenbach, “Geochemistry of light hydrocarbons in subduction-related volcanic and hydrothermal fluids,” *Society of Economic Geologists Special Publication*, vol. 10, no. 6, pp. 61–74, 2003.
- [57] M. Schoell, “The hydrogen and carbon isotopic composition of methane from natural gases of various origins,” *Geochimica et Cosmochimica Acta*, vol. 44, no. 5, pp. 649–661, 1980.
- [58] M. Schoell, “Multiple origins of methane in the Earth,” *Chemical Geology*, vol. 71, no. 1-3, pp. 1–10, 1988.
- [59] A. S. Bradley and R. E. Summons, “Multiple origins of methane at the Lost City hydrothermal field,” *Earth and Planetary Science Letters*, vol. 297, no. 1-2, pp. 34–41, 2010.
- [60] M. J. Whiticar, “Stable isotope geochemistry of coals, humic kerogens and related natural gases,” *International Journal of Coal Geology*, vol. 32, no. 1-4, pp. 191–215, 1996.
- [61] M. J. Whiticar, “Carbon and hydrogen isotope systematics of bacterial formation and oxidation of methane,” *Chemical Geology*, vol. 161, no. 1-3, pp. 291–314, 1999.
- [62] T. M. McCollom and J. S. Seewald, “Abiotic synthesis of organic compounds in deep-sea hydrothermal environments,” *Chemical Reviews*, vol. 107, no. 2, pp. 382–401, 2007.
- [63] Y. Kiyosu and S. Imaizumi, “Carbon and hydrogen isotope fractionation during oxidation of methane by metal oxides at temperatures from 400° to 530°C,” *Chemical Geology*, vol. 133, no. 1-4, pp. 279–287, 1996.
- [64] S. B. Cadieux, J. R. White, P. E. Sauer, Y. Peng, A. E. Goldman, and L. M. Pratt, “Large fractionations of C and H isotopes related to methane oxidation in Arctic lakes,” *Geochimica et Cosmochimica Acta*, vol. 187, pp. 141–155, 2016.
- [65] G. Etiope and M. Schoell, “Abiotic gas: atypical but not rare,” *Elements*, vol. 10, no. 4, pp. 291–296, 2014.
- [66] J. Du, W. Cheng, Y. Zhang et al., “Helium and carbon isotopic compositions of thermal springs in the earthquake zone of Sichuan, Southwestern China,” *Journal of Asian Earth Sciences*, vol. 26, no. 5, pp. 533–539, 2006.
- [67] J. Du, Y. Xu, and M. Sun, “³He/⁴He and heat flow in oil gas bearing basins, China’s mainland,” *Chinese Journal of Geophysics*, vol. 14, no. 2, pp. 239–247, 1998.
- [68] S. A. Miller, Y. Ben-Zion, and J. P. Burg, “A three-dimensional fluid-controlled earthquake model: behavior and

- implications," *Journal of Geophysical Research*, vol. 104, no. B5, pp. 10621–10638, 1999.
- [69] T. Rikitake, *Earthquake Forecasting and Warning*, Center for Academic Publications, Tokyo, 1982.
- [70] C. Y. King, N. Koizumi, and Y. Kitagawa, "Hydrogeochemical anomalies and the 1995 Kobe earthquake," *Science*, vol. 269, no. 5220, pp. 38–39, 1995.
- [71] S. P. Kingsley, P. F. Biagi, R. Piccolo et al., "Hydrogeochemical precursors of strong earthquakes: a realistic possibility in Kamchatka," *Physics and Chemistry of the Earth, Part C: Solar, Terrestrial & Planetary Science*, vol. 26, no. 10–12, pp. 769–774, 2001.
- [72] G. Chiodini, "CO₂/CH₄ ratio in fumaroles a powerful tool to detect magma degassing episodes at quiescent volcanoes," *Geophysical Research Letters*, vol. 36, no. 2, 2009.
- [73] J. M. L. Salazar, N. M. Pérez, P. A. Hernández et al., "Precursory diffuse carbon dioxide degassing signature related to a 5.1 magnitude earthquake in El Salvador, Central America," *Earth and Planetary Science Letters*, vol. 205, no. 1–2, pp. 81–89, 2002.
- [74] G. Chiodini, J. Selva, E. Del Pezzo et al., "Clues on the origin of post-2000 earthquakes at Campi Flegrei caldera (Italy)," *Scientific Reports*, vol. 7, no. 1, p. 4472, 2017.
- [75] M. Heidarzadeh, O. Necmioglu, T. Ishibe, and A. C. Yalciner, "Bodrum–Kos (Turkey–Greece) Mw 6.6 earthquake and tsunami of 20 July 2017: a test for the Mediterranean tsunami warning system," *Geoscience Letters*, vol. 4, no. 1, 2017.
- [76] A. Yalçiner, A. Annunziato, G. Papadopoulos et al., *The 20th July 2017 (22:31 UTC) Bodrum-Kos Earthquake and Tsunami: Post Tsunami Field Survey Report*, Technical Report Middle East Technical University, 2017.
- [77] W. D'Alessandro, L. Brusca, K. Kyriakopoulos, S. Bellomo, and S. Calabrese, "A geochemical traverse along the "Sperchios Basin — Evoikos Gulf" Graben (Central Greece): origin and evolution of the emitted fluids," *Marine and Petroleum Geology*, vol. 55, pp. 295–308, 2014.
- [78] J. N. Andrews, "The isotopic composition of radiogenic helium and Its use to study groundwater movement in confined aquifers," *Chemical Geology*, vol. 49, no. 1–3, pp. 339–351, 1985.
- [79] G. Chiodini, C. Cardellini, A. Amato et al., "Carbon dioxide Earth degassing and seismogenesis in central and southern Italy," *Geophysical Research Letters*, vol. 31, no. 7, 2004.
- [80] I. Wendt, "Fractionation of carbon isotopes and its temperature dependence in the system CO₂-gas-CO₂ in solution and HCO₃–CO₂ in solution," *Earth and Planetary Science Letters*, vol. 4, no. 1, pp. 64–68, 1968.
- [81] J. Zhang, P. D. Quay, and D. O. Wilbur, "Carbon isotope fractionation during gas–water exchange and dissolution of CO₂," *Geochimica et Cosmochimica Acta*, vol. 59, no. 1, pp. 107–114, 1995.
- [82] J. Szaran, "Achievement of carbon isotope equilibrium in the system HCO₃[−] (solution) - CO₂ (gas)," *Chemical Geology*, vol. 142, no. 1–2, pp. 79–86, 1997.
- [83] K. Emrich, D. H. Ehhalt, and J. C. Vogel, "Carbon isotope fractionation during the precipitation of calcium carbonate," *Earth and Planetary Science Letters*, vol. 8, no. 5, pp. 363–371, 1970.
- [84] G. Pecoraino, L. Brusca, W. D'Alessandro, S. Giammanco, S. Inguaggiato, and M. Longo, "Total CO₂ output from Ischia island volcano (Italy)," *Geochemical Journal*, vol. 39, no. 5, pp. 451–458, 2005.
- [85] S. Inguaggiato, A. Mazot, I. S. Diliberto et al., "Total CO₂ output from Vulcano island (Aeolian Islands, Italy)," *Geochemistry, Geophysics, Geosystems*, vol. 13, no. 2, 2012.
- [86] W. D'Alessandro, L. Brusca, K. Kyriakopoulos et al., "Diffuse and focused carbon dioxide and methane emissions from the Sousaki geothermal system, Greece," *Geophysical Research Letters*, vol. 33, no. 5, 2006.
- [87] W. D'Alessandro, L. Brusca, K. Kyriakopoulos, G. Michas, and G. Papadakis, "Methana, the westernmost active volcanic system of the South Aegean arc (Greece): insight from fluids geochemistry," *Journal of Volcanology and Geothermal Research*, vol. 178, no. 4, pp. 818–828, 2008.
- [88] M. M. Parks, S. Caliro, G. Chiodini et al., "Distinguishing contributions to diffuse CO₂ emissions in volcanic areas from magmatic degassing and thermal decarbonation using soil gas ²²²Rn–δ¹³C systematics: application to Santorini volcano, Greece," *Earth and Planetary Science Letters*, vol. 377–378, pp. 180–190, 2013.
- [89] C. Cardellini, G. Chiodini, and F. Frondini, "Application of stochastic simulation to CO₂ flux from soil: mapping and quantification of gas release," *Journal of Geophysical Research Atmospheres*, vol. 108, no. B9, article 2425, 2003.

Research Article

Heat and Helium-3 Fluxes from Teide Volcano, Canary Islands, Spain

Mar Alonso ^{1,2}, **Eleazar Padrón**^{1,2,3}, **Hirochika Sumino**⁴, **Pedro A. Hernández**^{1,2,3}, **Gladys V. Melián**^{1,2,3}, **María Asensio-Ramos**¹, **Fátima Rodríguez**¹, **Germán Padilla**^{1,2}, **Marta García-Merino**², **Cecilia Amonte**¹, and **Nemesio M. Pérez**^{1,2,3}

¹*Instituto Volcanológico de Canarias (INVOLCAN), 38320, San Cristóbal de La Laguna, Tenerife, Canary Islands, Spain*

²*Instituto Tecnológico y de Energías Renovables (ITER), 38600 Granadilla de Abona, Tenerife, Canary Islands, Spain*

³*Agencia Insular de la Energía de Tenerife (AIET), 38600 Granadilla de Abona, Tenerife, Canary Islands, Spain*

⁴*Department of Basic Science, Graduate School of Arts and Sciences, The University of Tokyo, 3-8-1 Komaba, Meguro-ku, Tokyo 153-0041, Japan*

Correspondence should be addressed to Mar Alonso; mar@iter.es

Received 11 February 2019; Revised 22 April 2019; Accepted 14 May 2019; Published 23 June 2019

Guest Editor: Guodong Zheng

Copyright © 2019 Mar Alonso et al. This is an open access article distributed under the Creative Commons Attribution License, which permits unrestricted use, distribution, and reproduction in any medium, provided the original work is properly cited.

During July 2016, the first integrated heat flow, CO₂, and ³He emission survey was conducted across 0.5 km² of the summit cone and crater of Teide volcano, Tenerife, Canary Islands, Spain. The thermal energy released from Teide summit cone by diffuse degassing was 2.2 MW, and the heat flux calculated through Dawson's method was 8.1 MW, difference due to the comparison of purely convective areas as the crater with diffusive areas as the flanks of the volcano. Diffuse CO₂ output was 211 ± 20 t d⁻¹, and ³He emission was estimated to be within a range between 0.35 and 0.89 mol y⁻¹. The obtained values of diffuse degassing and heat fluxes are close to others obtained for similar volcanic areas. The calculation of ³He/heat ratio for the first time in this volcanic system supports the presence of an important mantle source for the degassing of Teide volcano.

1. Introduction

The Earth's mantle is an important reservoir for compounds pertinent to surface and atmospheric processes such as water, carbon dioxide, sulphur, and noble gases. Advection of heat to the atmosphere via transportation of these gases remains an understudied phenomenon despite its potential importance [1, 2]. Volcanic activity represents focussed conduits for these fluxes and, as such, represents a key connection between the mantle and the atmosphere. Accurate measurements of both heat and gas flux from active volcanoes, and appraisal of their various sources, has contributed to a better understanding of the mantle-atmosphere link. In this study, we present the first data about the relationship between ³He and heat flux in the Teide volcanic system. This work is a new contribution to ³He global emission estimates.

Volcanoes emit large amounts of gases and volatiles to the atmosphere. These take the form of visible emanations

through volcanic plumes, fumaroles, and solfataras and through diffuse degassing (nonvisible emanations). Both types of gas emissions are controlled by local volcano-tectonic structures as a result of transport via diffusion and advection [3].

Among volcanic gases, helium has been considered as a useful tool in the geochemists' toolbox [4]. Helium is chemically inert, physically stable, nonbiogenic, sparingly soluble in water under ambient conditions, almost nonadsorbable, and, consequently, highly mobile. Due to these properties and its deep origin, helium is considered a tracer of magmatic activity and its speed of traversing the crust makes it an excellent precursor of volcanic eruptions [5–7].

There are two naturally occurring isotopes of helium: ⁴He and ³He, with an atmospheric ³He/⁴He ratio (R_A) of 1.384 · 10⁻⁶ [8]. ⁴He is produced mainly in the crust as α -particles from the radioactive decay of ²³⁸U, ²³⁵U, and ²³²Th, while nearly all of the ³He is primordial in origin and, by far, its

most important source is the Earth's interior. The $^3\text{He}/^4\text{He}$ ratio varies from high values ($>10^{-5}$) in mantle-derived lavas and fluids to low values ($\sim 10^{-8}$) in continental regions [9]. Helium production and the degree of tortuosity are the main parameters that control the uprising mantle-derived helium from the source to the atmosphere, showing a decreasing trend of the $^3\text{He}/^4\text{He}$ ratio with the distance in and around stratovolcanoes [6, 10]. However, in the case of Tenerife Island, Pérez et al. [11] demonstrated that the $^3\text{He}/^4\text{He}$ ratio remained constant regardless of the distance to Teide volcano.

In the case of the Canary Islands, the geographical distribution of the $^3\text{He}/^4\text{He}$ ratios shows the highest values on the westernmost islands (La Palma and El Hierro), which implies the existence of a helium source derived from the deep mantle [12–14]. Mass transfer of mantle helium to a fluid is accompanied by transfer of heat [15]. The presence of magmatic helium in a hydrothermal fluid therefore implies direct transport of heat from that magma to the fluid [15]. Previous studies have demonstrated a positive relation between helium isotopic composition and heat flux [16–18].

The calculated $^3\text{He}/\text{heat}$ production ratio in the upper mantle of the Earth is $\sim 0.5 \times 10^{-12} \text{ cm}^3 \text{ STP/J}$ [19] (where STP is $P = 1 \text{ atm}$ and $T = 25^\circ\text{C}$) and is spatially heterogeneous. For instance, the $^3\text{He}/\text{heat}$ production ratio associated with hot-spot volcanism is typically $\sim 24 \times 10^{-12} \text{ cm}^3 \text{ STP/J}$ [19, 20]. These values are much higher than that estimated for crustal regimes, $\sim 1 \times 10^{-15} \text{ cm}^3 \text{ STP/J}$, which are also dominated by radiogenic ^4He production [20]. Therefore, ^3He emission and heat flux studies at volcano-geothermal systems improve understanding not only of those systems but also the connection between mantle and atmosphere.

The measurement of the total thermal energy flux through the surface in volcanic areas is used to determinate changes in the magmatic activity and detecting changes in the energy balance of the volcanic system as a result of magmatic and tectonic processes [3, 21, 22].

The main objectives of this work are to compare ^3He emission estimated through different approaches, describe those estimates' relationship with heat flux, and calculate an indicative $^3\text{He}/\text{heat}$ production ratio at Teide volcano. It is important to highlight that it is the first study about the relationship between ^3He and heat flux in the Teide volcanic system. As such, this work is a new contributing value to ^3He global emission estimates.

2. Geological Setting

The Canarian archipelago is located in the Atlantic ocean about 100 km west of the African coast between $27^\circ 37'$ and $29^\circ 25' \text{N}$ and between $13^\circ 20'$ and $18^\circ 10' \text{W}$ (offshore Morocco). It consists of 7 main islands, decreasing ages from east to west, with the western islands still in the shield stage and the eastern-most in the erosional phase [23]. Their genesis continues to attract debate discussed below.

The most widely accepted “working” model is the one that combines three different hypotheses: hot spot, propagating fracture, and uplifted block hypothesis. It means that the

islands originate from a thermal anomaly in the mantle helped by regional fractures for the beginning of magmatism; meanwhile, the islands are in their present freeboard attitude due to the action of tectonic forces [24].

Tenerife ($2,034 \text{ km}^2$) (Figure 1), the central and largest island of the archipelago, is currently at the zenith of its volcanic development [23, 25]. The structure of Tenerife is controlled by a volcano-tectonic rift system with NW, NE, and NS directions. The oldest visible geological unit on Tenerife is called the “old basaltic series,” from central Miocene, and its forms by three strongly eroded edifices distributed in the corners of the island: Anaga (north-east), Teno (north-west), and Roque del Conde (south). This unit is formed by basaltic lavas and pyroclastics with some trachytes and phonolites [26]. A period of 2–3 M.y. of volcanic quiescence and erosion took place between “old basaltic series” and the eruptions which formed the younger volcanic series. Las Cañadas volcano grew on the eroded remains of the “old basaltic series” reaching about 40 km in diameter and 2,700–3,000 m of a complex succession of basalts, trachybasalts, trachytes, and phonolites that then collapsed 200 ky ago to form Las Cañadas caldera depression [23]. The caldera is located in the intersection of the three rifts, and the vertical collapse was associated with emptying of shallow magma chambers [27–29]. Other authors suggest the combination of vertical and lateral collapse for the formation of Las Cañadas caldera [30]. The youngest activity of the island is represented by basalts, trachytes, and phonolites of Teide-Pico Viejo volcanic complex and some individual basaltic cones scattered around the island, mainly located on the structural rift systems (NW, NE, and NS directions), characterized by the alignment of cinder cones and fissure systems, where historical eruptions occurred. Those monogenetic cones represent the most common eruptive activity during the last 1 M.y., and it is possible to easily recognize 297 of these cones in the island [31].

The 17 km long and 10 km wide caldera is the salient geomorphological feature of Tenerife partly because it hosts the highest stratovolcano in the Atlantic Ocean: Teide volcano (3,718 m.a.s.l.), a portion of Teide-Pico Viejo volcanic complex. Teide and Pico Viejo volcanoes overlap to form an elongate double cone. This volcanic complex was formed through different eruptive styles, ranging from strombolian to phreatomagmatic eruptions to cryptodome formation and dome extrusions [28, 32] forming basaltic, trachytic, and phonolitic products. The last eruption in this complex, Chahorra, occurred in 1798 through an adventive cone of Pico Viejo volcano.

Teide summit cone has been constructed during several phases. Its eruptive products are mainly phonolitic and basaltic-trachybasaltic lavas [32]. Persistent degassing activity has taken place at the summit of the volcano since the last eruption [33, 34].

Visible degassing in the summit cone of Teide volcano consists in low temperature fumaroles (around 83°C). Water is the major component of these fumaroles, followed by CO_2 , N_2 , H_2 , H_2S , Ar, CH_4 , and CO, a composition typical of hydrothermal fluids [34, 35]. Diffuse degassing is the principle degassing mechanism of Teide volcano, with the highest

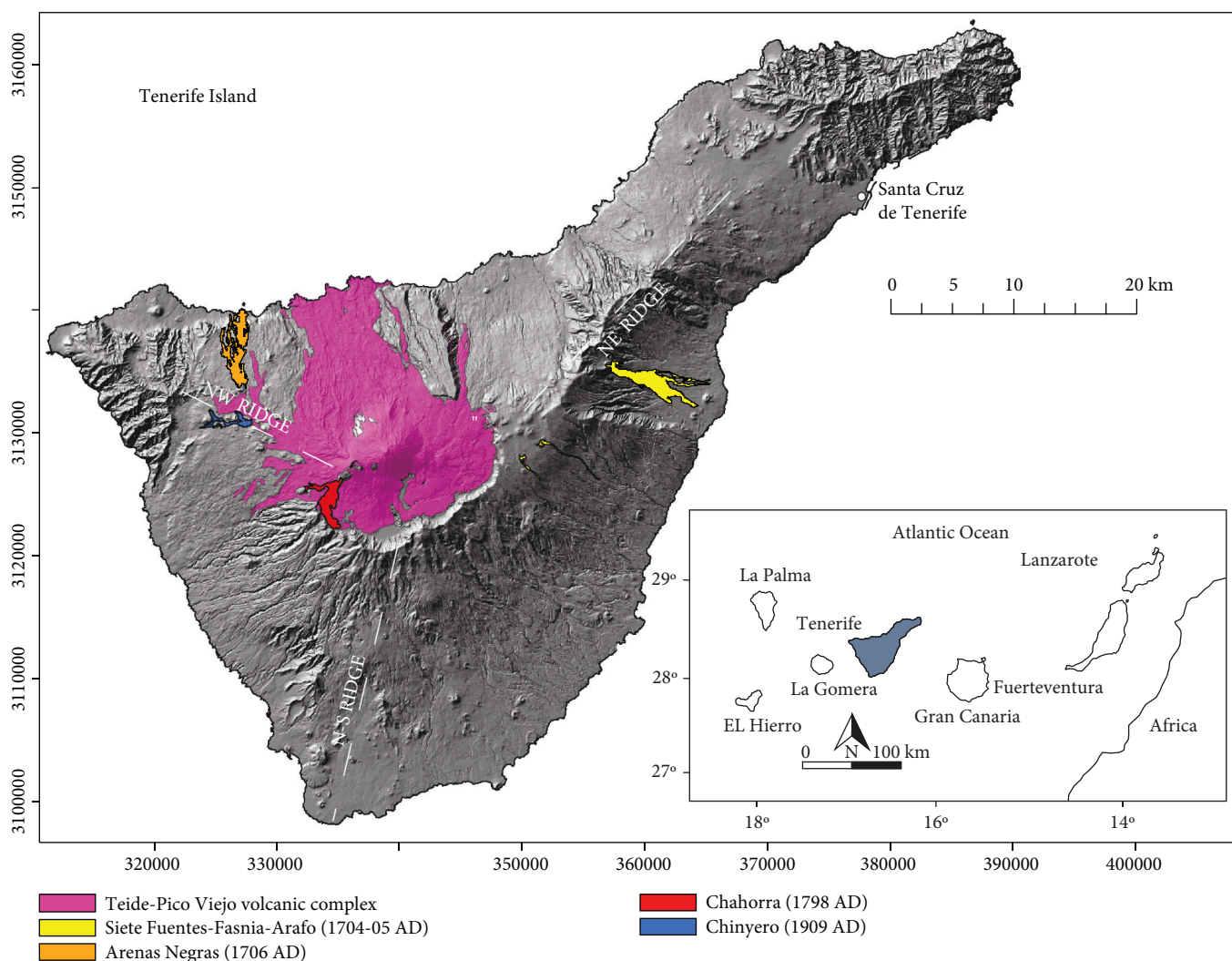


FIGURE 1: Tenerife Island marked with the location of the volcanic system studied, locations of historical eruptions and the three rifts. Inset: map of the Canarian archipelago highlighting Tenerife Island in grey.

rates emanated from the summit cone and crater of Teide volcano [36, 37].

3. Sampling Procedures, Analytical Methods, and Data Reduction

During July 2016, a soil gas survey comprised of 170 measurement sites was conducted at the summit cone of Teide volcano covering an area of 0.5 km^2 (Figure 2). The field work was carried out in the summer in order to minimize meteorological influences. The average distance between points of the summit cone was 45 meters on the slopes and 10 meters inside the crater, designed to tightly constrain the areal extent of visible degassing anomalies and arrive at more accurate overall estimates, while also achieving an evenly spaced distribution per domain.

3.1. Soil CO_2 Efflux and Temperature Measurements. Measurements of diffuse CO_2 were conducted at the soil surface using the accumulation chamber method [38] by means of West Systems portable CO_2 efflux meters equipped with a

nondispersive infrared CO_2 analyzer LICOR-820. This system is composed of a double beam infrared carbon dioxide sensor compensated for temperature and atmospheric pressure and an optical bench of 20,000 ppm of resolution. The gas flux meter was interfaced to a handheld computer running data acquisition software.

Soil temperature was determined by inserting a Type K thermocouple at each sampling site at 15 and 40 cm depth.

3.2. Soil Gas Sampling. At each measurement site, soil gas was collected in 20 cc glass vials. This was achieved by inserting a 50 cm stainless probe 40 cm depth into the ground connected to a hypodermic syringe. Residual gas inside the probe was purged before sampling.

Gaseous species as Ne , H_2 , O_2 , N_2 , CH_4 , CO_2 , and H_2O were analyzed by microchromatography with a VARIAN model 4900 (Agilent Technologies, USA), using a thermal conductivity detector and a 20 m PoraPLOT Q column using argon (Ar) as carrier gas. The temperature of the column and injector was 40°C and 80°C , respectively, and the injection time was 20 ms. The detection limit for CO_2 was

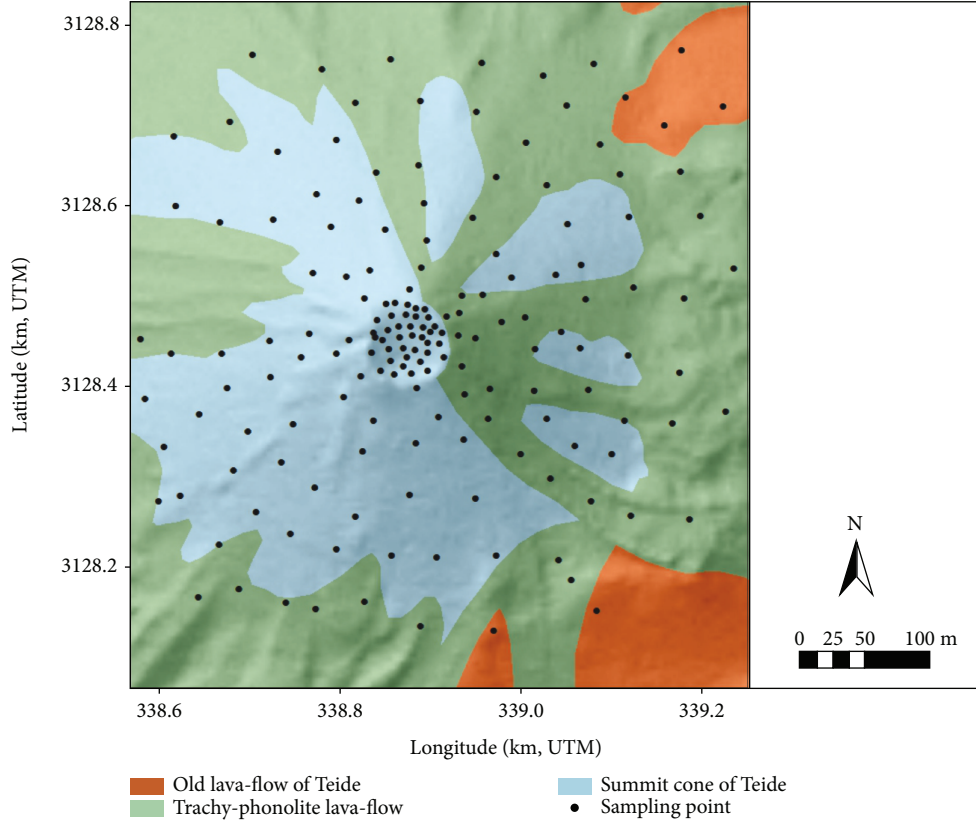


FIGURE 2: Geological map of Teide volcano summit cone and crater marked with the 170 measurement sites performed in the survey.

estimated to be about 10 ppmV, and the accuracy of the measurements was about 2.5% on the basis of standard sample measurements.

Helium was analyzed by a quadrupole mass spectrometer Pfeiffer Omnistar 422. The instrument accuracy of helium concentration was estimated to be ± 300 ppb, and the detection limit for helium is 1 ppm. Atmospheric gas was used periodically to calibrate the instrument.

The isotopic ratio expressed as $\delta^{13}\text{C}\text{-CO}_2\text{‰}$ vs. VPDB was measured by means of a Thermo Finnigan MAT 253 mass spectrometer. The analytical error for $\delta^{13}\text{C}$ values is of $\pm 0.1\text{‰}$.

3.3. Fumarole Sampling. Fumarolic gas samples were also collected in July 2016. Teide fumarolic activity consists of fluids discharged at approximately 83.5°C , close to the boiling point of water at 3,718 m.a.s.l. (87.5°C). A vent located inside the rim of the summit crater in the NE sector was the focus of the sampling effort.

A glass funnel was inserted into the vent and buried to prevent atmospheric air entering into the sampling system. The funnel was connected to a preevacuated glass flask filled with 50 ml of an alkaline solution (4N KOH). H_2O vapour condenses and acidic gases as CO_2 , SO_2 , and HCl dissolve into the alkaline solution, while noncondensable gases (N_2 , O_2 , He , H_2 , CH_4 , etc.) are concentrated in the gas phase of the sampling flask [35]. CO_2 concentration and $\text{CO}_2/\text{H}_2\text{O}$ molar ratio were analyzed by titration following the method described by Giggenbach and Goguel [39].

For the analysis of helium isotopes, lead-glass containers were filled with the fumarolic gas discharge. Helium concentration and $^3\text{He}/^4\text{He}$ isotopic ratios are expressed as $R_A = R/R_{\text{air}}$, where R is the measured $^3\text{He}/^4\text{He}$ ratio and R_{air} is that of the air; 1.384×10^{-6} [8] were analyzed using a high-precision noble gas mass spectrometer (modified-VG5400), following the procedure of Sumino et al. [40]. The correction factor for the helium isotope ratio was determined by measurements of interlaboratory helium standard named HESJ, with an established $^3\text{He}/^4\text{He}$ value of $20.63 \pm 0.10 R_A$ [41]. The analytical error for R_A was $< 2\%$. The measured $^3\text{He}/^4\text{He}$ ratios were corrected for air contamination based on the $^4\text{He}/^{20}\text{Ne}$ ratios measured with the mass spectrometer, assuming that all the neon has an atmospheric origin [16, 42].

3.4. Data Reduction and Spatial Interpolation

3.4.1. ^4He Flux Determination. The circulation of gases at superficial levels of volcanoes is governed by a combination of diffusive and advective mechanisms. Flows and velocities of gas moving by advective mechanisms, however, are much higher than those produced by diffusion. Diffusive and advective emission values were estimated at each sampling site as follows.

Diffusion is described by Fick's law:

$$F_i = -D_m \frac{dC}{dz}, \quad (1)$$

where D_m is the molecular diffusion coefficient ($\text{m}^2 \text{s}^{-1}$) and dC is the variation of gas concentration (kg m^{-3}) along dz (m).

The apparent diffusion coefficient (D) includes the effect of porosity (n) and tortuosity (τ) of the environment. For soils, Etiope and Martinelli [43] define this coefficient as

$$D = D_m n^2 = D_m \frac{n}{\tau}. \quad (2)$$

Advection is described by Darcy's law:

$$F_i = -C_i \frac{k \nabla P}{\mu Z}, \quad (3)$$

where C_i is the soil gas concentration (kg m^{-3}), k the permeability (m^2), μ the dynamic viscosity of the gas ($\text{kg m}^{-1} \text{s}^{-1}$), and ∇P the pressure difference ($\text{kg m}^{-1} \text{s}^{-2}$) between two points spaced at distance Z (m) [43].

Soil intrinsic permeability (k) is a key factor to estimate the theoretical emission of gases via Darcy's law. It depends on the hydraulic permeability (K_s) following Schaap and Lebron [44]:

$$k = \frac{\mu}{\rho g} K_s, \quad (4)$$

where μ is the gas viscosity ($\text{kg m}^{-1} \text{s}^{-1}$), ρ the gas density (kg m^{-3}), and g the gravitational constant (m s^{-2}).

In case of Teide volcano, pressure gradients are mostly generated by the geothermal gradient, which manifests by convection. We assume in this study, therefore, that the advective component of gas flux from the deep interior to the atmosphere is mainly governed by the efficiency of convection at the soil scale. Under this assumption, the pressure gradient is obtained from:

$$\nabla P = P_{\text{amb}} - P_{\text{soil}} = P_{\text{amb}} \left(1 - \frac{T_{\text{soil}}}{T_{\text{amb}}} \right), \quad (5)$$

where P_{soil} and P_{amb} are soil and ambient pressure and T_{soil} and T_{amb} are soil and ambient temperatures, respectively.

By combining equations (3), (4), and (5), we obtain the following expression for the convective flux:

$$F_i = -C_i \frac{K_s P_{\text{amb}}}{\rho g Z} \left(1 - \frac{T_{\text{soil}}}{T_{\text{amb}}} \right). \quad (6)$$

Direct measurements of diffuse CO_2 emission (F_{CO_2}), soil CO_2 concentration (C_{CO_2}), air temperature (T_{amb}), and soil temperature at 40 cm depth (T_{soil}) were used to estimate the hydraulic permeability (K_s) from equation (6) at each sampling site. These values were used later to estimate the convective flux of ^4He . To calculate the diffusive emission component for ^4He , we used a 7×10^{-5} as diffusion coefficient [43] and a value of 0.35 for porosity, as have been used in similar volcanic areas [45].

3.4.2. ^3He Flux Determinations. ^3He generally has low abundance, which leads to high analytical uncertainty for most gas samples. To arrive at an accurate estimate of flux across the study area, we must interpolate from ^3He measurements with high certainty using robust relationships with other gas fluxes. The ^3He output released to the atmosphere from the summit cone of Teide volcano can be estimated to be within the limits calculated by two end-member assumptions:

- (1) The $^3\text{He}/^4\text{He}$ ratio in the fumarolic gases (9.34×10^{-6}) is the same across the whole hydrothermal system, which is to assume the source of all helium is the same. In this case, ^3He emission (mol d^{-1}) is simply calculated using the $^3\text{He}/^4\text{He}$ ratio and the ^4He emission (mol d^{-1}) using the relationship:

$$\Phi_{^3\text{He}} = (^3\text{He}/^4\text{He}) \times \Phi_{^4\text{He}} \quad (7)$$

- (2) The ^3He flux is wholly derived from deep-seated source and therefore can be tied to the nonbiogenic component of the CO_2 flux. The estimated diffuse CO_2 emission, the $\text{CO}_2/^4\text{He}$ molar ratio, and the $^3\text{He}/^4\text{He}$ isotopic ratio measured in the fumarolic discharges of Teide can be used to estimate ^3He output using the relationships:

$$\begin{aligned} (\text{CO}_2/^4\text{He}) / (^3\text{He}/^4\text{He}) &= \text{CO}_2/^3\text{He}; \\ \Phi_{^3\text{He}} &= \Phi_{\text{CO}_2} / (\text{CO}_2/^3\text{He}) \end{aligned} \quad (8)$$

3.4.3. Heat Flow. CO_2 was used as a tracer of hydrothermal fluids to calculate the heat flow involved in the diffuse degassing process. Chiodini et al. [46] first demonstrated this method that rests on the assumption that the $\text{H}_2\text{O}/\text{CO}_2$ ratio is recorded, before steam condensation, by fumarolic effluents. These authors computed the heat flux adding the following contributions: (1) the heat released by H_2O gas moving from the hydrothermal reservoir to the steam condensation zone, (2) the heat given off by CO_2 passing from the hydrothermal reservoir to atmospheric conditions, (3) the enthalpy of steam condensation at 100°C , and (4) the heat loss by liquid water on cooling from 100°C to the average seasonal value.

In the July 2016 survey, the measured $\text{H}_2\text{O}/\text{CO}_2$ ratio was 2.24. On the basis of this ratio, we computed that 473 t d^{-1} of steam are condensed to produce the hydrothermal CO_2 output of 211 t d^{-1} following the procedure described by Frondini et al. [47]. The released thermal energy associated with the condensation of 473 t d^{-1} of steam was estimated on $1.26 \times 10^{12} \text{ J d}^{-1}$.

This value was obtained following two contributions. The enthalpy of steam condensation at 100°C ($1.07 \times 10^{12} \text{ J d}^{-1}$) is given by the product of the total amount of steam condensed in one day ($4.73 \times 10^8 \text{ g}$) times the enthalpy of evaporation at 100°C ($2,257 \text{ J g}^{-1}$) [48]. The heat loss by liquid water on cooling from 100°C to the average seasonal value of 3.2°C ($1.89 \times 10^{11} \text{ J d}^{-1}$) is given by the product of the enthalpy lost

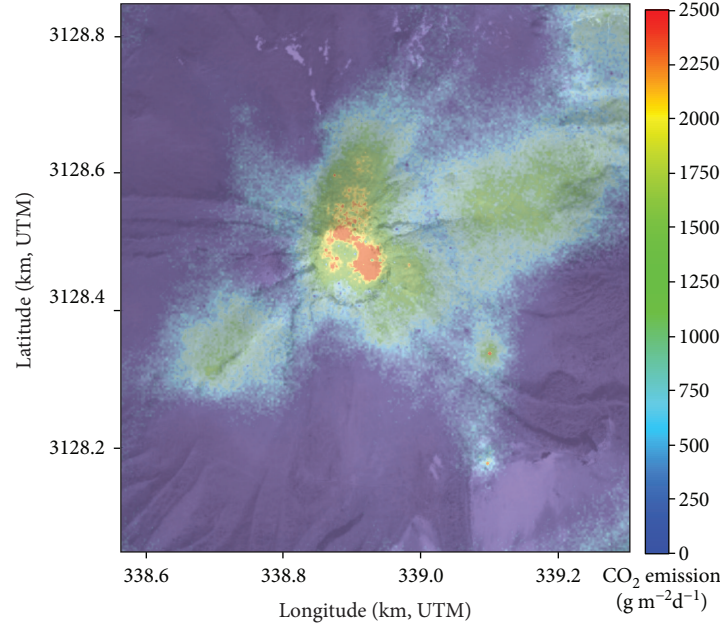


FIGURE 3: Diffuse CO₂ emission map of the summit cone and crater of Teide volcano.

by 1 g of water ($\Delta H = 398.7 \text{ J g}^{-1}$) times the mass of water ($4.73 \times 10^8 \text{ g}$).

The heat flux was also calculated following the method described by Dawson [49]. The method is based on correlation between soil temperature at 15 cm depth (t_{15}) and surface heat flux (q) by the following equation:

$$q = 5.2 \times 10^{-6} t_{15}^4, \quad (9)$$

where t_{15} was measured by a portable calorimeter at each point.

Sequential Gaussian simulation (sGs) using the sGsim program [50] was used to construct spatial distribution maps of CO₂, ⁴He, and heat fluxes. The sGs procedure allowed us to interpolate the different parameters at a nonsampled area between the sampling points and obtain the uncertainty of emissions. Emission of the entire area of study was estimated using these maps.

4. Results and Discussion

4.1. CO₂ Fluxes and Isotopic Signatures. Diffuse CO₂ efflux values ranged from below detection to $10,650 \text{ g m}^{-2} \text{ d}^{-1}$ with an average value of $879 \text{ g m}^{-2} \text{ d}^{-1}$. The spatially interpolated total diffuse CO₂ output released from the summit cone of Teide volcano was calculated as $211 \pm 20 \text{ t d}^{-1}$. Similar results were obtained by Pérez et al. [37]; an emission value of 180 ± 21 was calculated for the 2009 survey for an area of 0.11 km^2 .

The diffuse CO₂ emission map (Figure 3) shows higher values located inside the crater, along the crater rim mainly close to the fumarolic area and towards the north and north-east flanks. The areas with higher CO₂ efflux values also show relatively high temperatures and appear correlated to hydrothermal alteration at the surface, suggesting a mainly

advective degasification mechanism governing the gas emission regime at the study area. The north and north-east anomalies are probably related to radial fissures propagated from the volcanic axis [37]. Lower values are observed at other sectors of the flanks of the cone.

The total diffuse CO₂ output is comparable with the $219 \pm 36 \text{ t d}^{-1}$ released by Pico do Fogo volcano, Cape Verde, a similar volcanic system in a similar volcano-tectonic environment, measured during a survey in February 2010 [21].

Figure 4 summarizes the CO₂ isotopic composition and indicates that most of the analyzed samples correspond to a deep-seated source of CO₂, with different degrees of atmospheric contributions. The heaviest $\delta^{13}\text{C}(\text{CO}_2)$ values, indicative of deep-seated CO₂, were measured in soil gases in and around the summit crater, where fumarolic activity and thermal anomalies occur. The contribution of biogenic CO₂ can be considered negligible, which is consistent with the very limited vegetation and its related biological activity in the summit cone of Teide volcano.

4.2. ⁴He Emission. The total output of ⁴He from the studied area was estimated in $1.06 \pm 0.2 \text{ kg d}^{-1}$ ($265.15 \text{ mol d}^{-1}$) with the highest values observed where fumarolic activity is present, along the crater rim, and towards the north and north-east flanks, coinciding with the highest temperature and CO₂ efflux values measured (Figure 5). The average value of the convective component exceeded the average value of the diffusive component by almost an order of magnitude (4.2 vs. $0.44 \text{ mg m}^{-2} \text{ d}^{-1}$, respectively). For this reason, we can assume that most of the diffuse gas emission from the summit cone of Teide volcano is governed by convection.

Similar studies carried out in other volcanic systems of the Canary Islands have taken into account only the diffusive component due to the lack of geothermal anomalies in the surface environment of the study areas. Padrón et al.

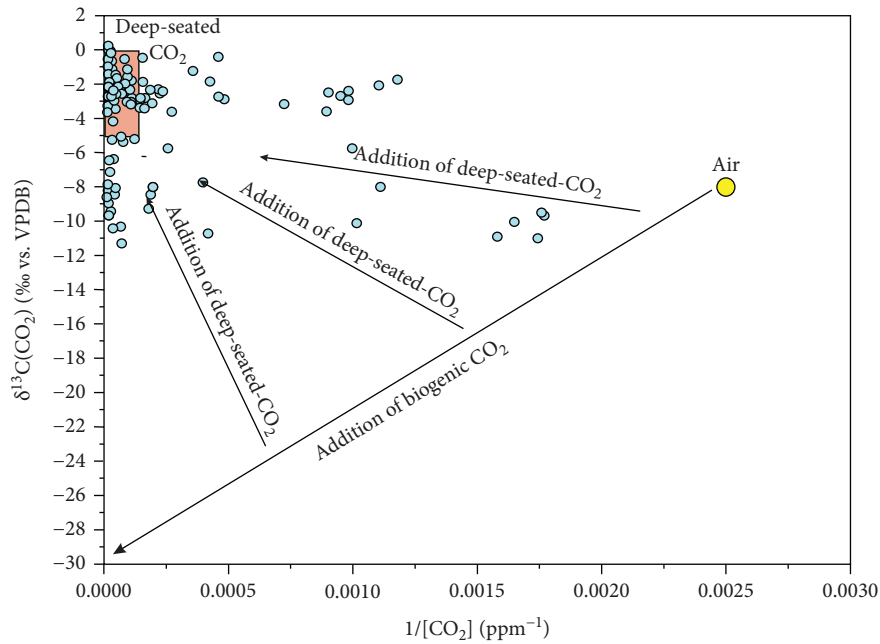


FIGURE 4: A plot of $\delta^{13}\text{C}(\text{CO}_2)$ versus $1/[\text{CO}_2]$ (ppmV^{-1}) data from the Teide summit cone and crater. This figure depicts three possible geochemical reservoirs: air, characterized by a $\delta^{13}\text{C}(\text{CO}_2) = -8\text{‰}$ and $[\text{CO}_2] = 0.04\%$, deep-seated CO_2 with $\delta^{13}\text{C}(\text{CO}_2) = -3.1\text{‰}$ and $[\text{CO}_2] = 100\%$, and biogenic CO_2 with $\delta^{13}\text{C}(\text{CO}_2) = -27.5\text{‰}$ and $[\text{CO}_2] = 100\%$. Mixing trend between biogenic, air-derived, and deep-seated CO_2 is represented by straight lines.

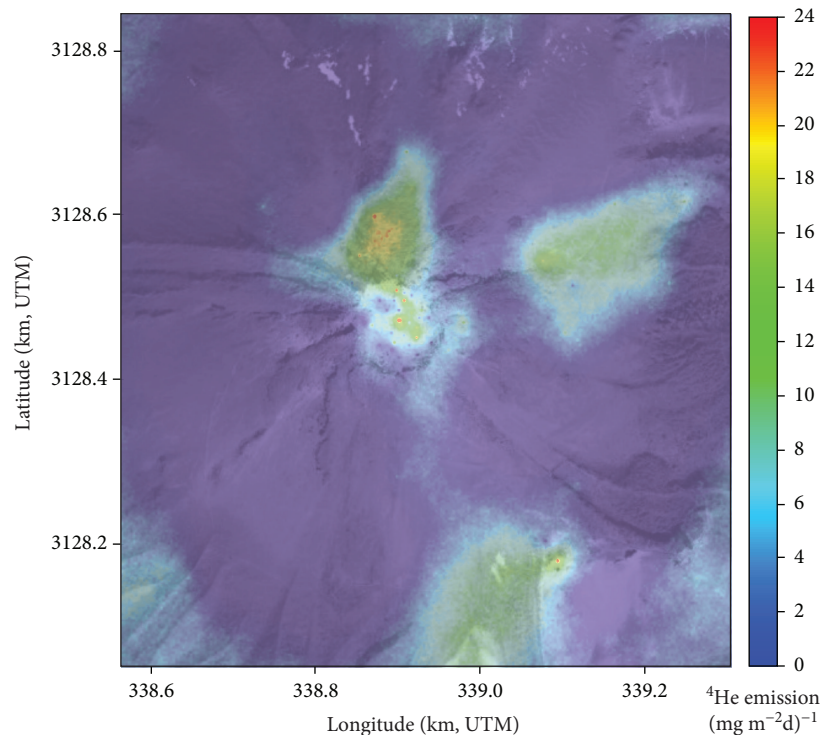


FIGURE 5: Diffuse ^4He emission map for the summit cone and crater of Teide volcano.

[51] estimate a ^4He emission between 15 and 38 kg d^{-1} from Cumbre Vieja volcano (La Palma) for an area of 220 km^2 . Padrón et al. [7] observed an increase in the diffusive component of ^4He emission from 9 to 38 kg d^{-1} of the whole El

Hierro island (278 km^2) prior to and during the 2011-2012 submarine eruption that took place 2 km off the southern coast of the island. In the case of the summit cone of Teide, with an area of 0.5 km^2 , the normalized ^4He emission rate is

TABLE 1: Outlet temperature, chemical, and isotopic composition of fumarolic gases from the summit crater of Teide volcano.

	T (°C)	$^4\text{He}/^{20}\text{Ne}$	$^3\text{He}/^4\text{He}$ (R/R_A)	$\delta^{13}\text{C}-\text{CO}_2$ (‰)	CO_2 (%)	Gas steam
Teide fumarole	83.3	33.613	6.723 ± 0.056	-3.13 ± 0.01	98.15	0.251

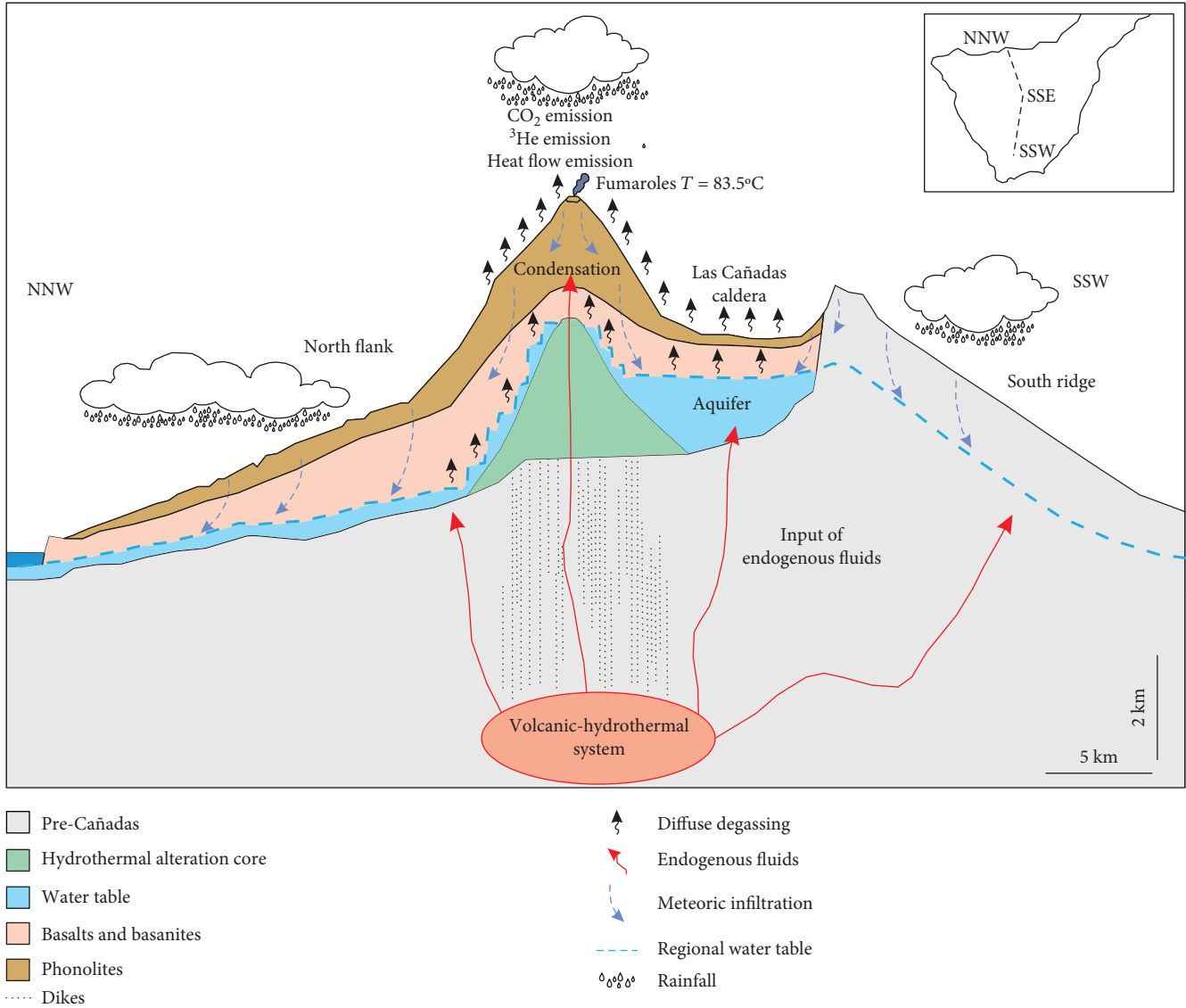


FIGURE 6: Hydrogeological model of Las Cañadas aquifer in the island of Tenerife. Fluid transport from the volcanic-hydrothermal system to the atmosphere is shown. Modified from Marrero-Díaz et al. [55].

$2.12 \text{ kg km}^{-2} \text{ d}^{-1}$, which represents a much higher value than that calculated for Cumbre Vieja and El Hierro (0.17 and $0.14 \text{ kg km}^{-2} \text{ d}^{-1}$, respectively).

The summit cone of Teide value for ^4He is comparable to Pico do Fogo volcano in Cape Verde. Dionis et al. [21] estimated a helium emission of 4.1 kg d^{-1} from the crater that has an area of 0.142 km^2 by considering a pure convective emission and a normalized emission rate of $28 \text{ kg km}^{-2} \text{ d}^{-1}$. It is worth noting that Pico do Fogo volcano has experienced a higher eruptive activity in the historical times (last 500 years) than Teide. This observation might suggest a more

general relationship between ^4He emission and volcanic activity than that demonstrated at the scale of the Cape Verde archipelago by Dionis et al. [21] using CO_2 and ^3He emission.

4.3. ^3He Emission. Chemical and isotopic composition of fumarolic gases from the summit crater of Teide volcano are summarized in Table 1.

Assuming that the $^3\text{He}/^4\text{He}$ ratio analyzed from the fumaroles is the same for the whole hydrothermal system, the calculated diffuse ^3He emission for the first assumption is $2.48 \times 10^{-3} \text{ mol d}^{-1}$ (0.89 mol y^{-1}). Nevertheless, because

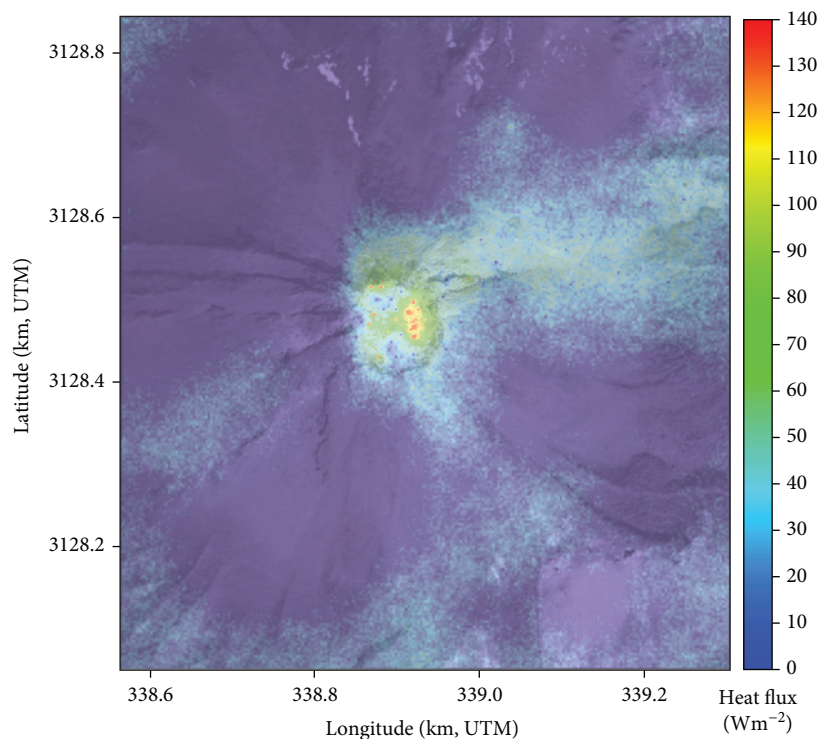


FIGURE 7: Heat flux emission map for the summit cone and crater of Teide volcano.

we have used the ^4He flux calculated before for our estimation, the ^3He emission could be overestimated because there must be some radiogenic ^4He from the crust. Anyway, that amount of ^4He from the crust is almost negligible for polygenetic volcanoes at oceanic islands as Tenerife [11]. For the second assumption, we use the CO_2 flux calculated before because we assume that the ^3He flux is wholly derived from deep-seated source. The calculated ^3He emission is $9.69 \times 10^{-4} \text{ mol d}^{-1}$ (0.35 mol y^{-1}). In this case, some amount of CO_2 derived from magma would be trapped by water in soil or groundwater during its ascent, so the true ^3He flux is underestimated and should be higher than the estimate. Marrero et al. [52] estimates through a CO_2 mass balance that $17.5 \times 10^8 \text{ mol y}^{-1}$ (211 t d^{-1}) of CO_2 is discharged by the groundwaters of Las Cañadas aquifer (144 km^2) (Figure 6). That means that there is a large amount of magmatic CO_2 that is trapped in the aquifer during its ascent to the atmosphere, suggesting that ^3He emission calculated using the second assumption is clearly subestimated.

These summit-cone wide values are consistent with the crater-only value which was reported by Hernández et al. [53] to be 0.51 mol y^{-1} (after correction of an error observed in the original calculation).

This work provides one more of the few values reported to date related to ^3He global emission, of which volcanic systems are highly significant. Other hot spot-type volcanic systems have shown similar (Piton de la Fournaise, La Réunion island, 1.1 mol y^{-1}) or higher emission values (Kilauea, Hawaii, $9\text{--}14 \text{ mol y}^{-1}$) [54], using fumarolic data. Other studies of soil ^3He emission in volcanic areas are rare. Padrón et al. [51] estimated a total output of ^3He in Cumbre Vieja

volcano (La Palma, Canary Islands) of $0.6\text{--}0.7 \text{ mol y}^{-1}$ considering a pure diffusive transport mechanism for an area of 220 km^2 .

4.4. Heat Flow. The computed thermal energy released by degassing of $1.26 \times 10^{12} \text{ J d}^{-1}$ corresponds to a total heat flow of 2.21 MW . We obtained a value of $8.1 \pm 0.97 \text{ MW}$ using the Dawson method. In the interpolation map, the areas with the highest heat flow occurred at the fumarolic areas inside the crater, the crater rim, and the NE flank (Figure 7). The fumarolic area in the crater of Teide volcano has an average temperature of 83.5°C that it is constant since it began to register in 1993. The major component of these fumaroles is the water vapour, which originates from the vaporization of the rainfall water [33] followed by CO_2 , N_2 , H_2 , H_2S , Ar , CH_4 , and CO , a composition typical of hydrothermal fluids [34, 35]. These data suggest that the fumarolic effluents are made by endogenous gases which cross the aquifer located somewhere in the postcaldera structure close to the surface [33]. At the same time, the heat flux in the crater of Teide volcano has been registered since 2009 and no significant changes have been detected. Most of the heat flow measured in Teide volcano is the result of the emitted heat by the phase change of water from gas to liquid in the condensation zone.

The difference between the heat emission calculations among two different methods is because the method proposed by Chiodini et al. [46] assumes that the $\text{H}_2\text{O}/\text{CO}_2$ molar ratio measured in the fumarolic discharges is the same for the whole hydrothermal system. In this study, we are comparing areas with higher convective component at the

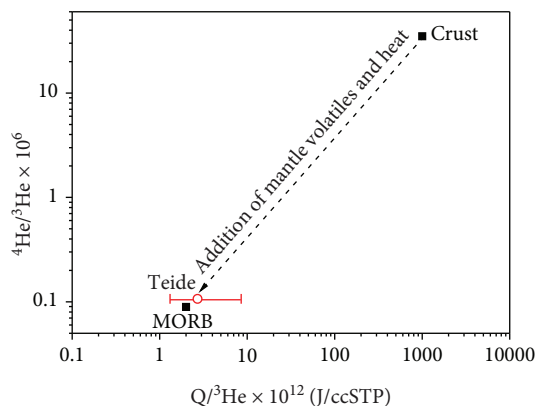


FIGURE 8: Schematic representation of the coherence between heat and helium.

crater with areas typified mainly by diffusive component at the flanks of the volcano, where there are no surface evidences of hydrothermal alteration.

To compare our data with other volcanic systems, Hernández et al. [3] estimated a total heat flow of 1.24 MW for the Hengill volcanic system; Chiodini et al. [2] reported the energy released by other volcanic areas as Campi Flegrei 100.8 MW, Ischia 40.1 MW, Vesuvio cone 16.6 MW, Vulcano crater 21 MW, and Comalito cinder cone 0.9 MW, and Dionis et al. [21] estimated a value of 10.3 MW released from the summit crater of Pico do Fogo volcano.

4.5. $^3\text{He}/\text{Heat}$ Ratio. Following from the end-member assumptions used to calculate the ^3He and heat flux, we calculated a plausible $^3\text{He}/\text{heat}$ ratio range from 0.117×10^{-12} to $0.764 \times 10^{-12} \text{ cm}^3 \text{ STP J}^{-1}$, with an average value of $0.370 \times 10^{-12} \text{ cm}^3 \text{ STP J}^{-1}$. This value is close to the $0.5 \times 10^{-12} \text{ cm}^3 \text{ STP J}^{-1}$ calculated for the $^3\text{He}/\text{heat}$ ratio for hydrothermal activity from the upper mantle [19, 20]. Figure 8 shows the relationship between heat and helium emissions, following the model of Kennedy et al. [17], which demonstrate that Teide volcano is a useful window to take measurements of volatiles and heat from the upper mantle of the Earth to the atmosphere. By extension, future studies that focus upon the temporal evolution of heat and volatile emission from Teide and similar windows to the mantle will improve understanding of mantle dynamics and the link between lithosphere and atmosphere.

5. Conclusions

Most of the volcano-hydrothermal fluid discharges occurring at the summit cone of Teide volcano occur in the crater area; yet, other important emission rates were measured along the north and north-east flanks. These extracrater emissions are suggestive of a strong structural control in the degassing process of Teide volcano. Given the prevalence of structural controls on the expression of volcanic systems worldwide, we can suggest that other important, yet not as obvious, emissions are likely to be encountered at other volcanic systems.

The estimated global volcanic emission of ^3He is $1250 \pm 250 \text{ mol y}^{-1}$ [54]. The contribution to this estimate emission obtained by Teide volcano in this work is about 0.62 mol y^{-1} , for an area of 0.5 km^2 , 0.05% of the total global emission. This study provides the first estimation of $^3\text{He}/\text{heat}$ from the Teide volcanic system and supports theoretical estimates at a global scale. The calculation of flux supports the presence of an important mantle source of volatiles and heat to the atmosphere.

Data Availability

The raw geochemical data used to support the findings of this study are stored on servers at ITER and can be made available by reasonable arrangement with the corresponding author.

Conflicts of Interest

The authors declare that there is no conflict of interest regarding the publication of this paper.

Acknowledgments

This research was financially supported by the projects (i) VOLRISKMAC from MAC 2014-2020, (ii) TFvolcano and TFinnova from the Cabildo Insular de Tenerife (Spain), and (iii) the Ministry of Science and Innovation from Spanish Government from DI-16-08974. We thank Iván Cabrera Pérez and Matthew James Pankhurst for their contribution to improve the quality of this paper and also Teleférico del Teide and Teide National Park for their assistance during the field work and for the logistic support.

Supplementary Materials

Supplementary materials 1: ambient and soil temperatures and CO_2 flux measured in each sampling site, and heat and ^4He fluxes calculated using the methodology described in the manuscript. Supplementary materials 2: data obtained from the analysis of the soil gases recollected in each sampling site. (*Supplementary Materials*)

References

- [1] T. A. Mather, "Volcanoes and the environment: lessons for understanding Earth's past and future from studies of present-day volcanic emissions," *Journal of Volcanology and Geothermal Research*, vol. 304, pp. 160–179, 2015.
- [2] G. Chiodini, D. Granieri, R. Avino, S. Caliro, A. Costa, and C. Werner, "Carbon dioxide diffuse degassing and estimation of heat release from volcanic and hydrothermal systems," *Journal of Geophysical Research*, vol. 110, no. B8, pp. 2156–2202, 2005.
- [3] P. A. Hernández, N. M. Pérez, T. Fridriksson et al., "Diffuse volcanic degassing and thermal energy release from Hengill volcanic system, Iceland," *Bulletin of Volcanology*, vol. 74, no. 10, pp. 2435–2448, 2012.
- [4] L. A. Pogorsky and G. S. Quirt, "Helium emanometry in exploring for hydrocarbons: part I," in *Unconventional Methods in Exploration for Petroleum and Natural Gas II-South*, pp. 124–135, Methodist University Press, 1981.

- [5] D. M. Thomas and J. J. Naughton, "Helium/carbon dioxide ratios as premonitors of volcanic activity," *Science*, vol. 204, no. 4398, pp. 1195–1196, 1979.
- [6] Y. Sano, Y. Nakamura, H. Wakita, A. Urabe, and T. Tominaga, "Helium-3 emission related to volcanic activity," *Science*, vol. 224, no. 4645, pp. 150–151, 1984.
- [7] E. Padrón, N. M. Pérez, P. A. Hernández et al., "Diffusive helium emissions as a precursory sign of volcanic unrest," *Geology*, vol. 41, no. 5, pp. 539–542, 2013.
- [8] W. B. Clarke, W. J. Jenkins, and Z. Top, "Determination of tritium by mass spectrometric measurement of ^3He ," *International Journal of Applied Radiation and Isotopes*, vol. 27, no. 9, pp. 515–522, 1976.
- [9] D. W. Graham, "Noble gas isotope geochemistry of mid-ocean ridge and ocean island basalts: characterization of mantle source reservoirs," *Reviews in Mineralogy and Geochemistry*, vol. 47, no. 1, pp. 247–317, 2002.
- [10] M. Sakamoto, Y. Sano, and H. Wakita, " $^3\text{He}/^4\text{He}$ ratio distribution in and around the Hakone volcano," *Geochemical Journal*, vol. 26, no. 4, pp. 189–195, 1992.
- [11] N. M. Pérez, S. Nakai, H. Wakita, P. A. Hernández, and J. M. Salazar, "Helium-3 emission in and around Teide volcano, Tenerife, Canary Islands, Spain," *Geophysical Research Letters*, vol. 23, no. 24, pp. 3531–3534, 1996.
- [12] N. M. Pérez, S. Nakai, H. Wakita, Y. Sano, and S. N. Williams, " $^3\text{He}/^4\text{He}$ isotopic ratios in volcanic-hydrothermal discharges from the Canary Islands, Spain: implications on the origin of the volcanic activity," *Mineralogical Magazine*, vol. 58A, no. 2, pp. 709–710, 1994.
- [13] D. R. Hilton, C. G. Macpherson, and T. R. Elliot, "Helium isotope ratios in mafic phenocrysts and geothermal fluids from La Palma, the Canary Islands Spain: implications for HIMU mantle sources," *Geochimica et Cosmochimica Acta*, vol. 64, no. 12, pp. 2119–2132, 2000.
- [14] J. M. D. Day and D. R. Hilton, "Origin of $^3\text{He}/^4\text{He}$ ratios in HIMU-type basalts constrained from Canary Island lavas," *Earth and Planetary Science Letters*, vol. 305, no. 1–2, pp. 226–234, 2011.
- [15] T. Torgersen and W. J. Jenkins, "Helium isotopes in geothermal systems: Iceland, The Geysers, Raft River and Steamboat Springs," *Geochimica et Cosmochimica Acta*, vol. 46, no. 5, pp. 739–748, 1982.
- [16] Y. Sano and H. Wakita, "Geographical distribution of $^3\text{He}/^4\text{He}$ ratios in Japan: implications for arc tectonics and incipient magmatism," *Journal of Geophysical Research*, vol. 90, no. B10, pp. 8729–8741, 1985.
- [17] B. M. Kennedy, T. P. Fischer, and D. L. Shuster, "Heat and helium in geothermal systems," *Twenty-Fifth Workshop on Geothermal Reservoir Engineering Stanford University*, 2000, Stanford, CA, USA, January 2000, 2000.
- [18] K. Umeda, Y. Sakagawa, A. Ninomiya, and K. Asamori, "Relationship between helium isotopes and heat flux from hot springs in a non-volcanic region, Kii Peninsula, southwest Japan," *Geophysical Research Letters*, vol. 34, no. 5, article L05310, 2007.
- [19] J. E. Lupton, E. T. Baker, and G. J. Massoth, "Variable ^3He /heat ratios in submarine hydrothermal systems: evidence from two plumes over the Juan de Fuca ridge," *Nature*, vol. 337, no. 6203, pp. 161–164, 1989.
- [20] H. Elderfield and A. Schultz, "Mid-ocean ridge hydrothermal fluxes and the chemical composition of the ocean," *Annual Review of Earth and Planetary Sciences*, vol. 24, no. 1, pp. 191–224, 1996.
- [21] S. M. Dionis, G. Melián, F. Rodríguez et al., "Diffuse volcanic gas emission and thermal energy release from the summit crater of Pico do Fogo, Cape Verde," *Bulletin of Volcanology*, vol. 77, no. 2, p. 10, 2015.
- [22] T. Fridriksson, B. R. Kristjánsson, H. Ármannsson, E. Margrétardóttir, S. Ólafsdóttir, and G. Chiodini, " CO_2 emissions and heat flow through soil, fumaroles and steam heated mud pools at the Reykjanes geothermal area, SW Iceland," *Applied Geochemistry*, vol. 21, no. 9, pp. 1551–1569, 2006.
- [23] J. C. Carracedo, E. R. Badiola, H. Guillou et al., "Eruptive and structural history of Teide volcano and rift zones of Tenerife, Canary Islands," *Geological Society of America Bulletin*, vol. 119, no. 9–10, pp. 1027–1051, 2007.
- [24] F. Anguita and F. Hernán, "The Canary Islands origin: a unifying model," *Journal of Volcanology and Geothermal Research*, vol. 103, no. 1–4, pp. 1–26, 2000.
- [25] H. Guillou, J. C. Carracedo, R. Paris, and F. J. Pérez Torrado, "Implications for the early shield-stage evolution of Tenerife from K/Ar ages and magnetic stratigraphy," *Earth and Planetary Science Letters*, vol. 222, no. 2, pp. 599–614, 2004.
- [26] E. Ancochea, J. M. Fuster, E. Ibarrola et al., "Volcanic evolution of the island of Tenerife (Canary Islands) in the light of new K/Ar data," *Journal of Volcanology and Geothermal Research*, vol. 44, no. 3–4, pp. 231–249, 1990.
- [27] J. Martí, J. Mitjavila, and V. Araña, "Stratigraphy, structure and geochronology of the Las Cañadas caldera (Tenerife, Canary Islands)," *Geological Magazine*, vol. 131, no. 6, pp. 715–727, 1994.
- [28] J. Martí and A. Gudmundsson, "The Las Cañadas caldera (Tenerife, Canary Islands); an overlapping collapse caldera generated by magma-chamber migration," *Journal of Volcanology and Geothermal Research*, vol. 103, no. 1–4, pp. 161–173, 2000.
- [29] M. J. Huertas, N. O. Arnaud, E. Ancochea, J. M. Cantagrel, and J. M. Fúster, " $^{40}\text{Ar}/^{39}\text{Ar}$ stratigraphy of pyroclastic units from the Cañadas Volcanic edifice (Tenerife, Canary Islands) and their bearing on the structural evolution," *Journal of Volcanology and Geothermal Research*, vol. 115, no. 3–4, pp. 351–365, 2002.
- [30] J. Martí, M. Hurlimann, G. J. Ablay, and A. Gudmundsson, "Vertical and lateral collapses on Tenerife (Canary Islands) and other volcanic ocean islands," *Geology*, vol. 25, no. 10, pp. 879–882, 1997.
- [31] J. Dóniz, C. Romero, E. Coello et al., "Morphological and statistical characterisation of recent mafic volcanism on Tenerife (Canary Islands, Spain)," *Journal of Volcanology and Geothermal Research*, vol. 173, no. 3–4, pp. 185–195, 2008.
- [32] G. J. Ablay and J. Martí, "Stratigraphy, structure, and volcanic evolution of the Pico Teide-Pico Viejo formation, Tenerife, Canary Islands," *Journal of Volcanology and Geothermal Research*, vol. 103, no. 1–4, pp. 175–208, 2000.
- [33] J. F. Albert-Beltrán, V. Araña, J. L. Diez, and A. Valentin, "Physical-chemical conditions of the Teide volcanic system (Tenerife, Canary Islands)," *Journal of Volcanology and Geothermal Research*, vol. 43, no. 1–4, pp. 321–332, 1990.
- [34] N. M. Pérez, N. C. Sturchio, S. N. Williams, J. C. Carracedo, and J. Coello, "Geochemical characteristics of the volcanic-hydrothermal gases in Teide, Timafaya, Taburiente, and

- Teneguia volcanoes, Canary Islands, Spain,” in *Proceedings of the Scientific Sessions: III Geological Congress of Spain, Volume I*, pp. 463–467, Graficas Varona, Salamanca, 1992.
- [35] G. Melián, F. Tassi, N. Pérez et al., “A magmatic source for fumaroles and diffuse degassing from the summit crater of Teide volcano (Tenerife, Canary Islands): a geochemical evidence for the 2004–2005 seismic–volcanic crisis,” *Bulletin of Volcanology*, vol. 74, no. 6, pp. 1465–1483, 2012.
- [36] T. Mori, P. A. Hernández, J. M. L. Salazar, N. M. Pérez, and K. Notsu, “An in situ method for measuring CO₂ flux from volcanic-hydrothermal fumaroles,” *Chemical Geology*, vol. 177, no. 1–2, pp. 85–99, 2001.
- [37] N. M. Pérez, P. A. Hernández, E. Padrón et al., “An increasing trend of diffuse CO₂ emission from Teide volcano (Tenerife, Canary Islands): geochemical evidence of magma degassing episodes,” *Journal of the Geological Society*, vol. 170, no. 4, pp. 585–592, 2013.
- [38] K. J. Parkinson, “An improved method for measuring soil respiration in the field,” *Journal of Applied Ecology*, vol. 18, no. 1, pp. 221–228, 1981.
- [39] W. F. Giggenbach and R. L. Goguel, *Collection and Analysis of Geothermal and Volcanic Water and Gas Discharges*, Unpublished report, Chemistry Division, DSIR-Petone, New Zealand, 1989.
- [40] H. Sumino, K. Nagao, and K. Notsu, “Highly sensitive and precise measurement of helium isotopes using a mass spectrometer with double collector system,” *Journal of the Mass Spectrometry Society of Japan*, vol. 49, no. 2, pp. 61–68, 2001.
- [41] J. Matsuda, T. Matsumoto, H. Sumino et al., “The ³He/⁴He ratio of the new internal He standard of Japan (HESJ),” *Geochemical Journal*, vol. 36, no. 2, pp. 191–195, 2002.
- [42] H. Craig and J. E. Lupton, “Primordial neon, helium and hydrogen in oceanic basalts,” *Earth and Planetary Science Letters*, vol. 31, no. 3, pp. 369–385, 1976.
- [43] G. Etiope and G. Martinelli, “Migration of carrier and trace gases in the geosphere: an overview,” *Physics of the Earth and Planetary Interiors*, vol. 129, no. 3–4, pp. 185–204, 2002.
- [44] M. G. Schaap and I. Lebron, “Using microscope observations of thin sections to estimate soil permeability with the Kozeny-Carman equation,” *Journal of Hydrology*, vol. 251, no. 3–4, pp. 186–201, 2001.
- [45] M. L. Carapezza and D. Granieri, “CO₂ soil flux at Vulcano (Italy): comparison between active and passive methods,” *Applied Geochemistry*, vol. 19, no. 1, pp. 73–88, 2004.
- [46] G. Chiodini, F. Frondini, C. Cardellini, D. Granieri, L. Marini, and G. Ventura, “CO₂ degassing and energy release at Solfatara volcano, Campi Flegrei, Italy,” *Journal of Geophysical Research*, vol. 106, no. B8, pp. 16213–16221, 2001.
- [47] F. Frondini, G. Chiodini, S. Caliro, C. Cardellini, D. Granieri, and G. Ventura, “Diffuse CO₂ degassing at Vesuvio, Italy,” *Bulletin of Volcanology*, vol. 66, no. 7, pp. 642–651, 2004.
- [48] J. H. Keenan, F. G. Keyes, P. G. Hill, and J. G. Moore, *Steam Tables Thermodynamic Properties of Water Including Vapor, Liquid and Solid Phases. International edition metric units*, Wiley, New York, NY, USA, 1969.
- [49] G. B. Dawson, “The nature and assessment of heat flow from hydrothermal areas,” *New Zealand Journal of Geology and Geophysics*, vol. 7, no. 1, pp. 155–171, 1964.
- [50] C. Deutsch and A. Journel, *GSLIB: Geostatistical Software Library and Users Guide*, Oxford University Press, New York, NY, USA, 2nd edition, 1998.
- [51] E. Padrón, N. M. Pérez, P. A. Hernández et al., “Helium emission at cumbre Vieja volcano, La Palma, Canary Islands,” *Chemical Geology*, vol. 312–313, pp. 138–147, 2012.
- [52] R. Marrero, D. L. López, P. A. Hernández, and N. M. Pérez, “Carbon dioxide discharged through the las Cañadas aquifer, Tenerife, Canary Islands,” *Pure and Applied Geophysics*, vol. 165, no. 1, pp. 147–172, 2008.
- [53] P. A. Hernández, N. M. Pérez, J. M. Salazar, S. Nakai, K. Notsu, and H. Wakita, “Diffuse emission of carbon dioxide, methane and helium-3 from Teide volcano, Tenerife, Canary Islands,” *Geophysical Research Letters*, vol. 25, no. 17, pp. 3311–3314, 1998.
- [54] P. Allard, “Global emissions of Helium-3 by subaerial volcanism,” *Geophysical Research Letters*, vol. 19, no. 14, pp. 1479–1481, 1992.
- [55] R. Marrero-Díaz, D. López, N. M. Pérez et al., “Carbon dioxide and helium dissolved gases in groundwater at Central Tenerife Island, Canary Islands: chemical and isotopic characterization,” *Bulletin of Volcanology*, vol. 77, no. 10, p. 86, 2015.

Research Article

Fluid Phase Simulation and Evolution of a Condensate Gas Reservoir in the Tazhong Uplift, Tarim Basin

Rui Deng,^{1,2} Chengsheng Chen,^{1,2} Shuyong Shi,^{1,2} and Yunpeng Wang¹ 

¹State Key Laboratory of Organic Geochemistry, Guangzhou Institute of Geochemistry, Chinese Academy of Sciences, Guangzhou 510640, China

²University of Chinese Academy of Sciences, Beijing 100039, China

Correspondence should be addressed to Yunpeng Wang; wangyp@gig.ac.cn

Received 30 January 2019; Revised 1 May 2019; Accepted 27 May 2019; Published 13 June 2019

Academic Editor: Julien Bourdet

Copyright © 2019 Rui Deng et al. This is an open access article distributed under the Creative Commons Attribution License, which permits unrestricted use, distribution, and reproduction in any medium, provided the original work is properly cited.

The fluid phase and the evolution of the condensate gas reservoir in the Lianglitage Formation (O_3), Well ZG7-5, Tazhong Uplift, were studied by integrating the PVTsim and the PetroMod software. The fluid phase was successfully simulated, and the burial, temperature, pressure, and pressure coefficient histories were reconstructed. The evolution of the fluid phase and its properties (density, viscosity, and gas-oil ratio) under the ideal and gas washing conditions was also explored. The simulated pressure-temperature (P - T) phase diagram confirms that the reservoir fluid is in the condensate gas phase at present, with an order of critical point-cricondenbar-cricondentherm (CP - P_m - T_m). The temperature and pressure show an overall increasing trend considering the entirety of geological evolution. Under ideal conditions, fluid transition from coexisting gas and liquid phases to a single condensate gas phase occurred during the Late Cretaceous (80 Ma, $T = 135.7^\circ\text{C}$, and $P = 58.19\text{ MPa}$). The density and viscosity of the liquid phase decreased gradually while the density and viscosity of the gas phase and the solution gas-oil ratio increased during geological processes. With the consideration of gas washing, the critical phase transition time points for 100% and 50% gas washing fluid are 394 Ma, 383 Ma, 331 Ma, and 23 Ma, as well as 266 Ma and 23 Ma, respectively. The average liquid phase density, gas phase density, and liquid phase viscosity under 100% gas washing are larger than those under 50% gas washing before 23 Ma (Miocene), while the gas phase viscosity values are similar for both cases. This study visually suggests that the temperature and pressure histories, which are controlled by the burial history and heat flow evolution, and gas washing have significant impacts on the formation of the condensate gas reservoirs and evolution of the fluid phase and its features in the Tazhong Uplift.

1. Introduction

The Tazhong Uplift is the most important oil and gas bearing area in the Tarim Basin of China. In recent decades, many different types of petroleum reservoirs have been discovered in the Tazhong Uplift, and the phase states of reservoir fluids vary among sand tar, super heavy oil, heavy oil, black oil, normal oil, light oil, condensate gas, and natural gas [1]. The condensate gas reservoirs serve as highly valued resources for energy supply, and their characteristic phase transitions during the accumulation and exploitation processes make them valuable for research [2].

Knowledge of the phase state and pressure-volume-temperature (PVT) properties of reservoir fluids is critical

to the exploration and development of the reservoirs and, therefore, of interest in petroleum engineering studies [3, 4]. For all conventional and unconventional petroleum reservoirs, it is essential to reconstruct the phase evolution history and the changes in the gas-oil ratio (GOR) and physical properties of the fluid over time, which are all closely related to the burial and thermal histories of the fluid [5]. In many previous works, phase simulation experiments have been conducted under high temperature and pressure using PVT-based methods to obtain PVT properties and determine the phase types of reservoir fluids; however, such experiments are complicated, time-consuming, and difficult to conduct [6–10]. In addition, the fluid phase and evolution of condensate gas reservoirs in the Tazhong Uplift have not

been intensively studied; there is a lack of systematic studies on the temperature and pressure recoveries for condensate gas reservoirs in the area, as well as a lack of the combination with PVT simulation and basin modeling. Therefore, the purpose of this study was to explore the fluid phase and evolution of a typical condensate gas reservoir, Well ZG7-5, in the Tazhong Uplift. We first simulated the phase envelope and PVT properties of the fluids by using the PVTsim software, which is an easy-to-use and widely used software for the phase simulation of reservoir fluids. We then reconstructed the burial, temperature, pressure, and pressure coefficient evolution histories of the target reservoir using the PetroMod software. Finally, we studied the evolution of the fluid phase and its features (density, viscosity, and solution GOR) under ideal and gas washing conditions considering the entirety of geological evolution, by integrating the results of the PVTsim and the PetroMod software.

2. Geological Setting

The Tarim Basin, encompassing an area of 560,000 km², is the largest petroleum-bearing basin in China and is also one of the most complex superimposed basins in the world [11, 12]. This basin is characterized by thick sediments, multiple cycles of uplift and erosion, and complex distribution of oil and gas accumulations [13]. The Tazhong Uplift is a long-term inherited paleouplift in the central Tarim Basin, which was formed during the Caledonian orogeny and shaped by the Early Hercynian orogeny [14]; its tectonic framework did not significantly change during the subsequent Indosinian-Himalayan orogeny [15]. The oil and gas in the Tazhong Uplift are mainly distributed in the Cambrian, Ordovician, Silurian, and Carboniferous strata, and most condensate gas reservoirs are found in the Ordovician reservoirs originated from the Cambrian-Lower Ordovician strata and the Middle-Upper Ordovician source rocks [16]. The Tazhong Uplift can be subdivided into several belts including the Tazhong no. 1 fault zone, Tazhong no. 10 structural belt, Tazhong central horst belt, and Tazhong 1-8 buried hill belt [17, 18]. Well ZG7-5 is in the Tazhong no. 1 gas field and is located on the north slope of the Tazhong Uplift (Figure 1). The borehole depth of Well ZG7-5 reaches 5718 m, encountering strata from the Quaternary to the Ordovician. The condensate gas reservoir was discovered in the Lianglitage Formation (O₃, 5655-5718 m) where there is a daily gas production of 20399 m³ but little oil production (inner report of the Tarim Oil Company, 2016).

3. Materials and Methods

3.1. Fluid Phase Simulation. The PVTsim software by the Calsep Company specializes in the calculation of fluid properties, employing several different equations of state (EOS); it is widely used in oil and gas reservoir studies [20]. The input data for the PVTsim software include well fluid components (C₁-C₃₀₊, molecular weight), constant mass expansion experimental data, and constant volume depletion experimental data; these were all derived from the PVT analysis report for Well ZG7-5 (inner report of the Tarim Oil Company,

2016) (Tables 1 and 2). The data in the report were measured using a phase analyzer (Schlumberger DBR) and a gas chromatograph (Agilent 7890A, 6890N). The simulation steps are as follows: First, the well fluid components (C₁-C₃₀₊, molecular weight) listed in Table 1 were input to the PVTsim software. The original *P-T* phase diagram showing the temperature and pressure of the critical point (CP), cricondetherm (*T_m*), and cricondenbar (*P_m*) was obtained after initially simulating with the Peng-Robinson equation of state (Figure 2(a)). Then, the relevant constant mass expansion experimental data and constant volume depletion experimental data listed in Table 2 were used to conduct a regression calculation. Afterward, the simulated values of CP, *T_m*, and *P_m* were tuned to achieve as much consistency as possible with the measured values by altering the parameters of EOS [21]. The final phase model was determined when the simulated *P-T* phase diagram was close to the measured one after repeated calculation and tuning; this simulated phase diagram was regarded as being representative of the actual fluid in the reservoir (Figure 2(b)). Additionally, the positional order of the critical point (CP), cricondetherm (*T_m*), cricondenbar (*P_m*), and in situ petroleum reservoir conditions (*T_i*, *P_i*) in the *P-T* phase diagram was used to identify the type of reservoir fluid.

3.2. One-Dimensional Basin Modeling

3.2.1. One-Dimensional Basin Modeling Method. The temperature and pressure histories of the Lianglitage Formation (O₃), Well ZG7-5, were determined by reconstructing a geological model using the PetroMod 2016 (1D) software by Schlumberger Limited. The input parameters for this purpose include stratigraphy (age, thickness, and lithology), tectonic events (unconformities, erosion time, and erosion thickness), and boundary conditions (heat flow, paleowater depth, and sediment-water interface temperature) [22–24]. During the simulation process, the measured temperature and maturity values were used to validate the modeling results. The burial, temperature, pressure, and pressure coefficient evolution histories of the target reservoir were confirmed when the modeled and measured results were consistent.

3.2.2. Input Data for One-Dimensional Basin Modeling. Erosion events have a significant influence on both the burial and thermal histories. The modeled stratigraphic succession of Well ZG7-5 starts from the Quaternary and continues down to the Lianglitage Formation (Ordovician), excluding the Jurassic, Devonian, and Upper Silurian strata which show the effects of multiple tectonic events. The concrete values of erosion thickness and erosion time were collected from Zhang et al. [25], Pang et al. [26], and Qi and Liu [27]. The main deposition and erosion events are listed in Table 3. The data for stratigraphy (age, thickness, and lithology) were gathered from the logging report from the Tarim Oil Company.

In terms of the boundary conditions, the heat flow values are vital to unearthing the reservoir thermal maturity history. Values of heat flow were derived from Qiu et al. [28], Wang et al. [29], and Feng et al. [30]. The values of the paleowater

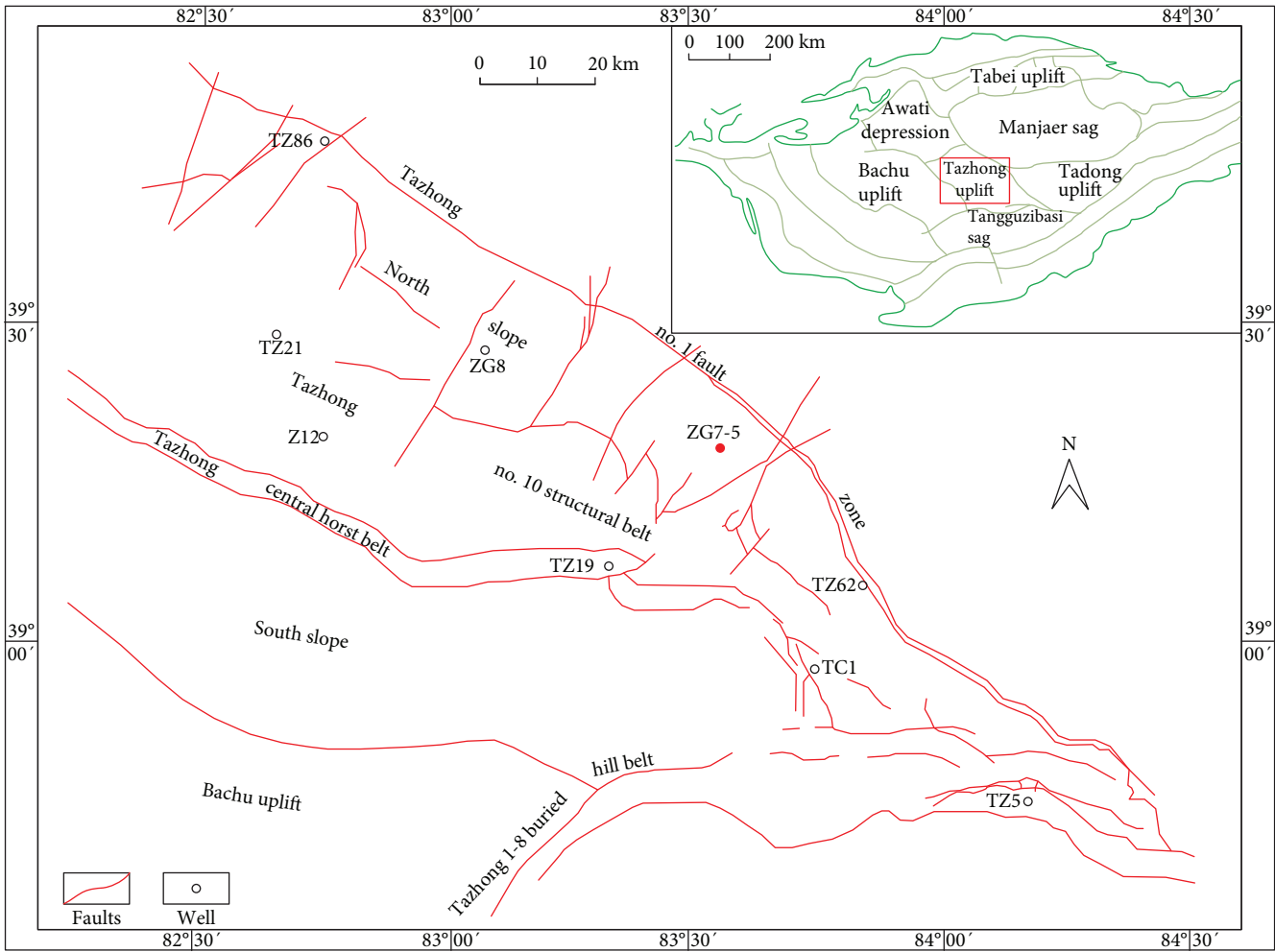


FIGURE 1: Map showing the location of Well ZG7-5 and the geological structures in the Tazhong Uplift (modified from [19]).

TABLE 1: Well fluid components (C_1 - C_{30+}) of the Lianglitage (O_3) reservoir in Well ZG7-5.

Components	Mol%	Molecular weight	Components	Mol%	Molecular weight
N ₂	4.232	28.014	C ₁₄	0.334	190
CO ₂	3.075	44.01	C ₁₅	0.260	206
C ₁	83.083	16.043	C ₁₆	0.177	222
C ₂	0.364	30.07	C ₁₇	0.143	237
C ₃	0.206	44.097	C ₁₈	0.118	251
iC ₄	0.078	58.124	C ₁₉	0.102	263
nC ₄	0.203	58.124	C ₂₀	0.091	275
iC ₅	0.147	72.151	C ₂₁	0.089	291
nC ₅	0.172	72.151	C ₂₂	0.085	305
C ₆	0.280	86.178	C ₂₃	0.075	318
C ₇	0.315	96	C ₂₄	0.059	331
C ₈	1.645	107	C ₂₅	0.054	345
C ₉	1.374	121	C ₂₆	0.041	359
C ₁₀	1.135	134	C ₂₇	0.024	374
C ₁₁	0.867	147	C ₂₈	0.014	388
C ₁₂	0.624	226	C ₂₉	0.007	402
C ₁₃	0.518	175	C ₃₀₊	0.011	416

TABLE 2: Experimental data for constant mass expansion and constant volume depletion.

Well	Constant mass expansion experiment			Constant volume depletion experiment		
	Pressure (MPa)	Temperature (°C)	Liquid vol% of Vd	Pressure (MPa)	Temperature (°C)	Z factor gas
ZG 7-5	61.46*	102.6	0.00			
	59.16*	122.6	0.00	56.81	142.6	1.374
	56.81*	142.6	0.00			

*Dew point pressure.

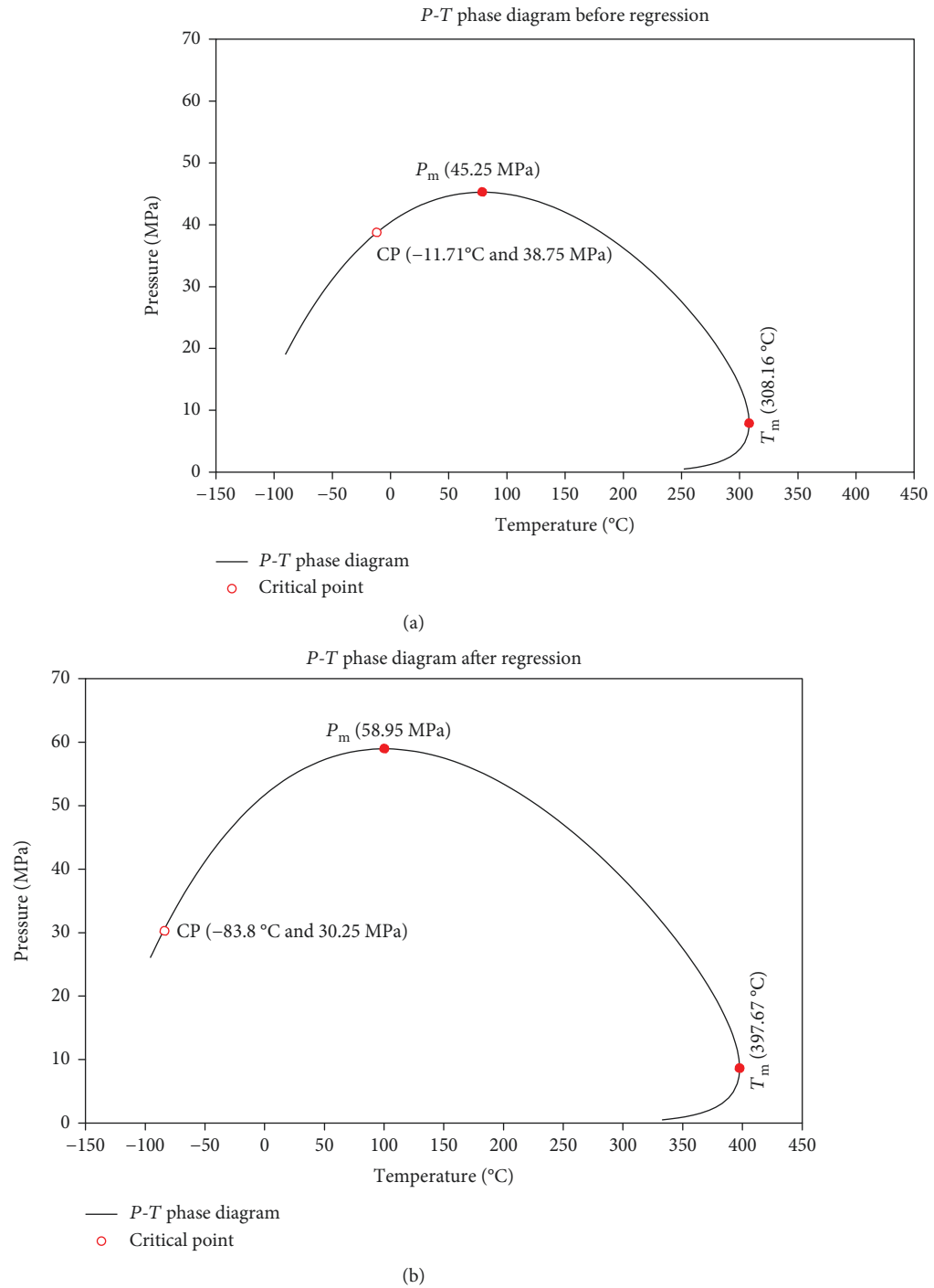
FIGURE 2: The original *P-T* phase diagram (before regression) and the final *P-T* phase diagram (after regression).

TABLE 3: The main deposition and erosion events in Well ZG7-5.

Age (Ma)	Strata	Depth (m)	Erosion thickness (m)	Lithology
0	Top N+Q	0		Sandstone, shale
23	Top E	1200		Sandstone
66	Top K	1834		Sandstone, shale
144	Erosion J		-150	
163	Top J		150	Sandstone, shale
201	Top T	2390		Shale, siltstone, conglomerate
247	Erosion P		-150	
254	Top P	2906	150	Shale, siltstone, conglomerate
298.9	Top C	3562		Shale, sandstone, limestone
358	Erosion D		-700	
387	Top D		700	Sandstone
417.6	Erosion S		-100	
427.4	Top S	4140	100	Sandstone, shale, siltstone
442	Erosion O ₃ s		-900	
443	Top O ₃ s	4482	900	Shale
453.4	Top O ₃ l ₁₋₂	5333		Limestone, sandstone
454.9	Target layer	5457		Limestone
458	Erosion O ₁ ys		-250	
459.9	Erosion O ₂ yif		-100	
460.7	Erosion O ₂ t		-50	
461	Top O ₂ t		50	Limestone
464.7	Top O ₂ yif		100	Limestone
470	Top O ₁ ys	5711	250	Limestone, dolomite
479.5	Top O ₁ p	6261		Dolomite, limestone
485.4	Base	6761		

depth (PWD) were estimated by sedimentary facies type and lithology, which are closely related to variations in the global sea level. The sediment-water interface temperatures (SWIT) were calculated using the PetroMod software upon identification of the location of the well. The plots for the concrete boundary conditions are presented in Figure 3. The temperature and maturity values measured for calibration were taken from the logging report and laboratory measurements by the Tarim Oil Company.

Finally, evolution of the fluid phase and its features (density, viscosity, and solution GOR) under ideal and gas washing conditions was studied by integrating the phase diagram from running the PVTsim software and the temperature-pressure values at each critical geological event point, derived by the PetroMod software.

4. Results and Discussion

4.1. *P-T* Phase Diagram for the Fluid. As mentioned above, the final phase diagram for the fluid was arrived at after several rounds of calculation and tuning, and the corresponding fluid features were calculated. Table 4 presents a comparison between the simulated and measured values of the fluid features of Well ZG7-5. The modeled features are consistent with the measured results. Further, the modeled density of oil on the ground and the solution GOR show relatively large

errors because oil density was measured with the loss of some light fractions, and the produced GOR, which slightly differs from the solution GOR, was measured. These comparisons illustrate that the modeling results are valid and the method is effective. The simulated *P-T* phase diagram for the fluids in the Lianglitage reservoir (O₃) is displayed in Figure 4. It can be seen that the temperature and pressure of the critical point (CP) are -83.8°C and 30.25 MPa, respectively, and the cricondentherm (T_m) and cricondenbar (P_m) are 397.67°C and 58.95 MPa, respectively. Furthermore, the *P-T* phase diagram is divided into the liquid phase zone, the condensate gas phase zone, the gas phase zone, and the coexistence phase zone for gas and liquid, by the positional order of the critical point (CP), cricondentherm (T_m), and cricondenbar (P_m). Based on the phase zone distribution of the *P-T* diagram and the in situ reservoir conditions ($T_i = 143.3^\circ\text{C}$, $P_i = 91.66\text{ MPa}$), the in situ reservoir fluid was classified as being of the condensate gas phase type. Under the conditions of normal temperature and pressure (20°C, 0.101 MPa), the fluid returns from the condensate gas phase to two separate phases of gas and liquid, which coincides with the current product type and macro compositions.

4.2. *Histories of Burial, Temperature, Pressure, and Pressure Coefficient.* As can be seen from Figure 5, the measured and modeled values of temperature and vitrinite reflectance

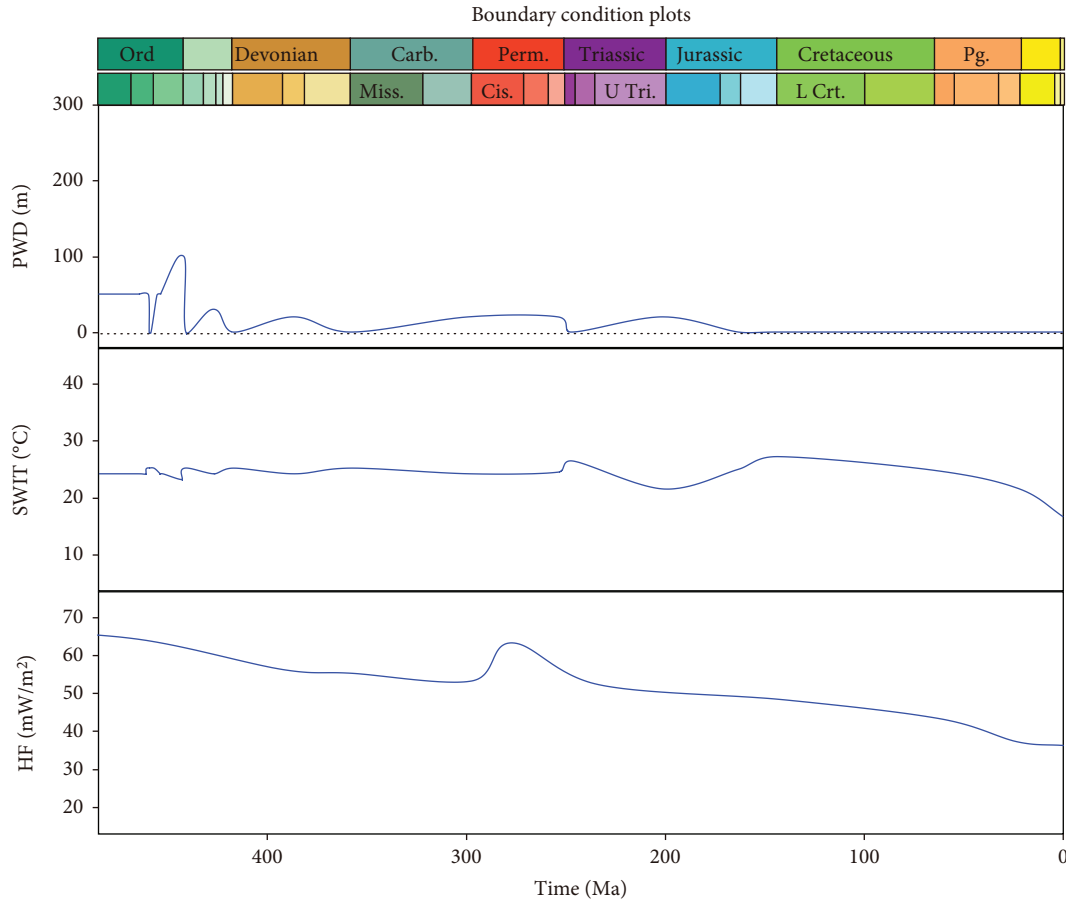


FIGURE 3: The boundary condition plots for Well ZG7-5.

TABLE 4: Comparison between simulated and measured features of the fluid.

Items	Simulated values	Measured values
Critical temperature (°C)	-83.80	-77.80
Critical pressure (MPa)	30.25	29.25
Cricondentherm (°C)	397.67	386.30
Cricondenbar (MPa)	58.95	57.71
Dew point pressure(142.6°C) (MPa)	58.00	56.81
Oil density at ground(20°C) (g/cm ³)	0.72	0.80*
Solution gas-oil ratio (GOR) (m ³ /m ³)	883	823**

*Measured with some loss of volatile fractions. **Produced GOR.

(Ro) fit well, indicating the reliability of burial, temperature, pressure, and pressure coefficient histories modeled using the PetroMod software.

The burial history overlaying with the thermal maturity history of Well ZG7-5 is shown in Figure 6, which indicates that the Tazhong Uplift has experienced multiple stages of uplift and erosion caused by multiple orogenies. Among all these orogenies, the Caledonian and Hercynian orogenies

had the most crucial impact on the study area. The Tarim Basin experienced a period of stable platform development during the Cambrian-Early Ordovician and encountered a slight erosion during the Late Middle Ordovician. Subsequently, the rapid subsidence and the following strong erosion of strata caused by the Middle Caledonian orogeny were the significant features of the Late Ordovician. This orogeny was also characterized by the strongest uplift and erosion (900 m) during the entire geological evolution history in the study area. During the Late Devonian, the Hercynian orogeny caused another strong uplift and erosion (700 m). The combined Caledonian and Hercynian orogenies caused an erosion thickness of more than 2000 m, and the Ordovician strata reached high-mature states (1.3-2.0%Ro) at the beginning of the Permian period. The orogeny events following this period had little impacts on the maturity. Currently, the Ordovician strata are buried to the maximum depth of over 6000 m.

Figure 7 shows the temperature and pressure histories of the Lianglitage Formation (O₃) in Well ZG7-5. The temperature history is significantly linked with the heat flow evolution and the burial history, while the pressure history is correlated with the burial history and lithology. Both the temperature and pressure histories depict overall increasing trends from the Ordovician to the present; however, decreasing trends caused by erosion events, heat flow

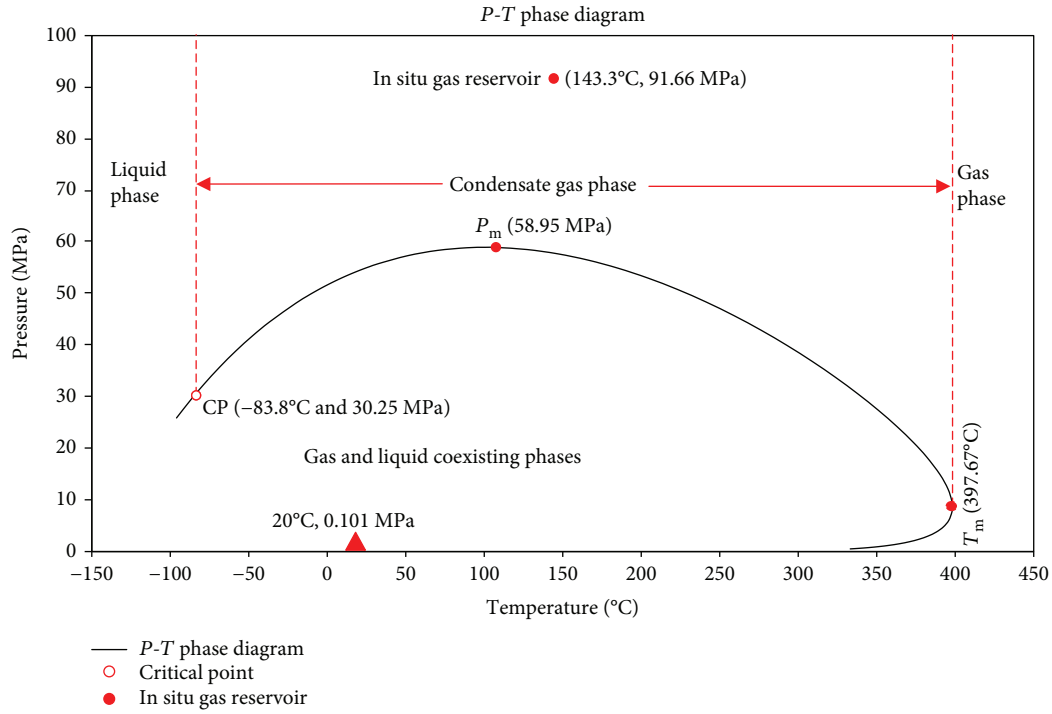
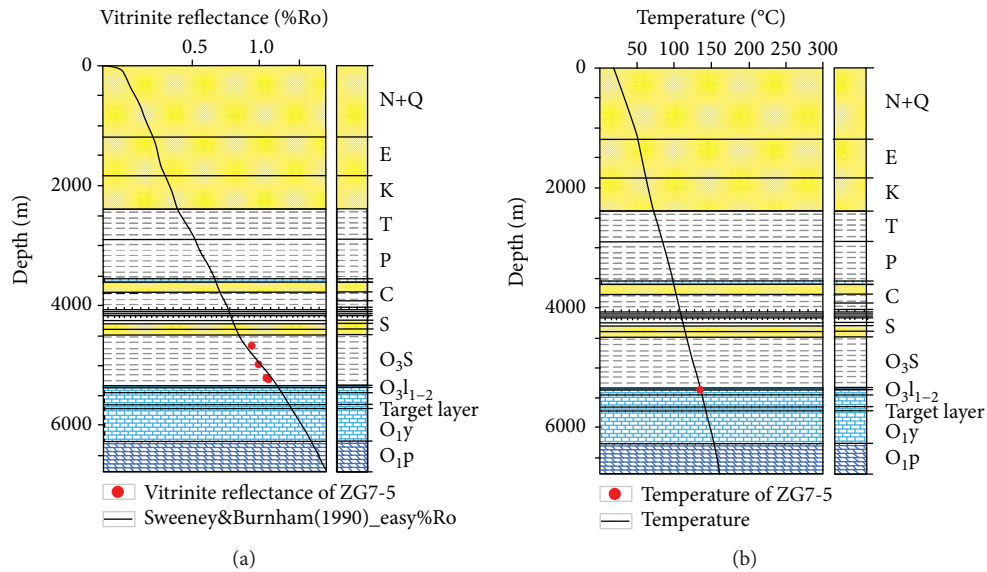
FIGURE 4: *P-T* phase diagram for the fluid in Well ZG7-5.

FIGURE 5: Good fit between the measured temperature and maturities and the modeled results of Well ZG7-5.

changes, or lithology variations were also observed. Moreover, the pressure coefficients throughout the evolution history were also calculated by the results derived from PetroMod (Figure 8). During the early stages, the reservoir was in normal pressure condition; these conditions changed to the state of overpressure (pressure coefficient > 1.2) during the Middle Permian (265 Ma) due to the deepening of the burial depth. After the Miocene, the pressure coefficient increased rapidly.

4.3. The Evolution of the Fluid Phase and Features

4.3.1. Ideal Conditions. Under ideal conditions, we assumed that the reservoir was formed without any destruction or change and the composition of the reservoir fluid was constant during the entire geological process. The simulated phase envelope and the modeled temperature-pressure values (labeled as the *P-T* line) at each time point of a critical geological event were overlapped in the same plot to

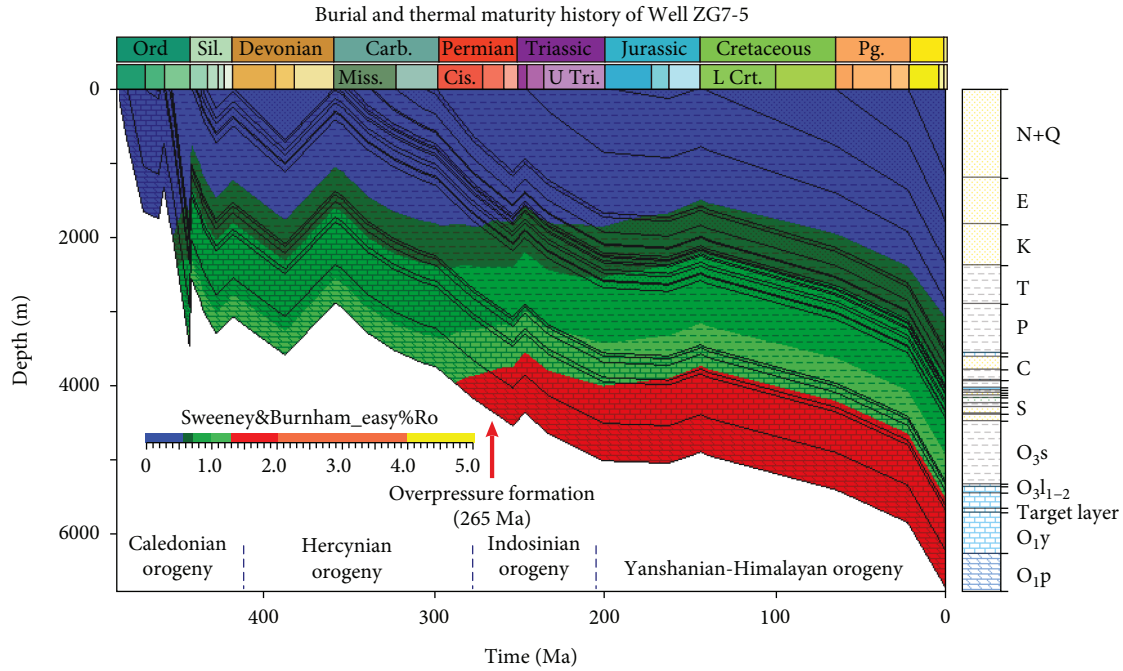


FIGURE 6: The burial history overlaying the thermal maturity history of Well ZG7-5.

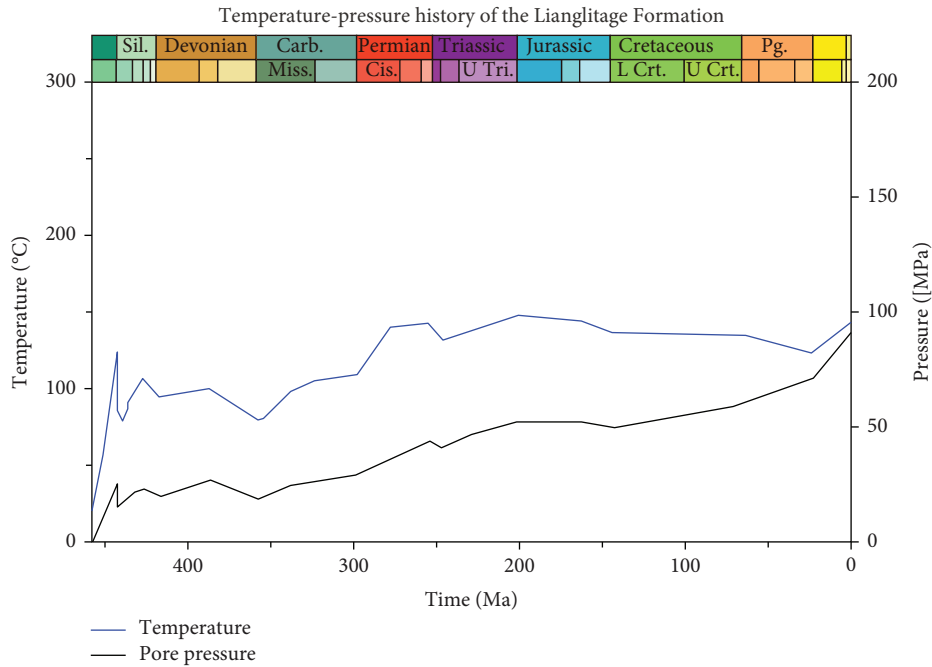


FIGURE 7: Temperature (T) and pressure (P) histories (upper) of the Lianglitage Formation (O_3) in Well ZG7-5.

investigate the reservoir evolution processes (Figure 9). The figure clearly shows that the P - T line goes across the coexisting phase zone of the gas and liquid to the condensate gas phase zone and the turning point (135.7°C , 58.19 MPa) corresponding to the age of 80 Ma (Late Cretaceous) appears at the point of intersection of the two lines. This suggests that the Lianglitage Formation (O_3) existed in the two-phase states of gas and liquid from Ordovician to 80 Ma (Late Cretaceous)

but, thereafter, turned to the condensate gas phase. This phenomenon clearly indicates that the condensate gas reservoir was formed after 80 Ma (Late Cretaceous) due to the changes in temperature and pressure conditions, which, in turn, were the result of the combined effect of multiple orogenies (the change of burial depth), as well as the heat flow evolution.

The changes in temperature and pressure controlled by heat flow evolution and multiple orogenies also affected fluid

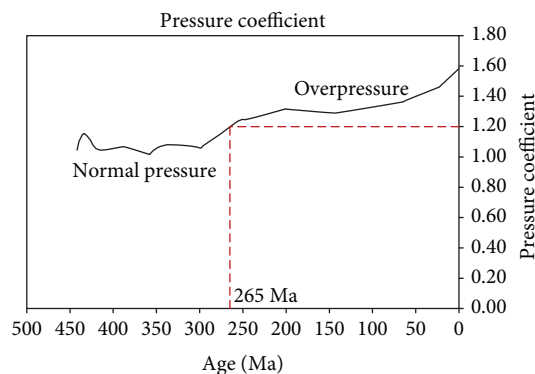


FIGURE 8: The pressure coefficient evolution of the Lianglitage Formation (O_3) in Well ZG7-5.

features. The evolutions of density, viscosity, and solution GOR during the entire geological processes are presented in Figure 10. From Ordovician to 80 Ma (Late Cretaceous), the fluid in the reservoir was composed of coexisting gas and liquid phases. The density of the liquid phase decreased gradually, while that of the gas fluctuated greatly and generally increased. On the contrary, the viscosity of the liquid phase fluctuated greatly, showing an overall decreasing trend and that of gas gradually increased. The fluctuations in density and viscosity are synchronized with the wave of burial depth. After 80 Ma (Late Cretaceous), the fluid turned into the condensate gas phase with increasing temperature and pressure. At the same time, the density and viscosity of the gas continually increased to reach the present values of 0.44 g/cm^3 and 0.0693 cP , respectively (Figures 10(a) and 10(b)). In the solution GOR, the amount of gas increased continuously; an increasing number of liquid hydrocarbons underwent the retrograde evaporation processes with continuous deep burial. This led the solution GOR to depict an overall increasing trend throughout the well-formation history; its value eventually reached $883 \text{ m}^3/\text{m}^3$ (Figure 10(c)). As mentioned above, after the Middle Permian (265 Ma), the overpressure state dominated the reservoir environment and the pressure coefficient increased rapidly after the Miocene. It is believed that the fluid expansion caused by retrograde evaporation is the main reason for the formation of overpressure. Moreover, the changes in pressure coefficient are also indirectly related with the alterations in GOR.

4.3.2. Gas Washing Conditions. From previous studies, it is known that oil charging occurred mainly in the Late Caledonian and Late Hercynian periods and that the gas filling that occurred mostly during the Late Himalayan period is one of the formation mechanisms of the condensate gas reservoirs in the Tazhong area [31]. In this context, it is hypothesized that the condensate gas reservoir of Well ZG7-5 was formed due to gas washing during the Late Himalayan. This assumes two different gas washing conditions: one, that the initial methane content is 0% (before being normalized) and that all the methane was a product of gas washing; therefore, the degree of gas washing can be set to 100%; the other is that half the methane (before being normalized) was from

gas washing, and therefore, the gas washing degree can be set to 50%. The specific fluid components (C_1 - C_{30+}) for these two cases are listed in Table 5 (only the amount of methane was varied; the other components were kept constant). We also assumed that 23 Ma (Late Himalayan) was the time at which the gas washing occurred, based on previous studies [32, 33]. The methods described above were then used to study the process of evolution with gas washing. The fluid phase evolution diagram of the Lianglitage Formation (O_3) in Well ZG7-5, considering gas washing, is shown in Figure 11. The P - T phase diagram in Figure 4 was also plotted in Figure 11 to represent the final P - T phase diagram of the gas-washed fluid.

In the 100% gas washing case, its initial phase diagram stayed in the high temperature and low pressure area because of the limited gas content and its critical point is 344.19°C and 11.79 MPa (Figure 11(a)). The fluid clearly existed as two phases, gas and liquid, from the Ordovician to the Middle Devonian (394 Ma). The fluid then transitioned quickly to the liquid phase before 383 Ma (Middle Devonian) and returned to the two-phase state again due to the changes in temperature and pressure conditions. After 331 Ma (Early Carboniferous), the fluid stayed in the liquid phase but turned into the condensate gas phase with gas washing in 23 Ma (Miocene) (Figure 11(a)).

There are some differences in the phase transition of the fluid when 50% of the gas was washed compared to when 100% of the gas was washed. The initial phase diagram of the former is in a lower temperature and higher pressure area compared to the latter because of its higher gas content, and its critical point is 149.09°C and 40.59 MPa (Figure 11(b)). The phase of the fluid remained in the two-state phase from the Ordovician to the Middle Permian (266 Ma), lasting longer than in the 100% gas washing case. Then, from 266 to 247 Ma (Middle Permian-Early Triassic), the fluid stayed in the liquid phase, with only a brief transition to the two-state phase. Finally, the fluid transitioned from the liquid phase to the condensate gas phase after gas washing in 23 Ma (Miocene). The occurrence time of the gas phase in the 50% gas washing case is longer than the 100% gas washing case. Thus, the critical phase turning time points for the 100% and 50% gas-washed fluid are 394, 383, 331, and 23 Ma, as well as 266 and 23 Ma, respectively.

The evolution of fluid density and viscosity in these two cases was also studied using the methods described above, and the results are shown in Figure 12. The figure also clearly shows the change of phase state. In the 100% gas washing case, the density of the liquid phase remained basically the same, fluctuating slightly in the 0.69 - 0.73 g/cm^3 range, while the gas phase existed for a shorter time but had values that changed more obviously (Figure 12(a)). Conversely, there was great fluctuation in the viscosity of the liquid phase but little fluctuation in the gas phase viscosity (Figure 12(b)).

In the 50% gas washing case, the fluctuations in density and viscosity were greater than those of the 100% gas washing case (Figures 12(c) and 12(d)). The density of the liquid phase first fluctuated greatly, with an overall decreasing trend, and then gradually increased. The density of the gas phase shows an increasing trend throughout. The sharp

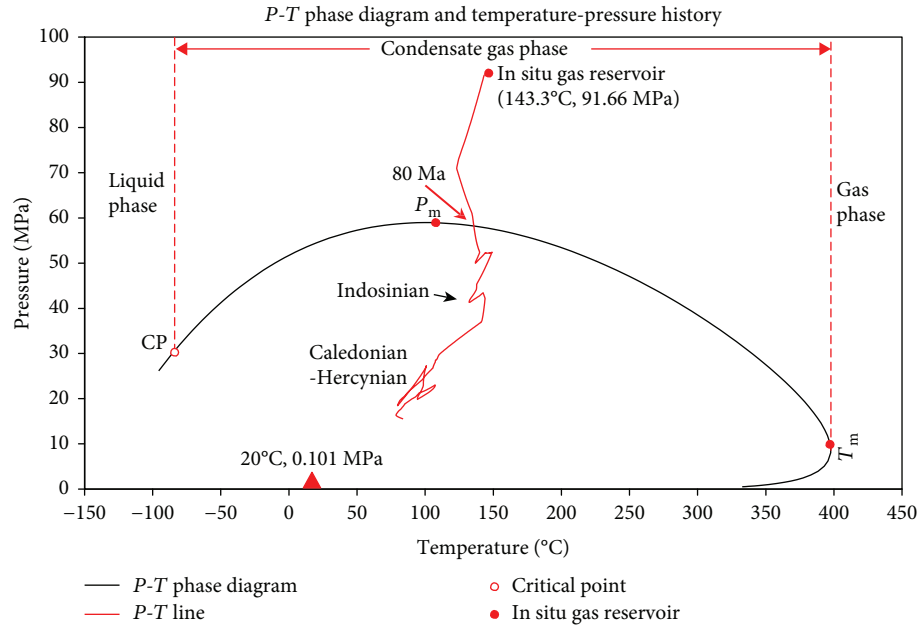


FIGURE 9: The fluid phase evolution diagram of the Lianglitage Formation (O_3) in Well ZG7-5 (under ideal conditions).

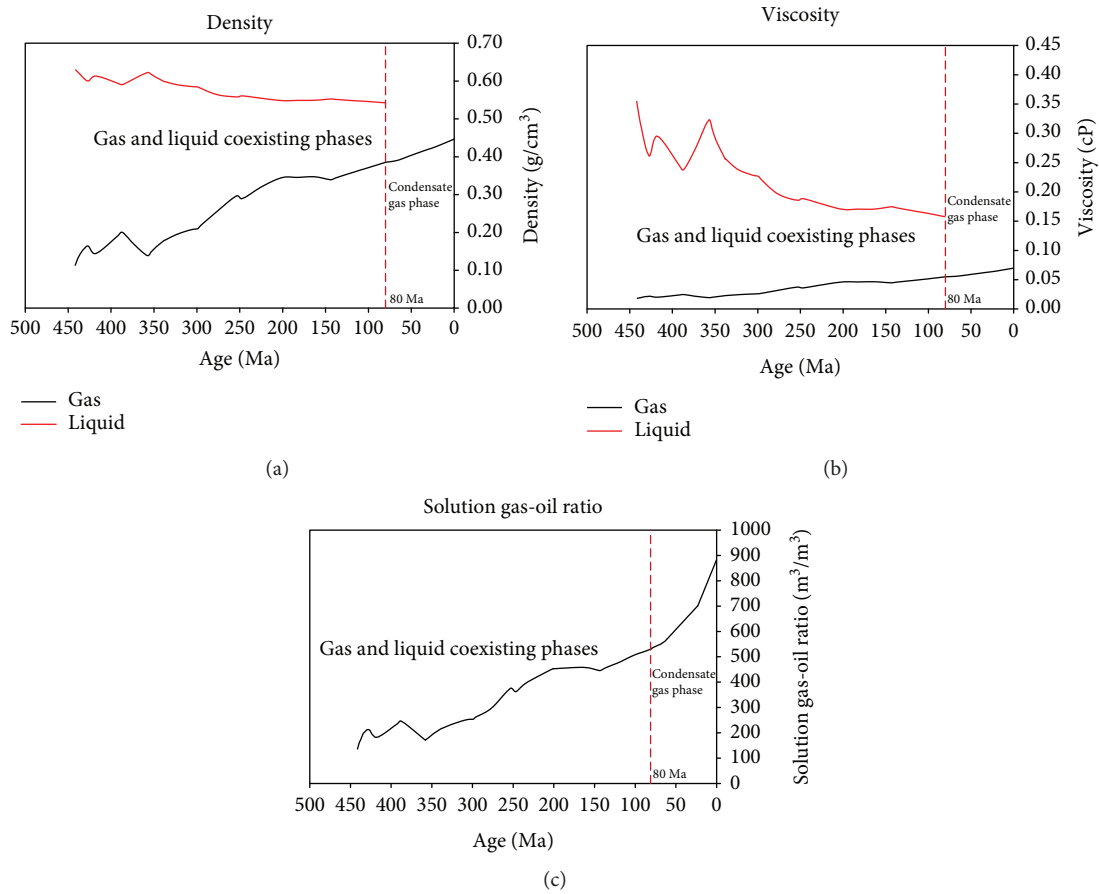


FIGURE 10: The evolution of fluid density, viscosity, and solution gas-oil ratio (GOR) under ideal conditions.

changes between 350 and 266 Ma (Early Carboniferous-Middle Permian) are believed to have been caused by the continuous burial and the high heat flow value during the

Carboniferous and Permian (Figure 12(c)) [34, 35]. The viscosity of the liquid phase also changed greatly while the viscosity of the gas phase increased gradually (Figure 12(d)).

TABLE 5: The specific well fluid components (C_1 - C_{30+}) of different gas washing degrees.

Gas washing degree		Components (%) (after normalized)																
		N ₂	CO ₂	C ₁	C ₂	C ₃	iC ₄	nC ₄	iC ₅	nC ₅	C ₆	C ₇	C ₈	C ₉	C ₁₀	C ₁₁	C ₁₂	C ₁₃
100%	25.013	18.175	0.000	2.151	1.218	0.461	1.200	0.869	1.017	1.655	1.862	9.723	8.121	6.708	5.124	3.688	3.062	
	C ₁₄	C ₁₅	C ₁₆	C ₁₇	C ₁₈	C ₁₉	C ₂₀	C ₂₁	C ₂₂	C ₂₃	C ₂₄	C ₂₅	C ₂₆	C ₂₇	C ₂₈	C ₂₉	C ₃₀₊	
	1.974	1.537	1.046	0.845	0.697	0.603	0.538	0.526	0.502	0.443	0.349	0.319	0.242	0.142	0.083	0.041	0.065	
50%	N ₂	CO ₂	C ₁	C ₂	C ₃	iC ₄	nC ₄	iC ₅	nC ₅	C ₆	C ₇	C ₈	C ₉	C ₁₀	C ₁₁	C ₁₂	C ₁₃	
	7.250	5.268	71.014	0.624	0.353	0.134	0.348	0.252	0.295	0.480	0.540	2.818	2.354	1.945	1.485	1.069	0.887	
	C ₁₄	C ₁₅	C ₁₆	C ₁₇	C ₁₈	C ₁₉	C ₂₀	C ₂₁	C ₂₂	C ₂₃	C ₂₄	C ₂₅	C ₂₆	C ₂₇	C ₂₈	C ₂₉	C ₃₀₊	
	0.572	0.445	0.303	0.245	0.202	0.175	0.156	0.152	0.146	0.128	0.101	0.093	0.070	0.041	0.024	0.012	0.019	

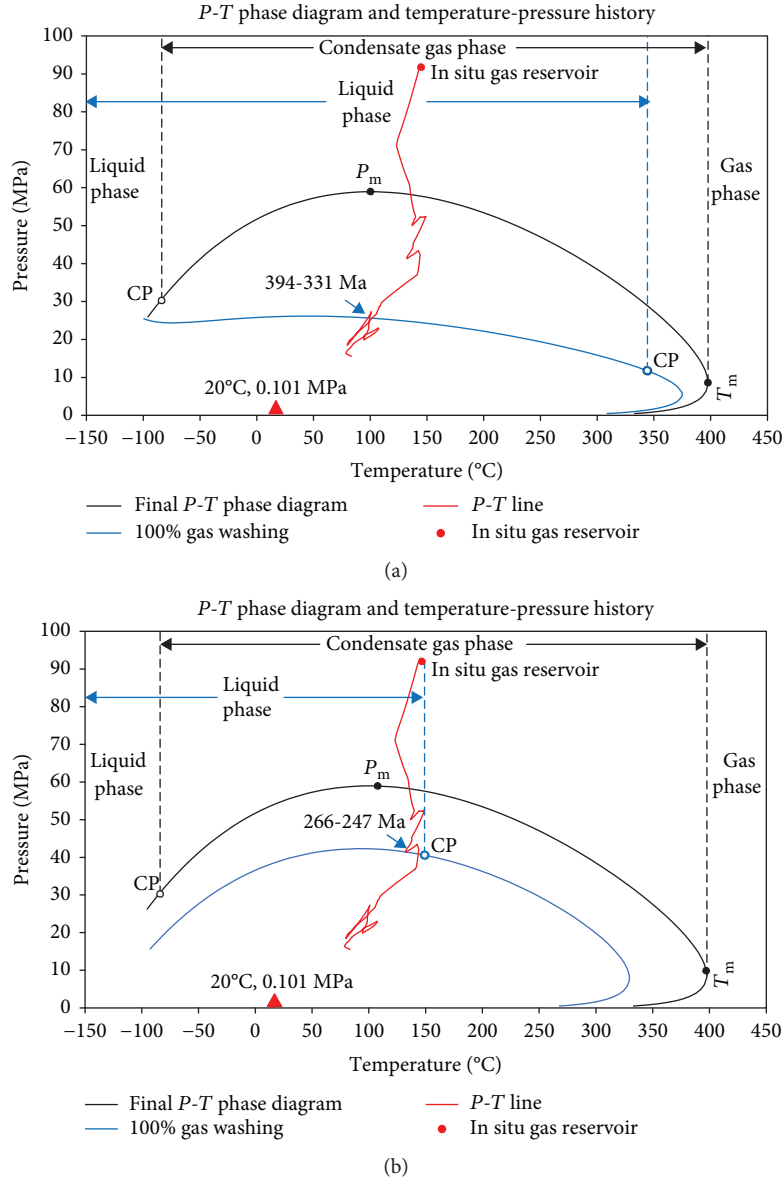


FIGURE 11: The phase evolution diagram of the fluid in the Lianglitage Formation (O_3) in Well ZG7-5, taking gas washing into account.

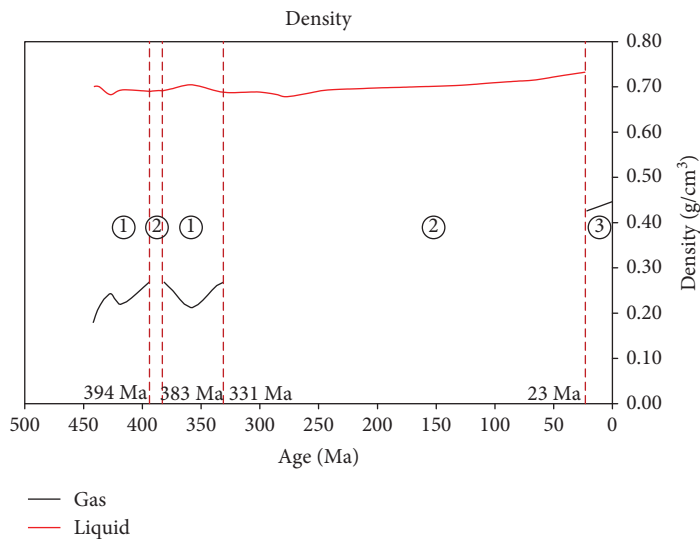
In general, the average liquid and gas phase densities and the liquid phase viscosity of the 50% gas washing case are smaller than those of the 100% gas washing case before 23 Ma (Miocene), whereas their gas phase viscosity values are similar. These results indicate that the degree of gas washing has a great impact on the fluid phase, phase transition point, and fluid features.

5. Conclusions

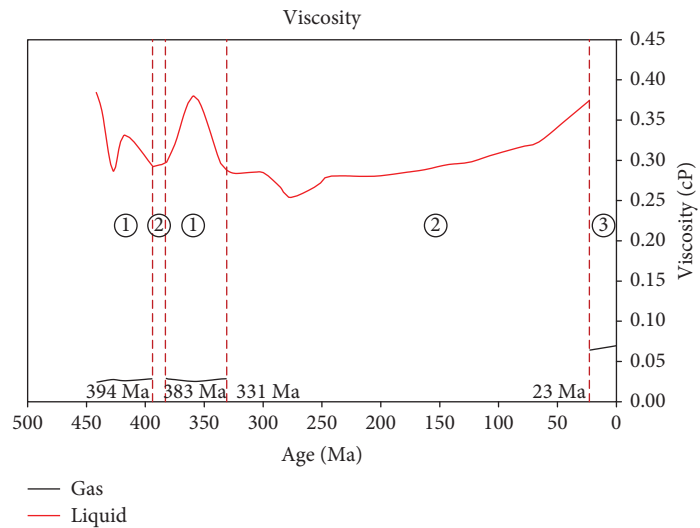
The simulated P - T phase diagram confirms that the studied reservoir is presently in the condensate gas phase, in the order CP - P_m - T_m . The modeled burial history shows that the Tazhong Uplift experienced multiple stages of uplift and erosion caused by multiple orogenies. The modeled temperature and pressure histories influenced by the burial history and the evolution of the heat flow show an overall

increasing trend from the Ordovician to the present. The reservoir experienced overpressure after the Middle Permian (265 Ma) because of the increasing pressure caused by the continuous subsidence; the pressure coefficient also increased rapidly after the Miocene.

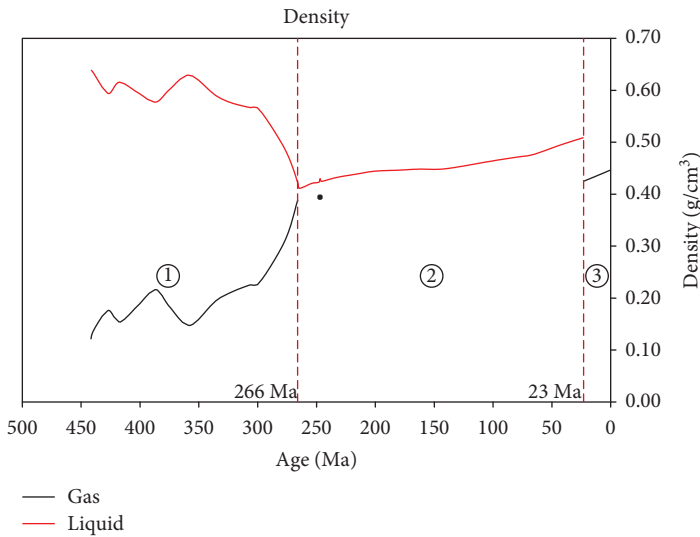
Under ideal conditions, the reservoir fluid was assumed to have formed without any destruction or change. The simulated results show that 80 Ma (Late Cretaceous, $T = 135.7^{\circ}\text{C}$, $P = 58.19$ MPa) was a key point in the phase transition from the two-state gas and liquid phases to the single-state condensate gas phase that led to the formation of the present condensate gas reservoir. The density and viscosity of the liquid phase decreased gradually while the density and viscosity of the gas phase increased with the increasing temperature and pressure during geological processes. The solution GOR increased throughout the history of the reservoir and eventually reached $883 \text{ m}^3/\text{m}^3$.



(a)



(b)



(c)

FIGURE 12: Continued.

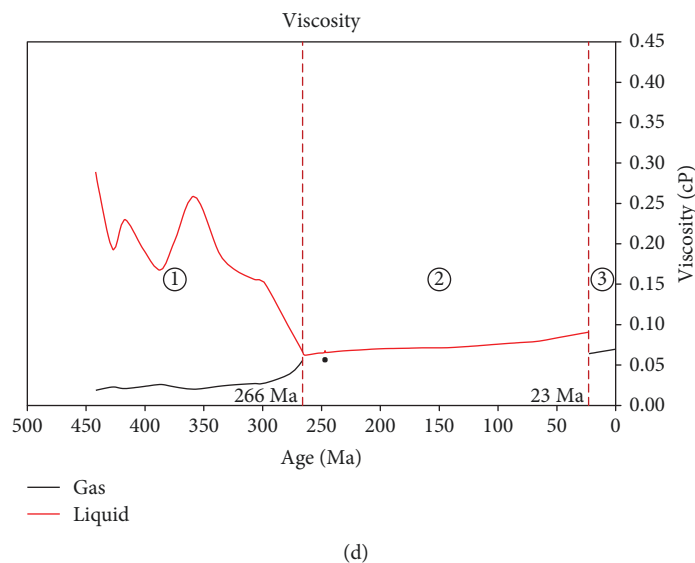


FIGURE 12: The evolution of the density and viscosity of the fluid in the Lianglitage Formation, taking gas washing into account. (a, b) 100% gas washing degree; (c, d) 50% gas washing degree. ①: coexisting gas and liquid phases; ②: liquid phase; and ③: condensate gas phase.

Taking the gas washing into consideration, it is hypothesized that the condensate gas reservoir was formed due to gas washing that occurred in the Late Himalayan (23 Ma). The simulations of gas washing degrees of 100% and 50% were designed to study how the gas washing affected the evolutionary history of the fluid phase. The results show that the critical time points in the change in the 100% and 50% gas washing cases are 394, 383, 331, and 23 Ma, as well as 266 and 23 Ma, respectively. The average liquid and gas phase densities and the liquid phase viscosity of the 100% gas washing case are greater than those of the 50% gas washing case before 23 Ma (Miocene). The gas phase viscosity of the two cases is similar.

The formation of condensate gas reservoirs in the Tazhong Uplift is associated not only with the changes in temperature and pressure controlled by burial history and the evolution of heat flow but also with the gas washing that occurred during the Late Himalayan, which played a critical role in forming the condensate gas reservoirs. This study confirms that both of these processes could result in the formation of condensate gas reservoirs. Moreover, it indicates that the method of integrating the PVTsim and the PetroMod software to study the phase simulations and evolution of a reservoir is useful and effective.

Data Availability

The data used to support the findings of this study are available from the corresponding author upon request.

Conflicts of Interest

The authors declare that there are no conflicts of interest regarding the publication of this paper.

Acknowledgments

This work was supported by the Strategic Priority Research Program of the Chinese Academy of Sciences (XDA14010103), the China National Major S&T Program (2017ZX05008-002-030), the GIG 135 Project (No. 135TP201602), and the NSFC Project (41372137). This is contribution No. IS-2716 from the Guangzhou Institute of Geochemistry, Chinese Academy of Sciences.

References

- [1] S. Zhang, G. Zhu, H. Yang et al., "The phases of Ordovician hydrocarbon and their origin in the Tabei uplift, Tarim Basin," *Acta Petrologica Sinica*, vol. 27, no. 8, pp. 2447–2460, 2011.
- [2] H. Yang and G. Zhu, "The condensate gas field geological characteristics and its formation mechanism in Tarim Basin," *Acta Petrologica Sinica*, vol. 29, no. 9, pp. 3233–3250, 2013.
- [3] S. Zendejboudi, M. A. Ahmadi, L. James, and I. Chatzis, "Prediction of condensate-to-gas ratio for retrograde gas condensate reservoirs using artificial neural network with particle swarm optimization," *Energy & Fuels*, vol. 26, no. 6, pp. 3432–3447, 2012.
- [4] E. Ganji-Azad, S. Rafiee-Taghanaki, H. Rezaei, M. Arabloo, and H. A. Zamani, "Reservoir fluid PVT properties modeling using adaptive neuro-fuzzy inference systems," *Journal of Natural Gas Science and Engineering*, vol. 21, pp. 951–961, 2014.
- [5] J. Tan, B. Horsfield, N. Mahlstedt et al., "Physical properties of petroleum formed during maturation of Lower Cambrian shale in the upper Yangtze Platform, South China, as inferred from PhaseKinetics modelling," *Marine and Petroleum Geology*, vol. 48, pp. 47–56, 2013.
- [6] R. Di Primio, V. Dieckmann, and N. Mills, "PVT and phase behaviour analysis in petroleum exploration," *Organic Geochemistry*, vol. 29, no. 1-3, pp. 207–222, 1998.
- [7] Z. Xingxi, W. Hongjun, C. Yicai, and X. Zhiming, "The study on the contributing factors of phase state of gas condensate:

- examples from Tarim Basin,” *Marine and Petroleum Geology*, vol. 15, no. 1, pp. 21–31, 1998.
- [8] H. Zhang, S. Zhou, D. Fu et al., “Petroleum phase state prediction in deep reservoir of Tashen-1 well in Tarim Basin,” *Natural Gas Geoscience*, vol. 24, no. 5, pp. 999–1004, 2013.
 - [9] Y. Tan, Y. Jiang, L. Zhao, X. Mu, and T. Xu, “Main controlling factors of phase evolution and charging pattern of hydrocarbons in northern Dongpu sag,” *Petroleum Geology & Experiment*, vol. 37, no. 1, pp. 28–34, 2015.
 - [10] S. Cui, H. Gu, S. Fang, and W. Yu, “Full component simulation of condensate gas in well Chunxiao 3 in Donghai oilfield,” *Petroleum Geology and Recovery Efficiency*, vol. 9, no. 1, pp. 54–56, 2002.
 - [11] L. Desheng, L. Digang, J. Chengzao, W. Gang, W. Qizhi, and H. Dengfa, “Hydrocarbon accumulations in the Tarim Basin, China,” *AAPG Bulletin*, vol. 80, no. 10, pp. 1587–1603, 1996.
 - [12] G. Zhu, A. V. Milkov, F. Chen et al., “Non-cracked oil in ultra-deep high-temperature reservoirs in the Tarim Basin, China,” *Marine and Petroleum Geology*, vol. 89, pp. 252–262, 2018.
 - [13] C. Jia, *Tectonic Characteristics and Petroleum, Tarim Basin*, Petroleum Industry Press, China, 1997.
 - [14] H. Pang, J. Chen, X. Pang et al., “Analysis of secondary migration of hydrocarbons in the Ordovician carbonate reservoirs in the Tazhong uplift, Tarim Basin, China,” *AAPG Bulletin*, vol. 97, no. 10, pp. 1765–1783, 2013.
 - [15] S. Li, X. Pang, Z. Jin et al., “Petroleum source in the Tazhong uplift, Tarim Basin: new insights from geochemical and fluid inclusion data,” *Organic Geochemistry*, vol. 41, no. 6, pp. 531–553, 2010.
 - [16] Q. Liu, Z. Jin, H. Li et al., “Geochemistry characteristics and genetic types of natural gas in central part of the Tarim Basin, NW China,” *Marine and Petroleum Geology*, vol. 89, pp. 91–105, 2018.
 - [17] X. Zhou, X. Pang, Q. Li et al., “Advances and problems in hydrocarbon exploration in the Tazhong area, Tarim Basin,” *Petroleum Science*, vol. 7, no. 2, pp. 164–178, 2010.
 - [18] J. Chen, X. Pang, and Z. Jiang, “Controlling factors and genesis of hydrocarbons with complex phase state in the upper Ordovician of the Tazhong area, Tarim Basin, China,” *Canadian Journal of Earth Sciences*, vol. 52, no. 10, pp. 880–892, 2015.
 - [19] Y. Zhang, X. Lyu, H. Yu, B. Jing, C. Zhang, and J. Cai, “Controlling mechanism of two strike-slip fault groups on the development of the Ordovician karst reservoirs in the Tazhong uplift, Tarim Basin,” *Oil & Gas Geology*, vol. 37, no. 5, pp. 663–673, 2016.
 - [20] P. Dimitrakopoulos, W. Jia, and C. Li, “An improved computational method for the calculation of mixture liquid–vapor critical points,” *International Journal of Thermophysics*, vol. 35, no. 5, pp. 865–889, 2014.
 - [21] W. A. England, “Empirical correlations to predict gas/gas condensate phase behaviour in sedimentary basins,” *Organic Geochemistry*, vol. 33, no. 6, pp. 665–673, 2002.
 - [22] X. Yao and Y. Wang, “Assessing shale gas resources of Wufeng-Longmaxi shale (O3w-S1l) in Jiaoshiba area, SE Sichuan (China) using PetroMod I: burial and thermal histories,” *Petroleum Science and Technology*, vol. 34, no. 11–12, pp. 1000–1007, 2016.
 - [23] M. Mei, K. K. (. A.). Bissada, T. B. Malloy, L. M. Darnell, and Z. Liu, “Origin of condensates and natural gases in the Almond Formation reservoirs in southwestern Wyoming, USA,” *Organic Geochemistry*, vol. 124, pp. 164–179, 2018.
 - [24] C. Shangbin, Z. Yanming, C. Si, H. Yufu, F. Changqing, and F. Junhua, “Hydrocarbon generation and shale gas accumulation in the Longmaxi Formation, southern Sichuan Basin, China,” *Marine and Petroleum Geology*, vol. 86, pp. 248–258, 2017.
 - [25] Y. Zhang, Z. Jin, G. Liu, and J. Li, “Study on the formation of unconformities and the amount of the eroded sedimentation in the Tarim Basin,” *Earth Science Frontiers*, vol. 7, no. 4, pp. 449–457, 2000.
 - [26] X. Pang, C. Jia, H. Pang, and H. Yang, “Destruction of hydrocarbon reservoirs due to tectonic modifications: conceptual models and quantitative evaluation on the Tarim Basin, China,” *Marine and Petroleum Geology*, vol. 91, pp. 401–421, 2018.
 - [27] Y. Qi and G. Liu, “Wave process analysis and erosion thickness study of unconformities in the sedimentary basin: examples of the Tarim Basin, Xinjiang,” *Journal of Jiaozuo Institute of Technology*, vol. 18, no. 3, pp. 161–165, 1999.
 - [28] N. Qiu, J. Chang, Y. Zuo, J. Wang, and H. Li, “Thermal evolution and maturation of lower Paleozoic source rocks in the Tarim Basin, Northwest China,” *AAPG Bulletin*, vol. 96, no. 5, pp. 789–821, 2012.
 - [29] L. Wang, C. Li, and Y. Shi, “Distribution of terrestrial heat flow density in the Tarim Basin,” *Acta Geophysica Sinica*, vol. 38, no. 6, pp. 855–856, 1995.
 - [30] C. G. Feng, S. W. Liu, L. S. Wang, and C. Li, “Present-day geothermal regime in Tarim Basin, Northwest China,” *Chinese Journal of Geophysics*, vol. 52, no. 6, pp. 1237–1250, 2009.
 - [31] H. Yang, G. Zhu, J. Han et al., “Conditions and mechanism of hydrocarbon accumulation in large reef-bank karst oil/gas fields of Tazhong area, Tarim Basin,” *Acta Petrologica Sinica*, vol. 27, no. 6, pp. 1865–1885, 2011.
 - [32] G. Zhu, B. Zhang, H. Yang, J. Su, K. Liu, and Y. Zhu, “Secondary alteration to ancient oil reservoirs by late gas filling in the Tazhong area, Tarim Basin,” *Journal of Petroleum Science and Engineering*, vol. 122, pp. 240–256, 2014.
 - [33] S. Zhang, B. Zhang, H. Yang, G. Zhu, J. Su, and X. Wang, “Adjustment and alteration of hydrocarbon reservoirs during the late Himalayan period, Tarim Basin, NW China,” *Petroleum Exploration and Development*, vol. 39, no. 6, pp. 712–724, 2012.
 - [34] J. Li, Z. Li, N. Qiu, Y. Zuo, J. Yu, and J. Liu, “Carboniferous–Permian abnormal thermal evolution of the Tarim Basin and its implication for deep structure and magmatic activity,” *Chinese Journal of Geophysics*, vol. 59, no. 9, pp. 3318–3329, 2016.
 - [35] H. Li, N. Qiu, Z. Jin, and Z. He, “Geothermal history of Tarim Basin,” *Oil & Gas Geology*, vol. 26, no. 5, pp. 613–617, 2005.

Research Article

Towards a Better Knowledge of Natural Methane Releases in the French Alps: A Field Approach

Frédéric Gal , Eric Proust, and Wolfram Kloppmann

BRGM, 45060 Orléans, France

Correspondence should be addressed to Frédéric Gal; f.gal@brgm.fr

Received 15 March 2019; Accepted 30 April 2019; Published 10 June 2019

Guest Editor: Guodong Zheng

Copyright © 2019 Frédéric Gal et al. This is an open access article distributed under the Creative Commons Attribution License, which permits unrestricted use, distribution, and reproduction in any medium, provided the original work is properly cited.

We report investigations performed at some hydrocarbon gas seeps located in the French Subalpine Chains in zones of outcropping Jurassic black shales, increasing the reported number of such occurrences in this part of the Alps. We present the characteristics of each of the seeps, based on soil flux measurements and soil gas measurements. Gases emitted are CH₄-rich (87–94%) with the exception of one site (78.5% CH₄ + 8.2% CO₂) where an active landslide may induce dilution by atmospheric air. CO₂ is generally measured at low levels (<1.6%). Concentrations in C₂H₆ are more variable, from less than 1% to more than 2.3%. Gas is emitted over areas of various sizes. The smallest gas emission area measures only 60 × 20 cm, characterized by a strong hydrocarbon flux (release of about 100 kg of CH₄ per year). At a second site, hydrocarbon emissions are measured over a surface of 12 m². For this site, methane emission is evaluated at 235 kg per year and CO₂ emission is 600 kg per year, 210 kg being related to gas seepage. At the third site, hydrocarbons are released over a 60 m² area but strong gas venting is restricted to localized seeps. Methane emission is evaluated at 5.1 tons per year and CO₂ emission at 1.58 tons per year, out of which 0.53 tons are attributed to gas seepage. Several historical locations remain uninvestigated at present, and numerous others may still be unknown. We outline strategies to search for such unrecorded sites. Considering the topography of the potential alpine and perialpine emission areas, the possibilities to detect gas emissions appear of the size recorded so far seem to be restricted to ground-based methods or to methods offering the possibility to point orthogonally to the soil towards the seep maximum. If such sites are to be investigated in the future in the frame of Environmental Baseline Assessment (EBA), even establishing appropriate monitoring protocols will be challenging.

1. Introduction

The occurrence of natural Earth degassing—and specifically hydrocarbon degassing—is known since very ancient times. In Europe, methane seeps are reported since the Roman period, e.g., in Greece [1], in Turkey [2], and in France [3]. Later, especially during the XIXth century, in conjunction with the hydrocarbon rush, some of these natural gas releases were investigated in more detail to assess their exploitability [3]. Nowadays, the growing interest for natural hydrocarbon seepage areas has two main angles: firstly, to better understand the production mechanisms of the hydrocarbon gas phases [4] and specifically to determine if the gas is produced by thermal or biological processes from organic matter [5, 6] or by abiotic reactions involving hydrogen [7]; secondly, to better describe the degassing patterns [8], to identify gas

migration pathways, and to quantify the amounts of gases released into the atmosphere [4, 9] and the related impacts onto the global atmospheric methane budget [10]. These investigations are in relation with environmental concerns related to the increasing share of unconventional gas exploitation [11] and to natural and man-induced gas emissions from hydrocarbon fields [12, 13] with a special focus on the integrity of gas and oil wells [14], including abandoned wells [15]. It is well established that gas seeps not only induce free gas emissions but also increase dissolved gas levels in aquifers [16–18] where their quantifications can be quite challenging [19, 20]. Here, we focus on the quantification of free gas leaks at the soil/atmosphere interface [10] where the influence of external parameters (temperature, soil properties, humidity, and so on) on the measurements of gas emissions needs to be taken into account [21].

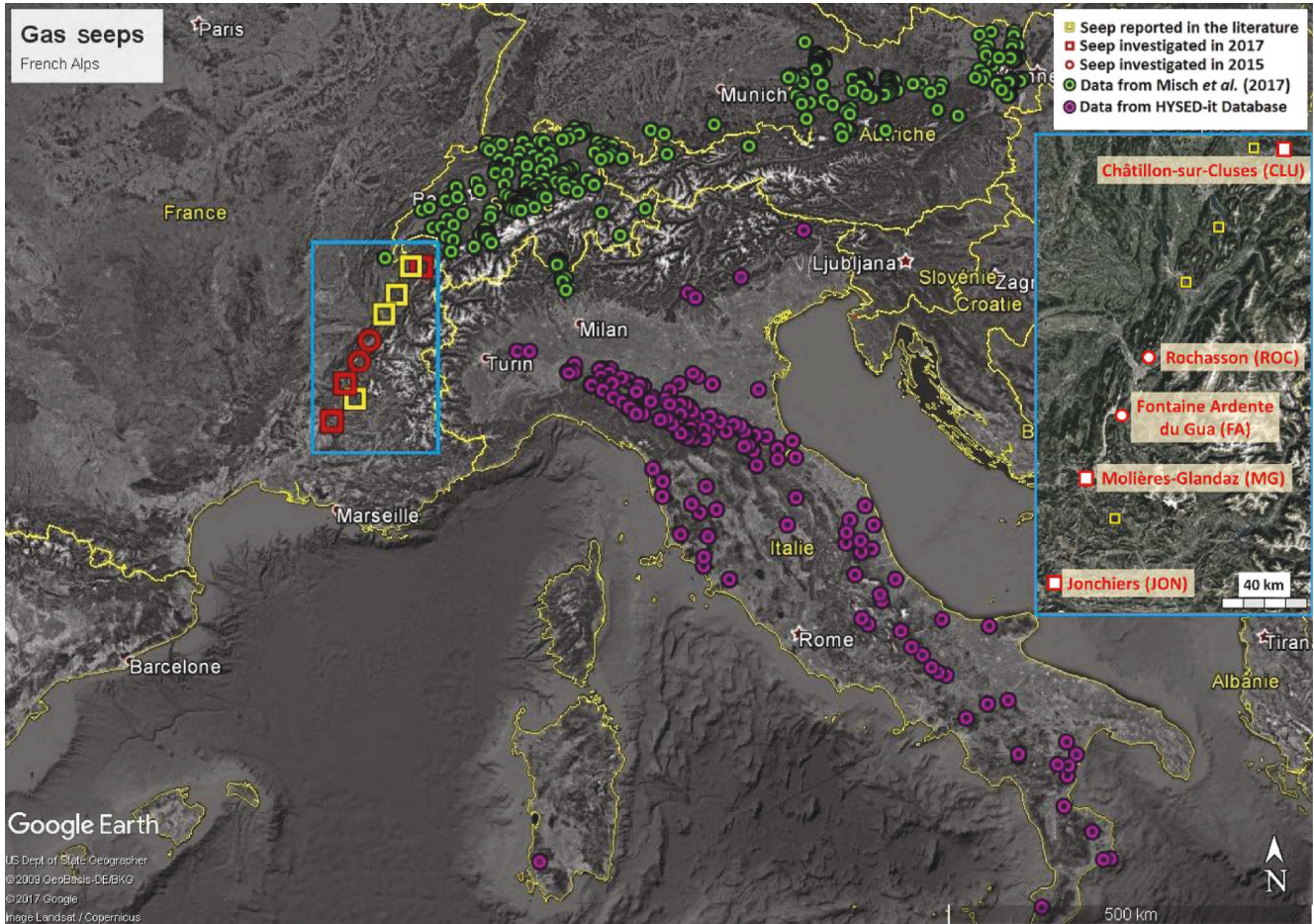


FIGURE 1: Gas seeps reported at the scale of the alpine chain. The blue inset details the locations of French CH_4 -rich seeps (in red: investigated locations).

Investigations of the most prominent French alpine gas seep, the Fontaine Ardente du Gua, have been recently reported [3] together with preliminary reconnaissance of a gas seep of lesser importance (Rochasson gas seep; [22]). When comparing the few known occurrences in the French Subalpine arc to the number of gas seeps reported for Italy (HYSED database; [23]) and for Switzerland, Germany, and Austria [5, 24, 25], mainly situated in the molasses basins, we suspect a significant knowledge gap, even though the lithological and tectonic contexts as well as the thermal history are not directly comparable. Thanks to an in-depth literature review, including “grey” historical literature, we localized several other sites prone to the release of hydrocarbon gases (Figure 1).

Here, we report field investigations performed at some of those newly localized sites (red symbols in Figure 1) as, from South to North, Jonchiers (JON), Molières-Glandaz (MG), and Châtillon-sur-Cluses (CLU). A fourth site (Rochasson (ROC)), already monitored in 2015, was investigated again because a landslide had modified its surface in 2016. Investigations were focused on the quantification and spatial patterns of gas emissions to the atmosphere as contributions to the greenhouse gas budget. Soil flux measurements using an accumulation chamber system were performed at all the sites

with the exception of JON. Soil gas analyses allowed estimating precisely the relative proportions of gas species.

2. Geological Settings

In their article in 1990, mainly focused on CO_2 emissions in the French southeast basin, Blavoux and Dazy [26] mentioned the occurrence of mofettes (natural gas seeps) among which some are methane-bearing including JON, MG, and the Fontaine Ardente du Gua (FA). For FA, we provided detailed information in Gal et al. [3]. Gas emissions reported at the Col de Cabre could not be investigated due to safety issues as these emissions were encountered during the drilling of a railway tunnel in 1887 [27]. Nonetheless, the probable source rocks for this site are black shale formations similar to those outcropping at Fontaine Ardente du Gua [3].

The Jonchiers site (JON; Figure 2) is located close to the town of Buis-les-Baronnies. This seep is associated with black shale formations of the Oxfordian age [27]. Local inhabitants discovered this methane seep indirectly by observing persistent flames after having practiced fire clearance (pers. comm.). Blavoux and Dazy [26] reported an analysis of the gas phase with dominant CH_4 (71.97%) and high concentrations in CO_2 (8.39%) and H_2 (5.19%), completed by N_2 (9.51%). These



FIGURE 2: Overview of the sites: from left to right and from top to bottom: Rochasson (ROC), Châtillon-sur-Cluses (CLU), Jonchiers (JON), and Molières-Glandaz (MG). FA: Fontaine Ardente du Gua (see [3]).

authors also reported an isotope analysis of the carbon of the methane ($\delta^{13}\text{C}_{\text{CH}_4} = -39.7\text{‰}$ vs. PDB), suggesting a dominant thermogenic origin for this gas phase. The location of this gas seep reported in the subsoil database BSS of the French Geological Survey (site BSS002BPZV; [28]) revealed to be erroneous (the real location is 730 m to the ESE).

The Molières-Glandaz site (MG; Figure 2) is not reported in any geological database. Blavoux and Dazy [26] only mentioned a location called “les Tiogaux” which corresponds to a farm. Nevertheless, they report a historical analysis from 1916: 70.16% of CH_4 , 14.05% of H_2 , 4.8% of C_2H_6 , 2.89% of N_2 , 1.2% of O_2 , and 0.3% of CO_2 . This alkane-rich gas is also seeping from black shale formations of the Callovian to Oxfordian age. Hints from the inhabitants oriented our investigations to a dry creek where we detected the seep organoleptically, through its characteristic hydrocarbon smell. Inhabitants have known the existence of this gas seep from immemorial times. It was discovered by observing gas bubbling in the creek during wet periods.

The Rochasson site (ROC; Figure 2) has been previously investigated [22]. This gas seep is again located in shale formations and has been only recently discovered in the 1970s in the course of geological investigations [29]. The gas phase is dominated by CH_4 (95%), with some C_2H_6 (1.9%) and only traces of CO_2 (0.4%), N_2 (0.35%), C_3H_8 (0.3%), and ^4He (0.007%). For comparison, the neighbouring Fontaine Ardente du Gua (FA) is less methane-rich (85 to 90%) and enriched in CO_2 (9 to 11%), other gas phases being N_2 (1%), Ar (<0.07%), ^4He (0.018 to 0.025%), and C_2H_6 (0.0002 to 0.058%), as measured in 2015 and 2016 [3].

The last investigated site is located much further in the north of the French Subalpine Chains, close to the municipi-

ality of Châtillon-sur-Cluses (CLU; Figure 2). Contrarily to the other seeps, it is not related to obvious Callovo-Oxfordian black shale outcrops. The existence of gas emission is reported since the XIXth century [30], and an analogy was made with the eternal flames occurring in the Caucasus or in Turkey (see references to Pliny the Elder in [2]). The gas was, at that time, collected at 16 m depth in argillaceous and gypsum formations covered by glacial deposits and used to light houses. Some decades later, a more detailed description was given by Omer [31]. Two locations were prone to gas emissions. The first emission zone was located in the backyard of a house, and some of the gas emerged from a crack of the floor inside a room. The second emission zone was located in a meadow and was discovered by a farmer who observed a bare surface of about 100 square meters, where the earth seemed “burned.” After having dug a hole in the ground, he heard a hissing gas, which caught fire instantly after approaching a burning match. These two locations are reported in the French BSS geological database (respectively, recordings BSS001RKMM and BSS001RKML; [28]). The gas phase is essentially methane, and production has been attributed in 1925, without proof, to the degassing of Eocene lignite-rich formations [32]. It can be noted that Lower Jurassic marls (Toarcian) outcrop near the site and have been noted as gas-bearing in a 45 m drillhole (BSS001RKML) even though their thickness cannot be compared to the sites further south. We report only the data from the first site, close to the house. The site owner provided instructive information on the zone (M. Dumont, pers. comm.): the area has been recently subject to a landslide which is currently monitored. Consequently, gas emissions to the atmosphere may be different from those described in the past.

3. Materials and Methods

The monitoring uses two well-established methods, soil gas flux measurements and soil gas concentration measurements. For all sites, soil gas flux measurements at the soil/atmosphere interface were performed. For most sites, these flux measurements were completed by soil gas measurements at 1 m depth. A detailed overview of these two techniques can be found in the literature [3, 33]; below, we provide a summary of the methods used.

Soil gas flux measurements were performed [using the accumulation chamber technique, with external recirculation] (Echo Instruments, Slovenia). The [...] chamber has a semi-spherical geometry with a basal area of 0.0289 m^2 and a volume of 0.0018 m^3 (soft ground) to 0.0023 m^3 (hard ground) [and is equipped with a fan with tunable speed for mixing of the headspace gas]. Pressure, temperature and relative humidity inside the chamber are continuously monitored. CO_2 and CH_4 [are measured] by Non-Dispersive Infra-Red (NDIR) detectors (0 to $5000 \text{ ppmv} \pm 2\%$ and 0 to $10000 \text{ ppmv} \pm 5\%$ [...] respectively), O_2 and H_2S by electrochemical cells (0 to $25\% \text{ vol.} \pm 2\%$ of the reading and 0 to $10000 \text{ ppmv} \pm 5\%$ of the reading respectively). [...] The flux measurement was based on the rate of CH_4 and CO_2 accumulation (positive fluxes) and possible opposite O_2 decrease (“negative” fluxes), in the chamber. Usually positive values indicate fluxes directed from the soil to the atmosphere and negative values flow from the atmosphere into the soil. [Most flux measurements were performed directly on the clayey soil surface with little to absent soil litter. Flux measurements at CLU site were performed on a grassy soil surface.] [3]

Soil gas concentrations were measured [in a 10 mm hole drilled down to 1 m depth. A copper] sampling tube was inserted [...] and an Infra-Red Gas Analyzer (IRGA, LFG20 by ADC Gas Analysis Ltd., UK) was plugged, pumping at low flow rate ($200 \text{ mL} \cdot \text{min}^{-1}$). [...] [Readings (CH_4 , CO_2 and O_2 gas concentrations) are taken once] steady state conditions [are reached, usually] within tens of seconds. Analytical precision for CO_2 and CH_4 was $\pm 0.5\%$ for low concentration range (0.01 – $10\% \text{ vol.}$), $\pm 3\%$ for higher concentrations (10 to $50\% \text{ vol.}$) and up to $\pm 5\%$ above $50\% \text{ vol.}$ [...]. The precision for oxygen was $\pm 0.4\%$ full scale reading (0 – $25\% \text{ vol.}$). [The most methane-rich samples were collected in Isotubes® for further laboratory characterization of the gas phase, encompassing] permanent gases (CO_2 , O_2 , N_2 , Ar), alkanes (CH_4 , C_2H_6 , C_3H_8) and ^4He . Detection limits are 10 ppm for permanent gases, 2 ppm for alkanes and 50 ppm for helium. Precision of the measurement is better than 2% at full scale. [3]

Flux measurements preceded soil gas measurements to avoid introducing artefacts due to altered soil permeability. The only exception is the ROC site where soil gas was measured during a previous campaign in 2015. This site was subject to a landslide in between the two surveys in 2015 and 2017, so that the ground surface has been totally reshaped and the locations where soil gas concentrations had been measured two years before have disappeared.

4. Results and Discussion

4.1. Meteorological Conditions. Meteorological conditions are known to have adverse effect on soil gas emissions from the soil under certain conditions, especially when weather is rainy [21, 34]. The field survey was performed during one week in early September 2017. During this period, weather conditions were dry and no rainfall event occurred (Figure 3). The atmospheric pressure was particularly high. If high-pressure conditions are sometimes reported to reduce gas emissions [34], this may not be always the case [33]. During the survey, the pressure conditions were stable. If gas emissions were reduced by the effect of high-pressure conditions, this effect would have concerned the complete monitoring period so that a hypothetical variability of the gas emissivity linked to pressure effects would be very low. Some thunderstorms occurred some days before the survey, but the amounts of rainfall were highly variable from one location to the other (from less than 10 mm up to 30 mm). Thunderstorms are also events that have generally a local influence, and their impact at a distance of some kilometers to tens of kilometers may be low to inexistent. We used the indications of the relative humidity sensor inside the flux chamber to assess local humidity conditions (Figure 3). Relative humidity in the air pumped from the soil is low, between 31% and 74% , with a mean value of 50.6% . This is in accordance with limited rainfall amounts and a 10-day period without any rainfall event at the end of August. The effect of humidity on gas emissions is thus negligible.

4.2. Soil Gas Fluxes and Soil Gas Concentrations. Data are presented in Figure 4 as boxplots. Datasets are provided as supplementary material (available here). At the JON site, no methane flux measurements could be performed. Soil background CO_2 flux in the surroundings of the seep is generally low ($<1 \text{ g} \cdot \text{m}^{-2} \cdot \text{h}^{-1}$) and matches with the values reported for biologically produced CO_2 flux [35]. Only one measurement is higher but still falls in the range of biological CO_2 fluxes reported in summer in France [36]. The CO_2 concentrations are between 1 and 2% with slight O_2 depletion compared to the atmosphere. Soil gas emitted at the seep is diluted by atmospheric air as drilling into the clayey formations, and the subsequent measurements were only possible to 30 cm of depth. By correcting this dilution, assuming zero O_2 , the gas composition was recalculated as follows: high CH_4 concentration (87%); abundant N_2 (10%); presence of CO_2 (1.6%), C_2H_6 (0.87%), and C_3H_8 (0.235%); and traces of C_4H_{10} (0.071%), C_5H_{12} (0.019%), and ^4He (0.025%).

At the MG site, only soil gas flux was measured (Figure 4) with the exception of one soil gas measurement sampled at the vent immediately after the flux measurements. CO_2 flux measurements outside the gas seepage area yielded values similar to those measured at the JON site. For about one-third of the measurements, elevated CH_4 fluxes were measured, ranging from less than 30 to $220 \text{ g} \cdot \text{m}^{-2} \cdot \text{h}^{-1}$. At the most emissive point, three repeated measurements obtained fluxes of 220 , 182 , and $204 \text{ g} \cdot \text{m}^{-2} \cdot \text{h}^{-1}$. Intrinsic “pulsations” [5] of the seep can explain this variability as suggested by short-term changes of flame size [37]. Nonetheless, the variations are

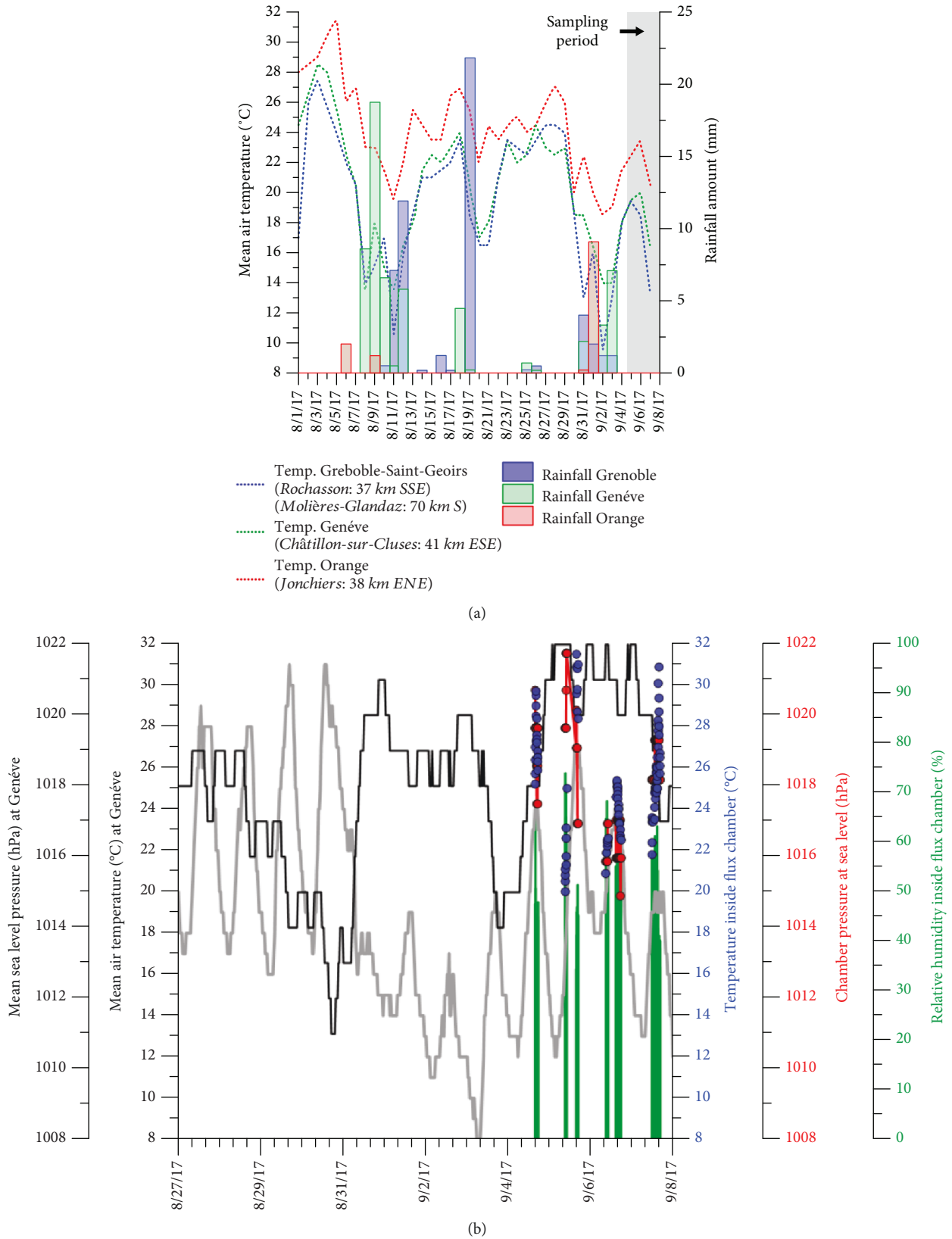


FIGURE 3: Meteorological parameters before and during the survey. (a) Daily mean air temperatures and rainfall amounts taken at the nearest airport weather stations (data from <https://freemeteo.fr>); distance between gas seeps and airports is indicated in the caption. (b) Hourly pressure and temperature data from Geneva (Genève) airport compared to temperature and pressure data measured using the flux chamber system during the measurements. Bar chart gives the relative humidity inside the chamber during the measurements.

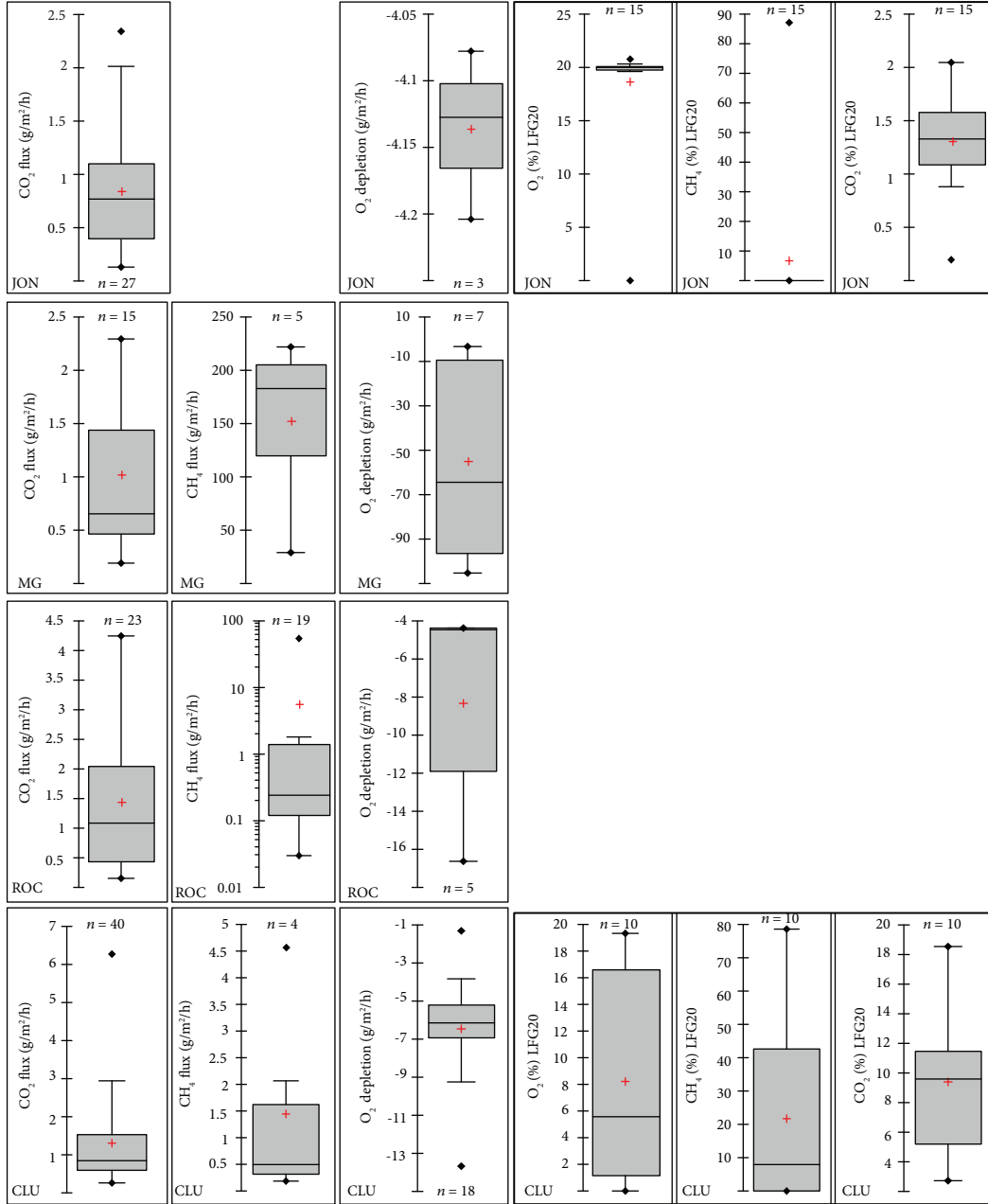


FIGURE 4: Boxplots for the four monitored locations; from left to right: CO₂ flux, CH₄ flux, O₂ depletion, and, if measured, O₂, CH₄, and CO₂ soil gas concentrations.

relatively weak with a standard deviation of less than $\pm 15\%$ [38], showing a good reproducibility of the flux measurements. If the lowest measured CH₄ flux is comparable to the upper range of diffuse seepage measured near the FA gas seep [3], the highest values are similar to some seeps reported by Etiope [2] in Greece or in Romania. In general, a strong depletion in oxygen in the chamber is linked to an increase in methane. The gas phase emitted at the MG site is CH₄-rich (94.2%), with abundant C₂H₆ (2.36%), residual N₂ (0.65%), and traces of CO₂ (0.31%), C₃H₈ (0.40%), C₄H₁₀ (0.056%), C₅H₁₂ (0.006%), and ⁴He (0.012%).

By comparison, the seepage intensity of the ROC site is apparently lower (maximum CH₄ flux of $54 \text{ g} \cdot \text{m}^{-2} \cdot \text{h}^{-1}$), but

the size of the degassing area is much larger (a CH₄ flux was detected for more than 80% of the points). The O₂ depletion inside the chamber is also lower. The CO₂ flux can punctually reach a relatively high value ($4.23 \text{ g} \cdot \text{m}^{-2} \cdot \text{h}^{-1}$) suggesting that part of the emitted CO₂ may originate from the seep. Strong CO₂ enrichment in the soil formations has been reported earlier at the ROC site [22].

The present-day methane emission at the CLU site is not as high as it could have been expected from historical literature. The highest value is only $4.56 \text{ g} \cdot \text{m}^{-2} \cdot \text{h}^{-1}$, and only 4 points from 40 showed methane emission. Nevertheless, O₂ depletion in the chamber was monitored more frequently, suggesting that even in cases where the CH₄ flux is not

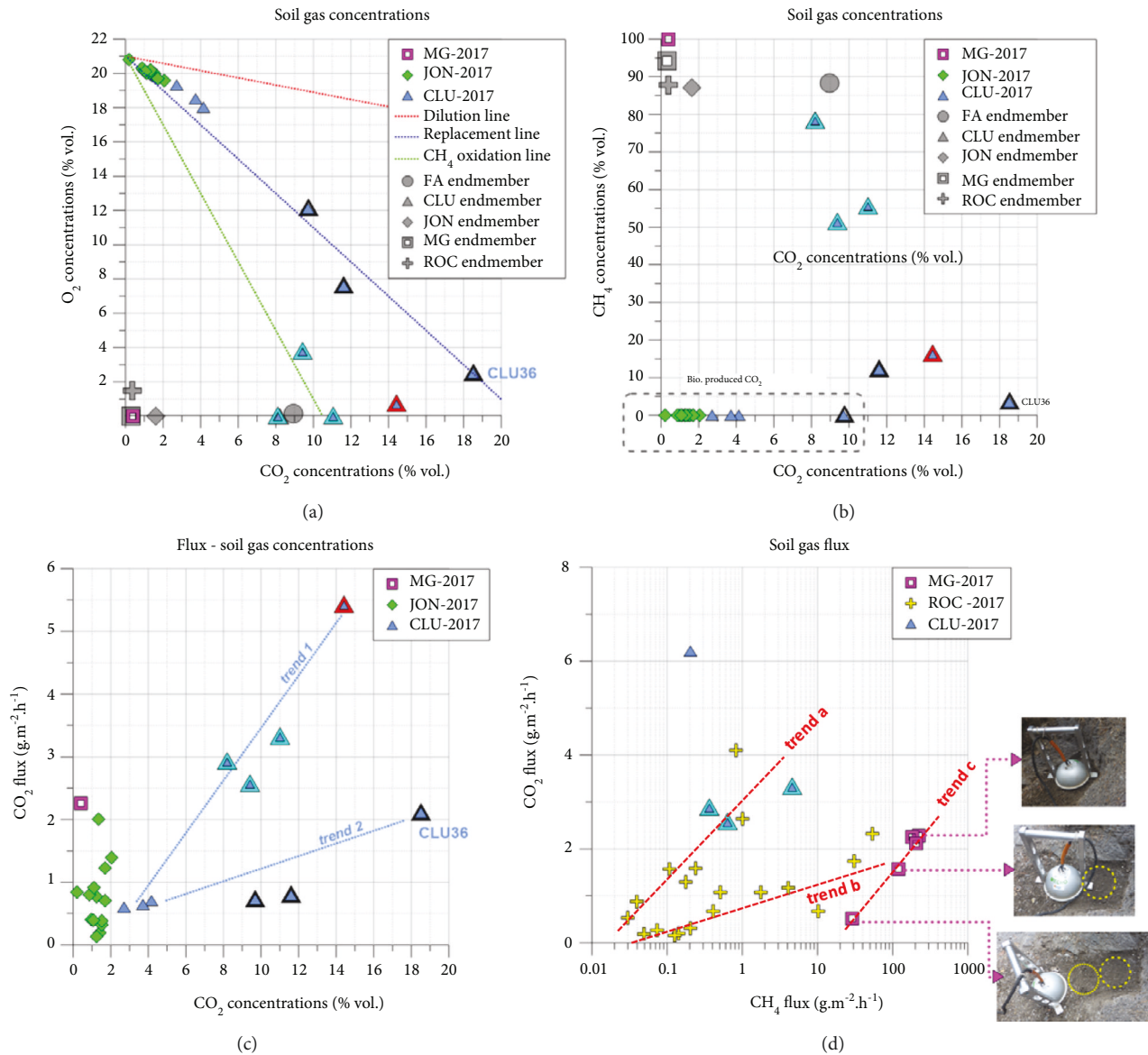


FIGURE 5: Binary plots showing (a) the O₂ concentrations vs. the CO₂ concentration, (b) the CH₄ concentration vs. the CO₂ concentration, (c) the CO₂ flux vs. the CO₂ concentration, and (d) the CO₂ flux vs. the CH₄ flux; diameter of the flux chamber: 20 cm. Lozenges: JON site, triangles: CLU site, squares: MG site, circle: FA site.

detectable, there is still an emission of deep oxygen-free gas diluting oxygen in the chamber volume [22]. This may be in relation with the active landslide that could have modified degassing patterns. Soil gas monitoring confirmed the existence of high CH₄ concentrations. The highest peak value was 78.5% monitored only during a short period. Lower CH₄ contents were measured in the laboratory (44.5%) accompanied by abundant nitrogen (47.8), CO₂ at 6.6%, and traces of C₂H₆ (0.60%), C₃H₈ (0.009%), C₄H₁₀ (0.0015%), and C₅H₁₂ (0.0002%). In spite of this supposed decline of methane supply, strong O₂ depletion and associated CO₂ enrichment were also monitored in soil.

4.3. Relationships between Gas Species. The binary plots in Figure 5 describe the relations between gas species. The

process-based approach [39] can be applied to the CO₂-O₂ relationship (Figure 5(a)). As expected, measurements at the JON site (green lozenges in Figure 5(a)) cover a reduced concentration range and plot close to the replacement line that characterizes respiration processes occurring in soils (aerobic respiration consumes 1 mole of O₂ to produce 1 mole of CO₂). The situation is different for the single sample taken at the centre of the JON gas seep (grey lozenge in Figure 5(a)), where O₂ is absent and CO₂ is present at ca. 2%. Similarly, only one point is available for the MG site (with on-site and laboratory measurements) so that it is not possible to characterize the CO₂-O₂ relation close to the MG gas seep.

Some of the measurements at the CLU site (small blue triangles in Figure 5(a)) plot on the replacement line

especially for relatively low CO_2 concentrations (<5%) which is common in summer in French soils [33]. At a CO_2 concentration greater than 9-10%, two behaviours exist. Some measurements (electric-blue-surrounded triangles in Figure 5(a)) plot close to the CH_4 oxidation line thus suggesting that part of the measured CO_2 is produced by CH_4 oxidation in the soil (2 moles of O_2 are needed to produce one mole of $\text{CO}_2 + \text{H}_2\text{O}$). This is coherent with the presence of CH_4 in sufficient amounts to allow for high CO_2 production in soil. Otherwise, with the exception of specific conditions, CH_4 amounts in soils are generally low [40]. Other measurements (black-surrounded triangles in Figure 5(a)) plot on the replacement line although their CO_2 concentrations may reach very high values (more than 18% for point CLU36). High CO_2 concentrations in soils, produced by biological processes, are sometimes reported (up to 12% [33]; up to 13% [41]; and up to 14% [42]) often in soils having high clay contents [43]. Higher concentrations seem to be exceptional even if locally excessive concentrations of CO_2 (up to 40% above the capillary fringe) are reported in the literature [44]. Point CLU36 being exactly on the replacement line, it must be hypothesized that there are local soil characteristics which allow the high concentrations of CO_2 may be in connection with the landslide phenomenon. Some of the CO_2 could be produced by CH_4 oxidation, but in amounts that are not sufficient for a noticeable deviation from the replacement line towards the CH_4 oxidation line. No influence of dilution of the $\text{O}_2 + \text{N}_2$ pool by a deep CO_2 endmember in near surface environments is visible from the CO_2 - O_2 binary plot.

Methane and CO_2 concentrations in soil are not well correlated for any of the sites (Figure 5(b)). Where biological processes in soil produce CO_2 by using O_2 (replacement line in Figure 5(a)), we would not expect elevated soil CH_4 (dashed rectangle in Figure 5(b) for the JON site and for some CLU points). The situation is different when some CH_4 is present in the soil gas. This is documented only for the CLU site. For the six measurements containing CH_4 , CO_2 appears inversely correlated to CH_4 . The existence of CH_4 oxidation in soil is only established for measurements with the highest CH_4 concentrations (electric-blue triangles in Figure 5(b)). These measurements also show the existence of a positive CH_4 flux at the soil surface (electric-blue triangles in Figure 5(d)). For these data, CH_4 oxidation may superpose to the biological production of CO_2 in soil. For the black-surrounded triangles, the CO_2 - O_2 relationship suggests that this is not the case (Figure 5(b)). Consequently, it is likely that biological processes are responsible even for very high CO_2 concentrations in soil (up to 18%).

A positive CO_2 flux was always measureable (Figure 5(c)). The positive correlation between CO_2 flux and soil CO_2 concentration is a common phenomenon in summer when biological activity is at its highest. The CLU site again shows a distinct behaviour. Biological CO_2 flux is less strong than at JON (blue triangles in Figure 5(c)). This can be a consequence of different soil conditions (texture, water content, and vegetation). Higher CO_2 flows (trend 1 compared to trend 2 in Figure 5(c)) demonstrate the additional production of CO_2 by CH_4 oxidation closer to the supposed CH_4 seepage areas.

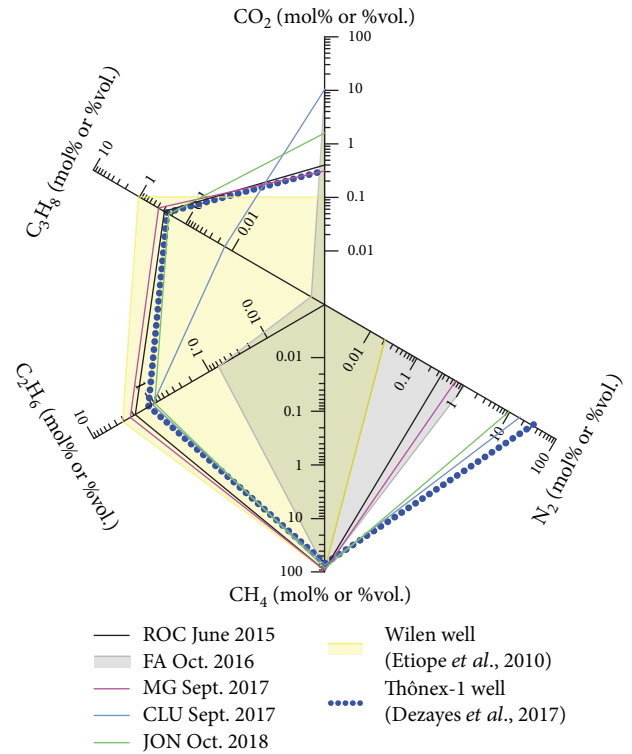


FIGURE 6: Radar diagram for the JON, MG, ROC, and CLU gas seeps; data from FA are indicated [3]. For comparison, data from two boreholes in Switzerland are reported [5, 45].

Figure 5(d) corroborates this assumption. The three measurements represented by electric-blue triangles have the highest CH_4 fluxes monitored at the CLU site. Part of the CO_2 release to the atmosphere is thus linked to CH_4 oxidation in soil. The CH_4 fluxes measured at the ROC site are more scattered. Below $10 \text{ g} \cdot \text{m}^{-2} \cdot \text{h}^{-1}$, it is difficult to define a clear relation between CH_4 and CO_2 fluxes. Two trends appear, one with relatively high CO_2 fluxes that also includes points from CLU (trend a) and one with a lower slope (trend b) reflecting different degrees of CH_4 oxidation. The trend for MG (trend c) has a similar slope to trend a and suggests, here again, a high rate of CO_2 production from CH_4 oxidation, at overall higher CH_4 fluxes, even though this is in apparent contradiction with the low CO_2 concentrations measured for this site (Figures 5(a) and 5(b)). Figure 5(d) shows the exponential decline of fluxes over a short distance (60 cm) from the main vent.

The gas dryness ratio ($= C_1 / (C_2 + C_3)$) provides some indication on the origin of alkane gases from the newly sampled methane seeps (Figure 6). The ratio is relatively low, from 34 (MG) up to 72-77 (CLU and JON, respectively). The ratio of ROC is in the same range (45) whereas the ratio of FA is much greater (1300). In the Western Alpine Arc, in Switzerland, ratios close to 50 are found in deep boreholes surrounding the Lemman lake (Thônex borehole; [45]), ratios close to 70 have been measured in gas seeps from the Giswil area [5], and ratios close to 20 were reported for boreholes located in the alpine flysch formations (Wilen well; [5]). Such ratios, lesser than 100, are often related to gas production

through thermogenic processes [46] whereas higher ratios may be related to a wider panel of production pathways or to secondary processes or mixing [47]. For the ROC, MG, and JON sites, situated in similar geological settings (lithology, geological age), similar mechanisms of light alkane production may be supposed. The situation may be different for the CLU site, with a comparable gas dryness ratios but where the seep likely to be associated with host rocks of different age and maturity, parameters known to be of prime importance [2]. For the FA site, if a genetic link of thermogenic methane generation with argillaceous host rocks, rich in organic matter, has certainly to be searched for, the higher dryness points potentially to secondary processes such as chemical fractionation upon transport or to biologically driven processes. This statement applies not only for alkane gas species but also for the origin of CO_2 .

4.4. Gas Emissions to the Atmosphere. On the basis of the data from this study for the JON, MG, ROC, and CLU sites and previous results for ROC [22] and for FA [3], it is obvious that the FA site remains the most important spot source of greenhouse gases (GHG) so far reported in the French Subalpine Chains. Nevertheless, the other seeps cannot be neglected altogether, especially if we consider them as indicators of the diffuse flux potentially related to a large number of undetected macro- or microseeps (see discussion below).

In the absence of flux measurements performed at the JON site, we refer to the other sites only. Nevertheless, the similarities in outcropping lithology, hydrographical, and topographic settings suggest that there may be comparable gas emission patterns for the JON and MG sites. Both are situated in creeks within the Middle Jurassic shales. The case of the MG site is particularly instructive. It is located in a very narrow riverbed (Figure 2), and the CH_4 emission was detected only in a 20×60 cm area (Figure 5(d)). As close as one meter away from this specific location, no CH_4 flux was measured at the soil surface. MG is thus the archetype of a tiny gas escape, with a very restricted seepage area, even though it falls in the macroseep category according to Etiope [2]. Calculation for MG is performed for the observed 0.12 m^2 emission area through which the gas is emitted (not extrapolated to 1 m^2). Taking into account the variability of the flux measurement reported above, CH_4 emissions can be estimated between 95 and 100 kg per year (ca. 270 g/day), with minor CO_2 emissions (1 kg). This corresponds to the amount of CH_4 released in two days by the FA seep [3]. This is a negligible absolute contribution to the overall regional methane budget, but not imperceptible when considering the small degassing area. Indeed, Mörner and Etiope [48] reported CH_4 emissions of 20 kg per year at San Vincenzo la Costa (Italy) but for an area of 300 m^2 (gas emission from a mud volcano and not from shales). Etiope et al. [6] reported seeps in the Appalachians where CH_4 emissions may be as low as 1 g/day (Chestnut Creek). Given the size of the seepage area, the MG site is thus remarkable.

Flux measurements performed at the ROC site cover an area of ca. 110 m^2 over which a CO_2 flux was always measurable whereas a CH_4 flux was detected only on approximately half of the area (Figure 7). The 2015 dataset on soil gas

measurements is used for comparison [22]. Interpolation uses standard kriging options in Surfer® software (Golden Software). Volume calculation of the amounts of gas released is also done using Surfer® software. The dataset is reduced, the size of the area is limited, so that definition of the data distribution and calculation of a variogram may fail to be successful or representative. The 2015 soil gas data indicated that gas venting was restricted to patchy seeps and two of them were identified as macroseeps. The 2017 flux measurements also revealed patchy gas emissions and poor correlation between CO_2 emissions and CH_4 emissions. It is not possible to identify any clear pattern related to geological or morphological features. When looking at the alkane emissions, little correspondence is found between soil gas and soil flux data. This is likely the consequence of a large time span between the acquisitions and the occurrence of a landslide in between the two surveys (Figure 2). Nowadays, the ROC site is more emissive on its western part, which corresponds to the upper part of the shales' outcrop. Over an area of ca. 60 m^2 , the global CH_4 emissions (macroseepage + miniseepage [2]) are evaluated at 5.1 tons per year. Gas seeps with similar annual releases are reported in Italy or in Romania [2]. The global CO_2 emission reaches 1.58 tons per year, 0.53 tons being related to gas seepage if a biological contribution to the CO_2 flux of $1.25 \text{ g} \cdot \text{m}^{-2} \cdot \text{h}^{-1}$ is considered [35].

At the CLU site, our investigations followed a more regular grid thanks to the flatness of the grassy terrain. The area of interest is only 50 m^2 large (Figure 8). Concentration measurements were performed over a half of this area. A CO_2 flux was always perceptible whereas a CH_4 flux was measureable over a surface of 12 m^2 only. Some decrease of the O_2 content inside the chamber was nevertheless measured even where no CH_4 was noticeable, suggesting that O_2 can be used as a proxy when the CH_4 efflux is very low. This is the case in the vicinity of points CLU22 and CLU28. As for other seeps, the correspondence between the patterns of CH_4 and CO_2 fluxes is not always obvious: the highest CO_2 fluxes are measured in the northern part of the area, whereas the highest CH_4 fluxes lie in the southeast corner. There is also a poor coherence between patterns of soil CH_4 concentrations and CH_4 fluxes, especially close to point CLU11 (yellow arrow in Figure 8(a)), likely due to varying soil properties. As tortuous the gas emission patterns may be, methane emission in the atmosphere is not negligible on a yearly basis. Over 12 m^2 , global methane emissions are evaluated around 235 kg per year. CO_2 emissions are larger (600 kg per year), a third of this value being related to the gas seep contribution if the biological contribution is assumed at $1.25 \text{ g} \cdot \text{m}^{-2} \cdot \text{h}^{-1}$ [35]. This evaluation needs certainly to be refined as it was not possible to assess the impact of the landslide phenomenon onto the gas emission pattern by a sole 1-day monitoring. Given the historical records, methane emissions can be expected to occur at other locations around the investigated site so that the overall emissions would be currently underestimated.

4.5. Are there Other Seepage Areas in the French Alps? An interesting conclusion can be drawn from the above-mentioned measurements. The sum of ROC, CLU, and MG

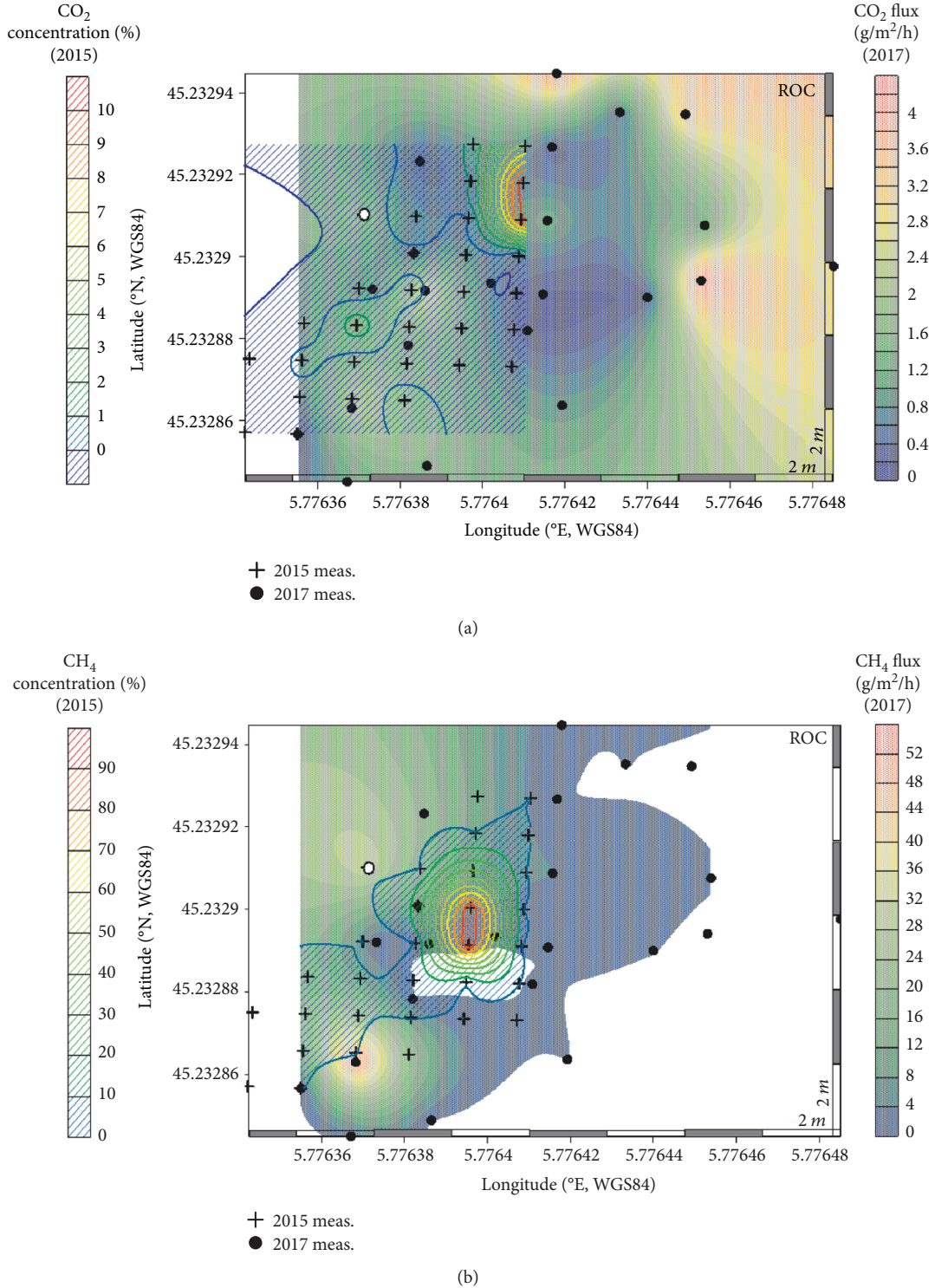


FIGURE 7: ROC site: interpolated maps for soil gas concentrations (hatched fill; data from [22]) and fluxes (full fill); (a) CO_2 gas specie; (b) CH_4 gas species. The light dot locates the main gas seep as represented in Figure 2 (no soil gas measurement done at this location).

contributions—and potentially the JON contribution if we assume it as similar to that of MG—to the CH_4 budget is close to 5.5 tons per year over a total degassing area of only 72 m^2 . This represents 29% of the yearly CH_4 emission from the FA site [3], but the cumulated seepage area of the other sites is equal to 30% of the surface of the macroseepage and

diffuse seepage areas of FA. The similarities of the different sites in terms of outcropping source rocks, topography, gas composition, and emission patterns may lead to the conclusion that we can assume an average annual release of 75 to 80 kg of CH_4 per square meter at a typical subalpine black shale seepage site.

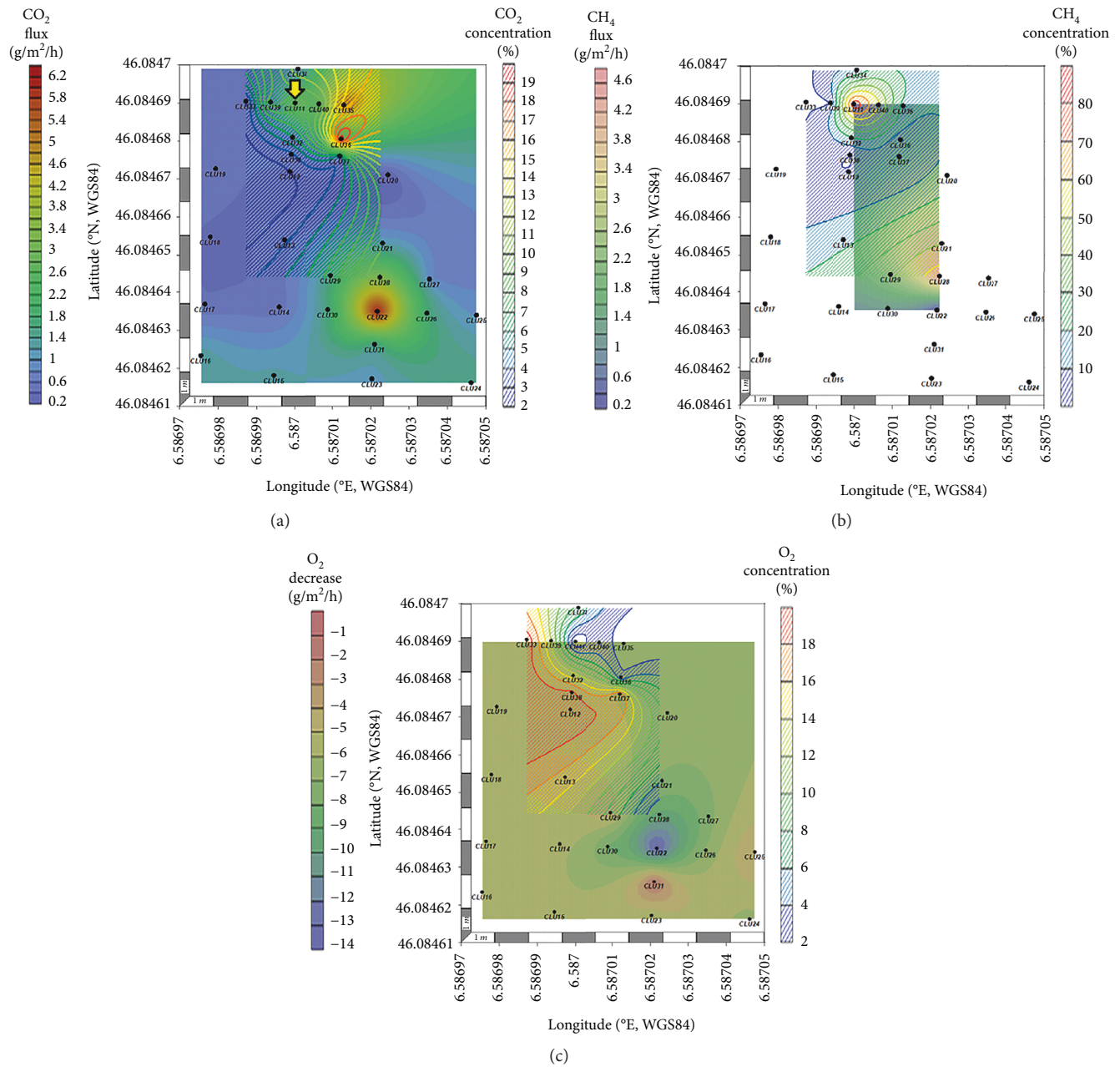


FIGURE 8: CLU site: interpolated maps for soil gas concentrations (lines) and fluxes (full fill); point CLU11 is located by the yellow arrow; (a) CO₂ gas; (b) CH₄ gas; (c) O₂ gas (for O₂, the data in g·m⁻²·h⁻¹ represent the decrease of gas content in the chamber during the measurement).

Several locations could not yet been localized and investigated (Figure 1), and many others may still be unknown or unreported. Black shale formations outcrop over hundreds of square kilometers in the French Subalpine Chains, and it is more than likely that other seepages exist in such a large area. Based on the knowledge gained on investigated seeps, the search of new degassing locations should probably focus on thalwegs and indented valleys crosscutting black shales. A rough estimate can be done in the case of the MG site. Over an area of 1 km², centred on the known gas seep, we can identify approximately 3.8 km (planar distance) of small valleys cutting into the outcropping black shales (Figure 9). Extrapolating this density to the total surface of black shale outcrops at the Subalpine Chains leads to tremendously high distances, which are, in most areas, only accessible by foot, given the rough topography and the dense vegetation on those agriculturally mostly unusable badlands.

The assessment of an environmental baseline with respect to potential uses of methane-containing argillaceous formations as well as any estimation of GHG releases from such formations would require a much more stringent approach to gas seep identification. Gal et al. [3] reported some aspects of gas detection in the context of environmental impact assessment-related shale gas exploration/exploitation.

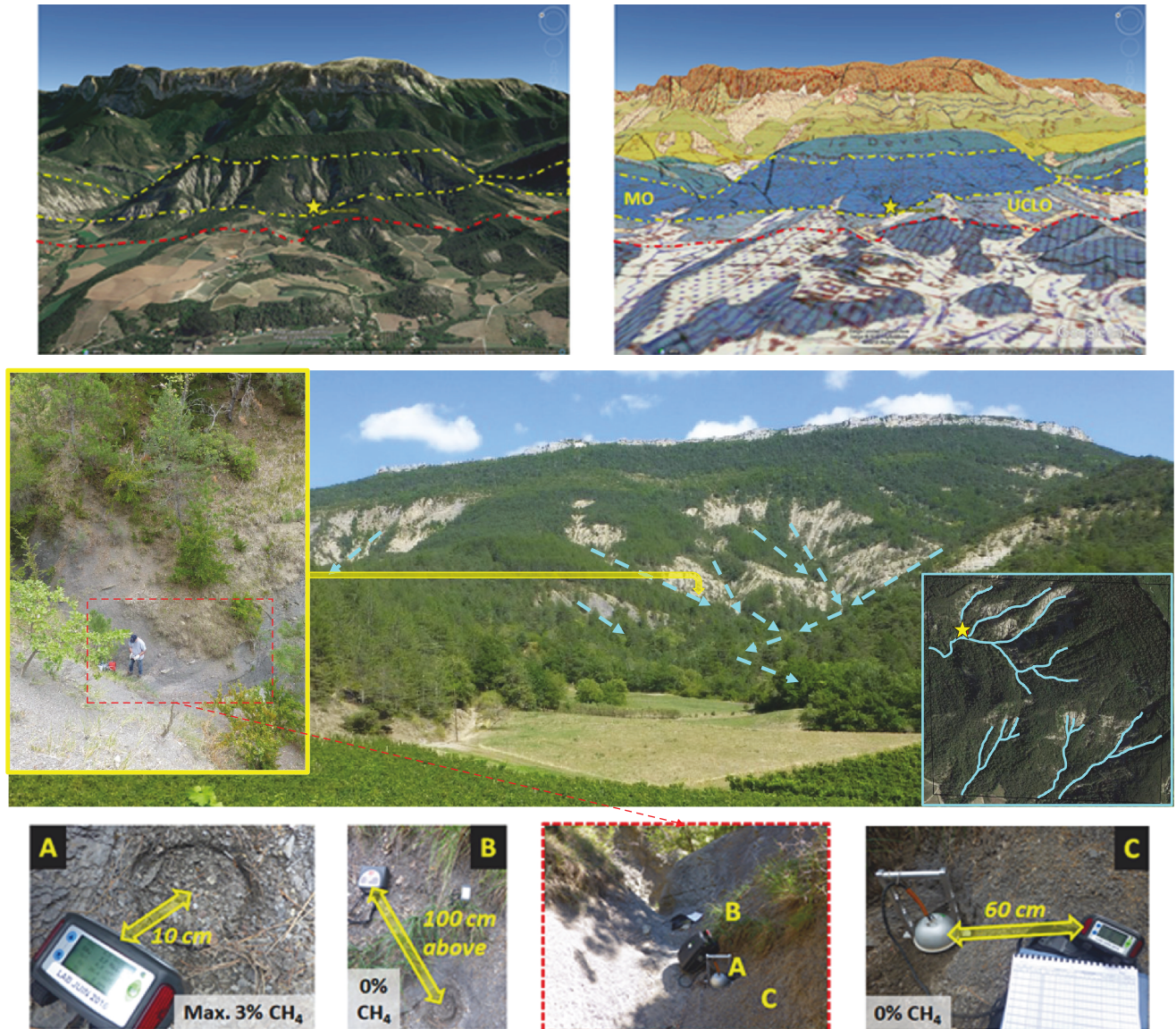


FIGURE 9: MG site: (top) overviews of reliefs surrounding the site and relief-shaped geological map (from Google Earth); location of the gas seep is indicated by the yellow star; MO: shales from the Middle Oxfordian age; UCLo: black shales from the Upper Callovian to the Lower Oxfordian age. (Middle) Photograph of the site and main thalwegs (dotted lines); right inset: aerial view of thalwegs (from Google Earth); left inset: topography of the seepage area (the character is in front of the seep). (Bottom) Locations of passive atmosphere monitoring (A, B, and C) and results of CH_4 measurements.

The example of the MG seep is very illustrative in that perspective. Contrarily to the FA site, the MG site represents a small seepage, but the mechanism may be similarly linked to fault structures, given that leakage rates along faults may be highly heterogeneous [49]. The MG site can be considered as point source macroseep. The photographs presented in Figure 9 illustrate how difficult it is to locate such a seepage in the field, using currently available monitoring equipment. Given the natural air movements, a gas detector held 10 cm above the seep will record maximum CH_4 values of only 3%, in spite of the fact that there is enough CH_4 seeping to the soil surface to light a flame directly above the seep. We noted significant variability in the readings even for a very light wind blowing through the narrow channel formed by the creek

bed. Moving the gas detector some tens of centimeters away from the source precludes any detection of CH_4 . This makes it highly improbable to detect such gas vents with any method outside a very restricted volume around the point of gas emission. Indeed, the human nose is in the present case one of the best tools owing to its ability to detect trace gases, such as H_2S , at levels far below the detection limits of common portable equipment [50].

Future detection of unknown seepage areas will thus be a difficult task. At the scale we consider here, neither methods relying on air gas monitoring nor airborne methods will be easily applicable because of the rapid dispersion of the CH_4 in the air. The use of unmanned systems (e.g., drones) may be possible but the rugged topography and often dense

natural vegetation will limit their use in regions comparable to the investigated areas of the Subalpine Chains.

At the present technological state of the art, the best way to proceed will be a fastidious ground monitoring with regular stops to check for active leakage. Laser systems seem here to be more appropriate than other detection techniques. The low concentrations imply that the best results can be expected if the sensors integrated in the monitoring equipment point directly, orthogonally to the soil. Direct laser pointing will integrate a CH_4 content (often expressed in ppm) over the distance between the sensor and a reflective source (soil/rock). In the case of the MG site, our flux measurements show that several hundreds of ppm of CH_4 are emitted each second into the atmosphere at the seep (up to $1500 \text{ ppm}\cdot\text{s}^{-1}$). Even for lower natural fluxes, a laser beam crossing the emission area, even at some distance, will detect such a release. Remote methane leak detectors built for pipeline leakage monitoring may be appropriate candidates. They often have a sensitivity of $5 \text{ ppm}\cdot\text{m}$, a working range of 0 to $50,000 \text{ ppm}\cdot\text{m}$ or more, and working distances from a few decimeters to 30–80 m [51–55]. Some sensors also exist as drone-mounted versions [54]. In the case of the MG site, such sensors should be able to detect the observed seepage at 10 to 20 m of distance (corresponding to max. $150 \text{ ppm}\cdot\text{m}$ and $75 \text{ ppm}\cdot\text{m}$, respectively), longer distances being not compatible with the lengths of the thalweg sections. The counterpart is that such kind of work implies a huge workload and is time and cost intensive. It is not adapted to operational day-to-day site surveillance of hydrocarbon plays.

5. Conclusions

The three newly investigated gas seeps situated in zones where argillaceous gas-bearing Jurassic host rock outcrop in the French Subalpine Chains complete our previous investigations reported for the most prominent alpine “eternal fire,” the Fontaine Ardente du Gua [3]. Again, methane is the dominant gas phase emitted to the atmosphere, over areas of variable size ranging from tens of square centimeters to tens of square meters. The integration of all data so far available for the French seeps leads to mean flux estimations with some statistical significance. Considering information from all macroseepage and miniseepage areas where a positive CH_4 flux is measured, mean CH_4 release is calculated at $76\text{--}79 \text{ kg}$ per square meter per year. This is far above microseepage rates recently reported by Etiope et al. [9] thus confirming the superposition of diffuse and focused degassing processes at macroseeps, highlighting the role of faults and fractures in gas emissions even from shale formations. Contrarily to most oil- and gas-bearing sedimentary basins with known gas and oil seeps (e.g., the recent inventory for China [56]), the French alpine seeps seem not linked to tectonic trap structures, seeping through younger brittle deformations. All are directly related to outcropping argillaceous host rocks, but alpine thrusting and faults certainly play an important role in creating pathways for gas accumulation and migration, similarly to what was postulated for the Appalachian Mountains [6]. Linking structural analysis of fault patterns

to gas emissions is certainly one of the most promising approaches for targeting ground-based investigations aiming at discovering new emitting structures in the restrained time-frame of environmental baseline assessment. The gas seeps described so far were found accidentally, by local inhabitants through spontaneous or induced ignition, bubbling in water-bearing creeks or by detecting the particular smell of higher alkanes or H_2S . Systematic “blind” monitoring of black shale outcrops will probably fail to succeed if ground investigations are not guided, e.g., by airborne analysis of fault patterns. Future work will be oriented towards the testing of ground-based and airborne laser-based detectors to check their capacities of detection on known seeps. If these tests are conclusive, then trials in uncovered areas will be performed.

The systematic detection of seeps becomes crucial in the context of monitoring the potential impact of shale gas exploration or exploitation as well as of underground storage of natural gas and CO_2 . Environmental baseline assessment is now a well-established prerequisite of Carbon Capture and Storage (CCS). As we attempt to demonstrate here, it is highly hypothetical that baseline investigations, as good as they may be from a technological point of view, will reveal all natural small-scale gas seeps. When then a site will shift to an operational stage, leakage from the exploitation infrastructure may be alleged if so far unreported natural seepage is discovered. This was the case at the CCS site of Weyburn in 2011 [57, 58]. Several studies have demonstrated the natural origin of the discovered CO_2 emission, related to specific processes in the soil formations close to the surface [59–61]. Nevertheless, eight years after the allegation has been raised, research is still ongoing aiming to discard or confirm CCS-induced leakage [62, 63]. In the context of shale gas, the situation is even more complex as the use of chemicals in hydraulic fracturing of the argillaceous host rocks has raised strong public concerns on health effects, both of flowback water spills and leaks to surface water or groundwater resources and of stray gas. [64, 65]. Much effort is put into optimizing water and groundwater monitoring [66, 67]. Monitoring during the activity of the site may be better focused than initial investigations of gas emission baselines over large areas. However, as shown for the Weyburn case, and other CCS test sites or demonstrators, as well as for areas with active unconventional gas exploitation, intrinsic fingerprinting of gas species as well as investigating chemical and isotopic characteristics of groundwater bears a great potential for system failure detection [68–73] and will usefully complete the identification and quantification of gas emanations.

Data Availability

Data are given as supplementary material.

Conflicts of Interest

The authors declare that there is no conflict of interest regarding the publication of this paper.

Acknowledgments

This research was conducted in the frame of the G-Baseline project, cofunded by the French Research Agency (ANR-14-CE05-0050 grant) and the Natural Sciences and Engineering Research Council of Canada (NSERC grant no. 463605).

Supplementary Materials

Soil gas flux values ($f\text{CO}_2$, $f\text{CH}_4$) are measured in the field, along with location and time of measurement. If a decrease of the O_2 concentration inside the chamber is measured together with an enrichment in CO_2 and/or CH_4 , then this depletion is reported. Soil gas concentrations (CO_2 , CH_4 , and O_2) are measured in the field, along with location and time of measurement. (*Supplementary Materials*)

References

- [1] G. Etiope, G. Papatheodorou, D. Christodoulou, M. Geraga, and P. Favali, "The geological links of the ancient Delphic Oracle (Greece): a reappraisal of natural gas occurrence and origin," *Geology*, vol. 34, no. 10, pp. 821–824, 2006.
- [2] G. Etiope, "Natural Gas Seepage," in *The Earth's Hydrocarbon Degassing*, Springer, 2015.
- [3] F. Gal, W. Kloppmann, E. Proust, and P. Humez, "Gas concentration and flow rate measurements as part of methane baseline assessment: case of the Fontaine Ardente gas seep, Isère, France," *Applied Geochemistry*, vol. 95, pp. 158–171, 2018.
- [4] G. Etiope and R. W. Klusman, "Geologic emissions of methane to the atmosphere," *Chemosphere*, vol. 49, no. 8, pp. 777–789, 2002.
- [5] G. Etiope, C. Zwahlen, F. S. Anselmetti, R. Kipfer, and C. J. Schubert, "Origin and flux of a gas seep in the northern Alps (Giswil, Switzerland)," *Geofluids*, vol. 10, no. 4, 485 pages, 2010.
- [6] G. Etiope, A. Drobniak, and A. Schimmelmann, "Natural seepage of shale gas and the origin of "eternal flames" in the northern Appalachian Basin, USA," *Marine and Petroleum Geology*, vol. 43, pp. 178–186, 2013.
- [7] G. Etiope and M. Schoell, "Abiotic gas: atypical, but not rare," *Elements*, vol. 10, no. 4, pp. 291–296, 2014.
- [8] G. Etiope and G. Martinelli, "Migration of carrier and trace gases in the geosphere: an overview," *Physics of the Earth and Planetary Interiors*, vol. 129, no. 3–4, pp. 185–204, 2002.
- [9] G. Etiope, G. Ciotoli, S. Schwietzke, and M. Schoell, "Gridded maps of geological methane emissions and their isotopic signature," *Earth System Science Data*, vol. 11, no. 1, pp. 1–22, 2019.
- [10] G. Etiope and R. W. Klusman, "Microseepage in drylands: flux and implications in the global atmospheric source/sink budget of methane," *Global and Planetary Change*, vol. 72, no. 4, pp. 265–274, 2010.
- [11] D. L. Pinti, Y. Gelinas, A. M. Moritz, M. Larocque, and Y. Sano, "Anthropogenic and natural methane emissions from a shale gas exploration area of Quebec, Canada," *Science of the Total Environment*, vol. 566–567, pp. 1329–1338, 2016.
- [12] D. R. Caulton, P. B. Shepson, R. L. Santoro et al., "Toward a better understanding and quantification of methane emissions from shale gas development," *Proceedings of the National Academy of Sciences of the United States of America*, vol. 111, no. 17, pp. 6237–6242, 2014.
- [13] G. Etiope, L. A. Doezeema, and C. Pacheco, "Emission of methane and heavier alkanes from the La Brea Tar Pits seepage area, Los Angeles," *Journal of Geophysical Research: Atmospheres*, vol. 122, no. 21, pp. 12,008–12,019, 2017.
- [14] S. Bachu, "Analysis of gas leakage occurrence along wells in Alberta, Canada, from a GHG perspective – gas migration outside well casing," *International Journal of Greenhouse Gas Control*, vol. 61, pp. 146–154, 2017.
- [15] G. Schout, J. Griffioen, S. M. Hassanizadeh, G. Cardon de Lichtbuer, and N. Hartog, "Occurrence and fate of methane leakage from cut and buried abandoned gas wells in the Netherlands," *Science of the Total Environment*, vol. 659, pp. 773–782, 2019.
- [16] M. Currell, D. Banfield, I. Cartwright, and D. I. Cendon, "Geochemical indicators of the origins and evolution of methane in groundwater: Gippsland Basin, Australia," *Environmental Science and Pollution Research*, vol. 24, no. 15, pp. 13168–13183, 2017.
- [17] P. Humez, B. Mayer, J. Ing et al., "Occurrence and origin of methane in groundwater in Alberta (Canada): gas geochemical and isotopic approaches," *Science of the Total Environment*, vol. 541, pp. 1253–1268, 2016.
- [18] J. T. Kulongoski, P. B. McMahon, M. Land, M. T. Wright, T. A. Johnson, and M. K. Landon, "Origin of methane and sources of high concentrations in Los Angeles groundwater," *Journal of Geophysical Research: Biogeosciences*, vol. 123, no. 3, pp. 818–831, 2018.
- [19] L. J. Molofsky, S. D. Richardson, A. W. Gorody et al., "Effect of different sampling methodologies on measured methane concentrations in groundwater samples," *Groundwater*, vol. 54, no. 5, pp. 669–680, 2016.
- [20] C. Rivard, G. Bordeleau, D. Lavoie, R. Lefebvre, and X. Malet, "Can groundwater sampling techniques used in monitoring wells influence methane concentrations and isotopes?," *Environmental Monitoring and Assessment*, vol. 190, no. 4, p. 191, 2018.
- [21] M. E. Hinkle, "Environmental conditions affecting concentrations of He, CO_2 , O_2 and N_2 in soil gases," *Applied Geochemistry*, vol. 9, no. 1, pp. 53–63, 1994.
- [22] G. Frederick, K. Wolfram, P. Eric et al., "Natural CH_4 gas seeps in the French Alps: characteristics, typology and contribution to CH_4 natural emissions to the atmosphere," *Energy Procedia*, vol. 114, pp. 3020–3032, 2017.
- [23] M. Pignone, "HYSED database," 2014, February 2019, <https://www.arcgis.com/home/webmap/viewer.html?webmap=03cc1bc26fd645228ad60bea403a1b26>.
- [24] E. Greber, W. Leu, D. Bernoulli, M. E. Schumacher, and R. Wyss, "Hydrocarbon provinces in the Swiss southern Alps—a gas geochemistry and basin modelling study," *Marine and Petroleum Geology*, vol. 14, no. 1, pp. 3–25, 1997.
- [25] D. Misch, W. Leu, R. F. Sachsenhofer, R. Gratzner, B. Rupperecht, and A. Bechtel, "Shallow hydrocarbon indications along the alpine thrust belt and adjacent foreland basin: distribution and implications for petroleum exploration," *Journal of Petroleum Geology*, vol. 40, no. 4, pp. 341–362, 2017.
- [26] B. Blavoux and J. Dazy, "Caractérisation d'une province à CO_2 dans le bassin du Sud-Est de la France," *Hydrogéologie*, vol. 4, pp. 241–252, 1990.

- [27] M. Gignoux and L. Moret, "Description géologique du bassin supérieure de la Durance," *Bulletin de la Société de statistique, des sciences naturelles et des arts industriels du département de l'Isère* 58(XVII), 1938, <https://gallica.bnf.fr/ark:/12148/bpt6k9610071m>.
- [28] BRGM, 2019, February 2019, <http://infoterre.brgm.fr/rechercher/default.htm>.
- [29] J. Debelmas, "Un dégagement de gaz naturel dans l'Oxfordien des environs de Grenoble (ravin du Rochasson, commune de Montbonnot, Isère)," *Géologie Alpine*, vol. 54, p. 15, 1978.
- [30] A. Favre, *Recherches géologiques dans les parties de la Savoie, du Piémont et de la Suisse voisines du Mont-Blanc, avec un atlas de 32 planches, Tome II, paragraphes*, Masson, 1867, February 2019, <http://docplayer.fr/34550274-Recherches-geologiques-dans-les-parties-de-la-savoie-du-piemont-et-de-la-suisse-voisines-du-mont-blanc-avec-un-atlas-de-32-planches-par.html>.
- [31] J. Omer, "Une source de gaz inflammable dans la Haute-Savoie," *La Nature, Revue des sciences et de leur application à l'art et à l'industrie*, vol. 1634, p. 246, 1904.
- [32] L. Moret, "Enquête critique sur les ressources minérales de la province de Savoie, précédée d'une esquisse géologique," *Bulletin de la Société Scientifique du Dauphiné*, vol. 46, no. 5, 1925.
- [33] F. Gal, K. Michel, Z. Pokryszka et al., "The SENTINELLE French research project: subsurface geochemical characterization prior CO₂ injection (baseline survey) – site of Rousse (TOTAL CCS pilot)," *International Journal of Greenhouse Gas Control*, vol. 21, pp. 177–190, 2014.
- [34] J. P. Toutain and J. C. Baubron, "Gas geochemistry and seismotectonics: a review," *Tectonophysics*, vol. 304, no. 1-2, pp. 1–27, 1999.
- [35] C. Werner and S. Brantley, "CO₂ emissions from the Yellowstone volcanic system," *Geochemistry, Geophysics, Geosystems*, vol. 4, no. 7, 2003.
- [36] Z. Pokryszka, F. Adelise, R. Farret, S. Lafortune, E. Michel, and S. Rupasinghe, "Valeurs de référence du flux de CO₂ et de CH₄ d'origine naturelle biogénique des sols, INERIS report DRS-17-164646-05731A," 2017, February 2019, https://www.ineris.fr/sites/ineris.fr/files/contribution/Documents/INERIS_DRS-17-164646-05731_Referentiel-flux-CO2-CH4-sols_ZPo.pdf.
- [37] G. Etiope, M. Schoell, and H. Hosgörmez, "Abiotic methane flux from the Chimaera seep and Tekirova ophiolites (Turkey): understanding gas exhalation from low temperature serpentinization and implications for Mars," *Earth and Planetary Science Letters*, vol. 310, no. 1-2, pp. 96–104, 2011.
- [38] G. Chiodini, F. Frondini, and B. Raco, "Diffuse emission of CO₂ from the fossa crater, Vulcano Island (Italy)," *Bulletin of Volcanology*, vol. 58, no. 1, pp. 41–50, 1996.
- [39] K. D. Romanak, P. C. Bennett, C. Yang, and S. D. Hovorka, "Process-based approach to CO₂ leakage detection by vadose zone gas monitoring at geologic CO₂ storage sites," *Geophysical Research Letters*, vol. 39, no. 15, 2012.
- [40] J. Le Mer and P. Roger, "Production, oxidation, emission and consumption of methane by soils: a review," *European Journal of Soil Biology*, vol. 37, no. 1, pp. 25–50, 2001.
- [41] G. Frédérick, P. Eric, B. Gaëtan et al., "What may be the consequences of a CO₂ leakage? Insights from soil gas measurements in an urban area – Clermont-Ferrand, French Massif Central," *Energy Procedia*, vol. 114, pp. 3006–3019, 2017.
- [42] N. R. Varley and M. A. Armienta, "The absence of diffuse degassing at Popocatepetl volcano, Mexico," *Chemical Geology*, vol. 177, no. 1-2, pp. 157–173, 2001.
- [43] R. H. Kiefer and R. G. Amey, "Concentrations and controls of soil carbon dioxide in sandy soil in the North Carolina coastal plain," *Catena*, vol. 19, no. 6, pp. 539–559, 1992.
- [44] H. Enoch and S. Dasberg, "The occurrence of high CO₂ concentrations in soil air," *Geoderma*, vol. 6, no. 1, pp. 17–21, 1971.
- [45] C. Dezayes, J. A. M. Mohammad, A. Bitri et al., "Application of exploration techniques on sedimentary basin fields, report IMAGE-D8.02, EU FP7 project IMAGE," 2017, February 2019, <http://www.image-fp7.eu/reference-documents/deliverables/IMAGE-D8.02-2017.09.18-Applications-of-Exploration-Techniques%20-%20public.pdf>.
- [46] B. B. Bernard, "Light hydrocarbons in marine sediments. PhD Dissertation," University of Texas, 1978, February 2019, <https://www.tdi-bi.com/wp-content/uploads/2015/04/BBB-1978-Diss-LIGHT-HYDROCARBONS-IN-MARINE-SEDIMENTS-r.pdf>.
- [47] A. V. Milkov and G. Etiope, "Revised genetic diagrams for natural gases based on a global dataset of >20,000 samples," *Organic Geochemistry*, vol. 125, pp. 109–120, 2018.
- [48] N.-A. Mörner and G. Etiope, "Carbon degassing from the lithosphere," *Global and Planetary Change*, vol. 33, no. 1-2, pp. 185–203, 2002.
- [49] C. E. Bond, Y. Kremer, G. Johnson et al., "The physical characteristics of a CO₂ seeping fault: the implications of fracture permeability for carbon capture and storage integrity," *International Journal of Greenhouse Gas Control*, vol. 61, pp. 49–60, 2017.
- [50] INERIS, "Toxicological and environmental data sheet for chemical substances - hydrogen sulfide. Report DRC-07-83451-15432B," 2011, February 2019, <https://substances.ineris.fr/fr/substance/getDocument/2848>.
- [51] Focused Photonics, 2019, February 2019, http://www.fpi-inc.com/en/index.php/pro_info/19?ctype=34.
- [52] Gazomat, 2019, February 2019, <https://www.gazomat.com/en/products/gazoscan/>.
- [53] Heath Consultants, 2019, February 2019, <https://heathus.com/products/remote-methane-leak-detector/>.
- [54] Hesai, 2019, February 2019, http://www.hesaitech.com/en/laser-based_remote_methane_leak_detector.html.
- [55] Tokyo Gas, 2019, February 2019, http://www.tokyogas-es.co.jp/en/business/eq/laser_methane_mini.html.
- [56] G. Zheng, W. Xu, G. Etiope et al., "Hydrocarbon seeps in petroliferous basins in China: a first inventory," *Journal of Asian Earth Sciences*, vol. 151, pp. 269–284, 2018.
- [57] K. Brown, S. Whittaker, M. Wilson, W. Srisang, H. Smithson, and P. Tontiwachwuthikul, "The history and development of the IEA GHG Weyburn-Midale CO₂ monitoring and storage project in Saskatchewan, Canada (the world largest CO₂ for EOR and CCS program)," *Petroleum*, vol. 3, no. 1, pp. 3–9, 2017.
- [58] A. D. Boyd, Y. Liu, J. C. Stephens et al., "Controversy in technology innovation: contrasting media and expert risk perceptions of the alleged leakage at the Weyburn carbon dioxide storage demonstration project," *International Journal of Greenhouse Gas Control*, vol. 14, no. 2013, pp. 259–269, 2013.
- [59] S. E. Beaubien, D. G. Jones, F. Gal et al., "Monitoring of near-surface gas geochemistry at the Weyburn, Canada, CO₂-EOR

- site, 2001–2011,” *International Journal of Greenhouse Gas Control*, vol. 16, pp. S236–S262, 2013.
- [60] D. Risk, M. Lavoie, and N. Nickerson, “Using the Kerr investigations at Weyburn to screen geochemical tracers for near-surface detection and attribution of leakage at CCS/EOR sites,” *International Journal of Greenhouse Gas Control*, vol. 35, pp. 13–17, 2015.
 - [61] K. Romanak, G. W. Sherk, S. Hovorka, and C. Yang, “Assessment of alleged CO₂ leakage at the Kerr farm using a simple process-based soil gas technique: implications for carbon capture, utilization, and storage (CCUS) monitoring,” *Energy Procedia*, vol. 37, pp. 4242–4248, 2013.
 - [62] S. M. V. Gilfillan, G. W. Sherk, R. J. Poreda, and R. S. Haszeldine, “Using noble gas fingerprints at the Kerr farm to assess CO₂ leakage allegations linked to the Weyburn-Midale CO₂ monitoring and storage project,” *International Journal of Greenhouse Gas Control*, vol. 63, pp. 215–225, 2017.
 - [63] C. D. Sandau, M. Prokipchuk, K. R. Dominato, and S. O. C. Mundle, “Soil gas investigation of an alleged gas migration issue on a residential farm located above the Weyburn-Midale CO₂ enhanced oil recovery project,” *International Journal of Greenhouse Gas Control*, vol. 81, pp. 11–20, 2019.
 - [64] T. J. Centner and L. K. O’Connell, “Unfinished business in the regulation of shale gas production in the United States,” *Science of the Total Environment*, vol. 476–477, pp. 359–367, 2014.
 - [65] Y. Yao, T. Chen, S. S. Shen et al., “Malignant human cell transformation of Marcellus shale gas drilling flow back water,” *Toxicology and Applied Pharmacology*, vol. 288, no. 1, pp. 121–130, 2015.
 - [66] S. Gamper-Rabindran, “Information collection, access, and dissemination to support evidence-based shale gas policies,” *Energy Technology*, vol. 2, no. 12, pp. 977–987, 2014.
 - [67] R. A. Howell, “UK public beliefs about fracking and effects of knowledge on beliefs and support: a problem for shale gas policy,” *Energy Policy*, vol. 113, pp. 721–730, 2018.
 - [68] D. Györe, R. McKavney, S. M. V. Gilfillan, and F. M. Stuart, “Fingerprinting coal-derived gases from the UK,” *Chemical Geology*, vol. 480, pp. 75–85, 2018.
 - [69] P. Humez, J. Lions, P. Negrel, and V. Lagneau, “CO₂ intrusion in freshwater aquifers: review of geochemical tracers and monitoring tools, classical uses and innovative approaches,” *Applied Geochemistry*, vol. 46, pp. 95–108, 2014.
 - [70] P. Humez, P. Negrel, V. Lagneau et al., “CO₂-water-mineral reactions during CO₂ leakage: geochemical and isotopic monitoring of a CO₂ injection field test,” *Chemical Geology*, vol. 368, pp. 11–30, 2014.
 - [71] B. Mayer, P. Humez, V. Becker et al., “Assessing the usefulness of the isotopic composition of CO₂ for leakage monitoring at CO₂ storage sites: a review,” *International Journal of Greenhouse Gas Control*, vol. 37, pp. 46–60, 2015.
 - [72] B. Mayer, P. Humez, V. Becker et al., “Prospects and limitations of chemical and isotopic groundwater monitoring to assess the potential environmental impacts of unconventional oil and gas development,” *Procedia Earth and Planetary Science*, vol. 13, pp. 320–323, 2015.
 - [73] P. Humez, B. Mayer, M. Nightingale et al., “Redox controls on methane formation, migration and fate in shallow aquifers,” *Hydrology and Earth System Sciences*, vol. 20, no. 7, pp. 2759–2777, 2016.

Research Article

Comparison on Rare Gas Geochemical Characteristics and Gas Originations of Kuche and Southwestern Depressions in Tarim Basin, China

Xiaobo Wang^{1,2,3}, Caineng Zou,³ Jian Li,^{1,2,3} Guoqi Wei,^{1,2,3} Jianfa Chen,⁴ Zengye Xie,^{1,2,3} Zhisheng Li,^{1,2,3} Jianying Guo,^{1,2,3} Shiguo Lin,^{1,2,3} Songqi Pan,^{1,2,3} Aisheng Hao^{1,2,3}, Chunlong Yang,^{1,2,3} and Xuening Qi^{1,2,3}

¹Gas Geology Research Center, PetroChina Research Institute of Petroleum Exploration and Development, Langfang 065007, China

²Key Laboratory of Gas Reservoir Formation and Development, CNPC, Langfang 065007, China

³PetroChina Research Institute of Petroleum Exploration and Development, Beijing 10083, China

⁴State Key Laboratory of Petroleum Resource and Prospecting, China University of Petroleum (Beijing), Beijing 100429, China

Correspondence should be addressed to Xiaobo Wang; wangxb69@petrochina.com.cn

Received 4 January 2019; Revised 19 March 2019; Accepted 26 March 2019; Published 2 June 2019

Academic Editor: Giovanni Martinelli

Copyright © 2019 Xiaobo Wang et al. This is an open access article distributed under the Creative Commons Attribution License, which permits unrestricted use, distribution, and reproduction in any medium, provided the original work is properly cited.

The Kuche Depression is considered as the most important gas resource potential and gas exploring area with great gas resource potential and prospect in the Tarim Basin. Based on geochemical experimental analyses and comprehensive geological studies, the general geochemical characteristics of molecular and isotope compositions of rare gases as well as hydrocarbon gases and nonhydrocarbon gases are comparatively studied in the Kuche and Southwestern Depressions. Then, their genetic types are separately identified and gas originations are comprehensively discussed. The main results are as follows. (1) Gas fields in the Kuche Depression have a higher methane abundance, accompanied with low N₂ and CO₂ abundances, but the Akemomu gas field in the Southwestern Depression has a relatively lower average methane abundance, accompanied with high average N₂ and CO₂ abundances. The helium abundance of natural gases in gas fields from the Kuche Depression general has 1 order of magnitude higher than the air value. Comparatively, it has more than 2 orders of magnitude higher than the atmospheric value in the Akemomu gas field from the Southwestern Depression. The neon, argon, krypton, and xenon abundances in both Kuche and Southwestern Depressions are lower than the corresponding air values. (2) Natural gases from gas fields in the Kuche Depression and the Southwestern Depressions are generally typical coal-formed gases. The rare gases in the Kuche Depression have typical crustal genesis, mainly deriving from the radioactive decay of elements in the crust, while in the Akemomu gas field from the Southwestern Depression, the rare gases have main crustal genesis with a proportion of 92.5%, probably accompanied with a little mantled genetic contribution. (3) Natural gases in the Kuche Depression are generally derived from coal measure source rocks of Jurassic and Triassic, which principally originated from Jurassic in strata period and coals in source rock types. The Jurassic source rocks account for 55%-75% and the Triassic source rocks account for 25%-45% approximately, while coals occupy 68% and mudstones occupy 32% separately. Natural gases from the Akemomu gas field in the Southwestern Depression mainly originated from humic mudstones of marine and continental transitional source rocks of Carboniferous to Permian.

1. Introduction

Rare gases mainly referring to helium, neon, argon, krypton, xenon, and radon are group zero elements with characteristics of inactive chemical properties, small resistance, heat conductivity coefficient, easy luminescence, and low melting,

boiling, and solubility, and so on. Although rare gases have extremely low abundance in nature, their distinctive physical and chemical properties can be used for tracing formation and evaluation processes of geological bodies ([1; Xu et al., 1994; [2–9]; Xu, 1996; [10–17]). It is considered as one of the most important hotspots and leading frontiers in

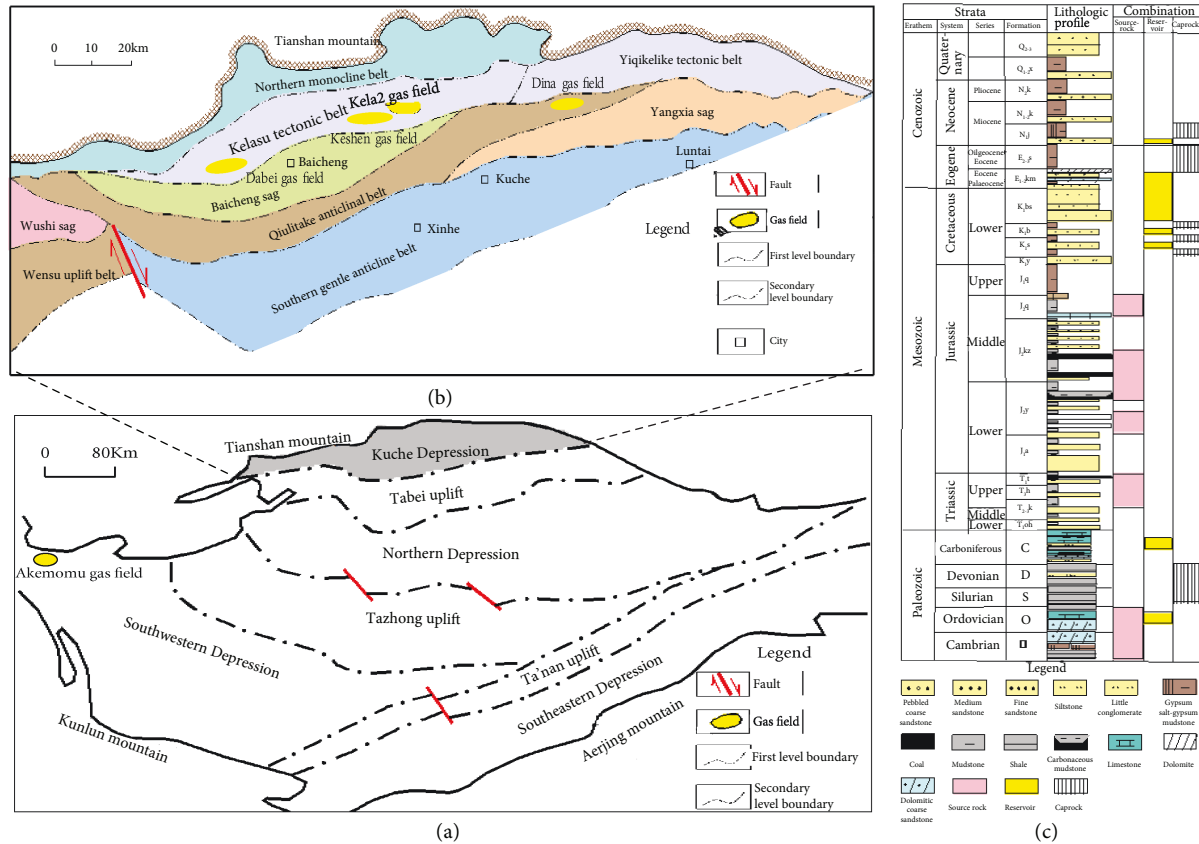


FIGURE 1: Gas field distribution and structural unit divisions of the Kuche and Southwestern Depressions, Tarim Basin (modified from [25]).

geosciences. The molecular and isotopic compositions of rare gases in natural gases can provide a lot of useful geochemical and geological information. They have extensive prospects on studies of gas genesis, migration, origination, deep mantle fluid action, volcanic moment, and earthquake activities ([1]; Xu et al., 1994; [5]; Liu and Xu, 1987; [18, 19]; Xu, 1996; [15–17, 20–24]). Because Rn is a radioactive element, the rare gas studies on oil and gas geology usually include helium, neon, argon, krypton, and xenon.

Sited in the north of the Tarim Basin, the Kuche Depression is one of the most important gas-bearing and exploration areas with the highest gas reserves. Many giant gas fields have been found in the Kulasu and Qiulitage tectonic belts such as the Kela2, Dina2, Dabei, Keshen2, and Keshen8 gas fields, showing huge gas resource potential and prospect for further exploration. Presently, many researchers in China have carried out a lot of studies and discussions on gas geochemical characteristics, genetic identifications, and gas originations, as well as mechanisms of gas reservoir forming and accumulation in the Kuche Depression ([25–33]; Li et al., 2018). However, geochemical characteristics of rare gases of the whole Kuche Depression have never been comprehensively and comparatively studied. By means of geochemical analyses and comprehensive geological studies, molecular and isotopic compositions of rare gases in the Kela2, Dabei, Dina2, and Keshen gas fields from the Kuche Depression as well as the Akemomu gas field from the Southwestern Depression are comparatively clarified firstly, then their

genetic types are identified and finally gas originations are comprehensively discussed.

2. Geological Setting

The Tarim Basin is one of the three biggest cratonic and foreland superimposed basins and the largest petroliferous basin in China. It can be divided into Tabei, Tazhong, and Ta'n'an uplifts, as well as Kuche, Northern, Southwestern, and Southeastern Depressions generally [34, 35]. The Kuche Depression is a Mesozoic and Cenozoic foreland basin, having northern monocline, southern gentle anticline, Qiulitage anticline, and Kela2 and Yiqikelike tectonic belts as well as Baicheng, Yangxia, and Wushi sags. The Kela2 tectonic belt is divided into Kela and Kela2 subsalt deep layers from north to south and 5 segments from west to east [26, 29]. The Kuche Depression has the most gas resource potential in the Tarim Basin, and many other large gas fields with gas reserve beyond 100 billion cubic meters have been found in recent two decades (Figure 1). Great breakthroughs have been achieved in the deep strata of the Kulasu and Qiulitage tectonic belts recently, showing great resource potential in the deep layer of the Kuche Depression.

The formation of the Kuche Depression from bottom to top mainly contains Triassic, Jurassic, and Shushanhe formation (K_1s), Baxigai formation (K_1b), and Bashijiqike formation (K_1bs) of Lower Cretaceous, Kumugeliemu group ($E_{1-2}km$) and Suweiyi formation ($E_{2-3}s$) of Paleogene, and

Jidike formation (N_{1j}), Kangcun formation (N_{1-2k}), and Kuche formation (N_{2k}) of Neogene, Quaternary (Figure 1). The main gas-producing layers include the Kumugeliemu group (E_{1-2km}) in the Paleogene strata and the Bashijiqi formation (K_{1bs}) and the Baxigai formation (K_{1b}) in the Lower Cretaceous strata. The gypsum mudstone and gypsum salt layers of the Kumugeliemu group of the Paleogene and the Jidike formation of the Neogene in the Kuche Depression are two sets of important regional caprocks. The coal measure source rocks of Jurassic to Triassic are well developed in the Kuche Depression. The organic matter of Jurassic source rocks is mainly Type III, with the thickness of dark mudstones ranging around 100–600 m and coal seams distributing around 5–40 m [28, 30, 33]. The organic matter of Triassic source rocks is generally Type II₂ and Type II₁, with the thickness of dark mudstones ranging around 200–600 m and coal seams reaching 10 m separately [28, 30, 33].

For comparing these gas fields from the Kuche Depression, the Akemomu gas field and the Tazhong I oil and gas field in the Tarim Basin as well as the Xushen and Changshen gas fields in the Songliao Basin are adopted. The Tazhong I oil and gas field is in the Tazhong low uplift of central uplift and has nearly 300 million tons of proven oil and gas reserves equivalent in platform margin reef-bank complex carbonate of Ordovician (Wang et al., 2011; Yang et al., 2011). Natural gases in the Tazhong I oil and gas field are oil-typed gas and mainly originated from marine sapropelic source rocks of Cambrian-Ordovician. The Akemomu gas field is located in the Southwestern Depression and natural gases are typical coal-formed gas. The Songliao Basin is located in northeast China and has an area of about 26×10^4 km². It is a Mesozoic and Cenozoic sedimentary basin with fault and depression dual structures which was developed on late Paleozoic basement. The Xusheng gas field is located in the Xujiaweizi fault depression, and the main gas reservoir is volcanic rock of the Yingcheng formation in Cretaceous. The Changshen gas field is located in the Changling fault depression, and the main reservoir is volcanic rock of the Yingcheng formation and clastic rock of the Dengloulou formation in Cretaceous. Natural gases in the Changshen and Xushen gas fields are mixed gases of organic coal-derived gas and deep inorganic gas [25].

3. Materials and Methods

A total of 21 gas samples including 19 from the Kela2, Dina2, Dabei, and Keshen gas fields in the Kuche Depression, as well as 2 from the Akemomu gas field in the Southwestern Depression, were specially selected and comprehensively studied, of which 8 were newly analyzed and 13 were collected from the author's previous researches. The relevant geochemical experimental analyses are completed in the Key Laboratory of Gas Reservoir Formation and Development of CNPC.

Conventional gas components were determined on an Agilent 6890N gas chromatograph (GC) equipped with a thermal conductivity detector (TCD), using helium as the carrier gas; a 30 m \times 0.32 mm \times 20 μ m PLOT Q or a 30 m \times 0.53 mm \times 25 μ m PLOT 5A MS column was used. The stable carbon isotopic compositions of natural gases

were determined on a Delta plus isotopic mass spectrometer equipped with an Agilent 6890N GC. Gas components were separated by gas chromatography, converted to CO₂ in a combustion interface, and then injected into the mass spectrometer. Gas samples were analyzed and the stable carbon isotopic values are reported in conventional δ notation in per mil (‰) relative to Vienna Pee Dee Belemnite (VPDB) standards. The reproducibility and accuracy are estimated to be $\pm 0.5\%$ with respect to the VPDB standard.

Molecular composition abundances and isotopic compositions of rare gases were measured in the Key Laboratory of Gas Reservoir Formation and Development of CNPC. In order to reduce impacts of rare gases in the air on sampling and experimentation and obtain correct rare gas analyzed results, some special gas sample collecting methods were adopted [23]. The detailed analytic processes were listed as follows [15, 23]. (1) A natural gas cylinder was connected to the injection port of the device through a pressure relief valve, and a mechanical pump, a molecular pump, and an ion pump were utilized to obtain low, high, and ultrahigh vacuum for the stainless steel pipeline separately. (2) The amount of natural gases was controlled by the sample injection control valve and vacuum gauge. (3) The active gases such as hydrocarbon gases, nitrogen (N₂), oxygen (O₂), carbon dioxide (CO₂), hydrogen sulfide (H₂S), and trace hydrogen gas (H₂) were purified by a zirconium base furnace, and an aspirator pump was used to enrich rare gases further. (4) The molecular composition abundances of rare gases were measured after purification. (5) Furthermore, a cryogenic pump, an activated carbon furnace, and liquid nitrogen were used to separate the components of helium (He), neon (Ne), argon (Ar), krypton (Kr), and xenon (Xe) according to different boiling points of different rare gases. (6) Finally, the separated rare gases were sent into rare gas isotope mass spectrometer to determine their isotopic compositions by method of peak height ratio on ion current signal intensity. The accuracies of molecular composition abundances of rare gases helium, neon, argon, krypton, and xenon were estimated to be $\pm 3.36\%$, $\pm 3.66\%$, $\pm 1.32\%$, $\pm 2.99\%$, and $\pm 6.96\%$ [23], and the accuracies of isotopic compositions of rare gases $^3\text{He}/^4\text{He}$, $^{20}\text{Ne}/^{22}\text{Ne}$, $^{40}\text{Ar}/^{36}\text{Ar}$, $^{38}\text{Ar}/^{36}\text{Ar}$, $^{129}\text{Xe}/^{130}\text{Xe}$, and $^{132}\text{Xe}/^{130}\text{Xe}$ were estimated to be $\pm 4.50\%$, $\pm 1.32\%$, $\pm 1.27\%$, $\pm 1.39\%$, $\pm 1.63\%$, $\pm 1.84\%$, and $\pm 2.13\%$, respectively.

4. Results and Discussion

4.1. Molecular Compositions of Hydrocarbon, Nonhydrocarbon, and Rare Gases. Natural gases in the Kela2, Dabei, Dina2, and Keshen gas fields from the Kuche Depression have high and wide-ranging methane abundance, mainly ranging from 87.3% to 98.4% (average is 95.52%). The abundances of C₁₋₄ distribute around 97.03%–99.26% (average is 98.51%) and the drying coefficient (C₁/C₁₊) is in the range of 0.892–0.995 (average is 0.972). The abundance of N₂ ranges from 0.36% to 1.67% (average is 0.74%), and CO₂ ranges around 0.05%–1.42% (average is 0.70%), excluding H₂S. On the contrary, natural gases in the Akemomu gas field from the Southwestern Depression have a relatively

low average methane abundance of 80.95% with high average carbon dioxide and nitrogen abundances of 10.75% and 8.11% separately and a high average drying coefficient of 0.997.

Compared to hydrocarbon and nonhydrocarbon gases, rare gas abundance in natural gases is extremely low. The general geochemical characteristics of each rare gas are as follows (Figures 2 and 3 and Table 1). (1) The helium abundance in gas fields from the Kuche Depression mainly distributes around $32\sim60 \times 10^{-6}$ (average is 49×10^{-6}), while it ranges around $1042\sim1062 \times 10^{-6}$ (average is 1054×10^{-6}) in the Akemomu gas field from the Southwestern Depression. (2) The neon abundance mainly distributes around $1.18\sim3.34 \times 10^{-6}$ (average is 1.76×10^{-6}) in the former and about $10.26\sim10.96 \times 10^{-6}$ (average is 10.608×10^{-6}) in the latter. (3) The argon abundance mainly distributes around $15\sim55 \times 10^{-6}$ (average is 27×10^{-6}) in the former. But it ranges around $342\sim394 \times 10^{-6}$ (average is 368×10^{-6}) in the latter. (4) The krypton abundance mainly distributes around $0.005\sim0.013 \times 10^{-6}$ (average is 0.008×10^{-6}) in the former. But it ranges around $0.042\sim0.056 \times 10^{-6}$ (average is 0.049×10^{-6}) in the latter. (5) The xenon abundance generally ranges $0.143\sim0.226 \times 10^{-8}$ (average is 0.174×10^{-8}) in the former. But it ranges around $1.081\sim1.402 \times 10^{-8}$ (average is 1.22×10^{-8}) in the latter.

Generally, the helium abundance in gas fields from the Kuche Depression is relatively 1 order of magnitude slightly higher than the air value, but it is more than 2 orders of magnitude in the Akemomu gas field from the Southwestern Depression. It is obviously not consistent with air from the distribution pattern of helium (Figure 3), obviously higher than the air value. The neon, argon, krypton, and xenon abundances in both areas are usually 1-3 orders lower than the corresponding air values. The distribution patterns of neon, argon, krypton, and xenon show that they are generally consistent with air (Figure 3). The relatively higher neon content indicates that neon in geological fluids of the gas field may be affected by air or air-saturated water before or during oil and gas reservoir forming.

4.2. Isotopic Compositions and Genetic Identification of Hydrocarbons and Rare Gases

4.2.1. Hydrocarbon Gases. The isotopic ratios of $\delta^{13}\text{C}_1$ and $\delta^{13}\text{C}_2$ in natural gases from the Kuche Depression generally range around $-34.5\text{‰}\sim-26.4\text{‰}$ (average value is -29.4‰) and $-24.2\text{‰}\sim-16.1\text{‰}$ (average value is 19.7‰) separately, while the average carbon isotopic values of $\delta^{13}\text{C}_1$ and $\delta^{13}\text{C}_2$ are -25.4‰ and -21.85‰ in the Akemomu gas field from the Kuche Depression correspondingly (Table 2).

According to the genetic identification index and charts provided by the former researchers [25, 36, 37], the $\delta^{13}\text{C}_2$ value of natural gases in the Kela2, Dabai, Dina2, and Keshen gas fields from the Kuche Depression mainly ranges from -24.2‰ to -16.1‰ with an average of -19.6‰ , which is obviously heavier than that of typical oil-typed gas in the Tazhong oil and gas field and can be considered as typical coal-formed gas (Figure 4). The average isotopic value ethane

value of (21.85‰) natural gases in the Akemomu gas field from the Southwestern Depression also shows the same characteristics of coal-formed gas as well.

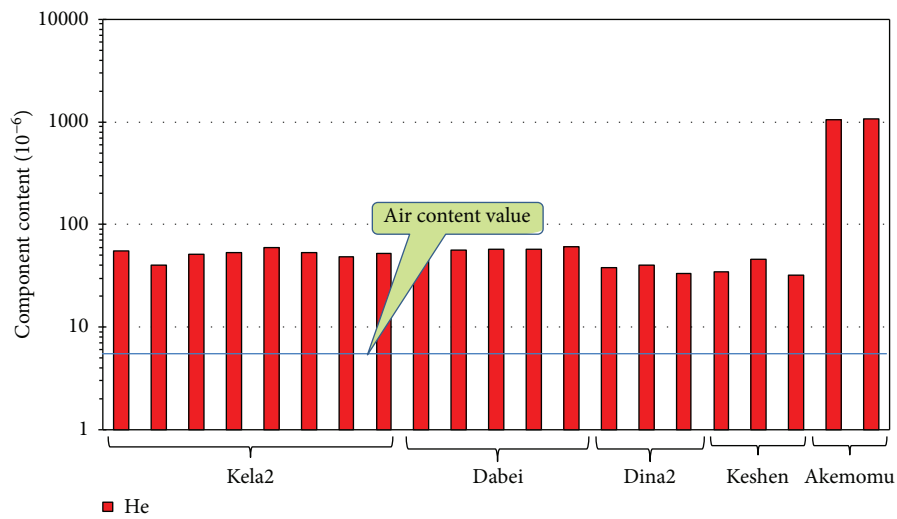
4.2.2. Helium. Helium has two stable isotopes: ^3He and ^4He . ^3He is a primordial nuclide, while ^4He is a radioactive nuclide which originated from radioactive elements [11, 38, 39]. The typical values of $^3\text{He}/^4\text{He}$ for air, mantle, and crust are 1.40×10^{-6} , 1.1×10^{-5} , and 2×10^{-8} separately [12, 14, 40, 41].

The $^3\text{He}/^4\text{He}$ value of natural gases in these gas fields from the Kuche Depression is generally distributed around $(3.33\sim11.24) \times 10^{-8}$ ($0.024\sim0.080R_a$) with an average of 6.04×10^{-8} ($0.043R_a$), indicating a typical crustal genesis characteristics with crustal proportion more than 98.8% (Table 2 and Figure 5). It is primarily derived from the decay of crustal radioactive elements, such as uranium (U) and thorium (Th). The $^3\text{He}/^4\text{He}$ value of natural gases in the Akemomu gas field from the Southwestern Depression is chiefly distributed around $(83.1\sim83.6) \times 10^{-8}$ ($0.0596\sim0.0597R_a$) with an average of 83.35×10^{-8} ($0.05965R_a$), showing main crustal genesis characteristics with crustal proportion around 92.5%, probably accompanied by a little mantled helium addition (Table 2 and Figure 5).

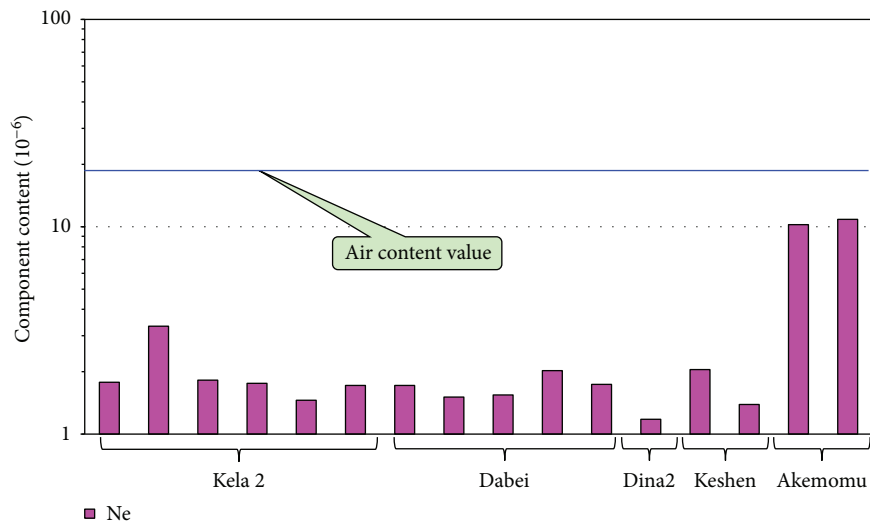
4.2.3. Neon. Neon has three stable isotopes, ^{20}Ne , ^{21}Ne , and ^{22}Ne , of which ^{20}Ne is a primordial nuclide, ^{21}Ne and ^{22}Ne are radioactive nuclides [42, 43]. The isotopic ratios of $^{20}\text{Ne}/^{22}\text{Ne}$ and $^{21}\text{Ne}/^{22}\text{Ne}$ in air usually keep stable, which are 9.800 and 0.0290 separately. The Mid Ocean Ridge Basalt (MORB) and Ocean Island Basalt (OIB) which originated from the mantle generally had an excessive primordial ^{20}Ne and then lead to a much higher $^{20}\text{Ne}/^{22}\text{Ne}$ value than that of air, while the radioactive elements in the crust such as uranium, thorium, oxygen, and fluorine (e.g., ^{18}O (n, a) ^{21}Ne and ^{19}F (n, a) ^{22}Ne) formed more enriched ^{21}Ne and ^{22}Ne and then caused a relatively lower $^{20}\text{Ne}/^{22}\text{Ne}$ value compared to that of the atmosphere.

The $^{20}\text{Ne}/^{22}\text{Ne}$ value of natural gases in gas fields from the Kuche Depression that ranged 9.50~9.74 with an average of 9.64 is generally lower than that of air, indicating that neon has crustal genesis and mainly originated from radioactive elements in the crust (Figures 6 and 7). In addition, the $^{20}\text{Ne}/^{22}\text{Ne}$ values of natural gases in gas fields from the Kuche Depression are positively correlated with $^3\text{He}/^4\text{He}$ values, indicating that ^{20}Ne possibly has the similar origination with ^3He and ^{22}Ne probably has the similar origination with ^4He (Figure 7). The $^{20}\text{Ne}/^{22}\text{Ne}$ value in the Akemomu gas field from the Southwestern Depression is about 9.71 and ^{20}Ne is relatively depleted, probably showing that neon has mainly crustal genesis (Figure 6). On the contrary, the $^{20}\text{Ne}/^{22}\text{Ne}$ value in the Changshen and Xushen gas fields is distributed around 9.88~10.07 and ^{20}Ne is relatively excessive compared with air, indicating that neon has an obvious mixture of mantle-derived genesis.

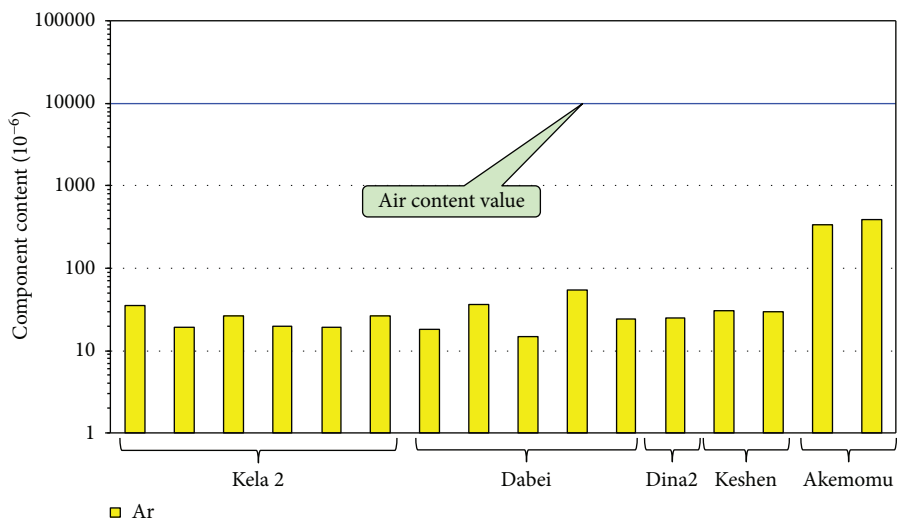
4.2.4. Argon. Argon generally has three stable isotopes, ^{36}Ar , ^{38}Ar , and ^{40}Ar , of which ^{36}Ar and ^{38}Ar are original nuclides, ^{40}Ar is a radioactive nuclide chiefly derived from the decay of ^{40}K ([5]; Liu and Xu, 1987; [7, 18]). The isotopic



(a)



(b)



(c)

FIGURE 2: Continued.

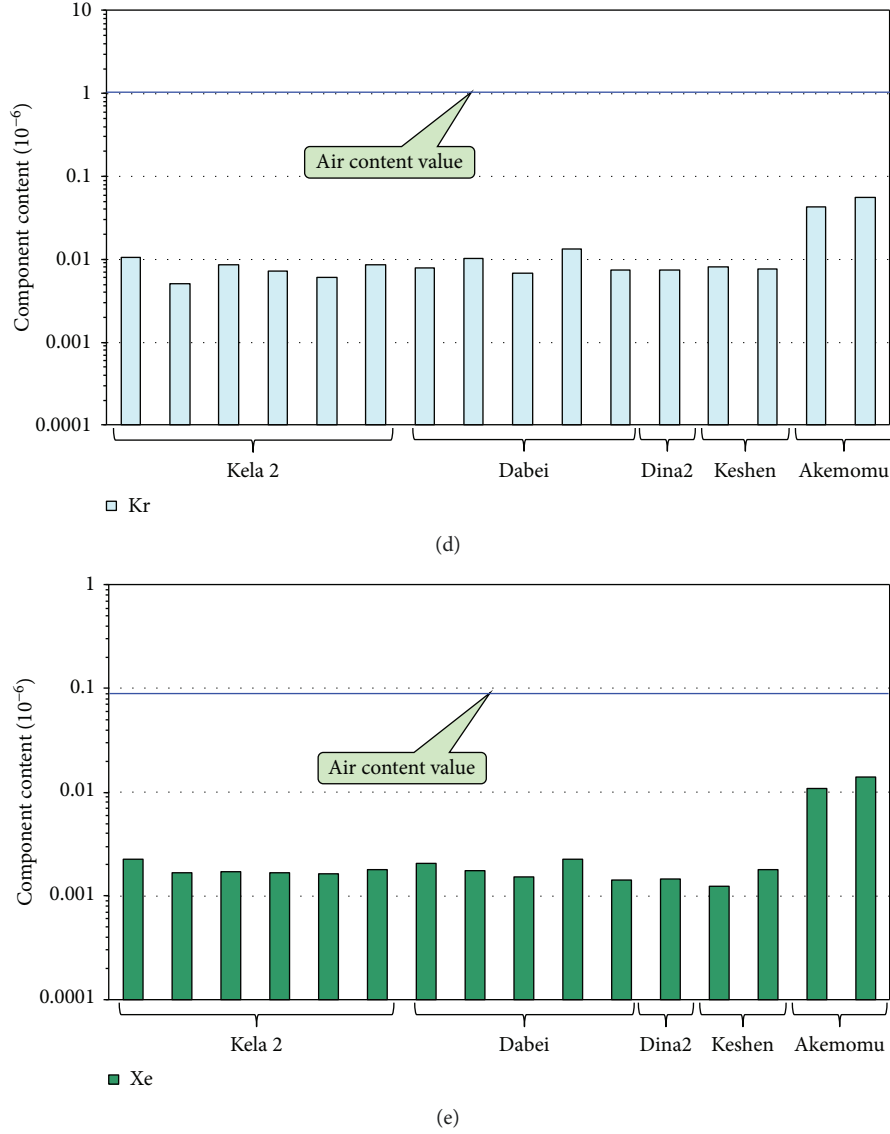


FIGURE 2: Histogram of helium, neon, argon, krypton, and xenon abundances in some gas fields from the Kuche and Southwestern Depressions, Tarim Basin.

compositions of argon in air are stable; the atmospheric $^{40}\text{Ar}/^{36}\text{Ar}$ and $^{38}\text{Ar}/^{36}\text{Ar}$ are 295.5 and 0.188 separately [5, 7, 20, 21]. Because of the uneven distribution of ^{40}K on the earth, the isotopic ratios of argon vary greatly in the crust and mantle.

The $^{40}\text{Ar}/^{36}\text{Ar}$ value of natural gases in gas fields from the Kuche Depression mainly distributes around 387~1323 (average of 659) and generally has a negative correlation with $^3\text{He}/^4\text{He}$ value, indicating that rare gas argon has typical crustal-derived genesis (Table 2 and Figure 8). The variation of argon isotope in the Kuche Depression is mainly caused by the uneven distribution of ^{40}K and possibly effected by different mixing ratios of air or air-saturated water during gas reservoir forming to some extent. In the Akemomu gas field from the Southern Depression, the $^{40}\text{Ar}/^{36}\text{Ar}$ value is relatively high and mainly distributed around 1653~1665 with an average of 1659, and the $^3\text{He}/^4\text{He}$ value is mainly distributed around $(8.31\sim 8.36) \times 10^{-7}$ with an average value

of 8.34×10^{-7} , indicating that rare gases have main crustal genesis possibly with a few mantle-derived contribution (Figure 8). However, the isotopic ratio of $^3\text{He}/^4\text{He}$ of natural gases in the Changshen and Xushen gas fields is generally larger than that of atmospheric value and has an obvious positive relationship with $^{40}\text{Ar}/^{36}\text{Ar}$, indicating that rare gases are of obvious mantle genesis mixing.

4.2.5. Xenon. Xenon has nine stable isotopes, of which ^{129}Xe , ^{130}Xe , ^{131}Xe , ^{132}Xe , ^{134}Xe , and ^{136}Xe are relatively useful in gas genetic identification. ^{129}Xe in earth's materials principally originated from the radioactive decay of the extinct ^{129}I , and $^{131}\sim^{136}\text{Xe}$ are usually derived from ^{238}U or extinct ^{244}Pu [17]. Because of short half-lives of ^{129}I (18 Ma) and ^{244}Pu (82 Ma), their decayed products ^{129}Xe and $^{131}\sim^{136}\text{Xe}$ are totally trapped in the mantle [44]. So, the relative excess of ^{129}Xe and its positive correlation with $^{131}\sim^{136}\text{Xe}$ in MORB show their origination of decay from ^{129}I and ^{244}Pu in the

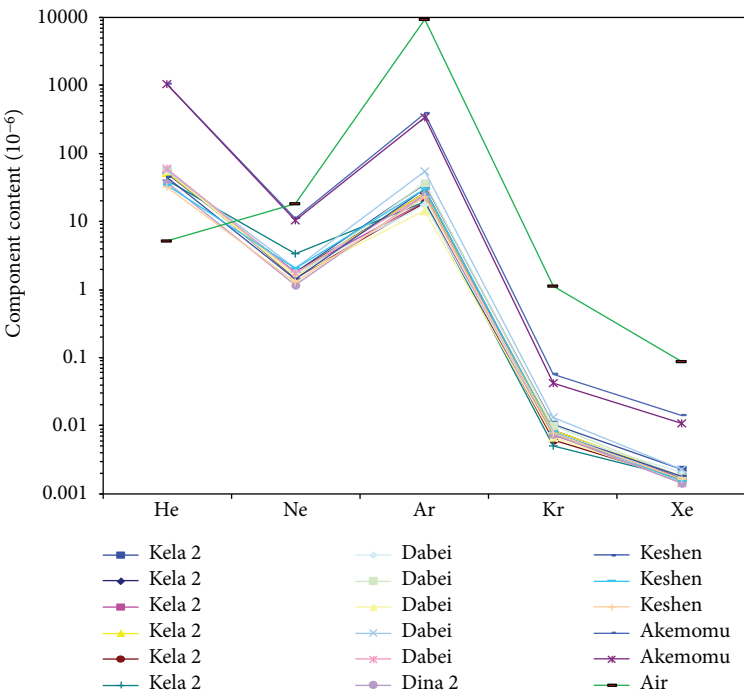


FIGURE 3: Broken line chart of helium, neon, argon, krypton, and xenon abundances in some gas fields from the Kuche and Southwestern Depressions, Tarim Basin.

TABLE 1: Molecular composition of hydrocarbon, nonhydrocarbon, and rare gases in some gas fields from the Kuche and Southwestern Depressions, Tarim Basin.

Tectonic unit	Gas field	Strata	CH ₄ (%)	CO ₂ (%)	N ₂ (%)	C ₁₋₄ (%)	C ₁ /C ₁₊	He (10 ⁻⁶)	Ne (10 ⁻⁶)	Ar (10 ⁻⁶)	Kr (10 ⁻⁶)	Xe (10 ⁻⁸)	References
Kuche Depression	Kela2	E	98.4	0.05	0.69	99.26	0.991	55	1.79	35	0.011	0.224	[15]
		K ₁ , E	97.5	0.60	0.37	99.03	0.985	41	3.34	19	0.005	0.167	
		K ₁ , E	93.7	0.53	0.36	99.11	0.995	52	1.82	26	0.009	0.172	
		K ₁ , E	98.1	0.70	0.56	98.74	0.994	53	1.77	20	0.007	0.166	
		K ₁ , E	97.4	0.69	0.38	98.93	0.985	59	1.46	19	0.006	0.162	
		K ₁ , E	98.3	0.69	0.58	98.73	0.994	53	1.73	27	0.009	0.180	
		K ₁ , E	97.7	0.43	0.36	99.2	0.985	48					This paper
		K ₁ , E	97.5	0.64	0.38	98.97	0.984	52					
	Dabei	K ₁ bs	95.8	1.42	0.44	98.15	0.976	59	1.73	18	0.008	0.204	[23]
		K ₁ bs	97.1	0.81	0.58	98.61	0.984	57	1.52	37	0.010	0.176	
		K ₁ bs	94.8	1.27	1.67	97.03	0.977	57	1.55	15	0.007	0.151	
		K ₁ bs	95.3	1.29	0.71	98.05	0.97	57	2.04	55	0.013	0.226	
		K ₁ bs	94.3	1.27	0.99	97.71	0.965	60	1.74	24	0.007	0.143	
	Dina	E	87.3	0.59	1.58	97.83	0.892	38	1.18	25	0.008	0.144	This paper
		E	88.5	0.33	1.11	97.95	0.904	40					
		E	89.1	0.36	1.08	98.34	0.906	33					
		K ₁ bs	97.9	0.61	0.86	98.53	0.994	36	2.05	30	0.008	0.151	
Keshen	K ₁ bs	98.3	0.30	0.72	98.98	0.993	45	1.40	30	0.007	0.178	This paper	
	K ₁ bs	97.9	0.78	0.70	98.45	0.994	32	1.30	23	0.008	0.165		
	Akemommu	K	81.1	10.20	8.40	81.40	0.996	1046	10.26	342	0.042		1.081
K		80.8	11.30	7.80	80.89	0.997	1062	10.96	394	0.056	1.402		
Southwestern Depression													
Air								5.24	18.18	9340	1.140	8.7	

Tectonic unit	Gas field	Strata	$\delta^{13}\text{C}_1$ (‰)	$\delta^{13}\text{C}_2$ (‰)	$^3\text{He}/^4\text{He}$ (10^{-8})	R/R_a	$^{20}\text{Ne}/^{22}\text{Ne}$	$^{21}\text{Ne}/^{22}\text{Ne}$	$^{40}\text{Ar}/^{36}\text{Ar}$	$^{38}\text{Ar}/^{36}\text{Ar}$	$^{129}\text{Xe}/^{130}\text{Xe}$	$^{132}\text{Xe}/^{130}\text{Xe}$	References
Kela2	Kela2	E	-27.6	-18	3.93	0.028	9.70	0.0298	1211	0.195	6.301	6.663	[15]
		K ₁ , E	-26.4	-17.8	4.31	0.031	9.65	0.0305	1323	0.196	6.433	6.706	
		K ₁ , E	-26.8	-18.4	6.77	0.048	9.74	0.0299	589	0.196	6.434	6.745	
		K ₁ , E	-28.1	-19.1	8.58	0.061	9.69	0.0307	719	0.198	6.418	6.628	
		K ₁ , E	-28	-18.7	5.68	0.041	9.63	0.0301	720	0.197	6.452	6.685	
		K ₁ , E	-27.8	-19	7.24	0.052	9.68	0.0302	462	0.195	6.399	6.715	This paper
		K ₁ , E	-27.3	-18.5	3.75	0.027							
		K ₁ , E	-27.4	-18.3	4.12	0.029							
		K ₁ bs	-30.9	-22.1	6.31	0.045	9.56	0.0291	858	0.201	6.446	6.689	
		K ₁ bs	-29.4	-19.4	8.73	0.062	9.60	0.0303	504	0.197	6.436	6.653	
Kuche Depression	Dabei	K ₁ bs	-30.4	-21.8	7.14	0.051	9.62	0.0307	521	0.204	6.422	6.638	[23]
		K ₁ bs	-30.7	-22.3	8.68	0.062			390	0.196			
		K ₁ bs	-31.9	-24.2	11.24	0.08	9.73	0.0299	485	0.199			
	Dina	E	-34.5	-21.3	3.33	0.024	9.50	0.0297	387	0.193	6.478	6.759	This paper
		E	-34.6	-22.4	3.56	0.025							
		E	-33.3	-22.5	3.82	0.027							
Southwestern Depression	Keshen	K ₁ bs	-27.8	-16.1	6.87	0.049	9.68	0.0304	841	0.194	6.381	6.809	This paper
		K ₁ bs	-27.7	-16.3	4.58	0.033	9.54	0.0306	456	0.191	6.422	6.704	
		K ₁ bs	-27.6	-17.3	6.07	0.043	9.64	0.0302	412	0.187	6.471	6.775	
	Akemommu	K	-25.6	-21.9	83.10	0.596			1653	0.198	6.437	6.754	
Air	Air	K	-25.2	-21.8	83.60	0.597	9.71		1665	0.202	6.389	6.828	
					140	1	9.8	0.029	295.5	0.188	6.496	6.607	

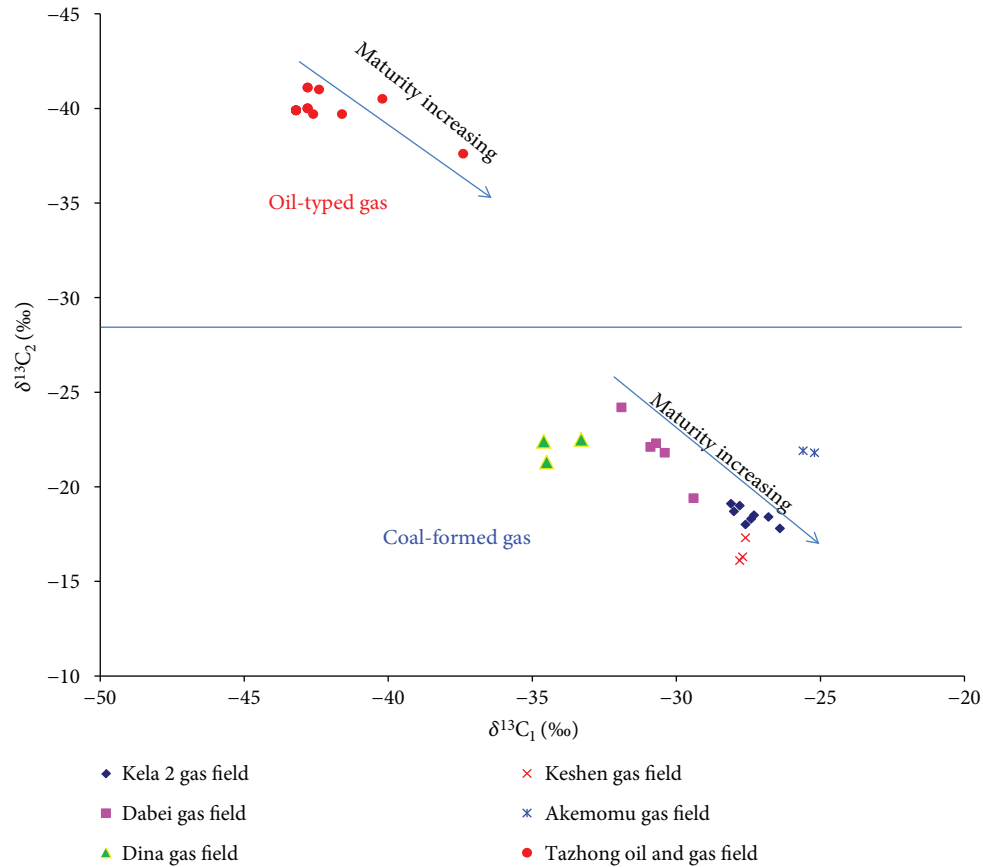


FIGURE 4: Genetic identification of $\delta^{13}\text{C}_1$ and $\delta^{13}\text{C}_2$ for natural gases of some gas fields from the Kuche and Southwestern Depressions, Tarim Basin (modified from [25, 36]).

mantle [11, 13, 17], while a relative excess of $^{131}\sim^{136}\text{Xe}$ rather than ^{129}Xe generally reflects the origination of spontaneous fission from ^{238}U in the crust.

The $^{129}\text{Xe}/^{130}\text{Xe}$ value of natural gases in gas fields from the Kuche Depression ranges around 6.301~6.471 with an average of 6.422 and distributes around 6.389~6.437 with an average of 6.413 in the Akemomu gas field from the Southwest Depression (Table 2). The $^{132}\text{Xe}/^{130}\text{Xe}$ value of natural gases ranges around 6.628~6.809 with an average of 6.705 in the former and 6.754~6.828 with an average of 6.791 in the latter (Table 2). The relatively depleted ^{129}Xe and the excessive ^{132}Xe in gas fields from the Kuche Depression as well as the Akemomu gas field from the Southwestern Depression indicate that xenon has chiefly crustal-derived genesis (Figure 9), while the Changshen and Xushen gas fields in the Songliao Basin have a relatively excessive ^{129}Xe rather than ^{132}Xe , showing that xenon is obviously mixed with mantle-derived genesis [23].

4.3. Gas Source Correlation. Previous genetic identification of hydrocarbon gas isotopes shows that natural gases of the Kela2, Dina2, Dabei, and Keshen gas fields in the Kuche Depression are typical coal-formed gases (Figure 4), principally generated from coal measure source rocks in the Kuche Depression. According to the correlation between methane

isotope ($\delta^{13}\text{C}_1$, ‰) of coal-formed gas and thermal evolution maturity (R_o , %) of coal measure source rocks [36, 37], $\delta^{13}\text{C}_1 = 14.131\lg(R_o) - 34.39$, the calculated maturity of coal-formed gases of these gas fields in the Kuche Depression is generally around 0.97%~3.68%. According to the relationship between coal-formed gas wetness (W , %) and maturity (R_o , %) (Dai et al., 2016), $R_o = -0.419\ln W + 1.908$, the calculated maturity of coal-formed gases of these gas fields in the Kuche Depression is about 0.96%~2.2%. From the comparison on the above calculated maturities, the former is more close to the actual thermal evolution of coal measure source rocks of Jurassic-Triassic in the Kuche Depression with maturity from mature to high mature even overmature. So, natural gases of these gas fields in the Kuche Depression generally originated from coal measure source rocks of Jurassic and Triassic with maturity from mature to high mature even overmature on conventional hydrocarbon gas source correlation.

Rare gases play a very important and useful role in identifying gas genesis and origination, enabling us to verify and deepen the understandings on conventional gas source correlation further. The average value of $^3\text{He}/^4\text{He}$ in gas fields from the Kuche Depression is about 6.04×10^{-8} , showing typical crustal-derived characteristics, so the chronological cumulative effect of argon isotopes can be adopted on gas

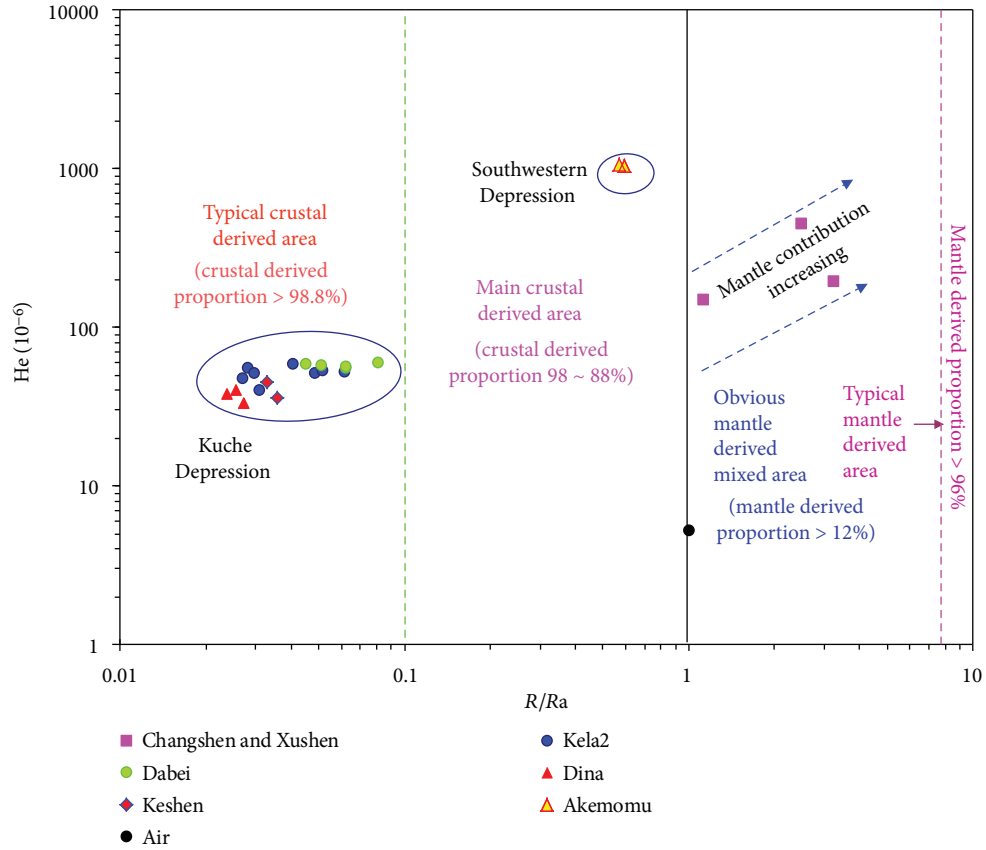


FIGURE 5: Genetic identification of He- R/R_a for some gas fields from the Kuche and Southwestern Depressions, Tarim Basin (chart modified from [23]).

source correlation in this area. Considering the carbonate source rocks having relatively old geologic age, the $^{40}\text{Ar}/^{36}\text{Ar}$ value of 387~1323 for natural gases in the Kuche Depression is obviously less than the calculated value of 2088~3686 from source rocks of Cambrian to Ordovician, so the carbonate source rocks of Cambrian to Ordovician can be excluded firstly. Coal measure source rocks of Triassic to Jurassic are greatly deposited in the Kuche Depression in the Mesozoic and Cenozoic periods. The average value of $^{40}\text{Ar}/^{36}\text{Ar}$ (659) in natural gases from the Kuche Depression mainly falls in the estimated range of gases generated from the Jurassic source rocks (571~767) and relatively deviates from the estimated range of gases generated from the Triassic source rocks (767~920). So, it can be concluded that natural gases of the Kuche Depression are probably derived from the coal measure source rocks of Jurassic and Triassic, principally from the Jurassic source rocks. According to obvious differences on $^{40}\text{Ar}/^{36}\text{Ar}$ value of natural gases that originated from different periods of source rocks, the calculated proportions of the Jurassic source rocks account for 55%-75% and the Triassic source rocks account for 25%-45%. As we know, the Jurassic source rocks are main coal measure source rocks and usually have a relatively higher gas potential, while the Triassic source rocks are main lake mudstone source rocks and generally have a relatively lower gas potential. The estimated proportion of the Jurassic and Triassic source

rocks shows that the contribution of the Jurassic source rock is obviously higher than that of the Triassic source rock. The above evaluated result is generally according to the current mainstream viewpoints that the Jurassic source rock is the main source rocks for natural gases in the Kuche Depression when taking gas generation potential into account ([27, 28, 33–35, 45]; Li et al., 2005; [25, 46]).

Furthermore, because of great differences on kalium-bearing minerals in mudstones and coals, the $^{40}\text{Ar}/^{36}\text{Ar}$ values of natural gases that originated from mudstones and coals have obvious differences [18, 47]. Natural gases derived from mudstones usually have relatively higher $^{40}\text{Ar}/^{36}\text{Ar}$ values while natural gases derived from coal rocks generally have relatively lower $^{40}\text{Ar}/^{36}\text{Ar}$ values. It can be used to discuss the proportional contributions of mudstones and coals in coal measure source rocks. According to the above methods, assuming that the maximum $^{40}\text{Ar}/^{36}\text{Ar}$ value of natural gases in the Kuche Depression represented the maximum end-member value for gas that originated from mudstones and the minimum $^{40}\text{Ar}/^{36}\text{Ar}$ value of experimental thermal simulation gas on coals (341) represented the minimum end-member value for gas that originated from coals, the proportional contributions of coals and mudstones on coal measure source rocks of Jurassic and Triassic in the Kuche Depression are preliminarily evaluated. The results show that the contributed proportions of coals and

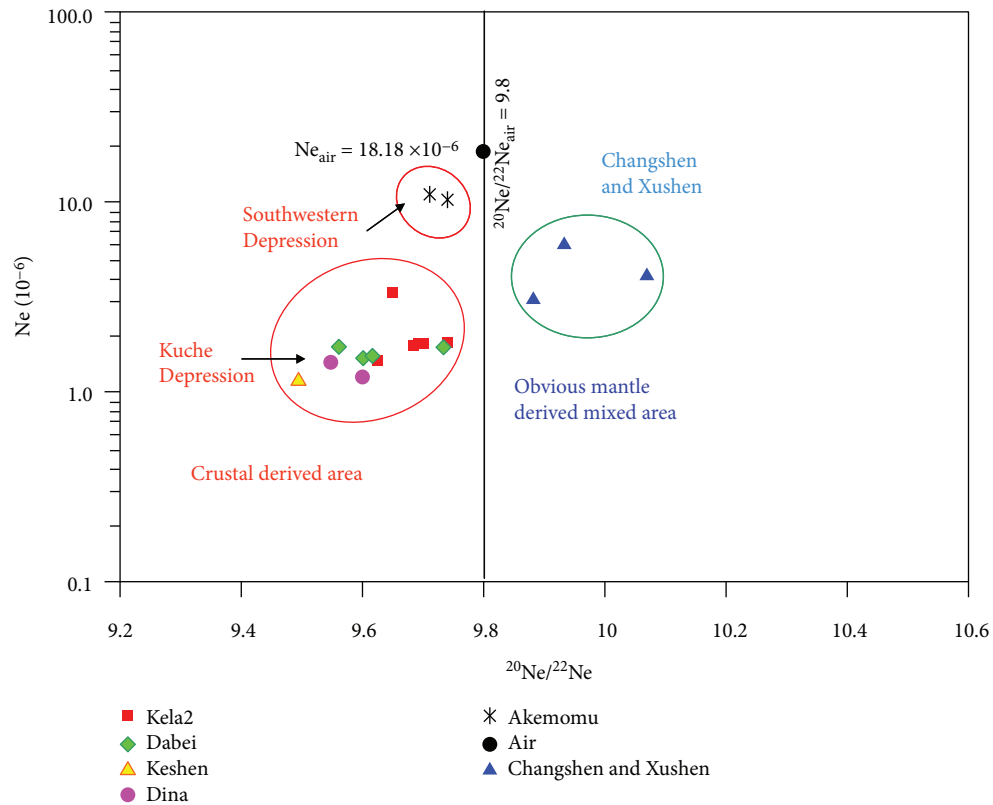


FIGURE 6: Genetic identification of Ne-²⁰Ne/²²Ne for some gas fields from the Kuche and Southwestern Depressions, Tarim Basin.

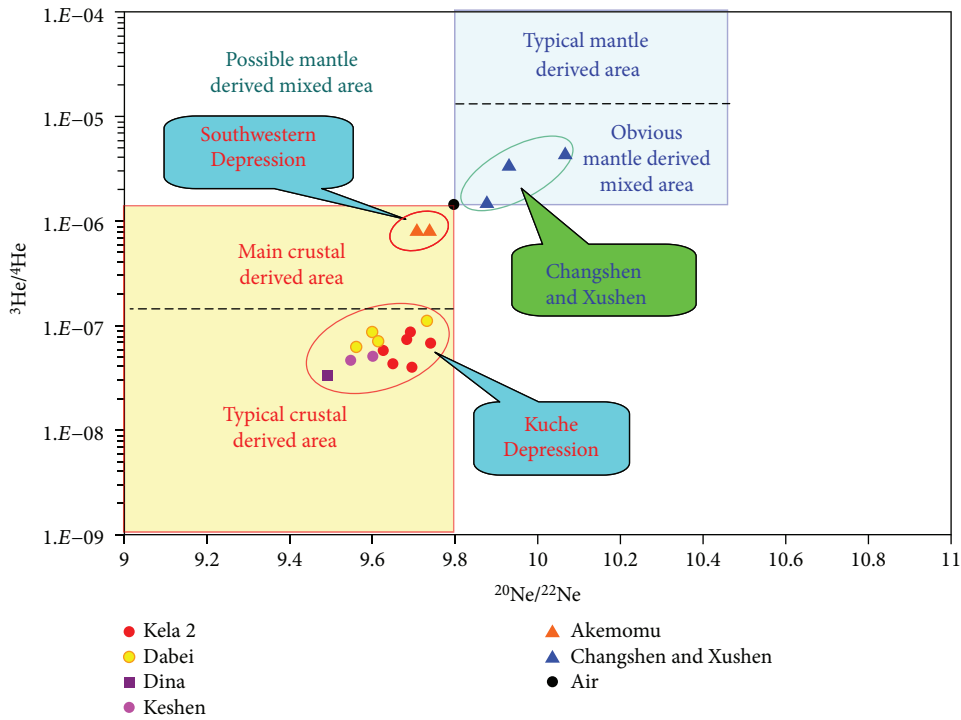


FIGURE 7: Genesis identification of ³He/⁴He-²⁰Ne/²²Ne for some gas fields from the Kuche and Southwestern Depressions, Tarim Basin (chart modified from [23]).

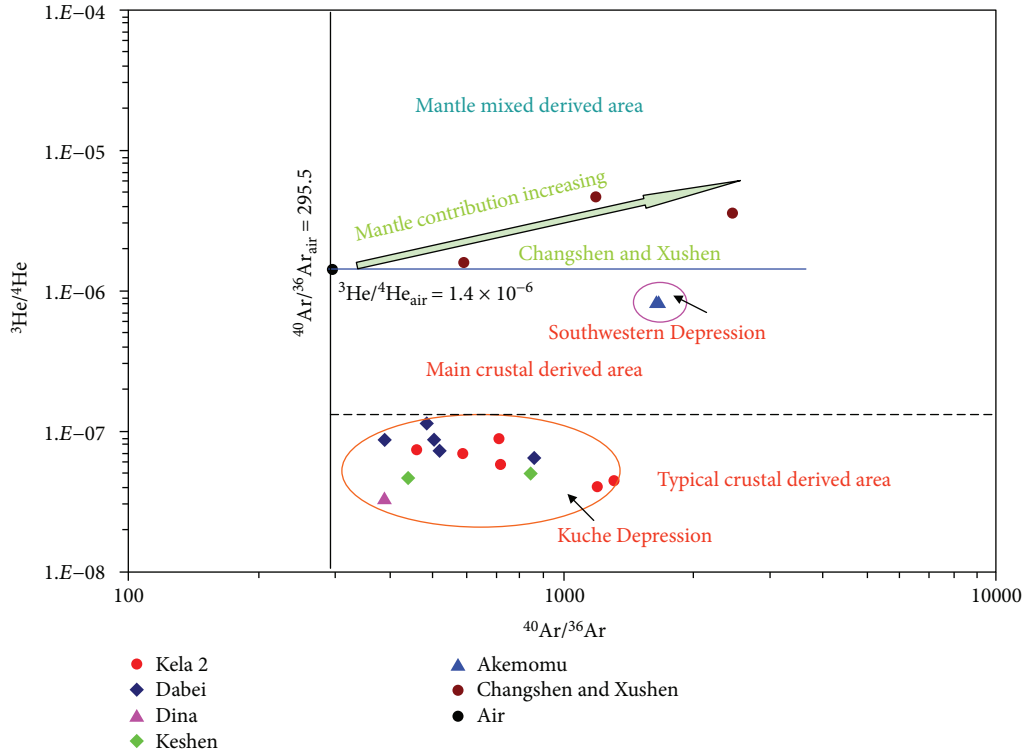


FIGURE 8: Genetic identification of $^3\text{He}/^4\text{He}$ - $^{40}\text{Ar}/^{36}\text{Ar}$ for some gas fields from the Kuche and Southwestern Depressions, Tarim Basin (chart modified from [23]).

mudstones in coal measure source rocks of Jurassic and Triassic are 68% and 32%, respectively. In addition, adopting the average $\delta^{13}\text{C}_1$ of -29.38‰ of natural gases in the Kuche Depression and taking the reported heaviest $\delta^{13}\text{C}_1$ of -25.1‰ [48] and the lightest $\delta^{13}\text{C}_1$ of -36.9‰ [25] in the Kuche Depression as the end-member values of natural gases from coals and mudstones, the evaluated contributions of coals and mudstones from coal measure source rocks of Jurassic and Triassic in the Kuche Depression are around 64% and 36%, respectively. The two methods have nearly the same results which show that the evaluated result is correct and reliable.

Natural gases from the Akemomu gas field in the Southwestern Depressions are generally typical coal-formed gases (Figure 4). The drying coefficients of natural gas and carbon isotope ratios of methane indicate that Akemomu gas source rocks have high maturity. The natural gases in the Akemomu gas field have a relatively higher helium and argon contents and argon isotope than those of gas fields from the Kuche Depression, showings their obvious differences on gas geochemical characteristics and origins. Coal measure source rocks of Triassic to Jurassic and marine and continental transitional source rocks of Carboniferous to Permian are developed in the Southwestern Depression. The average value of $^{40}\text{Ar}/^{36}\text{Ar}$ (1659) of natural gases from the Akemomu gas field is obviously larger than the estimated value of gas generated from the source rocks of Jurassic to Triassic (571~920), and the higher argon isotope indicates that their source rock has a relatively longer accumulating

time for gas accumulation, so the natural gases of the Akemomu gas field mainly originated from humic mudstones of marine and continental transitional source rocks of Carboniferous to Permian.

5. Conclusions

- (1) Gas fields in the Kuche Depression have a higher methane abundance, accompanied with low N_2 and CO_2 abundances, but the Akemomu gas field in the Southwestern Depression has a relatively lower average methane abundance, accompanied with high average N_2 and CO_2 abundances. The helium abundance of natural gases in gas fields from the Kuche Depression general has 1 order of magnitude higher than the air value. Comparatively, it has more than 2 orders of magnitude higher than the atmospheric value in the Akemomu gas field from the Southwestern Depression. The neon, argon, krypton, and xenon abundances in both Kuche and Southwestern Depressions are generally lower than the corresponding air values.
- (2) Natural gases from gas fields in the Kuche Depression and the Southwestern Depressions are generally typical coal-formed gases. The rare gases in the Kuche Depression have typical crustal genesis, mainly deriving from the radioactive decay of elements in the crust, while in the Akemomu gas field from the

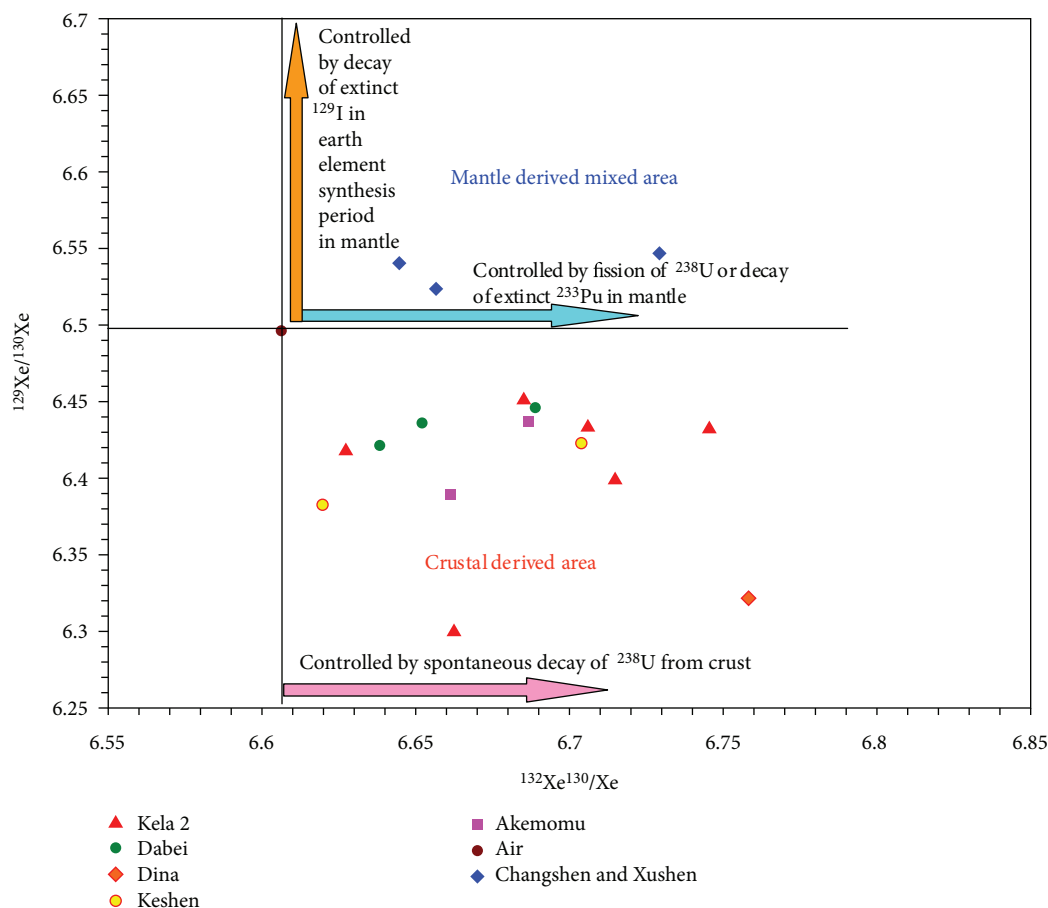


FIGURE 9: Genetic identification of $^{129}\text{Xe}/^{130}\text{Xe}$ - $^{132}\text{Xe}/^{130}\text{Xe}$ for some gas fields from the Kuche and Southwestern Depressions, Tarim Basin (chart modified from [23]).

Southwestern Depression, the rare gases have main crustal genesis with a proportion of 92.5%, probably accompanied with a little mantled genetic contribution.

- (3) Natural gases in the Kuche Depression are generally derived from coal measure source rocks of Jurassic and Triassic, which principally originated from Jurassic in strata period and coals in source rock types. The Jurassic source rocks account for 55%-75% and the Triassic source rocks account for 25%-45% approximately, while coals occupy 68% and mudstones occupy 32% separately. Natural gases from the Akemomu gas field in the Southwestern Depression mainly originated from humic mudstones of marine and continental transitional source rocks of Carboniferous to Permian.

Data Availability

The molecular and isotope composition geochemical data of natural gases used to support the findings of this study are included within the article. The experimental methods and processes are introduced in the manuscript. Some previously reported geochemical data are cited at relevant

places within the text as references [15, 23] in the manuscript to support this study and are available at DOI: 10.1177/0144598715623673 and DOI: 10.1016/j.marpetgeo.2017.02.013.

Conflicts of Interest

The authors declare that they have no conflicts of interest.

Acknowledgments

This paper was sponsored by the Major Project of National Special Science and Technology (2016ZX05007-003), the Strategic Priority Research Program of the Chinese Academy of Sciences (XDA14010403), and the Program of Petro-China Company Limited (2018D-500802, 2016B-0601, and 2016ycq03). Thanks are due to anonymous reviewers for their constructive suggestions.

References

- [1] Y. C. Xu, X. B. Wang, R. M. Wu, P. Shen, Y. X. Wang, and Y. P. He, "Rare gas isotopic composition of natural gases," *Geochimica*, vol. 8, no. 9, pp. 271-282, 1979.

- [2] C. J. Allegre, P. Sarda, and T. Staudacher, "Speculations about the cosmic origin of He and Ne in the interior of the Earth," *Earth and Planetary Science Letters*, vol. 117, no. 1-2, pp. 229-233, 1993.
- [3] C. J. Allegre, T. Staudacher, P. Sarda, and M. Kurz, "Constraints on evolution of Earth's mantle from rare gas systematics," *Nature*, vol. 303, no. 5920, pp. 762-766, 1983.
- [4] M. Honda, D. B. Patterson, I. McDougall, and T. J. Falloon, "Noble gases in submarine pillow basalt glasses from the Lau Basin: detection of a solar component in backarc basin basalts," *Earth and Planetary Science Letters*, vol. 120, no. 3-4, pp. 135-148, 1993.
- [5] M. Ozima and F. A. Podeseck, *Rare Gas Geochemistry*, Cambridge University Press, London, 1983.
- [6] R. J. Poreda and K. A. Farley, "Rare gases in Samoan xenoliths," *Earth and Planetary Science Letters*, vol. 113, no. 1-2, pp. 129-144, 1992.
- [7] X. B. Wang, *Rare Gas Isotope Geochemistry and Cosmochemistry*, Science Press, Beijing, 1989.
- [8] J. A. Welhan and H. Craig, "Methane, hydrogen and helium in hydrothermal fluids at 21°N on the East Pacific Rise," in *Hydrothermal Processes at Seafloor Spreading Centers. NATO Conference Series (IV Marine Sciences)*, vol. 12, P. A. Rona, K. Bostrom, and L. Laubier, Eds., pp. 391-410, Plenum Press, Boston, MA, USA, 1983.
- [9] J. A. Welhan, R. J. Poreda, W. Rison, R. Poreda, and P. Craig, "Geothermal gases of the Mud Volcano Area, Yellowstone Park," *Eos(Transactions, American Geophysical Union)*, vol. 64, p. 882, 1983.
- [10] A. Battani, P. Sarda, and A. Prinzhofer, "Basin scale natural gas source, migration and trapping traced by noble gases and major elements: the Pakistan Indus basin," *Earth and Planetary Science Letters*, vol. 181, no. 1-2, pp. 229-249, 2000.
- [11] P. Burnard, L. Zimmermann, and Y. Sano, "The noble gases as geochemical tracers: history and background," in *The Noble Gases as Geochemical Tracers. Advances in Isotope Geochemistry*, P. Burnard, Ed., pp. 1-16, Springer, Berlin, Heidelberg, 2013.
- [12] J. Lupton and L. Evans, "The atmospheric helium isotope ratio: is it changing?," *Geophysical Research Letters*, vol. 31, no. 13, pp. 482-485, 2004.
- [13] A. Prinzhofer, "Noble gas in oil and gas accumulations," in *The noble Gases as Geochemical Tracers. Advances in Isotope Geochemistry*, P. Burnard, Ed., pp. 225-247, Springer, Berlin, Heidelberg, 2013.
- [14] Y. Sano, T. Tokutake, and N. Takahata, "Accurate measurement of atmospheric helium isotopes," *Analytical Sciences*, vol. 24, no. 4, pp. 521-525, 2008.
- [15] X. Wang, G. Wei, J. Li et al., "Geochemical characteristics and origins of noble gases of the Kela 2 gas field in the Tarim Basin, China," *Marine and Petroleum Geology*, vol. 89, pp. 155-163, 2018.
- [16] S. Xu, Y. C. Xu, P. Shen et al., "The isotopic composition and its geological significance of neon in natural gas of eastern basin in China," *Chinese Science Bulletin*, vol. 41, no. 21, pp. 970-972, 1996.
- [17] S. Xu, Y. Xu, P. Shen, S. Nakal, and H. Wakita, "Noble gas isotopes in natural gases from Central and Northwest China," *Chinese Science Bulletin*, vol. 42, no. 10, pp. 838-841, 1997.
- [18] W. H. Liu and Y. C. Xu, "The significance of helium and argon isotopic composition in natural gases," *Chinese Science Bulletin*, vol. 38, no. 9, pp. 818-821, 1993.
- [19] M. L. Sun, Y. C. Xu, and X. B. Wang, "Mass spectrometer analysis for He isotope in natural gases," *Journal of Instrumental Analysis*, vol. 10, no. 5, pp. 50-55, 1991.
- [20] J. Y. Lee, K. Marti, J. P. Severinghaus et al., "A redetermination of the isotopic abundances of atmospheric Ar," *Geochimica et Cosmochimica Acta*, vol. 70, no. 17, pp. 4507-4512, 2006.
- [21] D. F. Mark, F. M. Stuart, and M. de Podesta, "New high-precision measurements of the isotopic composition of atmospheric argon," *Geochimica et Cosmochimica Acta*, vol. 75, no. 23, pp. 7494-7501, 2011.
- [22] X. Wang, Z. Li, J. Li et al., "Technique for total composition and isotope analyses of rare gases," *Acta Petrolei Sinica*, vol. 34, pp. 70-77, 2013.
- [23] X. Wang, J. Chen, Z. Li et al., "Rare gases geochemical characteristics and gas source correlation for Dabai gas field in Kuche depression, Tarim Basin," *Energy Exploration & Exploitation*, vol. 34, no. 1, pp. 113-128, 2016.
- [24] G. Wei, D. Wang, X. Wang et al., "Characteristics of noble gases in the large Gaoshiti-Moxi gas field in Sichuan Basin, SW China," *Petroleum Exploration and Development*, vol. 41, no. 5, pp. 585-590, 2014.
- [25] J. X. Dai, *Coal-Derived Large Gas Fields and Their Gas Sources in China*, Science Press, Beijing, 2014.
- [26] G. L. Lei, H. W. Xie, J. Z. Zhang et al., "Structural features and natural gas exploration in the Kelasu structural belt, Kuqa Depression," *Oil & Gas Geology*, vol. 28, no. 6, pp. 816-820, 2007.
- [27] J. Li, Z. Y. Xie, Z. S. Li, X. Luo, G. Y. Hu, and S. Gong, "Gas-source correlation of natural gas in Kuqa Depression, Tarim Basin," *Petroleum Exploration and Development*, vol. 28, no. 5, pp. 29-32, 2001.
- [28] D. Liang, S. Zhang, J. Chen, F. Wang, and P. Wang, "Organic geochemistry of oil and gas in the Kuqa Depression, Tarim Basin, NW China," *Organic Geochemistry*, vol. 34, no. 7, pp. 873-888, 2003.
- [29] Y. Neng, J. F. Qi, H. W. Xie, Y. Li, G. L. Lei, and C. Wu, "Structural characteristics of northern margin of Kuqa depression, Tarim Basin," *Geological Bulletin of China*, vol. 31, no. 9, pp. 1510-1519, 2012.
- [30] Y. Song, F. Hong, X. Y. Xia, G. Gao, and Y. G. Fu, "Syngensis relationship between abnormal overpressure and gas pool formation-with Kuqa Depression as an example," *Petroleum Exploration and Development*, vol. 33, no. 3, pp. 303-308, 2006.
- [31] N. Zhang, H. L. Guo, and Z. Y. Gao, "The characteristics of fluid inclusions and pool forming process of oil and gas reservoirs in the Kela 2 giant gas field, Tarim Basin," *Acta Petrologica Sinica*, vol. 16, no. 4, pp. 665-669, 2000.
- [32] S. Zhang, B. Zhang, G. Zhu, H. Wang, and Z. Li, "Geochemical evidence for coal-derived hydrocarbons and their charge history in the Dabai Gas Field, Kuqa Thrust Belt, Tarim Basin, NW China," *Marine and Petroleum Geology*, vol. 28, no. 7, pp. 1364-1375, 2011.
- [33] W. Zhao, S. Zhang, F. Wang et al., "Gas systems in the Kuche Depression of the Tarim Basin: source rock distributions, generation kinetics and gas accumulation history," *Organic Geochemistry*, vol. 36, no. 12, pp. 1583-1601, 2005.

- [34] C. Z. Jia, Y. Y. Hu, and Z. J. Tian, "The large gas fields exploration of Kuqa Depression in Tarim Basin," in *The Frontier Petroleum Exploration in China (Vol.1)*, G. Ruiqi and Z. Zhengzhang, Eds., pp. 254–268, Petroleum Industry Publish, Beijing, 2001.
- [35] C. Jia and G. Wei, "Structural characteristics and petroliferous features of Tarim Basin," *Chinese Science Bulletin*, vol. 47, no. S1, pp. 1–11, 2002.
- [36] J. X. Dai, "Identification and distinction of various alkenes gases," *Science in China Series B-Chemistry*, vol. 35, no. 10, pp. 1246–1257, 1992.
- [37] J. X. Dai and H. F. Qi, "The relationship between $\delta^{13}\text{C}$ and Ro in coal derived hydrocarbon in China," *Chinese Science Bulletin*, vol. 34, no. 9, pp. 690–692, 1989.
- [38] W. B. Clarke, W. J. Jenkins, and Z. Top, "Determination of tritium by mass spectrometric measurement of ^3He ," *The International Journal of Applied Radiation and Isotopes*, vol. 27, no. 9, pp. 515–522, 1976.
- [39] B. A. Mamyrin, G. S. Anufriev, I. L. Kamenskii, and I. N. Tolstikhin, "Determination of the isotopic composition of air helium," *Geochemistry International*, vol. 7, pp. 498–505, 1970.
- [40] J. E. Lupton, "Terrestrial inert gases: isotope tracer studies and clues to primordial components in the mantle," *Annual Review of Earth and Planetary Sciences*, vol. 11, no. 1, pp. 371–414, 1983.
- [41] R. J. Poreda, P. D. Jenden, I. R. Kaplan, and H. Craig, "Mantle helium in Sacramento basin natural gas wells," *Geochimica et Cosmochimica Acta*, vol. 50, no. 12, pp. 2847–2853, 1986.
- [42] J. G. Du, "The geochemistry of light rare gases," *Geology Geochemistry*, vol. 17, no. 4, pp. 56–59, 1989.
- [43] B. A. Mamyrin and I. N. Tolstikhin, "Helium isotopes in nature," in *Developments in Geochemistry 3*, p. 287, Elsevier, Amsterdam, 1984.
- [44] H. Hiyagon, M. Ozima, B. Marty, S. Zashu, and H. Sakai, "Noble gases in submarine glasses from mid-oceanic ridges and Loihi seamount: constraints on the early history of the Earth," *Geochimica et Cosmochimica Acta*, vol. 56, no. 3, pp. 1301–1316, 1992.
- [45] J. X. Dai, J. Li, W. W. Ding et al., "Geochemical characters of the giants gas accumulations with over one hundred billion cubic meters reserves in China," *Petroleum Exploration and Development*, vol. 32, no. 4, pp. 16–23, 2005.
- [46] S. Qin, J. Dai, and X. Liu, "The controlling factors of oil and gas generation from coal in the Kuqa Depression of Tarim Basin, China," *International Journal of Coal Geology*, vol. 70, no. 1–3, pp. 255–263, 2007.
- [47] D. W. Zhang, W. H. Liu, J. J. Zheng, X. F. Wang, and Q. Y. Nan, "Identification of main gas source in Kuqa Depression using argon isotope ratios," *Geochimica*, vol. 34, no. 4, pp. 405–409, 2005.
- [48] Z. Wang, T. Wang, Z. Xiao, Z. Xu, M. Li, and F. Lin, "Migration and accumulation of natural gas in Kela-2 gas field," *Chinese Science Bulletin*, vol. 47, Supplement 1, pp. 107–112, 2002.

Research Article

Occurrence and Origin of H₂S from Volcanic Reservoirs in Niudong Area of the Santanghu Basin, NW China

Xiangxian Ma,^{1,2} Guodong Zheng^{1,2}, Minliang Liang,³ Dianhe Xie,⁴ Giovanni Martinelli^{1,5}, Wasim Sajjad,^{1,2} Wang Xu,^{1,2} Qiaohui Fan,^{1,2} Liwu Li,^{1,2} Li Du,^{1,2} and Yidong Zhao⁶

¹Northwest Institute of Eco-Environment and Resources, Chinese Academy of Sciences, Lanzhou 730000, China

²Key Laboratory of Petroleum Resources, Gansu Province, Lanzhou 730000, China

³Institute of Geomechanics, Key Lab of Shale Oil and Gas Geological Survey, Chinese Academy of Geological Sciences, Beijing 100081, China

⁴Santanghu Oil Production Plant, Tuha Oilfield Company, PetroChina, Hami 839009, China

⁵ARPAE Emilia Romagna, 42100 Reggio Emilia, Italy

⁶Beijing Synchrotron Radiation Facility, Institute of High Energy Physics, Chinese Academy of Sciences, Beijing 100049, China

Correspondence should be addressed to Guodong Zheng; gdzhhj@mail.iggcas.ac.cn

Received 23 October 2018; Revised 8 January 2019; Accepted 30 January 2019; Published 2 June 2019

Academic Editor: Andri Stefansson

Copyright © 2019 Xiangxian Ma et al. This is an open access article distributed under the Creative Commons Attribution License, which permits unrestricted use, distribution, and reproduction in any medium, provided the original work is properly cited.

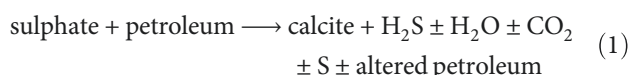
A series of samples including natural gas, formation water, and rocks were collected from volcanic rock reservoirs in the Niudong area of the Santanghu Oilfields and analyzed for their mineral and/or chemical compositions and sulfur and carbon isotopes in order to investigate the occurrence and origin of hydrogen sulfide (H₂S). H₂S was mostly dissolved in the formation water along with petroleum production in the study area. The $\delta^{34}\text{S}$ values of on-well H₂S samples varied in a range of 9.2‰ to 20.5‰, probably indicating thermochemical sulfate reduction (TSR) and/or thermal decomposition of organic sulfur-bearing compounds (TDS) as the genetic process for H₂S. However, the chemical composition of formation waters from the Kalagang Formation (C₂k) and their coefficient of desulfurization also revealed that TSR could be the main principle for H₂S formation. Considering the regional geological background, especially the tectonic structures and thermal evolution features of the basin, it was concluded that H₂S in the study area was dominantly produced by thermal genesis with TSR as a domain through interactions between hydrocarbons and aqueous sulfate dissolved from sulfate minerals.

1. Introduction

Hydrogen sulfide (H₂S) is one of the most perilous constituents of natural gases and also hazardous in several aspects such as diluting the proportion of hydrocarbons in natural gas, gravely altering its economic vitality, and being extremely lethal and corrosive to equipment used for oil and gas exploration and development [1, 2]. It is significantly important to study and get a better understanding of H₂S's occurrence and its origin for the reduction of health-related risks and to ensure safety, proper management of reservoirs, suitable construction facilities, and drilling-well design [3–5].

According to the literature, there are four major sources in geology for H₂S from a viewpoint of genesis: (1) inorganic (volcanic) source [6], (2) bacterial sulfate reduction (BSR) [7, 8], (3) thermal decomposition of organic sulfur-bearing compounds (TDS) in oil or kerogen [5, 9], and (4) thermochemical sulfate reduction (TSR) [7, 10, 11]. Inorganic (volcanic) H₂S genesis always occurs through volcanic activities and leads to a higher concentration of H₂S, whose sulfur isotope is normally in a range of –1‰ to –6–7‰ V-CDT [6, 11]. BSR is the typical and important source of H₂S genesis in sediments and many gas and oil reservoirs, being common in a low proportion of H₂S contribution (sulfur

concentration < 3–5%). The BSR source for H_2S genesis is generally considered to be active at temperatures below 80–100°C, and their sulfur isotopic ratios are mostly in a range of -5‰ and +5‰ V-CDT [7, 8, 11]. TDS normally takes place in the heating periods of organic matters and following petroleum formation. However, the H_2S contribution of TDS is very low and the isotopic ratios of sulfur range from 4‰ to 12‰ V-CDT, being always related to the secondary recovery of petroleum by using steam and/or hot water [7, 11]. Finally, the most influential source for H_2S production is TSR, contributing massive proportions of H_2S in natural gases and presenting in numerous petroliferous basins and even in some metal sulfide deposits [5, 7, 9, 12, 13]. Their sulfur isotopic ratios are normally between 8‰ and 25‰ V-CDT [3, 14]. The TSR reactions often occur along with interactions between hydrocarbons and aqueous sulfate which is always derived from the dissolution of sulfate minerals (primarily anhydrite and also barite and celestite). Both experimental studies and field inspections have revealed that the TSR process was kinetically practicable at outset temperatures > 10 0°C. Suitable temperature and pH values are the important essential factors to control the reaction rate and degree of TSR [8, 15–21]. A common chemical reaction of TSR can be summarized as follows [22].



With the progression of petroleum exploitation, unconventional oil and gas resources are the vital sources for exploration. Besides clastic and carbonate rocks, volcanic rocks as reservoirs are a potential target for oil and gas exploration as well in recent times [23]. Therefore, in the current scenario, the occurrence and origin of H_2S in volcanic reservoirs should be an important topic for exploration and as a supplement to the basic theory. About 100 ppm of H_2S was found in several wellheads in the Niudong area, Santanghu Basin, during the oil and gas development in 2010. Since then, growing concerns on the influence of H_2S on workers' health have led to the study on H_2S and measures were set up to reduce the negative influences on health and equipment. However, before controlling H_2S in these reservoirs, its occurrence and origin should be properly revealed. Therefore, a series of samples, including oil and gas, formation water, drilling core rocks, and on-well H_2S precipitant were collected and analyzed for this purpose.

2. Geological Settings

The Santanghu Basin, bordered by the Junggar Basin to the west, the Tuha Basin to the south, and the Mongolia Gebi to the northeast, is a special petroleum-bearing basin with volcanic rocks as reservoirs in NW China (Figure 1(a)). The basin in an area of $2.3 \times 10^4 \text{ km}^2$ and with accumulative petroleum reserves of more than 3×10^8 tons has been discovered at present. Since the initial formation in the Silurian period, this basin has experienced several tectonic movements, inducing well-developed regional faults and strongly

weathered local rocks [23–25]. Volcanic eruptions frequently occurred in and around the basin during the late Palaeozoic era which probably produced some fracture channels by faulting. However, the process of volcanism was extremely intensive during the Middle Permian period. A basalt layer in a thickness of 200–600 m was developed in several parts of the basin, mainly due to crustal thinning, lithospheric subsidence, and asthenosphere upwelling [25]. The present tectonic units of the Santanghu Basin can be divided into the northern thrust uplift zone, central depression zone, and southern thrusting nappe zone. The Niudong area belongs to the central depression in the front edge of the Tiaoshan uplift and pitches the Malang depression in the northwest-southeast direction with an area of 260 km^2 .

The Carboniferous sequences in the study area can be classified into five formations (from bottom to top, Figure 1(b)): the Donggulusitao Formation (C_1d), Jiangbasitao Formation (C_1j), Bashan Formation (C_2b), Harjiawu Formation (C_2h), and Kalagang Formation (C_2k). The Kalagang Formation is primarily composed of fundamental intermediate volcanic lava that is incorporated within basalt, andesite, and transitional rock types [24]. Beneath the Kalagang Formation is the Haerjiawu Formation which contains hydrocarbon source rocks. Hydrocarbons from these source rocks migrated vertically into the weathered volcanic crust through faults. Reservoirs developed oil wells in the areas where there were abundant faults, and the hydrocarbons are distributed mainly in the weathered volcanic crust near the faults. The volcanic rocks of the Haerjiawu Formation alternate with source rocks. Hydrocarbons were generated from these source rocks, migrated into the weathered volcanic crust directly or through the faults, and then accumulated to construct the petroleum reservoir in the study area [23].

The maximum burial depth of the Kalagang Formation reached 1637 m in the study area, and the present strata temperature is about 55°C [26]. Since the Santanghu Basin is just located at the junction of several major tectonic belts such as the Tianshan and Altai Mountains tectonic zones, the geothermal conditions should be changed in geological evolution history. The ancient geothermal gradient could be higher than that at present [27]. The geothermal history of the study area indicates the Middle Permian magmatism which caused locally thermal anomalies, and both the Late Indosinian movement (Late Triassic and Early Jurassic period) and Late Yanshan movement (Late Jurassic period) contributed to the increase of ancient geothermal gradients in the basin and led to the maturation of organic matters in the source rocks [26]. The temperature in oil and gas reservoirs of the Kalagang Formation (C_2k) reached more than 110°C during the Permian-Triassic period [26, 27].

3. Samples and Analysis

3.1. Sample Collection. Seventeen rock samples were selected from drilling cores of the Niudong area for the present study on geochemical and mineralogical characteristics of the volcanic rocks (Table 1). All the cored samples were rocks in the reservoir of Kalagang formation (C_2k), including 9 basalts, 4 andesites, 2 volcanic breccia, and 2 tuff samples.

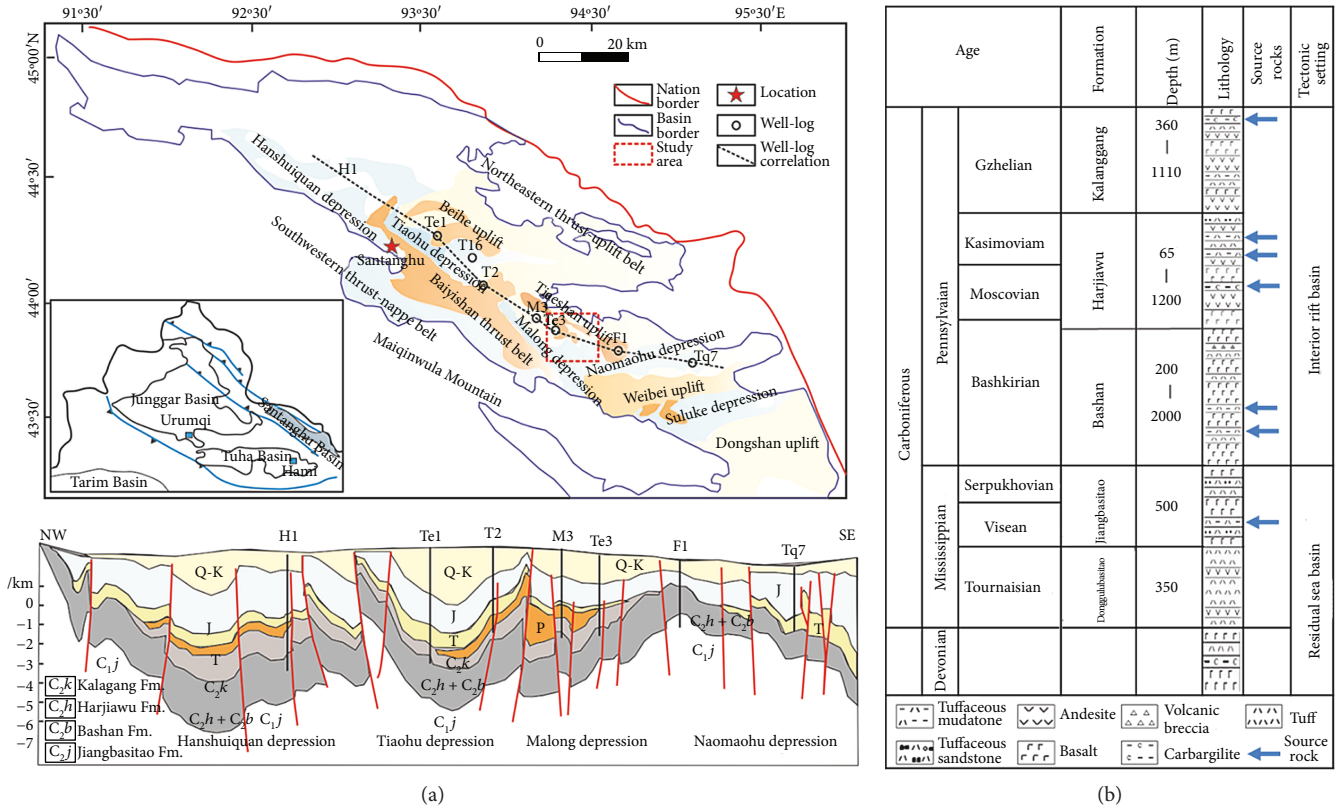


FIGURE 1: (a) Location of the study area, structure units, and section map of the Santanghu Basin. (b) Lithological column and sedimentary evolution of the Carboniferous (modified after Song et al. [24]).

TABLE 1: General property of study samples from the Kalangang Formation in the Santanghu Basin.

Sample no.	Depth (m)	Description
NDYX-01	1401.59-1401.80	Dark grey basalt
NDYX-02	1402.25-1402.39	Dark grey basalt with oil infected
NDYX-03	1403.38-1403.51	Taupe fluorescence basalt
NDYX-04	1410.81-1411.07	Taupe fluorescence basalt
NDYX-05	1416.44-1416.59	Purple basalt
NDYX-06	1420.84-1420.94	Brown basalt with oil infected
NDYX-07	1423.48-1423.62	Greyish-green breccia
NDYX-08	1429.38-1429.61	Purple oil spot andesite
NDYX-09	1429.61-1429.72	Purple oil spot andesite
NDYX-10	1430.05-1430.20	Purple oil spot andesite
NDYX-11	1433.82-1433.91	Taupe oil spot basalt
NDYX-12	1437.36-1437.51	Purple oil spot andesite
NDYX-13	1439.38-1439.49	Greyish-green breccia
NDYX-14	1444.68-1444.85	Brown-grey fluorescent basalt
NDYX-15	1447.23-1447.37	Brown-grey fluorescent basalt
NDYX-16	1508.63-1508.75	Taupe tuff
NDYX-17	1509.48-1509.56	Taupe tuff

The basalts were characterized by greyish-green and brownness and contained oil spots, air holes, and cracks. The andesites contained few and small purple oil spots and holes. The volcanic breccia and tuff were pyroclastic rocks with

TABLE 2: General properties of fillings in the crack of core samples obtained from the Kalangang Formation in the Santanghu Basin.

Sample no.	Depth (m)	Filling feature	Core
NDCT-01	1457.56-1457.68	Taupe	Dark grey basalt
NDCT-02	1552.85-1553.00	Transparent	Greyish-green basalt
NDCT-03	1540.69-1540.93	Greyish-green	Grey-brown basalt
NDCT-04	1508.63-1508.75	White	Taupe tuff
NDCT-05	1509.48-1509.56	White vein	Taupe tuff
NDCT-06	1430.05-1430.20	Milky white	Purple andesite

greyish-green and taupe, respectively. Six samples with clear veins were selected, and the vein fillings were extracted by indoor drilling for sulfur and carbon isotope analysis (Table 2 and Figure 2). The veins were in white color and transparent, some of which were characterized in an X-type of joints.

The samples for H₂S isotopes were obtained from twelve production wells and one gas gathering station. For sampling, the mixture of natural gases was introduced into a pre-prepared cadmium acetate solution (Cd (CH₃COO)₂·3H₂O), and then the precipitant of cadmium sulfide (CdS) was collected in situ by filtration for laboratory analysis.

3.2. Analytical Methods. All the rock samples without chemical pretreatment were crushed into powder by using an agate mortar and pestle. Mineralogical measurements were carried

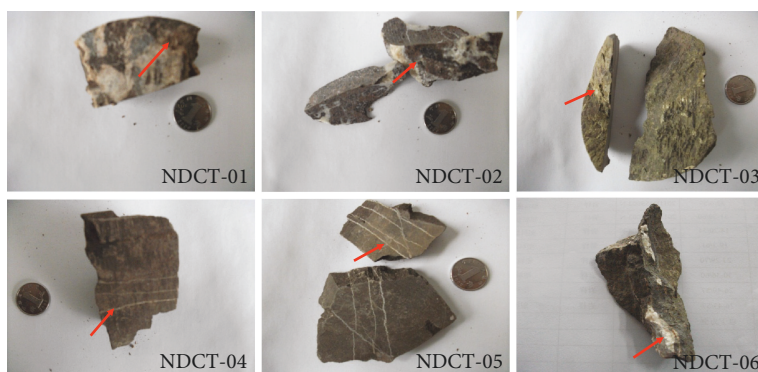


FIGURE 2: Photos showing the veins of cored samples.

out by the powder X-ray diffraction (XRD) method, using a D/Max-3B X-ray diffraction (XRD) Bruker diffractometer equipped with a graphite monochromator and operated at 40 kV and 100 mA using Cu $K\alpha$ radiation. A small portion of finely powdered sample crushed again in a clean mortar was properly mounted on a plastic holder ($\phi 25$ mm, depth 1 mm). Scanning of samples was performed over an interval of $2\text{--}60^\circ$ (2θ) at a scanning speed of $2^\circ/\text{min}$ for every 0.03° (2θ) step. Divergence, scattering, and receiving slits were 0.5° , 0.5 , and 0.10 mm, respectively.

Sulfur K-edge XANES analysis of well-crushed either cored rock or drilled vein samples were performed at beam-line 4B7A of the Beijing Synchrotron Radiation Facility (BSRF), Beijing. Both the beam path and samples were positioned in a vacuum to overcome the scattering of X-ray and their absorption by air when the crushed samples were exposed to the X-ray beam with an incident angle of 45° . The X-ray fluorescence emitted during analysis was quantified by using a solid-state detector (Si). As a reference, the spectrum of the blank filter was also measured for the comparison purpose and the absorption of sulfur was negligible [28].

The isotopic composition of sulfur (S) was analyzed by using an isotope mass spectrograph (Model MAT271) produced by Finnigan MAT Company. The mass range is 1 to 700 amu, and the mass resolution is 220 to 3000 used for gas composition and stable isotope analysis. CdS and CuO (copper oxide) obtained through precipitation were mixed in a 1:3 weight ratio into a quartz tube and rapidly heated to 850°C inside the reaction furnace for 30 minutes. Subsequently, the released gas was collected inside the cold trap by using liquid nitrogen for freezing the gas, and the vacuum pump was started to eliminate the impurities and pure SO_2 was released. The obtained gas was introduced into the instrument for isotope analysis and the $\delta^{34}\text{S}$ value of sulfide was ultimately obtained by using an international standard (CDT), with an accuracy of $\pm 0.5\text{‰}$.

Calcite presented inside the vein fillings of rock samples was extracted by using a small driller and was subjected to carbon and oxygen isotopic analysis. About 50–100 mg of calcite samples was treated with pure phosphoric acid for 4 hours at 72°C under a vacuumed container. The released CO_2 was analyzed for carbon and oxygen isotopes by using a Finnigan MAT253 plus mass spectrometer

standardized with GBW04416. The obtained data of carbon and oxygen were reported in units/mL relative to the V-PDB standard. The precision for both $\delta^{13}\text{C}$ and $\delta^{18}\text{O}$ measurements was $\pm 0.5\text{‰}$.

The composition of formation water and the concentration of H_2S were measured by the Sangtangu Oil Production Plant of Tuha Oilfield Company. A portable hydrogen sulfide detector was used to monitor the H_2S concentration at the wellhead of Oilfield, the precision being better than 5%.

4. Results and Discussion

4.1. Occurrence of H_2S . During the first recovery of oil in the Santanghu Oilfield, the H_2S content was reported in the oil-wellhead as 10–120 ppm/ m^3 air in 2010, and the relative content of H_2S in the dissolved air of formation water reached 0.19%. The average pressure value of reservoir strata C_2k in the study area was 10.5 MPa, of which the H_2S -bearing wells were mostly located in the area with low pressure (3–9 MPa) [29], and fractures were strongly developed in the surrounding rocks. Furthermore, the oil-wells containing H_2S more than 100 ppm were always characterized with a higher water cut (65–100%) while other oil-wells in lower H_2S concentration (<30 ppm) were assigned to a lower water cut (<60%). Thus, H_2S was mainly distributed in oil-wells with low formation pressure, high water cut, and fractures developed and mostly dissolved in formation water.

4.2. Minerals and Sulfur Characteristics of Reservoir Rocks. The reservoir rocks of the Santanghu Oilfields are typical volcanic rocks of the Carboniferous Kalagang Formation, which are dominated by basalt, andesite, volcanic breccia, and tuff [23]. The SiO_2 content of the volcanic rocks is 44% to 65%. There are a number of air holes and almond constructs in the rocks so that these rocks have relatively high porosity and proper connectivity; the porosity is 6% to 11% [23]. Weathering and leaching during the cessation of deposition should be the major controlling factor of favorable reservoirs in the Carboniferous volcanic rocks, and the secondary minerals such as clay minerals could be largely formed. The hydrolysis belt was mainly composed of mudstone and tiny volcanic grains, most of which were broken down into clay minerals [23]. The cracks or vein fillings in the

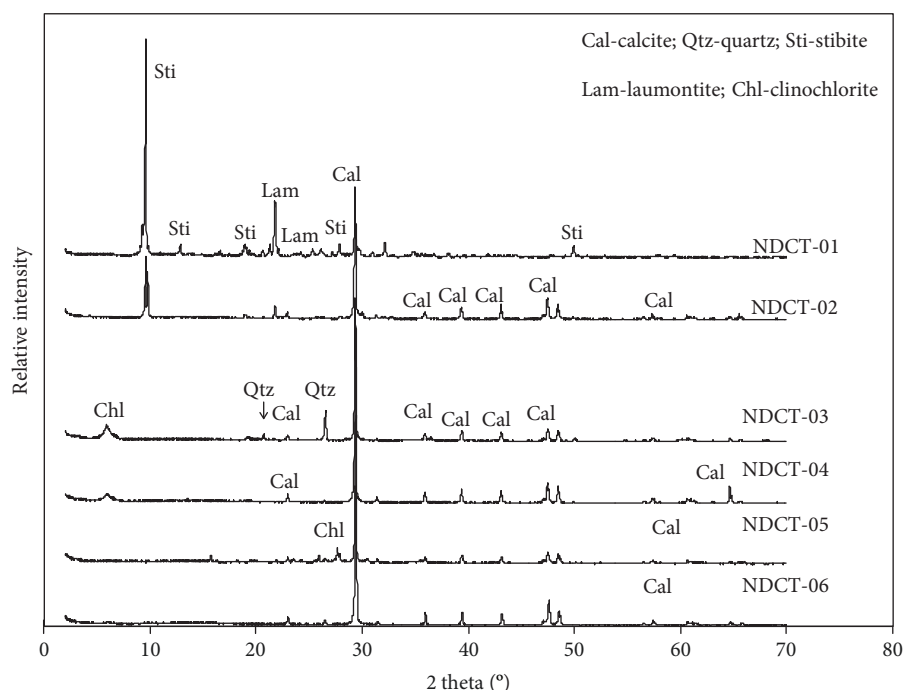


FIGURE 3: Powder X-ray diffraction patterns for the study samples.

core of volcanic rocks were widely developed and mainly consisted of volcanic zeolites, quartz, and/or calcite (Figure 3).

Sulfur species were herein referred to as the chemical status of sulfur, which was identified using XANES in this study by comparison of the obtained spectra for samples with those of selected sulfur-containing reference materials such as pyrite (FeS_2), pyrrhotite (FeS), calcium sulfate (CaSO_4), and sulfur (S^0). The impact of self-absorption associated with reference materials was investigated by using well-crushed mixtures of boron nitride in various concentrations of sulfur. The self-absorption impact was not detected in sulfur concentration < 0.5 wt.% [28]. The peak positions obtained from the cored samples were mostly positioned at two series of comparable energy range to those presented in the spectra of pyrite, pyrrhotite, and calcium sulfate, signifying that the foremost sulfur species were sulfide and sulfate, respectively. The absorbing peaks presented on the left (in range of 2.470–2.474 keV) indicate the presence of S^{2-} , S_2^{2-} , and also possibly elemental sulfur (S^0). On the other hand, the peak presented on the right (in range of 2.481–2.484 keV) denotes SO_4^{2-} species (Figure 4). The spectra thus obtained for all samples are shown in Figure 4, in which several composite variations within numerous sulfur species are displaced based on their spectrum structures as well as the location of the peak that is signified as sulfides and/or sulfate, respectively. In this study, it was found that both the sulfate (more than 90%) and sulfide minerals widely coexisted in the reservoir rocks, which could provide an effective sulfur source for the genesis of H_2S gas within the reservoirs.

4.3. Characteristics of Formation Water. The chemical compositions of formation water are shown in Table 3 and Figure 5. Relatively most samples belong to the group of

Na(K)-Cl or Ca-Cl_2 water while the existence of Ca(Mg)-SO_4 waters indicates possible evolutionary trends toward SO_4 -enriched waters. There are no samples belonging to the Ca(Mg)-HCO_3 and Na(K)-HCO_3 groups in the study area. In particular, the $\text{Na}^+ + \text{K}^+$ concentration of formation water in Kalagang Formation (C_2k) was in a range of 69–1008 mg/L and the Cl^- concentration in a range of 309–1955 mg/L, respectively. The range of Mg^{2+} concentration of C_2k formation water was from 1 to 291 mg/L with an average of 56.6 mg/L. Generally, the higher the Mg^{2+} concentration, the higher would be the H_2S yields, because ion Mg^{2+} could play a catalysis role in TSR [30–32]. The range of SO_4^{2-} concentration was from 27 to 1288 mg/L. The coefficient of desulfurization ($100 \times r \text{ SO}_4^{2-}/\text{Cl}^-$) was in a range of 2–160 with a mean value of 30. This coefficient could be used to reflect consumption of SO_4^{2-} during TSR and the redox conditions of formation water. The low mark means reduced condition and active TSR reactions [32]. The H_2S contraction rose with a decrease in the coefficient of desulfurization (Figure 6), exhibiting that TSR really occurred in the study reservoirs. The CO_3^{2-} concentration in most water samples was low (mostly not detected), and the average of HCO_3^- was 335.8 mg/L. In addition, the concentration of HCO_3^- decreased with the process of TSR reactions, strongly indicating the dilution of additional water under TSR conditions. This kind of dilution might be lowering the concentration of CO_3^{2-} and HCO_3^- in formation waters of volcanic reservoirs.

4.4. Sulfur Isotopes of H_2S . The sulfur isotopes of sulfates and/or sulfides presented in the volcanic rocks from wells ND89-9 and ND89-10 are quite close to each other, being 9.2‰ and 10.3‰, respectively. The natural gases at the

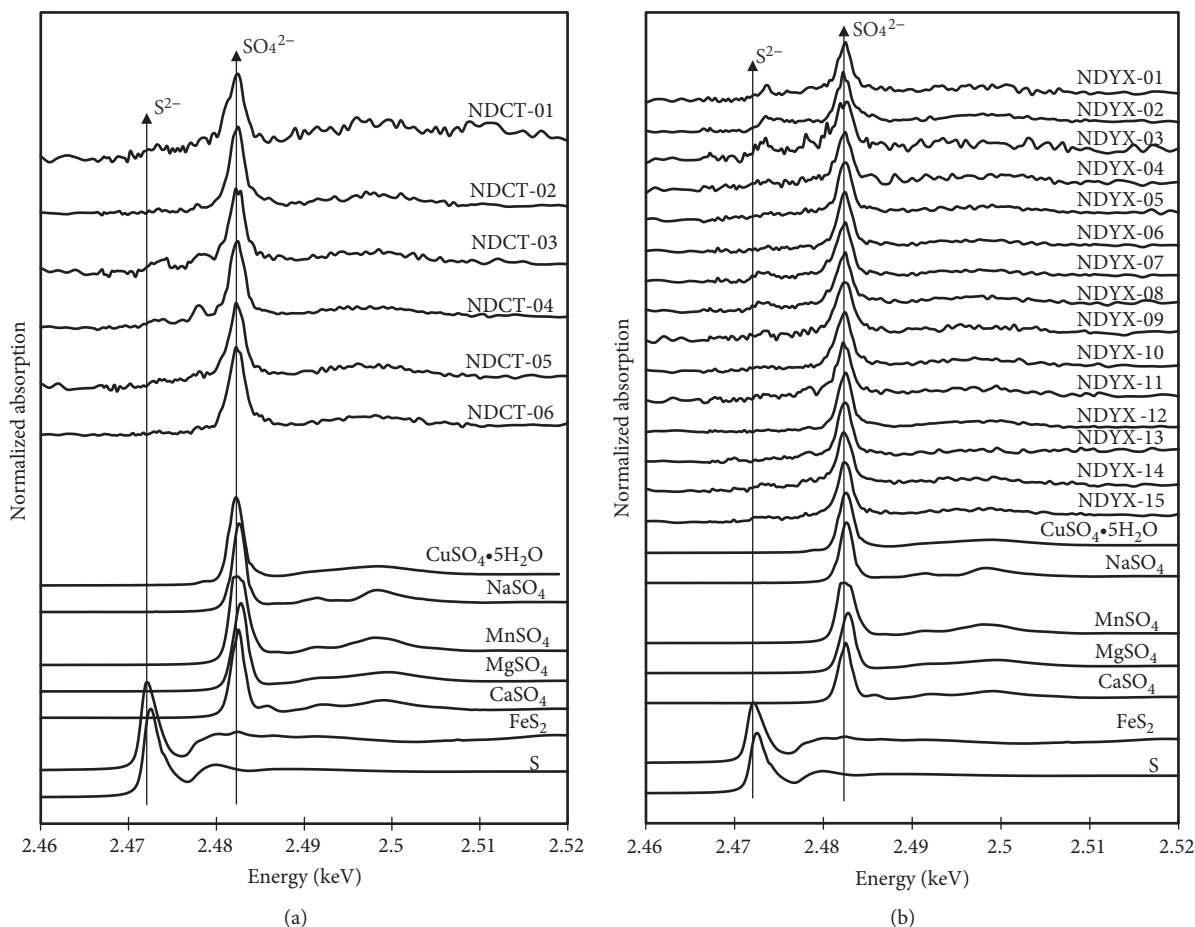


FIGURE 4: Spectra of sulfur species in the study samples. (a) Filling materials in the veins of cored rocks and (b) core samples. The absorbing peak on the left with a lower energy range corresponds to sulfides whereas the peak on the right with a higher energy range corresponds to sulfate.

TABLE 3: Hydrochemistry of the formation water from the Niudong area, Santanghu Basin.

Sample no.	Stratum	Sampling date	H ₂ S (ppm/m ³ air)	K ⁺ +Na ⁺	Ca ²⁺	Mg ²⁺	Cl ⁻	mg/L SO ₄ ²⁻	HCO ₃ ⁻	CO ₃ ²⁻	Total salinity	Type	pH
ND8-14	C ₂ k	2008/8/7	n.d.	410	864	291	1755	920	710	268	5218	CaCl ₂	9.3
ND78-9	C ₂ k	2008/8/6	115	592	545	1	1652	32	164	n.d.	2986	NaCl ₂	7.3
ND78-812	C ₂ k	2010/8/7	6	371	123	10	512	283	168	n.d.	1467	NaCl	6.0
ND89-10	C ₂ k	2010/10/8	44	647	442	24	1375	329	397	n.d.	3214	CaCl ₂	7.0
ND8-11	C ₂ k	2008/8/7	35	1008	683	67	1955	434	1171	n.d.	5318	NaCl	6.5
ND89-9	C ₂ k	2008/11/4	31	592	521	14	1544	349	123	n.d.	3143	NaCl ₂	6.0
ND8-111	C ₂ k	2010/5/1	13	194	566	98	1272	47	482	n.d.	2659	CaCl ₂	7.0
ND89-812	C ₂ k	2010/8/24	25	69	315	21	309	495	85	n.d.	1294	CaSO ₄	6.0
ND9-9	C ₂ k	2010/3/7	50	547	384	15	1393	188	57	n.d.	2584	CaCl ₂	7.0
ND89-91	C ₂ k	2010/6/5	44	869	369	15	1324	495	596	n.d.	3668	NaCl	6.0
ND 8-71	C ₂ k	2007/12/21	120	386	396	7	1264	27	36	10	2126	CaCl ₂	9.0
ND8-10	C ₂ k	2007/10/16	13	394	873	122	1475	1288	143	n.d.	4295	CaCl ₂	7.7
ND8-8	C ₂ k	2008/8/7	10	537	404	51	1368	255	234	n.d.	2849	NaCl ₂	6.5

Note: these data were provided by the Santanghu Oil Production Plant of Tuha Oilfield Company. pH was tested at room temperature.

Niudong pumping station have undergone a series of technological operations such as separation of oil and gas, whose sulfur isotopic ratios reached 20.5‰ (Table 4). As shown in

Figure 7, the $\delta^{34}\text{S}_{\text{V-CDT}}$ values for TSR-H₂S in this study were comparable with those in the Sichuan Basin (main frequency: 8‰ to 26‰) [14], the Tarim Basin (14‰ to 19‰) [17, 33],

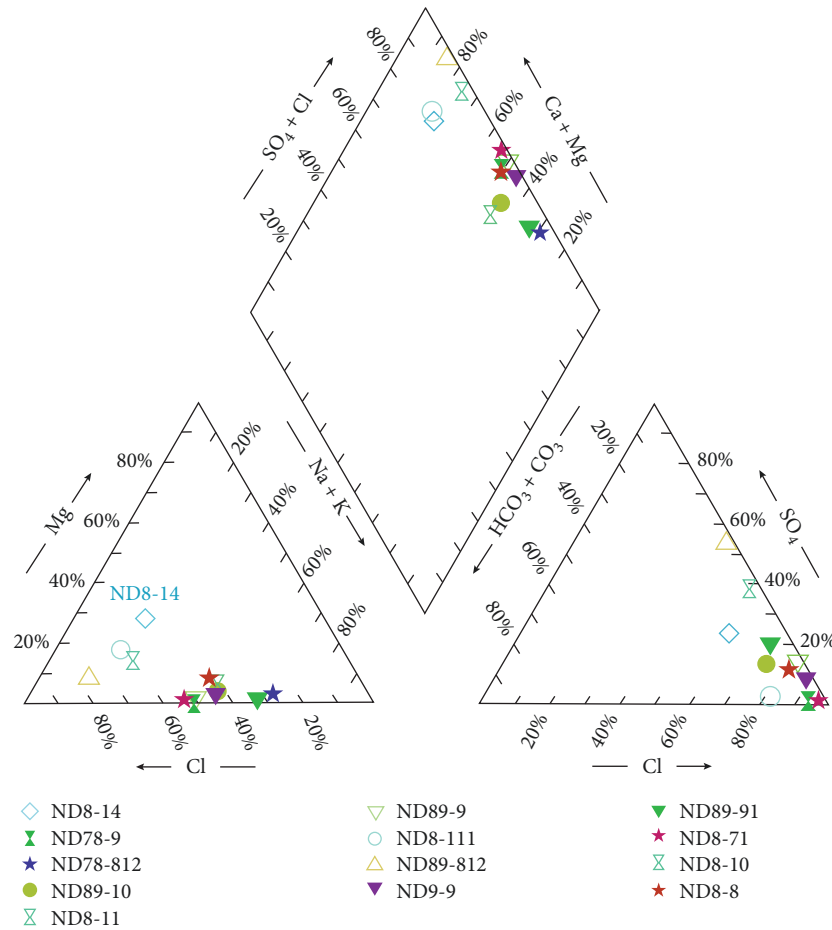


FIGURE 5: Piper diagram for ion composition of study formation waters.

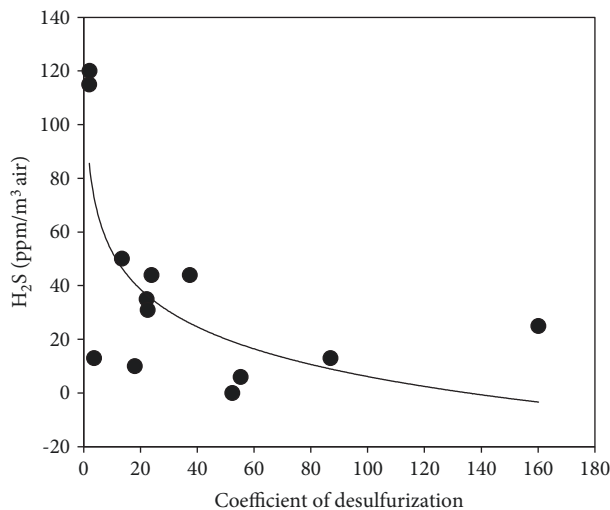


FIGURE 6: Relationship between the coefficient of desulfurization ratios and H_2S concentrations of oil wells.

and the Ordos Basin (16‰ to 20‰) [14]. Such comparison may indicate that H_2S presented in the oil wells of the Niudong area could probably be derived from TSR. $\delta^{34}S_{V-CDT}$ of TDS- H_2S in crude oils is usually from 3‰ to 15‰ [5]; thus, H_2S

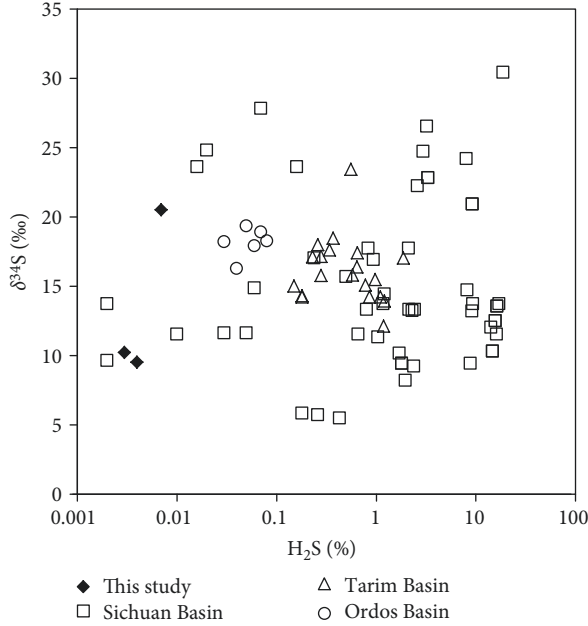
in the Niudong area could also be due to TDS. However, there is lack of meaningful evidence for the possibility of inorganic (volcanic) origin and BSR involvement for H_2S in the study area.

4.5. Carbon Isotopes of Calcite. The isotopic data of the calcite matrix from the Kalangang Formation exhibited a relatively wider range of carbon isotopic values between -10.7‰ and -3.3‰ V-PDB and a narrower range of oxygen isotopic values between -21.8‰ and -18.6‰ V-PDB, respectively (Table 4). These relatively negative carbon isotopic values may suggest a possible contribution of organic carbon into calcite, but the carbon and oxygen isotopic values failed on the boundary of TSR calcite [22] which was formed through TSR reactions. In addition, these carbon and oxygen isotopic values of vein calcite were also similar to those of primarily igneous carbonatite ($\delta^{13}C_{V-PDB}$ ‰: -5.0‰ to -8.0‰, $\delta^{18}O_{V-PDB}$ ‰: -21.7‰ to -23.7‰) [34], indicating the calcite formation with fluids from deep layers under low hydrothermal temperatures (<167°C) [35]. Therefore, calcite in the rock veins was mostly of magmatic origin and very less produced due to TSR reactions.

4.6. Origin of H_2S . As for the low concentration of H_2S in crude oils and natural gases, the BSR origin is always regarded as the first originating mechanism that may be

TABLE 4: Sulfur and carbon isotope of samples obtained from the Kalagang Formation in the Santanghu Basin.

Well or sample no.	Type	$\delta^{34}\text{S}_{\text{V-CDT}}\text{‰}$	$\delta^{13}\text{C}_{\text{V-PDB}}\text{‰}$	$\delta^{18}\text{O}_{\text{V-PDB}}\text{‰}$	Note
Gas pumping station	Gas	20.5			
ND89-9	Gas in water	9.2			
ND89-10	Gas in water	10.3			
NDCT-03	Rock		-10.7	-20.6	Calcite
NDCT-04	Rock		-5.8	-21.8	Calcite
NDCT-05	Rock		-5.7	-18.6	Calcite
NDCT-06	Rock		-3.3	-21.4	Calcite

FIGURE 7: Correlation between $\delta^{34}\text{S}$ values and H_2S contents of samples from the Santanghu Basin and other referenced TSR H_2S -bearing basins in China (data of Sichuan Basin, Tarim Basin, and Ordos Basin are from Zhu et al. [14] and Jiang et al. [22]).

caused by bacterial loadings during water injection. The sulfur isotopes of H_2S in the study area were 9.2‰ to 20.5‰, suggesting that BSR was probably not the most possible source in the Niudong Oilfield, where H_2S was found in the first recovery of oil without water injection in early oil and gas exploration. Additionally, the values of sulfur isotopes are not in favor of volcanic sources for the genesis of H_2S . Therefore, TSR and TDS should be their possible origins that were supported by the sulfur isotopic data. However, TDS usually occurred during the secondary recovery of oil under a relatively higher temperature than under the initial temperature of TSR [5], but no steam and/or hot water was utilized during the secondary recovery of heavy oils in the study reservoir and the heavy oils was typically low in sulfur content (about 0.17%). Based on these facts, either TDS should not be the origin or slightly contributed if TDS occurred. As for TSR, although gypsum and/or anhydrite in the cored rocks was not observed by naked eyes, trace sulfate and sulfide were detected by XANES. Such sulfur-bearing materials in the reservoir rocks could supply enough sulfur for TSR reactions

due to the huge volume of rocks. Secondly, the local geothermal temperature ($>110^\circ\text{C}$) reached the reaction conditions for TSR during the Permian-Triassic period as for the volcanic activity [27]. Finally, some increase in H_2S concentration was observed with a decrease in desulfurization coefficient, which confirmed the occurrence of TSR. Such formed H_2S in the reservoir of volcanic rocks is easily dissolved in the formation water. On the other hand, CO_3^{2-} and HCO_3^- concentrations in most samples were relatively low, indicating that the additional water formed along with TSR may dilute the concentrations of both CO_3^{2-} and HCO_3^- . Considering all the evidences above, TSR should be the main source for H_2S in the natural gases of the Niudong Oilfield, but the TDS origin could not also be excluded.

5. Conclusions

The volcanic reservoir rocks of the Carboniferous Kalagang Formation are dominated by basalt and andesite, whose cracks or vein fillings in the core are mainly composed of volcanic zeolites, quartz, and/or calcite. Both sulfate (more than 90%) and sulfide minerals extensively existed in the reservoir rocks, which could provide a potential sulfur source for H_2S gas formation through TSR in the reservoirs.

H_2S was distributed in the producing wells with low formation pressure and high water cut of the oil wells, which was mostly dissolved in the formation water. The sulfur isotopic data and ion compositions of formation water indicated that TSR should be the main source for H_2S genesis. The geological structures of the basin, the mineral compositions of the reservoir rocks, and the evolution characteristics of the paleogeothermal temperatures provided effective conditions for TSR reactions in the study area.

Data Availability

The data used to support the findings of this study are included within the article.

Conflicts of Interest

The authors declare that they have no conflicts of interest.

Acknowledgments

This work was supported by the Natural Science Foundation of China (41572352, 41872141) and the Santanghu Oil

Production Factory, partially supported by the CAS “Light of West China” Program, CAS Visiting Professorship for Senior International Scientists to GM (2018VMA0007), Technology Major Project of the Ministry of Science and Technology of China (2016ZX05007001-004), and the Key Laboratory Project of Gansu Province (Grant No. 1309RTSA041). The authors are grateful to the Santanghu Oil Production Factory for the support in fieldwork and permission to use the basic geological data.

References

- [1] R. H. Worden and P. C. Smalley, “H₂S-producing reactions in deep carbonate gas reservoirs: Khuff Formation, Abu Dhabi,” *Chemical Geology*, vol. 133, no. 1-4, pp. 157–171, 1996.
- [2] G. Zhu, S. Zhang, Y. Liang, J. Dai, and J. Li, “Isotopic evidence of TSR origin for natural gas bearing high H₂S contents within the Feixianguan Formation of the Northeastern Sichuan Basin, Southwestern China,” *Science in China Series D: Earth Sciences*, vol. 48, no. 11, pp. 1960–1971, 2005.
- [3] S. Zhang, G. Zhu, Y. Liang, J. Dai, H. Liang, and M. Li, “Geochemical characteristics of the Zhaolanzhuang sour gas accumulation and thermochemical sulfate reduction in the Jixian Sag of Bohai bay basin,” *Organic Geochemistry*, vol. 36, no. 12, pp. 1717–1730, 2005.
- [4] P. Mougin, V. Lamoureux-Var, A. Bariteau, and A. Y. Huc, “Thermodynamic of thermochemical sulphate reduction,” *Journal of Petroleum Science and Engineering*, vol. 58, no. 3-4, pp. 413–427, 2007.
- [5] G. Zhu, S. Zhang, H. Huang et al., “Induced H₂S formation during steam injection recovery process of heavy oil from the Liaohe Basin, NE China,” *Journal of Petroleum Science and Engineering*, vol. 71, no. 1-2, pp. 30–36, 2010.
- [6] P. Allard, “The origin of water, carbon, sulfur, nitrogen and rare gases in volcanic exhalations: evidence from isotope geochemistry,” *Forecasting Volcanic Events*, H. Tazieff and J.-C. Sabroux, Eds., pp. 337–386, Elsevier, 1983.
- [7] W. L. Orr, “Changes in sulfur content and isotopic ratios of sulfur during petroleum maturation—study of big horn basin Paleozoic oils,” *AAPG Bulletin*, vol. 58, pp. 2295–2318, 1974.
- [8] H. G. Machel, “Bacterial and thermochemical sulfate reduction in diagenetic settings — old and new insights,” *Sedimentary Geology*, vol. 140, no. 1-2, pp. 143–175, 2001.
- [9] R. H. Worden, P. C. Smalley, and S. A. Barclay, “H₂S and diagenetic pyrite in North Sea sandstones: due to TSR or organic sulphur compound cracking?,” *Journal of Geochemical Exploration*, vol. 78-79, pp. 487–491, 2003.
- [10] H. G. Machel, H. R. Krouse, and R. Sassen, “Products and distinguishing criteria of bacterial and thermochemical sulfate reduction,” *Applied Geochemistry*, vol. 10, no. 4, pp. 373–389, 1995.
- [11] Z. Guang-you, Z. Shui-chang, L. Ying-bo, and D. Jin-xing, “Stable sulfur isotopic composition of hydrogen sulfide and its genesis in Sichuan basin,” *Geochimica*, vol. 35, pp. 333–345, 2006.
- [12] Q. Y. Liu, R. H. Worden, Z. J. Jin et al., “TSR versus non-TSR processes and their impact on gas geochemistry and carbon stable isotopes in Carboniferous, Permian and Lower Triassic marine carbonate gas reservoirs in the Eastern Sichuan Basin, China,” *Geochimica et Cosmochimica Acta*, vol. 100, pp. 96–115, 2013.
- [13] C. Cai, L. Xiang, Y. Yuan et al., “Sulfur and carbon isotopic compositions of the Permian to Triassic TSR and non-TSR altered solid bitumen and its parent source rock in NE Sichuan Basin,” *Organic Geochemistry*, vol. 105, pp. 1–12, 2017.
- [14] G. Y. Zhu, A. G. Fei, J. Zhao, and C. Liu, “Sulfur isotopic fractionation and mechanism for thermochemical sulfate reduction genetic H₂S,” *Acta Petrologica Sinica*, vol. 30, no. 12, pp. 3772–3786, 2014.
- [15] R. H. Worden, P. C. Smalley, and N. H. Oxtoby, “Gas souring by thermochemical sulfate reduction at 140°C,” *AAPG Bulletin*, vol. 79, pp. 854–863, 1995.
- [16] M. M. Cross, D. A. C. Manning, S. H. Bottrell, and R. H. Worden, “Thermochemical sulphate reduction (TSR): experimental determination of reaction kinetics and implications of the observed reaction rates for petroleum reservoirs,” *Organic Geochemistry*, vol. 35, no. 4, pp. 393–404, 2004.
- [17] F. Hao, T. Guo, Y. Zhu, X. Cai, H. Zou, and P. Li, “Evidence for multiple stages of oil cracking and thermochemical sulfate reduction in the Puguang gas field, Sichuan Basin, China,” *AAPG Bulletin*, vol. 92, no. 5, pp. 611–637, 2008.
- [18] Q. Ma, G. S. Ellis, A. Amrani, T. Zhang, and Y. Tang, “Theoretical study on the reactivity of sulfate species with hydrocarbons,” *Geochimica et Cosmochimica Acta*, vol. 72, no. 18, pp. 4565–4576, 2008.
- [19] T. Zhang, G. S. Ellis, Q. Ma, A. Amrani, and Y. Tang, “Kinetics of uncatalyzed thermochemical sulfate reduction by sulfur-free paraffin,” *Geochimica et Cosmochimica Acta*, vol. 96, pp. 1–17, 2012.
- [20] T. G. Powell and R. W. Macqueen, “Precipitation of sulfide ores and organic matter: sulfate reactions at Pine Point, Canada,” *Science*, vol. 224, no. 4644, pp. 63–66, 1984.
- [21] J. S. Seewald, “Organic-inorganic interactions in petroleum producing sedimentary basins,” *Nature*, vol. 426, no. 6964, pp. 327–333, 2003.
- [22] L. Jiang, R. H. Worden, and C. Cai, “Generation of isotopically and compositionally distinct water during thermochemical sulfate reduction (TSR) in carbonate reservoirs: Triassic Feixianguan Formation, Sichuan Basin, China,” *Geochimica et Cosmochimica Acta*, vol. 165, pp. 249–262, 2015.
- [23] C. N. Zou, L. H. Hou, S. Z. Tao et al., “Hydrocarbon accumulation mechanism and structure of large-scale volcanic weathering crust of the Carboniferous in northern Xinjiang, China,” *Science China Earth Sciences*, vol. 55, no. 2, pp. 221–235, 2012.
- [24] D. Song, D. He, and S. Wang, “Source rock potential and organic geochemistry of Carboniferous source rocks in Santanghu Basin, NW China,” *Journal of Earth Science*, vol. 24, no. 3, pp. 355–370, 2013.
- [25] W. Li, Y. Q. Liu, Y. P. Dong et al., “The geochemical characteristics, geochronology and tectonic significance of the Carboniferous volcanic rocks of the Santanghu area in northeastern Xinjiang, China,” *Science China Earth Sciences*, vol. 56, no. 8, pp. 1318–1333, 2013.
- [26] W. M. Li and R. Y. Zhang, “Reservoir characteristics of composite petroleum system in Santanghu basin,” *Xinjiang Petroleum Geology*, vol. 21, pp. 275–278, 2000.
- [27] H. Jian-rong, L. Yi-qun, F. Qiao, X. Xiu-juan, and Z. Xiao-qin, “The tectonic-thermal evolution of the Santanghu Basin,” *Journal of Northwest University (Natural Science Edition)*, vol. 36, pp. 290–294, 2006.
- [28] L. Jun, B. Liang-Man, L. Wei et al., “Size distribution of sulfur species in fine and ultrafine aerosol particles using sulfur K-

- edge XANES,” *Chinese Physics C*, vol. 33, no. 11, pp. 965–968, 2009.
- [29] S. Xinhua, B. Guojuan, C. Changxu, C. Xiaoying, and W. Binwen, “Study on waterflooding feasibility of volcanic reservoir in Niudong,” *Tuha Oil & Gas*, vol. 15, pp. 262–266, 2010.
 - [30] T. Zhang, G. S. Ellis, K.-s. Wang et al., “Effect of hydrocarbon type on thermochemical sulfate reduction,” *Organic Geochemistry*, vol. 38, no. 6, pp. 897–910, 2007.
 - [31] K.-l. DING, S.-y. LI, C.-t. YUE, and N.-n. ZHONG, “Simulation experiments on thermochemical sulfate reduction using natural gas,” *Journal of Fuel Chemistry and Technology*, vol. 35, no. 4, pp. 401–406, 2007.
 - [32] H. Li, C. Cai, L. Jia, C. Xu, and K. Zhang, “The effect of water chemistry on thermochemical sulfate reduction: a case study from the Ordovician in the Tazhong area, Northwest China,” *Geofluids*, vol. 2017, Article ID 6351382, 11 pages, 2017.
 - [33] C. Cai, G. Hu, H. X. Li et al., “Origins and fates of H₂S in the Cambrian and Ordovician in Tazhong area: evidence from sulfur isotopes, fluid inclusions and production data,” *Marine and Petroleum Geology*, vol. 67, pp. 408–418, 2015.
 - [34] H. P. Taylor Jr, J. Frechen, and E. T. Degens, “Oxygen and carbon isotope studies of carbonatites from the Laacher See District, West Germany and the Alnö District, Sweden,” *Geochimica et Cosmochimica Acta*, vol. 31, no. 3, pp. 407–430, 1967.
 - [35] Y. Nan, Y. Q. Liu, D. W. Zhou, N. C. Zhou, X. Jiao, and P. Zhou, “Characteristics and origin of amygdale and crack fillers in volcanic rock of Late Carboniferous in Santanghu basin, Xinjiang,” *Acta Petrologica Sinica*, vol. 32, pp. 1901–1913, 2016.

Research Article

^{220}Rn (Thoron) Geohazard in Room Air of Earthen Dwellings in Vietnam

Dương Nguyễn-Thùy ¹, Hương Nguyễn-Văn ¹, Jan P. Schimmelmänn,²
Nguyệt Thị Ánh Nguyễn ¹, Kelsey Doiron ³ and Arndt Schimmelmänn³

¹Faculty of Geology, VNU University of Science, Vietnam National University, Hanoi, 334 Nguyen Trai Street, Thanh Xuan District, Hanoi, Vietnam

²University of Bremen, Institute of Geography, Celsiusstrasse FVG-M, D-28359 Bremen, Germany

³Department of Earth and Atmospheric Sciences, Indiana University, Bloomington, IN 47405-1405, USA

Correspondence should be addressed to Dương Nguyễn-Thùy; duongnt_minerals@vnu.edu.vn

Received 31 December 2018; Accepted 11 March 2019; Published 2 May 2019

Guest Editor: Yunpeng Wang

Copyright © 2019 Dương Nguyễn-Thùy et al. This is an open access article distributed under the Creative Commons Attribution License, which permits unrestricted use, distribution, and reproduction in any medium, provided the original work is properly cited.

Thoron's (^{220}Rn) contribution to α -radiation exposure is usually considered negligible compared to that of ^{222}Rn (radon). Despite its short half-life of 55.6 seconds, thoron can be exhaled from porous surface layers of building materials into indoor air where people subsequently inhale radioisotopes, including metallic radioactive progeny. Bare surfaces of dry porous soil with relatively high ^{232}Th content can pose a thoron radiation hazard in indoor air. On northern Vietnam's Đồng Văn karst plateau, the spatial distribution of thoron was determined in indoor air of traditional earthen and other types of dwellings using portable RAD7 and SARAD® RTM 2200 detectors. "Mud houses" are constructed with local compacted soil and typically do not have any floor or wall coverings (i.e., no plaster, wallpaper, or paint). Detailed measurements in a mud house revealed levels of thoron in room air averaging $>500 \text{ Bq m}^{-3}$. The spatial distribution of α -radiation from thoron in indoor air at a distance of about 1 m from interior walls was fairly homogeneous and averaged $\sim 200 \text{ Bq m}^{-3}$. Most concerning, from a human health perspective, were the high thoron concentrations of up to 884 Bq m^{-3} in sleeping areas near mud walls. The average annual thoron radiation dose to inhabitants of mud houses was estimated based on 13 hours of daily occupancy, including daily activities and sleeping. The estimated average thoron inhalation dose of 27.1 mSv a^{-1} during sleeping hours near mud surfaces accounts for nearly 75% of the total estimated radon and thoron inhalation dose of 37.4 mSv a^{-1} from indoor mud house air. Our conservative annual radiation dose estimates do not include subsequent radiation from inhaled metallic progeny of thoron. Our data demonstrate a significant human health risk from radiation exposure and a critical need for remediation in traditional northern Vietnamese mud house dwellings.

1. Introduction

Radon is a naturally occurring colorless, odorless, and tasteless gas, which, at high exposure levels, is recognized to cause lung cancer [1, 2]. Radon has more than thirty characterized radioactive isotopes [3, 4], but ^{222}Rn (called radon) of the uranium (^{238}U) decay series and ^{220}Rn (called thoron, commonly abbreviated Tn) of the thorium (^{232}Th) decay series are considered the major sources of natural radiation to the global human population [2]. The dangers of radon have been well established and constitute about 50% of natural

radiation exposure to humans. Additional significant sources of natural radiation include cosmic radiation and ^{40}K exposure. However, unlike indoor radon exposure, the latter sources cannot be managed [5]. The dangers of indoor radon exposure have led to guidelines by the World Health Organization (WHO) and public health legislation in many countries to require radon monitoring and mitigation [6]. The α -decay of radon isotopes generates multiple radioactive metallic progeny that tend to become adsorbed to aerosol and dust particles. These particles, once inhaled, collect in lung fluids and adsorb onto lung tissues, thereby concentrating

nuclear radiation near living cells. All types of radiation from radioactive decay can induce harmful random biochemical reactions, including damage to DNA [7]. The cell damage from exposure to high radon concentrations is known to increase the incidence of lung cancer.

Radon has been shown to pose a health risk to occupants if concentrations exceed 200 Bq m^{-3} in domestic residences and 300 Bq m^{-3} in workplaces [1, 8–12]. Unlike the focus that has been granted to ^{222}Rn studies for decades, acquiring data sets for indoor thoron concentrations and its decay products has been overlooked due to the general perception that its exposure levels are negligible. The disproportionate focus on ^{222}Rn ignored the contribution of ^{220}Rn to the total inhalation dose when evaluating significant sources of natural radiation. Thoron and its progeny have not even been officially considered into the contexts of official safety thresholds of indoor radiation exposure [5]. This misconception was based on knowledge of its relatively short half-life of 55.6 seconds and its short diffusion distance from emission sources ([13–16]).

Only in recent years has indoor thoron exposure gained attention as a public health concern when increased concentrations were found in dwellings dug into clay-rich soil and in certain types of traditional houses with unfired earthen architecture in China [17–19], India [20], Germany [21], Hungary [22], and Japan [23]. These studies demonstrated that in nearly all the housing types examined, thoron concentrations exceeded those of radon, especially in locations proximal to interior walls. Nearly all dry natural mud surfaces contain sufficient amounts of radioisotopes that provide a significant source for thoron exhalation [24]. The surface layer of soil or other earthen building materials containing ^{232}Th exhales thoron into indoor air [5, 25]. The results of these studies identified thoron as a significant contributor to the indoor radiation exposure of inhabitants.

High concentrations of thoron in Vietnam were initially discovered in karst caves and earthen dwellings of the Đồng Văn Karst Plateau Geopark (<http://www.globalgeopark.org/aboutggn/list/vietnam/6509.htm>), with values in excess of 1000 Bq m^{-3} [26–28]. The aforementioned recommendations, by UNSCEAR [9] and ICRP [29], for the control of radon radiation exposure in domestic and workplace dwellings are based on average environmental background concentrations of 10 Bq m^{-3} for thoron and 100 Bq m^{-3} for radon. Observed thoron levels inside evaluated earthen dwellings of northern Vietnam were orders of magnitude higher than the average environmental background thoron concentration in outdoor air.

The conventional earthen dwelling on the Đồng Văn karst plateau is constructed with fresh local clay-rich soil that is compacted and dried to form the walls and floor of the mud house. Traditional inexpensive mud houses have been used for centuries by several ethnic groups in the mountainous region of northern Vietnam where quality timber and bricks have been too costly. The inhabitants of mud houses often position their beds next to the bare mud walls inside their homes. This arrangement of furniture next to the uncovered exhaling source of thoron has not received adequate scrutiny in terms of the potential radiation health risk for occupants.

In this study, thoron and radon concentrations were systematically surveyed in the main room of a traditional mud house (termed ED 4) on the Đồng Văn karst plateau to establish the spatial distribution of ^{220}Rn and ^{222}Rn where inhabitants spend time during their daily activities. The primary emphasis of this study is the evaluation of thoron as a contributor to the total indoor radiation exposure affecting occupants of mud houses.

2. Materials and Methods

2.1. The Traditional Earthen Dwelling. The model mud house ED 4, a traditional ethnic house on the Đồng Văn karst plateau, was constructed using local soil with an earthen-wall thickness of 60 cm. The dimensions of the main room measured $5.5 \times 9 \times 2.8 \text{ m}$, which is typical of a mud house in the Đồng Văn karst region. The same local soil used to construct the walls also comprised the bare mud floor of the dwelling. As illustrated in Figure 1, the main entrance with a $1.2 \times 1.8 \text{ m}$ door (1) is located in the center of the front wall while two $60 \times 60 \text{ cm}$ windows (2) are symmetrically arranged in the front wall. This layout divides the main room of the mud house into two symmetric halves with their corners being bed positions (3) of inhabitants. A $0.8 \times 1.8 \text{ m}$ opening in the eastern mud wall (4) connects the mud-constructed kitchen room to the main room. The structure of the mud house provides ventilation through openings between the top of the walls and the loose fitting roof (Figure 1). Each earthen dwelling is usually occupied by a family of 6 to 8 people, typically with three generations in one household.

2.2. Measurements of Thoron and Radon Concentrations in Indoor Air. This study used two separate portable radon detectors. Most α -radiation of indoor air derives from ^{222}Rn and ^{220}Rn and their radiogenic progenies ^{218}Po , ^{214}Po , and ^{214}Bi from radon and ^{216}Po , ^{212}Po , and ^{212}Bi from thoron. The two instruments used α -spectroscopy to distinguish the nuclide-specific source of α -radiation in terms of radiation energy. (i) Air was sampled through a plastic hose, prefiltered, and measured using a SARAD® RTM 2200 instrument in “slow mode” to determine nuclide-specific α -radiation intensity in 10-minute intervals. The SARAD® RTM 2200 instrument additionally recorded temperature, barometric pressure, GPS location, relative humidity, and the carbon dioxide concentration. (ii) A RAD7 instrument (serial number 1572) sampled air through a plastic hose, filtered the air through a $1.0 \mu\text{m}$ membrane filter to retain airborne particulate matter, and passed the air sample through a Drierite desiccant trap before gas entered the detector chamber. The instrument quantified the α -decay of both radon isotopes in “sniff mode” [30].

Initial measurements indicating elevated thoron concentrations in indoor air, on the Đồng Văn karst plateau in March 2016, were performed with a SARAD® RTM 2200 instrument in different dwellings constructed with compacted soil, unfired-soil bricks, fired-clay bricks, and/or concrete. Measurements were performed at interior and exterior sites of the dwellings. In December 2016, both instruments

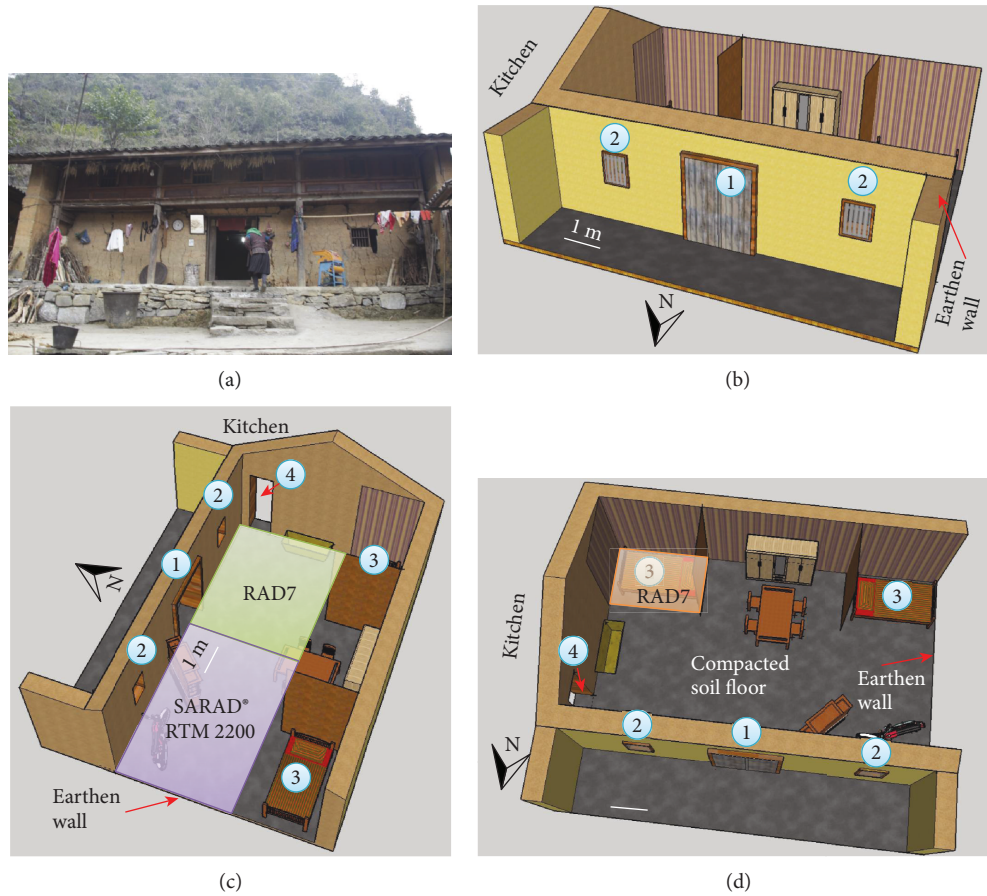


FIGURE 1: Model of the earthen dwelling used for our thoron survey from December 2016 to July 2017. (a) Front view of the traditional earthen dwelling on the Đồng Văn karst plateau. (b–d) Models of the earthen dwelling from different angles of view: (c) surveyed portions of the house with measurements by SARAD® RTM 2200 and RAD7 in violet and pastel green, respectively; (d) measured sleeping area by RAD7 in orange. (1) Main door, (2) two symmetrical windows, (3) positions of beds along mud walls, and (4) opening connecting the main room to a mud-built kitchen (kitchen not shown).

were simultaneously operated side by side to record thoron levels in room air at identical locations (i.e., 40 cm above the compacted earthen floor—comparable to the location of a bed or daily family life activities). Radon and thoron data from both instruments were compatible.

With the support of the builder and home owner of the traditional mud house ED 4 featured in Figure 1, we first visited the house in December 2016 (i.e., cold season) and surveyed the air with the SARAD® RTM 2200 in the western portion of the main room, whereas the RAD7 surveyed the eastern half of the main room (Figure 1(c)). We returned in July 2017 during the contrasting warm season [31] for repeat measurements using the RAD7. With door and windows closed, detailed measurements were taken in a grid-like pattern at ~1 m increments (Figure 1) to obtain the spatial distribution of radon and thoron concentrations at night. Duplicate measurements were recorded at each point. Reported results are averages of duplicate measurements.

3. Results and Discussion

3.1. Recognition of High Thoron Concentrations in Indoor Air of Earthen Dwellings on the Đồng Văn Karst Plateau. Radon

and thoron concentrations of indoor and outdoor air at the dwellings constructed from (i) compacted soil (4 mud houses), (ii) unfired-soil bricks (1 house), and (iii) fired-clay bricks and concrete (1 house) are summarized in Table 1. The average ^{222}Rn level of indoor air was $<100 \text{ Bq m}^{-3}$ in all housing types. The fired-clay brick house showed no significant ^{222}Rn difference when measurements were taken at the center of rooms versus areas close to walls. Conversely, a trend of increasing thoron concentrations was observed from the center of rooms to locations close to the interior walls of dwellings (Figure 2). In addition, thoron concentrations were far higher than radon in the majority of the surveyed dwellings. Maximum thoron concentrations of up to 725 Bq m^{-3} were measured in air close to mud walls and did not decrease below 100 Bq m^{-3} in the center of rooms. The indoor air thoron concentration of 480 Bq m^{-3} next to interior unfired-soil brick walls was similar to that of measurements next to compacted earthen walls, but swiftly declined to 86 Bq m^{-3} towards the center of the room. Thoron concentrations were generally below the detection limit in rooms constructed with fired-clay bricks and concrete, except 44 Bq m^{-3} in the immediate vicinity of some interior walls.

TABLE 1: Radon and thoron concentrations in indoor air and outside of several types of dwellings on the Đồng Văn karst plateau (numbers in regular font reflect average radon and thoron concentrations for a given location; numbers in brackets represent standard deviations).

Dwelling acronym	Radon concentrations (Bq m^{-3})			Thoron concentrations (Bq m^{-3})		
	Outside air	Air in center of room	Air next to wall	Outside air	Air in center of room	Air next to wall
ED 1	0 [0]	18 [36]	29 [50]	0 [0]	102 [18]	357 [113]
ED 2	101 [0]	4 [8]	0 [0]	148 [0]	197 [93]	535 [26]
ED 3	0 [0]	0 [0]	0 [0]	129 [183]	345 [130]	431 [140]
ED 4	46 [25]	41 [54]	59 [38]	107 [53]	438 [179]	725 [326]
EBD	0 [0]	58 [52]	29 [52]	12 [21]	86 [43]	480 [189]
FBH	0 [0]	19 [33]	77 [64]	0 [0]	0 [0]	44 [99]

ED = earthen mud house from compacted soil; EBD = unfired-earthen brick dwelling; FBH = dwelling built by fired-clay brick and/or concrete.

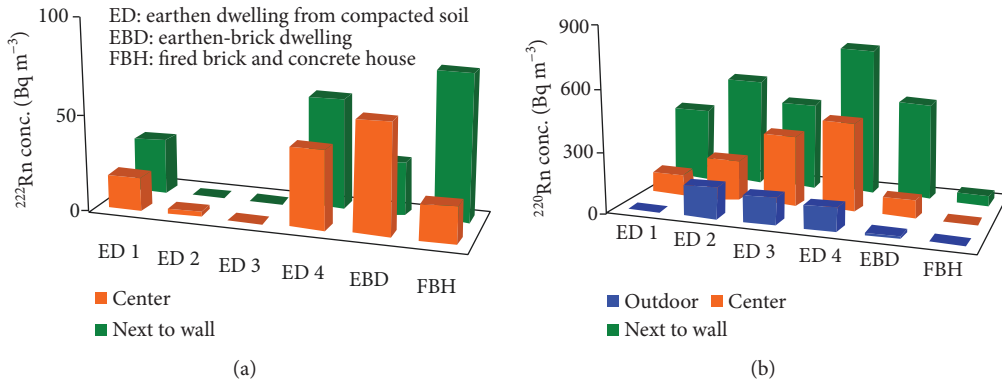


FIGURE 2: Average concentrations of radon in indoor air ((a) center of room and next to interior wall) and of thoron in indoor and outdoor air (b) of several types of dwellings on the Đồng Văn karst plateau.

Additional experiments in other mud houses evaluated the effects on thoron concentrations in the interstitial air between dry mud surfaces and inexpensive surface coverings like polyethylene foil or multiple layers of newspaper. Data from the SARAD® RTM 2200 measured at different locations with or without surface treatments along the interior and exterior of mud houses indicated that thoron concentrations in interstitial air behind surface covers increased drastically. In one instance, thoron levels were observed to exceed $3,000 \text{ Bq m}^{-3}$ behind polyethylene foil. In contrast, measurements of air in the center of the room showed concentrations of at least an order of magnitude less than the thoron levels recorded behind the polyethylene foil covering (Figure 3). These results further demonstrate that thoron is being exhaled from earthen-sourced building materials and diffuses further into the room air. Any surface covering impedes the advective dispersion of thoron into the room air [5] and results in enhanced thoron concentrations in the limited trapped air volume behind the coverings.

3.2. Detailed Thoron Distribution in Surveyed Traditional Earthen Dwelling. Detailed surveys of the distribution of radon and thoron in a traditional earthen dwelling were conducted in the compacted soil (mud) house ED 4 by both portable SARAD® RTM 2200 and RAD7 instruments (Figure 4(a)). Thoron concentrations in the air of the western half of the main room, furthest from the kitchen entrance,

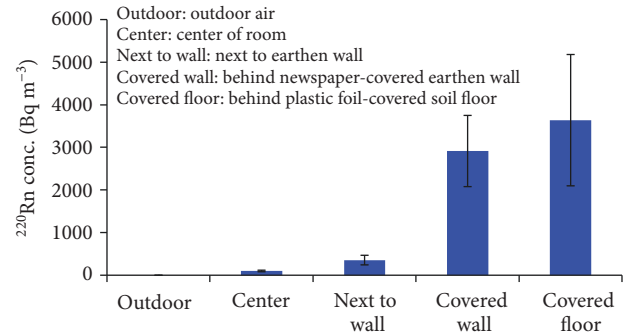


FIGURE 3: Thoron concentrations in interstitial air between dry mud surfaces and surface coverings in comparison to air near an untreated wall, in the center of the room, and outside of the mud house.

measured by SARAD® RTM 2200 in December 2016, varied from 258 to $2,383 \text{ Bq m}^{-3}$ with an average of 744 Bq m^{-3} (Figure 4(b)). The eastern half of the main room, adjacent to the kitchen entrance, measured by RAD7, featured thoron concentrations from 128 Bq m^{-3} to 798 Bq m^{-3} (average 456 Bq m^{-3}) in December 2016 (Figure 4(c)) and from 88 Bq m^{-3} to $2,030 \text{ Bq m}^{-3}$ (average 643 Bq m^{-3}) in July 2017 (Figure 4(d)). The highest concentrations of thoron in both

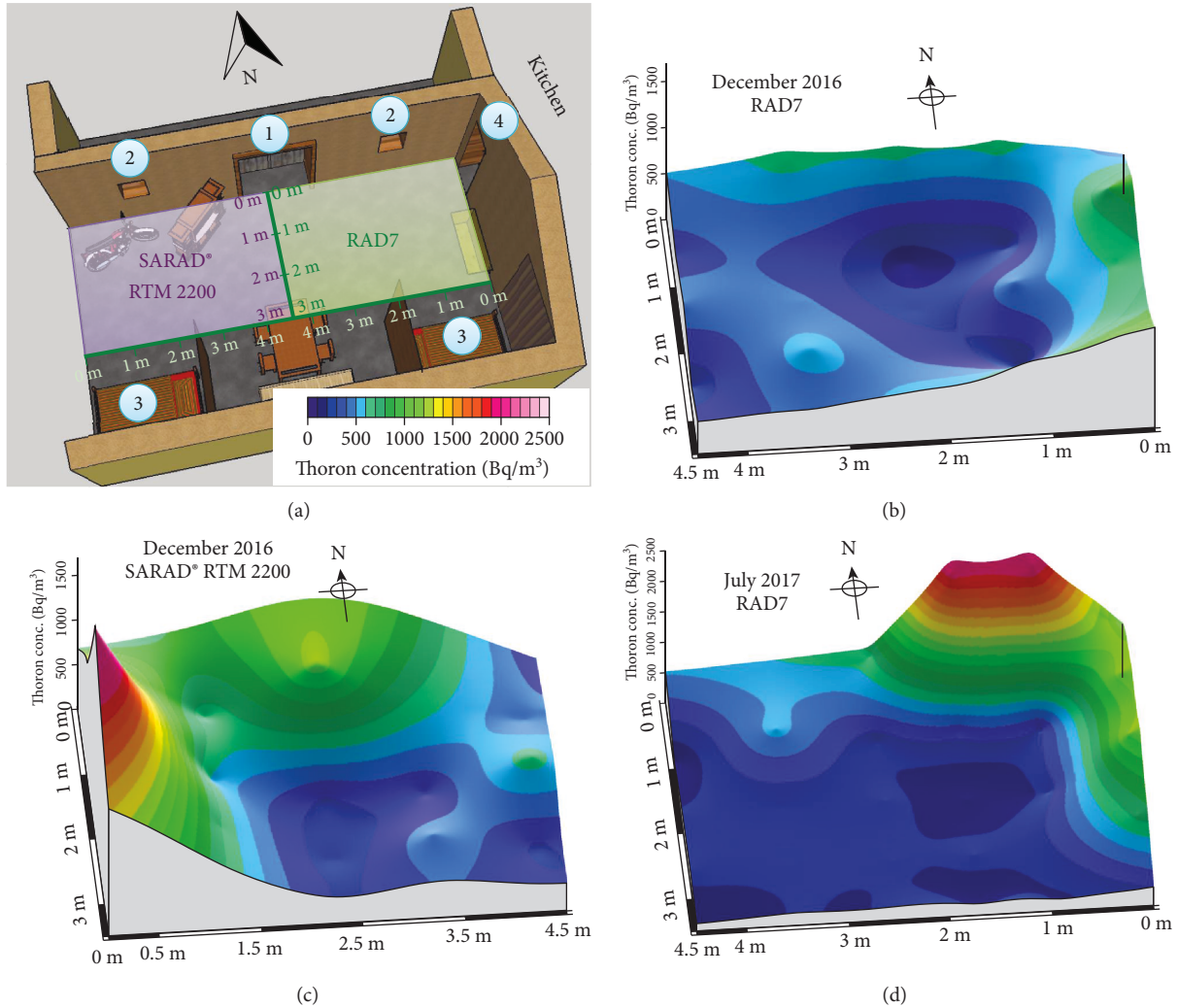


FIGURE 4: Detailed thoron distribution in the surveyed main room of mud house ED 4. (a) Map of the surveyed main room with indication of the parallel use of SARAD® RTM 2200 and RAD7 instruments in violet and pastel green, respectively. (b) Thoron distribution in the western half of the room (measured during the night by SARAD® RTM 2200 in December 2016). (c, d) Thoron distribution in the eastern half of the room (measured by RAD7 during the night in December 2016 and during the night in July 2017, respectively).

cold and warm seasons exceeded $2,000 \text{ Bq m}^{-3}$ at locations proximal to mud walls (Figures 4(b) and 4(d)).

In the eastern half of the main room, the average value of thoron in the warm season was higher than during the cold season. The discrepancy between seasons is from warmer air with higher humidity enhancing the diffusive exhalation of thoron from porous, more humid source materials [32, 33]. In the cold season, air in the western half of the room had higher thoron levels than the other half of the room. The difference is likely due to ventilation and uneven air flow in the room as well as through the kitchen entrance.

The results demonstrate that thoron concentrations tend to increase from the center of the room towards the surface of earthen walls (Figures 4(b)–4(d)) with maxima occurring near corners between two mud walls where air flow is limited and the ratio of thoron-exhaling mud surface versus adjacent air volume is highest (Figures 4(b) and 4(d)).

Despite emissions from multiple sources of dry mud in the dwelling, thoron in indoor air rapidly declines in

concentration outward from mud walls toward the center of the room. Thoron concentrations diminished by almost 70% at a distance of 120 cm from the walls (Figures 5 and 6). The center of the room measures only 20 to 25% of the thoron concentration measured proximal to mud walls. The observed spatial distribution of thoron in the mud house does not demonstrate an exponential decrease from the wall surface to the center of the structure, which is expected in the absence of convection ([14]). Instead, the observed pattern is consistent with a combination of factors, including an uneven distribution of thoron-exhaling mud surfaces, slow convection of room air (enhanced by the movement and thermal disturbance from the presence of people), and external wind forcing the mild ventilation through open spaces between the top of the mud walls and the roof, as well as through the imperfectly fitted door and windows.

From a human health perspective, it is important to note that the average thoron concentration in room air is far

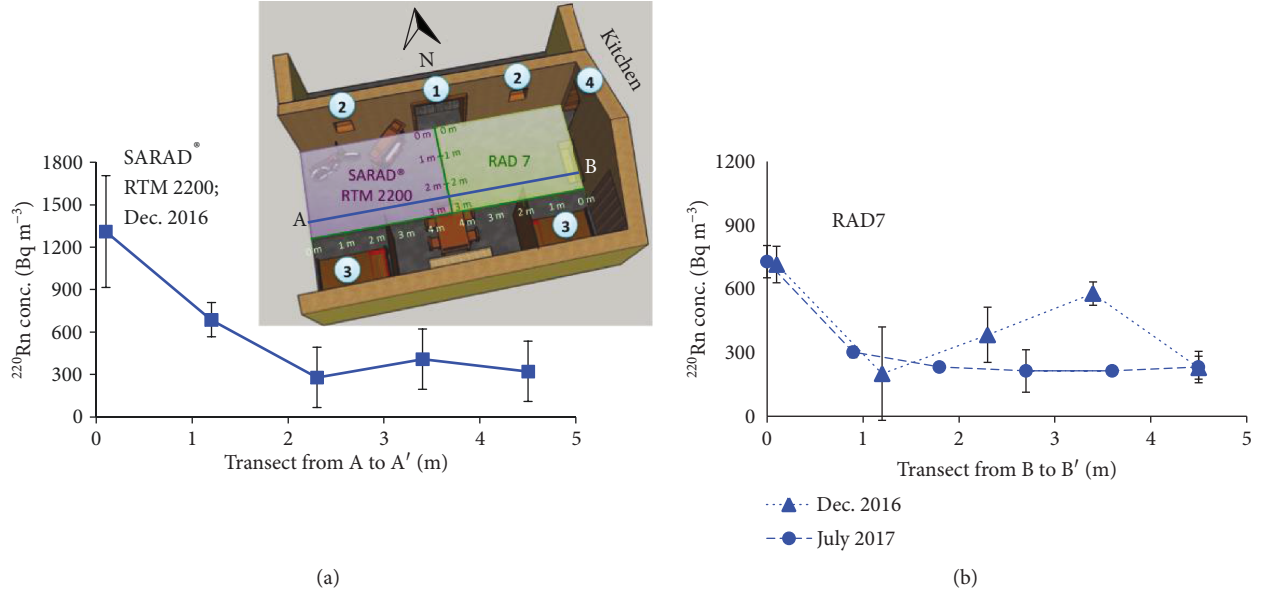


FIGURE 5: Thoron concentration profiles along western and eastern transects from the midpoint of earthen walls to the center of the main room in mud house ED 4. (a) Western transect from A to A', measured by SARAD® RTM 2200 in Dec. 2016. (b) Eastern transect from B to B', measured by RAD7 in Dec. 2016 and July 2017.

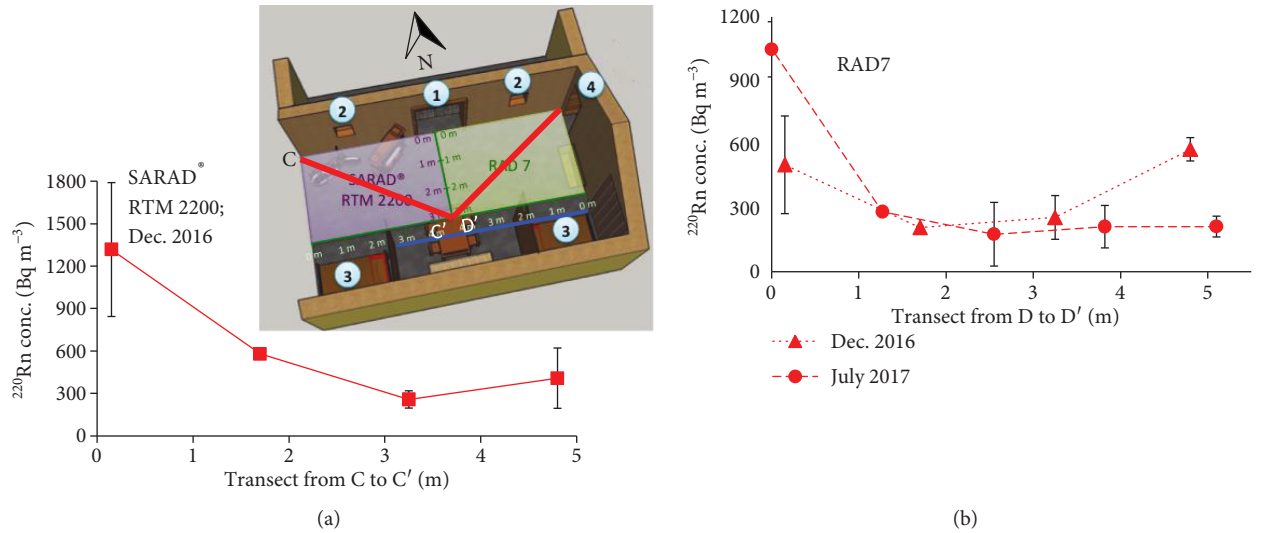


FIGURE 6: Thoron concentration profiles along diagonal transects of the western and eastern halves of the main room in mud house ED 4. (a) Diagonal transect of the western half from C to C', measured by SARAD® RTM 2200 in Dec. 2016. (b) Diagonal transect of the eastern half from D to D', measured by RAD7 in Dec. 2016 and July 2017.

higher in the sleeping area near earthen walls (up to $\sim 2,500 \text{ Bq m}^{-3}$) than in the center of the room (Figure 7). The inhabitants of earthen dwellings often place their beds at the corner of two mud walls and/or next to mud walls. Sleeping close to thoron-exhaling mud walls greatly enhances the radiation exposure for the inhabitants. The closure of doors and windows at night diminishes air convection and further exacerbates the indoor exposure from radionuclides during sleeping hours.

3.3. Estimated Annual Inhalation Dose for Inhabitants of Mud House ED 4. The effective dose of radon and thoron

inhalation, along with its radioactive progeny, was calculated for the main room of mud house ED 4 using the following UNSCEAR [2] algorithm:

$$D = [(k_{\text{Rn}} + n_{\text{Rn}} \times F_{\text{Rn}}) \times C_{\text{Rn}} + (k_{\text{Tn}} + n_{\text{Tn}} \times F_{\text{Tn}}) \times C_{\text{Tn}}] \times H \times 0.8 \times 10^{-6}, \quad (1)$$

with

D : total annual inhalation dose exposure to radon (mSv a^{-1});

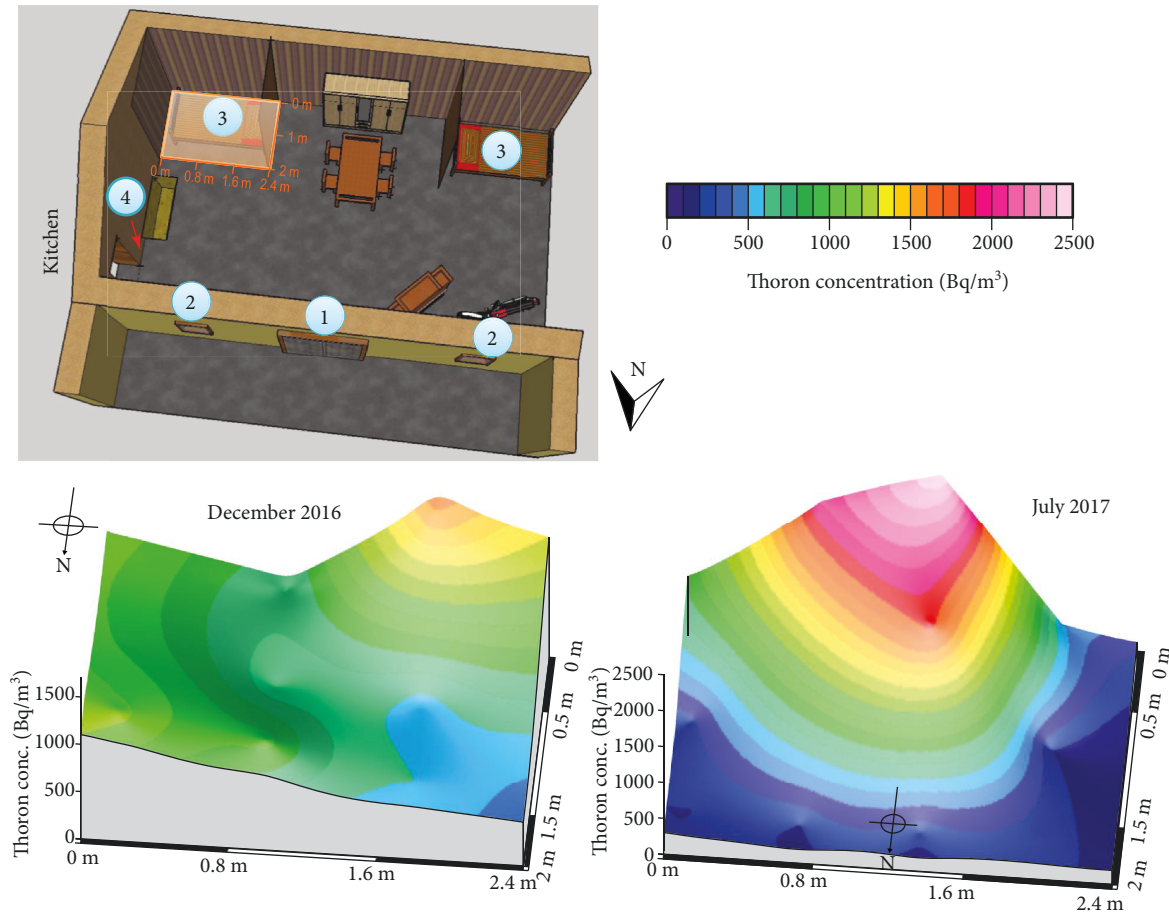


FIGURE 7: Thoron concentrations of indoor air in the sleeping area of mud house ED 4 at night for December 2016 and July 2017 (measured by RAD7).

Rn and Tn: abbreviations of radon and thoron, respectively;

k : solubility coefficient of radon in blood ($k_{Rn} = 0.17$; $k_{Tn} = 0.11$);

n : inhalation dose conversion factor ($nSv/(Bq\ h\ m^{-3})$) ($n_{Rn} = 9$; $n_{Tn} = 40$);

F : indoor equilibrium factor ($F_{Rn} = 0.4$; $F_{Tn} = 0.3$);

H : average duration of exposure per year (h);

C : concentration of radon ($Bq\ m^{-3}$);

0.8: occupancy factor for the study region with exposure duration of one year;

10^{-6} : factor to convert nSv into mSv.

Due to ethnic custom and economic constraints, a family living in a traditional northern Vietnamese mud house commonly encompasses three generations living together (i.e., infants to adolescents, working age adults ~16 to 50 in age, and elderly with ages above 50). All members of a family are usually at home together from the hours of 5:00 pm in the evening to 6:00 am the next morning. They stay at home approximately 13 hours per day with about 8 hours spent sleeping and 5 hours participating in family life activities (i.e., cooking, eating, children playing, etc.). Therefore, we assume that an inhabitant's average exposure to indoor radon and thoron lasts for a duration of at least 13 hours per day in mud houses. This estimate is most appropriately

applied to adults of working age, but exposure time for children and the elderly generation may be higher because of their likely extended time at the earthen structures. The elderly generation often stays at home, especially during colder months and during the rainy season, and children still attend school in some earthen buildings.

The average annual effective dose from radon and thoron and their progenies to mud house inhabitants was estimated to be $37.4\ mSv\ a^{-1}$. Thoron and its progenies account for 97% of the combined average radiation dose from radon and thoron, amounting to $36.2\ mSv\ a^{-1}$ (Table 2). Furthermore, the average annual inhalation dose due to the exposure of indoor thoron and its progenies amounts to $9.0\ mSv\ a^{-1}$ during 5 hours of daytime daily spent in mud houses, in addition to $27.1\ mSv\ a^{-1}$ while sleeping in mud houses for 8 hours daily. The annual inhalation dose during sleeping hours is 3 times higher than the dose of thoron during daytime activities in mud houses.

The spatial variation of the annual inhalation dose from thoron and its progenies in indoor air reflecting 5 hours per day of daytime presence in the mud house is represented in Figure 8. The annual inhalation doses from thoron and its progenies in proximity either to a single mud wall or at the corner of two adjoining mud walls have been estimated to be $\sim 13\ mSv\ a^{-1}$ and $\sim 19\ mSv\ a^{-1}$, respectively. These values

TABLE 2: Annual effective dose (mSv a^{-1}) due to inhaled indoor radon and thoron in the surveyed traditional mud house based on inhabitants staying at home for 5 hours during daytime and for 8 hours during the night, on a daily basis.

Measured time	Concentration of radon isotopes (Bq m^{-3})				Inhalation dose (mSv)			
	Living room Radon	Living room Thoron	Sleeping area Radon	Sleeping area Thoron	Living room (5 hours/day) Radon	Living room (5 hours/day) Thoron	Sleeping area (8 hours/day) Radon	Sleeping area (8 hours/day) Thoron
Dec. 2016 (i.e., cold half of the year)	43 (5-96)	456 (128-793)	33 (23-43)	1034 (976-1137)	0.2 (0.0-0.4)	4.0 (1.1-7.0)	0.2 (0.1-0.2)	14.6 (13.8-16.1)
Jul. 2017 (i.e., warm half of the year)	77 (18-116)	563 (89-2030)	119 (9-285)	884 (196-2475)	0.3 (0.1-0.5)	5.0 (0.8-18.0)	0.5 (0.0-1.3)	12.5 (2.8-35.0)
<i>Inhalation dose of radon and its progenies, and thoron and its progenies (mSv)</i>								
Average inhalation dose for daily occupancy on an annual basis (mSv a^{-1})					0.5	9.0	0.7	27.1
							37.4	

For each respective parameter, numbers in regular font represent average values, whereas numbers in italics and in brackets indicate observed ranges.

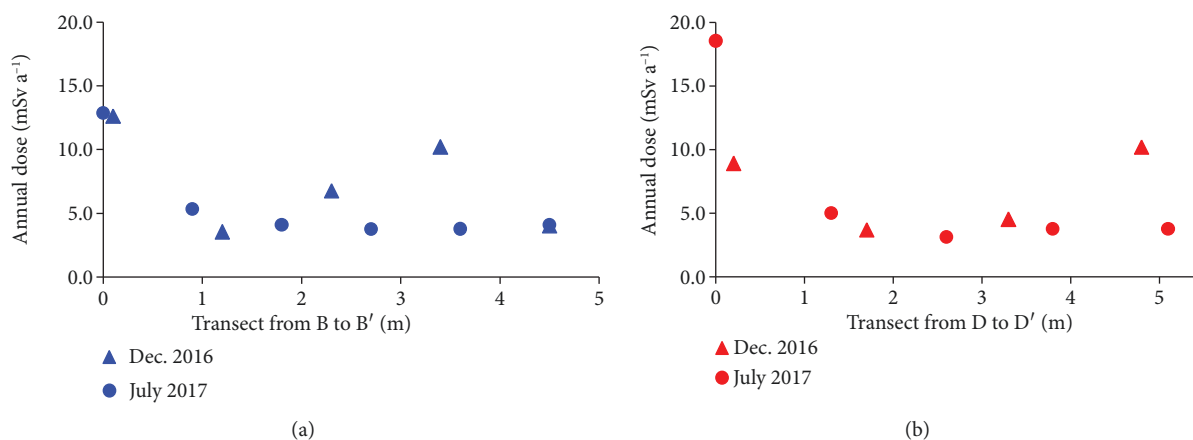


FIGURE 8: The profiles of annual dose from only thoron (in mSv a⁻¹) along the eastern transect from the midpoint of the earthen wall to the center of the room, transect B to B' in Figure 5 (a) and along the diagonal transect of the eastern half, transect D to D' in Figure 6 (b) pertaining to family life activities in the main room of mud house ED 4 for 5 hours per day. The exposure dose from thoron was estimated based on the concentrations of thoron measured by RAD7 at night in December 2016 and July 2017.

decrease to one-third at a distance of ~1 m from mud surfaces and remain rather constant towards the center of the room.

Based on the UNSCEAR [9] guidelines for annual doses of ionizing radiation by source, the recommended upper threshold inhalation dose of total radon and thoron and their progenies is 1.26 mSv a⁻¹, with a typical range of observed doses up to 10 mSv a⁻¹. The estimated average inhalation dose on an annual basis from only thoron and its progenies of 36.1 mSv a⁻¹ experienced by inhabitants in earthen dwelling ED 4 in northern Vietnam is substantially higher than the total annual average dose from natural sources of 2.4 mSv a⁻¹ [9].

4. Conclusions

Thoron and its airborne radioactive progeny were found to pose a significant health risk to inhabitants living in traditional earthen dwellings (i.e., mud houses) in northern Vietnam's karst region. High levels of thoron in indoor air with typical values of 450–650 Bq m⁻³ cannot be mitigated by enhanced ventilation because thoron's short half-life of 55.6 s causes a maximum concentration in the vicinity of exhaling mud surfaces. The distribution of thoron in the indoor air of mud houses is influenced by convection and also depends strongly on the available area and porosity of sources (i.e., mud walls and floors) as well as the distance from mud surfaces [34]. The common practice of positioning beds next to mud walls, especially in the corner of a room, exacerbates the radiation hazard during sleeping hours. The estimated average inhalation dose for daily occupancy, exclusively from thoron exposure during sleeping hours, on an annual basis reaches up to 37.4 mSv a⁻¹ and is 15 times larger than the recommended annual safety threshold for the public of 2.4 mSv a⁻¹ [9]. Most ethnic groups in the northern karst region of Vietnam live in earthen dwellings constructed with compacted local soil and thus are disproportionately at a higher risk of exposure to thoron compared to inhabitants of more modern homes made from nonearthen materials.

Practical mitigation strategies that are needed must be socially acceptable and economically feasible.

Data Availability

The data used to support the findings of this study are included within the article. No extra data were used to support this study.

Additional Points

Highlights. (i) Thoron exhales from bare dried mud walls and floors into indoor air of traditional northern Vietnamese mud houses. (ii) The thoron concentration in indoor air is elevated near mud surfaces and decreases towards the center of the room. (iii) The thoron inhalation dose of inhabitants increases in proportion to the amount of time spent near mud surfaces, especially when sleeping close to mud walls. (iv) High thoron concentrations in indoor air of traditional northern Vietnamese mud houses pose a human radiation health hazard.

Conflicts of Interest

The authors declare that there are no conflicts of interest regarding the publication of this paper.

Acknowledgments

The content of this manuscript is based upon work supported by the Vietnam National Foundation for Science and Technology Development (NAFOSTED) grant number 105.99-2016.16. Measurements with the SARAD® RTM 2200 were supported by the U.S. Department of Energy, Office of Science, Office of Basic Energy Sciences, Chemical Sciences, Geosciences, and Biosciences Division under Award Number DE-SC0006978. We are indebted to Mr. Nùng Văn Minh and his family for permission to use their home for measurements. We are grateful for the cultural

liaison and logistics facilitated by Minh Ngọc Schimmelmänn. We thank Dr. Thomas Streil from SARAD® GmbH and Assoc. Prof. Dr. Trần Tuấn Anh from the Institute of Geological Science, Vietnam Academy of Science and Technology, for the expert guidance on radon measurements.

References

- [1] United Nations Scientific Committee on the Effects of Atomic Radiation (UNSCEAR), "Report to the General Assembly, with scientific annexes," in *Sources and Effects of Ionizing Radiation*, United Nations, New York, NY, USA, 1993.
- [2] United Nations Scientific Committee on the Effects of Atomic Radiation (UNSCEAR), "UNSCEAR 2000 Report to the General Assembly, with scientific annexes," in *Sources and Effects of Ionizing Radiation, vol. I*, United Nations, New York, NY, USA, 2000.
- [3] M. E. Wieser, "Atomic weights of the elements 2005 (IUPAC Technical Report)," *Pure and Applied Chemistry*, vol. 78, no. 11, pp. 2051–2066, 2006.
- [4] D. Neidherr, G. Audi, D. Beck et al., "Discovery of ^{229}Rn and the structure of the heaviest Rn and Ra isotopes from Penning-trap mass measurements," *Physical Review Letters*, vol. 102, no. 11, 2009.
- [5] R. C. G. M. Smetsers and J. M. Tomas, "A practical approach to limit the radiation dose from building materials applied in dwellings, in compliance with the Euratom Basic Safety Standards," *Journal of Environmental Radioactivity*, vol. 196, pp. 40–49, 2019.
- [6] World Health Organization (WHO), *WHO Handbook on Indoor Radon: A Public Health Perspective*, World Health Organization, Geneva, 2009.
- [7] World Health Organization (WHO), *WHO Guidelines for Indoor Air Quality: Selected Pollutants*, World Health Organization, Geneva, 2010.
- [8] United Nations Scientific Committee on the Effects of Atomic Radiation (UNSCEAR), "UNSCEAR 2006 Report to the General Assembly, with scientific annexes," in *Effects of Ionizing Radiation, vol. I*, United Nations, New York, NY, USA, 2008.
- [9] United Nations Scientific Committee on the Effects of Atomic Radiation (UNSCEAR), "UNSCEAR 2008 Report to the General Assembly, with scientific annexes," in *Sources and Effects of Ionizing Radiation, vol. I*, United Nations, New York, NY, USA, 2010.
- [10] International Commission on Radiological Protection (ICRP), "Database of dose coefficients: workers and members of the public," in *Annals of the ICRP*, Elsevier Science, Amsterdam, 2003.
- [11] M. Tirmarche, J. D. Harrison, D. Laurier, F. Paquet, E. Blanchardon, and J. W. Marsh, "Lung cancer risk from radon and progeny and Statement on radon," *Annals of the ICRP*, vol. 40, no. 1, pp. 1–64, 2010.
- [12] S. Darby, D. Hill, A. Auvinen et al., "Radon in homes and risk of lung cancer: collaborative analysis of individual data from 13 European case-control studies," *British Medical Journal*, vol. 330, no. 7485, p. 223, 2005.
- [13] W. W. Nazaroff and A. V. J. Nero, "Radon and its decay products in indoor air," in *Environmental Science and Technology: A Wiley-Interscience Series of Texts and Monographs*, John Wiley and Sons, Inc, New York, 1988.
- [14] O. Meisenberg and J. Tschiersch, "Specific properties of a model of thoron and its decay products in indoor atmospheres," *Nukleonika*, vol. 55, no. 4, pp. 463–469, 2010.
- [15] V. Urosević, D. Nikezić, and S. Vulović, "A theoretical approach to indoor radon and thoron distribution," *Journal of Environmental Radioactivity*, vol. 99, no. 12, pp. 1829–1833, 2008.
- [16] P. Ujčić, I. Čeliković, A. Kandić et al., "Internal exposure from building materials exhaling ^{222}Rn and ^{220}Rn as compared to external exposure due to their natural radioactivity content," *Applied Radiation and Isotopes*, vol. 68, no. 1, pp. 201–206, 2010.
- [17] B. Shang, B. Chen, Y. Gao, Y. Wang, H. Cui, and Z. Li, "Thoron levels in traditional Chinese residential dwellings," *Radiation and Environmental Biophysics*, vol. 44, no. 3, pp. 193–199, 2005.
- [18] Y. Yamada, Q. Sun, S. Tokonami et al., "Radon-thoron discriminative measurements in Gansu Province, China, and their implication for dose estimates," *Journal of Toxicology and Environmental Health, Part A*, vol. 69, no. 7–8, pp. 723–734, 2006.
- [19] B. Shang, J. Tschiersch, H. Cui, and Y. Xia, "Radon survey in dwellings of Gansu, China: the influence of thoron and an attempt for correction," *Radiation and Environmental Biophysics*, vol. 47, no. 3, pp. 367–373, 2008.
- [20] M. Sreenath Reddy, P. Yadagiri Reddy, K. Rama Reddy, K. P. Eappen, T. V. Ramachandran, and Y. S. Mayya, "Thoron levels in the dwellings of Hyderabad city, Andhra Pradesh, India," *Journal of Environmental Radioactivity*, vol. 73, no. 1, pp. 21–28, 2004.
- [21] S. Gierl, O. Meisenberg, P. Feistenauer, and J. Tschiersch, "Thoron and thoron progeny measurements in German clay houses," *Radiation Protection Dosimetry*, vol. 160, no. 1–3, pp. 160–163, 2014.
- [22] Z. Szabó, G. Jordan, C. Szabó et al., "Radon and thoron levels, their spatial and seasonal variations in adobe dwellings — a case study at the great Hungarian plain," *Isotopes in Environmental and Health Studies*, vol. 50, no. 2, pp. 211–225, 2014.
- [23] H. Yonehara, S. Tokonami, W. Zhuo, T. Ishikawa, K. Fukutsu, and Y. Yamada, "Thoron in the living environments of Japan," *International Congress Series*, vol. 1276, pp. 58–61, 2005.
- [24] Y. Li, S. D. Schery, and B. Turk, "Soil as a source of indoor ^{220}Rn ," *Health Physics*, vol. 62, no. 5, pp. 453–457, 1992.
- [25] O. Meisenberg, R. Mishra, M. Joshi et al., "Radon and thoron inhalation doses in dwellings with earthen architecture: comparison of measurement methods," *Science of the Total Environment*, vol. 579, pp. 1855–1862, 2017.
- [26] D. Nguyen-Thuy, H. Nguyen-Van, A. Schimmelmänn, N. Nguyen-Anh, P. T. Dang, and H. P. Ta, "Radon concentrations in karst caves in Dong Van karst plateau," *VNU Journal of Science – Earth and Environmental Sciences*, vol. 32, no. 2S, pp. 187–197, 2016.
- [27] N. T. A. Nguyet, N. T. Duong, A. Schimmelmänn, and N. V. Huong, "Human exposure to radon radiation geohazard in Rong Cave, Dong Van Karst Plateau Geopark, Vietnam," *Vietnam Journal of Earth Sciences*, vol. 40, no. 2, pp. 117–125, 2018.
- [28] D. Nguyen-Thuy, H. Nguyen-Van, T. A. N. Nguyen, A. Schimmelmänn, and M. N. Schimmelmänn, "Recognition of health geohazard of thoron (Rn-220) exhalation into room air of earthen dwellings in northern Vietnam," in *4th*

International Conference on Radioecology & Environmental Radioactivity, pp. 125–127, Berlin, September 2017.

- [29] International Commission on Radiological Protection (ICRP), “The 2007 Recommendations of the International Commission on Radiological Protection,” *Annals of the ICRP*, vol. 37, no. 2–4, 2008.
- [30] DurrIDGE Company, “RAD7 electronic radon detector – user manual,” *DurrIDGE, Radon Capture & Analytics*, DurrIDGE Company Inc., 2017.
- [31] Ha Giang Statistics Office (GSO), “Mean air temperature at Ha Giang station,” in *Statistical Yearbook of Ha Giang 2017*, p. 24, Statistical Publishing House, Ha Giang, 2018, (in Vietnamese).
- [32] V. Balek and I. N. Beckman, “Theory of emanation thermal analysis XII. Modelling of radon diffusion release from disordered solids on heating,” *Journal of Thermal Analysis and Calorimetry*, vol. 82, no. 3, pp. 755–759, 2005.
- [33] M. Faheem and Matiullah, “Radon exhalation and its dependence on moisture content from samples of soil and building materials,” *Radiation Measurements*, vol. 43, no. 8, pp. 1458–1462, 2008.
- [34] M. Doi, K. Fujimoto, S. Kobayashi, and H. Yonehara, “Spatial distribution of thoron and radon concentrations in the indoor air of a traditional Japanese wooden house,” *Health Physics*, vol. 66, no. 1, pp. 43–49, 1994.

Research Article

An Areal Assessment of Subseafloor Carbon Cycling in Cold Seeps and Hydrate-Bearing Areas in the Northern South China Sea

Yanping Zhang ¹, Min Luo ^{2,3}, Yu Hu,³ Hongbin Wang,⁴ and Duofu Chen ^{1,3}

¹State Key Laboratory of Isotope Geochemistry, Guangzhou Institute of Geochemistry, Chinese Academy of Sciences, Guangzhou 510640, China

²Laboratory for Marine Geology, Qingdao National Laboratory for Marine Science and Technology, Qingdao 266061, China

³Shanghai Engineering Research Center of Hadal Science and Technology, College of Marine Sciences, Shanghai Ocean University, Shanghai 201306, China

⁴Guangzhou Marine Geological Survey, Guangzhou 510740, China

Correspondence should be addressed to Min Luo; mluo@shou.edu.cn and Duofu Chen; dfchen@shou.edu.cn

Received 25 November 2018; Accepted 20 January 2019; Published 17 March 2019

Academic Editor: Giovanni Martinelli

Copyright © 2019 Yanping Zhang et al. This is an open access article distributed under the Creative Commons Attribution License, which permits unrestricted use, distribution, and reproduction in any medium, provided the original work is properly cited.

Gas hydrates, acting as a dynamic methane reservoir, store methane in the form of a solid phase under high-pressure and low-temperature conditions and release methane through the sediment column into seawater when they are decomposed. The seepage of methane-rich fluid (i.e., cold hydrocarbon seeps) fuels the chemosynthetic biota-inhabited surface sediments and represents the major pathway to transfer carbon from sediments to the water column. Generally, the major biogeochemical reactions related to carbon cycling in the anoxic marine sediments include organic matter degradation via sulfate reduction (OSR), anaerobic oxidation of methane (AOM), methanogenesis (ME), and carbonate precipitation (CP). In order to better understand the carbon turnover in the cold seeps and gas hydrate-bearing areas of the northern South China Sea (SCS), we collected geochemical data of 358 cores from published literatures and retrieved 37 cores and corresponding pore water samples from three areas of interest (i.e., Xisha, Dongsha, and Shenhu areas). Reaction-transport simulations indicate that the rates of organic matter degradation and carbonate precipitation are comparable in the three areas, while the rates of AOM vary over several orders of magnitude (AOM: 8.3–37.5 mmol·m⁻²·yr⁻¹ in Dongsha, AOM: 12.4–170.6 mmol·m⁻²·yr⁻¹ in Xisha, and AOM: 9.4–30.5 mmol·m⁻²·yr⁻¹ in Shenhu). Both the arithmetical mean and interpolation mean of the biogeochemical processes were calculated in each area. Averaging these two mean values suggested that the rates of organic matter degradation in Dongsha (25.7 mmol·m⁻²·yr⁻¹) and Xisha (25.1 mmol·m⁻²·yr⁻¹) are higher than that in Shenhu (12 mmol·m⁻²·yr⁻¹) and the AOM rate in Xisha (135.2 mmol·m⁻²·yr⁻¹) is greater than those in Dongsha (27.8 mmol·m⁻²·yr⁻¹) and Shenhu (17.5 mmol·m⁻²·yr⁻¹). In addition, the rate of carbonate precipitation (32.3 mmol·m⁻²·yr⁻¹) in Xisha is far higher than those of the other two regions (5.3 mmol·m⁻²·yr⁻¹ in Dongsha, 5.8 mmol·m⁻²·yr⁻¹ in Shenhu) due to intense AOM sustained by gas dissolution. In comparison with other cold seeps around the world, the biogeochemical rates in the northern SCS are generally lower than those in active continental margins and special environments (e.g., the Black sea) but are comparable with those in passive continental margins. Collectively, ~2.8 Gmol organic matter was buried and at least ~0.82 Gmol dissolved organic and inorganic carbon was diffused out of sediments annually. This may, to some extent, have an impact on the long-term deep ocean carbon cycle in the northern SCS.

1. Introduction

Marine sediments are the Earth's largest methane reservoir, in which methane is dominantly preserved as gas hydrates that are commonly distributed along continental margins [1, 2]. It is estimated that at least 600 Gt methane is stored

as hydrates in the continental margin sediments characterized by relatively high-pressure and low-temperature conditions [3]. However, as a dynamic methane reservoir, gas hydrates tend to decompose when the equilibrium state breaks, potentially leading to ocean acidification, submarine slope instability, and global climate change [2–4]. In

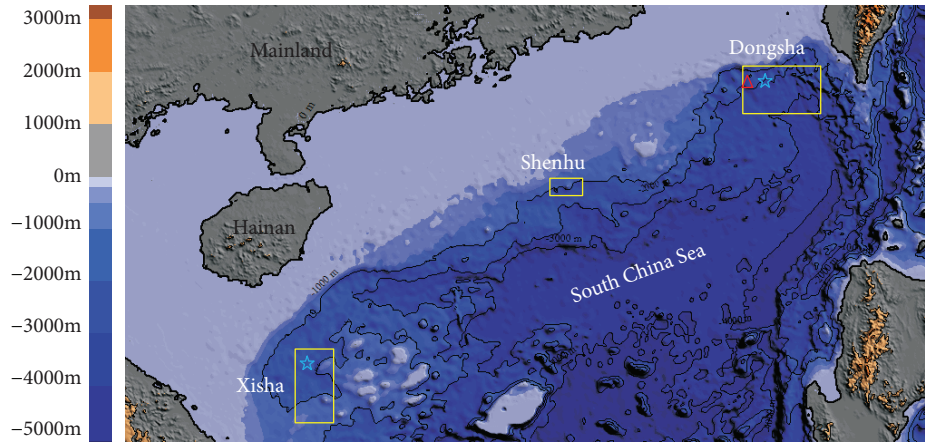


FIGURE 1: The bathymetric map of the northern South China Sea. Rectangle boxes denote study areas. Note that Xisha herein includes the Qiongdongnan basin and Xisha Uplift, and Dongsha comprises a broad area of the eastern Zhujiangkou basin and SW Taiwan basin. The blue stars denote active seepage sites. The red triangle represents the Jiulong methane reef covering an area of $\sim 400 \text{ km}^2$.

addition, in light of the resource potential and environmental effect, gas hydrate has drawn increasing attentions worldwide since its first discovery in 1970s.

Gas hydrates are usually closely coupled with cold seeps at continental slopes. On the continental margins, methane produced through either microbial methanogenesis or pyrolysis of organic matter can precipitate as hydrates when the dissolved methane concentration exceeds methane hydrate solubility within the gas hydrate stability zone [2, 5–7]. The gas hydrates will decompose and release large amounts of methane into the water column upon the pressure and/or temperature changes induced by global warming and sea level changes. The migration of methane-rich fluid towards the seafloor forms the cold seeps and associated seafloor expressions (e.g., mound or crater-like shape) [8]. Globally, the vast majority of methane in the sediments is consumed by the anaerobic oxidation of methane (AOM) mediated by anaerobic methane-oxidizing archaea and sulfate-reducing bacteria [9, 10]. AOM thus represents a microbial filter largely preventing dissolved methane from escaping the sediments. In the intensive seepage areas, a large amount of methane is usually transported in a gas phase as bubble, which cannot be fully consumed by AOM. The main product of AOM, dissolved inorganic carbon (DIC), can either precipitate as authigenic carbonate or migrate towards the seafloor. Other DIC sources in the sediments include organoclastic sulfate reduction and methanogenesis, which also makes important contribution to the DIC reservoir.

The South China Sea (SCS), as one of the major marginal seas around the west Pacific Ocean, is well known for its extensive distribution of high-saturation gas hydrate [11–14]. Since the 1990's, high-resolution seismic surveys have been carried out to delineate the distribution of bottom-simulating reflectors (BSR) and determine the prospecting area of gas hydrates. Through several hydrate survey expeditions, six promising hydrate-bearing areas including Dongsha, SW Taiwan, Xisha, Qiongdongnan, Shenhu, and Beikang have been confirmed to date [13–20]. Besides, more than 40 cold seepage sites have been indicated by

the occurrence of ^{13}C -depleted authigenic carbonate and seep-associated fauna and anomalous pore water and sediment geochemistry influenced by fluid seepage [6, 21–25]. Several pioneering studies have targeted at quantifying the rate of biogeochemical reactions and carbon fluxes at the seafloor using the reaction-transport model, in the specific seep sites of the northern SCS [16, 24, 26, 27]. Nevertheless, our quantitative understanding of the subsurface carbon cycle on a regional scale still remains limited. Therefore, the area-based carbon cycle calls for sufficient geochemical data combined with the numerical modeling approach to understand the relationship among different carbon reservoirs and their potential impact on the seawater carbonate system. In this study, 37 sediment cores were collected from the Shenhu area, Dongsha area, and Xisha area. The 1-D reaction-transport model was subsequently applied to quantify site-specific rates of biogeochemical processes and fluxes of DIC and methane. In combination with 358 published cores from the areas of interest, spatial interpolation was then used to explore the regional distribution of biogeochemical rates in the three regions. Finally, the areal assessments of surface carbon cycling in the northern SCS were provided to reveal the relationship among different carbon inventories.

2. Study Area

The SCS formed in the late Jurassic-early Cretaceous is located at the confluence of three plate collision, including the Pacific plate, Eurasia plate, and India-Australia plate [28]. The northern margin is a typical passive continental setting with a broad shelf, which is bounded to the west by the Indochina peninsula and to the east by a chain of island arcs [28]. The study area includes three areas in the northern slope of the SCS (Xisha, Shenhu, and Dongsha), with the water depth ranging from ~ 700 to ~ 2000 meters (see Figure 1). All these regions unanimously have experienced two tectonic stages, i.e., the syn-rift stage during the Paleocene and Oligocene and post-rift stage [29]. The infill of the northern continental marginal basins evolved simultaneously

from alluvial and lacustrine deposits to neritic deposits, followed by progradational packages of slope sediments [30]. The lacustrine sediments deposited in the depressions acted as important source rocks for hydrocarbon generation. The potential abundant gas hydrate reservoirs have been indicated by the widespread occurrence of bottom-simulating reflectors (BSRs) [12, 31] (see Figure 1). The gas hydrates, retrieved by GMGS1&3 hydrate-drilling expeditions conducted by the Guangzhou Marine Geology Survey at the water depth of ~2000 meters in the Shenhu area, are characterized by a high-saturation (up to 40%) and mixed gas source [12]. During the GMGS2 hydrate-drilling expedition in Dongsha, various gas hydrate morphologies including massive, fracture-filling, and disseminated hydrates were found in the collected cores [31]. In addition, active seepage sites were discovered during remotely operated vehicle (ROV) deployments in the Dongsha and Xisha areas [21, 32]. These active seepage sites are characterized by the existence of gas ebullition in the water column; living chemosynthesis-based communities, such as mussels, tubeworms, and clams; and abundant authigenic carbonate rocks in the form of crusts, nodules, and tubular concretion.

3. Sampling and Methods

3.1. Sampling. In total, the 37 sediment cores used in this study were collected from five expeditions by using different research vessels. Four cores were retrieved by gravity corers from the Dongsha area during the Haiyang-4 cruise conducted by the Guangzhou Marine Geological Survey in October 2013. The sediments consisted of homogeneous green-gray clay silt, embedded by several small authigenic carbonate nodules. The Dongsha area was visited twice by Shiyang-3 in April 2014 and by Haiyang-4 in May 2015. The sediments were sampled by piston-gravity corers and box corers. In the Xisha area, five piston cores were retrieved by Haiyang-4 in April 2015. The sediments change from brown silt clay to gray calcareous clay. Twenty-four cores in Shenhu were collected by piston corer using Haiyang-4 in May 2015 and September 2016. The lithology in the Shenhu area was similar to that in the Xisha area, consisting of brown to gray calcareous silt. Detailed information with regard to core lengths, water depths, and sampling gears were shown in Table S1. All the retrieved cores were immediately brought to the onboard laboratory for porewater extraction. Rhizon samplers were used to collect porewater at 20 cm or 40 cm intervals. Porewater aliquots were stored at 4°C with ultrapure concentrated HNO₃ and saturated HgCl₂ solution for anion and cation analyses, respectively.

3.2. Analytical Methods. Concentrations of total alkalinity (TA) and phosphate (PO₄³⁻) were measured onboard immediately after pore water collection. The TA concentrations were determined by direct titration with 0.006 M HCl using Bruevich's method [33]. The analysis was calibrated using standard seawater (IAPSO) with a precision of better than 2%. Phosphate concentrations were determined using a HITACHI U-5100 spectrophotometer with the analytical

precision of better than 5%. Concentrations of sulfate (SO₄²⁻), chloride (Cl⁻), and calcium (Ca²⁺) were determined onshore by a Dionex ICS-5000+ ion chromatography at the South China Sea Institute of Oceanology, Chinese Academy of Sciences (CAS), with the analytical precision better than 2%. Dissolved inorganic carbon (DIC) concentrations were measured by an IsoPrime 100 continuous flow isotope ratio mass spectrometer (CF-IRMS) at the State Key Laboratory of Isotope Geochemistry, Guangzhou Institute of Geochemistry, CAS, with the precision of better than 2%. Detailed analytical processes can be found in the study of Hu et al. [34].

3.3. Reaction-Transport Modeling. A one-dimensional, steady-state, reaction-transport model developed from previous approaches was applied to simulate one as a solid phase (POC) and five as dissolved species (SO₄²⁻, CH₄, DIC, Ca²⁺, and PO₄³⁻). Two partial differential equations were used to reproduce the depth concentration profiles of solid and dissolved species [35–37].

$$\phi \frac{\partial C_a}{\partial t} = \frac{\partial(\phi \cdot D_s \cdot (\partial C_a / \partial x))}{\partial x} - \frac{\partial(\phi \cdot v_p \cdot C_a)}{\partial x} + \phi \cdot \sum R + \phi \cdot R_{\text{Bui}}, \quad (1)$$

$$(1 - \phi) \frac{\partial \text{POC}}{\partial t} = - \frac{\partial((1 - \phi) \cdot v_s \cdot \text{POC})}{\partial x} + (1 - \phi) \cdot \sum R, \quad (2)$$

where t (year) is time, x (cm) is depth below the seafloor, ϕ (dimensionless) is porosity, D_s (cm²·yr⁻¹) is solute-molecular diffusion coefficient corrected by tortuosity, C_a (mol/L) is the concentrations of solutes in pore water, POC (wt.%) is the content of POC in dry sediment, v_p (cm·yr⁻¹) is the burial velocity of porewater due to steady-state compaction, v_s (cm·yr⁻¹) is burial velocity of solid, $\sum R$ is the sum of rates of all chemical reactions considered in the model, and R_{Bui} is the mixing rate of bottom water and porewater due to bubble irrigation.

Sediment porosity decreases with depth assuming steady-state compaction. v_p and v_s are variables changing with porosity under assumption of steady-state compaction. Equations can be described as follows:

$$\phi = \phi_f + (\phi_0 - \phi_f) \cdot e^{-px}, \quad (3)$$

where ϕ_f (dimensionless) is the porosity at depth and ϕ_0 (dimensionless) is the porosity at the sediment-water interface. p (cm⁻¹) denotes the attenuation coefficient of porosity.

In the absence of externally imposed fluid advection at the seafloor, the velocity of porewater and solids is directed downward under steady-state compaction relative to the seafloor:

$$\begin{aligned} v_p &= \frac{\phi_f \cdot w}{\phi}, \\ v_s &= \frac{(1 - \phi_f) \cdot w}{(1 - \phi)}, \end{aligned} \quad (4)$$

where w (cm·yr⁻¹) is the sedimentation velocity.

Calibration of diffusive coefficient with tortuosity was after the equation of Boudreau [36].

$$D_s = \frac{D_m}{1 - \ln(\phi)^2}, \quad (5)$$

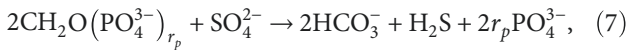
where D_m (cm²·yr⁻¹) is molecular diffusion coefficient in the in situ temperature, salinity, and pressure calculated according to Li and Gregory [38].

In sites 2015XS-R2 and 2015XS-50, gas ebullition during the ROV deployment was observed [32]. The porewater mixing with bottom water induced by rising gas bubbles can be described as a nonlocal transport similar to bioirrigation [39]:

$$R_{\text{Bui}} = \alpha_0 \cdot \frac{\exp(L_{\text{irr}} - x/\alpha_1)}{1 + \exp(L_{\text{irr}} - x/\alpha_1)} \cdot (C_0 - C_l), \quad (6)$$

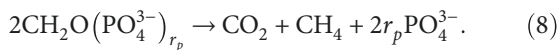
where α_0 (yr⁻¹) is the coefficient of irrigation intensity, L_{irr} (cm) is the depth of bubble irrigation, α_1 (cm) is the parameter determining how quickly bubble irrigation is attenuated to zero at an approximate depth of L_{irr} , C_0 is solute concentration at the SWI, and C_l is concentration at any depth within the irrigation zone.

As for biogeochemical reactions, organic matter decomposition via sulfate (OSR), methanogenesis (ME), anaerobic oxidation of methane (AOM), and authigenic carbonate precipitation (CP), as well as methane gas dissolution in a shallow hydrate-bearing site, are included in the model. Aerobic respiration, denitrification, manganese reduction, and iron reduction via organic matter remineralization were not taken into account in the model since these reactions were only restricted to the uppermost sediments (about 10–20 cm below the seafloor). Below the oxic and suboxic zones, sulfate serves as the main terminal electron acceptor for oxidizing organic matter [40–43]. Organic matter degradation via sulfate reduction was expressed as follows:



where r_p is the Redfield ratio of organic phosphorus to organic carbon.

Below the sulfate reduction zone, the organic matter was degraded via methanogenesis:



The rates of sulfate reduction and methanogenesis depend on the total rate of POC degradation according to Middelburg [44] and Wallmann et al. [37]:

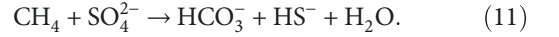
$$R_{\text{POC}} = \frac{K_c}{[\text{DIC}] + [\text{CH}_4] + K_c} \cdot \left(0.16 \cdot \left(a_0 + \frac{x}{w}\right)^{-0.95}\right) \cdot \text{POC}, \quad (9)$$

where K_c (M) is an inhibition coefficient of POC degradation, $[\text{DIC}]$ and $[\text{CH}_4]$ (mM) are concentrations of DIC and CH_4 , respectively, and a_0 (yr) is the initial age of organic matter, which was constrained using measured PO_4^{3-} concentrations. The rates of OSR and ME are thus expressed using the following equations:

$$\begin{aligned} R_{\text{OSR}} &= 0.5 \cdot \frac{\rho_s \cdot (1 - \phi) \cdot 10^6}{\text{MW}_c \cdot \phi} \cdot \frac{[\text{SO}_4^{2-}]}{[\text{SO}_4^{2-}] + K_{\text{SO}_4^{2-}}} \cdot R_{\text{POC}}, \\ R_{\text{ME}} &= 0.5 \cdot \frac{\rho_s \cdot (1 - \phi) \cdot 10^6}{\text{MW}_c \cdot \phi} \cdot \frac{K_{\text{SO}_4^{2-}}}{[\text{SO}_4^{2-}] + K_{\text{SO}_4^{2-}}} \cdot R_{\text{POC}}, \end{aligned} \quad (10)$$

where ρ_s (g·cm⁻³) is the density of dry sediments, MW_c (g·mol⁻¹) is the molecular weight of carbon, and $K_{\text{SO}_4^{2-}}$ is the Michaelis-Menten constant for the inhibition of sulfate concentration.

The AOM-coupled sulfate reduction mediated by a syntrophic consortium of methanotrophic archaea and sulfate-reducing bacteria is an important sink for methane in anoxic marine sediments [9, 45].

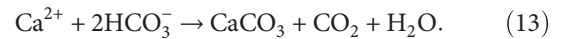


The rate of AOM was calculated using bimolecular kinetics:

$$R_{\text{AOM}} = k_{\text{AOM}} \cdot [\text{SO}_4^{2-}] \cdot [\text{CH}_4], \quad (12)$$

where k_{AOM} (cm³·mol⁻¹·yr⁻¹) is an apparent second-order rate constant.

The DIC produced by AOM and organic matter degradation can be consumed due to precipitation of authigenic carbonate [35, 46, 47]:



The rate of authigenic carbonate precipitation was simulated using the thermodynamic solubility constant as defined by Millero [48]:

$$R_{\text{CP}} = k_{\text{CP}} \cdot \left(\frac{[\text{Ca}^{2+}] \cdot [\text{CO}_3^{2-}]}{K_{\text{SP}}} - 1 \right), \quad (14)$$

where k_{CP} (mol·cm⁻³·yr⁻¹) is the kinetic constant and K_{SP} (mol²·l²) is the thermodynamic equilibrium constant. A typical porewater pH value of 7.6 was used to calculate CO_3^{2-} from modeled DIC concentration [49]. CaCO_3 is not simulated explicitly in the model.

At sites 2015XS-R2, 2015XS-50 where gas ebullition was observed, dissolution of rising gas bubble occurs if the

porewater is undersaturated with respect to in situ methane gas solubility:



where L_{MB} (mol/L) is a site-specific constant dependent on in situ salinity, pressure, and temperature using the algorithm in the work of Duan et al. [7, 50]. The rate of gas dissolution was described using a first-order kinetic expression of the departure from the local methane gas solubility concentration:

$$R_{\text{MB}} = k_{\text{MB}} \cdot (L_{\text{MB}} - [\text{CH}_4]), \quad (16)$$

where k_{MB} (yr^{-1}) is a first-order rate constant.

Gas hydrate precipitation occurred if the dissolved methane concentration exceeded the solubility of gas hydrate (L_{GH}):

$$R_{\text{GH}} = k_{\text{GH}} \cdot \left(\frac{[\text{CH}_4]}{L_{\text{GH}}} - 1 \right), \quad (17)$$

where k_{GH} ($\text{mol}\cdot\text{cm}^{-3}\cdot\text{yr}^{-1}$) is a fitting parameter constrained by the depth of the first occurrence of gas hydrate.

Upper and lower boundary conditions for all species were imposed as fixed concentrations with the exception of the intensive seepage site (2015XS-R2) whose lower boundary was imposed as a zero-concentration gradient. The continuous differential equations in equations (1) and (2) were solved using finite differences and the method-of-lines over an uneven grid with a higher spatial resolution at the surface and lower resolution towards the bottom. The model was solved using the NDSolve object of MATHEMATICA version 9.0. All simulations were run for long enough to achieve the steady state with a mass conservation of >99%. Parameter information and reaction terms of all species used in the model can be found in Table S2, Table S3, and Table S4.

3.4. Spatial Interpolation. Site-specific fluxes and rates were then used to explore area-based distribution in spatial coordinates by using the ordinary Kriging method. It is more accurate and realistic in this method to predict variables in the confined zone combining spatial distance with coordinate. According to Matheron [51], the mathematical principle of this method can be described as

$$Z'(x_0) = \sum_{i=1}^n \lambda_i Z(x_i), \quad (18)$$

where $Z(x_i)$ is a value which is situated at any place of the study area, x_0 is the predicted site, and λ_i is the weight factor, of which the sum is always equal to unity.

Spatial interpolation was implemented by ARCMAP version 10.5. Interpolation extent was derived by the point feature. The cell size of the output raster which was automatically created was 1/250 of the width and height of the extent.

4. Results

4.1. Porewater Geochemistry. We analysed 37 sediment cores, including 10 in Dongsha, 3 in Xisha, and 24 in Shenhu, and all the geochemical data are shown in Figure S1.

The sulfate concentration profiles in Dongsha generally show quasilinear depletion with depth. Especially in 2013DS-F, 2014DS-G4, and 2015DS17, sulfate concentrations show sharper decline towards the sulfate-methane transition zone (SMTZ) compared with those in other sites. Calcium concentration profiles in Dongsha display linear decline with depth. In contrast, DIC concentration profiles in Dongsha generally mirror the calcium concentration profiles.

The sulfate concentrations in Shenhu basically quasilinearly decline with depth but their gradients differ among sites. Similar to the calcium concentration profiles in Dongsha, calcium concentration profiles in Shenhu display linear decrease with depth and DIC concentration profiles show quasi-linear increase with depth.

The sulfate concentration profiles in Xisha do not follow the general trend of quasi-linear decrease. Instead, they show kink-type features with inflection points being located at 2 mbsf to 7 mbsf. The SO_4^{2-} concentrations in 2015XS-50 and 2015XS-R2 display near-seawater values in the upper 3-5 meters and then decline sharply towards the SMTZ. The seawater intrusion feature is also reflected by calcium concentration profiles, which is attributed to the irrigation of porewater caused by gas bubbling as demonstrated by previous studies [26, 52, 53]. At core 2015XS-44, the sulfate concentration profile does not show the feature of bubble irrigation but the calcium concentration profile still exhibits a kink at ~5 mbsf. The reason is not well understood at this moment, but it might be related to carbonate dissolution induced by organoclastic aerobic oxidation. At cores 2015XS-50 and 2015XS-R2, DIC concentration profiles also show the bubble irrigation feature and generally mirror the trend of sulfate concentration profiles.

4.2. Reaction-Transport Modeling. The simulation results for the three areas mostly reproduced the measured profiles. Model parameters used to constrain the model curve are listed in Table S2 and Table S3. In this model, phosphate concentration profiles were used to constrain the initial age of POC. Due to the lack of phosphate concentration profiles in the cores of Dongsha, initial ages in Dongsha (5000 yr) were adopted from Hu et al. [54]. For the same reason, the initial ages of 2015XS-44 and 2015XS-50 in Xisha were assumed to be the same as that of 2015XS-R2 derived from a measured phosphate concentration profile. Likewise, in the Shenhu area, the average initial age of TOC for the cores with phosphate data (200 ka) was taken to model those cores that lack phosphate sites. The modeled POC degradation rates are $11.2\text{--}24.5 \text{ mmol}\cdot\text{m}^{-2}\cdot\text{yr}^{-1}$ in Dongsha, $2.9\text{--}7.5 \text{ mmol}\cdot\text{m}^{-2}\cdot\text{yr}^{-1}$ in Xisha, and $7.2\text{--}30.7 \text{ mmol}\cdot\text{m}^{-2}\cdot\text{yr}^{-1}$ in Shenhu.

The depth-integrated rates and fluxes for the individual core are presented in Table S1. The rates of AOM in Dongsha range from 8.3 to $37.5 \text{ mmol}\cdot\text{m}^{-2}\cdot\text{yr}^{-1}$, which are similar to AOM rates in Shenhu (9.4 to $30.5 \text{ mmol}\cdot\text{m}^{-2}\cdot\text{yr}^{-1}$).

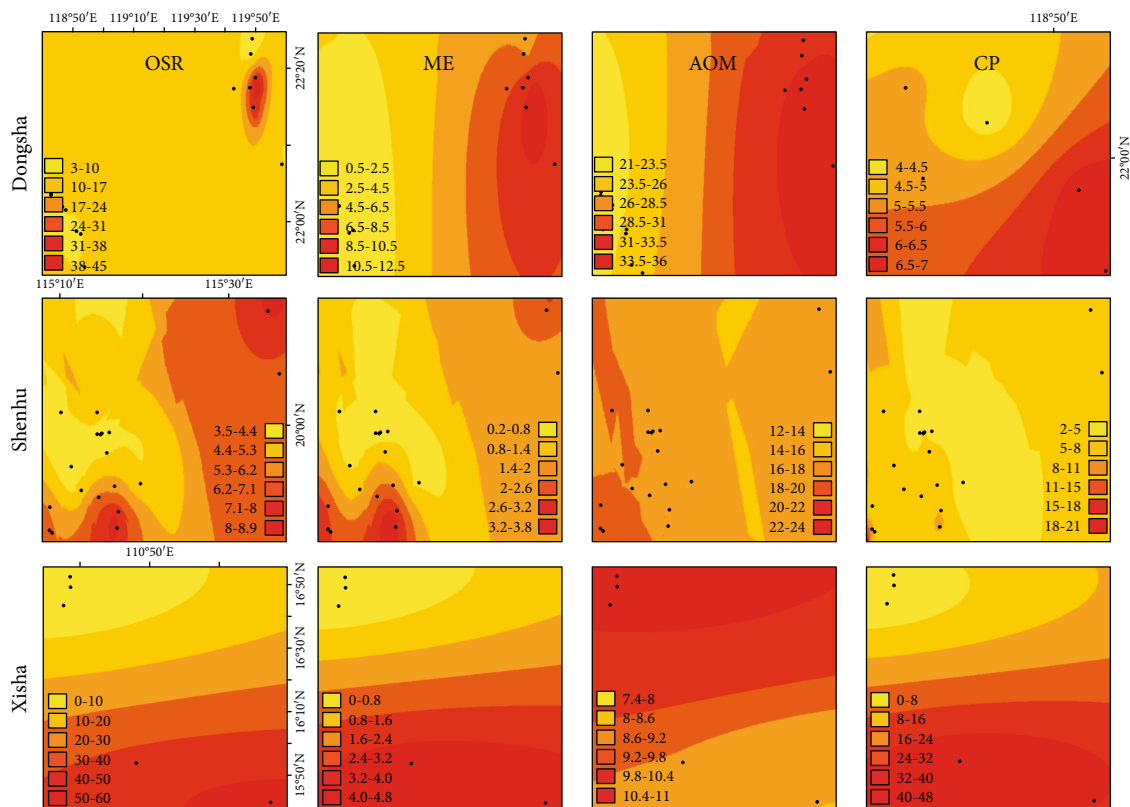


FIGURE 2: Spatial distribution of rates of organoclastic sulfate reduction (OSR), anaerobic oxidation of methane (AOM), methanogenesis (ME), and authigenic carbonate precipitation (CP) in the three areas. The black dots represent spatial distribution of sampling sites. Different colors denote different ranges of biogeochemical rates. In comparison to the interpolation rates of OSR, ME, and AOM in Dongsha, a smaller area was confined in the interpolation rate of CP. Additionally, rates of OSR, ME, AOM, and CP have the same interpolation region and so do those in Xisha.

In contrast, AOM rates in Xisha ($12.4\text{--}170.6\text{ mmol}\cdot\text{m}^{-2}\cdot\text{yr}^{-1}$) are greatly higher than those in Dongsha and Shenhu, because AOM was primarily supplied by methane gas dissolution. The methane fluxes at the top of the simulated sediment column are $0.002\text{--}0.2\text{ mmol}\cdot\text{m}^{-2}\cdot\text{yr}^{-1}$ in Dongsha, $0.002\text{--}0.3\text{ mmol}\cdot\text{m}^{-2}\cdot\text{yr}^{-1}$ in Shenhu, and $0.01\text{--}399.2\text{ mmol}\cdot\text{m}^{-2}\cdot\text{yr}^{-1}$ in Xisha. DIC fluxes in all three areas are approximately three to four orders of magnitude higher than methane fluxes with $13.1\text{--}26.1\text{ mmol}\cdot\text{m}^{-2}\cdot\text{yr}^{-1}$ in Dongsha, $10.1\text{--}31.7\text{ mmol}\cdot\text{m}^{-2}\cdot\text{yr}^{-1}$ in Shenhu, and $1\text{--}155\text{ mmol}\cdot\text{m}^{-2}\cdot\text{yr}^{-1}$ in Xisha. Rates of carbonate precipitation in Dongsha ($4.3\text{--}7.3\text{ mmol}\cdot\text{m}^{-2}\cdot\text{yr}^{-1}$), Shenhu ($3.6\text{--}9\text{ mmol}\cdot\text{m}^{-2}\cdot\text{yr}^{-1}$), and Xisha ($4.1\text{--}12.4\text{ mmol}\cdot\text{m}^{-2}\cdot\text{yr}^{-1}$) are comparable.

4.3. Spatial Interpolation. Interpolation was utilized to explore the spatial distribution of the biogeochemical rates of 395 cores, of which 37 cores are new in this study (see Table S1) and 358 cores were collected from literatures (see Table S5). As shown in Figure 2, rates of POC degradation via sulfate reduction and methanogenesis in Dongsha generally show high values in the east and gradually decrease towards the west. The rates of authigenic carbonate precipitation are mostly in agreement with those of AOM with higher values towards the east even though within a smaller region. The POC degradation rates in Xisha decrease from the south to the north. In contrast to that in the Dongsha area, the

distribution of AOM rates in the Xisha area is inconsistent with that of carbonate precipitation rates. This may be due to the lack of coordinates in some cores with high carbonate precipitation rates which are not incorporated in the north. Unlike the POC decomposition rate distribution in Dongsha and Xisha, two spots of intensified POC decomposition are located to the northeast and to the southwest in Shenhu. Rates of AOM and carbonate precipitation are generally low in the whole area.

5. Discussion

5.1. Regional Biogeochemical Rates and Fluxes of Methane and DIC. By upscaling the rates and fluxes in the specific sites into a region of interest, raster means were obtained by ARCMAP based on the small subareas divided automatically, which represent areal means. To better constrain the areal mean values of individual biogeochemical reactions in each area, we averaged arithmetical mean and raster mean values (see Table 1). Among the three areas, standard deviations of arithmetical means in the Xisha area were generally higher than 100, which indicate high heterogeneity of the biogeochemical rates. The arithmetical average of the rates of AOM in the Xisha area was much greater than those in the other two areas due to intensive methane bubbling. However, the raster mean of AOM rates in Xisha was slightly lower

TABLE 1: Biogeochemical rates and effluxes of methane and DIC in the three areas.

Location	CH4 efflux				DIC efflux				OSR				ME				AOM				CP				Cores
	RM	AM	SD	Average	RM	AM	SD	Average	RM	AM	SD	Average	RM	AM	SD	Average	RM	AM	SD	Average	RM	AM	SD	Average	
Dongsha	0.2	9.7	95	4.9	25.3	19.3	7	22.3	14.1	17.7	12	15.9	5.1	4.8	4	4.9	29.0	26.7	14	27.8	5.5	5.4	1	5.3	363
Xisha	0.1	144	366	72	36.0	246.2	136	141	27.6	14.6	20	21.1	2.6	1.5	1	2	9.4	261.1	385	135.2	27.3	37.4	28	32.3	8
Shenhu	0.0	0.1	1	0.0	17.1	19.8	5	18.4	5.8	9.8	2	7.8	1.4	2.8	1	2.1	16.8	18.2	5	17.5	5.4	6.3	1.6	5.8	24
North SCS	0.13	11.3	96	5.7	29.5	62.9	178	46.2	19.6	13.4	12	16.5	3.6	3.2	3	3.4	19.0	60.8	180	39.9	15.4	12	17	13.7	395

RM: raster mean; AM: arithmetical mean; SD: standard deviation.

TABLE 2: Areal comparison of biogeochemical rates and effluxes of methane and DIC with other cold seeps.

Location	CH ₄ efflux	DIC efflux	OSR	ME	AOM	CP	Reference
Northern SCS	5.7	46.2	16.5	3.4	39.9	13.7	This study
Hydrate Ridge	839.5	9000		51.83	6575		[60, 68, 69]
Gulf of Mexico	109.5				1718		[73]
Costa Rica	4562.5				5880		[59]
Black Sea	3017				11363		[61]
Blake Ridge			2.92	0.365	10.6		[37]
Sakhalin Island (Derugin Basin)			59.9	11.9	33.2	11	[37]
Skagerrak (Denmark)	36.5				62		[70]
Hikurangi Margin (New Zealand)	4380	5548	2.5	1.5	333		[53, 58]
Ulleung Basin			23	53.8	40	6.3	[71, 72]
Vestnesa Ridge			12.8		184.8		[74]

than those at the other two areas. The inconsistent result derived using two different methods is ascribed to the exclusion of intensive seepage sites due to unavailability of the sampling locations from the interpolation. Regardless of all the discrepancies between the two methods, a tentative comparison among the three regions indicates that the rates of AOM and carbonate precipitation in Xisha are overwhelmingly larger than those in the other two areas and that the rate of organic matter degradation in Xisha was slightly higher than those in Dongsha and Shenhu areas. The low rates of biogeochemical reactions in Shenhu are likely due to the absence of methane seepage and the occurrence of deep-seated hydrates [12]. The Dongsha area always shows the intermediate rates compared with the other two areas owing to the occurrence of sporadic methane seepage sites and gas hydrates in shallow sediments.

The Xisha area is characterized by high content of sedimentary organic matter (up to 2%) mainly sourced from marine algae [55, 56]. This may explain the relatively higher rate of organic matter degradation in Xisha compared to Dongsha and Shenhu. Applying the bimolecular kinetics to calculate the AOM rate, we assume that the adjustable rate constant (k_{AOM}) represents the integrated effects of a number of factors including the microbial community structure and abundance, bioenergetics, and enzyme kinetics. Therefore, different settings may have distinct rate constants, ranging over 6 orders of magnitude [57]. Similar to the other passive continental margin environments, the rate constant ($k_{\text{AOM}} = 1$) in this study is generally lower than those in active continental margin environments [26, 37, 58–61]. In the cold seeps and hydrate-bearing area, methane expulsion is usually associated with some specific structures, e.g., mud diapir, fault, and gas chimney. These structures provide conduits for the upward migration of methane-rich fluid. According to the geophysical imaging in Dongsha, large amounts of mud diapir and gas chimney are well developed in subsurface sediments [62]. Gas bubble release was indicated by hydroacoustic flares, and indeed, gas ebullition was observed during ROV investigation [21, 63]. In the Shenhu area, acoustic blank in shallow horizons, presumably caused by the dissociation of deep-seated hydrates, is connected with the gas

chimney [64, 65]. The derived AOM rate in Shenhu ($17.5 \text{ mmol} \cdot \text{m}^{-2} \cdot \text{yr}^{-1}$) is consistent with a pioneer work ($20.9 \text{ mmol} \cdot \text{m}^{-2} \cdot \text{yr}^{-1}$ and $11 \text{ mmol} \cdot \text{m}^{-2} \cdot \text{yr}^{-1}$) [27, 66]. In the Xisha area, gas chimneys, pockmarks, and gas bubble as well as chemosynthesis-based biota were also observed [32, 67]. These observations are consistent with the porewater profiles showing a bubble irrigation feature and shallow SMTZ in the Xisha area. The authigenic carbonate precipitation is due to the DIC production by AOM, resulting in the highest rate of carbonate precipitation in Xisha.

Synthetic biogeochemical rates and fluxes of methane and DIC in the cold seeps and hydrate-bearing area of the northern SCS are also estimated by combining raster means of the three regions and arithmetical means of all the cores. In the northern SCS, area-based biogeochemical rates and fluxes of CH₄ and DIC were far lower than estimates only based on few single points in the other regions (see Table 2). In the active continental margins, e.g., Hydrate Ridge, Costa Rica, and Hikurangi Margin, strong tectonic compression and structural fractures generally facilitate the ascension of internal methane-rich fluid across the sediment-seawater interface. Therefore, the rates of AOM and the fluxes of methane and DIC in the three areas are uniformly at least two orders of magnitude higher than those in the northern SCS [53, 58–60, 68, 69]. In the passive continental margins, e.g., Blake Ridge, Sakhalin Island, Skagerrak, and Ulleung Basin, AOM rates and fluxes of methane and DIC in the other regions worldwide are comparable with those in the northern SCS [37, 61, 70–72]. With the exception of the Gulf of Mexico and Vestnesa Ridge, the extraordinarily high AOM rates and the flux of methane can be attributed to cores retrieved near the gas chimney in the Gulf of Mexico [73] and around the pockmark in the Vestnesa Ridge [74]. As the world's largest anoxic basin and the largest surface reservoir of aqueous methane, the Black Sea was known for its extremely high AOM rate and methane flux compared with the northern SCS [61]. Additionally, recent works have revealed that the AOM rate in marine sediments worldwide is $\sim 7.9\text{--}10.7 \text{ mmol} \cdot \text{m}^{-2} \cdot \text{yr}^{-1}$ [75], which is less than the rate ($39.9 \text{ mmol} \cdot \text{m}^{-2} \cdot \text{yr}^{-1}$) in the cold seep area of the northern South China Sea.

5.2. DIC and Aqueous Methane Turnover in the Shallow Sediments. Generally, the sources of DIC in cold seeps include OSR, AOM, and methanogenesis, whereas the major DIC sinks are carbonate precipitation and diffusive loss towards the bottom water [76, 77]. The relative contributions of the 5 processes mentioned above influencing the DIC pool in Dongsha, Xisha, Shenhu, and all cold seep sites in the northern SCS were shown in Figure 3. The three areas and the northern SCS exhibit similar patterns in terms of the sources and sinks of DIC pool. As for the sources of DIC, the contributions of each reaction to DIC production decrease in the order of AOM, OSR, and ME, with AOM accounting for more than 60% of the DIC production in all the three areas. This trend in the SCS is inconsistent with that in the Ulleung basin (AOM > ME > OSR), probably as a result of the difference in the reactivity of organic matter and modelled depth [71]. As for sinks of DIC, the fluxes of DIC towards the seafloor accounted for more than 80% of DIC sinks in all the areas and the authigenic carbonate precipitation only occupied about 20% of DIC sinks. Differences between sources and sinks in the three regions and northern SCS are $6.1 \text{ mmol}\cdot\text{m}^{-2}\cdot\text{yr}^{-1}$ in Dongsha, $17 \text{ mmol}\cdot\text{m}^{-2}\cdot\text{yr}^{-1}$ in Xisha, $2.7 \text{ mmol}\cdot\text{m}^{-2}\cdot\text{yr}^{-1}$ in Shenhu, and $5.9 \text{ mmol}\cdot\text{m}^{-2}\cdot\text{yr}^{-1}$ in the northern SCS. Even though mass conservations are kept in each modeling exercise, the imbalance in DIC may be attributed to the inclusion of numerous published calculations (see Table S5).

There are four major factors, including methanogenesis, AOM, diffusive migration of methane, and phase transformation, that constrain methane cycling in shallow sediments. In Dongsha and Shenhu, AOM consumed a vast majority of methane moving up towards the seafloor. In contrast, AOM only consumed ~65% of methane and the residual was transported towards the seafloor in Xisha. As for the source of methane, bubble dissolution can widely take place if the dissolved methane concentration is lower than its phase equilibrium concentration [39]. In Xisha, bubble dissolution (99%) played a predominant role in methane supply and methanogenesis barely accounted for 1% of methane sources. However, constant diffusive supply of methane from the lower boundary provided the major source of methane in Dongsha and Shenhu. The diffusive migration of methane accounted for 47% and 82% of the methane source in Dongsha and Shenhu, respectively. Additionally, the methanogenesis played a similar role in supplying methane to the sediments (17% in Dongsha and 12% in Shenhu).

5.3. Influence of Shallow Carbon Cycling on the Carbon Reservoir of Seawater. As essential components of long-term carbon cycle, the confluence of organic carbon burial, organic matter degradation, and AOM mediates the carbon equilibrium between seawater reservoir and deep carbon and persistently affects the ocean environment [78]. Organic materials of both terrestrial and marine in origin undergo microbial decomposition during settling, and less than 1% of organic matter from the surface ocean reaches the seafloor [79]. Following the aerobic and anaerobic oxidation of organic matter in the sediments, the remaining refractory

organic matter is permanently buried. According to the model results in each site, average POC burial flux below 20 mbsf is $186 \text{ mmol}\cdot\text{m}^{-2}\cdot\text{yr}^{-1}$ in the cold seeps and hydrate-bearing area of the northern SCS, which means that 2.8 Gmol POC are buried annually (see Figure 4). As the final step of the organic matter, methanogenesis produces both methane and some other dissolved organic matters (DOM), e.g., formate and acetate [80]. The majority of methane is consumed by AOM, thereby generating DIC as the byproduct. The remaining methane and other DOM may migrate towards the sediment-water interface [81].

As we mentioned above, carbon entering the seawater from the sediments in the form of DIC and DOM can also, to some extent, influence the deep ocean carbon cycling, especially the carbonate saturation state in the water column [82, 83]. In the hydrate-bearing area of the northern SCS, DOM effluxes in the form of aqueous methane were $\sim 5 \text{ mmol}\cdot\text{m}^{-2}\cdot\text{yr}^{-1}$ (see Figure 4). By multiplying by the area of $1.6 \times 10^4 \text{ km}^2$, $9 \times 10^{-5} \text{ Tmol}$ aqueous methane is released out of the sediments annually. Irrespective of gaseous methane in the intensive gas seepage sites, such considerable amounts of DOM diffusing towards the bottom water may play an important role in the DOM cycling in the deep waters of the northern SCS. Recent studies have shown much greater DOM fluxes ($0.1 \text{ mol}\cdot\text{m}^{-2}\cdot\text{yr}^{-1}$) by accounting for other forms of DOM species such as volatile fatty acids [80, 83]. Thus, the widely distributed gas hydrates and cold seeps in the northern SCS could contribute far more than $9 \times 10^{-5} \text{ Tmol DOM/yr}$ to the ocean if gaseous methane and other organic acids are incorporated into the flux calculation. Additionally, DIC efflux ($46 \text{ mmol}\cdot\text{m}^{-2}\cdot\text{yr}^{-1}$) was several times higher than dissolved methane flux. Similarly, multiplying it by the area of cold seeps and hydrate-bearing areas gives an annual release amount of $7 \times 10^{-4} \text{ Tmol}\cdot\text{C}\cdot\text{yr}^{-1}$. Despite that this estimation is not comparable to the DIC flux on the shelf [84], it may have an impact on the bottom water chemistry in cold seeps and hydrate-bearing areas. Release of DIC into bottom water can, in some case, prompt the production and preservation of biogenic and authigenic carbonate. Nevertheless, aerobic oxidation of methane released from sediments produces CO_2 and lowers the seawater pH, thereby probably dissolving carbonate [82]. Accordingly, a total of $8.2 \times 10^{-4} \text{ Tmol}$ dissolved carbon is released into bottom water annually but its influence on bottom water carbonate systems is still unclear.

6. Conclusion

This study is aimed at quantitatively assessing the carbon turnover within the shallow sediments and quantifying the areal effluxes of methane and DIC in Xisha, Dongsha, and Shenhu, northern SCS. A 1-D reaction-transport model was used to calculate the biogeochemical rates and fluxes of methane and DIC in the 37 new collected cores. In addition, a total of 395 cores, including 358 cores reported in pioneer literatures, were used to extrapolate the areal rates and fluxes by spatial interpolation in the northern SCS. The average of the arithmetical mean and interpolation mean revealed that

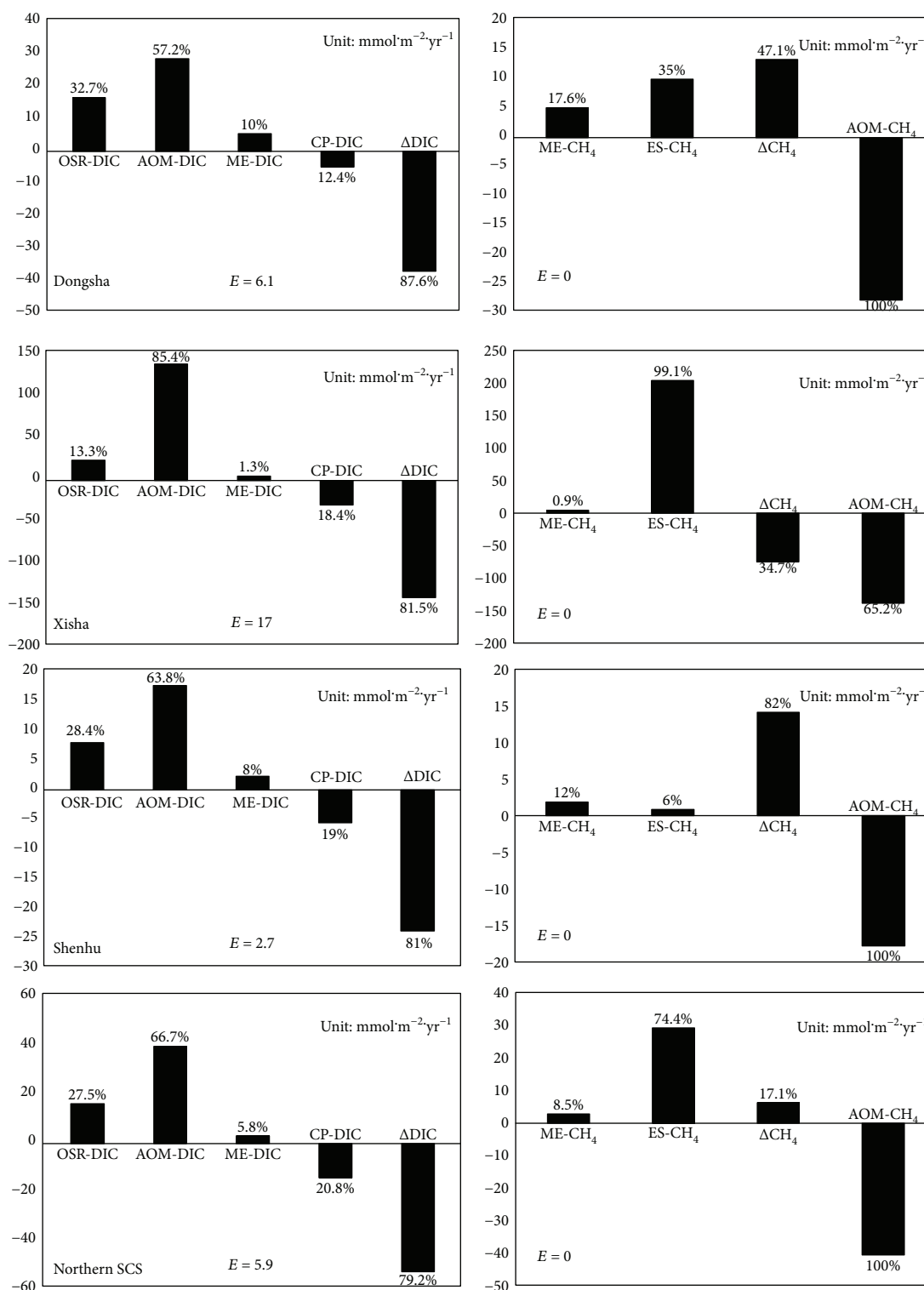


FIGURE 3: Sources and sinks of methane and DIC in the shallow sediments. Positive values denote sources of methane or DIC and negative values denote sinks of methane or DIC. OSR: organoclastic sulfate reduction; AOM: anaerobic oxidation of methane; ME: methanogenesis; CP: carbonate precipitation; ES: external methane from the bubble dissolution within modeled sediment columns. Δ represents difference between fluxes at the lower boundary and fluxes at the upper boundary. Percentages above or below each column represent the contributions of each biogeochemical reaction to the source/sink. E denotes the differences between sources and sinks of methane and DIC. Biogeochemical rates (OSR, AOM, ME, and CP) in the three regions and northern SCS are adopted from Table 1. The ES-CH₄ was obtained by assuming a complete mass conservation of methane.

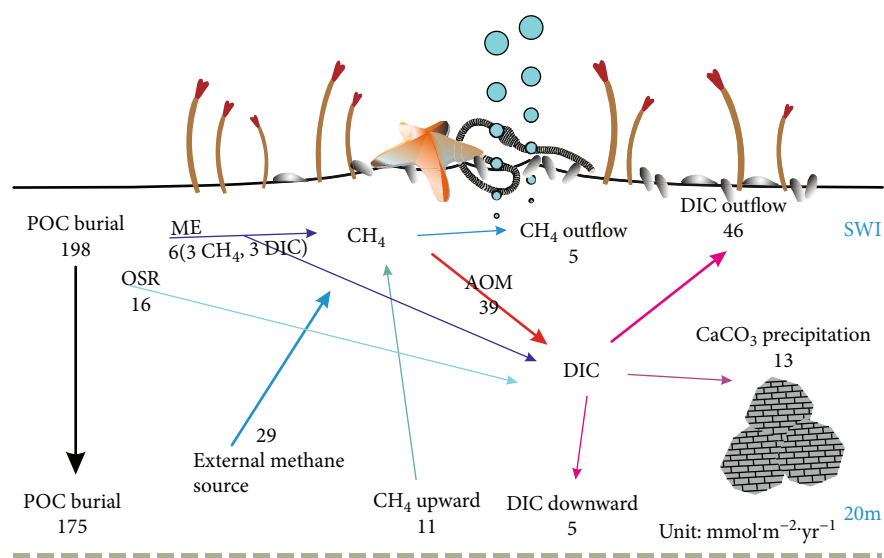


FIGURE 4: Shallow carbon cycling in the cold seeps and gas hydrate-bearing sediments in the northern South China Sea. The numbers in bold represent mean values of interpolation mean and arithmetic mean (Table 1). The numbers in italic are derived from the model. The number in grey is estimated considering methane mass conservation.

the rates of AOM and carbonate precipitation and effluxes of methane and DIC in Xisha were at least one order of magnitude higher than those in Dongsha and Shenhu and the rate of organic matter degradation in Xisha was slightly higher than those in the other two areas. This is because of the occurrence of intensive methane gas bubbling in Xisha. However, the diffusive source played the predominant role in methane supply in the other two areas. The majority of DIC mainly produced by AOM is diffused out of sediments in the three areas. In comparison to those in the active continental margin and euxinic environment, the AOM rates and fluxes of methane and DIC in the cold seeps of the northern SCS were much lower. Alternatively, source and sink analysis of methane revealed that the bubble dissolution in Xisha contributed most of the methane. According to the estimates in this study, $\sim 2.8 \text{ Gmol}$ organic matter was buried and at least $\sim 0.8 \text{ Gmol}$ dissolved carbon was released from marine sediments annually. Nonetheless, to what extent the impact of carbon release from the shallow sediments on the oceanic carbon reservoir remains to be investigated.

Data Availability

Data used in this article can be obtained upon request via the email address zhangyanping@gig.ac.cn.

Conflicts of Interest

The authors declare that there is no conflict of interest regarding the publication of this paper.

Acknowledgments

This study was supported by the National Key R&D Program of China (2018YFC0310003), National Natural Science Fund of China (Grant nos. 41730528 and 91228206),

and China Geological Survey project (DD20189310). We thank the crews of RVs Haiyang-4 and Shiyan-3 for their help with sampling at sea.

Supplementary Materials

There are 5 tables and 1 figure in the supplementary material. In Table S1, core length, water depth, sampling tools, and outputs of the reaction-transport models of the new 37 cores in this paper are listed. The fixed parameters and fitted parameters used in the reaction-transport models at the 37 sites are listed in Table S2 and Table S3. In the reaction-transport model, concentrations of every species modelled are constrained by biogeochemical reactions within the model depth in addition to physical transport processes. Each reaction term of all species is listed in Table S4. Figure S1 detailed the concentration depth profiles of the 37 cores and displayed the curve of model output. All those mentioned above are the detailed description of the reaction-transport model. Data listed in Table S5 are collected from pioneer works, which contribute to the subseafloor carbon cycling assessment of the study areas in Table 1 of the manuscript. (*Supplementary Materials*)

References

- [1] B. Buffett and D. Archer, "Global inventory of methane clathrate: sensitivity to changes in the deep ocean," *Earth and Planetary Science Letters*, vol. 227, no. 3-4, pp. 185-199, 2004.
- [2] K. A. Kvenvolden, "Gas hydrates-geological perspective and global change," *Reviews of Geophysics*, vol. 31, no. 2, pp. 173-187, 1993.
- [3] K. Wallmann, E. Pinero, E. Burwicz et al., "The global inventory of methane hydrate in marine sediments: a theoretical approach," *Energies*, vol. 5, no. 7, pp. 2449-2498, 2012.

- [4] A. V. Milkov, "Global estimates of hydrate-bound gas in marine sediments: how much is really out there?," *Earth-Science Reviews*, vol. 66, no. 3-4, pp. 183–197, 2004.
- [5] Y. Cao, D. Chen, and L. M. Cathles, "A kinetic model for the methane hydrate precipitated from venting gas at cold seep sites at Hydrate Ridge, Cascadia margin, Oregon," *Journal of Geophysical Research: Solid Earth*, vol. 118, no. 9, pp. 4669–4681, 2013.
- [6] D. F. Chen, Y. Y. Huang, X. L. Yuan, and L. M. Cathles III, "Seep carbonates and preserved methane oxidizing archaea and sulfate reducing bacteria fossils suggest recent gas venting on the seafloor in the Northeastern South China Sea," *Marine and Petroleum Geology*, vol. 22, no. 5, pp. 613–621, 2005.
- [7] Z. Duan, N. Møller, J. Greenberg, and J. H. Weare, "The prediction of methane solubility in natural waters to high ionic strength from 0 to 250°C and from 0 to 1600 bar," *Geochimica et Cosmochimica Acta*, vol. 56, no. 4, pp. 1451–1460, 1992.
- [8] E. Suess, "Marine cold seeps and their manifestations: geological control, biogeochemical criteria and environmental conditions," *International Journal of Earth Sciences*, vol. 103, no. 7, pp. 1889–1916, 2014.
- [9] A. Boetius, K. Ravensschlag, C. J. Schubert et al., "A marine microbial consortium apparently mediating anaerobic oxidation of methane," *Nature*, vol. 407, no. 6804, pp. 623–626, 2000.
- [10] K. Knittel and A. Boetius, "Anaerobic oxidation of methane: progress with an unknown process," *Annual Review of Microbiology*, vol. 63, no. 1, pp. 311–334, 2009.
- [11] D.-F. Chen, X.-X. Li, and B. Xia, "Distribution features of gas hydrate stable zones and resource prediction of the Qiongdongnan basin in the South China Sea," *Chinese Journal of Geophysics*, vol. 47, no. 3, pp. 548–555, 2004.
- [12] Y. Shengxiong, Z. Ming, L. Jinqiang et al., "Preliminary results of China's third gas hydrate drilling expedition: a critical step from discovery to development in the South China Sea," *Fire in the Ice*, vol. 15, no. 2, 2015.
- [13] G. X. Zhang, S. X. Yang, M. Zhang et al., "GMGS2 expedition investigates rich and complex gas hydrate environment in the South China Sea," *Center for Natural Gas and Oil*, vol. 412, pp. 386–7614, 2014.
- [14] H. Q. Zhang, S. Yang, N. Wu et al., "Successful and surprising results for China's first gas hydrate drilling expedition," *Fire in the Ice*, vol. 9, 2007.
- [15] H. Deng, P. Yan, H. Liu, and W. Luo, "Seismic data processing and the characterization of a gas hydrate bearing zone offshore of southwestern Taiwan," *Terrestrial, Atmospheric and Oceanic Sciences*, vol. 17, no. 4, pp. 781–797, 2006.
- [16] J. Feng, S. Yang, J. Liang et al., "Methane seepage inferred from the porewater geochemistry of shallow sediments in the Beikang Basin of the southern South China Sea," *Journal of Asian Earth Sciences*, vol. 168, pp. 77–86, 2018.
- [17] G. Hui, S. Li, L. Guo et al., "Source and accumulation of gas hydrate in the northern margin of the South China Sea," *Marine and Petroleum Geology*, vol. 69, pp. 127–145, 2016.
- [18] X. Wang, N. Li, D. Feng et al., "Using chemical compositions of sediments to constrain methane seepage dynamics: a case study from Haima cold seeps of the South China Sea," *Journal of Asian Earth Sciences*, vol. 168, pp. 137–144, 2018.
- [19] S. Wu, G. Zhang, Y. Huang, J. Liang, and H. K. Wong, "Gas hydrate occurrence on the continental slope of the northern South China Sea," *Marine and Petroleum Geology*, vol. 22, no. 3, pp. 403–412, 2005.
- [20] P. Yan, H. Deng, and H. Liu, "The geological structure and prospect of Gas Hydrate over the Dongsha Slope, South China Sea," *Terrestrial, Atmospheric and Oceanic Sciences*, vol. 17, no. 4, pp. 645–658, 2006.
- [21] D. Feng, M. Cheng, S. Kiel et al., "Using *Bathymodiolus* tissue stable carbon, nitrogen and sulfur isotopes to infer biogeochemical process at a cold seep in the South China Sea," *Deep Sea Research Part I: Oceanographic Research Papers*, vol. 104, pp. 52–59, 2015.
- [22] X. Han, E. Suess, Y. Huang et al., "Jiulong methane reef: microbial mediation of seep carbonates in the South China Sea," *Marine Geology*, vol. 249, no. 3-4, pp. 243–256, 2008.
- [23] Z. Lin, X. Sun, J. Peckmann et al., "How sulfate-driven anaerobic oxidation of methane affects the sulfur isotopic composition of pyrite: a SIMS study from the South China Sea," *Chemical Geology*, vol. 440, pp. 26–41, 2016.
- [24] M. Luo, L. Chen, S. Wang, W. Yan, H. Wang, and D. Chen, "Pockmark activity inferred from pore water geochemistry in shallow sediments of the pockmark field in southwestern Xisha Uplift, northwestern South China Sea," *Marine and Petroleum Geology*, vol. 48, pp. 247–259, 2013.
- [25] H. Tong, D. Feng, H. Cheng et al., "Authigenic carbonates from seeps on the northern continental slope of the South China Sea: new insights into fluid sources and geochronology," *Marine and Petroleum Geology*, vol. 43, pp. 260–271, 2013.
- [26] P.-C. Chuang, A. W. Dale, K. Wallmann et al., "Relating sulfate and methane dynamics to geology: accretionary prism offshore SW Taiwan," *Geochemistry, Geophysics, Geosystems*, vol. 14, no. 7, pp. 2523–2545, 2013.
- [27] Y. Hu, M. Luo, L. Chen et al., "Methane source linked to gas hydrate system at hydrate drilling areas of the South China Sea: Porewater geochemistry and numerical model constraints," *Journal of Asian Earth Sciences*, vol. 168, pp. 87–95, 2018.
- [28] B. Taylor and D. E. Hayes, "Origin and history of the South China Sea Basin," *The Tectonic and Geologic Evolution of Southeast Asian Seas and Islands: Part 2*, vol. 27, pp. 23–56, 1983.
- [29] P. Clift and J. Lin, "Preferential mantle lithospheric extension under the South China margin," *Marine and Petroleum Geology*, vol. 18, no. 8, pp. 929–945, 2001.
- [30] X. Xie, R. D. Müller, S. Li, Z. Gong, and B. Steinberger, "Origin of anomalous subsidence along the northern South China Sea margin and Its relationship to dynamic topography," *Marine and Petroleum Geology*, vol. 23, no. 7, pp. 745–765, 2006.
- [31] Z. Sha, J. Liang, G. Zhang et al., "A seepage gas hydrate system in northern South China Sea: seismic and well log interpretations," *Marine Geology*, vol. 366, pp. 69–78, 2015.
- [32] Q. Liang, Y. Hu, D. Feng et al., "Authigenic carbonates from newly discovered active cold seeps on the northwestern slope of the South China Sea: constraints on fluid sources, formation environments, and seepage dynamics," *Deep Sea Research Part I: Oceanographic Research Papers*, vol. 124, pp. 31–41, 2017.
- [33] V. N. Ivanenkov and Y. I. Lyakhin, "Determination of total alkalinity in seawater," in *Methods of Hydrochemical Investigations in the Ocean*, O. K. Bordovsky and V. N. Ivanenkov, Eds., pp. 110–114, Nauka Publ, House, 1978.
- [34] Y. Hu, D. Feng, Q. Liang, Z. Xia, L. Chen, and D. Chen, "Impact of anaerobic oxidation of methane on the geochemical cycle of redox-sensitive elements at cold-seep sites of the northern South China Sea," *Deep Sea Research Part II: Topical Studies in Oceanography*, vol. 122, pp. 84–94, 2015.

- [35] R. A. Berner, *Early Diagenesis: A Theoretical Approach*, Princeton University Press, 1980.
- [36] B. P. Boudreau, *Diagenetic Models and Their Implementation*, Springer, 1997.
- [37] K. Wallmann, G. Aloisi, M. Haeckel, A. Obzhairov, G. Pavlova, and P. Tishchenko, "Kinetics of organic matter degradation, microbial methane generation, and gas hydrate formation in anoxic marine sediments," *Geochimica et Cosmochimica Acta*, vol. 70, no. 15, pp. 3905–3927, 2006.
- [38] L. Yuan-Hui and S. Gregory, "Diffusion of ions in sea water and in deep-sea sediments," *Geochimica et Cosmochimica Acta*, vol. 38, no. 5, pp. 703–714, 1974.
- [39] M. Haeckel, B. P. Boudreau, and K. Wallmann, "Bubble-induced porewater mixing: A 3-D model for deep porewater irrigation," *Geochimica et Cosmochimica Acta*, vol. 71, no. 21, pp. 5135–5154, 2007.
- [40] G. E. Claypool, A. V. Milkov, Y.-J. Lee, M. E. Torres, W. S. Borowski, and H. Tomaru, "Microbial methane generation and gas transport in shallow sediments of an accretionary complex, southern hydrate ridge (ODP leg 204), Offshore Oregon, USA," in *Proceeding of the Ocean Drilling Program, Scientific Results*, A. M. Tréhu, G. Bohrmann, M. E. Torres, and F. S. Colwell, Eds., pp. 1–52, Ocean Drilling Program, College Station, TX, USA, 2006.
- [41] H. D. Schulz and M. Zabel, *Marine Geochemistry*, Springer, Berlin, Germany, 2006.
- [42] M. Thullner, A. W. Dale, and P. Regnier, "Global-scale quantification of mineralization pathways in marine sediments: a reaction-transport modeling approach," *Geochemistry, Geophysics, Geosystems*, vol. 10, no. 10, 2009.
- [43] J. T. Westrich and R. A. Berner, "The role of sedimentary organic matter in bacterial sulfate reduction: the G model tested," *Limnology and Oceanography*, vol. 29, no. 2, pp. 236–249, 1984.
- [44] J. Middelburg, "A simple rate model for organic matter decomposition in marine sediments," *Geochimica et Cosmochimica Acta*, vol. 53, no. 7, pp. 1577–1581, 1989.
- [45] W. S. Reece, "Oceanic methane biogeochemistry," *Chemical Reviews*, vol. 107, no. 2, pp. 486–513, 2007.
- [46] G. Bohrmann, J. Greinert, E. Suess, and M. Torres, "Authigenic carbonates from the Cascadia subduction zone and their relation to gas hydrate stability," *Geology*, vol. 26, no. 7, pp. 647–650, 1998.
- [47] L. D. Kulm, E. Suess, J. C. Moore et al., "Oregon subduction zone: venting, fauna, and carbonates," *Science*, vol. 231, no. 4738, pp. 561–566, 1986.
- [48] F. J. Millero, "Thermodynamics of the carbon dioxide system in the oceans," *Geochimica et Cosmochimica Acta*, vol. 59, no. 4, pp. 661–677, 1995.
- [49] R. E. Zeebe and D. Wolf-Gladrow, *CO₂ in Seawater: Equilibrium, Kinetics, Isotopes*, Elsevier, 2001.
- [50] Z. Duan, N. Møller, and J. H. Weare, "An equation of state for the CH₄-CO₂-H₂O system: I. Pure systems from 0 to 1000°C and 0 to 8000 bar," *Geochimica et Cosmochimica Acta*, vol. 56, no. 7, pp. 2605–2617, 1992.
- [51] G. Matheron, "Principles of geostatistics," *Economic Geology*, vol. 58, no. 8, pp. 1246–1266, 1963.
- [52] M. Haeckel, E. Suess, K. Wallmann, and D. Rickert, "Rising methane gas bubbles form massive hydrate layers at the seafloor," *Geochimica et Cosmochimica Acta*, vol. 68, no. 21, pp. 4335–4345, 2004.
- [53] M. Luo, A. W. Dale, L. Haffert et al., "A quantitative assessment of methane cycling in Hikurangi Margin sediments (New Zealand) using geophysical imaging and biogeochemical modeling," *Geochemistry, Geophysics, Geosystems*, vol. 17, no. 12, pp. 4817–4835, 2016.
- [54] Y. Hu, L. Chen, D. Feng, Q. Liang, Z. Xia, and D. Chen, "Geochemical record of methane seepage in authigenic carbonates and surrounding host sediments: A case study from the South China Sea," *Journal of Asian Earth Sciences*, vol. 138, pp. 51–61, 2017.
- [55] M. Cao, Q. Ma, Y. Wu, and J. Zhang, "Difference in organic matter distribution and degradation in surface sediment between northern South China Sea and Hainan island," *Oceanologia et Limnologia Sinica*, vol. 48, pp. 258–265, 2017.
- [56] C.-Y. Huang, S.-F. Wu, M. Zhao et al., "Surface ocean and monsoon climate variability in the South China Sea since the last glaciation," *Marine Micropaleontology*, vol. 32, no. 1–2, pp. 71–94, 1997.
- [57] P. Regnier, A. W. Dale, S. Arndt, D. E. LaRowe, J. Mogollón, and P. van Cappellen, "Quantitative analysis of anaerobic oxidation of methane (AOM) in marine sediments: a modeling perspective," *Earth-Science Reviews*, vol. 106, no. 1–2, pp. 105–130, 2011.
- [58] A. W. Dale, S. Sommer, M. Haeckel et al., "Pathways and regulation of carbon, sulfur and energy transfer in marine sediments overlying methane gas hydrates on the Opuawe Bank (New Zealand)," *Geochimica et Cosmochimica Acta*, vol. 74, no. 20, pp. 5763–5784, 2010.
- [59] P. Linke, K. Wallmann, E. Suess, C. Hensen, and G. Rehder, "In situ benthic fluxes from an intermittently active mud volcano at the Costa Rica convergent margin," *Earth and Planetary Science Letters*, vol. 235, no. 1–2, pp. 79–95, 2005.
- [60] R. Luff and K. Wallmann, "Fluid flow, methane fluxes, carbonate precipitation and biogeochemical turnover in gas hydrate-bearing sediments at Hydrate Ridge, Cascadia Margin: numerical modeling and mass balances," *Geochimica et Cosmochimica Acta*, vol. 67, no. 18, pp. 3403–3421, 2003.
- [61] K. Wallmann, M. Drews, G. Aloisi, and G. Bohrmann, "Methane discharge into the Black Sea and the global ocean via fluid flow through submarine mud volcanoes," *Earth and Planetary Science Letters*, vol. 248, no. 1–2, pp. 545–560, 2006.
- [62] J. Shang, Z. Sha, J. Liang, and L. Wu, "Seep gas acoustic features and its indication to gas hydrate exploration on the slope of the northeastern South China Sea," *Georesearch of Ecological South China Sea*, no. 1, pp. 25–36, 2013.
- [63] C. Jiang-Xin, S. Hai-Bin, G. Yong-Xian, Y. Sheng-Xiong, B. Yang, and G. Ming-Hui, "A preliminary study of submarine cold seeps by seismic oceanography techniques," *Chinese Journal of Geophysics*, vol. 60, no. 1, pp. 117–129, 2017.
- [64] S. Li, F. Chu, Y. Fang, Z. Wu, and Y. Ni, "Associated interpretation of sub-bottom and single-channel seismic profiles from slope of Shenhu Area in the northern South China Sea—characteristics of gas hydrate sediment," *Journal of Tropical Oceanography*, vol. 29, no. 4, pp. 56–62, 2010.
- [65] Y. Ni, Y. Zheng, and S. Li, "Preliminary interpretation of a typical sub-bottom profile from the upper slope of Shenhu area in the northern South China Sea," *Journal of Marine Sciences*, vol. 27, pp. 30–36, 2009.
- [66] L. S. Wu, S. X. Yang, J. Q. Liang et al., "Variations of pore water sulfate gradients in sediments as indicator for underlying gas hydrate in Shenhu Area, the South China Sea," *Science China Earth Sciences*, vol. 56, no. 4, pp. 530–540, 2013.

- [67] X. Wang, S. Wu, D. Dong, Y. Guo, and H. Deborah, "Control of mass transport deposits over the occurrence of gas hydrate in Qiongdongnan basin," *Marine Geology & Quaternary Geology*, vol. 31, no. 1, pp. 109–118, 2011.
- [68] S. Sommer, O. Pfannkuche, P. Linke et al., "Efficiency of the benthic filter: biological control of the emission of dissolved methane from sediments containing shallow gas hydrates at Hydrate Ridge," *Global Biogeochemical Cycles*, vol. 20, no. 2, 2006.
- [69] T. Treude, A. Boetius, K. Knittel, K. Wallmann, and B. Barker Jørgensen, "Anaerobic oxidation of methane above gas hydrates at Hydrate Ridge, NE Pacific Ocean," *Marine Ecology Progress Series*, vol. 264, pp. 1–14, 2003.
- [70] A. W. Dale, P. Regnier, N. J. Knab, B. B. Jørgensen, and P. Van Cappellen, "Anaerobic oxidation of methane (AOM) in marine sediments from the Skagerrak (Denmark): II. Reaction-transport modeling," *Geochimica et Cosmochimica Acta*, vol. 72, no. 12, pp. 2880–2894, 2008.
- [71] W.-L. Hong, M. E. Torres, J.-H. Kim, J. Choi, and J.-J. Bahk, "Carbon cycling within the sulfate-methane-transition-zone in marine sediments from the Ulleung Basin," *Biogeochemistry*, vol. 115, no. 1-3, pp. 129–148, 2013.
- [72] J.-H. Kim, M.-H. Park, U. Tsunogai et al., "Geochemical characterization of the organic matter, pore water constituents and shallow methane gas in the eastern part of the Ulleung Basin, East Sea (Japan Sea)," *Island Arc*, vol. 16, no. 1, pp. 93–104, 2007.
- [73] W. Ussler III and C. K. Paull, "Rates of anaerobic oxidation of methane and authigenic carbonate mineralization in methane-rich deep-sea sediments inferred from models and geochemical profiles," *Earth and Planetary Science Letters*, vol. 266, no. 3-4, pp. 271–287, 2008.
- [74] W.-L. Hong, S. Sauer, G. Panieri et al., "Removal of methane through hydrological, microbial, and geochemical processes in the shallow sediments of pockmarks along eastern Vestnesa Ridge (Svalbard)," *Limnology and Oceanography*, vol. 61, no. S1, pp. S324–S343, 2016.
- [75] M. Egger, N. Riedinger, J. M. Mogollón, and B. B. Jørgensen, "Global diffusive fluxes of methane in marine sediments," *Nature Geoscience*, vol. 11, no. 6, pp. 421–425, 2018.
- [76] S. Chatterjee, G. R. Dickens, G. Bhatnagar et al., "Pore water sulfate, alkalinity, and carbon isotope profiles in shallow sediments above marine gas hydrate systems: A numerical modeling perspective," *Journal of Geophysical Research*, vol. 116, pp. 1–25, 2011.
- [77] W. S. Borowski, T. M. Hoehler, M. J. Alperin, N. M. Rodriguez, and C. K. Paull, "Significance of anaerobic methane oxidation in methane-rich sediments overlying the Black Ridge gas hydrates," in *Proceeding of the Ocean Drilling Programs, Scientific Results*, vol. 164, pp. 87–99, 2000.
- [78] R. A. Berner, *The Phanerozoic Carbon Cycle: CO₂ and O₂*, Oxford university press, New York, NY, USA, 2004.
- [79] A. Boetius and F. Wenzhöfer, "Seafloor oxygen consumption fuelled by methane from cold seeps," *Nature Geoscience*, vol. 6, no. 9, pp. 725–734, 2013.
- [80] V. B. Heuer, J. W. Pohlman, M. E. Torres, M. Elvert, and K.-U. Hinrichs, "The stable carbon isotope biogeochemistry of acetate and other dissolved carbon species in deep seafloor sediments at the northern Cascadia Margin," *Geochimica et Cosmochimica Acta*, vol. 73, no. 11, pp. 3323–3336, 2009.
- [81] J. W. Pohlman, J. E. Bauer, W. F. Waite, C. L. Osburn, and N. R. Chapman, "Methane hydrate-bearing seeps as a source of aged dissolved organic carbon to the oceans," *Nature Geoscience*, vol. 4, no. 1, pp. 37–41, 2011.
- [82] A. J. Andersson, F. T. Mackenzie, and L. M. Ver, "Solution of shallow-water carbonates: an insignificant buffer against rising atmospheric CO₂," *Geology*, vol. 31, no. 6, pp. 513–516, 2003.
- [83] C. W. Hung, K. H. Huang, Y. Y. Shih et al., "Benthic fluxes of dissolved organic carbon from gas hydrate sediments in the northern South China Sea," *Scientific Reports*, vol. 6, no. 1, article 29597, 2016.
- [84] V. Krumins, M. Gehlen, S. Arndt, P. Van Cappellen, and P. Regnier, "Dissolved inorganic carbon and alkalinity fluxes from coastal marine sediments: model estimates for different shelf environments and sensitivity to global change," *Biogeochemistry*, vol. 10, no. 1, pp. 371–398, 2013.